



Lhadi Merhari
Editor

Hybrid Nanocomposites for Nanotechnology

Electronic, Optical, Magnetic and
Biomedical Applications

 Springer

Hybrid Nanocomposites for Nanotechnology

Lhadi Merhari
Editor

Hybrid Nanocomposites for Nanotechnology

Electronic, Optical, Magnetic
and Biomedical Applications

 Springer

Editor
Lhadi Merhari
CERAMEC
Limoges
France

ISBN: 978-0-387-72398-3 e-ISBN: 978-0-387-30428-1
DOI: 10.1007/978-0-387-30428-1

Library of Congress Control Number: 2007941080

© Springer Science+Business Media, LLC 2009

All rights reserved. This work may not be translated or copied in whole or in part without the written permission of the publisher (Springer Science+Business Media, LLC, 233 Spring Street, New York, NY 10013, USA), except for brief excerpts in connection with reviews or scholarly analysis. Use in connection with any form of information storage and retrieval, electronic adaptation, computer software, or by similar or dissimilar methodology now known or hereafter developed is forbidden.

The use in this publication of trade names, trademarks, service marks, and similar terms, even if they are not identified as such, is not to be taken as an expression of opinion as to whether or not they are subject to proprietary rights.

Printed on acid-free paper

springer.com

To the Loving Memory of my late Mother Eleonora

Preface

With the advent of nanoscience and nanotechnology, the dream of scientists to engineer new functional materials combining the best specific properties of organic and inorganic materials is closer to reality. The traditional targeted application has been the reinforcement of plastics with the addition of inorganic fillers. Accelerated research over the past two decades, as evidenced by the large bulk of literature on mechanical properties of organic–inorganic composites, focused on systems such as clay/polymer nanocomposites, which are now exploited by the automotive industry worldwide. Although, in the low filler loading range, clay/polymer nanocomposites can replace traditional fiber-reinforced composites, there is still a long way to go before understanding the mechanisms of enhancement of major engineering properties of polymers and to tailor their nanostructure.

The driving force to edit the present comprehensive book has been to show that the applications of organic–inorganic nanocomposites extend far beyond the above-mentioned traditional mechanical applications and that hybrid nanocomposites should be considered as an attractive, versatile, technological platform for future electronic, optical, magnetic, and biomedical applications. Indeed, taking up challenges such as homogeneous dispersion of inorganic nanoobjects into a polymer matrix or tailoring of the multiscale nano-to-macro structure of the composites will contribute to the establishment of a solid unified hybrid nanocomposite technological platform for commercially-viable products revolutionizing various industrial sectors.

The generally-accepted definition of a hybrid nanocomposite is a material created by dispersing inorganic nanoparticulates into a macroscopic organic matrix. Since the discovery that the markedly enhanced electrical and thermal conductivity, optical and dielectric properties, and mechanical properties such as stiffness and strength of the resulting material are essentially because of the extraordinarily large interfacial “third” phase, hybrid nanocomposites constitute a fast-growing area of the field of nanotechnology. Nanoscience is now recognized as essential to understanding and predicting the correlation between nanocomposites’ enhanced properties and high surface-to-bulk ratio of the constituting inorganic nanocomponent, and to direct the synthesis strategy for on-demand functional hybrid nanocomposites. Clearly, cost-effective strategies ensuring high-precision spatial and orientational

control of the hierarchical structure will broaden the spectrum of hybrid nanocomposite applications from commodity plastic applications to high-added-value components in active devices such as photovoltaic cells, biosensors, light emitting devices, and energy storage systems.

It is the hope of the editor that *Hybrid Nanocomposites for Nanotechnology: Electronic, Optical, Magnetic and Biomedical Applications* will become an invaluable reference book introducing the reader to this fascinating field and will stimulate the creativity of academic, industrial, and governmental researchers active in materials science, chemistry, polymer science, surface science, semiconductor physics, electrical engineering, electronics, surface microscopy, spectroscopy, microelectronics, electrochemistry, photonics, data storage, sensors, energy storage, computational engineering, biology, microbiology, bioengineering, biotechnology, pharmacy, medicine, and oncology.

As the aim of this book is to address a large audience of readers, from Ph.D. students to senior researchers in the academic world and also from engineers to business people in various industrial sectors, it has been organized by practical applications rather than by scientific disciplines. This book consists of 17 chapters written by 37 international leading experts from 12 different countries: Australia, Czech Republic, Germany, India, Ireland, Italy, Japan, Korea, the Netherlands, Portugal, Spain, and the USA. It will provide a large coverage of applications in the industrial sectors where nanocomposites can bring a specific value and decisive competitive edge.

Each chapter is self-contained with cross references. For the unity of the book, an overlap in the chapters – namely nanocomposite synthesis methods specific to the targeted application – has been purposely kept to play the role of scientific thread. For the first time, this book will offer a complete perspective on the topic of hybrid nanocomposites and should serve as a comprehensive reference with its 2,500 bibliographic citations. The chapters presenting cutting-edge research are classified into four parts:

- Part I “Synthesis and Characterization of Organic–Inorganic Nanocomposites” contains five chapters on the recent developments in synthesis, processing, and characterization of various types of nanocomposites.
- Part II “Electronic and Magnetic Applications of Hybrid Nanocomposites” contains six chapters describing specifically designed nanocomposites for applications mainly related to the electronic and energy storage sectors. Promising applications of magnetic nanocomposites are also reviewed.
- Part III “Optical Applications of Hybrid Nanocomposites” contains three chapters focusing on innovative photonic devices.
- Part IV “Biomedical Applications of Hybrid Nanocomposites” contains three chapters with an emphasis on biosensors.

The editor is grateful to the following publishers and authors for granting permissions to use their illustrations for the book: American Ceramics Society, American Chemical Society, American Institute of Physics, American Physical Society, Ceramic Society of Japan, CMC Publishing Corp., The Electrochemical

Society, Elsevier Science, IEEE, Indian Academy of Science, Institute of Physics Publishing Ltd., The International Society of Optical Engineering, Dr. Tetsuyoshi Ishii, John Wiley & Sons Inc., Kluwer Academic Publishers, Koninklijke Philips N.V., Dr. Frederik Krebs, Materials Research Society, Nature Publishing Group, Optical Society of America, Royal Society of Chemistry, Science, Springer Science, TIC Publishing Corp., Wiley-VCH Verlag.

This book is the result of the outstanding collaboration of all the distinguished authors who have dedicated their valuable time and effort to write state-of-the-art reviews. The editor is greatly indebted to all these leading experts for their commitment to excellence.

The editor wants also to express his deepest gratitude to Dr. Marie-Isabelle Baraton (University of Limoges, France), an internationally renowned expert in nanoscience and editor of leading books in the field, for her invaluable advice and critical review of the book.

Finally, special thanks are due to Ladislav Beránek, Christl Jeske, Helmut Lenhard, and Romana Leuschner for their kind support and encouragement.

Limoges, France

Lhadi Merhari

Contents

Part I Synthesis and Characterization

- 1 Epoxy-Silica/Silsesquioxane Polymer Nanocomposites..... 3**
Libor Matějka
- 2 Scale-Up Synthesis of Polymer-Grafted Nanoparticles
in Solvent-Free Dry-System and in Ionic Liquid..... 87**
Norio Tsubokawa
- 3 Inorganic–Organic Hybrid Porous Materials..... 131**
Nicola Hüsing and Sarah Hartmann
- 4 Synthesis of Mechanically Flexible Organic–Inorganic
Hybrid Nanocomposites from Polydimethylsiloxane
and Metal Alkoxides 173**
Shingo Katayama
- 5 Structural Characterization of Hybrid Organic–Inorganic
Nanocomposites: X-ray Scattering and Solid-State Nuclear
Magnetic Resonance Spectroscopy 193**
Tiziana Di Luccio and Marzia Pentimalli

Part II Electronic and Magnetic Applications

- 6 Development of Hybrid Nanocomposites
for Electronic Applications 231**
S.K. Samudrala and Sri Bandyopadhyay
- 7 Next-Generation Hybrid Nanocomposite Materials Based
on Conducting Organic Polymers: Energy Storage and
Conversion Devices 289**
Monica Lira-Cantú and Pedro Gómez-Romero

8 Hybrid Polymer-Inorganic Photovoltaic Cells	321
Waldo J.E Beek and René A.J. Janssen	
9 Fullerene Nanocomposite Resists for Nanolithography	387
Tetsuyoshi Ishii and Kiyotaka Shigehara	
10 Sol–Gel Hybrids for Electronic Applications: Hermetic Coatings for Microelectronics and Energy Storage	429
Andrei Jitianu and Lisa C. Klein	
11 Polymer–Iron Oxide Based Magnetic Nanocomposites	455
Mrinal Pal and Abhijit De	
 Part III Optical Applications	
12 Organic–Inorganic Hybrids for Light-Emitting Devices and Integrated Optics	509
L.D. Carlos, R.A. Sá Ferreira, and V. de Zea Bermudez	
13 Highly Photosensitive Sol–Gel Hybrid Nano Materials for Direct Photo-Fabrication of Micro-Optical Elements	587
Byeong-Soo Bae	
14 Photonic Structures of Luminescent Semiconductor Nanocrystals and Spherical Microcavities	653
Yury P. Rakovich, John F. Donegan, and Andrey L. Rogach	
 Part IV Biomedical Applications	
15 Biomedical Applications of Organic–Inorganic Hybrid Nanoparticles	707
María C. Gutierrez, María L. Ferrer, Pedro Tartaj, and Francisco del Monte	
16 Development of Bioactive Organic–Inorganic Hybrids Through Sol–Gel Processing	769
Toshiki Miyazaki, Masanobu Kamitakahara, and Chikara Ohtsuki	
17 Silica Sol–Gel Biocomposite Materials for Sensor Development	795
Wai Tak Yip, Yongyao Zhou, Tami A. Martyn, and James W. Gilliland	
Index	827

Part I
Synthesis and Characterization

Chapter 1

Epoxy-Silica/Silsesquioxane Polymer Nanocomposites

Libor Matějka

Abstract Organic–inorganic (O–I) polymer nanocomposites are multicomponent and multiphase systems. Research of such complex systems is focused on understanding hybrid formation and on elaborating a general approach to control their structure, in order to synthesize a material with the required properties.

The present chapter deals with the O–I nanocomposites composed of an epoxy network as the organic matrix and silica or silsesquioxane (SSQO) domains as the inorganic “filler.” The inorganic phase is introduced in the organic matrix via two approaches: (a) in situ generation within the matrix by the sol–gel processing of alkoxy silane precursors, and (b) incorporation of well-defined nanobuilding blocks such as polyhedral oligomeric silsesquioxanes (POSS). Both molecular and phase structure evolutions were followed during the O–I network build-up. Relationships between hybrid formation, its structure and morphology, and properties were determined.

Hybrids with a wide range of structures and morphologies were synthesized, depending on the type and composition of the system and on the conditions of the polymerization procedure. Their morphologies ranged from that of an epoxy matrix with well-dispersed POSS units (at the molecular level), to that of the same matrix with inorganic clusters and aggregates of various sizes, to a bicontinuous O–I phase structure. Moreover, ordered (lamellar) structures were formed under suitable conditions. The mechanical properties of the O–I hybrids are described in terms of reinforcement of the organic matrix with an inorganic phase, which is dictated by the morphology of the system and the interphase interaction. The ways of controlling the interaction between phases are shown. The interpretation of the mechanical behavior of the O–I polymers is based on the structure-properties relationship and on the theoretical evaluation using composite models.

L. Matějka

Institute of Macromolecular Chemistry, Academy of Science of the Czech Republic,
v.v.i. Heyrovský Sq. 2, 16206 Prague 6, Czech Republic
e-mail: matejka@imc.cas.cz

Abbreviations AFM: Atomic force microscopy; ASO: Alkoxysilane-encapped oligomer; ATEs: (3-Aminopropyl)triethoxysilane; BDMA: Benzyl dimethyl amine; DBTDL: Dibutyltin dilaurate; DDM: Diaminodiphenylmethane; DDS: Diaminodiphenylsulfon; DES: Dielectric spectroscopy; DGEBA: Diglycidylether of Bisphenol; DMA: Dynamic mechanical analysis; D2000: Poly(oxypropylene) diamine (Jeffamine), molecular weight $M = 2000$; EBM: Equivalent box model, theoretical model of mechanical behavior for composites with bicontinuous phase structure; EC: Epoxy-functional cluster; ET-1: DGEBA-D2000-TEOS network prepared by one-step polymerization; ET-2: DGEBA-D2000-TEOS network prepared by two-step polymerization including TEOS prehydrolysis; E1-T2: DGEBA-D2000-TEOS network prepared by sequential polymerization; GTMS: (3-Glycidioxypropyl) trimethoxysilane; IP: Isopropanol; IPN: Interpenetrating network; ITES: (3-Isocyanatopropyl)triethoxysilane; M600: Poly(oxypropylene) monoamine (Jeffamine), molecular weight $M = 600$; NBB: Nanobuilding block; O–I: Organic–inorganic; PGE: Phenyl glycidyl ether; POE: Poly(oxyethylene); POP: Poly(oxypropylene); POSS: Polyhedral oligomeric silsesquioxane; POSS_{DGEBA}: DGEBA with pendant POSS unit; POSS, En: POSS containing n epoxy groups; POSS_{oct}: POSS with isooctyl substituents; POSS_{ph}: POSS with phenyl substituents; Q8M8H8: Octakis(dimethylsilyloxy)-T8-silsesquioxane; SAXS: Small-angle X-ray scattering; SEC: Size exclusion chromatography; SEM: Scanning electron microscopy; SD_{*M*}: Silane-modified poly(oxypropylene) of the molecular weight M (bis(trialkoxysilane) – urea group); SM_{*M*}: Silane-modified poly(oxypropylene) of the molecular weight M (monoalkoxysilane – urea group); SPB2000: Silane-modified polybutadiene of the molecular weight $M = 2000$; SPCL2000: Silane-modified polycaprolactone of the molecular weight $M = 2000$; SPOE_{*M*}: Silane-modified poly(oxyethylene) of the molecular weight M (monoalkoxysilane – urethane group); SPOP_{*M*}: Silane-modified poly(oxypropylene) of the molecular weight M (bis(trialkoxysilane) – urethane group); SSQO: Silsesquioxane; TEM: Transmission electron microscopy; TEOS: Tetraethoxysilane; TGA: Thermal gravimetry analysis; TGDDM: Tetraglycidyl diaminodiphenylmethane; Ti: Structure unit with i siloxane bonds –O–Si– attached to the central atom; TMOS: Tetramethoxysilane; TSA: *p*-Toluenesulfonic acid; WAXS: Wide-angle X-ray scattering

Symbols α_c : Critical conversion, conversion at the point of gelation; D_m : Mass fractal dimension; f : Functionality of the reacting agent; G_c , G_m , G_f : Shear modulus of the composite, matrix and filler, respectively; G_e : Equilibrium shear modulus in the rubbery state; G' , G'' : Dynamic shear storage and loss modulus, respectively; I : Scattering intensity; K : Parameter characterizing strength of the interphase interaction; M_c : Molecular weight of the chain between junctions of the network; q : Scattering vector; R_G : Guinier radius; r_{AE} : Molar ratio of functional groups NH/epoxy; r_H : Molar ratio H₂O/Si; T_g : Glass transition temperature; T_i : Fraction of T_i unit; $T_{5\%}$: Temperature, at which 5% loss of mass occurs by thermal degradation; t_{gel} : Time of gelation; v : Volume fraction; ν : Crosslinking density of the network, (concentration of elastically active chains); ν_{EF} : Volume fraction of free epoxide

chains; v_{Eb} : Volume fraction of bound epoxide chains; v_{Si} : Volume fraction of the silica phase; v_{eff} : Effective volume of the filler; v_{f} : Volume fraction of the filler.

1.1 Introduction

High requirements on material properties result in the development of new types of multifunctional materials. A wide range of properties could be achieved in multicomponent polymer systems. These polymers form a complex structure and a multiphase morphology, which leads to a large variety of properties. Polymer nanomaterials have received a great deal of attention in basic and applied research in recent times.

Organic–inorganic (O–I) nanocomposite polymers, with an organic matrix filled with inorganic species of the size usually 1–100 nm, are a special category of nanomaterials [1–4]. Under convenient conditions, the O–I polymers show a synergetic effect of both phases, such as stiffness, thermal resistance, fireproof attributes in the inorganic phase, and toughness of the polymer. Generally, the O–I nanocomposites are synthesized by the top-down or bottom-up procedures. In the so-called top-down approach, the large micron-sized particles are disintegrated to form nanostructures. This method is typical of the nanocomposites prepared from layered silicates – clays.

The topic of this chapter is the preparation of the polymer nanocomposites by a bottom-up technique, i.e., by the build-up and growth of the inorganic nanostructures within a polymer matrix from a molecular level. The achievement of a fine dispersion of the nanofiller in a polymer matrix is a key problem of polymer nanocomposites. The small particle size and interparticle distances result in strong filler–filler interactions, and in a tendency to the formation of aggregates and agglomerates. Their presence could deteriorate the material properties. Therefore, the O–I polymers with in situ generated nanostructures are the prospective kinds of nanocomposites, because the initially reacting species are molecularly dispersed in a polymer. The integration of compatible organic and inorganic components at a molecular scale is achieved by the conventional sol–gel process chemistry [5, 6]. A variety of polymer systems – elastomers, thermoplastics, linear or crosslinked polymers – were filled with inorganic fillers formed in situ [7–10]. There are several methods of synthesis of the O–I polymer nanocomposites by this technique: (a) sol–gel polymerization of alkoxy silanes in the organic polymer matrix [1, 11–14], which is the most common procedure, (b) polymerization of organic monomers in silica gel pores or impregnation of the gel with an organic polymer [136], (c) simultaneous polymerization of organic and alkoxy silane monomers [137], (d) polymerization of reactants involving two types of functionalities as O–I precursors for formation of both organic and inorganic structures [15, 138].

The dimensions of an inorganic nanofiller are comparable with the size of a polymer, and therefore the nanocomposite behavior differs qualitatively from the classical microcomposites. The immense interfacial area is a typical feature of the

nanocomposites. Their exceptional properties are determined mainly by the interaction of the nanoparticles with the polymer at a molecular level, and by restriction of molecular dynamics at the interface. The interface interaction polymer-filler, immobilization of the polymer, interaction filler-filler, and nanostructure percolation in the polymer matrix play a crucial role. The improvement of mechanical properties (both stiffness and toughness) was observed when the interparticle distance was smaller than the particle diameter. In this case, the interphase can percolate through the system and dominate the properties [16]. To understand the behavior of the O-I nanocomposites, it is obvious that the perfect characterization of the nanocomposite structure at various length scales is necessary. This involves the geometry of the nanostructures, space and topological arrangement in the matrix, including the filler-filler and filler-polymer interactions.

The well-characterized nanocomposite systems are represented by the O-I polymers prepared from preformed nanoobjects, i.e., defined molecular nanobuilding blocks (NBB) [3, 17]. Various species have been used to serve as NBB, such as organically modified oligosilsesquioxanes, metal oxo-clusters, functionalized nanoparticles (metals, metal oxides), among others. Their synthesis was reviewed by Sanchez et al. [18]. The most promising NBB are functionalized metal oxo-clusters. Mainly, silicon-based NBB polyhedral oligomeric silsesquioxanes (POSS) exhibiting cage structures are of high importance.

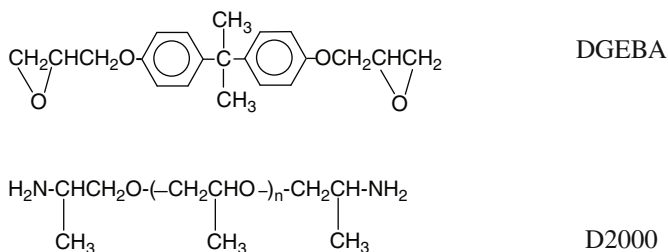
This chapter will present the O-I polymer nanocomposites based on the epoxy systems with inorganic silicon-based structures generated by the sol-gel process in situ in the polymer matrix, or incorporated in the epoxy network as the well-defined nanobuilding blocks POSS. The evolution of the molecular and phase structure during formation of the epoxy-inorganic network, as well as morphology and thermomechanical properties of the nanocomposites, will be discussed. The effect of the main factors governing the structure of the nanocomposites, including the interface interaction, will be presented. The aim of the chapter is to describe the relationships between formation of the O-I polymer nanocomposite, its structure, and the properties that make it possible to control the structure and morphology and predict the properties.

1.2 Epoxy-Silica/Silsesquioxane Networks

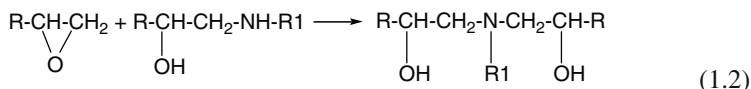
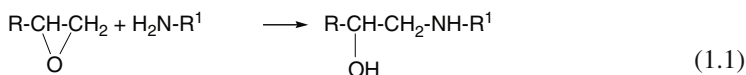
Epoxy networks, as the most widespread thermosets, are often used as a polymer matrix of the O-I nanocomposites. Mainly diglycidyl ether of Bisphenol A (DGEBA) epoxy resin or, to a lesser extent, tetraglycidyl diaminodiphenylmethane (TGDDM) cured with aromatic diamines, such as diaminodiphenylmethane (DDM), diaminodiphenyl sulfone (DDS), or 4,4'-[1,3 phenylenebis(1-methylidene)]bis(aniline) (BSA), are applied. However, epoxy matrices crosslinked with aliphatic amines, anhydrides, or dicyandiamide (among others) are also employed. Most often, high- T_g epoxy networks are used for synthesis of nanocomposites; nevertheless, the rubbery epoxy matrices have also been reinforced [19].

Silicon-based inorganic nanofillers of a variable structure are applied for the epoxide nanocomposites. The silica nanoparticles [20, 21], layered clays [22, 23], or the silica and silsesquioxane (SSQO) structures generated in situ by the sol-gel process [24–28] are the most common nanofillers. Moreover, POSS containing epoxy networks have also been investigated [29–33].

In this chapter, special attention will be paid to DGEBA – poly(oxypropylene) diamine (Jeffamine, Huntsman Int.) networks – and mainly to the rubbery network DGEBA-Jeffamine D2000. Due to low glass transition temperature, the DGEBA-D2000 network is very sensitive to mechanical reinforcement with inorganic nanodomains, in contrast to the glassy epoxide networks.



The following epoxide-amine reactions take place during the network formation:



Composition of the epoxy-amine network is characterized by the molar ratio of functional groups r_{AE} ($=\text{NH}/\text{epoxy}$). In most cases, the stoichiometric composition is employed, $r_{\text{AE}} = 1$.

Two ways of introducing the inorganic nanodomains in the network matrix will be discussed:

- (a) In situ generation of inorganic nanodomains by the sol-gel process within the organic medium will be reported in the first part of the chapter (Sect. 1.3). This procedure enables the generation of various inorganic structures, including the bicontinuous O-I phase morphology. However, the precise control of the final morphology is difficult, and the structures are polydisperse in size and heterogeneous in the chemical composition.
- (b) Incorporation of well-defined nanobuilding blocks – POSS – will be the topic of the second part (Sect. 1.4). The initial control of the particle size and volume fraction is the main advantage of this procedure. Formation of the nanocomposite morphology takes place by aggregation of the NBBs within the matrix.

The nanocomposites prepared by procedures (a) or (b) differ in the character of the inorganic nanodomains. While the sol-gel process generates chemical clusters with strong covalent structures, in the case of NBB the inorganic domains are formed by the physical aggregates of the nanosized units with weak physical intradomain interactions.

The phase or microphase separation of organic and inorganic structures is a typical feature occurring during the synthesis of the O-I networks. The interphase interaction is of primordial importance for the nanocomposite morphology. Physical interaction or even covalent bonding between O and I structures leads to an improvement of the system compatibility. In this case, homogeneous and transparent hybrid materials are produced. The common classification of O-I polymers [3] is based on the strength of the interphase interaction, and includes systems with no interactions or weak physical interactions and the polymers with strong covalent bonds between phases. Both types of epoxy-based O-I nanocomposites will be discussed – interpenetrating O-I networks without an intentional interphase bonding (Sect. 1.3.2) and the organic networks with defined grafting to the inorganic nanodomains (Sect. 1.3.3).

The organic matrix of the nanocomposites discussed in this chapter is formed by the epoxy network, with the exception of the alkoxy silane-endcapped oligomer (ASO) hybrid. This O-I network involves the urethane or urea groups, while no epoxide monomer contributes to the network build-up. However, by its characteristics (nature of the polymer network chains, SSQO nanodomains, topology of the O-I network), this hybrid closely corresponds to the discussed series of the epoxy-silica/SSQO networks, and hence it has been included in this chapter.

1.2.1 Experimental Techniques of Nanocomposite Characterization

A wide range of experimental techniques have been used to follow the process of formation of the hybrids and to characterize the structure, morphology, and properties of O-I nanocomposites.

1.2.1.1 Formation of O-I Hybrids

The process of O-I hybrids formation includes reaction kinetics, evolution of both molecular and phase structures during polymerization, gelation of polyfunctional systems, increase in crosslinking density in the postgel stage, as well as a possible vitrification.

Differential scanning calorimetry (DSC) or the spectroscopic methods like Fourier transform infrared (FTIR) and nuclear magnetic resonance (NMR) are typically used to follow the *kinetics of the polymerization* involving determination of conversion of functional groups. The *evolution of the molecular structure* during the polymerization is investigated in the pregel stage by using size exclusion chromatography (SEC) and

mass spectrometry (MALDI), while scattering techniques, chemorheology methods, or dielectric spectroscopy (DES) can be applied even in the postgel stage.

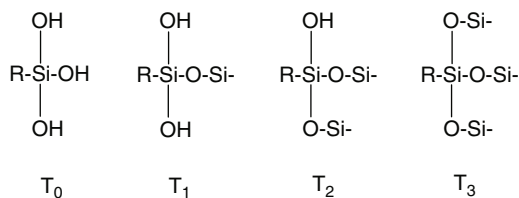
Chemorheology and dynamic mechanical analysis (DMA) are useful mainly for in situ study of network formation by polymerization of polyfunctional systems. *Gelation* is a crucial phenomenon in network build-up, and a simple way of in situ determination of the gel point is provided by chemorheology. The gel point is roughly characterized by a steep increase in the dynamic modulus $G'(t)$ during the reaction. A precise determination of the point of gelation is performed by using a power-law rheological behavior at the critical state [34]. The loss factor $\delta (=G''/G')$ measured during the crosslinking is independent of measurement frequency at the gel point.

The O–I hybrids are heterogeneous systems, and a phase or microphase separation takes place during polymerization. Small-angle X-ray scattering (SAXS) or dynamic light scattering (DLS) are the techniques used to follow *evolution of the phase structure* in formation of the O–I networks.

1.2.1.2 Characterization of O–I Hybrids

O–I hybrids are multicomponent and multiphase complex systems. Therefore, the multiscale approach of characterization is applied to fully describe the structure, morphology, and properties of the O–I hybrids.

Local structure at the atomic scale is determined by NMR and FTIR. In the case of the epoxy-silica/SSQO nanocomposites, the ^{29}Si NMR spectroscopy is a method to determine a local structure of the silica or SSQO domains. The NMR analysis provides fractions of the structural units Q_i^j , corresponding to Si atoms with j hydrolyzed groups (Si–OH) and i siloxane bridges (Si–O–Si). Distribution of these structure units characterizes the structure topology of silica. The condensation conversion is defined as $\alpha_{\text{Si}} = \Sigma iQ_i^j/4$. In the case of trialkoxysilanes, the formed SSQO structure is described by the distribution of T_i units, i.e., the structural units with i siloxane bonds –O–Si– attached to the central atom. The conversion is defined as $\alpha_{\text{Si}} = \Sigma iT_i/3$.



Macromolecular scale structure is investigated by the scattering methods – SAXS, neutron scattering (SANS), or static and dynamic light scattering. In addition to the size of the polymers or heterogeneity domains, the scattering methods also give a geometrical description of the structures using the *concept of fractal geometry*

[35], because random processes of polymerization or aggregation usually lead to the formation of fractal objects. The fractal structure is characterized by mass fractal dimension D_m , which is a measure of the compactness or the shape of the fractal object. D_m describes volume distribution of a mass, m , as $m \sim r^{D_m}$, where r is the radius of the fractal object. The relation $1 < D_m < 3$ holds for the mass fractals. The fractal dimension can be experimentally determined by the scattering methods, e.g., SAXS, from the slope x of a linear part of the scattering curve in log-log graph, $I(q) = q^{-x}$. I is the scattering intensity and $q(=4\pi/\lambda)\sin \theta$ is the magnitude of the scattering vector. The exponent x corresponds to mass fractals with fractal dimension $D_m = x$. The size of heterogeneities can be estimated by using the expression $d = 2\pi/q_{\min}$ (q_{\min} is a minimum q corresponding to the linear part of the scattering profile).

The larger length scale – *supramolecular structure* or *morphology* – is determined by electron microscopy – scanning electron microscopy (SEM), transmission electron microscopy (TEM), and atomic force microscopy (AFM). These techniques, of course, provide information on smaller length scales as well. DMA and DES are powerful indirect techniques to investigate the *phase structure*. Wide-angle X-ray scattering (WAXS) and DSC are employed to determine *crystallinity* of the material.

The *interphase (polymer-filler) interactions* in composites are examined using various techniques. Mainly, the viscoelastic properties (temperature, strain, or frequency dependence) are the perfect tool to detect the interaction between phases by DMA. Determination of the chain immobilization evidenced by a new relaxation process occurring at a higher temperature is the simplest approach. Moreover, the nonlinear behavior of composites manifests itself by a decrease in modulus at a low strain amplitude – the so-called Payne effect [36] – and is assumed to reflect the dynamics of polymer at the interface [37, 38], thus characterizing the polymer-filler interaction. In addition, other relaxation methods like DES, thermally stimulated depolarization currents (TSDC), or the NMR relaxation techniques are applied to follow the polymer chain dynamics and to investigate the interaction. In addition, swelling experiments are used to evaluate the interaction by assuming that the swelling of the matrix is completely restricted at the particle surface, in accordance with the Kraus theory [39].

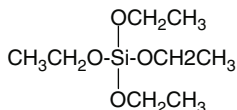
Mechanical properties are determined by DMA and stress-strain mechanical testing. Thermal properties such as glass transition temperature T_g , melting of crystalline domains, and thermal stability are determined by DSC, DMA, DES, or thermal gravimetry analysis (TGA).

1.3 Organic–Inorganic Networks with In Situ Generated Silica/SSQO Nanodomains

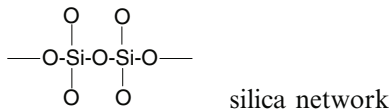
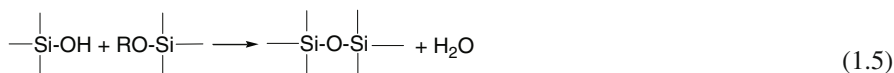
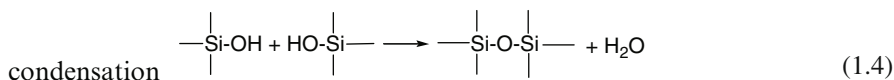
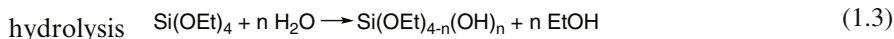
1.3.1 Sol–Gel Process

The sol–gel process includes a hydrolytic polycondensation of organometallic precursors such as silicates, titanates, and aluminates. The alkoxysilane compounds

$R_{4-n}-Si(OR')_n$ are mainly used as precursors of an inorganic phase formation. The sol-gel process (1.3–1.5) of alkoxy silanes results in the formation of linear polysiloxane (R_2SiO) $_n$ or branched and crosslinked silsesquioxane ($RSiO_{3/2}$) $_n$ from trialkoxy silanes, as well as silica (SiO_2) $_n$ structures from tetraalkoxy silanes. Tetramethoxysilane (TMOS) and tetraethoxysilane (TEOS) are the most common precursors of the in situ formed silica phase.



TEOS



The sol-gel reactions make possible a relatively easy incorporation of a pure inorganic phase into an organic matrix. A low-temperature procedure, high purity of reactants, and the possibility of mixing of precursors of organic and inorganic phases at the molecular level are the main advantages of this technique. Alcohols (ethanol, isopropanol) or THF are usually used as solvents for the sol-gel reactions. Water content is characterized by the mole ratio $r_H = H_2O/Si$. The stoichiometric water amount corresponds to the ratio $r_H = 2$ for tetraalkoxy silanes, and $r_H = 1.5$ for the trialkoxy silane monomers, taking into account both hydrolysis and condensation reactions.

The sol-gel process is acid- or base-catalyzed and the type of catalysis, water content, solvent, and temperature affect the reaction mechanism and the resulting structure of the silica phase [6, 40]. The kinetics of the process, including the simultaneous hydrolysis and condensation, were generally studied by Assink and Kay [41].

Two types of growth processes are proposed in the silicate systems: the reaction-limited cluster-cluster aggregation and the monomer-cluster aggregation [42]. The theory predicts the values of fractal dimension $D_m = 2.1$ for the reaction-limited

cluster-cluster reaction, and $D_m = 3.0$ for the monomer-cluster aggregation. Experimental SAXS results reveal [35] that mass fractals with $D_m \sim 2.1$ are formed during the sol-gel processes catalyzed with acid, which is consistent with the cluster-cluster reaction. In contrast, the monomer-cluster aggregation mechanism dominates in base catalysis, resulting in formation of more compact mass or surface fractals corresponding to colloidal particles with $D_m \leq 3.0$.

The effect of catalysis will be demonstrated by comparison of the action of the acidic, *p*-toluenesulfonic acid (TSA), basic benzyl dimethyl amine (BDMA), and pH neutral dibutyltin dilaurate (DBTDL) catalysts. Moreover, the typical epoxy hardeners, primary amines, show a catalytic effect for the sol-gel polymerization comparable to weak bases. The epoxy hardener Jeffamine D2000 has another special function in the hybrid system. In addition to being the crosslinker and catalyst, the poly(oxypropylene) chain of D2000 acts as a compatibilizer of the organic and formed silica phases.

1.3.1.1 Sol-Gel Polymerization of TEOS

The sol-gel polymerization of TEOS in isopropanol (IP) solution results in formation of silica gels. The catalysts govern the relative rates of hydrolysis and condensation, gelation of the system, and final morphology of the silica gels, including a possible phase separation. The rate of TEOS consumption, mainly due to hydrolysis, decreases in the series of catalysts with increasing basicity: TSA \gg DBTDL $>$ D2000 $>$ BDMA \gg no catalyst [43].

The acid catalysis by TSA promotes a fast hydrolysis; 50% of TEOS is reacted in 3 min at room temperature. As a result, a large fraction of the hydrolyzed products is formed. However, the condensation is slow, and only oligomer products are formed at room temperature during 24 h. Gelation of TEOS takes place at a reasonable time only on heating at a very high conversion (in 9 h at 80°C). The transparent gels are produced by using both TSA and DBTDL. The SAXS analysis reveals formation of small heterogeneities corresponding to the open mass fractals with fractal dimensions $(D_m)_{TSA} = 2.2$ and $(D_m)_{DBTDL} = 2.5$.

The reaction progress is different under nucleophilic catalysis with BDMA or D2000, and a more heterogeneous system is developed. The rate and extent of hydrolysis is lower compared to TSA catalysis, and less hydrolyzed products prevail. Half the TEOS is reacted in only 30 h at room temperature, using BDMA. In contrast, however, the condensation is effectively catalyzed, and high-molecular-weight products are formed from the very beginning of the reaction. Large compact silica structures of a high fractal dimension appear. The system phase-separates; precipitates or cloudy microgels emerge in the early stage and, in the case of BDMA, no macrogelation occurs. The morphology of the system prepared by using a higher concentration of D2000 becomes more homogeneous because of the solubilizing effect of poly(oxypropylene) chains on silica. Polymerization leads to an opalescent gel in a short time, at room temperature.

Structure evolution during TEOS polymerization includes formation of strongly cycled products – polyhedral cyclics [139, 140]. Due to the extensive cyclization, gelation is substantially delayed with respect to the theory, even under the relatively homogeneous conditions of acid catalysis. The classical theory of network formation predicts the critical conversion α_c for a gel formation in polymerization of an f -functional monomer in the ideal case [44]:

$$\alpha_c = 1/(f - 1) \quad (1.6)$$

For polymerization of a tetrafunctional monomer TEOS, the theoretical value is $\alpha_c = 0.33$, while the experimental critical conversion is $(\alpha_{s_i})_c = 0.83$ (Ng et al. 1995).

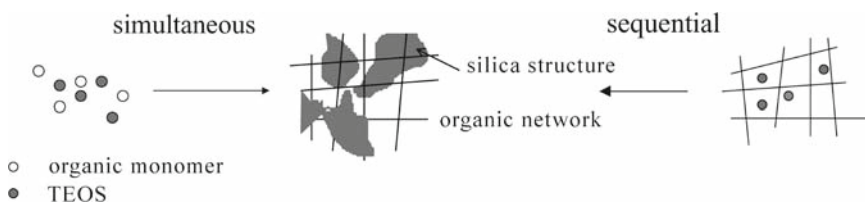
1.3.2 Interpenetrating Epoxy-Silica Networks

Various kinds of hybrid epoxy-silica networks with in situ formed silica have been synthesized and investigated [19, 24, 25, 28, 45, 141]. Usually, the silica phase was produced within the network matrix by the hydrolytic polycondensation of TEOS. However, the nonaqueous synthesis of nanosilica in an epoxy matrix has also been reported [46].

1.3.2.1 Network DGEBA-D2000-TEOS

We will describe the formation, structure, and properties of the epoxy-silica interpenetrating network (IPN) DGEBA-D2000-TEOS, consisting of the epoxide-amine network DGEBA-D2000 and the silica network in situ generated by the sol-gel process from TEOS [43, 47, 48]. Formation of the silica phase within the organic network depends on the method of preparation (see Scheme 1.1):

- The simultaneous polymerization of the organic monomers and TEOS,
- The sequential polymerization consisting in polymerization of TEOS within the preformed epoxide network.



Scheme 1.1 Synthesis procedures of the O-I networks with in situ generated silica

Synthesis Procedures of the Hybrid Networks

Simultaneous Polymerization

The network synthesis has been performed by one- or two-step procedures.

One-Step Polymerization

The reaction mixture of the monomers (DGEBA, D2000, TEOS) and water was homogenized with the cosolvent isopropanol (IP), and both formation of the DGEBA-D2000 network and sol-gel polymerization of TEOS proceeded simultaneously. Hydrolysis and condensation of TEOS was performed at a molar ratio $\text{TEOS:H}_2\text{O} = 1:3 (r_H = 3)$ in IP solutions in the volume ratio $\text{TEOS:IP} = 45:55$. The reaction was catalyzed with TSA or DBTDL and the polymer base catalyst D2000. While 2 mol% TSA/TEOS was used for catalysis, the concentration of the catalytic NH_2 groups in D2000 reaches 7–21 mol%/TEOS in different hybrid systems. Hence, an amine excess was applied in the hybrids. The synthesis temperature regime was as follows: $T = 20^\circ\text{C}$ 2 h, 90°C 2 days, 130°C 2 days. The one-step polymerized epoxy-TEOS hybrid is indicated as ET-1.

Two-Step Polymerization

TEOS was prehydrolyzed under acid catalysis at room temperature, and then mixed with the organic components DGEBA-D2000 to start the “simultaneous” formation of both organic and inorganic phases. The hybrid is indicated as ET-2.

Sequential Polymerization

The epoxide network was prepared first by reaction of DGEBA with D2000 at 130°C . The cured network was swollen in the mixture $\text{TEOS-H}_2\text{O-IP}$ at room temperature up to equilibrium. The swollen network was then heated in a closed vessel at 90°C for 5 days to polymerize TEOS under TSA or DBTDL catalysis, and to develop the silica phase within the epoxide network. Final curing was performed in vacuum at 130°C for 3 days. The content of silica in the network was controlled by composition of the swelling medium TEOS-IP. The hybrid is indicated as E1-T2.

Formation of the Epoxy-Silica Networks

Simultaneous Polymerization

During the simultaneous procedure of the hybrid IPN synthesis, the two independent reaction mechanisms are simultaneously operative, i.e., the reaction of the epoxy and amine monomers to form the DGEBA-D2000 polymer network, and the hydrolytic polycondensation of TEOS to form the silica phase. The structure evolution and final morphology of the epoxy-silica network is sensitive to the polymerization

procedure and mainly to catalytic conditions. The sol-gel process of TEOS in the DGEBA-D2000-TEOS hybrid system proceeds in the presence of both catalysts – TSA and D2000. In this case, the relative concentration of the catalysts is crucial for the sol-gel kinetics, silica structure, and morphology. Evolution of the silica structure by the sol-gel process is much faster under given experimental conditions than formation of the epoxide-amine network. While the silica system gels rapidly at room temperature, gelation of the stoichiometric epoxide network occurs only in 10 h at 80°C. Consequently, during the “simultaneous” polymerization, the silica network is formed first at room temperature, followed by a build-up of the epoxy-amine network at an increased temperature.

One-Step Polymerization

The sol-gel process in the one-step polymerization is base-catalyzed because of a molar excess of D2000 content over TSA concentration. The initially homogeneous mixture microphase-separates in the reaction, due to an early formation of high-molecular weight polysiloxane chains typical of base catalysis of TEOS polymerization. Evolution of the silica structures during polymerization is shown in Fig. 1.1a, depicting SAXS profiles of the reaction mixture at an increasing reaction time [47]. The scattered intensity of the SAXS profiles gradually increases during the reaction as the siloxane/silica structures grow. Gelation of the silica structure occurs in 81 min under given conditions at room temperature, according to independent chemorheology measurements.

The size of the forming siloxane polymers evaluated as the Guinier radius, R_G , from SAXS analysis is concentration-dependent, and is larger in the diluted solutions, $R_G \sim 15$ nm. This fact implies that in the reaction mixture an overlap of the forming polysiloxane clusters occurs from the beginning of the reaction. The Guinier analysis provides a spatial correlation length, ξ , within the overlapped polysiloxane clusters where intermolecular interferences contribute to the scattering profile. At the gel point, Guinier radius reaches the value of the spatial correlation length in the gel, $\xi \sim 10$ nm. A cluster overlap was also reported by Schaefer and Keefer [35] during the first step of the two-step acid-acid catalysis with sub-stoichiometric water content.

In the dilute system, the individual clusters are separated and their true size can be determined. SAXS intensity profiles of the reaction system after dilution, as shown in Fig. 1.1b, characterize the inner structure of the polysiloxane cluster. In contrast to the smooth scattering curves of the bulk reaction mixture, an increase in intensity at low q values as well as the break on the curve at $q \sim 0.1 \text{ \AA}^{-1}$ appear in the diluted solutions. The shape of this profile is interpreted by formation of small domains with a diameter $d \sim 3$ nm (according to the Guinier analysis) of a higher branching density within a large “heterogeneous” polysiloxane cluster ($R_G \sim 15$ nm). These domains are formed by nonrandom branching under base catalysis. The inner siloxane groups in the chain $(-\text{O}-)_2 \text{ Si } (-\text{OC}_2\text{H}_5)_{3-2n} (-\text{OH})_n$ and the branched groups $(-\text{O}-)_3 \text{ Si-OH}$ are more reactive than the terminal ones $-\text{O-Si}(-\text{OC}_2\text{H}_5)_{3-n} (-\text{OH})_n$ [6], which results in formation of more branched and compact domains

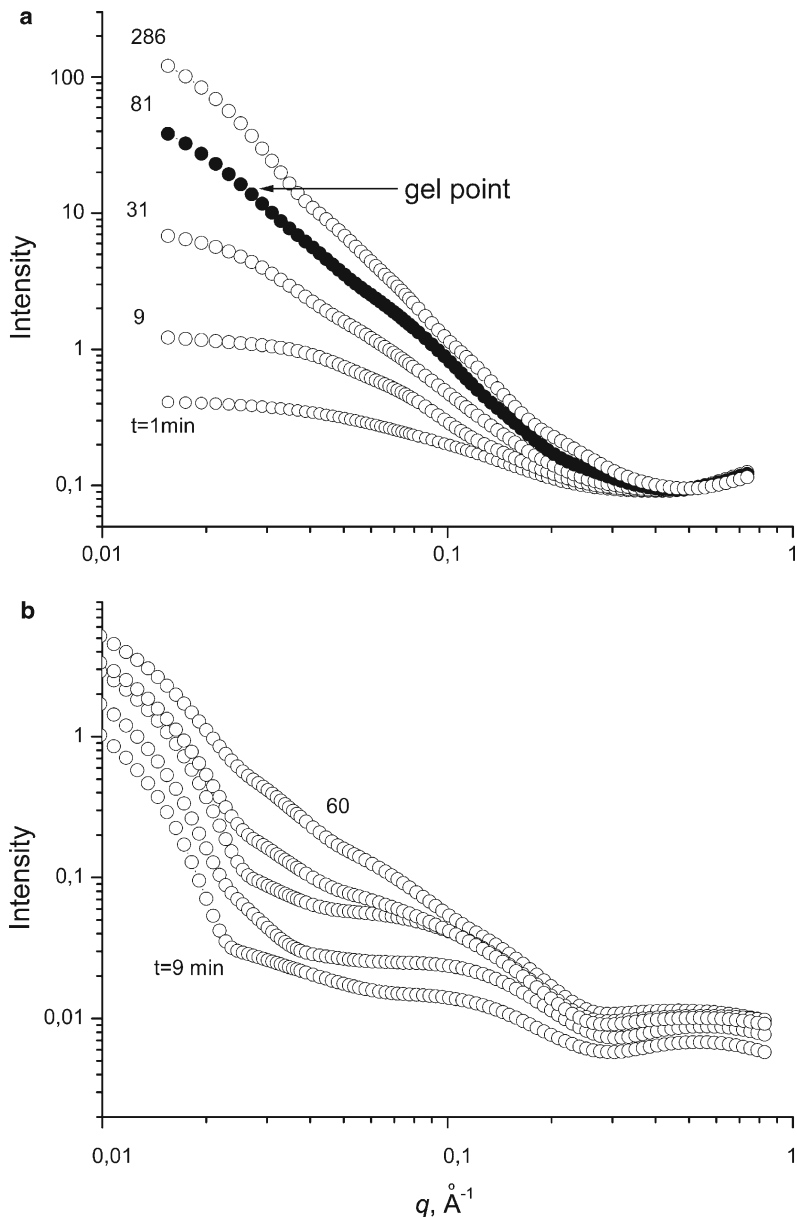


Fig. 1.1 Evolution of the SAXS profiles during the one-step polymerization of DGEBA-D2000-TEOS hybrid; the numbers indicate the reaction time. (a) reaction mixture, (b) diluted solution

within the “heterogeneous” chain. On the contrary, under acid catalysis, the terminal groups react preferably and the chain grows at the end to form linear sequences. The size of the “branched” subunits in the base-catalyzed system increases during

the polymerization and their number grows, as revealed by the shift of the break to lower q and by an increasing scattered intensity. The branched parts of the cluster become gradually interconnected, and finally fill in the whole cluster before the gel point and the break on the SAXS curve disappears. In bulk systems, the inner structure of the clusters is screened by their overlap, and hence no break on SAXS profiles corresponding to subunits is observed.

The forming structures show fractal behavior, as revealed from linearity of the intensity curves of the reaction mixture [35]. The change in the inner structure of the chain during the polymerization is shown by the gradual growth of the fractal dimension D_m of the polysiloxanes in the reaction mixture, as illustrated in Fig. 1.2. The high fractal dimension reaching the value $D_m > 2.5$ after the gel point corresponds to a relatively compact structure. The large value of the fractal dimension can be explained by the participation of the reaction-limited monomer-cluster type reaction mechanism. This is the result of the presence of the monomer in the reaction mixture even at a late reaction stage, due to slow hydrolysis under base catalytic conditions.

Two-Step Polymerization

Two-step acid-base polymerization is an optimum method for a fast formation of the inorganic structure. The procedure consists of prehydrolysis of TEOS in an acid medium in the first stage, followed by the build-up of a network in the presence of nucleophilic D2000 in the second stage. The formation of silanol groups in the acid medium serves as an initiation step for the subsequent condensation under base catalysis. Gelation of TEOS at the D2000-catalyzed reaction is significantly accelerated by the acid prehydrolysis. The dependence of gelation time t_{gel} on the time interval of the hydrolysis in the first step is shown in Fig. 1.3. Only 5 min of the

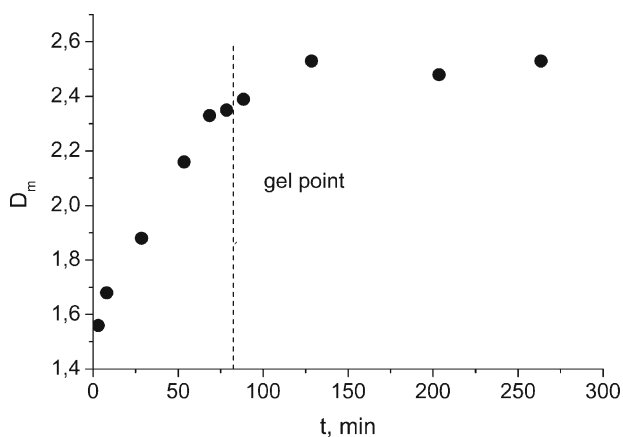


Fig. 1.2 Increase in fractal dimension D_m of the polysiloxane structures during the one-step polymerization of DGEBA-D2000-TEOS hybrid

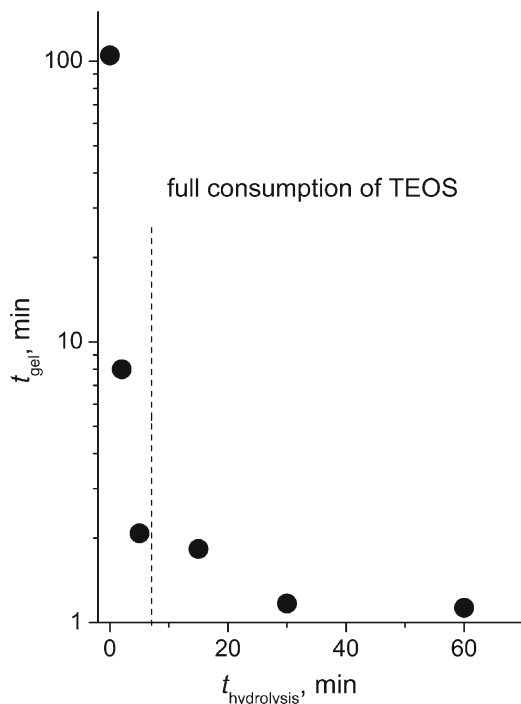


Fig. 1.3 Time of TEOS gelation catalyzed with D2000 as a function of the time interval of the acid prehydrolysis; $T = 23^\circ\text{C}$

acid prehydrolysis, corresponding to a conversion of more than 50% of TEOS, results in the dramatic acceleration of gelation in the second base-catalyzed step from ~ 100 to approximately 2 min. The prehydrolysis of TEOS also prevents precipitation of silica or microgel formation in the basic medium. The transparent gels are built-up under these conditions.

Evolution of the structure during the two-step polymerization of TEOS in the hybrid system DGEBA-D2000-TEOS significantly differs from that in the one-step process. In the first, acid-catalyzed step, a fast formation of the small particles with a size of ~ 2 nm takes place. The SAXS profiles in Fig. 1.4 illustrate the corresponding structure build-up at large scattering angles. These siloxane structures are low-molecular weight small cyclics formed by intramolecular condensation, in agreement with cage-like structures determined by Himmel et al. (1990) and Ng et al. (1995). Acid catalysis thus encourages not only fast hydrolysis but also condensation, to form small condensed structures in the early reaction stage.

The mixing of the prehydrolyzed TEOS with the system components DGEBA and D2000 results in a very fast polycondensation and gelation within 1–2 min. Figure 1.4 depicts an increase in the scattered intensity at low angles as the sizes of heterogeneities of the system grow. This second sol–gel step is catalyzed with

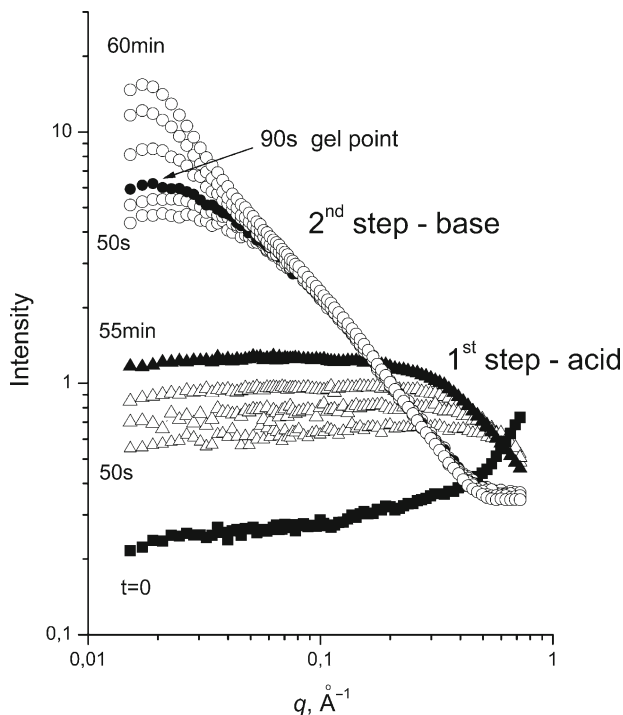


Fig. 1.4 Evolution of the SAXS profiles during the two-step polymerization of DGEBA-D2000-TEOS hybrid; the numbers indicate the reaction time of the particular reaction step. First step – acid-catalyzed, second step – base (D2000)-catalyzed

D2000, which leads to increased ionization of the unreacted SiOH groups and acceleration of the polycondensation. The primary particles formed in the acid medium immediately grow by aggregation to form large clusters and the system gels. Fast gelation results in a chemical quenching and slowing down of the diffusion, thus leading to diffusion control of the reaction. The monomer is consumed during the first fast hydrolysis acid step, and only clusters are available for the polycondensation in the second step, thus allowing only the cluster-cluster reaction. The clusters show a more open structure, compared to the one-stage process. The fractal dimension is low, $D_m = 1.7$, and does not change during polymerization (see Fig. 1.5). Such a low value of the fractal dimension is consistent with the model of diffusion-limited cluster-cluster reaction, which can be effective in fast polymerization processes [49] such as this one. The polymer chains grow; however, their inner structure remains unchanged (no change of fractal dimension). This is in contrast to gradual structure densification in the case of monomer-cluster aggregation in one-step polymerization.

The compact structures similar to those prepared in the one-stage process are formed when the neutral DBTDL catalyst was used instead of TSA in the first step.

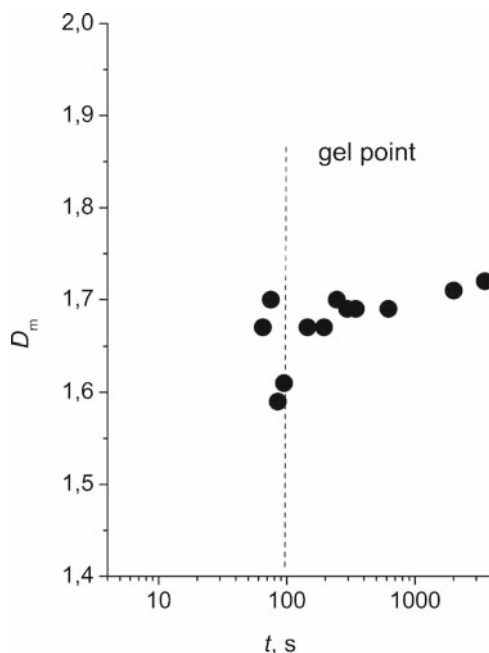


Fig. 1.5 Fractal dimension D_m of the polysiloxane structures as a function of the reaction time during the second step of the two-step polymerization of DGEBA-D2000-TEOS hybrid

The higher fractal dimension of these gels may refer to a low efficiency of DBTDL to catalyze the hydrolysis. As a result, a high content of the unreacted monomer, TEOS, is present in the second reaction stage. The participation of the reaction between monomers and large clusters (monomer-cluster growth) is likely, leading to formation of the compact structures.

Both structure evolution and final morphology of the O–I networks synthesized by the simultaneous polymerization are determined by the early reaction stages. Nucleophilic catalysis of the sol–gel process in the beginning stage brings about a gradual densification of the silica clusters during polymerization and formation of a more compact structure. Acid catalysis in the early stage prevents change of the inner chain structure and development of the fractal dimension (densification) during the reaction, despite the second step being base-catalyzed.

Sequential Polymerization

The silica structures grow within the preformed epoxide network. During swelling of the network with a TEOS–H₂O–IP mixture at room temperature, the hydrolysis of TEOS takes place while increasing the degree of swelling. The sol–gel polymerization of TEOS within the network is catalyzed with the acid or DBTDL, because the

polyamine D2000 already incorporated in the epoxide-amine network is not efficient as a base catalyst. Hence, under acid catalysis, the hydrolysis is very fast, and the structure evolution resulting in small particles corresponds to the first acid stage in the two-stage “simultaneous” process. However, the polycondensation proceeds only at an increased temperature. Nevertheless, diffusion of TEOS into the sample is slow, compared to the rate of formation of small clusters, and therefore a gradient of swelling degree and silica content throughout the sample appear.

Morphology and Structure of Epoxy-Silica Networks

In most cases, the generated silica phase percolates through the system and the epoxy-silica interpenetrating network with bicontinuous phase structure is formed. Heterogeneous microphase-separated hybrid IPNs DGEBA-D2000-TEOS are optically transparent because of the small size of the silica domains and the solubilizing effect of the poly(oxypropylene) chain of D2000. Only BDMA-catalyzed systems are opaque. Three polymerization procedures used to prepare the networks lead to different morphologies of the O–I network characterized by SEM (Fig. 1.6), and to different structures of the silica determined by SAXS (Fig. 1.7).

The morphology of the network synthesized by the one-step base-catalyzed simultaneous polymerization is the most heterogeneous one. The hybrid involves large siloxane-silica aggregates with a size of ~100–300 nm, composed of smaller particles/clusters of 20–70 nm in diameter (see SEM micrograph in Fig. 1.6a). The silica structure is very compact, as is obvious from the steep intensity curve of the SAXS profile in Fig. 1.7. The fractal dimension in the dry hybrid reaches the value of $D_m = 2.7$.

The networks prepared by the two-step acid-base polymerization show smaller silica structures. The silica domains are of size 50–100 nm in Fig. 1.6b. The very fast polymerization and gelation of the siloxane phase in this case result in quenching of microphase separation in the early reaction stage, and in formation of a fine structure. The relative rates of polymerization and microphase separation play a crucial role for the final morphology. The dried system exhibits the two-length scale structure revealed from two linear parts in a double logarithmic plot of the SAXS profile shown in Fig. 1.7. The structure corresponds to large, loose polysiloxane aggregates of low fractal dimension, $(D_m)_{\text{aggregate}} = 2.0$, composed of smaller, more compact particles, $(D_m)_{\text{particle}} = 2.7$.

The finest morphology of the O–I network is created by the sequential polymerization with the preformed epoxide network. The small inorganic domains with a size of ~10–20 nm are formed, and no larger aggregates are observed in the SEM micrographs (see Fig. 1.6c). The content of SiO_2 in the hybrids increases with the fraction of TEOS in the TEOS-IP mixture; however, the size of the siloxane structures formed within the epoxide network does not grow with the silica content. The distribution of the inorganic phase is not homogeneous throughout the sample, due to a nonhomogeneous swelling of the epoxide network. The surface skin appears with a higher SiO_2 concentration, compared to that in the inner part.

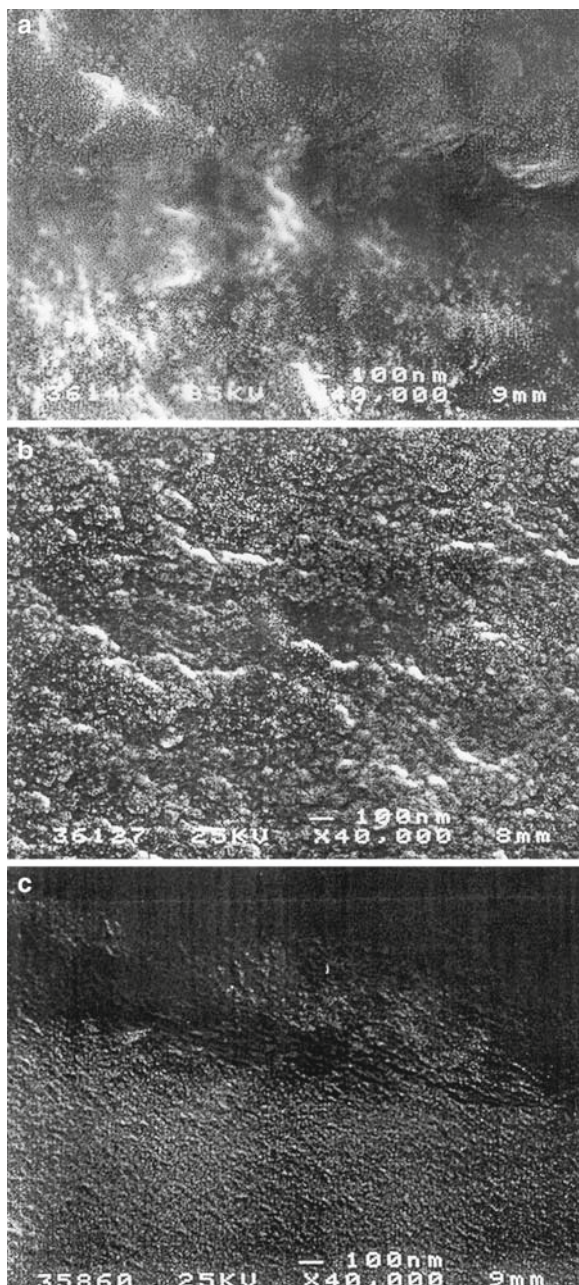


Fig. 1.6 SEM micrographs of the hybrid DGEBA-D2000-TEOS prepared by (a) one-step polymerization, (b) two-step polymerization, including acid prehydrolysis of TEOS, (c) sequential polymerization with preformed epoxide network

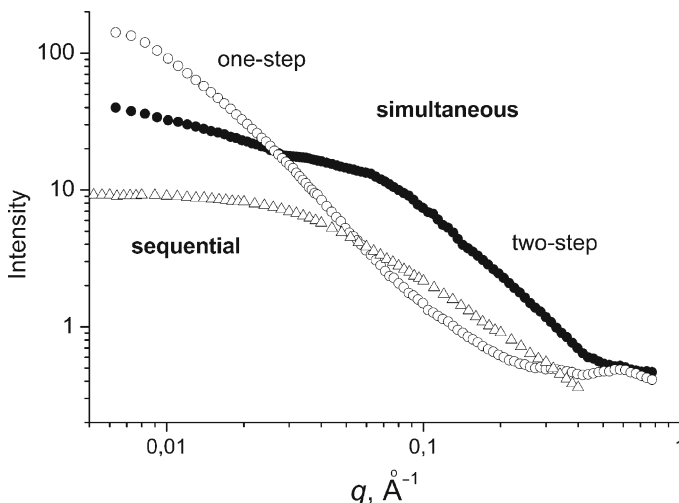


Fig. 1.7 SAXS profiles of the dry hybrids DGEBA-D2000-TEOS prepared by one-step polymerization, two-step polymerization including acid prehydrolysis of TEOS and sequential polymerization with preformed epoxide network, respectively

The sol-gel process in the sequential polymerization is acid-catalyzed throughout the synthesis procedure, which promotes formation of the most open and weakly ramified silica structures, compared to “simultaneously” prepared networks. Even the dry networks exhibit low fractal dimension, $D_m = 2.0$ (see Fig. 1.7). The compactness of the system catalyzed with TSA remains independent of silica content. The neutral catalysis with DBTDL results in a more compact structure, $D_m = 2.7$, due to the monomer-cluster reaction mechanism, as discussed above.

In addition to the catalytic conditions, the steric restrictions to the growth of the siloxane structures due to the rigid organic matrix are also important. The silica build-up proceeds within the epoxide network, preventing an aggregation of small particles and formation of large inorganic domains. The influence of the rigidity of the reaction medium on the progress of the sol-gel polymerization is obvious by comparing it with the model unrestricted TEOS system. Drying of the polymerized TEOS gel results in a significant densification and an increase in fractal dimension. In contrast, TEOS polymerized within the epoxide network DGEBA-D2000 exhibits an open gel structure in the dry hybrid similar to the non-dried model. The restrictions to an aggregation and silica structure densification by the preformed epoxide network are remarkable in the hybrid IPN. The effect of the crosslinking density and network mesh size on the size of the silica-particle aggregates was reported by Wen and Mark [50].

Generally, hybrid morphology is strongly dependent on an interaction between organic and inorganic phases. Presence of SiOH in the silica structures formed under acid catalysis leads to a chemical grafting between phases by the reaction with C–OH

of the epoxide network [19, 25, 43], and to a physical H-bond interaction with $-\text{CH}(\text{CH}_3)-\text{O}-\text{CH}_2-$ structures of the poly(oxypropylene) chain of D2000 diamine. Therefore, the networks prepared under acid catalysis show a more homogeneous morphology. This is the case with sequential polymerization and also with simultaneous polymerization with acid prehydrolysis.

Thermomechanical Properties and Interphase Interaction

In situ generated silica structures form hard glassy domains in the rubbery epoxide network, and serve as a reinforcing nanofiller. The glass transition temperature of the siloxane-silica clusters is 340°C . (T_g was determined by DSC using a model TEOS system polymerized under the same conditions as in the hybrid network up to the same conversion). Characteristics of the hybrid systems, including composition and moduli, are given in Table 1.1. The hybrids were compared with the reference classical composite DGEBA-D2000-Aerosil (EAe), prepared by physical blending of the silica Aerosil 200 with the reaction mixture of the epoxide system (DGEBA-D2000).

Generation of a relatively small number of silica structures results in a significant reinforcement of the rubbery DGEBA-D2000 network [48]. The polymer nanocomposites contain 3–13 vol% of the in situ formed SiO_2 (see Table 1.1). Shear storage modulus $G'(T)$ in the rubbery region increases with increasing content of silica, and the reinforcement is strongly dependent on the way the hybrid network is synthesized

Table 1.1 Characteristics of the hybrid DGEBA-D2000-TEOS networks

System	SiO_2 vol%	$v_{\text{Eb}}/v_{\text{E}}$	$v_{\text{EBg}}/v_{\text{Eb}}$	v_{eff}	$G_{\text{c}} \times 10^6$ (at 25°C) (Pa)
Simultaneous					
One-stage ET-1	3.8	0.14	0	0.04	2.1
	4.7	0.16	0	0.05	2.6
	9.5	0.48	0.10	0.14	6.9
Two-stage ET-2	3.7	0.42	0.10	0.08	3.6
	6.5	0.61	0.25	0.21	9.8
	13.2	0.83	0.50	0.49	160
DBTDL	8.9	0.51	0.15	0.16	10.7
Sequential E1-T2	4.2	0.75	0.25	0.22	29
	6.8	0.85	0.50	0.46	200
	6.9	0.87	0.65	0.60	274
DBTDL	4.7	0.48	0.05	0.07	7.8
DGEBA-D2000-Aerosil					
EAe	4.5	0.16	0	0.045	3.0
	6.8	0.23	0	0.07	3.7
	11.4	0.25	0	0.11	6.1

v_{E} , v_{Eb} , v_{EBg} volume fractions of the epoxide, bound epoxide phase and bound epoxide phase in the glassy state, respectively

v_{eff} effective volume fraction of the filler

(see Fig. 1.8). The efficiency of the reinforcement increases in the series $E Ae < ET-1 < ET-2 < E1-T2$. The sequential polymerization (E1-T2) with a preformed epoxide network was the most efficient procedure. The nanocomposite containing 6.9 vol% of silica shows a modulus higher by two orders of magnitude with respect to the reference DGEBA-D2000 network. Of high importance is the effect of the acid prehydrolysis of TEOS with TSA in the two-step polymerization (ET-2). The corresponding epoxy-silica network exhibits significantly higher modulus compared to that prepared by the one-step polymerization without prehydrolysis (E-T1). Nanocomposites of much lower moduli were prepared by using DBTDL as a catalyst for hydrolysis

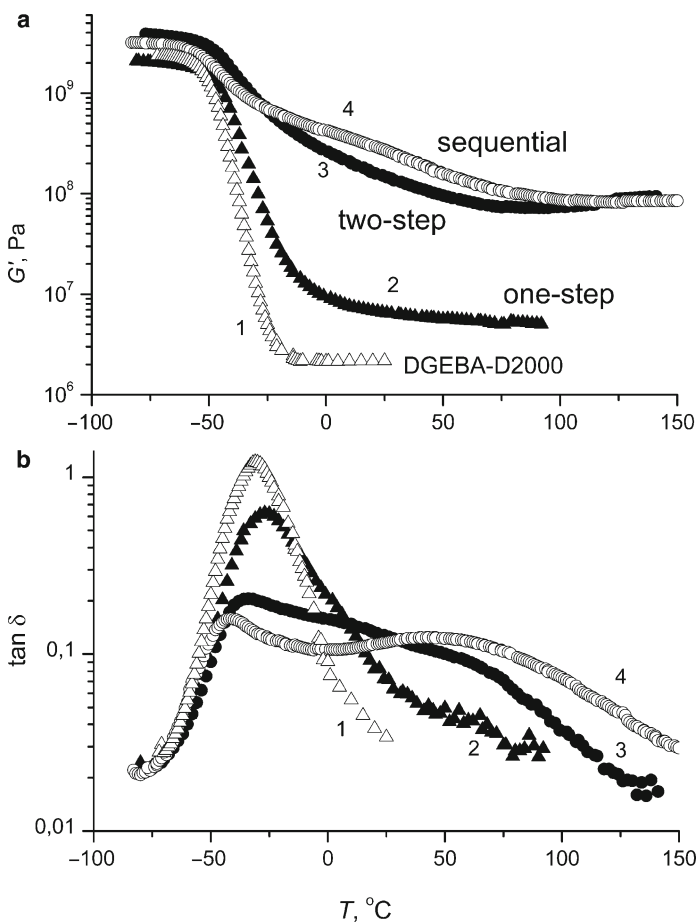


Fig. 1.8 Dynamic shear storage modulus (a) and loss factor $\tan \delta$ (b) of the network DGEBA-D2000 and the nanocomposites DGEBA-D2000-TEOS. 1 DGEBA-D2000, (2–4) DGEBA-D2000-TEOS nanocomposites prepared by (2) one-step polymerization (9.5 vol% SiO_2), (3) two-step polymerization with acid prehydrolysis of TEOS (13.2 vol% SiO_2), (4) sequential polymerization with preformed epoxide network (6.9 vol% SiO_2)

instead of TSA, both in the two-step simultaneous and sequential polymerization synthesis (see Table 1.1). However, all the epoxy-silica networks with the generated silica filler show higher moduli than the classical composite with Aerosil (EAe), taking into account a comparable content of the filler.

The hybrid networks exhibit a decrease and broadening of the peak of the loss factor $\tan \delta$ ($=G''/G'$) located at a temperature of approximately -30°C , which corresponds to the relaxation of the network chains and characterizes glass transition of the neat DGEBA-D2000 network. This effect is typical of most composite systems [51]. The nanocomposites display a new relaxation peak at a higher temperature, which provides evidence of the phase separation in the epoxy-silica hybrids. The new relaxation corresponds to the network chains immobilized by interaction with glassy silica domains. The interaction is very strong, due to the grafting between silica and epoxy network and possible hydrogen bonding. Formation of the immobilized interphase layer of the epoxide-amine network that is in contact with the silica phase leads to a decrease in the volume fraction of the “free” non-hindered chains of the epoxide network. As a result, the loss factor peak at $T = -30^\circ\text{C}$ diminishes. Broadening of the peak evidences the wide spectrum of relaxation times typical of composite materials. The area under the new relaxation peak corresponds to the fraction of the confined chains, and the position of this peak on the temperature scale is determined by the strength of the interphase interaction. On the contrary, in the ordinary composite DGEBA-D2000-Aerosil, the immobilized layer is absent due to a weak interaction between epoxide and silica phases. This is the main reason for the small reinforcing effect of the Aerosil filler (see Table 1.1).

The interphase interaction, which largely governs the mechanical properties of nanocomposites, can be quantitatively characterized by the fraction of the immobilized organic matrix. The hybrid nanocomposites are composed of three phases: the flexible epoxide-amine network (matrix), the immobilized (bound) chains of the epoxy network, and the inorganic phase with the corresponding volume fractions, v_{Ef} , v_{Eb} , v_{Si} , respectively. The amount of the bound epoxide phase, v_{Eb} , is determined from DMA results:

$$v_{\text{Eb}} = 1 - v_{\text{Si}} - v_{\text{Ef}} \quad (1.7)$$

The reduction of the fraction of free chains v_{Ef} in the composite can be roughly evaluated from the decrease in the loss factor peak $\tan \delta$ at -30°C . It has been empirically found [52] that the loss factor of a composite ($\tan \delta_c$) is approximately given as the sum of the constituting phases. For our nanocomposites, we obtain:

$$\tan \delta_c(T) = \tan \delta_{\text{Ef}}(T) v_{\text{Ef}} + \tan \delta_{\text{Eb}}(T) v_{\text{Eb}} + \tan \delta_{\text{Si}}(T) v_{\text{Si}} \quad (1.8)$$

This relationship is not generally valid, and could not be used for characterization of the composites with the different matrices of different rubbery moduli G' . However, it is useful for composites based on the same matrix of a given storage

modulus G' in the rubbery state. It can be assumed that the loss factor at -30°C is mainly given by the free chains, while the contribution of bound chains is much smaller and could be neglected, as also could the contribution of the silica phase. Then,

$$v_{\text{Ef}} = \tan \delta_c(-30^\circ\text{C}) / \tan \delta_{\text{Ef}}(-30^\circ\text{C}) \quad (1.9)$$

(The loss factor of the neat epoxide network was taken as the value of $\tan \delta_{\text{Ef}}$ ($T = -30^\circ\text{C}$)).

Table 1.1 shows the extent of the immobilization of network chains in various hybrids as a ratio $v_{\text{Eb}}/v_{\text{E}}$. The interphase interaction and volume fraction of the interphase v_{Eb} are controlled by the reaction mechanism and procedure of the O-I network formation, as discussed above. High content of silanols formed under acid catalysis favors grafting and a strong interphase interaction in the case of the acid-catalyzed two-step simultaneous networks (ET-2) and sequential nanocomposites (E1-T2). Moreover, very fine morphology – i.e., a large surface of the silica phase given by the small size and open structure of the domains in the case of the sequential and two-step simultaneous networks – favors the interaction with the epoxide network. On the contrary, grafting is weaker in the networks prepared in the one-step polymerization under catalysis with D2000 (ET-1) or with DBTDL catalysts, due to a low amount of silanols. The pyrolyzed Aerosil also contains a very low concentration of Si-OH, which accounts for weak adhesion between phases in the classical composite EAe.

Composite Models of Mechanical Properties

The O-I hybrids are usually described by Wilkes' morphological model [53], as corresponding to a composite with silica domains dispersed in an organic matrix. However, often morphology consisting of the co-continuous organic and inorganic phases is also assumed [19, 28, 54, 55]. In order to better understand the morphology of the epoxy-silica hybrid systems, we compared our experimental results on the moduli of studied nanocomposites with the prediction of existing models, assuming either particulate or bicontinuous phase morphology.

Particulate Composite Model

The elastic modulus of a two-phase system depends on the moduli and volume fractions of components, as well as on morphology. The Kerner model modified by Nielsen [51] (1.10) is frequently used to predict the mechanical behavior of the particulate composites:

$$G_c/G_M = (1 + ABv_f) / (1 - B\Psi v_f) \quad (1.10)$$

$$A = (7 - 5v_M) / (8 - 10v_M), B = ((G_f/G_M) - 1) / ((G_f/G_M) - A), \Psi = 1 + v_f(1 - v_{\text{max}}) / v_{\text{max}}^2$$

where G_c , G_M , G_f are moduli of the composite, matrix, and filler, respectively, ν_M is the Poisson ratio of the matrix, ν_f is the volume fraction of the filler, and ν_{\max} is the maximum packing fraction of the filler.

The analysis shows that the increase in modulus of rubbery DGEBA-D2000 network with in situ generated silica structures is too high to be explained by the model of the particulate composite. The theoretical prediction of the modulus for the composite of a rubbery matrix filled with hard particles, using the Kerner-Nielsen model, anticipates much lower values, as shown in Fig. 1.9a (curve 1). Only classical composite EAe approaches the theoretical values.

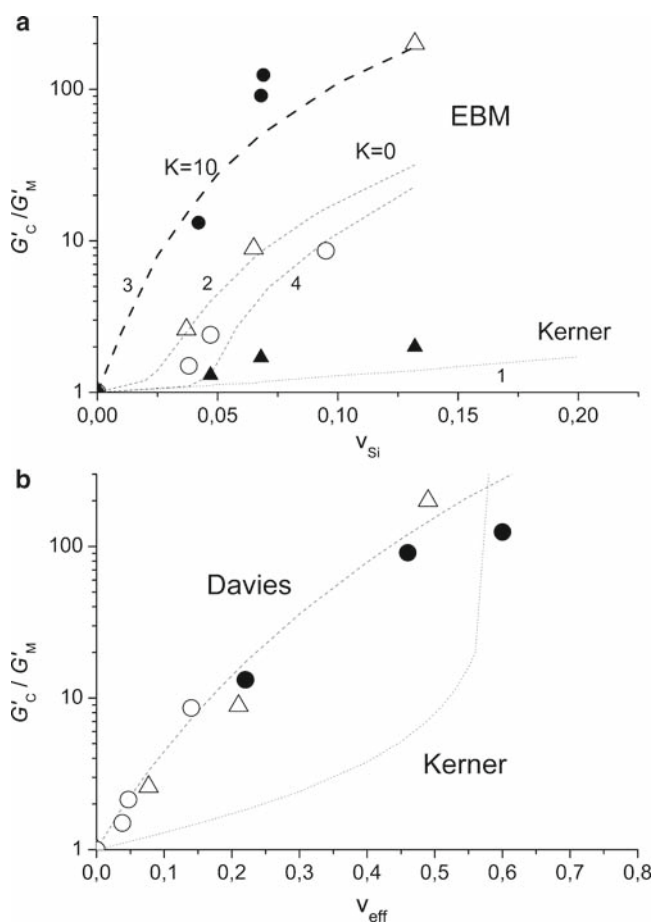


Fig. 1.9 Relative modulus of the composite as a function of the (a) volume fraction of the silica phase v_{Si} , (b) effective volume fraction of the filler v_{eff} : open circle ET-1, open triangle ET-2, filled circle E1-T2, filled triangle EAe; curves – theoretical models. (a) 1 Kerner-Nielsen model, 2–4 EBM model; 2 no interphase interaction $K = 0$, 3 strong interphase interaction $K = 10$, 4 $K = 0$, critical volume fraction $\nu_{Si,cr} = 0.02$. (b) Kerner-Nielsen and Davies models

The effect of morphology and interphase interaction must be considered. Due to the interphase interaction and the immobilized epoxide layer adhering to the silica domains, the effective volume of the filler, v_{eff} is higher than v_{Si} . However, only the bound epoxide regions, which are in glassy state at room temperature, could be efficient as a hard filler and contribute to the increase in modulus: $v_{\text{eff}} = v_{\text{Si}} + v_{\text{Ebg}}$, where v_{Ebg} is the fraction of the bound epoxide in the glassy state. In hybrid networks with strong interaction, the major part of the bound epoxide layer is in glassy state at room temperature, i.e., the $\tan \delta$ peak appears at temperatures above room temperature, as shown in Fig. 1.8b. However, in the case of weak interaction in the hybrid ET-1, the epoxy network part immobilized by silica is almost completely in the rubbery state at room temperature. Glassy fraction v_{Ebg} is negligible, and epoxide does not contribute to the filler effect (see Table 1.1). The fraction v_{Ebg} was determined from the areas under the loss factor curve above room temperature. However, even consideration of increased effective fractions of the filler in a particulate composite cannot account for the high values of the experimental moduli. The relative modulus of the composite, G_C/G_M , calculated using the effective volume fraction of the hard phase, is shown in Fig. 1.9b.

Bicontinuous Phase Morphology Model

High experimental moduli of the heterogeneous epoxy-silica nanocomposites can be explained by assuming that the hybrids consist of two co-continuous phases: the phase of the epoxy and silica interpenetrating networks and the phase of dispersed particles of the silica sol. The bicontinuous morphology of O-I hybrids was reported in the literature, based on the results of electron microscopy [55], light scattering [56], SAXS analysis [54], as well as mechanical tensile studies [57].

The effect of phase continuity on dynamic mechanical properties can be determined by using the equivalent box model (EBM) [58], assuming that each component is coupled partially in parallel (subscript p) (fraction continuous in the direction of acting force) and partially in series (subscript s) (discontinuous fraction). The following equation can be used for modulus of a binary system [59]:

$$G_C = (v_1)_p G_1 + (v_2)_p G_2 + v_s^2 / [(v_1)_s / G_1 + (v_2)_s / G_2] \quad (1.11)$$

The epoxy-silica hybrid network consists of three phases: rubbery epoxide phase (v_{ER}), glassy epoxide phase (v_{Ebg}), which is the fraction of the bound epoxide layer showing T_g above room temperature, and a silica phase (v_{Si}). In the composite with discontinuous phases, the resulting modulus is mainly determined by the modulus of the softest component. As $G_{\text{ER}} (=2.2 \cdot 10^6 \text{ Pa}) \ll G_{\text{Ebg}} (=2 \cdot 10^9 \text{ Pa}) < G_{\text{Si}} (=4 \cdot 10^9 \text{ Pa})$, the series branch of the EBM model can be neglected in comparison with the parallel branch, and a simplified expression can be used:

$$G_C \cong (v_{\text{Si}})_p G_{\text{Si}} + (v_{\text{Ebg}})_p G_{\text{Eg}} \quad (1.12a)$$

where G_{Ebg} is the modulus of the immobilized epoxide layer in glassy state, approximated by the glassy modulus of the epoxide.

The thickness of the glassy interphase layer or volume fraction v_{Ebg} in certain type of composites is proportional to the strength of the interphase interaction, which can be characterized by parameter $K = v_{\text{Ebg}}/v_{\text{Si}}$. The composite modulus then is expressed as a function of the strength of the interphase interaction K :

$$G_C \equiv (v_{\text{Si}})_p (G_{\text{Si}} + K G_{\text{Eg}}) \quad (1.12b)$$

The volume fractions of continuous (parallel) or discontinuous (series) phases for both components in the co-continuous system were determined using the percolation theory [59, 60]. The fraction of the continuous silica phase in the epoxy-silica hybrid is given by the following expression:

$$(v_{\text{Si}})_p = [(v_{\text{Si}} - v_{\text{Sicr}})/(1 - v_{\text{Sicr}})]^t \quad (1.13)$$

where v_{Sicr} is the critical volume fraction for a partial phase continuity of the component and t is the critical exponent. The theoretical critical volume fraction for spherical particles dispersed in a matrix is $v_{\text{cr}} = 0.156$ [61]. In the case of IPNs with covalent bonds, one can expect that the critical fraction will be close to zero. The composite modulus is described as:

$$G_C = [(v_{\text{Si}} - v_{\text{Sicr}})/(1 - v_{\text{Sicr}})]^t (G_{\text{Si}} + K G_{\text{Eg}}) \approx (v_{\text{Si}})^2 (G_{\text{Si}} + K G_{\text{Eg}}) \quad (1.12c)$$

The value of the critical exponent $t = 2.0$ was used [62].

The theoretical curves of the composite modulus in Fig. 1.9a (curves 2–4) were calculated according to the EBM model, using the various values of the parameter K characterizing the strength of interphase interaction. The curves correspond to systems (a) with very strong epoxy-silica interaction, $K = 10$ (curve 3), and (b) without any interaction, $K = 0$ (curve 2), respectively.

The “sequential networks” E1-T2 and the two-step networks ET-2 with a high silica content fit the theoretical curve for strong interaction, while ET-2 with a small silica content corresponds to a weak interaction. The critical volume fraction $v_{\text{Sicr}} = 0.02$ was found to better fit the data of the more heterogeneous one-stage systems (E-T1) with smaller phase continuity (see curve 4). The fact that (1.12c) (curves 2–4) well fits experimental data in contrast to the particulate model (curve 1) proves that the epoxy-silica nanocomposites can be viewed as IPNs.

The moduli of the systems containing two continuous phases are also often predicted using the empirical model of Davies [63, 64].

$$G_C^{1/5} = v_1 G_1^{1/5} + v_2 G_2^{1/5} \quad (1.14)$$

For our epoxy-silica system, an effective volume of hard phase, v_{eff} , is given by silica phase and glassy immobilized epoxide phase. The modulus of silica was used for the hard phase:

The prediction of the modulus, according to the Davies empirical model for the epoxy-silica networks, is given in Fig. 1.9b.

$$G_C^{1/5} = v_{\text{Ef}} G_E^{1/5} + v_{\text{eff}} G_{\text{Si}}^{1/5} \quad (1.15)$$

The analysis shows a satisfactory agreement of bicontinuous models with the experimental data (EBM model curves 2–4 in Fig. 1.9a and Davies model in Fig. 1.9b). The models fit the hybrid epoxy-silica systems with both weak and strong interphase interactions, assuming enhanced effective volume fraction of the hard phase. Thus, dynamic mechanical properties provide an experimental proof that the microphase-separated epoxy-silica hybrid forms an interpenetrating network.

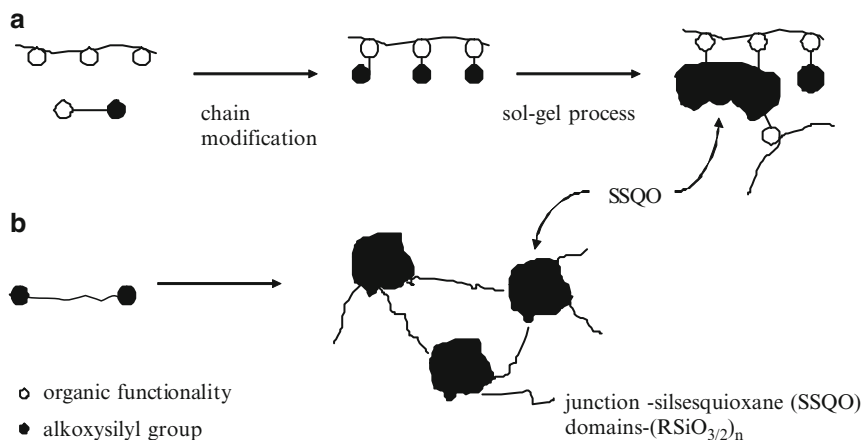
Crosslinking of the Matrix with Filler

Interphase crosslinking is another explanation of the excessive reinforcement of the O–I hybrids [65, 66]. The filler dispersed in the matrix can act as a multifunctional crosslink [67] in case of a covalent bond to the matrix or a good adhesion between phases. The plateau modulus above T_g in the linear PMMA-TEOS system [9] was interpreted as a result of crosslinking between the polymer matrix and silica clusters formed from TEOS. Physical and chemical interactions between organic and inorganic phases were proved [9, 13]. An increase in modulus with increasing crosslinking between silica phase and polymer was reported by Huang et al. [53] in the alkoxysilane-modified poly(tetramethyleneoxide)-TEOS system.

1.3.3 O–I Networks with Defined Interphase Covalent Bonding

The interface interaction is a crucial factor determining the structure, morphology, and properties of O–I polymer nanocomposites. Strengthening and control of the interaction is the main goal in the synthesis of nanocomposites. In the case of epoxy-silica nanocomposites discussed in Sect. 1.3.2, the silica domains generated in situ from TEOS are irregularly dispersed in the organic matrix. The epoxy network is grafted to the silica structures, and both covalent- and H-bonding exist in the epoxy-silica network. However, this interphase bonding is not well defined, and cannot be precisely controlled. Therefore, efforts are made to prepare the nanocomposites showing not only the strong but also the well-characterized and controlled interaction between phases, to determine and understand the effect of the interphase interaction on morphology and properties.

The coupling agents, used to improve an interaction between phases and miscibility of the O–I mixtures, are organic–inorganic precursors containing both organic and inorganic functionalities, thus providing a chemical bond between O and I phases.



Scheme 1.2 The O–I networks with an interphase covalent bonding. (a) SSQO grafted along the polymer chain, (b) SSQO as network junctions

Usually, organofunctional trialkoxysilanes are applied as coupling agents. Through the reaction with such an O–I precursor, a polymer is modified with the alkoxy groups along the chain. The hydrolytic condensation of these groups pendant on the chain results in generation of silsesquioxane (SSQO) domains grafted to the polymer in a well-characterized way (see Scheme 1.2a).

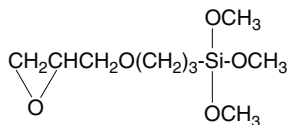
Another type of well-defined covalent bonding between phases can be produced by bis(trialkoxysilanes), as precursors of the so-called bridged polySSQO [68]. In these O–I networks, the inorganic SSQO structures are linked with organic bridges of various chemical characters and lengths. The “polymer-bridged” polySSQO, such as alkoxy silane-endcapped oligomers, are precursors of high interest. The hydrolytic condensation of the terminal alkoxy silane groups leads to the formation of the O–I block copolymer. The arising SSQO structures form inorganic crosslink domains of the O–I hybrid network linked with organic polymer chains (Scheme 1.2b). Investigation of these O–I hybrid polymers began in the 1980s [7, 11, 69], and resulted in the well-known Wilkes’ morphological model of the microphase-separated system with polymer-rich and SSQO-rich domains.

Scheme 1.2 shows the two above mentioned O–I systems with defined interphase covalent bonding – hybrid with the inorganic SSQO structure (a) grafted along the polymer chain, and (b) attached at the chain end-position as a network junction, respectively.

1.3.3.1 Polymerization of Trialkoxysilanes

Sol–gel polymerization of organotrialkoxysilanes $\text{RSi}(\text{OR}')_3$ results in the formation of polySSQO of the general formula $(\text{RSiO}_{3/2})_n$, composed of random branched polymers, ladder structures, and polyhedral products – “cages” [70, 71].

Sol-Gel Polymerization of (3-Glycidyloxypropyl)Trimethoxysilane (GTMS)



GTMS

(3-glycidyloxypropyl)trimethoxysilane (GTMS) is the typical organotrialkoxysilane used as a coupling agent. The structure evolution during hydrolytic polycondensation of GTMS is determined mainly by catalytic conditions, as is usual for the sol-gel process. The acid (TSA)-catalyzed polymerization is very slow, and the system finally gels in 15 days at 80°C, with the stoichiometric amount of water, $r_{\text{H}} = 1.5$ [72]. Under catalysis with DBTDL and BDMA, the polymerization is faster compared to TSA; however, mainly relatively stable low-molecular-weight products are formed in the early stage (see SEC record in Fig. 1.10). The dominant oligomer prevailing in the reaction mixture corresponds to the compact cubic octamer cage produced by intramolecular condensation of GTMS (Scheme 1.3a). Due to the preferential intramolecular reaction to form polyhedral cyclics, the trifunctional monomer does not gel under DBTDL catalysis. In addition to the fully condensed octamer cage, mass spectrometry also reveals distribution of products involving incompletely closed cages or nonamer and decamer cages present in the oligomer fraction. The most prominent structures proved by electrospray ionization mass spectrometry are illustrated in Scheme 1.3b. The fraction of the cages increases with dilution of the reaction mixture and with excess of water. A high yield of the cage (~90%) was obtained using BDMA catalyst and a water content of $r_{\text{H}} > 5$. On the contrary, only a small amount of low-molecular-weight polyhedral products arise in the reaction mixture catalyzed with TSA. In this case, the intermolecular condensation is preferred, high-molecular-weight polymers are formed slowly (see Fig. 1.10c), and GTMS gels. The structure is less branched and linear polysiloxane chains prevail.

In addition to the effect of catalysis, the size of the organic substituent R in organotrialkoxysilanes plays a crucial role in the reaction mechanism and final structure. The polymerization of small trialkoxysilanes, such as methyltrimethoxysilane or vinyltriethoxysilane, is relatively fast, and the systems quickly gel under both acid and basic conditions. An increasing length of R in octyltriethoxysilane and alkoxysilyl-encapped oligomers leads to a reduction of the reaction rate. Moreover, in this case *only* stable low-molecular weight products are formed, and no gelation occurs independent of catalysis [73]. The long organic substituents R in the trialkoxysilanes cause steric hindrance around the functional alkoxysilane groups, resulting in restriction to the intermolecular polycondensation. The SiOH groups mostly react intramolecularly to form polyhedral cyclics yielding a narrow distribution of almost fully condensed polyhedral frameworks that are very stable. No high-molecular-weight polymer is produced by polymerization of the long trialkoxysilanes, in contrast to polymerization of the GTMS/DBTDL system where

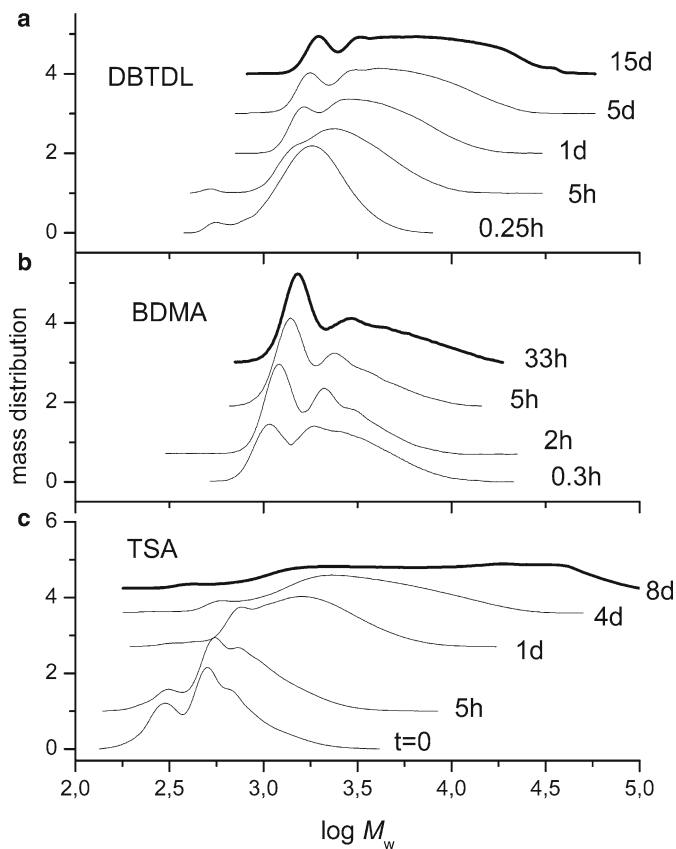


Fig. 1.10 Evolution of the molecular weight distribution during sol-gel polymerization of GTMS catalyzed with (a) DBTDL, (b) BDMA and (c) TSA. Curves are indicated by the reaction times; $T = 80^\circ\text{C}$

the octamer cage appears; however, a broad molecular weight distribution of polymers is formed as well (see Fig. 1.10a). In the case of alkoxyethyl-capped poly(oxyethylene) of the molecular weight $M = 350$, SPOE350, a gradual consumption of the long “macromonomer” takes place, and evolution of the molecular weight during polymerization leads to the bimodal distribution (see Fig. 1.11). The oligomer fraction corresponding to the “macrooctamer” is preferentially built-up from the beginning of the reaction. The distribution of the T_1 units, determined by NMR analysis of the octamer isolated from the reaction mixture of the polymerized oligomer SPOE350/DBTDL, is as follows: $T_0 = T_1 = 0$, $T_2 = 0.21$, $T_3 = 0.79$. The absence of T_1 units characterizing chain ends of the Si–O–Si sequences, and a high fraction of branched T_3 units in such a low-molecular-weight product, imply

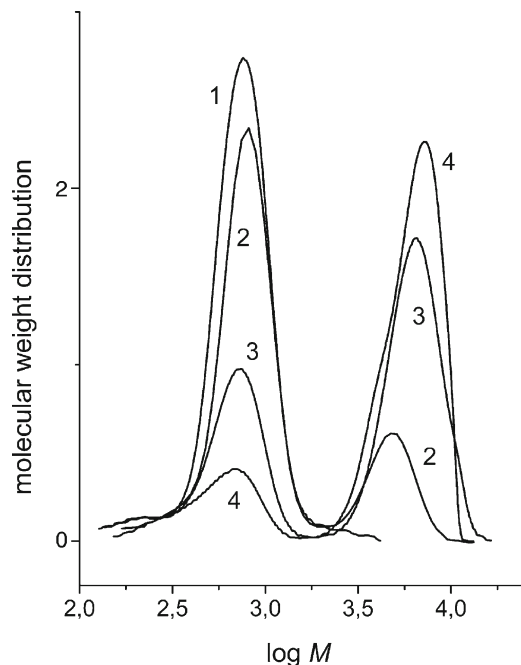


Fig. 1.11 Evolution of the molecular weight distribution during polymerization of SPOE350 catalyzed with DBTDL; $T = 80^\circ\text{C}$. Curves (reaction times): (1) $t = 0$, (2) $t = 24$ h, (3) $t = 120$ h, (4) $t = 288$ h

Self-Organization During the Sol–Gel Process

The SSQO structure evolution in polymerization of organotrialkoxysilanes is determined by a competition between the intermolecular polycondensation and intramolecular reactions to form cyclics, ladders, and cages. Moreover, because an O–I block copolymer is formed, the microphase separation occurring during the reaction is often accompanied by a spontaneous self-organization, typical of block copolymers.

The self-organization of GTMS during polymerization under DBTDL catalysis is revealed by SAXS analysis (Fig. 1.12a). The gradual structure ordering during the reaction manifests itself by a growth of the intensity maximum in SAXS curves at $q \sim 0.4 \text{ \AA}^{-1}$. The peak becomes apparent at a high condensation conversion, when the system is filled up predominantly with the compact microphase-separated cage-like structures and corresponds to the intermolecular interference coming from scattering on regularly arranged cages. The structure is organized into micelles, with the compact SSQO polyhedral core and protruding glycidylpropyl groups. The length of the organic group of these octopus-like molecules determines the separation distance of the cages, as shown in Scheme 1.4a. The correlation distance d is characterized by the position of the maximum q_{max} according to the expression, $d = 2\pi/q_{\text{max}}$. The experimentally determined value $d_1 = 15.7 \text{ \AA}$ is in good agreement with the theoretical estimate 15.0 \AA .

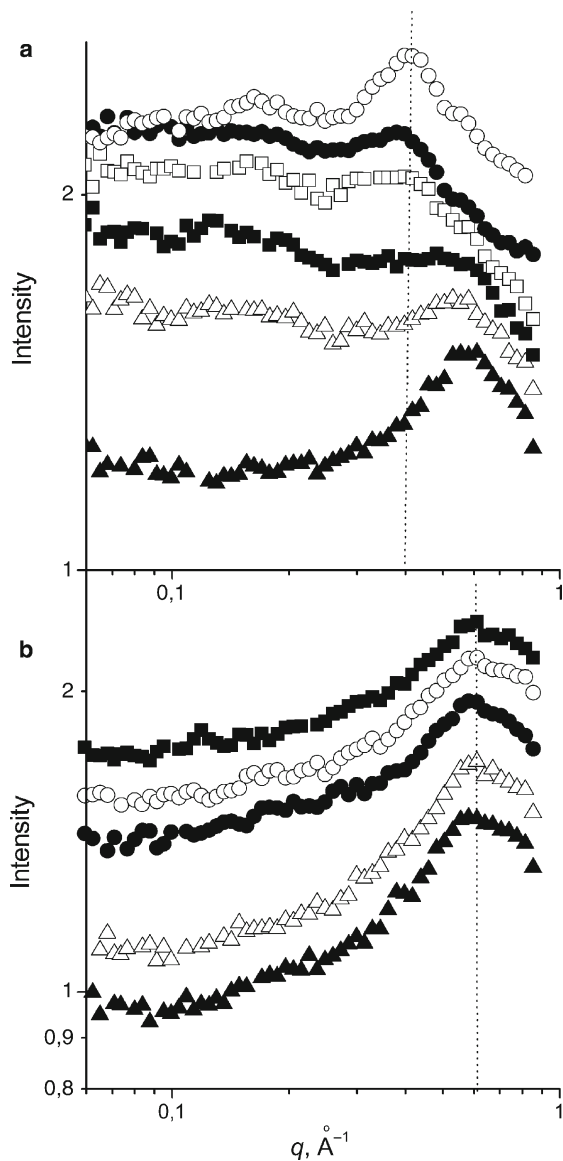
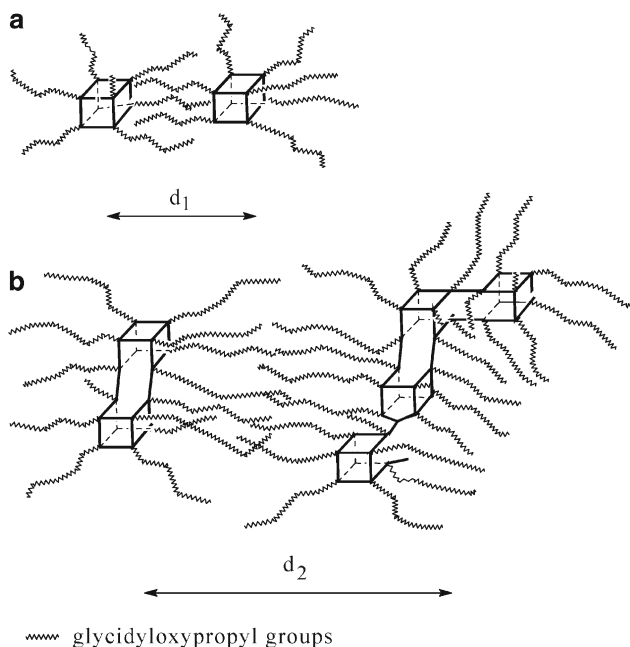


Fig. 1.12 Evolution of the SAXS profiles during polymerization of GTMS catalyzed with (a) DBTDL and (b) TSA; $T = 80^\circ\text{C}$. Curves (reaction times): (1) $t = 5$ min, (2) $t = 90$ min, (3) $t = 3$ h, (4) $t = 8$ h, (5) $t = 48$ h, (6) $t = 168$ h, (7) $t = 336$ h. Curves are mutually vertically shifted

The incompletely condensed cages also present in the system (see Scheme 1.3b) can interconnect to form a higher-molecular-weight branched polyhedral or ladder-like SSQO structures (Scheme 1.4b). Also Eisenberg et al. [76] found that most species are incompletely condensed, and the SSQO structure is built by combining



Scheme 1.4 Ordering of cage-like structures in the polymerized GTMS

fundamental octamer building blocks. In the case of higher-molecular-weight, ladder-like SSQO structures, the interpenetration of the organic dangling substituents, glycidioxypropyl groups, is less likely due to increasing steric hindrance. As a result, the structures with a larger separation distance d_2 are also formed, as displayed in the Scheme 1.4b. These structures are characterized by the second broad maximum at $q_{\max} = 0.15 \text{ \AA}^{-1}$ in Fig. 1.12a.

No self-assembly of the regularly arranged domains occurs under acid (TSA) catalysis of GTMS polymerization. A broad distribution of high-molecular-weight polySSQOs with dangling organic substituents formed in the acid polymerization (see Fig. 1.10c) does not allow for any regular arrangement. In this case, no interference maxima at $q < 0.50 \text{ \AA}^{-1}$ are observed in Fig. 1.12b. The initial maximum at $q \sim 0.6 \text{ \AA}^{-1}$ characterizes the intramolecular distances in GTMS and products. It does not suggest any intermolecular regular arrangement.

The significant ordering, more pronounced than in GTMS, takes place mainly during the polymerization of the trialkoxysilanes with long organic substituents. The structure evolution in the polymerization of SM600, i.e., the trialkoxysilane-capped poly(oxypropylene) of molecular weight $M = 600$, is characterized by the SAXS profiles in Fig. 1.13. The sharp maximum growing at $q = 0.18 \text{ \AA}^{-1}$ reveals a micro-phase separation and a high degree of ordering of the polyhedral domains. The self-organization of the long organotrialkoxysilanes happens both under DBTDL (Fig. 1.13a) and TSA (Fig. 1.13b) catalysis, unlike the GTMS polymerization. The

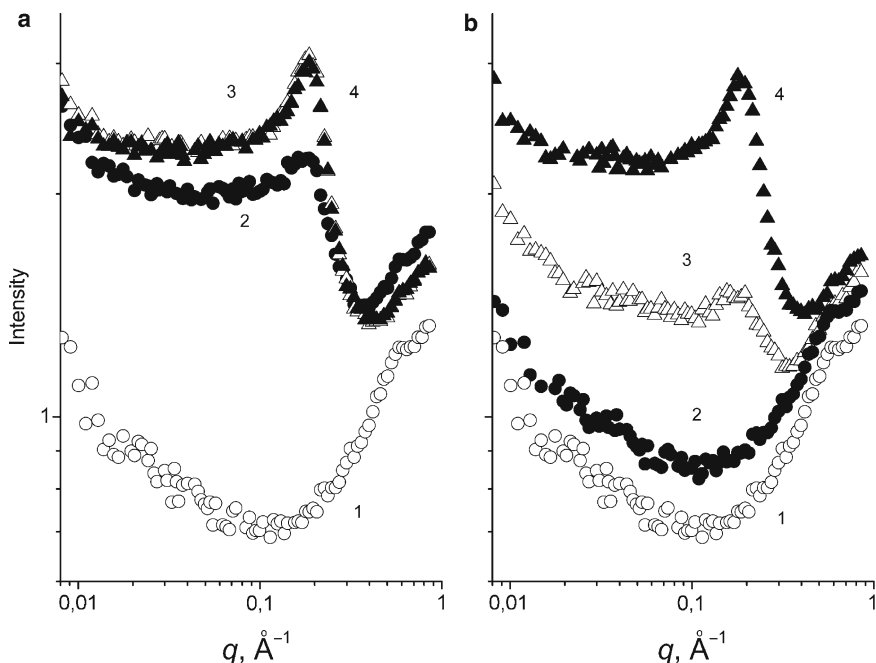


Fig. 1.13 Evolution of the SAXS profiles during polymerization of SM600 catalyzed with (a) DBTDL and (b) TSA; $T = 80^\circ\text{C}$. Curves (reaction times): (1) $t = 0$, (2) $t = 5$ h, (3) $t = 24$ h, (4) $t = 120$ h

position of the SAXS maximum correlates with the molecular weight of the organic chain, (refer to $q_{\max} = 2\pi/d$) (see Fig. 1.14, curves 4–6 for the substituents R = octyl and POP chains of $M = 600$ and 2000 , respectively) proving that its length controls the space separation of the cage frameworks in the micelle-like arrangement. The small trialkoxysilanes – methyltrimethoxysilane, vinyltriethoxysilane, and triethoxysilane – do not form ordered structures (Fig. 1.14, curves 1–3).

A perfect supramolecular ordering of the SSQO cages is directed by crystallization of a long poly(oxyethylene) chain in sol-gel polymerization of SPOE2000 and SPOE5000. During hydrolytic polycondensation at 135°C , the self-organization into micellar SSQO domains sets in, with a correlation distance corresponding to the POE coil size in the melt (Scheme 1.5). The melts of both polymerized SPOE oligomers exhibit SAXS interference maxima: $q_{\max}(\text{SPOE2000}) = 0.16 \text{ \AA}^{-1}$ (see Fig. 1.15a, curve 1) and $q_{\max}(\text{SPOE5000}) = 0.10 \text{ \AA}^{-1}$, corresponding to correlation lengths 39 and 63 Å, respectively, given by the POE chain length. The theoretical end-to-end distance r for SPOE2000 and SPOE5000 is 40 and 63 Å, respectively. During cooling, crystallization of fully extended POE chains in SPOE2000 or folded chains in SPOE5000 takes place. The crystallization of SPOE2000 chains on cooling manifested itself by a gradual appearance of the crystalline reflection in WAXS (Fig. 1.15b). Simultaneously, the micelle arrangement of the SSQO cages, characterized by a SAXS peak at 0.16 \AA^{-1} is gradually disappearing, and a new

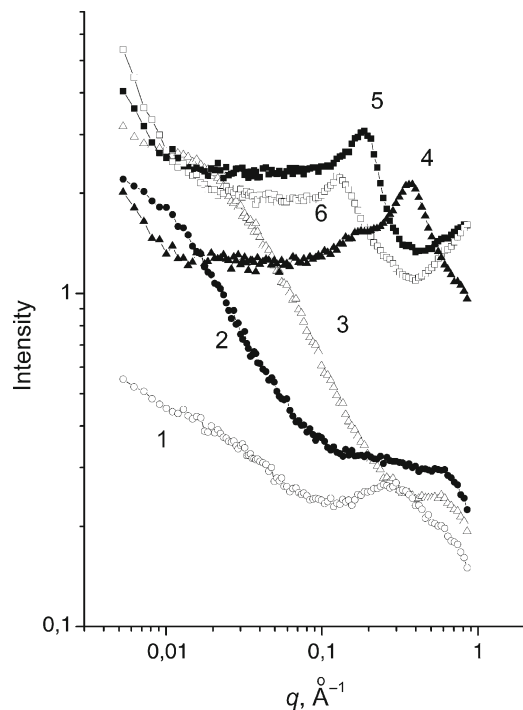
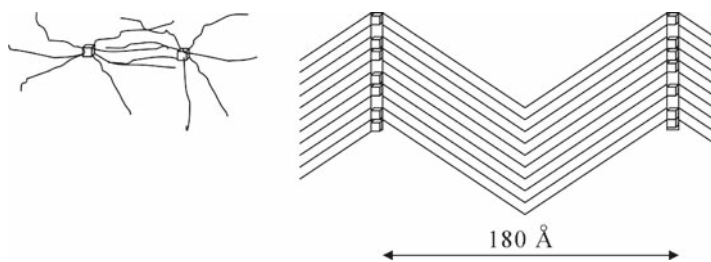


Fig. 1.14 SAXS profiles of the polymerized organotrialkoxysilanes of various sizes. (1) methyltrimethoxysilane, (2) vinyltriethoxysilane, (3) triethoxysilane, (4) octyltriethoxysilane, (5) SM600, (6) SM2005



Scheme 1.5 Ordering of the polymerized SPOE2000 in the melt and crystalline state

maximum given by the supermolecular ordering of crystalline and amorphous regions grows in the low- q region (Fig. 1.15a). The two low- q SAXS maxima of SPOE2000 and SPOE5000 in the solid state in Fig. 1.16 are the first and second order of the interference maximum, corresponding to the long period L_p of the regular alternation of crystalline and amorphous regions. $L_p = 180 \text{ \AA}$ for polymerized

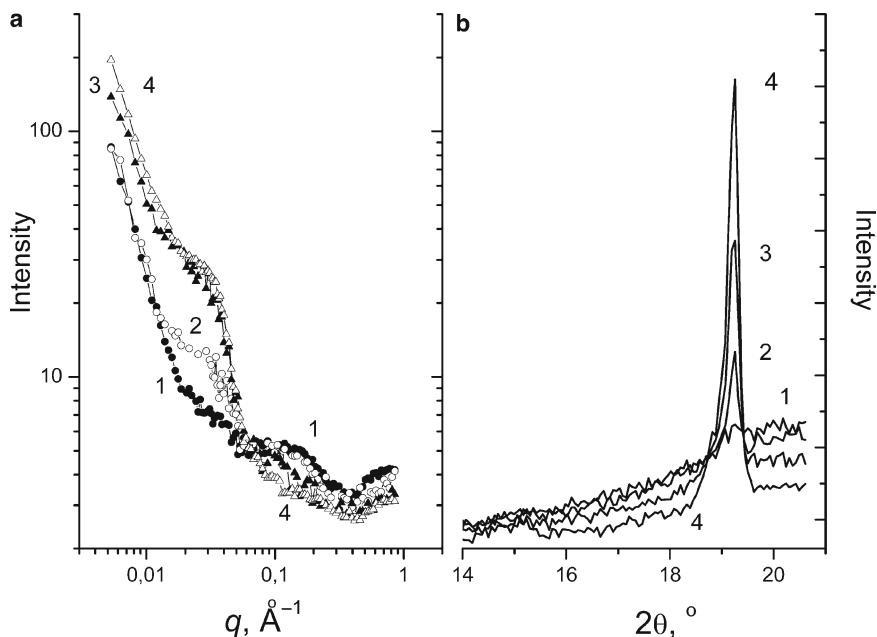


Fig. 1.15 Development of crystallinity at cooling of polymerized SPOE2000 followed by (a) SAXS and (b) WAXS. Curves (t – time of slow cooling the melt from $T = 135^\circ\text{C}$): (1) $t = 11$ min, (2) $t = 12$ min, (3) $t = 13$ min, (4) $t = 14$ min

SPOE2000 and $L_p = 233 \text{ \AA}$ for SPOE5000. The presence of the second order maximum is indicative of a lamellar structure. Either distorted bilayer lamellar arrangement (Scheme 1.5) or partly interpenetrated structures are assumed to be formed. The crystallization acts as a driving force for ordering of the SSQO cages into lamellae, and the lamellar SSQO structure is created.

Various kinds of organic templates have been used to direct self-assembly of the hybrid systems. Bridged SSQOs are very prospective materials in this area. The self-assembly tendency of the urea groups through H-bonding in the bridging organic unit was used in the ordering of the O–I hybrids. A combination of the urea groups and long alkyl chains providing hydrophobic interactions makes it possible to prepare long-range ordered hybrids. Different morphologies are formed, including lamellar bridged SSQO, layered sheets, or helical morphologies [77, 78, 142].

1.3.3.2 O–I Block Copolymer Networks with SSQO Junctions

Two types of O–I precursors can be used to synthesize the O–I block copolymer networks with SSQO domains in junctions of the network: the AlkoxySilane-encapped Oligomer (ASO) and the organically functionalized inorganic cluster [15, 79, 80]. Strategy of the network synthesis from the O–I precursors is illustrated

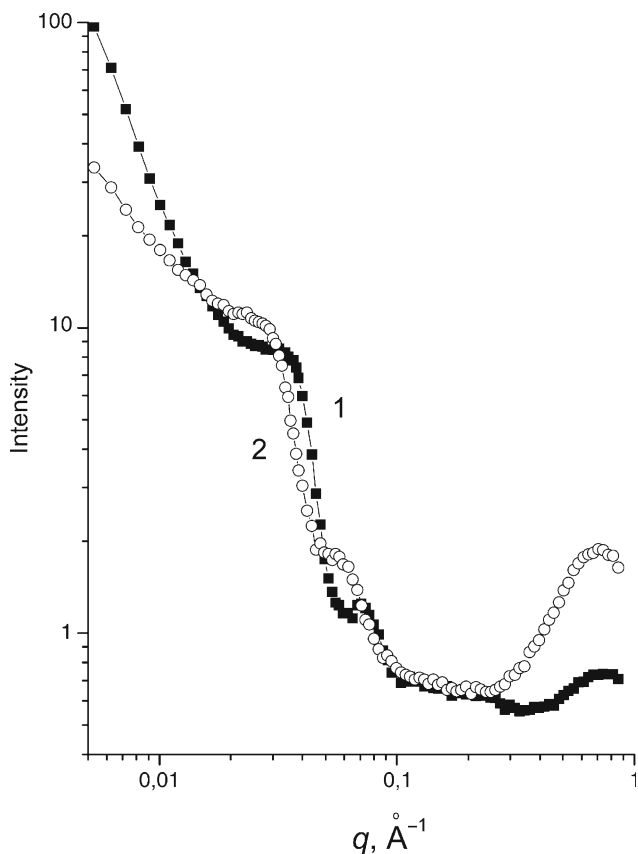
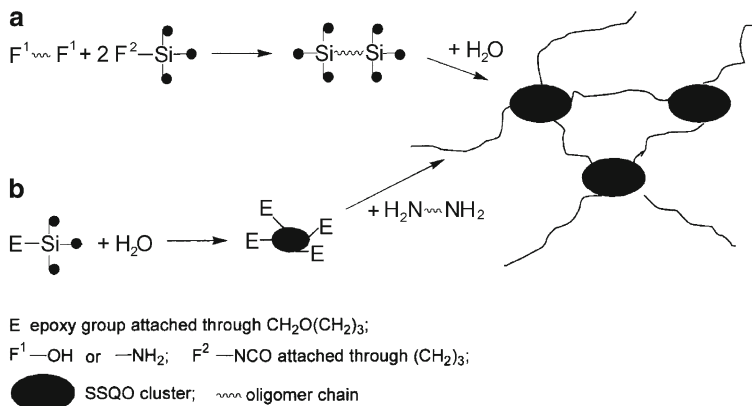


Fig. 1.16 SAXS profiles of the polymerized SPOE. (1) SPOE2000, (2) SPOE5000

in Scheme 1.6 showing the two approaches [81–83]. The first procedure consists of end-functionalization of an oligomer chain with alkoxy silane groups, followed by hydrolytic condensation of these terminal functionalities under formation of SSQO crosslinks (Scheme 1.6a). According to the second approach, the SSQO junction domains are prepared first, and then interlinked with an oligomer to form the O–I network (Scheme 1.6b). We have employed the Epoxy-functional SSQO Clusters (EC) crosslinked with diamine oligomers (Jeffamines). In both procedures, mainly POP oligomers of the molecular weight $M = 2000$ have been used to link the SSQO junctions and to form the corresponding hybrid networks, ASO2000 and EC-D2000.

The two network types differ slightly in the network structure. While the EC-diamine system forms the epoxy-SSQO network, the ASO crosslinking leads to an O–I network without presence of an epoxide.

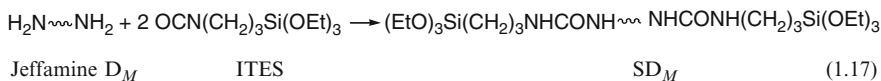
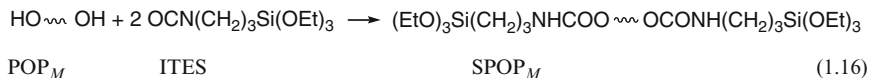


Scheme 1.6 Formation of the O-I block copolymer networks from (a) alkoxy silane endcapped oligomers and (b) epoxy-functional SSQO clusters

O-I Precursors of Hybrid Networks

AlkoxySilane-Endcapped Oligomers (ASO)

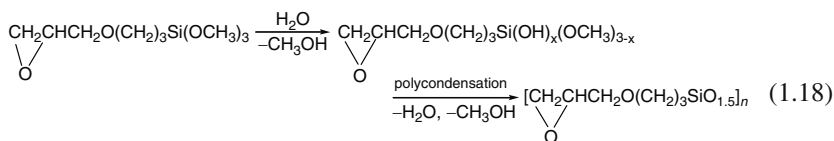
Alkoxy silane-endcapped oligomers, e. g. poly(oxypropylene) (POP) oligomers, polycaprolactones, or polybutadienes (PB) of molecular weight M were prepared by the reaction of $-\text{OH}$ or $-\text{NH}_2$ terminated oligomers with (3-isocyanatopropyl)triethoxysilane (ITES) [69, 82].



The silane-modified oligomers are denoted with S – SPOP _{M} (involving the urethane group) and SD _{M} (involving the urea group). The oligomers capped with the alkoxy silane groups at one end only were prepared similarly, by modification of α -hydro- ω -methoxy poly(oxyethylene) (POE) or poly(oxypropylene) monoamines (M600 and M2005) with ITES. The corresponding mono-trialkoxy silane oligomers are denoted SPOE _{M} and SM _{M} .

Epoxy-Functional Silsesquioxane Clusters (EC)

The SSQO clusters with pendant epoxy groups were prepared by hydrolysis and condensation of GTMS [72].



Depending on the reaction conditions, clusters with various molecular weights ($M = 500\text{--}2500$) and condensation conversions α_{Si} were synthesized. Using basic BDMA and DBTDL catalysts, the cyclic cage-like oligomers were preferably formed, and a relatively high conversion ($\alpha_{\text{Si}} = 0.95$ and $0.65\text{--}0.85$, respectively) was achieved in bulk reaction at 80°C for 1 or 3 h. On the contrary, under TSA, only low-conversion small SSQO oligomers ($\alpha_{\text{Si}} = 0.3\text{--}0.65$) were prepared by the reaction in bulk at 20°C for 1–4 days.

Synthesis Procedure of the O–I Block Copolymer Networks

The hydrolytic condensation of ASO reagents (SPOP or SD) was performed in the presence of a stoichiometric amount of water (for trialkoxysilanes, $r_{\text{H}} = 1.5$) under acid catalysis with TSA, by using DBTDL or basic BDMA, respectively. Crosslinking of EC with diamine proceeded at both stoichiometric, $r_{\text{AE}} = 1$, and off-stoichiometric compositions of the reaction mixture.

The reactions were performed in bulk, and only some cloudy reaction mixtures were homogenized with a small amount of isopropanol. The network samples were prepared at 80°C , postcured for 24 h at 120°C , and vacuum dried. All samples were transparent.

Formation of the O–I Block Copolymer Networks

Network formation from the O–I precursors and the resulting hybrid structure depend on the mechanism of the main crosslinking reaction. The O–I block copolymer networks are built by the sol–gel polymerization of the alkoxy-silane-encapped oligomers (ASO) or by the epoxide-amine reaction of the epoxyfunctional clusters (EC) with diamines (see Scheme 1.6).

The rate of network build-up significantly differs in various polyfunctional O–I systems. The hybrids gel in a wide range of reaction times, from 5 min up to 10 h at 50°C , depending on the type of the precursor and polymerization conditions. Figure 1.17 displays the growth of the modulus during polymerization, characterizing the molecular structure evolution and gelation of the O–I systems.

Crosslinking of Alkoxy-silane-Encapped Oligomers

The structure evolution and the rate of gelation in the case of crosslinking of ASO are affected mainly by catalysis of the sol–gel process. Hydrolysis initiating the polycondensation of the alkoxy-silane groups is the rate-determining step. Therefore,

the acid catalysis advancing hydrolysis leads to fast gelation. Alkoxysilane end-capped poly(oxypropylene) polymerized under TSA catalysis, SPOP2000/TSA, is the quickest gelling system under study (see Fig. 1.17). Hydrolysis with DBTDL or basic catalysts is slower, and gelation of SPOP2000 is substantially delayed. The faster network formation under TSA compared to DBTDL catalysis seems to contradict the common knowledge of slow polycondensation in an acid medium. This unusual behavior is due to the high functionality of the bistralkoxysilanes ($f_{\text{Si}} = 6$) and a resulting low critical condensation conversion for gelation, α_c . The theoretical value for a random reaction is $\alpha_c = 0.20$ (refer to (1.6)), and the experimental conversion at the gel point was determined to be $\alpha_c = 0.26$. Such a low condensation conversion corresponds to the formation of a dimer in the case of polymerization of the trialkoxysilanes, which is achieved in the very beginning of the reaction stage, despite the low condensation rate. (Polymerization degree P of an f functional monomer is $P = [1 - (f - 1)\alpha]^{-1}$, according to the statistical theory.) This explains the crucial role of the initiating hydrolysis reaction.

Network build-up from ASO proceeds by formation of SSQO crosslinks at the extremities of the oligomer chains. Evolution of the local SSQO structure during polymerization, described by distribution of T_i units, characterizes the formation of the SSQO junction domains and mechanism of gelation.

In the acid-catalyzed polymerization SPOP2000/TSA, the network “crosslinks” in the early postgel stage are composed of loose SSQO clusters, containing linear siloxane sequences and a high amount of unreacted SiOH. These clusters are inter-linked by oligomer chains. The structure of the O-I network near the gel point is shown in Scheme 1.7a. The distribution of T_i units in the cluster at the gel point is

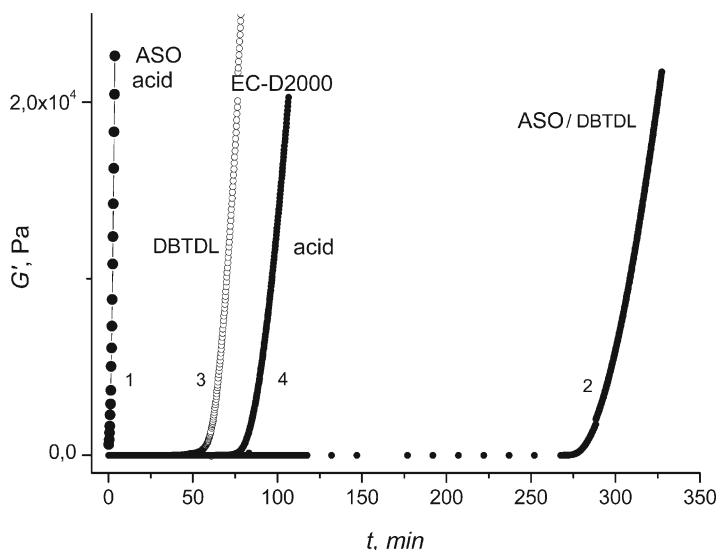


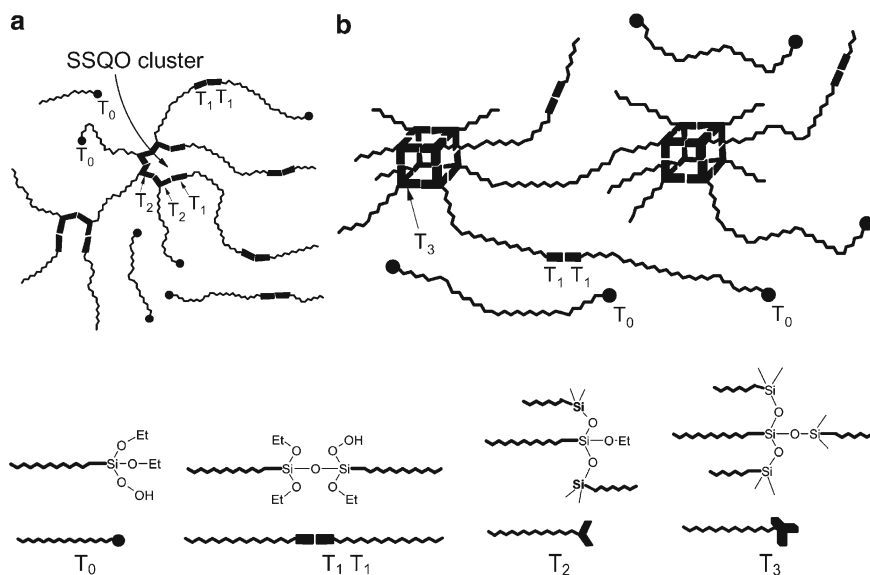
Fig. 1.17 Increase in dynamic storage modulus G' during network formation of O-I hybrids. (1) SPOP2000/TSA, (2) SPOP2000/DBTDL, (3) EC/DBTDL-D2000, (4) EC/TSA-D2000. $T = 50^\circ\text{C}$

as follows: $T_0 = 0.29$, $T_1 = 0.63$, $T_2 = 0.08$, $T_3 = 0$. Except for the unreacted T_0 units (SiOH), only the terminal silicon units T_1 and units T_2 of linear or cyclic SSQO structures are present at the ends of organic chains at the beginning of the polymerization up to gelation. The T_2 units at the chain ends issue three paths, including two reacted functionalities Si–O– and the oligomer chain path Si–CH₂–, thus forming the SSQO branching/crosslinking domain in the O–I block copolymer.

The network prepared by DBTDL-catalyzed polymerization of SD2000/DBTDL contains small polyhedral SSQO clusters as network junctions at both extremities of the SD2000 chain (see Scheme 1.7b). The local SSQO structure at the gel point is quite different, compared to the “acid” polymerization; $T_0 = 0.75$, $T_1 = 0.08$, $T_2 = 0.03$, $T_3 = 0.14$. This distribution of units – i.e., the low content of terminal T_1 units and T_2 units, and a high amount of branched SSQO structures T_3 – is consistent with intramolecular branching to form small polyhedral cyclics. During polymerization, T_3 units appear at the very beginning of the reaction, in contrast to polymerization under acid catalysis. Hence, the absence of T_2 units reveals a strong positive substitution effect and preferred formation of the “cage” with pendant alkoxy silane-terminated poly(oxypropylene) chains as a multifunctional building unit, which is a precursor of the network junction (see Scheme 1.7b). Formation of such cage-like network precursors was assumed in the model by Rankin et al. [84] for systems with fast cyclization.

Crosslinking of Epoxy-Functional SSQO Clusters

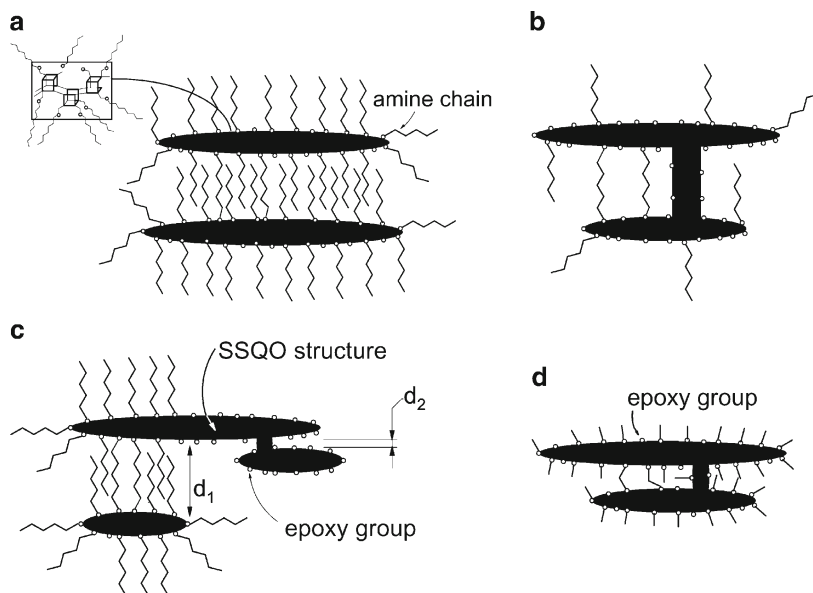
Network formation from the epoxy-functional cluster (EC) and diamines includes two independent reaction mechanisms contributing to the structure build-up. The



Scheme 1.7 Structure of the ASO-based networks near the gel point (a) SPOP2000/TSA, (b) SD2000/DBTDL

SSQO clusters prepared from GTMS (mainly those synthesized under acid conditions) are not quite stable, and during the reaction with amines the SSQO structures continue to grow. The basic medium of amines promotes condensation of the clusters, and hence both the epoxide-amine reactions and the sol-gel condensation take place in crosslinking of the EC with amines. The condensation of SiOH and alkoxy silane groups in EC dominates at the early stages of the reaction to form larger SSQO clusters, composed of interconnected incompletely condensed polyhedral cages with pendant epoxy groups (see Scheme 1.4b). Addition of the amine to the clusters by a slower epoxide-amine reaction occurs in the later stage [82]. The growing epoxyfunctional SSQO clusters become separated by the attached organic amine chains (Scheme 1.8a), thus being sterically protected from further growth by intermolecular condensation. The gelation then takes place by the epoxide-amine crosslinking reaction of the enlarged EC and D2000 to form the O-I block copolymer network (Scheme 1.8a).

Because of the crucial role of the slow epoxide-amine reaction in the network formation, the gelation of EC-D2000 sets in later, compared to polymerization of ASO under the most efficient conditions (see Fig. 1.17). In addition to the kinetic reactivity, the rate of gelation depends on the epoxy functionality of the SSQO cluster, f_E , which is proportional to the cluster size. The high functionality leads to a decrease in the critical conversion (refer to 1.6), and thus to earlier gel formation.



Scheme 1.8 Formation and structure of the network EC-D2000; effect of composition and length of the amine chain. (a) stoichiometric composition, $r_{AE} = 1$, block copolymer network; (b) deficiency of the amine oligomer, $r_{AE} < 1$, SSQO network; (c) $r_{AE} < 1$, two interdomain distances given by the size of the amine (d_1) and unreacted glycidyl groups (d_2); (d) short amine agent – SSQO network

The EC prepared under DBTDL catalysis is larger than that synthesized by using TSA, and therefore the EC/DBTDL-D2000 system gels slightly faster than EC/TSA-D2000 (see Fig. 1.17). For the typical EC, the functionality was $f_E \sim 20$ [82].

The hybrid network EC-D2000 displays a decisive dependence of formation on the composition of the reaction mixture. In fact, it is not the ratio of the amine and epoxy functionalities that is important, as in typical epoxy networks, but the relative content of the inorganic SSQO structures (EC) and polymer chains (D2000). However, this relative number of organic (amine functionality) and inorganic (epoxy functionality in SSQO) structures is conveniently characterized by the ratio r_{AE} .

In the stoichiometric composition, $r_{AE} = 1$, the hybrid system gels at the conversion of the epoxy groups ($\alpha_{E,C} = 0.20$), while condensation conversion in the inorganic phase is very high, reaching the value $\alpha_{Si} = 0.82$ at the gel point. The network is formed by the epoxide-amine reaction. No pure SSQO network exists at the gel point, despite such a high condensation conversion and a high fraction of branched units, $T_3 = 0.59$. This result is consistent with the formation of highly intramolecularly branched cage-like SSQO structures.

The structure evolution and network formation differ in polymerization of the non-stoichiometric composition EC-D2000. At a lower amount of organic amine chains, $r_{AE} < 1$, the steric shielding of the growing SSQO domains is less efficient. The intermolecular condensation between clusters can proceed, the clusters aggregate, and finally form the continuous SSQO network (Scheme 1.8b). Under such conditions, two percolation thresholds occur, and both the epoxy-amine O–I block copolymer network and the pure SSQO network are formed.

Structure and Morphology of O–I Block Copolymer Networks

Nanocomposite morphology is affected by the synthetic procedure, molecular architecture of the precursor, composition of the O–I system, and catalytic conditions during polymerization.

The block copolymer O–I networks are well ordered, and display a regular arrangement of the SSQO domains forming the network crosslinks. During formation of the network, the organized microphase-separated structure gradually develops. The regular spacing in a two-phase structure appears during polymerization after the gel point, as indicated by the growth of the interference maximum in SAXS profiles shown in Fig. 1.18. Such an ordered arrangement of the SSQO domains is in contrast to the irregular structure of the IPNs DGEBA-D2000-TEOS with randomly dispersed silica phase in the epoxy matrix.

The distance between SSQO crosslinks (determined from the position of the SAXS maximum) correlates with the length of the corresponding linking oligomer chain [85, 86]. The networks synthesized by using oligomers of molecular weight $M \sim 2000$, both from ASO and EC, exhibit SAXS intensity interference maxima in the region $q_{max} = 0.135\text{--}0.15 \text{ \AA}^{-1}$ (see Fig. 1.19a) [83]. These maxima correspond to the correlation distance 42–46.5 Å, in accordance with the results of Jordens and Wilkes [87], who found a spacing of 45 Å in the networks from silane-encapped D2000.

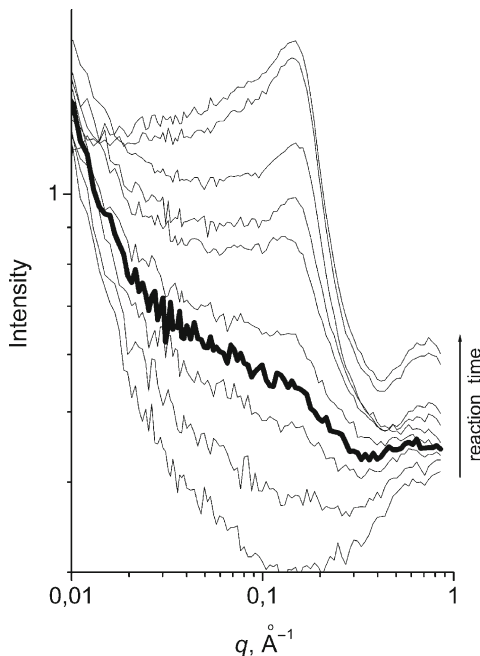


Fig. 1.18 Evolution of the SAXS profiles during polymerization of SD2000/DBTDL. Thick curve – gel point

Shortening of the interjunction distance occurs in the networks with increased interaction between organic and inorganic phases. The H-bonding of silanols in the SSQO clusters formed under acid catalysis with $-\text{OCH}_2-$ groups in POP chains leads to partial interpenetration of the organic chains and the SSQO domains. As a result, the separation distance between the compact frameworks diminishes. In SPOP2000 networks, the SAXS maximum shifts to a higher q -value ($q_{\text{max}} = 0.175 \text{ \AA}^{-1}$), corresponding to a shorter distance between SSQO junctions in the systems polymerized using the acid catalyst (TSA), compared to those catalyzed with the base (BDMA) (see Fig. 1.19b, curves 1 and 2). On the other hand, there is no interaction between SiOH and the chain in the networks based on alkoxyisilane-encapped polybutadiene, SPB2000. The SPB networks are strongly microphase separated, as indicated by the steep slope of the SAXS curves in Fig. 1.19b (curves 3 and 4), and no shift of the maximum takes place due to the catalysis.

The structure and morphology of the EC-D2000 nanocomposite is mainly controlled by composition of the reaction mixture, as discussed above.

The stoichiometric network EC-D2000 ($r_{\text{AE}} = 1$) is the microphase-separated hybrid containing the spherical domains of the SSQO clusters, of size 5–15 nm in diameter, shown in the AFM micrograph in Fig. 1.20a. These domains, composed of polyhedral SSQO structures, are interlinked by D2000 chains and regularly arranged, as proved by the SAXS maximum at $q = 0.135 \text{ \AA}^{-1}$ (Fig. 1.21, curve 1).

In the case of amine deficiency ($r_{AE} = 0.2$), i.e., deficiency of the organic polymer phase, the structure consists of large SSQO cylinders of size 30–150 nm in diameter (see Fig. 1.20b). The detailed view in Fig. 1.20c illustrates that the cylinders are interconnected, thus evidencing the existence of the continuous SSQO phase. The SAXS analysis provides an explanation of this SSQO network formation by a space closeness of the cylinders in the amine-deficient O–I networks. The maximum at

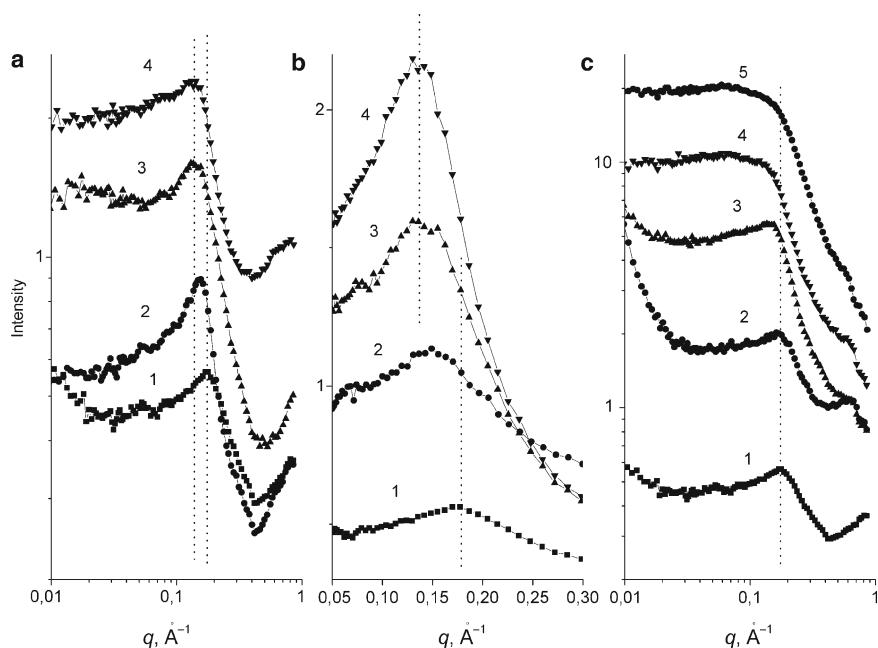


Fig. 1.19 SAXS profiles of the O–I networks prepared (a) from various precursors; (1) SPOP2000/TSA, (2) SD2000, (3) SPB2000/TSA, (4) EC/TSA-D2000; (b) under acid (TSA) and basic (BDMA) catalysis (1) SPOP2000/TSA, (2) SPOP2000/BDMA, (3) SPB2000/TSA, (4) SPB2000/BDMA; (c) with variable contents of TEOS (wt% of TEOS) (1) 0%, (2) 9.1 wt%, (3) 28.6 wt%, (4) 47.4 wt%, (5) 64.3 wt%

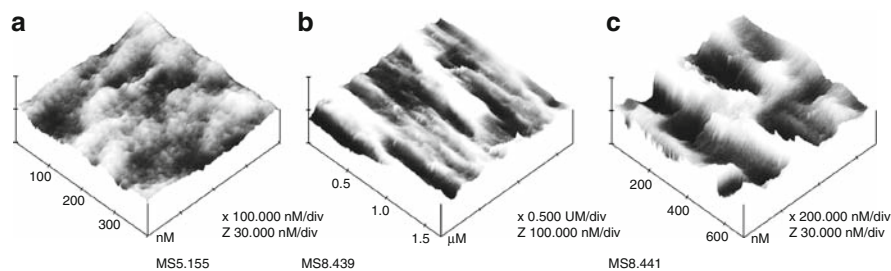


Fig. 1.20 AFM scans of EC/TSA-D2000 networks of various compositions: (a) $r_{AE} = 1$, (b) $r_{AE} = 0.2$, (c) $r_{AE} = 0.2$ – detail

$q = 0.135 \text{ \AA}^{-1}$ corresponding to D2000 the correlation distance ($d_1 = 46.5 \text{ \AA}$) becomes less pronounced at a composition $r_{AE} = 0.2$ (Fig. 1.21, curve 2), and it disappears completely at a composition $r_{AE} = 0.05$ (curve 3). The new interference maximum occurring in these networks at $q = 0.43 \text{ \AA}^{-1}$ characterizes the small correlation distance, $d_2 = 15 \text{ \AA}$, due to the short unreacted excessive (glycidyoxy)propyl groups separating the clusters (see Scheme 1.8c). Thus, decreasing the amine amount (i.e., polymer chains content) results in decreasing intercylinder distance, and enables formation of “crossbars” between the approaching SSQO clusters. The ordered ladder-like SSQO network structure involving SSQO “cylinders” is produced. The presence of the continuous hard SSQO phase in the networks with excess of EC ($r_{AE} < 1$) is also obvious from the mechanical behavior of the nanocomposite. The rubbery modulus of the EC-D2000 network grows with increasing amounts of EC due to the formation of the SSQO network, while the ordinary epoxy-amine networks achieve the maximum modulus at the stoichiometric composition under the adopted reaction conditions. The homopolymerization of the excessive epoxide groups was excluded at the given curing regime [83].

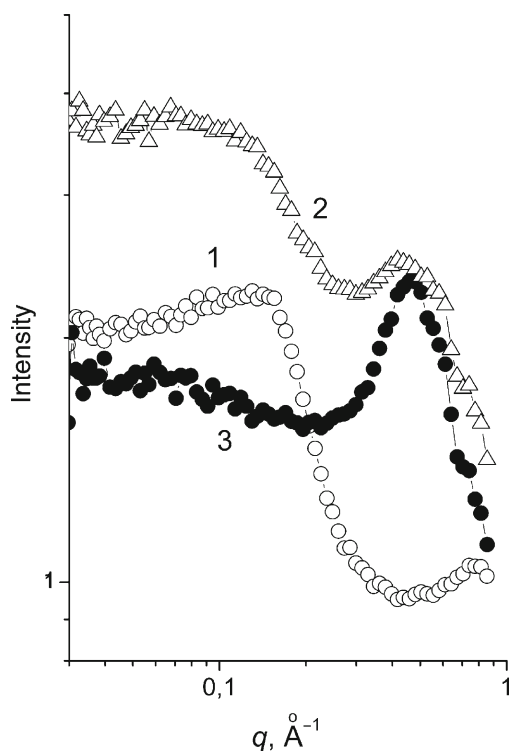


Fig. 1.21 The effect of composition of EC/TSA-D2000 networks on SAXS profiles. (1) $r_{AE} = 1$, (2) $r_{AE} = 0.2$, (3) $r_{AE} = 0.05$

The decreasing length of the oligomeric amine curing agent exhibits the same effect on the O–I network morphology as decreasing the number of the amine chains. Also, in this case, the EC cluster is less shielded by the smaller organic chain, and the intermolecular condensation proceeds to reach percolation of the SSQO structure (Scheme 1.8d).

The morphology of the ASO-based networks is characterized by small SSQO clusters with a size of 1–2 nm, as proved by the investigation of model systems [82]. AFM does not reveal any structures corresponding to objects larger than 3 nm. This is in agreement with the results of Cuney et al. [88], who found particles with a diameter of 1.5 nm at the chain ends in the network of silane-encapped hydrogenated polybutadiene. These small clusters are highly condensed ($\alpha_{\text{Si}} = 0.91\text{--}0.97$), compact cage-like structures in the case of DBTDL or BDMA catalysis. The acid-catalyzed networks involve less compact clusters ($\alpha_{\text{Si}} = 0.85\text{--}0.91$), including a high content of unreacted SiOH.

The networks with SSQO junctions prepared from O–I precursors with a long organic chain contain a low fraction of inorganic structures (~5 wt% in the case of the oligomer of $M = 2000$). The nanocomposites with a higher content of inorganic phase were synthesized by addition of TEOS to the hybrid SPOP2000. Sol–gel polymerization of TEOS leads to the formation of silica domains dispersed in a matrix; moreover, co-condensation with the alkoxy silane groups of SPOP2000 takes place, enlarging inorganic junction domains. Contrary to the neat SPOP2000 network, in the SPOP2000-TEOS nanocomposite the inorganic clusters are formed not only at the organic chain ends, but also irregularly along the chain. Because of this irregular arrangement, the interference maximum in SAXS profiles in Fig. 1.19c becomes less pronounced, the peak broadens, and disappears at a high TEOS content (~60 wt%). The high TEOS concentration also leads to increasing connectivity between silica domains and formation of the continuous phase.

Thermomechanical Properties

The glass transition temperature T_g of the O–I networks with SSQO junctions depends mainly on the chemical nature of the oligomer chain. The polybutadiene-based network SPB2000 exhibits a relatively high T_g (-27°C), while the glass transition temperature of the poly(oxypropylene)-based network SD2000 is $T_g = -55^\circ\text{C}$ (see Fig. 1.22). The polycaprolactone-based network (SPCL2000) shows a more complex behavior because of crystallization. In addition to glass transition at -60°C , melting of the backbone occurs at $T_m \sim 40^\circ\text{C}$.

The interphase interaction may contribute to an increase in the glass transition by creating a confined interface layer. The effect, however, is much lower, compared to the interpenetrating networks DGEBA-D2000-TEOS. In most block copolymer O–I networks, the interaction, if any, between the polymer and the SSQO junction is quite weak. The networks based on POP2000 oligomer prepared under various conditions (both ASO- and EC-based) possess a glass transition temperature in the range of approximately -55°C to -45°C (Fig. 1.23). The interphase

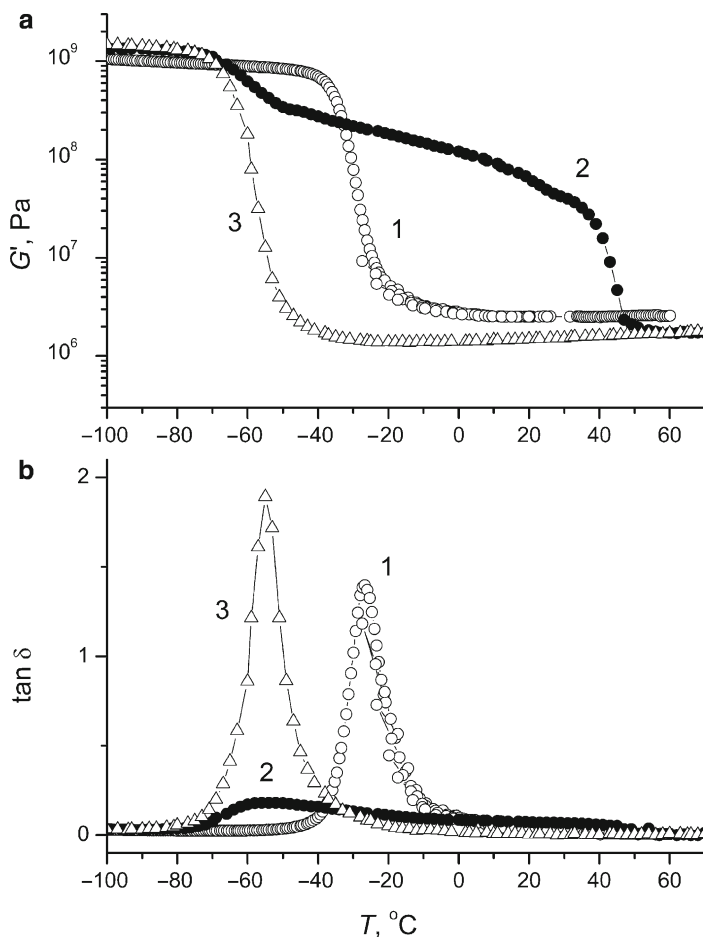


Fig. 1.22 Shear storage modulus G' (a) and loss factor $\tan \delta$ (b) of O-I networks with different backbones as a function of temperature. (1) SPB2000, (2) SPCL2000, (3) SD2000

interaction is affected by the internal structure of the SSQO domains, which is determined by catalysis. The presence of SiOH in SSQO clusters at the chain ends of SPOP2000 polymerized under acid catalysis results in an interaction with the oxygen of the neighboring part of the POP chain. Also, loose SSQO structures formed in this case are more efficient for the interaction with the organic matrix than the compact structures created under base catalysis. The interaction leads to immobilization of the part of the chain close to the SSQO domain, while the middle part of the chain remains free of restrictions [87, 89]. Hence, two relaxation peaks at -49 and -15°C (Fig. 1.23b, curve 3) in the network from SPOP2000/TSA correspond to the free and constrained POP chains. Similar effects have been

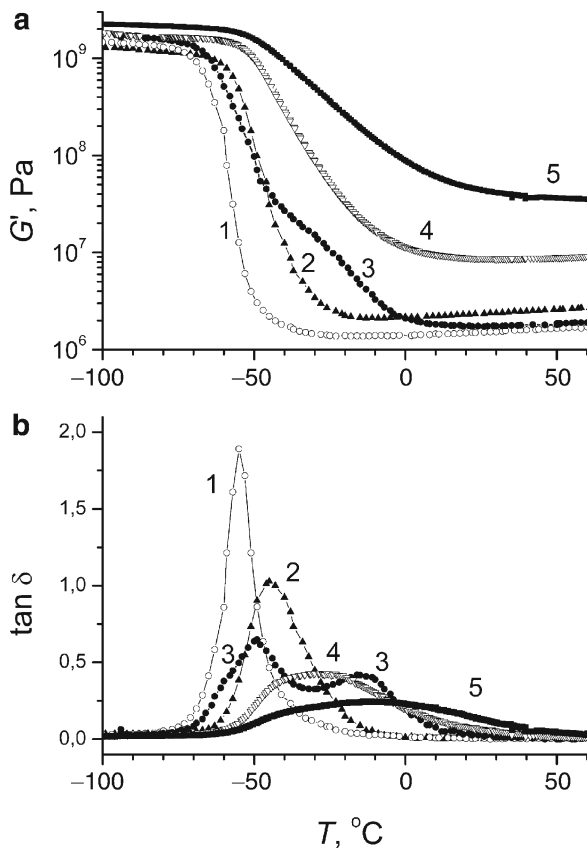


Fig. 1.23 Shear storage modulus G' (a) and loss factor $\tan \delta$ (b) of poly(oxypropylene)-based O-I networks as a function of temperature. (1) SD2000, (2) EC/TSA-D2000, (3) SPOP2000/TSA, (4) SPOP2000/TSA – TEOS (47 wt%), (5) SPOP2000/TSA – TEOS (64 wt%)

described in poly(tetramethylene oxide)-based O-I systems [85]. In contrast, the SPOP2000 networks with a low SiOH content, due to basic catalysis (BDMA) during synthesis or due to an understoichiometric amount of water ($r_{\text{H}} < 1.5$) used for hydrolysis, display no or a weak interphase interaction. One narrow peak of the loss factor $\tan \delta$ at $T_{\text{g}} = -55^{\circ}\text{C}$ indicates relaxation of the unconfined chains only (see Fig. 1.23, curve 1).

The presence of TEOS in the network SPOP2000-TEOS leads to a significant increase both in modulus and T_{g} (Fig. 1.23, curves 4 and 5). Broadening of the relaxation band corresponds to a broad distribution of immobilized chains. The strength of the interaction and the fraction of confined chains increase with the TEOS content.

Theoretical Prediction of the Modulus

The mechanical properties of the homogeneous network in the rubbery state are governed by the crosslinking density ν , defined as the concentration of elastically active network chains. In an ideal case, ν is determined by the molecular weight M_c of the chain between junctions, $\nu \sim 1/M_c$. According to the Flory-Erman (F-E) rubber elasticity theory [90], the crosslinking density is related to the equilibrium shear modulus G_e in the rubbery state:

$$G_e = \nu ART \quad (1.19)$$

($A = (f_{\text{eff}}^c - 2)/f_{\text{eff}}^c$ for a phantom network and $A = 1$ for the affine network, f_{eff}^c is an effective functionality of the crosslink). Contrary to classic networks with point-like crosslinks, in the O-I networks the junction is formed by a “crosslink domain.” Such networks can be treated by considering SSQO junctions as inelastic hard clusters of various sizes and “crosslink functionality.” Within hard clusters, the chains between branch points are too short, and therefore elastically inactive. However, according to the concept of hard clusters in heterogeneous networks [91], the loss of elastically active network chains in the cluster is fully compensated by higher cluster functionality. Hence, the crosslinking density can be calculated by the classic theory.

In heterogeneous systems, however, mechanical properties and the modulus depend on the composite morphology. The Kerner-Nielsen particulate composite model (see 1.10), taking into account the inorganic filler effect, and the empirical Davies model for bicontinuous morphology (1.14) were applied to treat the behavior of the O-I networks, in addition to the classical F-E theory.

Both experimental and theoretical values of the moduli in the rubbery state are given in Table 1.2. The experimental moduli of ASO-based networks are well predicted by the classic theory, using crosslinking density determined by the concentration

Table 1.2 Rubbery shear modulus of the O-I block copolymer networks

System	$G_c, 10^6$ (Pa) (at 25°C)			
	Experimental	Calculated		
		F-E	Kerner	Davies
SPOP2000	1.6	1.3	1.5	
EC-D2000, $r_{\text{AE}} = 1$	3.6	3.2 ^a	3.6 ^a	
SD400	4.1 ^a	4.4	5.7	
SPOP2000-TEOS (47 wt%)	8.7 ^a	1.5	2.2	9 ($c = 0.75$)
SPOP2000-TEOS (64 wt%)	44 ^a	1.5	2.8	36 ($c = 1$)
EC-D2000, $r_{\text{AE}} = 0.05$	9.5			12 ($c = 0.5$)

Davies model: c -fraction of the inorganic structure forming the continuous phase

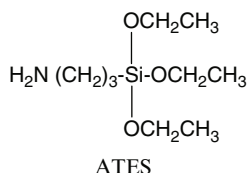
^aMeasured at T = 100°C

of the elastic oligomer and including the filler effect. The decreasing size of the oligomer corresponds to an increase in crosslinking density, and hence the networks prepared from shorter precursors ($M = 400$ compared to $M = 2000$) show higher moduli. The higher modulus of the EC-D2000 stoichiometric network with respect to SPOP2000 is the result of a higher crosslinking density. The primary amine group in diamine D2000 issues two branches to the epoxy agents, while the urethane or urea structure units in SPOP or SD networks issue one bond only [83]. An efficient reinforcement, however, was achieved, mainly in the systems with a high TEOS content where the continuous silica phase appears. Also, off-stoichiometric EC-D2000 network ($r_{AE} = 0.05$) comprising the continuous inorganic phase (see Fig. 1.20c) displays a high modulus. The hybrids with bicontinuous morphology are satisfactorily described by the Davies model, assuming that the fraction c of the inorganic structure forms the continuous phase.

1.3.3.3 Epoxy Networks with SSQO Grafted Along the Chain

In most cases, compatibilization of O–I systems by coupling agents is based on grafting inorganic structures along the polymer chain (see Scheme 1.2a). For the epoxy-silica nanocomposites, GTMS is the most widely employed coupling agent. The application of GTMS leads to improved thermal and mechanical properties of the nanocomposite. The effect of GTMS on hybrid synthesis and structure has been widely described [25–27, 92, 93].

In addition to the positive effect of grafting the silica structure to the epoxy network with GTMS, one has to also take into account a slight negative influence. GTMS is a monoepoxide agent, and its incorporation in the epoxy-amine network results in a decrease in crosslinking density of the organic phase and worsening of the initial matrix mechanical properties. A high GTMS amount could even lead to preventing the gelation of the epoxy-amine network. Therefore, composition of the system and content of GTMS must be optimized. Less detrimental to crosslinking density of the epoxy network is the application of another bifunctional coupling agent – (3-aminopropyl)triethoxysilane (ATES).



1.3.4 Network DGEBA-D2000-ATES

The DGEBA-D2000-ATES nanocomposite represents the epoxy-SSQO network containing inorganic domains grafted along the network chain, as shown in Scheme 1.2a, instead at the chain terminal position (see Scheme 1.2b) discussed in the

previous part. Upon synthesis of the network, a part of the tetrafunctional diamine crosslinker D2000 is replaced by ATEs, while the total ratio of amine and epoxy functionalities is kept constant and stoichiometric, $r_{AE} = 1$ [134]. The hybrid composition is characterized by the content of ATEs (x), corresponding to the molar fraction of NH groups of the system belonging to ATEs:

$$x = \frac{[-\text{NH}]_{\text{ATES}}}{\{[-\text{NH}]_{\text{ATES}} + [-\text{NH}]_{\text{D2000}}\}}$$

ATES is attached to the epoxy network by the reaction of the amino group with DGEBA. Due to a higher reactivity of the aliphatic amine ATEs toward DGEBA compared to D2000, stiff sequences $(\text{DGEBA-ATES})_n$ are formed in the case of one-step polymerization of the system DGEBA-D2000-ATES. Hydrolytic condensation of the pendant ethoxysilane groups results in formation of the SSQO structures covalently bonded to the network and finally producing the SSQO crosslinks. In addition, the reaction of SiOEt and SiOH, formed by hydrolysis of ATEs with C—OH, also takes place [25, 75, 94]. These condensation reactions are faster than epoxy-amine addition, and determine gelation of the system. As a result, the rate of gelation of the DGEBA-D2000-ATES hybrid increases with ATEs content.

The hybrid network shows a two-length scale character of the SSQO structures – the large aggregates composed of small particles. At low ATEs contents, the linear sequences of the SSQO particles grafted along the network chain are evidenced by TEM, as shown in Fig. 1.24a. The large aggregates formed in the network at a high ATEs content are illustrated in Fig. 1.24b. The size of the aggregates increases with ATEs amounts in the network.

The incorporation of ATEs in the epoxy network leads to increase in T_g and rubbery modulus (see Fig. 1.25). The O–I hybrid containing a sufficiently large amount of ATEs is microphase-separated, and displays two phases. The high- T_g phase corresponds to the stiff sequences ATEs-DGEBA confined by grafted SSQO structures, and flexible D2000 parts of the network chains form the low- T_g phase.

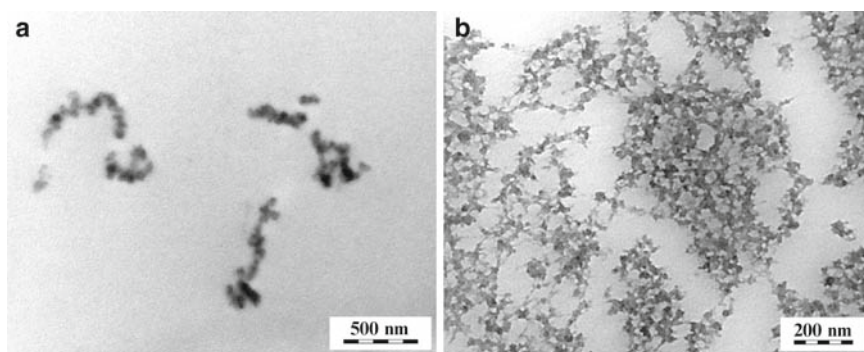


Fig. 1.24 TEM micrographs of DGEBA-D2000-ATES (x) nanocomposites. (1) $x = 0.50$, (2) $x = 0.75$

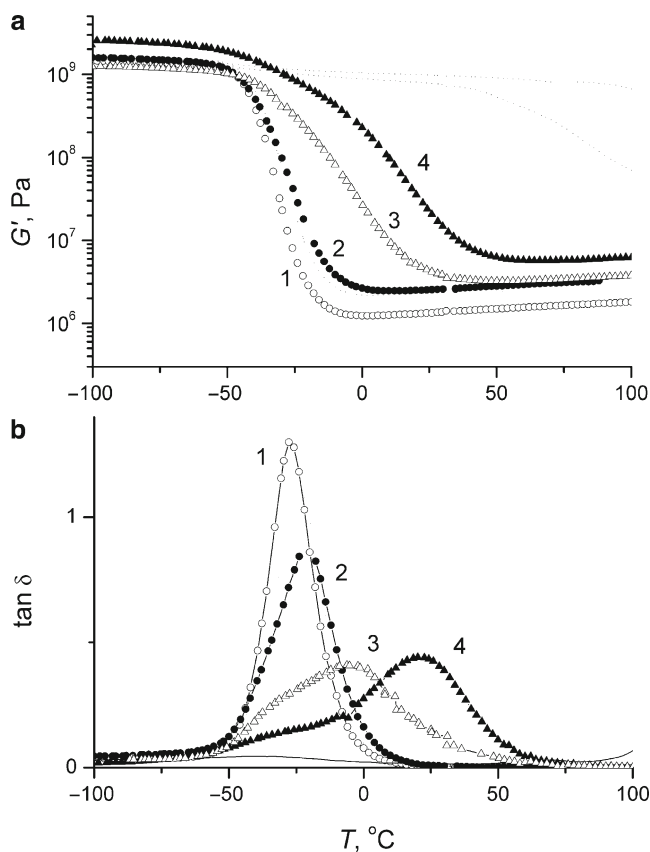


Fig. 1.25 Shear storage modulus G' (a) and loss factor $\tan \delta$ (b) of DGEBA-D2000-ATES (x) nanocomposites. (1) $x = 0.10$, (2) $x = 0.25$, (3) $x = 0.50$, (4) $x = 0.75$

The modulus increase is mainly a result of additional crosslinking through chemical junction domains of the SSQO aggregates.

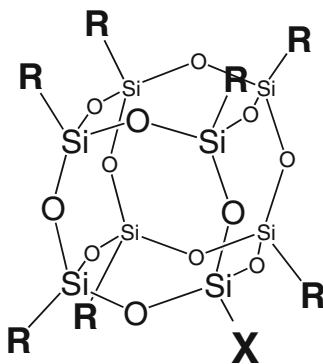
1.4 Epoxy Networks with Nanobuilding Blocks

1.4.1 Polyhedral Oligomeric Silsesquioxanes (POSS)

Defined inorganic clusters as nanobuilding blocks (NBB) are used to prepare well-characterized O-I nanocomposites. Incorporation of preformed organically functionalized dense inorganic structures into an organic polymer is widely described in the literature [3, 17]. Metal oxo-clusters of the nanoscale size based on silicon, tin, transition metals, or organically modified polyoxometalates are typical examples of NBB.

In recent times, polyhedral oligomeric silsesquioxanes (POSS) have been applied as the most common molecular building blocks. POSS are cluster-like oligomers with the general formula $(R-SiO_{1.5})_n$, mainly represented by cage-like octamer derivatives $(R-SiO_{1.5})_8$ – octasilsesquioxanes (T8 – POSS) [95]. The POSS molecule, with a size of 0.5–1.5 nm, is an ideal building block for the synthesis of new O–I polymers, as it resembles a nanosized particle of SiO_2 . Synthesis of POSS compounds was reviewed by Voronkov and Lavrentyev [96] and by Feher et al. [97]. POSS represents a core-shell nanosystem with the compact POSS core as a thermally robust framework and a shell of organic substituents (Scheme 1.9). These substituents control the miscibility of POSS with an organic matrix and make it possible to introduce POSS into polymer by physical blending. Functionalized POSS – i.e., a POSS unit with the reactive substituents X (Scheme 1.9) – is suitable for incorporation into a polymer by covalent bonding, either by grafting or copolymerization, to form linear or crosslinked POSS-polymers.

Incorporation of POSS into various polymers – polysiloxane [98], polymethacrylate [99], polystyrene [100], polyolefins [101], polyurethane [102] or polynorbornene [103] – results in an improvement of properties, such as increased glass-transition temperature, modulus, decomposition temperature, reduced flammability, and increased gas permeability. The compact nanometer-sized POSS unit in a polymer causes local chain reinforcement. POSS molecules in polymers tend to aggregate or even form crystallites [104, 105] acting as physical crosslinks. Lichtenhan et al. [106] suggested that POSS-POSS interactions have a dominant role in controlling the resulting physical properties of modified polymers. They revealed the critical POSS concentration above which POSS-POSS interactions percolate through the system. The properties are enhanced due to the formation of a physical network of the POSS continuous phase. In addition, the interchain interactions or inertia effect of a large mass POSS molecule are assumed to be responsible for retardation of polymer chain motion [104]. Theoretical simulation [107] of the POSS-polymer system shows that aggregation of POSS moieties is not required for slowing polymer chain relaxation. The main effect of POSS is serving as an anchoring point bound to the chain.



Scheme 1.9 POSS. R – inert organic substituents, X – reactive substituents

Fu et al. [108] have shown the effect of bonding of POSS moieties to a polymer chain. While POSS-POSS interactions dominate in physically blended systems resulting in aggregation of POSS molecules, the POSS-polymer interaction is more important in the polymers with the chemically grafted POSS. POSS covalently bound to the chain brings about a significant slowing down of chain relaxation [109]. However, no influence on the chain mobility was observed in the system with physically blended POSS molecules. Xu et al. [110] found that low content of unbound POSS behaves like a bulky diluent, decreasing the glass transition temperature T_g . In contrast, at high POSS contents, T_g increases due to POSS-chain and POSS-POSS interactions.

The monofunctional POSS cages are attached as dangling blocks to the polymer backbone, while the multifunctional POSS monomers are incorporated in the polymer as polyhedral crosslinks of the O–I networks. The networks based on vinyl polymers [111, 112], methacrylates [113], and based largely on epoxy resins were studied. In this case, often the single-phase polymer networks with POSS molecularly dispersed are formed. Recently, POSS-polymer nanocomposites have been reviewed by Li et al. [135] and by Joshi et al. [115].

1.4.2 Epoxy-POSS Networks

The Epoxy-POSS nanocomposites belong to the most studied POSS-polymer systems. The first POSS-containing epoxy networks were prepared by Crivello et al. [116] by homopolymerization of the octaepoxy-POSS monomer [117]. The polymerization resulted in the network of a low crosslinking density because of high extent of intramolecular reactions in the multifunctional monomer. Curing of polyepoxy-POSS with amines prevented the excessive cyclization reactions, and epoxy-POSS networks of a high crosslinking density were built-up. The polyepoxy-POSS units serve as junctions of the network, tethered with diamine molecules [31, 118–121]. In addition, octaamino-POSS derivatives were also applied to prepare epoxy-amine networks with POSS junctions [122, 123]. Moreover, POSS-triol compounds were incorporated in the DGEBA based epoxy network, as well [32, 124]. Both an increase [125] and decrease [30, 32] in glass transition temperature, as well as no change of T_g [114] or even absence of a transition [30], were determined. Two competing factors are decisive in affecting T_g of the POSS-polymers. Increase in free volume of the system by bulky POSS molecules leads to a decrease in T_g , while steric hindrance imposed by POSS to movement of the network chain tends to increase T_g . The rubbery modulus enhances due to a high crosslink density [30, 114] of the polyepoxy-POSS-based networks. The polyfunctional POSS is well dispersed in the matrix, even at a high content [30, 32, 114, 122]. The material is homogeneous at large length scale. However, POSS-rich aggregates were also detected in some systems [31, 112].

Less information is available about epoxy networks with POSS units dangling on the network backbone chain. Lee and Lichtenhan [29] proved that attachment of the monofunctional epoxy-POSS to the network DGEBA – butanediol diglycidyl

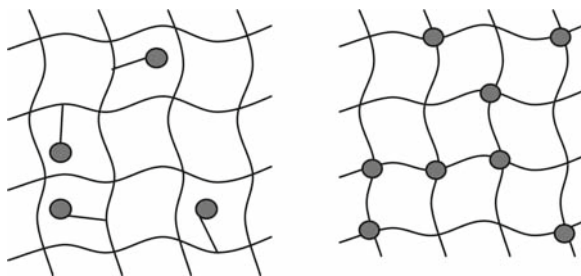
ether – poly(oxypropylene)diamine D230 (Jeffamine) resulted in broadening of the glass transition, increase in T_g , and slowing down of the chain relaxation in the glassy state. However, in the case of the monofunctional POSS, phase separation usually occurs due to incompatibility of the inorganic framework and organic matrix resulting in POSS aggregation. The phase separation in the POSS-polymer nanocomposites can be controlled by the type of POSS organic substituents and by covalent bonding to the polymer. The prereaction of the monofunctional epoxy-POSS with diamine [126] or of amino-POSS with a diepoxide monomer [127] partly suppresses POSS aggregation in the organic medium, and facilitates formation of a more homogeneous network. Moreover, the use of small curing agents such as dicyandiamide can avoid macrophase separation [127].

1.4.2.1 Network DGEBA-D2000-POSS

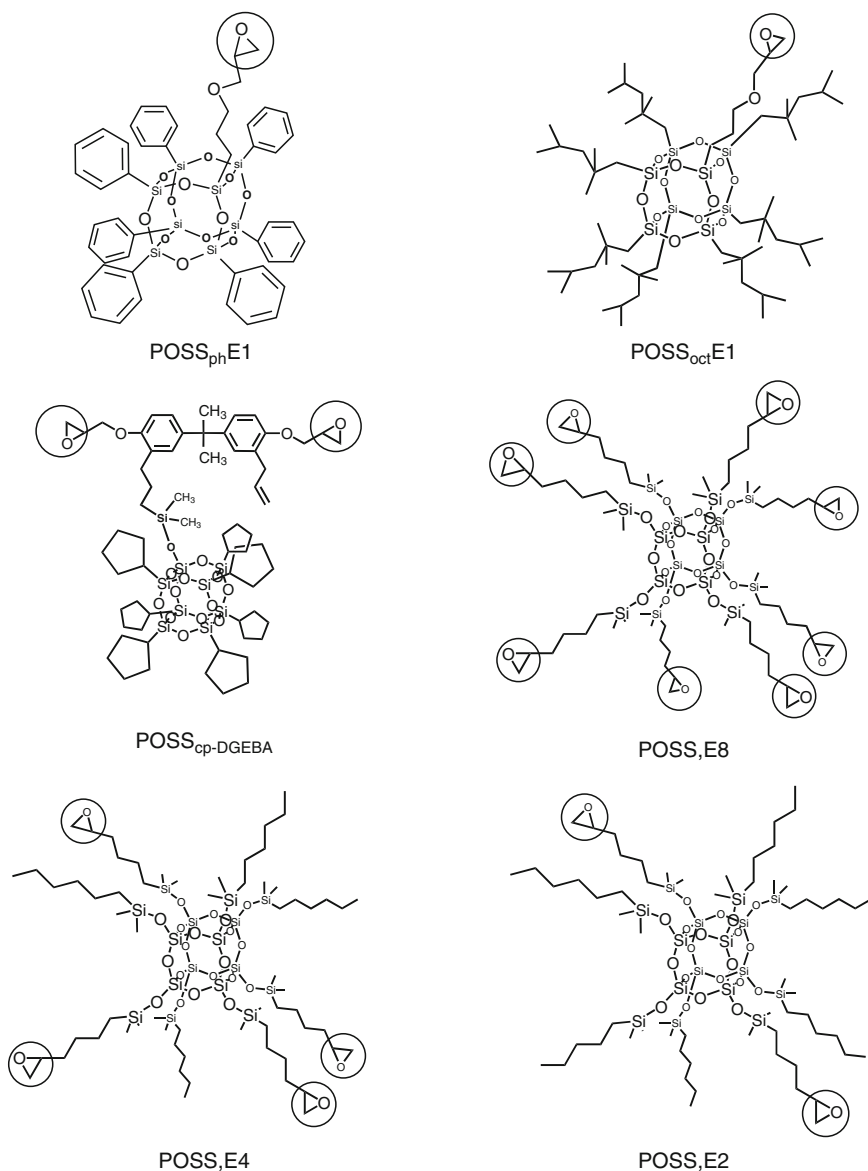
The effect of POSS on the network formation as well as on structure, morphology, and material properties of the Epoxy-POSS nanocomposites will be illustrated by using the system based on the epoxy network DGEBA-D2000 [128–130]. Two types of epoxide nanocomposites will be discussed: (a) networks with POSS attached as a pendant unit on the network chain, and (b) networks with POSS as a compact polyhedral network junction (Scheme 1.10). Mainly, the influence of the character of POSS substituents and topological localization of POSS in the network will be described.

POSS Monomers

The epoxy-functionalized POSS monomers (POSS,En) with various substituents are illustrated in Scheme 1.11. POSS with typical substituents – phenyl, isooctyl, or isobutyl and cyclopentyl – were used. The monoepoxy-POSS and DGEBA based



Scheme 1.10 POSS-containing networks. POSS as pendant units on the chain or as junctions of the network



Scheme 1.11 Epoxy-functional POSS monomers

cyclopentyl-substituted monomer POSS_{DGEBA} are available at Hybrid Plastics. The multifunctional epoxy-POSS with 2–8 epoxy groups was synthesized by hydrosilylation from the octasilane [octakis(dimethylsilyloxy)-T8-silsesquioxane] (Q8M8H8) and 5,6-epoxyhex-1-ene. POSS-tetraepoxide (POSS,E4) and POSS-diepoxy (POSS,E2) were prepared by using a mixture of 5,6-epoxyhex-1-ene and hex-1-ene,

the composition of which determines the ratio of functional and non-functional substituents in POSS [128]. While the monoepoxy-POSS monomers contain a T8 silsesquioxane core, the polyepoxy-POSS and $\text{POSS}_{\text{DGEBA}}$ involve a Q8M8H8 (octakis(dimethylsilyloxy)-T8-silsesquioxane) framework.

Synthesis of the DGEBA-POSS-D2000 Networks

The nanocomposite networks were synthesized by the crosslinking reaction of DGEBA and epoxy-POSS monomer with diamine D2000. The epoxy networks with pendant POSS were prepared using the monoepoxide-POSS compound, POSS,E1. A fraction x of the diepoxide DGEBA of the basic network DGEBA-D2000 was replaced by the monoepoxide and the content of dangling POSS units in the modified epoxy network $\text{DGEBA}(1-x) - \text{POSS,E1}(x) - \text{D2000}$, was controlled by the ratio of both epoxy monomers. The total concentration of epoxy groups was kept constant and equal to the concentration of NH groups in diamine D2000. Incorporation of the monofunctional monomer into the epoxy network, however, leads to a decrease in crosslinking density. Therefore, we prepared the epoxy networks with pendant POSS also using diepoxide DGEBA containing the cyclopentane-substituted POSS unit, $\text{POSS}_{\text{DGEBA}}$ (see Scheme 1.11). In this case, the network $\text{DGEBA} - \text{POSS}_{\text{DGEBA}}(x) - \text{D2000}$ displays no decrease in crosslinking density, compared to the reference DGEBA-D2000 network. The epoxy networks involving POSS units as network junctions of various functionality were synthesized by the reaction of D2000 with multifunctional epoxy-POSS monomers – octaepoxides (POSS,E8) and tetraepoxides (POSS,E4). Diepoxide-POSS monomer POSS,E2 was incorporated in the backbone of the network.

The epoxy-POSS systems were cured at 120°C for 3 days. The initially inhomogeneous reaction mixtures with POSS-monoepoxides $\text{POSS}_{\text{ph}}\text{E1}$ and $\text{POSS}_{\text{oct}}\text{E1}$ were homogenized by reaction blending. The system with a less compatible POSS monomer containing cyclopentane substituents $\text{POSS}_{\text{cp-DGEBA}}$ was cured as a 50% toluene solution. The reaction mixtures containing liquid multifunctional epoxy-POSS monomers (POSS,En) were transparent. The content of the POSS units in the DGEBA-POSS-D2000 networks ranges from 7 to 77 wt%.

1.4.2.2 Networks with Pendant POSS

Network DGEBA-POSS,E1-D2000

The structure and morphology of POSS-containing networks depend on the compatibility of the organic matrix with POSS monomers, given mainly by the type of substituents of the POSS core. Both octyl- and phenyl- substituted POSS (POSS_{oct} , POSS_{ph}) are immiscible with components of the organic medium, and show a tendency to aggregation. The procedure of reaction blending partly contributes to overcoming this problem. However, the prereaction of the POSS monomer in the two-step procedure [126, 127] is a more efficient way to avoid aggregation.

Network Formation

Both thermodynamic factors and kinetic aspects during network formation contribute to the evolution of the network structure. Contrary to the nanocomposites with in situ generated inorganic domains, in the case of the networks with POSS the epoxide-amine addition is the only reaction during the hybrid network formation. Structure evolution and incorporation of the POSS unit in the DGEBA-D2000 network is governed by the relative reactivity of the epoxy functionalities in both monomers, POSS_{E1} and DGEBA. Due to steric hindrance of the POSS epoxy group by neighboring POSS substituents, the reactivity of the epoxy-POSS monomer with amines is lower, compared to DGEBA [130]. Mainly, bulky branched isooctyl substituents in POSS_{oct}E1 significantly decrease the reactivity of the POSS epoxy group, while phenyl substituents in POSS_{ph}E1 display a smaller effect on the epoxy-POSS reactivity. As a result, the POSS_{E1} monomer is incorporated in the network DGEBA-D2000 only in the late reaction stage. Therefore, a non-random inhomogeneous distribution of POSS in the network is expected to be formed. Likely blocks of POSS units are attached to the chain in the DGEBA-POSS_{E1}-D2000 nanocomposite. The prereaction of POSS_{E1} with diamine D2000 eliminates the kinetic contribution to the system inhomogeneity.

Structure and Morphology

The phenyl-substituted POSS monomer (POSS_{ph}E1) is crystalline, and displays sharp reflections in the WAXS diffractogram (Fig. 1.26a). POSS crystallinity is not suppressed by polymerization and incorporation in the network; however, the covalently attached POSS unit is subjected to a significant steric restriction for the crystallization. Therefore, the structure of the crystalline domains in the networks with pendant POSS_{ph} is modified with respect to that of the monomer, crystallizing without any hindrance. This is evidenced by change of the WAXS profile (see Fig. 1.26a, b).

The nanocomposites show a morphology with more or less isotropic spherical crystal domains (see TEM micrograph in Fig. 1.27). The size of the crystallites in the network reaches the value $L = 25\text{--}40$ nm (determined from the width of the WAXS peak), in accordance with TEM results. The hybrid networks with a high POSS content (more than 25 wt% POSS) exhibit a slight structure ordering, as revealed by SAXS [128]. The ordered arrangement with a characteristic separation distance between POSS crystallites ($d \sim 12$ nm) is fixed only by crosslinking of the hybrid system. No ordering was observed in the uncrosslinked polymer with the same amount of POSS_{ph}.

The POSS monomer with isooctyl ligands, POSS_{oct}E1, is a liquid with no tendency to crystallize, and the network containing a pendant POSS_{oct} unit, DGEBA-POSS_{oct}E1-D2000, is amorphous. Due to poor compatibility with the matrix, the POSS units aggregate in the network, and the extent of aggregation increases with content of POSS. Figure 1.27c reveals broad amorphous maxima corresponding to POSS aggregates.

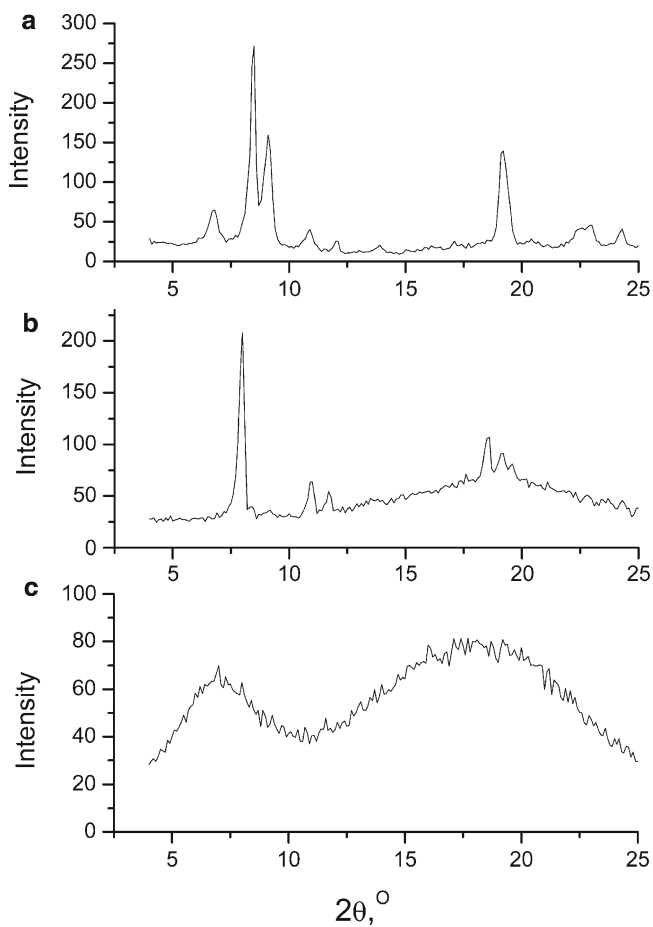


Fig. 1.26 WAXS profiles of the (a) monomer $\text{POSS}_{\text{ph}} \text{E1}$, (b) network $\text{DGEBA-POSS}_{\text{ph}} \text{E1-D2000}$, (c) network $\text{DGEBA-POSS}_{\text{oct}} \text{E1-D2000}$

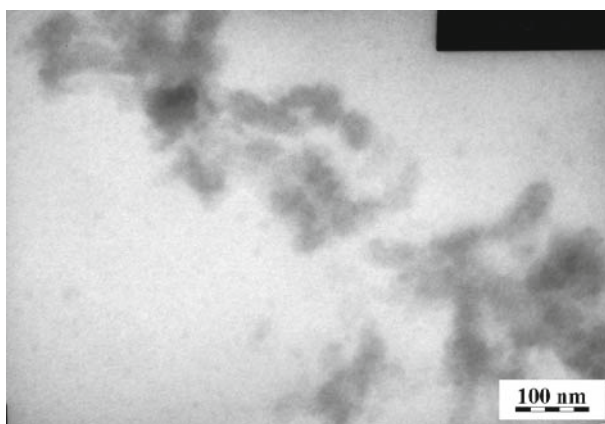


Fig. 1.27 TEM micrograph of the $\text{DGEBA-POSS}_{\text{ph}} \text{E1-D2000}$ nanocomposite

Thermomechanical Properties

The incorporation of a monofunctional monomer into a network leads to chain termination and formation of defects in the network. As a result, the crosslinking density and the rubbery modulus are reduced, compared to the diepoxy-diamine network (DGEBA-D2000). Therefore, the effect of pendant POSS on the network properties was determined by a comparison with the reference POSS-free network of a similar crosslinking density, prepared using the same molar fraction of the monoepoxide phenyl glycidyl ether (PGE), DGEBA-PGE(x)-D2000.

Mechanical properties of the Epoxy-POSS networks strongly depend on the type of substituents of the pendant POSS. While the network DGEBA-POSS_{oct}E1 ($x = 0.33$)-D2000 with isooctyl-substituted POSS shows a lower rubbery modulus compared to the reference system, the network with phenyl ligands, DGEBA-POSS_{ph}E1($x = 0.33$)-D2000 (25 wt% POSS), exhibits a higher modulus (see Fig. 1.28). The difference in mechanical properties reflects the nanocomposite morphology.

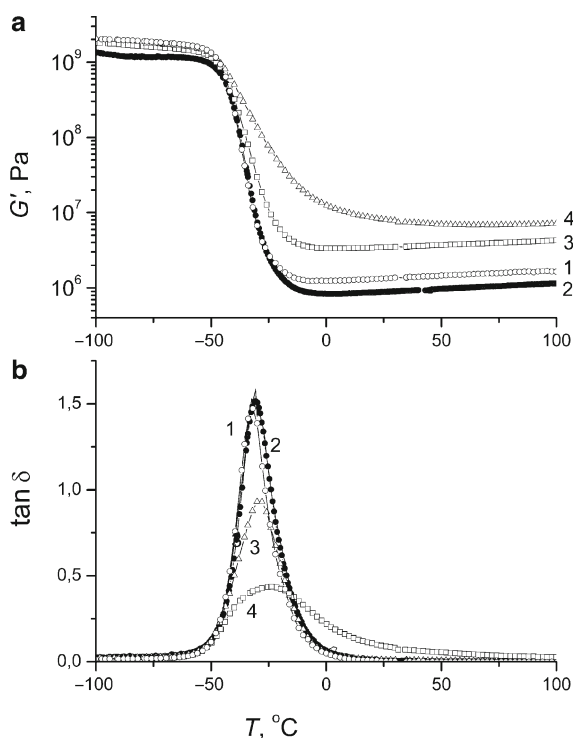
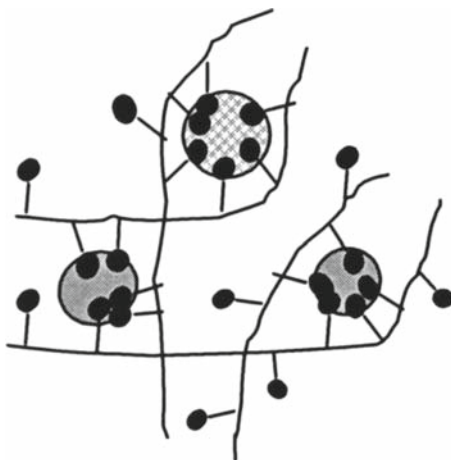


Fig. 1.28 Shear storage modulus G' (a) and loss factor $\tan \delta$ (b) of the networks containing pendant POSS as a function of temperature. (1) DGEBA-PGE($x = 0.33$)-D2000, (2) DGEBA-POSS_{oct}E1($x = 0.33$)-D2000, (3) DGEBA-POSS_{ph}E1($x = 0.33$)-D2000, (4) DGEBA-POSS_{ph}E1($x = 0.67$)-D2000

Scheme 1.12 Structure model of DGEBA- POSS_{ph} E1-D2000 network



The POSS crystalline domains in the nanocomposite DGEBA- POSS_{ph} E1-D2000 act as polyfunctional POSS clusters and create physical crosslinks, as depicted in Scheme 1.12. These crystalline junctions are responsible for the reinforcement of the epoxy network. In the network DGEBA- POSS_{ph} E1 ($x = 0.67$)-D2000 with a higher POSS content (48 wt% POSS), the chemical crosslinking density is very severely reduced (by an order of magnitude) due to presence of the monoepoxide. However, the experimental modulus is even higher than that of the network, with a lower monoepoxide-POSS content, $x = 0.33$. The modulus increases despite a lower chemical crosslinking. This is the result of a higher amount of POSS crystalline physical crosslinks.

In contrast, the amorphous aggregates of POSS_{oct} in the DGEBA- POSS_{oct} E1-D2000 network are presumably too weak to form stable physical crosslinks. The bulky pendant POSS_{oct} unit acts as a diluent, and the modulus decreases with respect to the reference DGEBA-PGE-D2000 network.

The POSS modified networks display no, or only a mild, change in the glass transition temperature (see Fig. 1.28), implying no, or a very weak, interaction between POSS and the polymer. A very high amount of POSS_{ph} (~50 wt%) is necessary to affect the polymer chain mobility. Due to severe incompatibility, the interphase layer around the POSS crystallites is narrow, and a very small fraction of the chains are involved and immobilized. At moderate POSS contents, the POSS-chain interaction is negligible and the POSS-POSS interactions dominate, being crucial for mechanical properties of the nanocomposites.

Network $\text{POSS}_{\text{DGEBA}}$ - D2000

The epoxy networks with pendant POSS and nonreduced crosslinking density are prepared using the diepoxide monomer $\text{POSS}_{\text{DGEBA}}$ with cyclopentyl substituents (see Scheme 1.11).

Network Formation, Structure and Morphology

During network formation, a gradual microphase separation takes place followed by ordering of the crystalline POSS domains in the epoxy-POSS network. The evolution of the structure in polymerization of the $\text{POSS}_{\text{DGEBA}} - \text{D2000}$ mixture, followed in situ by SAXS, is shown in Fig. 1.29. In the initial mixture, the small POSS crystallites are dispersed in the organic matrix. The sharp peaks at $q = 5.65$ and 7.6 nm^{-1} characterize crystallinity in the system. POSS crystallinity is not disturbed by the reaction; moreover, the crystalline structure of the $\text{POSS}_{\text{DGEBA}}$ unit is not even modified by incorporation in the network, in contrast to the case of POSS_{ph} . The dispersed POSS crystallites, however, are gradually transferred into the microphase-separated POSS-rich regions, as revealed by the decrease in scattered intensity background corresponding to dispersed POSS. Finally, the crystalline POSS domains assemble in the lamellar structure within the epoxy network. The SAXS maximum appearing at $q \sim 0.8 \text{ nm}^{-1}$ during polymerization, as well as a small second maximum at $q \sim 1.6 \text{ nm}^{-1}$, characterize lamellar arrangement. The crystallite size in one dimension determined by WAXS is $L = 19.5 \text{ nm}$. The layered structure in the $\text{POSS}_{\text{DGEBA}} - \text{D2000}$ nanocomposite is obvious from the TEM micrograph in Fig. 1.30. The correlation distance d between the scattering POSS layers is 8 nm , which is somewhat shorter than the contour length of the D2000 chain (10 nm). The regularity

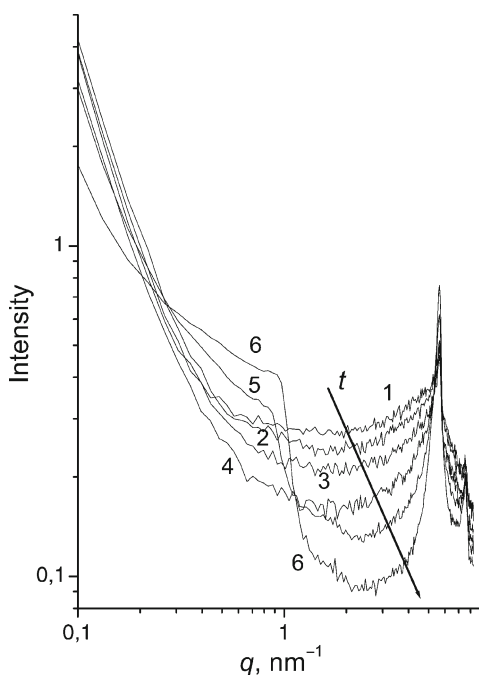


Fig. 1.29 Evolution of the SAXS profiles during formation of the $\text{POSS}_{\text{DGEBA}} - \text{D2000}$ network. Curves (reaction times): (1) $t = 0$, (6) $t = 563 \text{ min}$; $T = 120^\circ\text{C}$

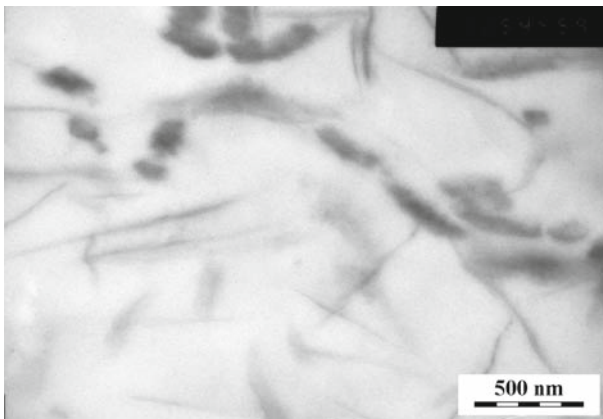
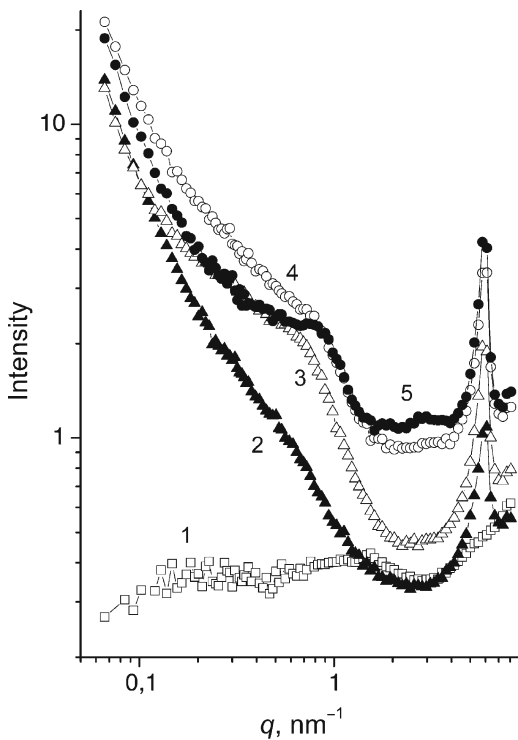
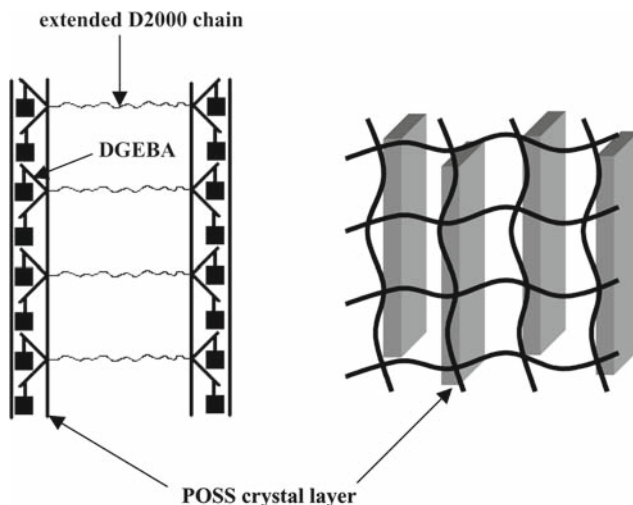


Fig. 1.30 TEM micrograph of the $\text{POSS}_{\text{DGEBA}}\text{-D2000}$ network

Fig. 1.31 SAXS profiles of the DGEBA- $\text{POSS}_{\text{DGEBA}}(x)\text{-D2000}$ networks of various $\text{POSS}_{\text{DGEBA}}$ content x . (1) $x = 0$ (DGEBA-D2000 network), (2) $x = 0.25$, (3) $x = 0.50$, (4) $x = 0.75$, (5) $x = 1$ ($\text{POSS}_{\text{DGEBA}}\text{-D2000}$ network)



of the arrangement decreases with diminishing content of the $\text{POSS}_{\text{DGEBA}}$ monomer (see Fig. 1.31). At the number of POSS units $x < 0.25$ in the network $\text{DGEBA}(1 - x)\text{-POSS}_{\text{DGEBA}}(x)\text{-D2000}$, the POSS ordering disappears.



Scheme 1.13 Structure model of $\text{POSS}_{\text{DGEBA}}\text{-D2000}$ network

The structure model of the $\text{POSS}_{\text{DGEBA}}\text{-D2000}$ network given in Scheme 1.13 consists of the lamellar ordering of the POSS crystal domains separated by the extended D2000 chain. This is an analogy to the organized block copolymers, where the chains are stretched along the direction perpendicular to the microdomain interface. The model is based on the structure ordering in the DGEBA-Jeffamine networks. Beck et al. [131] determined a regular arrangement in the DGEBA-Jeffamine system involving stiff polyepoxy-chain sequences separated by flexible poly(oxypropylene) Jeffamine chains. Such a network serves as a template to direct assembly of the POSS units pendant on DGEBA in the $\text{POSS}_{\text{DGEBA}}$ monomer into layered arrangement.

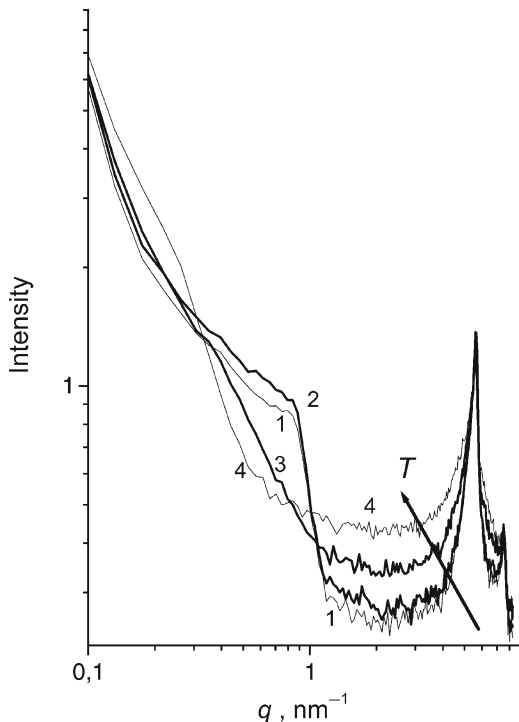
The structure of this epoxy-POSS network is temperature-dependent. The ordered arrangement disappears above the critical temperature $T \sim 120^\circ\text{C}$, as illustrated by SAXS profiles at different temperatures in Fig. 1.32. The order-disorder transition consists of disordering of the POSS crystal lamellar domains, while the crystallinity is preserved at this temperature.

Thermomechanical Properties

The POSS layered crystalline domains bring about a reinforcement of the polymer network due to physical crosslinking. The modulus above glass transition temperature increases with increasing content of POSS in the network $\text{DGEBA}(1-x)\text{-POSS}_{\text{DGEBA}}(x)\text{-D2000}$, as depicted in Fig. 1.33 [134]. The network $\text{POSS}_{\text{DGEBA}}(x=1)\text{-D2000}$, containing 21 wt% POSS, exhibits a modulus higher by 1.5 orders of magnitude, compared to the reference DGEBA-D2000 network.

A sufficiently high POSS amount, however, is necessary to develop the lamellar structure displaying a reinforcing effect. Small content of POSS, up to $x = 0.25$

Fig. 1.32 Effect of temperature on SAXS profiles of the POSS_{DGEBA}-D2000 networks. Curves (temperatures): (1) 100°C, (2) 120°C, (3) 150°C, (4) 200°C



(~10 wt%), almost does not affect the dynamic mechanical behavior of the network (see Fig. 1.33), because of the absence of ordered structure (see Fig. 1.31). Only a POSS fraction $x \geq 0.5$ leads to a substantial enhancement of the modulus and appearance of a distinctly microphase-separated morphology that is manifested by a new damping peak of the loss factor $\tan \delta$ curve in Fig. 1.33b. This new phase corresponds to the polymer confined within the region of the ordered lamellar POSS crystal domains. Above T_g of the neat network, there is a second relaxation transition, characterized by a more or less steep drop-off modulus to the equilibrium value. At increasing POSS content, this transition is more distinct and is shifted to a higher temperature. In the network POSS_{DGEBA}-D2000 with the best developed lamellar structure, the steep fall of the modulus occurs at a critical temperature $T \sim 120^\circ\text{C}$, in agreement with the order-disorder transition temperature determined by SAXS. The better ordered the lamellar arrangement, the narrower is the temperature range of the order-disorder transition and the steeper is the modulus drop. The transition and the thermomechanical behavior in the transition region are reversible. By cooling down the nanocomposite below the critical temperature, a relatively fast (within 5 min) increase in the modulus with respect to the initial value takes place.

The lamellar arrangement, however, is imperfect, and only a fraction of the network chains is confined, which results in the microphases of the unconfined and immobilized network chains. Glass transition of the microphase that comprises network

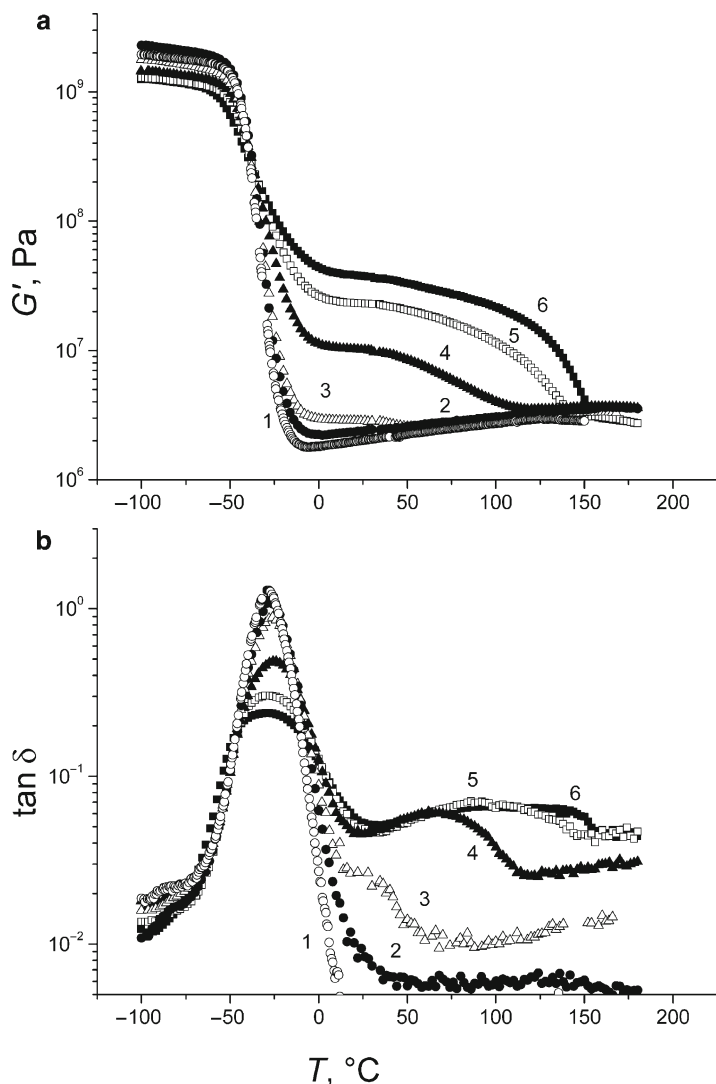


Fig. 1.33 Shear storage modulus G' (a) and loss factor $\tan \delta$ (b) of the DGEBA- $\text{POSS}_{\text{DGEBA}}(x)$ -D2000 networks of various $\text{POSS}_{\text{DGEBA}}$ content x . (1) $x = 0$ (DGEBA-D2000 network), (2) $x = 0.10$, (3) $x = 0.25$, (4) $x = 0.50$, (5) $x = 0.75$, (6) $x = 1$ ($\text{POSS}_{\text{DGEBA}}$ -D2000 network)

chains confined between the POSS layers dramatically enhances with increasing POSS content in the network (see Fig. 1.33). The increase in T_g exceeds 100°C in case of high POSS content $x > 0.5$. A two-phase model based on dielectric studies of molecular mobility has been recently proposed [132]. While a fraction of the polymer at the interface with the POSS layer is immobilized, the other polymer part displays slightly faster dynamics due to an increased free volume.

1.4.2.3 Network with POSS in Junctions

The formation of the networks from polyepoxy-POSS monomers, POSS,En, and the diamine D2000 is very slow, particularly in the case of POSS,E8. Steric hindrance around the POSS core is a reason for a low reactivity of the epoxy-POSS groups. Moreover, a preferential cyclization of the primary amine group with the two neighboring epoxy functionalities of the POSS,E8 monomer brings about a delay of gelation.

Structure and Morphology

The phase structure evolution during the network build-up is determined by competition between phase separation of the components and compatibilizing grafting reaction. Early chemical bonding of POSS to a polymer during formation of the epoxy-POSS hybrid prevents phase separation due to POSS aggregation [133]. The initially inhomogeneous reaction mixture POSS,E8 –D2000 contains POSS amorphous aggregates characterized by SAXS maximum at $q \sim 4.5 \text{ nm}^{-1}$, as shown in Fig. 1.34. During polymerization, these aggregates are gradually broken, and the POSS units become more dispersed in the organic medium. At the same time, an ordered structure develops, with regularly arranged POSS crosslinks domains separated by D2000 chains. The growing interference maximum at $q = 1\text{--}2 \text{ nm}^{-1}$ characterizes this ordering. The correlation distance d between crosslinks increases during the reaction,

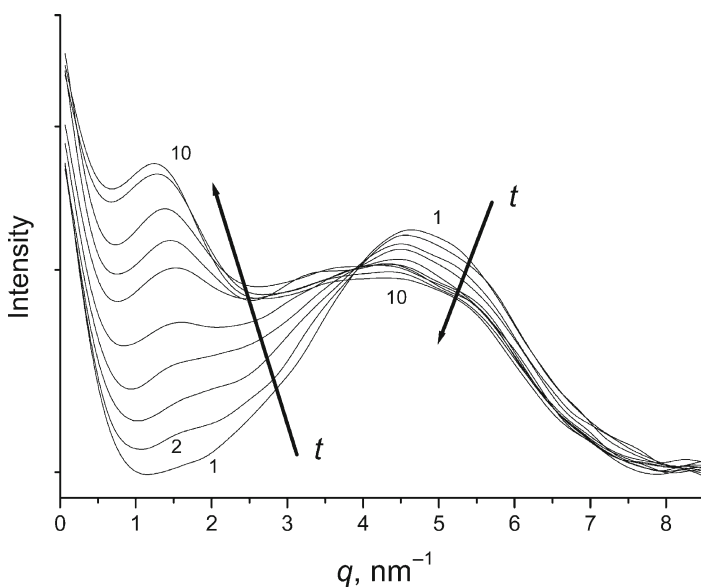
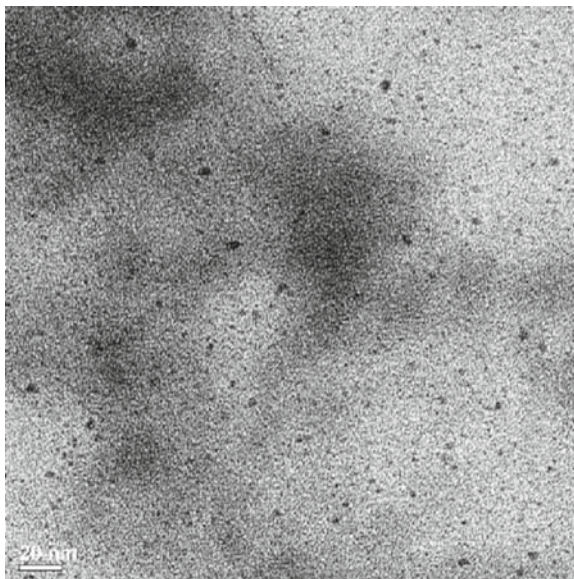


Fig. 1.34 Evolution of the SAXS profiles during formation of the POSS,E8-D2000 network. Curves (reaction times): (1) $t = 0$, (10) $t = 90 \text{ h}$; $T = 120^\circ\text{C}$

Fig. 1.35 TEM micrograph of the POSS,E8-D2000 nanocomposite



$d = 3.8\text{--}5.1$ nm, because D2000 chain tends to be more extended due to increasing steric restrictions and overcrowding space around the POSS junction.

In the cured network POSS,E8–D2000, the POSS in junctions are well dispersed in the matrix compared to the systems with pendant POSS (see Fig. 1.35). However, they are not completely dispersed at the molecular level. A small fraction of aggregates of size up to ~ 4 nm remain in the nanocomposite. The extent of aggregation increases with decreasing functionality of the POSS monomer in the series POSS,E8 < POSS,E4 < POSS,E2. The polyfunctional POSS units are shielded by D2000 chains attached during the reaction, thus enabling POSS dispersion. This steric hindrance diminishes at low POSS functionality, and therefore POSS,E2 in the backbone shows a higher extent of aggregation. In contrast, decreasing POSS functionality and formation of aggregates leads to a loss of long-range ordering. The POSS,E4-D2000 and POSS,E2-D2000 networks exhibit broader distribution of distances between POSS units and a decrease in the SAXS interference maximum intensity.

Thermomechanical Properties

The rubbery modulus of the hybrid networks increases with increasing crosslinking density, determined by functionality of the POSS monomers in the series POSS,E2-D2000 < POSS,E4-D2000 < POSS,E8-D2000 (Fig. 1.36). The network POSS,E8-D2000 is relatively homogeneous, and therefore the modulus could be successfully predicted by using the mean-field statistical theory of network formation and by the theory of rubber elasticity [90]. In contrast, the moduli of the inhomogeneous

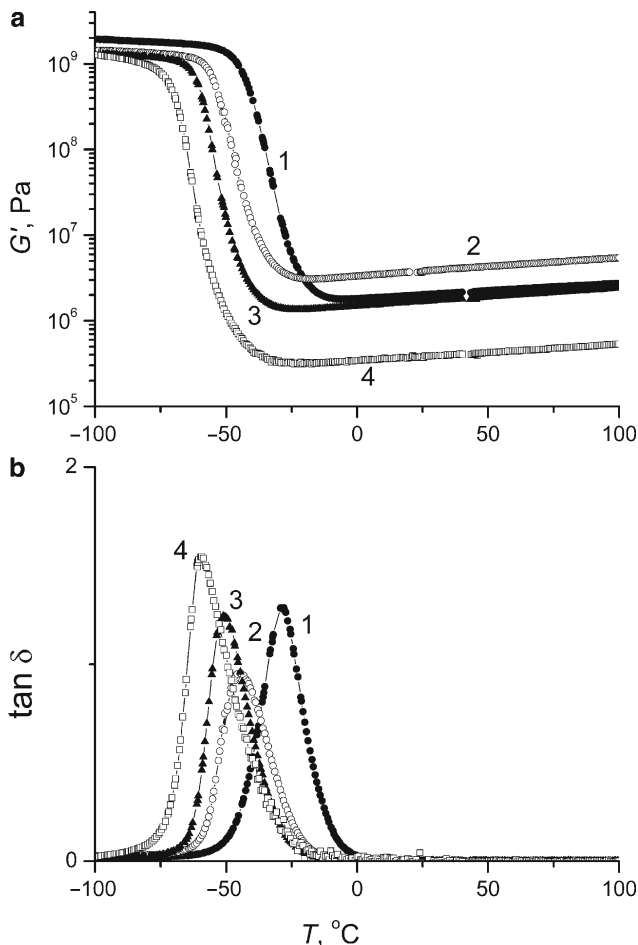


Fig. 1.36 Shear storage modulus G' (a) and loss factor $\tan \delta$ (b) of the networks with POSS in junctions of various functionality. (1) DGEBA-D2000, (2) POSS,E8-D2000, (3) POSS,E4-D2000, (4) POSS,E2-D2000

networks POSS,E4-D2000 and POSS,E2-D2000 are significantly lower with respect to the theory, and lower compared to the reference DGEBA-D2000 network. Due to POSS aggregation, the epoxy functional groups are buried in the aggregates and are not sterically accessible to the reactants. The incomplete conversion leads to a high sol fraction and a lower crosslinking density.

The multi-epoxy-POSS units contain flexible hexyl substituents, and act in the network as “soft” junctions. The networks chain mobility is less restricted by these POSS crosslinks than by the stiff DGEBA species in the DGEBA-D2000 network. Therefore, the glass transition temperature of these POSS-containing networks is lowered compared to the reference system (see Fig. 1.36). In addition, T_g drops with

decreasing functionality of the epoxy-POSS monomer because of decreasing crosslinking density.

Thermal Stability

The thermal stability of epoxy systems is improved by incorporation of POSS as pendant units and increases with increasing POSS content in the networks. The higher stability is significant mainly at heating in the air atmosphere, implying an improved thermal oxidation resistance, while in nitrogen the effect is much smaller. The temperature $T_{5\%}$, at which 5% loss of mass occurs, is increased by 20–25°C in the networks with phenyl- and cyclopentyl-substituted POSS (25 wt% POSS) in the air. “Soft POSS” in the network, containing isooctyl ligands, increases the $T_{5\%}$ only by 3°C. In contrast, the thermal stability of the networks with POSS in junction units is low and $T_{5\%}$ drops, compared to the reference network. The fast initial thermal degradation is a result of a higher mobility of network chains and lower T_g . Moreover, the POSS in junctions contains the core Q8M8H8, which is less thermally stable than the T8 core involved in the networks with pendant POSS.

The highest thermal stability was determined in the hybrid networks showing a strong POSS-network chain interaction. Because of this interaction, the organic chain is shielded by the inorganic structure. Consequently, the POSS–chain interaction, the POSS content, and the nature of the POSS ligands are the factors governing thermal stability of POSS-containing networks.

1.5 Conclusions

The epoxy-silica/SSQO nanocomposites belong to the most popular organic–inorganic polymer materials. In this chapter, we have discussed the rubbery epoxide networks with silica/SSQO nanodomains generated in situ by the sol–gel process and the networks containing well defined inorganic nanobuilding blocks. The formation, structure, and properties of the following O–I polymer networks have been investigated:

(a) The epoxy-silica network DGEBA-D2000-TEOS was prepared by hydrolytic polycondensation of TEOS in the epoxide-amine medium. (b) The controlled covalent bonding between phases was achieved by using the O–I precursors – alkoxy silane-encapped oligomers (ASO) or epoxyfunctional SSQO clusters (EC). Sol–gel polymerization of ASO or the reaction of EC with oligomeric diamine (D2000) resulted in the O–I block copolymer networks with SSQO crosslink domains. (c) The coupling agent ATEs was used to synthesize the epoxide network, grafted with the SSQO structures along the network chain (DGEBA-D2000-ATEs). (d) The well-defined functional inorganic units – POSS – were incorporated in the epoxide network. The monoepoxy-POSS monomers were applied to prepare the epoxy network with pendant POSS blocks (DGEBA-D2000-POSS,E1)

and the octaepoxy-POSS monomers for synthesis of the network with POSS junctions (POSS,E8-D2000).

1.5.1 Formation, Structure and Morphology of the O–I Networks

Process of the O–I hybrid network formation includes the *molecular structure evolution* during polymerization and, because of incompatibility of the reacting components or arising O and I structures, *phase structure evolution* is also of primary importance.

In situ generation of the silica/SSQO nanodomains within the epoxide network proceeds by the simultaneous or sequential polymerization of organic and inorganic monomers or O–I precursors. The polymerization is mostly performed in the initially homogeneous mixture (by using cosolvents, diluents) containing molecularly dispersed monomers. During network formation, however, depending on the reaction conditions, a polymerization-induced phase/microphase separation takes place.

In the *simultaneous polymerization* of the epoxy-TEOS system, the evolution of both organic and inorganic (siloxane, silica) molecular structures occurs via two independent reaction mechanisms: the epoxide-amine reaction and the sol–gel process. The hydrolytic polycondensation is sensitive to the reaction conditions, and this fact can be used to control formation and structure of the O–I polymers. In addition to the amount of water, solvent, or similar agent, the type of catalysis and the polymerization procedure are particularly decisive for the rate of polymerization, reaction mechanism, the structure growth, and the final morphology. The acid catalysts promote hydrolysis, while polycondensation, as well as formation of the gel, is slow. A relatively fine morphology with small and loose siloxane/silica structures containing a high amount of SiOH is produced. The nanocomposites display a *bicontinuous morphology* i.e., the IPN of silica and epoxy networks. Often, the phase separation by spinodal decomposition is the reason for the bicontinuous phase structure of the hybrids prepared by using TEOS [28]. In contrast, basic or DBTDL catalysis mainly accelerates polycondensation. Large and compact siloxane/silica structures are formed from the very beginning of the reaction, and early phase separation takes place to form more heterogeneous morphology compared to acid catalysis. The basic conditions initiate phase separation by nucleation, growth, and formation of particulate composites [28]. Due to the compatibilizing effect of D2000, however, all the DGEBA-D2000-TEOS networks show a bicontinuous structure with a variable degree of continuity.

The hybrid synthesis is performed either in one or two steps, thus allowing for optimization of the reaction conditions. From a practical point of view, the two-step acid-base polymerization is very efficient, involving prehydrolysis of the TEOS monomer under acid catalysis, followed by a very fast polycondensation and gelation in a basic medium. The epoxy-silica network of fine morphology with the small silica aggregates is produced by this procedure. This is the result of an early termination of the phase separation process, due to a very fast gelation that occurs during the polymerization. The system demonstrates the important

morphology-controlling factor – competition between the rates of polymerization and phase separation.

Sequential polymerization is another synthesis procedure. The epoxide network is formed first, and the sol–gel polymerization of TEOS proceeds within the network. In this case, the relative rates of diffusion of TEOS into the network and of the sol–gel process affect the growth of the silica structures. This procedure, however, generates the finest epoxy-silica morphology, due to the steric restrictions limiting silica growth within the network.

Crosslinking of the O–I precursors (ASO, EC-D2000) leads to formation of the O–I block copolymer network, with SSQO junction domains linked with organic chains. The crosslinking takes place by hydrolytic condensation of the terminal alkoxy silane groups in ASO, or by the epoxide-amine reaction in the case of EC-D2000.

The structure evolution during polymerization and morphology of the *O–I block copolymer network* from ASO is determined by catalysis of the sol–gel process and by the length of the ASO organic chain. The junctions of the network crosslinked under acid catalysis consist of small, loose SSQO clusters (1–3 nm) containing mainly linear siloxane sequences. On the contrary, basic or DBTDL catalysis results in a network with highly condensed, compact SSQO junctions. Decreasing the length of the endcapped oligomer leads to formation of larger SSQO clusters. The sol–gel polymerization of alkoxy silane groups undergoes competition between the intra- and intermolecular condensation reactions. In the long organic ASO chains, the intramolecular condensation dominates to produce small, compact clusters at the chain ends. In contrast, in the case of short ASO organic chains, the intermolecular polycondensation prevails, the SSQO clusters grow, and the continuous SSQO structure is formed. The O–I hybrid shows two percolation thresholds corresponding to formation of the O–I block copolymer network and build-up of the SSQO network. Hence, the bridged SSQO with the short organic bridges usually comprise the continuous inorganic phase.

The *epoxy-SSQO block copolymer network* EC-D2000 structure is governed mainly by the *composition of the system*. The stoichiometric network displays spherical SSQO domains (5–15 nm) dispersed in the epoxy matrix. With an excess of EC, the nanocomposite structure involves the large SSQO cylinders and even continuous SSQO phase.

Evolution of the molecular structure of the *Epoxy-POSS system* includes growth of the branched epoxide structures and incorporation of POSS into the network by the epoxide-amine reactions. The inorganic nanodomains are formed within the epoxide matrix by POSS aggregation. The nanostructuring of the epoxy-POSS nanocomposite is based on competition between POSS-POSS and POSS-polymer interactions. The compatibility of the POSS monomer with the organic medium controlled by the POSS substituents is a crucial aspect. POSS incorporation in the epoxy network during polymerization brings about homogenization of the hybrid, and topology of POSS attachment to the network plays also an important role. The pendant POSS tend to aggregate to form amorphous or crystalline domains. These POSS aggregates serve as physical crosslinks of the hybrid network. In contrast, POSS units in the network junctions are relatively well dispersed.

Reaction blending is the often-used approach to polymerize heterogeneous O–I systems. An initially heterogeneous mixture is gradually homogenized during the reaction by interphase bonding. The O–I precursors GTMS or ATEs are typical agents to improve compatibility of the O–I systems. Acid catalysis of the sol–gel process, advancing formation of SiOH in the silica structures, also encourages the covalent or H-bond interaction with an organic matrix, in contrast to the basic catalysis. In the case of the epoxy-POSS hybrids, the efficiency of reaction blending depends on POSS functionality.

1.5.2 Structure Ordering

The silica nanodomains generated in situ from TEOS or POSS domains attached as pendant blocks on the chain of the epoxy-POSS networks are irregularly dispersed in the epoxy matrix. However, the O–I block copolymers prepared from the O–I precursors create a microphase-separated organized structure, typical of block copolymers. The organotrialkoxysilanes with a sufficiently long organic chain form a micelle-like or lamellar arrangement. The ordered structure is fixed by gelation in the O–I networks prepared from ASO or EC. The correlation distance between the SSQO crosslinks in the hybrid networks is given by the size of the linking organic chains. Also, the epoxy networks containing POSS units as junctions exhibit structure ordering.

Organic templates can be used to direct a long-range ordering of inorganic domains in the O–I network. Self-assembly of urea groups or long alkyl chains, as well as a crystalline arrangement of particular oligomer chains are examples of the templates. The supramolecular self-assembly involving a crystalline POSS lamellar structure exists in the epoxy-POSS network containing POSS_{DGEBA} monomer. This supramolecular structure undergoes a sharp temperature-sensitive order-disorder transition.

1.5.3 Interphase Interaction

The interphase interaction is one of the most important factors determining the behavior of nanocomposites. Mainly, covalent and H-bonding provide a strong interaction between phases. Also of importance is the interfacial area, given by the volume content of dispersed nanodomains, by their internal structure, and by morphology (i.e., compactness and size of the nanodomains).

The silica structures generated in situ from TEOS in the *epoxy-silica networks* display an interaction with the organic matrix due to the presence of SiOH groups. The silanols tend to form both H-bonds with POP chains of the matrix and covalent bonds by the reaction with C–OH of the epoxide-amine networks. Therefore, acid catalysis is highly suitable. The fine morphology (i.e., the small size of inorganic

heterogeneities, providing a large interface surface) is another factor supporting the interaction. A very strong interphase interaction exists in the epoxy-silica nanocomposites prepared mainly by the sequential polymerization or the two-step (acid-base) polymerization procedure. The interaction is evidenced by the formation of an interphase layer, composed of the epoxy network chains immobilized by silica. This interphase shows a significant increase in glass transition temperature compared to the epoxide network, and contributes to the effective volume fraction of the hard filler in the epoxy-silica nanocomposite. The hybrid networks synthesized under basic or DBTDL catalysis exhibit a weak interphase interaction, due to a low content of SiOH and a rough morphology comprising large silica aggregates.

The *O-I block copolymer networks* with SSQO junctions display a mild interphase interaction. Due to a sharp microphase separation in the O-I block copolymer, there is only a thin interphase layer involving the surface of the SSQO junction domain and a small terminal part of the bonded oligomer chain (the covalent bond between phases is localized at the oligomer chain end only). Under acid catalysis, an interpenetration of the phases and thickening of the interphase layer occurs, thus strengthening the interaction. Stronger interaction exists in the network grafted with SSQO along the chain. The coupling agents, such as GTMS or ATEs, are commonly used to improve an interphase interaction in the epoxy-silica/SSQO nanocomposites.

The *epoxy-POSS networks* with pendant POSS are strongly microphase-separated. The POSS-chain interaction is quite weak because the POSS-POSS interactions to form aggregates prevail. The slight decrease in glass transition temperature in the networks containing POSS_{oct} with flexible substituents is a result of an increased free volume, due to a bulky POSS molecule acting as a plasticizer. Only a high content of POSS_{ph} with phenyl substituents leads to a significant confinement in network chains. Formation of a strong physical crosslink of the crystalline POSS_{ph} reduces mobility of the attached chains. The anchoring effect of the large POSS mass on chain mobility does not seem to be decisive. The very strong interaction and immobilization of chains due to POSS was observed in the networks with POSS_{DGEBA} monomer where the chains are confined between crystalline POSS layers. However, no interphase interaction occurs in the epoxy-POSS networks with POSS in junctions. The voluminous POSS crosslink involving flexible hexyl substituents is a reason for a decrease in the glass transition temperature with respect to the DGEBA-based network.

1.5.4 Mechanical Properties

Mainly, morphology determines the mechanical properties of the epoxy-silica/SSQO nanocomposites.

The hybrids with the bicontinuous morphology of the epoxy and silica phases display a dramatic increase in modulus. The rubbery modulus of the *epoxy-silica network* (DGEBA-D2000-TEOS, sequential polymerization) is enhanced by two

orders of magnitude at a low silica content, ~ 7 vol%, with respect to the reference epoxide network. The mechanical behavior and moduli, moreover, depend on the volume fraction of silica and on the interphase interaction.

The moduli of the *O-I block copolymer networks* (ASO and EC-based) are only slightly increased, compared to the homogeneous network, and correspond to the particulate nanocomposites. Significant reinforcement is achieved only in the networks with bicontinuous morphology (i.e., the ASO-networks containing a high amount of TEOS or the EC-D2000 networks with an excess of EC).

The *epoxy-POSS networks* with POSS units (POSS,E1) pendant on the network chain show dependence of the mechanical properties on the type of POSS substituent. The POSS aggregates covalently attached to the chain act as physical crosslinks, and the modulus depends on the strength of these aggregates. While POSS_{ph} crystallites increase the crosslinking density and modulus of the epoxy-POSS network, the amorphous aggregates of POSS_{oct} with flexible octyl substituents are too weak to contribute as the real physical network crosslinks. The very efficient reinforcement is provided by physical crosslinking with POSS crystalline lamellae in the ordered POSS_{DGEBA}-D2000 network. POSS in the network junctions (POSS,E8) are well dispersed as the polyfunctional chemical crosslink. These networks exhibit an increase in the modulus as a result of enhanced chemical crosslinking density due to high POSS functionality.

The elastic moduli in the rubbery state of the heterogeneous O-I networks could be predicted by combination of the theoretical models of mechanical behavior. The theory of rubber elasticity for homogeneous networks, the particulate composite model of Kerner-Nielsen, and the models describing the behavior of composites with bicontinuous morphology (EBM and Davies model) were applied to treat the hybrid nanocomposites.

Two basic types of nanocomposites discussed in this chapter involve the nanodomains of a different nature: the in situ generated chemical structures and the physical aggregates of the POSS blocks. The difference between the nanocomposites with the “chemical” and “physical” nanofillers is characterized by their behavior under a small mechanical deformation, the so-called Payne effect [134].

The rubbery homogeneous epoxide network DGEBA-D2000 displays a linear viscoelastic behavior up to a relatively high deformation, as shown in Fig. 1.37. The hybrid nanocomposite DGEBA-POSS_{ph}E1-D2000 contains the crystalline POSS aggregates. The physical intradomain interactions break under strain, and the typical composite behavior is observed. The rubbery modulus drops at a strain of about 0.5%. In contrast, the nanocomposite with the chemical SSQO structures as nanofillers (DGEBA-D2000-ATES) behaves like a homogeneous system, exhibiting a linear viscoelasticity without any decrease in the modulus up to a strain of $\sim 4\%$. The chemical SSQO structure of the nanodomain keeps the integrity during deformation, in contrast to the physical aggregates.

An interesting behavior under small deformation occurs in the case of the ordered hybrid network POSS_{DGEBA}-D2000 with the lamellar POSS crystalline structure. Figure 1.37 illustrates the breakage of the POSS-filler structure at a very low strain ($\sim 0.01\%$), due to disordering of the lamellar arrangement, followed by

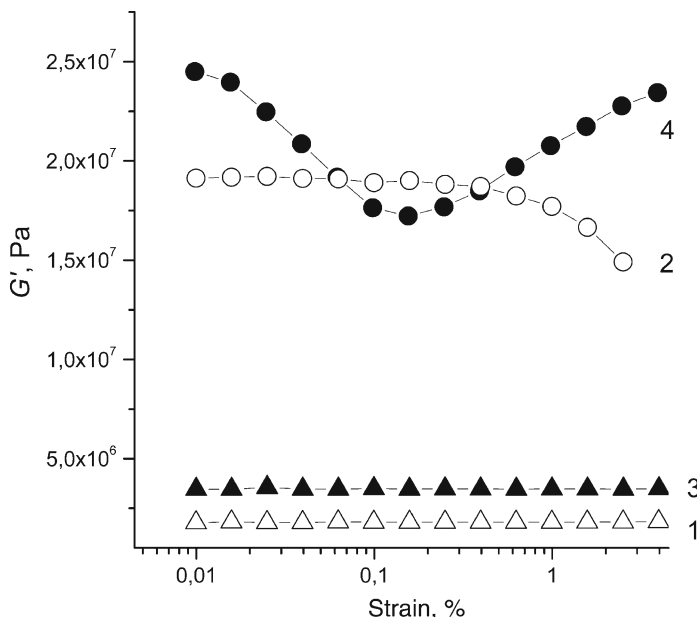


Fig. 1.37 Shear modulus of the nanocomposites as a function of small deformation. (1) DGEBA-D2000 network, (2) DGEBA-POSS_{ph}-E1-D2000 nanocomposite, (3) DGEBA-D2000-ATES nanocomposite, (4) POSS_{DGEBA}-D2000 nanocomposite

another reinforcement at a strain $\sim 0.2\%$. The modulus increase could correspond to a strain-induced new ordering of the POSS cages [134].

Acknowledgment The author acknowledges financial support of the Grant Agency of Academy of Science of the Czech Republic (IAA 400500701).

References

1. Mark JE (1996). *Polym Eng Sci* 36:2905
2. Novak BM (1993). *Adv Mater* 5:422
3. Sanchez C, Ribot F (1994). *New J Chem* 18:1007
4. Wen JY, Wilkes GL (1996). *Chem Mater* 8:1667
5. Schmidt HJ (1985). *J Non-Cryst Solids* 73:681
6. Brinker CJ, Scherer GW (1989). *Sol-Gel Science*, Academic Press, New York
7. Mark JE, Jiang C, Tang MY (1984). *Macromolecules* 17:2613
8. Wilkes GL, Orlor B, Huang HH (1985). *Polym Prepr* 26:300
9. Landry CJT, Coltrain BK, Brady BK (1992). *Polymer* 33:1486
10. Lam TM, Pascault JP (1993). *Trends Polym Sci* 3:317
11. Huang HH, Orlor B, Wilkes GL (1987). *Macromolecules* 20:1322
12. Kohjiya S, Ochiai K, Yamashita S (1990). *J Non-Cryst Solids* 119:132
13. Girard-Reydet E, Lam TM, Pascault P (1994). *Macromol Chem Phys* 195:149
14. Bokobza L, Chauvin JP (2005). *Polymer* 46:4144
15. Eisenberg P, Lucas JCC, Williams RJJ (1999). *Polimery* 44:735

16. Karger-Kocsis J, Zhang Z (2005). In: Friedrich K, Fakirov S, Zhang Z (eds.) Mechanical properties of polymers based on nanostructure and morphology. CRC, New York, p 547
17. Kicelbick G (2003). *Prog Polym Sci* 28:83
18. Sanchez C, Soler-Illia GJAA, Ribot F, Grosso D (2003). *CR Chim* 6:1131
19. Bauer BJ, Liu DW, Jackson CL, Barnes JD (1996). *Polym Adv Technol* 7:333
20. Liu YL, Hsu CY, Wei WL, Jeng RJ (2003). *Polymer* 44:5159
21. Ragosta G, Abbate M, Musto P, Scarinzi G, Mascia L (2005). *Polymer* 46:10506
22. Kommann X, Thoman R, Mulhaupt R, Finter J, Berglund LA (2002). *Polym Eng Sci* 42:1815
23. Wang MS, Pinnavaia TJ (2004). *Chem Mater* 6:468
24. Mascia L, Tang T (1998). *J Mater Chem* 8:2417
25. Ochi M, Takahashi R (2001). *J Polym Sci Part B: Polym Phys* 39:1071
26. Weng WH, Chen H, Tsai SP, Wu JC (2004). *J Appl Polym Sci* 91:532
27. Innocenzi P, Kidchob T, Yoko T (2005). *J Sol Gel Sci Technol* 35:225
28. Mascia L, Prezzi L, Haworth B (2006). *J Mater Sci* 41:1145
29. Lee A, Lichtenhan JD (1998). *Macromolecules* 31:4970
30. Choi J, Harcup J, Yee AF, Zhu QY, Laine RM (2001). *J Am Chem Soc* 123:11420
31. Kim GM, Qin H, Fang X, Sun FC, Mather PT (2003). *J Polym Sci Part B: Polym Phys* 41:3299
32. Pellice SA, Fasce DP, Williams RJJ (2003). *J Polym Sci Part B: Polym Phys* 41:1451
33. Mya KY, He CB, Huang JC, Xiao Y, Dai J, Siow YP (2004). *J Polym Sci Part A: Polym Chem* 42:3490
34. Winter HH, Mours M (1997). *Adv Polym Sci* 134:165
35. Schaefer DW, Keefer KD (1984). *Phys Rev Lett* 53:1383
36. Payne AR (1962). *J Polym Sci* 6:57
37. Berriot J, Lequeux F, Montes H, Pernot H (2002). *Polymer* 43:6131
38. Bandyopadhyay A, de Sarkar M, Bhowmick AK (2005). *J Polym Sci Part B: Polym Phys* 43:2399
39. Kraus G (1965). In: Kraus G (ed.) Reinforcement of elastomers. Wiley, New York
40. Iler RK (1979). *The chemistry of silica*. Wiley, New York
41. Assink RA, Kay BDJ (1988). *Non-Crystalline Solids* 99:359
42. Schaefer DW (1989). *Science* 243:1023
43. Matějka L, Dušek K, Pleštil J, Kříž J, Lednický F (1999). *Polymer* 40:171
44. Stockmayer WH (1952). *J Polym Sci* 9:69
45. Fujiwara M, Kojima K, Tanaka Y, Nomura R (2004). *J Mater Chem* 14:1195
46. Lee TM, Ma CCM (2006). *J Polym Sci Part A: Polym Chem* 44:757
47. Matějka L, Pleštil J, Dušek K (1998). *J Non-Cryst Solids* 226:114
48. Matějka L, Dukh O, Kolařík J (2000). *Polymer* 41:1449
49. Aubert C, Cannell DS (1986). *Phys Rev Lett* 56:738
50. Wen J, Mark JE (1994). *Rubber Chem Technol* 67:807
51. Nielsen LE, Landel RF (1994). *Mechanical properties of polymers and composites*. Marcel Dekker, New York
52. Nielsen LE (1969). *J Polym Sci* C12:249
53. Huang HH, Wilkes GL, Carlson JG (1989). *Polymer* 30:2001
54. Landry MR, Coltrain BK, Landry CJT, O'Reilly JM (1995). *J Polym Sci Part B: Polym Phys* 33:637
55. Silveria KF, Yoshida IVP, Nunes SP (1995). *Polymer* 36:1425
56. Nakanishi K, Soga N (1991). *J Am Ceram Soc* 74:2518
57. Mauritz KA, Storey RF, Jones CK (1989). *Multiphase polymer materials: blends, ionomers and interpenetrating networks*, ACS Symposium Series 395
58. Tomlins PE, Read BE (1991). *Plast Rubber Compos* 16:17
59. Kolařík J (1998). *Eur Polym J* 34:585
60. DeGennes PG (1976). *J Phys Lett (Paris)* 37:L1
61. Utracki LA (1991). *J Rheol* 35:1615
62. Stauffer D (1985). *Introduction to percolation theory*. Taylor and Francis, Philadelphia

63. Davies WEA (1971). *J Phys D* 4:1176
64. Donatelli AA, Sperling LH, Thomas DA (1976). *Macromolecules* 9:676
65. Schaefer DW, Mark JE (1990). *Polymer-based molecular composites*, vol. 171. Materials Research Society, Pittsburgh
66. Miller TM, Zhao L, Brennan AB (1998). *J Appl Polym Sci* 68:947
67. Karásek I, Meissner B (1994). *J Appl Polym Sci* 52:1925
68. Loy DA, Shea KJ (1995). *Chem Rev* 95:1431
69. Surivet F, Lam TM, Pascault JP (1991). *J Polym Sci Part A: Polym Chem* 29:1977
70. Baney RH, Itoh M, Sakakibara A, Suzuki T (1995). *Chem Rev* 95:1409
71. Loy DA, Baugher BM, Baugher CR, Schneider DA, Rahimian K (2000). *Chem Mater* 12:3624
72. Matějka L, Dukh O, Brus J, Simonsick WJ, Meissner B (2000). *J Non-Cryst Solids* 270:34
73. Matějka L, Dukh O, Hlavatá D, Meissner B, Brus J (2001). *Macromolecules* 34:6904
74. Feher FJ, Newman DA, Walzer JF (1989). *J Am Chem Soc* 111:1741
75. Fasce DP, Williams RJJ, Méchin F, Pascault JP, Liauro MF, Pétiard R (1999). *Macromolecules* 32:4757
76. Eisenberg P, Erra-Balsells R, Ishikawa Y, Lucas JC, Mauri AN, Nonami H, Riccardi CC, Williams RJJ (2000). *Macromolecules* 33:1940–1947
77. Moreau JJE, Vellutini L, Wong Chi Man M, Bied CJ (2001). *J Am Chem Soc* 123:1259
78. Moreau JJE, Vellutini L, Wong Chi Man M, Bied CJ, Dieudonné P, Bantignies JL, Sauvajol JL (2005). *Chem Eur J* 11:1527
79. Ellsworth MW, Novak BM (1993). *Polym Prepr* 34 (2):356
80. Ribot F, Sanchez C (1999). *Comment Inorg Chem* 20:327
81. Matějka L, Dukh O (2001). *Macromol Symp* 171:181
82. Matějka L, Dukh O, Meissner B, Hlavatá D, Brus J, Strachota A (2003). *Macromolecules* 36:7977
83. Matějka L, Dukh O, Kamišová H, Hlavatá D, Špírková M, Brus J (2004). *Polymer* 45:3267
84. Rankin SE, Kasehagen LJ, McCormick AV, Macosko CW (2000). *Macromolecules* 33:7639
85. Huang HH, Wilkes GL (1987). *Polym Bull* 18:455
86. Surivet F, Lam TM, Pascault JP, Mai C (1992). *Macromolecules* 25:5742
87. Jordens K, Wilkes GL (2000). *Pure Appl Chem* 37:145–175;177
88. Cuney S, Gerard JF, Dumon M, Pascault JP, Vigier G, Dušek K (1997). *J Appl Polym Sci* 65:2373
89. Brik M, Titman J, Bayle JP, Judenstein P (1996). *J Polym Sci Part B: Polym Phys* 34:2533
90. Erman B, Flory PJ (1978). *J Chem Phys* 68:5363
91. Dušek K, Šomvářský J (1995). *Faraday Discuss* 101:147
92. Macan J, Ivankovi H, Ivankovi , Mencer HJ (2004). *J Appl Polym Sci* 92:498
93. Brus J, Špírková M, Hlavatá D, Strachota A (2004). *Macromolecules* 37:1346
94. dell Erba IE, Fasce DP, Williams RJJ, Erra-Balsells R, Fukuyama Y, Nonami H (2003). *J Organometal Chem* 686:42
95. Bassindale AR, Gentle TR (1993). *J Mater Chem* 3:1319–1325
96. Voronkov MG, Lavrentyev VI (1982). *Top Curr Chem* 102:199
97. Feher FJ, Terroba R, Jin R, Wyndham KO, Lucke S, Brutchey R, Nguyen F (2000). *Polym Mater Sci Eng* 82:301
98. Lichtenhan JD, Vu NQ, Carter JA, Gilman JW, Feher FJ (1993). *Macromolecules* 26:2141
99. Lichtenhan JD, Otonari YA (1995). *Macromolecules* 28:8435–8437
100. Haddad TS, Lichtenhan JD (1996). *Macromolecules* 29:7302
101. Tsuchida A, Bolln C, Sernetz FG, Frey H, Muelhaupt R (1997). *Macromolecules* 30:2818
102. Hsiao BS, Mather PT, Chaffee KP, Jeon H, White H, Rafailovich M, Lichtenhan JD, Schwab JJ (1998). *Polym Mater Sci Eng* 79:389
103. Mather PT, Jeon Hong A, Romo-Urbe A, Haddad TS, Lichtenhan JD (1999). *Macromolecules* 32:1194

104. Romo-Urbe A, Mather PT, Haddad TS, Lichtenhan JD (1998). *J Polym Sci Part B: Polym Phys* 36:1857
105. Zheng L, Waddon AJ, Farris RJ, Farris RJ, Coughlin EB (2002). *Macromolecules* 35:2375
106. Lichtenhan JD, Haddad TS, Schwab JJ, Carr MJ, Chaffee KP, Mather PT (1998). *Polym Prepr* 39(1):489
107. Bharadwaj RK, Berry RJ, Farmer BL (2000). *Polymer* 41:7209
108. Fu BX, Gelfer MY, Hsiao BS, Phillips S, Viers B, Blanski R, Ruth P (2003). *Polymer* 44:1499
109. Haddad TS, Lee A, Phillips SH (2001). *Polym Prepr* 42(1):88
110. Xu HY, Kuo SW, Lee JS, Chang FC (2002). *Macromolecules* 35:8788
111. Zhang C, Babonneau F, Laine RM, Soles CL, Hristov, Yee AF (1998). *J Am Chem Soc* 120:8380
112. Li GZ, Wang LC, Toghiani H, Daulton TL, Pittman CU (2002). *Polymer* 43:4167
113. Bizet S, Galy J, Gerard JF (2006). *Macromolecules* 39:2574
114. Li GY, Wang L, Toghiani H, Daulton TL, Koyama K, Pittman CU Jr. (2001). *Macromolecules* 35:8686
115. Joshi M, Butola BS (2004). *J Macromol Sci Part C* 44:389
116. Crivello JV, Malik R (1997). *J Polym Sci Part A: Polym Chem* 35:407–425
117. Sellinger A, Laine RM (1996). *Macromolecules* 29:2327
118. Laine RM, Choi J, Lee I (2001). *Adv Mater* 13:800
119. Choi J, Yee AF, Laine RM (2003). *Chem Mater* 15:5666
120. Huang JC, He CB, Liu XM, Xu JW, Tay CSS, Chow SY (2005). *Polymer* 46:7018
121. Laine RM (2005). *J Mater Chem* 15:3690
122. Ni Y, Zheng SX, Nie KM (2004). *Polymer* 45:5557
123. Choi J, Kim SG, Laine R (2004). *Macromolecules* 37:99
124. Liu HZ, Zheng SX, Nie KM (2005). *Macromolecules* 38:5088
125. Lin EK, Snyder CR, Mopsik FI, Wallace WE, Wu WL, Zhang CX, Laine RM (1998). *Organic-inorganic hybrid materials*, *MRS* 519:15
126. Abad MJ, Barral L, Fasce DP, Williams RJJ (2003). *Macromolecules* 36:3128
127. Liu HZ (2006). *J Polym Sci Part A: Polym Chem* 44:1869
128. Matějka L, Strachota A, Pleštil J, Whelan P, Steinhart M, Šlouf M (2004). *Macromolecules* 37:9449
129. Strachota A, Kroutilová I, Kovářová J, Matějka L (2004). *Macromolecules* 37:9457
130. Strachota A, Whelan P, Kříž J, Brus J, Urbanová M, Šlouf M, Matějka L (2007). *Polymer* 48:3041
131. Beck Tan NC, Bauer BJ, Pleštil J, Barnes JD, Liu D, Matějka L, Dušek K, Wu WL (1999). *Polymer* 40 4603
132. Kourkoutsaki T, Logakis E, Kroutilová I, Matějka L, Nedbal J, Pissis P (2006). *Proceedings 20th Bratislava Int. Conference on Macromolecules Advanced Polymeric Materials*, Bratislava, Slovakia
133. Pittman CU, Li GZ, Ni HL (2003). *Macromol Symp* 196:301
134. Amici-Kroutilová I (2007). PhD Thesis, Institute of Macromolecular Chemistry, Prague.
135. Li GZ (2001). *J Inorg Org Polym* 11:123
136. Pope EJA, Asami M, MacKenzie JD (1989). *J Mater Res* 4:1018
137. Bauer BJ, Liu DW, Jackson CL, Barnes JD (1995). *Polym Adv Technol* 7:333
138. Schmidt H, Philipp G (1984) *J Non-Cryst Solids* 63:283
139. Himmel B, Gerber H, Burger J (1990). *J Non-Cryst Solids* 1:119
140. Ng LV, Thompson P, Sanchez J, Macosko CW, McCormick AV (1995). *Macromolecules* 28:6471
141. Hsiue GH, Liu YL, Liao HH (2001) *J Polym Sci Part A: Polym Chem* 39:986
142. Moreau JJE, Pichon BP, Wong CMM, Bied C, Pritzkow H, Bantignies JL, Diedonné P, Sauvajol JL (2004) *Angew Chem, Int Ed* 43:203

Chapter 2

Scale-Up Synthesis of Polymer-Grafted Nanoparticles in Solvent-Free Dry-System and in Ionic Liquid

Norio Tsubokawa

Abstract For the purpose of prevention of the environmental pollution and simplification of reaction process, the scale-up synthesis of polymer-grafted silica nanoparticles and carbon black in the solvent-free dry-system and in ionic liquid are summarized.

Scale-up synthesis of hyperbranched poly(amidoamine)-grafted silica nanoparticles was successfully achieved by using dendrimer synthesis methodology in solvent-free dry-system. The polymer was allowed to propagate from silica nanoparticle surface by repeating two steps: (1) Michael addition of methyl acrylate (MA) to amino group on the surface and (2) amidation of terminal methyl ester groups with ethylenediamine (EDA). MA was sprayed onto silica having amino group and the silica was agitated at 300 rpm at 50°C. After the reaction, unreacted MA was removed under high vacuum. Then, EDA was sprayed and the reaction was conducted at 50°C with agitation. After the reaction, unreacted EDA was also removed under high vacuum at 50 °C and MA was sprayed again. The procedures were repeated to grow poly(amidoamine) on the surface. The percentage of poly(amidoamine) grafting onto the surface was determined to be 141% with repeated reaction cycles of eight times.

In addition, the radical graft polymerizations of vinyl monomers onto silica nanoparticles and carbon black surfaces were successfully achieved by spraying monomers onto silica nanoparticles and carbon black having azo and peroxy-carbonate groups in solvent-free dry-system. It is interesting to note that the formation of ungrafted polymer was depressed in comparison with graft polymerization in solution; the grafting efficiency was 90–95%.

The radical graft polymerizations of vinyl monomers initiated by azo groups introduced onto silica nanoparticles and carbon black surfaces in ionic liquid were investigated. In this work, 1-butyl-3-methylimidazolium hexafluorophosphate was used as ionic liquid. The percentage of grafting in ionic liquid was much larger than

N. Tsubokawa

Department of Material Science and Technology, Faculty of Engineering, Niigata University,
Center for Transdisciplinary Research, Niigata University, 8050, Ikarashi 2-no-cho,
Nishi-ku, Niigata 950-2181, Japan
e-mail: ntsuboka@eng.niigata.u.ac.jp

those in 1,4-dioxane. The molecular weight of polystyrene grafted onto the silica nanoparticle surface in ionic liquid was almost equal to that in 1,4-dioxane. The result indicates that the number of grafted polystyrene in ionic liquid is five times that in 1,4-dioxane. This may be due to the fact that lifetime of the surface radical formed by the thermal decomposition of azo groups is prolonged because of high viscosity of ionic liquid. Therefore, the surface azo groups were effectively used as initiating sites for the graft polymerization. In addition, the reduction of waste solvent was achieved by the use of ionic liquid as reaction solvent medium, because unreacted monomer could be removed under high vacuum after the reaction and the reuse of ionic liquid could also be easily achieved. Therefore, the graft polymerization onto nanoparticle surface in ionic liquid enables us the scale-up synthesis of polymer-grafted nanoparticles.

The radical grafting onto carbon black surface initiated by the radical initiator in the presence of carbon black in ionic liquid is also discussed.

2.1 Introduction

Inorganic nanoparticles such as silica and titanium oxide are widely used industrially as fillers and pigments for polymer materials. Inorganic nanoparticles have excellent properties such as heat, chemical and weather resistance, lightweight, and low thermal expansion.

On the other hand, carbon materials, such as carbon black, graphite, activated carbon, and carbon nanotube, are well known as industrially important and commercially available carbon materials. Carbon materials have also outstanding properties such as electroconductivity, heat resistance, biocompatibility, and chemical resistance. Especially, carbon nanotubes have attracted attention as one class of nanotechnology related materials.

In general, dispersing nanoparticles, such as silica nanoparticles and carbon black, uniformly into a polymer or an organic solvent is very difficult because of aggregation of these particles. In addition, mechanical properties of the composite are considered to be dependent not only on the mechanical properties of the polymer matrix, but also on the properties of interfacial regions between the surface of nanoparticles and matrix polymer.

The chemical and physical modifications of silica nanoparticle and carbon black surfaces, therefore, have been extensively studied. The chemical modification of surfaces is permanent, but physical modification is temporary. We have pointed out that the dispersibility of silica nanoparticles and carbon black is extremely improved by surface grafting of polymers, namely, chemical binding of polymers, onto silica nanoparticle and carbon black surfaces [1–3]. In addition, grafting of polymers onto these surfaces is of interest to us for designing new functional organic–inorganic hybridmaterials which have excellent properties of both nanoparticles as mentioned above and grafted polymers, such as photosensitivity, curing ability, bioactivity, and pharmacological activity [1–3].

We have reported the grafting of various polymers such as vinyl polymer [4–7], polyester [8, 9], polyether [10, 11], poly(organophosphazene) [12], and poly(dimethylsiloxane) [13] onto silica nanoparticle and carbon black surfaces using surface functional groups as grafting sites. Furthermore, many experimental attempts by other researchers also have been made to graft polymers onto silica nanoparticle and carbon black surfaces. For example, it has been reported that grafting of polymers from nanoparticles (polymer brush) was successfully achieved by atom-transfer radical polymerization (ATRP), initiated by a system consisting of surface functional groups and transition metal complexes [14–18]. In situ radical-transfer addition polymerization [19] and emulsion polymerization from silica nanoparticles has been also reported [20]. Synthesis of a well-defined organic/inorganic nanocomposite via reverse ATRP was achieved by Wang et al. [21, 22]. Polymer grafting onto a colloidal silica surface was also reported by Yoshinaga et al. [23].

However, scale-up synthesis of polymer-grafted nanoparticles was hardly achieved, because complicated reaction processes, such as centrifugation, filtration, and solvent extraction, are required for the synthesis of polymer-grafted nanoparticles, and also a lot of solvent is wasted.

In this chapter, for the purpose of prevention of environmental pollution and simplification of reaction process, the scale-up synthesis of hyperbranched poly(amidoamine)-grafted silica nanoparticles and the radical graft polymerization of vinyl monomers onto silica nanoparticle surface initiated by surface initiating groups in the solvent-free dry-system are summarized.

In addition, the radical graft polymerization of vinyl monomers onto silica nanoparticle and carbon black surfaces by “grafting onto” and “grafting from” process in room temperature ionic liquid, well known as environmentally friendly “green solvent”, will be discussed.

2.2 Methodology of Surface Grafting of Polymers onto Nanoparticles

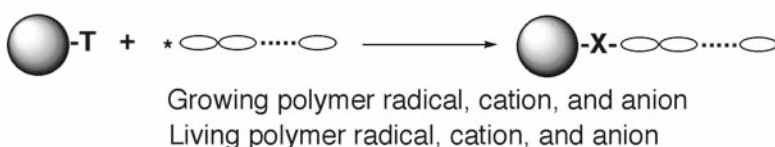
Several methodologies of the surface grafting of polymers onto nanoparticles have been developed for the preparation of various kinds of graft copolymers. These methodologies can be applied to the preparation of polymer-grafted nanoparticles. In general, one of the following principles may be applied to prepare polymer-grafted nanoparticles (Fig. 2.1) [1–3].

- (1) “Grafting onto” process: termination of growing polymer radical, cation, and anion, formed during the polymerization of various monomers; initiated by conventional initiator in the presence of nanoparticles and the deactivation of living polymerradical, cation, and anion with functional groups on nanoparticle surface.
- (2) “Grafting from” process: initiation of graft polymerization of various monomers from radical, cationic and anionic initiating groups previously introduced onto nanoparticle surfaces.

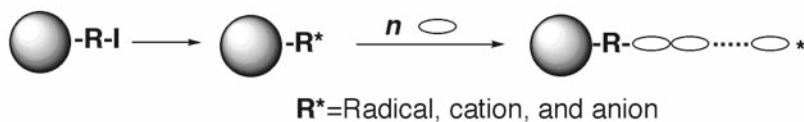
- (3) Polymer reaction process: reaction of surface functional groups on nanoparticles with polymers having functional groups, such as hydroxy, carboxyl, and amino groups.
- (4) Stepwise growth process: polymer chains are grown from surface functional groups on nanoparticles by repeated reaction of low-molecular-weight compounds by dendrimer synthesis methodology.

By the process (1), although polymer-grafted nanoparticles can be obtained, the percentage of grafting onto nanoparticles is less than 10% because of the preferential formation of ungrafted polymers. On the contrary, by the termination of living polymer polymers with well-defined molecular weight and narrow molecular weight distribution can be grafted onto nanoparticle surfaces.

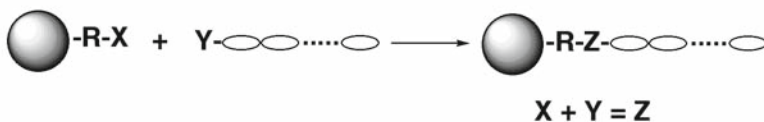
(1) "Grafting onto" process



(2) "Grafting from" process



(3) "Polymer reaction" process



(4) "Stepwise growth" process

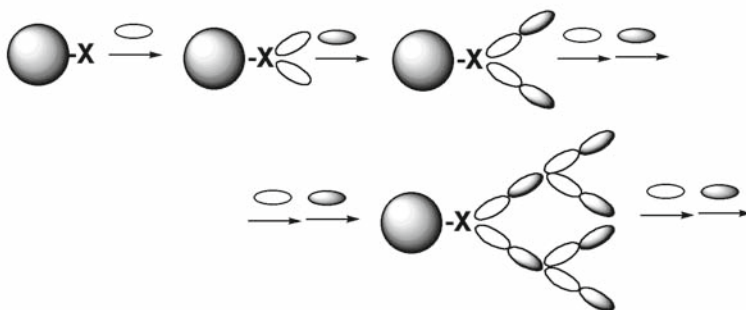


Fig. 2.1 Methodology of surface grafting of polymers onto silica nanoparticle and carbon black

Process (2) is the most favorable for the preparation of polymer-grafted nanoparticles with a high percentage of grafting. The molecular weight and number of grafted polymer chains can be controlled by use of surface-initiated living polymerization.

An important characteristic of process (3) is that not only the molecular weight and the number of grafted chains on nanoparticle surfaces are easily controlled, but also commercially available polymers having a well-defined structure can be grafted. But the number of grafted polymer chains on nanoparticle surface decreases with increasing molecular weight of polymer, because of steric hindrance.

By the process (4), although dendron with the theoretically predicted structure was not easily grafted, hyperbranched polymers having a large number of terminal functional groups can be grafted onto nanoparticle surfaces.

2.3 Grafting of Polymers onto Nanoparticle Surfaces in Solvent-Free Dry-System

2.3.1 What is the Advantage of Grafting in Solvent-Free Dry-System?

Figure 2.2 shows the comparison of the procedures of graft polymerization onto nanoparticles in solvent-free dry-system with those in solvent system. In solvent system, the purification and isolation of the resulting nanoparticles was achieved by

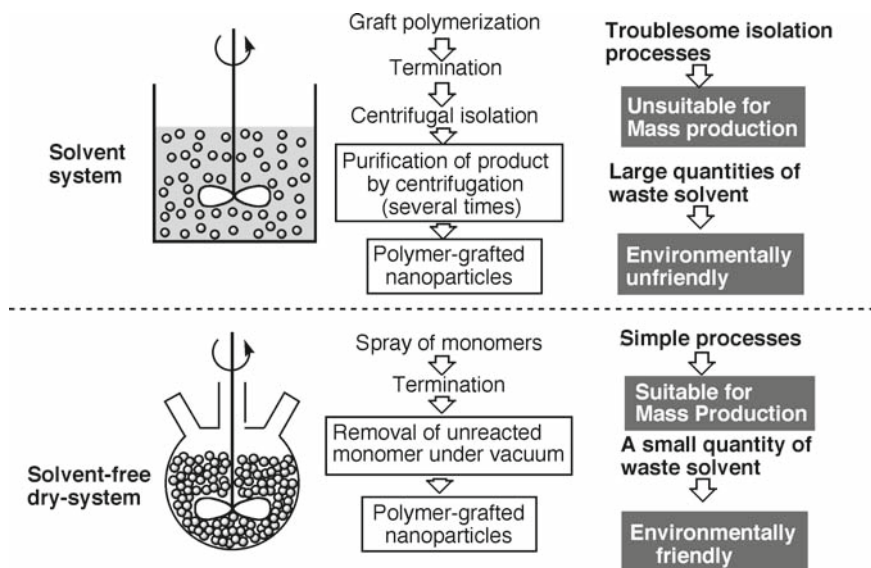


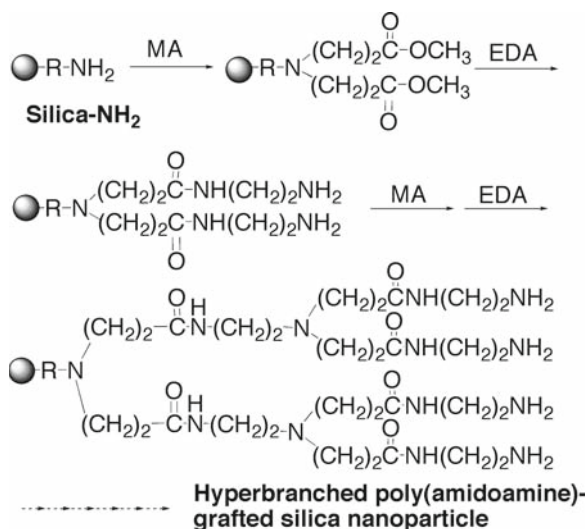
Fig. 2.2 Graft polymerization in solvent system vs. in solvent-free dry-system

cumbersome procedures, such as filtration and centrifugation. Therefore, the scale-up synthesis of polymer-grafted nanoparticles was hardly achieved and large quantities of solvent were wasted.

On the contrary, in the solvent-free dry-system, the isolation and purification of nanoparticle was easily achieved, because untreated monomer can be removed under high vacuum. Therefore, it is concluded that the solvent-free dry-system is environmentally friendly and graft polymerization onto nanoparticle surface in solvent-free dry system is expected to enable the scale-up synthesis of polymer-grafted nanoparticles.

2.3.2 Grafting of Hyperbranched Poly(Amidoamine) onto Silica Nanoparticles in Solvent-Free Dry-System

Recently, a great interest has been shown on “Dendrimer”, because the dendrimers have the fundamental building blocks, controlled molecular weight and controlled branching, and versatility in the modification of terminal groups [24, 25]. We have reported that hyperbranched poly(amidoamine) can be grown from amino group on silica nanoparticle, chitosan powder, and carbon black surface using dendrimer synthesis methodology in methanol as solvent [26–29]. The hyperbranched poly(amidoamine)-grafted nanoparticle has the possibility of being utilized as a support for catalyst and enzyme, and a curing agent of epoxy resin [30], because hyperbranched poly(amidoamine)-grafted nanoparticle has many terminal amino groups.



Scheme 2.1 Grafting of poly(amidoamine) onto silica nanoparticle surface by dendrimer synthesis methodology

Therefore, we have designed the scale-up synthesis of hyperbranched poly(amidoamine)-grafted silica nanoparticle in solvent-free dry-system [31] as shown in Scheme 2.1.

2.3.2.1 Experimental Method

Introduction of Amino Group onto Silica Nanoparticle Surface

The introduction of amino group onto the silica nanoparticle surface, i.e., preparation of a “grafting site”, was achieved by the treatment of surface silanol group with γ -aminopropyltriethoxysilane(γ -APS) in solvent-free dry-system [31]. A typical example is as follows. Into a 500-mL four-necked flask, as shown in Fig. 2.3, equipped with a mechanical stirrer having a semicircular blade, a thermometer, a purger of argon gas, and a reflux condenser, 15.0 g of silica nanoparticle was charged under an atmosphere of argon. Then, 3.0 g of γ -APS ethanol solution was sprayed onto the silica surface at 150°C under stirring at 300 rpm. After 30 min, unreacted γ -APS and ethanol were removed under high vacuum at 150°C. The silica nanoparticle (abbreviated as Silica-NH₂) was thus obtained.

Grafting of Hyperbranched Poly(Amidoamine) from Silica Nanoparticle Surface

Grafting of hyperbranched poly(amidoamine) onto silica nanoparticle surface was achieved by repeating two steps: (1) Michael addition of methyl acrylate(MA) to

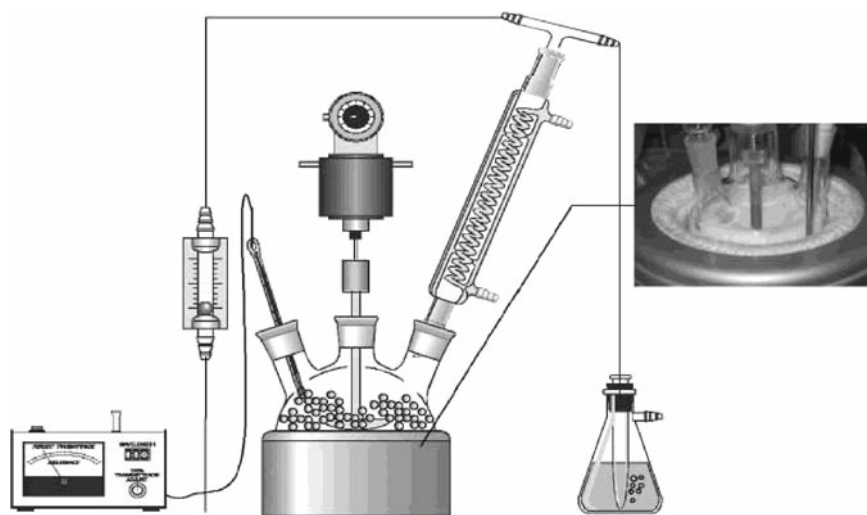


Fig. 2.3 Reaction apparatus for the synthesis of polymer-grafted silica nanoparticle in the solvent-free dry-system

the amino group on the surface and (2) amidation of terminal methyl ester group with ethylenediamine (EDA) (Scheme 2.1) [24–29].

Into a 500-mL four-necked flask (Fig. 2.3) containing 15.0 g of silica nanoparticles having amino groups, 3.0 g of MA (34.8 mmol, excess of surface amino groups) was sprayed and the mixture was stirred at 300 rpm at 50°C under argon gas. After 21 h, unreacted MA was removed under high vacuum at 50°C. After 2 hr, 3.0 g of EDA (50 mmol; excess of surface ester group) was sprayed into the flask and the reaction was conducted at 50°C with agitation. After 21 h, unreacted EDA was removed under vacuum at 50°C during 3 h and MA was sprayed again. Both the Michael addition and the amidation reactions were repeated to grow the poly(amidoamine) on the silica surface.

Determination of Percentage of Grafting

Silica nanoparticles obtained from the grafting reaction were dispersed in methanol, and the dispersion was allowed to centrifuge at 1.5×10^4 rpm. The silica precipitated was dispersed again in methanol and centrifuged. The procedures were repeated until no more ungrafted polymer could be detected in the supernatant solution. The percentage of grafting was determined by the following equation:

$$\text{Grafting (\%)} = (A/B) \times 100$$

where *A* is the weight of grafted poly(amidoamine) (g) and *B* is the weight of silica nanoparticles charged (g). The weight of poly(amidoamine) grafted onto the silica nanoparticle surface was determined from the weight loss when poly(amidoamine)-grafted silica nanoparticle was heated at 800°C by the use of a thermal analyzer.

2.3.2.2 Introduction of Amino Groups onto Silica Nanoparticles in Solvent-Free Dry-System

Generally, the introduction of functional groups onto silica and glass surface was achieved by the reaction of surface silanol group with silane-coupling agents in solvent [26]. In our new method, the introduction of amino group onto silica nanoparticle surface as a grafting site was achieved by the treatment of silica with γ -APS in solvent-free dry-system.

Figure 2.4a shows FT-IR spectrum of γ -APS-treated silica nanoparticles. The FT-IR spectrum of γ -APS-treated silica nanoparticles shows a new absorption peak at $1,640 \text{ cm}^{-1}$, which is characteristic of amino group. This suggests that amino group had also been introduced onto the silica surface in solvent-free dry-system.

The amount of amino group introduced onto silica nanoparticle surface was controlled by the concentration of γ -APS for the treatment of silica nanoparticle. In our study, silica nanoparticles containing 0.12, 0.19, 0.33, 0.45 and 0.62 mmol g^{-1} of amino group as a “grafting site” were prepared.

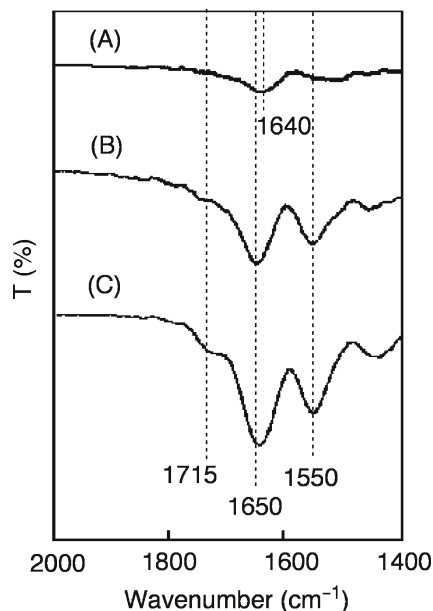


Fig. 2.4 FT-IR spectra of (A) γ -APS-treated silica nanoparticle, (B) hyperbranched poly(amidoamine)-grafted silica nanoparticle with repeated reaction cycles of three times (grafting = 38.3%), and (C) hyperbranched poly(amidoamine)-grafted silica nanoparticle with repeated reaction cycles of six times (grafting = 129.4%)

2.3.2.3 Grafting of Hyperbranched Poly(Amidoamine) onto Silica Nanoparticle Surface

The treatment of silica nanoparticles having amino group with MA and EDA in solvent-free dry-system was repeated n -times to obtain poly(amidoamine)-grafted silica nanoparticles as shown in Scheme 2.1. It is considered that poly(amidoamine) is grown from surface amino group and grafted onto silica nanoparticle surface [31].

Table 2.1 shows the amino group content of silica nanoparticle and the percentage of poly(amidoamine) grafting onto silica nanoparticle surface (wt% of grafted polymer on silica) after the grafting reaction. The amino group content and percentage of poly(amidoamine) grafting of the resulting silica nanoparticle increased with increasing repeated reaction cycles. On the other hand, when untreated silica nanoparticle was used, no increase of surface amino group and no grafting of poly(amidoamine) onto the surface was observed even with repeated reaction cycles of eight times.

During the grafting reaction, the formation of small amount of ungrafted polymer was observed: methanol soluble part (major product) was hyperbranched poly(amidoamine) and THF soluble part (minor product) was a mixture of polyMA and unknown viscous materials. This indicates that the removal of unreacted monomer in each step was incomplete because of strong adsorption of monomers on the silica nanoparticle surface.

Table 2.1 Grafting of hyperbranched poly(amidoamine) onto silica nanoparticle surface in solvent-free dry-system^a

Cycles of repeated reactions	Amino group content (mmol g ⁻¹)		Grafting (%)		
	Experimental	Calculated	Experimental	Calculated	R ^b
Two times	1.7	1.3	14.5	22.6	0.64
Four times	4.0	5.3	69.2	112.9	0.61
Six times	7.6	21.1	129.4	474.0	0.27
Eight times	8.8	84.5	141.0	1918.6	0.07

^aAmino group content of grafting site, 0.33 mmol g⁻¹^bR= Experimental value/calculated value**Table 2.2** Elemental analysis of hyperbranched poly(amidoamine)-grafted silica nanoparticle

Cycles of repeated reactions	C/N				
	C (%)	H (%)	N (%)	Experimental	Calculated
Two times	4.7	0.8	2.0	2.7	2.1
Four times	17.9	3.4	7.7	2.7	2.1

The amino group content of silica nanoparticle and percentage of poly (amidoamine) grafting, however, were considerably smaller than those of calculated value. The ratio of experimental value to calculated value, *R*, decreased with increasing repeated reaction cycles. The same tendency was observed in the grafting of poly(amidoamine) onto silica nanoparticle in methanol solvent system [26–29].

Table 2.2 shows the results of elemental analysis of poly(amidoamine)-grafted silica nanoparticle with repeated reaction cycles of two and four times. The C/N ratio of poly(amidoamine)-grafted silica nanoparticles was considerably larger than the theoretical C/N ratio of ideal poly(amidoamine). This suggests the incomplete amidation of terminal methyl ester group of poly(amidoamine).

Figure 2.4b, c also shows FT-IR spectra of poly(amidoamine)-grafted silica nanoparticle with repeated reaction cycles of three and six times. The absorption at 1,655 cm⁻¹, which is characteristic of amide group, increased with increasing repeated reaction cycles. The absorption (shoulder) at 1,715 cm⁻¹ suggests the presence of ester bonds, indicating the incomplete amidation of terminal methyl ester groups with EDA.

Figure 2.5 shows FT-IR spectra of poly(amidoamine)-grafted silica nanoparticles obtained in solvent-free dry-system and in methanol solvent system [31]. The intensity of ester bond in solvent-free dry-system is weaker than that in methanol solvent system. This indicates that the amidation of terminal methyl ester group proceeded more effectively in the solvent-free dry-system.

On the basis of the above results, it is concluded that theoretical propagation of poly(amidoamine) from silica nanoparticle surface was hardly achieved and hyperbranched poly(amidoamine) was grafted onto the surface as schematically shown in Fig. 2.6b.

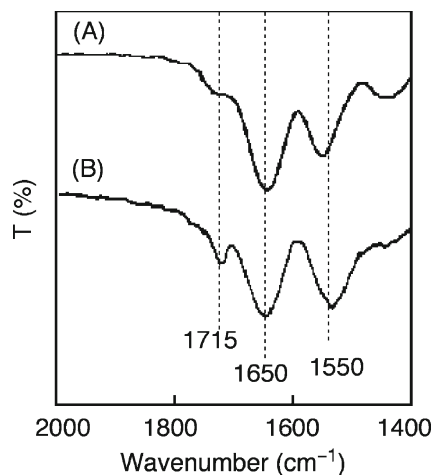


Fig. 2.5 FT-IR spectra of hyperbranched poly(amidoamine)-grafted silica nanoparticle with repeated reaction cycles of six times (A) in solvent-free dry-system (grafting = 129.4%) and (B) in methanol solvent system (grafting = 71.9%)

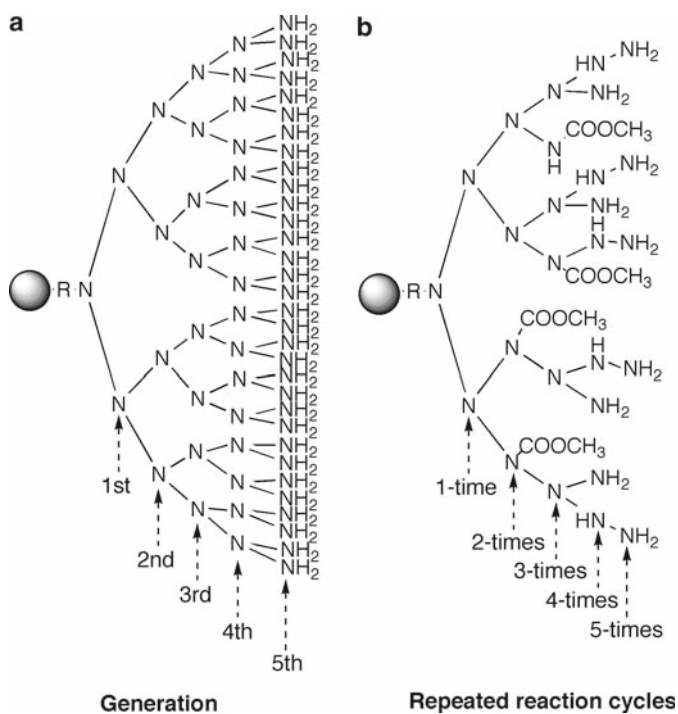


Fig. 2.6 Illustration of (a) theoretical poly(amidoamine) dendron-grafted silica nanoparticle and (b) hyperbranched poly(amidoamine)-grafted silica nanoparticle obtained from solvent-free dry-system

This may be due to the fact that (1) complete Michael addition and the amidation with surface amino and ester group hardly proceed because of aggregation of silica nanoparticles and (2) the grafted chains on the silica surface interfere with the propagation of dendron from the surface because of steric hindrances [26–29]

2.3.2.4 Effects of Polar Solvents on the Grafting of Hyperbranched Poly(Amidoamine) onto Silica Nanoparticle

In general, preparation of poly(amidoamine) dendrimer is achieved by an exhaustive Michael addition of amines to MA in a polar solvent such as methanol [24, 25]. Therefore, the effects of methanol and water on the Michael addition of surface amino groups to MA were examined. The Michael addition was conducted by spraying MA containing 25% of methanol or saturated aqueous solution of MA. The results are shown in Fig. 2.7.

It was found that the percentage of surface amino groups, which reacted with MA after the first Michael addition, was scarcely affected by the presence of polar solvents. The results indicate that about 75% of amino groups reacted with MA and poly(amidoamine) grows from amino group on silica nanoparticle surface even in the absence of methanol (solvent-free dry-system). Therefore, it seems that silanol groups on silica nanoparticle surface accelerates Michael addition of amino groups to MA.

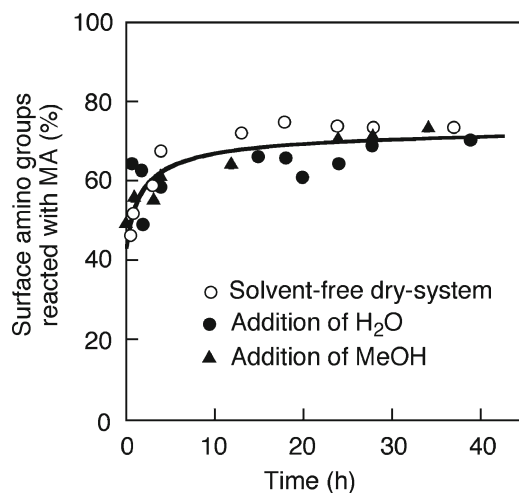


Fig. 2.7 Effects of methanol and water on the first Michael addition of surface amino groups with MA

2.3.2.5 Effects of Reaction Conditions on the Grafting of Hyperbranched Poly(Amidoamine)

The effects of reaction time and temperature on the grafting of hyperbranched poly(amidoamine) onto silica nanoparticle were investigated. The results are shown in Table 2.3. As shown in Table 2.3, the percentage of grafting increased with increase in reaction time, but the amount of ungrafted polymer also increased. This indicates that the formation of ungrafted polymer was accelerated because of thermal polymerization of MA during the prolonged reaction time. On the other hand, the grafting of poly(amidoamine) onto silica nanoparticle surface decreased at higher temperature.

2.3.2.6 Effect of Surface Amino Group Content on the Grafting of Hyperbranched Poly(Amidoamine) onto Silica Nanoparticle

Table 2.4 shows the effect of amino group content on the grafting of the hyperbranched poly(amidoamine) onto silica nanoparticle surface. It was found that the percentage of grafting with repeated reaction cycles of two times increased with increase in the initial amino group content on the surface. However, *R* (ratio of experimental value to theoretical value) decreased with increase in amino group content on the surface as grafting site.

Table 2.3 Effect of reaction conditions on the grafting of hyperbranched poly(amidoamine) onto silica nanoparticle surface^a

Temperature (°C)	Time (h)	Grafting (%)	Ungrafted polymer (%)
50	9	38.3	7.3
50	21	69.2	15.8
50	45	73.0	27.0
70	21	56.7	9.1

^aInitial amino group content of silica, 0.33 mmol g⁻¹. Repeated reaction cycles is four times

Table 2.4 Effect of amino group content of grafting site on silica nanoparticle on the poly(amidoamine) grafting in solvent-free dry-system

Amino group content (mmol g ⁻¹)	Grafting (%) ^a	<i>R</i> ^b
0.12	7.2	0.88
0.19	9.6	0.74
0.33	14.5	0.64
0.45	19.8	0.64
0.62	23.2	0.55

^aAfter repeated reaction cycles of two times

^b*R* = Experimental value/calculated value

This may be due to the fact that the steric hindrance to surface amino groups increased with increase in the density of surface amino groups [26].

2.3.3 Radical Grafting of Vinyl Polymers onto Silica Nanoparticle Initiated by Initiating Groups on the Surface

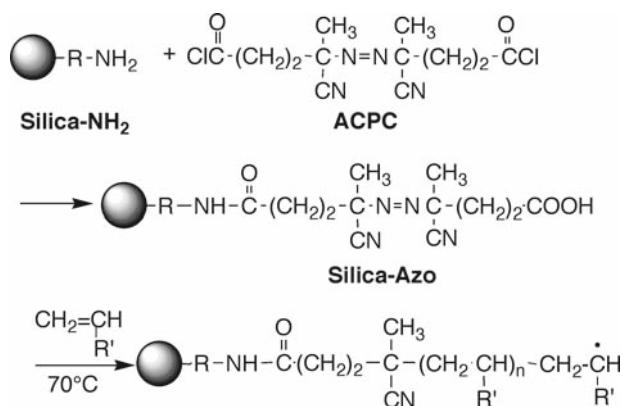
We have reported that the radical polymerizations of vinyl monomers are initiated by azo groups and peroxyester groups introduced onto nanoparticles, such as carbon black and silica [4–7, 32, 33]. In the polymerization, it was confirmed that the grafted polymer chains propagated from the surface radicals formed by the thermal decomposition of azo and peroxyester groups introduced onto the surface in organic solvents.

Therefore, we designed the radical graft polymerization of vinyl monomers onto silica nanoparticle surface initiated by azo and peroxycarbonate groups in solvent-free dry-system [34].

2.3.3.1 Experimental Methods

Introduction of Azo Groups onto Silica Nanoparticle

The introduction of azo groups onto silica nanoparticle surface was achieved by the reaction of surface amino groups with 4,4'-azobis(4-cyanopentanoic chloride) (ACPC) in the presence of pyridine as shown in Scheme 2.2 [5]. A typical experiment is as follows. Into a 500-mL Erlenmeyer flask, 9.6 g of Silica-NH₂, 500 mL of THF,



Scheme 2.2 Introduction of azo groups onto silica nanoparticle surface and radical graft polymerization of vinyl monomers initiated by surface azo groups

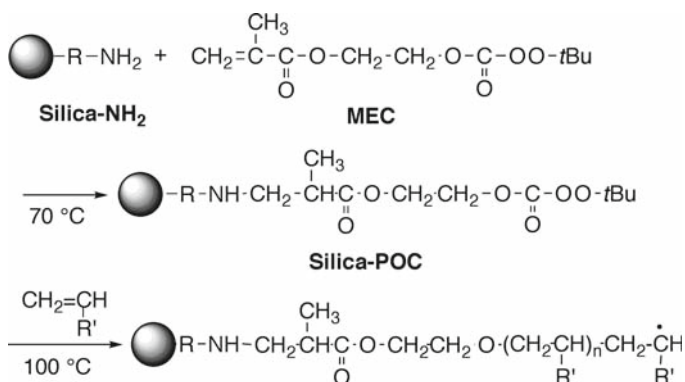
1.0 g of ACPC, and 1.0 mL of pyridine were charged. The reaction mixture was stirred for 24 h with a magnetic stirrer at room temperature under dry nitrogen. After the reaction, the resulting silica was repeatedly washed with THF and water. The treated silica was stored in the dark below -5°C . The silica having azo groups is abbreviated as Silica-Azo.

Introduction of Peroxycarbonate Groups onto Silica Nanoparticle Surface by Michael Addition in Solvent-Free Dry-System

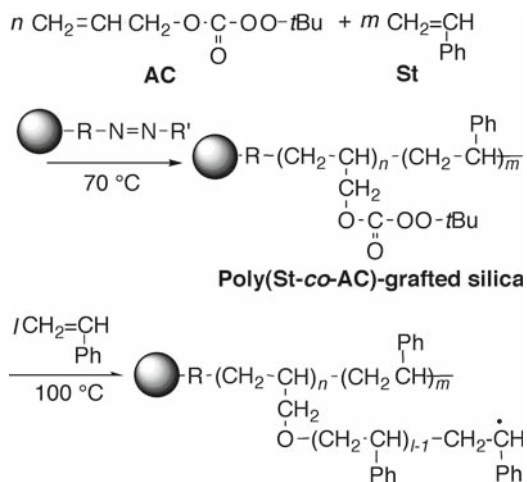
The introduction of peroxycarbonate groups onto silica nanoparticle surface was achieved by Michael addition of *t*-butylperoxy-2-methacryloyloxyethylcarbonate (MEC) to amino groups on the silica surface in solvent-free dry-system as shown in Scheme 2.3 [33]. Into a 200-mL four-necked flask (shown in Fig. 2.3) containing 8.8 g of Silica-NH₂, 2.5 g of MEC was sprayed and the silica was stirred at 120 rpm at 30°C under argon gas. After the reaction, unreacted MEC was removed under high vacuum. The silica nanoparticle having peroxycarbonate groups (abbreviated as Silica-POC) was thus obtained.

2.3.3.2 Grafting of Copolymer Having Pendant Peroxycarbonate Groups onto Silica Nanoparticle Surface in Solvent-Free Dry-System

The grafting of copolymer having pendant peroxycarbonate groups onto the silica nanoparticle surface was achieved by the copolymerization of styrene (St) with *t*-butylperoxyallylcarbonate (AC) initiated by azo groups on the silica nanoparticle surface as shown in Scheme 2.4 [32]. Into a 200-mL four-necked flask (shown in Fig. 2.3) containing 8.8 g of Silica-Azo, the mixture of monomers (St: AC =



Scheme 2.3 Introduction of peroxycarbonate groups onto silica nanoparticle surface by Michael addition of MEC and radical graft polymerization of vinyl monomers initiated by surface peroxycarbonate groups



Scheme 2.4 Grafting of copolymers having pendant peroxycarbonate groups onto silica nanoparticle surface and postgrafting of vinyl monomers onto the surface

0.013:0.013 mol) was sprayed and the silica was stirred at 120 rpm at 70°C under argon gas. After the reaction, unreacted monomers were removed under high vacuum. The poly(St-co-AC)-grafted silica having pendant peroxycarbonate groups (abbreviated as Silica-poly(St-co-AC)) was obtained.

Radical Graft Polymerization of Vinyl Monomers onto Silica Nanoparticle Initiated by Initiating Groups in Solvent-Free Dry-System

The radical graft polymerization of vinyl monomers onto the silica nanoparticle surface initiated by initiating groups on the surface in solvent-free dry-system was carried out as follows. Into a 200-mL four-necked flask (shown in Fig. 2.3) containing 8.8 g of silica having radical initiating groups (Silica-Azo, Silica-POC, and Silica-poly(St-co-AC)), 0.025 mol of vinyl monomer was sprayed and the silica was stirred at 120 rpm at 75°C under argon gas. After the reaction, unreacted monomers were removed under high vacuum.

2.3.3.3 Radical Grafting of Vinyl Monomers Initiated by Silica-Azo

The radical graft polymerization of St and methyl methacrylate(MMA), initiated by azo groups introduced onto the silica nanoparticle surface, in solvent-free dry-system was investigated. The results are shown in Table 2.5. In the presence of untreated silica nanoparticle and Silica-NH₂, polySt and polyMMA were scarcely grafted onto the surface.

Table 2.5 Graft polymerization of vinyl monomers initiated by azo groups introduced onto silica nanoparticle surface in solvent-free dry-system^a

Silica	Time (h)	Styrene		MMA	
		Grafting (%)	Grafting efficiency (%)	Grafting (%)	Grafting efficiency (%)
Untreated	4	trace	–	trace	–
Silica-NH ₂	4	trace	–	trace	–
Silica-Azo	1	8.5	36.0	6.0	92.3
Silica-Azo	2	11.5	55.0	6.8	98.6
Silica-Azo	3	11.6	48.5	6.6	93.0
Silica-Azo	4	11.5	50.2	7.0	77.8

^aSilica-Azo, 8.8 g; monomer, 0.025 mol; temperature, 75°C

On the contrary, it was found that the radical graft polymerizations of St and MMA were successfully initiated by azo groups introduced onto the silica surface in solvent-free dry-system. The polySt and polyMMA grafting reached 11.5% and 7.0%, respectively, at 75°C after 4 h, but no longer increased after 2 h.

Figure 2.8 shows DSC curves of (A) untreated silica nanoparticle, (B) Silica-Azo, (C) 4,4'-azobis(4-cyanopentanoic acid) (ACPA), and (D) polySt-grafted silica nanoparticle. As shown in Fig. 2.8(D), polySt-grafted silica nanoparticle shows no exothermic peak, indicating almost complete decomposition of azo groups during the polymerization.

Figure 2.9 shows FT-IR spectra of (A) Silica-NH₂ and (B) polyMMA-grafted silica nanoparticle. The FT-IR spectra of polyMMA-grafted silica nanoparticles show new absorptions at 1,736 and 1,454 cm⁻¹, which are characteristic absorption of polyMMA.

Figure 2.10 shows GC-MS of thermally decomposed gas of polySt-grafted silica nanoparticle. Gas chromatogram (GC) of decomposed gas was in agreement with that of polySt. Mass spectrum of the decomposed gas at retention time 2.0 min was also in agreement with that of polySt. The results also show that polySt was grafted onto silica nanoparticle surface.

In the previous paper, we have reported that the grafting efficiency (percentage of grafted polymer in the total polymer formed) in the graft polymerization initiated by azo groups on nanoparticle surfaces is about 50% at the initial stage of the polymerization, but immediately decreases to a small percentage at the middle and last stages of the polymerization [4–7]. This indicates that both surface radicals on the nanoparticle surface and fragment radicals formed by the thermal decomposition of azo groups on the surface initiate the polymerization: the surface radicals produce grafted polymer, but the fragment radicals produce ungrafted polymer as shown in Scheme 2.5. It is considered that at the last stage of the graft polymerization, the latter reaction preferentially proceeds which decreases the grafting efficiency.

Fig. 2.8 DSC curves of (A) untreated silica nanoparticle, (B) ACPA-immobilized silica nanoparticle (Silica-Azo), (C) ACPA, and (D) ACPA-immobilized silica nanoparticle after the graft polymerization

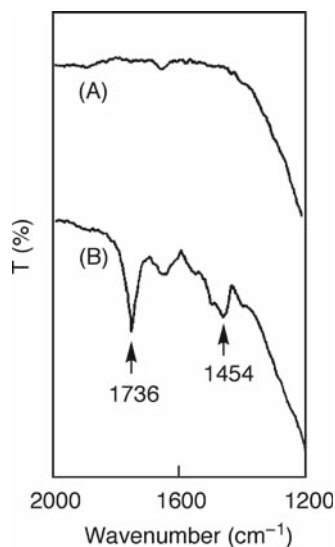
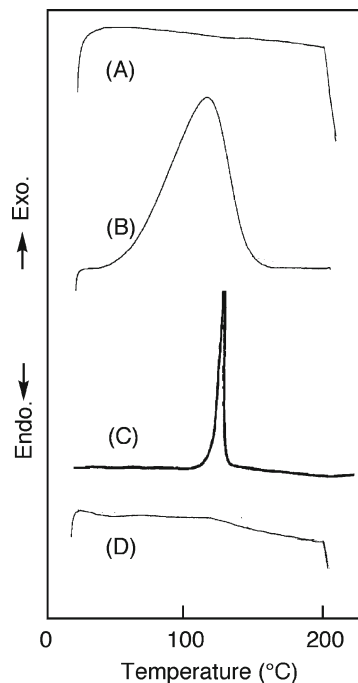


Fig. 2.9 FT-IR spectra of (A) untreated silica nanoparticle and (B) polyMMA-grafted silica nanoparticle

It is interesting to note that the grafting efficiency of polySt and polyMMA was extremely high in solvent-free dry system, 90–95%, as shown in Table 2.5, indicating depression in the formation of ungrafted polymer by the fragment radicals. This may be due to the fact that the graft polymerization proceeds on the silica nanoparticle surface.

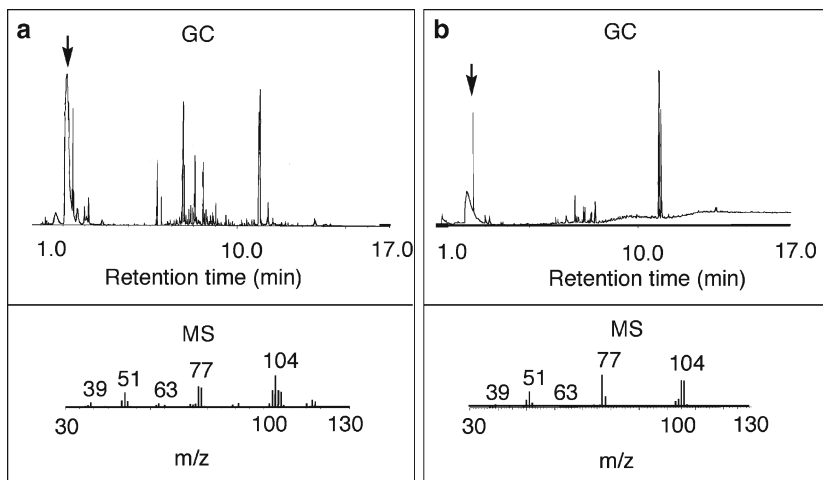
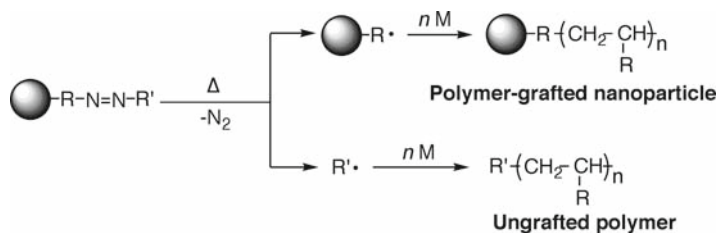


Fig. 2.10 GC-MS spectra (thermal decomposition) of (a) polySt and (b) polySt-grafted silica nanoparticle



Scheme 2.5 Grafting of polymers from surface radicals and formation of ungrafted polymer during polymerization initiated by surface azo groups on silica nanoparticle

On the basis of the above result, it is concluded that the radical graft polymerizations of St and MMA were initiated by the surface radicals formed by the decomposition of azo groups on the surface in the solvent-free dry system.

2.3.3.4 Grafting of Copolymer Having Pendant Peroxycarbonate Groups onto Silica Nanoparticle Surface

The grafting of copolymers having pendant peroxycarbonate groups onto the silica nanoparticle surface was achieved by the copolymerization of St with AC initiated by azo groups introduced onto the surface in solvent-free dry-system. The results are shown in Table 2.6. It was found that the copolymerization of St with AC was initiated by azo groups on the silica surface and poly(St-co-AC) having pendant peroxycarbonate groups was grafted onto the silica surface. The grafting efficiency was also very high and the formation of ungrafted polymer was depressed in solvent-free

dry-system. The AC content of the grafted copolymer was estimated to be 45 mol% from peroxycarbonate group content.

2.3.3.5 Postpolymerization of Vinyl Monomers Initiated by Poly(St-co-AC)-Grafted Silica Nanoparticle in Solvent-Free Dry-System

The radical postgraft polymerization of St and MMA initiated by pendant peroxycarbonate groups of grafted poly(St-co-AC) on the silica nanoparticle surface was investigated. The results are shown in Table 2.7. In the presence of untreated silica nanoparticle and Silica-NH₂, no polymerization of vinyl monomers was initiated. On the contrary, the postpolymerization of vinyl monomers was successfully initiated by pendant peroxycarbonate groups of grafted poly(St-co-AC) chain on the silica nanoparticle surface in the solvent-free dry-system.

The percentage of polySt and polyMMA postgrafting onto the silica nanoparticle was determined to be 15.8 and 7.5%, respectively. On the basis of the above result, it is concluded that the radical postgraft polymerizations of St and MMA was initiated by radicals on grafted poly(St-co-AC) chains by the thermal decomposition of pendant peroxycarbonate groups to give branched polymer-grafted silica nanoparticle. It became apparent that in the postpolymerization, the grafting efficiency was also high.

2.3.3.6 Introduction of Peroxycarbonate Groups onto Silica Nanoparticle by Michael Addition of MEC

The introduction of peroxycarbonate groups onto the silica nanoparticle surface by Michael addition of amino groups introduced onto the silica surface to t-butylperoxy-2-methacryloyloxyethylcarbonate (MEC) was investigated (Scheme 2.3). The results are shown in Table 2.8. It was found that the peroxycarbonate groups were successfully introduced onto the silica nanoparticle surface by the Michael addition of amino groups on the surface to MEC in the solvent-free dry-system: the peroxycarbonate group content of the silica nanoparticle reached 0.23 mmol g⁻¹. This indicates that about 70% of amino groups introduced onto silica nanoparticle surface reacted with MEC.

Table 2.6 Grafting of poly(AC-co-St) onto silica nanoparticle surface in solvent-free dry-system^a

Time (h)	Grafting (%)	Grafting efficiency (%)
0.5	4.8	72.7
1	5.0	76.9
2	5.1	87.9

^aSilica-Azo, 8.8 g; AC = St = 0.013 mol; temperature, 70°C

Table 2.7 Postgraft polymerization of St and MMA initiated by poly(St-co-AC)-grafted silica nanoparticle in solvent-free dry-system^a

Monomer	Time (h)	Grafting (%)	Grafting efficiency (%)
Styrene	0.5	10.1	74.8
Styrene	1	13.1	64.5
Styrene	2	15.8	67.2
MMA	2	7.5	74.5

^aPoly(St-co-AC)-grafted silica, 8.8 g, vinyl monomer, 0.025 mol; temperature, 100°C

Table 2.8 Introduction of peroxy carbonate groups onto the silica nanoparticle surface by Michael addition of MEC in solvent-free dry-system

Time (h)	Peroxy carbonate group (mmol g ⁻¹) ^a	R ^b
6	0.25	0.76
24	0.21	0.64
48	0.23	0.70

^aSilica-NH₂, 8.8 g; MEC, 0.022 mol; temperature, 30°C

^bRatio of amino groups that reacted with MEC

2.3.3.7 Graft Polymerization of Vinyl Monomers Initiated by Peroxy carbonate Groups Introduced onto Silica Nanoparticle by Michael Addition of MEC

The radical graft polymerization of vinyl monomers initiated by peroxy carbonate groups introduced onto the silica nanoparticle surface using MEC in solvent-free dry-system was investigated. The results are shown in Table 2.9. In the presence of untreated silica nanoparticle and Silica-NH₂, vinyl polymer was scarcely grafted onto the surface. On the contrary, it was found that the radical graft polymerization of St and MMA was successfully initiated by peroxy carbonate groups introduced onto the silica nanoparticle surface in solvent-free dry-system. The percentage of grafting of polySt and polyMMA onto the silica nanoparticle was determined to be 32.7 and 17.4%, respectively. The grafting efficiency was also found to be very high.

On the basis of the above result, it is concluded that the radical graft polymerization of vinyl monomers was initiated by the surface radicals formed by the decomposition of peroxy carbonate groups on silica nanoparticle surface.

2.3.4 Cationic Grafting of Polymers onto Silica Nanoparticles in Solvent-Free Dry-System

We have reported that silica nanoparticles having chloromethyl groups have the ability to initiate the cationic ring-opening polymerization of 2-methyl-2-oxazoline (MeOZO) to give the corresponding polymer-grafted silica nanoparticles [35].

Table 2.9 Graft polymerization of vinyl monomers initiated by peroxy carbonate groups introduced onto the silica nanoparticle surface in solvent-free dry-system^a

Monomer	Time (h)	Grafting (%)	Grafting efficiency (%)
Styrene	0.5	33.8	85.8
Styrene	1	31.0	91.1
Styrene	2	32.7	95.6
MMA	2	17.4	79.2

^aSilica-POC, 8.8 g, vinyl monomer, 0.025 mol; temperature, 100°C

It is well known that *p*-toluensulfonyl and methyl iodide are able to initiate the polymerization of 2-methyl-2-oxazoline (MeOZO) [36, 37]. Therefore, we designed the graft polymerization onto silica nanoparticle surface by cationic ring-opening polymerization of MeOZO initiated by silica nanoparticle having methylsulfonyl groups and 3-iodopropyl groups and carried out in solvent-free dry-system [38]. It is considered that polyMeOZO is grown from methoxysulfonyl and iodopropyl groups on silica nanoparticle surface to give the corresponding polymer grafted silica (Scheme 2.6).

2.3.4.1 Experimental Methods

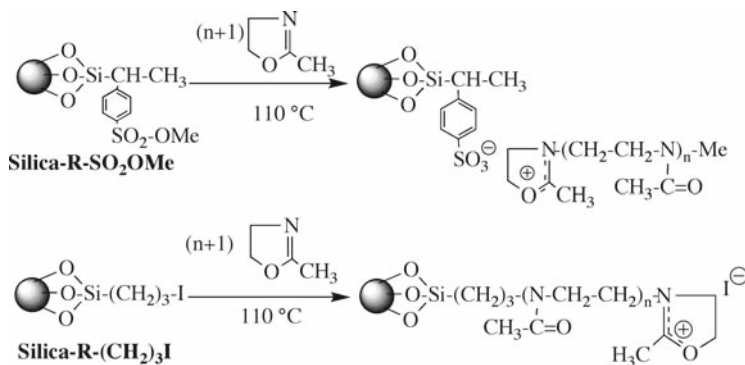
Introduction of Methoxysulfonyl and 3-Iodopropyl Groups onto Silica Nanoparticle in Solvent-Free Dry System

The introduction of methoxysulfonyl and 3-iodopropyl groups onto silica nanoparticle surface was achieved by the treatment of surface silanol groups with 2-(4-methoxysulfonylphenyl)ethyltrimethoxysilane and 3-iodopropyltrimethoxysilane, respectively, in solvent-free dry-system [38].

These treatments were achieved in solvent-free dry-system by the same manner as mentioned above (2.3.2.1). The resulting silica nanoparticles having methoxysulfonyl and 3-iodopropyl groups are abbreviated as Silica-SO₂OMe and Silica-(CH₂)₃I, respectively.

Cationic Ring-Opening Graft Polymerization in Solvent-Free Dry-System

Cationic ring-opening graft polymerization of MeOZO onto silica nanoparticle surface initiated by Silica-SO₂OMe and Silica-(CH₂)₃I in solvent-free dry-system was achieved as follows. Into a 200-mL three-necked flask (shown in Fig. 2.3) containing 4.0 g of Silica-SO₂OMe (Silica-(CH₂)₃I), MeOZO was sprayed and the silica nanoparticle was stirred at 100 rpm at 110°C (boiling point of MeOZO) under argon gas. After the reaction, unreacted MeOZO was removed under high vacuum.



Scheme 2.6 Cationic ring-opening graft polymerization of MeOZO initiated by methylsulfonyl groups and 3-iodopropyl groups on silica nanoparticle surface

2.3.4.2 Cationic Ring-Opening Graft Polymerization of MeOZO onto Silica Nanoparticle in Solvent-Free Dry-System

Table 2.10 shows the result of the cationic ring-opening graft polymerization of MeOZO in the presence of Silica–SO₂OMe and Silica–(CH₂)₃I in solvent-free dry-system. It was found that Silica–SO₂OMe and Silica–(CH₂)₃I were able to initiate the cationic ring-opening polymerization of MeOZO to give polyMeOZO-grafted silica nanoparticle. PolyMeOZO grafting onto silica nanoparticle surface initiated by 3-iodopropyl group increased to nearly 100% by increasing the MeOZO monomer concentration.

This may be due to the fact that in solvent-free dry-system, the polymerization occurs on silica nanoparticle surface. Consequently, the monomer concentration of silica surface became very high in solvent-free dry-system.

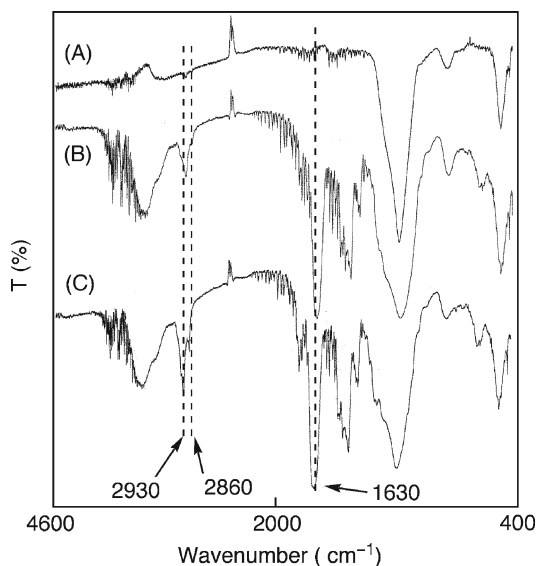
On the other hand, the percentage of grafting efficiency decreased with increase in the amount of MeOZO. The results suggest that chain transfer reaction increased with increase in MeOZO monomer concentration.

Figure 2.11 shows FT-IR spectrum of untreated silica nanoparticle, polyMeOZO-grafted silica nanoparticle, and polyMeOZO. The FT-IR spectra of polyMeOZO-grafted silica show new absorptions at 1,630 cm⁻¹, 2,860 cm⁻¹ and 2,930 cm⁻¹. The absorptions at 2,860 cm⁻¹ and 2,930 cm⁻¹ are characteristic of methylene group of polyMeOZO. The absorption at 1,630 cm⁻¹ is characteristic of C = O bond of polyMeOZO. These results also suggest that polyMeOZO had been grafted onto silica nanoparticle surface.

The polymerization of MeOZO onto silica surface in solvent-free dry-system was compared with that in solution. The results are shown in Table 2.11. As shown in Table 2.11, the conversion, grafting, and grafting efficiency in solvent-free dry-system were larger than those in solution. In addition, the grafting efficiency in solvent-free dry-system did not decrease with the progress of polymerization. The result suggests that in solvent-free dry-system, chain transfer reaction was depressed, because the polymerization occurs on silica nanoparticle surface.

Table 2.10 Graft polymerization of MeOZO onto silica nanoparticle surface initiated by methoxysulfonyl group and 3-iodopropyl group in solvent-free dry-system

Silica	MeOZO (g)	Conversion (%)	Grafting (%)	Grafting efficiency (%)
Silica ^a	1.8	0	—	—
Silica-R-SO ₂ OMe ^b	7.2	90.3	23.3	14.6
Silica-R-(CH ₂) ₃ I ^c	1.8	48.3	17.4	40.0
Silica-R-(CH ₂) ₃ I ^c	3.2	87.8	47.7	26.5
Silica-R-(CH ₂) ₃ I ^c	5.4	99.0	44.3	19.2

^aSilica, 2.0 g; 24 h; 110°C^bSilica-R-SO₂OMe, 4.0 g; 24 h; 110°C^cSilica-R-(CH₂)₃I, 2.0 g; 24 h; 110°C**Fig. 2.11** FT-IR spectra of (A) untreated silica nanoparticle, (B) polyMeOZO-grafted silica nanoparticle, and (C) polyMeOZO

2.3.5 Cationic Grafting of Polymers onto Carbon Black Surface Initiated by Carboxyl Groups in Solvent-Free Dry-System

We pointed out that carboxyl groups of carbon black surface have the ability to initiate the cationic ring-opening polymerization of MeOZO [39] and the cationic polymerization of vinyl monomers, such as isobutyl vinyl ether and *N*-vinyl-2-pyrrolidone (NVPD) [40–42]. In the cationic polymerization, the corresponding polymers were grafted onto carbon black depending on the termination of growing polymer cation with carboxylate groups of the surface as shown in Scheme 2.7. Therefore, we designed the cationic grafting of polymers onto carbon black surface initiated by carboxyl groups in solvent-free dry-system [43].

2.3.5.1 Experimental Procedure

Cationic Ring-Opening Polymerization of MeOZO Initiated by Carboxyl Groups on Carbon Black

Cationic ring-opening graft polymerization of MeOZO onto carbon black surface initiated by carboxyl groups in solvent-free dry-system was achieved as follows. Into a 200-mL four-necked flask (shown in Fig. 2.3) containing 4.0 g of carbon black, MeOZO was sprayed and the carbon black was stirred at 100 rpm at 110°C (boiling point of MeOZO) under argon gas. After the reaction, unreacted MeOZO was removed under high vacuum.

Cationic Polymerization of NVPD Initiated by Carboxyl Groups on Carbon Black

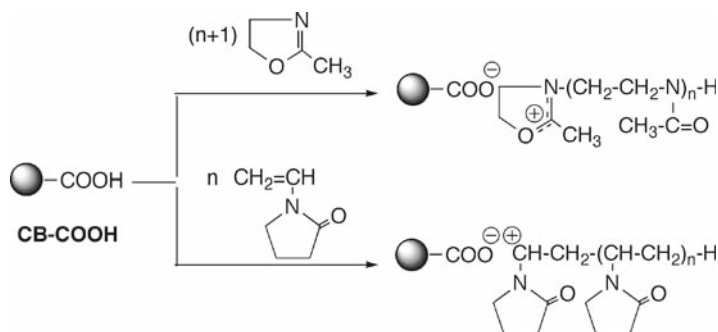
Cationic graft polymerization of NVPD onto carbon black surface initiated by carboxyl groups in solvent-free dry-system was achieved as follows. Into a 200-mL four-necked flask (shown in Fig. 2.3) containing 4.0 g of carbon black, NVPD was sprayed and the carbon black was stirred at 100 rpm at 110°C under argon gas. After the reaction, unreacted NVPD was removed under high vacuum.

Table 2.11 Graft polymerization of MeOZO onto silica nanoparticle surface initiated by 3-iodopropyl group in solution and solvent-free dry-system

System	Time (h)	Conversion (%)	Grafting (%)	Grafting efficiency (%)
Solvent-free dry-system ^a	2	99.8	44.0	22.0
Solvent-free dry-system ^a	6	94.0	44.5	26.2
Solution ^b	2	0.53	9.7	25.0
Solution ^b	6	2.1	8.6	6.4

^aSilica-R-(CH₂)₃I, 4.0 g; MeOZO, 7.2 g; 110°C

^bSilica-R-(CH₂)₃I, 0.2 g; MeOZO, 16 g; 110°C



Scheme 2.7 Cationic graft polymerization of MeOZO and NVPD initiated by carboxyl groups on carbon black surface

2.3.5.2 Cationic Ring-Opening Polymerization of MeOZO Initiated by Carbon Black Surface in Solvent-Free Dry-System

MeOZO was sprayed onto carbon black and the reaction was conducted in solvent-free dry-system to obtain polyMeOZO-grafted carbon black.

The conversion, grafting, and grafting efficiency of polyMeOZO onto carbon black are shown in Table 2.12. It was found that the cationic ring-opening polymerization of MeOZO was successfully initiated by carboxyl groups on carbon black surface.

The percentage of grafting reached was 53.8%. The percentage of grafting efficiency increased to 77.3% by increasing the MeOZO monomer concentration. The conversion, grafting, and grafting efficiency in solvent-free dry-system were much larger than those in solution [39]. In addition, the grafting efficiency in solvent-free dry-system did not decrease with the progress of polymerization.

The result suggests that in solvent-free dry-system, chain transfer reaction was depressed, because the polymerization occurs on carbon black surface.

The FT-IR spectra of polyMeOZO-grafted carbon black show new absorptions at 1,630 cm^{-1} , 418 cm^{-1} , 470 cm^{-1} , and 592 cm^{-1} . These absorptions are characteristic of polyMeOZO. These results suggest that polyMeOZO had been grafted onto carbon black surface.

2.3.5.3 Cationic Polymerization of NVPD Initiated by Carbon Black Surface in Solvent-Free Dry-System

It has been reported that the cationic polymerization of NVPD is successfully initiated by carboxyl groups on carbon black surface [40–42]. Therefore, the cationic polymerization of NMVD initiated by carboxyl groups on carbon black surface was carried out in solvent-free dry-system as shown in Scheme 2.7.

The conversion, grafting and grafting efficiency of poly NVPD onto carbon black are shown in Table 2.13. It was found that the cationic polymerization of NVPD was successfully initiated by carboxyl groups on carbon black surface to give poly(NVPD)-grafted carbon black. The percentage of grafting reached was 27.7%.

Table 2.12 Graft polymerization of MeOZO onto carbon black surface initiated by carboxyl groups in solvent-free dry-system^a

MeOZO (g)	Conversion (%)	Grafting (%)	Grafting efficiency (%)
1.8	86.4	25.0	66.7
3.6	79.2	29.9	41.2
7.2	38.6	53.8	77.3

^aCarbon black, 4.0 g; 110°C; 24 h

Table 2.13 Cationic graft polymerization of NVPD initiated by carbon black surface in solvent-free dry-system^a

NVPD (g)	Conversion (%)	Grafting (%)	Grafting efficiency (%)
1.8	28.3	8.0	60.8
3.6	47.5	24.1	56.1
7.2	56.3	27.7	27.1

^aCarbon black, 4.0 g; 110°C; 24 h

2.4 Radical Grafting of Vinyl Polymers in Ionic Liquid

Recently, organic synthesis and polymerization in ionic liquid (IL) as a reaction solvent has been reported. Ionic liquids are nonvolatile, nonflammable, and thermally stable solvents. These properties are promising replacements for the traditional volatile organic solvents. Therefore, the number of studies on ionic liquids as organic synthesis and polymerization media has increased markedly [44–46].

For example, the polymerization of vinyl monomers initiated by benzoyl peroxide (BPO) and 2,2'-azobisisobutyronitrile (AIBN) in ionic liquid has been reported [44–47]. The rate of the radical polymerization and molecular weight of polymer in ionic liquid were much larger than those in benzene [47].

In addition, Carmichael et al. have used 1-butyl-3-methylimidazolium hexafluorophosphate, an air and water-stable ionic liquid, as solvent for the Cu^I-*N*-propyl-2-pyridylmethanimine mediated “living” radical polymerization of MMA [48]. They found that the rate of polymerization enhanced in comparison to other polar/coordinating solvents. Moreover, the polymerization product was made copper-free by a simple solvent wash, which avoids contamination of the polymer product by the catalyst [48]. Other atom-transfer radical polymerizations in ionic liquids have recently been reported [49, 50].

2.4.1 What is the Advantage of Grafting in Ionic Liquid?

Figure 2.12 shows the comparison of procedures of graft polymerization onto nanoparticles in conventional organic solvents with those in ionic liquids. In organic solvent system, the purification and isolation of resulting silica was achieved by cumbersome procedures, such as filtration and centrifugation as mentioned above. Therefore, the scale-up synthesis of polymer-grafted silica was hardly achieved and large quantities of solvent were wasted.

On the contrary, in ionic liquids the isolation and purification were easily achieved, because untreated monomer can be removed under high vacuum, the medium being a solvent-free dry-system as well. Therefore, it is expected that we

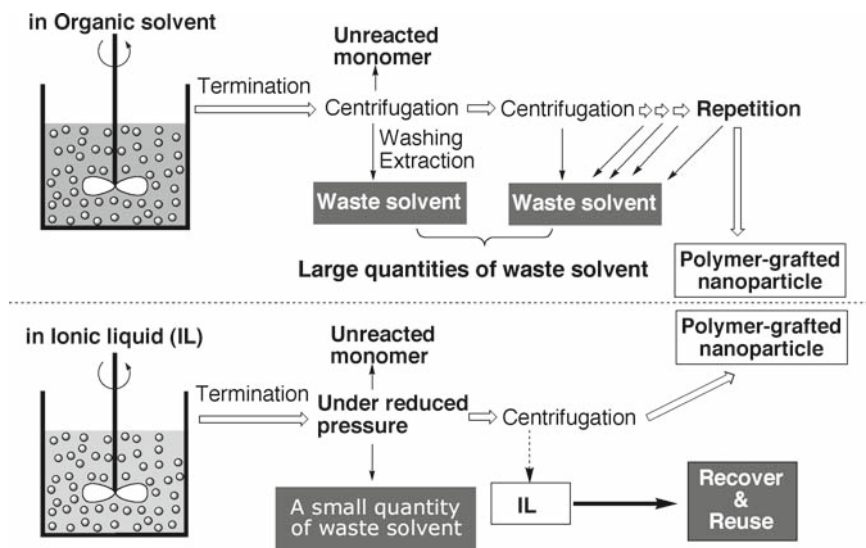


Fig. 2.12 Graft polymerization in solvent system vs. in ionic liquid

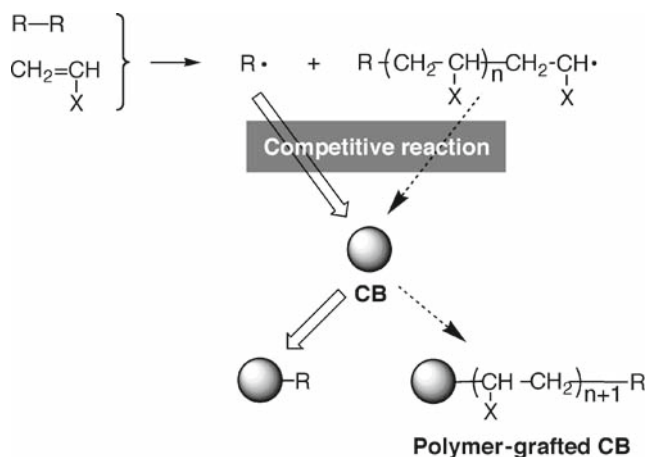
can achieve scale-up synthesis of polymer-grafted nanoparticles by the use of ionic liquid as solvent.

2.4.2 Grafting of Vinyl Polymers onto Carbon Black by “Grafting onto” Method in Ionic Liquid

As mentioned above, we have reported that the radical polymerization of vinyl monomers, initiated by BPO and AIBN, was remarkably retarded in the presence of carbon black and during the polymerization, a part of the polymer formed was grafted onto the surface based on the termination (trapping) of growing polymer radical by carbon black [51, 52]. That is, it is considered that competitive reactions of initiator radicals and growing polymer radicals onto the surface proceed during the polymerization (Scheme 2.8). Therefore, the effect of 1-butyl-3-methylimidazolium hexafluorophosphate as ionic liquid on the radical polymerization in the presence of carbon black was investigated [53].

2.4.2.1 Experimental Procedures

The radical graft polymerization of vinyl monomers initiated by benzoyl peroxide (BPO) and 2,2'-azobisisobutyronitrile (AIBN) in the presence of carbon black was



Scheme 2.8 Competitive reactions of polymer radical and fragment radical to carbon black surface

carried out in a sealed tube under high vacuum [4–7]. A typical example was as follows. Into a polymerization tube, 0.10 g of carbon black, 5.0 ml of vinyl monomer, 10.0 ml of solvent, 0.10 g of BPO (AIBN) and a stirrer bar were charged. The mixture was frozen in a liquid nitrogen bath, degassed with a vacuum pump and then thawed. After this operation was repeated three times, the tube was sealed under vacuum. The sealed tube was heated with stirring. After the graft polymerization, small amount of methanol was added into the reaction mixture in order to terminate the polymerization.

2.4.2.2 Radical Graft Polymerization of Vinyl Monomers Initiated by BPO in the Presence of Carbon Black

Figures 2.13 and 2.14 show effect of ionic liquid on the radical polymerization of St and MMA, respectively, initiated by BPO in the presence of carbon black. It was found that when toluene was used as solvent, the polymerization was remarkably retarded. It is interesting to note that the retardation of polymerization observed in the presence of carbon black almost disappeared in the initial stage of the polymerization in ionic liquid.

Figures 2.15 and 2.16 show the relationship between the reaction time and percentage of polySt and polyMMA grafting, respectively, onto carbon black surface. In toluene, the grafting of polySt onto the carbon black surface was less than 1%. On the contrary, in ionic liquid, the percentage of polySt grafting increased with increasing reaction time and reached 4%.

On the other hand, effective grafting of polyMMA onto carbon black was achieved in ionic liquid: the percentage of grafting reached 35% after 30 h.

Fig. 2.13 Effect of ionic solvent on the polymerization of St initiated by BPO in the presence of carbon black: Carbon black, 0.10 g; BPO, 0.10 g; St, 5.0 mL; solvent, 10.0 mL; 60°C

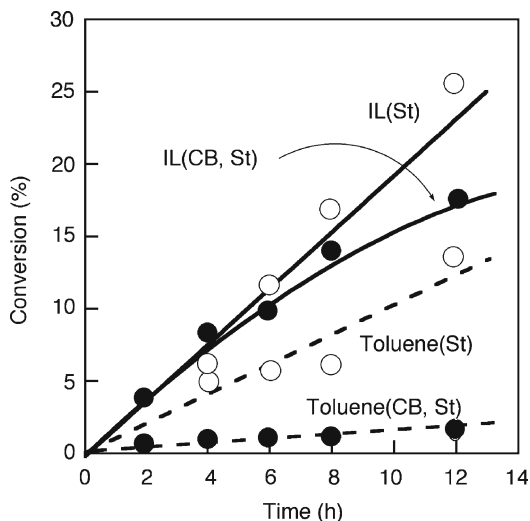


Fig. 2.14 Effect of ionic liquid on the polymerization of MMA initiated by BPO in the presence of carbon black: Carbon black, 0.10 g; BPO, 0.10 g; MMA, 5.0 mL; solvent, 10.0 mL; 60°C

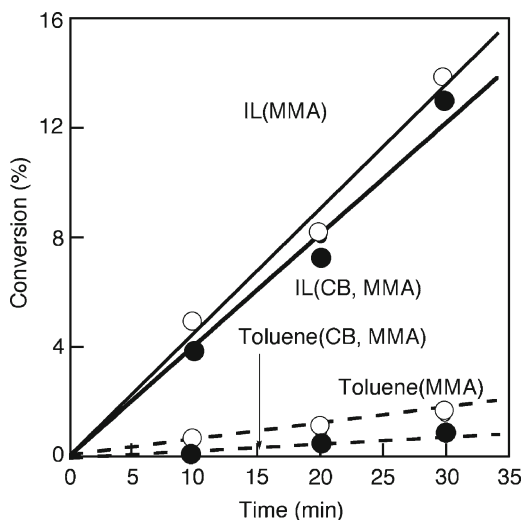


Figure 2.17 shows relationship between conversion and grafting efficiency in the polymerization shown in Fig. 2.13. It is interesting to note that the grafting efficiency in ionic liquid was larger than that in toluene. It was found that the grafting efficiency in ionic liquid also remarkably decreased with increasing conversion as well as in toluene.

The grafting of polySt and polyMMA onto carbon black surface was confirmed by FT-IR and thermal decomposition GC-MS. These results may be explained as follows. In toluene, the initiating radicals (benzoyloxy radicals) were preferentially

Fig. 2.15 Relationship between polySt grafting and reaction time. Polymerization conditions are given in Fig. 2.13

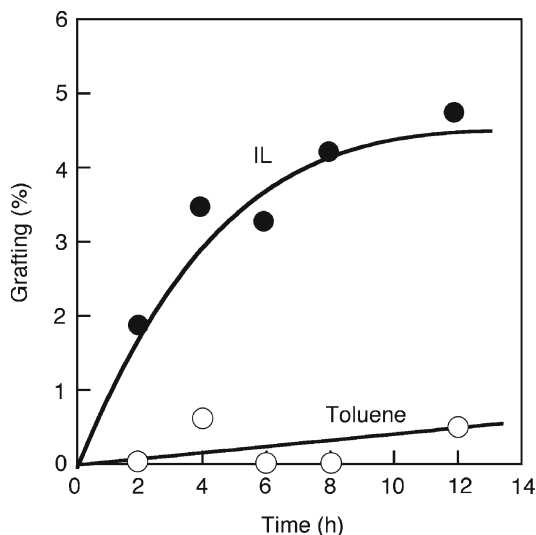
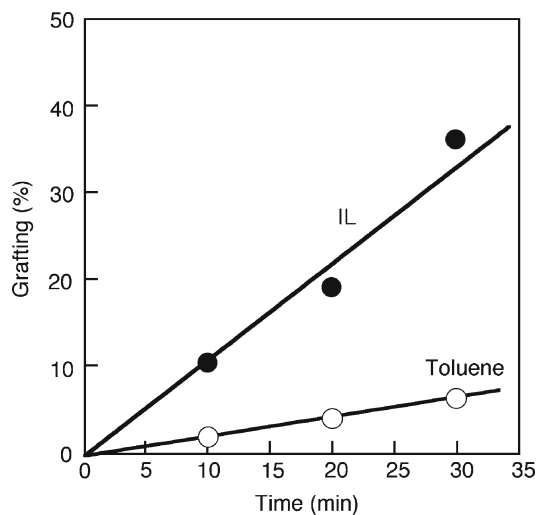


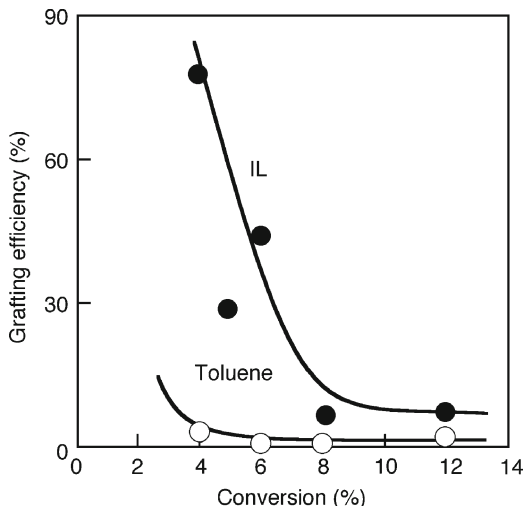
Fig. 2.16 Relationship between polyMMA grafting and reaction time. Polymerization conditions are given in Fig. 2.14



trapped by carbon black surface and the polymerization is retarded. During the polymerization, a part of growing polySt radicals was trapped by carbon black surface; the percentage of grafting was very small. This indicates that very low molecular weight of polySt was grafted onto the surface in toluene.

On the contrary, in ionic liquid growing polySt radicals with relatively high molecular weight were trapped by carbon black surface to give polySt-grafted carbon black, because of stabilization of radicals in ionic liquid (Scheme 2.8).

Fig. 2.17 Relationship between conversion and grafting efficiency of polySt in ionic liquid. Polymerization conditions are given in Fig. 2.13



2.4.2.3 Radical Graft Polymerization of MMA Initiated by AIBN in the Presence of Carbon Black

Figure 2.18 shows the results of the radical polymerization of MMA in the presence of carbon black initiated by AIBN in ionic liquid and toluene. It was found that the retardation of the radical polymerization of MMA in the presence of carbon black was also remarkably reduced in ionic liquid. The polymerization behavior of MMA initiated by AIBN shows almost the same tendency as that initiated by BPO in the presence of carbon black.

Figure 2.19 shows the relationship between reaction time and percentage of polyMMA grafting. It was found that the percentage of grafting increased with increase in reaction time. The percentage of grafting in ionic liquid was also much larger than that in toluene.

2.4.3 Grafting of Vinyl Polymers onto Silica Nanoparticles and Carbon Black by “Grafting from” Method in Ionic Liquid

As mentioned above, the radical graft polymerization of vinyl monomers were initiated by the surface azo groups previously introduced onto silica nanoparticle and carbon black, and the corresponding polymer-grafted silica nanoparticle and carbon black can be obtained by “grafting from” method [5, 6]. The effect of ionic liquid on the radical grafting of vinyl polymers onto silica nanoparticle and carbon black by “grafting from” method was investigated [54].

Fig. 2.18 Effect of ionic liquid on the polymerization of MMA initiated by AIBN in the presence of carbon black: Carbon black, 0.10 g; AIBN, 0.10 g; MMA, 5.0 mL; solvent, 10.0 mL; 60°C

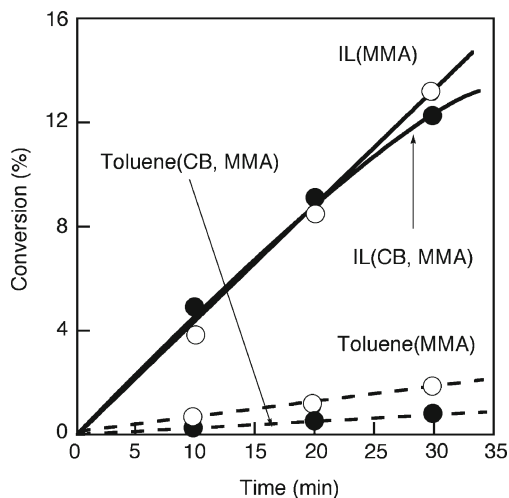
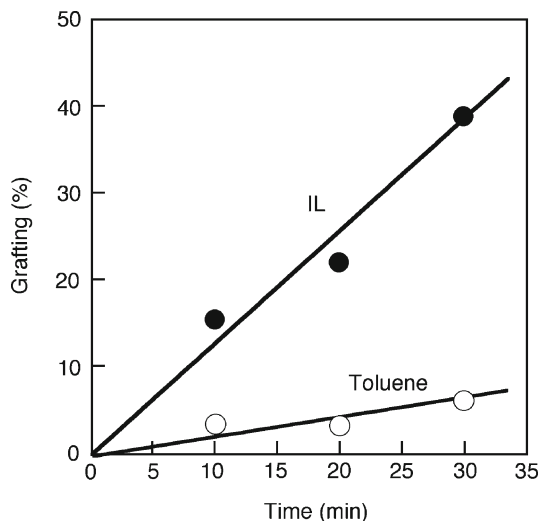


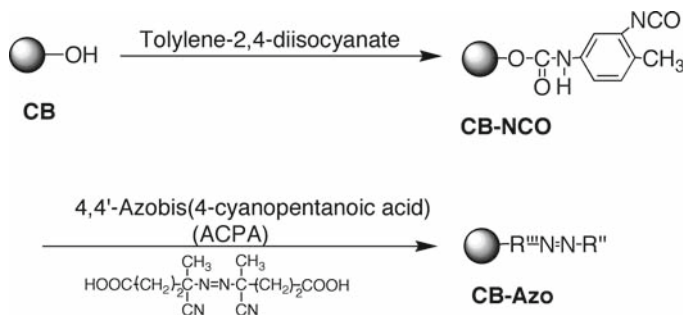
Fig. 2.19 Relationship between polyMMA grafting and reaction time. Polymerization conditions are given in Fig. 2.18



2.4.3.1 Experimental Procedures

Introduction of Azo Groups onto Carbon Black Surface

The introduction of azo groups onto carbon black surface was achieved by the reaction of 4,4'-azobis(4-cyanopentanoic acid) (ACPA) with isocyanate groups, which were introduced by the reaction of carboxyl and phenolic hydroxyl groups on carbon black surface with toluene-2,4-diisocyanate (TDI) as shown in Scheme 2.9 [4]. Into a 100-mL flask, 2.0 g of carbon black, 60 mL of dimethyl sulfoxide (DMSO), 0.6 mL of TDI, and α -picoline were charged. The mixture was stirred for 4 h with a



Scheme 2.9 Introduction of azo groups onto carbon black surface

magnetic stirrer at room temperature under dry nitrogen. After the reaction for 4 h, the flask was cooled to room temperature. Then 1.0 g of ACPA was added into the flask and the reaction was continued with stirring for 8 h at 25°C. After the reaction, carbon black was repeatedly washed with methanol and dried in vacuo at room temperature. The treated carbon black was stored in the dark below -5°C. The content of azo groups was determined to be 0.11 mmol g⁻¹ by DSC. The resulting carbon black is abbreviated as CB-Azo.

Radical Graft Polymerization of Vinyl Monomers Initiated by Azo Groups Introduced onto Silica Nanoparticle and Carbon Black Surface in Ionic Liquid

The radical graft polymerization of vinyl monomers initiated by azo groups introduced onto silica nanoparticle and carbon black in ionic liquid were carried out in a sealed tube under vacuum. A typical experiment is as follows. Into a polymerization tube, 0.20 g of Silica-Azo (0.15 g of CB-Azo), 5.0–10.0 mL of vinyl monomer, 5.0–10.0 mL of solvents, and a stirrer bar magnet were charged. The mixture was frozen in a liquid nitrogen bath, degassed with a vacuum pump and then thawed. After this, operation was repeated three times and the tube was sealed under high vacuum. The sealed tube was heated under stirring. After the graft polymerization, a small amount of MeOH was added into reaction mixture in order to terminate the polymerization. The precipitate was filtered and dried in vacuo at 30°C.

Isolation of Grafted PolySt from Silica Nanoparticle Surface

To isolate grafted polySt from the silica nanoparticle surface, the polySt-grafted silica nanoparticle was treated with aqueous alkali. A typical experiment is as follows. Into a flask, 1.0 g of polySt-grafted silica nanoparticle and 100 mL of 12% NaOH aqueous solution were charged and the reaction mixture was stirred at 110°C for 8 h. The resulting solution was extracted with toluene twice. The toluene phase was washed with water

and dried over sodium sulfate. By the evaporation of toluene, polySt was obtained and purified by reprecipitation from THF solution to methanol.

2.4.3.2 Radical Graft Polymerization of Styrene and MMA Initiated by Azo Groups Introduced onto Silica Nanoparticle Surface in Ionic Liquid

The effect of ionic liquid as solvent on the radical graft polymerization of styrene and MMA initiated by Silica-Azo was investigated. Figures 2.20 and 2.21 show the

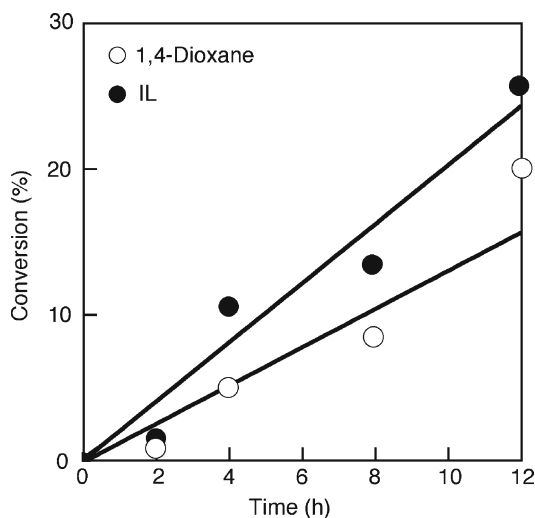


Fig. 2.20 Effect of ionic liquid on the graft polymerization of St initiated by azo groups introduced onto the silica nanoparticle surface: Silica-Azo, 0.20 g; St, 5.0 mL; solvent, 10.0 mL; 70°C

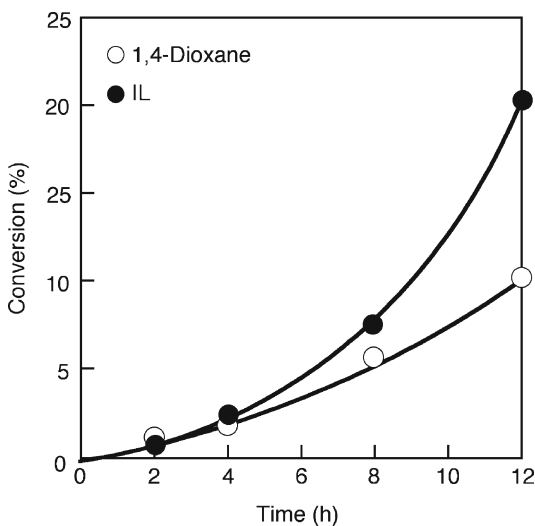


Fig. 2.21 Effect of ionic liquid on the graft polymerization of MMA initiated by azo groups introduced onto the silica nanoparticle surface: Silica-Azo, 0.20 g; MMA, 5.0 mL; solvent, 10.0 mL; 70°C

effect of ionic liquid on the rate of polymerization of styrene and MMA, respectively. It was found that the rate of the polymerization of both monomers initiated by Silica-Azo in ionic liquid was considerably larger than those in 1,4-dioxane.

Figures 2.22 and 2.23 shows the effect of ionic liquid on the grafting of polySt and polyMMA onto the silica nanoparticle surface obtained from the graft polymerization shown in Figs. 2.20 and 2.21, respectively. It was found that the percentage of grafting onto the silica surface increased with increases in reaction time in both the

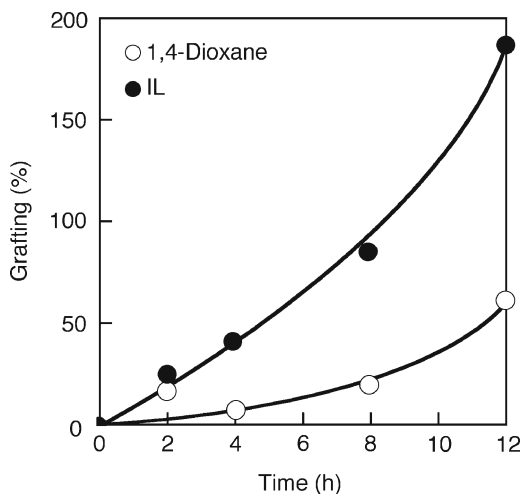


Fig. 2.22 Relationship between polySt grafting and reaction time. Polymerization conditions are shown in Fig. 2.20

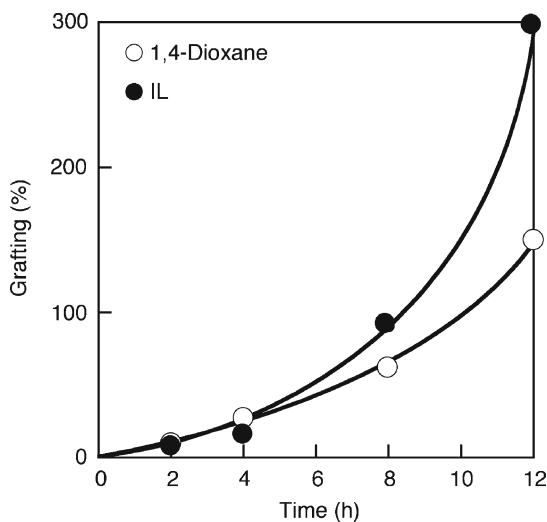


Fig. 2.23 Relationship between polyMMA grafting and reaction time. Polymerization conditions are shown in Fig. 2.21

solvents. It is interesting to note that the percentage of grafting in ionic liquid was much larger than those in 1,4-dioxane: the percentage of grafting exceeded 200%.

This may be due to the fact that the lifetime of radicals are prolonged because of the high viscosity of ionic liquid [44–47].

In the previous paper, we pointed out that the formation of ungrafted polymer preferentially proceeded by chain transfer of the growing polymer chain with the progress of the polymerization and the propagation of grafted chain was blocked by the grafted chain on the surface with the progress of the reaction. Therefore, the grafting efficiency was relatively high, about 50% at the initial stage of the polymerization, but immediately decreased at the middle and last stages of the polymerization as mentioned above (Scheme 2.5).

On the contrary, it is considered that in ionic liquid the propagation of grafted chains from surface radicals formed by the thermal decomposition of azo groups effectively proceeded, because of the stabilization of surface radicals and depression of chain transfer reaction.

2.4.3.3 Radical Graft Polymerization of MMA Initiated by Azo Groups Introduced onto Carbon Black Surface in Ionic Liquid

The effect of ionic liquid as solvent on the radical graft polymerization of MMA initiated by CB-Azo was investigated. Figure 2.24 shows the relationship between the reaction time and conversion, in ionic liquid and 1,4-dioxane. It was found that the rate of the polymerization in ionic liquid was also larger than that in 1,4-dioxane.

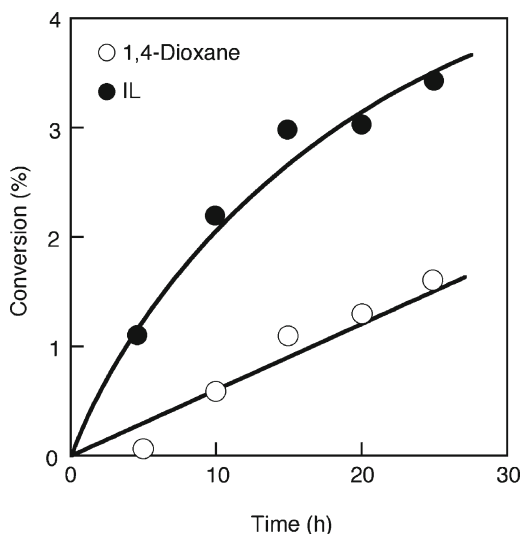


Fig. 2.24 Effect of ionic liquid on the graft polymerization of MMA initiated by azo groups introduced onto carbon black: CB-Azo, 0.15 g; MMA, 10.0 mL; solvent, 5.0 mL; 70°C

Figure 2.25 shows the effect of ionic liquid on the polyMMA grafting onto the carbon black surface obtained from the graft polymerization shown in Fig. 2.24. It was found that the percentage of grafting increased with increase in reaction time in both the solvents and the percentage of grafting in ionic liquid was larger than that in 1,4-dioxane.

2.4.3.4 Effect of Ionic Liquid on the Molecular Weight of Grafted Polymer

PolySt grafted onto silica nanoparticle was isolated by the alkali treatment of polySt-grafted silica nanoparticle. Table 2.14 shows the molecular weight of grafted polySt on silica nanoparticle surface and ungrafted polySt obtained from the graft polymerization in ionic liquid and 1,4-dioxane. It was found that the molecular weight and molecular weight distribution in ionic liquid were almost equal to those in 1,4-dioxane.

On the basis of the above result, the number of the grafted polymers on the silica surface was calculated. The results are shown in Table 2.15. The number of grafted polymers on silica obtained from the polymerization in ionic liquid was about five

Fig. 2.25 Relationship between grafting of polyMMA and reaction time. Polymerization conditions are shown in Fig. 2.24

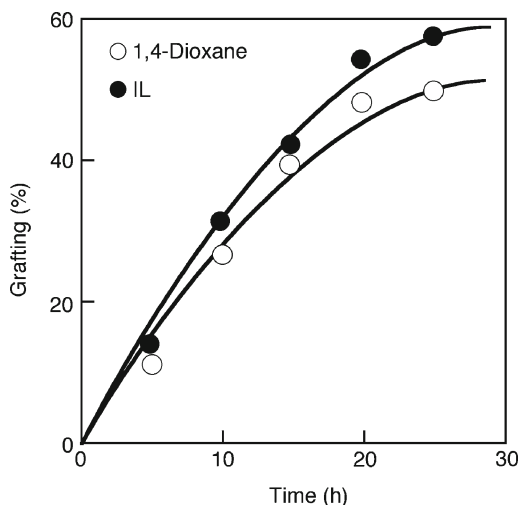


Table 2.14 Molecular weight of polystyrene grafted onto silica nanoparticle surface

Solvent	$M_w \times 10^{-4}$		M_w/M_n	
	Ungrafted Polymer	Grafted polymer	Ungrafted polymer	Grafted polymer
1,4-Dioxane	5.16	5.45	2.01	1.95
IL	5.17	5.47	2.08	2.12

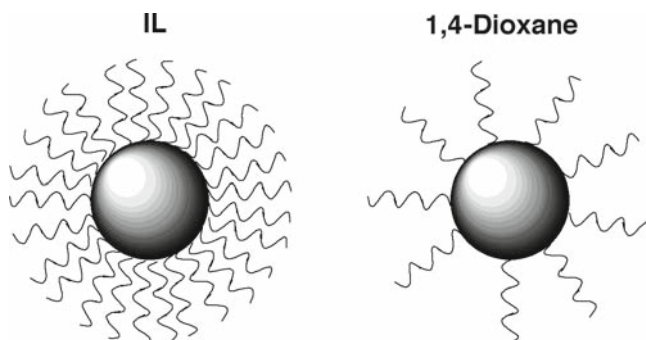


Fig. 2.26 Polymer chains grafted onto silica nanoparticle surface in RT IL and 1,4-dioxane

Table 2.15 Number of grafted polystyrene chains grafted onto silica nanoparticle surface^a

Solvent	No. of grafted polymer	<i>R</i> (%) ^b
1,4-Dioxane	2.1×10^{18}	5.5
IL	9.6×10^{18}	25.0

^aSilica-azo, 0.20 g; styrene, 5.0 mL; solvent, 10 mL; 70°C; 8 h

^b $R = [\text{Grafted polymer (mmol g}^{-1}) / \text{Azo group (mmol g}^{-1})] \times 100$

times larger than that in 1,4-dioxane, as schematically shown in Fig. 2.26. The proportion used for the grafting site to azo group on the surface was about 5% in 1,4-dioxane, but about 25% in ionic liquid, because of stabilization by ionic liquid.

These may be due to the fact that in 1,4-dioxane the growth of grafted polymer chain from silica nanoparticle surface is inhibited by the blocking effect of surface radical by grafted polymer chain, but in ionic liquid, the blocking effect is reduced, because of stabilization by ionic liquid.

2.4.4 *Recycle of Ionic Liquid after the Radical Graft Polymerization*

Ungrafted polymer precipitated because polymer is insoluble in ionic liquid. After the graft polymerization, polymerization was terminated by the addition of small amount of methanol. Therefore, ionic liquid contains polymer-grafted nanoparticles, unreacted monomer, ungrafted polymer, and methanol. The precipitate, containing polymer-grafted nanoparticle and ungrafted polymer, was removed by filtration.

On the other hand, filtrate contains unreacted monomer and methanol. Methanol and monomer were removed from the filtrate under high vacuum at 70°C and the resulting ionic liquid was recovered after washing with water followed by drying under high vacuum at 50°C. The ionic liquid recovered can be reused.

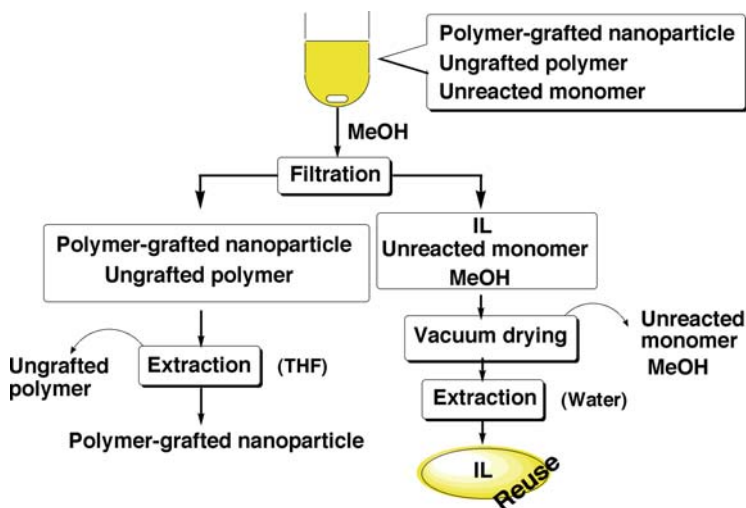


Fig. 2.27 Recycle procedures of ionic liquid after the graft polymerization

Therefore, the reduction of wastage of solvent by recycle and scale-up synthesis of polymer-grafted nanoparticles were achieved by the use of ionic liquid as a reaction solvent (Fig. 2.27).

Acknowledgment This study was partly supported by a Grant in Aid for Scientific Research from the Ministry of Education, Culture, Sport, Science and Technology of Japan (No. 15360357), which is gratefully acknowledged.

References

1. Tsubokawa N (1992) Functionalization of carbon black by surface grafting of polymers. *Prog Polym Sci* 17: 417–470
2. Tsubokawa N (1999) Modification of Inorganic particles by Grafting of Functional Polymers. In: Blits JP, Little CB (eds) *Fundamental and Applied Aspects of Chemically Modified Surface*. The Royal Soc Chem, London, pp 36–51
3. Tsubokawa N (2002) Functionalization of carbon materials by surface grafting of polymers. *Bull Chem Soc Japan* 75: 2115–2136
4. Tsubokawa N, Fujiki K, Sone Y (1988) Graft polymerization of vinyl monomers initiated by peroxyester groups initiated onto carbon black surface. *Polym J* 20: 213–220
5. Tsubokawa N, Kogure A, Maruyama K, Sone Y, Shimomura M (1990) Graft polymerization of vinyl monomers from inorganic ultrafine particles initiated by azo groups introduced onto the surface. *Polym J* 22: 827
6. Fujiki K, Tsubokawa N, Sone Y (1990) Radical grafting from carbon black. Graft polymerization of vinyl monomers initiated by azo groups introduced onto carbon black surface. *Polym J* 22: 661–670
7. Tsubokawa N, Ishida H (1992) Graft polymerization of vinyl monomers by peroxyester groups introduced onto the surface of inorganic ultrafine particles. *Polym J* 24: 809–816

8. Tsubokawa N, Funaki A, Hada Y, Sone Y (1982) Grafting onto carbon black: Graft polymerization of β -propiolactone onto carbon black surface. *J Polym Sci Polym Chem Ed* 20: 3297–3304
9. Tsubokawa N, Yamada A, Sone Y (1983) Grafting of polyester onto carbon black. 4. Copolymerization of epoxide with phthalic anhydride initiated by COOK groups on carbon black surface. *Polym Bull* 10: 63–69
10. Tsubokawa N, Nunokawa H, Sone Y (1986) Cationic grafting from carbon black. 4. Grafting of poly(oxytetramethylene) to carbon black by ring-opening polymerization of tetrahydrofuran initiated by CO⁺CIO⁻ groups on carbon black. *Macromol Sci Pure Appl Chem A23*: 105–115
11. Tsubokawa N, Jian Y, Sone Y (1988) Cationic grafting from carbon black. VIII. Cationic ring-opening polymerization and copolymerization of oxepane initiated by acylium perchlorate groups on carbon black. *J Polym Sci Polym Chem Ed* 26: 2715–2724
12. Tsubokawa N, Tsuchida H (1992) Heat-resistant polymer-grafted carbon black: grafting of poly(organophosphazenes) onto carbon black surface. *J Macromol Sci Pure Appl Chem A29*: 311–321
13. Tsubokawa N, Yanadori K (1922) Reaction of polymer radicals formed by the decomposition of azopolymer with carbon black surface. *Kobunshi Ronbunshu* 49: 865–870
14. Pyun J, Matyjaszewski K (2001) Synthesis of nanocomposite organic/inorganic hybrid materials using controlled living radical polymerization. *Chem Matter* 13: 3436–3448
15. Ohno K, Koh K, Tsuji Y, Fukuda T (2002) Synthesis of gold nanoparticles coated with well-defined, high-density polymer brushes by surface-initiated living radical polymerization. *Macromolecules* 35: 8989–8993
16. Lui T, Jia S, Kowalewski T, Matyjaszewski K, Casadio-Portilla R, Belmont J (2003) Grafting poly(*n*-butyl acrylate) from a functionalized carbon black surface by atom transfer radical polymerization. *Langmuir* 19: 6342–6345
17. Harrak AE, Carrot G, Oberdisse J, Jestin J, Bou F (2005) Atom transfer radical polymerization from silica nanoparticles using grafting from method and structural study via small angle neutron scattering. *Polymer* 46: 1095–1104
18. Lui T, Casadio-Portilla R, Belmont J, Matyjaszewski K (2005) ATRP of butyl acrylates from functionalized carbon black. *J Polym Sci Part A Polym Chem* 43: 4695–4709
19. Liu P, Liu WM, Xue QJ (2004) In situ radical transfer addition polymerization of styrene from silica nanoparticles. *Eur Polym J* 40: 267–271
20. Ding X, Zhao J, Liu Y, Zhang H, Wang Z (2004) Silica nanoparticles encapsulated by polystyrene via surface grafting and in situ emulsion polymerization. *Mater Lett* 58: 3126–3130
21. Wang Y-P, Pei X-W, He Z-Y, Yuan K (2005) Synthesis of well-defined, polymer-grafted silica nanoparticles via reverse ATRP. *Eur Polym J* 41: 1326–1332
22. Wang Y-P, Pei X-W, Yuan K (2005) Reverse ATRP grafting from silica surface to prepare well-defined organic/inorganic hybrid nanocomposite. *Mater Lett* 59: 520–523
23. Yoshinaga K, Teramoto M (1996) Bindings of a secondary polymer to monodisperse colloidal silica particles modified with poly(maleic anhydride-styrene) for controlling the surface polarity. *Bull Chem Soc Jpn* 69: 2667–2672
24. Tomalia DA, Baker H, Dewald J, Hall M, Kallos G, Martin S, Roeck J, Ryder J, Smith P (1985) A New Class of Polymers: Starburst-dendritic macromolecules. *Polym J* 17: 117–132
25. Tomalia DA, Berry V, Hall M, Hedstrand DM (1987) Starburst dendrimers. 4. Covalently fixed unimolecular assemblages reminiscent of spheroidal micelles. *Macromolecules* 20: 1164–1167
26. Tsubokawa N, Ichioka H, Satoh T, Hayashi S, Fujiki K (1998) Grafting of dendrimer onto ultrafine silica surface. *React Funct Polym* 37: 75–82
27. Tsubokawa N, Satoh T, Murota M, Sato S, Shimizu H (2001) Grafting of hyperbranched poly(amidoamine) onto carbon black surface using dendrimer synthesis methodology. *Polym Adv Technol* 12: 569–602
28. Tsubokawa N, Takayama T (2000) Surface modification of chitosan powder by grafting of “dendrimer-like” hyperbranched polymer onto the surface. *React Funct Polym* 43: 341–350

29. Fujiki K, Sakamoto M, Satoh T, Tsubokawa N (2000) Postgrafting of hyperbranched dendritic polymer from terminal amino groups of polymer chains grafted onto silica surface. *J Macromol Sci Pure Appl Chem* A37: 357–377
30. Okazaki M, Murota M, Kawaguchi Y, Tsubokawa N (2001) Curing of epoxy resin by ultrafine silica modified by grafting of hyperbranched poly(amidoamine) using dendrimer synthesis methodology. *J Appl Polym Sci* 80: 573–573
31. Murota M, Sato S, Tsubokawa N (2002) Scale-up synthesis of hyperbranched poly(amidoamine)-grafted ultrafine silica using dendrimer synthesis methodology in solvent-free dry system. *Polym Adv Technol* 13: 144–150
32. Hayashi S, Tsubokawa N (1998) Grafting of polymers having pendant peroxycarbonate groups onto carbon black and postpolymerization of vinyl monomers. *J Macromol Sci Pure Appl Chem* A35: 1781–1796
33. Hayashi H, Takeuchi Y, Eguchi E, Iida T, Tsubokawa N (1999) Graft polymerization of vinyl monomers initiated by peroxycarbonate groups introduced onto silica surface by Michael addition. *J Appl Polym Sci* 71: 1491–1497
34. Ueda J, Sato S, Tsunokawa A, Yamauchi T, Tsubokawa N (2005) Scale-up synthesis of vinyl polymer-grafted nano-sized silica by radical polymerization of vinyl monomers initiated by surface initiating groups in the solvent-free dry-system. *Eur Polym J* 41: 193–200
35. Tsubokawa N (1989) Ring-opening polymerization of 2-oxazolines initiated by chloromethyl groups introduced onto carbon black surface. *Polym Bull* 22: 55–62
36. Saegusa T, Ikeda H, Fujii H (1972) Isomerization Polymerization of 2-Oxazoline. II. Propagating Species and Mechanism of unsubstituted 2-oxazoline polymerization. *Polym J* 3: 176–180
37. Saegusa T, Ikeda H, Fujii H (1972) Isomerization polymerization of 2-oxazoline. I. preparation of unsubstituted 2-oxazoline polymer. *Polym J* 3: 35–39
38. Ueda J, Gang W, Shirai K, Yamauchi T, Tsubokawa N (2008), Cationic graft polymerization onto silica nanoparticle surface in a solvent-free dry-system. *Polym Bull* 60: 617–624
39. Tsubokawa N, Asano I, Sone Y (1987) Cationic ring-opening polymerization of 2-substituted-2-oxazoline initiated by carbon black surface. *Polym Bull* 18: 377–384
40. Tsubokawa N, Takeda N, Kudoh K (1980) Carbon black as an initiator of cationic polymerization of isobutyl vinyl ether. *Carbon* 18: 163
41. Tsubokawa N, Takeda N, Kudoh K (1980) Cationic polymerization of isobutyl vinyl ether initiated by carbon black surface. *Nippon Kagaku Kaishi* 1980: 1264–1268
42. Tsubokawa N, Takeda N, Iwasa T (1981) Cationic polymerization of vinyl monomers initiated by carbon black surface. *Polym J* 13: 1093–1097
43. Ueda J, Yamauchi T, Shirai K, Tsubokawa N (2005) Graft polymerization onto nano-sized particle surface in solvent-free dry-system. *Polym Preprints Jpn* 54: 2706
44. Brazel CS, Rogers RD (2005) Ionic liquids in polymer systems: solvents, additives, and novel applications. ACS symposium series 913. American Chemical Society, Washington, DC
45. Carmichael AJ, Haddleton DM (2003) Polymer synthesis in ionic liquids. In: Wasserscheid P, Welton T (eds) *Ionic Liquids in Synthesis*. Wiley-VHC, Weinheim, pp 319–335
46. Wilkes JS (2002) A short history of ionic liquids—from molten salts to neoteric solvents. *Green Chem* 4: 73–80
47. Harrison S, Mackenzie SR, Haddleton DM (2002) Unprecedented solvent-induced acceleration of free-radical propagation of methyl methacrylate in ionic liquids. *Chem Commun* 23: 2850–2851
48. Carmichael AJ, Haddleton DM, Bon SAF, Seddon KR (2000) Copper(I) mediated living radical polymerization in an ionic liquid. *Chem Commun* 14: 1237–1238
49. Sarbu T, Matyjaszewski K (2001) ATRP of methyl methacrylate in the presence of ionic liquids with ferrous and cuprous anions. *Macromol Chem Phys* 202: 3379–3391
50. Biendron T, Kubisa P (2001) Atom-Transfer Radical Polymerization of Acrylates in an Ionic Liquid. *Macromol Rapid Commun* 22: 1237–1242
51. Ohkita K, Tsubokawa N, Kadoi H, Suneya Y (1972) Polymerization reaction of vinyl monomers in the presence of carbon black. *Nippon Gomu Kyokaishi* 45: 1074–1080

52. Ohkita K, Tsubokawa N, Takashina N (1976) The free radical polymerization of vinyl monomers in the presence of carbon black. *Nippon Gomu Kyokaishi* 49: 223–230
53. Ueda J, Yamaguchi H, Shirai K, Yamauchi T, Tsubokawa N (2008) Radical polymerization of vinyl monomers in the presence of carbon black initiated by 2,2'-azobisisobutyronitrile and benzoyl peroxide in ionic liquid. *J Appl Polym Sci* 107: 3300–3305
54. Ueda J, Yamaguchi H, Yamauchi Y, Tsubokawa N (2007), Radical graft polymerization of vinyl monomers onto nanoparticles in ionic liquid initiated by azo groups introduced onto the surface. *J Polym Sci Part A Polym Chem* 45: 1143–1149

Chapter 3

Inorganic–Organic Hybrid Porous Materials

Nicola Hüsing and Sarah Hartmann

Abstract Hybrid materials are becoming increasingly important because of the possibility of combining inorganic, organic, and even biological entities and functions in a well-defined host matrix.

Soft chemistry-based processes (i.e., chemical pathways at low temperatures and pressures, from molecular, colloidal, or polymeric precursors) clearly offer the most favourable paths towards hybrid materials. Especially the mild reaction conditions and the high adaptability of the sol–gel process are very promising in the design of hybrid inorganic–organic matrices.

For a porous material many favourable properties are derived from its specific porous structure. This structure is typically built-up by a deliberate positioning of the different building blocks to form the inorganic framework, which determines the pores' size, shape, and arrangement. Many of the properties of these materials, e.g. extremely low thermal conductivity, large adsorption capacity, etc are a consequence of the highly porous structure. Therefore, any chemical modification of the inorganic network must retain this specific structure.

For many inorganic porous materials modifications of the backbone are necessary to provide a certain specific functionality, surface chemistry, or even active sites. These modifications make the material more suitable for application in catalysis, sensing, or separation technologies. A significant surface modification for materials is performed in chromatography, in which very often long alkyl chains as hydrophobic surface groups are incorporated.

This chapter on hybrid porous materials will focus the discussion on the chemical functionalization of different types of hybrid porous materials that are zeolites, aerogels, M41S materials, and frameworks with a hierarchical organization of the pore structure. Each of these materials has a distinct way of preparation to produce the pore structure, therefore, different pathways give optimal results for an organic functionalization.

Following a short introduction on soft chemistry-based approaches toward the formation of oxidic inorganic networks in general (sol–gel chemistry), we will

N. Hüsing (✉) and S. Hartmann
Ulm University, Inorganic Chemistry I, Albert-Einstein-Allee 11, 89081 Ulm, Germany
e-mail: nicola.huesing@uni-ulm.de

discuss the specific properties of the different porous matrices, starting from microporous, to mesoporous, macroporous materials and finally networks with hierarchical organization of the pore structure. In the second part of this chapter, different alternatives for the functionalization and modification of these porous networks are discussed, starting with different strategies such as grafting of organic groups, co-condensation reactions, or incorporation of the organic moieties as an integral part of the pore wall for the different porous matrices. It will be shown that, in principle, the general strategies for the modification of both types of porous materials are the same, but that different problems are encountered, which means that the applicability of various methods for different materials can vary significantly.

3.1 Introduction

3.1.1 General Principles of Sol–Gel Processing

The sol–gel process can be described as the creation of an oxide network by progressive polycondensation reactions via a sol, gelation of the sol and finally removal of the solvent. Starting from homogeneous liquid mixtures of all components enables mixing on a nanometric scale, and thereby easy processing of different macro-morphologies such as fibres, monoliths, films, and powders [1–3]. Sol–gel systems typically solidify under kinetic control. Therefore, slight changes of the experimental parameters such as pH, temperature, concentration of the precursors, choice of solvent, and counter-ions, etc can lead to substantial differences in the final material properties, e.g. structure, morphology, etc.

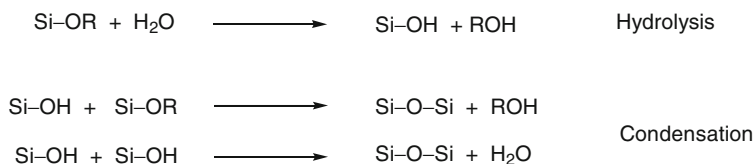
Before going into detail to the mechanisms by which the solids are eventually formed, the terms “sol” and “gel” must be defined. A *sol* is a stable suspension of colloidal solid particles or polymers in a liquid. These particles can be amorphous or crystalline. A *gel* consists of a porous, three-dimensionally continuous solid network surrounding and supporting a continuous liquid phase. In most “inorganic” sol–gel systems, gelation is due to the formation of covalent bonds, e.g. for silica, siloxane bonds are formed.

3.1.1.1 Silica-Based Materials

Various types of precursors can be used to prepare silica gels by sol–gel processing. The most common precursors are aqueous solutions of sodium silicates (“water glass”) and silicon alkoxides ($\text{Si}(\text{OR})_4$).

Hydrolysis and Condensation

The chemical reactions during sol–gel processing of silica-based materials can be formally described by three equations (Scheme 3.1). In alkoxide-based systems,



Scheme 3.1 Basic sol–gel reactions

hydrolysis reactions generate Si–OH groups from Si–OR groups before condensation can take place. Condensation can occur either via an alcohol-producing mechanism, or via a water-producing mechanism.

These chemical reactions seem to be straightforward and easy to understand, however, the overall picture is much more complex, since hydrolysis and condensation reactions occur simultaneously and compete with each other during all steps of the sol–gel process. Thus, a large variety of different species can be found in a single reaction mixture. In addition, parameters such as pH, temperature, concentration of the precursors, etc influence the reaction rates of the hydrolysis and condensation reactions to a different degree. The final properties of the obtained gel depend to a large extent on the structural evolution that is governed by the relative rate of the hydrolysis and condensation reactions.

Two chemically different situations have to be considered for silicon-containing sol–gel precursor systems: reactions under acidic or basic conditions, respectively. The point of zero charge (PZC) of Si–OH-containing species lies between pH 1.5 and 4.5, depending on the degree of condensation (the higher the degree of condensation, the lower the PZC). Acidifying the solution to a pH below the PZC means that the siliceous species are positively charged, and increasing the pH above the PZC (more basic) means that the species are negatively charged.

Under acidic conditions the oxygen atom of an Si–OH or an Si–OR group is protonated in a rapid first step and a good leaving group (with water or alcohol) is created. In addition electron density is withdrawn from the central silicon atom, making it more electrophilic and thus more susceptible to be attacked by water (hydrolysis) or silanol groups (condensation). Under basic conditions, to which we generally refer when the reactions occur at a pH > 3, the reaction proceeds via a nucleophilic attack of either an OH[−] or ≡Si–O[−] ion to the silicon atom by an S_N2-type mechanism.

Some general trends in the reactivity of alkoxy silanes: the rate of hydrolysis of alkoxy silanes decreases as the steric bulk of the alkoxide group increases. The relative rates for the first hydrolysis of alkoxy silanes reveal that MeO >> EtO > n-PrO > n-BuO. In most cases the methoxy or ethoxy derivatives are used, with the latter being favored because of the lower toxicity of ethanol. In organotrialkoxy silanes, which are often used in the synthesis of hybrid materials, the nature of the organic group (R') has strong electronic and steric effects on the hydrolysis and condensation chemistry and therefore, exerts a profound influence on the progress and ultimate product of the sol–gel process. These effects are especially important when mixtures

of tetra- and organically modified trialkoxysilanes are employed. Due to the different reaction mechanisms that have been discussed above, electron-donating groups such as alkyls (methyl, ethyl, etc) increase the rates of hydrolysis and condensation relative to tetraalkoxysilanes under acidic conditions. The opposite is true in an alkaline environment, in which electron-donating groups decrease the reaction rates of the organotrialkoxysilane compared to the tetraalkoxysilane [2, 4].

In addition hydrolysis reactions of alkyltrialkoxysilanes and condensation of the corresponding silanols are very sensitive to the steric bulk of the alkyl group with the rate of reaction decreasing as the alkyl substituent changes from methyl to ethyl, propyl or butyl. Functional groups, e.g. such as aminopropyl moieties might interfere with the sol–gel reactions due to the basic properties and thus lead to complete mechanistic changes. For more information on sol–gel processing of organo trialkoxysilanes see the corresponding references [5–9].

Very important modifications of sol–gel materials are based on a covalent linkage of organic groups to the inorganic network. The mild processing conditions (“chimie douce”) allow the integration of a wide variety of organic groups. In silica-based processes, organotrialkoxysilanes such as $R'-Si(OR)_3$ or $(RO)_3Si-R'-Si(OR)_3$ can be used in the same way as tetraalkoxysilanes. The covalent Si–C bonds are hydrolytically stable and therefore, the organic group is retained in the final material. The choice of R' is almost unlimited (see wide infra), and many functional groups can be used. Materials that are built from those modified trialkoxysilanes only, are usually termed silsesquioxanes – describing an average stoichiometry of 1.5 or sesqui oxygens per silicon.

Only very few studies report on the formation of porous materials from pure silsesquioxanes, e.g. methyltrialkoxysilanes, and these synthesis procedures are typically performed under extreme pH conditions [8, 10–13]. This can probably be attributed to (a) the lower degree of cross-linking that is expected when precursors are used with only three potential reaction sites (resulting in long gelation times), (b) the mechanical instability of the resulting gels due to the lower connectivity and (c) phase separation phenomena of oligomeric or polymeric silsesquioxanes due to the polarity differences within the precursor molecule [8].

Gelation, Aging, and Drying

The sol–gel transition (gel point) is reached when a continuous three-dimensional network is formed. The faster the condensation reactions, the faster gel formation takes place. The final network structure – polymeric versus colloidal – does strongly depend on the reaction conditions chosen in the beginning. An extremely important aspect of the preparation of inorganic gels by sol–gel processing is that the chemical reactions are not completed with the formation of the solid network. The pore liquid still contains condensable particles, and structural rearrangements of the gel network might take place (Ostwald ripening, syneresis). Therefore, the gel needs to be aged for a certain period of time before it can be dried [1, 2, 9].

While reaction rates and physical changes slow down in the gel state, one must remember that the system is still dynamic. This can easily be seen by the syneresis that is shrinkage of the gel body with expulsion of the solvent from the gel. Thus it is very critical to control the aging time, because syneresis and other processes can have a profound effect on the porosity and texture of the resulting gels. The final step during sol–gel processing is the drying of the wet gel structure. Here different routes can be followed: The sample can either be dried traditionally in vacuum, typically resulting in strong shrinkage of the gel network, or by surface modification or supercritical drying giving access to porous gels.

3.1.2 Silica-Based Porous Materials

A wide variety of different porous materials are known. Following the classification by IUPAC, they can be grouped by the size of their pores: microporous solids with pore diameters up to 2 nm with zeolites and metal-organic frameworks (so-called MOF structures) as the most prominent representatives, mesoporous solids with pore sizes between 2 and 50 nm, e.g. aerogels, pillared clays, or M41S phases, and macroporous solids with pore sizes larger than 50 nm, such as foams or glasses. In addition, these materials can be distinguished by the arrangement of the pores – periodic or random – and the pore radii distribution, which can either be narrow or quite broad.

3.1.2.1 Statistical Arrangement of Pores: Aerogels

Aerogels are characterized by an extremely high porosity with well-accessible, cylindrical, branched mesopores typically prepared by sol–gel processing followed by supercritical drying. In rare cases, the highly porous structure is retained after surface modification and subsequent drying. The bulk densities of aerogels are very low and typically in the range of 0.003–0.500 gcm⁻³.

Aerogels can be prepared as monoliths, granulates, or powders. The filigrane solid network and, as a result, the pore structure of aerogels is formed by condensation of primary particles which have diameters in the lower nanometer range. Figure 3.1 shows schematically the structural build-up of a silica aerogel. The generation and aggregation of the network forming particles are typically controlled via the conditions chosen for sol–gel processing. There are some recent review articles on various aspects of aerogels [14–21].

One of the big problems particularly for the technical use of unmodified SiO₂ aerogels is their long-term stability in humid atmosphere. The large number of silanol groups on the inner surface results in adsorption and capillary condensation of water, and eventually in the cracking of the gel body by the resulting capillary forces. Therefore, approaches to modify the aerogel network, e.g. with organic

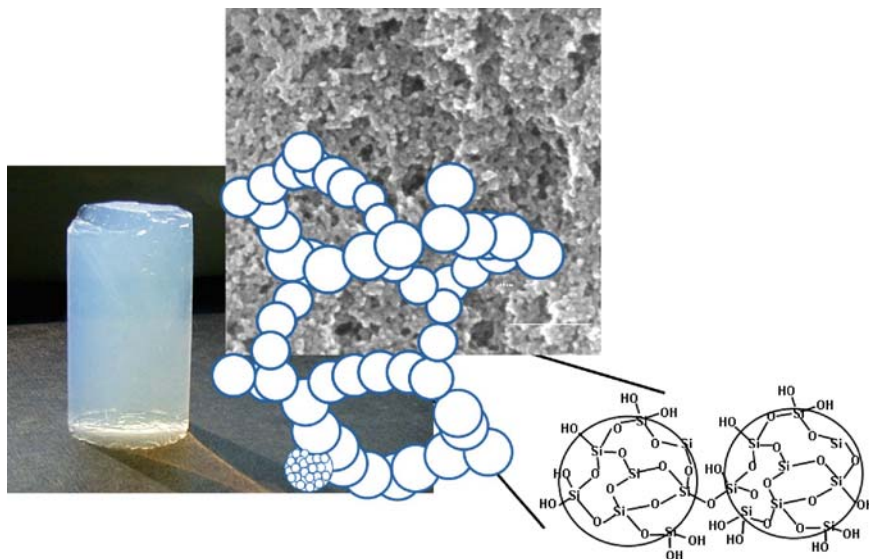


Fig. 3.1 Photograph and schematic representation of a silica aerogel structure

groups to permanently hydrophobize the inner surface, but simultaneously retain the typical structure were investigated quite early.

3.1.2.2 Periodic Arrangement of Pores: Zeolites, M41S-materials and Inverse Opal Structures

Zeolites are microporous crystalline oxides, typically composed of silicon, oxygen, and aluminum with cavities that are interconnected by smaller windows. Since their first discovery in the middle of the eighteenth century, zeolites had been generally regarded as microporous crystalline aluminosilicates having ion-exchangeable cations and reversibly desorbable water molecules (analogue to natural zeolites). Today this definition has been extended for several reasons, i.e. in 1978, a purely siliceous zeolitic material, silicalite, was synthesized, which does not have an ion-exchanging ability (it is an aluminum-free material) and in 1982, the first aluminophosphates were prepared as microporous crystalline molecular sieves again with electrostatically neutral frameworks. It would be far beyond the scope of this chapter to cover all aspects of zeolite chemistry and their microporous analogues. The reader is referred to the literature given in this chapter and specifically to the Handbook of Porous Solids, which covers many different aspects of zeolites [21].

In zeolites, the pores are formed as an inherent feature of the crystalline inorganic framework – thus the pores are also periodically arranged. When discussing pores in zeolites, the reader has to be aware of the fact that one has to distinguish between a cage, in which molecules can be accommodated and the windows to this cage,

which are typically smaller than the actual cage. Therefore, molecules that fit into the cage are not necessarily able to cross the windows, thus diffusion within the material can be drastically limited. The size of the cage (pore) must be spacious enough to accommodate at least one molecule. For the accommodation of water molecules the pore diameter must exceed 0.25 nm which is the lower limit for the pore size in zeolites. Today a wide variety of zeolitic structures either natural or synthetic is well known, covering the pore size regime from 0.25 to 1.5 nm. In addition to the different pore sizes, zeolites can be classified as uni-, bi- and tridirectional zeolites, depending on whether the channel system is arranged along one, two, or the three Cartesian axes. This directionality is extremely important with respect to the ability of guest molecules to diffuse within the zeolite matrix.

Zeolites owe their importance to their use as catalysts in gas-phase, large-scale petrochemical processes, such as catalytic cracking, Friedel-Crafts alkylation and alkylaromatic isomerisation and disproportionation. In addition to their importance in heterogeneous catalysis, it is likely that these solids will also attract interest in the development of functional materials and in nanotechnology, for which zeolites provide an optimal rigid matrix which allows inclusion of some active components.

M41S materials: Since the early 1990s a novel synthetic approach has been available for the preparation of porous solids; this entails the use of supramolecular aggregates (e.g., of surfactants, or amphiphilic block copolymers) serving as templates, thus providing access to porous materials with larger pore sizes from 2 to 50 nm [21]. The first materials with periodic mesoporosity, termed FSM (Folded Sheet Materials) and MCM (Mobil Composition of Matter), were independently developed by the two groups of Yanagisawa et al. and Kresge et al. [22, 23] The latter group developed a synthetic “templating” approach similar to the synthesis of zeolites by applying supramolecular aggregates of surfactants as structure-directing agents (Fig. 3.2), while the former used amphiphilic molecules to swell an inorganic clay material (Kanemite).

Although most of the pathways leading to periodically arranged composites rely on cooperative mechanisms, where the interaction between the inorganic precursor and the amphiphilic structure-directing agent leads to the formation of the lyotropic mesophases far below the critical micelle concentration, some synthetic routes also start from an already preformed liquid crystalline phase of the amphiphile in water,

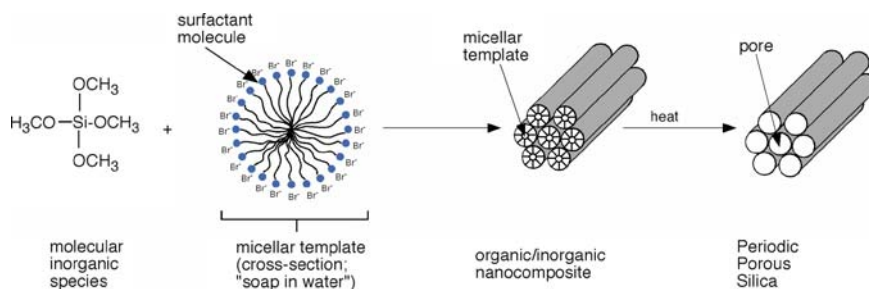


Fig. 3.2 Synthesis scheme of the formation of MCM-41 [adapted from [24]]

thus a true liquid crystal templating (TLCT) pathway is taken. However, in most cases, the organic-inorganic mesophase, which can be converted to a porous material by removing the organic moieties, is formed by the cooperative organization of the liquid crystal-forming organic moieties and inorganic condensable precursors.

So far, the synthetic pathways and the compositional variability of these mesostructured materials have been extensively developed. Silica and alumina are no longer the only two components for mesoporous solids, but various materials composed of transition metal oxides and even pure metals have been prepared. In addition, the pore size, wall thickness, etc. can strongly be influenced by the choice of the structure-directing agent, which can be ionic but also non-ionic. Besides the cationic surfactants of long chain alkyl ammonium molecules mostly applied in the first years as structure-directing agents, amphiphilic block copolymers can also be used as templates for preparing large-pore mesostructured materials [21, 24, 25]. Table 3.1 gives selected examples of the most often prepared periodically organized materials.

Inverse opals: Macroporous solids that are templated from spherical packings of e.g., latexes or Stöber particles (opal structures) will result in inverse opal materials after removal of the spherical packings. Thus a macroporous structure with a periodic arrangement of the macropores is obtained [31, 32]. The general steps for production of such macroporous solids are shown in Figure 3.3.

To obtain a perfectly organized material, much effort is invested in the production of a perfect face-centered cubic (FCC) or hexagonally dense (HDP) sphere packing. To use spheres as templates, several requirements must be met: (a) they must be removable without destruction of the residual porous framework; (b) they must be compatible with the process conditions, (c) they should be wettable with the precursor for the framework, and (d) for a high-quality, low-defect concentration structure they should have a narrow particle-size distribution with a variance of less than 5–8%. These requirements drastically reduce the choice of mould materials to basically two different cases – as already mentioned above: silica spheres produced by the Stöber

Table 3.1 Relevant mesoporous matrices, their structure, abbreviations, pore connectivity and synthesis conditions

Designation	Pore system/symmetry	Synthesis conditions (explanation for the abbreviation, full name of the material)
MCM-41 [24, 26]	2D Hexagonal/ P_6	Basic conditions, cationic template (Mobil composition of matter no. 41)
MCM-48 [24, 26]	Cubic/ I_{a3d}	Basic conditions, cationic template (Mobil composition of matter no. 48)
FSM-16 [22]	2D Hexagonal	From Kanemite (layered clay), cationic surfactant (folded sheet materials no. 16)
HMS [27]	Wormhole-like organization	Acidic conditions, neutral amine templates (hexagonal molecular sieves)
SBA-15 [28]	2D Hexagonal, P_6	Acidic conditions, neutral block copolymer (Santa Barbara no. 15)
KIT-6 [29, 30]	Cubic, I_{a3d}	Acidic conditions, neutral block copolymer, butanol (Korea Advanced Institute of Science and Technology no. 6)

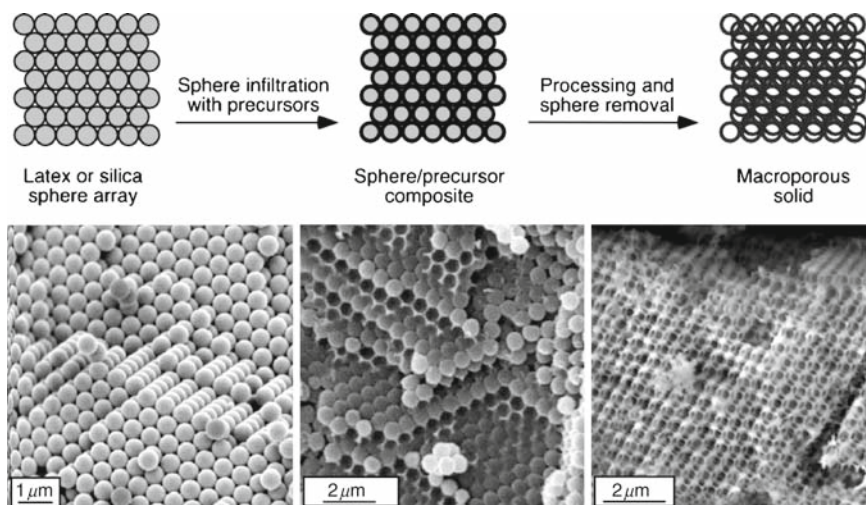


Fig. 3.3 Inverse opal structures and production pathway [31]

process or polymer latexes, which are typically produced by emulsion polymerization processes – both in a narrow particle-size distribution [21]. These preformed particle arrangements are in a second synthesis step infiltrated with a liquid precursor solution (e.g., sol–gel process based). After condensation, the solid composite matrix is dried and the spheres are removed by either calcination or extraction depending on the choice of template (for organic polymers high temperatures are used, for Stöber silica spheres leaching with HF or NaOH can be applied).

The underlying chemistry for the formation of inverse opal structures is very similar to the processes already discussed for M41S materials, the network is typically formed of amorphous silica and the pores are aligned in a periodic fashion – only the pore size varies. As a consequence the same modification procedures apply for the formation of inorganic–organic hybrid materials and the reader is referred to the sections on M41S materials.

3.1.2.3 Materials with Hierarchical Porosity

Materials with hierarchical porosity exhibiting pore sizes over at least two of the aforementioned pores size regimes can also be prepared. These can, e.g., be macroporous materials with zeolitic framework walls, but also M41S type of materials as network forming component in a nonperiodic macroporous foam-like structure. Typical synthesis strategies towards these materials are based on dual/multiple templating or nanocasting approaches applying either hard or soft templates [33–36]. Another simple and reproducible, however, more chemical method is based on sol–gel processing accompanied by phase separation. In a sol, containing a soluble polymer, phase separation can be induced because of changes in the miscibility and

polarity due to the continuous condensation reactions and formation of more hydrophobic siloxane species. At some point during the reaction, the phase-separated structure is just frozen. [37–40]. This approach, also termed polymerization-induced phase separation has been proven a rather successful and variable approach especially in the synthesis of monolithic inorganic but, also inorganic–organic hybrid materials. The bicontinuous structure, in which each separated phase is interconnected in three-dimensions, is spontaneously formed when the transient structure of the phase separation is frozen in by the ongoing inorganic condensation reaction. Nakanishi et al. published a series of papers in which they reported the use of water-soluble organic polymers, such as poly(ethylene oxide) (PEO), to control macroscopic phase separation parallel to the sol–gel transition. Lindén and Nakanishi extended this approach by applying the macroscopic, PEO-polymer-controlled phase separation of silica particles in combination with an ionic or non-ionic surfactant as structure-directing agent in the nanometer regime [41–43]. The material they obtained exhibited interconnected porosity on several length scales, for which the macropore diameter is controlled via PEO-nanoparticle interactions, and the mesopore diameter by the presence of the surfactant e.g., cetyltrimethylammonium bromide or a poly(ethylene oxide)-based polymer.

Figure 3.4 shows a schematic time evolution of the transient structure of the phase separation that can in principle occur by nucleation and growth or spinodal decomposition mechanisms depending on the relative starting concentrations and the choice of the precursors [37].

Silica monoliths exhibiting a unique hierarchical network structure with a bimodal pore size distribution and high surface areas can also be prepared from polyol-modified silanes, e.g., tetrakis(2-hydroxyethyl)-, tetrakis(2-hydroxypropyl)- and tetrakis(2,3-hydroxypropyl)-orthosilicate by sol–gel processing in the presence of amphiphilic block copolymers. For ethylene glycol- and propane-1,2-diol-modified silanes, simply the release of the corresponding diols during sol–gel processing in

Domain Formation by Phase Separation

1. Nucleation and Growth

Dispersed domains with sharp interfaces grow by diffusion controlled kinetics.



2. Spinodal Decomposition

Interconnected domains with diffuse interfaces grow exponentially with time. (Initial stage)



Fig. 3.4 Schematic evolution of networks by either nucleation and growth or spinodal decomposition [37]

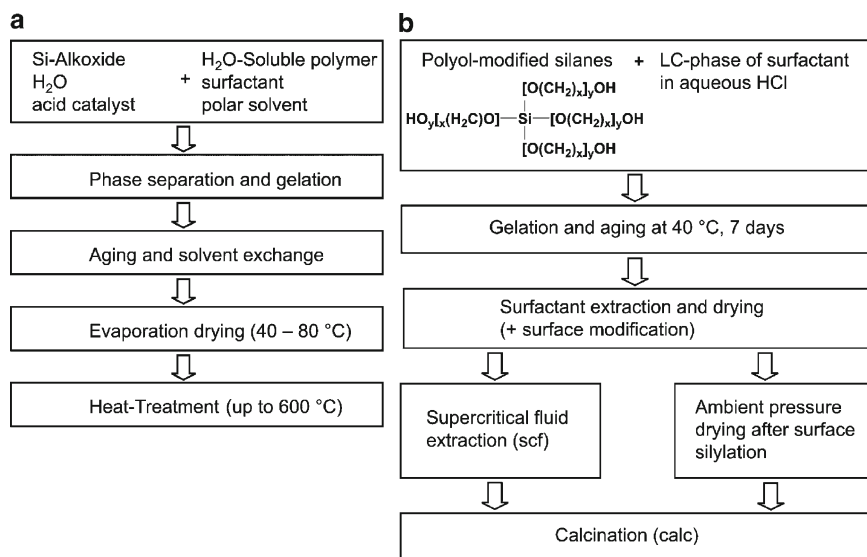


Fig. 3.5 Schematic description of the synthesis protocol towards hierarchically organized silica-based materials (route presented by Nakanishi (a), by Huesing (b))

the presence of the block copolymer surfactant such as Pluronic P123 results in phase separation on several different levels. Figure 3.5 shows a schematic comparison of the two different synthetic approaches by Nakanishi et al. and Huesing et al. In approach (a) phase separation is induced by the addition of an additional polymer e.g., poly(ethylene oxide), in the second one (b) phase separation is induced due to the release of ethylene glycol in the presence of the blockcopolymeric structure-directing agent.

In addition to an extraordinary cellular porous network structure of amorphous silica with interconnected macropores of several hundreds of nanometers up to micrometers in diameter, the material exhibits a well-ordered mesostructure with periodically arranged mesopores of about 6–7 nm in diameter as displayed in Fig. 3.6 [44–46].

3.2 Hybrid Porous Materials

Hybrid inorganic–organic materials are not just physical mixtures of inorganic and organic moieties. They can be defined as nanocomposites with organic and inorganic components that are intimately mixed on a molecular level. The general concept is to combine the properties of organic groups, biomolecules and polymers (functionalization, ease of processing at low temperatures, toughness) with properties of glass- or ceramic like materials (hardness, chemical, and thermal stability), in order to generate

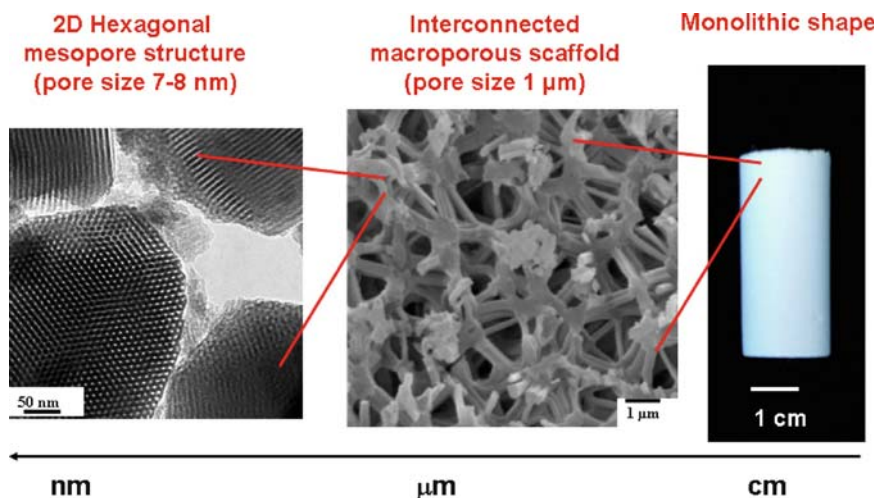


Fig. 3.6 Hierarchical network build-up of a silica gel prepared from tetrakis(2-hydroxyethyl)-orthosilicate in the presence of P123 as structure-directing agent

new and synergetic properties not accessible otherwise. Hybrids are typically either homogeneous systems derived from monomers or miscible organic and inorganic components, or heterogeneous systems (nanocomposites) in which at least one of the components' domains has dimensions ranging from some Å to several nanometers. The properties of the final materials certainly depend to a large degree on the chemical nature of the compounds, however, the synergistic effects arising from the combination of the different moieties cannot be underestimated. Therefore, one key aspect in the synthesis of hybrid inorganic–organic materials is the deliberate positioning of the various species in the network and the design of the nature, the extent and accessibility of the interface between the various parts. One very prominent natural inorganic–organic nanocomposite material is nacre with its alternating layers composed of calcium carbonate and an organic polymer.

Hybrid inorganic–organic materials are typically divided into different classes: [47, 48] Class I materials are typically composed of organic or inorganic moieties embedded in an inorganic or organic matrix, respectively, by only weak chemical bonding (hydrogen, van der Waals or sometimes ionic bonds). In class II materials, the different components are linked on a molecular level by strong bonds (covalent or ionic-covalent bonds). (For further information see also the excellent review articles and the special issue devoted to Hybrid Materials in *J. Mater. Chem.* in 2005 [49] and references herein) [48, 50–56].

In the synthesis of hybrid inorganic–organic materials with an inorganic backbone in general, but also more specifically for porous materials, the sol–gel process plays an essential role, due to its mild processing conditions (metal-organic precursors, organic solvents, low processing temperatures, processing variability of the colloidal state). It allows not only the intact integration of a large variety of organic functions

into an inorganic framework (due to the low temperatures) but also for homogeneous mixing of all components on a nanometric level.

There is a wide range of possibilities to vary the composition and structure and thus the properties of the materials, starting from the chemical composition, the ratio of the inorganic to organic components, the structure and distribution of the building blocks [49]. The ability to entrap molecular species (class I) has been largely used to prepare functional materials applicable in catalysis, optical, electrochemical, and other applications. For porous materials simple entrapment of functional molecules inside the matrix always bears the risk of leaching of the active compound. Therefore, for many applications, covalent bonding to the backbone greatly enhances the lifetime and stability of the material.

Siloxane-based class II materials can be easily synthesized due to the high hydrolytic stability of the Si–C(sp³) bond. A large variety of organo-substituted silanes of the general formula R'–Si(OR)₃ or the corresponding bridged species (RO)₃Si–R'–Si(OR)₃ are available, where R' can be almost any organofunctional group (e.g., an alkyl group, a polymerizable group, a group that complexes metal centres, an organic dye, etc) (Fig. 3.7).

The chemical synthesis pathway that is used to design a given hybrid network structure is one of the most important parameters in the preparation process. General strategies towards the synthesis of hybrid materials are discussed in detail in several review articles [49] and references herein), [48, 50–56]. With respect to porous hybrid matrices many of these synthetic approaches can be used, but in many cases have to be adapted to the specific porous host material.

Chemical modification of porous materials in principle, and covalent modification by organic entities in particular, can be achieved at various stages of the preparation process.

1. Post-synthesis modification of the final dried porous product by gaseous, liquid or dissolved organic or organometallic species
2. Addition of molecular, but non-reactive compounds to the precursor solution
3. Liquid-phase modification in the wet nanocomposite stage or – for mesostructured materials or zeolites – prior to removal of the template
4. Co-condensation reactions by the use of organically substituted co-precursors
5. Application of “single source precursors” in which the organic entity is an integral part of the network-forming species

These approaches open the door to a large variety of porous hybrid materials that benefit from the properties of both parts by the combination of inorganic and organic building blocks. The purpose for is to improve the spectrum of properties without deteriorating the existing positive characteristics by modifying porous materials by organic groups. The favorable physical and derived properties of porous materials are a consequence typical of the highly porous structure. Therefore, any chemical modification of the material must retain this structure. In the case of crystalline microporous materials, the crystallinity and stability of the material should remain unchanged, and for mesostructured porous materials, the periodicity of the structure must be retained [57, 58]. For example, unmodified M41S silica-based materials are

hydrophilic, which is undesired for many applications. The material can be rendered hydrophobic by the introduction of hydrophobic organic groups, e.g., methyl or phenyl groups (*vide infra*). The organic groups can selectively be placed on the internal and/or the external pore surfaces or even within the pore walls. The organic modification in principle permits a very selective fine tuning of material properties, including potential interaction to guest molecules. In addition, surface reactivities can be altered, the surface can be protected by organic groups from chemical attack, and bulk properties, e.g., mechanical or optical properties can be modified. This flexibility in choosing organic, inorganic, or even hybrid building blocks allows control over the materials properties to optimize them for each desired application.

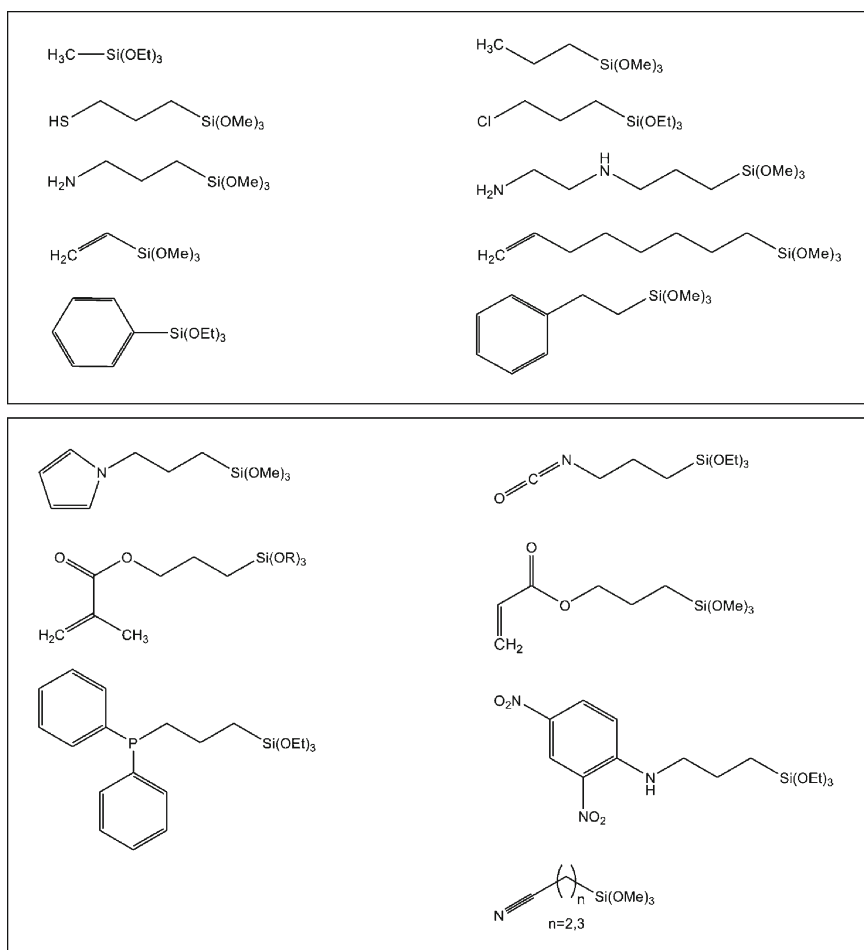


Fig. 3.7 Selection of representative organofunctional silanes available for the preparation of inorganic–organic hybrid materials (APTS = aminopropyltrialkoxysilane)

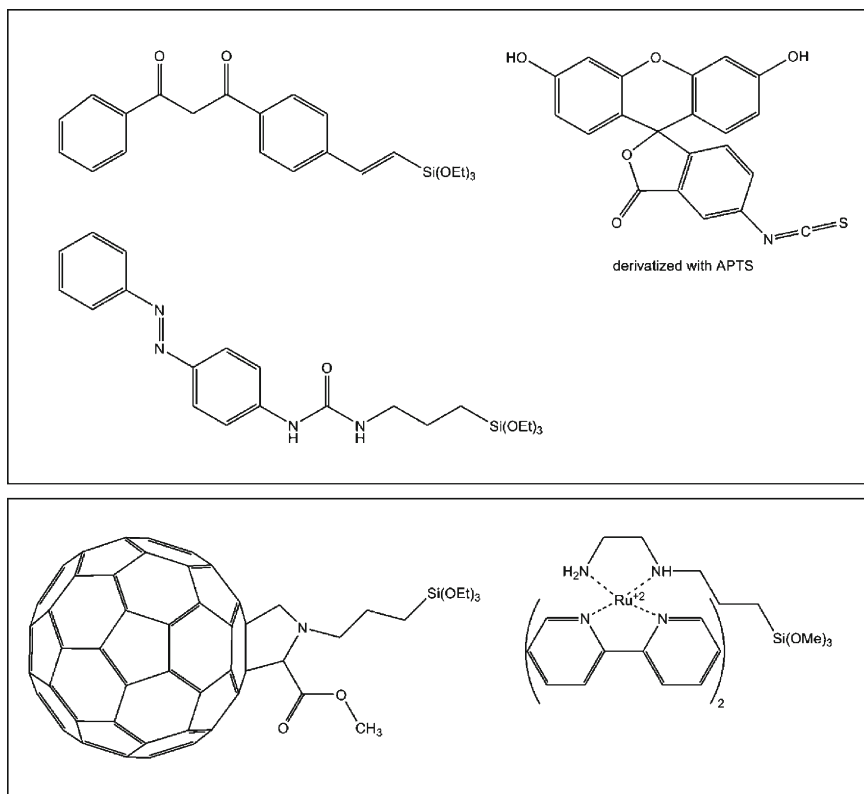


Fig. 3.7 (continued)

The selection of porous matrices that are discussed in the following sections of this chapter is somewhat arbitrary, but represents the general reaction schemes and the problems associated with the different pathways in the synthesis of hybrid porous materials.

3.2.1 *Post-Synthesis Treatment*

The easiest way to modify a porous material with organic groups is to synthesize the porous inorganic network first and add the functionalizing species in a second step. A large number of examples can be found in the literature not only for the different porous matrices, but also for a variety of organic entities. Therefore, the selection of examples given in this section can only be a general overview and the reader is referred to more specialized literature (see references).

The focus of this section lies on the possibilities and problems related to post-synthesis modification of the various porous matrices, the different types of post-synthesis treatments (covalent grafting versus simple impregnation without chemical

attachment) and the various stages of the synthesis process at which the modification can be performed.

3.2.1.1 Zeolites

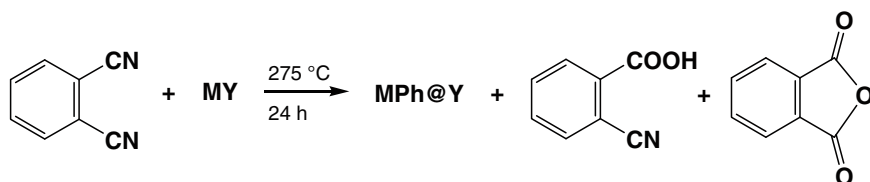
In general – not only for zeolites – a post-synthesis grafting process may be limited in its efficiency, since the organic groups may concentrate near the opening of the channels and show only a limited diffusion into the pores. The smaller the pores, the more severe this problem may become.

Inclusion chemistry in zeolites has already been well reviewed [57, 59, 60]. Just as an example at this point, inclusion of *p*-nitroaniline in ALPO-5 from the gas phase as well as from the liquid phase into the porous zeolitic host is mentioned and very common is also the inclusion of luminescent dye molecules in zeolite L [61–64]. One major aspect in these studies is the alignment of the organic guests in the matrix and subsequent supramolecular organisation to obtain a material with novel electronic properties. For microporous materials, e.g., zeolites, adsorption from the liquid phase is always a competitive process between the adsorption of the guest molecule and the solvent. Here solvents that are sufficiently big to be completely excluded from the micropore system can be used [62].

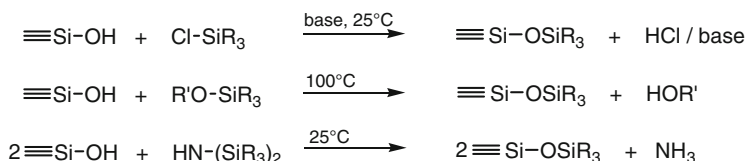
Ions can easily be incorporated into the pore system of porous materials in which the framework walls carry charges. Classical zeolitic frameworks are an excellent example of negative framework charges that can be modified by “simple” aqueous ion exchange processes. These reactions, however, can pose severe problems in some cases, e.g., upon exchange reactions, the crystallinity of the matrix can decrease. The pH is a very critical parameter, especially if metal ions which easily might precipitate as metal hydroxides are involved. In addition, ion exchange is an equilibrium process, which makes it difficult to get quantitative exchange. Nevertheless, a large variety of metal ions and even larger organic molecules can be incorporated into zeolitic frameworks by this approach.

Larger entities that cannot pass the apertures of the pore system of the porous matrix can be formed by the so-called “*ship-in-the-bottle*”-synthesis. Here, small precursors are brought into the pore system, e.g., by simple impregnation via the liquid phase, and are subsequently reacted with each other to produce a bigger guest molecule. One archetypical reaction of a “*ship-in-the-bottle*”-reaction is the synthesis of metallic phthalocyanines inside faujasite X by treating 1,2-dicyanobenzene with a transition metal-exchanged faujasite at temperatures above 200°C (Scheme 3.2). This synthesis allows the incorporation of species into the cavities of zeolites which would otherwise not be able to diffuse through the smaller windows [65–67].

The “*ship in the bottle*”-synthesis has been extended to the preparation of a large variety of molecules for various applications. Metal carbonyl clusters such as Pd₁₃(CO)_x or Rh₆(CO)₁₆ or the heteropolyacid H₃PW₁₂O₄₀ have been successfully synthesized for catalytic applications [67–69]. By a similar approach, a conducting organic polymer – polyaniline – was synthesized in the pores of zeolites after loading the corresponding monomers [70].



Scheme 3.2 Ship in the bottle synthesis (M = metal ion, Ph = phthalocyanine, and Y = zeolite Y)



Scheme 3.3 Possible surface silylation reactions with chlorosilanes, alkoxy silanes and silazanes and R' = organic (functional) group

Grafting refers to a post-synthesis modification of a pre-fabricated porous host by attaching functional/organic moieties to the inner surface. Grafting reactions can be performed prior to or after drying the porous material. If templates or structure-directing agents are employed in the synthesis of the material, grafting is typically performed after removal of the template, however, some examples show that grafting can also be used to catch two birds with one stone: template removal and surface functionalization e.g., for zeolites and M41S materials. Scheme 3.3 gives the three possible reaction schemes that are routinely used for the functionalization of siliceous matrices.

These grafting reactions of organosilanes to silanol-containing surfaces are not straightforward for microporous zeolites because a large fraction of the grafted functional groups becomes instead attached to the exterior surface of the zeolite crystals. One also has to keep in mind that the number of reactive silanol groups at the surface of zeolites is not as large as for amorphous materials and that steric constraints due to the small pore sizes may influence the grafting reactions. Nevertheless, in principle the same reactions as discussed in the next section for mesoporous solids apply to zeolites.

3.2.1.2 M41S materials

Introduction of organic groups into the pores of mesoporous ordered materials has been reviewed extensively [49, 71–76]. Many different organic species, organometallic complexes, and even biomolecules can be entrapped into the mesoporous framework via gas or liquid phase without any strong linkage to the pore walls. One of the major problems connected with this approach is leaching of the organic entity with time. However, the post-synthesis functionalization is not limited to

small molecules, but even large entities such as proteins, fullerenes, phthalocyanines, etc. can be included [77–80].

The synthesis of organic polymers inside the pore channel system of mesoporous silica is of high interest, especially with respect to one-dimensional conductivity, if conductive polymers are used. The nanoscale channels of the mesoporous host can act as confinement for the polymerization reaction and thus, limit the formation of polymer side-chains. Consequently a more ordered growth of the polymer chains along the channels is favored. Bein and co-workers have prepared polyaniline nanowires inside the channels of MCM-41 [79, 80]. By polymerizing formaldehyde and phenol inside the pore channels of MCM-41 and subsequent removal of silica by etching with HF. Ozin and coworkers have obtained high aspect ratio, controlled diameter mesoscale poly(phenolformaldehyde) fibers [81]. All these approaches are based on a post-synthesis loading of the monomeric species into the preformed porous silica host matrix. Li et al. have chosen a different approach by using structure-directing agents based on polymerizable thiophene groups. Here, the organic polymer is formed in situ after obtaining the silica/structure-directing agent composite by addition of FeCl_3 [82].

Incorporation of functional groups by grafting reactions to the surface of the pore walls offers a further possibility to tailor the chemical properties of the porous material. This post-synthetic grafting process has been widely employed to anchor various organic groups, including organometallic species, amine and thiol groups, and epoxide functions. However, this method quite often leads to low loadings, an inhomogeneous distribution of the functional groups and a decrease of the pore volume [83]. For an effective grafting via silylation reactions, it is desired to have a large number of surface silanols in the material. If the surfactant has been removed prior to the grafting reaction by calcination, many of the silanol groups are lost due to condensation to neighbouring silanols. In this case, it is advantageous to rehydrate the surface by treatment in boiling water, or by acid hydrolysis or steam treatment. Removal of the surfactant by extraction processes minimizes this loss of silanols. However, without a heat treatment, many silanols show a lower reactivity due to intersilanol-hydrogen bonding. Grafting of enantioselective catalysts has been carried out with a large variety of different species. Hydrogenations, oxidations, dehydrations, hydrolysis, epoxidations, Diels-Alder reactions, and other catalytic systems have been investigated by the grafting of catalytically active material to the pore walls. Especially chiral catalytic centers are of high interest in this context [71–74, 83].

3.2.1.3 Aerogels

For aerogels, post-synthesis treatment of the highly porous dried gel bodies with a liquid phase is difficult, because the wet gels are formed again and the laborious drying process has to be repeated. When a liquid is evaporated from a wet gel, the different stages during drying – shrinkage or gel deformation, condensation of surface silanols due to the shrinkage and finally cracking of the gel body, result in a collapse of the highly porous network structure.

Two processes are of main importance for this collapse upon drying: First, the slower shrinkage of the network in the interior of the gel body results in a pressure gradient which causes cracks. Second, larger pores will empty faster than smaller ones during drying for a gel with differently sized pores, thus the meniscus of the liquid drops faster in larger pores. The walls between pores of different size are therefore subject to uneven stress and crack.

Still the most common method to overcome this network collapse is supercritical drying. In this procedure, the pore liquid is put into the supercritical state. Above the critical point, liquid/gas interfaces no longer exist, and the capillary forces are thus avoided. The supercritical fluid is then slowly vented without crossing the phase boundary between the liquid and the gas [14–20].

Ambient-pressure methods for preparing highly porous aerogels are just emerging. One approach is based on a surface modification of the wet gel by grafting reactions and subsequent solvent exchange. The contact angle between the pore liquid and the pore walls has to be influenced by deliberate modification of the inner surface and variation of the solvent to minimize the capillary forces.

Smith et al. published the first synthesis of ambient pressure dried SiO_2 aerogels in 1992 [84–86]. The procedure involves, in principle, the passivation of the inner surface by silylation of the Si–OH groups with trimethylchlorosilane (see also Scheme 3.3, that is conversion in Si–OSiR₃ groups), thereby inverting the polarity. The gel shrinks strongly during evaporation of the solvent from the pores at ambient pressure, as expected. However, no irreversible narrowing of the pores by formation of Si–O–Si bonds is possible because of the surface silylation (passivation). Therefore, the gel is able to expand to nearly its original size after the pores have been emptied, when its mechanical stability is high enough. This is called “spring-back” effect [87].

3.2.1.4 Hierarchically Organized Materials

A similar approach also using organochlorosilanes and organoalkoxysilanes as post treatment reagents was recently published not for drying, but for the extraction of ionic surfactants from self-assembled silica-surfactant powders [88, 89]. The driving force for this reaction is the replacement of electrostatic interactions at the inorganic–organic interface by covalent siloxane bonds, that is the formation of Si–O–SiR₃ (Fig. 3.8).

Large, low-density silica monoliths with multimodal pore size distribution as prepared by the application of ethylene-glycol modified silanes in the presence of amphiphilic molecules are already high performance materials. However, for many applications, the spectrum of properties of these materials needs to be improved by additional functions, e.g., hydrophobic groups, metal-coordinating groups, etc, without deteriorating the existing structural features such as porosity, periodic ordering, large surface area, etc. Inspired by the successful simultaneous drying, surface modification and surfactant extraction of silica materials as demonstrated by Smith et al. for silica aerogels and Jaroniec et al. for MCM powders, large silica

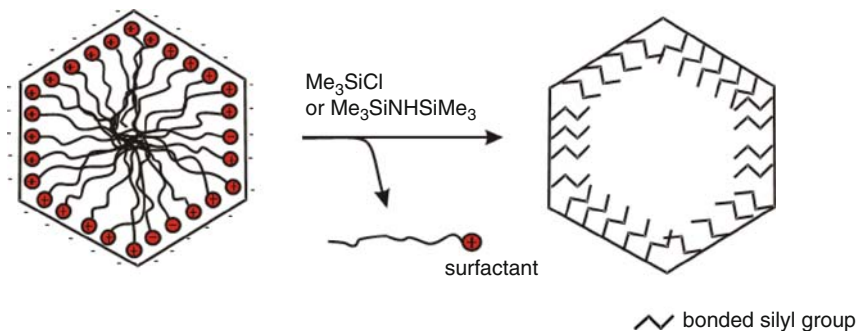


Fig. 3.8 Schematic depiction of the silylation reaction of surface silanols with trimethylchlorosilane or hexamethyldisilazane and concomitant change of surface polarity

monoliths with a hierarchical network organization have been modified by this simple surface silylation reaction of the wet gel structure with simultaneous extraction of the block copolymer amphiphile to almost 100% [90].

A variety of organofunctional silanes such as trimethylchlorosilane, 3-mercaptopropyl-trimethoxysilane, phenyl-trimethoxysilane, 3-[(2,2-dimethyl-1-aza-2-silacyclopent-1-yl)dimethylsilyl]-1-propanamine, a cyclic silazane resulting in aminopropyl-dimethyl-silyl groups on the silica surface, and (methylmethacryloyl) dimethyl-methoxysilane, has been successfully applied in this interfacial modification of the silica surface. Figure 3.9 shows exemplarily the SEM and TEM images of a methacrylate-modified hierarchically structured silica gel. The delicate gel structure is completely retained during the post-synthesis treatment and a rather high bonding density of functional groups to the silica surface with 2–4 mmol $\text{g}(\text{SiO}_2)^{-1}$ is achieved (Fig. 3.9) [45, 46]. This approach can in principle be extended to many many more functional groups. Even further reactions at the functional centres now located on the pore walls are possible.

The resulting material is still characterized by a high surface area (above $500 \text{ m}^2 \text{ g}^{-1}$), narrow pore diameter distribution in the mesoporous regime with pores of about 7 nm and macropores of about 1–2 μm .

3.2.2 *In-situ Synthesis*

As already mentioned above, two different situations have to be distinguished when discussing inorganic–organic hybrid materials: intercalation into the porous host by either weak non-covalent (class I) or strong covalent (class II) interactions.

Organic species can always be added to the precursor solution when a solution based approach such as sol–gel processes are used. Here, the organic components (e.g., a dye, metal complex, etc.) initially present in the precursor solution are typically embedded in the growing metal-oxo-based network. From a preparative point of view, it is desirable to increase interfacial interactions such as hydrogen bonding,

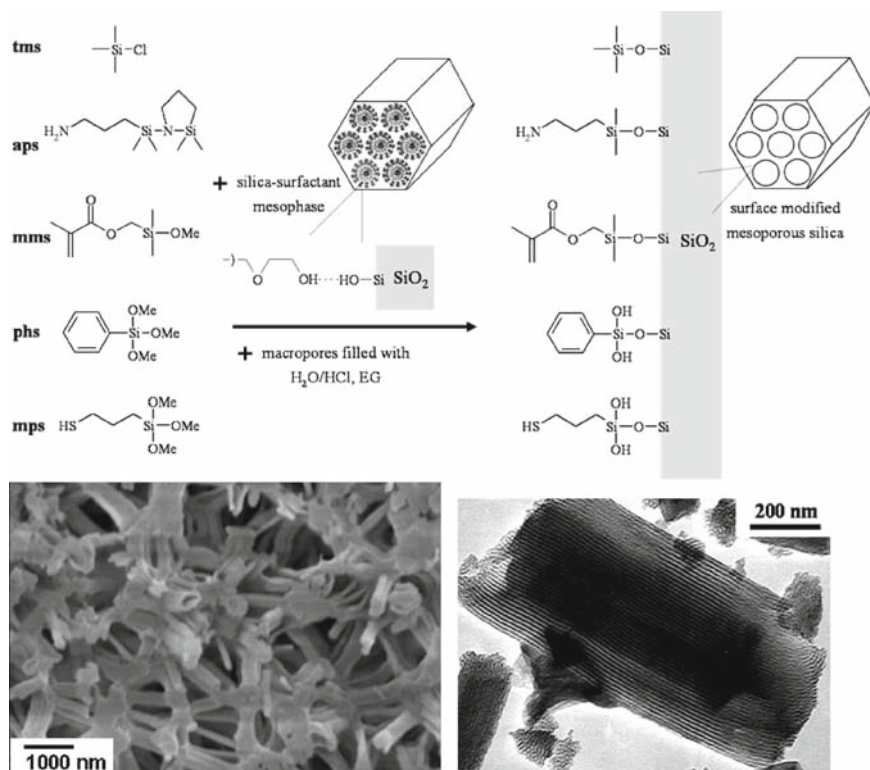


Fig. 3.9 Schematic description of the reaction of organofunctional silanes with a preformed silica gel body, and the corresponding SEM and TEM image for a methacrylate-modified sample

π – π -interactions, etc., to achieve a homogeneous and intimate mixing of all species. However, this very simple way, does not always result in the desired material. Especially when networks with a periodic organization of the pore system are prepared by templating approaches, network formation is very often disturbed by the addition of organic species and non-organized materials or even phase separated structures are formed. For many sol–gel-based materials, the organic component is nevertheless entrapped in the final matrices, which exhibit a wide variety of interesting properties with respect to their mechanical, optical, electrical, ionic, sensor, catalytic behaviour. For porous materials, leaching has always to be discussed as a big problem.

As already discussed above, the sol–gel process offers the possibility to apply organically substituted precursors, such as functional trialkoxysilanes, $R'-Si(OR)_3$, where R' can be almost every organic group (see also Fig. 3.7). The use of these organofunctional precursors results in materials in which the organic group is covalently linked to the inorganic network.

The connectivity of the organotrialkoxysilanes is reduced with respect to the ability to form siloxane bonds. Therefore, it is typically much more difficult to form

stable three-dimensional gel networks in reasonable time scales. To circumvent this problem, but still benefit from the presence of the organic moiety, these precursors are typically processed in the presence of an unsubstituted tetraalkoxysilane. However, one has to keep in mind, that the addition, of the organically substituted trialkoxysilane can have a profound influence on the hydrolysis and condensation reactions. In addition, homo- versus heterocondensation processes have to be considered depending on the reaction kinetics of the different precursors [1–9].

3.2.2.1 Zeolites

For zeolites, typical problems that might be encountered in the synthesis of class I or class II materials by the in-situ approach include:

- *Structural impacts*: The addition of small amounts of organic species to a synthesis mixture can have an extreme influence on the structure. For zeolites, not only mixtures of crystalline phases are obtained, but in some cases crystallization does not occur at all.
- *Phase separation*: Phase separation of the organic phase from the aqueous zeolite synthesis gel is commonly observed.
- *Porosity*: not only structural defects, but also loss of porosity can be a problem. The organic groups are located in the micropores, thus spoiling the microporosity.
- *Loading*: Only a very low amount of organic groups can be incorporated by co-condensation reactions with organically modified silanes of about 1–3% of the Si-atoms into zeolitic frameworks.
- *Template removal*: One methodological disadvantage is the question of the removal of the template (typically calcination) without deteriorating the organic functional moieties on the inner surface.

Addition of organic species to the synthesis solution typically results in loss of crystallinity and periodicity of the zeolite structure. One option is to apply a functional structure-directing agent for two different functions: a) it serves as the structure-directing entity, and b) it adds a specific functionality to the final zeolite nanocomposite structure. This approach was successfully demonstrated for organometallic complexes in zeolite structures such as cobalticinium fluoride nonasil.

In principle, it is possible to synthesize zeolites with pendant organic functionalities. However, attempts at modifying zeolites by co-condensation with organically modified precursors usually create structural defects (loss of crystallinity) or block the internal channels with large pendant groups. By carefully choosing the system, some organically modified zeolites have been prepared. For example, phenethyltrimethoxysilane has been used as modification agent for the preparation of zeolites with *BEA structure and intracrystalline phenethyl groups. Even polar groups have been successfully incorporated into zeolitic structures, e.g., aminopropyl-, mercaptopropyl-, 2-(4-chlorosulfonylphenyl)ethyl-, 3-bromopropyl-moieties, etc. In addition, so-called follow-up reactions to convert functional groups have been successfully performed; such as the sulfonation reaction of the phenethyl-moiety [91, 92].

3.2.2.2 Aerogels

Permanently hydrophobic aerogels were prepared in a simple one-step process using a mixture of tetra- and organo-trialkoxysilanes in alkaline conditions. Sol–gel processing of mixtures of $\text{Si}(\text{OR})_4$ and $\text{R}'\text{-Si}(\text{OR})_3$ ($\text{R}' = \text{alkyl, aryl, or } (\text{CH}_2)_n\text{A}$ ($n = 2, 3$; $\text{A} = \text{SH, OCH}_2\text{-epoxy, OC(O)C(Me) = CH}_2, \text{NCO, Cl, NHC(O)OMe, PPh}_2$) under alkaline conditions proceeds in two steps (see also the discussion of the reaction mechanisms of sol–gel reactions above). Hydrolysis and condensation rates of the organically modified trialkoxysilane are slower than that of the corresponding tetraalkoxysilane in basic media. Therefore, in the first stage of the reaction, the gel network is formed only by hydrolysis and condensation of $\text{Si}(\text{OR})_4$, while $\text{R}'\text{-Si}(\text{OR})_3$ behaves as a kind of co-solvent. Hydrolysis and condensation of $\text{R}'\text{-Si}(\text{OR})_3$ are delayed under these conditions. Once $\text{R}'\text{Si}(\text{OR})_{3-n}(\text{OH})_n$ species are formed, the organically substituted moieties condense to the already preformed silica network (formed from the tetraalkoxysilane). Thus, the $\text{R}'\text{-Si}\equiv$ are positioned specifically on the inner surface of the pores and truly modify the silica particles. Organically substituted silica aerogels with the typical aerogel properties retained in the material have been prepared successfully by this approach [93–96]. Surprisingly the structure of aerogels (porosity, specific inner surface area) is much more influenced by the $\text{Si}(\text{OR})_4/\text{R}'\text{-Si}(\text{OR})_3$ ratio than by the properties of the group R' . Because the trialkoxysilane basically acts as a co-solvent in the first stage of the reaction, the tetraalkoxysilane is more diluted in this stage (resulting in a decrease of the network density), and a larger relative amount of water and catalyst is available for the reaction, thus resulting in larger particles.

Sol–gel processing of $\text{TEOS}/(\text{MeO})_3\text{Si}(\text{CH}_2)_3\text{NR}'_2$ mixtures ($\text{NR}'_2 = \text{NH}_2, \text{NHCH}_2\text{CH}_2\text{NH}_2$), followed by drying of the wet gels with supercritical CO_2 have also resulted in organically functionalized aerogels. However, due to the basic amino groups (which can undergo hydrogen bonding), both silanes appear to be involved in the build up of the aerogel network, by contrast with alkoxysilanes without basic properties [97].

3.2.2.3 M41S Materials

The co-condensation approach (also termed one-pot synthesis) can also be used in the synthesis of organically modified M41S materials. Mixtures of tetraalkoxysilanes and organotrialkoxysilanes in the presence of surfactant template molecules were employed in either a hydrothermal synthesis of mesostructured hybrid powders or in sol–gel based approaches towards mesoporous thin films and bulk materials. Many examples of hybrid mesostructured materials can be found in the excellent review articles [71–74, 98, 99]. Compared to post-synthetic grafting reactions, the co-condensation approach leads to higher loadings and the organic groups do not tend to block the pores. However, for mesostructured materials it does not only offer advantages, but shows some distinct disadvantages, e.g., the degree of mesostructural ordering typically drastically decreases with increasing amount of

organotrialkoxysilane; above a limit of about 40% of $R'-Si(OR)_3$ groups the periodic mesostructure typically collapses completely and the amount incorporated into the final matrix is often lower than the one in the starting solution. Systematic studies of the hydrolysis and condensation kinetics of the different precursors similar to the ones for aerogels have not been performed, but the incorporation of the organic groups has been in most cases confirmed by ^{29}Si MAS NMR spectra. With respect to template removal, the same problems arise: it remains difficult to selectively degrade the template without deteriorating the organic function. Therefore, the template has to be removed by time-consuming and tedious extraction processes.

Since the first publications by Mann, Macquarrie and Stein many different mesostructured silica-based materials have been synthesized via the co-condensation approach [100–102]. The large choice of organofunctional silanes allows access to surface-functionalized mesostructured silica with alkyl-, thiol-, amino-, cyano-, phosphine-, vinyl-, methacrylate-, epoxide-, aromatic, etc groups covering the pore walls (see also Fig. 3.7 for some examples from the various choices of organosilanes) [103–108].

These chemical functions on the pore surface can be used in subsequent chemical reactions, e.g., hydroboration or bromination of vinyl groups, adsorption of heavy metals, especially Hg^{2+} -ions, or even catalytic reactions such as heterogeneous acid or base catalysis, in Knoevenagel reactions, etc. [102, 109]. Many more examples such as modifications with dye, cyclodextrines, photosensitive molecules, chelating ligands, etc. could be given, but the reader is referred to the more specific review articles [98, 99].

Another approach towards hybrid mesostructured materials lies in the possibility of combining the template and inorganic precursor within one compound. This “self-templating synthesis” of organic-inorganic silica-grafted surfactant materials – so called SGS materials – is shown by applying a starting reagent such as a cationic surfactant covalently bonded to an alkoxysilane, which is able to hydrolyze and polymerize giving spontaneously self-assembled entities with layered (like organoclays) or hexagonal (like silica micelle intermediates of MCM-41) arrangements [110].

In addition, the co-condensation approach can be used to tailor the microstructure of the final material. This was reported by Che et al. [111] They have prepared a chiral mesoporous silica-based material based on the self-assembly of chiral anionic surfactants and simultaneous co-condensation of tetraethoxysilane and a quaternized aminosilane. The latter one is required for charge matching. (Fig. 3.10) [111].

3.2.2.4 Hierarchically Organized Materials

Co-condensation reactions between tri- and tetraalkoxysilanes can also be used for the formation of hierarchically organized materials. The same problems as already discussed above apply here: strong influence on network formation, only limited amounts of organic groups can be incorporated without deteriorating the hierarchical structure, homo- versus hetero-condensation, limited degree of loading, etc.

Only very few studies report on the formation of highly porous hybrid materials from pure silsesquioxanes, e.g., methyltrialkoxysilanes in a well-defined macroscopic

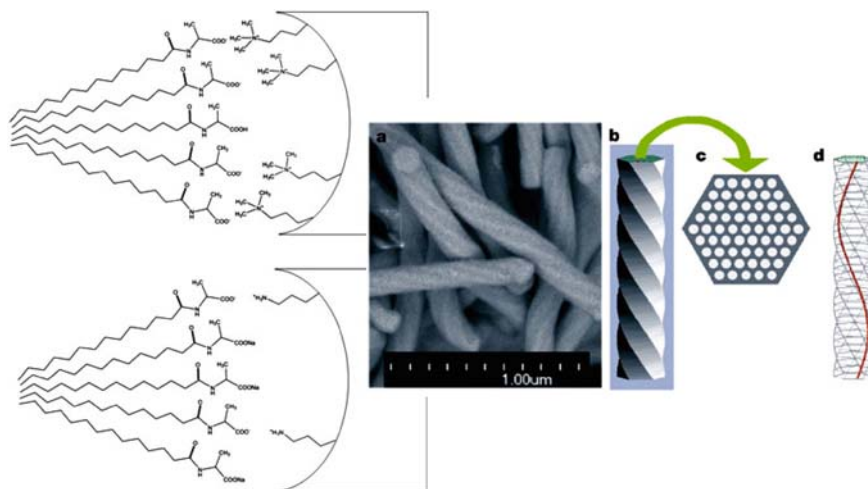


Fig. 3.10 Schematic description of the interaction between the chiral surfactant molecules and the ammonium-group modified silica pore wall surface (*left*), and the corresponding SEM image and schematic drawing of the mesoporous, silica fibres with helical-chiral topology after calcination (*right*) [adapted from [111]]

morphology [8, 10–13, 42, 112–114]. This can probably be led back to the lower degree of cross-linking that is expected when precursors are used with only three potential reaction sites (resulting in long gelation times) as well as the mechanical instability of the resulting gels due to the lower connectivity, and phase separation phenomena of oligomeric or polymeric silsesquioxanes due to the polarity differences within the precursor molecule.

Siloxane-based inorganic–organic hybrid monoliths with well-defined macropores and mesopores have been synthesized by sol–gel processing of trialkoxysilanes accompanied by phase separation [42]. In this work, Nakanishi et al. investigated the hydrolysis/condensation and phase separation behaviour of methyltrimethoxysilane in the presence of formamide and methanol in detail. They found that the phase separation tendency is increased compared to tetraalkoxysilanes, but can be deliberately controlled by the choice and concentration of the solvent phase. Another important parameter which governs the final network structure are the relative reaction rates of sol–gel transition and phase separation.

Similar materials were prepared by Brennan et al. by using a two-step acid/base processing methodology [112, 113]. They first hydrolyzed methyltrimethoxysilane in methanol and aqueous hydrochloric acid and added ammonium hydroxide as a basic catalyst in a second step. Again phase separated structures, exhibiting rather high surface areas and porosities are obtained. A tight control over macropore size is obtained by simply changing the duration of the acid hydrolysis. With longer times in the acidic medium, the gelation is retarded and phase separation occurs, thus resulting in an increase of pore size.

Other silica-based materials with hierarchical organization of the pore structure and more pronounced mesoporosity can be obtained by using glycol-modified silanes.

Pure silsesquioxane gels were prepared from tris-(2-hydroxyethoxy)methylsilane and tris-(2-hydroxyethoxy)phenylsilane. Interestingly, these organically substituted precursors exhibit a much faster gelation time than the corresponding ethylene glycol-modified tetraalkoxysilane in acidic medium, but still show gelation, not precipitation [115, 116]. These precursors can also be processed in the presence of the tetrakis (2-hydroxyethyl)orthosilicate and a surfactant, similar to the co-condensation route described previously. Mechanically stable monoliths, exhibiting macropores and periodically arranged mesopores were obtained. Again, the final network structure is strongly influenced by the amount of organosilane used to substitute the SiO_4 -entities. Figure 3.11 shows SEM images for gels prepared from tris-(2-hydroxyethoxy)methylsilane with various degrees of substitution from 10 mol% (Me10) up to 100 mol% (Me100) and at different pH-values. It can clearly be seen that the macrostructure is strongly influenced by the pH and the amount of organosilane (degree of substitution). The corresponding SAXS curves at the bottom part of Figure 3.11, in addition, indicate that not only the macrostructure, but also the mesostructure is strongly influenced. Under the given set of synthesis conditions, periodic ordering was only achieved up to 25 mol% of tris-(2-hydroxyethoxy)methylsilane.

3.2.3 Bridged Polysilsesquioxanes

Bridged polysilsesquioxanes are a rather new family of hybrid inorganic–organic materials that are prepared via sol–gel processing of monomers that contain a bridging organic group and two or more trialkoxysilyl groups [53, 117, 118]. The use of these bridged precursors, such as $\text{X}_3\text{Si}-\text{R}'-\text{SiX}_3$ (R' is an organic spacer, $\text{X} = \text{Cl}, \text{Br}, \text{OR}$) allows the formation of homogeneous molecular hybrid inorganic–organic materials, which have a high degree of local organization.

The organic spacer can be varied in length, rigidity, geometry of substitution, and functionality (Fig. 3.12).

The most intriguing aspect related to bridged polysilsesquioxanes is the fact that materials derived from these precursors are characterized by organic entities that are integral parts of the structural network and not only surface decorating/modifying species. Therefore, the large variability of the organic spacer provides an opportunity to engineer bulk properties such as porosity, thermal stability, refractive index, optical clarity, chemical resistance, hydrophobicity, and dielectric constant. Today, many precursors for bridged polysilsesquioxanes are available (either commercially or via rational synthetic approaches); a few representative examples are presented in Figure 3.12. The variety of organic spacers in the monomers is rather endless and range from rigid arylenic, acetylenic, and olefinic bridging moieties to flexible alkylenes ranging from 1 to 14 methylene groups in length. In addition, a large variety of functional groups such as amines, ethers, sulfides, phosphines, amides, ureas, carbamates, carbonates, azobenzenes, or even organometallics, e.g., ferrocenyl-bridged monomers or η -6-arenechromiumtricarbonyl complexes, can be incorporated as the bridge between two or more alkoxyisilyl-moieties.

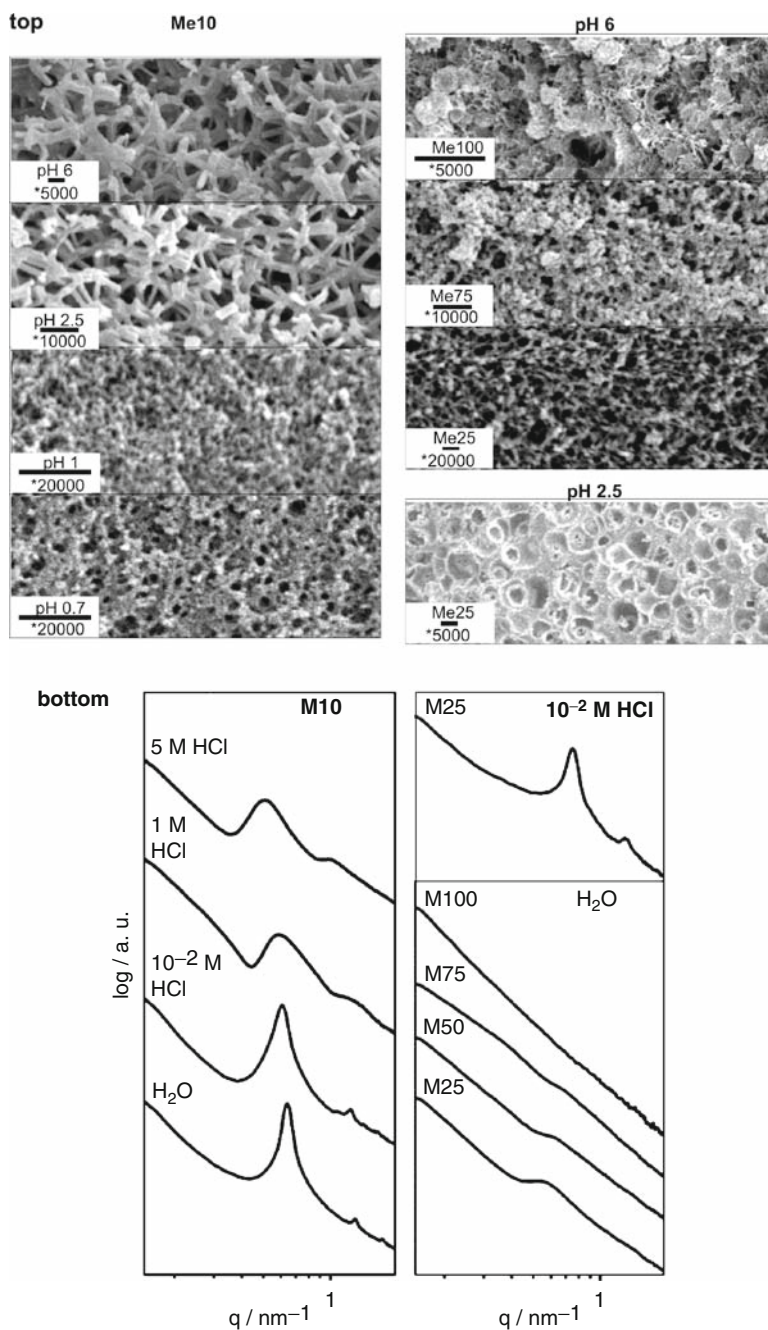


Fig. 3.11 SEM images of the methyl silsesquioxane monoliths (Me = methyl) at different pH and for different degrees of substitution and the corresponding small angle X-ray scattering patterns

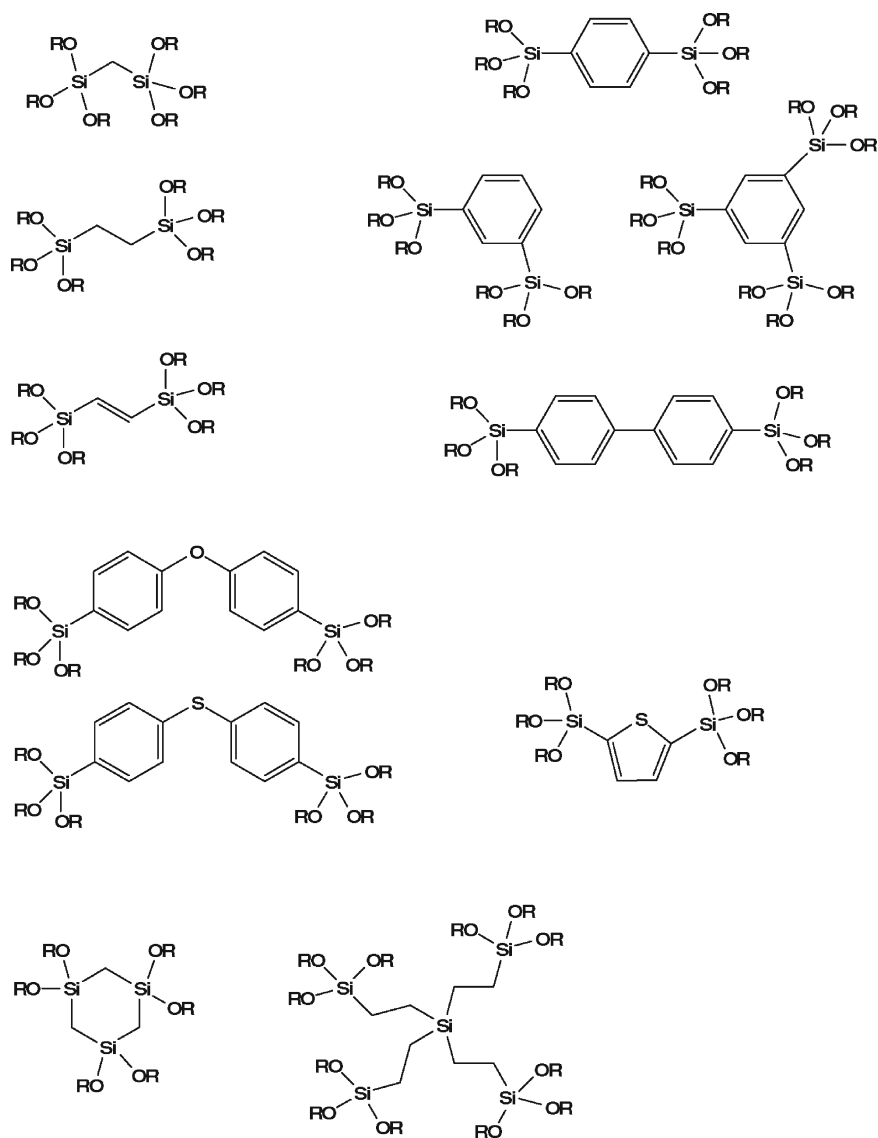


Fig. 3.12 Representative examples of bridged organosilanes that have been used in the formation of micro/mesoporous frameworks

3.2.3.1 Porous Silsesquioxanes by Sol–Gel Processing

Sol–gel processing of these precursors in acidic or basic environment results in the formation of bridged silsesquioxane gels (Fig. 3.13), which can be converted – depending on the drying conditions – into porous or nonporous hybrid materials. As already discussed above, hydrolysis and condensation rates of alkyl- and aryltrialkoxysilanes

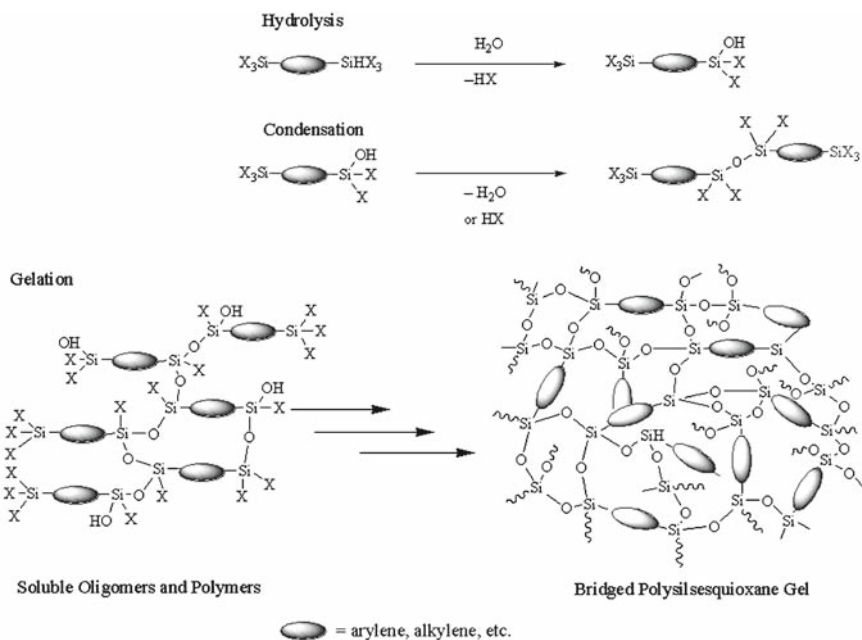


Fig. 3.13 Formation of bridged polysilsesquioxanes by hydrolysis and condensation of monomers with two or more trialkoxysilyl groups attached to the organic bridging group [taken from [4]]

are significantly faster than the rates of tetraalkoxysilanes under acidic conditions and slower under basic conditions. These trends have so far not been verified for bridged bis-silyl precursors, but it seems reasonable to suspect a similar behavior depending on the electronic properties of the organic spacer.

The majority of organotrialkoxysilanes will not form gels when used as the sole network forming precursor (100% $\text{R}'\text{-Si}(\text{OR})_3$) under any sol–gel conditions, due to the low degree of cross-linking resulting from only three condensable groups per silicon. In contrast, the bridged precursor molecules very rapidly form gels due to the hydrolytically stable Si-X-Si spacer and the six reactive alkoxide groups thus resulting in a connectivity of four per silicon.

Depending on the gelation and drying conditions, the final pore structure of bridged silsesquioxane gels can be deliberately tailored. Simple air-drying of the obtained gels typically results in large shrinkage of the gel body (depending on the concentration of monomers used in the synthesis). This shrinkage can result in gels that are non-porous, however most bridged silsesquioxane xerogels still exhibit a certain degree of porosity and surface areas between 200 and 1200 $\text{m}^2 \text{g}^{-1}$. Highly porous hybrid materials can be obtained via supercritical extraction procedures (as already applied in the synthesis of aerogels, Fig. 3.14). When precursors of the type $(\text{RO})_3\text{Si}(\text{CH}_2)_n\text{Si}(\text{OR})_3$ with $n = 2, 6, 8, 10, 14$ are processed under either acidic or basic conditions and are dried supercritically, the length of the spacer (n) has a decisive

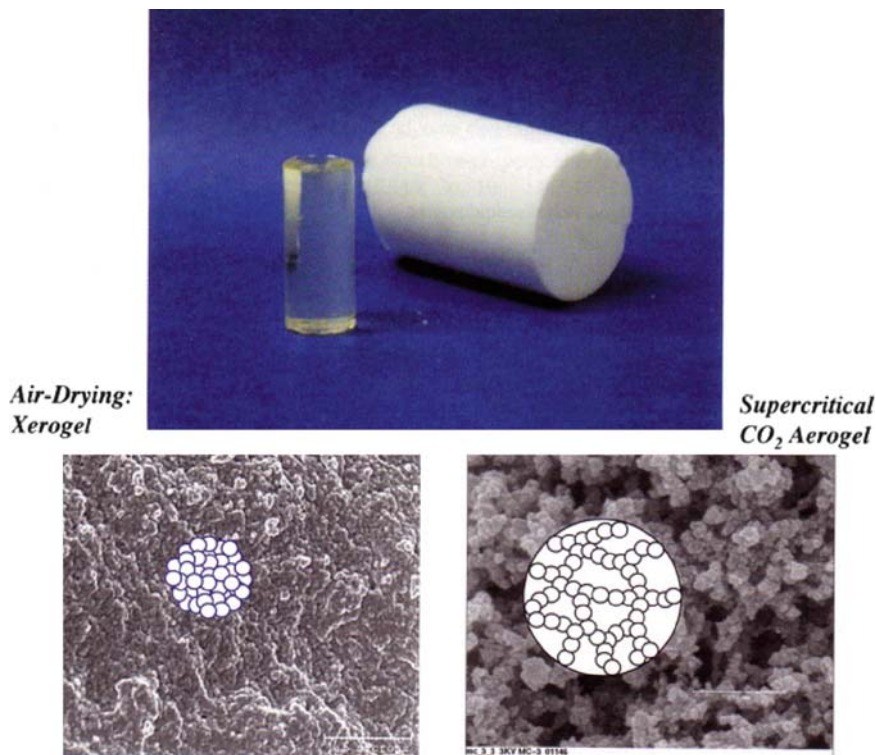


Fig. 3.14 Scanning electron micrographs of a hexylene-bridged polysilsesquioxane xerogel (*left*) and the analogous aerogel (*right*) [taken from [4]]

influence on the later aerogel structure. Most of the alkylene-bridged aerogels are mesoporous, high surface area materials. However, the specific surface area decreases with increasing n and the base-catalyzed sample with $n = 14$ is even non-porous.

Another strategy for creating porosity is to use the organic group as the template for porosity. This templating relies on the ability of the organic group to occupy space until calcination, chemical oxidation or chemical rearrangement of the template. This will leave a pore whose size and shape roughly corresponds to that of the organic molecule. A variety of chemical processes have been developed for cleaving, chemically modifying, or removing portions of the organic groups, including retro-Diels-Alder reactions, decarboxylation or thermal decomposition (Fig. 3.15).

3.2.3.2 Templated Bridged Silsesquioxanes (PMOs and ZOLs)

Periodic Mesoporous Organosilicas *PMOs*: Most of the available precursors can also be condensed in the presence of a structure-directing agent such as a liquid crystalline phase of surfactant molecules or amphiphilic block copolymers, necessary for the preparation of periodically arranged mesoporous frameworks.

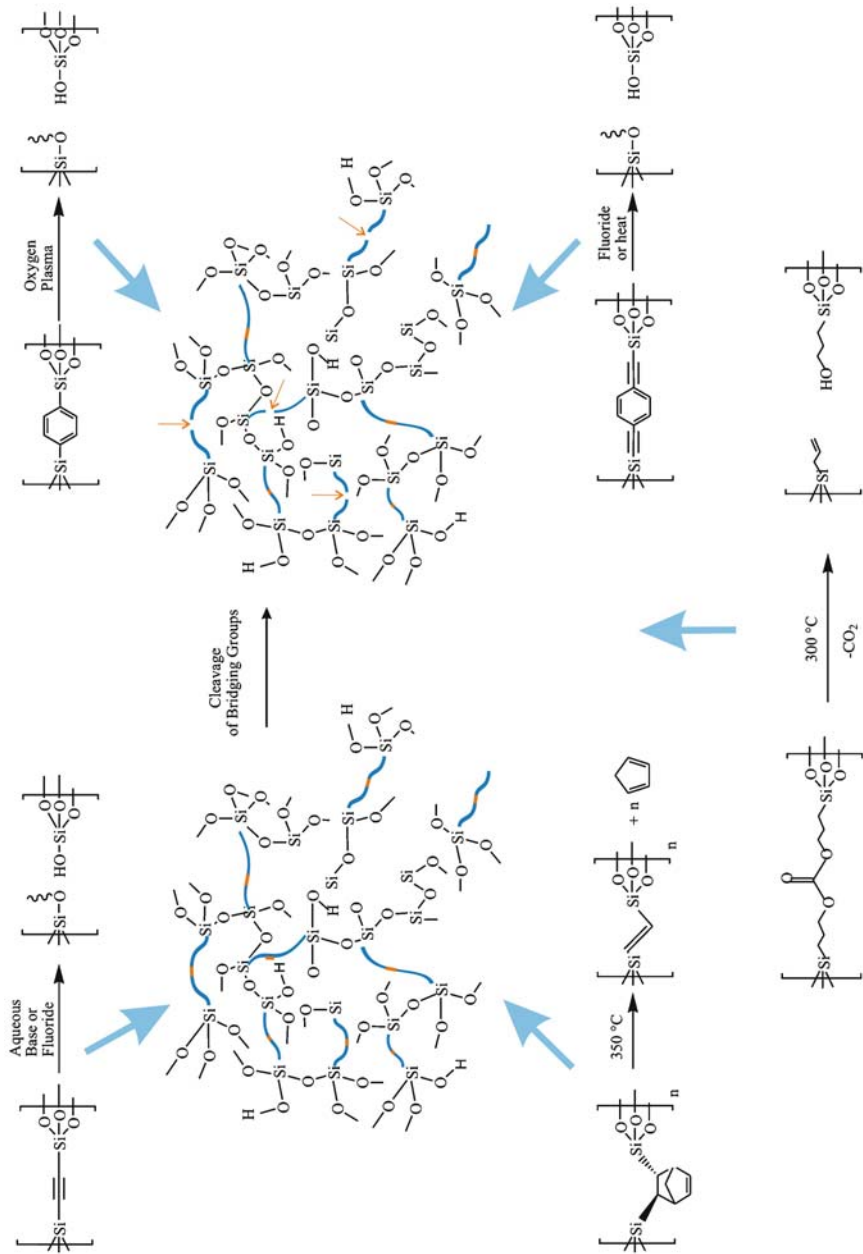


Fig. 3.15 Templating porosity in bridged silsesquioxanes by selective chemical degradation etc. of the organic spacer [adapted from [4]]

The first synthesis of a periodically arranged mesostructured silsesquioxane material with an organic bridge as an integral part of the network was reported in 1999, independently by three different groups [119–121]. Today these materials are often called periodic mesoporous organosilicas (PMOs).

PMOs exhibit several unique features built into their structure:

1. High loading of organic groups
2. Insignificant pore blocking
3. Chemical reactive sites in the pore wall
4. Homogeneously distributed groups
5. Easily modified physical and chemical properties by flexible tuning of the organic bridge
6. High surface area, uniform pore and channel size with nanoscale dimensions

Furthermore, different periodic pore geometries (cubic – with a 3D-channel system or hexagonal – with a 1D-channel system) are accessible, depending only on the supramolecular templating agent used in the synthesis.

The largest pores (cage-like pores of 10 nm) in a well-ordered mesostructured silica material with integrated organic groups have been reported by using a large block copolymer as surfactant and bis(triethoxysilyl)ethane as the framework-forming component. In contrast, super-microporous organic-integrated silica with periodic and uniform pore sizes of 1–2 nm have been prepared from alkylamine surfactants and bis(triethoxysilyl)ethane. This already indicates that the synthesis of PMOs is very flexible with regard to the porous matrix, but also the chemical reactivity of the final material can be varied, e.g., by applying a functional bridging molecule.

The amount of organic bridging units can easily be controlled by using mixtures of the bridged silsesquioxane precursor and a tetraalkoxysilane. This has been demonstrated by mixing a photoresponsive bissilyl-derivatized propylureido azobenzene moiety and tetraethoxysilane in the presence of hexadecyltrimethylammonium bromide as the structure-directing agent. The resulting material exhibits periodic ordering of the mesopores and the possibility of photochemical switching of the azobenzene moieties from *cis* to *trans* configuration and thus, a reversible change in the pore dimensions (therefore the adsorption capacity) [122].

In addition, two different functions can be incorporated simultaneously into the network, by using two different precursor molecules, e.g., co-condensation of ethane and propyl ethylenediamine bridged bissilyl compounds [123]. To obtain optimal results, the mobile diamine bridge was complexed with Cu^{2+} -ions prior to sol–gel processing to decrease the flexibility. This approach can be extended to an almost unlimited choice of precursors.

In principle, a bistralkoxysilyl precursor can also be co-condensed with an organically modified trialkoxysilane to obtain a material that contains functional groups as an integral part of the network, but also located at the pore walls. To mention just one example of a successful synthesis, the combination of bis(triethoxysilyl)ethane and mercaptopropyltrimethoxysilane is named [124, 125].

Typically, the framework of the MCM-type mesostructured materials is amorphous. However, an interesting feature has been discovered when 1,4-bis(triethoxysilyl)

benzene is used as network former. The reaction of a mixture of 1,4-bis(triethoxysilyl)benzene, octadecyltrimethylammonium salt, sodium hydroxide and water results in a material possessing a crystal-like pore-wall structure. This additional periodicity is attributed to a regular arrangement of $O_{1.5}Si-C_6H_4-SiO_{1.5}$ units in the pore walls due to non-covalent hydrophobic and $\pi-\pi$ -intermolecular interactions between the phenylene groups and hydrogen bonding through C–SiOH groups [126]. It was shown that these groups are accessible for further reaction, such as sulfonation of the phenylene moieties.

Zeolites with organic groups as lattice, *ZOLs*: As discussed above, modifying zeolites by adding organic groups is not trivial due to the steric constraints and the inherent structural defects imposed to the zeolite matrix. However, would it be possible to incorporate bridging organic groups?

ZOL materials are zeolite matrices with organic groups as an integral part of their lattice [127, 128]. In the synthesis of zeolites, these bridging moieties are limited to hybrid zeolites with methylene groups ($-CH_2-$) replacing a lattice oxygen atom by starting with bis(triethoxysilyl)methane having a bridging methylene group ($Si-CH_2-Si$) between two ethoxysilanes as the silicon source (Fig. 3.16). Different organic-inorganic hybrid zeolitic phases have been synthesized. However, due to the reaction conditions, the synthesis is not as straightforward as anticipated.

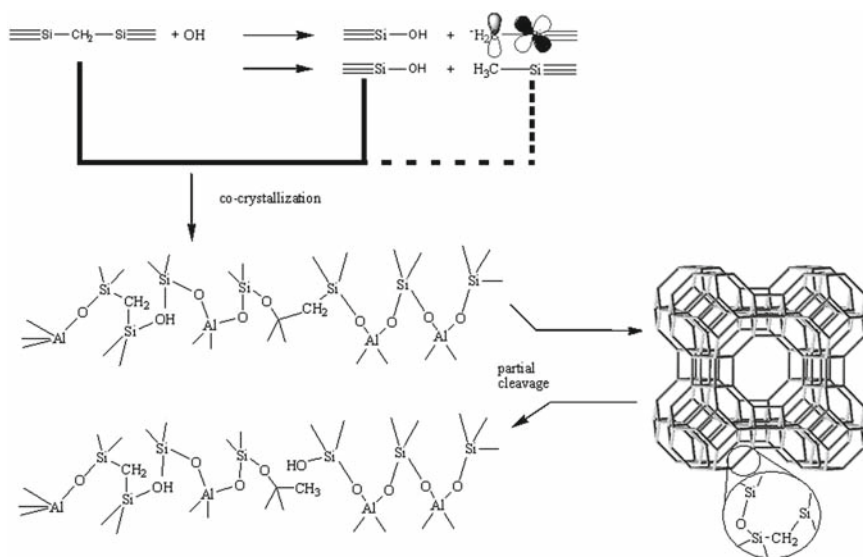


Fig. 3.16 Possible pathways to ZOL materials [adapted from [127]]

Although the Si–C-bond is generally strong enough to be resistant against hydrolysis, Si–CH₂–Si is relatively easy to be cleaved by nucleophilic substitution via possible intermediate species, e.g., Si–CH[–]. This carbanion can presumably be stabilized by the vacant d-orbital of the adjacent Si atom. Supposedly, purely inorganic Si species thus formed and organically modified species co-crystallize to form the organically modified material, which can be seen in the ²⁹Si-MAS NMR spectra of the final zeolite material that contains, Q(SiO₄) and T(–CH₂–SiO₃ and CH₃–SiO₃) species. The amount of organic groups can be quantified by measuring the amount of T-units in the ²⁹Si-NMR spectra, which is about 30% of total Si. Compared to their purely inorganic counterparts very long crystallization times up to several weeks can be observed for the synthesis of these hybrid systems.

The use of other organosilanes, such as bis(triethoxysilyl)ethane, have not yielded crystalline materials, presumably because two CH₂-groups are too large to replace a lattice oxygen atom.

Why is it so difficult to substitute the oxygen atom by a methylene group? Bond length and angles have to match rather closely to crystallize in a typical zeolite structure. The typical bond length of Si–C is 1.88 Å, which is longer than that of Si–O with 1.6 Å. In addition, the steric demand of a CH₂-unit is higher than a single oxygen. However, the Si–C–Si bond angle (~109°) is usually smaller than the Si–O–Si angle. This smaller bond angle compensates for the distance of two silicon atoms thus enabling crystallization of this type of inorganic–organic hybrid zeolitic material, but the limits are already seen when the size of the organic spacer is increased.

3.2.3.3 Bridged Silsesquioxanes with Hierarchical Porosity

The first reports on organo-silica materials in monolithic form with a bimodal pore-structure in the form of interconnected macropores and periodically ordered mesopores have been published by Nakanishi et al. [129]. They describe the synthesis of alkylene-bridged silica monoliths using a non-ionic block copolymer (P123) as template in combination with 1,3,5-trimethylbenzene as swelling agent, an additive that enhances the self-organization of structure-directing agents.

A different approach to synthesize silica monoliths with a hierarchical build up of highly ordered mesopores and interconnected, uniform macropores has been recently presented by Hüsing and coworkers (Fig. 3.17) [130]. The key of this work has been the substitution of ethoxy-/methoxy groups of conventional tetraalkoxy-silane precursors with short chain glycols as they show much better compatibility with the self-assembly of silica/surfactant mesophases compared to ethanol or methanol. Furthermore, the glycol-modified silanes, e.g., tetrakis-(2-hydroxyethyl) orthosilicate (EGMS), are water-soluble and can be hydrolyzed/condensed without the addition of an acid or base catalyst at neutral conditions in purely aqueous medium. The synthetic process is therefore simplified, as no toxic and/or expensive additives like swelling-agents and co-solvents are required. In summary, a simple, versatile method has been demonstrated to fabricate phenylene-bridged silica monoliths with a hierarchical build up on at least four levels – (a) deliberate macroscopic

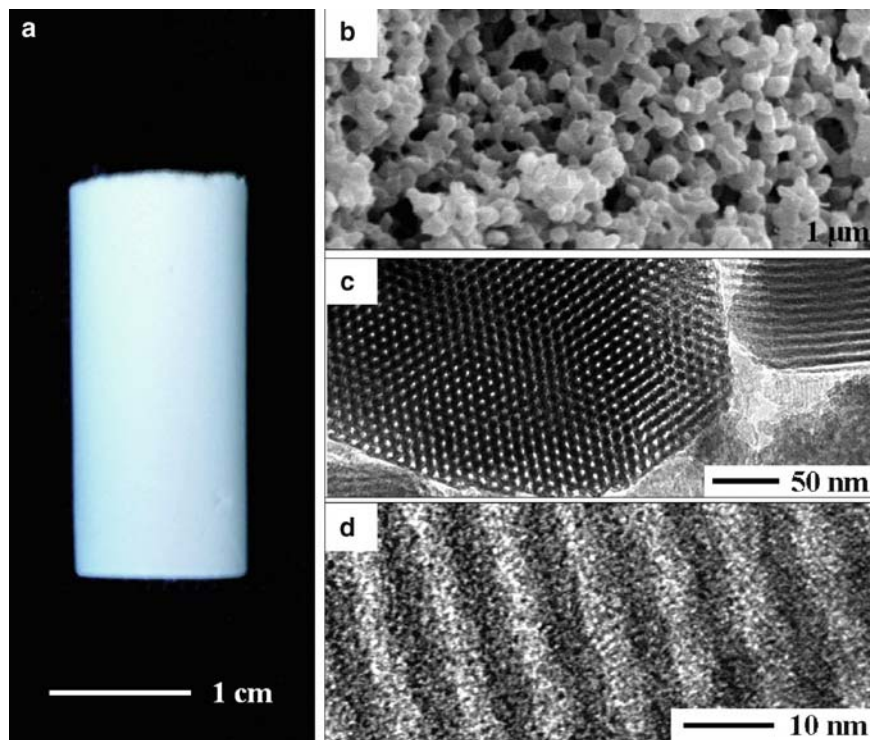


Fig. 3.17 Hierarchy on four levels: Photograph (a), SEM image (b), and TEM images (c, d) of the dried phenylene-bridged silica monolith bPh_a, exhibiting its hierarchical build-up

shape, (b) uniform macropores, (c) highly ordered mesopores (plus micropores), and (d) molecular periodicity of the phenylene moieties within the pore walls. The underlying notion of substituting the alkoxygroups of conventional organo-alkoxysilane precursors with ethylene glycol can be readily extended to other organic functionalities. This method represents a versatile tool to tailor the chemical functionality of monolithic materials with well-defined, multi-modal pore structures, thus increasing their potential application significantly.

3.3 Conclusions

Hybrid inorganic–organic materials have been and are becoming increasingly important for a large variety of technologies, especially since researchers from different fields such as physics, chemistry, materials science and even biology are starting to exploit the apparent benefits that arise from the combination of the different areas.

Porous materials that are built-up from inorganic and organic moieties have been used for a long time already. Prominent examples are reversed-phase silicas used in

chromatographic applications. Today reversed-phase silicas with n-octadecyl- and n-octyl ligands are among the most common adsorbents in high performance liquid chromatography (HPLC). The variety and broad applicability of approaches towards inorganic–organic hybrid materials has been discussed in this chapter. The presented examples display only a small selection of the possible hybrid porous structures, but show that chemists can practically tailor-make any porous inorganic–organic hybrid material.

The scientific work in the field of hybrid inorganic–organic materials is growing tremendously in recent years. Another interesting example – not discussed in this chapter – but nevertheless of high interest is the research on metal–organic frameworks (MOFs) that represent the ultimate hybrid porous material built-up from inorganic metal ion complexes bridged by organic linkers to form a three-dimensional network. These materials have almost no dead volume and due to that display world-record surface areas of up to 6000 m² g⁻¹. One potential application is envisioned in the area of gas storage.

In general, the explosion of novel synthetic strategies to all kind of inorganic–organic hybrid materials will definitely lead to numerous scientific breakthroughs in the field of porous materials.

References

1. Brinker CJ, Scherer GW (1990) *Sol–Gel Science: The Physics and Chemistry of Sol–Gel Processing*. Academic Press, New York
2. Schubert U, Hüsing N (2004) *Synthesis of Inorganic Materials*. Wiley-VCH, Weinheim
3. Sakka S (2005) Current and future possibilities of sol–gel process. *Trans Ind Ceram Soc* 64: 13–19
4. Shea KJ, Moreau J, Loy DA, Corriu RJP, Boury B (2004) Bridged polysilsesquioxanes. Molecular-engineering nanostructured hybrid organic–inorganic materials. In: Gómez-Romero P, Sanchez C (eds) *Functional Hybrid Materials*. Wiley-VCH, pp. 50–85
5. Loy DA, Mather B, Straumanis AR, Baugher C, Schneider DA, Sanchez A, Shea KJ (2004) Effect of pH on the gelation time of hexylene-bridged polysilsesquioxanes. *Chem Mater* 16: 2041–2043
6. Loy DA (2001) Hybrid organic–inorganic materials. *MRS Bull* 26: 364–365
7. Schneider DA, Baugher BM, Loy DA, Rahimian K, Alam T (2001) Sol–gel chemistry of trialkoxysilanes. *Mater Res Soc Symp Proc* 628: CC6.35.1–CC6.35.6
8. Loy DA, Baugher BM, Baugher CR, Schneider DA, Kamyar K (2000) Substituent effects on the sol–gel chemistry of organotrialkoxysilanes. *Chem Mater* 12: 3624–3632
9. Barton TJ, Bull LM, Klemperer WG, Loy DA, McEnaney B, Misono M, Monson PA, Pez G, Scherer GW, Vartuli JC, Yaghi OM (1999) Tailored porous materials. *Chem Mater* 11: 2633–2656
10. Gun J, Lev O, Regev O, Pevzner S, Kucernak A (1998) Sol–gel formation of reticular methyl-silicate materials by hydrogen peroxide decomposition. *J Sol Gel Sci Technol* 13: 189–193
11. Kanamori K, Yonezawa H, Nakanishi K, Hirao K, Jinnai H (2004) Structural formation of hybrid siloxane-based polymer monolith in confined spaces. *J Sep Sci* 27: 874–886
12. Shirtcliffe NJ, McHale G, Newton MI, Perry CC (2003) Intrinsically superhydrophobic organosilica sol–gel foams. *Langmuir* 19: 5626–5631

13. Rao AV, Kulkarni MM, Amalnerkar DP, Seth T (2003) Superhydrophobic silica aerogels based on methyltrimethoxysilane precursor. *J Non-Cryst Solids* 330: 187–195
14. Ayen RJ, Iacobucci PA (1988) Metal oxide aerogel preparation by supercritical extraction. *Rev Chem Eng* 5: 157–198
15. Gesser HD, Goswami PC (1989) Aerogels and related porous materials. *Chem Rev* 89: 765–788
16. Pajonk GM (1991) Aerogel catalysts. *Appl Catal* 72: 217–266
17. Fricke J, Emmerling A (1992) Aerogels – preparation, properties, applications. *Struct Bonding* 77: 37–87
18. Schneider M, Baiker A (1995) Aerogels in catalysis. *Catal Rev Sci Eng* 37: 515–556
19. Hüsing N, Schubert U (1998) Aerogels – airy materials: Chemistry, structure, and properties. *Angew Chem Int Ed Engl* 37: 22–45
20. Rolison DR, Dunn B (2001) Electrically conductive oxide aerogels: new materials in electrochemistry. *J Mater Chem* 11: 963–980
21. Schüth F, Sing KSW, Weitkamp J (eds) (2002) *Handbook of Porous Solids*, Wiley-VCH, Weinheim
22. Yanagisawa T, Shimizu T, Kuroda K, Kato C (1990) The preparation of alkyltrimethylammonium–kaneinite complexes and their conversion to microporous materials. *Bull Chem Soc Jpn* 63: 988–992
23. Kresge CT, Leonowicz ME, Roth WJ, Vartuli JC, Beck JS (1992) Ordered mesoporous molecular sieves synthesized by a liquid-crystal template mechanism. *Nature* 359: 710–712
24. Biz S, Occelli ML (1998) Synthesis and characterization of mesostructured materials. *Catal Rev-Sci Eng* 40: 329–407
25. Patarin J, Lebeau B, Zana R (2002) Recent advances in the formation mechanisms of organized mesoporous materials. *Curr Opin Ion Intef Sci* 7: 107–115
26. Beck JS, Vartuli JC, Roth WC, Leonowicz ME, Kresge CT, Schmitt KD, Chu CTW, Olson DH, Sheppard EW, McCullen SB, Higgins JB, Schlenker JL (1992) A new family of mesoporous molecular sieves prepared with liquid crystal templates. *J Am Chem Soc* 114: 10834–10843
27. Tanev PT, Pinnavaia TJ (1995) A neutral templating route to mesoporous molecular sieves. *Science* 269: 865–868
28. Zhao D, Huo Q, Feng J, Chmelka BF, Stucky GD (1998) Non-ionic triblock and star diblock copolymer and oligomeric surfactant syntheses of highly ordered, hydrothermally stable, mesoporous silica structures. *J Am Chem Soc* 120: 6024–6036
29. Ryoo R, Kim JM, Ko CH, Shin CH (1996) Disordered molecular sieve with branched mesoporous channel network. *J Phys Chem* 100: 17718–17721
30. Kleitz F, Choi SH, Ryoo R (2003) Cubic Ia3d large mesoporous silica: synthesis and replication to platinum nanowires, carbon nanorods and carbon nanotubes. *Chem Commun* 2136–2137
31. Holland BT, Blanford C, Stein A (1998) Synthesis of macroporous minerals with highly ordered three-dimensional arrays of spheroidal voids. *Science* 281: 538–541
32. Stein A, Schrodin RC (2001) Colloidal crystal templating of three-dimensionally ordered macroporous solids: materials for photonics and beyond. *Curr Opin Solid State Mater Sci* 5: 553–564
33. Yang P, Deng T, Zhao D, Feng P, Pine D, Chmelka BF, Whitesides GM, Stucky GD (1998) Hierarchically ordered oxides. *Science* 282: 2244–2247
34. Velev OD, Jede TA, Lobo RF, Lenhoff AM (1998) Microstructured porous silica obtained via colloidal crystal templates. *Chem Mater* 10: 3597–3602
35. Antonietti M, Berton B, Göltner C, Hentze HP (1998) Synthesis of mesoporous silica with large pores and bimodal pore size distribution by templating of polymer latices. *Adv Mater* 10: 154–159
36. Holland BT, Abrams L, Stein A (1999) Dual templating of macroporous silicates with zeolitic microporous frameworks. *J Am Chem Soc* 121: 4308–4309
37. Nakanishi K (1997) Pore structure control of silica gels based on phase separation. *J Porous Mater* 2: 67–112

38. Nakanishi K (2006) Sol–gel process of oxides accompanied by phase separation. *Bull Chem Soc Jpn* 79: 673–691
39. Nakanishi K, Takahashi R, Nagakane T, Kitayama K, Koheija N, Shikata H, Soga N (2000) Formation of hierarchical pore structure in silica gel. *J Sol Gel Sci Technol* 17: 191–210
40. Sato Y, Nakanishi K, Hirao K, Jinnai H, Shibayama M, Melnichenko YB, Wignall GD (2001) Formation of ordered macropores and templated nanopores in silica sol–gel system incorporated with EO-PO-EO triblock copolymer. *Colloids and Surfaces A* 187–188: 117–122
41. Smått J-H, Schunk S, Lindén M (2003) Versatile double-templating synthesis route to silica monoliths exhibiting a multimodal hierarchical porosity. *Chem Mater* 15: 2354–2361
42. Nakanishi K, Kanamori K (2005) Organic-inorganic hybrid poly(silsesquioxane) monoliths with controlled macro- and mesopores. *J Mater Chem* 15: 3776–3786
43. Konishi J, Fujita K, Nakanishi K, Hirao K (2006) Phase-separation-induced titania monoliths with well-defined macropores and mesostructured framework from colloid-derived sol–gel systems. *Chem Mater* 18: 864–866
44. Hüsing N, Raab C, Torma V, Roig A, Peterlik H (2003) Periodically mesostructured silica aerogel monoliths from diol-modified silanes. *Chem Mater* 15: 2690–2692
45. Brandhuber D, Peterlik H, Huesing N (2005a) Simultaneous drying and chemical modification of hierarchically organized silica monoliths with organofunctional silanes. *J Mater Chem* 15: 3896–3902
46. Brandhuber D, Torma V, Raab C, Peterlik H, Kulak A, Hüsing N (2005b) Glycol-modified silanes in the synthesis of mesoscopically organized silica monoliths with hierarchical porosity. *Chem Mater* 17: 4262–4271
47. Sanchez C, Ribot F (1994) Design of hybrid organic-inorganic materials synthesized via sol–gel chemistry. *New J Chem* 18: 1007–1047
48. Sanchez C, de AA, Soler-Illia GJ, Ribot F, Lalot T, Mayer CR, Cabuil V (2001) Designed hybrid organic-inorganic nanocomposites from functional nanobuilding blocks. *Chem Mater* 13: 3061–3083
49. Sanchez C, Julián B, Belleville P, Popall M (2005) Applications of hybrid organic-inorganic nanocomposites. Special issue on Functional hybrid materials, Sanchez C (eds). *J Mater Chem* 35/36: 3559–3592
50. Chujo Y, Saegusa T (1992) Organic polymer hybrids with silica gel formed by means of the sol–gel method. *Adv Polym Sci* 100: 11–29
51. Novak BM (1993) Hybrid nanocomposite materials – between inorganic glasses and organic polymers. *Adv Mater* 5: 422–433
52. Schubert U, Hüsing N, Lorenz A (1995) Hybrid inorganic–organic materials by sol–gel processing of organofunctional metal alkoxides. *Chem Mater* 7: 2010–2027.
53. Loy DA, Shea KJ (1995) Bridged polysilsesquioxanes. Highly porous hybrid organic-inorganic materials. *Chem Rev* 95: 1431–1442
54. Judeinstein P, Sanchez C (1996) Hybrid organic-inorganic materials: a land of multidisciplinary. *J Mater Chem* 6: 511–525
55. Corriu RJP (1998) Monophasic organic-inorganic hybrid materials. *CR Acad Sci* 1: 83–89
56. Sanchez C, Ribot F, Lebeau B (1999) Molecular design of hybrid organic-inorganic nanocomposites synthesized via sol–gel chemistry. *J Mater Chem* 9: 35–44.
57. Corma A (1997) From microporous to mesoporous molecular sieve materials and their Use in catalysis. *Chem Rev* 97: 2373–2420
58. Wight AP, Davis ME (2002) Design and preparation of organic-inorganic hybrid catalysts. *Chem Rev* 102: 3589–3614
59. Ozin GA, Kuperman A, Stein A (1989) Advanced zeolite, materials science. *Angew Chem Int Ed* 28: 359
60. Stucky GD, MacDougall JE (1990) Quantum confinement and host/guest chemistry: Probing a new dimension. *Science* 247: 669–678
61. Marlow F, Demuth D, Stucky G, Caro J, Schüth F (1995) Polarized IR spectra of *p*-nitroaniline-loaded AlPO_4^{-5} single crystals. *J Phys Chem* 99: 1306–1310

62. Striebel C, Hoffmann K, Marlow F (1997) The microcrystal prism method for refractive index measurements on zeolite-based nanocomposites. *Microporous Mater* 9: 43–50
63. Calzaferri G, Huber S, Maas H, Minkowski C (2003) Host-guest antenna materials. *Angew Chem Int Ed* 42: 3732–3758
64. Brühwiler D, Calzaferri G (2004) Molecular sieves as host materials for supramolecular organization. *Microporous Mesoporous Mater* 72: 1–23
65. Meyer G, Woehrl D, Mohl M, Schulz-Ekloff G (1984) Synthesis of faujasite supported phthalocyanines of cobalt, nickel and copper. *Zeolites* 4: 30–34
66. Schulz-Ekloff G, Ernst S (1997) Zeolite-entrapped metal complexes. In: Ertl G, Knözinger H, Weitkamp J (eds) *Handbook of Heterogeneous Catalysis*, vol 1. Wiley-VCH, Weinheim, pp 374
67. Sheu LL, Knoezinger H, Sachtler WMH (1989) Palladium carbonyl clusters entrapped in NaY zeolite cages: ligand dissociation and cluster-wall interactions. *J Am Chem Soc* 111: 8125–8131
68. Nandhini UK, Arabindoo B, Palanichamy M, Murugesan V (2004) *t*-Butylation of phenol over mesoporous aluminophosphate and heteropolyacid supported aluminophosphate molecular sieves. *J Mol Catal A* 223: 201–210
69. Corma A, Garcia H (2004) Supramolecular host-guest systems in zeolites prepared by ship-in-a-bottle synthesis. *Eur J Inorg Chem* 6: 1143–1164
70. Enzel P, Bein T (1989) Inclusion of polyaniline filaments in zeolite molecular sieves. *J Phys Chem* 93: 6270–6272
71. Möller K, Bein T (1998) Inclusion chemistry in periodic mesoporous hosts. *Chem Mater* 10: 2950–2963
72. Stein A, Melde BJ, Schroden RC (2000) Hybrid inorganic–organic mesoporous silicates – nanoscopic reactors coming of age. *Adv Mater* 12: 1403–1419
73. Scott BJ, Wirnsberger G, Stucky GD (2001) Mesoporous and mesostructured materials for optical applications. *Chem Mater* 13: 3140–3150
74. Sayari A, Hamoudi S (2001) Periodic mesoporous silica-based organic-inorganic nanocomposite materials. *Chem Mater* 13: 3151–3168
75. Thomas JM, Raja R (2004) Catalytic significance of organometallic compounds immobilized on mesoporous silica: economically and environmentally important examples. *J Organomet Chem* 689: 4110–4124
76. Ogawa M (2002) Photoprocesses in mesoporous silicas prepared by a supramolecular templating approach. *J Photochem Photobiol C* 3: 129–146
77. Hartmann M (2005) Ordered mesoporous materials for bioadsorption and biocatalysis. *Chem Mater* 17: 4577–4593
78. Yiu HHP, Wright PA (2005) Enzymes supported on ordered mesoporous solids: a special case of an inorganic-organic hybrid. *J Mater Chem* 15: 3690–3700
79. Wu CG, Bein T (1994a) Conducting carbon wires in ordered, nanometer-sized channels. *Science* 266: 1013–1016
80. Wu CG, Bein T (1994b) Conducting polyaniline filaments in a mesoporous channel host. *Science* 264: 1757–1760
81. Johnson SA, Khushalani D, Coombs N, Mallouk TE, Ozin GA (1998) Polymer mesofibres. *J Mater Chem* 8: 13–14
82. Li G, Bhosale S, Wang T, Zhang Y, Zhu H, Fuhrhop JH (2003) Gram-scale synthesis of sub-micrometer-long polythiophene wires in mesoporous silica matrices. *Angew Chem Int Ed* 42: 3818–3821.
83. Hüsing N, Schubert U (2004) Porous inorganic–organic hybrid materials. In: Sanchez C, Gómez-Romero P (eds) *Functional Hybrid Materials*. Wiley-VCH, Weinheim, pp.86–121
84. Davis PJ, Brinker CJ, Smith DM (1992a) Pore structure evolution in silica gel during aging/drying I. Temporal and thermal aging. *J Non-Cryst Solids* 142: 189–196
85. Davis PJ, Brinker CJ, Smith DM, Assink RA (1992b) Pore structure evolution in silica gel during aging/drying II. Effect of pore fluids. *J Non-Cryst Solids* 142: 197–207
86. Deshpande R, Hua DW, Smith DM, Brinker CJ (1992) Pore structure evolution in silica gel during aging/drying. III. Effects of surface tension. *J Non-Cryst Solids* 144: 32–44

87. Smith DM, Stein D, Anderson JM, Ackerman W (1995) Preparation of low-density xerogels at ambient pressure. *J Non-Cryst Solids* 186: 104–112
88. Antochshuk V, Jaroniec M (1999) Simultaneous modification of mesopores and extraction of template molecules from MCM-41 with trialkylchlorosilanes. *Chem Commun* 2373–2374
89. Antochshuk V, Jaroniec M (2000) Functionalized mesoporous materials obtained via interfacial reactions in self-assembled silica-surfactant systems. *Chem Mater* 12: 2496–2501
90. Hüsing N, Raab C, Torma V, Brandhuber D, Peterlik H (2005) Cellular mesoscopically organized silica monoliths with tailored surface chemistry by one-step drying/extraction/surface modification processes. *J Mater Chem* 15: 1801–1806
91. Tsuji K, Jones CW, Davis ME (1999) Organic-functionalized molecular sieves (OFMSs): I. Synthesis and characterization of OFMSs with polar functional groups. *Microporous Mesoporous Mater* 29: 339–349
92. Jones CW, Tsuji K, Davis ME (1999) Organic-functionalized molecular sieves (OFMSs): II. Synthesis, characterization and the transformation of OFMSs containing non-polar functional groups into solid acids. *Microporous Mesoporous Mater* 33: 223–240
93. Schwertfeger F, Glaubitt W, Schubert U (1992) Hydrophobic aerogels from $\text{Si}(\text{OMe})_4/\text{MeSi}(\text{OMe})_3$ mixtures. *J Non-Cryst Solids* 145: 85–89
94. Schwertfeger F, Hüsing N, Schubert U (1994) Influence of the nature of organic groups on the properties of organically modified aerogels. *J Sol Gel Sci Technol* 2: 103–108
95. Riegel B, Plittersdorf S, Kiefer W, Hüsing N, Schubert U (1997) Raman spectroscopic analysis of the sol–gel processing of $\text{RSi}(\text{OMe})_3/\text{Si}(\text{OMe})_4$ mixtures. *J Mol Struct* 410–411: 157–160
96. Hüsing N, Schubert U, Misof K, Fratzl P (1998) Formation and structure of porous gel networks from $\text{Si}(\text{OMe})_4$ in the presence of $\text{A}(\text{CH}_2)_n\text{Si}(\text{OCH}_3)_3$. *Chem Mater* 10: 3024–3032
97. Hüsing N, Schubert U, Mezei R, Fratzl P, Riegel B, Kiefer W, Kohler D, Mader W (1999) Formation and structure of gel networks from $\text{Si}(\text{OEt})_4/(\text{MeO})_3\text{Si}(\text{CH}_2)_3\text{NR}'_2$ mixtures. *Chem Mater* 11: 451–457
98. Nicole L, Boissière C, Grosso D, Quach A, Sanchez C (2005) Mesostructured hybrid organic-inorganic thin films. *J Mater Chem* 15: 3598–3627
99. Hoffmann F, Cornelius M, Morell J, Fröba M (2006) Silica-based mesoporous organic-inorganic hybrid materials. *Angew Chem Int Ed* 45: 3216–3251
100. Burkett S, Sims SD, Mann S (1996) Synthesis of hybrid inorganic-organic mesoporous silica by co-condensation of siloxane and organosiloxane precursors. *Chem Commun* 1367–1368
101. Macquarrie DJ (1996) Direct preparation of organically modified MCM-type materials. Preparation and characterisation of aminopropyl-MCM and 2-cyanoethyl-MCM. *Chem Commun* 1961–1962
102. Lim MH, Blanford CF, Stein A (1997) Synthesis and characterization of a reactive vinyl-functionalized MCM-41: Probing the internal pore structure by a bromination reaction. *J Am Chem Soc* 119: 4090–4091
103. Mercier L, Pinnavaia TJ (2000) Direct synthesis of hybrid organic-inorganic nanoporous silica by a neutral amine assembly route: Structure-function control by stoichiometric incorporation of organosiloxane molecules. *Chem Mater* 12: 188–196
104. Walcarius A, Delacôte C (2003) Rate of access to the binding sites in organically modified silicates. 3. Effect of structure and density of functional groups in mesoporous solids obtained by the co-condensation route. *Chem Mater* 15: 4181–4192
105. Che S, Garcia-Bennett AE, Yokoi E, Sakamoto K, Kunieda H, Terasaki O, Tatsumi T (2003) A novel anionic surfactant templating route for synthesizing mesoporous silica with unique structure. *Nature Mater* 2: 801–805
106. Cagnol F, Grosso D, Sanchez C (2004) A general one-pot process leading to highly functionalised ordered mesoporous silica films. *Chem Commun* 1742–1743
107. Liu N, Assink RA, Smarsly B, Brinker CJ (2003) Synthesis and characterization of highly ordered functional mesoporous silica thin films with positively chargeable $-\text{NH}_2$ groups. *Chem Commun* 1146–1147

108. Ji X, Hampsey JE, Hu Q, He J, Yang Z, Lu Y (2003) Mesoporous silica-reinforced polymer nanocomposites. *Chem Mater* 15: 3656–3662
109. Asefa T, Kruk M, MacLachlan MJ, Coombs N, Grondley H, Jaroniec M, Ozin GA (2001) Sequential hydroboration-alcoholysis and epoxidation–ring opening reactions of vinyl groups in mesoporous vinylsilica. *Adv Funct Mater* 11: 447–456
110. Ruiz-Hitzky E, Letaief S, Prévot V (2002) Novel organic–inorganic mesophases: Self-templating synthesis and intratubular swelling. *Adv Mater* 14: 439–443
111. Che S, Liu Z, Osuna T, Sakamoto K, Terasaki O, Tatsumi T (2004) Synthesis and characterization of chiral mesoporous silica. *Nature* 429: 281–284
112. Dong H, Brennan JD (2006a) Controlling the morphology of methylsilsesquioxane monoliths using a two-step processing method. *Chem Mater* 18: 541–546
113. Dong H, Brennan JD (2006b) Macroporous monolithic methylsilsesquioxanes prepared by a two-step acid/acid processing method. *Chem Mater* 18: 4176–4182
114. Loy DA (2007) Sol–gel processing of inorganic–organic materials based on polysilsesquioxanes. In: Kickelbick G (ed) *Hybrid Materials*, Wiley-VCH, pp. 225–254
115. Hüsing N, Brandhuber D, Kaiser P (2006) Glycol-modified organosilanes in the synthesis of inorganic–organic silsesquioxane and silica monoliths. *J Sol Gel Sci Technol* 40: 131–139
116. Hüsing N, Brandhuber D, Hartmann S (2007) Glycol-modified silanes: Novel possibilities for the synthesis of hierarchically organized (hybrid) porous materials. *Acc Chem Res* 40(9): 885–894
117. Corriu RJP, Leclercq D (1996) Recent developments of molecular chemistry for sol–gel processes. *Angew Chem Int Ed Engl* 35: 1420–1436**
118. Shea KJ, Loy DA (2001) Bridged polysilsesquioxanes. *Molecular-engineered hybrid organic–inorganic materials*. *Chem Mater* 13: 3306–3319
119. Inagaki S, Guan S, Fukushima Y, Ohsuna T, Terasaki O (1999) Novel mesoporous materials with a uniform distribution of organic groups and inorganic oxide in their frameworks. *J Am Chem Soc* 121: 9611–9614
120. Melde BJ, Holland BT, Blanford CF, Stein A (1999) Mesoporous sieves with unified hybrid inorganic/organic frameworks. *Chem Mater* 11: 3302–3308
121. Asefa T, MacLachlan MJ, Coombs N, Ozin GA (1999) Periodic mesoporous organosilicas with organic groups inside the channel walls. *Nature* 402: 867–871
122. Alvaro M, Benitez M, Das D, Garcia H, Peris E (2005) Reversible porosity changes in photore sponsive azobenzene-containing periodic mesoporous silicas. *Chem Mater* 17: 4958–4964
123. Zhu H, Jones DJ, Zajac J, Dutartre R, Rhomari M, Rozière J (2002) Synthesis of periodic large mesoporous organosilicas and functionalization by incorporation of ligands into the framework wall. *Chem Mater* 14: 4886–4894
124. Yang Q, Liu J, Yang J, Kapoor MP, Inagaki S, Li C (2004) Synthesis, characterization, and catalytic activity of sulfonic acid-functionalized periodic mesoporous organosilicas. *J Catal* 228: 265–272
125. Asefa T, Yoshina-Ishii C, MacLachlan MJ, Ozin GA (2000) New nanocomposites: putting organic function “inside” the channel walls of periodic mesoporous silica. *J Mater Chem* 10: 1751–1755
126. Inagaki S, Guan S, Ohsuna T, Terasaki O (2002) An ordered mesoporous organosilica hybrid material with a crystal-like wall structure. *Nature* 416: 304–307
127. Yamamoto K, Sakata Y, Nohara Y, Takahashi Y, Tatsumi T (2003) Organic–inorganic hybrid zeolites containing organic frameworks. *Science* 300: 470–473
128. Yamamoto K, Nohara Y, Domon Y, Takahashi Y, Sakata Y, Plévert J, Tatsumi T (2005) Organic–inorganic hybrid zeolites with framework organic groups. *Chem Mater* 17: 3913–3920
129. Nakanishi K, Kobayashi Y, Amatani T, Hirao K, Kodaira T (2004) Spontaneous formation of hierarchical macro-mesoporous ethane-silica monolith. *Chem Mater* 16: 3652–3658
130. Brandhuber D, Peterlik H, Hüsing N (2006) Facile self-assembly processes to phenylene-bridged silica monoliths with four levels of hierarchy. *Small* 2: 503–506

Chapter 4

Synthesis of Mechanically Flexible Organic–Inorganic Hybrid Nanocomposites from Polydimethylsiloxane and Metal Alkoxides

Shingo Katayama

Abstract Organic–inorganic hybrid nanocomposites derived from polydimethylsiloxane (PDMS) and metal alkoxides are reviewed as “flexible ceramics” candidates, which have both high thermal and mechanical flexibility. The synthesis, structure and mechanical properties of the PDMS-based organic–inorganic hybrid nanocomposites are discussed. In addition to the mechanical flexibility, some additional properties such as tribological, surface, bioactive, and thermally conductive properties are discussed in the PDMS-based organic–inorganic hybrid nanocomposites for practical uses.

4.1 Introduction

Materials used around us can be divided broadly into two categories, organic and inorganic materials. Organic materials are organic polymers and rubbers, which have characteristics such as soft, elastic, low density and low refractive index. Inorganic materials are metals, ceramics and glasses, which have characteristics such as hardness, strength, thermal stability, high density and high refractive index. Considering the mechanical flexibility (elastic modulus or Young’s modulus) and thermal stability of both materials, a materials map can be drawn as shown in Fig. 4.1 [1]. Inorganic materials have high thermal stability but low mechanical flexibility (low Young’s modulus). Organic materials, on the contrary, have high mechanical flexibility but low thermal stability. No material exists with both, high thermal stability and high mechanical flexibility. This is an undeveloped region as shown in Fig. 4.1. Organic materials endowed with thermal stability, “thermally stable elastomers,” and inorganic materials endowed with mechanical flexibility, “flexible ceramics,” are required as materials going into the undeveloped region. While an effort has been made to improve properties in the individual fields of

S. Katayama
Nippon Steel Materials Co., Ltd., 4-14-1, Sotokanda, Chiyoda-Ku,
Tokyo 101-0021 Japan
e-mail: katayama.shingo@nsmat.nsc.co.jp

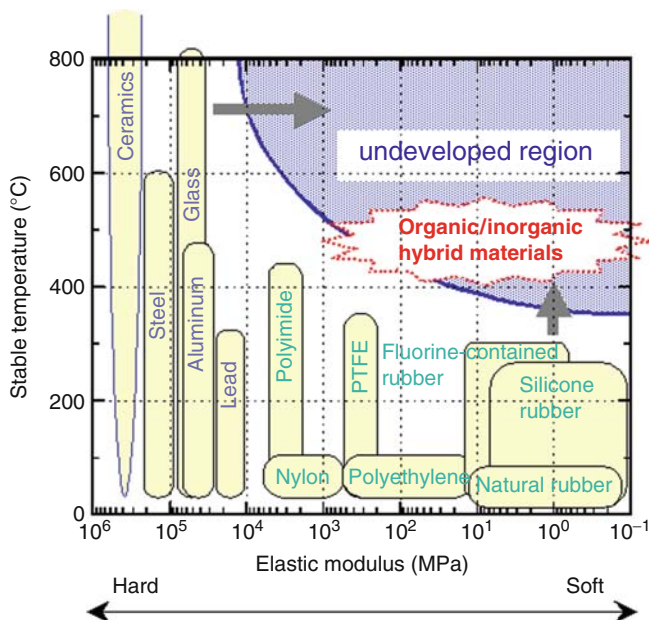


Fig. 4.1 Materials map of relationship between thermal stability and elastic modulus

conventional organic and inorganic materials, organic–inorganic hybrid nanocomposites are expected to be the first ones to go into the undeveloped region in Fig. 4.1.

As mentioned above, organic–inorganic hybrid nanocomposites, in which organic and inorganic components are combined at a nano- or molecular-scale, are attracting attention because they provide the desirable properties of both inorganic and organic compounds within a single composite. However, it is not easy to synthesize organic–inorganic hybrid nanocomposites because of large differences in process temperature between organic and inorganic materials. In general, the process temperature of organic materials is low, from room temperature to $\sim 200^{\circ}\text{C}$, but that of inorganic materials is high, $1,000^{\circ}\text{C}$ or above. Since the sol–gel process is a low-temperature route for preparing ceramics and glasses [2–4], it has been also employed to synthesize organic–inorganic hybrid nanocomposites, especially the organosiloxane-based system [3]. The synthesis of the organosiloxane-based organic–inorganic hybrid nanocomposites by the sol–gel process has been researched since the 1980s [5, 6]. Recently, there has been increased activity in the research of organosiloxane-based organic–inorganic hybrid nanocomposites aiming at numerous applications in optical [6, 7], mechanical [8, 9], chemical [10–14], electrical [15, 16], biological [17] and other fields. Despite large research on organosiloxane-based organic–inorganic hybrid nanocomposites, not many reports on bulk materials such as mechanically flexible sheets are available.

One of the organosiloxane-based organic–inorganic hybrid nanocomposites, “Cramer” has been synthesized from tetraethoxysilane (TEOS) and silanol-terminated

polydimethylsiloxane (PDMS) precursors and its mechanical properties have been studied by Wilkes et al. [5, 18–21]. In succession, Mackenzie et al. have investigated the rubbery behavior of the PDMS-based system prepared from TEOS and PDMS, “rubbery Ormosils,” based on the viewpoint that the sol–gel derived oxide networks were modified by the incorporation of organic groups to improve ductility [8, 22–33]. It is possible that the rubbery Ormosils are thermally more stable than pure organic rubbers because the inorganic component derived from TEOS is incorporated and can act as a thermally stable cross-linking species of PDMS [30, 32]. Although rubbery Ormosils have only the TEOS-derived siloxane network as an inorganic component, we can also consider the use of various metal alkoxides instead of TEOS, such as Al, Ti, Zr and Ta alkoxides, which is expected to alter the structure and properties of the PDMS-based system due to differences in molecular weight, valence and coordination number between silicon and other metallic elements. Since the metal alkoxides other than TEOS are generally so reactive toward water that they give a precipitate such as the corresponding oxides and hydroxides [34–36], it is very difficult to synthesize the PDMS-based organic–inorganic hybrid nanocomposites containing an inorganic component derived from metal alkoxides other than TEOS. However, the metal alkoxides can be chemically modified by ethyl acetoacetate (EAcAc) to prevent precipitation [36–40], resulting in the synthesis of PDMS-based organic–inorganic hybrid nanocomposites containing an inorganic component metal alkoxides other than TEOS [41, 42]. This review will concentrate in particular on the mechanically flexible bulk materials of PDMS-based organic–inorganic hybrid nanocomposites. Material design, properties and applications will be discussed.

4.2 Mechanical Flexibility of Organosiloxane-Based Organic–Inorganic Hybrid Nanocomposites

Silica glass with inorganic three-dimensional networks of $-\text{O}-\text{Si}-\text{O}-\text{Si}-$ has high Young’s modulus (7.5×10^{10} Pa) due to rigidity of oxide networks. However, rigidity can be relaxed by the incorporation of methyl groups ($-\text{CH}_3$) into the siloxane networks as shown in Fig. 4.2, thereby providing a decrease in Young’s modulus ($\sim 10^9$ Pa) [43].

Dimethylsiloxane is effective for further decrease in Young’s modulus, reaching rubbery regions (10^6 – 10^7 Pa) [19, 24, 44, 45]. The rotation energy of the Si–O bond of PDMS chains is low because the Si–O bond has longer bond-distance and lower electron-density than the C–C bond. The bond angle of O–Si–O is the same as that of C–C–C, but the bond angle of Si–O–Si is larger than that of C–C–C as shown in Fig. 4.3. In addition, since the Si–O bond has an ionic character of 50%, the bond angle of O–Si–O is easily varied with low energy. Thus, it is very easy for PDMS chains to move and bend. PDMS chains are bulky because two methyl groups are bonded to a Si atom. PDMS chains vibrate with relatively large amplitude. Thus, it is difficult for PDMS chains to approach each other. That is, the intermolecular forces or cohesive forces of PDMS chains are low, the distance among PDMS chains is large, and the

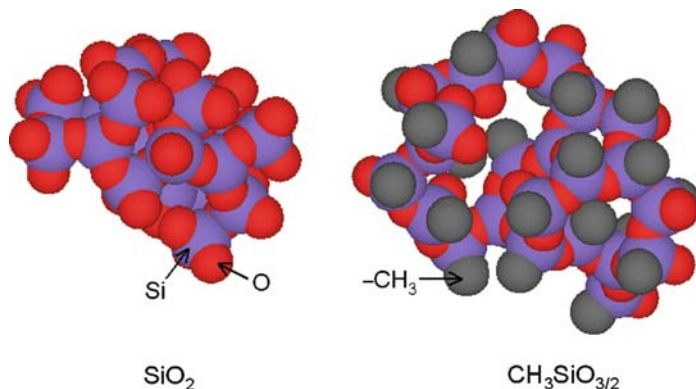
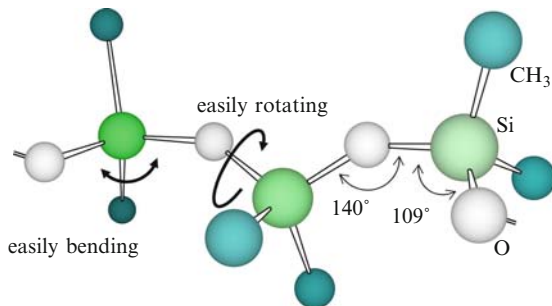


Fig. 4.2 Schematic structures of siloxane (SiO_2) and methyl siloxane ($\text{CH}_3\text{SiO}_{2/3}$)

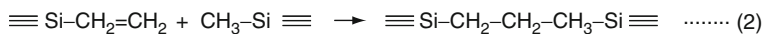
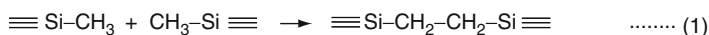
Fig. 4.3 Characteristics of PDMS chain



occupying space of PDMS chains is very large. PDMS chains are easily deformed by adding a compressive or tensile stress, resulting in mechanical flexibility.

The nature of PDMS chains described above causes the mechanical flexibility in the PDMS-based organic–inorganic hybrid nanocomposites. Silicone rubbers are also well known as an elastomer based on the flexibility of PDMS chains [46], which can fall into the category of organic–inorganic hybrid materials in the broad sense. However, the difference between silicone rubbers and PDMS-based organic–inorganic hybrid nanocomposites is a cross-linking species in PDMS chains. While PDMS-based organic–inorganic hybrid nanocomposites have an inorganic cross-linking species, silicone rubbers have an organic cross-linking species. The organic cross-linkers in silicone rubbers are formed by vulcanization as shown in Fig. 4.4. The representative vulcanization is carried out by means of curing with free-radical initiators like peroxides [46]. On the other hand, the inorganic cross-linkers in PDMS-based organic–inorganic hybrid nanocomposites are derived from metal alkoxides as shown in Fig. 4.4. The species formed by hydrolysis of metal alkoxides react with the silanol of PDMS chains, connecting PDMS chains via M–O–Si bonds [47].

Cross-linking of silicone rubbers



Cross-linking of PDMS-based organic/inorganic hybrids

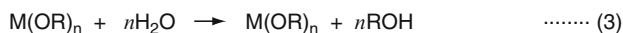


Fig. 4.4 Cross-linking reactions of silicone rubbers and PDMS-based organic–inorganic hybrids

Higher thermal stability is expected in the PDMS-based organic–inorganic hybrid nanocomposites because the inorganic cross-linkers are thermally stable.

4.3 TEOS-PDMS-Derived Organic–Inorganic Hybrid Nanocomposites

TEOS has been used as a precursor of fine fillers for silicone rubbers because fine silica particles can be prepared by appropriate hydrolysis of TEOS. Mark et al. have investigated the filled silicone elastomers prepared by simultaneous curing and filling [48–56]. During curing of PDMS, silica particles with a diameter of 15–25 nm are in-situ generated by hydrolysis of TEOS [55]. Differing from a viewpoint of inorganic fillers, Wilkes et al. have synthesized “Ceramer” from TEOS and PDMS, in which silica formed from TEOS mainly plays the role of cross-linkers between PDMS chains rather than that of fillers [5].

According to (3) and (4) in Fig. 4.4, TEOS is hydrolyzed under acidic condition and then condensed with silanol groups of PDMS. The size of the inorganic component derived from TEOS ranges over several nm and depends on the reaction condition [19, 32]. For example, the size of silica clusters increases when increasing the amount of acid catalyst because of the progress of the self-condensation reaction of TEOS [8]. Transparent bulk samples can be synthesized under appropriate reaction conditions [18, 19] and spongy flexible bulk samples can also be synthesized by aero-gelation [22]. The mechanical flexibility of TEOS-PDMS-derived organic–inorganic hybrid nanocomposites is affected by synthesis conditions such as the amount of acid catalyst, TEOS/PDMS ratio and molecular weight of PDMS [19].

TEOS-PDMS-derived organic–inorganic hybrid nanocomposites have a thermal stability superior to that of silicone rubbers because of inorganic cross-linking by silica. However, thermal stability must be still improved to aim at “thermally stable elastomers” and “flexible ceramics” in the undeveloped region of Fig. 4.1. Mackenzie et al. have further investigated the improvement of TEOS-PDMS-derived organic–inorganic hybrid nanocomposites by adding small amounts of iron chloride

[27, 30, 33]. Since iron chloride is known as an improving agent for thermal stability of silicone rubbers, the same effect can be expected. This involves suppression of the oxidation of methyl groups by redox reactions of ferrous and ferric ions with O_2 . However, it is difficult to apply such a mechanism to TEOS-PDMS-derived organic–inorganic hybrid nanocomposites as the amount of added Fe ion is too small to prevent oxidation of many methyl groups. In the case of TEOS-PDMS-derived organic–inorganic hybrid nanocomposites, it is proposed that the improvement of thermal stability by adding Fe ions is due to the development of silica cross-linking structures of PDMS chains with the effect of Fe ions in the formation process [33].

4.4 $M(OR)_n$ -PDMS-Derived Organic–Inorganic Hybrid Nanocomposites

4.4.1 Chemical Modification of Metal Alkoxides

Metal alkoxides, $M(OR)_n$, have been frequently used as a starting material (precursor) for the sol–gel process for preparing ceramics and glasses [4, 57, 58]. Metal alkoxides are readily hydrolyzed and condense to form an inorganic network with M–O–M bonds at low temperatures as shown in Fig. 4.5 [59]. Since the sol–gel process involves the inorganic network of M–O–M at relatively low temperatures, it is one of the promising methods of hybridizing inorganic compounds such as ceramics and glasses with organic compounds that are unstable at high temperatures.

Though the hydrolysis and condensation reactions of metal alkoxides easily occur as shown in Fig. 4.5, the reactivity of metal alkoxides actually depends on

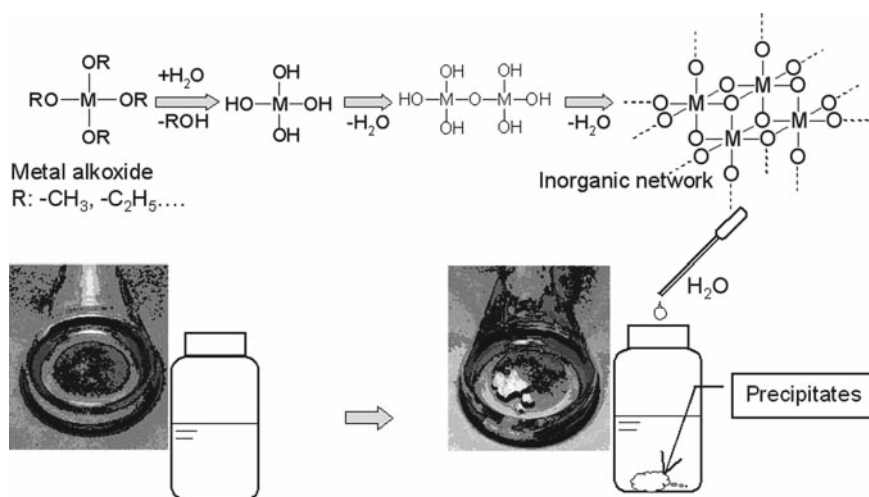


Fig. 4.5 Reactivity of metal alkoxides

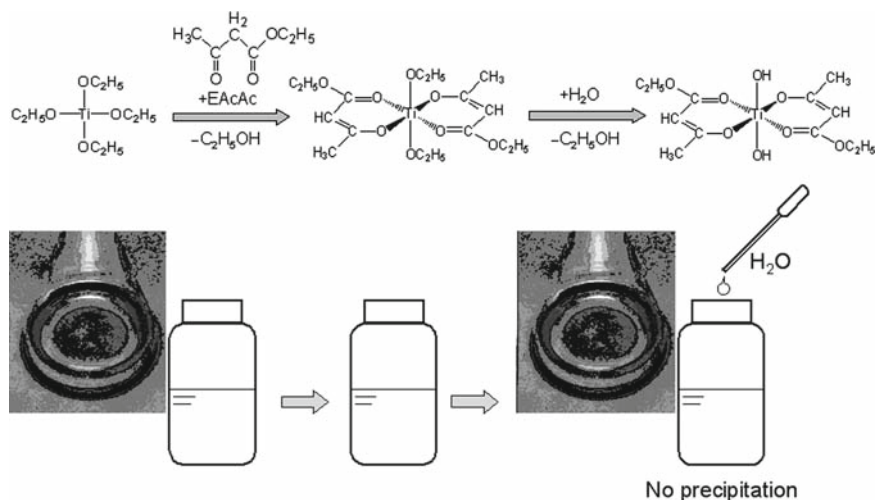


Fig. 4.6 Reactivity of metal alkoxides chemically modified with EAcAc

metals and alkoxy groups. Alkoxides of Si, for example TEOS, are less reactive, so it is easy for us to handle them. Most of the metal alkoxides other than Si are highly reactive, and it is difficult to handle them especially in the atmosphere. Therefore, if highly reactive metal alkoxides such as transition metal alkoxides are directly used, inorganic networks will largely grow without reaction with PDMS and the corresponding oxide or hydroxide will precipitate separately from PDMS as shown in Fig. 4.5. Consequently, metal alkoxides have been chemically modified with chelating agents such as EAcAc to reduce reactivity during formation of PDMS-based organic–inorganic hybrid structures [41, 42]. Figure 4.6 shows a schematic example of $\text{Ti}(\text{OC}_2\text{H}_5)_4$ modified with EAcAc, in which no precipitation occurs even after adding water [59]. The chelating EAcAc groups prevent rapid growth of oxide or hydroxide particles.

The behavior of modified metal alkoxides with EAcAc during the formation of $\text{M}(\text{OR})_n$ -PDMS-derived organic–inorganic hybrid nanocomposites will be discussed. Figure 4.7 shows sequential FT-IR spectra at each step of the process, comprising (a) metal alkoxides mixed with EAcAc in a molar ratio of $\text{EAcAc}/\text{M}(\text{OR})_n = 2$, (b) hydrolyzed solutions of modified metal alkoxides in the presence of PDMS, (c) gels prepared at 70°C for 2 days and (d) samples synthesized by heat-treatment at 150°C for 3 days [42]. Presence of peaks around $1,530$ and $1,620\text{ cm}^{-1}$ in Fig. 4.7a suggests formation of $\text{M}(\text{OR})_{n-x}(\text{EAcAc})_x$, because formation of the chelate complex is confirmed by the appearance of the peak around $1,620\text{ cm}^{-1}$ assigned to C–O bonding with M, and the peak around $1,530\text{ cm}^{-1}$ assigned to C=C vibration of six-membered ring of the chelate complex [37, 38]. In the case of Al(III), Ti(IV) and Zr(IV) alkoxides, almost all the added EAcAc react with metal alkoxides, indicating that two alkoxy groups in one alkoxide molecule are replaced with two EAcAc molecules. On the other hand, strong absorption peaks of free EAcAc are also observed around

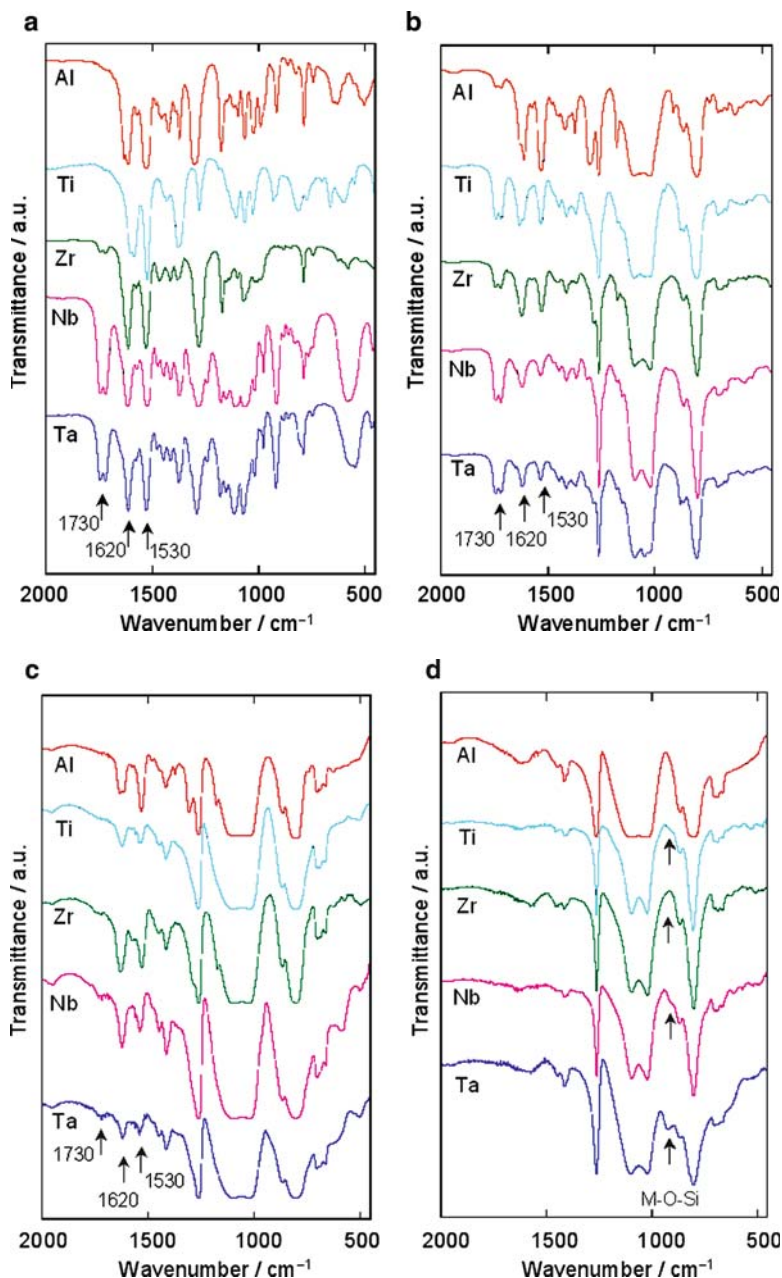


Fig. 4.7 Sequential FT-IR spectra at each step of the process, comprising (a) metal alkoxides mixed with EAcAc in a molar ratio of EAcAc/M(OR)_n = 2, (b) hydrolyzed solutions of modified metal alkoxides in the presence of PDMS, (c) gels prepared at 70°C for 2 days and (d) samples synthesized by heat-treatment at 150°C for 3 days

1,730 cm^{-1} in Nb(V) and Ta(V) alkoxides. One alkoxy group in an alkoxide molecule may be replaced with one EAcAc molecule and EAcAc not reacted with Nb(V) and Ta(V) alkoxides remains free in a keto form. As a result of the chemical modification with EAcAc in a molar ratio of $\text{EAcAc}/\text{M}(\text{OR})_n = 2$, the number of remaining alkoxy groups in one modified alkoxide molecule is thought to be reduced to four in the case of Nb(V) and Ta(V) alkoxides, about two in Ti(IV) and Zr(IV) alkoxides and one in Al(III) alkoxide.

After hydrolysis with water of $\text{H}_2\text{O}/\text{M}(\text{OR})_n = 2$ in the presence of PDMS, the absorption peaks corresponding to alkoxy groups around 500–700 cm^{-1} [60] disappear and that corresponding to free EAcAc around 1,730 cm^{-1} appears or becomes stronger as compared with the absorption peaks of chelating EAcAc around 1,620 and 1,530 cm^{-1} , as shown in Fig. 4.7b. Although part of the EAcAc forming a chelate complex is released upon hydrolysis and exists as free EAcAc, the absorption peaks of EAcAc forming a chelate complex still remain in all the hydrolyzed metal alkoxides.

In a gel prepared at 70°C, the absorption peaks of free EAcAc almost disappear whereas those of EAcAc forming a chelate complex still remain as shown in Fig. 4.7c. Although part of the EAcAc bonded to these alkoxides is released upon hydrolysis, the chelating EAcAc still exists in hydrolyzed solutions and gels, preventing growth of large inorganic particles.

In the samples obtained after the heat-treatment at 150°C, however, no absorption peaks corresponding to EAcAc were observed as shown in Fig. 4.7d. A new absorption peak around 930 cm^{-1} is clearly observed in the sample derived from Ta(V) alkoxide. The samples derived from Ti(IV), Zr(IV) and Nb(V) alkoxides also show a small new peak from 910 to 930 cm^{-1} as indicated by arrows. These peaks attributed to the $\nu(\text{M}-\text{O}-\text{Si})$ vibrations [61, 62] result from M–O–Si bonds formed by the reaction of hydrolyzed alkoxides with silanol groups of PDMS.

4.4.2 Formation Behavior and Structure

Figure 4.8 shows a representative sample of organic–inorganic hybrid nanocomposite sheet synthesized from chemically modified $\text{Zr}(\text{OC}_4\text{H}_9)_n$ and PDMS [47].

The sheet is flexible, homogeneous and transparent without inorganic particles precipitated from the metal alkoxide. This means that the incorporated inorganic component has a size smaller than the Rayleigh scattering size, which is at least smaller than the visible wavelength. The size of the inorganic component was confirmed by HRTEM and SAXS [47]. Figure 4.9 shows the HRTEM of a sample synthesized from chemically modified $\text{Zr}(\text{OC}_4\text{H}_9)_4$ and PDMS. The TEM images indicate larger dark regions with 2–3 nm size distributed over the whole area, which is likely the inorganic component with high electron density, derived from $\text{Zr}(\text{OC}_4\text{H}_9)_4$. The size of the inorganic component is extremely small, compared to silica fillers with ~20 nm size that were dispersed in the PDMS network by using TEOS [55].

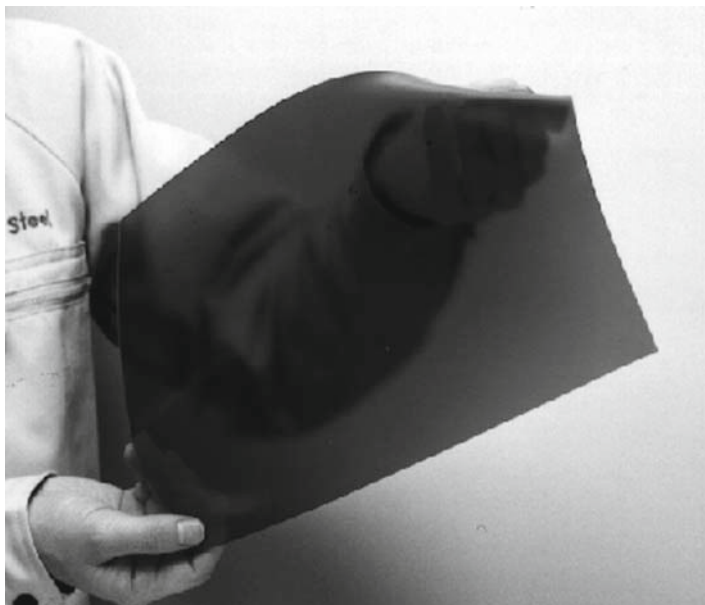
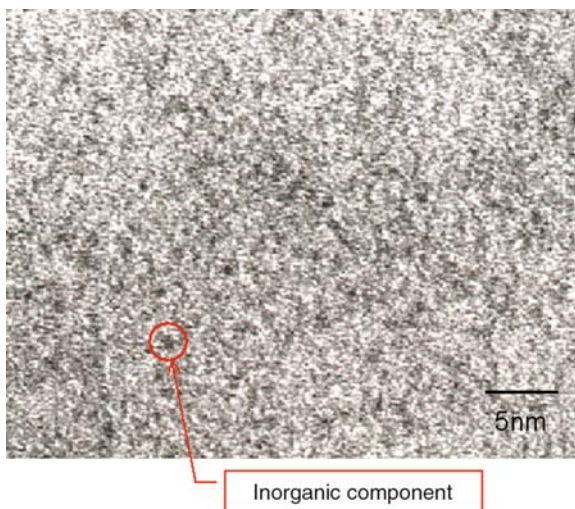


Fig. 4.8 Representative sample of organic–inorganic hybrid nanocomposite sheets synthesized from chemically modified $\text{Zr}(\text{OC}_4\text{H}_9)_n$ and PDMS

Fig. 4.9 HRTEM of sample synthesized from chemically modified $\text{Zr}(\text{OC}_4\text{H}_9)_4$ and PDMS



The formation behavior of organic–inorganic hybrid nanocomposites from $\text{M}(\text{OR})_n$ and PDMS is schematically shown in Fig. 4.10 [42, 47].

Chemically modified metal alkoxides are subject to hydrolysis and condensation reactions, providing the inorganic clusters. However, these inorganic clusters cannot grow into large particles identified as precipitates. Therefore, inorganic components

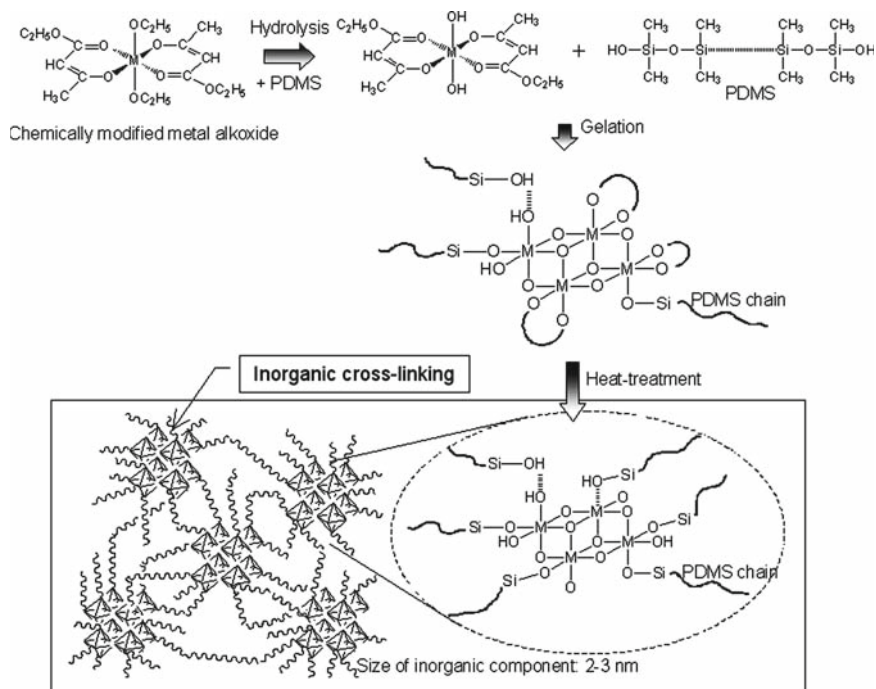


Fig. 4.10 Formation behavior of organic–inorganic hybrid nanocomposites from PDMS and chemically modified $M(OR)_n$

derived from metal alkoxides are present as oxide-like clusters with several nm sizes or below, which are attached to PDMS via M–O–Si bonds and hydrogen bonds. Since the inorganic components are close to molecular-level size, they are thought to behave as cross-linkers of PDMS chains rather than simple fillers such as inorganic particles [42, 47, 63].

4.4.3 Mechanical Properties

Flexible bulks or sheets are also synthesized from $M(OR)$ -PDMS-derived organic–inorganic hybrid nanocomposites as exhibited in Fig. 4.8. Figure 4.11 shows a typical example of dynamic mechanical behaviors depending on temperature for the flexible samples [47]. The dynamic elastic modulus exhibits a high value at low temperatures but at temperatures between 0 and 300°C, it is low and approximately constant in the rubbery region. The abrupt decrease in dynamic elastic modulus and the peak of $\tan \delta$ around -120°C are attributed to the glass transition of PDMS chains.

Mechanical flexibility depends not only on synthesis conditions such as $M(OR)_n$ /PDMS ratio and molecular weight of PDMS but also on the type of inorganic components derived from metal alkoxides [42, 47, 63]. Figure 4.12 shows

Fig. 4.11 Dynamic mechanical properties of organic–inorganic hybrid nanocomposite synthesized from chemically modified $Zr(OC_4H_9)_4$ and PDMS

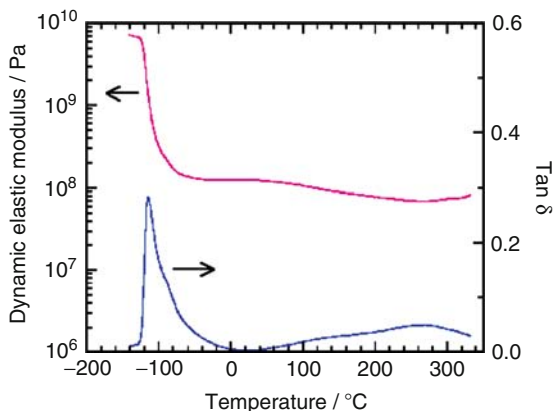
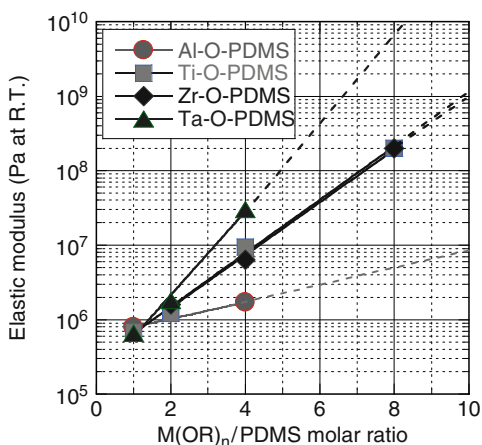


Fig. 4.12 Effect of inorganic component on mechanical flexibility



the effect of inorganic component on the property of mechanical flexibility. The elastic modulus is influenced by type and content of inorganic components. Generally, when inorganic content increases, elastic modulus also increases. This effect depends on the type of inorganic components derived from metal alkoxides. This is due to the difference in interaction between the inorganic component and PDMS chains [47].

4.4.4 Use of Dimethyldiethoxysilane (DMDES)

Dimethyldiethoxysilane (DMDES, $(CH_3)_2Si(OC_2H_5)_2$) can be hydrolyzed and can condense to form PDMS as shown in Fig. 4.13. Thus, PDMS-based organic–inorganic hybrid nanocomposites can also be synthesized using DMDES and TEOS although it is difficult for DMDES to form a long chain of PDMSs like the PDMS used as a starting material.

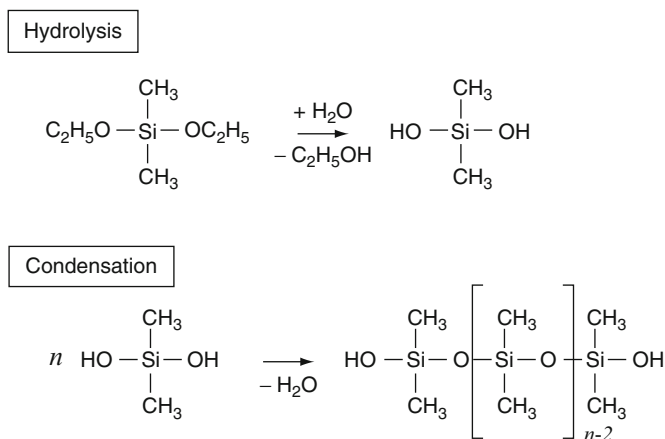


Fig. 4.13 Hydrolysis and condensation reactions of dimethyldiethoxysilane

Not only TEOS [64, 65] but also $\text{M}(\text{OR})_n$ such as Ti, Zr and Al alkoxides [66–68] have been used as starting materials of the inorganic component in the PDMS-based organic–inorganic hybrid nanocomposites synthesized using DEMDMS. Whereas transition-metal alkoxides are highly reactive to water, they can be used without chemical modifiers in the case of the DMEDES-derived system. Metal alkoxides act not only as precursors of inorganic cross-linking species but also as catalysts for the hydrolysis and condensation reactions of DMEDES [69, 70].

4.5 MultiFunctionality and Applications of Mechanically Flexible Organic–Inorganic Hybrid Nanocomposites

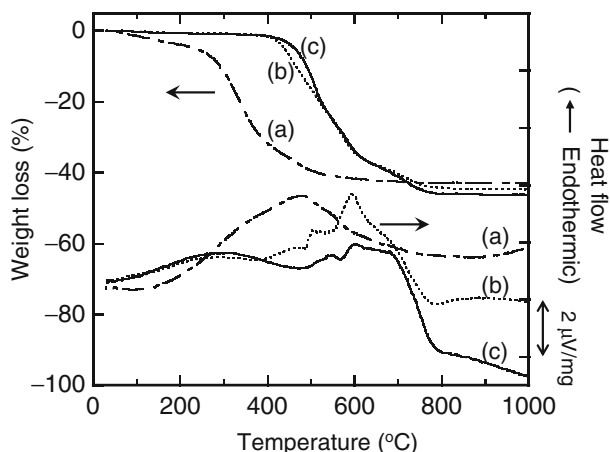
The application of mechanically flexible hybrid nanocomposites such as the PDMS-based organic–inorganic hybrid nanocomposite sheets and bulks has been limited as yet. Some examples are listed in Table 4.1. In addition to mechanical flexibility, some additional properties have been investigated in the PDMS-based organic–inorganic hybrid nanocomposites for practical uses.

4.5.1 Tribological Property

The wettability to engine oil in organosiloxane-based organic–inorganic hybrid nanocomposites has been investigated, aimed at the development of low friction materials under boundary and fluid lubrication conditions for automobile components, especially a piston ring without a gap [71–73]. In conventional materials such as cast iron and steel of piston rings, a gap is needed for assembling it into a piston.

Table 4.1 Examples of applications and additional properties of PDMS-based organic–inorganic hybrid nanocomposites

Application	Additional property	Method for approaching to the additional property	Refs.
Piston rings (low friction materials)	Tribological property	incorporating phenyl groups	[72-74]
Thermal-fixation rolls for electro-photographic printers	Surface property	optimizing the content and condition of organic and inorganic components	[78, 79]
Biomedical materials	Bioactive property	adding Ca(II) ions	[16, 79-85]
Thermally conductive sheets for electric assemblies	Thermally conductive Property	dispersing fillers	[86]

**Fig. 4.14** TG-DTA curves of (a) PDMS-based inorganic–organic hybrid, (b) PDMDPS-based inorganic–organic hybrid and (c) PDMDPS-based inorganic–organic hybrid with addition of FeCl_3

These piston rings face the problem of combustion gases slightly leaking through the gap, leading to low fuel efficiency. A flexible piston ring made out of organic–inorganic hybrid nanocomposites would be stretched to fit the piston even without a gap. In order to apply flexible organic–inorganic hybrid nanocomposites to the piston ring, not only mechanical flexibility but also lubrication properties must be optimized.

The organosiloxane-based organic–inorganic hybrid nanocomposites containing phenyl groups derived from phenyltriethoxysilane were found to have high wettability with engine oil and good friction property [71]. In addition, flexible sheets of organosiloxane-based organic–inorganic hybrid nanocomposites containing phenyl groups have been synthesized from starting materials of polydimethyldiphenylsiloxane

(PDMDPS), phenyltriethoxysilane ($\text{PhSi}(\text{OEt})_3$) and zirconium n-butoxide ($\text{Zr}(\text{O}^i\text{C}_4\text{H}_9)_4$) [73]. The incorporation of phenyl groups provides not only high wettability with engine oil and good friction property but also high thermal stability. The PDMDPS-based system has higher thermal stability than the PDMS-based system as shown in TG-DTA curves of Fig. 4.14. In the PDMDPS-based system, no weight loss is observed until 400°C and large weight loss corresponding to the thermal decomposition occurs above 400°C with endothermic peaks of DTA. On the other hand, the PDMS-based system has large weight loss from 300°C with an endothermic peak of DTA corresponding to the thermal decomposition. It is known that the phenyl group is one of the thermodynamically stable organic components in organosiloxanes because of the thermal stability of the aromatic structure. The inductive effect of the phenyl group also strengthens Si–O bonds of a phenylsiloxane network [74]. These effects are thought to result in high thermal stability of PDMDPS-based organic–inorganic hybrid nanocomposites. As mentioned above, the addition of FeCl_3 into TEOS-PDMS-derived organic–inorganic hybrid nanocomposites is effective in thermal stabilization [27, 30, 33]. In the PDMDPS-based system, the addition of FeCl_3 is effective in thermal stabilization but its effect is small, as shown in the TG-DTA curves of Fig. 4.14.

4.5.2 Surface Property

There are very few studies on the surface properties of PDMS-based organic–inorganic hybrid nanocomposites. As a fundamental study, Rubio et al. reported on the surface energy of silica-TEOS-PDMS ormosils and TEOS-TBOT(tetrabutyl orthotitanate)-PDMS hybrids, which was measured by inverse gas chromatography [75, 76]. The surface is covered mainly with methyl groups from PDMS chains, but acidic hydroxyl groups originating from silica particles are also present and lower surface energy. As a practical study, Shindo et al. reported on the surface properties of the $\text{Ti}(\text{OC}_3\text{H}_7)_4$ -PDMS-derived system with the aim of applying it on the thermal-fixation roll for electro-photographic printers [77, 78]. In order to achieve a higher quality print, the toners need to be globular and finer. But such toners are prone to adhere easily to the surface of the thermal-fixation roll. The next generation thermal-fixation rolls need not only mechanical flexibility but also a surface property avoiding adhesion of the toners - so-called “toner-offset” property. In the $\text{Ti}(\text{OC}_3\text{H}_7)_4$ -PDMS-derived system, the surface was characterized in terms of the contact angle of water and the surface morphology by AFM. The effect of heat-treatment and composition on the surface property was elucidated. Practical evaluation showed an excellent “toner-offset” property.

4.5.3 Bioactive Property

In addition to mechanical flexibility, the introduction of the property of bioactivity into the TEOS-PDMS-derived system has been investigated for biomedical applications. Tsuru et al. found that the addition of Ca(II) ions derived from calcium nitrate was

effective for making the TEOS-PDMS-derived system bioactive - the so-called “ormosils” [17, 79–85]. The Ca(II)-containing ormosils deposit apatite spontaneously on their surface when soaked in human physiological fluids, whereas ormosils without Ca ions do not show such effect.

4.5.4 *Thermally Conductive Property*

Silicone rubber sheets filled with ceramic particles are used as electrically insulating and thermally conductive spacers for electric assemblies. There is a growing demand for high-performance thermally conductive sheets since heat-management is becoming more important for power transistors, power modules, and so on. PDMS-based organic–inorganic hybrid nanocomposites have high potential for the above applications because they not only have the same PDMS chains as silicone rubbers but also inorganic components derived from metal alkoxides as an inorganic cross-linking species. The inorganic components may be effective for making a strong interaction with fillers. The $Zr(OC_3H_7)_4$ -PDMS-derived organic–inorganic hybrid nanocomposite filled with alumina particles shows high thermal conductivity above 5 W/m K [86]. Further improvement of thermal conductivity is expected in the near future.

4.6 Conclusions

Organosiloxane-based organic–inorganic hybrid nanocomposites have been actively investigated for a variety of applications because they have potential due to extraordinary properties resulting from the synergistic effect of organic and inorganic components. In particular, many attempts have been made to apply the films and coatings for practical uses but application of bulks and coatings is limited. Typical applications of bulks and sheets are “thermally stable elastomers” and “flexible ceramics” shown in Fig. 4.1, which are essentially required for our applications. In order to apply bulk and sheet materials to individual practical uses, however, we have to consider and design additional properties beside flexibility. Fortunately, the design of organosiloxane-based organic–inorganic hybrid nanocomposites can take advantage of a wide range of combinations of organic and inorganic components, which can lead to the desired property. Bulk and sheet materials, especially mechanically flexible materials of organic–inorganic hybrid nanocomposites should be further improved and spread out in the near future, to target applications beyond those listed in Table 4.1

References

1. Katayama S (2005) Flexible ceramics. In: Makishima A (ed) *The Latest Technology of Nano Hybrid Materials*. CMC, Tokyo, pp. 327.

2. Mackenzie JD (1984) Applications of sol–gel methods for glass and ceramics processing. In: Hensch LL, Ulrich DR (eds) *Ultrastructure Processing of Ceramics, Glasses and Composites*. Wiley, New York, pp. 15–26.
3. Pierre AC (1998) *Introduction to Sol–Gel Processing*. Kluwer, Boston, pp 1–9.
4. Wright JD, Sommerdijk NAJM (2001) *Sol–Gel Materials Chemistry and Applications*. Gordon and Breach Science, Amsterdam, pp. 1–14.
5. Wilkes GL, Orlor B, Huang HH (1985) “Ceromers” hybrid materials incorporating polymeric/oligomeric species into inorganic glasses utilizing a sol–gel approach. *Polym. Prepr.* 26: 300–301.
6. Philipp G, Schmidt H (1984) New materials for contact lenses prepared from Si- and Ti-alkoxides by the sol–gel process. *J. Non Cryst. Solids* 63: 283–292.
7. Krung H, Schmidt H (1994) Organic-inorganic nanocomposites for micro optical applications. *New J. Chem.* 18: 1125–1134.
8. Mackenzie JD, Chung YJ, Hu Y (1992) Rubbery ormosils and their applications. *J. Non Cryst. Solids* 147/148: 271–279.
9. Izumi K, Tanaka T, Uchida Y, Tohge N, Minami T (1993) Hydrolysis of trifunctional alkoxy silane and corrosion resistance of steel sheets coated with alkoxy silane-derived films. *J. Mater. Sci. Lett.* 12: 724–727.
10. Avnir D, Braun S, Lev O, Levy D, Ottolenghi M (1994) Organically doped sol–gel porous glasses: Chemical sensors, enzymatic sensors, electrooptical materials, luminescent materials and photochromic materials. In: Klein LC, (ed) *Sol–Gel Optics: Processing and Applications*. Kluwer, Dordrecht, pp. 539–582.
11. Selliner A, Weiss PM, Nguyen A, Lu Y, Assink RA, Gong W, Brinker CJ (1998) Continuous self-assembly organic-inorganic nanocomposite coatings that mimic nacre. *Nature* 349: 256–260.
12. Inagaki S, Guan S, Ohsuna T, Terasaki O (2002) An ordered mesoporous organosilica hybrid material with a crystal-like wall structure. *Nature* 416: 304–307.
13. Stein A, Meide BJ, Schroden RC (2000) Hybrid inorganic-organic mesoporous silicates – Nanoscopic reactors coming of age. *Adv. Mater.* 12: 1403–1419.
14. Sayari A, Hamoudi S, (2001) Periodic mesoporous silica-based organic-inorganic nanocomposite materials. *Chem. Mater.* 13: 3151–3168.
15. Remenar JF, Hawker CJ, Hedrick JL, Kim SM, Miller RD, Nguyen C, Trollsas M, Yoon DY (1998) Templating nanopores into poly(methylsilsequioxane): New low-dielectric coatings suitable for microelectronic applications. *Mater. Res. Soc. Symp. Proc.* 511: 69–74.
16. Park Y, Nagai M (2001) Proton exchange nanocomposite membranes based on 3-glycidoxypropyltrimethoxysilane silicotungstic acid and α -zirconium phosphate hydrate. *Solid State Ionics* 145: 149–160.
17. Tsuru K, Aburatani Y, Yabuta T, Hayakawa S, Ohtsuki C, Osaka A (2001) Synthesis and behavior of organically modified silicate containing Ca ions. *J. Sol Gel Sci. Tech.* 21: 89–96.
18. Huang H, Orlor B, Wilkes GL (1985) Ceramers: Hybrid materials incorporating polymeric/oligomeric species with inorganic glasses by a sol–gel process. *Poly. Bull.* 14: 557–564.
19. Huang H, Orlor B, Wilkes GL (1987) Structure-property behavior of new hybrid materials incorporating oligomeric species into sol–gel glasses. 3. Effect of acid content, tetraethoxysilane content, and molecular weight of poly(dimethylsiloxane). *Macromolecules* 20: 1322–1330.
20. Rodrigues DE, Brennan AB, Bétrabet C, Wang B, Wilkes GL (1992) Structural features of sol–gel derived hybrid inorganic-organic network ceramer materials by small-angle X-ray scattering. *Chem. Mater.* 4: 1437–1446.
21. Huang H, Glaser RH, Brennan AB, Rodrigues DE, Wilkes GL (1992) Structure-property study of hybrid materials incorporating organic oligomers into sol–gel systems. In: Uhlmann DR, Ulrich DR (eds) *Ultrastructure Processing of Advanced Materials*. Wiley, New York, pp. 425–438.
22. Chung YJ, Ting S-J, Mackenzie JD (1990) Rubbery ormosils. *Mater. Res. Soc. Symp. Proc.* 180: 981–986.
23. Morita K, Hu Y, Mackenzie JD (1992) The effect of ultrasonic radiation on gelation and properties of ormosils. *Mater. Res. Soc. Symp. Proc.* 271: 693–698.

24. Hu Y, Mackenzie JD (1992) Rubber-like elasticity of organically modified silicates. *J. Mater. Sci.* 27: 4415–4420.
25. Hu Y, Mackenzie JD (1992) Structure-related mechanical properties of ormosils by sol–gel process. *Mater. Res. Soc. Symp. Proc.* 271: 681–686.
26. Iwamoto T, Morita K, Mackenzie JD (1993) Liquid state ^{29}Si NMR study on the sol–gel reaction mechanisms of ormosils. *J. Non Cryst. Solids* 159: 65–72.
27. Kramer SJ, Mackenzie JD (1994) Thermal stability enhancement of rubbery ormosils. *Mater. Res. Soc. Symp. Proc.* 346: 709–714.
28. Hu Y, Chung YJ, Mackenzie JD (1993) Gelation kinetics of an organically modified silicate. *J. Mater. Sci.* 28: 6549–6554.
29. Iwamoto T, Mackenzie JD (1994) Ormosils of high hardness. *Mater. Res. Soc. Symp. Proc.* 346: 397–402.
30. Mackenzie JD, Huang Q, Rubio-Alonso F, Kramer SJ (1996) Effects of temperature on properties of ormosils. *Mater. Res. Soc. Symp. Proc.* 435: 229–236.
31. Kramer SJ, Rubio-Alonso F, Mackenzie JD (1996) Organically modified silicate aerogels, “aeromosils”. *Mater. Res. Soc. Symp. Proc.* 435: 295–300.
32. Mackenzie JD, Huang Q, Iwamoto T (1996) Mechanical properties of ormosils. *J. Sol Gel Sci. Tech.* 7: 151–161.
33. Bescher E, Hoshino Y, Nishizawa Y, Cooley K, Mackenzie JD (2003) The role of Fe in the thermal stabilization of ormosils. *J. Sol Gel Sci. Tech.* 26: 297–301.
34. Bradley DC, Mehrotra RC, Gaur DP (1978) *Metal Alkoxides*. Academic, London, pp. 150–167.
35. Brinker CJ, Scherer GW (1990) *Sol–Gel Science, the Physics and Chemistry of Sol–Gel Processing*. Academic, Boston, pp. 42–44.
36. Turova NY, Turevskaya EP, Kessler VG, Yanovskaya MI (2002) *The Chemistry of Metal Alkoxides*. Kluwer, Boston, pp. 107–125.
37. Yamamoto A, Kambara S (1959) Structure of the reaction products of tetraalkoxytitanium with acetylacetone and ethyl acetoacetate. *J. Am. Chem. Soc.* 79: 4344–4348.
38. Uchhashi H, Tohge N, Minami T (1989) Preparation of amorphous Al_2O_3 thin films from stabilized Al-alkoxides by the sol–gel method. *J. Ceram. Soc. Jpn.* 97: 396–399.
39. Bradley DC, Mehrotra RC, Gaur DP (1978) *Metal Alkoxides*. Academic, London, pp. 209–217.
40. Brinker CJ, Scherer GW (1990) *Sol–Gel Science, the Physics and Chemistry of Sol–Gel Processing*. Academic, Boston, pp. 52–59.
41. Yamada N, Yoshinaga I, Katayama S (1997) Synthesis and dynamic mechanical behavior of inorganic–organic hybrids containing various inorganic components. *J. Mater. Chem.* 7: 1491–1495.
42. Yamada N, Yoshinaga I, Katayama S (2000) Formation behavior and optical properties of transparent inorganic–organic hybrids prepared from metal alkoxides and polydimethylsiloxane. *J. Sol Gel Sci. Tech.* 17: 123–130.
43. Lee J, Chopra N, Ma J, Lu Y, Huang T, Willecke R, Yau W, Cheung D, Yieh E (2000) Integration and characterization of low carbon content $\text{SiO}_x\text{C}_y\text{H}_z$ low k materials for <0.18 μm dual damascene application. *Mater. Res. Soc. Symp. Proc.* 612: D3.4.1–D3.4.6.
44. Katayama S, Yoshinaga I, Yamada N (1996) Synthesis of inorganic–organic hybrids from metal alkoxides and silanol-terminated Polydimethylsiloxane. *Mater. Res. Soc. Symp. Proc.* 435: 321–326.
45. Yamada N, Yoshinaga I, Katayama S (1998) Processing and properties of inorganic–organic hybrids containing various inorganic components. *J. Sol Gel Sci. Soc.* 13: 445–449.
46. Warrick EL, Pierce OR, Polmanteer KE, Saam JC (1979) Silicone elastomer developments 1967–1977. *Rubber Chem. Tech.* 52: 437–525.
47. Katayama S, Kubo Y, Yamada N (2002) Characterization and mechanical properties of flexible dimethylsiloxane-based inorganic–organic hybrid sheets. *J. Am. Ceram. Soc.* 85: 1157–1163.

48. Mark JE, Pan S-J (1982) Reinforcement of polydimethylsiloxane networks by in situ precipitation of silica: A new method for preparation of filled elastomers. *Makromol. Chem. Rapid Commun.* 3: 681–685.
49. Mark JE, Jiang C-Y, Tang M-T (1984) Simultaneous curing and filling of elastomers. *Macromolecules* 17: 2613–2616.
50. Mark JE (1986) Conformational analysis of some polysilanes, and the precipitation of reinforcing silica into elastomeric poly(dimethylsiloxane) networks. In: Hensch LL, Ulrich DR (eds) *Science of Ceramic Chemical Processing*. Wiley, New York, pp. 434–454.
51. Mark JE (1988) In-situ generation of ceramic particles for the reinforcement of elastomeric matrices. In: Mackenzie JD, Ulrich DR (eds) *Ultrastructure Processing of Advanced Ceramics*. Wiley, New York, pp. 623–633.
52. Mark JE (1989) Generate reinforcing particles in place. *Chemtech* 19: 230–233.
53. Ning YP, Zhao MX, Mark JE (1992) Siloxane-silica composites prepared by sol–gel technique with hydrolysis water generated in situ. In: Hensch LL, West JK (eds) *Chemical Processing of Advanced Materials*. Wiley, New York, pp. 745–751.
54. Schaefer DE, Mark JE, Jian L, Sun C-C, McCarthy DW, Jiang C-Y, Ning Y-P, Spooner S (1992) Structure-property relationships in silica-siloxane molecular composites. In: Uhlman DR, Ulrich DR (eds) *Ultrastructure Processing of Advanced Materials*. Wiley, New York, pp. 361–375.
55. Kumudinie C, Mark JE (1999) Tear strengths of poly(dimethylsiloxane) networks reinforced with in-situ precipitated silica. *Mater. Res. Soc. Symp. Proc.* 576: 331–336.
56. Mark JE (2000) Some scattering results on organic-inorganic composites. *Mater. Res. Soc. Symp. Proc.* 628: CC8.4.1–CC.8.4.9.
57. Brinker CJ, Scherer GW (1990) *Sol–Gel Science, the Physics and Chemistry of Sol–Gel Processing*. Academic, Boston, pp. 1–18.
58. Pierre AC (1998) *Introduction to Sol–Gel Processing*. Kluwer, Boston, pp. 50–70.
59. Katayama S, Yoshinaga S, Yamada N (1999) Inorganic–organic hybrid materials. *Mater. Integr.* 12: 51–56.
60. Bradley DC, Mehrotra RC, Gaur DP (1978) *Metal Alkoxides*. Academic, London, pp. 117–122.
61. Schraml-Marth M, Walther KL, Wokaun W, Handy BE, Baiker A (1992) Porous silica gels and $\text{TiO}_2/\text{SiO}_2$ mixed oxides prepared via the sol–gel process: characterization by spectroscopic techniques. *J. Non Cryst. Solids* 143: 93–111.
62. Gunji T, Nagao Y, Misono T, Abe Y (1989) Preparation of $\text{SiO}_2\text{–TiO}_2$ fibers from polytitanosiloxanes. *J. Non Cryst. Solids*, 107: 149–154.
63. Yamada N, Yoshinaga I, Katayama S (1998) Effect of inorganic components on the mechanical properties of inorganic–organic hybrids synthesized from Metal alkoxides and polydimethylsiloxane. *J. Mater. Res.* 14: 1720–26.
64. Babonneau F, Bois L, Livage J (1992) Structural characterization of gels prepared from co-hydrolysis of tetraethoxysilane and dimethyldiethoxysilane. *Mater. Res. Soc. Symp. Proc.* 271: 237–242.
65. Babonneau F, Toutou C, Gaveriaux S (1997) ^{17}O NMR investigation of chemical homogeneity in hybrid systems. *J. Sol Gel Sci. Tech.* 8: 553–556.
66. Dire S, Babonneau F, Carturan G, Livage J (1992) Synthesis and characterization of siloxane-titania materials. *J. Non Cryst. Solids* 147/148: 62–66.
67. Dire S, Babonneau F, Sanchez C, Livage J (1992) Sol–gel synthesis of siloxane-oxide hybrid coatings $[\text{Si}(\text{CH}_3)_2\text{O.MOX}]$: $\text{M} = \text{Si, Ti, Zr, Al}$ with luminescent properties. *J. Mater. Chem.* 2: 239–244.
68. Julian B, Gervais C, Cordocillo E, Escribano P, Babonneau F, Sanchez C (2003) Synthesis and characterization of transparent PDMS-metal-oxo based organic-inorganic nanocomposites. *Chem. Mater.* 15: 3026–3034.
69. Sanchez C, Ribot F (1994) Design of hybrid organic-inorganic materials synthesized via sol–gel chemistry. *New J. Chem.* 18: 1007–1047.

70. Katayama S, Yoshinaga I, Kubo Y, Yamada N (2003) Catalytic effect of chemically modified metal alkoxides on hydrolysis and condensation reactions of methyl- and phenyl-ethoxysilanes. *J. Ceram. Soc. Jpn.* 111: 743–748.
71. Sakai T, Shibata Y, Satake S, Katayama S, Yamada N (2001) Lubrication properties of inorganic-organic hybrids. *J. Ceram. Soc. Jpn.* 109: 322–325.
72. Katayama S, Yamada N, Shibata Y, Sakai T, Satake S (2002) Preparation of organosiloxane-based inorganic-organic hybrids with high affinity toward engine oil. *J. Ceram. Soc. Jpn.* 110: 549–553.
73. Katayama S, Yamada N, Shibata Y, Noda K (2003) Fabrication and properties of PDMDPS-based inorganic-organic hybrid sheets. *J. Ceram. Soc. Jpn.* 111: 391–395.
74. Grassie N, Francey KF, Macfarlane IG (1980) The thermal degradation of polysiloxane – Part 4: Poly(dimethyl)diphenyl siloxane). *Polym. Degrad. Stab.* 2: 67–83.
75. Martos C, Rubio F, Rubio J, Oteo JL (2001) Surface energy of silica-TEOS-PDMS ormosils. *J. Sol Gel Sci. Tech.* 20: 197–210.
76. Pena-Alonso R, Tellez L, Rubio J, Rubio F (2006) Surface chemical and physical properties of TEOS-TBOT-PDMS hybrid materials. *J. Sol Gel Sci. Tech.* 38: 133–145.
77. Shindou T, Katayama S, Yamada N, Kamiya K (2003) Surface properties of Polydimethylsiloxane-based inorganic-organic hybrid films deposited on polyimide sheets by the sol-gel method. *J. Sol Gel Sci. Tech.* 27: 15–21.
78. Shindou T, Katayama S, Yamada N, Kamiya K (2004) Effect of composition on surface properties of Polydimethylsiloxane-based inorganic-organic hybrid films. *J. Sol Gel Sci. Tech.* 30: 229–237.
79. Tsuru K, Ohtsuki C, Osaka A, Iwamoto T, Mackenzie JD (1996) Synthesis of bioactive ormosils by sol-gel method. *Mater. Res. Soc. Symp. Proc.* 435: 403–408.
80. Tsuru K, Ohtsuki C, Osaka A, Iwamoto T, Mackenzie JD (1997) Bioactivity of sol-gel derived organically modified silicates: Part I: In vitro examination. *J. Mater. Sci. Mater. Med.* 8: 157–161.
81. Aburatani Y, Tsuru K, Hayakawa S, Osaka A (2003) Bioactivity of viscoelastic ormosil-type organic-inorganic hybrids containing colloidal silica particles. *J. Ceram. Soc. Jpn.* 111: 318–322.
82. Aburatani Y, Tsuru K, Hayakawa S, Osaka A (2003) Mechanical property and microstructure of bioactive organic-inorganic hybrids containing colloidal silica particles. *J. Ceram. Soc. Jpn.* 111: 247–251.
83. Yabuta T, Bescher EP, Mackenzie JD, Tsuru K, Hayakawa S, Osaka A (2003) Synthesis of PDMS-based porous materials for biomedical applications. *J. Sol Gel Sci. Tech.* 26: 1219–1222.
84. Yabuta T, Tsuru K, Hayakawa S, Osaka A (2004) Synthesis of blood compatible PDMS-based organic-inorganic hybrid coatings. *J. Sol Gel Sci. Tech.* 31: 273–276.
85. Tsuru K, Hayakawa S, Osaka A (2004) Synthesis of bioactive and porous organic-inorganic hybrids for biomedical applications. *J. Sol Gel Sci. Tech.* 32: 201–205.
86. Takuya S (2004) Surface properties of inorganic-organic hybrids prepared by sol-gel method and application to novel heat-resistant materials. *Res. Rep. Fac. Eng. Mie Univ.* 29: 79–78.

Chapter 5

Structural Characterization of Hybrid Organic–Inorganic Nanocomposites: X-ray Scattering and Solid-State Nuclear Magnetic Resonance Spectroscopy

Tiziana Di Luccio and Marzia Pentimalli

Abstract The properties of hybrid composites result from a complex cooperation between the organic and inorganic species constituting the nanocomposites. A continuous, increasing demand of the detailed knowledge of such properties at the nanoscale has contributed to the development of the characterization techniques. The chapter provides an overview on two specific characterization tools widely used in nanocomposites research: X-ray scattering (XRS) and Solid-State Nuclear Magnetic Resonance spectroscopy (SSNMR). We briefly describe some fundamentals of both the methods and present several relevant results from the literature in this field. Specific emphasis is devoted to nanoparticle polymer nanocomposites and polymer-layered silicate nanocomposites.

Abbreviations CP: Cross-polarization; CSA: Chemical shift anisotropy; DD: Dipolar decoupling; FWHM: Full width half-maximum; GID: Grazing-incidence diffraction; GISAXS: Grazing-incidence small-angle X-ray scattering; MAS: Magic-angle spinning; MDEA: MMA/2-(*N*-methyl-*N,N*-diethylammonium iodide) ethyl acrylate; MMT: Montmorillonite; MQ-MAS: Multiple-quantum magic-angle spinning; PL: Photoluminescence; PLS: Polymer-layered silicate; PS: Polystyrene; RD: Recycle delay; SAXS: Small-angle X-ray scattering; SPE: Single-pulse excitation; SSNMR: Solid-state nuclear magnetic resonance; TEM: Transmission electron microscopy; TOPAS: Thermoplastic cyclic olefin copolymer; USAXS: Ultra-small-angle X-ray scattering; WAXS: Wide-angle X-ray scattering; XRD: X-ray diffraction.

T. Di Luccio (✉) and M. Pentimalli
ENEA Centro Ricerche Portici, P.le Enrico Fermi, I-80055 Portici (Napoli), Italy
e-mail: tiziana.diluccio@portici.enea.it

5.1 X-ray Scattering Methods

5.1.1 Introduction

X-ray scattering represents a powerful tool to study the structure and dynamics in hybrid composites. To this purpose, different X-ray scattering techniques are available; from traditional methods of powder diffraction to modern synchrotron radiation techniques that allow the study of structures such as molecular monolayers, quantum dots, supported islands, nanoparticles and proteins, otherwise difficult to determine because of their low scattering power. The choice of the specific technique depends on the system under investigation, length scales involved and information required. In this chapter, we will illustrate most of them, namely, X-ray diffraction (XRD), wide- and small-angle X-ray scattering (WAXS and SAXS, respectively) and grazing incidence small angle scattering (GISAXS) and will report selected results on hybrid nanocomposites. A comprehensive distinction among such methods can be made in terms of the *scattering vector* (or *momentum transfer*) q defined as the difference between the scattered and the incident wave vectors. The atomic scale corresponds to values of $q > 0.1 \text{ nm}^{-1}$. Both XRD and WAXS provide information at this scale. Traditionally, XRD is used in reflection geometry (Fig. 5.1b); best suitable

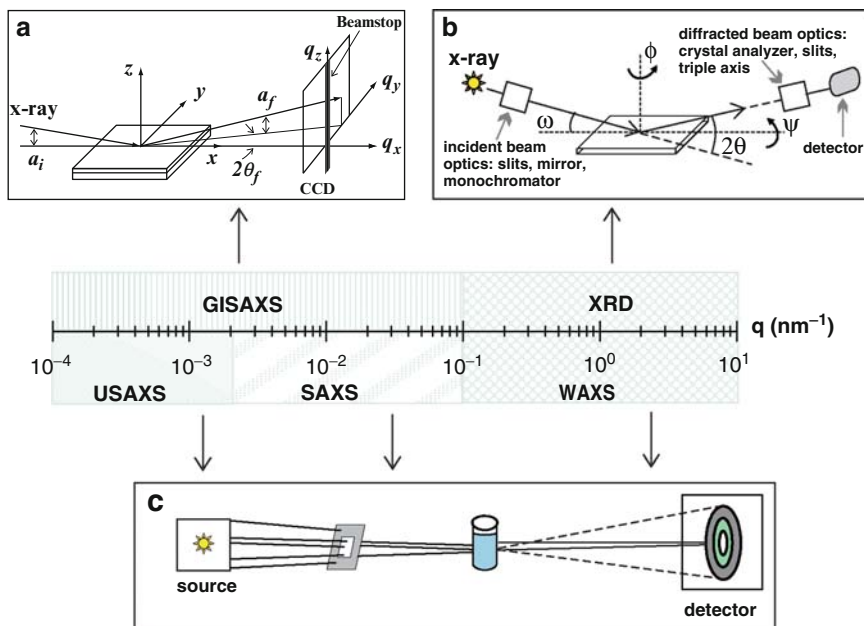


Fig. 5.1 Schematic view of the momentum range q where different scattering techniques apply. Fig. 5.1a has been reprinted in part with permission from [1]. Copyright © (2005) American Chemical Society

for samples with a defined surface such as films deposited on opaque substrates. On the other hand, WAXS is performed in transmission (Fig. 5.1c) and is suitable for solutions, powders in small quantities and polymers. In SAXS, the q -range extends from about 1 nm^{-1} down to 0.01 nm^{-1} or below, entering the ultra-small-angle scattering regime (USAXS).

The experimental setup is essentially the same for USAXS, SAXS and WAXS, as schematically represented in Fig. 5.1c. SAXS has gained popularity in the last years because it permits to access periodicities from 0.1 to 100 nm, typical of large atomic aggregates, such as nanostructures or molecules, and their combination in organic/inorganic nanocomposites. At these length scales, scattering of the X-ray radiation is due essentially to strong variations of the mean electronic density rather than the specific atomic configuration. GISAXS and X-ray reflectivity (XRR) are the two scattering techniques that investigate the electronic density in thin films. XRR probes variations of electronic density along the surface normal and allows the determination of thickness of thin films and multi-layers and interface roughness along such direction [1]. GISAXS is complementary to XRR because it involves off-specular measurements (Fig. 5.1a) that provides information about lateral correlations [2, 3], roughness of a surface [4, 5], size, shape and distribution of quantum dots distributed on a substrate [6, 7]. Nowadays, the use of GISAXS and other surface techniques is continuously increasing in the research field of nanocomposite materials. Thanks to the enormous advances in the synchrotron radiation sources and equipments, both traditional diffraction methods and scattering techniques have received a great development. The potentiality of the synchrotron radiation experiments is the in-situ sample preparation assisted by the most suitable scattering technique, with usually very versatile equipments (vacuum or controlled atmosphere and thermal heating or cooling).

Some generic concepts of X-ray scattering and their main usefulness regarding the structural study of nanocomposites will be given in the next section. The experimental results from different research groups will be presented in the two successive sections. The first one is about nanoparticle nanocomposites and the second one is about polymer-layered silicate nanocomposites. The same topics will be treated in Sect. 5.2 wherein the characterization by NMR will be discussed.

5.1.2 Generalities

X-ray diffraction (XRD) is probably the most popular X-ray scattering technique since it has been traditionally employed as a method to investigate the microscopic structure of crystalline solids, in the form of single crystals, powders, pellets or thin films. In this section, we will discuss a few elements of the X-ray scattering theory in order to understand the application of the several X-ray scattering techniques in the field of nanocomposites. For further readings on the theory of XRD, we recommend, among others, some good books [8–10].

In the general case of an imperfect crystal, the atoms are placed at arbitrary positions. If the crystal is irradiated by a monochromatic parallel X-ray beam, each atom behaves as a scattering centre by emitting a wave coherent with the incident radiation. The observed diffracted wave results from the interference of all the waves emitted by the single atoms. The amplitude of the diffracted wave in the reciprocal space is the superposition of all the waves scattered by an object constituted by N atoms

$$A(\mathbf{s}) = \sum_{n=1}^N f_n \exp(-2\pi i \mathbf{s} \cdot \mathbf{x}_n) = \int \rho(\mathbf{x}) \exp(-2\pi i \mathbf{s} \cdot \mathbf{x}), \quad (5.1)$$

where f_n is the atomic scattering factor, $\mathbf{s} = (\mathbf{k}_{\text{out}} - \mathbf{k}_{\text{in}})$ is the unitary scattering vector, λ is the X-ray beam wavelength and \mathbf{x}_n is the position of the atom in the real space. Since the atomic scattering factor f_n is related to the electronic density $\rho(\lambda)$, the right-hand side of the above definition expresses the scattered amplitude as the Fourier transform of the electronic density. What is really measured in a diffraction experiment is not the amplitude, since the phase in (5.1) is not a measurable quantity, but its square modulus, that is the diffracted intensity or scattering power

$$I_N(\mathbf{s}) = |A(\mathbf{s})|^2. \quad (5.2)$$

When a group of atoms is considered, it is useful to consider the interference function

$$\mathfrak{I}(\mathbf{s}) = \frac{I_N(\mathbf{s})}{NF^2}. \quad (5.3)$$

The value of \mathfrak{I} is determined by the interference between the scattered waves, being equal to unity if the scattering is incoherent.

Among hybrid nanocomposites, it is very likely that powder-like diffracting systems are encountered. A powder is composed of identical objects that are randomly oriented. In this case, the scattering power is given by the Debye formula:

$$I_N(\mathbf{S}) = \sum_{n=1}^N \sum_{n'=1}^N f_n f_{n'} \frac{\sin(2\pi \mathbf{s} \cdot \mathbf{x}_{nn'})}{2\pi \mathbf{s} \cdot \mathbf{x}_{nn'}}, \quad (5.4)$$

where I_N is the average observed intensity and $\mathbf{x}_{nn'} = \mathbf{x}_n - \mathbf{x}_{n'}$. The corresponding interference function assumes the following expression:

$$\mathfrak{I}(\mathbf{s}) = 1 + \frac{2}{N} \sum \frac{\sin(2\pi \mathbf{s} \cdot \mathbf{x}_{mm'})}{2\pi \mathbf{s} \cdot \mathbf{x}_{mm'}}. \quad (5.5)$$

The experimental diffraction pattern of a powder shows only a dependence on the interatomic distances $x_{mm'}$, but does not contain any information about the orientation.

When the diffraction is applied to crystals, a different formula of the scattering power is given, based on the concepts of crystal and reciprocal lattices. The scattering amplitude per unit cell is the Fourier transform of the electron density of the crystal $\rho_c(\mathbf{x})$ that can be expressed as the convolution of the Fourier transforms of the electron

density inside the unit cell $\rho(x)$, the crystal lattice function $z(x)$ and the form factor of the crystal $\sigma(x)$ according to the following expression:

$$\rho_c(\mathbf{x}) = \rho(\mathbf{x}) * [z(\mathbf{x})\sigma(\mathbf{x})].$$

Correspondingly, the scattering power per unit cell assumes the form:

$$I(s) = \frac{F_{hkl}}{VV_c} \sum_h \sum_k \sum_l \left| \Sigma(s - \mathbf{r}_{hkl}^*) \right|^2, \quad (5.6)$$

where V is the entire volume of the crystal, V_c is the volume of the unit cell, F_{hkl} is the structure factor of the crystal relative to the lattice plane identified by the Miller indices (hkl) . The plane (hkl) corresponds in the reciprocal lattice to a point in the position \mathbf{r}_{hkl}^* and the function Σ is the Fourier transform of the form factor. Σ has its maximum at the node of the reciprocal lattice $\mathbf{s} = \mathbf{r}_{hkl}^*$ and is different from zero except in a small region around such node.

Among the two formulations given by (5.4) and (5.6), the Debye formula is sometimes more convenient to use, for example, in the case of a crystal with a small number of atoms. On the other hand, (5.6) has the advantage to show the explicit dependence on the reciprocal lattice and its integral value is used to calculate observable quantities. The Bragg's law

$$\lambda = 2d \sin(\theta) \quad (5.7)$$

is easily derived from (5.6) considering that $I(s)$ differs significantly from zero only if the vector \mathbf{r}_{hkl}^* belongs to the reciprocal lattice, i.e., it lies on the surface of the Ewald sphere, centred at the tip of the incident wave vector \mathbf{k}_{in} and having modulus $|\mathbf{k}_{in}| = |\mathbf{k}_{out}| = |\mathbf{k}|$.

In order to estimate the grain size L of the powder grains, the Scherrer formula is very useful:

$$\Delta'(2\theta) = \frac{0.9\lambda}{L \cos(\theta_0)}. \quad (5.8)$$

In this expression, $\Delta'(2\theta)$ (expressed in rad) is the full width at half-maximum (FWHM) of the diffraction peak corresponding to the Bragg angle θ_0 while λ is the wavelength used in the experiment. The grain size calculated by using (5.8) is termed “apparent size” of the grain, while the “true” size is defined as the cube root of the crystalline volume. To be rigorous, rather than the FWHM one should know the integral width, defined as the total area under the diffraction maximum divided by the peak intensity, or the complete line profile and take into account other factors that might influence the peak broadening beyond the crystal size, such as the crystallite shape and size distribution, instrumental contribution or lattice defects [11]. To this purpose, very long and accurate measurements should be performed and the “true” Scherrer formula given by (5.8) without the factor 0.9 should be used [9, p 143]. However, the computation of the real crystal size in nanometric crystals by means of the Scherrer formula is not correct, as stated by several authors [12, 76], mostly when the nanocrystals contain less than a thousand

atoms. The correct approach would involve the calculation of the FWHM by means of theoretical approaches based on the Debye formula (4) [13] or line profile analysis [14–16].

While the theory for XRD and WAXS is essentially the same and the two techniques differ only for the measurement geometry (reflection and transmission, respectively) (Fig. 5.1), SAXS needs a separate treatment [17, 18] because the scattering region is located at small angles in the vicinity of the primary beam where it has different properties with respect to the high-angle region. The scattering features at these angles extend from tens to thousands of Angstroms and at these lengthscales the mean electronic density plays the major role in the scattering mechanism with respect to the detailed atomic structure. SAXS is applied to systems of identical particles to determine the nanoparticle size distributions [19] or the size and shape of colloidal core–shell nanoparticles [20]. It is also employed to study crystallization phenomena in polymers [21, 22] or the biomineralization of inorganic nanostructures in DNA templates [23]. The interpretation of SAXS data can be very difficult because the curves are often featureless and require a proper model to be correctly interpreted in conjunction with other techniques, such as microscopy. The scattering intensity in the vicinity of the reciprocal space origin $\mathbf{r}_{hkl}^* = 0$ can be written in terms of the mean electronic density of the crystal ρ and of the Fourier transform of the form factor Σ :

$$I(s) = \rho^2 |\Sigma(s)|^2. \quad (5.9)$$

This expression is obtained from (5.6) at $\mathbf{r}_{hkl}^* = 0$ and considering that $F/V_c = \rho$. Since the function $\Sigma(s)$ has its maximum at $s = 0$, at these conditions the scattering curve is characterised by a central peak that depends only on the external shape of the object. The central peak is not observed very often because very narrow and consequently is completely hidden by the direct beam. Since its angular width $\varepsilon \approx \lambda / d$, where d is of the order of the size of the object, the central peak is likely to be observed at dimensions below $0.1 \mu\text{m}$. For systems of identical particles that are randomly oriented and not interacting, the scattering intensities for each particle are simply summed (no interference). In that case, the function $\Sigma(s)$ can be easily calculated for a specific shape of the particles [8, Appendix A]. When $\Sigma(s)$ is inserted in (5.9) the scattering intensity will depend on the geometrical factors of the particles, for example, the radius in the case of a sphere. For powder-like systems, the experimental SAXS diffraction patterns are usually recorded on photographic plates and are characterised by a central spot (the direct beam shadowed by a beam stop) and a certain number of concentric rings of decreasing intensity. This two-dimensional pattern has to be integrated to get a one-dimensional curve of $I(s)$ as a function of s . For a system of spherical particles, the radius can be calculated by the conditions at which the intensity vanishes.

At very small angles ($s \sim 0$), the exponential approximation for $I(s)$ is considered:

$$I(s) = n^2 \exp\left(-\frac{4\pi^2 R^2 \varepsilon}{3\lambda^2}\right). \quad (5.10)$$

This is valid for particles of any shape and also when the particles are not identical. From the slope near the origin, it is possible to evaluate the gyration radius R . The limit of higher angles is called Porod region of the SAXS curve. In this region, $I(s)$ has the asymptotic form:

$$I(s) = \frac{(\rho - \rho_0)^2 S}{8\pi^3 s^4}, \quad (5.11)$$

where S is the total surface of the particles. This expression is valid for particles of any shape, randomly oriented and also for not homogenous and dense systems. The shape of the particles obtained from the $s \sim 0$ region can be used in this limit to get the surface-to-volume ratio of the scattering objects. Many other useful informations can be achieved by means of SAXS. For example, the area under the curve gives the so-called “invariant,” and any change in the invariant can be indicative of the crystallisation process of polymers.

When the particles are close to each other, the interference effects in the function $I(s)$ cannot be neglected, but if the particles are randomly distributed it is possible to give an analytic form to $I(s)$. For particles with spherical symmetry, the scattering intensity is the sum of a term due to the single-particle scattering plus an interference term. As the scattering vector s increases, the interference term first decreases and then has a hump that becomes a maximum at high concentrations. The value of s at the maximum gives a length d that is of the order of magnitude of the nearest particles distance. Such a maximum is often observed in semiconducting nanoparticles, as reported in the next section.

Other scattering techniques are available to study other properties of the materials. For example, GISAXS has been developed to measure thin films and surfaces and it is a combination of grazing-incidence diffraction (GID), which uses reflection geometry to obtain surface-sensitive X-ray scattering, and SAXS. Examples of GISAXS will be given in the Sect. 5.1.2. Beyond GISAXS, anomalous SAXS (ASAXS) uses the atomic scattering factor dependence on the energy of the incident X-ray beam to enhance the scattering signal in proximity of the X-ray absorption edges. This effect, termed “anomalous effect,” makes the technique very sensitive to the chemical composition of the samples and is very useful to reveal elements present in small percentages, such as metals contained in polymers, or to define the stoichiometry of binary alloys [77–79].

5.2 Nanoparticles Nanocomposites

XRD is widely applied to nanocomposites of semiconducting and magnetic nanocrystals embedded in a polymer matrix, or nanoparticles functionalised by different functional groups, such as thiols or silane groups for specific applications. In many cases, XRD serves to characterise the crystal structure of the nanoparticles, estimate their size and shape and individuate lattice defects. On the other hand,

SAXS is related to the spatial distribution of nanoparticles and at the same time is used to study the polymer-related properties.

Murray et al. [24] used XRD to investigate the structure of CdE (E = S, Se or Te) nanocrystals synthesised by the TOP/TOPO route. The nanocrystals prepared by such a technique have mainly a wurtzite structure and are nearly monodisperse, as shown by TEM, with a size tuneable between 1.2 and 11.5 nm. They show very regular redshift in the absorption and luminescence spectra with decreasing size. The effect of the finite size of the crystals and the contribution of defect broadening were included in the Debye formula (4) to fit the experimental XRD data. The best fit is obtained by assuming a wurtzite structure with stacking faults along the [002] direction, which is responsible for the broadening of the 102 and 103 reflections.

Many fundamental works towards the synthesis of CdS [25] and CdSe [26] nanocrystals and related core-shell structures [27] are from Weller's group. Both WAXS and SAXS are used to characterise the nanocrystals. A crystal structure change from the cubic to hexagonal phases is observed from smaller (~2 nm) to larger (~4 nm) nanocrystals. At small-angle regime, the presence of a sharp first-order peak and a weaker second-order peak are the signatures of ordered nanoparticles at short range, as expected from dense systems of identical particles (see the *Generalities* paragraph).

In core-shell nanostructures, as in the case of CdS/ZnS shells on colloidal CdSe nanorods [28], by combining TEM and XRD it was established that the shell grows epitaxially with the core. The core dimensions varied between 4.4 and 7.3 nm while the shell dimensions varied between 24.2 and 29.8 nm. The diffraction peaks shift towards higher angles with the shell thickness and confirm epitaxial growth except for the thickest shell.

The above cited works are a few examples to show how the size, shape and spatial distribution of nanoparticles can be characterized by XRD. When the nanoparticles are used to prepare nanocomposites with organic materials, such as polymers, the same methods can be applied. The main difficulties encountered in the dispersion of nanoparticles in polymers are phase separation and agglomeration. Reducing these effects is of utmost importance to enhance the efficiency of fullerene/polymer photovoltaic devices or to control the polymer viscosity by nanoparticles addition. In-situ growth of the nanoparticles inside a polymer matrix is an alternative way to control their dispersion.

A route for a new kind of hybrid nanocomposites is offered by employing dendrimers that can be used as template to form metallic [29] or metal sulphide nanoparticles [30] within the polymer matrices. SAXS, SANS and TEM provide in these cases full characterization of the system.

5.2.1 Case of CdS Nanoparticles Grown in a Polymer Matrix by Thermolysis

An example of in-situ preparation of nanoparticles/polymer nanocomposites is given by CdS nanoparticles grown within amorphous transparent polymer matrices

such as polystyrene (PS) [31–33] or topas (TP) [34, 35]. The nanocomposites were prepared by a thermolysis process that consists of thermally induced decomposition of a suitable precursor molecule and successive formation of a given micro- or nanocrystals. In particular, we used this method to prepare CdS nanoparticles in amorphous polymer matrices by first dispersing a Cd thiolate precursor $\text{Cd}(\text{SR})_2$ ($\text{R} = \text{C}_n\text{H}_{2n+1}$) in the polymer solution. Successively, a precursor/polymeric foil of about 2-mm thick was obtained by drop-casting the solution and the solvent was allowed to evaporate during 1 or 2 days. If heated at temperatures above the precursor decomposition temperature, CdS nanoparticles become embedded in the polymer matrix. For these nanocomposites, ex situ WAXS and SAXS, together with NMR spectroscopy (see Sect. 5.2) allowed a careful study of the synthesis parameters (annealing conditions and role of the polymer).

WAXS and SAXS analyses were performed on samples previously annealed at different temperatures [34]. The distance between the sample and the detector position can be varied in such a way that the momentum transfer q covers both the SAXS ($0.05\text{--}10\text{ nm}^{-1}$) and the WAXS ($10\text{--}40\text{ nm}^{-1}$) regions.

The SAXS/WAXS experiments were very useful in clarifying the role of the matrix, as can be seen from Fig. 5.2. In this figure curves (a) and (b) refer to polystyrene (PS) at room temperature and after annealing at 250°C , respectively, while the curve (c) refers to CdS/PS obtained upon annealing at 237°C . The WAXS curves relative to the pure polymer are the same before and after the thermal treatment. Moreover, in the WAXS curve of the precursor/polymer foil (c) we distinguish the polymer

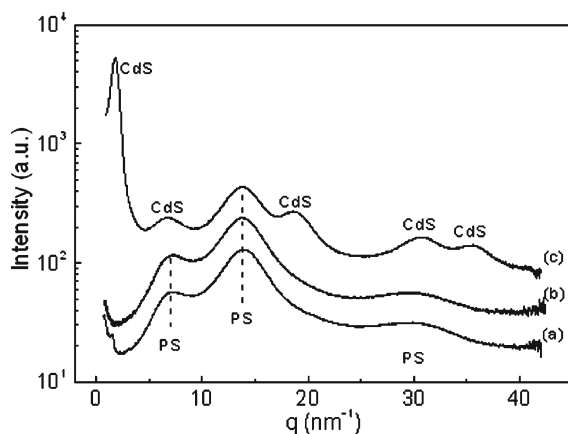


Fig. 5.2 WAXS curves relative to nanocomposites of CdS nanoparticles embedded in a polystyrene (PS) matrix obtained by thermolysis of a cadmium-(bis)thiolate precursor with 12 carbon atoms (C12) dispersed in a PS foil: (a) PS only, before annealing; (b) PS only, after annealing at 250°C ; (c) C12/PS after annealing at 237°C . The annealing allows the formation of CdS nanoparticles, confirmed by the Bragg peaks indicated in (c) while the PS signal remains the same as was before the annealing

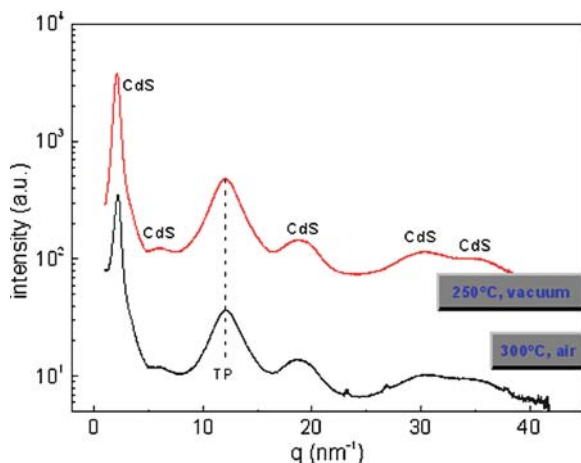


Fig. 5.3 WAXS curves relative to C12/TP (where TP is an acronym for topas, a cyclic olephin copolymer) after annealing at 250°C in vacuum and at 300°C in air. The two processes produce nanoparticles of the same size and spatial distribution, since the scattering spectra are the same in both cases

peaks equal to those observed in (a) and (b), and additional peaks from the crystalline CdS nanoparticles. Considering these results, one can conclude that the polymer has the function of template where the precursor transformation occurs.

The small size of the nanoparticles broadens the peaks making it difficult to distinguish, at least without a proper simulation, between the cubic and the hexagonal phases, because the peaks of the two phases are often overlapped. The nanoparticles size, evaluated by the Scherrer formula applied to the cubic (220)/hexagonal (110) peak, is about 1.5 nm. At small values of the q - vector, a strong peak, similar to that observed by Murray et al. [24–27], centred at $q = 1.8 \text{ nm}^{-1}$ corresponds to an average distance of 3.5 nm, showing that the nanoparticles produced at this annealing temperature are well separated. By means of WAXS and NMR (see Sect. 5.2) it was shown that it is preferable to perform the annealing process under vacuum instead of air, where unwanted polymer reactions can take place. The same WAXS spectrum is obtained by annealing two identical precursor/polymer samples, one in vacuum and the other one in air (Fig. 5.3) at different temperatures. In fact, in vacuum the annealing temperature needed to obtain 1-nm CdS nanoparticles in topas (TP) is 250°C, instead of 300°C in air. The matrix can be chosen among amorphous polymers, such as PS and TP, that are suitable for optical applications because of their high transparency. From the structural point of view, TP offers the advantage that the amorphous peak is not too much overlapped with the first Bragg reflection from CdS.

The kinetics of the reaction from the precursor to the nanoparticles was followed by in-situ synchrotron XRD experiments, in order to understand the underlying growth process [35]. The size and crystal structure of the so-prepared nanoparticles

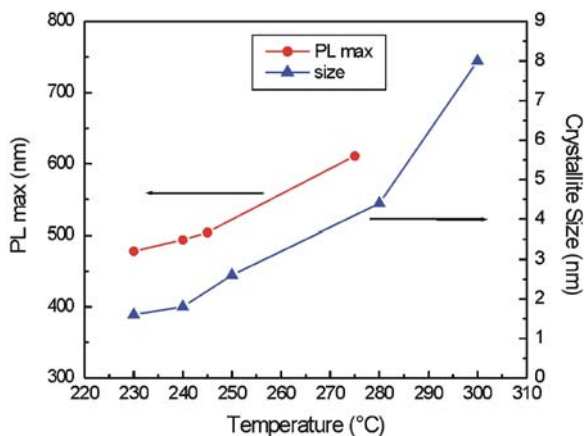


Fig. 5.4 PL maximum and crystal size of the CdS nanoparticles in CdS/PS nanocomposites obtained by thermolysis, as a function of the annealing temperature. Reprinted with permission from [35]. Copyright © (2006) American Chemical Society

were found to depend mainly on the annealing temperature. Annealing temperatures between 230 and 300°C under vacuum produce nanoparticles with a size of 1 and 8 nm (Fig. 5.4). In this figure, the temperature dependence of nanoparticle size and of the photoluminescence peak position (PL) are reported on the right and left axis, respectively. In particular, the size has been evaluated from simulation of the in situ synchrotron XRD data as described below. The temperature dependence of several precursors $\text{Cd}(\text{SR})_2$, $\text{R} = \text{C}_n\text{H}_{2n+1}$ ($n = 3, 5, 12, 18$) dispersed in TP matrix was followed by in situ synchrotron XRD measurements. The experiments were performed at the beamline W1.1 of Hasylab (DESY) by using an incident beam energy of 10.5 KeV ($\lambda = 1.18 \text{ \AA}$). A piece of precursor/polymer foil was mounted on a Cu holder heated by resistors, and measured in reflection by detector 2θ -scans at fixed incident angle of 2° under vacuum. The data were acquired in temperature steps of 10°C from room temperature to 300°C. The results are reported in Fig. 5.5 for the precursor with $n = 12$ carbon atoms in the thiol chain, named C12 and the corresponding polymer composite, named C12/TP.

In the temperature range 100–200°C (Fig. 5.5a), we observe the precursor transformation, while the nanoparticle growth happens in the high-temperature range 200–300°C as shown in (Fig. 5.5b, c) for the small and large q - values. The diffraction curve at 100°C is characterised by regularly separated peaks SL1–SL5 that arise from the lamellae structure of the C12 precursor (Fig. 5.5a). The peak separation corresponds to a periodicity of the lamellae along the aliphatic chain of 35 Å. The SL peak intensity decreases with the temperature until the peaks completely disappear at 160°C. Meantime, new peaks P1–P4 arise from metastable phases from the decomposition process. The peak P1 is present between 100 and

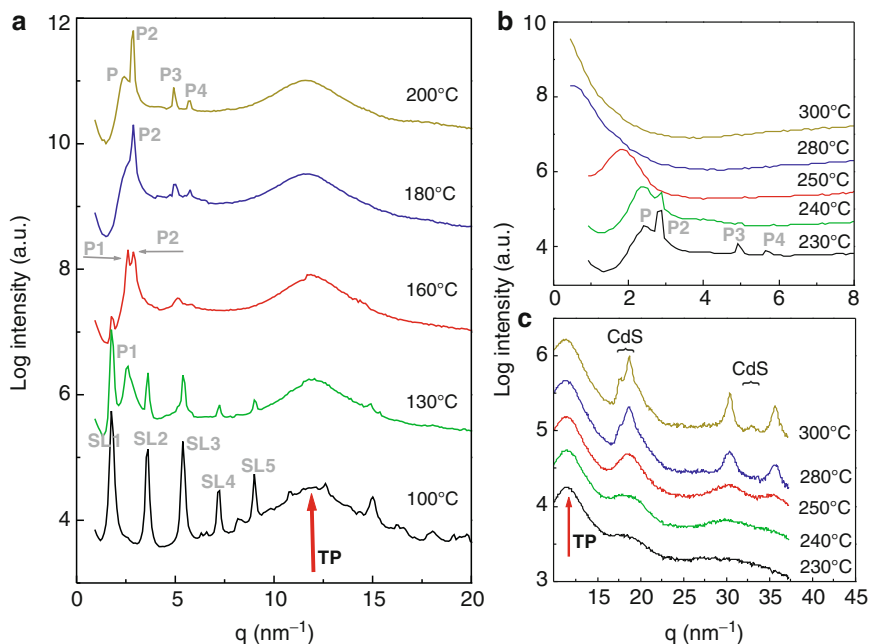


Fig. 5.5 Synchrotron X-ray diffraction curves of C12/TP as a function of annealing temperature. (a) $T = (100\text{--}200)^\circ\text{C}$. The C12 precursor peaks are indicated by SLi. The peaks P_i ($i = 1, 4$) are transitory peaks induced by the thermolysis of the C12. P is related to the mean distance among the growing CdS nanoparticles, TP is the topas peak. (b) $T = (230\text{--}300)^\circ\text{C}$, $q = (1\text{--}8\text{ nm}^{-1})$ and (c) $T = (230\text{--}300)^\circ\text{C}$, $q = (10\text{--}40)\text{ nm}^{-1}$. The q -range is plotted in two parts, the high q regime, where the crystalline reflections from CdS are measured, and the small q regime, where the decomposition of the precursor is followed. Reprinted with permission from [35]. Copyright © (2006) American Chemical Society

160°C, while the other three peaks appear at 180°C and disappear at 240°C, where the precursor decomposition is complete. The peaks P2, P3 and P4 are compatible with the structure factors of the 11, 02 and 22 reflections of a hexagonal lattice with centred rectangular unit cell of lattice parameters $a = 4.45\text{ nm}$ and $b = 2.55\text{ nm}$. Such a structure is a possible configuration of the S and Cd atoms because of the flexibility or partial decomposition of the long alkyl chains in the lamellae precursor. In Fig. 5.5a, we observe that the peak P is present from 200°C and shifts to smaller values of the scattering vector q as the temperature is increased (Fig. 5.5b). This peak in the diffraction curve is the equivalent of the SAXS first-order reflection, indicative of a mean distance among the nanoparticles which in this specific case is temperature-dependent. A weak and broad signal from the CdS Bragg reflection, located in the region $q = 15\text{--}40\text{ nm}^{-1}$, appears at 230°C (Fig. 5.5c) but becomes very well defined at higher annealing temperatures. Two are the main effects of the temperature on the nanoparticle structure: (1) the reduction of the peak broadening, sign of larger crystals and (2) a structural evolution, from mostly zinc-blende below 250°C to the presence of all the peaks of the wurtzite phase at 300°C. The diffraction

curves were simulated by using a diffraction peak intensity profile from spherical crystallites of the zinc-blende (zb) or wurtzite (w) phase, according to Ida et al. [36]:

$$I^{zb,w}(\mathbf{q}) = \sum_{hkl} m_{hkl} L_{hkl} |F_{hkl}^{zb,w}|^2 \frac{\pi D^4}{2s(\mathbf{q})^2} \left[1 - \frac{2}{s(\mathbf{q})} \sin(s(\mathbf{q})) + \left[\frac{2}{s(\mathbf{q})} \sin\left(\frac{s(\mathbf{q})}{2}\right) \right]^2 \right] \quad (5.12)$$

with

$$s(\mathbf{q}) = 2\pi\mathbf{q}D,$$

where \mathbf{q} is the usual scattering vector, D is the diameter of the nanoparticle, L_{hkl} is the Lorentz polarization factor and m_{hkl} and F_{hkl} are the multiplicity and structure factor of the hkl reflection, respectively. The calculated curves that better approximate the experimental data show that a mixture of both zb and w phases is present. With the hypothesis that each phase contributes to the total scattered intensity by 50%, we obtained a good fit of the experimental curves.

We report the results relative to the samples annealed at 240 and 300 °C (Fig.5.6) where the nanoparticle diameter D is evaluated as 1.8 and 8 nm, respectively. This study,

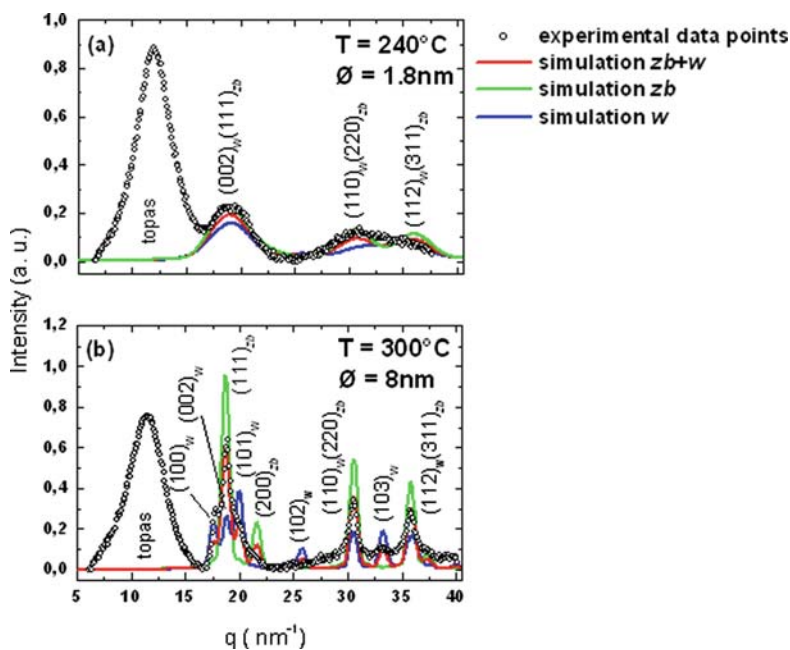


Fig. 5.6 Theoretical simulations of the in situ synchrotron XRD data of C12/TP at annealing temperatures $T = 240$ °C (a) and 300 °C (b), by considering spherical CdS nanoparticles with zincblende (zb) and wurtzite (w) phases of diameter $\varnothing = 1.8$ nm (a) and 8.0 nm (b). In both (a) and (b): (i) the dots represent the experimental data points, the green curve is the calculated for nanoparticles with zb phase, the blue curve for nanoparticles with w phase, the red curve is obtained by considering 50% zb and 50% w mixed phase; (ii) the peaks are labelled by the relative Miller indexes of the zb and w phases. Reprinted with permission from [35]. Copyright © (2006) American Chemical Society

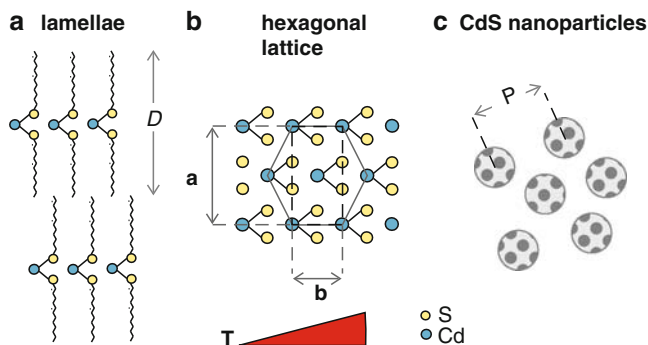


Fig. 5.7 Schematic view of the chemical transformation of the thiolate precursors and the nucleation and growth of the CdS nanoparticles from the precursor thermolysis: (a) lamellae structure of the precursor from room temperature up to 100°C; (b) hexagonal structure due to the flexibility of the alkyl chains in the temperature range between 160 and 240 °C; (c) final state (above 240 °C) consisting of CdS nanoparticles only. The organic component has completely decomposed. The crystalline structure of the nanoparticles has been simplified in the sketch. Reprinted with permission from [35]. Copyright © (2006) American Chemical Society

together with supporting analyses from TEM, PL and Gas chromatography/Mass spectrometry, allowed to draw a possible mechanism for the CdS nanoparticle formation from the thermolysis of the long-chain thiol precursors (Fig. 5.7): below 100 °C, the precursor has a lamellae structure (a) that changes to an hexagonal lattice formed by the sulphur atoms (b) because of the flexibility of the organic chains induced by the increased temperature (160–240 °C). Above 240 °C, (c) the precursor molecules are completely decomposed and the CdS nanoparticles are grown dispersed in the polymer matrix.

5.3 Polymer-Layered Silicate Nanocomposites

Polymer-layered silicate nanocomposites represent a large group of nanocomposites materials that has developed in the last 15 year. Publications in this field started appearing in around year 1995, increased up to 50 in 2000 and was about 200 in 2005. The reason is that the combination of a few percents of inorganic-layered silicates (or clays) with polymers can produce a final composite with improved physical and mechanical properties and with final economical advantages. The nanocomposites are obtained when the sheets of the clay unit cells are more or less intercalated in the polymers. In the case of no intercalation, the clay and the polymer are phase-separated and no composite is obtained. At an intermediate level of the polymer intercalation, the clay sheets distance is increased compared to the original distance without the polymer (intercalated nanocomposites). In the opposite limit, the clay sheets are pushed so far away that a complete exfoliation occurs (exfoliated nanocomposites). The exfoliation is usually favoured when the clay is organically

modified by the addition of quaternary ammonium surfactants that improve the interactions between the polymer and the clay. A complete review that covers both the preparation and processing methods is given by Sinha Ray and Okamoto [37] and the references therein. Other reviews are important as well [38–40]. The review by Ray and Okamoto contains a detailed bibliography on most of the polymers used, from vinyl polymers to polyolefins and condensation step polymers, poly(N-vinylcarbazole) and polyaniline. The most used layered silicates are Montmorillonite [$M_x(Al_{4-x}Mg_x)Si_8O_{20}(OH)_4$], Hectorite [$M_x(Mg_{6-x}Li_x)Si_8O_{20}(OH)_4$], Saponite [$M_xMg_6(Si_{8-x}Al_x)O_{20}(OH)_4$]. Traditional X-ray diffraction experiments in reflection are widely employed in the field of polymer-layered silicate nanocomposites to reveal the degree of exfoliation of the clay material by the polymer intercalation. This preliminary information helps to optimise the processing conditions. As the length scale of the clay sheet distance is above 1 nm, the interesting part of the diffraction pattern is located below 10° (with Cu radiation). The position, intensity and width of the diffraction peaks in this range are used to distinguish among immiscible, intercalated or exfoliated silicate composites.

In some cases, transmission measurements (WAXS and SAXS) are preferred when a low amount of material is available. SAXS allows to obtain important information about the organization and correlation of the nanostructures [41, 42]. Some examples will be given below. Microstructural properties such as the mutual orientation of the clay sheets with respect to the polymer matrix can be derived by means of SAXS.

Varlot et al. reported on the preferential orientation of the montmorillonite sheets and polyamide crystalline lamellae [43]. The nanocomposites were prepared by extrusion-injection of two kinds of montmorillonite, a slightly swollen and a highly swollen montmorillonite, after modification with quaternary ammonium ions. They performed conventional XRD at different depths in the samples by abrading the surface. At the surface level, they found three peaks, the first one at the diffraction angle 2.3° and the other two at higher angles, interpreted as higher order peaks. The presence of these reflections proves that the intercalated structure is formed only when the highly swollen montmorillonite is used (Fig. 5.8). In this graph, the curve PA1 refers to the polymer only. The three reflections become much weaker when the inner part of the sample is measured. Very interesting are the results of the SAXS experiments on the PA2 sample, oriented in four possible directions with respect to the incident beam (Fig. 5.9). The highest intensity of the low-angle peak is observed in case 1, when the beam is aligned along the injection direction and a good signal is also recorded in orientation 2. This result is interpreted as a preferential orientation of most of the sheets parallel to the largest area of the sample. In the case of slightly swollen montmorillonite/polyamide, the absence of diffraction peak is typical of a completely exfoliated structure (Fig. 5.8). Nevertheless, from a change in the curvature at low q , a characteristic length of 35 nm is interpreted as the distance among the sheets homogeneously dispersed in the polyamide.

A reference paper on diffraction studies of polymer-layered silicate nanocomposites has been published by Vaia and Liu [44]. The interpretation of the diffraction data are often compromised by several factors, such as layer disorder, silicate volume fraction below 10% and experimental conditions. They calculate the ideal scattering pattern for

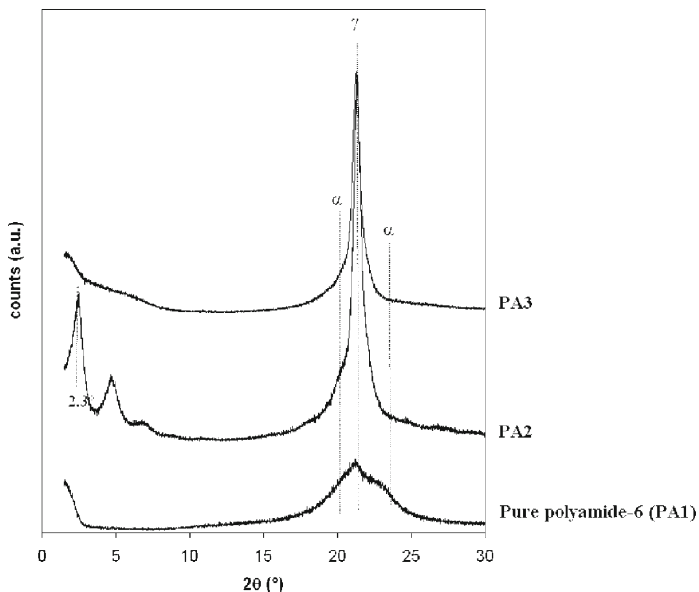


Fig. 5.8 XRD spectra of polyamide crystalline lamellae reinforced by montmorillonite (MMT) sheets, as measured at the level of the surface of two samples (PA2 and PA3) extruded by using highly and slightly swollen MMT, respectively, and compared with pure polyamide (PA1). Montmorillonite is completely exfoliated in the sample PA3, while it is intercalated in the sample PA2. The α - and γ -phases of polyamide are indicated by dotted lines. Reprinted with permission of John Wiley & Sons, Inc. from [43]; Copyright © (2001) John Wiley & Sons, Inc.

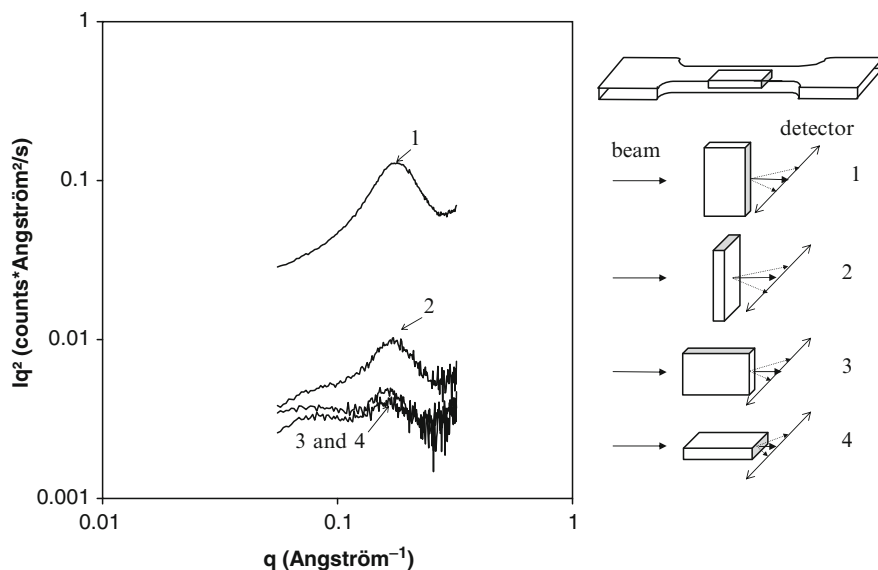


Fig. 5.9 SAXS experiment results on the sample PA2 of Fig. 5.8, performed at different sample orientation with respect to the incident X-ray beam as indicated by the scheme at the right. The intensity of the correlation peak shows that MMT is preferentially oriented in the injection direction. Reprinted with permission of John Wiley & Sons, Inc. from [43]; Copyright © (2001) John Wiley & Sons, Inc.

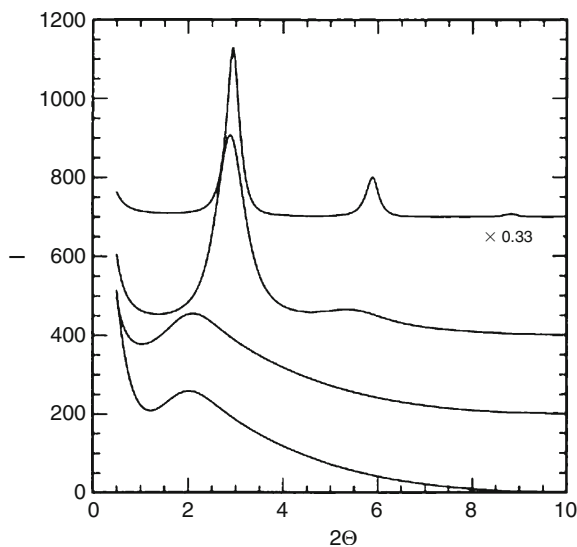


Fig. 5.10 Calculated diffraction profiles for MMT layers with distance among the sheet $D = 3.0$ nm, and random crystalline distribution. From top to bottom, the mean number of layers in a crystallite $\langle N \rangle$ is 5, 5, 5 and 2, while the mean strain indicative of disorder, α , has the values 0.0, 0.5, 1.5 and 1.5 nm, correspondingly. The top curve has been multiplied by a factor 0.33. Reprinted with permission of John Wiley & Sons, Inc. from [44]; Copyright © (2002) John Wiley & Sons, Inc.

the nanocomposites given by the product of the structure factor of a single, independent, randomly oriented clay layer, by the interference function of the stacks of layers in the clay, and by the Lorentz polarization factor. The interference function contains information about the stack size, size polydispersity and structural disorder.

The results of the calculations by Vaia and Liu indicate that a nanocomposite without disorder in the stacking layer structure should have a spectrum characterized by three peaks, the (001) peak and the second and third order peaks, of decreasing intensity and similar breadth (Fig. 5.10). The higher order peaks are usually broadened by internal disorder. From the calculations, the internal disorder causes also a shift of the (001) peak and a general decrease of the intensity, that reduces the features observed in the diffraction curves as seen from Fig. 5.10. Therefore, the shift of the (001) peak, commonly assumed to indicate the distance variation among the silicate layers, might be influenced by other factors, such as disorder, sample alignment and choice of the source slit. For this reason, the XRD technique has to be supported by other techniques, such as microscopy, to provide a complete characterization of the morphology and structure of the layered silicate nanocomposites. A generalization of this work was extended from XRD to SAXS analyses of organically modified montmorillonite suspension [45].

Other works have focused on the crystallization properties of the polymer [22]. In this case, scattering experiments in real time need to be performed during the crystallization process. Nair and Ramesh reported a study on the crystallization of

nanocomposites of nylon-6 with montmorillonite. Nylon-6 is polymorphic and can crystallize in two phases, α and γ . In particular, the γ -phase is less readily obtained than the α -phase but when nylon-6 is combined with clay materials the γ -phase is easily formed. In situ variable temperature WAXS experiments allowed to observe the intercalation from the clay point of view, and to follow the whole crystallisation process of the polymer, the evolution of the two phases and the appearance of a metastable phase. The metastable phase is present between 150 and 210°C, which is the crystallization temperature of the γ -phase. Such features are completely reversible with the temperature. The extent of crystallization into the γ -phase has been observed to depend on the clay content, while, on the other hand, the gallery height of the clay decreases when the temperature is reduced because of the crystallization of nylon-6. This result shows that a mutual influence between the clay and polymer contributes for determining their structural properties.

In situ WAXS is used also to study the mechanical properties of polymer–clay nanocomposites under deformation. For example, Wang et al. studied two nanocomposites, one constituted of polyethylene grafted with maleic anhydride (PEMA) and montmorillonite 20A (PE/20A), and the other made of PEMA and SiO₂ nanoparticles [46]. In general, the nanocomposites employing MMT 20A have a better dispersion in the PEMA than those with the SiO₂ nanoparticles, as observed in the TEM images (Fig. 5.11), and have a better interfacial adhesion upon deformation. The WAXS experiments, performed while cold-drawing is applied to the samples, show a martensitic transformation of the polyethylene. Such transformation consists of a structural phase transition from orthorhombic to monoclinic structure, as can be seen from Fig. 5.12. Here, at low strain the (110) and (200) of the orthorhombic phase are visible, while at higher strain the (001) of the monoclinic phase appears. Close to the beam stop, in the low-angle region, an anisotropic signal suggests a certain orientation of the clays during the cold-drawing reported also by other authors [47].

Porous silicate-based nanocomposites can find application as low dielectric constant films. To this end, nano-porous organosilicate thin films were prepared by Lee et al. by mixing a poly(ϵ -caprolactone) (PCL4) precursor and poly(methylsilsesquioxane) (PMSSQ). PCL4 is a porogen, while the PMSSQ is the organosilicate polymer matrix [1]. Thin films of about 100 nm thickness were obtained by spin-coating the solutions at different precursor/polymer wt % concentrations. GISAXS measurements were conducted by means of synchrotron radiation to characterize the pores and understand their formation. A scheme of the GISAXS experimental setup used by Lee et al. is reported in Fig. 5.13. The incoming X-ray beam is sent at an incident angle α_i on the film surface under total reflection conditions, i.e., α_i below the critical angle of the film. The scattered beam exits at an angle α_f with respect to the film surface and at a diffraction angle $2\theta_f$ with respect to the incidence plane. The scattered radiation is collected by a 2D CCD detector. The GISAXS theory is based on the evaluation of the differential cross-section

$$I_{\text{GISAXS}} = \frac{d\sigma}{d\Omega} = \mathbf{r}^2 \left\{ \Psi(\mathbf{r}) \Psi^*(\mathbf{r}) \right\}, \quad (5.13)$$

Fig. 5.11 TEM images of nanocomposites containing polyethylene grafted with maleic anhydride and MMT 20A (PEMA/20A), and PEMA and SiO₂ nanoparticles (PEMA/SiO₂). Reprinted with permission from [46]. Copyright © (2002) American Chemical Society

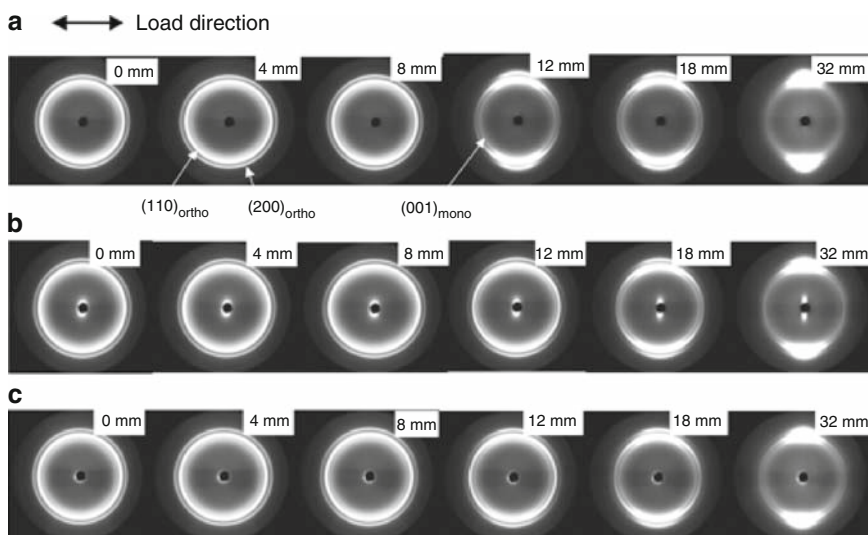
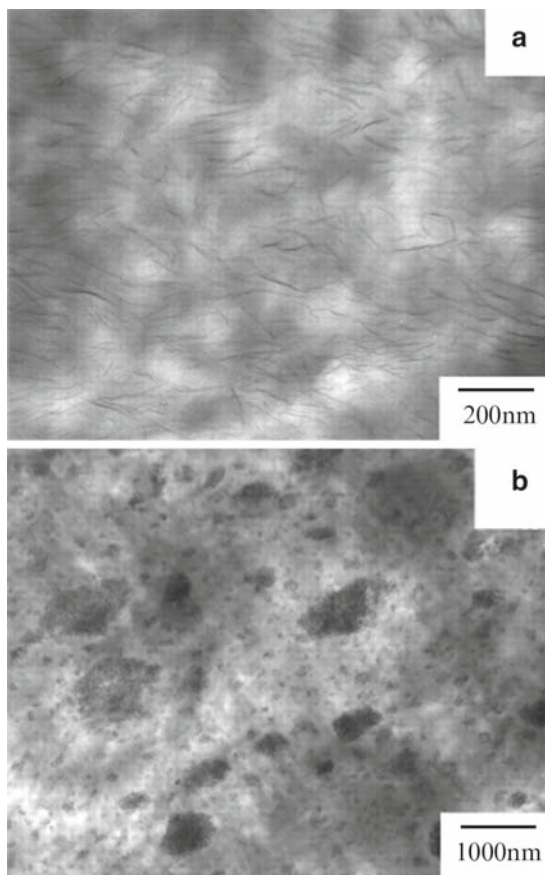


Fig. 5.12 In situ WAXS patterns measured during the tensile deformation: (a) PEMA, (b) PEMA/20A, (c) PEMA/SiO₂. Reprinted with permission from [46]. Copyright © (2002) American Chemical Society

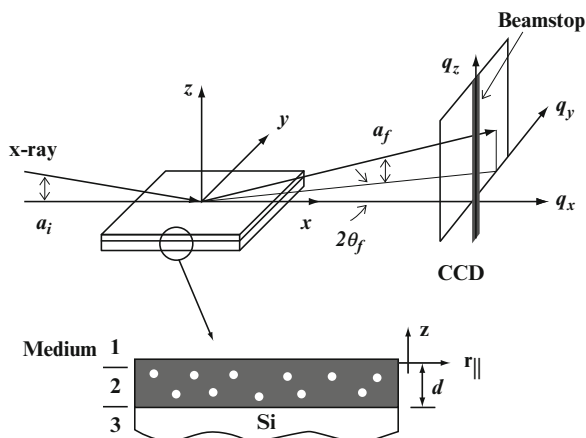


Fig. 5.13 Geometry of grazing-incidence small-angle scattering (GISAXS) and schematic diagram of the sample measured, a nanoporous film deposited on silicon substrate: medium 1, vacuum; medium 2, film of thickness d ; medium 3, silicon substrate. Reprinted with permission from [1]. Copyright © (2005) American Chemical Society

where $\psi(\mathbf{r})$ is the solution of the Schrödinger equation with a scattering potential V given, in the specific case, by a potential of a thin film without the pores plus a potential that takes into account the presence of the pores. The potential due to the pores, or other structures such as quantum dots, metallic islands or roughness that are responsible for the diffuse scattering are treated as a perturbation to the unperturbed systems described by the Parratt formalism commonly used in X-ray reflectivity. The perturbation is treated by the distorted-wave Born approximation (DWBA) since the interface roughness is small with respect to the film thickness and can thus be neglected. More details on the theory can be found in the paper by Lee [1], in the SAXS theory references [18, 48] and in the paper by Lazzari [49], and references therein. The PLC4/PMSSQ films were measured both by static and in situ GISAXS. In the latter case, the data were recorded during the thermal treatment from room temperature to 400°C and during the cooling; the duration of each scan was between 1 and 2 min. The data analysis, based on distorted-wave Born approximation (DWBA), allowed the calculation of pore size and size distribution, gyration radius, porosity, electron density and miscibility of the two components. On the basis of the GISAXS results and TGA measurements, a picture of the formation mechanism of the pores was drawn. The PMSSQ precursor undergoes a thermal curing that causes phase separation and porogen aggregates at temperatures below 200°C. At 293°C, the porogen aggregates are completely degraded leaving their imprint in the matrix as pores. The pore parameters (size density, etc.) depend on the porogen wt%.

5.4 Solid-State NMR Methods

5.4.1 Introduction

From the previous section, we have seen that the preparation of homogeneous organic–inorganic hybrid nanocomposites with specific enhanced properties requires a high control of both the synthesis process and material structure. Furthermore, the structure of a hybrid composite is the result of a complex cooperation between the organic and inorganic species. In order to elucidate the successive steps of the nanocomposites preparation, it is necessary to apply a combination of advanced characterization techniques. Solid-state nuclear magnetic resonance (SSNMR) spectroscopy is a powerful tool capable of providing information both about the structure of materials and the dynamics of processes occurring within those materials.

In particular, SSNMR has been widely used for polymer characterization over a wide range of length scales. The focus of many studies is a molecular-level understanding of polymers in their functional state.

In the following section, some generalities on NMR in the solid state and its use for the structural study of nanocomposites will be given. Examples of organic–inorganic hybrid nanocomposites, as characterized by different NMR techniques in the solid state, will be presented in the two successive sections: semiconductor nanoparticle and polymer-layered silicate nanocomposites.

5.4.2 Generalities

In this section, a few aspects of the NMR theory will be pointed out aiming to give the reader some fundamentals to understand the discussed applications in the field of nanocomposites. Nevertheless, the interested reader is encouraged to consult some of the existing excellent books dealing with different aspects of NMR spectroscopy and solid-state NMR with a different emphasis and perspective. Among these, let us mention the book by Abragam [50–52] for the background to the physics of NMR. Ernst et al. [53] have discussed in detail the physical basis of multi-dimensional NMR techniques. Ample literature is devoted to ^{13}C NMR of organic materials including the book of Stejskal and Memory [54]. Schmidt-Rohr and Spiess [55] have presented a comprehensive background to modern NMR techniques for characterizing solid polymeric materials. A recent book on solid-state NMR of inorganic materials is by MacKenzie and Smith [56].

In liquid samples, the molecules typically move rapidly and randomly in such a way that the time-averaged dipole–dipole interactions among nuclei do not affect the NMR spectrum; whereas in solid samples, the motion of atoms and molecules is restricted and therefore the effect of their interactions does not average to zero. The resonance frequency of a particular nucleus depends on the magnetic field at

its site. Since the local field due to neighbour nuclei varies from place to place through out the sample, in solid samples a significant spread in the resonance frequencies occurs. This effect produces a broadening of the lines in the NMR spectrum of solid samples, for mononuclear dipolar coupling, by several order of magnitude with respect to the lines obtained from liquid samples.

Another source of line broadening in solid samples is the chemical shift anisotropy (CSA). The chemical shift depends on the orientation of the molecules with respect to the external field. In a powdered sample, the small crystals exhibit a range of orientations with respect to the applied static field and one observes a dispersion of peak positions because of CSA. The magnitude of CSA depends upon the nucleus and its chemical environment.

Finally, spectra of quadrupolar nuclei (nuclei with spin $> 1/2$) are also enlarged by the presence of quadrupolar interactions between the nuclear quadrupole moment and the electric-field gradient at the site of the nucleus. As a consequence, the direct application of solution-state NMR techniques to solid samples would give very broad and featureless spectra. However, the nature of the different sources of line broadening in solids is well known and it is possible to tailor experiments in which different techniques are applied at the same time to obtain well-resolved spectra. These experiments include the rotation of the sample at the magic angle (MAS), the dipolar decoupling (DD) for removing interactions between abundant nuclei (protons) and rare nuclei (carbon, silicon, etc.), and the cross-polarization (CP) for enhancing the signal/noise ratio of rare nuclei. Moreover, very recently developed 2D experiments known as multiple-quantum magic-angle spinning (MQ-MAS) allow to obtain well-resolved 2D map of quadrupolar nuclei, such as ^{27}Al , ^{23}Na , ^{87}Rb and ^{11}B .

We will briefly describe some types of SSNMR experiments which can be used for studying hybrid nanocomposites.

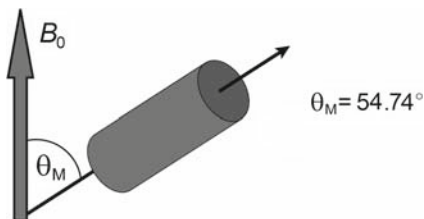
The Hamiltonians, which take into account the dipolar interactions, for the chemical shift anisotropy and, only partially, for the quadrupolar interaction contain a term $(3 \cos^2 \theta - 1)$. In solution, rapid isotropic tumbling averages this spatial component to zero.

Magic-angle spinning introduces artificial motion by rotating the axis of the sample at the magic angle with respect to the static magnetic field B_0 [54, 57].

The average of the term $(3 \cos^2 \theta - 1)$ is equal to zero when $\theta = 54.74^\circ$ (Fig. 5.14). In order to fully average the interactions to zero, the spin rate must be greater than or equal to the magnitude of the interactions (this however does not hold for quadrupolar interaction because the second-order quadrupolar interaction is not averaged at MAS). Otherwise, residual interactions, even if at a minor extent, will anyway affect the spectrum. With the CP-MAS technique, the polarization from abundant spins such as ^1H or ^{19}F is transferred to dilute spins, such as ^{13}C , ^{29}Si , and ^{15}N . Two types of advantages are thus obtained:

1. Cross-polarization enhances signals of dilute spins potentially by a factor of γ_I / γ_S , where γ_I is the magnetogyric ratio of the abundant spin I and γ_S is referred to the dilute spin S .

Fig. 5.14 Schematic draw of magic-angle spinning rotor where the sample is inserted



2. The CP experiment is repeatable on a timescale determined by the ^1H spin–lattice relaxation times which are usually much shorter than those of ^{13}C .

In other words, the recycle delay between successive scans is much shorter than the recycle delay to be used when performing the experiment without cross-polarization [54, 57].

The commonly used sequence scheme is reported in Fig. 5.15 for a sample containing carbon and proton atoms.

During the CP experiment, a 90° pulse on the ^1H channel creates a magnetization along the y axis and during the spin-lock pulse, the simultaneous double-frequency irradiation of the ^1H and ^{13}C spins matches the Hartmann–Hahn condition: $\gamma_C B_C = \gamma_H B_H$; under this condition the two species of spin exchange energy via the dipolar interaction [54, 57].

The key for obtaining an efficient cross polarization is to set the Hartmann–Hahn match properly (see Fig. 5.15). In this case, the precession frequency of the dilute spin (e.g., ω_C) is made equal to that of the abundant spin (e.g., ω_H) by adjusting the radio frequency field on both channels. Under these conditions, proton and carbon magnetizations precess in the rotating frame at the same frequency, i.e. $\omega_H = \omega_C$ (valid for static conditions), allowing the magnetization to be transferred from the abundant to the dilute spins (Fig. 5.16).

5.5 Semiconductor Nanoparticles in Polymeric Matrices

Semiconductor nanoparticles have been widely investigated because of their enhanced optical, luminescent and electrical properties resulting from the quantum size effect and from their increased surface/volume ratio [24]. In particular, we focused our NMR studies on a cadmium sulphide-polystyrene nanocomposite obtained as described by [32] using a thermolytic synthesis method [31]. The same compounds were studied by X-ray scattering: results and more details on their preparation can be found in the Sect. 5.1.1.

In this case, the SSNMR contributed especially to optimize the synthesis conditions. The work started with the characterization of a CdS/polystyrene composite prepared by annealing in air at 300°C a polystyrene film containing a certain amount of cadmium-(bis)thiolate as precursor. Direct evidence of the CdS formation

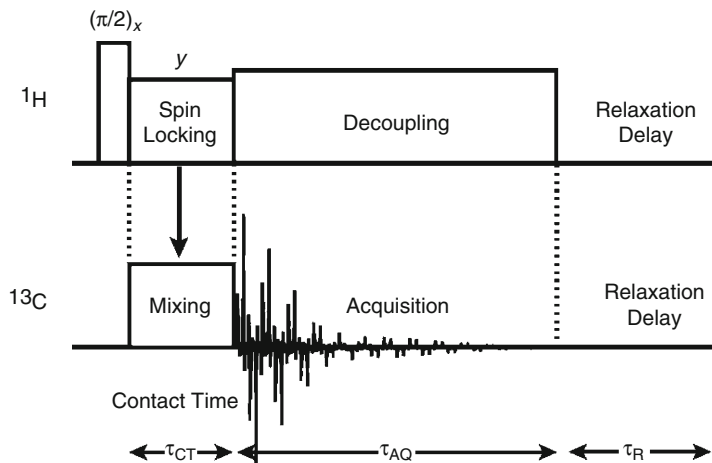


Fig. 5.15 Scheme of the sequence commonly used in a cross-polarization experiment

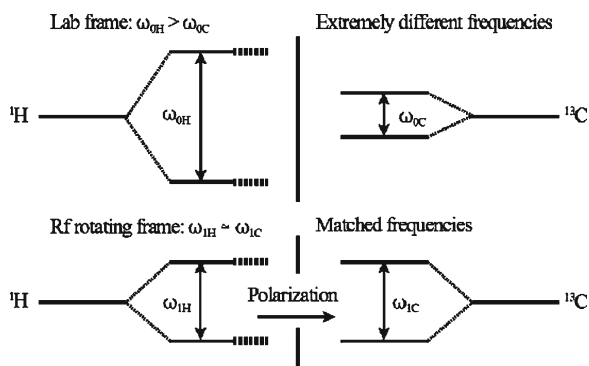


Fig. 5.16 Scheme of Hartmann-Hahn match for the system ^1H - ^{13}C

was obtained by performing solid-state ^{113}Cd NMR measurements of the samples before and after the annealing. In Fig. 5.17, we report the ^{113}Cd CP MAS spectra of the precursor/polystyrene films before (a) and after (b) the annealing. In the spectrum (b) the signal at 715 ppm arises from the CdS nanoparticles formed after 10 min of annealing. These measurements directly probed the presence of CdS and some unreacted precursor, and other reaction products (signal at 648 ppm) as well. Generally, depending on the type of nanoparticles, by appropriate choice of the observable NMR nucleus one can follow the formation reactions of the nanoparticles as well.

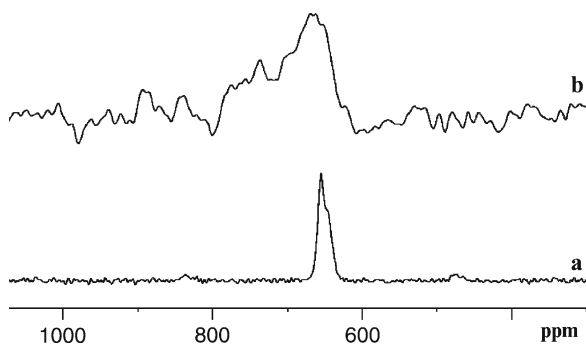


Fig. 5.17 ^{113}Cd CP MAS spectra of cadmium-(bis)thiolate/polystyrene films before (a) and after (b) annealing in air at $T = 300\text{ }^\circ\text{C}$. Spectra are carried out at 44.366 MHz on a Bruker ASX-200 spectrometer. Spin rate 8 kHz; $\pi/2$ pulse width 4 μs ; recycle delay 3 s; contact time 15 ms; number of scans 32,000. Chemical shifts are reported with respect to $\text{Cd}(\text{ClO}_4)_2 \cdot 6\text{H}_2\text{O}$. Reprinted from [32], supporting information, copyright (2005), with permission from Elsevier

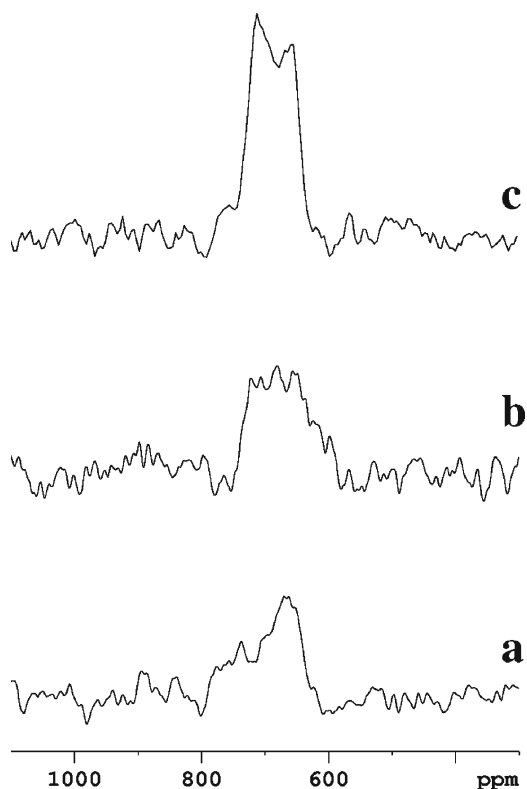
The second important point concerns the purity of the obtained nanocomposite samples. The presence of undesired species in the final sample prompted us to optimize the thermolytic process for obtaining enhanced quality CdS/PS nanocomposites. Thus, we performed ^{113}Cd CP MAS spectra of samples annealed in different atmospheres (see Fig. 5.18). Depending on the annealing conditions, the intensity of the CdS peak at 715 ppm increases from air to nitrogen, reaching the maximum value in the vacuum-annealed sample (Fig. 5.18c). These data qualitatively identify annealing under vacuum as the treatment that produces the best quality sample.

The great chemical shift dispersion of ^{113}Cd (800 ppm) with respect to the other spin ($-1/2$) nuclei, such as ^1H (12 ppm), ^{29}Si (200 ppm) and ^{13}C (300 ppm), indicates that the shielding of the ^{113}Cd nuclei may possibly be most sensitive to the local environment [58]. However, ^{113}Cd solid-state NMR spectra need both long signal averaging and the use of cross-polarization (CP) [59, 60] and magic angle spinning (MAS) techniques to overcome problems such as low natural abundance, low gyromagnetic ratio and large spin–lattice relaxation times of these nuclei. Thus, when applied in studying the in situ synthesis of organic–inorganic nanocomposites, solid-state cadmium NMR spectroscopy is a valid tool for a qualitative assessment of the principal features of the material (formation of nanoparticles and purity of the composite). Its only limit is the concentration of the inorganic part which should be at least 10% wt/wt.

5.5.1 ^{13}C on polymer

The organic counterpart of hybrid nanocomposites often plays a role of matrix serving as dispersion media for nanoparticles precursors (in situ synthesis) or as a physical

Fig. 5.18 ^{113}Cd CP MAS spectra of cadmium-(bis)thiolate/polystyrene films annealed in (a) air; (b) nitrogen; (c) vacuum. Reprinted from [33], copyright (2006) with permission from Elsevier

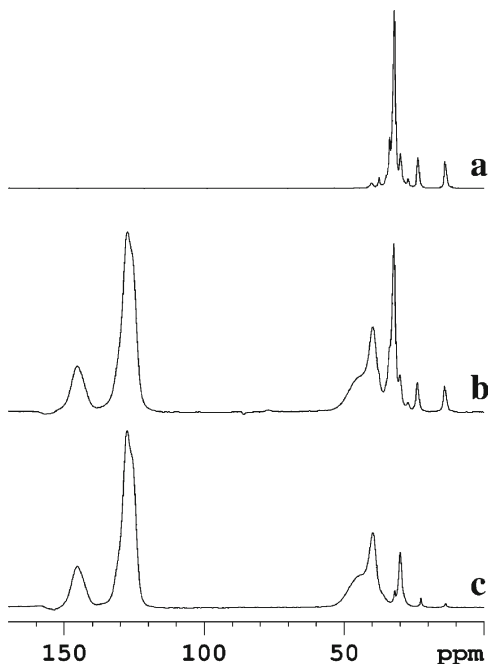


obstacle to particles agglomeration. However, in some cases the polymeric component interacts with the inorganic counterpart through molecular mechanisms.

It is well established that solid-state ^{13}C NMR spectroscopy is a powerful method to characterize completely polymers and probe the nature of the molecular interactions between the organic and inorganic phases of polymer-based nanocomposites.

In our work, CdS/polystyrene nanocomposites were studied by ^{13}C NMR in the solid state. The first step was the assignment of polystyrene and of the precursor cadmium-(bis)thiolate resonances. In Fig. 5.19a, we reported the ^{13}C CP MAS NMR spectrum of $\text{Cd}(\text{SR})_2$ as synthesized, and compared the spectra of $\text{Cd}(\text{SR})_2/\text{PS}$ samples before (b) and after (c) the annealing in air. In the spectrum of Fig. 5.19b, the resonance at 127.7 ppm is due to the protonated aromatic carbons $\text{C}_2\text{--C}_6$ of polystyrene, while the signal at 146 ppm is from the non-protonated carbon C_1 . C_α and the C_β carbons of polystyrene resonate at 39.8 and 45 ppm, respectively. The resonances of cadmium thiolate are found in the 12–40 ppm region: the terminal methyl C_{12} at 13.6 ppm and the methylene C_{11} bound to C_{12} at 22.6. The comparison of the spectra in Fig. 5.19b, c evidences that all the resonances of the polystyrene matrix are not affected by the thermal treatment, while weak signals due to reaction by-products are observed in the 12–30 ppm region. Since ^{13}C CP MAS experiments

Fig. 5.19 ^{13}C CP MAS spectra of (a) cadmium-(bis)thiolate as synthesized and cadmium-(bis)thiolate/polystyrene film before (b) and after (c) the annealing in air. Reprinted from [33], copyright (2006), with permission from Elsevier



are not quantitative, evaluating the amount of the unwanted substances cannot be performed by simply integrating the 12–30 ppm resonances. Therefore, according to the procedure reported in the following paragraph, the cross-polarization dynamic process was investigated for all the samples. As an example, we report the correlation between the intensity of the carbon resonances C_1 and $C\alpha$ of polystyrene, and C_{11} of thiolate, and the contact time τ for a CdS/PS sample annealed in air (see Fig. 5.20). It is worth to note that the $T_{1\rho}(^1H)$ value (120 ms) of the resonance C_{11} is definitely much longer than the corresponding ones (9, 10 ms) obtained for the resonances C_1 and $C\beta$ of polystyrene. Therefore, in order to obtain a semi-quantitative analysis, SPE spectra were carried out. It is well known that the simplest experiment for obtaining quantitative measurements in solid-state high-resolution NMR is the Single-Pulse excitation (SPE) experiment. A single $\pi/2$ pulse is applied to excite the carbon signal that is recorded in the presence of MAS and dipolar decoupling (DD). The recycle delay RD between successive scans must be chosen to ensure that the longitudinal nuclear magnetization has recovered to equilibrium following the preceding pulse.

The ^{13}C SPE NMR spectra of the CdS/PS sample obtained by annealing in different conditions are shown in Fig. 5.21: (a) air, (b) nitrogen and (c) vacuum; only the 0–60 ppm region is shown. We compared the integral of some signals of polystyrene resonating in the 36–60 ppm range (region A) with the ones resonating in the 12–30 ppm range (region B). In all the spectra, the integral of region A was

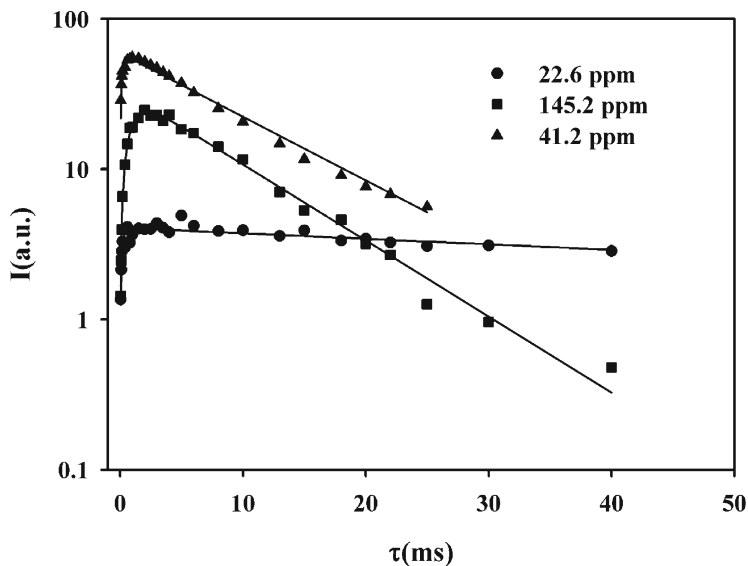


Fig. 5.20 Correlation between the area of the carbon resonances C_1 , C_{α} and C_{11} and the contact time τ . Lines through experimental points have been obtained by fitting the experimental data to (5.14). Reprinted from [33], copyright (2006), with permission from Elsevier

normalized to 1. In this way, it was possible to quantitatively evaluate the amount of the impurities in all the samples. In the case of annealing in air, the integral of region B is found to be 0.8. When the annealing is conducted in vacuum, the integral decreases down to 0.4, whereas an intermediate value of 0.6 is found in the sample annealed in nitrogen. To summarize, the ^{13}C NMR semi-quantitative analysis confirmed the ^{113}Cd NMR qualitative results, and established that the best CdS/PS nanocomposites, with a low amount of impurities, are obtained when annealing the samples in vacuum.

5.5.2 ^{13}C CP MAS Cross-Polarization Dynamic

Because ^{13}C intensities depend on the cross-polarization rates which may be different for different carbon atoms [57, 61], CP MAS spectra are not quantitative. The rate of the process strongly depends on the number of the abundant spin I near the dilute spin S and on their distance from S. The question arises when we wish to obtain a quantitative analysis of the intensity of resonances due to carbon nuclei of different types.

In simple cases, the problem can be solved by investigating the cross-polarization dynamic [54].

The kinetic of the cross-polarization dynamic is described by the equation [61]:

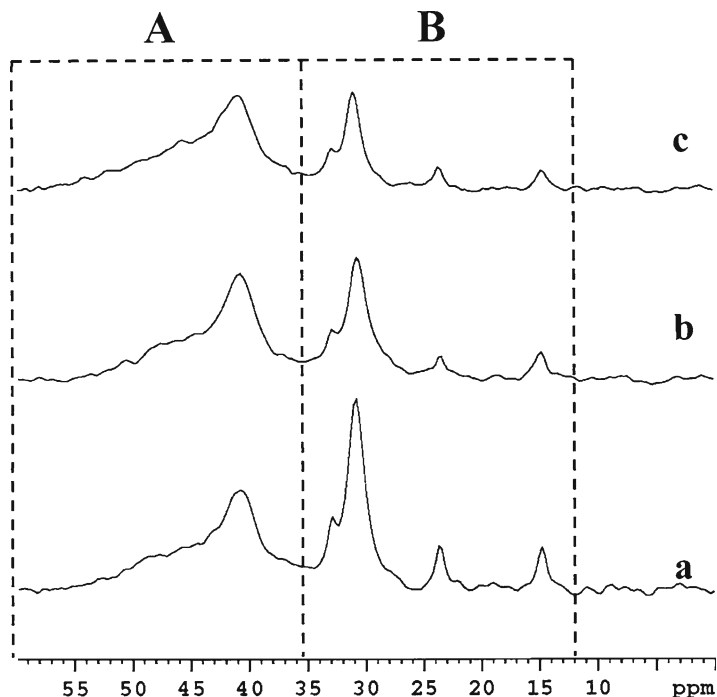


Fig. 5.21 ^{13}C SPE spectra of the CdS/PS samples obtained by annealing in different atmospheres; (a) air, (b) nitrogen and (c) vacuum. Integrals were calculated in the region A, 36–60 ppm and in the region B, 12–30 ppm. Reprinted from [33], copyright (2006), with permission from Elsevier

$$\frac{S(\tau)}{S_0} = \frac{1}{\lambda} \left[1 - \exp\left(-\frac{\lambda\tau}{T_{IS}}\right) \right] \exp\left(-\frac{\tau}{T_{1\rho}({}^1\text{H})}\right) \quad (5.14)$$

$$\lambda = 1 + \frac{T_{IS}}{T_{1\rho}({}^{13}\text{C})} - \frac{T_{IS}}{T_{1\rho}({}^1\text{H})},$$

where S_0 is the area of the resonance at time $\tau=0$, $T_{1\rho}({}^1\text{H})$ and $T_{1\rho}({}^{13}\text{C})$ are the proton and the carbon spin–lattice relaxation times in the rotating frame, T_{IS} is the cross-relaxation time between protons and carbons. In homogeneous systems, the spin-diffusion process averages the $T_{1\rho}({}^1\text{H})$ values of all carbon resonances; in this case the S_0 values obtained fitting the data to the equation are the “true” areas of the resonances. Whereas, in inhomogeneous systems the $T_{1\rho}({}^1\text{H})$ values are different from each other as the spin-diffusion process is ineffective; in this case the S_0 values cannot be used for a quantitative analysis. Under these circumstances, the only possibility for obtaining a semi-quantitative analysis lies in performing SPE spectra with a proper recycle delay. ^{13}C CP-MAS spectra were carried out with the contact time τ ranging from 0.05 to 40 ms. The area of three selected resonances was

reported as a function of the contact time. By fitting the experimental data to (5.14), $T_{1\rho}$ (1H) and S_0 were evaluated.

5.6 Polymer-Layered Silicates

Polymer-layered silicate (PLS) nanocomposites are hybrid organic(polymers)–inorganic(silicates) nanocomposites. The inorganic counterpart belongs to the family of layered silicates, the phyllosilicates, such as talc, montmorillonite, mica, hectorite, saponite, etc [62, 63]. They have a two-dimensional layer crystalline structure and each layer is separated from its neighbours by a van der Waals gap. When the polymer chains are intercalated between the silicate layers, the distance between them is of a few nanometers. In other cases, the silicate can be totally delaminated and dispersed in the polymer matrix and the distance between the layers is of the order of the polymer gyration radius.

The good potential of SSNMR in the study of both polymers [57] and clays [64] gave an impulse in experimenting the NMR characterization for the determination of the structure of clay/methyl methacrylate copolymer nanocomposites [65]. They prepared interlayer complexes of several MMA/2-(*N*-methyl-*N,N*-diethylammonium iodide) ethyl acrylate (MDEA) copolymers with two different clays, bentonite and hectorite, using two different preparations. These complexes were studied by means of solid-state ^{13}C NMR. Given the relatively high content of paramagnetic centres in bentonite, which is ~50 times more paramagnetic than hectorite, the SPE/MAS and CP/MAS spectra of the different nanocomposites with bentonite show differences according to the proximity of the different copolymer moieties to the clay surface. The dynamics of the organic molecules in the organic interlayers were investigated by NMR relaxation time measurements. The paramagnetism of the clay, when relevant, strongly influences the relaxation times whereas in the other cases the different relaxation times allow one to discern differences in the structural organization and mobility of the organic molecules depending on the preparation method. Finally, the structure of the nanocomposite was determined by combining both the NMR and WAXD results. Some authors [66, 67] also used FTIR spectroscopy to understand the structure of the nanocomposites. Recently, do Nascimento et al. [68] presented for the first time the resonance Raman characterization of a polymer/clay nanocomposite formed by aniline polymerization in the presence of MMT.

VanderHart et al. [69] first used 1H and ^{13}C NMR as a tool for gaining greater insight about the surface chemistry, morphology and dynamics of exfoliated polymer clay nanocomposites. In particular, they were interested in developing NMR methods to quantify the level of clay exfoliation which is a very important aspect in the nanocomposite characterization. The extent and the homogeneity of the dispersion of the silicate layers within the polymer matrix are very important for determining physical properties. The main objective in solid-state NMR measurements is the correlation between the measured longitudinal relaxation times T_1^H of proton (and ^{13}C nuclei) with the quality of clay dispersion.

The surfaces of naturally occurring layered silicates, such as montmorillonite, are mainly made of silica tetrahedra while the central plane of layers contains octahedrally coordinated Al^{3+} with frequent non-stoichiometric substitutions, where Al^{3+} is replaced by Mg^{2+} and, although less frequently, by Fe^{3+} . The concentration of the latter ion is very important because Fe^{3+} is strongly paramagnetic. Typical concentration of Fe^{3+} in naturally occurring clays leads to nearest-neighbour Fe–Fe distances of about 1.0–1.4 nm [70], and at such distances, the spin-exchange interaction between the unpaired electrons of different Fe atoms is expected to produce magnetic fluctuations in the vicinity of the Larmor frequencies for protons or ^{13}C nuclei [70]. The spectral density of these fluctuations is important because the T_1^{H} of proton (and ^{13}C nuclei) within about 1 nm of the clay surface can be directly shortened. If that mechanism is sufficiently efficient [71], the proton relaxation time will also propagate into the bulk of the polymer by spin diffusion (Abragam 1961). Thus, this paramagnetically induced relaxation will influence the overall measured T_1^{H} to an extent that will depend on both Fe concentration in the clay layer and on the average distances between clay layers. The latter dependence suggests a potential relationship between measured T_1^{H} values and the quality of the clay dispersion. When the clay particles are stacked and poorly dispersed in the polymer matrix, the average distances between polymer/clay interfaces are larger, and the average paramagnetic contribution to T_1^{H} is weaker. The same authors employed this method to understand the stability of a particular organically modified layered silicate under different processing conditions [72, 73].

Yang and Zax [70] also used NMR to determine the relative mobility of bulk and interphase polymers in intercalated polyethylene oxide nanocomposites, while Mathias et al. [74] used NMR to determine the phase structure of polyamide-6/clay nanocomposites.

In a more recent paper, the structure and dynamics of the polymer chains inserted between the montmorillonite lamellae were studied by NMR [75]. Solid-state NMR and X-ray diffraction measurements demonstrated a spontaneous polymerization of 2-ethanypyridine within the galleries of montmorillonite.

5.7 Conclusion

Nanoscience and nanotechnology represent a challenge for the research of new hybrid organic–inorganic materials with specific tuneable properties and at the same time have stimulated the development of more and more sophisticated experimental techniques for characterizing and testing their functionalities. Among the numerous characterization techniques of hybrid organic–inorganic nanocomposites, two of them have been presented herein: X-ray scattering and NMR in the solid state. These two techniques are both non-destructive tools to investigate the structural aspects at the nanoscale, from crystalline and morphological properties to chemical surroundings and molecular reconstruction. Particular emphasis was given to two classes of nanocomposites: nanoparticles-polymer nanocomposites and polymer-layered silicate

nanocomposites. Advanced characterization setups, such as in situ synchrotron radiation experiments and CP-MAS NMR experiments have been applied to understand the structure of the materials, in an effort to improve the synthesis conditions and the final properties of the nanocomposites.

Acknowledgements The authors' experiments were partially supported by (a) the European Community – Research and Infrastructure Action under the FP6 program Structuring the European Research Area through the Integrated Infrastructure Initiative Integrating Activity on Synchrotron and Free Electron Laser Science; (b) Consiglio Nazionale delle Ricerche (CNR) and Deutsche Forschungsgemeinschaft (DFG).

References

1. Lee B, Yoon J, Oh W, Hwang Y, Heo K, Jin KS, Kim J, Kim K-W, Ree M (2005) In-situ grazing incidence small-angle X-ray scattering studies on nanopore evolution in low-k organosilicate dielectric thin films. *Macromolecules* 38:3395–3405
2. Dailliant J, Gibaud A (1999) X-ray and Neutron Reflectivity: Principles and Applications. Springer, Berlin/Heidelberg
3. Metzger TH, Kegel I, Paniago R, Lorke A, Peisl J, Schulze J, Eisele I, Schittenhelm P, Abstreiter G (1998) Shape, size, strain and correlations in quantum dots systems studied by grazing incidence X-ray scattering methods. *Thin Solid Films* 336(8):1–8
4. Metzger TH, Kegel I, Paniago R, Lorke A, Peisl J (1999) Grazing incidence X-ray scattering: an ideal tool to study the structure of quantum dots. *J. Phys. D Appl. Phys.* 32:A202–A207
5. Boer DKG (1994) Influence of the roughness profile on the specular reflectivity of X-rays and neutrons. *Phys. Rev. B* 49(9):5817–5820
6. Sinha SK, Sirota EB, Garoff S, and Stanley HB (1988) X-ray and neutron scattering from rough surfaces. *Phys. Rev. B* 38(4):2297–2311
7. Stangl J, Holý V, Mikulík P, Bauer G, Kegel I, Metzger TH, Schmidt OG, Lange C, Eberl K (1999) Self-assembled carbon-induced germanium quantum dots studied by grazing-incidence small-angle scattering. *Appl. Phys. Lett.* 74(25):3785–3787
8. Zhang K, Heyn Ch, Hansen W, Schmidt Th, and Falta J (2001) Grazing incidence structural characterization of InAs quantum dots on GaAs(001). *Appl. Surf. Sci.* 175–176:606–612
9. Guinier A (1994) X-ray Diffraction in Crystals, Imperfect Crystals, and Amorphous Bodies. Dover, New York
10. Warren BE (1969) X-ray Diffraction. Addison-Wesley, Reading
11. Klug HP (1954) X-ray Diffraction. Wiley, New York
12. Langford JJ, Wilson JC (1978) Scherrer after sixty years: a survey and some new results in the determination of crystallite size. *J. Appl. Cryst.* 11:102–113
13. Hall BD, Zanchet D, Ugarte D (2000) Estimating nanoparticle size from diffraction measurements. *J. Appl. Cryst.* 33:1335–1341
14. Pinna N (2005) X-ray diffraction from nanocrystals. *Progress in Colloid and polymer Science* 130:29–32
15. Langford JJ, Louër D and Scardi P (2000) Effect of a crystallite size distribution on x-ray diffraction line profiles and whole-powder-pattern fitting. *J. Appl. Cryst.* 33:964–974
16. Ungár T, Gubicza J, Ribárik G, Borbély A (2001) Crystallite size distribution and dislocation structure determined by diffraction profile analysis: principles and practical application to cubic and hexagonal crystals. *J. Appl. Cryst.* 34:298–310
17. Ida T, Toraya H (2002) Deconvolution of the instrumental functions in powder x-ray diffractometry. *J. Appl. Cryst.* 35:58–68

18. Glatter O, Kratky O (1982) *Small Angle X-ray Scattering*. Academic Press, New York
19. Beaucage G, Kammler HK, Pratsinis SE (2004) Particle size distributions from small angle scattering using global scattering functions. *J. Appl. Cryst.* 37:523–535
20. Lu S-Y, Wu M-L, Chen H-L (2003) Polymer nanocomposites containing CdS-ZnS core-shell particles: optical properties and morphology. *J. Appl. Phys.* 93(9):5789–5793
21. Panine P, Urban V, Boesecke P, Narayanan T (2003) Combined small- and wide-angle X-ray scattering study of early stage of polymer crystallization. *J. Appl. Cryst.* 36:991–994
22. Nair S and Ramesh C (2005) Studies on the crystallization behaviour of nylon-6 in the presence of layered silicates using variable temperature WAXS and FTIR. *Macromolecules* 38:454–462
23. Liang H, Angelini TE, Ho J, Braun PV, and Wong GCL (2003) Molecular imprinting of biomineralized CdS nanostructures: crystallographic control using self-assembled DNA-membrane templates. *J. Am. Chem. Soc.* 125:11786–11787
24. Murray CB, Norris DJ, Bawendi MG (1993) Synthesis and characterization of nearly monodisperse CdE (E = S, Se, Te) semiconductor nanocrystallites. *J. Am. Chem. Soc.* 115:8706–8715
25. Vossmeier T, Katsikas L, Giersig M, Popovic IG, Diesner K, Chemseddine A, Eychmüller A, Weller H (1994) CdS nanoclusters: synthesis, characterizations, size dependent oscillator strength, temperature shift of the excitonic transition energy, and reversible absorbance shift. *J. Phys. Chem.* 98:7665–7673
26. Rogach AL, Kornowski A, Gao Minguyan, Eychmüller A, Weller H (1999) Synthesis and characterization of a size series of extremely small thiol-stabilized CdSe nanocrystals. *J. Phys. Chem. B* 103:3065–3069
27. Talapin DV, Rogach AL, Kornowski A, Haase M, Weller H (2001) Highly luminescent monodisperse CdSe and CdSe/ZnS nanocrystals synthesized in a hexadecylamine-trioctylphosphine oxide-trioctylphosphine mixture. *Nano Lett.* 1:207–211
28. Manna L, Scher EC, Li LS, Alivisatos AP (2002) Epitaxial growth and photochemical annealing of graded CdS/ZnS shells on colloidal CdSe nanorods. *J. Am. Chem. Soc.* 124:7136–7145
29. Gröhn F, Kim G, Bauer BJ, Amis EJ (2001) Nanoparticle formation within dendrimers-containing polymer networks: route to new organic-inorganic hybrid materials. *Macromolecules* 34:2179–2185
30. Beck Tan NC, Balogh L, Trevino SF, Tomalia DA, Lin JS (1999) A small angle scattering study of dendrimers-copper sulphide nanocomposites. *Polymer* 40:2537–2545
31. Carotenuto G, Martorana B, Perlo P, Nicolais L (2003) A universal method for the synthesis of metal and metal sulfide clusters embedded in polymer matrices. *J. Mater. Chem.* 13:2927–2930
32. Antolini F, Pentimalli M, Di Luccio T, Schioppa M, Re M, Mirengi L, Tapfer L (2005) Structural characterization of CdS nanoparticles grown in polystyrene matrix by thermolytic synthesis. *Mater. Lett.* 59:3181–3187
33. Pentimalli M, Antolini F, Bauer EM, Capitani D, Di Luccio T, Viel S (2006) A solid state nuclear magnetic study on the thermolytic synthesis of CdS nanoparticles in a polystyrene matrix. *Mater. Lett.* 60:2657–2661
34. Di Luccio T, Nickel B, Antolini F, Pentimalli M, Tapfer L (2005) Structure of nanocomposites films of CdS nanoparticles in a polymer matrix. *Mater. Res. Soc. Symp. Proc.* 847:EE13.22.1
35. Di Luccio T, Laera AM, Tapfer L, Kempter S, Kraus R, Nickel B (2006) Controlled nucleation and growth of CdS nanoparticles in a polymer matrix. *J. Phys. Chem. B* 110:12603–12609
36. Ida T, Shimazaki S, Hibino H, and Toraya H (2003) Diffraction peak profiles from spherical crystallites with lognormal size distribution. *J. Appl. Cryst.* 36:1107–1115
37. Sinha Ray S, Okamoto M (2003) Polymer/layered silicate nanocomposites: a review from preparation to processing. *Progr. Polym. Sci.* 28:1539–1641
38. Alexandre M, Dubois P (2000) Polymer-layered silicate nanocomposites: preparation, properties and uses of a new class of materials. *Mat. Sci. Eng.* 28:1–63

39. Zanetti M, Lomakin S, Camino G (2000) Polymer layered silicate nanocomposites. *Macromol. Mater. Eng.* 279:1–9
40. LeBaron PC, Wang Z, Pinnavaia TJ (1999) Polymer-layered silicate nanocomposites: an overview. *Appl. Clay Sci.* 15:11–29
41. Nam PH, Maiti P, Okamoto M, Kotaka T, Hasegawa N, Usuki A (2001) A hierarchical structure and properties of intercalated polypropylene/clay nanocomposites. *Polymer* 42:9633–9640
42. Chin IJ, Thurn-Albrecht T, Kim HC, Russel TP, Wang J (2001) On exfoliation of montmorillonite in epoxy. *Polymer* 42:5947–5952
43. Varlot K, Reynaud E, Kloppfer MH, Vigier G, Varlet J (2001) Clay-reinforced polyamide: preferential orientation of the montmorillonite sheets and the polyamide crystalline lamellae. *J. Polym. Sci. B* 39:1360–1370
44. Vaia RA, Liu W (2002) X-ray powder diffraction of polymer/layered silicate nanocomposites: model and practice. *J. Polym. Sci. Part B* 39:1360–1370
45. Vaia RA, Liu W, Koerner H (2003) Analysis of small angle scattering of suspensions of organically modified montmorillonite: implications to phase behavior of polymer nanocomposites. *J. Polym. Sci. Part B* 41:3214–3236
46. Wang KH, Chung IJ, Jang MC, Keum JK, Song HH (2002) Deformation behaviour of polyethylene/silicate nanocomposites as studied by real-time wide-angle X-ray scattering. *Macromolecules* 35:5529–5535
47. Bafna A, Beaucage G, Mirabella F, Metha S (2003) 3D hierarchical orientation in a polymer-clay nanocomposite films. *Polymer* 44:1103–1115
48. Guinier A, Fournet G (1955) *Small-Angle Scattering of X-rays*. Wiley, New York
49. Lazzari R (2002) *IsGISAXS: a tool for grazing incidence small angle X-ray scattering analysis for nanostructures*. Available at: <http://www.insp.jussieu.fr/axe2/Oxydes/IsGISAXS/figures/doc/manual.html>
50. Abragam A (1961) *The Principles of Nuclear Magnetism*. Oxford University Press, New York
51. Munowitz M (1988) *Coherence and NMR*. Wiley, New York
52. Slichter CP (1990) *Principles of Magnetic Resonance*. Springer, Berlin
53. Ernst RR, Bodenhausen G, Wokaun A (1988) *Principles of Nuclear Magnetic Resonance in One and Two Dimensions*. Oxford University Press, Oxford
54. Stejskal EO, Memory JD (1994) *High Resolution Solid State NMR*. Oxford University Press, New York
55. Schmidt-Rohr K, Spiess HW (1996) *Multidimensional Solid-State NMR and Polymers*. Academic, San Diego
56. MacKenzie KJD, Smith ME (2002) *Multinuclear Solid-State NMR of Inorganic Materials*. Pergamon Materials Series 6, Pergamon-Elsevier: Oxford
57. McBrierty VJ, Packer KJ (1993) *Nuclear magnetic resonance in solid polymers*. Cambridge University Press: Cambridge, UK
58. Cheung TTP, Worthington LE, DuBois Murphy P, Gerstein BC (1980) Solid-state NMR studies of cadmium: ^{113}Cd -1H cross polarization and magic angle spinning. *J. Magn. Res.* 41:158–168
59. Hartmann SR, Hahn EL (1962) Nuclear double resonance in the rotating frame. *Phys. Rev.* 128:2042–2053
60. Pines A, Gibby MG, Waugh JS (1973) Proton-enhanced NMR of dilute spins in solids. *J. Chem. Phys.* 59:569–590
61. Harris RK (1998) In: *Multinuclear Magnetic Resonance in Liquids and Solids – Chemical Application*. Granger P, Harris RK (eds.). NATO ASI Series C, 322, Kluwer, Dordrecht, The Netherlands, p 301–302
62. Bridley SW, Brown G (1980) *Crystal Structure of Clay Minerals and Their X-ray Diffraction*. Mineralogical Society, London
63. Pinnavaia TJ (1983) Intercalated clay catalyst. *Science* 220:365–371

64. Tennakoon DTB, Thomas JM, Jones W, Carpenter TA, Subramaniam R (1986) Characterization of clays and clay-organic systems: cation diffusion and dehydroxylation. *J. Chem. Soc. Faraday Trans. 1*(82):545–562
65. Forte C, Geppi M, Giamberini S, Ruggeri G, Veracini CA, Mendez B (1998) Structure determination of clay/methyl methacrylate copolymer interlayer complexes by means of ^{13}C solid state n.m.r. *Polymer* 39(12):2651–2656
66. Wu HD, Tseng CR, Chang FC (2001) Chain conformation and crystallization behavior of the syndiotactic polystyrene nanocomposites studied using Fourier transform infrared analysis. *Macromolecules* 34:2992–2999
67. Loo LS, Gleason KK (2003) Fourier transform infrared investigation of the deformation behavior of montmorillonite in nylon-6/clay nanocomposite. *Macromolecules* 36:2587–2590
68. do Nascimento GM, Constantino VRL, Temperini MLA (2002) Spectroscopic characterization of a new type of conducting polymer-clay nanocomposite. *Macromolecules* 35:7535–7537
69. VanderHart DL, Asano A, Gilman JW (2001a) NMR measurements related to clay-dispersion quality and organic modifier stability in nylon-6/clay nanocomposites. *Macromolecules* 34:3819–3822
70. Yang DK, Zax DB (1991) Li^+ dynamics in a polymer nanocomposite: an analysis of dynamic line shapes in nuclear magnetic resonance. *J. Phys. Chem.* 110:5325–36
71. Blumberg WE (1960) Nuclear spin-lattice relaxation caused by paramagnetic impurities. *Phys. Rev.* 119:79–84
72. VanderHart DL, Asano A, Gilman JW (2001b) Solid –state NMR investigation of paramagnetic nylon-6 clay nanocomposites. 1. Crystallinity, morphology and the direct influence of Fe^{3+} on nuclear spins. *Chem. Mater.* 13:3781–3795
73. VanderHart DL, Asano A, Gilman JW (2001c) Solid –state NMR investigation of paramagnetic nylon-6 clay nanocomposites. 2. Measurements of clay dispersion, crystal stratification and stability of organic modifiers. *Chem. Mater.* 13:3796–3809
74. Mathias LJ, Davis RD, Jarret WL (1999) Observation of α - and γ -crystal forms and amorphous regions of nylon 6-clay nanocomposites using solid-state ^{15}N nuclear magnetic resonance. *Macromolecules* 32:7958–7960
75. Sahoo SK, Kim DW, Kumar J, Blumstein A, Cholli AL (2003) Nanocomposites from in-situ polymerization substituted polyacetylene within lamellar surface of montmorillonite: a solid-state NMR study. *Macromolecules* 36:2777–2784
76. Lee JW, Stein GD (1987) Structure change with Size of Argon Clusters Formed in Laval Nozzle Beams. *J. Phys. Chem.* 91:2450–2457
77. Goerigk G, Haubold H-G, Klingshirn C, Uhrig A (1994) ASAXS from $\text{CdS}_{(1-x)}$ -doped silicate glasses. *J. Appl. Cryst.* 27:907–911
78. Ramos A, Lyon O, Levelut (1995) Stoichiometry of $\text{Cd}(\text{S}, \text{Se})$ nanocrystals by anomalous small-angle x-ray scattering. *J. Appl. Phys.* 78(12): 6916–6922
79. Prado LASA, Wittich H, Schulte K, Goerigk G, Garamus VM, Willumeit R, Vetter S, Ruffmann B, Nunes SP (2003) Anomalous Small-Angle X-Ray Scattering characterization of composites Based on Sulfonated Poly(ether ether ketone), zirconium phosphates and zirconium oxide. *J. Polym. Science: Part B: Polymer Physics*, 42: 567–575

Part II
Electronic and Magnetic Applications

Chapter 6

Development of Hybrid Nanocomposites for Electronic Applications

S.K. Samudrala and Sri Bandyopadhyay

Abstract Hybrid inorganic–organic nanocomposite materials with their widely varying electrical and mechanical properties offer promising applications in many areas of the electronic industry and have been traditionally employed as insulators and dielectrics. The development of new materials has broadened their utilization into areas where their semi-conducting and conducting properties have encouraged use in many novel applications. In this chapter we have reviewed on the material aspects of nanocomposites used in the following electronic applications: integrated circuits, embedded capacitors, transistors, lithium ion batteries, light emitting diodes, information storage, and briefly about liquid crystal, flat panel displays and ultra large scale integrated (ULSI) devices.

6.1 Introduction

Hybrid organic–inorganic materials are nanocomposites with organic and inorganic components that are either homogeneous systems derived from monomers and miscible organic and inorganic components, or heterogeneous systems (nanocomposites) where at least one of the components' domains has a dimension ranging from some Angstrom to several nanometers. The improved or unusual features related to multi-phase structures of these materials not only represent an alternate to design new multifunctional materials and compounds for academic research, but also result in the development of innovative industrial applications [1–3]. These new generations of hybrid materials, offer a land of promising applications in many areas including electronics, ionics, mechanics, energy, environment, biology,

S.K. Samudrala and S. Bandyopadhyay (✉)
School of Materials Science and Engineering, University of New South Wales,
Sydney, NSW 2052 Australia
e-mail: s.bandyopadhyay@unsw.edu.au

optics, medicine (for example as separation devices and membranes), functional smart coatings, solar and fuel cells, catalysts, sensors, etc [1, 4–19].

Nanocomposites represent the current trend in novel nanostructured materials. Properties of these materials are not only limited to the sum of the individual contributions of both phases, but also the role of the inner interfaces could be predominant. Based on the nature of the interface, nanocomposites can be divided into two distinct classes [1, 5, 20, 21] where (a) organic and inorganic components are embedded and only weak hydrogen, van der Waals or ionic bonds give the cohesion to the whole structure and (b) the two phases are linked together through strong chemical covalent or ionic-covalent bonds.

Nanocomposites being at the interface of organic and inorganic realms offer a wide range of possibilities to elaborate tailor-made materials in terms of processing, chemical and physical properties. Hybrid materials generate smart microelectronic, or intelligent therapeutic vectors that combine targeting, imaging, therapy and controlled release properties. Electronic technologies that allow for a reduction in size, weight, and cost while improving functionality and performance are highly desired for military and commercial applications, including telecommunications, network systems, automobiles, and computer electronic devices [1, 4–19]. Hybrid inorganic–organic nanocomposites with their widely varying electrical and mechanical properties have been traditionally employed as insulators and dielectrics but, the development of new materials has broadened their utilization into areas where their semiconducting and conducting properties have encouraged use in many novel applications. This review will focus on the material aspects of nanocomposites used for electronic applications such as: integrated circuits, embedded capacitors, transistors, lithium ion batteries, light emitting diodes, information storage, and briefly about liquid crystal, flat panel displays and ULSI devices. Before going into the review it is appropriate to briefly introduce these applications.

6.1.1 Background

6.1.1.1 Transistors

A transistor is a three-terminal semiconductor device that can be used for amplification, switching, voltage stabilization, signal modulation and many other functions. Transistor is a fundamental building block of both digital and analog integrated circuits. In analog circuits, transistors are used in amplifiers, (direct current amplifiers, audio amplifiers, radio frequency amplifiers), and linear regulated power supplies. Transistors are also used in digital circuits such as logic gates, random access memory (RAM), microprocessors, and digital signal processors (DSPs) where they function as electronic switches.

Transistors are divided into two main categories: bipolar junction transistors (BJTs) and field effect transistors (FETs). The vast majority of transistors are fabricated into integrated circuits (also called *microchips* or simply *chips*) along

with diodes, resistors, capacitors and other electronic components to produce complete electronic circuits. A logic gate comprises about twenty transistors whereas an advanced microprocessor, as of 2006, can use as many as 1.7 billion transistors [22]. Field-effect transistors (FETs), sometimes called unipolar transistors, use either electrons (N-channel FET) or holes (P-channel FET) for conduction. Like bipolar transistors, FETs can be made to conduct with light (photons) as well as voltage. Devices designed for this purpose are called phototransistors.

Transistors have the applications in and as [23–25]:

- (1) **Electronic Switches:** for both high power applications including switched-mode power supplies and low power applications such as logic gates.
- (2) **Amplifiers:** from mobile phones to televisions, vast numbers of products include amplifiers for sound reproduction, radio transmission, and signal processing. Transistors are commonly used in modern musical instrument amplifiers, where circuits up to a few hundred watts are common and relatively cheap. They have largely replaced valves in instrument amplifiers. In some cases of musical instrument amplifiers both transistors and vacuum tubes are used in the same circuit, to utilize the inherent benefits of both the devices.
- (3) **Computers:** development of transistors was the key to computer miniaturization and reliability. Transistors incorporated into integrated circuits have replaced most discrete transistors in modern digital computers.

Some advantages of transistors over conventional vacuum tubes include [1, 5, 12, 22, 26–32]: smaller size, highly automated manufacture, lower cost (in volume production), lower possible operating voltages, no warm-up period, lower power dissipation, higher reliability, longer life, and ability to control large currents.

6.1.1.2 Integrated Circuits

Integrated circuits (ICs) were made possible by technology advancements in semiconductor device fabrication (by mid-twentieth century) and by the experimental discoveries that showed semiconductor devices could perform the functions of vacuum tubes [33–35]. The integration of large numbers of tiny transistors into a small chip was an enormous improvement over the manual assembly of circuits using discrete electronic components. The integrated circuit's mass production capability, reliability, and building-block approach to circuit design ensured the rapid adoption of standardized ICs in place of designs using discrete transistors. There are two main advantages of ICs over discrete circuits: cost and performance. As of 2006, chip areas range from a few square mm to around 250 mm², with up to 1 million transistors per mm² [22].

Microprocessors are the most advanced integrated circuits, which control computers to cellular phones to digital microwave ovens. Digital memory chips are another family of integrated circuits that are crucially important to the modern information society [36]. While the cost of designing and developing a complex integrated circuit

is quite high, when spread across typically millions of production units the individual IC cost is minimized. Since the speed and power consumption gains are apparent to the end user, there is fierce competition among the manufacturers to use finer geometries [33–35].

Integrated circuits can be classified into analog, digital and mixed signal (both analog and digital on the same chip) [37]. Digital integrated circuits contain from one to millions of logic gates, flip-flops, multiplexers, and other circuits in a few square millimeters [38]. The small size of these circuits allows high speed, low power dissipation, and reduced manufacturing cost compared with board-level integration [39]. In 1986 the first one megabit RAM chips were introduced, which contained more than one million transistors. Microprocessor chips produced in 1994 contained more than three million transistors. The latest server processor from Intel had four billion transistors on a chip [22].

6.1.1.3 Capacitors

Capacitors, (energy-storage devices in electrical circuits) can also be used to differentiate between high-frequency and low-frequency signals which make them useful in electronic filters.

Capacitors have various uses in electronic and electrical systems such as [40–42]:

- (a) Energy storage, filtering, signal coupling, noise filters, motor starters,
- (b) Signal processing (energy stored in a capacitor can be used to represent information, either in binary form, or in analogue form, as in analog sampled filters),
- (c) Tuned circuits (capacitors and inductors are applied together in tuned circuits to select information in particular frequency bands),
- (d) Sensor applications [43, 44]:
 - I. Capacitors with an exposed and porous dielectric can be used to measure humidity in air; by changing the distance between the plates, capacitors can also be used to accurately measure the fuel level in airplanes
 - II. Capacitors with a flexible plate can be used to measure strain or pressure
 - III. Capacitors are used as sensors in condenser microphones,
 - IV. Some accelerometers use MEMS capacitors etched on a chip to measure the magnitude and direction of the acceleration vector
 - V. They are used to detect changes in acceleration, e.g., as tilt sensors or to detect free fall, as sensors triggering airbag deployment, and fingerprint sensors

6.1.1.4 Lithium Ion Batteries

Lithium (Li) ion batteries are rechargeable batteries that are commonly used in consumer electronics. They are the most popular type of batteries, with one of the

Table 6.1 Permanent capacity loss vs. storage conditions in lithium ion batteries at different temperatures [45]

Storage Temperature (°C)	100% Charge	40% Charge
0	6% loss after 1 year	2% loss after 1 year
25	20% loss after 1 year	4% loss after 1 year
40	35% loss after 1 year	15% loss after 1 year
60	40% loss after 3 months	25% loss after 1 year

best energy-to-weight ratios, no memory effect and a slow loss of charge when not in use. Lithium ion batteries can be formed into a wide variety of shapes and sizes, so as to efficiently fill available space in the devices they power. The forte of the Li-ion chemistry is the high open circuit voltage in comparison to aqueous batteries (such as lead acid, nickel metal hydride and nickel cadmium). However, a unique drawback of the Li-ion battery is its life span that is dependent upon aging from the time of manufacturing regardless of the number of charge/discharge cycles. Table 6.1 [46] lists the permanent capacity loss of Li ion batteries vs. storage conditions at different temperatures.

6.1.1.5 Light Emitting Diodes

Organic light-emitting diodes (OLEDs) are a special type of light-emitting diodes (LEDs) in which the emissive layer comprises a thin-film of certain organic compounds. The emissive electroluminescent layer can include a polymeric substance that allows the deposition of very suitable organic compounds, for example, in rows and columns on a flat carrier by using a simple “printing” method to create a matrix of pixels which can emit different color light [47]. One of the great benefits of an OLED display over the traditional liquid crystal displays (LCDs) is that OLEDs do not require a backlight to function. This means that they draw far less power and, when powered from a battery, can operate longer on the same charge. It is also known that OLED based display devices can be more effectively manufactured than LCD and plasma displays [47].

6.2 Applications

6.2.1 *Embedded Capacitors*

Lighter, smaller, compact, cheaper, finer function and further miniaturization are the keywords of today’s electronics industry. To satisfy these goals, electronic packaging technology has to play a vital role [8, 19, 42, 48–53]. Discrete passives (capacitors)

are useful in applications such as noise suppression, tuning, filtering, decoupling, bypassing, termination, and frequency determination. Passives account for a very large part of today's electronic assemblies especially for digital products such as cellular phones, camcorders, computers and defense devices [19, 48–50, 52, 53]. However, they outnumber the active integrated circuits (ICs) by several times and occupy more than 70% of the substrate in a typical electronic system with the increase of frequency. Also, current interconnect technology to accommodate surface mounted passives impose certain limits on board design, which limit the overall circuit speed. Thus discrete passives have become major barriers to the miniaturization of an electronic system especially when the ratio of capacitors to total passive components could be more than 60% [54]. Many efforts were on to increase the integration density of printed circuit boards (PCBs) as part of the general effort to miniaturize electronic equipment. Additionally, as they occupy a substantial amount of surface area on a substrate, there are limitations in the number of capacitors that can be placed around a chip [53]. Hence, an obvious strategy is to reduce the number of surface mounted passives by embedding them in the substrate or printed wire board.

Embedded passives provide increased real estate on the printed wiring board (PWB), reduced parasitic effects and conversion cost, miniaturization of interconnect distance, reduced part count and improved performance [55]. For this reason, embedded passive technology, which aims at removing passive components (capacitors, resistors, and inductors) from the PCB surface and integrating them into the bulk of the boards has attracted considerable interest [50]. System-in-a-package (SIP), a novel technology, is an assembly of several types of chips such as logic, memory, analog, and passives in a package, working as one system [56]. Embedded passives, components placed between the interconnecting substrates of a PWB, play an important role in SIP technique. Integration of the passives in packages also has the benefits of higher reliability, and improved design options. Such embedded capacitors demand materials with a high dielectric constant (especially at high frequency over MHz), a low processing temperature, a low leakage current, and a reasonable high breakdown field [49, 50, 52].

Thin film deposition and anodization have been used for manufacturing embedded capacitors [57]. But, these techniques need relatively expensive equipment and are not easily implemented into large-area MCM-L (multi chip module laminated) substrates [52]. Metal organic chemical vapor deposition (MOCVD) can also be used for fabrication of high value integral capacitors where cost may not be a critical factor. MOCVD can be employed as a low temperature dielectric deposition technique as required by the PWB multi-layer fabrication technology. This technique was implemented to deposit TiO_2 thin film dielectrics at temperatures below 180°C with higher capacitance densities [52]. Two different metal-dielectric-metal type parallel plate capacitor structures on silicon and PWB substrates were developed for relatively high frequency (45 MHz–1 GHz) and low frequency (100 Hz–1 MHz) characterization (Fig. 6.1 [52]). Copper was used as the ground and upper electrodes with a 10 nm Cr adhesion layer between the dielectric and the electrodes. Specific capacitance as high as 200 nF/cm^2 was reported at 1 MHz from devices built on silicon substrates and at 100 kHz from devices on PWB substrates.

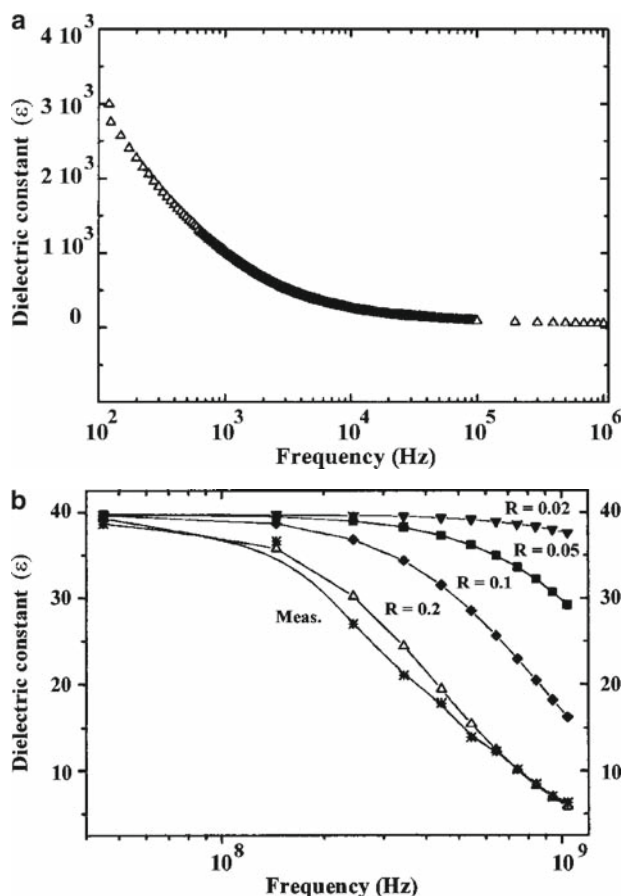


Fig. 6.1 Relative dielectric constant vs. frequency in the range (a) 100 Hz–1 MHz (b) 45 MHz–1 GHz (Reprinted with permission from [58]. Copyright (2000) Kluwer Academic Publishers)

For cost driven applications such as mobile phones and personal computers, polymer composites are the preferred materials. Polymer composite materials have emerged as a potential candidate for integral capacitors, because they satisfy the requirements of low processing temperature and reasonably high dielectric constant [53]. Many polymer nanocomposite studies focused on processing of high capacitance density thin films within small substrates/wafers where the important processing issue was to achieve high capacitance density on large coatings [54, 59, 60]. The uniqueness of polymer-based nanocomposites, compared with other nano-size objects, lies in the influence of the matrix resin on composites' performance and matrix-nanoparticle interaction. Another distinctive feature of these systems is the cooperative behavior of interacting particles in the case of highly filled composites, which becomes observable at the so-called percolation threshold where certain continuous structures of fillers are formed [61]. Novel integral passive component

materials with extraordinarily high dielectric constants ($K > 1,000$) and high reliability performances were demonstrated by Yang and Wong (Patented in 2001). These materials (although needed precision filler concentration control) were characterized by high dielectric constant based on the mechanism of interfacial polarization [53].

Two types of fillers have been investigated in polymers to suit as embedded capacitors: ferroelectric ceramic fillers and conducting (metallic) fillers. Properties of polymer/ferroelectric composites have been widely investigated for capacitor integration [8, 54, 59]. The dielectric constant of these composites was reported to be in the range of 10–100, depending on the ferroelectric filler concentration [62]. Also, in some cases, a high dielectric constant above 100 was reported; for example, epoxy/ceramic composites [58, 63]. Epoxy is a suitable polymer for the ceramic/polymer composites, because of its inertness to electroless plating solution and the compatibility with PWBs. Barium titanate (BaTiO_3) is a well-known ferroelectric material, and has a high dielectric constant around 6,000 at a fine grain size of $\sim 1 \mu\text{m}$, and of 1,500–2,000 at a coarse grain size [64]. Despite this, the micrometer range ceramic particles used in polymer matrix composites form weak interfaces between ceramic particles and the polymer, where more pores would form and hence lower the dielectric permittivity [65–67].

To overcome these problems, additives with high dielectric constant were used, surface modification of ceramic particles was done to improve their dispersion in the matrix, curing temperature of polymer matrix was lowered, and dielectric constant of the polymer matrix was increased [51]. Also chemical additives or shifters have been applied to the dielectric ceramics to move the Curie peak value (towards room temperature) and to smooth the Curie peak to improve the capacitance, and to have lower temperature coefficient of capacitance respectively. However these isovalent and aliovalent shifters can either decrease or increase the Curie point and change the dielectric constant. In case of modified BaTiO_3 high dielectric constants have been reported [64]. It is also reported that dielectric properties and the behavior of BaTiO_3 ceramics are highly dependent upon the particle size, grain size, phase contents, and the types of dopants added. Removal of grain boundaries, elimination of constrained forces from neighboring grains and a drop in domain density with the decreased particle size reduced the dielectric constant of the BaTiO_3 powders [64].

Further, conventionally to achieve high dielectric constant, the ceramic particle loading in the polymer-ceramic composite is increased. However, a high ceramic loading may lead to poor processability, poor dispersion, and therefore poor adhesion of the composite due to large loose aggregates, which in turn will effect the reliability of embedded capacitors [51]. Bai et al. [68] reported that the polymer–matrix composite with a high dielectric constant of 250 with a 50% (volume) concentration of relaxor ferroelectric ceramic particles, lost its flexibility. It was reported that a ceramic loading of above 80 vol% is impracticable. Table 6.2 lists the dielectric properties of commercial polymer-ceramic composites developed world-wide [51, 71]. Commercially available composites have only a dielectric constant of less than 40, which is far lower from the requirements for the next generation electronics. Hence, novel polymer-ceramic composites approaching the highest margin of

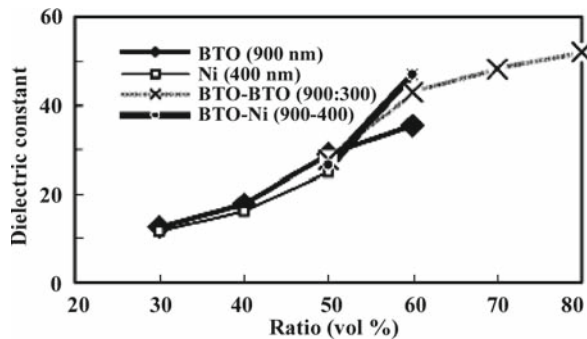
Table 6.2 Different commercial organic/inorganic composite materials with high dielectric constant [69, 70]

	Hadoco	3M	Dupont	Vantico
Trade name	EmCap	C-Ply	Hi-K	CFP
Composite	Epoxy/Ceramic	Epoxy/BTO	Polyimide/BTO	Epoxy/Ceramic
Thickness (μm)	100	4–25	25	12
Capacitance (pF/mm^2)	3.3	15.5–16.5	2.3	16
Dielectric constant @ 1 GHz	36	22	11.6	20.5
Dielectric loss @1 GHz	0.06	0.10	0.01	–

ceramic loading based on new concepts are needed for embedded capacitor applications. But, as per the 1998 National Electronics Manufacturing Technology Roadmap [72], a required capacitance density of $\sim 50 \text{ nF}/\text{cm}^2$ by 2001 is needed for successful implementation of integral passive technology, polymer/ceramic nanocomposites proved to be a viable option for values only up to $20 \text{ nF}/\text{cm}^2$ [73]. Since, for higher values these nanocomposites have not been proven to be a viable solution for integration with the printed wiring boards, alternative material systems were evaluated for the critical needs as evident in the NEMI Roadmap [72].

Metal nanoparticles exhibit unique physical, chemical, optical, magnetic, and electrical properties. Many researchers have exploited their properties in a readily usable form by incorporating them into polymers [53]. The solution for the capacitors consists in embedding those components in the form of metal/insulator/metal (MIM) stacks in between the inner interconnection lines of multilayer PCBs. The advantages of this technology include increased integration density, improved reliability (reduction of solder bumps) and better electrical performances (capacitors can be located closer to active circuits) [50]. Wong et al. demonstrated metal/epoxy composites [74] for embedded capacitor applications. They fabricated epoxy/silver flakes composites with a dielectric constant of more than 1,000 which is ten times higher than ferroelectric/epoxy composites [74]. This approach is based on the fact that in metal/insulator composites, the dielectric constant is predicted to diverge at the percolation threshold [75, 76]. Li et al. [51] evaluated nickel (400 and 150 nm)-filled nanocomposite as a candidate for embedded capacitors. They reported that with highly dispersed filler even at loadings of 60 vol%, a high dielectric constant of over 90 was achieved. The change in the dielectric constant with volume ratio of the filler is demonstrated in Fig. 6.2 [51]. When the surface modification of a barium titanate (Phthalocyanine coated BTO) particle was attempted in nanocomposite, its dielectric constant was observed to be over 80 at 1 MHz, which was much higher than that of composite derived from commercial BTO. Further, to improve the processability of the nanocomposite, 4, 4'-diphenylmethane bismaleimide (BMI) was selected as a matrix polymer by the combination with polyamide (PA). Higher dielectric constant nanocomposite derived from PA/BMI and Pc-coat BTO was obtained, and its potential application towards embedded capacitors was also evaluated.

Fig. 6.2 Relationship between dielectric constant and filler volume ratio (Reprinted with permission from [69]. Copyright (2005) IEEE)



Pothukuchi et al. [53] used an in situ reduction approach to incorporate silver particles in epoxy matrix for possible use in embedded capacitor applications. Reduction of metal salt was carried out in an epoxy matrix using a reducing agent. BaTiO₃-epoxy based polymer nanocomposites having the potential to surpass conventional composites to produce high capacitance density, low loss, and applicable over large surface areas, in thin film capacitors were reported by Das et al. [49]. The effects of particle size, thickness and loading parameters on the observed electrical performance and the reliability of the embedded capacitors were shown. Electrical properties of nanocomposites made of epoxy (used in majority of the PCBs) resin filled with 70 nm silver particles were investigated by Gonon et al. [50] ac conductivity and dielectric constant were plotted (Fig. 6.3 [50]) in the 10⁻¹–10⁵ Hz range frequency for different concentrations of silver nanoparticles. The composites exhibited electrical properties that do not obey standard percolation laws. A very low percolation threshold obtained ($\Phi_c = 1\%$) was related to a segregated distribution of the fillers in the epoxy matrix. Also, they reported a very high dc critical exponent ($t = 5$), which was attributed to the inter particle electrical contact. Pecharroman et al. [78] have reported Ni/BaTiO₃ metal/ceramic composites with high dielectric constant of 80,000, but the metal/ceramic composites still need to be sintered at high temperature of about 1,300°C under the special protection of preventing from oxidation of Ni. Dang et al. [79] reported a three phase (Ni/BaTiO₃/PVDF) composite based on the mixture rules and percolation theory, with dielectric constant of above 500. These composites were prepared by simple blending and hot molding procedures and they are reported to be flexible.

Conventionally, according to percolation theories, the dielectric constant takes very large values for filler concentrations close to the percolation threshold [80–82]. So, in principle, provided one stays on the “insulating side” (filler concentrations below the percolation threshold) it is possible to get a very high dielectric constant while keeping insulating properties. Though it appears appealing, in practice this approach is not so simple to implement. Indeed, there were many examples of conductor/insulator composites for which divergence of the permittivity is not observed at the percolation threshold. For instance, in carbon black/polymer composites it was observed that the dielectric constant *smoothly* increases through

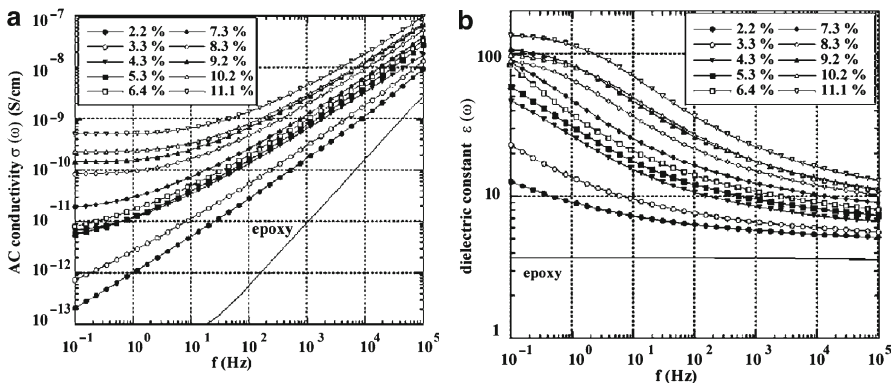


Fig. 6.3 (a) ac conductivity and (b) dielectric constant vs. frequency for various silver nanoparticles volume fraction (Reprinted with permission from [77]. Copyright (2006) AIP)

the percolation threshold (no sharp increase is observed at the percolation threshold) [83, 84]. The practical consequence is that it is not possible to get a high dielectric constant while maintaining insulating characteristics.

In a more fundamental context, conductor/insulator mixtures of several kinds were extensively studied to understand the insulator conductor transition in percolative networks [75, 76]. Concerning a segregated particle network it has been proposed that for spherical particles the following relationship should hold [85]:

$$\frac{\varphi_c}{100 - \varphi_c} = 2.99 \frac{D_n}{D_p}$$

where φ_c is the percolation threshold in vol% and D_p and D_n are the diameters of the polymer and the nanoparticle respectively. In a very recent work Luechinger et al. [86] studied electrical conductivity of C/Co-PEO and C/Co-PMMA nanocomposites whereby a very low percolation threshold of 0.81 vol% C/Co could be obtained. This low threshold resulted from a segregated C/Co-network located at the polymer-polymer interfaces which was corroborated by SEM-micrographs and a theoretical model. Despite numerous studies, metal/insulator composites are still motivating basic studies because deviations from standard percolation theories have been observed in many systems and some of them remain largely unexplained (as cited above, one of the “anomalous” behaviors observed in metal/insulator mixtures is the absence of permittivity divergence at the percolation threshold). A recent paper of McLachlan and Chiteme gives a good summary of such singular systems and the questions they raise about percolation theories [69].

To obtain thinner high-dielectric permittivity ceramic/polymer composite films, it is necessary to study nanocomposites that could endure the repeated changes of the heating-cooling processes when the films serve as dielectric in multilayer embedded micro-capacitors. As dielectric materials, dielectric permittivity should

increase as high as possible. But in a few cases [58, 87] results showed that the dielectric permittivity of polymer-matrix composite with micrometer-sized ceramic particles was a little higher than that with nanosized particles. This was because, tetragonality of the micrometer-sized particle is better than that of the nanosized one. Nevertheless, the thermal stability and mechanical properties of the composites will be improved when the inorganic nano-filler replaces the micro-filler in the polymer composites. Also, frequently, nanoparticles impart some particular properties to the composite only when the particles are homogeneously dispersed in the polymer matrix. The polymer composites with electro-active ceramic nanoparticles were prepared using ball-milling and a sol-gel process [58, 87, 88]. BaTiO₃/polyvinylidene fluoride (BT/PVDF) nanocomposites were prepared via a natural adsorption action, which occurred between the nano-sized BT and PVDF particles [48]. The BT/PVDF nanocomposites without obvious BT agglomerations provided the hope of the application of the BT/PVDF nanocomposites as an alternative dielectric to embedded micro-capacitors as a result of this simple and convenient technology. Figure 6.4 [48] shows the dependence of the dielectric permittivity and loss of the BT/PVDF nanocomposites on the volume fraction of nanosized BT at different frequencies at room temperature.

Despite the positive effects of embedded nanocomposite capacitors, there is a critical issue that needs to be considered in-depth: “yield” in the manufacturing process, since embedded passive technology does not offer the luxury of reworkability, as in the case of discrettes. A single defect could result in discarding the entire board with hundreds of pre-fabricated components.

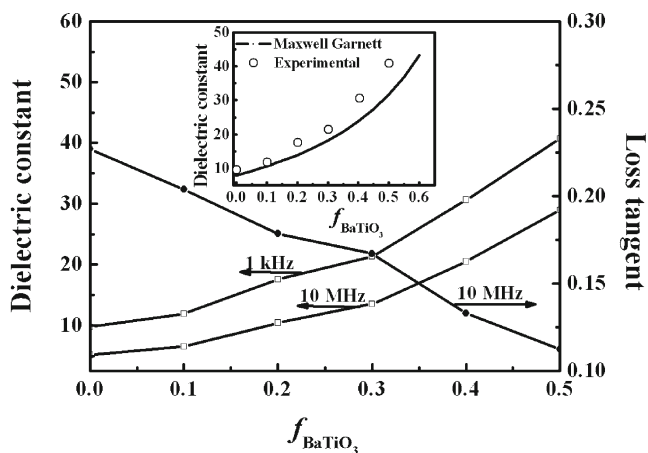


Fig. 6.4 Dependence of dielectric permittivity (*left*) and loss (*right*) of the BT/PVDF nanocomposite on the volume fraction of nanosized BT at different frequencies at room temperature. The inset is a comparison of the experimental value in dielectric permittivity to the calculated results using the Maxwell-Garnett approximation. (Reprinted with permission from [80]. Copyright (2005) Wiley VCH)

6.2.2 Lithium Ion Batteries

The improvement of preparation technology and electrochemical performance of electrode materials is a major focus of research and development in today's world. Particularly, the large scale demand for lithium rechargeable batteries or secondary batteries in day-to-day electronics (cellular phones, laptop computers, camcorders, and so forth) provided the thrust to improve their energy density, cycle life, and safety. Lithium rechargeable batteries have higher voltage (nominal voltage for Lithium ion battery is 3.6 V), higher energy density or specific energy (125 W h/kg L), and longer cycle life (>1,000 cycles) compared to conventional batteries, such as lead-acid, [89, 90] Ni–Cd, Ni–MH, [91, 92] and Ag–Zn. The performance characteristics of secondary batteries are listed in Table 6.3 [93]. Also, large-scale Li-ion batteries have great potential for electric vehicles and stationary energy storage systems.

The performances of Li-ion batteries are mainly influenced by the specific capacity and quality of the anode and cathode. During charge and discharge processes, Li ions from cathode intercalate into the crystal structure of anode and then the ions reverse direction, leaving the anode, and re-entering the cathode structure, respectively [94–96]. To achieve high cycling efficiency and long cycle life, the movement of Li ions in anode and cathode systems should not change or damage the crystal structure. Hence the physical, structural, and electrochemical properties of the cathode materials are critical to the performance of the whole battery as they provide the lithium ion source for the intercalation reaction. Figure 6.5 [98] shows a graphical representation of the energy storage capability of common types of secondary batteries.

Metallic lithium with excellent energy density was used in earlier batteries as an anodic material despite its high reactivity, which resulted in severe safety problems. For example, the dendrites grown while electroplating of Li onto the anode during charging reach the cathode resulting in an internal short, thereby leading to combustion of the Li. To overcome the problems of metallic lithium, a number of approaches/efforts were made. Scrosati et al. reported replacing metallic Li anode in Li secondary batteries with Li-insertion type of anodes [99]. Use of carbonaceous materials like graphite and artificial carbon having a graphite structure as anode materials for commercial lithium-ion batteries was also reported [100, 101]. However, the capacity of

Table 6.3 Comparison of the performance characteristics of some secondary batteries [38].

Battery	Nominal voltage (V)	Specific energy		Volumetric energy	
		(W h/kg)	(kJ/kg)	(W h/l)	(kJ/l)
Pb-acid	2	35	126	70	252
Ni–Cd	1.2	40	144	100	360
Ni–MH	1.2	90	324	245	882
Ag–Zn	1.5	110	396	220	792
Li-Ion	3.6	125	450	440	1584
Li-SPE	3.1	400	1,440	800	2,880

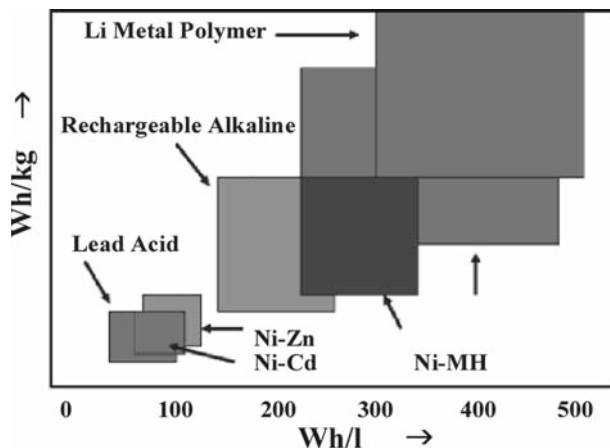


Fig. 6.5 Energy storage capability of common rechargeable batteries (Reprinted with permission from [97]. Copyright (2004) American Chemical Society)

graphite (372 mAh/g) was limited compared to that of lithium metal (3,860 mAh/g) [102]; but on the positive side, this has opened up new avenues for the deployment of transition metal oxides [103–105], metal–metal alloys [106–108], transition metal vanadates [109], ATCO anodes [77, 110], metalloids, lithium metal oxides [111], such as LiMSnO_4 [112], phosphates [113], niobates [114], and spinel-type ferrite anodes, viz. CoFe_2O_4 [115], NiFe_2O_4 [116, 117], ZnFe_2O_4 [118], and CaFe_2O_4 [119] for their high specific capacities and facile synthesis.

The introduction of Stalion lithium ion cells by Fuji Photo Film Celltec [95, 120, 121] whose anodes consisted of amorphous tin-based oxides instead of carbonaceous-based materials also laid the foot steps to a new generation of Li ion rechargeable batteries in the early 1990s. Materials such as SnO_2 , SnO and tin glass were shown to have twice the theoretical gravimetric capacity and four times more theoretical volumetric capacity as anode active materials than carbonaceous materials [122–126]. This led to the investigation of new materials that are capable of alloying with lithium such as Al, Sn, Pb, In, Bi, Cd, Ag, Mg, Zn, Si, and Sb [123, 124, 127]. These materials though showed satisfactory Li-ion transport properties, good lithium packing density and electrochemical potential, a substantial change in specific volume of the electrode upon continuous cycling resulted in loss of electrical contact, and thus capacity loss as well as macroscopic dimensional problems within the cell structure. For example, a large irreversible capacity loss at the first cycle due to a reduction reaction [127] prevented tin oxide anode materials from having any practical application. According to previous reports, tin oxides are reduced during the first discharge to form fine particles of tin and inactive phases like Li_2O , which slowed the growth of tin [123] leading to an excessive usage of cathode materials. Also, large tin oxide particles pulverize rapidly during discharge and charge cycles due to volume mismatch, resulting in a rapid drop in reversible capacity upon cycling.

In case of small particles, because the nanometer sized cavities within powders absorb the expansion of materials during the formation of lithium compounds, pulverization was thought to be less extensive. Silicon has the highest theoretical capacity of 4,000 mAh/g when forming $\text{Li}_{4.2}\text{Si}$ alloys. However, this alloying process is associated with a 300% volume dilatation, pulverizing the brittle electrode and inducing poor cyclability [6]. Limitation of cycling depth with a very thin reaction layer [128, 129], reducing the metal particle size [95, 130], or construction of bonded electrodes using Li^+ -conducting intermetallic phases [6, 131] were among the several methods proposed to solve the problem of volume expansion. It was thus postulated that nanostructured or amorphous electrodes may reduce the extent of pulverization, and thereby improve the cycle life of the electrode [132, 133].

Since many nanomaterials show higher reversible capacity than the corresponding micro-sized materials for anodes of lithium ion batteries, they have attracted great interest for lithium secondary batteries [134–138]. Carbon nanotubes [139–143], intermetallics, nanocomposites [98, 144], nano-oxides [104, 144–146], nanocrystalline thin films [147] are some examples, which have been reportedly used as anode materials to improve lithium storage capacities. Among these, single walled carbon nanotubes (SWNTs) showed a reversible capacity of 600 mAh/g [143]; a nanocomposite of Si [148] exhibited better cycling performance and reversible capacity of over 1,700 mAh/g at room temperature; and nano-sized transition-metal oxides delivered a Li storage capacity of ~ 700 mAh/g with 100% capacity retention for up to 100 cycles [104]. Chen et al. [45] reported the usage of nanocomposites of carbon nanotubes with Sn_2Sb alloy nanoparticles as anode material for Li ion batteries and showed that the first cycle de-lithiation capacity of 580 mAh/g from a carbon nanotube-56 wt% Sn_2Sb nanocomposite was reduced to 372 mAh/g after 80 cycles. Moreover, Sony commercialized [149] the first tin-based anode battery in February 2005, and Toshiba Corporation in March 2005 announced [149] a breakthrough technology using nanoparticles as negative electrode of Li-ion batteries.

Further, Li et al. [134, 135] reported high capacity and good cyclability for nanostructured tin oxides prepared by templating technique. Likewise, Yang et al. [133, 138] found that ultra-fine Sn-SnSb particles with $d_p < 300$ nm substantially raise the electrochemical performance of tin based alloys. The authors have attributed the improvement to the stabilization of the nano-sized alloy particles against agglomeration during Li insertion and extraction reactions. Carbon nanotubes were also used as one-dimensional hosts for the intercalation of Li and other alkali metals. It was demonstrated that multi-walled carbon nanotubes (MWNTs) could accommodate very high Li concentrations if insertion was carried out in the molten state at high pressures [150]. Reversible capacities were found to be in the range of 80–640 mAh/g for carbon nanotubes, in general, and further increase after ball milling. For example, Chen et al. reported the reversible capacities for single-walled nanotube electrodes after ball milling from 600 to 1,000 mAh/g [141, 151, 152]. However, a large voltage hysteresis in the first electrochemical extraction reaction of Li^+ was observed in all studies, in turn dampening the interest in using nanotubes as a viable Li-ion storage compound.

In addition, aggregation of nanotubes during cycling is a major challenging problem, which gives rise to poor cycling performance and thus limiting their practical applicability. Many efforts were put-forth to disperse the nanoparticles homogeneously in a matrix [153] and also to synthesize metal-encapsulated spherical hollow carbon [154], in order to improve their cycling behavior. But, none of these methods resulted in significant progress. A few studies were also focused at the usage of nanocomposites as anode materials in Li-ion batteries [6, 45, 95–98, 100, 102, 131, 155–157]. 10.3 wt% 3.5 nm Sn-graphite nanocomposite made from an in situ formed SnCl_4 precursor displayed a high reversible Li^+ storage capacity of 415 mAh/g, of which 91.3% was retained after 60 charge and discharge cycles, and demonstrated that particle size and distribution are both very important factors determining the applicability of Sn-based nanoparticles in Li-ion batteries [158].

It is always highly desirable to apply simple and highly productive techniques to produce both the anode and cathode materials despite the various methods available for the production of the ultrafine nanoparticles used in Li-ion batteries. Spray pyrolysis, an in situ fabrication technique, is one such method because it is inexpensive, versatile, industrially oriented, and can be operated over a large temperature range (100–1,000°C) [128, 129, 159, 160]. Martos et al. [129, 159] used sprayed lead oxide powders as anode material in Li-ion batteries and showed that the specific capacity fades on cycling when bulk powders were used. Recently, Ng et al. [95] have suggested the addition of a carbon source (sucrose solution) to enhance the electric conductivity of PbO [160–162]. The combination of spray technology and carbon addition increased the specific surface area (above 6 m²/g and the conductivity of PbO, improved the specific capacity, and maintained a cycle life with a reversible capacity above 100 mAh/g beyond 50 cycles) [95]. The increase in capacity retention for PbO–carbon compared to pure PbO was attributed to the presence of a conductive and highly developed carbon matrix (an excellent electric conductor) that can absorb large volume changes during alloying/dealloying of lead with [163, 164] lithium over the 1.50–0.01 V potential range. Also, with increasing carbon content, an improved cycle life of the PbO–carbon nanocomposites was reported (Fig. 6.6 [95]).

Different from the traditional methods (polymer coating, self assembly and layer by layer formation [136]) to synthesize core/shell nanocomposites, Fu et al. employed emulsion polymerization method followed by heat treatment to synthesize the core/shell structured TiO_2/C nanocomposites [155, 165]. These nanocomposites proved to be a good way of improving the cycling behavior and kinetics of lithium intercalation and de-intercalation of nano-titanium oxides [156]. They have shown that the thickness of carbon shell and the number of TiO_2 nanoparticles in the shell can also be controlled. In Fig. 6.7, [156] the discharge and charge curves of virgin TiO_2 and TiO_2/C nanocomposite electrodes are shown. The charge capacity of TiO_2/C nanocomposite remained at 96.7% (i.e., 118 mAhg⁻¹ titania) of its original capacity (i.e., 122 mAh/g titania) even after 10 cycles, which was much higher than that of virgin TiO_2 nanoparticles whose anode retained only 67.5% of the original capacity. This was thought to be due to the suppression of the aggregation

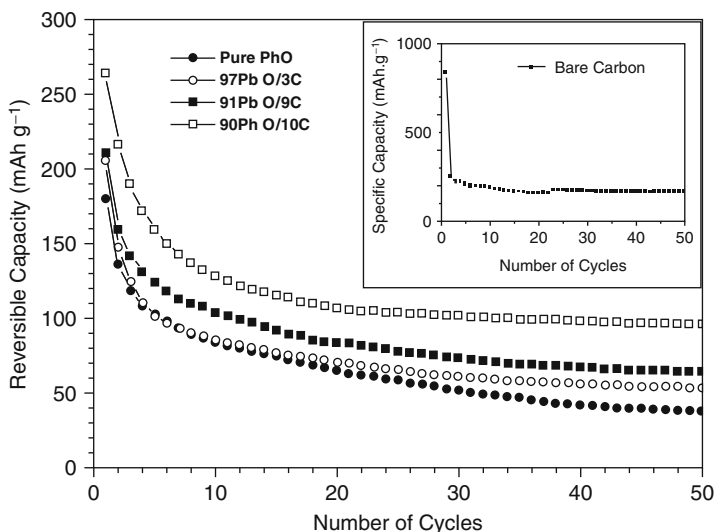


Fig. 6.6 Cycle life of PbO–C nanocomposites. The current density was 0.100 mA/cm^2 . The inset figure presents the specific capacity vs. cycle number data for the bare carbon powder and the current density applied was also 0.100 mA/cm^2 (Reprinted with permission from [40]. Copyright (2006) Electrochemical Society)

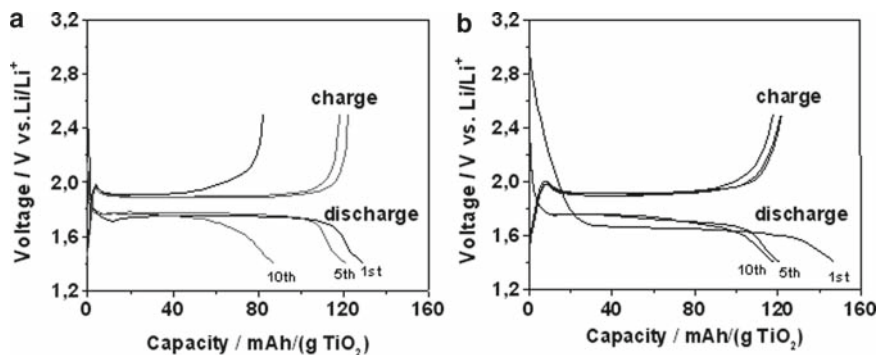


Fig. 6.7 Discharge and charge profiles of: (a) the virgin TiO_2 nanoparticles and (b) the TiO_2/C core-shell nanocomposite at a constant current density of 0.1 mA/cm^2 (0.25 C) in the voltage range $1.4\text{--}2.5 \text{ V}$ (Reprinted with permission from [37]. Copyright (2006) Elsevier)

of nanoparticles by the coated carbon shell. They also reported that the nanocomposites exhibited higher apparent diffusion coefficients of lithium ions compared with virgin TiO_2 nanoparticles.

For the first time, Selvan et al. [96] have reported the use of $\text{CuFe}_2\text{O}_4/\text{SnO}_2$ nanocomposites (synthesized by means of a urea–nitrate combustion method) as anode materials for Li-ion batteries. They showed that the electrochemical activity of native CuFe_2O_4 was enhanced through the incorporation of SnO_2 and also identified

the advantages of deployment of nanocomposite electrodes and the effect of SnO_2 dopant in reducing the Li^+ ion diffusion path lengths so as to enhance the diffusion kinetics and impart improved charge–discharge characteristics. The coulombic efficiency of copper ferrite anodes is improved from 65 to 99.5% through SnO_2 doping. Figure 6.8 [96] represents the charge–discharge profiles exhibited by CuFe_2O_4 and $\text{CuFe}_2\text{O}_4/\text{SnO}_2$ anodes. The high specific capacity values exhibited by both the ferrite anodes (>800 mAhg [20]) were attributed to the electrochemically driven size confinement of the nano electrodes.

The nano CuFe_2O_4 anode and $\text{CuFe}_2\text{O}_4/\text{SnO}_2$ nanocomposites delivered an improved specific capacity of 1,193 and 849 mAhg^{-1} , respectively, which were almost three times higher than that of a carbon anode (372 mAh/g). Ahn et al. [102] also have investigated the effect of dispersion of alumina particles on the electrochemical properties of Sn, SnO_2 , and tin based intermetallic Ni–Sn as anode materials for Li-ion batteries. They have synthesized various tin-based nanocomposite anodes with Al_2O_3 , using high-energy ball milling. The first charge (Li-insertion) capacities were found to be very high for these composite electrodes. However the nanosize oxide dispersion did not improve cycle properties of tin-based anodes.

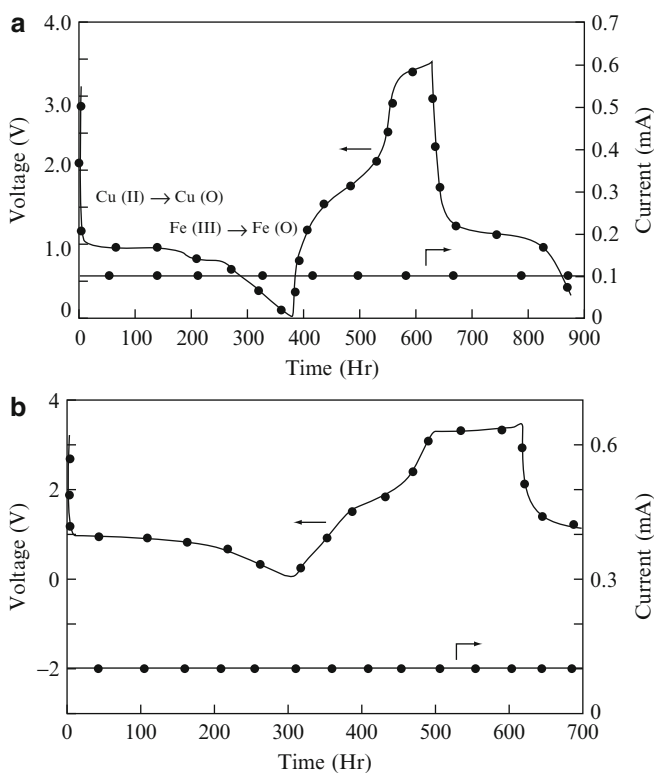


Fig. 6.8 Charge–discharge profiles exhibited by (a) CuFe_2O_4 and (b) $\text{CuFe}_2\text{O}_4/\text{SnO}_2$ anodes (Reprinted with permission from [131]. Copyright (2006) Elsevier)

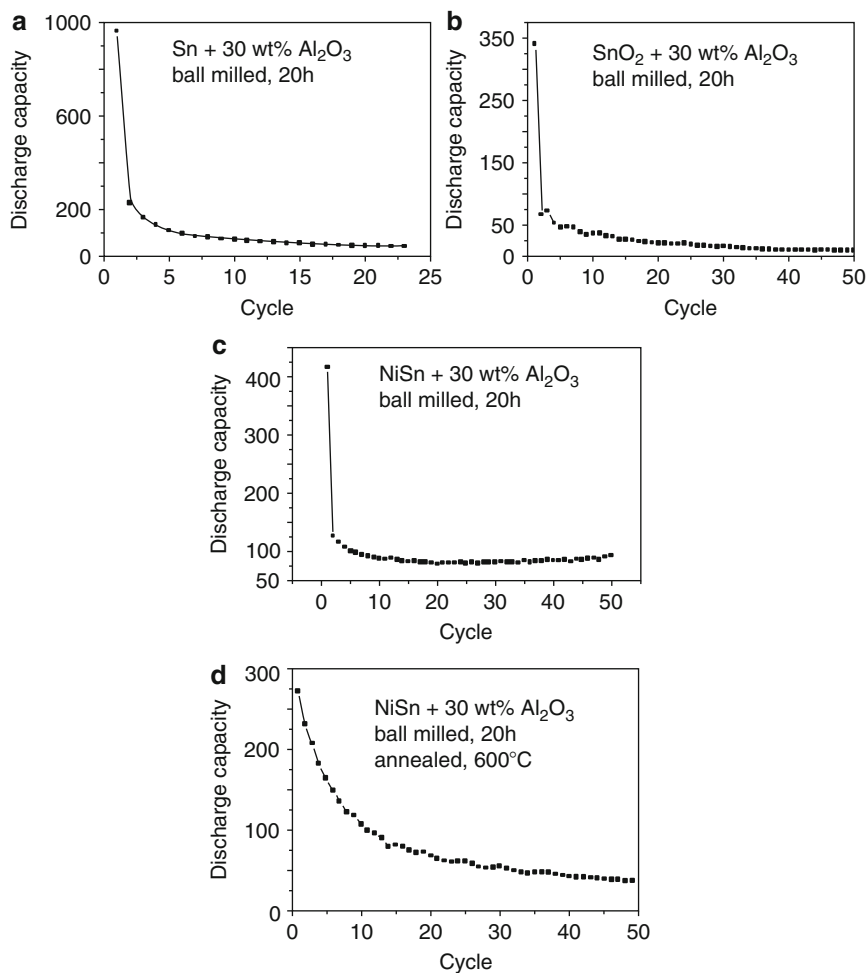


Fig. 6.9 Change in charge capacities on cycling for different nanocomposites (Reprinted with permission from [22]. Copyright (2003) Elsevier)

Figure 6.9 [102] shows the change in charge capacities for different nanocomposites on cycling.

Furthermore, nano-dispersed Si in carbon synthesized by chemical vapor deposition (CVD) had demonstrated a reversible capacity of 500 mAhg⁻¹. However, the CVD approach produced SiC and the morphology of Si and C cannot be controlled [166]. Nanostructured thin-film form of Si electrode was investigated by some researchers and they reported a specific capacity of around of 1,100 mAh/g [167, 168]. Nano Si-C composite prepared by hand mixing has been reported to have a high reversible capacity of 1,700 mAh/g by Li et al. [148]. Also crystalline Si powders have been dispersed in sol-gel graphite [169], in a TiN matrix [153], and in synthetic graphite [170], by ball milling. All the Si-C composites mentioned, exhibited increased specific capacity

compared to bare graphite, and improved cyclability compared to bare Si electrodes. Wang et al. [157] have reported the synthesis of nanostructured Si–C composites by dispersing nanocrystalline Si in carbon aerogel. A reversible capacity of $1,450 \text{ mAhg}^{-1}$ for Si–C composite electrodes (Fig. 6.10a [157]) was reported. The good cyclability was attributed to the usage of nano-sized Si powders and their homogeneous distribution (Fig. 6.10b [157]) in an amorphous carbon matrix.

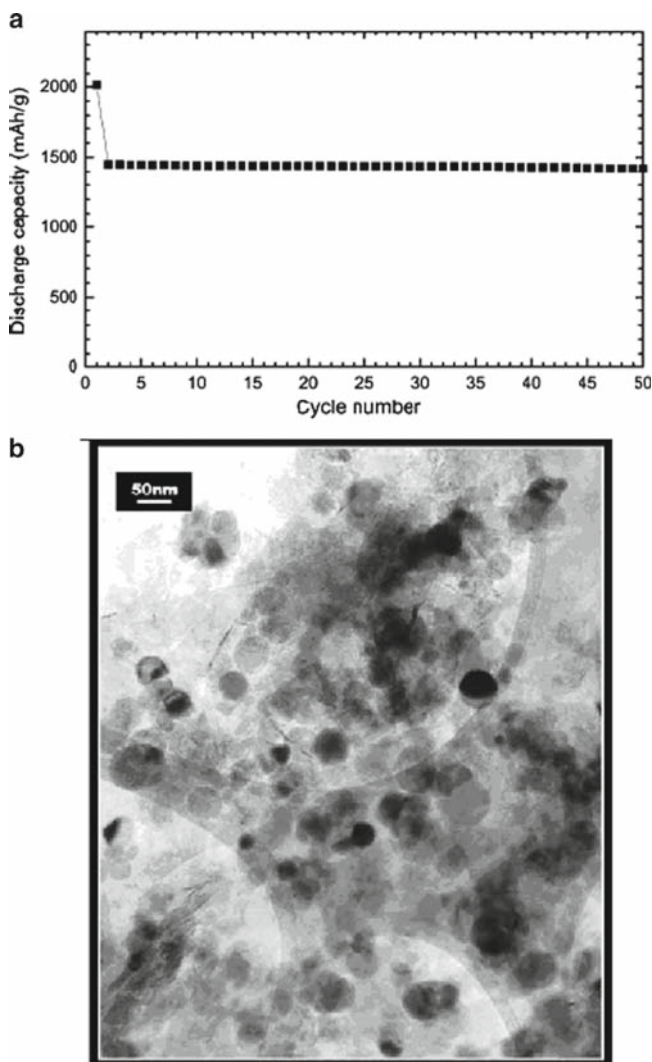


Fig. 6.10 (a) The discharge capacity vs. cycle number for Si–C electrode. (b) TEM image of nanocrystalline Si–C composites (Reprinted with permission from [171]. Copyright (2004) Elsevier)

A challenge in working with nanocomposites and nanostructured materials derives from difficulties in obtaining adequate structural characterization, especially, as they often lack long-range order. For example, although XRD can yield valuable information regarding structural changes that occur in the host material during Li^+ insertion, the poor crystallinity of organic–inorganic hybrid nanocomposites limits the applicability of this technique. So the results obtained exclusively from this technique should be addressed in terms of their accuracy. Nuclear magnetic resonance technique is proved to be a better alternative for this purpose.

6.2.3 *Integrated Circuits*

Meso-, micro-, and nano-porous materials are of much interest in the microelectronics industry due to their potential use as low dielectric constant (low- k) interdielectrics [35, 122, 172–174], in integrated circuits (ICs) with multilayer structures. They can lower line-to-line noise in interconnects and alleviate power dissipation issues by reducing the capacitance between the interconnect conductor lines. In addition to providing device speed improvements, low- k interdielectrics also provide lower resistance-capacitance delay, making them superior to low resistivity metal conductors such as copper and silver [33, 173, 175]. Thus, interdielectric materials with $k \ll 2.5$ are in high demand in the microelectronics industry, which is rapidly developing advanced ICs with multilayer structures that have improved functionality and speed in a smaller package and also consume less power [33, 173, 175].

As per “The Semiconductor Industry Association’s International Technology Roadmap” for semiconductor materials, materials with an effective k of 2.5–3.0 are in production today, and that in the near future, material systems that deliver an effective $k < 1.9$ are expected to be available, in particular for 50 nm or less feature size technology based on copper metallization [175]. However low- k dielectric materials must meet the thermal stability requirements of the metallization processing of ICs. For example, low- k nanoporous materials should withstand high temperatures during the processes like copper metallization, which are conducted at $<250^\circ\text{C}$; and generally, are followed by thermal annealing in the range $400\text{--}450^\circ\text{C}$ to ensure the production of void-free copper deposits. Moreover, these materials also have to meet conditions such as [35, 176]: low moisture uptake, high purity, good adhesion to silicon, silicon oxide and metals, good planarization behavior, and appropriate plasma etching behavior. Interdielectric materials also have to be able to withstand harsh chemical mechanical polishing (CMP) conducted with an aqueous slurry containing an abrasive (e.g., alumina particles) and an oxidant and/or complexing agent (e.g., nitric acid or ammonium hydroxide) to remove excess metal during the metal inlay process [35, 176].

A wide variety of polymers have been reported as potential low- k materials for use in the development of advanced ICs such as polyimides, heteroaromatic polymers, polyaryl ethers, fluoropolymers, non-polar hydrocarbon polymers, and polysilsesquioxanes [34, 164, 177, 178]. The dielectric films of these materials can be deposited from the gas phase with chemical deposition, plasma enhanced chemical vapor deposition, and other techniques. Polytetrafluoroethylene has a k value of 2.2, the lowest reported so far for such polymers. However, its very poor mechanical properties, poor interfacial adhesion and poor processability out-list PTFE for use in the fabrication of ICs. Nevertheless, the k value of these polymers ($k \sim 2.5$) is lower than those of today's workhorse dielectrics silicon dioxide ($k = 3.9\text{--}4.3$) and silicon nitride ($k = 6.0\text{--}7.0$), and still much higher than that of air (or vacuum), $k = 1.01$, which is possibly the lowest value attainable. So, the idea of incorporating air into dielectric materials as nano-pores to produce nanoporous materials with low k values has attained much interest [33, 173, 174]. To prevent the metal diffusion into the interdielectric layers during the IC fabrication, the nano-pores have to be at least 5–10 times smaller than the minimum IC metal feature size.

The dielectric constant obtained is limited primarily due to the intrinsic dielectric constant of the matrix and the sizes of the dispersion pores in the materials. The ultimate aim of the introduction of nanometer-sized pores into these materials is to increase the amount of free space. Matrices containing homogeneous, nanometer-scaled, and closed pores were preferred in terms of their electrical and mechanical properties and the effect porosity on dielectric constant can be predicted using simple models, such as the Bruggeman effective medium approximation [34]:

$$f_1 \frac{k_1 + k_e}{k_1 + 2k_e} + f_2 \frac{k_2 - k_e}{k_2 + 2k_e} = 0$$

where, f_1 and f_2 represent the fractions of the two components, k_1 and k_2 are the dielectric constants of the components, and k_e is the effective dielectric constant of the material. The assumption here is that the material has two components, matrix and pores. When the porosity exceeds 30%, the pores will become percolated or interconnected causing local trapping of moisture and chemicals, which leads to an increase in dielectric constant, and crack formation.

Films of poly(*p*-phenylene biphenyltetracarboximide) containing 27 wt% hollow sphere silica nanoparticles (with refractive index of 1.7007 at a wavelength of 830 nm) were prepared by thermal sintering of monolithic silica aerogels [35]. These hollow nanoparticles were thermally stable and withstood temperatures of up to 500°C, which made them useful for incorporation in organic polymers such as polyamide, other high temperature polymer dielectrics and inorganic dielectrics such as silicates and organosilicates. However the size of these nanoparticles (150 nm) was larger than the actual metal features of the advanced ICs.

Generally, studies on porous materials were based on two routes: (a) thermal decomposition of polymer blends or by block copolymers and (b) blending of a highly thermal stable polymer [179–181] with an unstable one. Carter et al. [180] developed a highly fluorinated polyimide with low dielectric constant of $k < 2.3$ by

Table 6.4 Dielectric constant of polyamide nanoporous materials [29]

Sample	PEO-POSS in feed		Dielectric constant (K)	Thermal expansion coefficient (ppm) 50–250 (°C)	Measured density (g/cc)
	wt%	mol%			
PI-0P	0	0	3.25	38.2	1.38
PI-2P	2	0.0007	2.88	42.3	1.31
PI-5P	5	0.0017	2.43	46.5	1.18
PI-10P	10	0.0034	2.25	55.8	1.09

using the nano-foam approach. However, fluorinated polymers have inadequate thermal stability for use in integration procedures, and there are issues for fluoric acid evolution during processing and reactions with the metals used [182, 183]. Block copolymers usually consist of a highly temperature-stable block and a thermally labile block that acts as the dispersed phase through the curing process, which makes them good candidates for templates. Thermolysis of the labile blocks leaves pores of sizes and shapes that correspond to those present in the initial copolymer's morphology. A number of reports [179, 180, 182] described the synthesis of porous structures of high temperature thermoplastic materials ($T_g > 350^\circ\text{C}$) from block copolymers. Lee et al. [184] synthesized nano-porous polyimide films through the use of a hybrid poly(ethylene oxide)–polyhedral oligosilsesquioxane (PEO-POSS) template. Reduced dielectric constant of $k = 3.25$ – 2.25 of the porous hybrid films with pore sizes in the range of 10–40 nm were reported. Table 6.4 [184] gives the dielectric constants of the various composites having different POSS contents.

6.2.4 Transistors

Field effect transistors (FETs) play a significant role in modern electronics as they are inherent parts of various devices, for example, computer chips. It is crucial to develop novel device geometries to optimize gate electrostatics needed for efficient ON-OFF switching for highly scaled molecular transistors with short channels [1]. Composite materials based on the coupling of conducting organic polymers (COPs) and carbon nanotubes (CNTs) offer an attractive route to introduce electronic properties [20, 185–188]. Some of the COPs used are polyaniline (PANI) [5, 189–191], polypyrrole (PPY) [192–194], polythiophene (PTh) [195], poly(3,4-ethylenedioxy thiophene) (PEDOT) [193, 194, 196], poly(*p*-phenylene vinylene) (PPV) [186], and poly(*m*-phenylene vinylene-co-2,5-dioctoxy-*p*-phenylene) (PmPV) [192, 197]. It was also suggested that in COP/CNT composites, either the polymer functionalizes the CNTs or the COPs are doped with CNTs, i.e., a charge transfer occurs between the two constituents [1]. Qi et al. [198] showed that SWNT-contacted P3HT FETs exhibited higher current modulation of three orders of magnitude than the metal contacted devices over a same gate voltage (–2 to 2 V gate range). However, there

are many problems associated with the use of carbon nanotubes to be overcome, if their potential towards the field of transistors has to be fully realized, which will be briefly discussed in this section.

Carbon nanotubes, particularly, single-walled carbon nanotubes (SWNTs) generated much interest as they possess unique electronic properties, high chemical stability, impressive mechanical strength and excellent thermal and electrical stability [12, 26, 27]. Their potential use in a variety of technologically important applications, such as electronic devices, field effect transistors, molecular diodes, memory elements, logic gates, molecular wires, high strength fibers, sensors, and field emission is very well established [12, 32]. Dekker [199–201], Lieber [202–204], and Avouris [205] demonstrated that SWNTs can be used as semiconducting channels in functional field effect transistors (FETs) and also outperform comparable Si-based devices [32]. Dai and co-workers showed that SWNTs can act as chemical sensors, where exposure to specific gases, including ammonia, hydrogen and NO_2 alters nanotube conductivity by up to three orders of magnitude within several seconds of exposure [32]. However, their structural resemblance to graphene, limits their flexibility for practical applications due to their high chemical stability and insolubility in most organic and aqueous solvents. This limiting factor must be overcome if carbon nanotubes are to be utilized, especially in the preparation of blends with conventional polymers, molecular electronics, and the production of homogeneously dispersed conducting layers within electroluminescent devices [12, 32].

To modify their structure, especially to improve their solubility, compatibility, chemical reactivity, and electronic properties [12] generally, CNTs are functionalized with various organic, inorganic, and organometallic structures using both covalent and non-covalent approaches with a primary focus of improving the solubility properties. Initial success was achieved by functionalizing carboxylic acid groups, formed at the ends and defective sites of SWNTs during oxidative purification/shortening through amidation with alkylamines such as octadecylamine [206]. Later, this approach has been extended to the attachment of organometallic complexes, including Vaska's complex [207] and Wilkinson's catalyst [208], inorganic nanocrystals such as CdSe [209] and Au, DNA, and various other biological molecules, dendrons, and polymers. Another strategy for SWNT functionalization involves the use of side-wall reactions such as fluorination with elemental fluorine, 1,3-dipolar cyclo addition, electrochemical reduction of diazonium salts, and direct addition of nitrenes, carbenes, and radicals to the unsaturated π -system of the nanotubes. The covalent functionalization strategies opened up a wide range of chemistry that can be performed on the sidewalls of carbon nanotubes, which allow chemists to control the properties of these nanoscale materials.

Functionalization with monolayer protected nanoclusters (MPCs) is highly promising and many researchers have focused on gold nanoclusters because of their special optical properties, unusual electronic properties, remarkably high catalytic activity, and so forth. MPCs are generally organized on pre-functionalized nanotube surface either by covalent, hydrophobic or hydrogen bonding. Geckeler et al. arranged gold nanoparticles on SWNTs by the addition of metal salts to surfactant-suspended SWNTs in water using the solution phase dispersion technique [12].

Recently, Mahima et al. [12] reported an electrochemical route to assemble monolayer protected gold nanoclusters (AuMPCs) on the surface of SWNT bundles, by applying an external potential. This electrochemical process for preparing hybrid nanoscale materials has added advantages compared to other chemical routes, which normally include undesirable sidewall reactions, tedious purification processes, and shortening of the tubes due to the use of strong oxidizing agents, which introduces defects on the side-walls, making them less useful for potential electronic applications. The authors reported significant enhancement in double layer capacitance (almost ten times greater) for these hybrid materials as compared to bare SWNTs.

Further, a number of recent reports have concentrated on supramolecular functionalization of SWNTs, especially with polymeric structures. Aromatic side-walls of nanotubes provide the possibility for π -stacking interactions with conjugated polymers as well as polycyclic aromatic hydrocarbons [32]. Substituted pyrene molecules were also employed for surface attachment of a number of functionalities where the appended structure has been used to attach proteins, polymerization initiators, or aqueous solubilizing groups in a non-covalent fashion. So far, covalent attachment of polymers to carbon nanotubes has been mainly accomplished using a “grafting to” approach, in which the polymer is first prepared and then reacted with the carboxylic acid functionalities of the SWNTs.

As different from that approach, Yao et al. [32] described a “grafting from” approach to the “growth” of polymers from the surface of nanotubes by first covalently attaching polymerization initiators and then exposing the nanotube-based macro-initiators to monomers. It was believed that a higher incorporation of polymers would result relative to the “grafting to” approach because this approach strictly involves the reaction of the nanotubes with small molecules. They investigated the use of atom transfer radical polymerization (ATRP) which has been shown to be a highly versatile technique for the controlled radical polymerization of acrylate based monomers from the surface of nanoscale structures. SWNTs were functionalized along their side-walls with phenol groups using the 1,3-dipolar cyclo addition reaction and the phenols were further derivatized with 2-bromoisobutryl bromide, resulting in the attachment of atom transfer radical polymerization initiators to the sidewalls of the nanotubes. They also reported that nanotubes functionalized with poly(methyl methacrylate) were found to be insoluble, while those functionalized with poly(tert-butyl acrylate) were soluble in a variety of organic solvents. The tert-butyl groups of these appended polymers were removed to produce nanotubes functionalized with poly(acrylic acid), resulting in structures that were soluble in aqueous solutions [32].

Due to their low carrier mobility, conducting polymer based thin film transistors suffer from inferior performance when compared to inorganic crystalline semiconductors [1, 5]. The properties of the individual molecules and structural order of the molecules are the key factors determining the macroscopic properties of the organic semiconductor materials. Large π -conjugation length, high degree of ordering, and molecular packing are important factors for carrier mobility in conducting polymers [210, 211]. Polyaniline is an outstanding conducting polymer in which the conductivity results from a process of partial oxidation. It is interesting because of its good stability

in the doped form and electronic properties. Based on morphological modification or electronic interaction between the two components, carbon nanotubes in conducting polymers were shown to possess properties of the individual components with a synergistic effect [20, 186, 194]. Carbon nanotubes will not only allow the carriers to be transported by providing percolation paths, but also help to improve the mobility. The transfer characteristics' analysis of the field effect transistors (FETs) suggested that the carbon nanotubes have a higher carrier density than graphite and a hole mobility comparable to that of heavily p-doped silicon [212].

In the core shell structure of the polyaniline (shell)/CNT (core) nanocomposites obtained by in situ polymerization, the presence of CNTs have improved the polymer properties by (a) inducing additional structural ordering of the polymer; (b) enhancing thermal stability; (c) enhancing delocalization of charges in the composite; (d) improving the compactness and conjugation or chain length; and (e) improving charge carrier mobility [8]. These properties are desired for a material in the field of organic electronics. DuPont have developed polyaniline/carbon nanotube composites as printable conductors for organic electronics applications [29]. Ramamurthy et al. [213] reported that improvement in material consistency and reduction in defect densities will make these composites suitable for use in fabricating organic electronic devices. It was suggested that by finely dispersing the carbon nanotubes in a polymerization medium, during in situ polymerization, a good level of homogeneity can be achieved further enhancing the material quality.

Kuo et al. demonstrated polyaniline without any side chains to be the active layer in an organic thin film transistor (TFT) and high field effect mobility was observed [214]. Carbon nanotube nanocomposites used for thin-film transistors provide one of the first technologically-relevant test beds for two-dimensional heterogeneous percolating systems. The characteristics of these TFTs are predicted by considering the physics of heterogeneous finite-sized networks and interfacial traps at the CNT/gate-oxide interface. TFTs based on two-dimensional networks of carbon nanotubes or silicon nanowires were recently explored for low voltage, high reliability, and high-speed applications in flexible macro-electronics [171, 215, 216] as well as in CNT microelectronics [217, 218]. A number of technical difficulties remain, despite their promise to improve the performance of micro- and macro-electronics, such as: poor sub-threshold characteristics and lack of understanding of on-off current dependence on parameters such as the channel length, tube length, and the fraction of metallic tubes. Properties of these two dimensional CNT networks are controlled by the competition between heterogeneous networks of metallic and semi-conducting CNTs, a regime that has never before been explored. A predictive model is required to interpret experimental results and to expedite the development of this new class of TFTs.

Kumar et al. [27] have developed a heterogeneous finite-size percolation model to explore the dependence of gate characteristics in the linear regime on tube density and metallic contamination for thin films made of randomly oriented nanotubes. The authors explained the on-off ratio before and after the breakdown of metallic tubes. The developed model also answered two questions of fundamental technological importance: (1) What are the performance limits of network transistors free

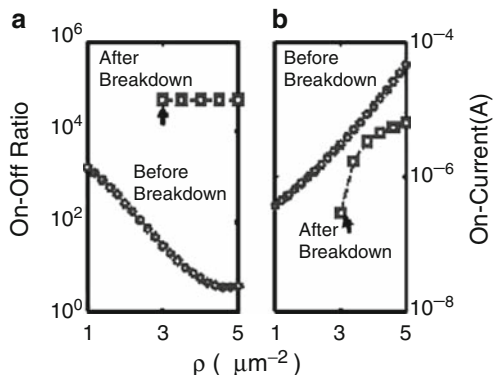


Fig. 6.11 Dependence of (a) On-off ratio and (b) On-current on network density before and after the removal of metallic tubes. $L_s = 10 \mu\text{m}$, $L_c = 2 \mu\text{m}$, and $H = 35 \mu\text{m}$. The network drops below the percolation limit after breakdown for the tube density indicated by arrows (Reprinted with permission from [7]. Copyright (2006) AIP)

from metallic tubes (f_m (metallic tube fraction) = 0)?, and (2) given a technology-specific f_m , what is the maximum density of tubes that will preserve a high on-off ratio? Figure 6.11 [27] represents the results obtained from the model for the on-off ratio before and after the break down. Close agreement between numerical results and different experimental observations was also achieved demonstrating the capability of this model to predict the characteristics of CNT/nanowire-based TFTs. Such predictive models would simplify device optimization and expedite the development of this nascent TFT technology.

Organic thin film transistors though attracted a great deal of interest (as critical components for the fabrication of low cost and large area flexible displays and sensors), the major problem in using them in the logic circuits is the requirement of high operating voltage. This problem needs to be focused in order to realize the full practical applicability of these materials.

6.2.5 Information Storage

It is evident that modern information systems, in particular, electronic systems inevitably reach the fundamental technological, physical, and functional limitations. The fact that fiber optics communications is an advanced field of business today shows that from the view-point of information carrier, photon is considered as an alternative to electron [10]. Telecommunication networks mainly develop in a so-called “third telecommunication window,” i.e., in the range of silica fiber (minimum absorption near the wavelength of $\sim 1.5 \mu\text{m}$), and erbium doped optical fibers (generally, used for amplification of optical signals [70] to achieve high amplification with low noise [219]).

Photonic devices based on integrated optics and hybrid systems that use micro-laser and other micro- and nano-optical elements are playing a significant role. These systems demand a short effective gain length and, consequently, a higher concentration of active medium. To meet this new active media, methods that obtain high doping concentrations should be used and also concentration quenching be surmounted.

Photonic crystals (periodic quantum-dimensional systems) present a new type of artificial media possessing a spatial periodicity of optical properties with the period of the order of optical wavelength [219]. There are possibilities to control photons in such media, which are advanced in various fields of modern optics and nanophotonics. It was reported that most promising technologies for forming new media with quantum-dimensional properties are those based on self-organizing systems [219]. Photoluminescence of nanocomposites based on cubic packing SiO_2 nanospheres (opal matrices) and porous anodic alumina (PAA) doped with erbium and other rare earth elements, vs. the element structure, concentration of rare earth ions, matrix composition, optical properties, and technology was studied by Tsvetkov et al. [219]. Fig. 6.12 [219] shows the images of these materials. They also discussed the possible application of 3D-(space) and 2D-(planar) nanocomposites in systems of optical information transfer, storage, and processing.

The progress of information technology depends critically on the development of new materials for high density optical and magnetic memory storage. The last decade has seen a great research effort in the case of optical data storage, geared towards development of bit-oriented 3D, or multilayered, optical memories based on a variety of materials. 3D media promises a dramatic increase in memory capacity as the storage density scales as $1/\lambda^2$ and $1/\lambda^3$, where λ is the wavelength of the reading beam, for 2D and 3D optical memories, respectively [221]. Rentzepis et al. [222] explained the approach of bit-oriented 3D optical memory based on two-photon writing for the first time. It was shown that simultaneous absorption of two photons from overlapping laser beams led to excitation of the photochromic molecule, spirobenzopyrane, which was molecularly dispersed in a polymeric matrix. The intersection of the two laser beams at different spots in the material led to spatially resolved photochemical changes in the bulk material. The “written” state was sufficiently stable to be accessed or “read” [221].

A variety of media, have explored the use of photoinduced effects such as photochromism, photorefractivity, photobleaching, carbonization, microexplosions, photoluminescence, and photopolymerization as the basis for information storage, while a broad range of microscopy techniques have been used to read the data written in 3D space [219, 223–225]. All these research studies have considered homogeneous recording medium (storage density can be as high as 10^{12} bits/cm³) [219, 223, 225]. In other words, it was either represented by a single-component photosensitive film material or contained low-molecular-weight photosensitive species uniformly dispersed in a film-forming matrix. Siwick et al. [10] reported the use of a hexagonally close-packed (HCP) array of fluorescent particles periodically embedded in an optically inert polymer matrix. Optical recording in the nanocomposite was accomplished by photo bleaching the fluorescent dye incorporated in the particles with a laser confocal fluorescence microscope [10]. However, they showed that their approach did not exploit the periodically modulated optical properties of the nanocomposite since

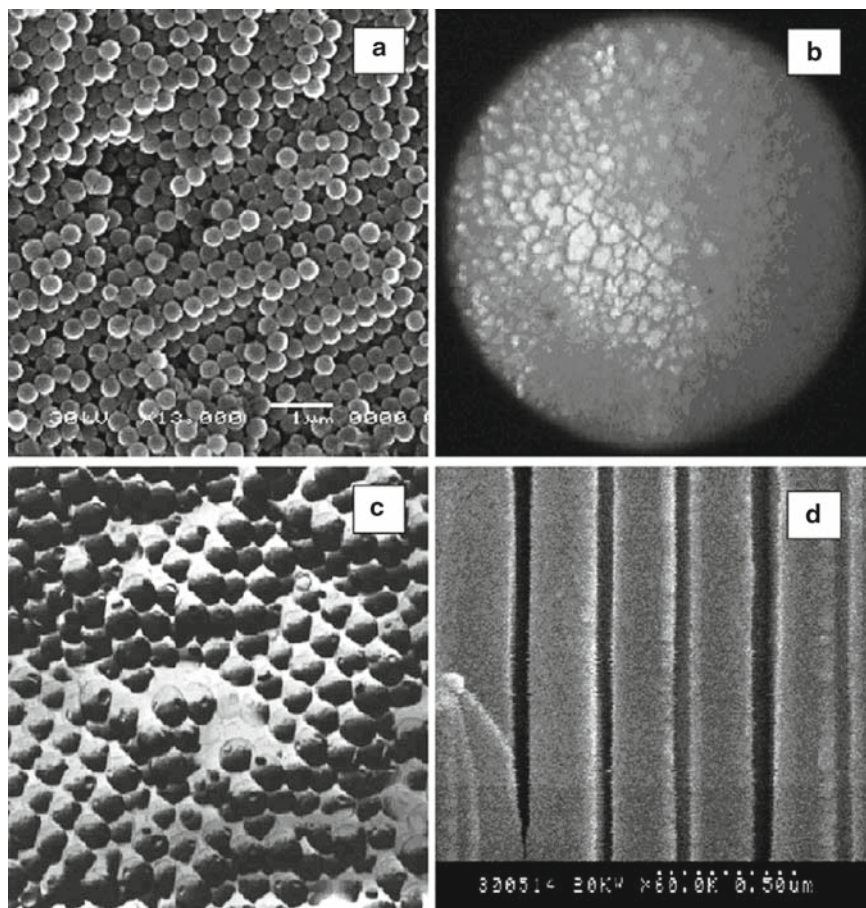


Fig. 6.12 Images of (a) opal matrix, (c) Er³⁺-doped opal matrix, and (d) porous anodic alumina obtained by electron microscopy; (b) image of opal film obtained by optical microscope (Reprinted with permission from [220]. Copyright (2005) Elsevier)

each “written” mark contained up to 500 fluorescent beads. Later, they reported another study in which the full potential of the nanocomposite was realized by using every photo-sensitive core particle as a bit storage bin. Two-photon fluorescent dye excitation was employed to induce local photo-bleaching of the fluorescent microbeads. The effective optical storage density was increased by a factor of two over conventional bulk materials. Figure 6.13 [221] shows the intensity distribution of a bit pattern photo bleached in homogenous material and nanostructured material composed of fluorescent particles.

In general, the major advantages of using nanocomposites in 3D optical data storage applications include [10, 41, 219, 221, 223]:

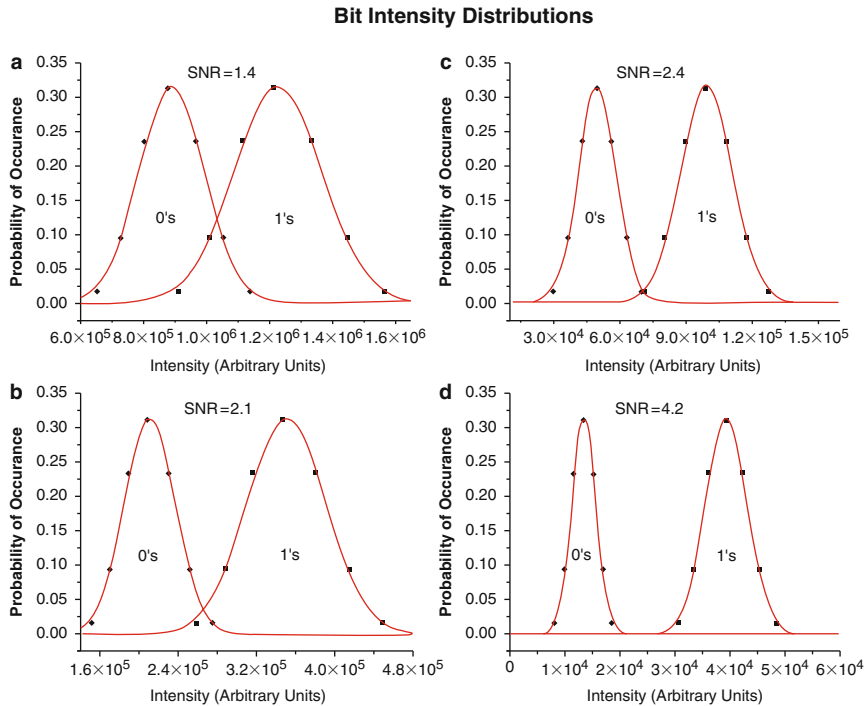


Fig. 6.13 Bit intensity distributions in the material with a homogenous structure (a, b) and the nanostructured material (c, d) (Reprinted with permission from [10]. Copyright (2001) AIP)

- (1) Nanocomposites provide a greater flexibility in the design of new recording media compared to homogeneous materials. The rigid latex cores can be replaced with two-layer particles composing of a fluid core and a thin rigid shell, where the fluid core is synthesized from a low- T_g polymer. Since the high viscosity of polymers above the glass transition temperature imposes a significant barrier to photochemical processes involving molecular rearrangements or bimolecular processes (atomic displacements in general), the photochemical reactions in the fluid cores will occur at higher speeds [227]. Hence, the quantum yield increases significantly in fluid environments and accordingly, the write speed.
- (2) Spatially periodic modulation of the photosensitive material.
- (3) Significant reduction in the cross talk in writing and reading processes that results from the compartmentalization of information carrying domains with respect to optically inert regions, which create “dead space” barriers against cross talk.
- (4) Additional filter mechanism and ability to better tune the photochemistry within composite materials makes nanocomposite polymeric systems highly attractive candidates as future high density optical storage media [221].

Another major application of photopolymers is with respect to the development of holographic data storage devices because of their high sensitivity and large refractive index change [228]. They have been extensively investigated as holographic recording media for many applications, including holographic scanners, LCD displays, helmet-mounted displays, optical interconnects, waveguide couplers, holographic diffusers, narrowband wavelength filters, laser eye protection devices, automotive lighting, and security holograms [226, 228–230].

Holograms are stored in photopolymer materials as spatial modulations of refractive index created in response to an interference pattern generated by incident laser beams. Because of photoreactions, the refractive index of irradiated areas of a material differs from that of dark areas. The bigger the difference in the refractive index between these two regions, the greater will be the data storage capacity of the material. The storage capacity of the material is also enhanced if the medium is thick, as this enables recording of many holograms in a given volume of material and results in improved diffraction efficiency of phase grating (modulated index) [226, 228–230].

Among the photopolymers, an organic–inorganic hybrid film is proposed to yield rigid media with low dimensional changes during holographic recording. Further, optical transparency and ease of film processing with sol–gel solutions for the organic–inorganic hybrids ensure the preparation of a thick film [228]. Many researchers showed that inclusion of nanoparticles contributed to rapid grating build-up and noticeable suppression of polymerization shrinkage, yielding high recording sensitivity and dimensional stability. The grating formation in nanoparticle-dispersed photopolymers is explained in terms of the mutual diffusion of monomer molecules and nanoparticles during holographic exposure because reactive monomer is consumed more in the bright region than in the dark one under holographic illumination and monomer molecules diffuse from the dark to the bright regions due to the difference of chemical potential between the bright and the dark regions. At the same time nanoparticles counter-diffuse from the bright to the dark regions. This is because the chemical potential of nanoparticles becomes higher in the bright region owing to their photo-insensitivity. As a result, compositional and density modulations of the formed polymer and nanoparticles having different refractive indices are spatially created, leading to the formation of a refractive index modulation (Δn) as large as 10^{-2} [226].

Transparent inorganic oxides such as TiO_2 and ZrO_2 possess refractive indices much higher than those of available monomer and polymeric binder materials (>2) in the visible region: e.g., bulk refractive indices of 2.55 and 2.1 at 589 nm for TiO_2 and ZrO_2 , respectively. Therefore such high-refractive-index inorganic nanoparticles may be used to increase Δn further [226]. In these photopolymer nanocomposite films, holographic recording is achieved through photo-induced refractive index contrast arising from a compositional variation induced by polymerization and the subsequent diffusion of monomers into the polymerized areas (the high-intensity region of irradiation, the bright region) of the film under the constructive and destructive interference of multiwaves [228]. Achieving the desired storage capacity that would make holographic data storage commercially viable (~ 100 bits/ μm^2)

will therefore require developing a large index contrast in thick photopolymer materials [230].

Suzuki et al. proposed holographic photopolymer incorporated with inorganic TiO_2 , SiO_2 and organic (hyperbranched polymer) nanoparticles for permanent volume holographic storage with high diffraction efficiency [220, 231–233]. TiO_2 nanoparticles with an average diameter of 15 nm dispersed in methacrylate photopolymers gave Δn as large as 5.1×10^{-3} and the polymerization shrinkage suppression of approximately 69% was achieved at the nanoparticle concentration of 15 vol%. Sanchez et al. [234] also reported a similar 4 nm (average diameter) TiO_2 nanoparticles dispersed in the mixture of two kinds of acrylate monomers. They performed holographic recording at a wavelength of 351 nm and obtained Δn as large as 15.5×10^{-3} at 633 nm. However the systems reported by both Suzuki et al. and Sanchez et al. suffered scattering losses as high as 20 and 29%, respectively, for the 40 μm film thickness.

Further development of modern optical devices for information storage, transfer, and processing requires a transition from “classical” optical media to materials with quantum-dimensional parameters, in which an interaction of optical radiation with medium on interfaces of the medium play the fundamental role [219]. Such an approach results in considerably modified optical characteristics of materials, in particular, a substantial increase in the optical response of the medium. New possibilities are open for creating advanced devices for telecommunications and other modern industrial segments.

6.2.6 Light Emitting Diodes (LEDs)

LED technology is being used in commercial applications such as small screens for mobile phones and portable digital music players (MP3 players), car radios and digital cameras and also in high resolution micro displays for head-mounted displays. Organic light emitting diodes are found in models of the Sony Walkman and of some of the Sony Ericsson phones, notably the Z610i, as well as most Motorola color cell phones [47].

6.2.6.1 Si-Based Nanocomposite Materials in LEDs:

Efficient visible photoluminescence from etched and as-anodized porous silicon and observation of a blue shift in absorption edge triggered attention on the opto-electronic behavior of nano-sized silicon from the view-points of scientific and technological interests [235]. Fig. 6.14 [2] shows a nanostructured composite of silicon quantum dots in an amorphous matrix. Although Si is the base material of modern microelectronics, unfortunately, it does not efficiently emit light, due to its indirect band gap and the exciton binding energy of a few meV. Photoluminescence (PL) from Si is observed only at low temperature, which makes it impractical for

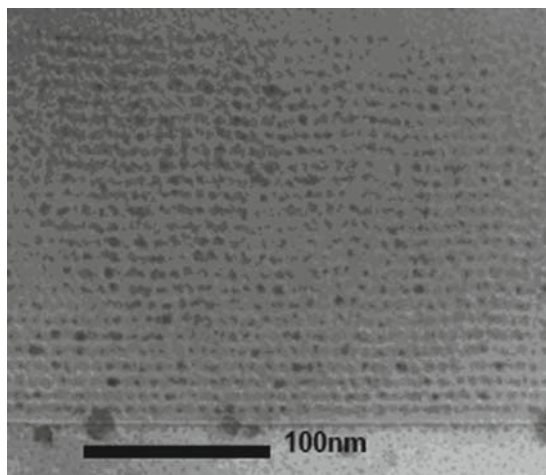


Fig. 6.14 TEM image of nanostructured silicon quantum dots in an amorphous matrix for photovoltaic applications. (Reprinted with permission from [20]. Copyright Proceedings of ACUN-5 International Composites Conference: Developments in Composites: Advanced, Infrastructural, Natural and Nanocomposites, Sydney)

use in optoelectronic circuits and devices. To overcome this problem and to achieve high emission yield from Si, several different systems have been proposed [11, 236–240] and one among such systems is based on nanostructured Si (nanocrystalline and porous Si), where quantum confined effects and exciton localization play a major role in the light emission process [238, 239].

Silicon nanocrystals as a light source had an additional advantage over bulk silicon in that the electrical carriers were confined to a region in which no defects were present due to the fact that the host material (normally SiO_2) ensures an efficient passivation of defects and recombination centers. This opened gates for different systems based on Si and SiO_2 to be investigated, like SiO_2 layers doped with Si nanocrystals [238], Si/ SiO_2 superlattices [11], oxidized porous Si or single nanometer-thick quantum wells of crystalline silicon. Above all, the insulating effect of SiO_2 makes it even difficult to inject electrical charges into Si nanocrystals, and thus efficient light-emitting diodes are troublesome to make. Moreover, large currents passing through an oxide film will eventually make it fail, resulting in a short circuit. Amato et al. [4] proposed a completely different approach to produce Si/ SiO_2 nanocomposites by investigating the possibility of infiltrating Si into porous silicon oxide (PSO) by CVD. PSO in which the pores are interconnected acted as a template for the growth of the Si network so that the complete pore filling gives rise to a percolated Si network inside SiO_2 . The authors reported that the system was absent of consequent effects to porosity such as instability, reactivity, and fragility. Additionally, several alternative ways have been pursued to deal with its inability of Si to luminescence efficiently. Some examples are crystalline silicon doped with rare earth ions, crystallized silicon quantum dots

[240], and porous silicon [239]. Luminescent PS layer (formed by anodic conversion of single-crystal silicon c-Si) consists of highly packed, isolated and/or interconnected silicon nanocrystallites with a mean diameter of 2–3 nm, which is below the critical level for the occurrence of quantum confinement. Koshida and Gelloz [235] reviewed wet and dry porous silicon, their characterization, and properties at greater depth.

In addition, silicon-based materials were also used as hosts for erbium doping. They showed a 1.54 μm emission (falls in the window of maximum transmission for silica-based optical fibers) stimulating both academia and industries on erbium-doped materials. 4f-shell luminescence from erbium-doped crystalline silicon was reported for the first time in 1983 [2], and after that, erbium has been incorporated in numerous other materials. Porous silicon was also used as a host for the incorporation of erbium ions. The ability to manufacture high reflectivity multilayer structures [238], efficient visible photoluminescence [239], and compatibility with standard silicon processes in making integrated optoelectronic devices [11] has attracted porous silicon. The large surface area of nanostructured matrix of porous silicon allows easy infiltration of the ions into the matrix. The structure of porous silicon readily oxidizes, producing large concentrations of oxygen necessary for efficient erbium emission. Different doping techniques have been proposed for porous silicon, such as ion implantation [241], diffusion [242], and electrochemical migration [243]. Among these, cathodic electrochemical migration was preferred because it offers the advantages of deeper erbium penetration (10–20 μm), lower cost, and simplicity of processing. However, erbium-doped crystalline silicon structures were usually prepared by expensive and time consuming processes like ion implantation, epitaxial growth, and chemical vapor deposition, which also require specialized equipment, and limited to very shallow doping profiles [4].

Lopez et al. [244] infiltrated erbium in the pores by cathodic electrochemical migration of the ions followed by high temperature annealing (600–1,100°C) to produce a composite material made of silicon nano-crystals and silicon dioxide. The devices exhibited exponential electroluminescence dependence in both bias conditions (Fig. 6.15 [244]) as a function of the driving current and driving voltage. It was reported that in reverse bias, the external quantum efficiency reached 0.01%; the electroluminescence intensity decreased by a factor of 24 in reverse bias and 2.6 in forward bias when the temperature increased from 240 to 300 K; and the photoluminescence from the erbium-doped micro cavity resonators was enhanced by more than one order of magnitude and tuned to emit in areas where the natural erbium emission was very weak.

6.2.6.2 Polymer-Based Materials in LEDs

Polymers are very promising candidates for cost-effective micro- and nano-photonic devices in optical communication networks, chip-to-chip interconnections and sensors. They have many desirable properties, such as easy fabrication, low production cost, device integration, and compatibility with Si and GaAs fabrication

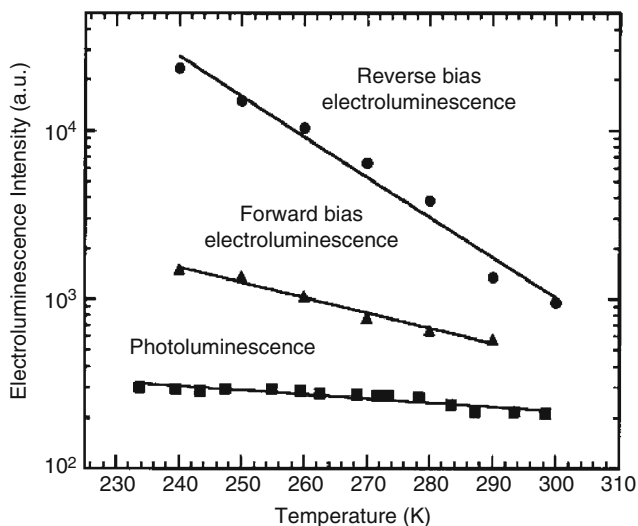


Fig. 6.15 Temperature dependence of photoluminescence and electroluminescence under forward and reverse bias. Data for electroluminescence was taken at a constant current density of 34 mA/cm² (Reprinted with permission from [165]. Copyright (2001) Elsevier)

technologies [245]. They can also be deposited directly on any kind of substrates and tune their optical properties by different combinations of monomers and dopants. Different classes of polymers have been developed for micro-photonics: photosensitive polymers (e.g., polyimides and photoresists), olefins, fluorinated polymers, acrylates, elastomers [245].

π -conjugated polymers are extensively studied for their potential use in light emitting diodes, photovoltaic cells (solar cells), and organic thin-film transistors. Poly(*p*-phenylene vinylene) (PPV) and its derivatives were promising in this regard because of their particular structure and highly interesting electroluminescent, electrical, nonlinear optical and lasing properties [246]. Besides PPV and its derivatives, polyfluorene (PF) and its derivatives are promising conjugated polymers for PLEDs because of their thermal and chemical stability, good solubility, and high fluorescence quantum yields. Despite this, the use of PF and its derivatives for PLED applications has several disadvantages arising from the aggregation and excimer formation and/or thermal oxidation (keto defect), as well as intermolecular cross-linking between PF chains. These include relatively low electroluminescence quantum efficiencies and unstable color purities. Although many approaches were used to overcome these problems, like introducing solubilizing substitutes to control the aggregation, there are still problems like complicated synthesis process and difficult to access fully aromatic materials. Thus, further improvements are still needed to achieve the commercialization of full-color displays [247] demonstrating the need for more stable and efficient conjugated polymers.

An alternate approach to polyaromatics with multiple advantages in terms of ease of synthesis, robustness, versatility in functionality, and high solubility was

reported by Brick et al. [26]. Cubic octasilsesquioxanes novel compounds are used as model catalytic surfaces, molecular catalysts, porous media, NMR standards, fluoride encapsulants, and building blocks for nanocomposite materials. They reported that polybromophenylsilsesquioxane $\text{Br}_{5.3}\text{OPS}$ reacts readily with borates of phenyl, biphenyl, naphthyl, 9,9-dimethylfluorene, and thiophene using standard Suzuki conditions to produce the corresponding polyaromatic and heteroaromatics with complete substitution of all bromines. The resulting materials were completely soluble in a variety of common organic solvents and were also stable at temperatures exceeding 400°C in air. Photoluminescence measurements showed standard aromatic behavior with typical quantum efficiencies [26].

Polyhedral oligomeric silsesquioxanes (POSSs), have unique cube-shaped molecular structure and nanoscale dimensions, and POSS-functionalized organic–inorganic hybrid materials were used as modifiers for nanoparticle applications [247]. POSS-substituted organic–inorganic hybrid PFs were also developed by several groups. Lee et al. [247] reported POSS-pendant PF copolymers and showed that they have higher luminescence, efficiency, and color stability than POSS-free pristine PF. Later, they hypothesized that small amounts of nanoscale POSS attached to the C-9 position of fluorine in PF derivatives would reduce the intermolecular π – π interactions between polymer chains and thus suppress aggregation and thermal oxidative degradation [247]. Also, photoluminescence and electroluminescence studies of POSS-functionalized PF derivatives showed that the inclusion of POSS strongly suppresses the intermolecular aggregation and thermal oxidation and thus, enhanced the light-emitting performance.

Recently, super radiance in PPV and PPV analogues was achieved suggesting the prospect of polymer semiconductor lasers [246]. PPV exhibits a strong two-photon pumped up-conversion emission when excited by near-IR laser pulses of 800 nm, which also opens up another prospect, upconversion lasing [246]. PPV is traditionally made by a base catalyzed reaction of a water-soluble salt monomer precursor. However, many questions and difficulties still remain in spite of the rapidity with which PPV has been developed for electroluminescence applications. It is extremely difficult to achieve a narrow distribution of molecular weight of PPV due to the difficulty in controlling the base-catalyzed reaction and therefore leads to large polymer chains. Moreover, since the final polymer is insoluble, it is difficult to process it in various forms such as a bulk sample or in the form of a blend with other polymers. Lal et al. [246] demonstrated a controlled, nanoscale polymerization of the PPV monomer conducted within the size-controlled cavity of reverse micelles, which yields processable PPV. These PPV analogues (oligomers) were also readily processed through dispersion to prepare polymer blends. Figure 6.16 [246] shows the Fluorescence emission from poly(*p*-phenylenevinylene) of different conjugation lengths synthesized within reverse micelles. Ho et al. [248] demonstrated that PPV- SiO_2 nanocomposites exhibited a composition dependence of refractive index that can be utilized to fabricate all polymer photonic structures in the visible-NIR region. They fabricated conjugated polymer distributed Bragg reflectors and micro-cavity light-emitting diodes [176, 248]. In this PPV- SiO_2 system, a very large refractive index contrast was also achieved ($>40\%$). This system also has other advantages such as:

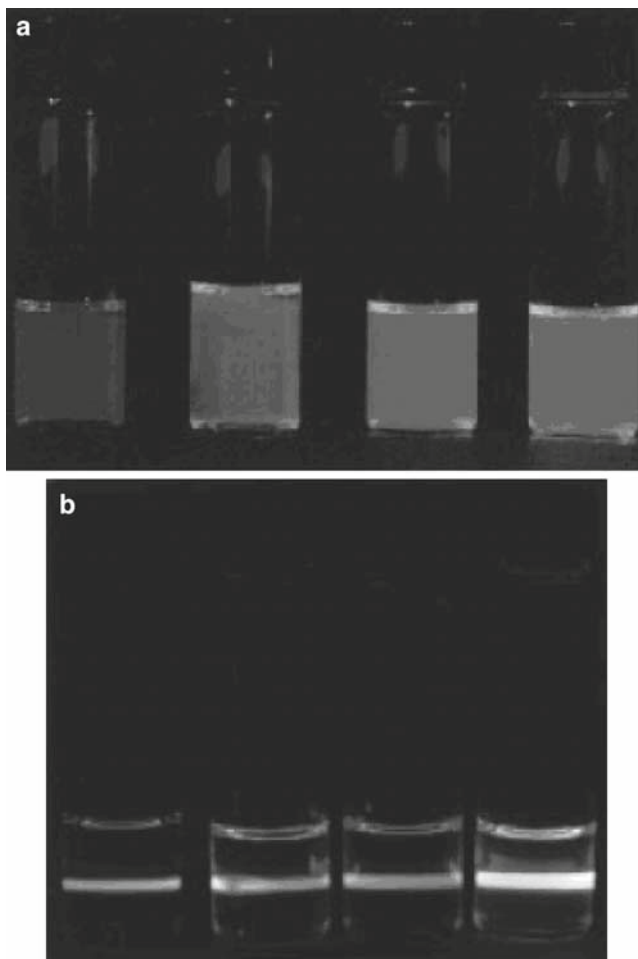


Fig. 6.16 Fluorescence emission from poly(*p*-phenylenevinylene) of different conjugation lengths synthesized within reverse micelles (from left to right: $W_0 = 5, 10, 15, 20$). (a) UV excitation; (b) two-photon excitation at 800 nm (Reprinted with permission from [108]. Copyright (1998) ACS)

- (a) silica is transparent over the key electronic and vibrational bands of PPV, also inert to the acidic thermal elimination reaction that generates PPV,
- (b) silica is a wide band gap insulator (hydrolytic silica is expected to have few chemical defects; e.g., dangling bonds, so neither bulk/surface charge trapping nor excitation energy transfer occurs)
- (c) spectroscopic properties of PPV and its oligomers are well characterized and
- (d) simple repeat structural unit of PPV leads to sharp spectroscopic features that are more sensitive to disorder than those of many other conjugated polymers.

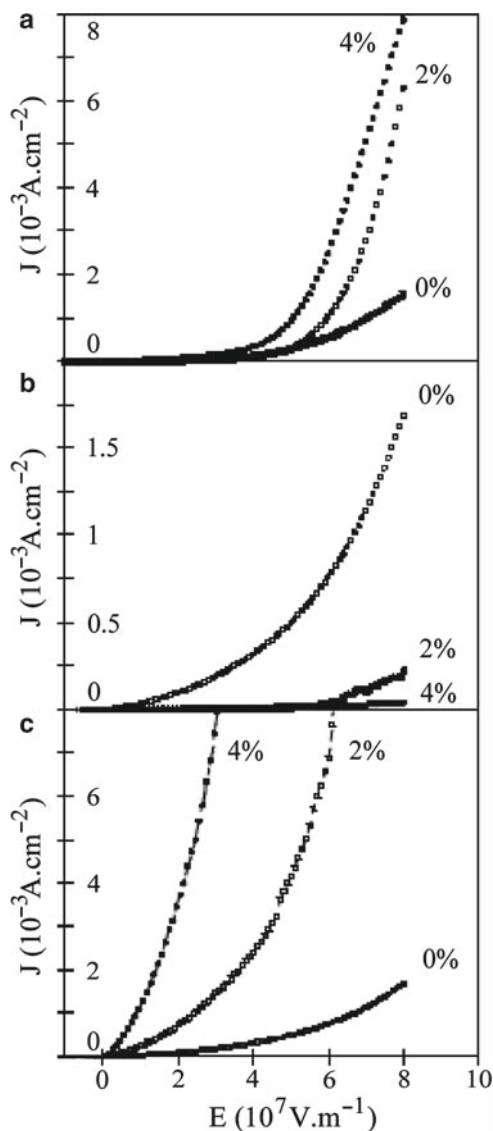
In the light-emitting diodes made of *p*-type polymers such as PPV derivatives, the majority of the carriers of the emissive polymers are holes. It is thus, necessary to

improve the electron injection ability at the interface of the polymer cathode and to block the holes effectively before they reach the cathode, to improve the EL quantum efficiency. For this purpose cathodes with low work function such as Ca and Mg have been employed [247]. Since metals are susceptible to degradation upon exposure to air an inert atmospheric condition is required to deal with them. To overcome this problem, an electron injecting or transporting layer or an insulating layer such as Al_2O_3 and LiF were employed for the stable and efficient EL device with an Al cathode. Later, the EL device with Al cathode was greatly improved by the post-deposition annealing above the glass transition temperature of an emitting polymer without any additional layer. A quantum well structure for the charge confinement was also employed to improve the electron-hole recombination rate of the organic EL device by An et al. [249]. In spite of all these efforts, fabrication of multilayer devices by successive spin casting of polymer solutions is not easy. Hence, to commercialize the polymeric EL devices the improvement of device stability was urgently required.

Both chemical and physical methods were used to enhance the performance of PPV-based devices. Using chemical methods, structure of the polymer was changed by adding functional groups to the backbone, thereby improving the solubility or modifying the band gap of the material [250]. Although, the chemical techniques gave good results, they strongly depend on the synthesis of the polymer. Regarding physical methods, the properties of a polymer can be improved by adding "selective" inorganic nanoparticles to the host material and this process is also believed to increase the electrical conduction of the polymer, and in addition, improve its stability. Many researchers have reported nanocomposites of silica/titania nanoparticles with PPV or its derivatives [251, 252]. Silica nanoparticles had a good effect on the conductivity of the polymer host while the titania nanoparticles influenced photovoltaic properties. In both cases, modification of the polymer luminescence was observed. However, contradictory results were reported in very similar materials; for example poly(2-methoxy-5(2'-ethyl) hexoxy-phenylene vinylene) blended with SiO_2 was found to have an improved conductivity as compared to the bare polymer; while PPV with similar nanoparticles showed a lower conductivity than the polymer alone. Lee et al. [251] reported that conjugated polymer layered silicate nanocomposites with high environmental stability against oxygen and moisture showed greatly improved photoluminescence intensity and its EL device also possesses hugely improved external quantum efficiency. Nguyen et al. [252] performed isolation of a conjugated polymer chain within mesoporous silica to control chain conformation and energy migration. It was also reported that the conjugation length of the polymer could be altered by the incorporation of the nanoparticles, modifying its optical and electrical properties [250]. The main consideration here should be that the polymers used in these works were not synthesized by the same technique and the analysis of the results should also mind the quality of the polymer materials.

Yang et al. [250] studied diodes made using PPV/ SiO_2 and PPV/ TiO_2 nanocomposites by depositing the composite thin film onto indium tin oxide (ITO) substrates followed by thermal evaporation of a MgAg cathode of thickness 500 nm. Figure 6.17 [250] represents the current density vs. applied field for devices with different concentrations of PPV/ SiO_2 and PPV/ TiO_2 composites.

Fig. 6.17 Current density vs. applied field in diodes with different nanoparticle concentrations: (a) ITO–PPV/SiO₂ (100 nm)–MgAg; (b) ITO–PPV/SiO₂ (20 nm)–MgAg; (c) ITO–PPV/TiO₂ (20 nm)–MgAg (Reprinted with permission from [137]. Copyright (2005) Elsevier)



The authors reported different behavior patterns in devices of PPV/SiO₂, depending on the particle sizes; for smaller particles, the conductivity of the composite decreased with the increasing concentration, while for larger particles, it increased with the concentration. Qian et al. [253] showed almost forty times increase in photoluminescence from nanotubed titania, compared to that of nanoparticles. This increase was attributed to the translational symmetry in TiO₆ octahedron that remains along the tube axis; and no longer exists around its circumference.

Since nanoparticles and nanotubes have different characteristics of surface area, morphology, etc, the changes in the electronic band structure resulted in increasing luminescence of titania nanotubes. They also reported blue electroluminescence from titania nanotubes [253] doped into a poly (2-methoxy-5-(2-ethyl hexyloxy)-*p*-phenylene vinylene) (MEH-PPV) matrix which directly comes from band to band transitions of titania nanotubes. The onset voltages of the polymer light-emitting diodes were lowered after doping with titania nanotubes and the doped devices gave higher current compared with the undoped ones. Figure 6.18 [253] shows the normalized EL spectra of the PLEDs.

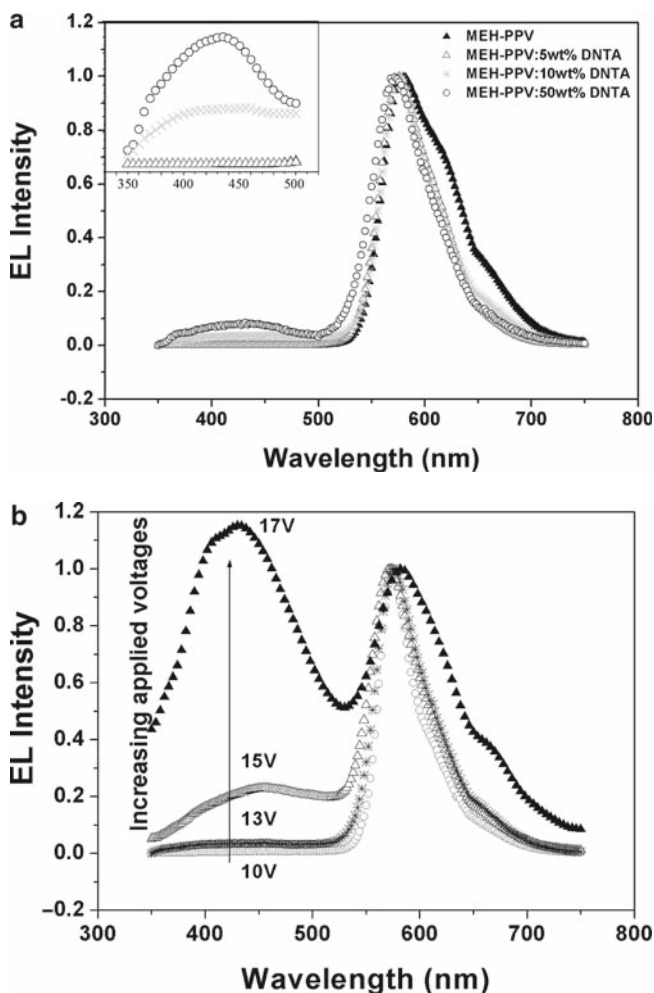


Fig. 6.18 (a) Normalized EL spectra of PLEDs with different concentrations of titania nanotubes (applied voltages at 13 V). (b) Normalized EL spectra of PLEDs doped with titania nanotubes at weight ratio 10 wt% under different applied voltages (Reprinted with permission from [31]. Copyright (2006) Institute of Physics)

Effective charge confinement of the nanocomposite devices plays a critical role in improving the luminescent efficiency. Lee et al. [254] determined the charge (electronic and ionic) carrier mobility of the LED made of nanostructured polymer/clay composites by measuring pulsed- and steady-state transient EL. The authors reported that the clay within the nanocomposite acted as a barrier against both electronic and ionic charges. Figure 6.19 [254] represents the transient current and EL as a function of time of different devices for a steady state electric field.

Furthermore, conducting polymer nanostructures not only have advantages/applications in light emitting diodes, but also in various other electronic devices such as flexible electronic circuits, field effect transistors and so on due to their ease of controlling the conductivity (from insulator to conductor) by changing the doping level. However, Lewis acid a commonly used dopant is reactive enough to damage the electronic devices limiting long lifetime and device stability. On the other hand,

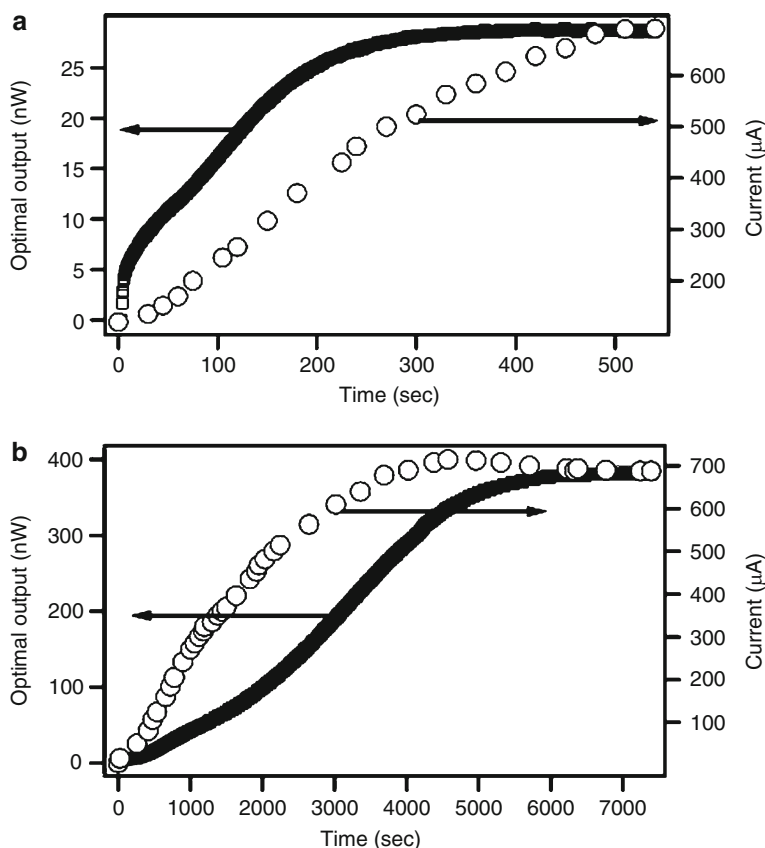


Fig. 6.19 Transient current and EL as a function of time while applying a steady state electric field (9.5×10^7 V/m). (a) ITO/MEH-PPV/Al; (b) ITO/(MEH-PPV/Clay)/Al (Reprinted with permission from [201]. Copyright (2001) Elsevier)

small organic compounds have been applied to the semiconductors capable of being fabricated into thin-film transistor (TFT). Examples include oligothiophenes, substituted naphthalenes, phthalocyanines, and pentacene. The conduction mechanism for these classes of organic semiconductors involves charge transport across π electrons in these molecules. Most of them are known to carry electrons by positive charge (hole). Triphenylamine derivatives such as *N,N'*-bis-(4-methylphenyl)-*N,N'*-diphenylbenzidine (TPD), transport hole were used as organic conductors or in organic electroluminescence devices. A new method to fabricate semi-conductor by solution process based on the composite of organic hole transporting compound, TPD, and titanium dioxide (TiO_2) nanoparticles by sol-gel process was reported by Yokozumi et al. [255]. The conductivity of the composite increased up to six orders of magnitude higher than that of TPD itself when TPD was doped with TiO_2 nanoparticles.

In sum, multifunctional polymers (exhibiting simultaneously more than one property) are a new generation of materials that hold considerable promise for numerous applications in the field of electronics and photonics [246]. Manipulation of molecular architecture and the morphology at nano level provides a powerful approach to control the electronic and optical properties of a material as well as its processability. So far, most of the research was carried out on inorganic semiconductors in the design and preparation of quantum confined structures such as quantum dots, quantum wires, and quantum wells [246]. Electron-hole pairs can be quantum confined to control the band gap of materials by the correct choice of physical sizes. In case of inorganic materials (semi-conductors and metal clusters) the electronic and photonic properties, which are strongly dependent on their band gaps, are well documented. However, nano-scale processing of polymers in a restricted geometry to produce quantum confined structures and composites is less explored. By tuning the morphologies, band gaps, and charge-transport properties of these polymers, device stabilities have been increased, and emitters at a wide variety of wavelengths have been fabricated [246, 251, 254, 256, 257].

6.2.7 Miscellaneous Applications

6.2.7.1 Ultra Large Scale Integration (ULSI) Devices

Multilayer polymer ceramic structures are important for many applications such as the need for thin film polymers for electronic packaging, coatings, passivation layers, lubrication, biocompatible materials, and intermetallic dielectrics for ULSI devices. [258]. A major need exists to replace silicon dioxide with a low dielectric constant material such as a polymer to reduce RC-delay and cross-talk in integrated circuits. However, to realize this goal both synthesis techniques and a fundamental understanding of polymer thin films are needed. Different integration schemes were proposed which used SiO_2 and functionalized poly(*p*-xylylene) derivatives to take advantage of silica's good adhesion properties and thermal stability while also

taking advantage of the polymer's low dielectric constant, which would ultimately reduce the RC-delay in ULSI devices [258, 259]. The presence of SiO_2 specific interactions and physical confinement causes thin film polymers to have more complex morphology compared to the complex anisotropic morphology of the polymers. Crystallization behavior of the polymer is a noticeable effect of the specific interactions. In this regard ultrathin films of polystyrene (formed by spin casting/coating technique) on H-terminated Si and on native oxide silicon have been studied and it was reported that they exhibited opposite behavior in terms of their glass transition temperature as a function of film thickness [258, 259]. These polymeric films are not advantageous in fabricating ULSI devices due to their low processing throughput, poor conformality, purity incorporation and the presence of casting solvent, which is an environmental concern. Senkevich et al. [258] have deposited both SiO_2 and PPXC (poly (chloro-*p*-xylylene)) polymer layer at near room temperature by thermal CVD. CVD is very promising, but it is not very cost effective. They reported that the introduction of a polymer with SiO_2 raised the refractive index from 1.44 to 1.59 (at 630 nm) and lowered the dielectric constant from 4.0 to 3.30 (at 10 kHz) with a PPXC thickness fraction of ~ 0.80 .

Ezhilvalavan and Tseng [260] reviewed the use of tantalum pentoxide (Ta_2O_5) thin films for ULSI circuits applications. They investigated the deposition of Ta_2O_5 films by reactive sputtering, photo-CVD (chemical vapor deposition) and LPCVD (low pressure CVD) and reported that LPCVD is more appropriate for high density device applications owing to its good step coverage. Also maximum dielectric constant and low leakage current density obtained with LPCVD- Ta_2O_5 films were better than those of other processing methods.

6.2.7.2 Liquid Crystal Displays (LCDs)

Nanocomposites consisting of spatially confined liquid crystals are of great interest due to the prospects of their application in optoelectronic devices, photonic crystals, depolarizers, scattering displays, information storage and recording devices, and windows with adjustable transparency. In these systems, applied external electric field causes switching between the scattering and transparent states, and, under some conditions, these states can be retained after the field switching off. In case of spherical aerosol particles, it was found that the memory effect is achieved due to formation of ordered branched network of the aerosol particles in the liquid crystal matrix. But in the case of anisometric particles of a clay mineral an important contribution for the memory effect can be from the influence of the clay surface on the alignment of adjacent liquid crystal (LC) layers, which can be controlled by the application of hydrophobic organic modifier on the clay mineral.

The effect of modification of the montmorillonite (MMT) clay mineral with different organic surfactant ions on the electro-optical properties of the MMT + 5CB (4-pentyl-4'-cyanobiphenyl nematic liquid crystal) heterogeneous LC-clay nano systems have been studied by Chashechnikova et al. [261]. Using IR and Raman

spectroscopy techniques, it was shown that in the LC-clay nanocomposites consisting of organically modified MMT and 5CB, mutual influence of 5CB molecules and the clay particles occurred that resulted in the ordering of the near-surface layers of both inorganic and organic components of the composites. Because of this Van der Waals interaction, the system became transparent under the action of electrical field, and preserved the transparent state when the voltage was switched-off, i.e., the contrast and electro-optical memory effect were observed. They also reported that the use of polar additive (acetone) for preparation of the nanocomposite increases the uniformity of the composites and considerably improves their electro-optical properties.

6.2.7.3 Flat Panel Displays

The velocity of electrons approaching the speed of light ($3 \times 10^8 \text{ ms}^{-1}$) in vacuum is limited to only a saturation velocity of 10^5 ms^{-1} in solids by lattice scattering; thus, making vacuum electronic devices attractive for high speed and high frequency applications [262]. Conventional vacuum electronic devices use electrons liberated by thermionic emission from hot filaments that are large and need much energy in heating up the filament. So, replacing the thermionic cathode by a cold cathode (uses field emission, FE, electrons where the electrons are liberated by tunneling from the cathode material at room temperature under intense electric field) can reduce the size of the device and also improve the power efficiency. Cold electron FE materials, with low threshold fields, are seen as potential candidates for flat panel displays (FPD). Some of the novel cold field emission materials include metallic-dielectric nanocomposites such as resin-carbon coatings [263, 264] graphitic clusters embedded in amorphous carbon (a-C) films, metal doped a-C films and metal implanted SiC layers [264]. Due to a local electric field enhancement by virtue of the electrical inhomogeneity between nano-sized conductive clusters and insulating dielectric matrix, these materials have excellent field emission properties and very low threshold fields for electron emission, smaller than $20 \text{ V}/\mu\text{m}$ compared to several thousand volts per micron values of flat metallic cathodes.

Tsang et al. [264] have studied the electron field emission properties of the Ag-SiO₂ nanocomposite layers. Threshold fields as low as $13 \text{ V}/\mu\text{m}$ was reported. Figure 6.20 [264] shows the electron field emission characteristics of the nanocomposite layers at different Ag doses. SiO₂ as a host matrix has the advantages of chemical stability, efficient fabrication process by thermal oxidation, and fast well characterized etching process of SiO₂ which is convenient to create differently patterned FE devices. Ag has excellent electrical and thermal conductivities (beneficial in FE device applications), does not react chemically with the SiO₂ matrix, and the formation of nano-sized pure Ag clusters in silica is possible with small Ag doses ($1 \times 10^{15} \text{ cm}^{-2}$) [264]. Hence, the combination of Ag-SiO₂ has the added benefit that the whole fabrication process is compatible with existing IC technology and thus the nanocomposite layers as the cathode material for vacuum microelectronic devices take advantage of the possibility for integrating the devices with other circuit elements on a single chip.

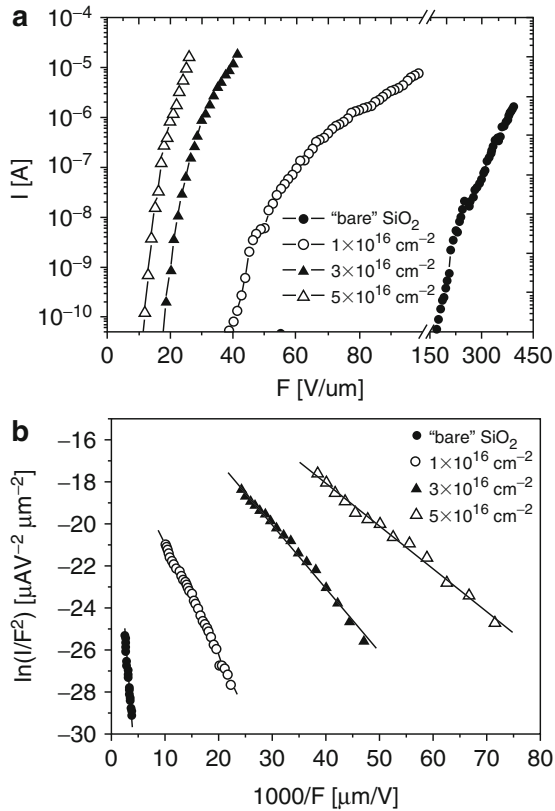


Fig. 6.20 Electron field emission characteristics of samples implanted with various Ag doses. (a) I - F characteristics and (b) the corresponding Fowler-Nordheim plots (Reprinted with permission from [175]. Copyright (2005) Elsevier)

6.3 Summary

In this chapter, we discussed the material aspects of some of the nanocomposites used in different electronic applications as: embedded capacitors, integrated circuits, lithium ion batteries, transistors, light emitting diodes, ULSI devices, LCDs, and flat panel displays. The potential of these hybrid materials has been realized in various modern day applications like: iMac G5 by Apple[®] Inc., OLEDs (Nanohorizons[®], Motorola[®], NUVUE AM55OL by Eastman Kodak[®], Dupont[®], Samsung[®], Sony[®] corporation, Universal display corporation[®], RiT display corporation[®]), Pioneer[®] organic electro luminescent display (OEL), Sanyo[®] OEL display, surface conduction electron emitter display by Canon[®], television display coating by ecology coatings[®], and in processors (Athlon[®] AMD[™] 64 FX, AMD[™] Athlon[®] 64 X2 dual-core, IBM power PC 970 FX/970 MP, Intel[®] Celeron[®] 4, Intel[®] Core[™] duo, Intel[®] Pentium[®] 4, Intel[®] Pentium[®] D) [22, 265].

Nonetheless, it is evident from this review and the unwanted break downs in consumer electronics that more studies should be focused towards the fundamental understanding of these materials. Recall that with increasing ceramic loading, the dielectric constant of polymer/ceramic nanocomposite materials was increased for embedded capacitor applications, but the role of processing methods and conditions, filler size, shape, orientation, dispersion, percolation, and crystal structure are still not very clear. Likewise, nanoparticle dispersion is another critical issue that controls the use of these materials for commercial applications. Although, the research work discussed in this review is mainly oriented in terms of electronic behavior of the nanocomposites, it is very important to consider other properties of these materials (mechanical, thermal, rheological, or any combination there-of) in order to preserve the structural integrity of the material as a whole.

Acknowledgments S.K. Samudrala acknowledges University of New South Wales for the Visiting Fellow Position in the School of Materials Science and Engineering. Permissions from various publishers and authors to reproduce tables and figures in the manuscript are much appreciated.

References

1. Baibarac M, Gomez-Romero P (2006) Nanocomposites based on conducting polymers and carbon nanotubes: from fancy materials to functional applications. *Journal of Nanoscience and Nanotechnology* 6:289–302
2. Green MA (2006) Synthesizing semiconducting material using silicon – a nanostructured composite of silicon quantum dots in an amorphous matrix. In: Bandyopadhyay S, Berndt CC, Rizkalla S, Gowripalan N, Matisons J, Zeng Q (eds) ACUN-5 International Composites Conference: Developments in Composites: Advanced, Infrastructural, Natural and Nanocomposites Sydney, pp 513–518
3. Sanchez C, Julian B, Belleville P, Popall M (2005) Applications of hybrid organic-inorganic nanocomposites. *Journal of Materials Chemistry* 15:3559–3592
4. Amato G, Borini S, Rossi AM, Boarino L, Rocchia M (2005) Si/SiO₂ nanocomposite by CVD infiltration of porous SiO₂. *Physica Status Solidi A-Applications and Materials Science* 202:1529–1532
5. Baibarac M, Baltog I, Lefrant S, Mevellec JY, Chauvet O (2003) Polyaniline and carbon nanotubes based composites containing whole units and fragments of nanotubes. *Chemistry of Materials* 15:4149–4156
6. Besenhard JO, Hess M, Komenda P (1990) Dimensionally stable Li-alloy electrodes for secondary batteries. *Solid State Ionics* 40–41:525–529
7. Bhattacharya A, Ganguly KM, De A, Sarkar S (1996) A new conducting nanocomposite – PPy-zirconium(IV) oxide. *Materials Research Bulletin* 31:527–530
8. Bhattacharya SK, Tummala RR (2001) Integral passives for next generation of electronic packaging: application of epoxy/ceramic nanocomposites as integral capacitors. *Microelectronics Journal* 32:11–19
9. Caseri WR (2006) Nanocomposites of polymers and inorganic particles: preparation, structure and properties. *Materials Science and Technology* 22:807–817
10. Siwick BJ, Kalinina O, Kumacheva E, Dwayne Miller RJ, Noolandi J (2001) Polymeric nanostructured material for high-density three-dimensional optical memory storage. *Journal of Applied Physics* 90:5328–5334
11. Lockwood DJ, Lu ZH, Baribeau JM (1996) Quantum confined luminescence in Si/SiO₂ superlattices. *Physical Review Letters* 76:539–541

12. (a) Kim DS, Lee T, Geckeler KE (2006) Hole-doped single-walled carbon nanotubes: ornamenting with gold nanoparticles in water. *Angewandte Chemie (International ed. in English)* 45: 104–107
12. (b) Mahima S, Chaki NK, Sharma J, Kakade BA, Pasricha R, Rao AM, Vijayamohan K (2006) Electrochemical organization of monolayer protected gold nanoclusters on single-walled carbon nanotubes: Significantly enhanced double layer capacitance. *Journal of Nanoscience and Nanotechnology* 6:1387–1391
13. Merhari L, Belorgeot C, Moliton JP (1990) Etch rate modeling for ion-irradiated nitrocellulose. *Applied Physics Letters* 57:2785–2787
14. Merhari L, Moliton JP, Belorgeot C (1990) Fourier-transform infrared study of ion irradiated nitrocellulose. *Journal of Applied Physics* 68:4837–4845
15. Merhari L, Lehue C, Belorgeot C, Bahna Z (1991) Ion-implantation profile modeling of nitrocellulose coated substrates. *Applied Physics Letters* 59:2856–2858
16. Merhari L, Belorgeot C, Moliton JP (1991) Ion irradiation induced effects in polyamidoimide. *Journal of Vacuum Science & Technology B* 9:2511–2522
17. Merhari L, Belorgeot C, Quintard P (1994) Helium ion-irradiated polyamidoimide films – a ft-ir and raman follow-up. *Journal of Materials Science Letters* 13:286–288
18. Merhari L, Gonsalves KE, Hu Y, He W, Huang WS, Angelopoulos M, Bruenger WH, Dzionk C, Torkler M (2002) Nanocomposite resist systems for next generation lithography. *Microelectronic Engineering* 63:391–403
19. Ogitani S, Bidstrup-Allen SA, Kohl PA (2000) Factors influencing the permittivity of polymer/ceramic composites for embedded capacitors. *IEEE Transactions on Advanced Packaging* 23:313–322
20. Ago H, Petritsch K, Shaffer MSP, Windle AH, Friend RH (1999) Composites of carbon nanotubes and conjugated polymers for photovoltaic devices. *Advanced Materials* 11:1281–1285
21. Bakueva L, Musikhin S, Sargent EH, Schulz S (2003) Fabrication and investigation of nanocomposites of conducting polymers and GaSb nanocrystals. *Surface Science* 532:828–831
22. http://www.intel.com/technology/silicon/65nm_technology.htm.
23. Amos SW, James MR (1999) *Principles of Transistor Circuits*. Butterworth-Heinemann, Oxford
24. Horowitz, Paul, Hill (1989) *The Art of Electronics*. Cambridge University Press, Winfield
25. Warnes L (1998) *Analogue and Digital Electronics*. Macmillan, New York
26. Brick CM, Ouchi Y, Chujo Y, Laine RM (2005) Robust polyaromatic octasilsesquioxanes from polybromophenylsilsesquioxanes, BrxOPS, via Suzuki coupling. *Macromolecules* 38:4661–4665
27. Kumar S, Pimparkar N, Murthy JY, Alam MA (2006) Theory of transfer characteristics of nanotube network transistors. *Applied Physics Letters* 88:123505 (1–3)
28. Kumar TP, Ramesh R, Lin YY, Fey GTK (2004) Tin-filled carbon nanotubes as insertion anode materials for lithium-ion batteries. *Electrochemistry Communications* 6:520–525
29. Philip B, Xie JI, Abraham JK, Varadan VK (2004) A new synthetic route to enhance polyaniline assembly on carbon nanotubes in tubular composites. *Smart Materials & Structures* 13: N105–N108
30. Torsi L, Cioffi N, Di Franco C, Sabbatini L, Zambonin PG, Blevè-Zacheo T (2001) Organic thin film transistors: from active materials to novel applications. *Solid-State Electronics* 45:1479–1485
31. Yao KJ, Song M, Hourston DJ, Luo DZ (2002) Polymer/layered clay nanocomposites: 2 polyurethane nanocomposites. *Polymer* 43:1017–1020
32. Yao ZL, Braidly N, Botton GA, Adronov A (2003) Polymerization from the surface of single-walled carbon nanotubes – preparation and characterization of nanocomposites. *Journal of the American Chemical Society* 125:16015–16024
33. Ree M, Goh WH, Kim Y (1995) Thin-films of organic polymer composites with inorganic aerogels as dielectric materials – polymer-chain orientation and properties. *Polymer Bulletin* 35:215–222
34. Ree M, Shin TJ, Lee SW (2001) Fully rod-like aromatic polyimides: Structure, properties, and chemical modifications. *Korea Polymer Journal* 9:1–19

35. Ree MH, Yoon JW, Heo KY (2006) Imprinting well-controlled closed-nanopores in spin-on polymeric dielectric thin films. *Journal of Materials Chemistry* 16:685–697
36. Kang S, Leblebici Y (2002) *CMOS Digital Integrated Circuits Analysis & Design*. McGraw-Hill, New York
37. Mead C, Conway L (1980) *Introduction to VLSI systems*. Addison Wesley, Reading, MA
38. Hodges DA, Jackson HG, Saleh R (2003) *Analysis and Design of Digital Integrated Circuits*. McGraw-Hill, New York
39. Rbaey JM, Chandrakasan A, Nikolic B (1996) *Digital Integrated Circuits*. Prentice Hall, Englewood Cliffs, NJ
40. Huelsman LP (1972) *Basic Circuit Theory with Digital Computations*. Prentice-Hall, Englewood Cliffs, NJ
41. Maini AK (1998) *Electronic Projects for Beginners*. Pustak Mahal, India
42. Zorpette G (2005) Super charged: a tiny South Korean company is out to make capacitors powerful enough to propel the next generation of hybrid-electric cars. *IEEE Spectrum* 42:32–37
43. Carpick RW, Sasaki DY, Marcus MS, Eriksson MA, Burns AR (2004) Polydiacetylene films: a review of recent investigations into chromogenic transitions and nanomechanical properties. *Journal of Physics-Condensed Matter* 16:R679–R697
44. Murugaraj P, Mainwaring D, Mora-Huertas N (2006) Thermistor behaviour in a semiconducting polymer-nanoparticle composite film. *Journal of Physics D-Applied Physics* 39:2072–2078
45. Chen WX, Lee JY, Liu ZL (2002) Electrochemical lithiation and de-lithiation of carbon nanotube-Sn₂Sb nanocomposites. *Electrochemistry Communications* 4:260–265
46. batteryuniversity.com.
47. <http://en.wikipedia.org>.
48. Dang ZM, Wang HY, Zhang YH, Qi JQ (2005) Morphology and dielectric property of homogeneous BaTiO₃/PVDF nanocomposites prepared via the natural adsorption action of nanosized BaTiO₃. *Macromolecular Rapid Communications* 26:1185–1189
49. Das D, Chakravorty D (2001) Alternating current conductivity of the interfacial phase in copper oxide-silica gel nanocomposites. *Journal of Materials Research* 16:1047–1051
50. Gonon P, Boudefel A (2006) Electrical properties of epoxy/silver nanocomposites. *Journal of Applied Physics* 99
51. Li L, Takahashi A, Hao JJ, Kikuchi R, Hayakawa T, Tsurumi TA, Kakimoto MA (2005) Novel polymer-ceramic nanocomposite based on new concepts for embedded capacitor application (I). *IEEE Transactions on Components and Packaging Technologies* 28:754–759
52. Misman O, Bhattacharya SK, Erbil A, Tummala RR (2000) PWB compatible high value integral capacitors by MOCVD. *Journal of Materials Science-Materials in Electronics* 11:657–660
53. Pothukuchi S, Li Y, Wong CP (2004) Development of a novel polymer-metal nanocomposite obtained through the route of in situ reduction for integral capacitor application. *Journal of Applied Polymer Science* 93:1531–1538
54. Rao Y, Ogitani S, Kohl P, Wong CP (2002) Novel polymer-ceramic nanocomposite based on high dielectric constant epoxy formula for embedded capacitor application. *Journal of Applied Polymer Science* 83:1084–1090
55. Jillek W, Yung WKC (2005) Embedded components in printed circuit boards: a processing technology review. *International Journal of Advanced Manufacturing Technology* 25:350–360
56. Tummala RR, Rymaszewski EJ, Klopfenstein AG (1999) *Microelectronics Packaging Handbook*. Kluwer, Norwell
57. Clearfield HM, Wijeyesekera S, Logan EA, Luu A, Gieser D, Lin CM, Jing J (1998) Integrated passive devices using Al/BCB thin films. In *Third Advanced Technology on Workshop Integrated Passives Technol*, Denver
58. Cho YH, Park JM, Park YH (2004) Preparation and properties of polyimides having highly flexible linkages and their nanocomposites with organoclays. *Macromolecular Research* 12:38–45
59. Ramesh S, Shutzberg BA, Huang C, Gao J, Giannelis EP (2003) Dielectric nanocomposites for integral thin film capacitors: Materials design, fabrication, and integration issues. *IEEE Transactions on Advanced Packaging* 26:17–24

60. Rao Y, Wong CP (2004) Material characterization of a high-dielectric-constant polymer-ceramic composite for embedded capacitor for RF applications. *Journal of Applied Polymer Science* 92:2228–2231
61. Godovski, Yu D (1995) *Advances in Polymer Science* 119:79–122
62. www.3m.com/us/electronics_mfg/microelectronic_packaging/materials.
63. Rao Y, Yue J, Wong CP (2001) High K polymer-ceramic nano-composite development, characterization and modeling for embedded capacitor RF application. *Proceedings of the Electronic Components Technology Conference*, 1408–1419
64. Kuo DH, Chang CC, Su TY, Wang WK, Lin BY (2004) Dielectric properties of three ceramic/epoxy composites. *Materials Chemistry and Physics* 85:201–206
65. Bidstrup-Allen SA, Kohl PA (2002) *IEEE Transactions on Advanced Packaging* 23:313
66. Vrejoiu I, Pedarnig JD, Dinescu M, Bauer-Gogonea S, Bauerle D (2002) Flexible ceramic-polymer composite films with temperature-insensitive and tunable dielectric permittivity. *Applied Physics A-Materials Science & Processing* 74:407–409
67. Xu J, Bhattacharya S, Moon K, Lu J, Englert B, Wong CP, Pramanik P (2006) Large Area Processable High k Nanocomposite-Based Embedded Capacitors. *IEEE Electronic Components and Technology Proceedings* 56:1520–1532
68. Bai Y, Cheng ZY, Bharti V, Xu HS, Zhang QM (2000) High-dielectric-constant ceramic-powder polymer composites. *Applied Physics Letters* 76:3804–3806
69. Chiteme C, McLachlan DS (2003) ac and dc conductivity, magnetoresistance, and scaling in cellular percolation systems. *Physical Review B* 67(2), pp. 024206.1–024206.18
70. Desurvire E (1994) *Erbium Doped Fiber Amplifiers*. Wiley, New York
71. Kozeki M (2002) The condensor film and its property. *Proceeding of Eighth JIEP Microfabrication Research Report*, 31
72. NEMI (1998) *National Electronics Manufacturing Technology Roadmap*. National Electronics Manufacturing Initiative, Herndon
73. Chahal P, Tummala R, Allen M, Swaminathan M (1999) *IEEE Transactions on Components, Packaging and Manufacturing Technology* B21:184
74. Rao Y, Wong CP (2002) *Proceedings of the Eight International Symposium on Advanced Packaging Materials*, 243
75. Bergman DJ, Stroud D (1992) Physical properties of macroscopically inhomogenous media. *Solid State Physics* 46:147
76. Clerc JP, Giraud G, Laugier JM, Luck JM (1990) *Advances in Physics* 39:191
77. Choi SH, Kim JS, Yoon YS (2004) Fabrication and characterization of SnO₂-RuO₂ composite anode thin film for lithium ion batteries. *Electrochimica Acta* 50:547–552
78. Pecharroman C, Esteban-Betegon F, Bartolome JF, Lopez-Esteban S, Moya JS (2001) New percolative BaTiO₃-Ni composites with a high and frequency-independent dielectric constant (epsilon(r) approximate to 80,000). *Advanced Materials* 13:1541–1544
79. Dang ZM, Shen Y, Nan CW (2002) Dielectric behavior of three-phase percolative Ni-BaTiO₃/polyvinylidene fluoride composites. *Applied Physics Letters* 81:4814–4816
80. Chou YC, Jaw TS (1988) Divergence of dielectric-constant near the percolation-threshold. *Solid State Communications* 67:753–756
81. Chung KT, Sabo A, Pica AP (1982) Electrical permittivity and conductivity of carbon-black polyvinyl-chloride composites. *Journal of Applied Physics* 53:6867–6879
82. Grannan DM, Garland JC, Tanner DB (1981) Critical-behavior of the dielectric-constant of a random composite near the percolation-threshold. *Physical Review Letters* 46:375–378
83. Flandin L, Prasse T, Schueler R, Schulte K, Bauhofer W, Cavaillie JY (1999) Anomalous percolation transition in carbon-black-epoxy composite materials. *Physical Review B* 59: 14349–14355
84. McLachlan DS, Heaney MB (1999) Complex ac conductivity of a carbon black composite as a function of frequency, composition, and temperature. *Physical Review B* 60:12746–12751
85. Bhattacharyya SK, Basu S, DE SK (1975) *Composites Part A-Applied Science and Manufacturing* 9:177

86. Luechinger N, Wendelin JS, Bandyopadhyay S, Heness G (2006) Processing, Structure and Electrical Properties of C/Co-Polymer Nanocomposites. Internal Report ETH Zurich/UNSW/UTS
87. Cho SD, Lee JY, Hyun JG, Paik KW (2004) Study on epoxy/BaTiO₃ composite embedded capacitor films (ECFs) for organic substrate applications. *Materials Science and Engineering B-Solid State Materials for Advanced Technology* 110:233–239
88. Dong LJ, Xiong CX, Chen J, Nan CW (2004) Dielectric behavior of BaTiO₃/PVDF nanocomposites *in-situ* synthesized by the sol-gel method. *Journal of Wuhan University of Technology-Materials Science Edition* 19:9–11
89. Wang J, Guo ZP, Zhong S, Liu HK, Dou SX (2003) Lead-coated glass fibre mesh grids for lead-acid batteries. *Journal of Applied Electrochemistry* 33:1057–1061
90. Wang J, Zhong S, Liu HK, Dou SX (2003) Beneficial effects of red lead on non-cured plates for lead-acid batteries. *Journal of Power Sources* 113:371–375
91. Chen J, Bradhurst DH, Dou SX, Liu HK (1998) Electrode properties of Mg₂Ni alloy ball-milled with cobalt powder. *Electrochimica Acta* 44:353–355
92. Luan B, Liu HK, Dou SX (1997) On the elemental substitutions of titanium-based hydrogen-storage alloy electrodes for rechargeable Ni-MH batteries. *Journal of Materials Science* 32:2629–2635
93. Sadoway DR, Mayes AM (2002) Portable power: advanced rechargeable lithium batteries. *Mrs Bulletin* 27:590–592
94. Liu HK, Wang GX, Guo ZP, Wang JZ, Konstantinov K (2006) Nanomaterials for lithium-ion rechargeable batteries. *Journal of Nanoscience and Nanotechnology* 6:1–15
95. Ng SH, Wang J, Konstantinov K, Wexler D, Chen J, Liu HK (2006) Spray pyrolyzed PbO-carbon nanocomposites as anode for lithium-ion batteries. *Journal of the Electrochemical Society* 153:A787–A793
96. Selvan RK, Kalaiselvi N, Augustin CO, Doh CH, Sanjeevraja C (2006) CuFe₂O₄/SnO₂ nanocomposites as anodes for Li-ion batteries. *Journal of Power Sources* 157:522–527
97. Huggins RA (2002) Alternative materials for negative electrodes in lithium systems. *Solid State Ionics* 152:61–68
98. Winter M, Brodd RJ (2004) What are batteries, fuel cells, and supercapacitors? *Chemical Reviews* 104:4245–4269
99. Scrosati B (1992) Lithium rocking chair batteries – an old concept. *Journal of the Electrochemical Society* 139:2776–2781
100. Besenhard JO, Wagner MW, Winter M, Jannakoudakis AD, Jannakoudakis PD, Theodoridou E (1993) Inorganic film-forming electrolyte additives improving the cycling behavior of metallic lithium electrodes and the self-discharge of carbon lithium electrodes. *Journal of Power Sources* 44:413–420
101. Imanishi N, Kashiwagi H, Ichikawa T, Takeda Y, Yamamoto O, Inagaki M (1993) Charge-discharge characteristics of mesophase-pitch-based carbon-fibers for lithium cells. *Journal of the Electrochemical Society* 140:315–320
102. Ahn JH, Wang GX, Yao J, Liu HK, Dou SX (2003) Tin-based composite materials as anode materials for Li-ion batteries. *Journal of Power Sources* 119:45–49
103. Hibino M, Abe K, Mochizuki M, Miyayama M (2004) Amorphous titanium oxide electrode for high-rate discharge and charge. *Journal of Power Sources* 126:139–143
104. Poizot P, Laruelle S, Grugeon S, Dupont L, Tarascon J-M (2000) *Nature* 407:496–499
105. Sides CR, Martin CR (2005) Nanostructured electrodes and the low-temperature performance of Li-ion batteries. *Advanced Materials* 17:125–128
106. Cheng XQ, Shi PF (2005) Electroless Cu-plated Ni₃Sn₄ alloy used as anode material for lithium ion battery. *Journal of Alloys and Compounds* 391:241–244
107. Kim YU, Lee SI, Lee CK, Sohn HJ (2005) Enhancement of capacity and cycle-life of Sn_{1+delta}P₃ (0 <= delta <= 1) anode for lithium secondary batteries. *Journal of Power Sources* 141:163–166
108. Xie J, Zhao XB, Cao GS, Zhong YD, Zhao MJ, Tu JP (2005) Solvothermal synthesis of nanosized CoSb₂ alloy anode for Li-ion batteries. *Electrochimica Acta* 50:1903–1907

109. Reddy MV, Wannek C, Pecquenard B, Vinatier P, Levasseur A (2003) LiNiVO₄-promising thin films for use as anode material in microbatteries. *Journal of Power Sources* 119:101–105
110. Idota Y, Kubota T, Matsufuji A, Maekawa Y, Miyasaka T (1997) Tin-based amorphous oxide: A high-capacity lithium-ion-storage material. *Science* 276:1395–1397
111. Nishijima M, Takeda Y, Imanishi N, Yamamoto O (1994) Li deintercalation and structural change in the lithium transition metal nitride Li₃FeN₂. *Journal of Solid State Chemistry* 113:205–210
112. Kishore M, Varadaraju UV, Raveau B (2004) Electrochemical performance of LiM₂SnO (M = Fe, In) phases with ramsdellite structure as anodes for lithium batteries. *Journal of Solid State Chemistry* 177:3981–3986
113. Kalaiselvi N, Doh CH, Park CW, Moon SI, Yun MS (2004) A novel approach to exploit LiFePO₄ compound as an ambient temperature high capacity anode material for rechargeable lithium batteries. *Electrochemistry Communications* 6:1110–1113
114. Son JT (2004) Novel electrode material for Li ion battery based on polycrystalline LiNbO₃. *Electrochemistry Communications* 6:990–994
115. Chu YQ, Fu ZW, Qin QZ (2004) Cobalt ferrite thin films as anode material for lithium ion batteries. *Electrochimica Acta* 49:4915–4921
116. Alcantara R, Jaraba M, Lavela P, Tirado JL, Jumas JC, Olivier-Fourcade J (2003) Changes in oxidation state and magnetic order of iron atoms during the electrochemical reaction of lithium with NiFe₂O₄. *Electrochemistry Communications* 5:16–21
117. NuLi YN, Qin QZ (2005) Nanocrystalline transition metal ferrite thin films prepared by an electrochemical route for Li-ion batteries. *Journal of Power Sources* 142:292–297
118. NuLi YN, Chu YQ, Qin QZ (2004) Nanocrystalline ZnFe₂O₄ and Ag-doped ZnFe₂O₄ films used as new anode materials for Li-ion batteries. *Journal of the Electrochemical Society* 151:A1077–A1083
119. Sharma N, Shaju KM, Rao GVS, Chowdari BVR (2003) Iron-tin oxides with CaFe₂O₄ structure as anodes for Li-ion batteries. *Journal of Power Sources* 124:204–212
120. Idota Y, Mishima M, Miyaki Y, Kubota T, Miyasaka T (1994) Canadian Patent Application 2:134
121. Idota Y, Mishima M (1995) Canadian Patent Application 2:143
122. Brousse T, Retoux R, Herterich U, Schleich DM (1998) Thin-film crystalline SnO₂-lithium electrodes. *Journal of the Electrochemical Society* 145:1–4
123. Courtney IA, McKinnon WR, Dahn JR (1999) On the aggregation of tin in SnO composite glasses caused by the reversible reaction with lithium. *Journal of the Electrochemical Society* 146:59–68
124. Goward GR, Leroux F, Power WP, Ouvrard G, Dmowski W, Egami T, Nazar LF (1999) On the nature of Li insertion in tin composite oxide glasses. *Electrochemical and Solid State Letters* 2:367–370
125. Liu W, Huang X, Wang Z, Li H, Chen L (1998) *J. Electrochem. Soc.* 145:59
126. Wolfenstine J, Sakamoto J, Huang CK (1998) Tin oxide tin composite anodes for use in Li-ion batteries. *Journal of Power Sources* 75:181–182
127. Courtney IA, Dahn JR (1997) Electrochemical and in situ X-ray diffraction studies of the reaction of lithium with tin oxide composites. *Journal of the Electrochemical Society* 144:2045–2052
128. Cruz M, Hernan L, Morales J, Sanchez L (2002) Spray pyrolysis as a method for preparing PbO coatings amenable to use in lead-acid batteries. *Journal of Power Sources* 108:35–40
129. Martos M, Morales J, Sanchez L, Ayouchi R, Leinen D, Martin F, Barrado JRR (2001) Electrochemical properties of lead oxide films obtained by spray pyrolysis as negative electrodes for lithium secondary batteries. *Electrochimica Acta* 46:2939–2948
130. Yang J, Winter M, Besenhard JO (1996) Small particle size multiphase Li-alloy anodes for lithium-ion-batteries. *Solid State Ionics* 90:281–287
131. Huggins RA (1999) Lithium alloy negative electrodes. *Journal of Power Sources* 82:13–19
132. Mao O, Turner RL, Courtney IA, Fredericksen BD, Buckett MI, Krause LJ, Dahn JR (1999) Active/inactive nanocomposites as anodes for Li-ion batteries. *Electrochemical and Solid State Letters* 2:3–5

133. Yang J, Wachtler M, Winter M, Besenhard JO (1999) Sub-microcrystalline Sn and Sn-SnSb powders as lithium storage materials for lithium-ion batteries. *Electrochemical and Solid State Letters* 2:161–163
134. Li NC, Martin CR (2001) A high-rate, high-capacity, nanostructured Sn-based anode prepared using sol-gel template synthesis. *Journal of the Electrochemical Society* 148:A164–A170
135. Li NC, Martin CR, Scrosati B (2000) A high-rate, high-capacity, nanostructured tin oxide electrode. *Electrochemical and Solid State Letters* 3:316–318
136. Whitehead AH, Elliott JM, Owen JR (1999) Nanostructured tin for use as a negative electrode material in Li-ion batteries. *Journal of Power Sources* 82:33–38
137. Yang J, Takeda Y, Imanishi N, Yamamoto O (1999) Ultrafine Sn and SnSb_{0.14} powders for lithium storage matrices in lithium-ion batteries. *Journal of the Electrochemical Society* 146:4009–4013
138. Yang J, Takeda Y, Imanishi N, Ichikawa T, Yamamoto O (1999) Study of the cycling performance of finely dispersed lithium alloy composite electrodes under high Li-utilization. *Journal of Power Sources* 79:220–224
139. Che GL, Lakshmi BB, Fisher ER, Martin CR (1998) Carbon nanotubule membranes for electrochemical energy storage and production. *Nature* 393:346–349
140. Dahn JR, Zheng T, Liu YH, Xue JS (1995) Mechanisms for lithium insertion in carbonaceous materials. *Science* 270:590–593
141. Gao B, Kleinhammes A, Tang XP, Bower C, Fleming L, Wu Y, Zhou O (1999) Electrochemical intercalation of single-walled carbon nanotubes with lithium. *Chemical Physics Letters* 307:153–157
142. Guo ZP, Zhao ZW, Liu HK, Dou SX (2005) Electrochemical lithiation and de-lithiation of MWNT-Sn/SnNi nanocomposites. *Carbon* 43:1392–1399
143. Tans SJ, Verschueren ARM, Dekker C (1998) Room-temperature transistor based on a single carbon nanotube. *Nature* 393:49–52
144. Wang GX, Yao J, Liu HK (2004) Characterization of nanocrystalline Si-MCMB composite anode materials. *Electrochemical and Solid State Letters* 7:A250–A253
145. Badway F, Pereira N, Cosandey F, Amatucci GG (2003) Carbon-metal fluoride nanocomposites – structure and electrochemistry of FeF₃:C. *Journal of the Electrochemical Society* 150:A1209–A1218
146. Wang Y, Lee JY (2005) Microwave-assisted synthesis of SnO₂-graphite nanocomposites for Li-ion battery applications. *Journal of Power Sources* 144:220–225
147. Fleischauer MD, Topple JM, Dahna JR (2005) Combinatorial investigations of Si–M (M = Cr plus Ni, Fe, Mn) thin film negative electrode materials. *Electrochemical and Solid State Letters* 8:A137–A140
148. Li H, Huang XJ, Chen LQ, Wu ZG, Liang Y (1999) *Electrochemical and Solid-State Letters* 2:547
149. <http://www.physorg.com/news3061.html>.
150. Nalimova VA, Sklovsky DE, Bondarenko GN, Alvergnat-Gaucher H, Bonnamy S, Beguin F (1997) Lithium interaction with carbon nanotubes. *Synthetic Metals* 88:89–93
151. Claye AS, Fischer JE, Huffman CB, Rinzler AG, Smalley RE (2000) Solid-state electrochemistry of the Li single wall carbon nanotube system. *Journal of the Electrochemical Society* 147:2845–2852
152. Frackowiak E, Gautier S, Gaucher H, Bonnamy S, Beguin F (1999) Electrochemical storage of lithium multiwalled carbon nanotubes. *Carbon* 37:61–69
153. Kim I, Kumta PN, Blomgren GE (2000) Si/TiN nanocomposites – novel anode materials for Li-ion batteries. *Electrochemical and Solid State Letters* 3:493–496
154. Lee KT, Jung YS, Oh SM (2003) Synthesis of tin-encapsulated spherical hollow carbon for anode material in lithium secondary batteries. *Journal of the American Chemical Society* 125:5652–5653
155. Besenhard JO (1999) *Handbook of Battery Materials*. Wiley VCH, Weinheim
156. Fu LJ, Liu H, Zhang HP, Li C, Zhang T, Wu YP, Holze R, Wu HQ (2006) Synthesis and electrochemical performance of novel core/shell structured nanocomposites. *Electrochemistry Communications* 8:1–4

157. Wang GX, Ahn JH, Yao J, Bewlay S, Liu HK (2004) Nanostructured Si-C composite anodes for lithium-ion batteries. *Electrochemistry Communications* 6:689–692
158. Wang GX, Chen Y, Yang L, Yao J, Needham S, Liu HK, Ahn JH (2005) *Journal Power Sources* 146:487
159. Martos M, Morales J, Sanchez L (2003) Lead-based systems as suitable anode materials for Li-ion batteries. *Electrochimica Acta* 48:615–621
160. Yuan L, Konstantinov K, Wang GX, Liu HK, Dou SX (2005) Nano-structured SnO₂-carbon composites obtained by in situ spray pyrolysis method as anodes in lithium batteries. *Journal of Power Sources* 146:180–184
161. Bewlay SL, Konstantinov K, Wang GX, Dou SX, Liu HK (2004) Conductivity improvements to spray-produced LiFePO₄ by addition of a carbon source. *Materials Letters* 58: 1788–1791
162. Yoshio M, Wang HY, Fukuda K, Umeno T, Dimov N, Ogumi Z (2002) Carbon-coated Si as a lithium-ion battery anode material. *Journal of the Electrochemical Society* 149:A1598–A1603
163. Kim Y, Goh WH, Chang T, Ha CS, Ree M (2004) Optical and dielectric anisotropy in polyimide nanocomposite films prepared from soluble poly(amic diethyl ester) precursors. *Advanced Engineering Materials* 6:39–43
164. Yu J, Ree M, Shin TJ, Park YH, Cai W, Zhou D, Lee KW (2000) Adhesion of poly(4,4'-oxydiphenylene pyromellitimide) to copper metal using a polymeric primer: Effects of miscibility and polyimide precursor origin. *Macromolecular Chemistry and Physics* 201:491–499
165. Wu YP, Dai XB, Ma JQ, Chen YJ (2004) *Lithium Ion Batteries – Practice and Applications*. Chemical Industry Press, Beijing
166. Wilson AM, Dahn JR (1995) Lithium Insertion in Carbons Containing Nanodispersed Silicon. *Journal of the Electrochemical Society* 142:326–332
167. Gratz J, Ahn CC, Yazami R, Fultz B, A194. (1999) *Electrochemical Solid-state letters* 6:A 194
168. Ohara S, Suzuki J, Sekine K, Takamura T (2003) Li insertion/extraction reaction at a Si film evaporated on a Ni foil. *Journal of Power Sources* 119:591–596
169. Niu J, Lee JY (2002) *Electrochemical Solid-State Letters* 5:A107
170. Wang CS, Wu GT, Zhang XB, Qi ZF, Li WZ (1998) Lithium insertion in carbon-silicon composite materials produced by mechanical milling. *Journal of the Electrochemical Society* 145:2751–2758
171. Menard E, Lee KJ, Khang DY, Nuzzo RG, Rogers JA (2004) A printable form of silicon for high performance thin film transistors on plastic substrates. *Applied Physics Letters* 84:5398–5400
172. Chan VZH, Hoffman J, Lee VY, Iatrou H, Avgeropoulos A, Hadjichristidis N, Miller RD, Thomas EL (1999) Ordered bicontinuous nanoporous and nanorelief ceramic films from self assembling polymer precursors. *Science* 286:1716–1719
173. Maex K, Baklanov MR, Shamiryani D, Iacopi F, Brongersma SH, Yanovitskaya ZS (2003) Low dielectric constant materials for microelectronics. *Journal of Applied Physics* 93:8793–8841
174. Morgen M, Ryan ET, Zhao JH, Hu C, Cho TH, Ho PS (2000) Low dielectric constant materials for ULSI interconnects. *Annual Review of Materials Science* 30:645–680
175. Semiconductor Industry Association (2004) *International Technology Roadmap for Semiconductors*. Semiconductor Industry Association, San Jose
176. Ho PKH, Friend RH (2002) pi-electronic and electrical transport properties of conjugated polymer nanocomposites: Poly(*p*-phenylenevinylene) with homogeneously dispersed silica nanoparticles. *Journal of Chemical Physics* 116:6782–6794
177. Maier G (2001) Low dielectric constant polymers for microelectronics. *Progress in Polymer Science* 26:3–65
178. Moylan CR, Best ME, Ree M (1991) Solubility of water in polyimides – quartz crystal microbalance measurements. *Journal of Polymer Science Part B-Polymer Physics* 29:87–92
179. Carter KR, DiPietro RA, Sanchez MI, Russell TP, Lakshmanan P, McGrath JE (1997) Polyimide nanofoams based on ordered polyimides derived from poly(amic alkyl esters): PMDA/4-BDAF. *Chemistry of Materials* 9:105–118

180. Carter KR, DiPietro RA, Sanchez MI, Swanson SA (2001) Nanoporous polyimides derived from highly fluorinated polyimide/poly(propylene oxide) copolymers. *Chemistry of Materials* 13:213–221
181. Mikoshiba S, Hayase S (1999) Preparation of low density poly(methylsilsequioxane)s for LSI interlayer dielectrics with low dielectric constant. Fabrication of angstrom size pores prepared by baking trifluoropropylsilyl copolymers. *Journal of Materials Chemistry* 9:591–598
182. Azzam RMA, Bashara NM (1977) *Ellipsometry and Polarized Light*. North-Holland, Amsterdam
183. Licata TJ, Colgan EG, Harper JME, Luce SE (1995) Interconnect fabrication processes and the development of low-cost wiring for CMOS products. *IBM Journal of Research and Development* 39:419–435
184. Lee YJ, Huang JM, Kuo SW, Chang FC (2005) Low-dielectric, nanoporous polyimide films prepared from PEO-POSS nanoparticles. *Polymer* 46:10056–10065
185. Chen GZ, Shaffer MSP, Coleby D, Dixon G, Zhou WZ, Fray DJ, Windle AH (2000) Carbon nanotube and polypyrrole composites: coating and doping. *Advanced Materials* 12:522–526
186. Curran SA, Ajayan PM, Blau WJ, Carroll DL, Coleman JN, Dalton AB, Davey AP, Drury A, McCarthy B, Maier S, Strevens A (1998) A composite from poly(m-phenylenevinylene-co-2,5-dioctoxy-p-phenylenevinylene) and carbon nanotubes: A novel material for molecular optoelectronics. *Advanced Materials* 10:1091–1093
187. Dai L (1999) Effective bandwidths and performance bounds in high-speed communication systems. *Journal of Optimization Theory and Applications* 100:549–574
188. Saito Y, Uemura S, Hamaguchi K (1998) Cathode ray tube lighting elements with carbon nanotube field emitters. *Japanese Journal of Applied Physics Part 2-Letters & Express Letters* 37:L346–L348
189. Downs C, Nugent J, Ajayan PM, Duquette DJ, Santhanam SV (1999) Efficient polymerization of aniline at carbon nanotube electrodes. *Advanced Materials* 11:1028–1031
190. Valter B, Ram MK, Nicolini C (2002) Synthesis of multiwalled carbon nanotubes and poly(o-anisidine) nanocomposite material: Fabrication and characterization of its Langmuir-Schaefer films. *Langmuir* 18:1535–1541
191. Zengin H, Zhou WS, Jin JY, Czerw R, Smith DW, Echegoyen L, Carroll DL, Foulger SH, Ballato J (2002) Carbon nanotube doped polyaniline. *Advanced Materials* 14:1480–1483
192. Coleman JN, Curran S, Dalton AB, Davey AP, McCarthy B, Blau W, Barklie RC (1998) Percolation-dominated conductivity in a conjugated-polymer-carbon-nanotube composite. *Physical Review B* 58:R7492–R7495
193. Lefrant S, Baibarac M, Baltog I, Godon C, Mevellec JY, Wery J, Faulques E, Mihut L, Aarab H, Chauvet O (2005) SERS, FT-IR and photoluminescence studies on single-walled carbon nanotubes/conducting polymers composites. *Synthetic Metals* 155:666–669
194. Woo HS, Czerw R, Webster S, Carroll DL, Park JW, Lee JH (2001) Organic light emitting diodes fabricated with single wall carbon nanotubes dispersed in a hole conducting buffer: the role of carbon nanotubes in a hole conducting polymer. *Synthetic Metals* 116:369–372
195. Kymakis E, Amaratunga GAJ (2002) Single-wall carbon nanotube/conjugated polymer photovoltaic devices. *Applied Physics Letters* 80:112–114
196. Woo HS, Kim YB, Czerw R, Carroll DL, Ballato J, Ajayan PM (2004) Tailoring hole transport in organic light-emitting devices using carbon nanotube-polymer nanocomposites. *Journal of the Korean Physical Society* 45:507–511
197. Star A, Stoddart JF, Steurman D, Diehl M, Boukai A, Wong EW, Yang X, Chung SW, Choi H, Heath JR (2001) Preparation and properties of polymer-wrapped single-walled carbon nanotubes. *Angewandte Chemie-International Edition* 40:1721–1725
198. Qi PF, Javey A, Rolandi M, Wang Q, Yenilmez E, Dai HJ (2004) Miniature organic transistors with carbon nanotubes as quasi-one-dimensional electrodes. *Journal of the American Chemical Society* 126:11774–11775
199. Bachtold A, Hadley P, Nakanishi T, Dekker C (2001) Logic circuits with carbon nanotube transistors. *Science* 294:1317–1320

200. Postma HWC, Teepen T, Yao Z, Grifoni M, Dekker C (2001) Carbon nanotube single-electron transistors at room temperature. *Science* 293:76–79
201. Yao Z, Dekker C, Avouris P (2001) Carbon Nanotubes. 80:147–171
202. Duan XF, Huang Y, Lieber CM (2002) *Nano Letters* 2:487–490
203. Ouyang M, Huang JL, Cheung CL, Lieber CM (2001) *Science* 291:97–100
204. Rueckes T, Kim K, Joselevich E, Tseng GY, Cheung CL, Lieber CM (2000) *Science* 289:94–97
205. Avouris P (2002) Molecular Electronics with Carbon Nanotubes. *Accounts of Chemical Research* 35:1026–1034
206. Liu J, Rinzler AG, Dai HJ, Hafner JH, Bradley RK, Boul PJ, Lu A, Iverson T, Shelimov K, Huffman CB, Rodriguez-Macias F, Shon YS, Lee TR, Colbert DT, Smalley RE (1998) Fullerene pipes. *Science* 280:1253–1256
207. Banerjee S, Wong SS (2002) Functionalization of carbon nanotubes with a metal-containing molecular complex. *Nano Letters* 2:49–53
208. Banerjee S, Wong SS (2002) Structural characterization, optical properties, and improved solubility of carbon nanotubes functionalized with Wilkinson’s catalyst. *Journal of the American Chemical Society* 124:8940–8948
209. Banerjee S, Wong SS (2002) Synthesis and characterization of carbon nanotube-nanocrystal heterostructures. *Nano Letters* 2:195–200
210. Dimitrakopoulos CD, Mascaro DJ (2001) Organic thin-film transistors: a review of recent advances. *IBM Journal of Research and Development* 45:11–27
211. Lodha A, Singh R (2001) Prospects of manufacturing organic semiconductor-based integrated circuits. *IEEE Transactions on Semiconductor Manufacturing* 14:281–296
212. Martel R, Schmidt T, Shea HR, Hertel T, Avouris P (1998) Single- and multi-wall carbon nanotube field-effect transistors. *Applied Physics Letters* 73:2447–2449
213. Ramamurthy PC, Malshe AM, Harrell WR, Gregory RV, McGuire K, Rao AM (2004) Polyaniline/single-walled carbon nanotube composite electronic devices. *Solid-State Electronics* 48:2019–2024
214. Kuo CT, Chiou WH (1997) Field-effect transistor with polyaniline thin film as semiconductor. *Synthetic Metals* 88:23–30
215. Javey A, Guo J, Paulsson M, Wang Q, Mann D, Lundstrom M, Dai HJ (2004) High-field quasiballistic transport in short carbon nanotubes. *Physical Review Letters* 92(10):106804/1–4
216. Snow ES, Novak JP, Lay MD, Houser EH, Perkins FK, Campbell PM (2004) Carbon nanotube networks: Nanomaterial for macroelectronic applications. *Journal of Vacuum Science & Technology B* 22:1990–1994
217. Seidel R, Graham AP, Unger E, Duesberg GS, Liebau M, Steinhögl W, Kreupl F, Hoenlein W (2004) High-current nanotube transistors. *Nano Letters* 4:831–834
218. Seidel RV, Graham AP, Rajasekharan B, Unger E, Liebau M, Duesberg GS, Kreupl F, Hoenlein W (2004) Bias dependence and electrical breakdown of small diameter single-walled carbon nanotubes. *Journal of Applied Physics* 96:6694–6699
219. Tsvetkov MY, Kleshcheva SM, Samoilovich MI, Gaponenko NV, Shushunov AN (2005) Erbium photoluminescence in opal matrix and porous anodic alumina nanocomposites. *Microelectronic Engineering* 81:273–280
220. Suzuki N, Tomita Y (2003) Diffraction properties of volume holograms recorded in SiO₂ nanoparticle-dispersed methacrylate photopolymer films. *Japanese Journal of Applied Physics Part 2-Letters* 42:L927–L929
221. Siwick BJ, Kalina O, Kumacheva E, Miller RJD, Noolandi J (2001) Polymeric nanostructured material for high-density three-dimensional optical memory storage. *Journal of Applied Physics* 90:5328–5334
222. Parthenopoulos DA, Rentzepis PM (1989) *Science* 245:843
223. Caruso RA, Antonietti M (2001) Sol–gel nanocoating: an approach to the preparation of structured materials. *Chemistry of Materials* 13:3272–3282

224. Kawata S, Kawata Y (2000) Three-dimensional optical data storage using photochromic materials. *Chemical Reviews* 100:1777–1788
225. Malini KA, Anantharaman MR, Sindhu S, Chinnasamy CN, Ponpandian N, Narayanasamy A, Balachandran M, Pillai VNS (2001) Effect of cycling on the magnetization of ion exchanged magnetic nanocomposite based on polystyrene. *Journal of Materials Science* 36:821–824
226. Suzuki N, Tomita Y (2006) Highly transparent ZrO₂ nanoparticle-dispersed acrylate photopolymers for volume holographic recording. *Optics Express* 14:12712–12719
227. Kalinina O, Kumacheva E (2001) Nanostructured polymer films with liquid inclusions. 1. Structural blocks. *Macromolecules* 34:6380–6386
228. Kim E, Park J, Shin C, Kim N (2006) Effect of organic side-chains on the diffraction efficiency of an organic-inorganic hybrid nanocomposite film. *Nanotechnology* 17:2899–2906
229. Judeinstein P, Oliveira PW, Krug H, Schmidt H (1997) Photochromic organic-inorganic nanocomposites as holographic storage media. *Advanced Materials for Optics and Electronics* 7:123–133
230. Trentler TJ, Boyd JE, Colvin VL (2000) Epoxy resin-photopolymer composites for volume holography. *Chemistry of Materials* 12:1431–1438
231. Suzuki N, Tomita Y (2004) Silica-nanoparticle-dispersed methacrylate photopolymers with net diffraction efficiency near 100%. *Applied Optics* 43:2125–2129
232. Suzuki N, Tomita Y, Kojima T (2002) Holographic recording in TiO₂ nanoparticle-dispersed methacrylate photopolymer films. *Applied Physics Letters* 81:4121–4123
233. Tomita Y, Nishibiraki H (2003) Improvement of holographic recording sensitivities in the green in SiO₂ nanoparticle-dispersed methacrylate photopolymers doped with pyromethene dyes. *Applied Physics Letters* 83:410–412
234. Sanchez C, Escuti MJ, van Heesch C, Bastiaansen CWM, Broer DJ, Loos J, Nussbaumer R (2005) TiO₂ nanoparticle-photopolymer holographic recording. *Advanced Functional Materials* 15:1623–1629
235. Koshida N, Gelloz B (1999) Wet and dry porous silicon. *Current Opinion in Colloid & Interface Science* 4:309–313
236. Altukhov PD, Kuzminov EG (1999) Condensation of a hot electron-hole plasma in tunneling silicon MOS structures. *Solid State Communications* 111:379–384
237. Green MA, Zhao JH, Wang AH, Reece PJ, Gal M (2001) Efficient silicon light-emitting diodes. *Nature* 412:805–808
238. Pavese L, Dal Negro L, Mazzoleni C, Franzo G, Priolo F (2000) Optical gain in silicon nanocrystals. *Nature* 408:440–444
239. Simons AJ, Cox TI, Loni A, Canham LT, Blacker R (1997) Investigation of the mechanisms controlling the stability of a porous silicon electroluminescent device. *Thin Solid Films* 297:281–284
240. Sticht A, Neufeld E, Luigart A, Brunner K, Abstreiter G, Bay H (1998) Characteristics of surface and waveguide emitting SiGe: Er: O diodes. *Journal of Luminescence* 80:321–327
241. Amato G, Boarino L, Midellino D, Rossi AM (2000) *Philosophical Magazine B* 80:679
242. Lu ZH, Grozea D (2002) Crystalline Si/SiO₂ quantum wells. *Applied Physics Letters* 80:255–257
243. Parisini A, Angelucci R, Dori L, Poggi A, Maccagnani P, Cardinali GC, Amato G, Lerondel G, Midellino D (2000) TEM characterisation of porous silicon. *Micron* 31:223–230
244. Lopez HA, Fauchet PM (2001) Infrared LEDs and microcavities based on erbium-doped silicon nanocomposites. *Materials Science and Engineering B-Solid State Materials for Advanced Technology* 81:91–96
245. Cristea D, Obreja P, Kusko M, Manea E, Rebigan R (2006) Polymer micromachining for micro- and nanophotonics. *Materials Science & Engineering C-Biomimetic and Supramolecular Systems* 26:1049–1055
246. Lal M, Kumar ND, Joshi MP, Prasad PN (1998) Polymerization in a reverse micelle nano-reactor: Preparation of processable poly(*p*-phenylenevinylene) with controlled conjugation length. *Chemistry of Materials* 10:1065–1068

247. Lee J, Cho HJ, Cho NS, Hwang DH, Kang JM, Lim E, Lee JI, Shim HK (2006) Enhanced efficiency of polyfluorene derivatives: Organic-inorganic hybrid polymer light-emitting diodes. *Journal of Polymer Science Part A-Polymer Chemistry* 44:2943–2954
248. Ho PKH, Kim JS, Tessler N, Friend RH (2001) Photoluminescence of poly(*p*-phenylenevinylene)-silica nanocomposites: Evidence for dual emission by Franck-Condon analysis. *Journal of Chemical Physics* 115:2709–2720
249. An HY, Chen BJ, Hou JY, Shen JC, Liu SY (1998) Exciton confinement in organic multiple quantum well structures. *Journal of Physics D-Applied Physics* 31:1144
250. Yang SH, Nguyen TP, Le Rendu P, Hsu CS (2005) Optical and electrical investigations of poly(*p*-phenylene vinylene)/silicon oxide and poly(*p*-phenylene vinylene)/titanium oxide nanocomposites. *Thin Solid Films* 471:230–235
251. Lee TW, Park OO, Kim JJ, Hong JM, Kim YC (2001) Efficient photoluminescence and electroluminescence from environmentally stable polymer/clay nanocomposites. *Chemistry of Materials* 13:2217–2222
252. Nguyen T-Q, Wu J, Doan W, Schwartz BJ, Tolbert SH (2000) *Science*:288
253. Qian L, Zhang T, Wageh S, Jin ZS, Du ZL, Wang YS, Xu XR (2006) Study of blue electroluminescence from titania nanotubes doped into a polymeric matrix. *Nanotechnology* 17:100–104
254. Lee TW, Park OO, Hong JM, Kim DY, Kim YC (2001) Carrier mobilities of polymer/organo-clay nanocomposite electroluminescent devices. *Thin Solid Films* 393:347–351
255. Yokozumi T, Kim SH, Washino K, Lee HC, Ogion K, Usui H, Sato H (2003) Semiconducting nanocomposite from titanium dioxide and organic charge transporting compound. *Synthetic Metals* 139:151–154
256. Lee HC, Lee TW, Lim YT, Park OO (2002) Improved environmental stability in poly(*p*-phenylene vinylene)/layered silicate nanocomposite. *Applied Clay Science* 21:287–293
257. Lee TW, Park OO, Yoon J, Kim JJ (2001) Enhanced quantum efficiency in polymer/layered silicate nanocomposite light-emitting devices. *Synthetic Metals* 121:1737–1738
258. Senkevich JJ, Desu SB (1998) Poly(chloro-*p*-xylylene)/SiO₂ multilayer thin films deposited near room temperature by thermal CVD. *Thin Solid Films* 322:148–157
259. Senkevich JJ, Desu SB (2000) Compositional studies of near-room-temperature thermal CVD poly(chloro-*p*-xylylene)/SiO₂ nanocomposites. *Applied Physics A-Materials Science & Processing* 70:541–546
260. Ezhilvalavan S, Tseng TY (1999) Preparation and properties of tantalum pentoxide (Ta₂O₅) thin films for ultra large scale integrated circuits (ULSIs) application: A review. *Journal of Materials Science: Materials in Electronics* 10:9–31
261. Chashechnikova I, Dolgov L, Gavrilko T, Puchkovska G, Shaydyuk Y, Lebovka N, Moraru V, Baran J, Ratajczak H (2005) Optical properties of heterogeneous nanosystems based on montmorillonite clay mineral and 5CB nematic liquid crystal. *Journal of Molecular Structure* 744–747:563–571
262. Zhu W (2001) *Vacuum Microelectronics*. Wiley, New York
263. Bajic S, Latham RV (1988) Enhanced cold-cathode emission using composite resin-carbon coatings. *Journal of Physics D: Applied Physics* 21:200
264. Tsang WM, Stolojan V, Wong SP, Sealy BJ, Silva SRP (2005) The electron field emission properties of ion beam synthesized metal-dielectric nanocomposite layers on silicon substrates. *Materials Science and Engineering B-Solid State Materials for Advanced Technology* 124:453–457
265. <http://www.nanotechproject.org/>.

Chapter 7

Next-Generation Hybrid Nanocomposite Materials Based on Conducting Organic Polymers: Energy Storage and Conversion Devices

Monica Lira-Cantú and Pedro Gómez-Romero

Abstract This review deals with the most recent developments in the field of hybrid nanocomposite materials based on conducting organic polymers (COPs) with special emphasis on their impact on energy-related devices. Our aim is to introduce the reader to the fascinating world of conducting organic polymers, from basic aspects related to their working mechanism to their interplay with inorganic compounds to form hybrid organic–inorganic functional materials. The multifunctionality observed from these nanocomposite materials empower their application in a wide variety of energy-related devices capable to produce, convert or save energy. In addition to the later is their low-cost fabrication capability, linked to COPs processability, which makes hybrid organic–inorganic materials a powerful resource for the energy sector. In this review, we will focus on the design of hybrid nanocomposite materials based on COPs and their application in the “state-of the art” energy-related devices such as electrochemical supercapacitors and photovoltaic devices

Abbreviations C: Carbon; C2A: Carboxylated diacetylene; CNs: Carbon nanotubes; CNT: Carbon nanotube; COP: Conducting organic polymer; CV: Cyclic voltammetry; ETA: Extremely thin absorbers; FF: Fill factor; HTM: Hole-transport material; HSC: Hybrid organic–inorganic solar cell; J_{sc} : Current density in the short-circuit mode; MDMO-PPV: Poly[2-methoxy-5-(3,7-dimethyloxy)-1,4-phenylenevinylene]; MEH-PPV: Poly[2-methoxy-5-(2'-ethylhexyloxy-*p*-phenylenevinylene)]; MWNT: Multiwalled carbon nanotube; POTP: Poly(9,9'-dioctylfluorene-co-bithiophene) PAni: Polyaniline; PA-PPV: Poly[*N*-phenylimino-1, 4-phenylene-1, 2-ethenylene-1, 4-(2,5-dioctoxy) phenylene-1, 2-ethenylene-1, 4-phenylene]; PCBM: 1-(3-methoxycarbonyl) propyl-1-phenyl[6,6]C₆₁; PEP: Photoelectrochemical polymerization; PEDOT: Poly(3,4-ethylenedioxythiophene); PEP: Photoelectrochemical polymerization;

M. Lira-Cantú (✉) and P. Gómez-Romero
Centre d' Investigació en Nanociència i Nanotecnologia (CIN2, CSIC), Escola Tècnica Superior d' Enginyeria (ETSE) Campus UAB, Edifici Q 2nd Floor - QC/2111, Bellaterra (Barcelona), Spain E-08193
e-mail: monica.lira@cin2.es

PPy: Polypyrrole; PVK: Poly(*N*-vinylcarbazole); PU2T: Poly(3-undecyl-2,2'-bithiophene); P3HT: Poly(3-hexylthiophene); P3OT: Poly(3-octylthiophene); P4BTH: Poly(4-undecyl-2,2'-bithiophene); SWNT: Single-walled carbon nanotube; PMOs: Polyoxometalates; PW12: Phosphotungstic acid; ($H_3PW_{12}O_{40}$); PMo12: Phosphomolybdic acid; ($H_3PMo_{12}O_{40}$); SiW12: Silicotungstic acid; ($H_4SiW_{12}O_{40}$); Spiro-OMeTAD: 2,2',7,7'-Tetrakis(*N,N*-di-*p*-methoxyphenyl-amine)9,9'-spirobifluorene; ss-DSSC: Solid-state dye-sensitized solar cell; V_{oc} : Voltage in open-circuit mode; VK: *N*-Vinyl carbazole

7.1 Introduction

We are witnessing the prelude of what has been called a “technological wave,” with Energy playing a vital role. Innovation, strongly supported by advances in nanotechnology and alternative energy devices, is the focal point for this new technological era. The different energy-related systems, where hybrid nanocomposite materials have created a breakthrough impact, can be divided into energy storage (batteries, supercapacitors or hydrogen storage), conversion/production (solar cells, fuel cells, thermal solar cells or thermoelectricity) and energy saving (insulation, more efficient lighting, OLEDs, or combustion). In all of them, renewable energy resources must be adequate to meet energy needs but energy demand will only be met by the combination of different technologies. For example, energy conversion devices like solar cells will have an important impact in energy economy. The technology will have to evolve towards low-cost manufacturing in the future years, but it will also show a direct dependency on energy storage systems like batteries, capacitors or supercapacitors [1, 2]. Also, for an apparently self-sufficient device like a fuel cell, complementary storage might be necessary as is becoming evident in the design of hydrogen cars in which supercapacitors will be needed to provide peak currents [3]. Batteries are best suited to store relatively large amounts of charge, thanks to their high energy densities [4, 5]. However, the ionic diffusion processes are relatively slow, which is the reason why batteries score low in power density and why complementary devices related to conventional capacitors are under development. Electrochemical supercapacitors fill in the gap between batteries and conventional capacitors, resulting in devices that provide higher power density than a battery and higher energy density than a conventional parallel-plate capacitor [6].

Recent developments on polymer photovoltaics revealed the requirement of inorganic materials in order to improve solar charge-transfer limitations observed in conducting organic polymers (COPs). These solar cells are called hybrid organic–inorganic solar cells (HSC) and the key factor behind the operation is the close contact between the inorganic and organic materials. The latter enables for a large-area interface between the organic and inorganic counterparts demonstrating promising results. In a different approach, COPs are also applied as hole-transport material working together with nonporous semiconductor oxides; the latter

photovoltaic device is called solid-state dye-sensitized solar cell showing large efficiencies and promising lifetimes.

Double-layer supercapacitors, based on electrodes formed by porous carbon materials, represented a first step towards improving energy density in capacitors. The next generation was heralded by electrochemical supercapacitors, bringing electrochemical systems for the first time into the picture and decreasing the conceptual gap between supercapacitors and batteries. Both conducting organic polymers and metal oxide nanoparticles (notably RuO_2) have been exploited as active electrode materials in this type of systems [7]. Exploring the possibilities of hybrid organic–inorganic materials made of COPs and active inorganic species was a logical prospective strategy to take advantage of the best properties of each of the components.

But, beyond the possibility of dispersing the polymers on porous carbon or combining them with oxide nanoparticles, there is a more chemical approach in which molecular species are integrated within a conducting polymer network, or else, in which the polymer is grown “in situ” by polymerization on nanometric substrates. These chemical approaches make use of molecular components which can be bound together either through covalent bonds or just as ionic adducts.

Concerning electrochemical supercapacitors, we would like to mention here the recent work in our group with special emphasis on two particular cases and illustrate each of these two cases. We will describe first the ionic adducts formed between polyoxometalates and conducting polymers and will finally discuss the chemical modification of carbon nanotubes with conducting polymers through covalent bonding. With respect to photovoltaic devices, we have been able to fabricate hybrid solar cells applying COPs and semiconductor oxides as an initial attempt to study the interaction of both the components. In both the applications, the interplay between the organic and inorganic counterparts enhance final device performance. In the following section, we will present an overview of COPs and discuss how their properties are directly related to the applications. That section will be followed by a brief summary of the inclusion of inorganic materials within the conducting polymers to form hybrid nanocomposite materials and description of the synergic effects taking place between the counterparts. Description of some of the energy-related devices applying hybrid organic–inorganic nanocomposite materials will follow giving special emphasis to electrochemical supercapacitors and hybrid solar cells.

Before starting our review, a brief introduction to the basic principles behind the mechanisms of energy storage devices, such as batteries, capacitors or supercapacitors, and energy production devices like fuel cells and solar cells is given.

7.1.1 Energy Storage vs. Energy Conversion Devices

Although each energy storage and conversion device is characterized by its particular structural and functional dissimilarities, they share common electrochemical foundations. In general terms, we can envisage these devices as electrode pairs in

contact with a charge-carrier medium. The negative electrode is called the anode (oxidation reactions take place) where electrons are delivered to the external circuit. The positive electrode is called the cathode, where reduction reactions take place. Electrons flow from the negative to the positive electrode while conventional current flows in the opposite direction from high to low potential. In a battery, fuel cell and electrochemical supercapacitor, the charge carrier medium is called the electrolyte and is, in general terms, an ion-conducting media. In a solar cell, charge carriers are driven by a different principle based on the photon absorption from light, exciton dissociation at the p–n junction and charge transport through the hole and electron transport materials (see Fig. 7.1).

The difference between energy storage and energy conversion devices is that the first type is a closed system where energy production occurs within the same compartment as in a battery or an electrochemical supercapacitor. The second type, an energy conversion device, is an open system where the anode and cathode perform just as charge transfer media where the active mass providing energy is delivered from outside of the cell, for example, oxygen and hydrogen from an external source (tank) in fuel cells or photons from light in solar cells.

In a battery, energy is indirectly stored as chemical energy and a faradaic oxidation and reduction reaction of the corresponding reactants is required for current generation and electrical work production. Thus, chemical reactions and reactants phase change take place. In a capacitor, energy is stored directly as negative and positive electric charges by a process known as non-faradaic electrical energy storage. Thus, only an excess or a deficiency of electron charges on the capacitor plates are involved in the charge storage process. In general, capacitors can deliver large quantities of charge in a small period of time (e.g., to start the engine of a car), while batteries can deliver less charge for a longer period of time (e.g., to drive a car with a limited speed). An electrochemical supercapacitor, however, is a new type of device with an energy density in between that of batteries and capacitors, able to provide higher power density than a battery and higher energy density than a capacitor [8]. In these devices, double-layer processes, that is, the charge at

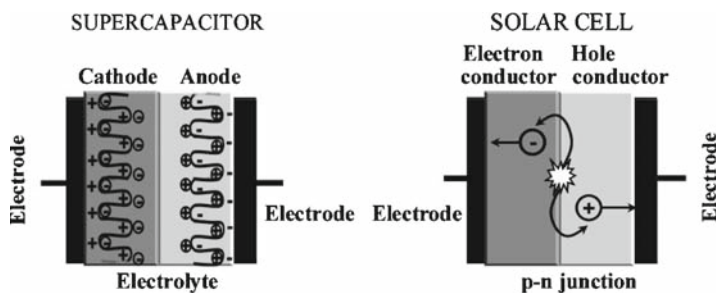


Fig. 7.1 Schematic representation of an electrochemical supercapacitor (*left*) and a bilayer solar cell (*right*)

electrode/electrolyte interfaces, play a fundamental factor. A double-layer capacitor with relatively small capacitance (e.g., $100 \mu\text{F}/\text{cm}^2$) and plates with high surface area (e.g., $1,000 \text{ m}^2/\text{g}$) becomes a device with the capability to store large amount of energy (e.g., about hundreds of F/g). Some examples of materials used for this purpose are high surface area carbon powders, aerogels or, more recently, conducting organic polymers like polyaniline [9] or polypyrrole, among others [3, 10]. Thus, it becomes evident that a large-surface-area interface of the active materials is the most important feature in order to develop high-performance devices. In an electrochemical supercapacitor, main interactions take place at the electrode/electrolyte interface (see Fig. 7.1), whereas in an organic solar cell it is dependent on the n-p bulk-heterojunction interface (see Fig. 7.3), as will be explained within the course of this brief review.

7.2 Conducting Organic Polymers Within Hybrid Nanocomposite Materials

Notwithstanding their many remarkable properties, the prominence of conducting organic polymers (COPs) has been related to two crucial historical events: first, the discovery of their electrical conductivity in 1977 by Shirakawa et al. [12] and later the finding of their electroluminescence in 1990 [13]. Their conductivity and functionality can be controlled by means of two characteristic mechanisms: redox doping and acid-base doping, allowing for the incorporation of charge-balancing doping counterions. A careful choice of the latter has a direct influence on the final properties such as redox activity and electrochemical properties, catalytic activity, gas sensor capability or processability, among others, and represents a simple way to design tailor-made materials. Obviously, this leads to whole new possibilities for their applications, like conductive plastics, catalysts, membranes, batteries, sensors, etc. On the other hand, under their undoped form COPs behave as intrinsic semiconductors and their properties can be modulated by the modification of the polymer backbone or by substitutions on the polymer chain. This versatility has placed COPs in the center of a constantly growing research area and has made them key players in many different state-of-the-art applications like in the plastic electronic industry as polymer lasers, OLEDs, photovoltaic cells, field-effect transistors, etc [14].

As part of the active component in energy storage systems, COPs present some drawbacks. For example, the application of COPs as electrodes for rechargeable lithium batteries led to relatively low specific capacities, high self-discharge rates and proved to be unfavorable because of the anion intercalation-deintercalation mechanism characteristic of the most promising p-doped COPs. The latter revealed uneven changes in current density during battery lifetime, but more problematical was the physical volume changes observed within the electrolyte because of the intermittent presence of anions. In other applications like photovoltaics, devices based on single-layer COPs are able to produce good voltage values but the photo-generated current has been observed to be low. The main reason for this is due to

the strong tendency of COPs to form bound excitons that are difficult to dissociate into the useful electron and hole counterparts responsible for current generation.

To overcome these limitations, COPs have been combined with inorganic materials to form hybrid organic–inorganic nanocomposite materials where the synergy between the organic and the inorganic counterparts improve final device properties. The anion-intercalation mechanism characterizing COPs has been transformed into a cation insertion by anchoring large-size oxide clusters into the polymer matrix [15, 16]. This modification in the insertion/deinsertion mechanism of COPs makes them ideal as Li^+ intercalation electrodes for rechargeable batteries solving some problems for their application. Another example is the inclusion of inorganic semiconductors within the COPs which has been proved to enhance exciton dissociation and enhance photovoltaic properties in hybrid solar cells [8]. These are only two of many examples where the interplay of COPs with inorganic materials works together to enhance device properties.

7.3 Hybrid Organic–inorganic Materials in Electrochemical Supercapacitors

Conducting organic polymers by themselves can be active materials for electrochemical supercapacitors when doped, delivering high specific power for a short period of time (10–100 s). The most desirable configuration for supercapacitors based on COPs is when an n-doped polymer is used as negative electrode and a p-doped polymer is applied as the positive electrode. This configuration is the most promising in terms of energy and power.

Hybrid nanocomposite materials can provide the added activity of the inorganic clusters in electrochemical supercapacitors. This option represents a different (and complementary) approach to batteries for the storage of charge, based on interfacial processes, and allow for higher power density but lower energy density than batteries. Originally, supercapacitors harnessed double-layer charge storage on the interface between microporous carbon materials and suitable electrolytes in a purely electro-physical capacitive mechanism, but more recently electrochemical supercapacitors are leading the way toward higher specific energy systems. These are based on redox-active materials able to cycle repeatedly between two oxidation states and therefore represent an approximation between traditional supercapacitors and batteries. Current research in electrochemical supercapacitors has been carried out with emphasis on the development of new electrode materials. In this line of work, we can find three kinds of electrode materials, namely, high-surface-area carbons [17], metal oxides [18–23] and conducting polymers [24–27]. In addition to these conventional types, novel alternative materials such as hybrid organic–inorganic nanocomposites are being considered because of their potential for synergic behavior. There are many possible combinations following this line of thought and work has been carried out on composite materials based on conducting polymers and carbon and also combining conducting polymers and electroactive metal oxides. Some of these examples are listed in Table 7.1.

Table 7.1 Some examples of hybrid nanocomposite materials applied in electrochemical supercapacitors

Inorganic	Polymer	Q (F/g) – from CVs	Q (F/g)	Ref
MnO ₂	PAni	–	500	[28]
RuO ₂	PEDOT:PSS	1,490	–	[28]
PMo ₁₂ O ₄₀	PPy	–	4	[29]
PMo ₁₂ O ₄₀	PAni	–	120	[8]
SiMo ₁₂ O ₄₀	PPy	–	3.5	[29]
PV ₂ Mo ₁₀ O ₄₀	PPy	–	7	[28]
Ir(VI)	PAni	–	–	[30]
SiO ₂	PAni	–	226	[31]
RuO ₂	PEDOT	420	–	[5]
RuO ₂	PAni	1,210	–	[32]
Stainless steel	PAni	–	800	[33]
Ni	PAni	–	405	[33]
C	PAni	–	420	[34]
SWNT	PPy	350	–	[28]

Two types of electrochemical supercapacitors have been developed in our group applying COPs: a) polyoxometalates and b) carbon nanotubes. The first type of materials makes use of the reversible redox chemistry of both COPs and polyoxometalates [35] which are known to suffer reversible reduction processes with a concomitant protonation, a mechanism which must be at work during cycling of the supercapacitor. The application of carbon nanotubes presents the advantage of high surface area and high conductivity [8]. A brief review of our most recent results follows.

7.3.1 *Nanocomposites of Conducting Polymers and Polyoxometalates*

Polyoxometalates (POMs) resemble clusters of metal oxides both from the structural and electronic point of view; they are formed by a small number of metal centers (typically 6–18 W or Mo) coordinated by bridging oxygen atoms, presenting well-known structures [36] and undergoing reversible multielectron reduction processes both electrochemically or photochemically similar to quantum-sized oxide particles [37]. Nevertheless, their solubility derived from their molecular nature has caused them to be ignored as active compounds for electrodes or for any kind of application where collective properties were needed. POMs have been extensively studied from a chemical point of view and have been used in catalysis and photocatalysis, either as homogeneous catalyst or supported onto polymers. Some examples are known of POMs doping conducting organic polymers such as polyaniline for application in catalysis and in energy storage [15].

The similarities between POMs and oxides are not limited to their composition and topologies. Their electrochemical and photochemical behaviors are also parallel. Thus, POMs can be electrochemically or photochemically reduced to form blue species. These reduced species are chemically and spectroscopically equivalent to tungsten or molybdenum bronzes in the form of colloidal semiconducting quantum dots, with the added advantage for POMs of a well-known structure that is stable in solution [38]. One such structure is the Keggin structure, common to many heteropolyacids. In addition to their reversible redox activity, these species present high proton conductivities in their solid (acid) form. Furthermore, they represent the ultimate limit for the dispersion of oxide species, since all metal centers can be considered to be “surface” centers, in contact with an electrolyte. This makes them good “a priori” candidates for electrode materials for electrochemical supercapacitors.

Conducting organic polymers (COPs) on the other hand have been extensively studied as promising novel materials, based on their possible use for rechargeable batteries [38–42] and electrochemical supercapacitors [43–45]. Yet, one of the frequent problems related to the application of COPs is a relatively low capacity to store charge in such devices.

The combination of conducting polymers and electroactive molecular, cluster or extended inorganic species, to form nanocomposite hybrid materials represents an opportunity for the design of novel concept materials with improved properties and enhanced energy storage capabilities, a line of work that we have recently developed in our laboratory [15, 46]. In particular, the anchoring of POMs within the network of COPs such as PANi leads to the fabrication of molecular hybrid materials in which the inorganic clusters keep their integrity and activity while benefiting from the conducting properties and polymeric nature of the hybrid structure. Some of these hybrid materials have been studied in nonaqueous solvents as lithium-inserting electrodes for the potential use in lithium batteries. However, under such conditions, the electroactivity of POMs could not be harnessed for too many charging–discharging cycles. Furthermore, the electroactivity of these inorganic clusters integrated in a hybrid material is heavily dependent of the electrolyte used. Thus, the use of aqueous acidic electrolytes facilitates the counterion flux and promotes the concomitant protonation of the cluster upon reduction, leading to quick and reversible redox chemistry [44]. All of these considerations, added to the fact mentioned above that POM clusters effectively constitute the ultimate degree of dispersion for an oxide phase, strongly suggest that POM species could act as ideal active materials for electrochemical supercapacitors when combined with acidic electrolytes [8, 47, 48].

Figure 7.2 shows the electrochemical supercapacitor behavior of a hybrid organic–inorganic material based on polyaniline and PMo12. The graph shows the variation in capacitance with successive charge/discharge cycles applying a current density of 400 mA/g. A stabilization period was observed during the initial cycles indicating an electroactivation process. The final capacitance value obtained was 120 F/g with good cyclability [8]. Our work constituted the first example of the use of hybrid molecular nanocomposite materials formed by polyaniline (PANi) and polyoxometalates, $H_4SiW_{12}O_{40}$ (SiW12), $H_3PW_{12}O_{40}$ (PW12) or $H_3PMo_{12}O_{40}$ (PMo12) as electrodes in solid-state electrochemical supercapacitors.

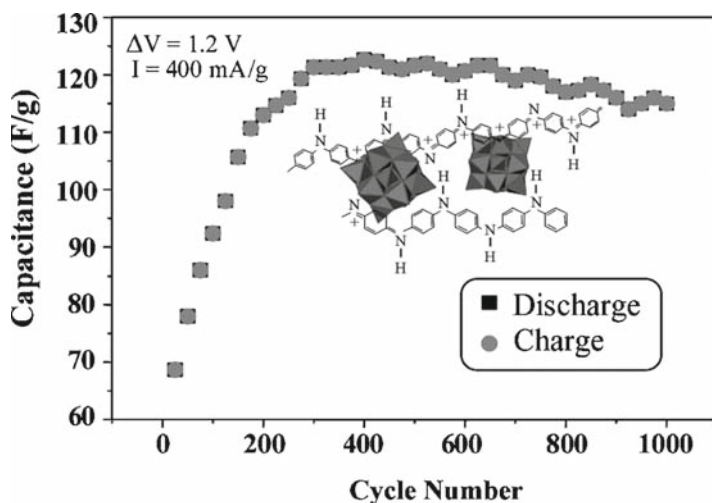


Fig. 7.2 Electrochemical supercapacitor made of polyaniline and polyoxometalate $\text{PMo}_{12}\text{O}_{40}$. The graph shows the capacitance values obtained for the first 1,000 cycles [8]

7.3.2 Nanocomposites of Carbon Nanotubes and Conducting Polymer

The synthesis of carbon nanotube/polymer composites is a promising approach to the effective incorporation of carbon nanotubes (CNs) into practical devices [49]. The combination of the unique properties of CNs with conducting organic polymers makes these materials interesting multifunctional systems with great potential in many applications not only as supercapacitors, but also in sensors, advanced transistors, high-resolution printable conductors, electromagnetic absorbers, photovoltaic cells, photodiodes and optical limiting devices [13]. As a result of their optical limiting performance and good photoconductivity, special attention has been given to CNs functionalized with poly (*N*-vinyl carbazole)(PVK) [23, 50–53]. Two methods of synthesis of PVK/CNs composites have been reported: direct mixing of the polymer with CNs, and chemical polymerization of monomer in the presence of carbon nanoparticles [53, 54]. When preparing a composite, it is essential to determine the type of interaction between the host matrix and the guest nanoparticles. The main functionalization possibilities of CNs reported so far are: (a) generation and functionalization of defect sites at the tube ends and side walls by oxidation and subsequent conversion into derivatives; (b) covalent functionalization of side walls by addition reactions and subsequent nucleophilic substitution; (c) noncovalent exohedral functionalization with surfactant-type molecules and (d) endohedral functionalization with C_{60} [55]. We note that, in the case of conducting

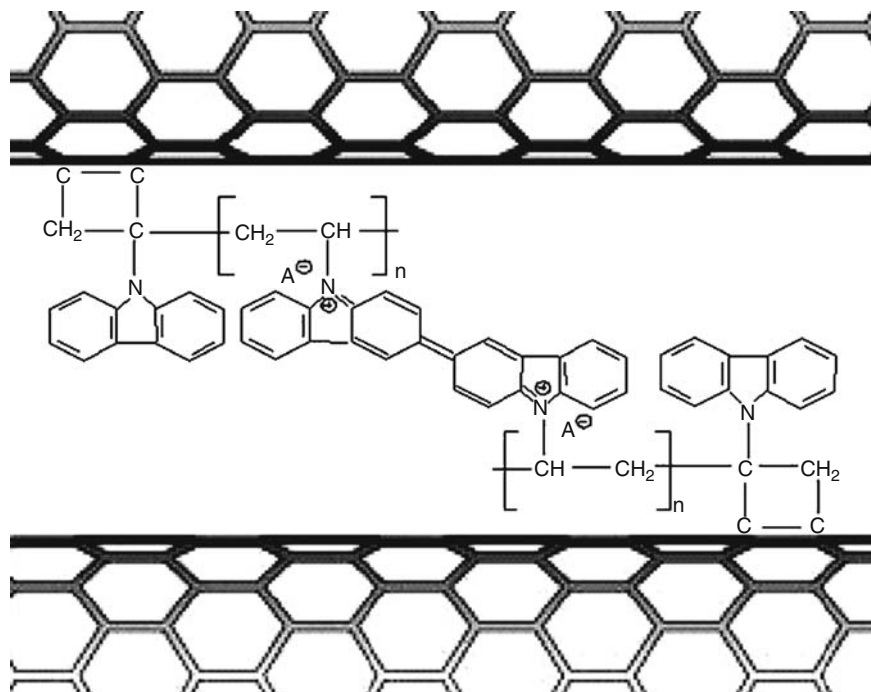


Fig. 7.3 Schematic representation of a hybrid nanocomposite material based on carbon nanotubes and conducting organic polymer (PVK) [11]

organic polymer/carbon nanotube composites (COP/CNs), it has been suggested that either the polymer functionalizes the CNs or the COP is doped with CNs; that is, a charge transfer occurs between the two constituents [50]. Consequently, two kinds of composites can be obtained: polymer-functionalized CNs and polymer doped with CNs.

Figure 7.3 shows the chemical structure of a hybrid nanocomposite material developed in our laboratory based on PVK-functionalized SWNTs doped with perchlorate and SWNT radical anion. The material has been applied as active electrode in lithium batteries as well as electrochemical supercapacitors with promising results [15, 180–181, 184–186].

7.4 Hybrid Nanocomposite Materials in Hybrid Solar Cells

In the race towards highly efficient, low-cost and large-area photovoltaic technology, conducting organic polymers (COPs) have found an important niche. The light-harvesting and hole-conducting properties that characterize some

COPs, together with the easy processing from solution and thus the possibility of large-scale printing technologies, make polymer photovoltaics a promising technological area.

Although, the application of a single COP in solar cells is possible, it is limited by the nonspontaneous separation of the free holes and electrons. In addition, they are also characterized by low electron mobility, typically around 10^{-4} cm²/Vs. Thus, polymer photovoltaics has shown enhanced performance with the introduction of electron transport and charge transfer materials. The formation of a donor–acceptor semiconductor system yields a charge-separation state [30, 56]. Nevertheless, owing to the short lifetime and low mobility of excitons in organic polymers, their diffusion length is limited to ~10 nm range. To ensure these conditions, Heeger and Friend et al. proposed the bulk-heterojunction concept [57, 58]. In this concept, an intimate mixture at the nanoscale range between the n-type and p-type materials allows for large-area donor–acceptor interface for efficient exciton dissociation [30]. The electron is accepted by the larger electron affinity material and the hole by the material with lower ionization potential [59]. Usually, conducting organic polymers act as hole transport in these systems.

One of the most interesting types of bulk-heterojunction solar cell was made by applying blends between a light-harvesting polymer and C₆₀-type molecules. It was first reported by Sariciftci et al. [60] and several reviews can be found in the literature about this type of solar cells [15, 30, 59, 61–63]. The concept, however, has been extended to other n–p type systems, where inorganic materials are applied as electron acceptors such as, for example, applying nanoparticles of inorganic semiconductor (Table 7.2) and semiconductor oxides (Table 7.3). These latter types of solar cells are known as hybrid solar cells (HSC) and their fabrication is relatively easy. The major advantages are the ease of processing, mechanical flexibility and versatility of chemical structure of the polymer within the hybrid blend.

It is well established that the structure and morphology of the active layer on these systems play an essential role to obtain good photovoltaic properties [99]. Phase separation and miscibility of the components are two of the many issues to be addressed during blend preparation [56, 59]. Yet, the morphology at the nanoscale

Table 7.2 Examples of hybrid solar cells made with inorganic semiconductor nanocrystals and conducting organic polymers

Polymer	Inorganic compound	V_{oc} (V)	J_{sc} (mA/cm ²)	η (%)	FF	Ref
P3HT	CdSe	0.7	5.8	1.7	0.4	[64]
P3HT	HgTe	0.4	2	0.4	0.5	[65]
P3HT	PbSe	0.35	1.08	0.14	0.32	[66]
MEH-PPV	PbS	0.36	0.0035	–	–	[67]
POHT	GaAs	0.63	3.8	4.2	0.7	[68]
PEDOT/PCBM	CuInS ₂	0.22	0.84	0.07	0.26	[69]

Table 7.3 Photovoltaic properties of hybrid solar cells applying semiconductor oxides and conducting organic polymers

Polymer	Oxide	V_{oc} (V)	J_{sc} (mA/cm ²)	η (%)	FF	Ref
P3HT	TiO ₂	0.72	1.4	1.5	0.51	[70–72]
P3HT	TiO ₂	0.44	2.67	0.42	0.36	[73]
P3HT	TiO ₂	0.66	0.68	0.69	0.6	[74]
POHT	TiO ₂	0.45	0.7	0.17	0.41	[75]
POHT	TiO ₂	0.72	0.25	0.06	0.35	[76]
PU2T	TiO ₂	0.67	0.448	0.10	0.28	[77]
PU2T	TiO ₂	0.92	0.1	–	–	[78]
POTP	TiO ₂	0.80	0.3	–	–	[79]
MDMO-PPV	TiO ₂	0.52	0.6	–	0.42	[80, 81]
MDMO-PPV	TiO ₂	0.60	0.6	0.22	–	[75]
MDMO-PPV	TiO ₂	0.52	0.79	–	0.38	[82]
MEH-PPV	TiO ₂	0.86	3.3	0.71	0.28	[83]
MEH-PPV	TiO ₂	0.86	1	0.40	0.5	[84, 85]
PA-PPV	TiO ₂	0.85	–	–	0.52	[86]
PAni	TiO ₂	0.25	0.12	–	–	[87]
MEH-PPV	TiO ₂	1.10	0.4	–	0.42	[18]
MEH-PPV	TiO ₂	0.70	0.57	0.51	0.64	[88]
MEH-PPV	TiO ₂	0.63	0.008	–	–	[89]
MDMO-PPV	ZnO	0.81	2.4	1.60	0.56	[90–93]
MDMO-PPV	ZnO	1.14	2.3	1.10	0.42	[91–93]
P3HT	ZnO	0.69	2.19	0.92	0.55	[94]
P3HT	ZnO	0.44	2.2	0.56	0.53	[95]
P3HT	ZnO	0.30	1.73	0.20	0.38	[96]
P3HT	ZnO/dye	0.25	2	0.20	–	[97]
P3HT/PCBM	ZnO	0.47	10	2.03	0.43	[95]
MEH-PPV	Nb ₂ O ₅	0.76	0.28	–	0.44	[98]

level of these blends is difficult to control [56], thus the homogeneous distribution of the n-type and the p-type materials within the 10-nm exciton diffusion length required for efficient charge transport becomes a challenge. To overcome all these problems, many solutions have been proposed. For example, the functionalization of C₆₀ derivatives has been shown to improve solubility. The application of bicontinuous, interpenetrating networks [30] or ordered bulk heterostructures [56] could, in principle, help to minimize these problems. Figure 7.4 shows a schematic representation of the active layer of different n-type/p-type heterojunctions, from the bilayer structure to the well-ordered bulk heterostructures.

Besides the well-known bulk-heterojunction solar cell, based on C₆₀ molecules [60], conducting organic polymers can be found as part of different hybrid organic–inorganic photovoltaic systems: for example, within the hybrid organic nanocrystal solar cells [100], as hybrid organic–inorganic solar cells [8], solid-state or quasi-solid-state dye-sensitized solar cells [101] or within extremely thin absorber (ETA) solar cells. Usually COPs are utilized because of their exceptional light-harvesting properties, and also because of their capability to work as hole-transport material

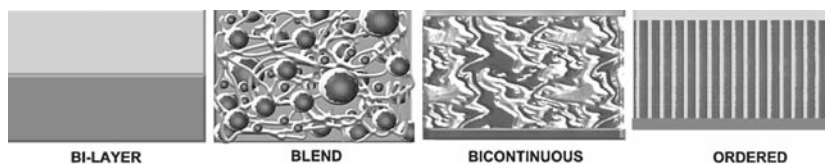


Fig. 7.4 The bulk-heterojunction concept. From *left to right*: bilayer structure (*far left*), nanoparticle/polymer blends, bicontinuous interpenetrating networks and well-ordered bulk heterostructures (*far right*)

(HTM) and, in many cases, they serve both purposes. The highest efficiency reported to date applying COPs in photovoltaics can be attributed to bulk-heterojunction solar cells utilizing C_{60} derivatives. In small-area devices efficiency can approach 5%. If we consider that the goal for efficiency has been set at 10% [69], one can argue that COPs-based photovoltaics are far away from these objectives. Nevertheless, the optimization of several parameters, like open-circuit voltage or charge-carrier mobility of electrons and holes, can lead to higher solar cell efficiencies. In the following section, a brief overview based on new hybrid solar cell concepts is given.

7.4.1 Hybrid Solar Cells with Inorganic Semiconductors

The group of Alivisatos developed in 2002 [64] hybrid solar cells making use of inorganic semiconductor nanoparticles. This type of device, called hybrid nanocrystal-polymer solar cell (HNSC) was initially made of blends of a conducting organic polymer, poly-3(hexylthiophene), and nanorods of an inorganic semiconductor, CdSe. The authors reported an initial 1.7% efficiency [64]. Examples of crystalline inorganic semiconductors applied in HSC are $CuInS_2$ [102–105], $CuInSe_2$ and $CuInTe_2$ [105], PbS [67, 106–109], GaAs [68, 110], PbSe [111] or HgTe nanocrystals [65]. Table 7.2 shows some examples of HSC applying inorganic semiconductor nanocrystal/polymer bulk-heterojunctions and their photovoltaic properties.

In order to fabricate highly efficient HNSC, several requirements should be taken into consideration: a) the absorption within the inorganic semiconductor must be complementary to the conducting polymer absorption, b) a clear driving force for charge transfer must be present and c) enough morphology control must be achieved for percolation [112]. Inorganic semiconductors by themselves can address the first two aspects. Nevertheless, greater efforts should be made in order to control morphology of the semiconductor/polymer blend during the incorporation of the inorganic semiconductor within the thin film. An advantage of this type of solar cells, however, is that transport within a single nanocrystal (nanorods) is likely to be highly efficient [112, 113]. Thus, the electron mobility in noncontinuous inorganic networks like in nanocrystalline or nanocrystal/polymer blends is limited

by the nanocrystal–nanocrystal hopping [112]. Thus, reducing the hopping effects will improve transport efficiency. This has been demonstrated by increasing the length of the inorganic nanorods from 7 nm to 30 nm and to 60 nm within the blend. Improvement in EQE when increasing nanorod lengths was observed and solar cell efficiency as high as 1.7% was achieved for the longest nanorods. If nanorods are replaced by branched nanocrystals, the EQE almost double and solar cell efficiencies of 1.8% can be achieved. Various strategies have been applied to enhance the solar cell efficiency by modifying the inorganic semiconductor, by tailoring the composition of the blend or the shape of the nanocrystal, as for example, in branched cadmium telluride (CdTe) tetrapods [114]. Although the increase in efficiency can be achieved by modification of the shape of the inorganic semiconductor, another problem arises from the fact that both inorganic semiconductors and some conjugated polymers (e.g., P3HT) applied to date absorb light in the visible part of the solar spectrum, leaving a considerable amount of near-infrared solar energy unused. Promising approaches have been reported to “displace” the absorption range into the infrared by the utilization of low-band-gap polymers [66] like MEH-PPV [62] or P3OT [115].

Inorganic semiconductors in their oxide form constitute a different approach. Their first application as electron acceptors in hybrid solar cells involved interpenetrating networks of TiO_2 and the conjugated polymer MEH-PPV [8, 86]. The authors demonstrated the effective application of the bulk-heterojunction concept in a system integrating nanoparticles of TiO_2 . A significant improvement in photovoltaic properties when compared to the bilayer-structured device was demonstrated and the good photovoltaic performance of the system opened up the research area of hybrid solar cells with semiconductor oxides. Since then, many systems applying all kinds of semiconductor oxides have been studied like TiO_2 [8, 18, 73, 75, 82, 84–86, 98, 116–118], Nb_2O_5 [98, 118–120], ZnO [90–94, 96, 97, 118, 119], SnO_2 [121], CeO_2 or CeO_2 - TiO_2 [118, 119]. Because semiconductor oxides are easier to fabricate as rigid heterostructures (than, for example, C_{60} derivatives), HSC can be found as thin porous films, blends (nanoparticles, nanorods, tetrapods), bicontinuous networks and more recently well-ordered bulk heterostructures. In the last two years, the application of ZnO nanoparticles blended within a COP has awakened great interest because of the encouraging performance observed in these devices. First reports have shown efficiencies up to 1.6% with a J_{sc} of 2.4 mA/cm², a V_{oc} of 0.8 V and a 0.59 FF (see Table 7.3). The feasibility to fabricate semiconductor oxides in large scale and in almost any substrate led to well-ordered heterostructured electrodes [73, 97]. As a result, high-efficient photovoltaic devices have been obtained.

Special consideration should be taken of the fact that all of these bulk-heterojunction photovoltaic systems are characterized by the direct physical contact between the electron-acceptor and hole-transport material. Despite their good photovoltaic properties and the excellent exciton dissociation observed at the interface, some reports predict the need for the separation of the electron- and hole-transporting components [122, 123]. Separation of both components could, in principle, improve charge collection and prevent charge recombination [123].

In the case of bulk-heterojunction solar cells applying semiconductor oxides, however, the separation becomes a necessity because oxygen release and exchange have been proved to take place in HSC during irradiation [98, 119, 120]. The reported mechanism is directly linked to the semiconductor oxide thin film that shows a light-driven oxygen exchange mechanism. The latter affects the performance of the solar cell under different atmospheres because of the semiconductor oxide requirement (“breathing”) of oxygen [98]. The removal of oxygen from the environment decreases photovoltaic activity in these types of solar cells as shown in Fig. 7.5. The graphs in Fig. 7.5 show how current density decreases steadily under vacuum but can be recovered once the HSC is transferred to ambient atmosphere.

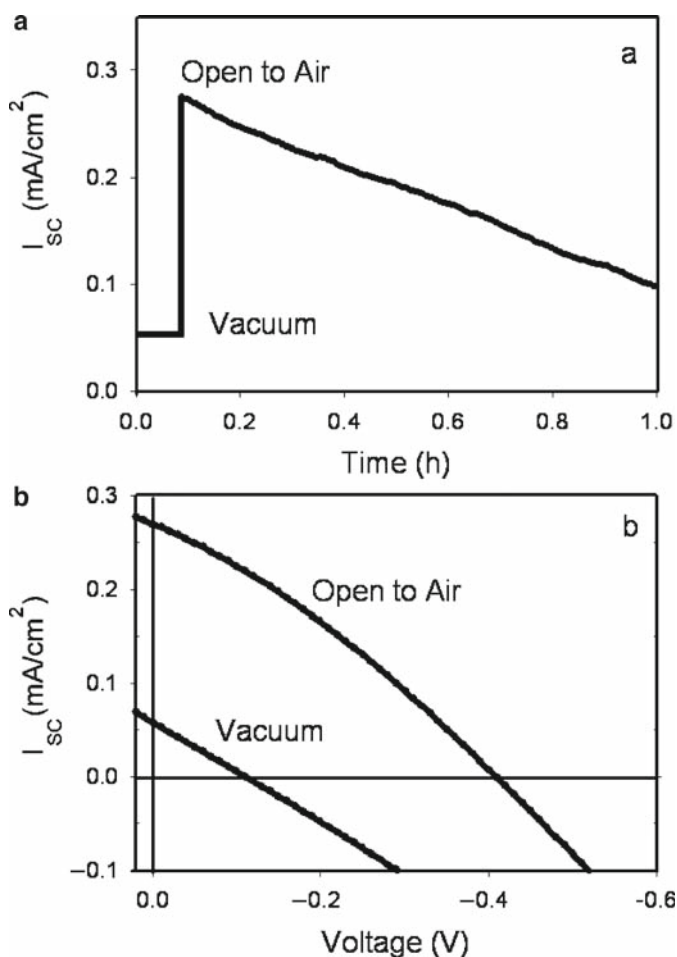


Fig. 7.5 The effect of vacuum atmosphere on a glass/ITO/ Nb_2O_5 /MEH-PPV/Ag hybrid solar cell. (a) Vacuum (1×10^{-6} mBar) with introduction of air and (b) IV-curves in vacuum and once the device is transferred to the open atmosphere [82]

IV curves obtained under vacuum conditions and once the device is transferred to the ambient atmosphere show higher photovoltaic response under oxygen-containing atmosphere as observed in Fig. 7.5b. The same behavior has been reported in systems based on TiO_2 /polymer nanocomposites [124] and similar solar cells [98]. Moreover, the oxygen exchange taking place on the surface of the semiconductor oxide during irradiation is able to react with the components of the solar cell, especially with the conducting polymer which is irreversibly degraded with time, thus reducing solar cell stability and lifetime [119].

These results indicate that in a HSC, exploiting a direct mixture of conducting polymer and semiconductor oxide, the photooxidation (photobleaching) of the polymer with time is inevitable and cannot be avoided by the application of UV filters or inert atmospheres [98]. A possible solution to this problem could then be the physical separation of the electron- and hole- transporting components as suggested in already published reports [122, 123]. This separation could avoid the polymer degradation and improve the lifetime of HSC integrating semiconductor oxides. But, equally important is the possibility to enhance charge separation and avoid or retard recombination in this and all the other types of bulk-heterojunction solar cells [122, 123]. The latter has been recently proved in an interesting report published by Ravirejan et al. [97]. In this work, HSC were fabricated from ZnO, used in three different configurations: flat layer structure, vertical aligned nanorods and nanoparticles. The authors applied the polymer in an intimate contact with the ZnO but also added an amphiphilic molecular interface layer (a dye) in between the ZnO and polymer. A transient absorption spectroscopy technique was used to obtain the photoinduced electron-transfer yield and the charge-recombination kinetics.

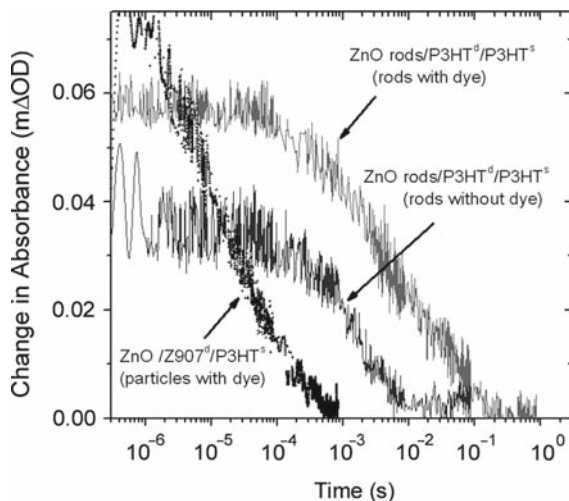


Fig. 7.6 Photoinduced change in absorbance for structures consisting of dye-treated ZnO rod/Z907/P3HT, dye-treated ZnO nanoparticle/Z907/P3HT and P3HT-treated ZnO rod/P3HT/P3HT [97]. With permission from J. Nelson

Comparison between the devices with bare ZnO and ZnO coated with the dye showed that the dye-treated ZnO devices presented a) longer lifetime of the hole polarons, b) improvement of 50% in the charge transfer yield and c) shorter half-life by a factor of 4–5, as shown in Fig. 7.6.

The improved *charge separation yield* observed was attributed to the “cascade” type of interface (ZnO/Dye/polymer) which blocked the hole transfer. Another positive factor was the orientation of the dye which is believed to attach its polar side group to the oxide while maintaining its nonpolar side towards the polymer, thus improving wettability. A direct charge transfer between the ZnO and P3HT would promote recombination, but it was effectively retarded by the application of a dye as a spatial separation between the hole- and electron-transfer materials.

These findings prove the beneficial effect of separating the hole and the electron transport materials. The research is now focusing on the lifetime of these devices and the role of oxygen when the new configuration is adopted.

7.4.2 In between Hybrid Solar Cells (HSC) and Solid-state Dye-Sensitized Solar Cells (ss-DSSC)

The application of a dye in conjunction with an electron-acceptor semiconductor oxide and a COP as the hole-transport material (HTM), as described in the above example, is one of many types of what is known as solid-state or quasi-solid-state dye-sensitized solar cell (ss-DSSC). The ss-DSSC concept was first reported around 1995 [125, 126] as a possible solution to the practical problems related to the liquid electrolyte such as leakages, corrosion of electrodes and dye evaporation, among others [126–128]. Efforts to replace the liquid electrolyte by a HTM include the investigation of different compounds from p-type inorganic semiconductors [126], polymer or gel electrolytes [126, 128–137], ionic liquids [138–143], ionic liquid crystals [126, 143, 144], conducting organic polymers [145, 178, 179] or redox molecules covalently linked to the dye and the TiO₂ forming a triad [122, 146]. The possibility to fabricate DSSC made completely of solid components represents a step forward into a solar cell technology capable of being fabricated by large-scale techniques with the technological advantages described before for plastic solar cells.

In a ss-DSSC, light is absorbed by a dye to form an excited electronic state (a), called an exciton. The formed electron is then injected in the conduction band of the nanostructured titanium oxide (b) which is then transported to the electrode (c). At the same time, the hole produced within the dye is transferred from the oxidized dye to a hole-transporting molecule (d) and then collected at the counter electrode (e) [147].

Although there are many HTMs alternatives, in this review we will focus on the application of conducting organic polymers as HTM in ss-DSSC. One of the most important requirements of any COP to act as the HTM is its wettability [147]. The polymer must penetrate into the pores of the semiconductor oxide nanoparticles used as electron transport to effectively fill the pores of the semiconductor oxide. But, there are also other requirements that must be fulfilled, like high transparency in the spectral

range of the dye, maintaining dye integrity, high hole mobility to prevent charge recombination, etc [147]. Several attempts to apply COPs in ss-DSSC have been reported [178, 179, 182–183] and some of the polymers already used are listed in Table 7.4.

The first report of the application of COP, specifically polypyrrole, as hole-transport compound in solid-state DSSC was first reported by Yanagida et al. in 1997 [152]. To ensure close contact between the dye and the hole-conducting polymer, an innovative in situ photoelectrochemical polymerization technique was applied. Unfortunately, it was found that polypyrrole itself absorbs in the visible range leading to low-efficiency solar cells. Tests were also carried out applying polyaniline with similar results (see Table 7.4). In 2001, Grätzel et al. applied a bithiophene-type polymer as hole conductor [155]. In that report, the authors compared solar cells with and without the application of the light-harvesting dye. In the latter case, the polymer was coated on top of the TiO_2 /Dye layer by the spin-coating method. The main difficulty found was the incomplete pore filling [155] which is also a well-known problem in bulk-heterojunction solar cells [56]. It was not until 2004 that poly(3,4-ethylenedioxythiophene) (PEDOT) was applied with an initial photovoltaic efficiency of 0.53%, as reported by Yanagida et al. This value has increased up to 2.6% nowadays [99] and is the highest value reported to date from that laboratory. The ability to obtain such high efficiencies is possibly because of the

Table 7.4 Examples of conducting organic polymers working as hole-transport materials (HTMs) in ss-DSSC and comparison with the best ss-DDSC applying spiro-OMeTAD hole conductor

COP (as HTM)	J_{sc} (mA/cm ²)	V_{oc} (V)	η (%)	FF	Ref
PAni	0.0021	0.31	–	–	[148]
PAni	0.045	0.56	0.12	–	[149]
PAni	–	–	1.15	–	[150, 151]
PAni	0.77	0.34	0.10	–	[85, 150]
PPy	0.070	0.63	–	–	[101]
PPy	–	–	0.10	–	[152]
PPy	0.094	0.77	0.20	–	[153]
P3OT	0.027	0.57	–	0.43	[37]
P3OT	0.45	0.65	0.16	–	[38]
P3OT	3.90	0.58	1.30	0.61	[154]
P4BTH	0.060	0.65	–	–	[155]
P4BTH	0.068	0.44	–	–	[156]
PEDOT	3.2	0.7	1.26	0.58	[35]
PEDOT	0.075	0.4	0.01	0.37	[156, 182]
PEP·PPy	0.32	0.72	0.34	0.78	[153]
PEP·PEDOT	1.7	0.47	0.32	0.40	[145]
PEP·PEDOT/C	2.3	0.47	0.53	0.50	[157]
PEP·PEDOT	1.2	0.56	0.26	0.26	[158, 159]
PEP·PEDOT	4.5	0.78	2.60	0.74	[99]
PEP·PEDOT	4.9	0.50	1.69	0.68	[160]
C2A	4.25	0.46	0.82	0.44	[161]
PVK	1.18	0.71	2.40	0.66	[162]
PAni/C/iodide	12.8	0.58	3.48	0.47	[163]
spiro-OMeTAD			3.2		[164]

elegant method applied to improve wettability and overcome pore-filling problems. The method applied is called photoelectrochemical polymerization (PEP) and it is initiated by the photoexcitation of the ruthenium dye. Once the dye is oxidized, it can carry out the oxidative polymerization of the monomer in solution offering close contact between the photosensitizer (dye) and the HTM (polymer). The oxidation potential of the EDOT monomer, however, is about 1.0 V vs. Ag/AgCl and cannot be oxidized by the Ruthenium dye (HOMO potential: 0.59 V vs. Ag/AgCl). Thus, an optimization of the PEP process was performed by applying a bi-monomer, bis-EDOT, whose oxidation potential is lower, about 0.4 V vs. Ag/AgCl [157–159]. The latter allowed the polymerization to take place with excellent results.

Figure 7.7 shows the curve of current density vs. time obtained during photochemical polymerization of bis-EDOT at 22 mW/cm². The figure also shows the device structure and the path followed by the electrons in the complete ss-DDSC. The PEP curve in Fig. 7.7 shows that after an initial spike, current density increases until reaching a maximum between 420 and 600 s depending on the TiO₂-layer thickness. The shape of the curve could be analyzed as follows: increase in current density during photoelectrochemical polymerization could be an indication of the formation of COP in its conductive state [16]. During photopolymerization, the growth of the polymer slowly covers the surface of the electrode, thus light reaching the surface of the dye decreases steadily with time as well as the possibility for the dye to maintain the oxidizing potential required to polymerize bis-EDOT. After about 30 min, the process ends and current reaches almost zero. Careful control of parameters like TiO₂-layer thickness, light intensity, total charge used during

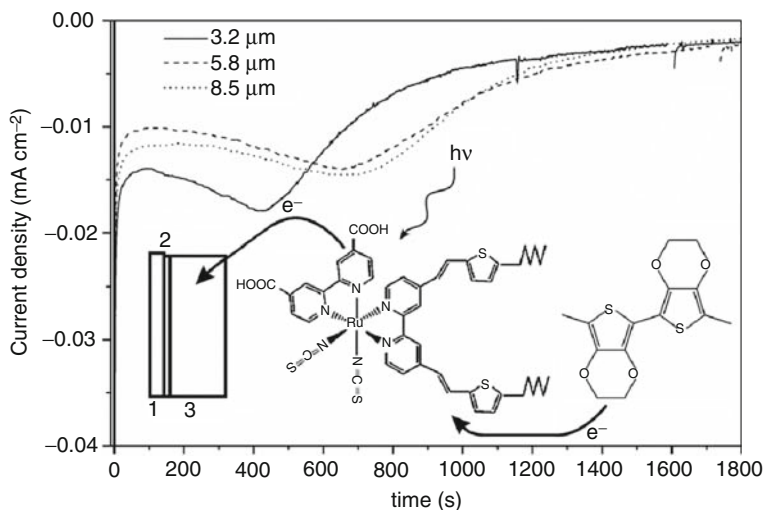


Fig. 7.7 Current density vs. time recorded during the photochemical polymerization of bis-EDOT. The inset shows the device structure and the polymerization process. (1) FTO, (2) dense TiO₂ barrier layer, (3) porous TiO₂ layer [99]. With permission from S. Yanagida

photopolymerization, the application of an ionic liquid or the selection of the right counter electrode are only some examples of what is taken into account to enhance final device performance.

A simplified approach has been recently published by the group of Sanchez et al. where an all-solid-state dye-sensitized solar cell was fabricated by applying nanoporous TiO₂ and a dye as the light-harvesting specie. In this configuration, a conjugated polymer (P3TH) deposited by the spin-coating method was applied as the hole conductor. The device showed a V_{oc} of 0.58 V, a J_{sc} of 3.75 mA/cm², a fill factor of 0.61 and an overall solar cell efficiency of 1.3% [154, 165]. The authors reported very good reproducibility in a set of 60 devices demonstrating the possibility for large-scale industrial production of these hybrid solar cells.

7.4.3 Hybrid Solar Cells: Processability and Large-Scale Fabrication

As shown from the latter example, many encouraging advantages were obtained thanks to the processability offered by COPs and thus, the low-cost manufacturing-when applying solution processing of film-forming polymers. The possibility to replace inorganic photovoltaic devices produced at high cost by solar cells made on thin plastic substrates via printing techniques is an attractive alternative. Assuming that a significant cost reduction can be achieved, a device and module efficiency of 10 and 5% respectively, would be critical to enter the market. The technology, however, must achieve simultaneously three basic requirements in order to reach commercialization: high efficiency, long lifetime and low cost per Wp¹ [166]. Although the three requirements are difficult to achieve, the fabrication of large-area photovoltaic devices (>2 × 2 cm² cell unit) by printing techniques is already a reality.

Some examples are solar cells made by doctor blade [167], spin coating [168] or silkscreen [169] as listed in Table 7.5. As an example, Fig. 7.8 shows an image

Table 7.5 Some examples of large-area (>2 × 2 cm unit cell) bulk-heterojunction solar cells from different laboratories

Active area	η (%)	Applied technique	Ref
10 × 15 cm ²	–	Doctor blade	[167]
2 × 2.1 cm ²	0.2	Spin coating	[168]
5 × 5 cm ²	1.54	Spin coating	[170]
5 × 5 cm ²	3	Spin coating	[171]
1 m ²	0.0046	Silkscreen	[172]
0.1 m ²	0.1	Silkscreen	[169]

¹Wp: watt-peak, a unit of power output representing the maximum output in watt of a 1 m² solar panel at 25°C.

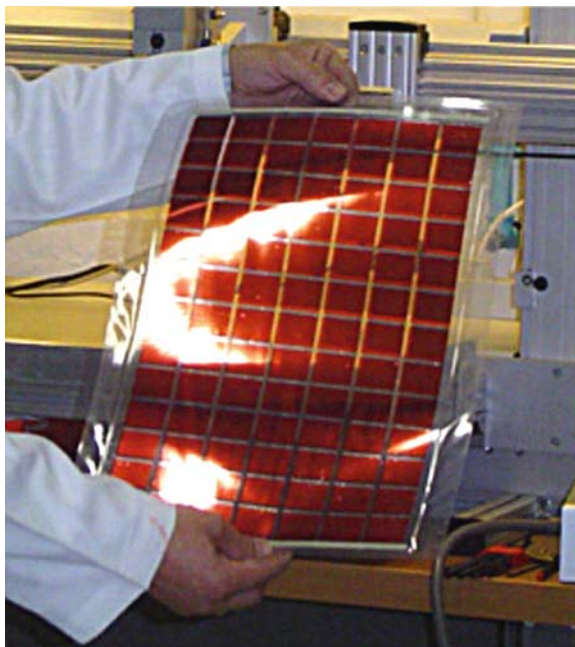


Fig. 7.8 A 0.1 m² polymer solar cell produced by screen printing at RISO National Laboratory using MEH-PPV. Courtesy of F.C. Krebs, RISO National Laboratory

of a 0.1m² polymer solar cell produced by screen printing at RISO National Laboratory using MEH-PPV polymer [169]. Moreover, an example of hybrid solar cells made by printing techniques which can already be found in the market belongs to the company Konarka, the first developer of photovoltaic devices printed on light-weight, flexible substrates [173].

Although 10% efficiency seems possible, it has not been achieved yet [69] and several attempts to improve PV properties are being made by different laboratories. Promising results are observed during post-fabrication treatments like annealing of the solar cell. Li et al. [174] demonstrated the possibility to obtain high efficiency by reducing series resistance of a polymer bulk-heterojunction solar cell. The latter was achieved by controlling the growth rate of the active polymer layer from solution to solid state leading to a self-organized polymer [174]. The possibility of self-assembly and self-organization in conducting organic polymers is not new as shown by several reports that can be found in the literature [175–177]. The variability observed in device performance depends critically on molecular packing of COPs [175]. Thus, from the study and control of polymer behavior in solar cell fabrication, a possible improvement of device efficiency can be foreseen.

7.5 Conclusion and Prospects

Hybrid nanocomposite materials based on conducting organic polymers have become an important part for the development of energy-related applications. Especially in the area of energy storage and conversion devices, conducting organic polymers, in synergy with a wide range of inorganic materials, have established a new path for the generation of new materials with improved and novel properties.

In this chapter, we have focused our discussion on the progress that hybrid nanocomposite materials have revealed in two main research areas; electrochemical supercapacitors and photovoltaic applications. Among different energy-related devices, these applications demonstrate the versatility of conducting organic polymers and how the modulation of their properties can be tuned to work within a well-defined purpose. Properties like high electrical conductivity and high surface area are required for the application of COPs in electrochemical supercapacitors, whereas light-harvesting and hole-conducting properties are needed for photovoltaic applications. A common point for both applications is the interface; an increasing importance of the interaction between active inorganic and organic materials at the nanosize scale and molecular level is a key factor to obtain well-functioning and efficient devices. Interface engineering, from flat plate to high surface area, has followed the historical evolution of hybrid nanocomposite materials, especially those made with conducting organic polymers, and is correlated with the improvement observed within their applications.

It is clear that the main feature of these materials based on COPs is the ease of fabrication and compatibility with low-cost printing techniques for final device production. Research efforts have been focused on the synthesis of new hybrid nanocomposites toward the improvement of material properties and final device efficiency. However, an important void is observed in the understanding of materials stability, device degradation and lifetime. The latter are, with no doubt, the main drawbacks in order to reach industrial stage. In solar cell applications, for example, the efficiency goal of 10% is not a reality yet, but research and development efforts carried out in many laboratories show that this objective can be achieved in the near future. Thus, knowledge-based research must focus on larger-surface-area devices, reliability and longer lifetime studies. As hybrid nanocomposite materials progress towards commercialization, the need to understand their main strengths and drawbacks will provide the basis for further development in a growing number of energy-related applications.

Acknowledgments M.L.-C. would like to thank Dr. Frederik C. Krebs (Denmark) and Dr. Shozo Yanagida (Japan) for their support during the visit to their laboratories. She is also grateful to AGAUR for the support to visit RISO National Laboratory (Denmark, 2004), to the Canon Foundation in Europe for the visiting grant to the Centre for Advanced Science and Innovation (Japan, 2006), to the Spanish Ministry of Science and Technology (MAT 2005-07683-C02-01 and ENE2008-04373/ALT) and to the “Ramon y Cajal” program (Spain) for the support.

References

1. Nanoroad SME. Nanomaterial roadmap 2015. Roadmap report concerning the use of nanomaterials in the energy sector. <http://www.nanoroad.net/index.php?topic=download>.
2. Schell International. (2001) Energy needs, choices and possibilities. Scenarios to 2050. <http://www.shell.com/scenarios>.
3. Winter M. and Brodd RJ. (2004) What are batteries, fuel cells and supercapacitors? *Chem. Rev.* 104:4245–4269.
4. Edwards JH, Badwal SPS, Duffy GJ, Lasich J, Ganakas G. (2002) The application of solid-state ionic technology for novel methods of energy generation and supply. *Solid State Ionics* 152–153:843–852.
5. Hong JI, Yeo IH, Paik WK. (2001) Conducting polymer with metal oxide for electrochemical capacitor – poly(3,4-ethylenedioxythiophene) RuO₂ electrode. *J. Electrochem. Soc.* 148(2): A156–A163.
6. Conway BE. (1999) *Electrochemical Supercapacitors. Scientific Fundamentals and Technological Applications*. Kluwer Academia/Plenum, New York.
7. Huang LM, Wen T-C, Gopalan A. (2006) Electrochemical and spectroelectrochemical monitoring of supercapacitance and electrochromic properties of hydrous ruthenium oxide embedded poly(3,4-ethylenedioxythiophene)-poly(styrene sulfonic acid) composite. *Electrochem. Acta* 51:3469–3476.
8. Cuentas-Gallegos K, Lira-Cantú M, Casañ-Pastor P, Gómez-Romero P. (2005) Nanocomposite hybrid molecular materials for application in solid-state electrochemical supercapacitors. *Adv. Funct. Mater.* 15:1125–1133.
9. Prasad KR, Munichandraiah N. (2002) Fabrication and evaluation of 450 F electrochemical redox supercapacitors using inexpensive and high-performance, polyaniline coated, stainless-steel electrodes. *J. Power Sources* 112(2):443–451.
10. Shukla AK, Sampath S, Vijayamohanan K. (2000) Electrochemical supercapacitors: Energy storage beyond batteries. *Curr. Sci.* 79(12):1656–1661.
11. Baibarac M, Gómez-Romero P. (2005) Nanocomposites based on conducting polymers and carbon nanotubes: from fancy materials to functional applications. *J. Nanosci. Nanotechnol.* 6(2):289–302.
12. Shirakawa H, Louis EJ, McDiarmid AG, Chaing CK, Heeger AJ. (1997) Synthesis of electrically conducting organic polymers: halogen derivatives of poly(acetylene), (CH)_x. *J. Chem. Soc. Commun.* 16:578–579.
13. Burroughes JH, Bradley DDC, Brown AR, Marks RN, Mackay K, Friend RH, Burns PL, Holmes AB. (1990) Light-emitting diodes based on conjugated polymers. *Nature* 347:539–541.
14. Pron A. and Rannou P. (2002) Processible conjugated polymers: from organic semiconductors to organic metals and superconductors. *Prog. Polym. Sci.* 27:135–190.
15. Gómez-Romero P. (2001) Hybrid organic-inorganic materials. In search for synergic activity. *Adv. Mater.* 13:163–174.
16. Lira-Cantú M. and Gómez-Romero P. (1998) Electrochemical and chemical syntheses of the hybrid organic-inorganic electroactive material formed by phosphomolybdate and polyaniline. Application as cation-insertion electrodes. *Chem. Mater.* 10:698–704.
17. Zheng JP, Huang J, Jow TR. (1997) The limitations of energy density for electrochemical capacitors. *J. Electrochem. Soc.* 144:2026–2031.
18. Breeze AJ, Schlesinger Z, Carter SA, Brock PJ. (2001) Charge transport in TiO₂/MEH-PPV polymer photovoltaics. *Phys. Rev. B* 64:125205.
19. Hu CC. and Tsou TW. (2003) The optimization of specific capacitance of amorphous manganese oxide for electrochemical supercapacitors using experimental strategies. *J. Power Sources* 115:179–182.
20. Jiang J. and Kucernak A. (2002) Electrochemical supercapacitor material based on manganese oxide: Preparation and characterization. *Electrochim. Acta* 47:2381–2386.

21. Kudo T, Ikeda Y, Watanabe T, Hibino M, Miyayama M, Abe H, Kajita K. (2002) Amorphous V_2O_5 /carbon composites as electrochemical supercapacitors electrodes. *Solid State Ionics* 152–15:833–841.
22. Wohlfahrt-Mehrens M, Schenk J, Wilde PM, Abdelmula E, Axmann P, Garche J. (2002) New materials for supercapacitors. *J. Power Sources* 105:182–188.
23. Wu NL, Wang SY, Han CY, Wu DS, Shiue LR. (2003) Electrochemical capacitor of magnetite in aqueous electrolytes. *J. Power Sources* 113:173–178.
24. Chen WC, Wen TC, Hsisheng T. (2003) Polyaniline-deposited porous carbon electrode for supercapacitors. *Electrochim. Acta* 48:641.
25. Mastragostino M, Arbizzani C, Soavi F. (2002) Conducting polymers as electrode materials in supercapacitors. *Solid State Ionics* 148:493–498.
26. Park JH, Park OO. (2002) Hybrid electrochemical capacitors based on polyaniline and activated carbon electrodes. *J. Power Sources* 111:185–190.
27. Ryu KS, Kim KM, Park NG, Park YJ, Chang SH. (2002) Synthesis and electrochemical properties of V_2O_5 intercalated with binary polymer. *J. Power Sources* 103:305.
28. Zhou Z, Cai N, Zhou Y. (2005) Capacitive characteristics of manganese oxides and polyaniline composite thin film deposited on porous carbon. *Mater. Chem. Phys.* 94:371–375.
29. White AM and Slade RCT. (2003) Polymer electrodes doped with heteropolymetallates and their use within solid-state supercapacitors. *Synth. Met.* 139:123–131.
30. Janssen RAJ, Hummelen JC, Sariciftci NS. (2005) Polymer-fullerene bulk heterojunction solar cells. *MRS Bull.* 30:33–36.
31. Takel T, Yoshimura K, Yonesaki Y, Kumada N, Kinomura N. (2005) Preparation of polyaniline/mesoporous silica hybrid and its electrochemical properties. *J. Porous Mater.* 12(4):337–343.
32. Machida K, Furuuchi K, Min M, Naoi K. (2004) Mixed proton-electron conducting nanocomposite based on hydrous RuO_2 and polyaniline derivatives for supercapacitors. *Electrochemistry* 72(6):402–404.
33. Girija TC, Sangaranarayanan MV. (2006) Analysis of polyaniline-based nickel electrodes for electrochemical supercapacitors. *J. Power Sourc.* 156:705–711.
34. Wang XF, Ruan DB, Wang DZ, Liang J. (2005) Hybrid electrochemical supercapacitors based on polyaniline and activated carbon electrodes. *Acta Phys. Chim. Sin.* 21(3):26–266.
35. Gómez-Romero P, Lira-Cantú M. (1997) Chemical polymerization of polyaniline and polypyrrole by phosphomolibdic acid. In situ formation of hybrid organic-inorganic materials. *Solid State Ionics* 101–103:875–880.
36. Pope MT, Müller A. (eds.). (1994) Polyoxometalates: from platonic solids to anti-retroviral activity. In *Topics in Molecular Organization and Engineering*. Kluwer, Dordrecht.
37. Gómez-Romero P. and Casañ-Pastor N. (1996) Photoredox chemistry in oxide clusters. Photochromic and redox properties of polyoxometalates in connection with analog solid state colloidal systems. *J. Phys. Chem.* 100:12448.
38. Gómez-Romero P. and Lira-Cantú M. (1997) Hybrid organic-inorganic electrodes: The molecular material formed between polypyrrole and the phosphomolybdate anion. *Adv. Mat.* 9:144.
39. Barbero C, Miras MC, Schnyder B, Haas O, Kotz R. (1994) Sulfonated polyaniline films as cation insertion electrodes for battery applications. Part 1 – Structural and electrochemical characterization. *J. Mater. Chem.* 4:1775–1783.
40. Novak P, Mueller K, Santhanam KSV, Haas O. (1997) Electrochemically active polymers for rechargeable batteries. *Chem. Rev.* 97:207.
41. Oyama N, Tatsuma T, Sato T, Sotomura T. (1995) Dimercaptan-polyaniline composite electrodes for lithium batteries with high-energy density. *Nature* 373:6515.
42. Scrosati B. Electrochemical properties of conducting polymers. (1988) *Progress in Solid State Chem.* 18(1):1–77.
43. Chen WC, Wen TC. (2003) Electrochemical and capacitive properties of polyaniline-implanted porous carbon electrode for supercapacitors. *J. Power Sources.* 117(1–2):273–282.

44. Hashmi SA, Upadhyaya HM. (2002) Polypyrrole and poly(3-methyl thiophene)-based solid state redox supercapacitors using ion conducting polymer electrolyte. *Solid State Ionics* 152:883–889.
45. Ryu KS, Kim KM, Park NG, Park YJ, Chang SH. (2002) Redox supercapacitor using poly-aniline doped with Li salt as electrode. *Solid State Ionics* 152:861–866.
46. Gómez-Romero P and Sanchez C. (2004) *Functional hybrid materials*. Wiley, Weinheim (ISBN 3-527-30484-3).
47. Kulesza PJ, Malik MA, Karwowska B, Miecznikowski K, Dzwolak W, Gursynska A, Grzybowski IN. (1997) *Electrochemical Capacitors*, (FM Delnick, D Ingersoll, X Andrieu, K Naoi eds.). Electrochemical Society, Pennington, UK. PV 96–2; 89.
48. Torres-Gómez G, Lira-Cantú M, Gómez-Romero P. (1999). Molecular hybrid materials based on conducting organic polymers and electroactive/photoactive inorganic species. *J. New Electrochem. Syst.* 2:145.
49. Dai L. (1999) Advanced syntheses and microfabrication of conjugated polymers, C₆₀-containing polymers and carbon nanotubes for optoelectronic applications. *Polym. Adv. Technol.* 10(7):357–420.
50. Baibarac M, Mihut L, Preda N, Lefrant S. (2005) Surface-enhanced Raman scattering studies on C-60 fullerene self-assemblies. *Carbon* 43(1):1–9.
51. Baibarac M, Baltog I, Godon C, Lefrant S, Chauvet O. (2004) Covalent functionalization of single-walled carbon nanotubes by aniline electrochemical polymerization. *Carbon* 42(15):3143–3152.
52. Li C, Liu CL, Li FS, Gong QH. (2003) Optical limiting performance of two soluble multi-walled carbon nanotubes. *Chem. Phys. Lett.* 380(1–2):201–205.
53. Wu W, Li J, Liu L, Yanga L, Guo ZX, Dai L, Zhu D. (2002) The photoconductivity of PVK-carbon nanotube blends. *Chem. Phys. Lett.* 364(1–2):196–199.
54. Wang W, Lin Y, Sun YP. (2005) Poly(*N*-vinyl carbazole)-functionalized single-walled carbon nanotubes: Synthesis, characterization, and nanocomposite thin films. *Polymer* 46(20):8634–8640.
55. Hirsch A. (2002) Functionalization of single-walled carbon nanotubes. *Ang. Chemie. Intl. Ed.* 41(11):1853–1859.
56. Coakley KM, Liu Y, Goh C, McGehee MD. (2005) Ordered organic-inorganic bulk heterojunction photovoltaic cells. *MRS Bull* 30:37–40.
57. Halls JMM, Walsh CA, Greenham NC, Marsaglia E, Friend RH, Moratti SC, Holmes AB. (1995) Efficient photodiodes from interpenetrating polymer networks. *Nature* 376(6540):498–500.
58. Yu G, Gao J, Hummelen JC, Wudl F, Heeger AJ. (1995) Polymer photovoltaic cells – enhanced efficiencies via network of internal donor-acceptor heterojunctions. *Science* 270:1789.
59. Spanggaard H, Krebs FK. (2004) A brief history of the development of organic and polymeric photovoltaics. *Sol. Energ. Mater. Sol. Cell* 83:125–146.
60. Sariciftci NS, Braun D, Zhang C, Srdanov VI, Heeger AJ, Stucky G, Wudl F. (1993) Semiconducting polymer-buckminsterfullerene heterojunctions – diodes, photodiodes, and photovoltaic cells. *Appl. Phys. Lett.* 62:585–587.
61. Hoppe H and Sariciftci NS. (2006) Organic solar cells: An overview. *J. Mater. Res.* 19(7):1924–1945.
62. Lira-Cantú M. and Gómez-Romero P. (2004) Multifunctional hybrid materials based on conducting organic polymers. Nanocomposite systems with photo-electro-ionic properties and applications. In *Functional Hybrid Materials* (Gómez-Romero P and Sanchez C eds.). Wiley, Weinheim, pp. 210.
63. Singh TB. and Sariciftci NS. (2006) Progress in plastic electronics devices. *Ann. Rev. Res.* 36:199–230.
64. Huynh WU, Dittmer JJ, Alivisatos AP. (2002) Hybrid nanorods-polymer solar cells. *Science* 295(5564):2425–2427.
65. Günes S, Neugebauer H, Sariciftci NS, Roither H, Kovalenko M, Pillwein G, Heiss W. (2006) Hybrid solar cells using HgTe nanocrystals and nanoporous TiO₂ electrodes. *Adv. Funct. Mater.* 16(8):1095–1099.

66. Cui DH, Xu J, Zhu T, Paradee G, Ashok S, Gerhold M. (2006) Harvest of linear infrared light in PbSe nanocrystal-polymer hybrid photovoltaic cells. *Appl. Phys. Lett.* 88(18):1831-11.
67. McDonald SA, Konstantatos G, Zhang SG, Cyr PW, Klem EJD, Levina L, Sargent EH. (2005) Solution-processed PbS quantum dot infrared photodetectors and photovoltaics. *Nat. Mater.* 4(2):138-142.
68. Ackermann J, Videlot C, El Kassimi A, Guglielmetti R, Fages F. (2005) Highly efficient hybrid solar cells based on an Octithiophene-GaAs heterojunction. *Adv. Funct. Mater.* 15(5):810-817.
69. Scharber MC, Mühlbacher D, Koppe M, Denk P, Waldauf C, Heeger AJ, Brabec J. (2006) Design rules for donors in bulk-heterojunction solar cells- Towards 10% energy-conversion efficiency. *Adv. Mater.* 18:789-794.
70. Coakley KM, McGehee MD. (2003) Photovoltaic cells made from conjugated polymers infiltrated into mesoporous titania. *Appl. Phys. Lett.* 83(16):3380-3382
71. Coakley KM, Liu Y, McGehee MD, Frindell KL, Stucky GD. (2003) Infiltrating semiconducting polymers into self-assembled mesoporous titania films for photovoltaic applications. *Adv. Funct. Mater.* 13(4):301-306
72. Coakley KM, Srinivasan BS, Ziebarth JM, Goh C, Liu Y, McGehee MD. (2005) Enhanced hole mobility in regioregular polythiophene infiltrated in straight nanopores. *Adv. Funct. Mater.* 15:1927-1932.
73. Kwong CY, Choy WCH, Djuricic AB, Chui PC, Cheng KW, Chan WK. (2004) Poly(3-hexylthiophene): TiO₂ nanocomposites for solar cell applications. *Nanotechnol.* 15(9):1156-1161.
74. Liu YX, Summers MA, Edder C, Frechet JMJ, McGehee MD. (2005) Using resonance energy transfer to improve exciton harvesting in organic-inorganic hybrid photovoltaic cells. *Adv. Mater.* 17(24):2960-2965.
75. Slooff LH, Wienk MM, Kroon JM. (2004) Hybrid TiO₂/polymer photovoltaic cells made from a titanium oxide precursor. *Thin Solid Films* 451:634-638.
76. Huisman CL, Goossens A, Schoonman J. (2003) Preparation of a nanostructured composite of titanium dioxide and polythiophene: a new route towards 3D heterojunction solar cells. *Synth. Met.* 138:237-241.
77. Grant CD, Schwartzberg AM, Smedstad GP, Kowalik J, Tolbert LM, Zhang JZ. (2002) Characterization of nanocrystalline and thin film TiO₂ solar cells with poly(3-undecyl-2,2'-bithiophene) as a sensitizer and hole conductor. *J. Electroanal. Chem.* 522:40-48.
78. Grant CD, Schwartzberg AM, Smedstad GP, Kowalik J, Tolbert LM, Zhang JZ. (2003) Optical and electrochemical characterization of poly(3-undecyl-2,2'-bithiophene) in thin film solid state TiO₂ photovoltaic solar cells. *Synth. Met.* 132:197-204.
79. Ravirajan P, Haque SA, Poplavskyy D, Durrant JR, Bradley DDC, Nelson J. (2004) Nanoporous TiO₂ solar cells sensitized with a fluorine-thiophene copolymer. *Thin Solid Films* 451-452:624-629.
80. van Hal PA, Wienk MM, Kroon JM, Verhees WJH, Slooff LH, van Gennip WJH, Jonkheijm P, Janssen RAJ. (2003) Photoinduced electron transfer and photovoltaic response of a MDMO-PPV:TiO₂ bulk-heterojunction. *Adv. Mater.* 15(2):118-120
81. van Hal PA, Christiaans MPT, Wienk MM, Kroon JM, Janssen RAJ. (1999) Photoinduced electron transfer from conjugated polymers to TiO₂. *J. Phys. Chem. B* 103(21):4352-4359.
82. Slooff LH, Kroon JM, Loos J, Koetse MM, Sweelssen J. (2005) Influence of the relative humidity on the performance of polymer/TiO₂ photovoltaic cells. *Adv. Funct. Mater.* 15(4):689-694.
83. Wang H, Oey CC, Djuricic AB, Xie MH, Leung YH. (2005) Titania bicontinuous network structures for solar cell applications. *Appl. Phys. Lett.* 87:023507.
84. Ravirajan P, Bradley DDC, Nelson J, Haque SA, Durrant JR, Smit HJP, Kroon JM. (2005) Efficient charge collection in hybrid polymer/TiO₂ solar cells using poly(ethylenedioxythiophene) polystyrene sulfonate as hole collector. *Appl. Phys. Lett.* 86(14):143101

85. Ravirajan P, Haque SA, Durrant JR, Bradley DDC, Nelson J (2005). The effect of polymer photoelectronic properties on the performance of multilayer hybrid polymer/TiO₂ solar cells. *Adv. Funct. Mater.* 15(4):609–618.
86. Arango AC, Johnson LR, Bliznyuk VN, Schlesinger Z, Carter SA, Horhold HH. (2000) Efficient titanium oxide/conjugated polymer photovoltaics for solar energy conversion. *Adv. Mater.* 12:1689.
87. Liu Z, Zhou J, Xue H, Shen L, Zang H, Chen W. (2006) Polyaniline/TiO₂ solar cells. *Synth. Met.* 156:721–723.
88. Song MY, Kim KJ, Kim DY. (2005) Enhancement of photovoltaic characteristics using PEDOT interlayer in TiO₂/MEHPPV heterojunction devices. *Sol. Energ. Mater. Sol. Cells* 85:31–39.
89. Fan Q, McQuillan B, Bradley DDC, Whitelegg S, Seddon AB. (2001) A solid state solar cell using sol–gel processed material and a polymer. *Chem. Phys. Lett.* 347:325–330.
90. Beek WJE, Wienk MM, Janssen RAJ. (2004) Efficient hybrid solar cells from zinc oxide nanoparticles and conjugated polymers. *Adv. Mater.* 16:1009–1013.
91. Beek WJE, Wienk MM, Kemerink M, Yang XN, Janssen RAJ. (2005) Hybrid zinc oxide conjugated polymer bulk heterojunction solar cell. *J. Phys. Chem. B* 109:9505–9516
92. Beek WJE, Wienk MM, Janssen RAJ. (2005) Hybrid polymer solar cells based on zinc oxide. *J. Mater. Chem.* 15:2985–2988
93. Beek WJE, Slooff LH, Wienk MM, Kroon JIM, Janssen RAJ (2005). Hybrid solar cells using a zinc oxide precursor and a conjugated polymer. *Adv. Funct. Mater.* 15:1703–1707.
94. Beek WJE, Wienk MM, Janssen RAJ. (2006) Hybrid solar cells from regioregular polythiophene and ZnO nanoparticles. *Adv. Funct. Mater.* 16:112–1116.
95. Olson DC, Piris J, Collins RT, Shaheen SE, Ginley DS. (2006) Hybrid photovoltaic devices of polymer and ZnO nanofiber composites. *Thin Solid Films* 496(1):26–29.
96. Peiro AM, Ravirajan P, Govender K, Boyle DS, O'Brien P, Bradley DDC, Nelson J, Durrant JR. (2006) Hybrid polymer/metal oxide solar cells based on ZnO columnar structures. *J. Mater. Chem.* 16(21):2088–2096.
97. Ravirajan P, Peiro AM, Nazeeruddin MK, Graetzel M, Bradley DDC, Durrant JR, Nelson J. (2006) Hybrid polymer/zinc oxide photovoltaic devices with vertically oriented ZnO nanorods and amphiphilic molecular interface layer. *J. Phys. Chem. B* 110(15):7635–7639.
98. Lira-Cantú M, Norrman K, Andreasen JW, Krebs FC. (2006) Oxygen release and exchange in niobium oxide MEH-PPV hybrid solar cells. *Chem. Mater.* 18:5684–5690.
99. Mozer AJ, Wada Y, Jiang KJ, Masaki N, Yanagida S, Mori SN. (2006) Efficient dye-sensitized solar cells based on a 2-thiophen-2-yl-vinyl-conjugated ruthenium photosensitizer and conjugated polymer hole conductor. *Appl. Phys. Lett.* 89:043509.
100. Greenham NC, Peng XG, Alivisatos AP. (1996) Charge separation and transport in conjugated-polymer/semiconductor-nanocrystal composites studied by photoluminescence quenching and photoconductivity. *Phys. Rev. B* 54(24):17628–17637.
101. Murakoshi K, Kogure R, Wada Y, Yanagida S. (1998) Fabrication of solid-state dye-sensitized TiO₂ solar cells combined with polypyrrole. *Sol. Energ. Mater. Sol. Cell* 55(1–2):113–125.
102. Arici E, Sariciftci NS, Meissner D. (2003) Hybrid solar cells based on nanoparticles of CuInS₂ in organic matrices. *Adv. Funct. Mater.* 13(2):165–171.
103. Arici E, Hoppe H, Schaffler F, Meissner D, Malik MA, Sariciftci NS. (2004) Morphology effects in nanocrystalline CuInSe₂-conjugated polymer hybrid systems. *Appl. Phys. A Mat. Sci. Proc.* 79(1):59–64.
104. Bereznev S, Kononov I, Opik A, Kois J. (2005) Hybrid CuInS₂/polymer and CuInS₂/poly(3,4-ethylenedioxythiophene) photovoltaic structures. *Synth. Met.* 152(1–3):81–84.
105. Jayadevan KP, Tseng TY. (2005) One-dimensional semiconductor nanostructures as absorber layers in solar cells. *J. Nanosci. Nanotech.* 5(11):1768–1784.
106. Gao LL, Tong B, Yao GJ, Dong YP, Zhang MF, Lam J, Yip W, Tang BZ. (2005) In situ complexes of self-assembled films of conjugated polymers with PbS nanoparticles and their photovoltaic properties. *Acta Polym. Sin.* 3:313–316.

107. Watt AAR, Meredith P, Riches JD, Atkinson S, Rubinsztein-Dunlop H. (2004) A PbS quantum-cube: conducting polymer composite for photovoltaic applications. *Curr. Appl. Phys.* 4(2–4):320–322.
108. Watt AAR, Blake D, Warner JH, Thomsen EA, Tavenner EL, Rubinsztein-Dunlop H, Meredith P. (2005) Lead sulfide nanocrystal: conducting polymer solar cells. *J. Phys. D Appl. Phys.* 38(12):2006–2012.
109. Zhang S, Cyr PW, McDonald SA, Konstantatos G, Sargent EH. (2005) Enhanced infrared photovoltaic efficiency in PbS nanocrystal/semiconductor polymer composites: 600-fold increase in maximum power output via control of the ligand barrier. *App. Phys. Lett.* 87(23):233101.
110. Ackermann J, Videlat C, El Kassimi A. (2002) Growth of organic semiconductors for hybrid solar cell application. *Thin Solid Films* 403–404:157–161.
111. Hu CC and Chu CH. (2000) Electrochemical and textural characterization of Iridium-doped polyaniline films for electrochemical capacitors. *Mater. Chem. Phys.* 65:329–338.
112. Milliron D, Gur I, Alivisatos AP. (2005) Hybrid organic-nanocrystal solar cells. *MRS Bull.* 30:41–44.
113. Milliron DJ, Hughes SM, Cui Y, Manna L, Li JB, Wang LW, Alivisatos AP. (2004) Colloidal nanocrystal heterostructures with linear and branched topology. *Nature* 430(6996):190–195.
114. Manna L, Milliron DJ, Meisel A, Scher EC, Alivisatos AP. (2003) Controlled growth of tetrapod-branched inorganic nanocrystals. *Nat. Mater.* 12:382–385.
115. Maria A, Cyr P, Klem E, Levina L, Sargent H. (2005) Solution-processed infrared photovoltaic devices with >10% monochromatic internal quantum efficiency. *Appl. Phys. Lett.* 87:213112.
116. Kroeze JE, Savenije TJ, Vermeulen MJW, Warman JM. (2003) Contactless determination of the conductivity action spectrum, exciton diffusion length, and charge separation efficiency in polythiophene-sensitized TiO₂ bilayers. *J. Phys. Chem. B* 107(31):7696–7705.
117. Kwong CY, Djurisic AB, Chui PC, Cheng KW, Chan WK. (2004) Influence of solvent on film morphology and device performance of poly(3-hexylthiophene):TiO₂ nanocomposite solar cells. *Chem. Phys. Lett.* 384(4–6):372–375.
118. Lira-Cantú M, Krebs FC. (2005) Polymer Photovoltaics: From Conjugated Polymers to Hybrid Organic-Inorganic Solar Cells. In *Recent Research Developments in Applied Physics Vol. 8* (S.G. Pandalai eds.). Transworld Research Network (ISBN:81-7895-187-8).
119. Lira-Cantú M and Krebs FC. (2006) Hybrid solar cells based on MEH-PPV and thin film semiconductor oxides (TiO₂, Nb₂O₅, ZnO, CeO₂ and CeO₂-TiO₂): Performance improvement during long time irradiation. *Sol. Energ. Mater. Sol. Cells* 90:2076–2086.
120. Lira-Cantú M, Norrman K, Andreasen JW, Casan-Pastor N, Krebs FC. (2007) Detrimental effect of inert atmospheres on hybrid solar cells based on semiconductor oxides. *J. Electrochem. Soc.* 154(6):B508–B513.
121. Kroeze JE, Savenije TJ. (2004) The application of a low-bandgap conjugated oligomer for the sensitization of SnO₂ and TiO₂. *Thin Solid Films* 451–45:54–59.
122. Moser J-E. (2005) Solar Cells. Later rather than sooner. *Nat. Mater.* 4:723–724.
123. Snaith HJ, Zakeeruddin SM, Schmidt-Mende L, Klein C, Graetzel M. (2005) Ion-coordinating hybrid sensitizer in solid-state hybrid solar cells. *Angew. Chem. Int. Ed.* 44:6413–6417.
124. Xiao-e L, Green ANM, Haque SA, Mills A, Durtant JR. (2004) Light-driven oxygen scavenging by titania/polymer nanocomposite films. *J. Photochem. Photobio. A Chem.* 162(2–3):253–259.
125. Cao F, Oskam G, Searson PC. (1995) A solid state, dye sensitized photoelectrochemical cell. *J. Phys. Chem.* 99:17071–17073.
126. Li B, Wang L, Kang B, Wang P, Qiu Y. (2006) Review of recent progress in solid-state dye-sensitized solar cells. *Sol. Energ. Mater. Sol. Cells* 90:549–573.
127. Durrant JR, Haque SA. (2003) Solar cells. A solid compromise. *Nat. Mater.* 2:362–363.

128. Yanagida S. (2006) Recent research progress of dye-sensitized solar cells in Japan. *C.R. Chimie* 9:597–604.
129. Graetzel M. (2004) Conversion of sunlight to electric power by nanocrystalline dye-sensitized solar cells. *J. Photochem. Photobio. A Chem.* 164(1–3):3–14.
130. Guo L, Dai SY, Wang KJ, Fang XQ, Shi CW, Pan X. (2005) Dye-sensitized Nano-TiO₂ thin membrane solar cells based on (PVDF-HFP)-type gel electrolytes. *Chem. J. Chin. Univ. Chin.* 26(10):1934–1937.
131. Kubo W, Kambe S, Nakade S, Kitamura T, Hanabusa K, Wada Y, Yanagida S. (2003) Photocurrent-determining processes in quasi-solid-state dye-sensitized solar cells using ionic gel electrolytes. *J. Phys. Chem. B* 107(18):4374–4381.
132. Mohmeyer N, Wang P, Schmidt HW, Zakeeruddin SM, Graetzel M. (2004) Quasi-solid-state dye sensitized solar cells with 1,3: 2,4-di-O-benzylidene-D-sorbitol derivatives as low molecular weight organic gelators. *J. Mater. Chem.* 14(12):1905–1909.
133. Stangar UL, Orel B, Neumann B, Stathatos E, Lianos P. (2003) A sol–gel type of electrolyte for a dye-sensitized solar cell: Attenuated total reflectance (ATR) vibrational spectra studies. *J. Sol Gel Sci. Tech.* 26(1–3):1113–1118.
134. Stathatos E, Lianos P. (2002) Organic–inorganic nanocomposite gels employed as electrolyte supports in dye-sensitized photoelectrochemical cells. *Int. J. Photoenerg.* 4(1):11–16.
135. Stathatos E, Lianos P, Vuk AS, Orel B. (2004) Optimization of a quasi-solid-state dye-sensitized photoelectrochemical solar cell employing a ureasil/sulfolane gel electrolyte. *Adv. Funct. Mater.* 14(1):45–48.
136. Stathatos E, Lianos R, Zakeeruddin SM, Liska P, Graetzel M. (2003) A quasi-solid-state dye-sensitized solar cell based on a sol–gel nanocomposite electrolyte containing ionic liquid. *Chem. Mater.* 15(9):1825–1829.
137. Wang P, Zakeeruddin SM, Moser JE, Nazeeruddin MK, Sekiguchi T, Graetzel M. (2003) A stable quasi-solid-state dye-sensitized solar cell with an amphiphilic ruthenium sensitizer and polymer gel electrolyte. *Nat. Mater.* 2(6):402–407.
138. Kato T, Okazaki A, Hayase S. (2006) Latent gel electrolyte precursors for quasi-solid dye sensitized solar cells – The comparison of nano-particle cross-linkers with polymer cross-linkers. *J. Photochem. Photobio. A Chem.* 179(1–2):42–48.
139. Kawano R, Tokuda H, Katakabe T, Nakamoto H, Kokubo H, Imabayashi S, Watanabe M. (2006) Specific charge transport in ionic liquids and ion gels and the importance in material science. *Kob. Ronbu.* 63(1):31–40.
140. Matsui H, Okada K, Kawashima T, Ezure T, Tanabe N, Kawano R, Watanabe M. (2004) Application of an ionic liquid-based electrolyte to a 100 mm × 100 mm sized dye-sensitized solar cell. *J. Photochem. Photobio. A Chem.* 164(1–3):129–135.
141. Oda T, Tanaka S, Hayase S. (2006) Analysis of dominant factors for increasing the efficiencies of dye-sensitized solar cells: Comparison between acetonitrile and ionic liquid based electrolytes. *Jpn. J. Appl. Phys. Part I.* 45(4A):2780–2787.
142. Ogomi Y, Kato T, Hayase S. (2006) Dye sensitized solar cells consisting of ionic liquid and solidification. *J. Photopoly. Sci. Technol.* 19(3):403–408.
143. Wang L, Fang SB, Lin Y, Zhou XW, Li MY. (2005) A 7.72% efficient dye sensitized solar cell based on novel necklace-like polymer gel electrolyte containing latent chemically cross-linked gel electrolyte precursors. *Chem. Commun.* 45:5687–5689.
144. Yamanaka N, Kawano R, Kubo W, Kitamura T, Wada Y, Watanabe M, Yanagida S. (2005) Ionic liquid crystal as a hole transport layer of dye-sensitized solar cells. *Chem. Commun.* 6:740–742.
145. Saito Y, Azechi T, Kitamura T, Hasegawa Y, Wada Y, Yanagida S. (2004) Photo-sensitizing ruthenium complex for solid state dye sensitized solar cells in combination with conducting polymers as hole conductors. *Coord. Chem. Rev.* 248:1469–1478.
146. Haque SA, Handa S, Peter K, Palomares E, Thelakkat M, Durrant JR. (2005) Supermolecular control of charge transfer in dye-sensitized nanocrystalline TiO₂ films: towards a quantitative structure-function relationship. *Angew. Chem. Int. Ed.* 44:5740–5744.

147. Nogueira AF, Longo C, De Paoli M.A. (2004) Polymers in dye sensitized solar cells: Overview and perspectives. *Coord. Chem. Rev.* 248:1455–1468.
148. Tan XS, Zhai J, Wan MX, Jaing L, Zhu DB. (2003) Polyaniline as a hole transport material to prepare solid solar cells. *Synth. Met.* 137:1511–1512.
149. Senadeera GKR, Kitamura T, Wada Y, Yanagida S. (2004) Deposition of polyaniline via molecular self-assembly on TiO₂ and its use as a sensitizer in solid-state solar cells. *J. Photochem. Photobio. A Chem.* 164(1–3):61–66.
150. Tan S, Zhai J, Xue B, Wan M, Meng Q, Li Y, Jiang L, Zhu D. (2004) Property influence of polyanilines on photovoltaic behaviors of dye-sensitized solar cells. *Langmuir* 20:2934–2937.
151. Tan SX, Zhai J, Wan MX, Meng OB, Li YL, Jiang L, Zhu DB. (2004) Influence of small molecules in conducting polyaniline on the photovoltaic properties of solid-state dye-sensitized solar cells. *J. Phys. Chem. B* 108(48):18693–18697.
152. Murakoshi K, Kogure R, Wada Y, Yanagida S. (1997) Solid state dye-sensitized TiO₂ solar cell with polypyrrole as hole transport layer. *Chem. Lett.* 5:471–472.
153. Kitamura T, Maitani M, Matsuda M, Wada Y, Yanagida S. (2001) Improved solid-state dye solar cells with polypyrrole using carbon-based counter electrode. *Chem. Lett.* 10:1054–1055.
154. Lancelle-Beltran E, Prené P, Boscher C, Belleville P, Buvat P, Sanchez C. (2006) All-solid-state dye-sensitized nanoporous TiO₂ hybrid solar cells with high energy conversion efficiency. *Adv. Mater.* 18:2579–2582.
155. Spiekermann S, Smestad G, Kowalik J, Tolbert LM, Graetzel M. (2001) Poly(4-undecyl-2,2-bithiophene) as hole conductor in solid state dye sensitized titanium dioxide solar cells. *Synth. Met.* 121:1603–1604.
156. Saito Y, Kitamura T, Wada Y, Yanagida S. (2002) Poly(3,4-ethylenedioxythiophene) as a hole conductor in solid state dye sensitized solar cells. *Synth. Met.* 131(1–3):185–187.
157. Saito Y, Fukuri N, Senadeera R, Kitamura T, Wada Y, Yanagida S. (2004) Solid state dye sensitized solar cells using in situ polymerized PEDOTs as hole conductor. *Electrochem. Commun.* 6:71–74.
158. Saito R, Dresselhaus G, Dresselhaus MS. (1998) *Physical Properties of Carbon Nanotubes*. Imperial college press, London.
159. Saito Y, Uemura S, Hamaguchi K. (1998) Cathode ray tube lighting elements with carbon nanotube field emitters. *Jpn. J. Appl. Phys.* 37(3B):L346–L348.
160. Lira-Cantu M, Krebs FC, Gomez-Romero P, Yanagida S. (2008) Conjugated polymers as part of multifunctional organic-inorganic hybrid materials for photovoltaic applications. *Mater. Res. Soc. Symp. Proc.* 1007:249–257.
161. Wang Y, Yang K, Kim S-C, Nagarajan R, Samuelson LA, Kumar J. (2006) In situ polymerized carboxylated diacetylene as a hole conductor in solid-state dye-sensitized solar cell. *Chem. Mat.* 18:4215–4217.
162. Ikeda N, Miyasaka T. (2005) A solid-state dye-sensitized photovoltaic cell with poly(*N*-vinyl-carbazole) hole transporter mediated by alkali iodide. *Chem. Comm.* 1886–1888.
163. Ikeda N, Teshima K, Miyasaka T. (2006) Conductive polymer-carbon-imidazolium composite: a simple means for constructing solid-state dye-sensitized solar cells. *Chem. Comm.* 1733–1735.
164. Kruger J, Plass R, Graetzel M, Matthieu HJ. (2002) Improvement of the photovoltaic performance of solid-state dye-sensitized device by silver complexation of the sensitizer cis-bis(4,4'-dicarboxy-2,2' bipyridine)-bis(isothiocyanato) ruthenium(II). *Appl. Phys. Lett.* 81(2):367–369.
165. Lancelle-Beltran E, Prené P, Boscher C, Belleville P, Buvat P, Lambert S, Guillet F, Boissiere C, Grosso D, Sanchez C. (2007) Nanostructured Hybrid Solar Cells Based on Self-Assembled Mesoporous Titania Thin Films. *Chem. Mater.* 18(26):6152–6156.
166. Brabec CJ, Hauch JA, Schilinsky P, Waldauf C. (2005) Production aspects of organic photovoltaics and their impact on the commercialization of devices. *MRS Bull.* 30:50–52.
167. Padinger F, Brabec CJ, Fromherz T, Hummelen JC, Sariciftci NS. (2000) Fabrication of large area photovoltaic devices containing various blends of polymer and fullerene derivatives by using the doctor blade technique. *Opt. Elect. Rev.* 8(4):280–283.

168. Winther-Jansen B, Krebs FC. (2006) High-conductivity large-area semi-transparent electrodes for polymer photovoltaics by silk screen printing and vapour-phase deposition. *Sol. Energ. Mat. Sol. Cells* 90:123–132.
169. Krebs F. Alternative PV. (2005) Alternative PV Large scale organic photovoltaics. *Refocus* 6(3):38–39.
170. Al-Ibrahim M, Roth HK, Zhokhavets U, Gobsch G, Sensfuss S. (2005) Flexible large-area polymer solar cells based on poly(3-hexylthiophene)/fullerene. *Sol. Energ. Mater. Sol. Cells* 85:13–20.
171. Al-Ibrahim M, Klaus H, Sensfuss S. (2004) Efficient large-area polymer solar cells on flexible substrates. *Appl. Phys. Lett.* 85(9): 1481–1483.
172. Krebs FC, Alstrup J, Spanggaard H, Larsen K, Kold E. (2004) Production of large-area polymer solar cells by industrial silk screen printing, lifetime considerations and lamination with polyethyleneterephthalate. *Sol. Energ. Mater. Sol. Cell* 83:293–300.
173. <http://www.konarkatech.com/>
174. Li G, Shrotriya V, Huang J, Yao Y, Moriarty T, Emery K, Yang Y. (2005) High-efficiency solution processable polymer photovoltaic cells by self-organization of polymer blends. *Nat. Mater.* 4:864–868.
175. Kim Y, Cook S, Tuladhar SM, Choulis SA, Nelson J, Durrant JR, Bradley DDC, Giles M, McCulloch I, Ha CS, Ree M. (2006) A strong regioregularity effect in self-organizing conjugated polymer films and high-efficiency polythiophene:fullerene solar cells. *Nat. Mater.* 5:1897–203.
176. Österbacka R, An CP, Jiang XM, Vardeny ZV (2000) Two-dimensional electronic excitations in self-assembled conjugated polymer nanocrystals. *Science* 4:839–842.
177. Siringhaus H, Brown PJ, Friend RH, Nielsen MM, Bechgaard K, Langeveid-Voss BMW, Spiering AJH, Janssen RAJ, Meijer EW, Herwig P, de Leeuws DM (1999) Two-dimensional charge transport in self-organized, high-mobility conjugated polymers. *Nature* 401:685–688.
178. Gebeyehu D, Brabec CJ, Sariciftci NS, Vangeneugden D, Kiebooms R, Vanderzande D, Kienberger F, Schindler H. (2002) Hybrid solar cells based on dye-sensitized nanoporous TiO₂ electrodes and conjugated polymers as hole transport materials. *Synth. Met.* 125:279–287
179. Gebeyehu D, Brabec CJ, Sariciftci NS. (2002) Solid-state organic–inorganic hybrid solar cells based on conjugated polymers and dye-sensitized TiO₂ electrodes. *Thin Solid Films* 403–404:271–274.
180. Baibarac M, Lira-Cantú M, Oró Solé J, Casañ-Pastor N, Gómez -Romero P. (2006) Electrochemically functionalized carbon nanotubes and their application to rechargeable Li batteries. *Small* 2(8–9):1075–1082.
181. Dell RM, Rand DAJ. (2001) Energy storage – a key technology for global energy sustainability. *J. Power Sources* 100(1):2–17.
182. Fukuri N, Saito Y, Kubo W, Senadeera GKR, Kitamura T, Wada Y, Yanagida S. (2004) Performance improvement of solid-state dye-sensitized solar cells fabricated using poly(3,4-ethylenedioxythiophene) and amphiphilic sensitizing dye. *J. Electrochem. Soc.* 151(10):A1745–A1748.
183. Gebeyehu D, Brabec CJ, Padinger F, Fromherz T, Spiekermann S, Valchopoulos N, Kienberger F, Schindler H, Sariciftci NS. (2001) Solid state dye-sensitized TiO₂ solar cells with poly(3-octylthiophene) as hole transport layer. *Synth. Met.* 121:1549–1550.
184. Gómez-Romero P, Chojak M, Cuentas-Gallegos K, Asensio JA, Kulesza PJ, Casañ-Pastor N, Lira-Cantú M. (2003) Hybrid organic-inorganic nanocomposite materials for application in solid state electrochemical supercapacitors. *Electrochem. Commun.* 5:149.
185. Arango AC, Carter SA, Brock PJ. (1999) Charge transfer in photovoltaics consisting of interpenetrating networks of conjugated polymer and TiO₂ nanoparticles. *Appl. Phys. Lett.* 74:1698–1700.
186. Kim H, Popov BN. (2003) Study and characterization of MnO₂-based mixed oxides as supercapacitors. *J. Electrochem. Soc.* 150:D56–D62.

Chapter 8

Hybrid Polymer-Inorganic Photovoltaic Cells

Waldo J.E. Beek and René A.J. Janssen

Abstract Composite materials made from organic conjugated polymers and inorganic semiconductors such as metal oxides attract considerable interest for photovoltaic applications. Hybrid polymer-inorganic solar cells offer the opportunity to combine the beneficial properties of the two materials in charge generation and transport with easy and cheap processing in large areas. Various strategies, for creating hybrid polymer solar cells have been explored in recent years. Many of these methods aim at creating an intimately mixed bulk-heterojunction microstructure of the two materials on a nanometer scale, ensuring efficient charge generation at the interface and effective percolating pathways for photogenerated electrons and holes to the electrodes. Progress in the basic understanding of the operation principles and in the actual performance of these devices has been very significant. This review highlights the state of the art in the field and discusses the scope and limitations of hybrid polymer-inorganic photovoltaic cells for future energy production.

8.1 Introduction

8.1.1 Introduction to Solar Cells

Edmond Becquerel discovered the photovoltaic effect in 1838, when he observed a small voltage and current when two silver halide coated platinum plates immersed in an acidic solution were exposed to light. Only far into the next century a major improvement was achieved: over 50 years ago, the first silicon solar cell was developed by Chapin, Fuller, and Pearson of Bell Telephone Laboratories [1].

W.J.E. Beek and R.A.J. Janssen (✉)
Molecular Materials and Nanosystems, Eindhoven University of Technology, PO Box 513,
5600 MB Eindhoven, The Netherlands
e-mail: r.a.j.janssen@tue.nl

Silicon solar cells consist of p- and n-type silicon (Fig. 8.1). In-between these two layers there is a transition layer, a p–n junction. The internal field over this junction separates the photogenerated charges, the holes are swept into the p-layer and the electrons are swept into the n-layer. Although these opposite charges attract each other, most of them can only recombine by passing through an external circuit outside the material because of the internal potential energy barrier.

Since the first silicon solar cell, many other types of cells, often based on new materials, new deposition methods, or novel device architectures have been described. The operation principle of each photovoltaic device, however, involves three basic steps, i.e., absorption of photons, creation and separation of free and mobile charges, and transport of these charges towards electrodes for collection. When each of these steps is efficient and occurs with minimal energy losses, a photovoltaic device can convert solar light into electrical free energy, with a maximum thermodynamic efficiency of about 31% in the radiative limit assuming detailed balance and a single band gap absorber [2].

Many different designs of this general p–n junction type silicon solar cell have been developed. Nowadays, single crystalline and multi-crystalline silicon solar cells have reached solar energy conversion efficiencies of 24.7 and 20.3%, respectively [3–5]. In essence silicon is not the optimal material for solar cells, its band gap of 1.1 eV (crystalline Si) is at the lower limit for optimal solar light conversion. The ideal solar cell would have a band gap between 1.1 and 1.7 eV for good photovoltaic conversion efficiency, a direct band gap for a high absorption coefficient, and consist of non-toxic, readily available materials that can be easily and reproducibly deposited with a technique that is suitable for large areas [6]. Of course such ideal solar cell would also have excellent long term stability.

Silicon suffers from its disadvantage of being an indirect semiconductor; as a result it is only a weakly absorbing material. For a silicon layer to absorb 90% of the light, at least a 100 μm thick film is needed. Using direct band gap semiconductors,

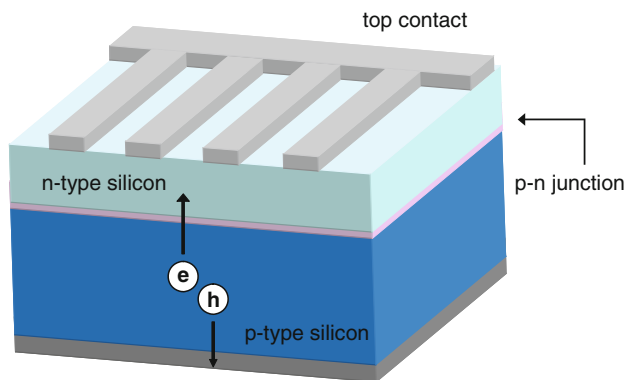


Fig. 8.1 A simple scheme of a silicon solar cell, showing the basic elements: p- and n-type silicon and the junction in between

like GaAs, a 1 μm thin film is sufficient. Because the photocarriers have to reach the p–n junction for separation, the silicon used in solar cells has to be of very high purity and crystalline perfection. For this reason the production of crystalline silicon is far from easy and cheap, and much attention is paid to the development of micro-crystalline and amorphous silicon solar cells, promising high efficiencies at lower costs. Nonetheless single crystalline silicon solar cells still have a market share of 31.0, vs. 59.6% for multi-crystalline silicon, 3.1% for ribbon silicon and 5.3% for amorphous silicon, leaving $\sim 1\%$ for non-silicon based solar devices [7]. One of the major challenges for future photovoltaic devices will be to overcome the high material- and production-cost of silicon and other semiconductor materials. Relatively new materials like semiconducting polymers and hybrid composites with metal oxides promise to become an attractive alternative.

8.1.2 Conducting Polymers

The discovery of conducting polymers by MacDiarmid, Shirakawa, and Heeger in 1977, and the ability to dope these polymers to cover the full range from insulator to metal [8, 9], has created a new field of research at the crossroads of polymer chemistry and condensed matter physics. These newly discovered conjugated polymers with conducting and semiconducting properties provide exciting opportunities for application in opto-electronic devices. The origin of the appealing properties of π -conjugated polymers (Fig. 8.2) that enable their application in devices is related to the extended nature of the electronic wave functions that is created by the alternating single and double bonds of their molecular structure. This provides the basis for charge transport and gives rise to a range of linear and nonlinear optical properties.

Semiconducting polymers offer the promise of achieving a new generation of materials, exhibiting the electrical and optical properties of metals or semiconductors and retaining the attractive mechanical properties and processing advantages of polymers. Many of the envisioned applications of conjugated polymers require transport of charges and therefore high charge carrier mobility. Hole mobilities in highly ordered regioregular polythiophenes [10, 11] and electron mobilities in ladder type polymers [12] as high as 0.1 cm^2/Vs have been obtained. In general, the family of n-type conjugated polymers is much less developed than that of p-type

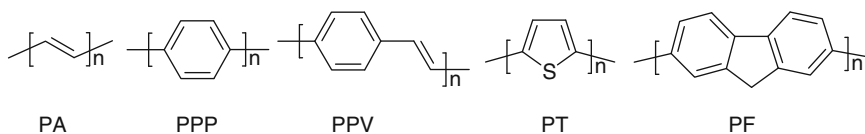


Fig. 8.2 Structures of archetypal π -conjugated polymers polyacetylene (PA), poly-*p*-phenylene (PPP), poly(*p*-phenylene vinylene) (PPV), polythiophene (PT), and polyfluorene (PF)

conjugated polymers. In fact, the electron mobility of most conjugated polymers is still low compared to the hole mobility in p-type conjugated polymers and the electron mobility in inorganic materials. Increasing attention is therefore given to hybrid conjugated polymer – inorganic materials, that represent a synergistic approach to overcome the limitations of semiconducting polymer devices without losing their beneficial processability properties. New insights show that these materials might strengthen and enhance their intrinsic properties and will eventually lead to a yet newer class of exciting materials with a wide span of applications.

8.1.3 Hybrid – polymer Solar Cells

The high absorption coefficients ($>10^7/\text{m}$) found in conjugated polymers like poly(*p*-phenylene vinylene) (PPV) make them viable candidates to use in a combination with n-type semiconducting inorganic materials, which will lead to a simple and effective solar cell. In contrast to inorganic semiconductors, photoexcitation of organic semiconductors generally results in a strongly bound electron-hole pair, called an exciton [13, 14]. In organic semiconductors these excitons are only effectively separated at an interface between a p-type (electron donating) and n-type (electron accepting) material. Hence, in polymer photovoltaic devices, the primary step after absorption of a photon is a photoinduced electron transfer between donor and acceptor type semiconducting materials, yielding a charge-separated state. This photoinduced electron transfer between donor and acceptor boosts the photogeneration of free charge carriers compared to the individual, pure materials. In general, the exciton lifetime and diffusion length in organic semiconductors are limited by radiative and non-radiative decay. As a consequence only excitons generated in close vicinity of a p–n interface will give rise to charges. For PPVs the exciton diffusion length is about 5–10 nm [15–17], this implies that for effective charge separation the photogeneration of excitons should occur within a few nanometers from a p–n junction. For polythiophenes the exciton diffusion length is on the same order of magnitude, ~ 5 nm [18]. These short exciton diffusion lengths impose an important condition for efficient charge generation. Anywhere in the active layer, the distance to the interface should be on the order of the exciton diffusion length. Despite their high absorption coefficients, exceeding $10^7/\text{m}$, a 10 nm double layer of donor and acceptor materials would not be optically dense, allowing most photons to pass freely. The solution to this dilemma is elegantly simple [19, 20]. By mixing the p- and n-type materials and relying on the intrinsic tendency of polymer materials to phase-separate on a nanometer dimension, junctions throughout the bulk of the material are created that ensure quantitative dissociation of photogenerated excitons, irrespective of the thickness (Fig. 8.3).

In the past decade significant progress has been reported for these so-called bulk heterojunction photovoltaic devices using solution processed p-type conjugated polymers, either in combination with polymers [19, 21, 22] or fullerenes [20, 23–25] as the n-type material. In these devices the active layer is sandwiched between charge-selective electrodes, one being transparent to light (Fig. 8.3). Photovoltaic

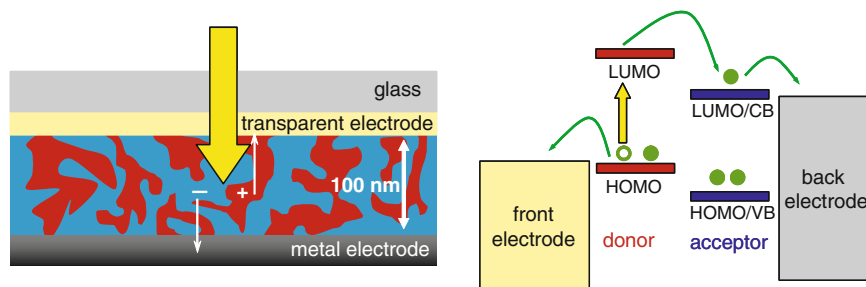


Fig. 8.3 Schematic representation of a bulk heterojunction solar cell, showing the phase separation between donor (*red*) and acceptor (*blue*) materials and the schematic energy diagram involving the energy levels of the highest occupied and lowest unoccupied molecular orbitals (HOMO and LUMO) and valence and conduction bands (VB and CB)

devices with efficiencies of 4–5% have been obtained using a combination of a fullerene derivative (PCBM) and regioregular poly(3-hexylthiophene) (P3HT) [26–29]. Presently, the efficiency of polymer: polymer blends is somewhat less, mainly due to limitation of electron transport in the acceptor type of polymers.

On the other hand, the use of wide band gap semiconductor oxides materials is well established, and shows a great revival after the application of TiO_2 in dye sensitized solar cells (DSSC), following the work of Grätzel et al. [30]. The best dye sensitized solar cells currently reach efficiencies of 11.04% [31, 32]. The main drawback of the traditional DSSC, hampering its wide use, seems the application of a liquid electrolyte. This liquid electrolyte is often related to the limited thermostability of the cell and is responsible for the corrosion of the Pt covered counter electrode. For this reason alternatives for the liquid electrolyte are being developed, aiming at a solid-state version of the DSSC [33–35]. Current “state of the art” quasi-solid-state dye-sensitized solar cells based on the iodide/triiodide redox couple, reach stable and are >6% efficient [36]. Also the use of solvent-free dye-sensitized solar cell based on an ionic liquid electrolyte and using $\text{SeCN}^-/(\text{SeCN})_3^-$ as the redox couple, replacing the iodide/triiodide redox couple has been considered. This solar cell reaches measured AM1.5 efficiencies of 8% [37].

Given these developments, it is not surprising that the combination of organic or polymer p-type semiconductors with n-type inorganic materials attracts considerable interest for photovoltaic applications. These hybrid materials would have the processing properties of polymers, i.e., allowing spin coating, doctor blading, or printing techniques to deposit thin films, have a high absorption coefficient in the visible range, and would benefit from the high charge carrier mobility for holes in the polymer and for electrons in the inorganic material.

Different approaches to create hybrid polymer solar cells have been explored. Many of these aim at creating an intimately mixed bulk-heterojunction microstructure

of the two materials on a nanometer scale, ensuring percolating pathways for both charge carriers to the relevant electrodes. In this chapter five methods to create active layers will be considered:

8.1.3.1 Blending Nanoparticles with Conjugated Polymers

By mixing nanoparticles of inorganic semiconductors with conjugated polymers, p–n junctions can be created throughout the thin film that give rise to efficient charge generation from photogenerated excitons. The approach is in essence simple and applicable to large areas. The challenge, however, is to create sufficient particle-particle contacts to sustain charge transport. Moreover, it is crucial to use a solvent that allows processing of the inorganic and the organic materials at the same time, which may not be trivial because of the different nature of the two components. This may require modification of the inorganic material or conjugated polymer.

8.1.3.2 Flat Bilayer Architectures

Covering flat inorganic semiconductor layers with a conjugated polymer is the most direct approach to hybrid photovoltaic cells. While bilayers with a flat interface suffer from a low interface area between the two components, which – in a first approach – limits the effective thickness of active layer for charge generation to the exciton diffusion length (~5 nm for many polymers). This cell architecture has received considerable interest. In addition, the well-defined flat interface offers several advantages in investigating charge generation and has often been used for scientific purposes.

8.1.3.3 Infiltrating Polymers into Nanoporous Inorganic Semiconductors

With respect to increasing the interface area between the p-type and n-type materials, infiltrating a nanoporous semiconductor electrode with a conjugated polymer is an attractive option. It is a logical extension of the solid-state DSSC concept in which the semiconducting polymer takes care of light absorption and hole transport, replacing both the dye and electrolyte.

8.1.3.4 Filling Nanostructured Inorganic Electrodes with Conjugated Polymers

Hybrid bulk heterojunctions based on well-ordered inorganic semiconductor nanostructures such as for e.g., vertical pillars, straight pores, or inverted opal structures are a promising approach to create effective photoactive layers for solar cells. By controlling the dimensions into the range of the exciton diffusion length,

charge generation can be optimized while efficient charge transport can be ensured by creating short, straight direct pathways for both charge carriers [38].

8.1.3.5 In Situ Synthesis of the n-Type Semiconductor in the p-Type Polymer Layer

This approach differs in an essential way from the previous methods, in the sense that the inorganic material is made only after film formation. For this goal a precursor for the semiconductor is mixed with a conjugated polymer, cast into a thin film, and subsequently converted in situ into the inorganic phase inside the polymer. This is an attractive method as it promises a very simple procedure for making hybrid bulk heterojunctions and can make use of well established sol-gel chemistry. Similar to the two other methods, the challenge is to control the morphology of the blend and the crystalline nature of the inorganic phase after conversion, as these are likely to affect the electron transport in the material. One drawback of this method is that the applied precursor or sol-gel chemistry should be compatible with the use of conjugated polymers, limiting it to the application of organic media and low temperatures.

8.1.4 Solar Cell Characterization

Several efficiencies exist that describe the electrical characteristics of solar cells under illumination. The most relevant one is the power conversion efficiency η being the ratio of the maximum obtainable electrical power P_{\max} and the incident light power (I_L).

$$\eta = \frac{P_{\max}}{I_L} \times 100\%. \quad (8.1)$$

The point of maximum obtainable electrical power P_{\max} is located in the fourth quadrant on the current density-voltage (J - V) curve where the product of current density J and voltage V reaches its maximum value (Fig. 8.4).

In order to relate this maximum power point to the short-circuit current density J_{sc} , the open-circuit voltage V_{oc} , and the diode behavior of the solar cell, the fill factor (FF) is introduced. The FF describes the ratio of (or the rectangle of) P_{\max} with the product of (or the rectangle defined by) J_{sc} and V_{oc} .

$$FF = \frac{P_{\max}}{J_{sc} V_{oc}}. \quad (8.2)$$

For a simple single-semiconductor photovoltaic model FF lies in between 0.25 and 1.0. With (8.2), (8.1) can be written in its most practical form as:

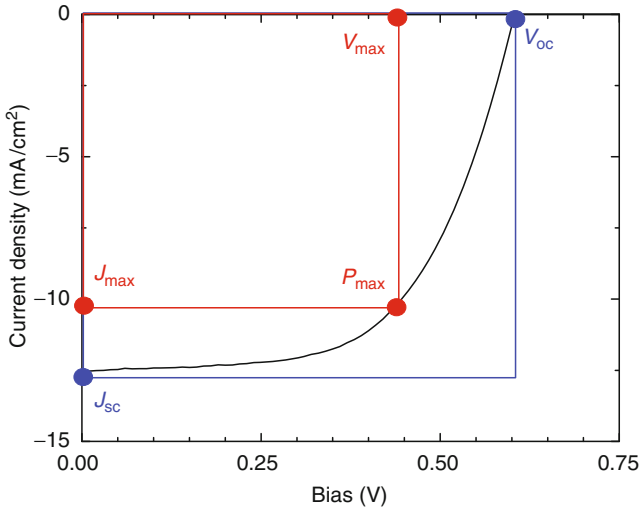


Fig. 8.4 Current density-voltage (J - V) curve of solar cell under illumination. The maximum obtainable electrical power (P_{\max}) is depicted as the red rectangle

$$\eta = \frac{J_{sc} V_{oc} \text{FF}}{I_L} \times 100\%. \quad (8.3)$$

Hence optimization of the performance of a solar cell involves maximizing each of the three parameters J_{sc} , V_{oc} and FF.

The power conversion efficiency η should be measured under standard test conditions. These conditions are specified as a radiant density of 100 mW/cm^2 with a spectral distribution defined as “Air Mass 1.5 Global” (AM1.5G, IEC 904-3) at a cell temperature of 25°C . AM1.5 approximates the intensity of sunlight that would be received on a tilted plane surface on a clear day, and for a model atmosphere containing specified concentrations of, as for e.g., water vapor, and aerosol.

Apart from η , the external quantum efficiency (EQE), is often used. The EQE compares the number of charge carriers collected at zero bias (J_{sc}) to the number of incident monochromatic photons:

$$\text{EQE}(\lambda) = \frac{1,240 J_{sc}(\lambda)}{\lambda I_L(\lambda)} \times 100\%, \quad (8.4)$$

where J_{sc} is in mA/cm^2 , λ in nm, and I_L in mW/cm^2 . Measuring the EQE at different wavelengths results in a spectral response of the solar cell. Because the short-circuit current density (J_{sc}) does not necessarily increase linearly with incident light power (I_L), the EQE values generally depend on the I_L of the monochromatic light. The same, of course, holds for η . This explains the necessity for both η and EQE measurements under appropriate standard test conditions. Hence, apart from the

monochromatic light, continuous irradiation under standard test conditions is required for meaningful comparison of the EQE spectra. In the literature many “ill-defined” efficiencies are often reported. This hampers a meaningful comparison of the solar cell data reported. One of the reasons for this fact is the difficulty in measuring the absolute light intensities at different wavelengths and the various different types of white light that are being used. Therefore, we have tried in this chapter to quote the efficiencies as they were reported together with the light sources and intensities used. Nevertheless, white light sources and AM1.5 solar simulators may still differ significantly in spectral output and hence one has to be cautious in comparing the absolute efficiencies.

8.1.5 General Outline

In this chapter we will further focus on the five different approaches that have been explored for polymer-inorganic hybrid solar cells. We will summarize the most salient results that have been reported in this area and address in more detail the results that have followed from our own research in this area.

8.2 Nanoparticle-polymer Hybrid Solar Cells

The hybridization of inorganic nanoparticles and conjugated polymers potentially combines all the advantages of inorganic and polymeric semiconductors. Polymers allow for simple, large scale, deposition techniques and, hence, combining with soluble inorganic nanoparticles into bulk heterojunction layers opens a versatile route towards hybrid photovoltaic devices [39].

8.2.1 CdSe and CdTe Nanoparticles

So far, the best photovoltaic response for hybrid devices has been realized using cadmium selenide (CdSe) nanoparticles mixed with conjugated polymers as explored by Alivisatos and Greenham. CdSe nanoparticles also harvest solar light and the size of the nanoparticles can be tuned for optimal light absorption. First examples on CdSe nanoparticles (nc-CdSe) in poly [2-methoxy-5-(2'-ethylhexyloxy)-1,4-phenylene vinylene] (MEH-PPV) showed external (monochromatic) quantum efficiencies up to 12% [40, 41]. In these devices, the nc-CdSe:MEH-PPV blend was sandwiched between a transparent indium tin oxide (ITO) front electrode and an aluminum (Al) metal back electrode, to harvest the photogenerated holes and electrons respectively. It appeared to be of extreme importance to control the surface chemistry of the nanoparticles. During synthesis capping agents such as trioctylphosphineoxide (TOPO)

are used to control the solubility of the nanoparticles. For efficient electron transfer between the polymer and the nanoparticle and subsequent electron transport between the particles, this capping agent has to be removed. TOPO can be removed by treatment with pyridine, and the crystals can then be redissolved in chloroform and mixed with the polymer.

The photoinduced electron transfer from conjugated polymers to CdSe has been studied in detail by Greenham et al. using photoluminescence (PL) and photoinduced absorption spectroscopy (PIA) for three different poly(*p*-phenylene vinylene) derivatives and monodisperse nanoparticles with diameters from 2.5 to 4.0 nm [42, 43]. For MEH-PPV, the PL was quenched and the PIA spectrum revealed the characteristic spectral features of long-lived positive polarons (radical cations) on the polymer. Both the PL quenching and the PIA spectra were insensitive to the nanocrystal size. Two high-electron-affinity, cyano-substituted PPVs, were also investigated with these techniques. One of the polymers (MEH-CN-PPV) behaved very similarly to MEH-PPV, but for the second polymer (DHeO-CN-PPV), having two linear hexyloxy side chains instead of the methoxy en 2-ethylhexyloxy side chains in MEH-CN-PPV, no photoinduced charge transfer could be observed. Apparently the symmetric dihexyloxy side chains inhibit electron transfer, either by creating a spatial barrier or by creating a less well mixing of the polymer with the crystals. Similar results have been observed by Dyakonov et al. for mixtures of CdSe and poly [2-methoxy-5-(3' 7'-dimethyloctyloxy)-1,4-phenylene vinylene] (MDMO-PPV) [44]. By extending the wavelength range of the PIA spectra to the infrared, down to 0.23 eV, these authors were able to observe the spectral characteristics of trapped electron in CdSe at 0.31 eV. Electron spin resonance (ESR) spectra for CdSe:MDMO-PPV composite layers under illumination with 514 nm light, gave a strong signal at $g = 2.0025$. This g -value is characteristic for polymer radical cations (positive polarons). Together with the absence of light-induced ESR (LESr) signals in pure MDMO-PPV or CdSe, the LESr signal at $g = 2.0025$ could be attributed to the photoinduced electron transfer reaction between the polymer and the nanocrystals [44].

A major improvement of the photovoltaic effect came with the introduction of CdSe rods combined with P3HT [45–47]. CdSe rods allow for a more efficient electron transport through the film, and the P3HT is a better hole-transporting polymer. Figure 8.5 shows the device layout and TEM-pictures of CdSe rods and dots.

For film preparation, the challenge is to keep these rods soluble in organic solvents. This has been achieved by replacing TOPO with pyridine, which makes these rods soluble in pyridine-chloroform mixtures. Photovoltaic devices prepared in this way give external quantum efficiencies up to EQE = 55%, a short circuit current density of $J_{sc} = 5.7$ mA/cm², an open circuit voltage of $V_{oc} = 0.7$ V, and a fill factor of FF = 0.4, under AM1.5 (100 mW/cm²) illumination with power conversion efficiency of $\eta = 1.7\%$ [45]. The high efficiency was attributed to the effective dispersing of CdSe nanorods in P3HT by using pyridine-chloroform solvent mixture and subsequent removal of the pyridine through thermal treatment. The fine dispersion creates a high interfacial area and the removal of pyridine causes a strong enhancement of the photocurrent. The latter effect has been attributed to result from

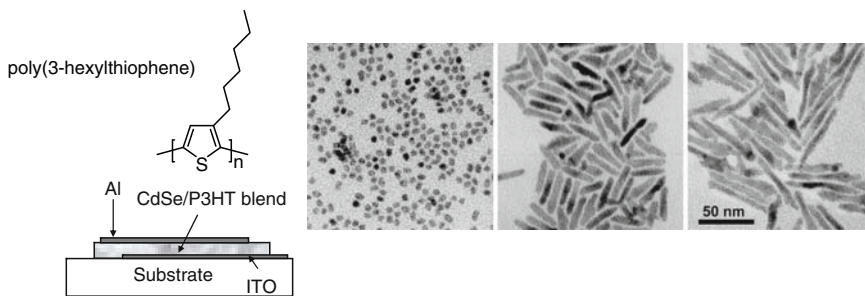


Fig. 8.5 *Left:* Schematic layout of a hybrid solar cell consisting of CdSe nanorods (90 wt%) in P3HT. Reprinted with permission from Adv. Funct. Mater. 2003, 13, 73 [47]. Copyright 2003 Wiley-VCH. *Right:* TEM pictures of dots and rods, with high aspect ratios are shown on the right. From Science 2002, 295, 2425 [46]. Reprinted with permission from AAAS

an improved photoinduced charge transfer between the polymer and the rods by a closer contact and by the fact that pyridine may act as a nonradiative recombination site for excitons in the polymer [47].

The charge transport in these CdSe-rod:P3HT blends has been studied in some detail and modeled using the Shockley equation including the presence of a space-charge limited region at high currents [48]. It was found that, especially, the low mobility of the holes in the blends limits the transport and thereby the performance of the solar cell. From the light intensity dependence of the V_{oc} for nanocrystals with different band gaps, it was inferred that Fermi-level pinning occurs at the interface with the aluminum electrode and the nanocrystal.

While surfactants can be stripped from the nanocrystals during film processing to afford direct contact between the nanocrystals and the polymer, it is difficult to control the morphology and dispersion of nanocrystals within the polymer when using this process. To address this challenge, Fréchet et al. have prepared well-defined oligo(3-hexylthiophenes) (T_n , n = number of 3-hexylthiophenes) with a phosphonic acid (PA) functional group that binds strongly to the CdSe surface [49]. By varying the conjugation length (n) of the oligomer it was found that for T3 and T5, the PL of the oligothiophene was quenched, but by different mechanisms as inferred from the increase or decrease of the CdSe emission. Photoexciting T3 results in energy transfer, enhancing the CdSe emission, while for T5 charge transfer occurs that results in a concomitant reduction of the PL intensity of CdSe. In a subsequent study Fréchet et al. have synthesized a P3HT derivative with an alkyl amino end group that effectively disperses CdSe nanocrystals to afford intimate nanocomposites with favorable morphology that shows a much better mixing and considerably less phase segregation than the common P3HT. Using this end-functional polythiophene, an improved performance of P3HT:CdSe hybrid solar cell was obtained [50].

In a related approach, quantum dots have been tailored with poly(*p*-phenylene vinylene). The method involves the growth of the CdSe quantum dots with a functional (phenyl bromide phosphineoxide) complexing ligand that is subsequently copolymerized

with 2,5-dioctyl-1,4-divinylbenzene and 2,5-dioctyl-1,4-dibromobenzene, to obtain a CdSe-surface grafted PPV [51]. Layers made with the CdSe-PPV composite showed improved dispersion and an almost complete quenching of the PPV luminescence, while that of the CdSe remained.

One evident drawback of nanocrystal rods is that they only improve transport in the direction of their alignment, which in a thin film device is unlikely to be from one electrode to the other. CdSe tetrapods, i.e., nanocrystals with four crystalline arms in a tetrahedral configuration, can be used to overcome this drawback, because these tetrahedral branched structures cannot lie in a plane. Greenham et al. showed that branched CdSe tetrapods in MDMO-PPV give an improved electron transport compared to linear CdSe nanorods, leading to solar cells with an efficiency of 2.4–2.8% [52, 53]. They have also used branched CdSe nanoparticles in combination with a reduced band gap copolymer, poly(2,7-(9,9-dioctyl-fluorene)-alt-5,5-(4',7'-di-2-thienyl-2',1',3'-benzothiadiazole)) (APFO-3), to improve the absorption of light to the parts of the solar emission [54]. This has resulted in cells with an efficiency of $\eta = 2.4\%$ ($J_{sc} = 7.23 \text{ mA/cm}^2$, $V_{oc} = 0.95 \text{ V}$, FF = 0.38).

Li et al. has synthesized a series of ternary tetrapodal nanocrystals of $\text{CdSe}_x\text{Te}_{1-x}$ with $x = 0$ (CdTe), 0.23, 0.53, 0.78, and 1 (CdSe) [55], and fabricated hybrid nanocrystal/polymer solar cells with MEH-PPV as an electron donor [56]. It was found that the V_{oc} , J_{sc} , and η of the devices all increased with decreasing Te content in the $\text{CdSe}_x\text{Te}_{1-x}$ nanocrystals. Tetrapodal CdSe nanocrystals and MEH-PPV (9:1 w/w) showed the highest power conversion efficiency of 1.13% under AM 1.5 with an EQE = 47% at 510 nm. The influence of nanocrystal composition on the photovoltaic properties of the hybrid solar cells was explained by the difference of the band level positions between MEH-PPV and the nanocrystals. The band-edge positions of the nanocrystals of CdSe, $\text{CdSe}_x\text{Te}_{1-x}$, and CdTe were systematically studied by cyclic voltammetry. It was established that the valence and conduction band energy levels of the nanocrystals shift upwards from CdSe to CdTe with decreasing x , making electron transfer from a polymer to the $\text{CdSe}_x\text{Te}_{1-x}$ less likely for smaller x values [55]. A similar result was found in photophysical studies of blends of a polythiophene derivative with CdTe quantum dots [57].

A new approach for controlled assembly of hybrid bulk heterojunction solar cells has been reported using sequential deposition of tetrapod-shaped cadmium telluride (CdTe) nanocrystals and P3HT. First nanocrystal tetrapods are deposited on an electrode surface [58]. The unique tetragonal structure gives rise to natural ordering, with three arms in contact with the surface and one arm pointing up, perpendicular to the surface. The tetrapods can be anchored to the ITO electrode surface by means of carboxylic or siloxane functionalities. Figure 8.6 shows several of the hybrid layers that can be obtained when P3HT is deposited by spin coating from chloroform solution onto the tetrapod layer. Preliminary studies on photovoltaic devices, using an aluminum top electrode, showed that devices with partial covering (Fig. 8.6b), performed best, but that the efficiency of these devices remained low, less than 1%. Apart from the fact that further optimization of the composition, morphology, and annealing may result in improvement, the abovementioned effect that electron transfer at the CdTe/P3HT interface is not very efficient [55–57] may also affect the conversion efficiency.

Alignment of the inorganic component (like rods and tetrapods) is one way to improve properties, alignment of the organic component might be a way to improve hole transport properties of the blend. Surface initiated polymers (polymer brushes) containing hole conducting moieties have been investigated to prove the viability of the advantage of the increased order in the organic component. CdSe nanoparticles, impregnated into a polymer poly(triphenylamine acrylate) (PTPAA) brush containing triphenylamine hole transporting moieties, indeed show an improved photovoltaic effect compared to spin cast blends [59].

8.2.2 *PbS*, *PbSe*, and *PbTe* Nanoparticles

8.2.2.1 Photovoltaic Devices

Lead sulfide (PbS) and lead selenide (PbSe) colloids absorb light in the near- to mid-infrared region and can be beneficial to increase the overlap of the absorption spectrum of the photoactive layer with the emission of the sun. The optical properties of colloidal semiconductor nanocrystals strongly depend on the size of the particle.

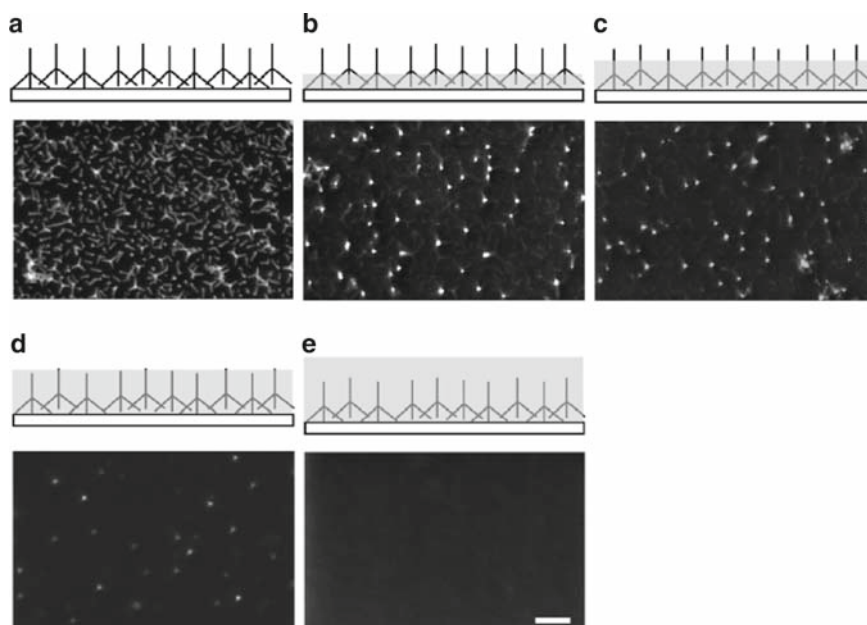


Fig. 8.6 Scanning electron micrographs of an original template of tetrapod array on ITO (a) and several composites produced by subsequent deposition of P3HT. P3HT was spin-cast from solution in chloroform with concentrations of 5 mg/mL (b), 7.5 mg/mL (c), 10 mg/mL (d), and 15 mg/mL (e), allowing for controlled thickness and exposure of the inorganic nanocrystals. Scale bar, 200 nm. Reprinted with permission from *J. Phys. Chem. B* 2006, 110, 25543 [58]. Copyright 2006 American Chemical Society

This follows from the fact that when a particle (electron, hole, or exciton) is confined to a volume in space it acquires kinetic energy (confinement energy) and its energy spectrum becomes discrete. For semiconductor quantum dots this confinement can be directly noticed from an increase of the exciton energy with decreasing size. The extent of confinement depends on the radius R of the quantum dot and the Bohr radius a_b of the particle. When $R/a_b \ll 1$, the system is strongly confined and the effects of confinement become more pronounced. Especially quantum dots of IV-VI semiconductors (such as PbS and PbSe) provide unique access to the limit of strong confinement because the electron, hole, and exciton all have large Bohr radii (for PbS: $a_e = a_h = 10$ nm, $a_{exc} = 20$ nm; for PbSe: $a_e = a_h = 23$ nm, $a_{exc} = 46$ nm) compared to II-VI and III-V semiconductors [60, 61]. Moreover, PbS and PbSe are direct gap semiconductors in the bulk with band gaps of 0.41 and 0.27 eV at room temperature. The low band gap and the strong confinement result in a widely size-tunable band gap ($-0.3 \leq E_g \leq 1.3$ eV) and a strong absorption from the UV to the near-IR region. These characteristics are advantageous for solar cell applications.

The use of these infrared active lead salts has been explored in bulk heterojunction type devices. Sargent et al. studied nanocomposites consisting of MEH-PPV and PbS nanocrystals, whose optical absorption was tuned by the quantum size effect [62, 63]. In a solution-processed device, they achieved sensitivity far beyond 800 nm, harvesting of infrared-photogenerated carriers and demonstrated an infrared photovoltaic effect. They used the wavelength tunability afforded by the nanocrystals to tailor the photocurrent spectra to three different regions of the infrared spectrum [62]. The photovoltaic devices consist of a sandwich structure of glass, an ITO front electrode, nc-PbS:MEH-PPV active layer, and a magnesium metal (Mg) back contact. The short-circuit current EQE at 975 nm, however, was extremely small ($\sim 0.0008\%$), which leaves serious doubt as to the question whether the electron transfer between the PbS and MEH-PPV is efficient. In fact, the same authors showed previously that MEH-PPV with embedded PbS nanocrystals transfers the excitation energy rather than a charge after photoexcitation with up to 60% efficiency for ligands with relatively short octylamine side chains [64], and they used the same nc-PbS/MEH-PPV material system to demonstrate electroluminescence [65]. To improve the photovoltaic devices, the effect of thermal annealing was investigated. Annealing of nc-PbS:MEH-PPV above 160°C, lead to noticeable changes in J_{sc} and a ~ 25 -fold rise of quantum efficiency to EQE = $\sim 0.002\%$ [66]. The same authors also proposed a device architecture in which the infrared absorbing active layer was based only on pure PbS nanocrystals layer, in combination with shorter butylamine surface passivating ligands to increase electron transport [67]. The EQE of the best devices fabricated in this way increased considerably to 0.4% compared to the blends, but it remained low on an absolute scale.

A different approach to make nc-PbS:MEH-PPV blends was followed by Meredith et al. [68] who reasoned that the common approach in which the nanoparticles were synthesized separately and subsequently mixed with a conducting polymer has two shortcomings: first the surfactant used to prepare the nanocrystals has to be removed. Any proportion of this surfactant that is incorporated into the final composite, will inhibit efficient charge transfer between the nanocrystal

and conducting polymer. Second, the mixing approach requires often the use of co-solvents, which adversely affect nanocrystal solubility and polymer chain orientation. Meredith et al. developed a new nanocrystal synthesis which eliminates these synthetic problems by using the conducting polymer to control nanocrystal growth [69]. The composite material was produced via a new single-pot synthesis in which, PbS was synthesized from lead acetate and sulfur in the presence of MEH-PPV. The advantage of this method is that it does not use specific surfactants. The devices were reported to have white light power conversion efficiencies under AM1.5 illumination (at 5 mW/cm^2) of $\eta = 0.7\%$, with $J_{sc} = 0.13 \text{ mA/cm}^2$, $V_{oc} = 1 \text{ V}$, and $FF = 0.28$ [68]. The electron and hole mobilities of the nc-PbS:MEHPPV composite made using this surfactant free synthesis have been studied using TOF and steady-state techniques [70]. It was found that the nanocrystals act to balance and dramatically increase both electron and hole mobilities. It is believed that transport in the composite system is due to two conduction pathways in the material: a polymer-nanocrystal donor-acceptor pathway, and a purely nanocrystal percolation pathway arising from the equal electron and hole mobilities in PbS. A similar synthetic approach has also been used to make nc-PbS:P3HT composites, but their optoelectronic properties have not been reported so far [71].

Also PbSe has been tested in combination with conjugated polymers to make hybrid photovoltaic devices. Prasad et al. used monodisperse PbSe nanocrystals in combination with poly-*N*-vinylcarbazole (PVK) for making polymer composites, that comprised $\sim 40\text{--}50 \text{ wt}\%$ of nc-PbSe [72]. These nc-PbSe:PVK blends, sandwiched between ITO and Al electrodes exhibited a photoconductivity (quantum efficiency $\sim 3\%$) under high bias (34 V) at excitation wavelengths of 1.34 and $1.55 \mu\text{m}$, but a photovoltaic response was not reported. Zakhidov et al. were the first to report a photovoltaic effect in nanocomposites of P3HT and nc-PbSe [73]. The thin film devices showed a good diode behavior with $J_{sc} = 0.24 \text{ mA/cm}^2$, $V_{oc} = 0.32 \text{ V}$, $FF = 0.43$ and $\eta = 0.04\%$, giving evidence of electron transfer between the polymer and the infrared active nc-PbSe. Also the quenching of the nc-PbSe has been studied to gain more understanding of energy and charge transfer in this system. Xu et al. have also reported the use of nc-PbSe by blending with P3HT. The fabricated device (ITO/PEDOT:PSS/nc-PbSe:P3HT/Al) exhibited an EQE = 1.3% at 805 nm, and a power conversion efficiency of $\eta = 0.14\%$ under 1 sun AM1.5 illumination, with $J_{sc} = 1.08 \text{ mA/cm}^2$, $V_{oc} = 0.35 \text{ V}$, and $FF = 0.37$ [74].

8.2.2.2 Multiple Exciton Generation in Lead Salts

The use of PbSe has the additional advantage of the possibility of multiple carrier generation. Quantum dot solar cells have the potential to reach efficiencies exceeding the thermodynamic conversion efficiency by utilizing the photon energy above the band gap (E_g). Nanosized semiconductor crystals can provide a regime where energetic hot carriers produce a second electron-hole pair through impact ionization. Impact

ionization is a process where a high-energy exciton, created in a semiconductor by absorbing a photon of energy $\geq 2E_g$, relaxes to the band edge via transfer of energy to a valence band electron that is concomitantly excited above the band gap (Fig. 8.7). The result of this energy transfer is that two electron-hole pairs are formed for each absorbed photon. For impact ionization to occur, the rate must be greater than the rate for carrier cooling and any other relaxation process. Because of the slower carrier cooling, nanosized semiconductor crystals can provide a regime where energetic hot carriers produce a second electron-hole pair through impact ionization.

Rather than increasing the photovoltage, impact ionization has the potential to increase the photocurrent because more than one electron hole pairs are formed per (high energy) photon. Broad band impact ionization efficiency has been analyzed theoretically by several authors [75, 76], and may give power efficiencies close to 40% at 1 sun for $E_g = 1$ eV [77]. So far there have been very few reports on impact ionization in solar cells. Nozik was the first to propose that nanosized semiconductor crystals might provide a regime where carrier multiplication via impact ionization could be greatly enhanced [78, 79]. The first actual demonstration of impact ionization in nanocrystals was published by Klimov et al. [80] showing that this process occurs with a high efficiency in lead selenide (PbSe). In their experiment Klimov et al. demonstrated that two (or more) excitons are formed when pump photon energies are more than 3 times the band gap energy in PbSe nanocrystals. The process was found to occur on an ultrafast (picosecond) timescale with up to 100% efficiency. This breakthrough discovery lead to a new, intriguing challenge for (hybrid) solar cells: is it possible to extract both electron-hole pairs as a photocurrent in an external circuit?

Since its discovery, several other examples of impact ionization or multiple exciton generation have been reported, not only for PbSe [81], but also for PbS [81], PbTe [82], and CdSe [83, 84]. More recently, Klimov et al. have even shown that it is possible to generate seven excitons from a single photon with an energy of 7.8 energy gaps, which corresponds to only $\sim 10\%$ energy loss, while in the normal

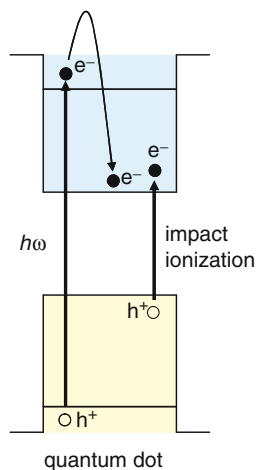


Fig. 8.7 In impact ionization, a high-energy exciton created by absorbing a photon of energy $\geq \omega \geq 2E_g$, relaxes to the band edge via transfer of energy to a valence band electron that is concomitantly excited above the band gap

scenario (one photon produces one exciton) ~90% of the photon energy would be dissipated as heat. Such large photon-to-exciton yields (conversion efficiency up to 700%) have the potential to increase the performance of photovoltaic cells when all charge carriers can be extracted [85, 86]. The actual mechanism of multiple exciton generation is not completely clear yet and different models ranging from impact ionization [80], or resonance between single-exciton and multi-exciton states [81], to direct photogeneration via multiple virtual single-exciton states [87], have been proposed, studied theoretically [88, 89] and reviewed [90].

Different device configurations that can exploit the multiple carrier generation have been proposed [91], some of which employ hybrid versions involving electron or hole conducting polymer layers. The maximum efficiencies that can be attained in cells with carrier multiplication have also been addressed. Nozik et al. used detailed balance model with 1 sun AM1.5G illumination, to find that for single gap photovoltaic devices the maximum efficiency increases from 33.7%, the Shockley-Queisser limit occurring at $E_g = 1.34$ eV, for cells with no carrier multiplication to 44.4% for a band gap $E_g = 0.7$ eV, for cells with a maximum possible number of multiplications of 6 [92]. Here the main step is the first one because a high efficiency of 41.9% was still obtained with a maximum multiplication of only 2, which is 94% of the absolute maximum [92]. They also found that the maximum efficiency of an ideal two gap tandem PV device increases from 45.7 to 47.7% when carrier multiplication absorbers are used in the top and bottom cells. Klimov also analyzed the impact of carrier multiplication on the power conversion limits of solar cells using detailed balance considerations that also took into account practical efficiencies measured in experimental studies [93]. For PbSe nanocrystals that exhibit a $\sim 3E_g$ threshold for carrier multiplication, the calculated maximum efficiency is 36%. If carrier multiplication would occur at its theoretical minimum of $2E_g$, an increase to 42% is possible [93].

So far there has been one publication claiming photocurrent gain in an actual diode structure, which was attributed to the carrier multiplication in PbSe nanocrystal quantum dots via multiple exciton generation [94]. Šelmic et al. described the fabrication and properties of photodetectors based on MEH-PPV and nc-PbSe. Photocurrent measurements at -8 V bias were reported for several devices using two different sizes of PbSe quantum dots: one with the IR absorption peak at 1,100 nm (1.13 eV, diameter ~ 4.5 nm) and the second with the absorption at 1,900 nm (0.65 eV, diameter ~ 8 nm). EQEs greater than 100% were observed in the range of 450–575 nm for nc-PbSe:MEH-PPV blends containing 95 wt% MEH-PPV and 5 wt% of the larger PbSe quantum dots (1,900 nm), with a maximum of EQE = 150% at 510 nm [94]. This appealing result has been attributed to multiple carrier generation but, on the other hand, seems not compatible with the low (5 wt%) PbSe content and thin (60 nm) films used. The density of PbSe (7.5 g/cm³) is almost an order of magnitude larger than that of MEH-PPV (~ 0.9 g/cm³), suggesting that the PbSe content is about ~ 0.7 vol%, corresponding to an equivalent PbSe layer thickness of only 0.4 nm. Clearly this is too thin to absorb all photons at 510 nm. Moreover, it must be noted that independent of the particle size, the spectral response of the photocurrent followed the absorption spectrum of MEH-PPV closely, indicating that absorption by the polymer occurred, rather than by PbSe.

8.2.3 Other Light Absorbing Nanoparticles

While the majority of hybrid nanoparticle-polymer solar cells involving quantum dots that absorb light outside the UV region relate to cadmium and lead salts as described in the previous paragraphs, other particles also have received some attention. In each case the rationale behind this approach is to utilize the extended wavelength absorption of the inorganic quantum dot into the near infrared to enhance the spectral coverage and harvest more photons from the sunlight.

8.2.3.1 CuInS₂ and CuInSe₂ Nanoparticles

Interesting achievements in this area were reported by Meissner and Sariciftci using copper indium sulfide (CuInS₂, CIS) [95, 96] and selenide (CuInSe₂, CISE) [97, 98] particles mixed with conducting and semiconducting polymers. CIS and CISE are promising materials to replace silicon in thin film solar cells. The synthesis of CIS nanoparticles was achieved using a colloidal route. Bulk heterojunctions involving a blend of PEDOT:PSS and CIS nanoparticles at a flat interface with a fullerene derivative (PCBM) showed photovoltaic response with external quantum efficiencies of up to 20% at 400 nm [96]. CISE nanoparticles have been blended with P3HT and showed a photovoltaic effect with $J_{sc} = 0.3 \text{ mA/cm}^2$, $V_{oc} = 1.0 \text{ V}$, FF = 0.50 at 80 mW/cm² ($\eta = 0.19\%$) in a ITO/PEDOT/CISE:P3HT/Al device configuration and a 6:1 weight ratio of CISE:P3HT [97, 98].

8.2.3.2 HgTe Nanoparticles

An example of a combination of a hybrid bulk heterojunction and a solid state dye sensitized solar cell has been reported by Günes et al. [99]. A nanoporous TiO₂ substrate was impregnated by HgTe nanoparticles (acting as a dye) and covered with a blend of HgTe nanoparticles and P3HT. The HgTe crystals offer the possibility to push the wavelength operation of the devices to longer wavelengths. The device combines two solar cell concepts, a solid-state nanocrystal-sensitized solar cell and a nanocrystal/polymer-blend solar cell, where the bulk heterojunction helps in creating more mobile charges and the high surface area TiO₂ acts as an efficient collection electrode. These solar cells give a small photoresponse (EQE < 2%) in the near infrared region (800–1,500) and a higher response (EQE = 10% at 550 nm) in the visible range where P3HT absorbs. Under simulated AM1.5 (100 mW/cm²) white light irradiation, the cell performance parameters are $J_{sc} = 2.0 \text{ mA/cm}^2$, $V_{oc} = 0.4 \text{ V}$, and FF = 0.5, providing an estimated power conversion efficiency of $\eta = 0.4\%$.

8.2.3.3 InP Nanoparticles

Compared to for e.g., CdSe, InP absorbs light further in the red part of the spectrum. Dyakonov et al. studied InP nanocrystals with a diameter of 4.2 nm in combination

with MDMO-PPV [44]. When mixed with InP nanocrystals, the PL of the MDMO-PPV polymer was quenched by almost three orders of magnitude, compared to a pristine MDMO-PPV layer. The PIA spectrum of nc-InP:MDMO-PPV solid films showed two bands at 0.31 and 1.34 eV, which are the clear signatures of radical cations on MDMO-PPV. The high intensity that was observed for the low-energy band is consistent with electrons in the InP nanocrystals. These photogenerated charges were only observed in the PIA when the TOPO/TOP ligand shell around the InP was removed by washing with pyridine. Without the exchange with pyridine, the PIA spectra of InP-TOPO-TOP nanoparticles did not indicate photoinduced charge transfer, even though the PL was quenched to a similar extent. This last result has been interpreted as being the consequence of resonance energy transfer. A LESR signal was observed at $g = 2.002$ for pyridine washed InP nanocrystals blended with MDMO-PPV that could be attributed to radical cations on the polymer. The corresponding unpaired electron in InP was not detected in the LESR experiment.

Selmarten et al. found that the steady state PL of a solution of InP nanocrystals was quenched by addition of P3HT [100]. By studying the time-resolved PL, it was concluded that the quenching is static in origin, i.e., it is the consequence of a complex formed between nc-InP and P3HT in solution. The PL quenching has been attributed to the fact that an electron is transferred from the P3HT, to the excited InP quantum dot, suggesting that this particular combination of materials may be a suitable candidate for a future photovoltaic cell.

8.2.4 TiO_2 Nanoparticles

Transparent semiconducting metal oxides like TiO_2 and ZnO are promising materials to be used as the electron accepting material in combination with p-type conjugated polymers. These metal oxides are not considered to be toxic and are available in abundance. First examples of blends from TiO_2 nanoparticles and PPV have shown only moderate external quantum efficiencies of a few percent and short circuit currents of tens of microamperes. In one example, PPV was obtained by thermal conversion of a methanol soluble precursor mixed with 20 nm TiO_2 nanocrystals and spin casting on fluorinated tin oxide ($\text{SnO}_2:\text{F}$) [101, 102]. The resulting $\text{SnO}_2:\text{F}/\text{TiO}_2:\text{PPV}/\text{Al}$ devices with 20 wt% TiO_2 gave $J_{\text{sc}} = 25 \mu\text{A}/\text{cm}^2$ and $V_{\text{oc}} = 0.65$ V, with $\text{EQE} = 2\%$ in the absorption range of PPV [101, 102]. Later TEM and PL studies on similarly prepared $\text{TiO}_2:\text{PPV}$ blends revealed the large phase separation between the TiO_2 crystals and PPV [103]. In another attempt to create bulk heterojunction solar cells [104], MEH-PPV was mixed with TiO_2 nanoparticles dispersed in *p*-xylene and cast into thin films [105]. ITO/nc- $\text{TiO}_2:\text{MEH-PPV}/\text{Ca}$ devices prepared in this way, containing 70 wt% TiO_2 , gave $J_{\text{sc}} \approx 20 \mu\text{A}/\text{cm}^2$ and $V_{\text{oc}} \approx 1$ V.

These examples show that it is not straightforward to make bulk heterojunction solar cells by blending TiO_2 nanoparticles with conjugated polymers; poor mixing of the polymer and the nanoparticles leads to agglomerates of nanoparticles in the blend, which limited the performance of the first photovoltaic devices thereof.

The synthesis of TiO_2 nanoparticle powders mainly occurs in water or alcohol based media. Transferring these nanoparticle powders into organic solvents regularly leads to aggregate formation and therefore a low miscibility with conjugated polymers. For this reason the application of TiO_2 nanoparticle powders in the bulk heterojunction approach is often limited. Only recently it was shown that 20–40 nm TiO_2 nanoparticles and conjugated polymers can be blended from common organic solvents. Kwong et al. demonstrated solar cells with an efficiency of approximately $\eta = 0.42\%$ [106, 107], providing a first account showing that the ideas advanced by Alivisatos and Greenham for CdSe, also work for TiO_2 nanoparticles. The most efficient devices incorporated 60 wt% TiO_2 and a ~ 100 nm thick TiO_2 :P3HT film, spin coated from xylene. The solutions for fabricating the films were prepared in a heated ultrasonic bath (at 50°C) to increase solubility of P3HT. The films were baked in a vacuum oven for 24 h at 110°C . The completed ITO/PEDOT:PSS/nc- TiO_2 :P3HT/Al devices gave $J_{\text{sc}} = 2.759$ mA/cm², $V_{\text{oc}} = 0.44$ V, FF = 0.396, and $\eta = 0.424\%$ under AM1 spectral conditions at 100 mW/cm². The maximum EQE amounted to 15% at 475 nm. For blend compositions with less than 40% or more than 70% TiO_2 the performance was significantly less, due to extensive recombination (at low concentration) or poor film quality (at high concentration).

Agostiano et al. have performed an extensive optical and photoelectrochemical study of blended systems composed of organic-capped TiO_2 crystals with a spherical ($d \sim 5$ nm) or rodlike ($d \sim 3\text{--}4$ nm, $l = 25\text{--}30$ nm) morphology and MEH-PPV [108, 109]. PL quenching experiments indicated that photoinduced charge separation occurs at the interface for both oleic acid and *n*-tetradecylphosphonic acid capping layers. Photoelectrochemical measurements in three-electrode cell employing an ITO working electrode covered with the nc- TiO_2 :MEH-PPV blends provided photocurrents that were higher for the spherical particles than for the rodlike counterparts, and also increased when replacing the bulky oleic acid with the phosphonic acid capping layer.

An interesting alternative method to develop hybrid solar cells using an aerosol technique has been proposed by Huisman et al. [110, 111]. In this technique, ultrasonically formed droplets of titanium(IV) isopropoxide are pyrolyzed to deposit thin films of nanosized anatase TiO_2 particles. This method eliminates the need for a sintering step after deposition. Using these films, cells could be constructed by spin coating poly(3-octylthiophene) (P3OT) on top. Devices with a 1 μm thick active layer give $J_{\text{sc}} = 0.25$ mA/cm², $V_{\text{oc}} = 0.72$ V, FF = 0.35, and $\eta = 0.06\%$ under 100 mW/cm² white light illumination and EQE = 2.5% at 488 nm. Devices prepared by adding P3OT during the deposition of the porous layer showed a similar performance.

8.2.5 ZnO Nanoparticles

Beek et al. chose to use ZnO instead of TiO_2 or CdSe [112]. ZnO is a non-toxic, crystalline material and at room temperature the stable phase is a wurtzite type crystal. In contrast to TiO_2 , crystalline ZnO is already formed at temperatures as

low as 4°C [113]. ZnO has a direct band gap at 3.2 eV, a conduction band level of -4.4 V vs. vacuum [114], and an electron mobility exceeding $100 \text{ cm}^2/\text{Vs}$ [115, 116]. Crystalline ZnO nanoparticles (nc-ZnO), soluble in organic solvents, have been mixed with conjugated polymers without the use of surfactants [112]. Fig. 8.8a shows a transmission electron microscopy (TEM) image of crystalline ZnO nanoparticles of approximately 4.9 nm in diameter (according to UV absorption onset). X-ray analysis confirmed the presence of the crystalline wurtzite crystal (Fig. 8.8b) [117].

8.2.5.1 Photophysics of Nanocrystalline ZnO – Polymer Blends

Spin casting a mixed solution of these nc-ZnO particles and a conjugated polymer (MDMO-PPV) from a common solvent (chlorobenzene:methanol 95:5 v/v) can be used to prepare thin bulk heterojunction films. PIA spectroscopy performed on these films (Fig. 8.9a) gave direct spectral evidence that under illumination, electron transfer occurred from the polymer to the ZnO nanoparticles. The PIA spectrum (solid line) of the nc-ZnO:MDMO-PPV blend exhibits the characteristic absorption bands of the polymer radical cation at 0.4 and 1.3 eV [118]. Compared to the spectrum of TiO_2 :MDMO-PPV (dashed line), the increased intensity of the 0.4 eV band indicates the presence of negatively charged nc-ZnO [119]. The presence of the radical cation on the MDMO-PPV and the electron on the ZnO nanoparticle proves that after photoexcitation the electron is transferred from the MDMO-PPV to the ZnO, leaving a hole on the conjugated polymer. Pump-probe spectroscopy (Fig. 8.9b) revealed that the photoinduced charge transfer occurs within a picosecond, similar to the ultrafast electron injection (<300 fs) reported by Bauer et al. [120] for electron injection in a dye sensitized solar cell utilizing $\text{Ru}(\text{dcbpy})_2(\text{NSC})_2$ dyes on

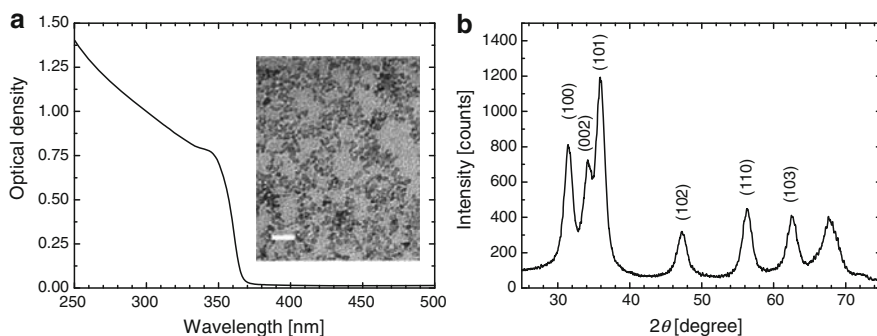


Fig. 8.8 ZnO nanoparticles. (a) TEM image (white bar = 20 nm) and UV-vis absorption spectrum in a chloroform:methanol (v:v = 90:10) mixture. (b) Powder X-ray diffraction pattern. Reprinted in part with permission from *J. Phys. Chem. B.* 2005, 109, 9505 [117]. Copyright 2005 American Chemical Society

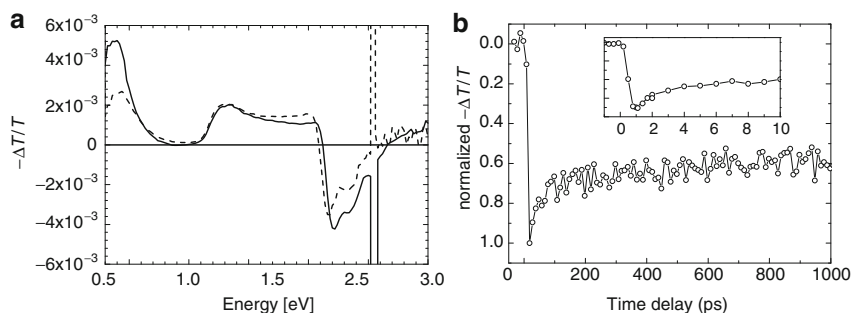


Fig. 8.9 (a) PIA spectrum of a nc-ZnO:MDMO-PPV blend on quartz (solid line) and of MDMO-PPV on TiO₂ (dashed line). (b) Time-resolved pump-probe spectroscopy, monitoring the intensity of the radical cation band at 0.56 eV, after excitation at 2.43 eV (510 nm). The inset shows the transient absorption at short time delays. Reprinted with permission from Adv. Mater. 2004, 16, 1009 [112]. Copyright 2004 Wiley-VCH

nanoparticulate ZnO electrodes. The occurrence of fast electron injection into the ZnO and the formation of long-lived charges on the polymer and the ZnO, show that this combination of materials has promising properties for application in photovoltaic devices.

In a subsequent study, composite films of P3HT and nc-ZnO, spin cast from chloroform, have been characterized with absorption and photoluminescence spectroscopy [121]. The UV-vis spectra of these blends (Fig. 8.10a) show that the relative contribution of the ZnO absorbance (at 350 nm) increases compared to the π - π^* band of P3HT in the 400–650 nm region with increased concentration of ZnO in the blend. Simultaneously, a slight blue shift of the P3HT band has been observed and a concomitant loss of the (weak) vibronic structures. The shift has been attributed to a loss of P3HT polymer chain stacking and conformational disorder, caused by the mixing with the ZnO nanoparticles. With increased ZnO concentration, the photoluminescence intensity of the blend increased initially compared to the intensity of pristine P3HT (Fig. 8.10, inset), only after addition of more ZnO (>26 vol%), the photoluminescence eventually dropped below the initial intensity. The initial increase of photoluminescence intensity is unexpected because a photoinduced electron transfer between P3HT and ZnO would rather result in photoluminescence quenching. However, the photoluminescence quantum yield of P3HT is low and known to be sensitive to the degree of chain order. Hence, the changes in PL intensity with ZnO concentration were rationalized by a competition between an intensity increase due to more disordered P3HT chains and an intensity decrease due to photoinduced electron transfer to the ZnO.

Photoinduced charge separation between P3HT and nc-ZnO was confirmed by PIA spectroscopy (Fig. 8.10b). The PIA spectrum of a nc-ZnO:P3HT blend exhibits a vibronically resolved photobleaching band (1.98, 2.15, and 2.41 eV) of the neutral P3HT and the characteristic absorption bands of the P3HT radical cation around 0.4 eV and 1.26 eV [122]. The intensity ratio of these bands is different from the usual

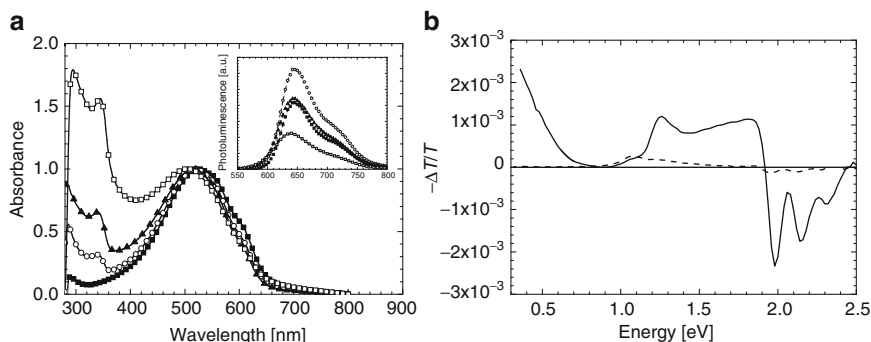


Fig. 8.10 (a) Absorbance spectra of nc-ZnO:P3HT blends, with 15 vol% nc-ZnO (*open circle*), with 26 vol% nc-ZnO (*filled triangle*), and 42 vol% nc-ZnO (*open square*) compared to pristine P3HT (*filled square*). The inset shows the effect of the addition of these amounts of nc-ZnO on the photoluminescence of P3HT. (b) PIA spectrum of a nc-ZnO:P3HT blend (26 vol% ZnO) on quartz (solid line), measured at 80 K with modulated (275 Hz) excitation at 2.54 eV (488 nm). The pump power was 25 mW with a beam diameter of 2 mm. The dashed line gives the PIA spectrum of a P3HT film. Reprinted with permission from Adv. Funct. Mater. 2006, 16, 1112 [121]. Copyright 2006 Wiley-VCH

[122], and we attribute the higher intensity of the 0.4 eV band to electrons injected into the nc-ZnO [123]. In addition to the spectral features of photoinduced charges in P3HT and ZnO, a small signal at 1.06 eV is observed for the blend. This band is also present in the PIA spectra of pure P3HT (dashed line) and is due to the triplet-triplet absorption of P3HT. Its presence indicates that not all absorbed photons give rise to charges, consistent with the partial photoluminescence quenching (Fig. 8.10a) and indicating the presence of relatively large P3HT domains.

Savenije et al. have studied the photogeneration and decay of charge carriers in blend films of ZnO nanoparticles and MDMO-PPV and P3HT by means of time resolved microwave conductivity (TRMC) experiments [124]. This technique allows measuring the AC conductivity without applying electrodes to the sample. Excitation of the polymer was found to lead to a long-lived transient photoconductance signal, due to charge formation at the nc-ZnO:polymer interface. The signal has been attributed to be mainly due to excess electrons in ZnO. Increasing the weight fraction of nc-ZnO in the blends, leads to a higher photoconductance via the generation of more charge carriers.

8.2.5.2 Photovoltaic Properties of nc-ZnO-polymer Blends

Hybrid bulk heterojunction photovoltaic devices (Fig. 8.11) have been made using a nc-ZnO MDMO-PPV blend, sandwiched between poly(3,4-ethylenedioxythiophene):poly(styrenesulfonate) (PEDOT:PSS) on ITO as front electrode and Al as back electrode (Fig. 8.11a) [112].

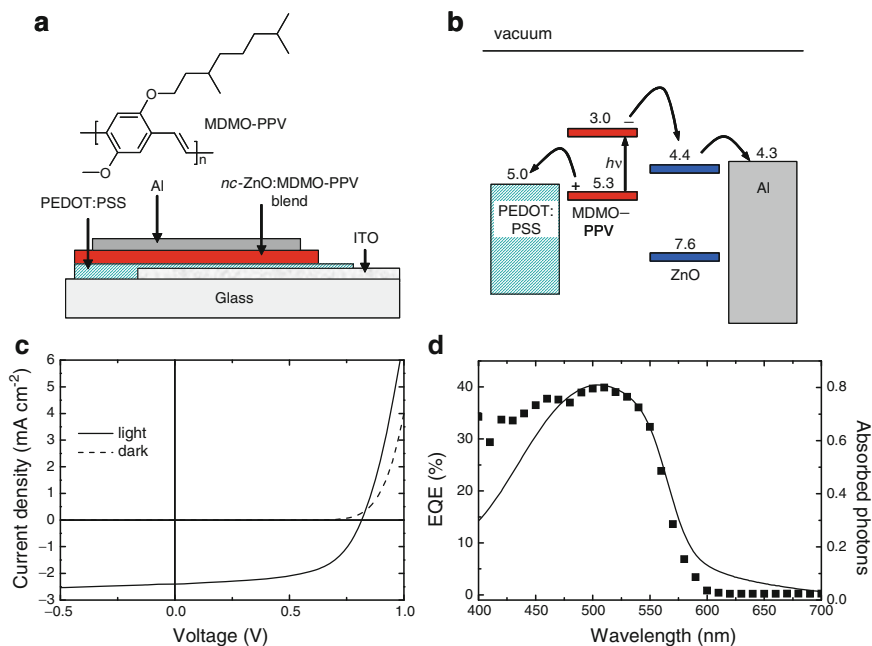


Fig. 8.11 (a) Solar cell consisting of an 80 nm thick *nc*-ZnO:MDMO-PPV blend, sandwiched between ITO/PEDOT:PSS (80 nm) and Al (100 nm) electrodes. (b) Schematic energy level diagram for the cell, with energy levels in eV relative to vacuum. (c) Current density voltage (J - V) characteristic of a *nc*-ZnO:MDMO-PPV cell (67 wt% *nc*-ZnO) in the dark and under illumination with white light from a tungsten halogen lamp estimated at 0.71 sun equivalent intensity. (d) EQE as function of the wavelength of monochromatic irradiation, co-plotted with the fraction of photons absorbed by the blend. Reprinted in part with permission from Adv. Mater. 2004, 16, 1009 [112]. Copyright 2004 Wiley-VCH

The EQE of the hybrid *nc*-ZnO:MDMO-PPV solar cell with 26 vol% ZnO (Fig. 8.11d) has been measured with white light bias illumination to create conditions resembling operation under solar illumination. The EQE spectrum reaches a value of 40% at the absorption maximum of MDMO-PPV. Integration of the EQE with the solar spectrum (AM1.5 standard, normalized to 100 mW/cm^2) affords an estimate of the short-circuit current density of $J_{sc} = 3.3 \text{ mA/cm}^2$ under AM1.5 (1 sun) conditions. J - V measurements measured with white-light illumination (equivalent to AM1.5 at 71 mW/cm^2) are shown in Fig. 8.11c. Under these conditions $J_{sc} = 2.40 \text{ mA/cm}^2$ has been obtained, together with $V_{oc} = 0.814 \text{ V}$ and FF = 0.59. At this light intensity the power conversion efficiency is $\eta = 1.6\%$.

The effect of the ZnO concentration on the photovoltaic performance is significant. Hybrid *nc*-ZnO:MDMO-PPV devices with different amounts of *nc*-ZnO show different J - V characteristics under illumination [117]. The experiments were performed in a short period of time to rule out variations in performance due to changes in the

surrounding atmosphere. The effects of the ZnO concentration and layer thickness on the maximum power point (*MPP*) under white light illumination are shown in Fig. 8.12. The maximum performance is observed for devices containing 26–35 vol% ZnO and a layer thickness between 100 and 150 nm.

Regioregular P3HT is an interesting material to apply in nc-ZnO hybrid polymer solar cells. P3HT can have a high hole mobility, up to $\sim 0.1 \text{ cm}^2/\text{Vs}$ in field-effect transistors [10, 11]. Compared to MDMO-PPV the improved hole mobility, together with a more “red-shifted” absorbance of the material, might lead to an improved performance of photovoltaic devices. Beek et al. have demonstrated that in combination with nc-ZnO, solution processed bulk heterojunction solar cells can be obtained [121]. Thermal annealing of the nc-ZnO:P3HT blend further enhanced the photovoltaic performance [121]. Fig. 8.13 shows the effects of the annealing step on the photovoltaic properties of nc-ZnO:P3HT solar cells. The effects of annealing are very obvious in blends with low amounts of nc-ZnO, the short circuit current density and the open circuit voltage increase, leading to a pronounced increase in efficiency. In some respect these solar cells behave very similarly to P3HT:PCBM solar cells, where the performance also improves with annealing [125, 126]. The improvement in cell efficiency in both types of cells mainly results from an increased, almost doubled, short circuit current density, attributed to an increased crystallinity and hence higher charge carrier mobility.

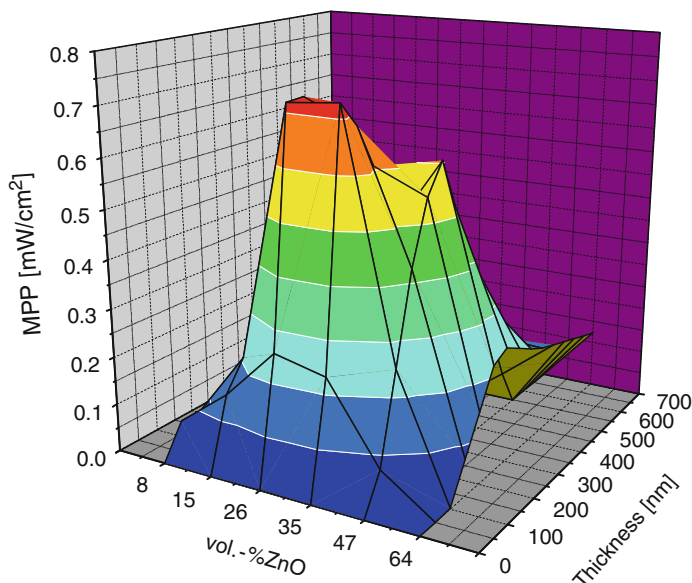


Fig. 8.12 The maximum power point (*MPP*) of nc-ZnO:MDMO-PPV solar cells, as a function of vol% ZnO and the thickness of the active layer. Reprinted with permission from J. Phys. Chem. B. 2005, 109, 9505 [117]. Copyright 2005 American Chemical Society

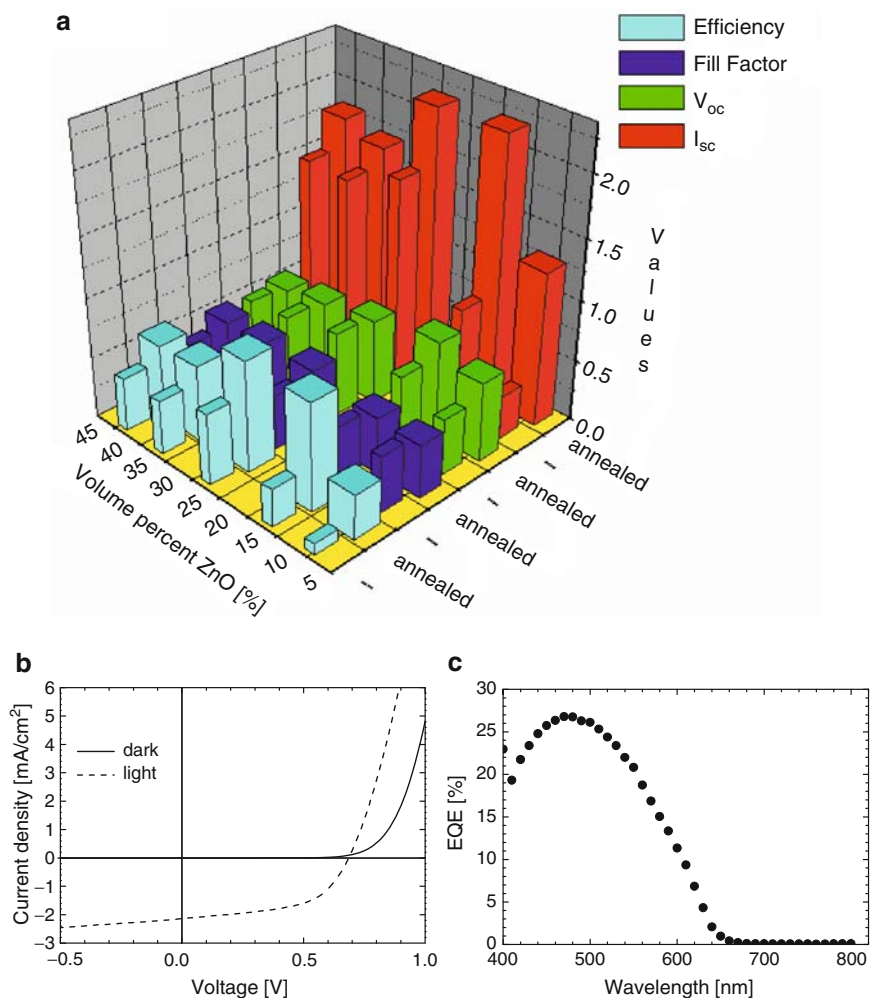


Fig. 8.13 (a) Performance of nc-ZnO:P3HT solar cells as function of thermal annealing composition. (b) Current density voltage (J - V) characteristics of an nc-ZnO:P3HT blend (with 26 vol% nc-ZnO) in dark and under illumination with white light from a tungsten-halogen lamp (75 mW/cm^2) (c) EQE as a function of the wavelength of monochromatic irradiation. Reprinted in part with permission from Adv. Funct. Mater. 2006, 16, 1112 [121]. Copyright 2006 Wiley-VCH

Figure 8.13a indicates that the largest effect of annealing is found in blends with low amounts of ZnO, i.e., the highest amount of polymer. This shows that the annealing step mainly influences P3HT phase and therefore is likely to have a beneficial effect on the hole transport properties of this phase [121, 127]. The J - V characteristics of the optimized nc-ZnO:P3HT cell under white-light illumination using a tungsten-halogen lamp (75 mW/cm^2) are shown in Fig. 8.13b. Under these conditions $J_{sc} = 2.14 \text{ mA/cm}^2$, $V_{oc} = 0.685 \text{ V}$, and $FF = 0.55$, giving an overall

power-conversion efficiency of $\eta = 0.9\%$. Compared to $\eta = 1.6\%$ of the nc-ZnO:MDMO-PPV the lower value for nc-ZnO:P3HT seems unexpected, given the higher (pristine) hole mobility of the P3HT and the red-shifted absorbance. However, difficulties during processing and film formation indicated that the processing conditions and the blend-morphology play a significant role.

8.2.5.3 Morphology of nc-ZnO: Polymer Blends

For bulk heterojunction solar cells, the phase separation between the two components is of utmost importance because it will determine the effectiveness of charge generation and of charge transport [126, 128]. Charge generation requires a high surface to volume ratio, whereas charge transport requires the presence of pathways consisting of almost pure phases of the starting compounds, formed by phase separation. Transmission electron microscopy (TEM) of a thin (50 nm) film (Fig. 8.14) containing 26 vol% nc-ZnO in MDMO-PPV revealed phase separation on nanometer scale. Dark nc-ZnO regions and bright polymer regions, some larger than 10 nm, can be seen. The occurrence of pure polymer domains, larger than the exciton diffusion length, shows that not all excitons can dissociate into photogenerated charges, i.e., lowering the charge generation efficiency. From photoluminescence quenching data it appeared that a maximum of 85% of the absorbed photons gave rise to charge separation [112].

The TEM image seems to indicate that the desired morphology is present; however the phase-separated morphology was more difficult to observe with tapping mode atomic force microscopy (AFM) (Fig. 8.15). When mixing the ZnO nanoparticles

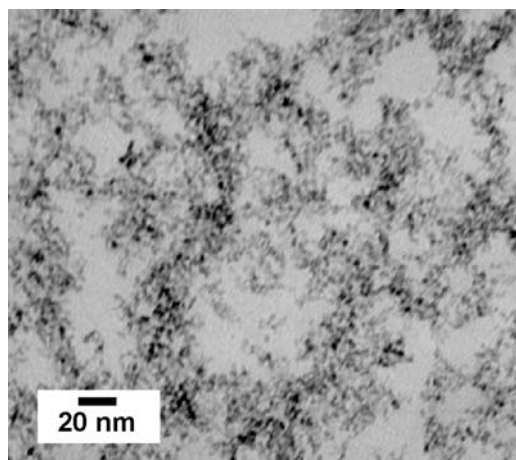


Fig. 8.14 TEM image of a 50 nm thin film of a nc-ZnO:MDMO-PPV blend with 26 vol% ZnO. Reprinted with permission from *J. Phys. Chem. B.* 2005, 109, 9505 [117]. Copyright 2005 American Chemical Society

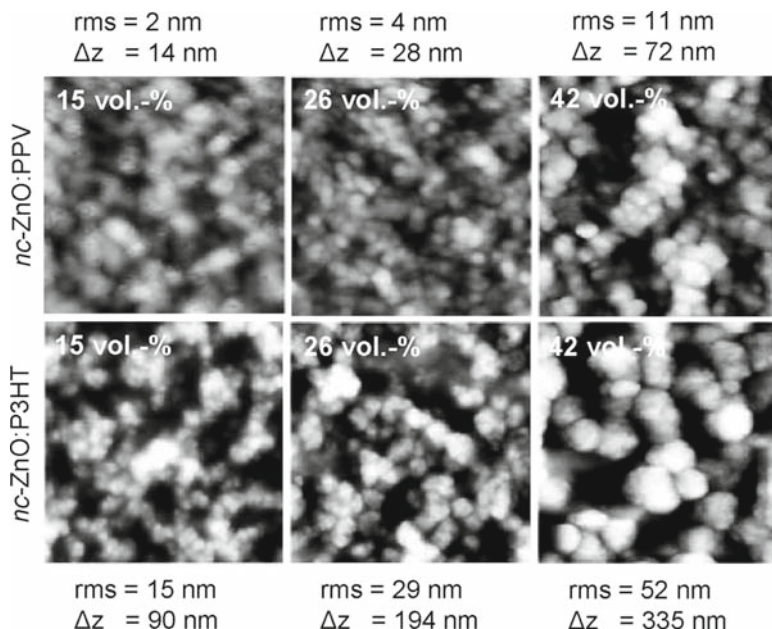


Fig. 8.15 Tapping mode AFM pictures (500×500 nm) of *nc-ZnO:MDMO-PPV* (*top*) and *nc-ZnO:P3HT* (*bottom*) blends for different compositions. Reprinted in part with permission from *J. Phys. Chem. B.* 2005, 109, 9505 [117]. Copyright 2005 American Chemical Society

with MDMO-PPV or P3HT spherical aggregates and clusters thereof appeared, the spherical structures appeared to consist of a mixture of polymer and ZnO, but no clear phase separation has been observed at the surface of the *nc-ZnO:MDMO-PPV* film.

Closer examination of the AFM images revealed that there is a significant difference in morphology between the P3HT and MDMO-PPV based blends. The MDMO-PPV based blends appeared much smoother and the spherical structures and aggregates were much smaller. This is a likely explanation for the differences in photovoltaic effect. The roughness of the *nc-ZnO:P3HT* films increased dramatically when the amount of ZnO in the blend had been increased. The likelihood of shunted films increases, which limits the photovoltaic performance that can be reached. The *nc-ZnO:MDMO-PPV* blends also showed an increase in roughness with ZnO addition, but much less. This allows a further loading of the *nc-ZnO:MDMO-PPV* films with sufficient ZnO nanoparticles to improve charge generation and separation. Figures 8.12 and 8.13 show that the optimum volume percent of ZnO in the *nc-ZnO:P3HT* cells is slightly lower than in the case of the *nc-ZnO:MDMO-PPV* cells. This seems to be further evidence that it is the morphology that limits the performance of the *nc-ZnO:P3HT* devices.

8.3 Flat Bilayers Cells

Bulk heterojunctions are not the only way to create hybrid polymer-inorganic solar cells. Devices consisting of two layers on top of each other, one being the polymer and the other the inorganic semiconductor, have the advantage that photogenerated charge carriers can easily be transported to the electrodes. The small interfacial area between polymer and inorganic semiconductor, however, limits the charge carrier generation, especially when the exciton diffusion length is small. Because of this fundamental limit, the progress in terms of power conversion efficiency for hybrid bilayers has been modest since the publication of a first $\text{TiO}_2/\text{MEH-PPV}$ solar cell [17], but the structure allows for investigating several interesting issues with respect to device operation.

Apart from hybrid p–n semiconductor junctions, p-doped (conducting) polymers have also been combined with n-type inorganic semiconductors in bilayer photovoltaic devices. With respect to the operation of these devices, various mechanisms have been proposed, varying from a metal-insulator-semiconductor structure and p–n heterojunction to a Schottky diode in which the conducting polymer merely modifies the contact between the metal electrode and the inorganic semiconductor. It seems that in each of these cells, the inorganic semiconductor is the photoactive layer and light absorbed by the polymer does not contribute significantly to the energy conversion efficiency.

8.3.1 Bilayers with TiO_2

8.3.1.1 $\text{TiO}_2/\text{Poly}(\rho\text{-Phenylene Vinylene})$

Savenije et al. have used the flash-photolysis TRMC to monitor charge separation between a smooth film of anatase TiO_2 (ca 80 nm) and spin coated layers of MEH-PPV (20–140 nm thick) on nanosecond flash-photolysis in the polymer absorption band at 544 nm [129]. The quantum efficiency of electron injection into the TiO_2 per incident photon is ca 6% for thicknesses in the range of 30–50 nm of the polymer layer. The charge separation persisted well into the microsecond region.

Carter et al. have described bilayer devices containing a transparent planar TiO_x layer and a conjugated polymer based on a phenylamino-*p*-phenylene vinylene (PA-PPV) repeating unit [130]. The amino electron donor units in PA-PPV enhance the hole mobility of the polymer. When used in an ITO/ TiO_x /PA-PPV/Au configuration an 80 nm thick PA-PPV film gave $V_{oc} = 0.85$ V and FF= 0.52 under 100 mW/cm² white light illumination and an EQE of 25% at 440 nm. Similar bilayer devices made from MEH-PPV on top of flat TiO_2 gave rather low efficiencies of $\eta \leq 0.1\%$ ($J_{sc} = 0.24$ mA/cm², $V_{oc} = 0.7$ V, FF= 0.42) with a maximum EQE= 3.3% for a 65 nm thick layer [131], consistent with the TRMC results of Savenije et al. [129]. When the MEH-PPV was replaced with the better hole transporting poly [2,5-dimethoxy-1,4-phenylene-1,2-ethenylene-2-methoxy-5-(2-ethylhexyloxy)

(1,4-phenylene-1,2-ethynylene)] (M3EH-PPV) a bilayer device with an estimated efficiency of 0.4% and an EQE of ca 7.5% has been obtained [132]. Spin casting a mixture of M3EH-PPV and (poly[oxa-1,4-phenylene-1,2-(1-cyano)ethynylene-2,5-dioctyloxy-1,4-phenylene-1,2-(2-cyano)ethynylene-1,4-phenylene]) (PCNEPV) on top of the TiO₂ layer, increases this efficiency to 0.75% ($J_{sc} = 3.3$ mA/cm², $V_{oc} = 0.65$ V, FF= 0.28, EQE= 23.5% at 480 nm) [132], but in this case the actual bulk heterojunction layer and charge separation are likely to be dominated by the p-type M3EH-PPV and the n-type PCNEPV.

Similar cells and results using PPV derivatives have been reported by many others. Fan et al. presented a planar heterojunction photovoltaic cell, fabricated from sol-gel TiO₂ anatase and MEH-PPV with a peak power conversion efficiency of 1.6% when illuminated with monochromatic light at 500 nm at low intensity (0.20 mW/cm²) [133]. Likewise, Krebs et al. found $J_{sc} = 0.39$ mA/cm², $V_{oc} = 0.7$ V, FF= 0.25, $\eta = 0.07\%$ for ITO/TiO₂/MEH-PPV/Ag devices [134]. Krebs et al. used various different metal oxides (Nb₂O₅, ZnO, CeO₂, and CeO₂-TiO₂) thin films prepared via sol-gel methods but found that none of the oxides surpassed the performance of TiO₂ layers when investigated using an ITO/oxide/MEH-PPV/Ag device structure under identical conditions [134]. Photocurrents were generally low although they increased somewhat with time (except for ZnO). Slooff et al. have reported an estimated AM1.5 efficiency of 0.3% ($J_{sc} = 0.96$ mA/cm², $V_{oc} = 0.508$ V, FF= 0.61) for planar bilayer devices constructed from MDMO-PPV and TiO₂ using a cell configuration in which the TiO₂/MDMO-PPV bilayer is sandwiched between an ITO bottom electrode and a PEDOT:PSS/Au top electrode [135].

The influence of oxygen on ITO/TiO₂/MDMO-PPV/Hg cells has been studied by Goossens et al. [136, 137] They found that in the presence of oxygen, illumination causes an increase of the dark reverse and forward currents when the cell is held at open-circuit voltage. However, this effect did not occur under short-circuit conditions. The results were explained by considering that under open-circuit conditions the photoexcited electron is not transferred to TiO₂, but remains in the LUMO of MDMO-PPV and interacts with available oxygen to form O²⁻ and a charge transfer complex, increasing the acceptor density and conductivity. Under short-circuit conditions, the photoexcited electrons are injected into TiO₂, removed from the interface by the electric field at the junction and do not cause oxygen doping. However, this explanation seems not consistent with the result that, irrespective of the presence of an electric field, photoinduced electron transfer readily occurs in many conjugated polymer/TiO₂ composites [122] and that the lifetime of an electron in the LUMO of MDMO-PPV is at best a few nanoseconds [138].

8.3.1.2 TiO₂/Polythiophene

Polythiophene derivatives have also been used in combination with flat TiO₂ layers. In a study on solid state dye-sensitized TiO₂ solar cells with P3OT as hole transport layer Sariciftci et al. reported the performance of a flat-TiO₂/P3OT control cell with $J_{sc} = 9$ μ A/cm², $V_{oc} = 0.56$ V, FF= 0.36 under 64 mW/cm² white light illumination

[139]. Kim et al. have described a comparison of devices made with regiorandom and regioregular P3HT [140]. ITO/TiO₂/P3HT/Au devices were studied at different temperatures. For regiorandom P3HT, V_{oc} decreased from ~0.9 to 0.55 V going from 140 to 300 K, while J_{sc} increased from less than 1 to ~20 $\mu\text{A}/\text{cm}^2$ (under 25 mW/cm^2 AM1.5 illumination). For regioregular P3HT, $J_{sc} \approx 30 \mu\text{A}/\text{cm}^2$ and is almost constant in the 200–295 K temperature range. Similar bilayer solar cells constructed from poly(3-undecyl-2,2'-bithiophene) (P3UBT) and flat TiO₂ were reported by Smestad et al. [141]. The best initial performance of FTO/TiO₂/P3UBT/graphite devices gave $J_{sc} = 55 \mu\text{A}/\text{cm}^2$ and $V_{oc} = 0.7$ V under 100 mW/cm^2 AM1.5 illumination. However, performance vs. time measurements revealed that photocurrent and voltage improve over time to $J_{sc} = 85 \mu\text{A}/\text{cm}^2$, $V_{oc} = 0.78$ V, FF= 0.30, and $\eta = 0.02\%$ [142, 143].

The photophysics of polythiophenes on TiO₂ layers has been studied by Goossens et al. [144]. Contrary to their expectations, they observed that the photoluminescence of a 5 nm P3OT layer on TiO₂ is much stronger than when the same layer is on glass. The authors ascribe the enhancement to the interaction of long-lived positive polarons (P3OT radical cations created by electron transfer to TiO₂) with subsequently generated excitons. Although the exact nature of this interaction was not clear, the authors postulated that a fraction of the nonemissive triplet excitons is converted to emissive singlet excitons. This process, however, would be most remarkable as it has been firmly established that positive polarons are effective in quenching singlet excitons in conjugated polymers [145–148] and moreover it is not clear what could provide the extra ~0.7 eV energy that is required to excite the triplet exciton to a singlet exciton in P3HT.

Savenije et al. have studied the charge separation efficiency in polythiophene-sensitized P3HT/TiO₂ bilayers using flash photolysis TRMC [149]. The transient photoconductivity was monitored from nanoseconds to milliseconds following a single 3 ns pulse. Interfacial charge separation and electron injection was found to persist well into the millisecond domain. The action spectrum of the photoconductivity followed the photon attenuation spectrum with a maximum wavelength of 540 nm. By studying both front-side and back-side illumination for different P3HT layer thicknesses and comparing the results to direct band gap excitation of TiO₂ the efficiency of charge separation per incident photon (IPCSE) could be determined. At 540 nm, the IPCSE reached a maximum of 0.8% for 10 nm P3HT films. In principle, the IPCSE may be taken as an upper limit for the EQE that would be expected in a similar cell for the same composition and excitation wavelength. Although this value is considerably lower than the EQE=4.6% that was subsequently reported by Fréchet and McGehee for a TiO₂/P3HT cell [150], it does demonstrate that reaching high efficiencies in bilayer devices is a challenging task.

Fréchet et al. have used a polythiophene derivative (Fig. 8.16) with a thermally removable solubilizing group to increase the performance of TiO₂/polymer solar cells [150]. The structure of the ester-functionalized polythiophene was based on several considerations: (1) the tertiary ester can be cleaved at relatively low temperatures; (2) the branched side chains increase solubility that facilitates synthesis, purification, and deposition; (3) the carboxylic groups that remain after thermal cleavage allow

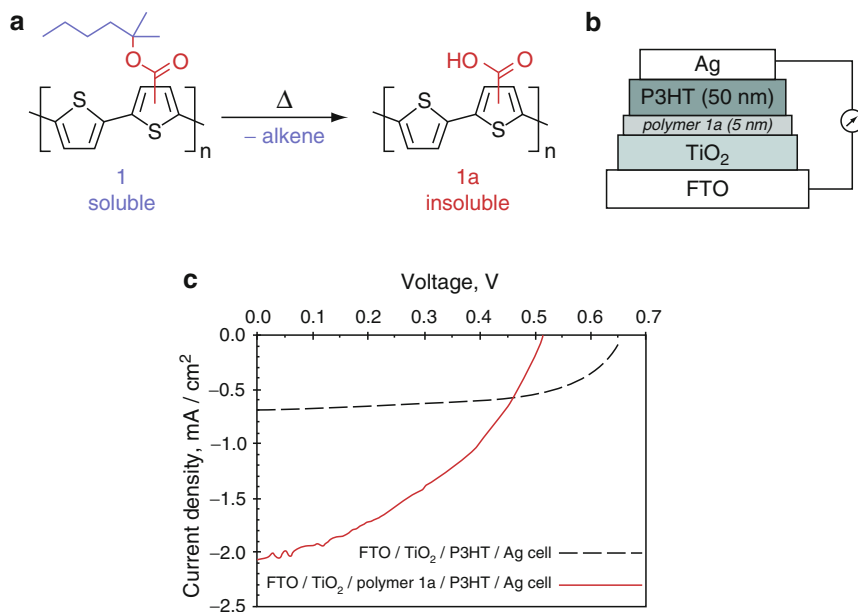


Fig. 8.16 (a) Ester-Functionalized polythiophene 1 and its thermal conversion into insoluble acid-functionalized polymer 1a (b) Device architecture (c) *I-V* curves of FTO/TiO₂/polymer 1a/P3HT/Ag cell (solid line) and FTO/TiO₂/P3HT/Ag cell (dashed line) under 39 mW/cm² 514 nm illumination. Reprinted with permission from J. Am. Chem. Soc. 2004, 126, 9486 [150]. Copyright 2004 American Chemical Society

tuning of the energy levels but also enhance the interface interaction with TiO₂; and (4) after conversion the acid functionalized polythiophene is insoluble, which allows making multilayer devices.

For device fabrication, a TiO₂ layer was deposited on a fluorine doped tin oxide (FTO) electrode on glass (Fig. 8.16b). Subsequently a 5 nm ester-functionalized polythiophene was deposited from solution and then converted to the acid-functionalized derivative at 210°C for 45 min. Finally, the device was completed by spin coating P3HT and evaporation of 80 nm Ag. This FTO/TiO₂/polymer 1a/P3HT/Ag device performed appreciably better than a control cell (FTO/TiO₂/P3HT/Ag) (Fig. 8.16c). Under monochromatic (514 nm) illumination the EQE of this cell is 12.6%, compared to 4.2% for the control cell. The enhanced photocurrent has been ascribed to the advantageous properties of polymer 1a, viz. a higher chromophore density, an enhanced exciton diffusion length because of a shorter interchain distance, and chelation of the carboxylic acid groups to the TiO₂. For the FTO/TiO₂/polymer 1a/P3HT/Ag cell the power conversion efficiency at 39 mW/cm² 514 nm illumination is about 1.10% ($J_{sc} = 2.06$ mA/cm², $V_{oc} = 0.52$ V, FF= 0.40). Compared to the control cell ($J_{sc} = 0.68$ mA/cm², $V_{oc} = 0.66$ V, FF= 0.60) this represents a tripling of the photocurrent but a simultaneous loss of V_{oc} and FF. The effect of carboxylic acid groups on the V_{oc} has been studied in more detail by McGehee et al. [151]. By using polythiophenes with different densities of carboxylic acid groups and Kelvin probe measurements,

they showed that the decrease of the open-circuit voltage originates from interfacial dipoles. These create a reduction in the band offset between the conduction band of TiO_2 and HOMO of the polymer interface resulting in loss of V_{oc} .

A similar multi-polymer layer structure has been used in combination with resonance energy transfer to improve exciton harvesting in organic-hybrid photovoltaic cells by McGehee et al. [152]. In this cell a thin layer of a low band gap polymer (poly(*N*-dodecyl-2,5-bis(2'-thienyl)pyrrole-2,1,3-benzothiadiazole, PTPTB) is inserted between P3HT and TiO_2 to triple the efficiency of a polymer/titania solar cell. The rationale behind this interesting idea is that the thicker P3HT layer can efficiently transfer its excitation energy via a Förster mechanism to the thin low band gap PTPTB layer that subsequently injects an electron into TiO_2 , followed by hole injection into P3HT. Indeed the PL of P3HT on a thin TiO_2 layer was stronger, quenched when a PTPTB interlayer was used. The use of Förster transfer to increase the distance over which an exciton can be transferred beyond the normal diffusion length, has been studied by the same group recently including optical interference effects in multilayer configurations [153, 154]. Clear evidence for the effect was obtained from studying the solar cells performance. A control device of FTO/ TiO_2 /P3HT/Ag without the PTPTB interlayer provides $J_{sc} = 0.46 \text{ mA/cm}^2$, $V_{oc} = 0.64 \text{ V}$, FF= 0.63 and an overall power conversion efficiency of $\eta = 0.19\%$ under simulated AM1.5, 100 mW/cm^2 solar illumination (Fig. 8.17). The device with PTPTB was three times better, with $J_{sc} = 1.33 \text{ mA/cm}^2$, $V_{oc} = 0.67 \text{ V}$, FF= 0.63, and $\eta = 0.56\%$ [152]. Importantly, the spectral response of the device corresponds to the absorption spectrum of P3HT, which shows that excitons initially generated in P3HT are effectively transferred to PTPTB.

With respect to this multi-polymer cell, it is interesting to note that Kroeze and Savenije have studied the photoinduced charge separation in a double-layer of the low-band gap PTPTB spin-coated onto a smooth layer of SnO_2 or TiO_2 , using the TRMC technique [155]. As explained above, the TRMC technique allows intrinsic properties such as the charge separation efficiency to be measured without the necessity of applying electrodes. It was found that SnO_2 that has a high electron affinity

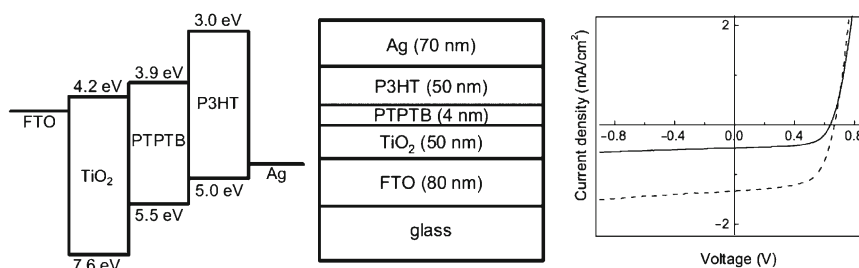


Fig. 8.17 Energy levels, device structure, and performance of FTO/ TiO_2 /PTPTB/P3HT/Ag devices. The J - V characteristics measured under 100 mW/cm^2 AM1.5 illumination with PTPTB (solid line) and without (PTPTB) (dashed line). Reprinted with permission from Adv. Mater. 2005, 17, 2960 [152]. Copyright 2005 Wiley-VCH

(low lying conduction band) could successfully be applied as the electron acceptor in combination with PTPTB that has relatively low excited-state energy level. Ultimately, the major advantage of using such a low-band gap material is the improved overlap with the solar energy spectrum. As a result of the lower-lying SnO_2 conduction band edge and the increased driving force for photoinduced charge transfer, the charge separation efficiency per incident photon is increased by a factor of 30 as compared to the TiO_2 acceptor. Hence SnO_2 /low-band gap polymer combinations form an interesting candidate for application in photovoltaic devices.

8.3.2 Junctions of Doped Polymers with Inorganic Semiconductors

Hybrid organic-inorganic thin film photovoltaic junctions between conducting polymer and various inorganic semiconductors have been studied by various authors following the first report by Horowitz and Garnier on the combination of monocrystalline n-GaAs and poly(3-methylthiophene) (P3MT) as the p-type conjugated polymer. P3MT was electrochemically grown on n-GaAs and initially obtained in a doped state, but then undoped at negative potentials. Compared to a classical Schottky GaAs/Au cell ($J_{\text{sc}} = 10 \text{ mA/cm}^2$, $V_{\text{oc}} = 0.42 \text{ V}$, $\text{FF} = 0.67$, $\eta = 2.8\%$) the GaAs/P3MT(25 nm)/Au cell gave a lower current but higher voltage ($J_{\text{sc}} = 8.4 \text{ mA/cm}^2$, $V_{\text{oc}} = 0.7 \text{ V}$, $\text{FF} = 0.64$, $\eta = 3.5\%$) [156, 157]. The role played by the P3MT layer could not be clearly identified; it may be acting as a real p-type semiconductor (i.e., p-n heterojunction) or instead as an insulator or a passivation layer (i.e., a metal-insulator-semiconductor (MIS) structure) [158].

Frank et al. studied the combination of highly doped P3MT with n-CdS [159]. For a solid state CdS/P3MT/Au device the photoresponse matches the absorption spectrum of CdS, indicating that the inorganic semiconductor, rather than the polymer is the photoactive component of the cell and that charge generation occurs at the CdS/P3MT interface. Under 50 mW/cm^2 illumination of a tungsten-halogen lamp $J_{\text{sc}} = 1.0 \text{ mA/cm}^2$, $V_{\text{oc}} = 0.37 \text{ V}$, $\text{FF} = 0.6$, and $\eta = 0.4\%$ were obtained compared to $J_{\text{sc}} = 1.0 \text{ mA/cm}^2$, $V_{\text{oc}} = 0.25 \text{ V}$, $\text{FF} = 0.4$, and $\eta = 0.2\%$ for a CdS/Au cell. The improved photovoltaic characteristics of the n-CdS:conductive polymer contact was ascribed to be due to a better electronic coupling between n-CdS and P3MT compared with that between the semiconductor and gold.

Chartier et al. have reported the use of various semi-transparent semiconductors in combination with highly doped electrochemically grown P3MT in solid-state Schottky junctions between semiconductors, viz. CdS [160–164], CdSe [165, 166], CdTe [167, 168], and CuInSe_2 [167, 169]. The best electrical contact between the organic and inorganic phases, from an electrochemical viewpoint and in solution, was obtained with the P3MT(PF_6)/CdS(Sb) junction. For this combination the photovoltaic performance in solid state maximized at higher short-circuit current,

open-circuit photovoltage and energy conversion ($J_{sc} = 8.0 \text{ mA/cm}^2$, $V_{oc} = 0.47 \text{ V}$, $\text{FF} = 0.53$, and $\eta = 3.5\%$) at 56 mW/cm^2 light intensity.

Bereznev et al. investigated multilayer structures consisting of electrochemically deposited n-type bulk CIS and CISE with p-type polypyrrole (PPy) for photovoltaic applications. Using bilayer configurations of ITO/CIS/PPy/Ag a $V_{oc} = \sim 0.5 \text{ V}$ and a $J_{sc} = 6.5 \text{ mA/cm}^2$ have been realized at an illumination intensity of 100 mW/cm^2 [170, 171]. More recently, this has been improved using a polycrystalline CIS film that was deposited on Cu tape. By spin coating PEDOT:PSS from a dispersion in water [172], the best obtained hybrid PV structure Cu/CIS/PEDOT:PSS/Au-grid reached an efficiency of 4.14% ($J_{sc} = 20.4 \text{ mA/cm}^2$, $V_{oc} = 0.512 \text{ V}$, $\text{FF} = 0.40$).

Camaioni investigated the photovoltaic effect of p-doped, conducting poly(4,4'-dipentoxy-2,2'-bithiophene) on n-doped silicon [173]. The polymer was electrochemically grown and the cell was sandwiched between two evaporated aluminum contacts. Although the junction between poly(4,4'-dipentoxy-2,2'-bithiophene) and n-Si showed rectification properties and an evident photovoltaic effect, the conversion efficiency was limited ($\eta < 0.6\%$) mainly by a high series resistance which could arise from a non-perfect contact between silicon and conducting polymer.

Wang and Jabbour et al. used silicon in combination with polymers. In a first paper they described the fabrication and properties of an intrinsic (*i*) hydrogenated amorphous silicon (*a*-Si:H) layer and a n-type microcrystalline silicon ($\mu\text{c-Si}$) deposited by hot-wire chemical vapor deposition on spin coated PVK [174]. Compared to a glass/ITO/*a*-Si:H(*i*)/ $\mu\text{c-Si}$ (n)/Pd control cell the photovoltaic effect was completely lost when the PVK layer was inserted (glass/ITO/PVK/*a*-Si:H(*i*)/ $\mu\text{c-Si}$ (n)/Pd). The PVK blocks photogenerated carriers which thus cannot be extracted. On the other hand, under +1.5 V forward bias, a significant photoconductivity could be measured [174]. In a subsequent publication an organic-inorganic hybrid solar cell with a p-i-n stack was produced. Here the p-layer was a spin coated layer of PEDOT:PSS, again with an *a*-Si:H *i*-layer and a $\mu\text{c-Si}$ n-layer [175]. These devices exhibited good photovoltaic performance with ($J_{sc} = 4.55 \text{ mA/cm}^2$, $V_{oc} = 0.883 \text{ V}$, $\text{FF} = 0.51$, and $\eta = 2.1\%$) at 100 mW/cm^2 light intensity. Comparison of these devices with those incorporating *a*-SiC:H:B p-layers indicated that the polymer layer was acting as an ideal p-layer.

8.4 Filling Nanoporous Semiconductors with Conjugated Polymers

Porous TiO_2 electrodes like those used in the DSSCs have a high surface area. When used in a bulk heterojunction of a conjugated polymer and a nanoporous semiconductor, this high surface area is advantageous for charge generation. Consequently, the idea of replacing the dye and liquid electrolyte by a semiconducting polymer that takes care of light absorption, electron injection, and hole transport has been explored in recent years. While this principle is very attractive and would also lead to a morphologically stable heterojunction, the main challenge that has been encountered in this approach is efficient filling of the pores and ultimately

reaching high solar energy conversion efficiencies. As will be shown in this paragraph, these are only slowly approaching the 1% threshold.

Van Hal et al. have performed PIA and photoinduced ESR experiments to investigate the electron transfer from MEH-PPV, MDMO-PPV, P3HT and poly(3,4-dihexyloxy-2,5-thiophene) (PDHOT)) to nanoporous TiO_2 [122]. The PIA spectra of the conjugated polymers on nanoporous TiO_2 recorded at 80 K showed two strong bands at ~ 0.5 and 1.5 eV that are characteristic of cation radicals (polarons) generated on the polymer chains. Photoinduced ESR experiments confirmed this result by the appearance of an ESR signals at $g = 2.0022\text{--}2.0026$ due to photogenerated spins on the polymers, whose intensity could be modulated by changing the light intensity. A complex range of lifetimes for the charge-separated state was observed. In PIA spectroscopy a decay mechanism with a steady state lifetime of 2–10 ms gave an important contribution but other, slower processes occurred as well. The complex decay behavior has been attributed to the inhomogeneous nature of the polymer/nanoporous TiO_2 interface, giving rise to a range of trapping depths. Photoinduced ESR at 130 K on MEH-PPV/ TiO_2 and PDHOT/ TiO_2 shows that recombination occurs with time constants of 10 s and longer. Importantly, only a partial quenching of the polymer photoluminescence was observed when it was in contact with the nanoporous TiO_2 . The residual photoluminescence was attributed to polymer chains that are at a longer distance from the interface with TiO_2 than the exciton diffusion range. This will result in fluorescence, even when an ultrafast forward electron transfer is possible in regions of improved contact. Luzzati et al. confirmed these results for a polydithenothiophenedioxide (PTOX) derivative [176]. The optical absorption spectra of this polymer showed a remarkable interaction with the TiO_2 as compared to other alkyl substituted thiophene based conjugated polymers. Moreover, the PL quenching and the PIA spectra evidenced that TiO_2 acts as an efficient electron acceptor toward PTOX in the excited state.

Lian et al. used femtosecond infrared transient absorption spectroscopy to study the separation and recombination dynamics of the electron transfer of photoexcited MEH-PPV to nanoporous SnO_2 and TiO_2 films [177]. The forward electron transfer is indeed ultrafast with timescales of 800 fs (SnO_2) and <100 fs (TiO_2). Despite a lower level of its conduction band the injection rate for SnO_2 is less than for TiO_2 , demonstrating that the rate is not only determined by the energetics of the band offsets. $\text{SnO}_2/\text{MEH-PPV}$ showed no carrier recombination within 1 ns, but a significant signal decay was observed for $\text{TiO}_2/\text{MEH-PPV}$. In both systems some charges persisted for microseconds to seconds.

One of the first attempts, in terms of solar cells, to infiltrate a polymer into nanoporous TiO_2 has been reported by Carter et al. [104]. Sintered nanocrystalline TiO_2 layers were made by coating an ITO/glass substrate with a viscous TiO_2 water solution and subsequent annealing at 500°C to fuse the particles. This resulted in 4–6 μm thick layers with TiO_2 particles of ~ 80 nm and a pore diameter of 20 nm. The pores were filled with MEH-PPV by spin coating. The best devices based on a ITO/ $\text{TiO}_2/\text{MEH-PPV}/\text{Au}$ cell architecture gave $J_{\text{sc}} = 40 \mu\text{A}/\text{cm}^2$, $V_{\text{oc}} = 0.7$ V, FF = 0.43 at 2 mW/cm² light intensity over the absorption region of the polymer. Subsequent devices made using 200 nm thick sintered TiO_2 nanoparticle layers with a surface

roughness of up to 100 nm showed noticeable improvements and provided $J_{sc} = 0.4$ mA/cm², $V_{oc} = 1.1$ V, FF = 0.40, at incident light intensity near 100 mW/cm², giving a power conversion efficiency of 0.18% [131]. The improvement can be possibly rationalized by the fact that a thinner TiO₂ film (100–200 nm) allows for a better transport of the photogenerated holes, and allows filling the porous material better than in the case of a TiO₂ film that is several micrometers thick.

Sariciftci et al. studied sintered nanocrystalline TiO₂ layers in combination with P3OT. Sandwiched between an ITO or FTO front electrode and an Au back electrode, these devices provided $J_{sc} = 0.17$ mA/cm², $V_{oc} = 0.70$ V and FF = 0.40 under 60 mW/cm² white light illumination [139]. These characteristics improved significantly to $J_{sc} = 0.33$ mA/cm², $V_{oc} = 0.64$ V and FF = 0.44 when a sensitizer layer of *cis*-bis(isothiocyanato)bis(2,2'-bipyridyl-4,4'-dicarboxylato)ruthenium(II) bistetrabutylammonium was inserted between the TiO₂ and P3OT. In this last device the conjugated polymer acts as a solid state hole conductor, replacing the liquid electrolyte of standard DSSCs. Conjugated polymers have attracted more attention as hole conductor in solid state ruthenium dye sensitized solar cells [178–180], but given the fact that solid-state dye sensitized solar cells are a vast research area by itself [181, 182], these cells will not be discussed here. Similarly, we excluded liquid dye-sensitized solar cells in which the dye is a conjugated oligomers [183] or polymer [184, 185] from this overview.

Nelson et al. have studied photovoltaic devices consisting of poly(9,9'-dioctylfluorene-co-bithiophene) (F8BT) and nanocrystalline TiO₂ [186, 187]. In this system, efficient photoinduced charge transfer occurs while charge recombination is relatively slow (~100 μs–10 ms). In the best ITO/TiO₂/F8BT/Au device the EQE maximized at 13% at a wavelength of 440 nm. In these devices a dense “hole-blocking layer” TiO₂ layer, about 50 nm thick, was introduced between the ITO and the nanoporous TiO₂ to prevent direct contact between the polymer and the substrate. Under simulated AM1.5 illumination, the device produced $J_{sc} = 0.40$ mA/cm², $V_{oc} = 0.92$ V, FF = 0.44, and $\eta = 0.16\%$. The authors proposed that the performance of these devices is limited by the energy step at the polymer/metal interface.

Consistently, Kim et al. were the first to show that by inserting a conducting PEDOT:PSS layer between the Au back contact and the polymer layer the device efficiency of nanoporous TiO₂ cells in combination with MEH-PPV can be significantly enhanced [188]. The PEDOT modified device (ITO/TiO₂/MEH-PPV/PEDOT:PSS/Au) cell has $J_{sc} = 0.97$ mA/cm², $V_{oc} = 0.74$ V, FF = 0.48, and $\eta = 0.44\%$ at 80 mW/cm² AM1.5 illumination. Without PEDOT, the fill factor was very small (FF = 0.16). The enhancing effect of PEDOT:PSS was explained by a better ohmic contact.

Seeking optimization of power conversion efficiency of hybrid solar cells based on nanostructured TiO₂ and a MEH-PPV based conjugated polymer Ravirajan and Nelson et al. also established that the charge collection efficiency and device performance were enhanced by introducing a PEDOT:PSS layer under the gold electrode as the hole collector [189, 190]. Several possible reasons for the improvement in J_{sc} resulting from insertion of the PEDOT layer were proposed, viz. (1) PEDOT may cause a chemical doping of the polymer that reduces the contact resistance between the polymer and metal contact, (2) the PEDOT layer may protect the polymer

film from damage during evaporation of the Au electrode, and (3) PEDOT improves collection by minimizing the energy step between polymer and top contact. Maximum device performance was obtained for a 100 nm thick active layer, giving an EQE of 40% at the polymer's maximum absorption wavelength and $J_{sc} = 2.10$ mA/cm², $V_{oc} = 0.64$ V, FF = 0.43, and $\eta = 0.58\%$ under AM1.5 conditions with 100 mW/cm², 1 sun [190].

The results mentioned above show that filling the porous material with (conjugated) polymers or other hole conducting materials is seriously hampered by the densely agglomerated TiO₂. Long polymer strands will find it more difficult to infiltrate into a porous network than smaller strands [191]. This subject has been studied in detail by Heeger et al. [191]. By combining surface analysis, imaging, and depth-profiling they have studied the infiltration of regioregular P3HT into nanoporous TiO₂ networks. A very low incorporation of the polymer was found (0.5%), even for highly porous ($\approx 65\%$) networks. Strategies to increase the incorporation via heat treatment, surface derivatization, and the use of polymer with low molecular weight resulted in a high value of 22% P3HT of the total volume. These authors concluded that if semi-conducting polymers can be incorporated at a high level, efficient hybrid cells will result [191]. Circumventing filling problems by in situ polymerization of polythiophene in the pores of the TiO₂ layer has led to moderate photovoltaic effects so far [192], and this effect is dependent on the doping level of the polythiophene [193].

8.5 Filling Structured Inorganic Semiconductors with Polymers

Creating structured inorganic semiconductors with a pre-defined morphology may be useful to resolve the problems encountered in filling the random nanoporous semiconductors described in the previous sections. Nanostructuring the inorganic material allows for optimizing dimensions, small enough for all excitons to reach the junction, but still allowing a simple and effective filling of the electrodes. A controlled height of the structures will also lead to an improved hole transport and collection efficiency at the top electrode. Since most conjugated polymers still have rather low hole mobilities, the height of the structures, and therefore the maximally achievable increase in contact area and light absorption are likely to limit the device. Ultimately, major improvements can be expected to come from polymers with significantly higher hole mobilities, an expectation that actually holds for all hybrid solar cells described in this chapter.

8.5.1 Structured Porous TiO₂

McGehee et al. have reported an elegant example of nanostructured TiO₂ [194, 195]. Mesoporous TiO₂ films were synthesized using the structure-directing

properties of block copolymers. Using titanium(IV) tetraethoxide as the titania precursor and a Pluronic poly(ethylene oxide)-poly(propylene oxide)-poly(ethylene oxide) tri-block copolymer (P123, average composition HO-PEO₂₀-PPO₇₀-PEO₂₀-OH) as a template, TiO₂ films were formed that have a regular and open structure with pores of approximately 10 nm (Fig. 8.18), which have been filled with regioregular P3HT. Infiltration of the mesoporous TiO₂ has been performed by heat treatment of a spin-cast polymer film. External quantum efficiencies of EQE=10% have been obtained for cells that have a FTO front electrode, a Ag back electrode and a 30 nm P3HT. By combining the measured $V_{oc} = 0.72$ V and FF = 0.51 with the AM1.5 integrated spectral response a power conversion efficiency of $\eta = 0.45\%$ was estimated, corresponding to $J_{sc} = 1.22$ mA/cm² at 100 mW/cm².

Djurišić et al. followed a similar approach as McGehee et al. to create a TiO₂ interconnected network structure for photovoltaic applications using a polystyrene-block-polyethylene oxide diblock copolymer (PS-*b*-PEO) as the templating agent and MEH-PPV as the light absorbing and hole transporting polymer. The pore structure could be controlled by the amount of Ti precursor provided. The best heterojunction solar cells provided $J_{sc} = 3.3$ mA/cm², $V_{oc} = 0.86$ V, FF = 0.28, and $\eta = 0.71\%$ under AM 1.5 solar illumination and used a 20 nm compact TiO₂ layer between the porous TiO₂ and the ITO electrode. The maximum EQE for optimum MEH-PPV thickness was 34% in these ITO/TiO₂/MEH-PPV/Au devices [196, 197].

An interesting approach for nanostructuring TiO₂ has been reported by McGehee et al. (Fig.8.19) [198]. Starting with an anodic alumina template (AAO) with pore diameters of 35–65 nm, high modulus polymethylmetacrylate (PMMA) was thermally infiltrated, followed by covering with a poly(dimethylsiloxane) (PDMS) coating and wet etching the AAO template. By subsequently embossing the resulting PMMA mold into a sol gel, a TiO₂ replica of the AAO was obtained. These deep narrow straight pores could be useful for hybrid photovoltaic applications when infiltrated with a semiconducting polymer. This seems an attractive approach

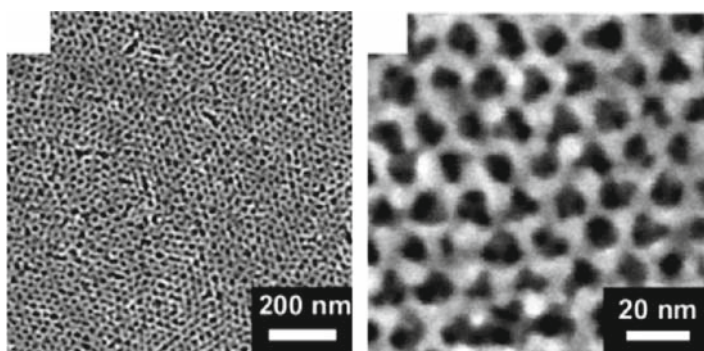


Fig. 8.18 Mesoporous TiO₂ films made using the structure directing properties of block copolymers, after the TiO₂ network is formed the polymers are removed and the TiO₂ is crystallized by calcination at 400°C. Reprinted with permission from Adv. Funct. Mater. 2003, 13, 301 [195]. Copyright 2003 Wiley-VCH

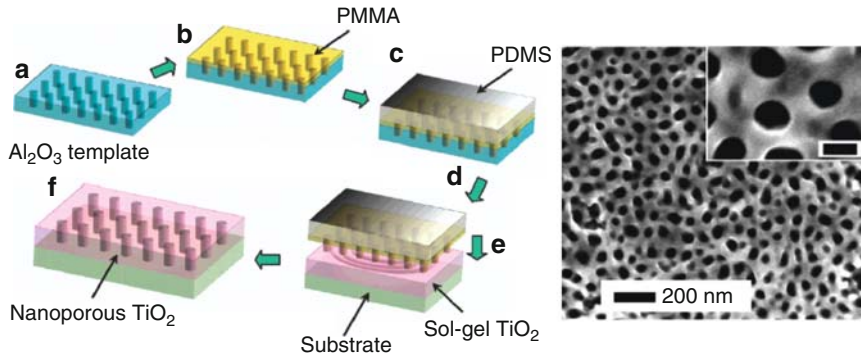


Fig. 8.19 Left: Schematic diagram of the processes involved in embossing titania: (a) preparing AAO template, (b) infiltrating PMMA, (c) coating on PDMS, (d) retrieving mold by wet chemical etching, (e) embossing sol-gel TiO_2 , and (f) removing the mold. Right: embossed TiO_2 structures after PMMA removal, the average pore diameter is 45 nm, the scale bar in the inset corresponds to 50 nm. Reprinted with permission from Nano Lett. 2005, 5, 1545 [198]. Copyright 2005 American Chemical Society

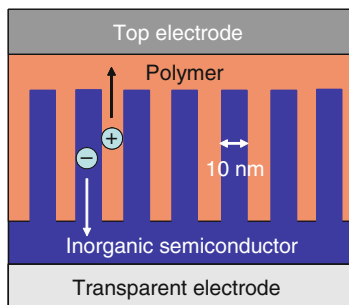
because it was shown that the mobility of regioregular P3HT can be enhanced by a factor of 20 by infiltrating into straight pores of anodic alumina, because the polymer chains align along the inorganic surface [199].

A simple coating method to produce TiO_2 films with orthogonally tilted cylindrical nanopore arrays has been reported by Rankin et al. [200]. In this method a surfactant templated sol-gel made from titanium(IV) ethoxide and Plurion (P123) was dipcoated on a substrate covered with PEO-*r*-PPO copolymer. After aging in a humid environment and subsequent calcinations, orthogonally tilted 2D hexagonally packed TiO_2 nanopores arrays were obtained. In this method, the orientation of the mesophases out of the plane of the film is directed by the chemically neutral PEO-*r*-PPO sacrificial copolymer layer, which is removed during calcination.

8.5.2 Oriented Nanorods

Ultimately the ideal bulk heterojunction structure (Fig. 8.20) would be one where ordered nanosized channels or pillars of both the inorganic material and the polymer are present throughout the bulk of the film [201, 202]. When the typical dimensions on the order of the exciton diffusion length can be realized, high charge generation efficiency and good charge transport can be possibly combined.

Fig. 8.20 Schematic representation of the ideal bulk heterojunction hybrid solar cell in which an ordered inorganic semiconductor is infiltrated with a conjugated polymer and typical dimensions are on the order of the exciton diffusion length



8.5.2.1 CdTe and CdS Pillars

Following this idea Kang et al. have reported results of the fabrication and characterization of CdTe nanorods/poly(3-octylthiophene) (P3OT) hybrid solar cells [203]. CdTe is a promising photovoltaic material for inorganic solar cells because of its optimum band gap energy of 1.45 eV and high absorption coefficient of $10^6/\text{m}$ in the visible solar spectrum. As a template, Kang used anodic aluminum oxide (AAO) with pores having a diameter, length, and density of about 200 nm, 30 μm , and $5 \times 10^8/\text{cm}^2$, respectively. CdTe nanorods were fabricated by electrodeposition from an aqueous solution. The top view images of CdTe nanorods (Fig. 8.21) revealed that CdTe filled the pores uniformly and that the nanorods reproduced the dimension of the membrane pores. Hall effect measurements established that the electrode-deposited CdTe shows an n-type behavior. The active layer was formed by drop casting or spin coating P3OT. Au front electrodes were thermally evaporated in vacuum. The device characteristics under AM1.5 illumination were $J_{\text{sc}} = 3.12 \text{ mA}/\text{cm}^2$, $V_{\text{oc}} = 0.714 \text{ V}$, $\text{FF} = 0.477$, resulting in an overall efficiency of $\eta = 1.06\%$. To date this is the highest efficiency that has been obtained using a combination of an ordered nanostructured inorganic semiconductor and a conjugated polymer. In CdTe nanorods/P3OT cells, both components absorb a considerable portion of the solar emission, and photoexcitation of both the polymer and the CdTe leads to photo-generation of charges.

In a similar fashion as for CdTe, also CdS nanorods (diameter 200 nm, length 30 μm) were grown vertically by Kang et al. via cathodic electrochemical deposition through a porous anodic aluminum oxide (AAO) substrate, which had been covered on one side by a Ti layer that functioned as the working electrode [204]. After removing the AAO template in sodium hydroxide, MEH-PPV was spin coated onto the CdS nanorod surface, thermally annealed in a forming gas (10% H_2 in Ar). The device was completed by evaporating an Au front electrode. The device characteristics were $J_{\text{sc}} = 1.397 \text{ mA}/\text{cm}^2$, $V_{\text{oc}} = 0.858 \text{ V}$, $\text{FF} = 0.496$ under AM1.5 illumination (100 mW/cm^2) resulting in an overall efficiency of $\eta = 0.60\%$.

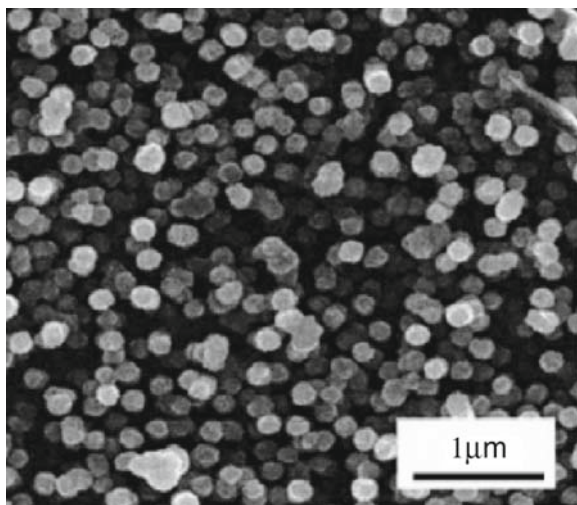


Fig. 8.21 Top view scanning electron microscopy (SEM) image of the vertical aligned CdTe nanorods. Reprinted with permission from *Appl. Phys. Lett.* 2005, 86,113101 [203]. Copyright 2005 American Institute of Physics

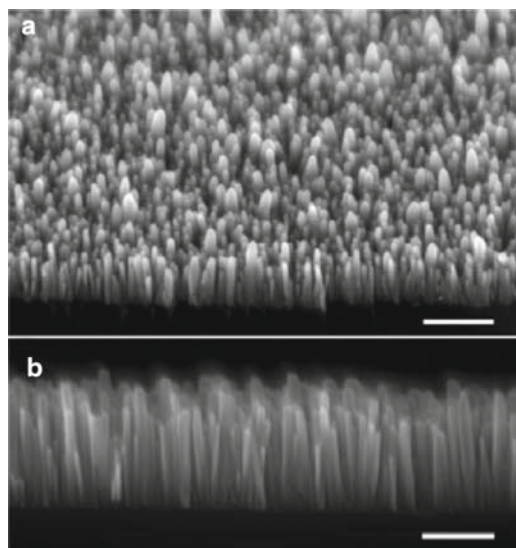


Fig. 8.22 SEM characterization of vertical ZnO nanowire arrays on silicon. (a) Image taken at a 45° tilt. Wire lengths and diameters are 250–400 nm and 15–65 nm, respectively. Scale bar, 500 nm. (b) Cross-sectional image of a different array. Scale bar, 200 nm. Reprinted with permission from *Nano Lett.* 2005, 5 1231 [206]. Copyright 2005 American Chemical Society

8.5.2.2 ZnO Pillars

Nanocrystalline ZnO can adopt a wide range of interesting morphologies [205]. Fabrication of well-defined ZnO nanopillars is an appealing approach for hybrid polymer solar cells (Fig. 8.22) [206], especially when the dimensions of the rods, and the spacing in between, can be controlled to create a structure with a high interface contact area, but still allowing a proper filling of the voids with polymer.

The actual realization of hybrid solar cells involving ZnO nanopillars has been reported by two groups independently [207–209]. Olson et al. have grown ZnO nanofibers hydrothermally from a ZnO nucleation layer on a conducting ITO/glass substrate (Fig. 8.23) [207]. Then P3HT was spin coated from solution, followed by thermal annealing at 200°C for 1 min before completing the device with an Ag top electrode. The best device gave a significant photovoltaic effect with $J_{sc} = 2.2 \text{ mA/cm}^2$, $V_{oc} = 0.475 \text{ V}$, and $FF = 0.56$, providing an efficiency of $\eta = 0.53\%$ with a maximum EQE of 17% at 520 nm. Incorporation of PCBM as an additional acceptor in the blend gave an increase in performance to 2.03%. In this case, the active layer is the P3HT:PCBM blend, which is known to give very high conversion efficiencies of 4–5% [26–29]. The power efficiency in the ZnO-fiber/P3HT devices seems to be limited by the 0.2 V reduction in V_{oc} compared to the nanoparticle cells and by the spacing between the ZnO nanofibers, which is in the order of 100 nm and therefore substantially larger than the exciton diffusion length in P3HT [207].

Nelson et al. have performed an extensive study on the different solution-based chemical routes for preparing columnar ZnO structures on a dense ZnO backing layer, that act as a seed-growth layer for the rods in relation to hybrid photovoltaic devices [209]. They established that the growth of ZnO nanorod arrays depends on the morphological and structural characteristics of the seed layers. Different polymers (high hole mobility MEH-PPV and P3HT) were tested in devices. A unique feature of this approach is that the ZnO nanorods were covered with an amphiphilic dye *cis*-RuLL'(SCN)₂ ($L = 4,4'$ -dicarboxylic acid-2,2'-bipyridine, $L' = 4,4'$ -dinonyl-2,2'-

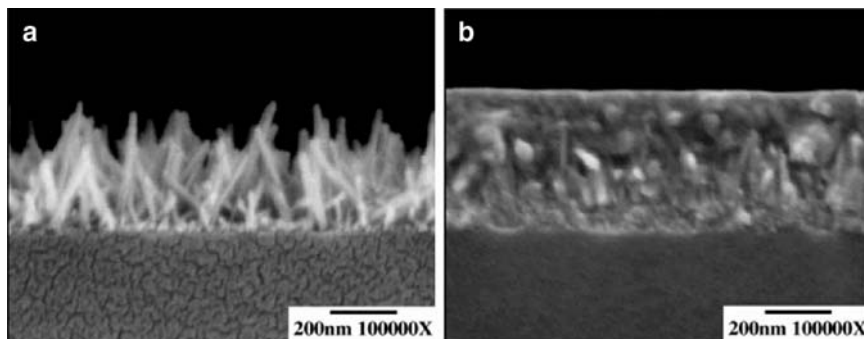


Fig. 8.23 (a) SEM image of a glass/ZnO nucleation layer/ZnO nanofiber structure. (b) SEM image of P3HT intercalated into the ZnO nanofiber structure. Reprinted with permission from *Thin Solid Films* 2006, 496, 26 [207]. Copyright 2006 Elsevier

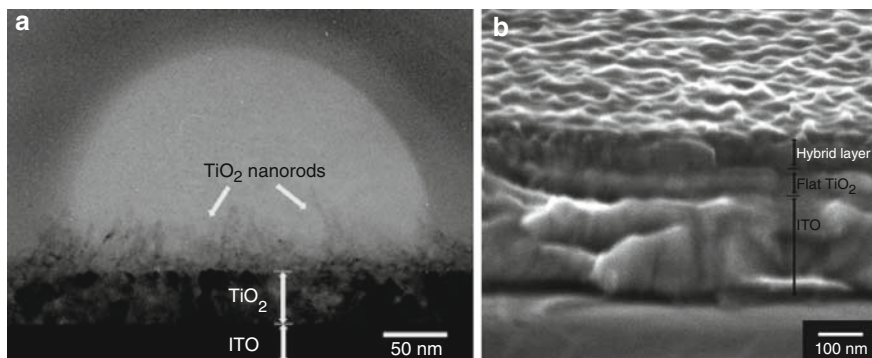


Fig. 8.24 (a) TEM cross-sectional image of the nanostructured TiO_2 substrate (b) FE-SEM cross-sectional images of the MEH-PPV films deposited on the nanostructured TiO_2 substrates. Reprinted with permission from Chem. Mater. 2006, 18, 5080 [210]. Copyright 2006 American Chemical Society

bipyridine), referred to as Z907, before applying P3HT by spin coating [208]. The rationale for this approach is that the dye helps in wetting the ZnO surface by the polymer and that the dye can assist in the interfacial electron transfer from the polymer to the ZnO. For the top contact, a layer of PEDOT:PSS was spin coated followed by deposition of Au. The PEDOT:PSS improves the smoothness of the top surface and the electrode quality. The best ZnO nanorod:P3HT device using the Z907 interfacial layer, gave $J_{sc} = 1.73 \text{ mA/cm}^2$, $V_{oc} = 0.30 \text{ V}$, and $\text{FF} = 0.39$, providing an efficiency of $\eta = 0.2\%$ [209], with a maximum $\text{EQE} = 14\%$ at 550 nm [208]. Devices with the high hole mobility MEH-PPV derivative showed an overall efficiency of 0.15% . Without the Z907 dye or the PEDOT:PSS, the devices showed large leakage currents and very low V_{oc} .

8.5.2.3 TiO_2 Pillars

Based on low-temperature sol-gel synthesis of anatase TiO_2 nanorods in a reversed micelle solution, Hashimoto et al. succeeded in depositing an array of TiO_2 nanostructure assemblies with a height of $\sim 40 \text{ nm}$ selectively on a TiO_2 substrate [210]. Cross sectional TEM showed that each nanostructure is an assembly of TiO_2 nanorods with a diameter and length of 4 and 40 nm , respectively (Fig. 8.24). The fabricated array of TiO_2 rods was applied to construct photovoltaic devices in combination with MEH-PPV. The best devices showed $J_{sc} = 0.95 \text{ mA/cm}^2$, $V_{oc} = 0.88 \text{ V}$, and $\text{FF} = 0.47$, providing an efficiency of $\eta = 0.39\%$, which is a considerable improvement compared to a flat $\text{TiO}_2/\text{MEH-PPV}$ control device ($J_{sc} = 0.33 \text{ mA/cm}^2$, $V_{oc} = 0.87 \text{ V}$, $\text{FF} = 0.49$, and $\eta = 0.13\%$). The EQE of the nanostructure $\text{TiO}_2/\text{MEH-PPV}$ maximized at 15% at a wavelength of 510 nm .

8.6 Metal Oxide Networks and Conjugated Polymers

In the previous sections it was shown that hybrid conjugated polymer – inorganic solar cells can give energy conversion efficiencies close to 3%. However, both mixing conjugated polymers with inorganic nanoparticles and filling of (nanostructured) pores still pose processing challenges with respect to reaching higher efficiencies. For the nanoparticles, a difficult issue is to find conditions that allow efficient mixing of the particles with the polymer and that which create good electrical contacts between the particles to obtain a percolating pathway. The hybrid polymer – nanoporous inorganics face the problem that the small (~20 nm) pores, that are required to ensure that the majority of photoexcitations in the polymer reach the interface with an inorganic semiconductor, are difficult to fill efficiently.

In an attempt to overcome these disadvantages, Van Hal et al. introduced the use of a molecular precursor for the inorganic semiconductor to create a metal oxide network inside the polymer film [211]. Because the metal oxide precursor is readily soluble in organic media, it can be cast into a thin film together with the polymer from solution. Upon exposure to moisture from air, the precursor is converted into a metal oxide semiconductor within the polymer layer, ensuring intimate mixing and concomitantly efficient photoinduced charge generation.

8.6.1 *In Situ Blends Based on TiO_x*

The validity of this approach was first demonstrated using titanium(IV) isopropoxide ($\text{Ti}(i\text{-PrO})_4$) as precursor for TiO_2 and MDMO-PPV [211]. To fabricate the hybrid bulk heterojunction, $\text{Ti}(i\text{-PrO})_4$ was added to a solution of MDMO-PPV in dry tetrahydrofuran (THF) prior to spin casting the mixture into a thin solid film. The $\text{Ti}(i\text{-PrO})_4$ precursor was subsequently converted in situ into TiO_2 by exposure of the cast film to moisture from the air to promote hydrolysis and a consecutive high vacuum treatment to promote condensation of the formed titanium hydroxide into titania. As a consequence of the formation of a TiO_2 network, the bulk heterojunction film became resistant to scratching and could no longer be wiped off the substrate or dissolved in organic solvents. X-ray photoelectron spectroscopy (XPS) of the in situ- TiO_2 :MDMO-PPV indicated that the conversion of $\text{Ti}(i\text{-PrO})_4$ into TiO_2 in the bulk heterojunction was at least 65% under these conditions [211]. The characteristic distance of this in situ- TiO_x :MDMO-PPV bulk heterojunction was in the nanometer range as inferred from AFM studies (Fig. 8.25) [211].

The PL at 580 nm of the in situ- TiO_x :MDMO-PPV bulk heterojunction was significantly quenched compared to that of a pristine MDMO-PPV film. The PL intensity decreased with increasing amount of TiO_2 and was quenched by a factor of 19 in the 50% blend (Fig. 8.26a), implying a fast deactivation of the MDMO-PPV singlet excited state. The significantly reduced PL intensity corroborates with the fine scale phase separation inferred from AFM (Fig. 8.25) and indicates an efficient formation of photoinduced charges. The PIA spectrum of in situ- TiO_x :MDMO-PPV

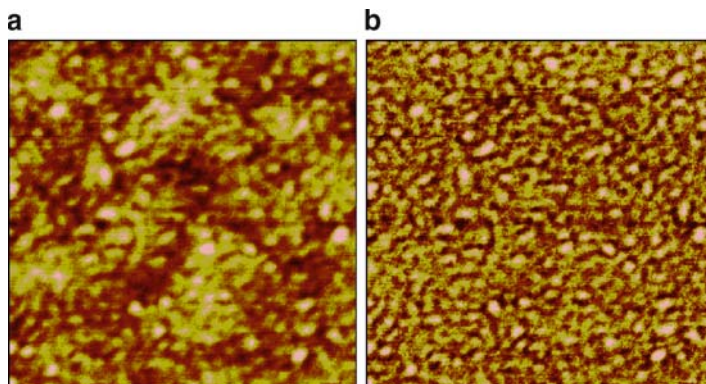


Fig. 8.25 (a) Tapping mode AFM height image of a 1:1 (v/v) in situ-TiO_x:MDMO-PPV bulk heterojunction ($2 \times 2 \mu\text{m}^2$, z -range = 10 nm) created by the in situ method. (b) Corresponding AFM phase image (z -range = 7.5°). Reprinted with permission from Adv. Mater. 2003, 15, 118 [211]. Copyright 2003 Wiley-VCH

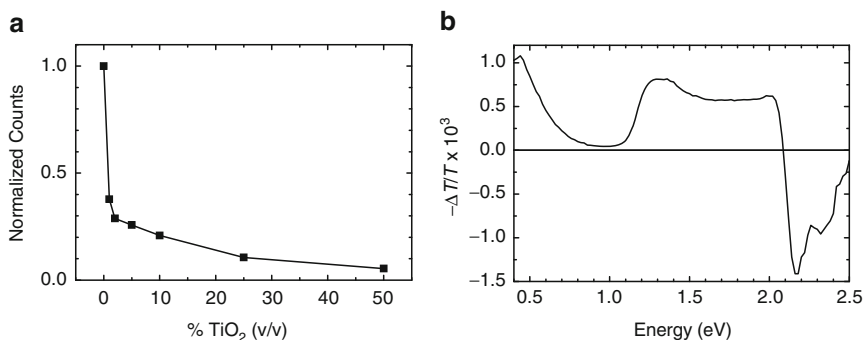


Fig. 8.26 (a) Photoluminescence intensity of in situ-TiO_x:MDMO-PPV bulk heterojunctions with varying amounts of TiO₂, with excitation at $\lambda = 488 \text{ nm}$. (b) PIA spectrum of 1:1 (v/v) in situ-TiO_x:MDMO-PPV a bulk heterojunction. Reprinted with permission from Adv. Mater. 2003, 15, 118 [211]. Copyright 2003 Wiley-VCH

recorded at 80 K exhibits two absorptions at 0.42 and 1.32 eV and a bleaching signal at 2.18 eV with a shoulder at 2.32 eV (Fig. 8.26b) and gives direct spectral evidence of the formation of photogenerated charges. The absorption bands are due to the two dipole-allowed transitions of the radical cation of MDMO-PPV, while the two bleaching signals are attributed to the MDMO-PPV ground state [122].

The spectral response of a ITO/PEDOT-PSS/in situ-TiO_x:MDMO-PPV/LiF/Al solar cell prepared using this simple approach gave an EQE= 11% at 450 nm (Fig. 8.27a) for a 4:1 (v/v) blend. J - V measurements on these cells under illumination with a halogen lamp (~ 0.7 sun intensity) revealed a moderate performance with $J_{\text{sc}} = 0.6 \text{ mA/cm}^2$, $V_{\text{oc}} = 0.520 \text{ V}$, and FF= 0.42 (Fig. 8.27b), representing an energy

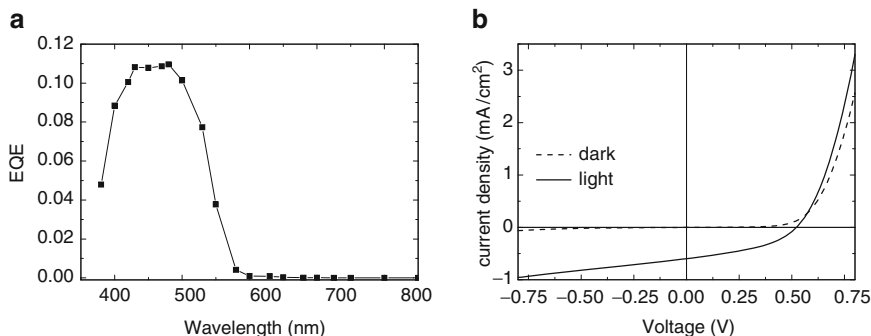


Fig. 8.27 Photovoltaic properties of ITO/PEDOT-PSS/in situ-TiO_x:MDMO-PPV/LiF/Al devices 4:1 (v/v) (a) External quantum efficiency. (b) J - V curve in the dark (dashed line) and under illumination (~ 70 mW/cm²) (solid line). Reprinted with permission from Adv. Mater. 2003, 15, 118 [211]. Copyright 2003 Wiley-VCH

conversion efficiency of $\eta = 0.2\%$. Integration of the measured spectral response of the cell with the AM1.5 solar spectrum affords an estimate for the short circuit current density under AM1.5 conditions (1,000 W/m²) of $J_{sc} = 0.87$ mA/cm² [211]. In a subsequent study, Slooff et al. confirmed these results for in situ-TiO_x:MDMO-PPV ($J_{sc} = 0.6$ mA/cm², $V_{oc} = 0.60$ V, and FF = 0.43, $\eta = 0.22\%$ at 70 mW/cm²) and showed that the procedure is also applicable to polythiophene derivatives [212]. For an in situ-TiO_x:P3OT active layer they found $J_{sc} = 0.7$ mA/cm², $V_{oc} = 0.45$ V, and FF = 0.41, $\eta = 0.17\%$ at 70 mW/cm²).

Wang et al. followed a similar approach using a triethoxysilane-containing poly(3-nonylthiophene) (P3NT) and Ti(*i*-PrO)₄ to make hybrid in situ-TiO_x/P3NT material [213]. The presence of the silane group effectively prevented the macroscopic aggregation of TiO₂ during the sol-gel reaction, leading to more uniform distribution of TiO₂ throughout the sample and a better PL quenching. This promising material, however, has not been tested in solar cells so far.

While the in situ TiO_x synthesis has various potential advantages in terms of creating an intimate mixing, the main drawback of the use of in situ prepared TiO_x is that the resulting inorganic phase is essentially amorphous. Crystallization of TiO₂ would require high temperatures (>350°C [214]). Hence, it is likely that the presence of an amorphous TiO_x phase, rather than a crystalline network of TiO₂, limits the charge transport in photovoltaic devices based on this method.

8.6.2 In Situ Blends Based on ZnO

Due to the poorly-defined, amorphous nature of the formed TiO_x phase, the power conversion efficiency of the resulting photovoltaic cells described in the previous section remained rather low at ca. 0.2%. Improvement can be expected from

crystallization of TiO_2 . However, this would require high temperatures ($>350^\circ\text{C}$ [214]) that are not compatible with the presence of the semiconducting polymer. ZnO , on the other hand, is known to crystallize at much lower temperatures [113]. To overcome the limitations encountered in the in situ synthesis of TiO_2 , Beek et al. introduced in situ- ZnO :polymer bulk heterojunction solar cells [215]. The active layer was prepared by spin coating a solution containing an organozinc compound and a conjugated polymer, followed by thermal annealing at moderate temperature. This affords a crystalline ZnO network in the polymer phase. The resulting photovoltaic devices exhibit a significantly increased power conversion efficiency compared to the amorphous in situ- TiO_2 :polymer cells.

The new method to make crystalline ZnO films starts from diethylzinc. Like other sol-gel processes, the conversion of diethylzinc into ZnO requires two steps: hydrolysis and condensation. These reactions initiate very rapidly when diethylzinc is exposed to air. To obtain smooth ZnO films the hydrolysis and condensation reactions need to be moderated. This has been achieved by the addition of THF to the solution. THF stabilizes diethylzinc by coordination to the zinc atom. Room temperature conversion of diethylzinc does not result in the direct formation of ZnO as evidenced from the lack of absorption above 250 nm in the absorption spectrum of a pristine spin coated film. However, upon heating to 110°C the absorption onset shifted towards 375 nm, indicating that ZnO is formed [215]. The ZnO formed via this route appears to be crystalline by powder X-ray diffraction. The observed peak positions correspond very well to the values expected for crystalline ZnO [215, 216]. The line broadening that was present in the XRD spectrum indicated the formation of 6 ± 1 nm small domains of ZnO .

Because of the moderate conversion temperature, the diethylzinc route is compatible with conjugated polymers. Composite films on glass were made by spin coating solutions of diethylzinc and MDMO-PPV in chlorobenzene/THF/toluene mixtures. Because water is one of the reagents, the relative humidity is a critical processing parameter. The best results were obtained when spin coating was performed in air under relative humidity of 40%, followed by aging for 15 min and annealing at 110°C for 30 min in nitrogen at 40% relative humidity. The UV-vis absorption spectrum revealed the presence of ZnO at $\lambda < 360$ nm (Fig. 8.28b). At the same time a distinct 26 nm blue shift of the MDMO-PPV absorbance was observed, indicating partial degradation of the polymer [215].

The photoluminescence of in situ- ZnO :MDMO-PPV films was significantly quenched compared to a pristine, annealed MDMO-PPV film, consistent with an electron transfer in the blend from the singlet-excited state of the polymer to ZnO precursor. The residual photoluminescence amounted to $\sim 20\%$ and was attributed to excitons that cannot reach a junction between MDMO-PPV and ZnO [215]. Hence, up to 80% of the absorbed photons may result in charge formation. Evidence for long-lived charges was provided by PIA measurements. The PIA spectrum of an annealed in situ- ZnO :MDMO-PPV film shows the photobleaching band of neutral MDMO-PPV at 2.2 eV and the characteristic absorption bands of the polymer radical cation at around 0.4 and 1.5 eV (Fig. 8.28b) [215]. The band at 1.5 eV also contained a residual signal from the MDMO-PPV triplet excited state absorption. Some triplet formation via intersystem crossing is likely

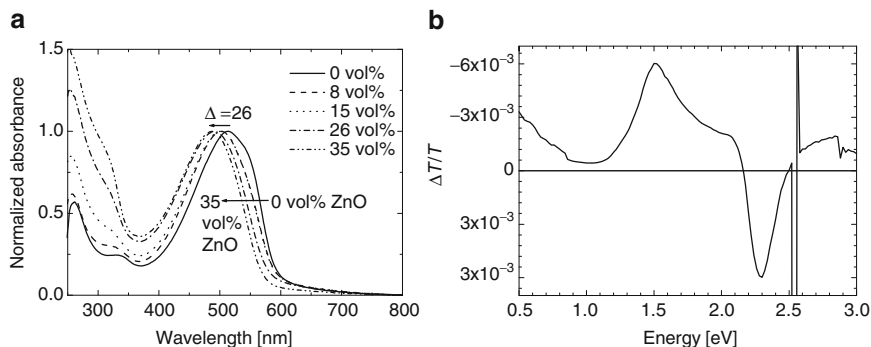


Fig. 8.28 (a) Normalized UV-vis absorption spectra of in situ-ZnO:MDMO-PPV films after annealing at 110°C. (b) PIA spectrum of an in situ-ZnO:MDMO-PPV blend on quartz, measured at 80 K with modulated (275 Hz) excitation at 2.54 eV (488 nm). Reprinted with permission from *Adv. Funct. Mater.* 2005, 15, 1703 [215]. Copyright 2005 Wiley-VCH

to occur because the competing intrinsic process, photoluminescence of the polymer, was not completely quenched. No distinct contribution of ZnO to the PIA spectrum was observed, but this absorption may be obscured by the low energy absorption of the cation radical. The formation of charge carriers in in situ-ZnO:MDMO-PPV bulk heterojunctions has also been studied by Savenije et al. by the electrodeless TRMC technique [217]. Photoexcitation of the polymer at 510 nm leads to a long-lived (up to 10 μ s) conductance signal indicating efficient charge separation from the polymer to ZnO.

The morphology of the in situ-ZnO:MDMO-PPV films has been examined with the tapping mode AFM and SEM. With AFM, conglomerates of spherical aggregates have been identified. The roughness of the film increases significantly with increasing ZnO content (Fig. 8.29a–c). A similar conclusion can be drawn from the SEM images (Fig. 8.29d–f). The increased roughness at higher ZnO content leads to formation of large pores as observed with AFM and SEM (Figs. 8.29c and 8.29f). However, the increased roughness and larger pores do not seem to change the morphology on a smaller scale, as the same spherical aggregates are observed with AFM.

Photovoltaic devices were fabricated by spin coating, aging, and annealing the photoactive layer under controlled relative humidity on glass substrates covered with ITO and PEDOT:PSS and completed by deposition of an Al top electrode. Under white-light illumination (90 mW/cm^2), the hybrid device gives $J_{\text{sc}} = 2.0 \text{ mA}/\text{cm}^2$, $V_{\text{oc}} = 1.14 \text{ V}$, and $\text{FF} = 0.42$ (Fig. 8.30). The EQE reached 27% at 520 nm and integrating the spectral response with the AM1.5 spectrum gave an estimate for $J_{\text{sc}} = 2.3 \text{ mA}/\text{cm}^2$ and a calculated power conversion efficiency of $\eta = 1.1\%$. This efficiency is five times higher than for optimized cells based on TiO_2 precursors [211] and demonstrates the effectiveness of crystalline ZnO as n-type material in hybrid bulk heterojunction solar cells. Moreover, such photovoltaic effect is consistent with the formation of a

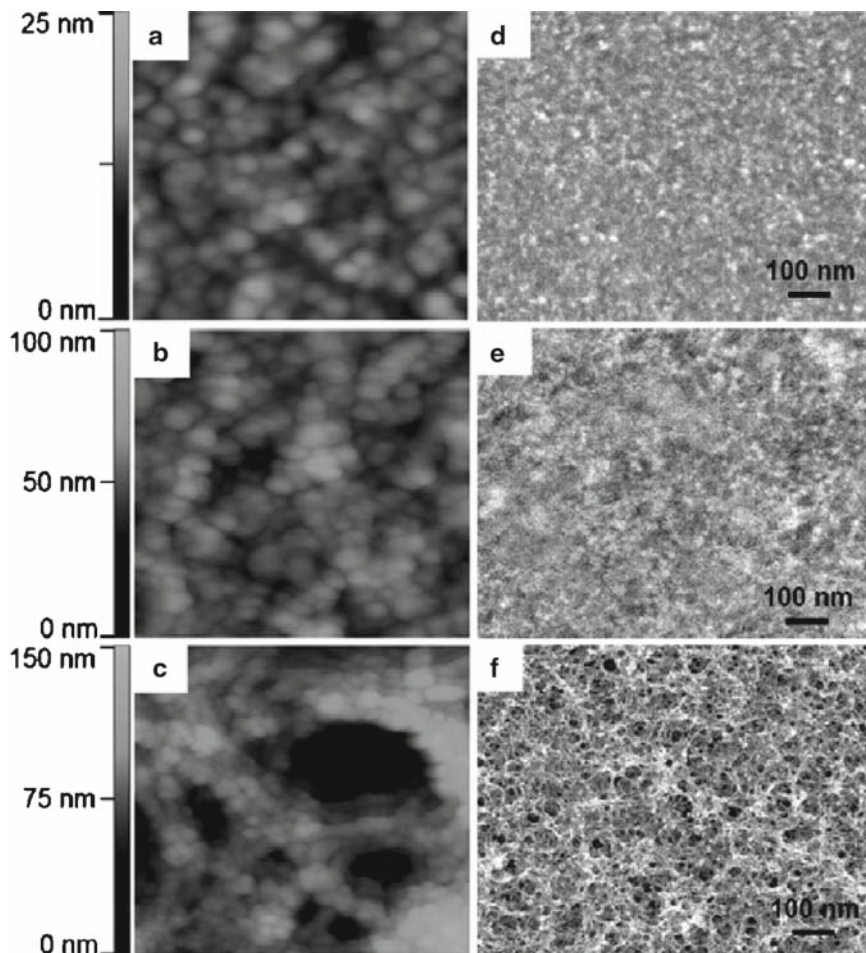


Fig. 8.29 (a–c) AFM tapping mode images of in situ-ZnO:MDMO-PPV blends, image size is 500 by 500 nm: (a) 8 vol% ZnO (height scale = 25 nm, Δh (peak-to-peak roughness) = 7 nm); (b) 26 vol% ZnO (height scale = 100 nm, Δh = 40 nm); (c) 47 vol% ZnO (height scale = 150 nm, Δh = 100 nm). (d–f) SEM images: (d) 15 vol% ZnO; (e) 26 vol% ZnO; (f) 35 vol% ZnO. Reprinted with permission from Adv. Funct. Mater. 2005, 15, 1703 [215]. Copyright 2005 Wiley-VCH

bicontinuous network of both materials. It is important to note that a non-annealed in situ-ZnO:MDMO-PPV blend shows only a very small photovoltaic effect with $J_{sc} = 0.05 \text{ mA/cm}^2$, $V_{oc} = 1.15 \text{ V}$, and $\text{FF} = 0.18$. This shows the necessity of the annealing step and obtaining crystalline ZnO for preparing well performing photovoltaic devices.

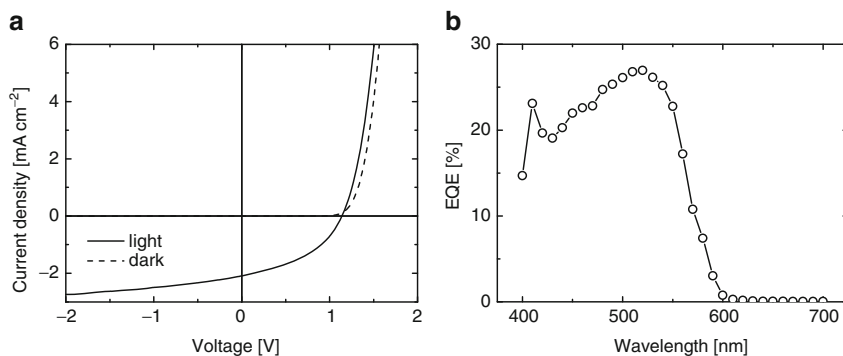


Fig. 8.30 (a) J - V of a in situ-ZnO:MDMO-PPV photovoltaic device (15 vol% ZnO). (b) EQE of the device Reprinted with permission from Adv. Funct. Mater. 2005, 15, 1703 [215]. Copyright 2005 Wiley-VCH

8.7 Conclusions and Outlook

The field of hybrid polymer-inorganic solar cells has attracted strong interest and progressed enormously over the last decade. An overview of the different cell architectures and their performance as published up to the end of 2006 is collected in Table 8.1. The best cells in which the photoinduced electron transfer between the conjugated polymer and the inorganic semiconductor reach efficiencies above 1% [45] are mostly based on nanoparticles blended into the polymer [50, 52–54, 56, 112] with a record efficiency of $\eta = 2.4$ –2.8% for cells based on P3HT and CdSe tetrapods [53]. However cells based on flat inorganic layers [150], inorganic pillars filled with polymers [203], and polymers with in situ synthesized metal oxides [215] also have reached efficiencies above this 1% threshold. Although these efficiencies slowly approach the 4–5% obtained for the best polymer/fullerene cells, hybrid cells still face some important challenges in closing the gap. One of the most important questions to solve is the creation of the bulk heterojunction itself. The different nature of the organic and inorganic materials makes the creating of an intimate blend with two fully percolating pathways not trivial and it is our opinion that this remains the most important hurdle to be taken. It will be up to the imagination and creativity of researchers to come up with novel techniques and approaches to solve this issue. This will pave the way for further improving the cells by optimizing the optical band gap of the polymer to the solar emission and by minimizing voltage losses at electrodes and in the actual charge transfer step.

Finally, it should be noted that apart from being part of the active layer transparent inorganic layers are emerging as additional layers in improving the efficiency of polymer/fullerene solar cells. In this respect Krausch et al. [218] and more recently Heeger et al. [219] have used a TiO₂ layer as an optical spacer between the active layer and the Al back electrode. The optical spacer affects the spatial

Table 8.1 Performance of hybrid polymer-inorganic photovoltaic cells. Short-circuit current (J_{sc}), open-circuit voltage (V_{oc}), fill factor (FF), power conversion efficiency (η), light intensity (I_L), and external quantum efficiency (EQE) at wavelength (λ)

Cell configuration	J_{sc} (mA/cm ²)	V_{oc} (V)	FF	η (%)	I_L (mW/cm ²)	EQE (%) λ (nm)	Ref.
Blends of nanoparticle and polymers							
ITO/CdSe:MEH-PPV/Al	5.7	0.70	0.40	1.7	100	12 514	[40,41]
ITO/PEDOT:PSS/CdSe(rods):P3HT/Al	~3.2	~0.45	~0.35	~0.6	100	55 485	[45]
ITO/PEDOT:PSS/CdSe(rods):P3HT/Al	~6.3	~0.60	~0.38	~1.5	100		[50]
ITO/PEDOT:PSS/CdSe(rods):P3HT-CH ₂ NH ₂ /Al	7.30	0.65	0.35	1.8	93	45 480	[52]
ITO/PEDOT:PSS CdSe(tetrapods):MDMOPPV/Al	6.42	0.76	0.44	2.4	90	48 500	[53]
ITO/PEDOT:PSS CdSe(tetrapods):MDMOPPV/LiF:Al	7.23	0.95	0.38	2.4	100	44 565	[54]
ITO/PEDOT:PSS/CdSe(branched particles):APFO-3/Al	2.86	0.69	0.46	1.1	80	47 410	[56]
ITO/PEDOT:PSS/CdSe(tetrapods):MEH-PPV/Al	0.024	0.33	0.33	0.003	80	47 410	[56]
ITO/CdTe(tetrapods):P3HT/Al				<1			[58]
ITO/PTPA.A(polymer brush):CdSe/Al		0.75			20	340	[59]
ITO/PEDOT:PSS/PTPAA(polymer brush):CdSe(dots)/Al	0.007	0.85			8		[59]
ITO/PbS:MEH-PPV/Mg					0.0008	975	[62,63]
ITO/PbS:MEH-PPV/Mg annealed	0.13	1.00	0.28	0.7	5	0.002 975	[66]
ITO/PEDOT:PSS/PbS:MEH-PPV/Al	0.24	0.32	0.43	0.04	100		[68]
ITO/PEDOT:PSS/PbSe:P3HT/Al	1.08	0.35	0.37	0.14	100	1.3 805	[73]
ITO/PEDOT:PSS/PbSe:P3HT/Al	0.26	0.75	0.44	0.086	80	5 400	[74]
ITO/PEDOT:PSS/CIS/PCBM/LiF/Al	0.84	0.22	0.26	0.07	80	20 400	[95,96]
ITO/CIS:PEDOT:PSS/PCBM/LiF/Al	0.30	1.00	0.50	0.19	80		[97,98]
ITO/CIS:P3HT/Al	2.0	0.40	0.50	0.4	100	10 550	[99]
ITO/TiO ₂ /HgTe/P3HT/Au	0.025	0.65	~0.25	0.004	100	2 450	[101,102]
FTO/TiO ₂ :PPV/Al	~0.020	~1.00			2		[104]
ITO/TiO ₂ :MEH-PPV/Ca	2.76	0.44	0.40	0.42	100	15 475	[106,107]
ITO/PEDOT:PSS/TiO ₂ :P3HT/Al	0.25	0.72	0.35	0.06	100	2.5 488	[110,111]
FTO/TiO ₂ /P3OT/Au aerosol deposition	2.40	0.81	0.59	1.6	71	40 510	[112]
ITO/PEDOT:PSS/ZnO:MDMO-PPV/Al	2.14	0.69	0.55	0.9	100	27 490	[121]

Flat semiconductor-polymer bilayers									
ITO/TiO ₂ /PA-PPV/Au	~0.5	0.85	0.52	-0.2	100	25	425	[130]	
ITO/TiO ₂ /MEH-PPV/Au	0.24	0.70	0.42	0.07	100	3.3	500	[131]	
ITO/TiO ₂ /M3EH-PPV/Au	1.2	0.65	0.40	0.40	80	7.5	480	[132]	
ITO/TiO ₂ /M3EH-PPV/PCNEPV/Au	3.3	0.65	0.28	0.75	80	23.5	475	[132]	
ITO/TiO ₂ /MEH-PPV/Au	0.008	0.63	0.67	1.6	0.2 ^a	9.5	300	[133]	
ITO/TiO ₂ /MEH-PPV/Ag	0.4	0.74	0.25	0.07	100			[134]	
ITO/TiO ₂ /MDMO-PPV/PEDOT:PSS/Au	0.96	0.51	0.61	0.30	100	12	540	[135]	
ITO/TiO ₂ /P3OT/Au	0.009	0.56	0.36	0.003	64			[139]	
ITO/TiO ₂ /P3HT/Au	0.030	0.55			25			[140]	
FTO/TiO ₂ /P3UBT/graphite	0.085	0.78	0.30	0.02	100			[142,143]	
FTO/TiO ₂ /P3HT/Ag	0.68	0.66	0.60	0.79	39 ^b	4.2	514	[150]	
FTO/TiO ₂ /PT-COOH/P3HT/Ag	2.06	0.52	0.40	1.10	39 ^b	12.6	514	[150]	
FTO/TiO ₂ /P3HT/Ag	0.46	0.64	0.63	0.19	100			[152]	
FTO/TiO ₂ /PTBTB/P3HT/Ag	1.33	0.67	0.63	0.56	100			[152]	
ITO/TiO ₂ /MEH-PPV/Au	0.33	0.87	0.49	0.13	100			[210]	
Junctions of doped polymers and inorganic semiconductors									
GaAs/Au	10.0	0.42	0.67	2.8	100			[156,157]	
GaAs/P3MT/Au	8.4	0.70	0.64	3.5	100			[156,157]	
CdS/Au	1.0	0.25	0.40	0.2	50			[159]	
CdS/P3MT/Au	1.0	0.37	0.60	0.4	50			[159]	
ITO/CdS(Sb)/P3MT(PF ₆)/graphite	8.0	0.47	0.53	3.5	56			[164]	
ITO/CIS/PPV/Ag	6.5	0.50			100			[170,171]	
Cu/CIS/PEDOT:PSS/Au	20.4	0.51	0.40	4.14	100			[172]	
ITO/PEDOT:PSS(α -Si:H(i))/ μ c-Si(m)/Pd	4.55	0.88	0.51	2.1	100			[175]	
Nanoporous TiO ₂ filled with polymers									
ITO/TiO ₂ /MEH-PPV/Au	0.40	1.10	0.40	0.18	100			[131]	
ITO/TiO ₂ /P3OT/Au	0.17	0.70	0.40	0.08	60			[139]	
ITO/TiO ₂ /Ru-dye/P3OT/Au	0.33	0.64	0.44	0.16	60			[139]	
ITO/TiO ₂ /F8BT/Au	0.40	0.97	0.44	0.16	100	13	440	[186,187]	
ITO/TiO ₂ /MEH-PPV/PEDOT:PSS/Au	0.97	0.74	0.48	0.44	80			[188]	

(continued)

Table 8.1 (continued)

Cell configuration	J_{sc} (mA/ cm ²)	V_{oc} (V)	FF	η (%)	I_L (mW/ cm ²)	EQE (%) λ (nm)	Ref.
ITO/TiO ₂ /TPDs-M4-MEH-M3EH-PPV/PEDOT:PSS/Au	2.10	0.64	0.43	0.58	100	40 425	[190]
Nanostructured semiconductors filled with polymers							
FTO/TiO ₂ /P3HT/Ag	1.22	0.72	0.51	0.45	100	10 514	[194]
ITO/TiO ₂ /MEH-PPV/Au	3.30	0.86	0.28	0.71	100	34 -	[196,197]
Ti/CdTe(pillars)/P3HT/Au	3.12	0.714	0.48	1.06	100	20 830	[203]
Ti/CdS(pillars)/MEH-PPV/Au	1.397	0.858	0.50	0.60	100	17 540	[204]
ITO/ZnO(pillars)/P3HT/Ag	2.20	0.475	0.56	0.53	100	17 540	[207]
ITO/ZnO(pillars)/P3HT/PCBM/Ag	10.0	0.475	0.43	2.0	100	57 515	[207]
ITO/ZnO(pillars)/Ru-dye/P3HT/PEDOT:PSS/Au	1.73	0.30	0.39	0.20	100	14 550	[208,209]
ITO/ZnO(pillars)/Ru-dye/TPD(4M)-MEH-M3EH-PPV/ PEDOT:PSS/Au	~1.50	~0.30	~0.33	0.15	100		[209]
ITO/TiO ₂ (pillars)/MEH-PPV/Au	0.95	0.88	0.47	0.39	100	15 510	[210]
Metal oxide networks							
ITO/PEDOT:PSS/TiO ₂ :MDMO-PPV/LiF/Al	0.6	0.52	0.42	0.20	60	11 450	[211]
ITO/PEDOT:PSS/TiO ₂ :MDMO-PPV/LiF/Al	0.6	0.60	0.43	0.22	70	14 490	[212]
ITO/PEDOT:PSS/TiO ₂ :P3OT/LiF/Al	0.7	0.45	0.41	0.17	70	10 490	[212]
ITO/PEDOT:PSS/ZnO:MDMO-PPV/Al	2.0	1.14	0.42	1.10	90	27 520	[215]

^aMonochromatic light of 500 nm^bMonochromatic light of 514 nm

distribution of the optical field strength in the devices and causes an increased absorption of light. Krausch et al. have shown that the optical effect alone cannot explain the increased performance and concluded that the TiO_2 layer also acts as a charge-transfer interface. For ITO/PEDOT:PSS/P3HT:PCBM/ TiO_x /Al cells, the introduction of the TiO_x layer has resulted in a more than twofold improvement of the power conversion efficiency compared to a similarly prepared device without the TiO_x layer.

Likewise, White et al. developed inverted organic photovoltaic devices based on a blend of P3HT and PCBM by inserting a solution-processed ZnO interlayer between the ITO electrode and the active layer using Ag as a hole-collecting back contact [220]. Efficient electron extraction through the ZnO and hole extraction through the Ag, with minimal loss in open-circuit potential, was observed with a certified power conversion efficiency of 2.58%. The inverted architecture removes the need for the use of PEDOT:PSS as an ITO modifier and for the use of a low-work-function metal as the back contact in the device.

Hybrid materials have also contributed to the development of double and triple junction solar cells. Gilot et al. [221] have presented a first example of solution processed multiple junction solar cells incorporating polymer:fullerene bulk heterojunctions as active layers and a hybrid recombination layer. The hybrid recombination layer, deposited between the active layers, was fabricated by spin coating ZnO nanoparticles, followed by spin coating neutral pH PEDOT from water, and short UV illumination of the completed device. The key advantage of this procedure is that each step does not affect the integrity of the previously deposited layers. The open-circuit voltage (V_{oc}) for double and triple junction solar cells is close to the sum of the V_{oc} 's of individual cells. This simple procedure to create multi junction devices will enable increasing the overall efficiency when active materials with different optical band gaps are used.

In conclusion, hybrid polymer-inorganic photovoltaic cells are one of the various strategies that are currently explored for creating renewable sources of sustainable energy. While the progress in the basic understanding of their operating principles and in the actual performance of these devices has been very significant, it is evident that breakthroughs will be needed before we can start thinking of using these devices for large scale energy production. Yet, the importance of this subject for society and the interesting opportunities for fundamental research, make exploring this fascinating area worth all the effort.

Acknowledgement The authors thank Dr. Martijn Wien (Eindhoven University of Technology) for his invaluable contributions to the development of hybrid solar cells and numerous helpful discussions.

References

1. Chapin DM, Fuller CS, Pearson GL (1954) A new silicon p-n junction photocell for converting solar radiation into electrical power. *J Appl Phys* 25: 676.
2. Shockley W, Queisser HJ (1961) Detailed balance limit of efficiency of p-n junction solar cells. *J Appl Phys* 32: 510.

3. Zhao J, Wang A, Green MA, Ferrazza F (1998) 19.8% efficient “honeycomb” textured multi-crystalline and 24.4% monocrystalline silicon solar cells. *App Phys Lett* 73: 1991.
4. Shultz O, Glunz SW, Goldschmidt JC, Lautenschlager H, Leimenstoll A, Scheiderlochner E, Willeke GP (2004) 19th European Photovoltaic Solar Energy Conference, Paris, France.
5. Green MA, Emery K, King DL, Hishikawa Y, Warta W (2006) Solar cell efficiency tables (Version 28). *Prog Photovolt Res Appl* 14: 455.
6. Goetzberger A, Hebling C, Schock H-W (2003) Photovoltaic materials, history, status and outlook. *Mater Sci Eng R40*: 1.
7. Basic Research Needs for Solar Energy Utilization (2005) Report of the Basic Energy Sciences Workshop on Solar Energy Utilization, Washington.
8. Shirakawa H, Louis EJ, MacDiarmid AG, Chiang CK, Heeger AJ (1977) Synthesis of electrically conducting organic polymers: Halogen derivatives of polyacetylene, (CH)_x. *J Chem Soc, Chem Commun* 474: 578.
9. Chiang CK, Fincher CRJr, Park YW, Heeger AJ, Shirakawa H, Louis E (1977) Electrical conductivity in doped polyacetylene. *Phys Rev Lett* 39: 1098.
10. Bao Z, Dodabalapur A, Lovinger A (1996) Soluble and processable regioregular poly(3-hexylthiophene) for thin-film field-effect transistor applications with high mobility. *Appl Phys Lett* 69: 4108.
11. Sirringhaus H, Brown PJ, Friend RH, Nielsen MM, Bechgaard K, Langeveld-Voss BMW, Spiering AJH, Janssen RAJ, Meijer EW, Herwig PT, de Leeuw DM. (1999) Two-dimensional charge transport in self-organised, high-mobility conjugated polymers. *Nature* 401: 685.
12. Babel A, Jenekhe SA (2003) High electron mobility in ladder polymer field-effect transistors. *J Am Chem Soc* 125: 13656.
13. Schweitzer B, Bäessler H (2000) Excitons in conjugated polymers, *Synth Met* 109: 1.
14. Sariciftci NS (ed.) (1998) Primary Photoexcitations in Conjugated Polymers: Molecular Exciton Versus Semiconductor Band Model. World Scientific Publishers, Singapore.
15. Markov DE, Amsterdam E, Blom PWM, Sieval AB, Hummelen JC (2005) Accurate measurement of the exciton diffusion length in a conjugated polymer using a heterostructure with a side-chain cross-linked fullerene layer. *J Phys Chem A* 109: 5266.
16. Halls JJM, Pichler K, Friend RH, Moratti SC, Holmes AB (1996) Exciton diffusion and dissociation in a poly(p-phenylenevinylene)/C-60 heterojunction photovoltaic cell. *Appl Phys Lett* 68: 3120.
17. Savenije TJ, Warman JM, Goossens A (1998) Visible light sensitisation of titanium dioxide using a phenylene vinylene polymer. *Chem Phys Lett* 287: 148.
18. Kroeze JE, Savenije TJ, Vermeulen MJW, Warman JM (2003) Contactless determination of the photoconductivity action spectrum, exciton diffusion length, and charge separation efficiency in polythiophene-sensitized TiO₂ bilayers. *J Phys Chem B* 107: 7696.
19. Halls JJM, Walsh CA, Greenham NC, Marseglia EA, Friend RH, Moratti SC, Holmes AB (1995) Efficient photodiodes from interpenetrating polymer networks. *Nature* 395: 498.
20. Yu G, Gao J, Hummelen JC, Wudl F, Heeger AJ. (1995) Polymer photovoltaic cells – enhanced efficiencies via a network of internal donor-acceptor heterojunctions. *Science* 270: 1789.
21. Veenstra SC, Verhees WJH, Kroon JM, Koetse MM, Sweelssen J, Bastiaansen JJAM, Schoo HFM, Yang X, Alexeev A, Loos J, Schubert US, Wienk MM (2004) Photovoltaic Properties of a Conjugated Polymer Blend of MDMO—PPV and PCNEPV. *Chem Mater* 16: 2503.
22. Koetse MM, Sweelssen J, Hoekerd KT, Schoo HFM, Veenstra SC, Kroon JM, Yang X, Loos J (2006) Efficient polymer: polymer bulk heterojunction solar cells. *Appl Phys Lett* 88: 083504.
23. Shaheen SE, Brabec CJ, Sariciftci NS, Padinger F, Fromherz T, Hummelen JC (2001) 2.5% efficient organic plastic solar cells. *Appl Phys Lett* 78: 841.
24. Schilinsky P, Waldauf C, Brabec CJ (2002) Recombination and loss analysis in polythiophene based bulk heterojunction photodetectors. *Appl. Phys Lett* 81: 3885.
25. Wienk MM, Kroon JM, Verhees WJH, Knol J, Hummelen JC, van Hal PA, Janssen RAJ (2003) Efficient methano[70]fullerene/MDMO-PPV bulk heterojunction photovoltaic cells. *Angew Chem Int Ed* 42: 3371.

26. Ma W, Yang C, Gong X, Lee K, Heeger A (2005) Thermally stable, efficient polymer solar cells with nanoscale control of the interpenetrating network morphology. *J Adv Funct Mater* 15: 1617.
27. Brabec CJ (2004) Organic photovoltaics: Technology and market. *Sol Energ Mater Sol Cells* 83: 273.
28. Padinger F, Rittberger RS, Sariciftci NS (2003) Effects of postproduction treatment on plastic solar cells. *Adv Funct Mater* 13: 85.
29. Li G, Shrotriya V, Huang J, Yao Y, Moriarty T, Emery K, Yang Y (2005) High-efficiency solution processable polymer photovoltaic cells by self-organization of polymer blends. *Nat Mater* 4: 864.
30. O'Regan B, Grätzel M (1991) A low-cost, high-efficiency solar cell based on dye-sensitized colloidal TiO₂ films. *Nature* 353: 737.
31. Nazeeruddin MK, Kay A, Rodicio I, Humphrybaker R, Muller E, Liska P, Vlachopoulos N, Grätzel M (1993) Conversion of light to electricity by cis-X₂bis(2,2'-bipyridyl)-4,4'-dicarboxylate)ruthenium(II) charge-transfer sensitizers (X = Cl⁻, Br⁻, I⁻, CN⁻, and SCN⁻) on nanocrystalline titanium dioxide electrodes. *J Am Chem Soc* 115: 6382.
32. Grätzel M (2004) Conversion of sunlight to electric power by nanocrystalline dye-sensitized solar cells. *J Photochem Photobiol A* 164: 3.
33. Bach U, Lupo D, Comte P, Moser JE, Weissörtel F, Salbeck J, Spreitzer H, Grätzel M (1998) Solid-state dye-sensitized mesoporous TiO₂ solar cells with high photon-to-electron conversion efficiencies. *Nature* 395: 583.
34. Li B, Wang L, Kang B, Wang P, Qiu Y (2006) Review of recent progress in solid-state dye-sensitized solar cells. *Sol Energ Mater Sol Cells* 90: 549.
35. Grätzel M (2005) Dye-sensitized solid-state heterojunction solar cells. *MRS Bull* 30: 23
36. Wang P, Zakeeruddin SM, Moser JE, Nazeeruddin MK, Sekiguchi T, Grätzel M (2003) A stable quasi-solid-state dye-sensitized solar cell with an amphiphilic ruthenium sensitizer and polymer gel electrolyte. *Nat Mater* 2: 402.
37. Wang P, Zakeeruddin SM, Moser JE, Humphry-Baker R, Grätzel M (2004) A solvent-free, SeCN⁻/(SeCN)₃⁻ based ionic liquid electrolyte for high-efficiency dye-sensitized nanocrystalline solar cells. *J Am Chem Soc* 126: 7164.
38. Coakley KM, Liu Y, Goh C, McGehee MD (2005) Ordered organic-inorganic bulk heterojunction photovoltaic cells. *MRS Bull* 30: 37.
39. Milliron DJ, Gur I, Alivisatos AP (2005) Hybrid organic – nanocrystal solar cells. *MRS Bull* 30: 41.
40. Greenham NC, Peng X, Alivisatos AP (1996) Charge separation and transport in conjugated-polymer/semiconductor-nanocrystal composites studied by photoluminescence quenching and photoconductivity. *Phys Rev B* 54: 17628.
41. Greenham NC, Peng X, Alivisatos AP (1997) Charge separation and transport in conjugated polymer/cadmium selenide nanocrystal composites studied by photoluminescence quenching and photoconductivity. *Synth Met* 84: 545.
42. Ginger DS, Greenham NC (1999) Photoinduced electron transfer from conjugated polymers to CdSe nanocrystals. *Phys Rev B* 59: 10622.
43. Ginger DS, Greenham NC (1999) Charge separation in conjugated-polymer/nanocrystal blends. *Synth Met* 101: 425.
44. Pientka M, Dyakonov V, Meissner D, Rogach A, Talapin D, Weller H, Lutsen L, Vanderzande D (2004) Photoinduced charge transfer in composites of conjugated polymers and semiconductor nanocrystals. *Nanotechnology* 15: 163.
45. Huynh WU, Peng X, Alivisatos AP (1999) CdSe nanocrystal rods/poly(3-hexylthiophene) composite photovoltaic devices. *Adv Mater* 11: 923.
46. Huynh WU, Dittmer JJ, Alivisatos AP (2002) Hybrid nanorod-polymer solar cells. *Science* 295: 2425.
47. Huynh WU, Dittmer JJ, Libby WC, Whiting GL, Alivisatos AP (2003) Controlling the morphology of nanocrystal-polymer composites for solar cells. *Adv Funct Mater* 13: 73.
48. Huynh WU, Dittmer JJ, Teclamarium N, Milliron DJ, Alivisatos AP, Barnham KWJ (2003) Charge transport in hybrid nanorod-polymer composite photovoltaic cells. *Phys Rev Lett* 67: 115326.

49. Milliron DJ, Alivisatos AP, Pitois C, Edder C, Fréchet JMJ (2003) Electroactive surfactant designed to mediate electron transfer between CdSe nanocrystals and organic semiconductors. *Adv Mater* 15: 58.
50. Liu J, Tanaka T, Sivula K, Alivisatos AP, Fréchet JMJ (2004) Employing end-functional polythiophene to control the morphology of nanocrystal-polymer composites in hybrid solar cells. *J Am Chem Soc* 126: 6550.
51. Skaff H, Sill K, Emrick T (2004) Quantum dots tailored with poly(para-phenylene vinylene). *J Am Chem Soc* 126: 11322.
52. Sun BQ, Marx E, Greenham NC (2003) Photovoltaic devices using blends of branched CdSe nanoparticles and conjugated polymers. *Nano Lett* 3: 961.
53. Sun BQ, Snaith HJ, Dhoot AS, Westenhoff S, Greenham NC (2005) Vertically segregated hybrid blends for photovoltaic devices with improved efficiency. *J Appl Phys* 97: 014914.
54. Wang P, Abrusci A, Wong HMP, Svensson M, Andersson MR, Greenham NC (2006) Photoinduced charge transfer and efficient solar energy conversion in a blend of a Red polyfluorene copolymer with CdSe nanoparticles. *Nano Lett* 6: 1789.
55. Li Y, Zhong H, Li R, Zhou Y, Yang C, Li Y (2006) High-yield fabrication and electrochemical characterization of tetrapodal CdSe, CdTe, and CdSexTe1-x nanocrystals. *Adv Funct Mater* 16: 1705.
56. Zhou Y, Li YC, Zhong HZ, Hou JH, Ding YQ, Yang CH, Li YF (2006) Hybrid nanocrystal/polymer solar cells based on tetrapod-shaped CdSexTe1-x nanocrystals. *Nanotechnology* 17: 4041.
57. van Beek R, Zoombelt AP, Jenneskens LW, Van Walree CA, De Mello Donéga C, Veldman D, Janssen RAJ (2006) Side chain mediated electronic contact between a tetrahydro-4H-thiopyran-4-ylidene- appended polythiophenes and CdTe quantum dots. *Chem Eur J* 12: 8075.
58. Gur I, Fromer NA, Alivisatos AP (2006) Controlled assembly of hybrid-heterojunction solar cells by sequential deposition. *J Phys Chem B* 110: 25543.
59. Snaith HJ, Whiting GL, Sun B, Greenham NC, Huck WTS, Friend RH (2005) Self-organization of nanocrystals in polymer brushes. *Application in heterojunction photovoltaic diodes*. *Nano Lett* 5: 1653.
60. Kang I, Wise FW (1997) Electronic structure and optical properties of PbS and PbSe quantum dots. *J Opt Soc Am B* 14: 1632.
61. Wise FW (2000) Lead salt quantum dots: the limit of strong quantum confinement. *Acc Chem Res* 33: 773.
62. McDonald SA, Cyr PW, Levina L, Sargent EH (2004) Photoconductivity from PbS-nanocrystal/semiconducting polymer composites for solution-processible, quantum-size tunable infrared photodetectors. *Appl Phys Lett* 85: 2089.
63. McDonald SA, Konstantatos G, Zhang S, Cyr PW, Klem EJD, Levina L, Sargent EH (2005) Solution-processed PbS quantum dot infrared photodetectors and photovoltaics. *Nat Mater* 4: 138.
64. Chang TWF, Musikhin S, Bakueva L, Levina L, Hines MA, Cyr PW, Sargent EH (2004) Efficient excitation transfer from polymer to nanocrystals. *Appl Phys Lett* 84: 4295.
65. Bakueva L, Musikhin S, Hines MA, Chang TWF, Tzolov M, Scholes GD, Sargent EH (2003) Sizable infrared (1,000–1,600 nm) electroluminescence from PbS quantum-dot nanocrystals in a semiconducting polymer. *Appl Phys Lett* 82: 2895.
66. Zhang S, Cyr PW, McDonald SA, Konstantatos G, Sargent EH (2005) Enhanced infrared photovoltaic efficiency in PbS nanocrystal/semiconducting polymer composites: 600-fold increase in maximum power output via control of the ligand barrier. *Appl Phys Lett* 87: 233101.
67. Maria A, Klem EJD, Levina L, Sargent EH (2005) Solution-processed infrared photovoltaic devices with >10% monochromatic internal quantum efficiency. *Appl Phys Lett* 87: 213112.
68. Watt AAR, Blake D, Warner JH, Thomsen EA, Tavenner EL, Rubinsztein-Dunlop H, Meredith P (2005) Lead sulfide nanocrystal: conducting polymer solar cells. *J Phys D Appl Phys* 38: 2006.
69. Watt AAR, Thomsen E, Meredith P, Rubinsztein-Dunlop H (2004) A new approach to the synthesis of conjugated polymer: nanocrystal composites for heterojunction optoelectronics. *Chem Commun* 2334.

70. Watt AAR, Eichmann T, Rubinsztein-Dunlop H, Meredith P (2005) Carrier transport in PbS nanocrystal conducting polymer composites. *Appl Phys Lett* 87: 253109.
71. Warner JH, Watt AAR, Tilley RD (2005) Controlling PbS nanocrystal aggregation in conducting polymers. *Nanotechnology* 16: 2381.
72. Choudhury KR, Sahoo Y, Ohulchanskyy TY, Prasad PN (2005) Efficient photoconductive devices at infrared wavelengths using quantum dot-polymer nanocomposites. *Appl Phys Lett* 87: 073110.
73. Jiang X, Lee SB, Altfeder IB, Zakhidov AA, Schaller RD, Pietryga JM, Klimov VI (2005) Nanocomposite solar cells based on conjugated polymer/PbSe quantum dot. *Proc SPIE* 5938: 59381F-1.
74. Cui D, Xu J, Zhu T, Paradee G, Ashok S, Gerhold M (2006) Harvest of near infrared light in PbSe nanocrystal-polymer hybrid photovoltaic cells. *Appl Phys Lett* 88: 183111.
75. Landsberg PT, Nussbaumer H, Willeke GJ (1993) Band-band impact ionization and solar cell efficiency. *Appl Phys* 74: 1451.
76. Würfel P (1997) Solar energy conversion with hot electrons from impact ionisation. *Sol Eng Mater Sol Cells* 46: 43.
77. de Vos A, Desoete B (1998) On the ideal performance of solar cells with larger than unity quantum efficiency. *Sol Eng Mater Sol Cells* 51: 413.
78. Guyot-Sionnest P, Shim M, Matranga C, Hines M (1999) Intraband relaxation in CdSe quantum dots. *Phys Rev B* 60: R2181.
79. Nozik A (2002) Quantum dot solar cells. *J Physica E* 14: 115.
80. Schaller RD, Klimov VI (2004) High efficiency carrier multiplication in PbSe nanocrystals: implications for solar energy conversion. *Phys Rev Lett* 92: 186601.
81. Ellingson RJ, Beard MC, Johnson JC, Yu P, Micic OI, Nozik AJ, Shabaev A, Efros AL (2005) Highly efficient multiple exciton generation in colloidal PbSe and PbS quantum dots. *Nano Lett* 5: 865.
82. Murphy JE, Beard MC, Norman AG, Ahrenkiel SP, Johnson JC, Yu P, Micic OI, Ellingson RJ, Nozik AJ (2006) PbSe colloidal nanocrystals: synthesis, characterization, and multiple exciton generation. *J Am Chem Soc* 128: 3241.
83. Schaller RD, Sykora M, Jeong S, Klimov VI (2006) High-efficiency carrier multiplication and ultrafast charge separation in semiconductor nanocrystals studied via time-resolved photoluminescence. *J Phys Chem B* 110: 25332.
84. Schaller RD, Petruska MA, Klimov VI (2005) The effect of electronic structure on carrier multiplication efficiency: A comparative study of PbSe and CdSe nanocrystals. *Appl Phys Lett* 87: 253102.
85. Schaller RD, Sykora M, Pietryga JM, Klimov VI (2006) Seven excitons at a cost of one: Redefining the limits for conversion efficiency of photons into charge carriers. *Nano Lett* 6: 424.
86. Schaller RD, Klimov VI (2006) Non-poissonian exciton populations in semiconductor nanocrystals via carrier multiplication. *Phys Rev Lett* 96: 097402.
87. Schaller RD, Agranovich VM, Klimov VI (2005) High-efficiency carrier multiplication through direct photogeneration of multi-excitons via virtual single-exciton states. *Nat Phys* 1: 189.
88. Allan G, Delerue C (2006) Role of impact ionization in multiple exciton generation in PbSe nanocrystals. *Phys Rev B* 73: 205423.
89. Franceschetti A, An JM, Zunger A (2006) Impact ionization can explain carrier multiplication in PbSe quantum dots. *Nano Lett* 6: 2191.
90. Klimov VI (2006) Mechanisms for photogeneration and recombination of multiexcitons in semiconductor nanocrystals. *J Phys Chem B* 110: 16827.
91. Nozik AJ (2005) Exciton multiplication and relaxation dynamics in quantum dots: applications to ultrahigh-efficiency solar photon conversion. *Inorg Chem* 44: 6893
92. Hanna MC, Nozik AJ (2006) Solar conversion efficiency of photovoltaic and photoelectrolysis cells with carrier multiplication absorbers. *J Appl Phys* 100: 074510.
93. Klimov VI (2006) Detailed-balance power conversion limits of nanocrystal-quantum-dot solar cells in the presence of carrier multiplication. *Appl Phys Lett* 89: 123118.

94. Qi D, Fischbein M, Drndic M, Šelmic S (2005) Efficient polymer-nanocrystal quantum-dot photodetectors. *Appl Phys Lett* 86: 093103.
95. Arici E, Sariciftci NS, Meissner D (2002) Photovoltaic properties of nanocrystalline CuInS₂/methanofullerene solar cells. *Mol Cryst Liq Cryst* 385: 129.
96. Arici E, Sariciftci NS, Meissner D (2003) Hybrid solar cells based on nanoparticles of CuInS₂ in organic matrices. *Adv Funct Mater* 13: 165.
97. Arici E, Hoppe H, Schäffler F, Meissner D, Malik MA, Sariciftci NS (2004) Morphology effects in nanocrystalline CuInSe₂-conjugated polymer hybrid systems. *Appl Phys A* 79: 59.
98. Arici E, Hoppe H, Schäffler F, Meissner D, Malik MA, Sariciftci NS (2004) Hybrid solar cells based on inorganic nanocluster and conjugated polymers. *Thin Solid Films* 451–452: 612.
99. Günes S, Neugebauer H, Sariciftci NS, Roither J, Kovalenko M, Pillwein G, Heiss W (2006) Hybrid solar cells using HgTe nanocrystals and nanoporous TiO₂ electrodes. *Adv Funct Mater* 16: 1095.
100. Selmarten D, Jones M, Rumbles G, Yu P, Nedeljkovic J, Shaheen S (2005) Quenching of semiconductor quantum dot photoluminescence by a pi-conjugated polymer. *J Phys Chem B* 109: 15927.
101. Salafsky JS, Lubberhuizen WH, Schropp REI (1998) Photoinduced charge separation and recombination in a conjugated polymer-semiconductor nanocrystal composite. *Chem Phys Lett* 290: 297.
102. Salafsky JS (1999) Exciton dissociation, charge transport, and recombination in ultrathin, conjugated polymer-TiO₂ nanocrystal intermixed composites. *Phys Rev B* 59: 10885.
103. Zhang J, Wang B, Ju X, Liu T, Hu T (2001) New observations on the optical properties of PPV/TiO₂ nanocomposites. *Polymer* 42: 3697.
104. Arango AC, Carter SA, Brock PJ (1999) Charge transfer in photovoltaics consisting of interpenetrating networks of conjugated polymer and TiO₂ nanoparticles. *Appl Phys Lett* 74: 1698.
105. Carter SA, Scott JC, Brock PJ (1997) Enhanced luminance in polymer composite light emitting diodes. *Appl Phys Lett* 71: 1145.
106. Kwong CY, Djurišić AB, Chui PC, Cheng KW, Chan WK (2004) Influence of solvent on film morphology and device performance of poly (3-hexylthiophene): TiO₂ nanocomposite solar cells. *Chem Phys Lett* 384: 372.
107. Kwong CY, Choy WCH, Djurišić AB, Chui PC, Cheng KW, Chan WK (2004) Poly (3-hexylthiophene):TiO₂ nanocomposites for solar cell applications. *Nanotechnology* 15: 1156.
108. Petrella A, Tamborra M, Cozzoli PD, Curri ML, Striccoli M, Cosma P, Farinola GM, Babudri F, Naso N, Agostiano A (2004) TiO₂ nanocrystals – MEH-PPV composite thin films as photoactive material. *Thin Solid Films* 451–452: 64.
109. Petrella A, Tamborra M, Curri ML, Cosma P, Striccoli M, Cozzoli PD, Agostiano A (2005) Colloidal TiO₂ nanocrystals/MEH-PPV nanocomposites: Photo(electro)chemical study. *J Phys Chem B* 109: 1554.
110. Huisman CL, Goossens A, Schoonman J (2003) Preparation of a nanostructured composite of titanium dioxide and polythiophene: A new route towards 3D heterojunction solar cells. *Synth Met* 138: 237.
111. Huisman CL, Goossens A, Schoonman J (2003) Aerosol synthesis of anatase titanium dioxide nanoparticles for hybrid solar cells. *Chem Mater* 15: 4617.
112. Beek WJE, Wienk MM, Janssen RA (2004) Efficient hybrid solar cells from ZnO nanoparticles and a conjugated polymer. *J Adv Mater* 16: 1009.
113. Meulenkamp EA (1998) Synthesis and growth of ZnO nanoparticles. *J Phys Chem B* 102: 5566.
114. Hagfeldt A, Grätzel M (1995) Light-induced redox reactions in nanocrystalline systems. *Chem Rev* 95: 49.
115. Hutson AR (1957) Hall effect studies of doped zinc oxide. *Phys Rev* 108: 222.
116. Hunger R, Iwata K, Fons P, Yamada A, Matsubara K, Niki S, Nakahara K Takasu H (2001) Control of optical and electrical properties of ZnO films for photovoltaic applications. *Mat Res Soc Symp Proc* 668: H2.8.1.

117. Beek WJE, Wienk MM, Kemerink M, Yang X, Janssen RAJ (2005) Hybrid zinc oxide conjugated polymer bulk heterojunction solar cells. *J Phys Chem B* 109: 9505.
118. Wei X, Vardeny ZV, Sariciftci NS, Heeger A (1996) Absorption-detected magnetic-resonance studies of photoexcitations in conjugated-polymer/C60 composites. *J Phys Rev B* 53: 2187.
119. Shim M, Guyot-Sionnest P (2001) Organic-Capped ZnO Nanocrystals: synthesis and n-type character. *J Am Chem Soc* 123: 11651.
120. Bauer C, Boschloo G, Mukhtar E, Hagfeldt A (2001) Electron injection and recombination in Ru(dcbpy)₂(NCS)₂ sensitized nanostructured ZnO. *J Phys Chem B* 105: 5585.
121. Beek WJE, Wienk MM, Janssen RAJ (2006) Hybrid solar cells from regioregular polythiophene and ZnO nanoparticles. *J Adv Funct Mater* 16: 1112.
122. Van Hal PA, Christiaans MPT, Wienk MM, Kroon JM, Janssen RAJ (1999) Photoinduced electron-transfer from conjugated polymers to TiO₂. *J Phys Chem B* 103: 4352.
123. Shim M, Guyot-Sionnest P (2001) Organic-capped ZnO nanocrystals: Synthesis and n-type character. *J Am Chem Soc* 123: 11651.
124. Quist PAC, Beek WJE, Wienk MM, Janssen RAJ, Savenije T, Siebbeles LDA (2006) Photogeneration and decay of charge carriers in hybrid bulk heterojunctions of ZnO nanoparticles and conjugated polymers. *J Phys Chem B* 110: 10315.
125. Padinger F, Rittberger RS, Sariciftci NS (2003) Effects of postproduction treatment on plastic solar cells. *Adv Funct Mater* 13: 85.
126. Yang X, Veenstra SC, Verhees WJH, Wienk MM, Janssen RAJ, Kroon JM, Michels MAJ, Loos J (2005) Nanoscale morphology of high-performance polymer solar cells. *Nano Lett* 5: 579.
127. Mihailetchi VD, Xie H, De Boer B, Popescu LM, Hummelen JC, Blom PWM, Koster LJA (2006) Origin of the enhanced performance in poly(3-ethylthiophene):methanofullerene solar cells using slow drying. *Appl Phys Lett* 89: 012107.
128. Van Duren JKJ, Yang XN, Loos J, Bulle-Lieuwma CWT, Sieval AB, Hummelen JC, Janssen RAJ (2004) Relating the morphology of poly(p-phenylene vinylene)/methanofullerene blends to solar-cell performance. *J Adv Funct Mater* 14: 425.
129. Savenije TJ, Vermeulen MJW, de Haas MP, Warman JM (2000) Contactless determination of the efficiency of interfacial charge separation in a TiO₂/phenylene vinylene polymer junction. *Sol Energ Mater Sol Cells* 61: 9.
130. Arango AC, Johnson LR, Bliznyuk VN, Schlesinger Z, Carter SA, Hörhold HH (2000) Efficient titanium oxide/conjugated polymer photovoltaics for solar energy conversion. *Adv Mater* 12: 1689.
131. Breeze AJ, Schlesinger Z, Carter SA, Brock P (2001) Charge transport in TiO₂/MEH-PPV polymer photovoltaics. *Phys Rev B* 64: 125205/1.
132. Breeze AJ, Schlesinger Z, Carter SA, Tillmann H, Hörhold H.-H (2004) Improving power efficiencies in polymer—polymer blend photovoltaics. *Sol Energ Mater Sol Cells* 83: 263.
133. Fan Q, McQuillin B, Bradley DDC, Whitelegg S, Seddon AB (2001) A solid state solar cell using sol-gel processed material and a polymer. *Chem Phys Lett* 347: 325.
134. Lira-Cantu M, Krebs F (2006) Hybrid solar cells based on MEH-PPV and thin film semiconductor oxides: TiO₂, Nb₂O₅, ZnO, CeO₂ and CeO₂-TiO₂ performance improvement during long-time illumination. *Sol Energ Mater Sol Cells* 90: 2076.
135. Slooff LH, Kroon JM, Loos J, Koetse MM, Sweelssen J (2005) Influence of the relative humidity on the performance of polymer/TiO₂ photovoltaic cells. *Adv Funct Mater* 15: 689.
136. Van der Zanden B, Goossens A, Schoonman J (2001) Photodoping of PPV/TiO₂ solar cells. *Synth Met* 121: 1601.
137. Van der Zanden B, Goossens A (2003) Oxygen doping of TiO₂/poly(phenylene-vinylene) bilayer solar cells. *J Appl Phys* 94: 6959.
138. Meskers SCJ, Janssen RAJ, Haverkort JEM, Wolter JH (2000) Relaxation of photo-excitations in films of oligo- and poly(paraphenylene-vinylene) derivatives. *Chem Phys* 260: 415.
139. Gebeyehu D, Brabec CJ, Padinger F, Fromherz T, Spiekermann S, Vlachopoulos N, Kienberger F, Schindler H, Sariciftci NS (2001) Solid state dye-sensitized TiO₂ solar cells with poly(3-octylthiophene) as hole transport layer. *Synth Met* 121: 1549.

140. Song MY, Kim JK, Kim KJ, Kim DY (2003) Temperature effect on photocurrent generation of TiO₂/conjugated polymer photovoltaic devices. *Synth Met* 137: 1389.
141. Roberson LB, Poggi MA, Kowalik J, Smestad GP, Bottomley LA, Tolbert LM (2004) Correlation of morphology and device performance in inorganic-organic TiO₂-polythiophene hybrid solid-state solar cells. *Coord Chem Rev* 248: 1491.
142. Grant CD, Schwartzberg AM, Smestad GP, Kowalik J, Tolbert LM, Zhang JZ (2003) Optical and electrochemical characterization of poly(3-undecyl-2,2'-bithiophene) in thin film solid state TiO₂ photovoltaic solar cells. *Synth Met* 132: 197.
143. Grant CD, Schwartzberg AM, Smestad GP, Kowalik J, Tolbert LM, Zhang JZ (2002) Characterization of nanocrystalline and thin film TiO₂ solar cells with poly(3-undecyl-2,2'-bithiophene) as a sensitizer and hole conductor. *J Electroanal Chem* 522: 40.
144. Van der Zanden B, van de Krol R, Schoonman J, Goossens A (2004) Enhanced photoluminescence at poly(3-octylthiophene)/TiO₂ interfaces. *Appl Phys Lett* 84: 2539.
145. Dyreklev P, Inganäs O, Paloheimo J, Stubb H (1992) Photoluminescence quenching in a polymer thin-film field-effect luministor. *J Appl Phys* 71: 2816.
146. List EJW, Kim C-H, Naik AK, Scherf U, Leising G, Graupner W, Shinar J (2001) Interaction of singlet excitons with polarons in wide band-gap organic semiconductors: a quantitative study. *Phys Rev B* 64: 155204.
147. Scheblykin I, Zorinians G, Hofkens J, De Feyter S, Van der Auweraer M, De Schryver FC (2003) Photoluminescence intensity fluctuations and electric-field-induced photoluminescence quenching in individual nanoclusters of poly(phenylenevinylene). *Chem Phys Chem* 4: 260.
148. Yu J, Song NW, McNeill JD, Barbara PF (2004) Efficient exciton quenching by hole polarons in the conjugated polymer MEH-PPV. *Isr J Chem* 44: 127.
149. Kroeze JE, Savenije TJ, Vermeulen MJW, Warman JM (2003) Contactless determination of the photoconductivity action spectrum, exciton diffusion length, and charge separation efficiency in polythiophene-sensitized TiO₂ bilayers. *J Phys Chem B* 107: 7696.
150. Liu J, Kadnikova EN, Liu Y, McGehee MD, Fréchet JMJ (2004) Polythiophene containing thermally removable solubilizing groups enhances the interface and the performance of polymer-titania hybrid solar cells. *J Am Chem Soc* 126: 9486.
151. Liu Y, Scully SR, McGehee MD, Liu J, Luscombe CK, Fréchet JMJ, Shaheen SE, Ginley DS (2006) Dependence of band offset and open-circuit voltage on the interfacial interaction between TiO₂ and carboxylated polythiophenes. *J Phys Chem B* 110: 3257.
152. Liu Y, Summers MA, Edler C, Fréchet JMJ, McGehee MD (2005) Using resonance energy transfer to improve exciton harvesting in organic-inorganic hybrid photovoltaic cells. *Adv Mater* 17: 2960.
153. Liu Y, Summers MA, Scully SR, McGehee MD (2006) Resonance energy transfer from organic chromophores to fullerene molecules. *J Appl Phys* 99: 093521.
154. Scully SR, McGehee MD (2006) Effects of optical interference and energy transfer on exciton diffusion length measurements in organic semiconductors. *J Appl Phys* 100: 034907.
155. Kroeze JE, Savenije TJ (2004) The application of a low-bandgap conjugated oligomer for the sensitization of SnO₂ and TiO₂. *Thin Solid Films* 451–452: 54.
156. Horowitz G, Garnier F (1986) Polythiophene-GaAs p-n heterojunction solar cells. *Sol Energ Mater* 13: 47.
157. Horowitz G, Garnier F (1987) Organic semiconducting polymers as molecular material for electronic devices. *Synth Met* 18: 693.
158. Garnier F (2002) Hybrid organic-on-inorganic photovoltaic devices. *J Opt A Pure Appl Opt* 4: S247.
159. Frank AJ, Glenis S, Nelson AJ (1989) Conductive polymer-semiconductor junction: characterization of poly(3-methylthiophene): Cadmium sulfide based photoelectrochemical and photovoltaic cells. *J Phys Chem* 93: 3818.
160. Nguyen-Cong H, Sene C, Chartier P (1993) Cadmium sulfide thickness effect on the photoresponse of the CdS(A1) spray/poly(3-methylthiophene) solid state junction. *Sol Energ Mater Sol Cells* 29: 209.

161. Nguyen-Cong H, Sene C, Chartier P (1993) Photovoltaic cell based on cadmium sulfide sprayed film and electrolytic poly(3-methylthiophene): Solvent nature effect. *Sol Energ Mater Sol Cells* 30: 127.
162. Nguyen-Cong H, Sene C, Chartier P (1996) Poly(3-methylthiophene) structural change effect on characteristics of CdS(A1):PMeT photovoltaic junction. *Sol Energ Mater Sol Cells* 40: 261.
163. Sene C, Nguyen-Cong H, Chartier P (1997) Effect of the structural and electronic changes induced in poly(3-methylthiophene), PMeT, by the monomer concentration on the characteristics of sprayed CdS(A1)-PMeT based photovoltaic junctions. *J Mater Sci* 8: 85.
164. Nguyen-Cong H, Dieng M, Sene C, Chartier P (2000) Hybrid organic-inorganic solar cells: case of the all thin film PMeT(Y)/CdS(X) junctions. *Sol Energ Mater Sol Cells* 63: 23.
165. Chartier P, Nguyen-Cong H, Sene C (1998) Hybrid organic-inorganic photovoltaic junctions: case of the all thin-film CdSe/poly(3-methylthiophene) junction. *Sol Energ Mater Sol Cells* 52: 413.
166. Sene C, Nguyen-Cong H, Dieng M, Chartier P (2000) Hybrid photovoltaic structures based on polymer/chemically grown cadmium selenide films: Effect of silicotungstic acid on the junction properties. *Mater Res Bull* 35: 1541.
167. Gamboa SA, Nguyen-Cong H, Chartier P, Sebastian PJ, Calixto ME, Rivera MA (1998) Photovoltaic structures based on polymer/semiconductor junctions. *Sol Energ Mater Sol Cells* 55: 104.
168. Gamboa SA, Sebastian PJ, Mathew X, Nguyen-Cong H, Chartier P (1999) A CdTe/PMeT photovoltaic structure formed by electrodeposition and processing. *Sol Energ Mater Sol Cells* 59: 115.
169. Sebastian PJ, Gamboa SA, Calixto ME, Nguyen-Cong H, Chartier P, Perez R (1998) Poly-3-methylthiophene/ CuInSe2 solar cell formed by electrodeposition and processing. *Semicond Sci Technol* 13: 1459.
170. Bereznev S, Kois J, Mellikov E, Öpik A, Meissner D (2001) CuInSe2/polypyrrole photovoltaic structure prepared by electro-deposition. 17th European Photovoltaic Solar Energy Conference, Munich, Germany.
171. Bereznev S, Konovalov I, Kois J, Mellikov E, Öpik A (2003) CuInS2/PEDOT photovoltaic structure. *MRS Symp Proc* 771: 243.
172. Bereznev S, Konovalov I, Öpik A, Kois J (2005) Hybrid CuInS2/polypyrrole and CuInS2/poly(3,4-ethylenedioxythiophene) photovoltaic structures. *Synth Met* 152: 81.
173. Camaioni N, Beggiato G, Casalbone-Miceli G, Gallazzi MC, Geri A, Martelli A (1997) Photovoltaic effect of heterojunctions between poly(4,4 ϵ -dipentoxy-2,2 ϵ -bithiophene) and n-doped silicon. *Synth Met* 85: 1369.
174. Wang Q, Shaheen SE, Williams EL, Jabbour GE (2003) Hybrid organic-inorganic photoconductive diode. *Appl Phys Lett* 83: 3404.
175. Williams EL, Jabbour GE, Wang Q, Shaheen SE, Ginley DS (2005) Conducting polymer and hydrogenated amorphous silicon hybrid solar cells. *Appl Phys Lett* 87: 223504.
176. Luzzati S, Basso M, Catellani M, Brabec CJ, Gebeyehu D, Sariciftci NS (2002) Photo-induced electron transfer from a dithieno thiophene-based polymer to TiO2. *Thin Solid Films* 403-404: 52.
177. Anderson NA, Hao E, Ai X, Hastings G, Lian T (2001) Ultrafast and long-lived photoinduced charge separation in MEH-PPV/nanoporous semiconductor thin film composites. *Chem Phys Lett* 347: 304.
178. Gebeyehu D, Brabec CJ, Sariciftci NS, Vangeneugden D, Kiebooms R, Vanderzande D, Kienberger F, Schindler H (2001) Solid state dye-sensitized TiO2 solar cells with poly(3-octylthiophene) as hole transport layer. *Synth Met* 121: 1549.
179. Spiekermann S, Smestad G, Kowalik J, Tolbert LM, Grätzel M (2001) Poly(4-undecyl-2,2'-bithiophene) as a hole conductor in solid state dye sensitized titanium dioxide solar cells. *Synth Met* 121: 1603.
180. Smestad GP, Spiekermann S, Kowalik J, Grant CD, Schwartzberg AM, Zhang J, Tolbert LM, Moons E (2003) A technique to compare polythiophene solid-state dye sensitized TiO2 solar cells to liquid junction devices. *Sol Energ Mater Sol Cells* 76: 85.

181. Bach U (2002) Solid state dye-sensitized solar cells - an alternative route towards low-cost photovoltaic devices, in S. Licht (ed.) *Encyclopedia of Electrochemistry*, Vol 6, Wiley, Weinheim, p. 475.
182. Nogueira AF, Longo C, De Paoli MA (2004) Polymers in dye sensitized solar cells: overview and perspectives. *Coord Chem Rev* 248: 1455.
183. Van Hal PA, Wienk MM, Kroon JM, Janssen RAJ (2003) TiO₂ sensitized with an oligo(p-phenylene vinylene) carboxylic acid: a new model compound for a hybrid solar cell. *J Mater Chem* 13: 1054.
184. Senadeera GKR, Nakamura K, Kitamura T, Wada Y, Yanagida S (2003) Fabrication of highly efficient polythiophene-sensitized metal oxide photovoltaic cells. *Appl Phys Lett* 83: 5470.
185. Kim YG, Walker J, Samuelson LA, Kumar J (2003) Efficient light harvesting polymers for nanocrystalline TiO₂ photovoltaic cells. *Nano Lett* 3: 523.
186. Ravirajan P, Haque SA, Poplavskyy D, Durrant JR, Bradley DDC, Nelson J (2004) Nanoporous TiO₂ solar cells sensitised with a fluorene–thiophene copolymer. *Thin Solid Films* 451–452: 624.
187. Ravirajan P, Haque SA, Durrant JR, Poplavskyy D, Bradley DDC, Nelson J (2004) Hybrid nanocrystalline TiO₂ solar cells with a fluorene–thiophene copolymer as a sensitizer and hole conductor. *J Appl Phys* 95: 1473.
188. Song MY, Kim JK, Kim KJ, Kim DY (2003) Photovoltaic characteristics of TiO₂/conjugated polymer junctions. *Synth Met* 137: 1387.
189. Ravirajan P, Haque SA, Durrant JR, Bradley DDC, Nelson J (2005) The effect of polymer optoelectronic properties on the performance of multilayer hybrid polymer/TiO₂ solar cells. *Adv Funct Mater* 15: 609.
190. Ravirajan P, Bradley DDC, Nelson J, Haque SA, Durrant JR, Smit HJP, Kroon JM (2005) Efficient charge collection in hybrid polymer/TiO₂ solar cells using poly(ethylenedioxythiophene)/polystyrene sulphonate as hole collector. *Appl Phys Lett* 86: 143101.
191. Bartholomew GO, Heeger AJ (2005) Infiltration of regioregular poly[2,2 ϵ -(3-hexylthiophene)] into random nanocrystalline TiO₂ networks. *Adv Funct Mater* 15: 677.
192. Huisman CL, Huijser H, Donker H, Schoonman J, Goossens A (2004) UV polymerization of oligothiophenes and their application in nanostructured heterojunction solar cells. *Macromolecules* 37: 5557.
193. Kajihara K, Tanaka K, Hirao K, Soga N (1997) Photovoltaic effect in titanium dioxide/polythiophene cell. *Jpn J Appl Phys* 36: 5537.
194. Coakley KM, McGehee MD (2003) Photovoltaic cells made from conjugated polymers infiltrated into mesoporous titania. *Appl Phys Lett* 83: 3380.
195. Coakley KM, Liu Y, McGehee MD, Frindell KL, Stucky GD (2003) Infiltrating semiconducting polymers into self-assembled mesoporous titania films for photovoltaic applications. *Adv Funct Mater* 13: 301.
196. Wang H, Oey CC, Djurišić AB, Xie MH, Leung YH, Man KKY, Chan WK, Pandey A, Nunzi JM, Chui PC (2005) Titania bicontinuous network structures for solar cell applications. *Appl Phys Lett* 87: 023507.
197. Oey CC, Djurišić AB, Wang H, Man KKY, Chan WK, Xie MH, Leung YH, Pandey A, Nunzi JM, Chui PC (2006) Polymer–TiO₂ solar cells: TiO₂ interconnected network for improved cell performance. *Nanotechnology* 17: 706.
198. Goh C, Coakley KM, McGehee MD (2005) Nanostructuring titania by embossing with polymer molds made from anodic alumina templates. *Nano Lett* 5: 1545.
199. Coakley KM, Srinivasan BS, Ziebarth JM, Goh C, Liu Y, McGehee MD (2005) Enhanced hole mobility in regioregular polythiophene infiltrated in straight nanopores. *Adv Funct Mater* 15: 1927.
200. Koganti VR, Dunphy D, Gowrishankar V, McGehee MD, Li X, Wang J, Rankin SE (2006) Generalized coating route to silica and titania films with orthogonally tilted cylindrical nanopore arrays. *Nano Lett* 6: 2567.

201. Salafsky JS (2001) A 'channel' design using single, semiconductor nanocrystals for efficient (opto)electronic devices. *Solid-State Electron* 45: 53.
202. Kannan B, Castelino K, Majumdar A (2003) Design of nanostructured heterojunction polymer photovoltaic devices. *Nano Lett* 3: 1729.
203. Kang Y, Park N-G, Kim D (2005) Hybrid solar cells with vertically aligned CdTe nanorods and a conjugated polymer. *Appl Phys Lett* 86: 113101.
204. Kang Y, Kim D (2006) Well-aligned CdS nanorod conjugated polymer solar cells. *Sol Energ Mater Sol Cells* 90: 166.
205. Wang ZL (2004) Nanostructures of zinc oxide. *Mater Today* 7: 26.
206. Greene LE, Law M, Tan DH, Montano M, Goldberger J, Somorjai G, Yang P (2005) General route to vertical ZnO nanowire arrays using textured ZnO seeds. *Nano Lett* 5: 1231.
207. Olson DC, Piris J, Collins RT, Shaheen SE, Ginley DS (2006) Hybrid photovoltaic devices of polymer and ZnO nanofiber composites. *Thin Solid Films* 496: 26.
208. Ravirajan P, Peiró AM, Nazeeruddin MK, Graetzel M, Bradley DDC, Durrant JR, Nelson J (2006) Hybrid polymer/zinc oxide photovoltaic devices with vertically oriented ZnO nanorods and an amphiphilic molecular interface layer. *J Phys Chem B* 110: 7635.
209. Peiró AM, Ravirajan P, Govender K, Boyle DS, O'Brien P, Bradley DDC, Nelson J, Durrant JR (2006) Hybrid polymer/metal oxide solar cells based on ZnO columnar structures. *J Mater Chem* 16: 2088.
210. Wei Q, Hirota K, Tajima K, Hashimoto K (2006) Design and synthesis of TiO₂ nanorod assemblies and their application for photovoltaic devices. *Chem Mater* 18: 5080.
211. Van Hal PA, Wienk MM, Kroon JM, Verhees WJH, Slooff LH, Van Gennip WJH, Jonkheijm P, Janssen RAJ (2003) Photoinduced electron transfer and Photovoltaic response of a MDMO-PPV:TiO₂ bulk-heterojunction. *Adv Mater* 15: 118.
212. Slooff LH, Wienk MM, Kroon JM (2004) Hybrid TiO₂: polymer photovoltaic cells made from a titanium oxide precursor. *Thin Solid Films* 451(452): 634.
213. Wang L, Ji JS, Lin YJ, Rwei SP (2005) Novel poly (3-nonylthiophene)-TiO₂ hybrid materials for photovoltaic cells. *Synth Met* 155: 677.
214. Okuya M, Nakade K, Kaneko S (2002) Porous TiO₂ thin films synthesized by a spray pyrolysis deposition (SPD) technique and their application to dye-sensitized solar cells. *Sol Energ Mater Sol Cell* 70: 425.
215. Beek WJE, Slooff LH, Wienk MM, Kroon JM, Janssen RA (2005) Hybrid solar cells using a zinc oxide precursor and a conjugated polymer. *J Adv Funct Mater* 15: 1703.
216. Albertsson J, Abrahams SC, Kvik A (1983) Atomic displacement, anharmonic thermal vibration, expansivity and pyroelectric coefficient thermal dependences in ZnO. *Acta Cryst B* 45: 34.
217. Quist PAC, Slooff LH, Donker H, Kroon JM, Savenije TJ, Siebbeles LDA (2005) Formation and Decay of Charge Carriers in Hybrid MDMO-PPV: ZnO bulk heterojunctions produced from a ZnO precursor. *Superlatt Microstruct* 38: 308.
218. Hänsel H, Zettl H, Krausch G, Kisselev R, Thelakkat M, Schmidt H-W (2003) Optical and electronic contributions in double-heterojunction organic thin-film solar cells. *Adv Mater* 15: 2056.
219. Kim JY, Kim SH, Lee HH, Lee K, Ma W, Gong X, Heeger AJ (2006) New architecture for high-efficiency polymer photovoltaic cells using solution-based titanium oxide as an optical spacer. *Adv Mater* 18: 572.
220. White MS, Olson DC, Shaheen SE, Kopidakis N, Ginley DS (2006) Inverted bulk-heterojunction organic photovoltaic device using a solution-derived ZnO underlayer. *Appl Phys Lett* 89: 143517.
221. Gilot J, Wienk MM, Janssen RA (2007) Double and triple junction polymer solar cells processed from solution. *J Appl Phys Lett* 90: 143512.

Chapter 9

Fullerene Nanocomposite Resists for Nanolithography

Tetsuyoshi Ishii and Kiyotaka Shigehara

Abstract Fullerene nanocomposite resists that incorporate sub-nanometer fullerene molecules into a resist material have been developed for nanolithography. Fullerene has both physically and chemically resistant qualities and its incorporation reinforces the original resist material. A system composed of fullerene (C_{60} and/or C_{70}) and a positive-type electron-beam resist (ZEP520) exhibits about a 10–40% enhancement of dry-etch resistance, which enables us to improve resolution by resist thinning. In addition the system also enhances pattern contrast, mechanical strength, and thermal resistance. The readily changeable sensitivity of the system provided by the dissolution-inhibiting effect of fullerene can be used to construct a fullerene-incorporated bilayer resist system for lift-off. Because chemically modified fullerene derivatives have better solubility in the casting solvent and better miscibility with ZEP520, it is possible to prepare nanocomposite resist systems by incorporating a large amount of fullerene derivatives (at least up to 50 wt%). The derivative systems exhibit a moderate resistance enhancement (about 10–25%) with a minimal decrease in sensitivity and without losing the potential resolution. Furthermore, a chemically amplified nanocomposite resist system comprising a fullerene derivative and a chemical amplification resist can be a candidate for future extreme ultraviolet resists as well as for electron-beam resists.

T. Ishii (✉)

NTT Photonics Laboratories, 3-1 Morinosato Wakamiya, Atsugi, Kanagawa 243-0198, Japan
e-mail: tishii@aecl.ntt.co.jp

K. Shigehara

Department of Applied Chemistry, Faculty of Technology, Tokyo University of Agriculture and Technology, 2-24-16 Naka-cho, Koganei, Tokyo 184-8533, Japan

9.1 Introduction

Microchips are widely used in a variety of products, ranging from cell phones to personal computers to automobiles. Over the past several decades, microchip circuits have been continually integrated to ever-higher scales to improve their performance, and it appears that this trend will continue endlessly. Circuit patterns with minimum linewidths of 50 nm and below are increasingly in demand for the fabrication of next-generation ultra-large-scale integrated circuits (ULSIs). In addition to ULSI fabrication, nanometer patterns with dimensions smaller than 10 nm are needed for the research and development of revolutionary new devices. Pattern fabrication technology, which is generally known as lithography, is a key technology in device fabrication. Lithography has the same roots as photography. It was invented to fix an image permanently on a flat surface by using a light-induced chemical change [1, 2].

The lithographic process is illustrated in Fig. 9.1. First, a photosensitive resin called a resist is spin-coated on a substrate. Second, the resist film is exposed to ultraviolet light through a mask having circuit patterns. Third, the unnecessary part of the resist dissolves during development to form resist patterns on the substrate. There are two types of resist patterns: positive ones, in which the exposed area of the resist is removed during development, and negative ones, in which the exposed area remains after development; that is, the unexposed area is removed during development. Then using the resist patterns as a protective film, the substrate is etched with a reactive solution or gas and the original mask patterns are transferred to the substrate. The resist sets its name from its “resistance” against etching. Finally, the residual

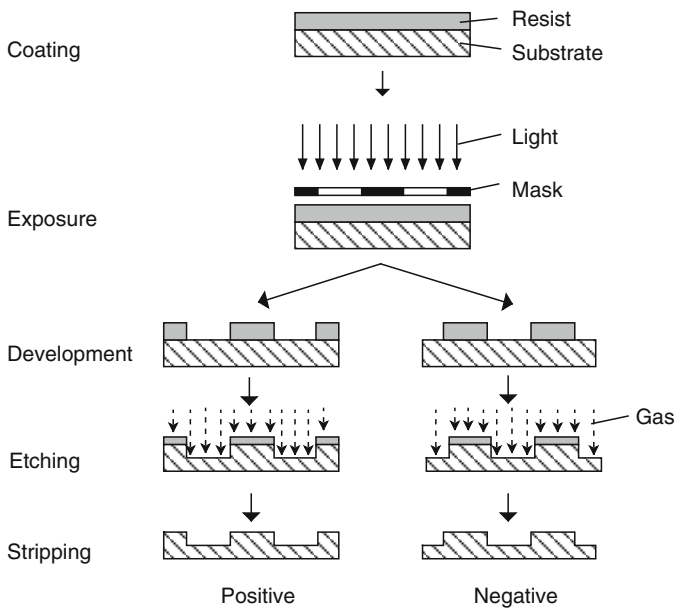


Fig. 9.1 Lithographic process for device fabrication

resist film is stripped off the substrate. In Fig. 9.1, 1:1 proximity exposure process is shown for simplification. In actual LSI production, however, 4 :1 or 5:1 reduction projection exposure systems (called steppers) are used for circuit pattern fabrication. Steppers substantially improve resolution by means of a reduction lens system between a mask and a substrate. According to the 2005 International Technology Roadmap for Semiconductors [3], ULSIs with minimum linewidths of 90 and 65 nm are currently fabricated on a commercial basis and 45-nm ULSIs are being developed using argon fluoride (ArF) excimer laser steppers (Fig. 9.2).

Electron or laser-beam exposure systems can also be used for pattern fabrication, but they are limited to small-scale production, mask writing, or device research due to their low throughput.

As described above, lithography plays an important role in device fabrication. To ensure that its role continues in the years to come, further improvement is required in resist performance, particularly the enhancement of etch resistance.

Figure 9.3a shows the trend in the gate lengths of microprocessor units (MPUs) (plotted with squares) and half-pitches of dynamic random access memories (DRAMs) (plotted with circles) as assessed in the ITRS2005 roadmap. It is expected that device size will shrink by about 70% every 3 years. Figure 9.3b shows the trend in resist thickness required for making corresponding ULSIs for MPUs (squares) and DRAMs (circles). At present, the thickness of resist used for the fabrication of sub-100-nm ULSIs ranges from 130 to 230 nm. However, in 2010 the range will be

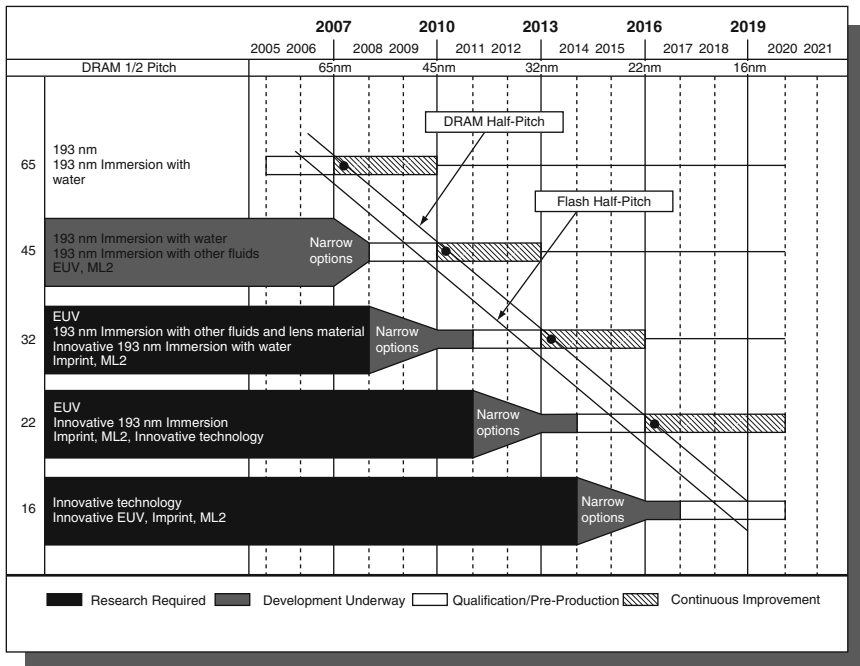


Fig. 9.2 Lithography exposure tool potential solutions (from 2005 International Technology Roadmap for Semiconductors, ITRS)

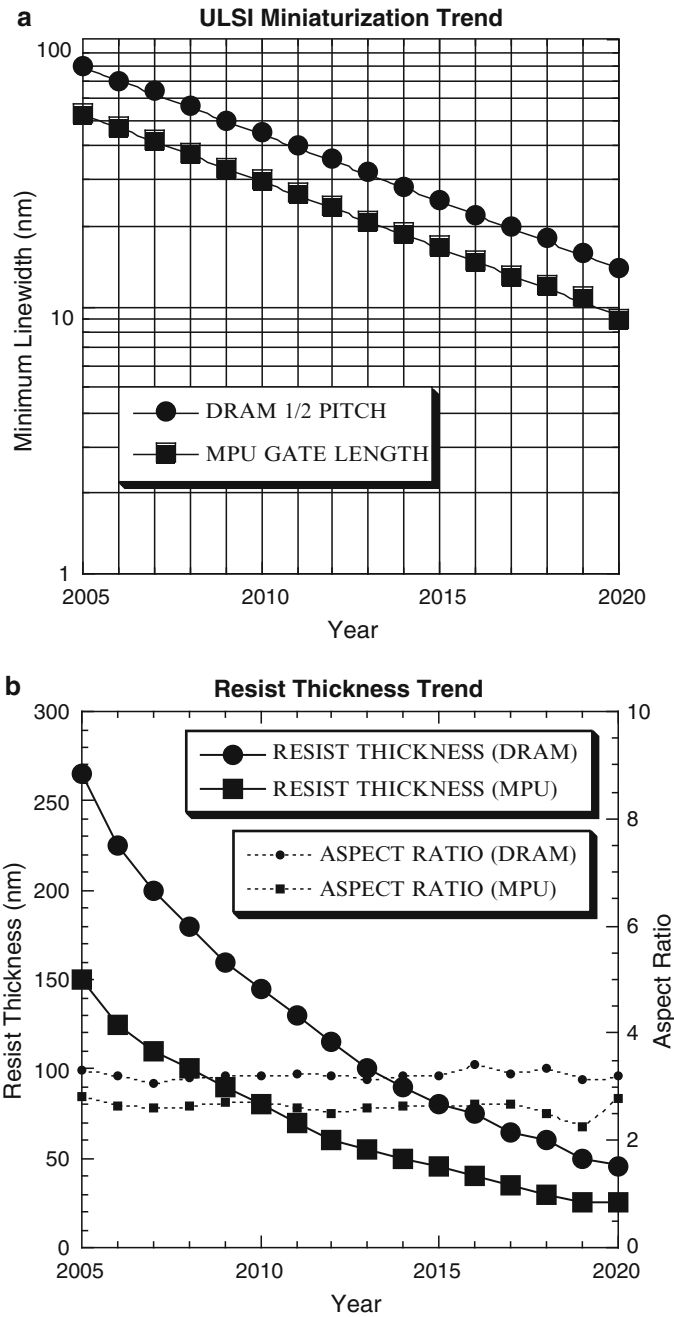


Fig. 9.3 (a) ULSI miniaturization trend (from ITRS2005). (b) Resist thickness trend (from ITRS2005)

80–150 nm for 30–45-nm ULSIs and in 2020 it will be below 50 nm for 10-nm-level ULSIs. This trend clearly demonstrates that resist thinning is essential for device miniaturization. Resolution improvement by resist thinning is a general principle that holds regardless of exposure means. In a thinner film, the effect of defocusing is smaller in photolithography and also the effect of scattering is smaller in electron-beam lithography (EBL). And, interestingly, the aspect ratio, defined as the ratio of pattern height to pattern width, will stay around three (dashed lines). This means that when pattern size is reduced by half, so is resist thickness. In other words, resist thinning proceeds at the same rate as miniaturization. Considering the need for ultra-thin resist films in the coming future, we believe that the enhancement of etch resistance is absolutely necessary. A conventional way to enhance etch resistance is to introduce as many highly resistant groups (like aromatic rings) as possible into a polymer molecule using synthetic approaches. However, the number of the groups that can be introduced is limited because of limited reaction sites and steric hindrance.

As a next-generation highly etch resistant resist, we have developed a fullerene nanocomposite resist by incorporating fullerene molecules into a conventional resist material, taking advantage of the smallness and stableness of fullerene molecules [4]. Fullerene is a carbon material and carbon has a history as a highly etch-resistant material. Broers first showed that contamination produced by electron beam irradiation in an electron microscope is highly dry-etch resistant and used the contaminated material as a resist for the fabrication of nanometer-size devices [5, 6]. This “contamination” resist is presumably polymerized carbon-rich hydrocarbon and is sometimes called “carbon resist.” Gokan et al. investigated the effect of the carbon content of various resist materials on dry-etch resistance and found that resistance generally increases as the carbon content increases. The degree of carbon content is represented by a parameter called the “Ohnishi parameter” [7]. Kakuchi et al. reported direct and more explicit proof of the high dry-etch resistance and also the excellent mechanical and thermal stability of carbon. They successfully fabricated nanometer Si patterns by reactive ion etching (RIE) using an amorphous carbon film as an etching mask for the Si substrate in a bilayer resist system [8]. More recently, Tada et al. used fullerene C_{60} as a negative-type electron-beam resist and showed, through the fabrication of Si nanopillars, that its dry-etch resistance is higher than that of novolac resists [9].

From the viewpoint of composite preparation, fullerene is an excellent material for incorporation. It is an ultrasmall particle with a diameter of ~ 0.7 nm and soluble in some organic solvents. It can be removed completely by oxygen plasma as CO_2 gas, which is a prerequisite for resist materials in device fabrication.

Three types of fullerene nanocomposite resists have been developed (Table 9.1). The first-generation resist is the simplest one. It is composed of fullerene (C_{60} and/or C_{70}) and a polyacrylate-type resist. The second generation is a nanocomposite of a C_{60} derivative and a polyacrylate-type resist. Many more of the highly soluble C_{60} derivatives can be incorporated into the polyacrylate-type resist than C_{60} or C_{70} can. The third generation is a nanocomposite of a C_{60} derivative and a chemical amplification resist. This is intended not only for EBL but also for extreme ultraviolet (EUV) lithography.

Section 2 describes the concept of fullerene nanocomposite resists. Section 3 covers the preparation and characteristics of the first-generation nanocomposite

Table 9.1 Development of fullerene nanocomposite resists

Generation	Fullerenes	Matrix resists
First	C ₆₀ and/or C ₇₀	Polyacrylates (PMMA, ZEP520)
Second	C ₆₀ derivatives	Polyacrylate (ZEP520)
Third	C ₆₀ derivatives	Chemical amplification (CAPI12PM)

resists and provides some examples of their device applications. Section 4 examines the synthesis of C₆₀ derivatives and the characteristics of the second- and third-generation nanocomposite resists.

9.2 Concept of Fullerene Nanocomposite Resists

A film of conventional resist materials spin-coated on a substrate appears to be a closely packed film, but from a microscopic viewpoint, such a thin organic polymer film contains spaces not occupied by polymer molecules and is porous in nature (Fig. 9.4a). Developer or an etching species easily passes through the pores in the resist film, which results in degradation of pattern contrast or causes etching defects. In addition, such porous organic film generally has poor mechanical strength and tends to collapse during development due to its inability to bear the surface tension caused by the rinsing solvent. Filling those spaces with fullerene (C₆₀ and/or C₇₀) blocks the intrusion of both the developer and the etching species and thereby enhances pattern contrast and etch resistance (Fig. 9.4b).

Figure 9.5 illustrates the resistance enhancement mechanism by fullerene C₆₀ during etching in a fluorocarbon (CmFn) gas. Electrons and various kinds of ions (CxFy⁺) and radicals (CmFn[·]) are produced in the plasma by radio-frequency application. Ultraviolet light is also emitted by discharge. In the case of physical etching by the ions, fullerene molecules reduce the sputtering impact of the ions by bouncing them back or absorbing their kinetic energy. On the other hand, in the case of chemical etching by the radicals, the fullerene molecules deactivate the radicals by dispersing the excited energy into the three-dimensional resonance structure of the fullerene molecules. Moreover, the fullerene molecules act as acceptors or absorbers of electrons and ultraviolet light. All the effects mentioned above contribute to protect the resist film, thereby enhancing the etch resistance of the resist material. It is also expected that close packing with such ultrasmall particles can increase the rigidity or strength of the film by increasing its density. Furthermore, the compactness of the film contributes to the stability of chemical amplification resists because acid in the resist film is protected from acid-quenching species, such as amines and water, in the surrounding environment.

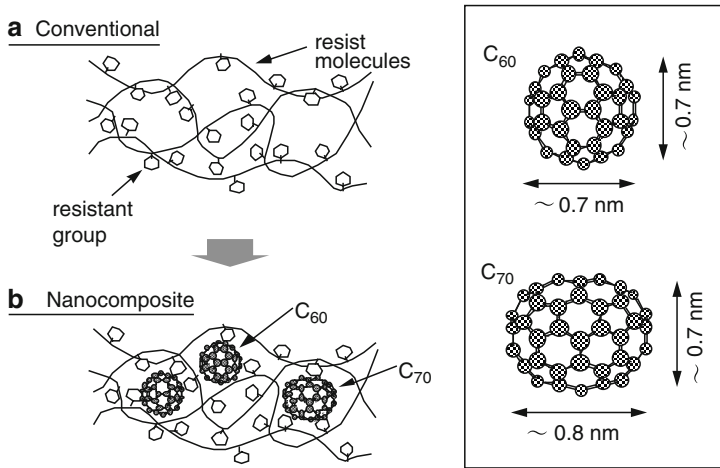


Fig. 9.4 A schematic drawing of nanocomposite resist system. Fullerene molecules fill up spaces among matrix resist molecules to form a closely packed and reinforced resist film

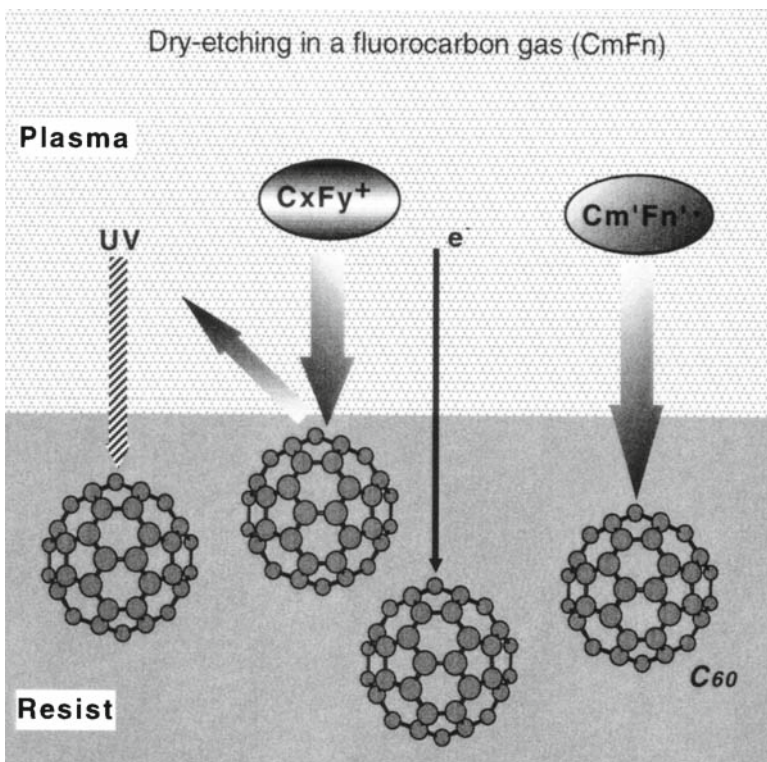


Fig. 9.5 Enhancement mechanism of dry-etch resistance by fullerene

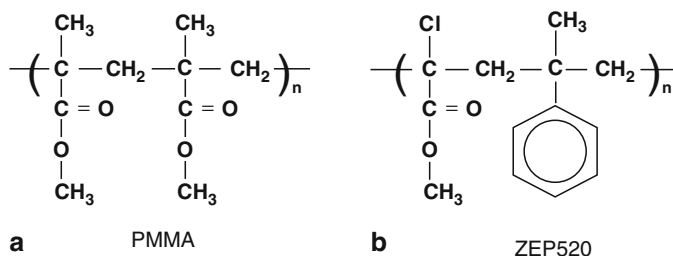


Fig. 9.6 Chemical structures of (a) PMMA and (b) ZEP520

9.3 Fullerene (C_{60} and/or C_{70}) Nanocomposite Resists

We selected PMMA [poly(methyl methacrylate)] and ZEP520 as matrix resists because the former is known as a high-resolution standard positive-type electron-beam resist and the latter is a widely used practical positive-type electron-beam resist with high resolution, high sensitivity, and high resistance. The chemical structures of PMMA and ZEP520 are shown in Fig. 9.6a, b, respectively.

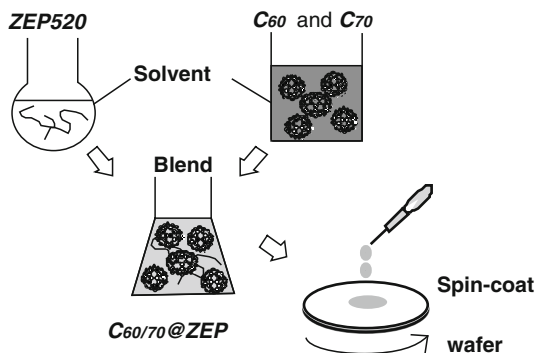
PMMA is a radiation-sensitive polymer and undergoes main-chain scission upon electron-beam irradiation. The detailed scission mechanism is described in [10]. ZEP520 is a copolymer of methyl α -chloroacrylate and α -methylstyrene [11]. Like PMMA, it also undergoes main-chain scission, but owing to the inductive effect of chlorine atoms and the phenyl group's energy dispersion effect, ZEP520 is much more sensitive and etch resistant than PMMA. The intrinsic resolution of PMMA is considered to be 5–7 nm [12, 13] and that of ZEP520 is assumed to be in the same range because of the similarity of their bond-scission mechanisms. Considering the size of C_{60} and C_{70} (0.7–0.8 nm), the resolution of the fullerene nanocomposite resists could be limited by the size of fullerene and the minimum achievable linewidths of PMMA and ZEP520 nanocomposite resists should be around 10 nm on a practical basis.

Hereafter, the nanocomposite resist of C_{60} and PMMA is denoted C_{60} @PMMA. Those comprising C_{60} , C_{70} , or a C_{60}/C_{70} mixture, and ZEP520 are denoted C_{60} @ZEP, C_{70} @ZEP, and $C_{60/70}$ @ZEP, respectively. ZEP520 is denoted ZEP for simplicity.

9.3.1 Preparation

Fullerene C_{60} , C_{70} , and C_{60}/C_{70} mixture (mole ratio: 4:1), which is available at a much lower price than C_{60} or C_{70} alone, were procured from Tokyo Chemical Industry Co. PMMA is supplied under the product name OEER-1000 (Molecular weight: 600,000; OEER stands for Ohka electron-beam resist) from Tokyo Ohka Kogyo Co. ZEP520 was purchased from Nippon Zeon Co. (Molecular weight: 55,000; ZEP means Zeon's electron-beam positive resist).

Fig. 9.7 Preparation of fullerene nanocomposite resist ($C_{60/70}$ @ZEP)



The preparation of $C_{60/70}$ @ZEP is illustrated in Fig. 9.7. The black powder of C_{60} and C_{70} is first dissolved in *ortho*-dichlorobenzene (*o*-DCB) and then mixed with resist solutions by shaking by hand. For C_{60} @PMMA, some quantity of *o*-DCB must be added to the resist solution in advance to facilitate the mixing because PMMA's solvent is 2-ethoxyethyl acetate (cellosolve acetate), which is a poor solvent for C_{60} . The preparation for C_{60} @ZEP or $C_{60/70}$ @ZEP is much simpler than for C_{60} @PMMA because the resist solvent is also *o*-DCB. The C_{60} dissolved in *o*-DCB readily mixes with the ZEP solution to form a uniform resist solution. In the same manner as pure PMMA or ZEP, the corresponding nanocomposite resist films can be formed on a substrate by spin-coating.

Although *o*-DCB is a better solvent than xylene or benzene for fullerene, the amount of fullerene that can be dissolved in *o*-DCB is limited, and this makes it difficult to prepare nanocomposite resists. Fullerene molecules tend to form aggregates in the resist solution some time after they are mixed with the matrix resist. Those aggregates have micrometer dimensions and definitely degrade resolution. Figure 9.8a shows photographs of C_{60} aggregates observed in C_{60} @ZEP. The aggregates appeared in both the 30 and 50 wt% resist solutions 1 week after nanocomposite preparation and in the 10 wt% 3 weeks after preparation. In the $C_{60/70}$ @ZEP system, however, aggregates appeared only in the 50 wt% 1 week after preparation, as shown in Fig. 9.8b. No aggregates were observed in the 10 wt% even after 6 months and in the 30 wt% after 3 months.

As described above, the solubility of fullerene in *o*-DCB should be known in advance, otherwise, fullerene cannot be dissolved properly and tends to form aggregates. The solubility data for fullerenes can provide a supportive basis for aggregate minimization. The reported solubility of C_{60} is 24.6 g/L [14] and 27.0 g/L [15], but the solubility of C_{70} and a mixture of C_{60} and C_{70} has not been reported. We have measured the solubility of fullerenes in *o*-DCB by ultraviolet (UV) absorption spectroscopy.

Figure 9.9 shows UV spectra of saturated solutions of C_{60} , C_{70} , and a 4:1 mixture in *o*-DCB measured at 23°C (A saturated solution of each fullerene was first prepared and then diluted 1,000-fold for measurement due to the strong absorption of fullerenes, and the absorption of *o*-DCB was subtracted from the spectra by using the subtraction software of the apparatus). By comparing absorption peak heights at wavelengths of

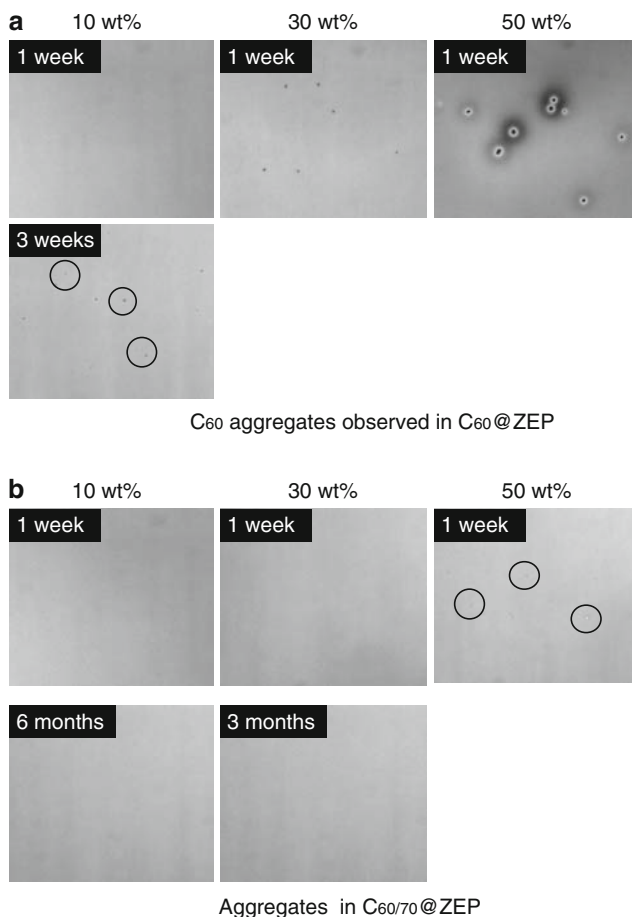


Fig. 9.8 Aggregates formation in fullerene nanocomposite resists: (a) aggregates observed in C₆₀@ZEP and (b) aggregates in C_{60/70}@ZEP

332.5 (C₆₀) and 466 nm (C₇₀) with the absorption intensity of each calibration curve of C₆₀ and C₇₀, which was obtained in advance by changing the concentration of fullerenes, we estimated the solubility of C₆₀, C₇₀, and the 4 :1 mixture. The measured solubility of each fullerene is 25.0, 26.6, and 73.4 g/L, respectively (Table 9.2).

The 25.0 g/L for C₆₀ agrees well with the reported solubility of 24.6 and 27.0 g/L, and this verifies that the measured solubility of C₇₀ and the 4 :1 mixture is reliable. There is no significant difference in solubility between C₆₀ and C₇₀, and the solubility of the mixture is approximately three times larger than that of C₆₀ or C₇₀ alone. This supports a significantly smaller tendency to aggregate formation in the C_{60/70}@ZEP system than in the C₆₀@ZEP. One possible explanation for the enhanced solubility of the mixture is the formation of ultrasmall stable clusters composed of C₆₀ and C₇₀ that would prevent each other from forming aggregates. A detailed analysis of UV spectra from the mixture revealed an interesting phenomenon.

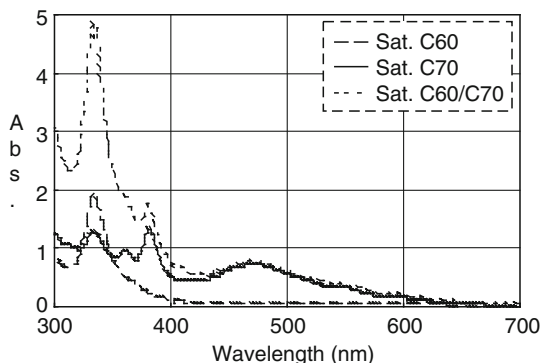


Fig. 9.9 UV spectra of *o*-DCB solutions of C_{60} , C_{70} , and a 4:1 mixture of C_{60} and C_{70} (23°C). A saturated solution of each fullerene was first prepared and then diluted 1,000-fold for measurement. The absorption of *o*-DCB was subtracted from the spectra by using the subtraction software of the apparatus

Table 9.2 Solubility of fullerenes in *o*-DCB (23°C)

Fullerenes	Solubility (g/L)	References (g/L)
C_{60}	25.0	24.6 [14] 27.0 [15]
C_{70}	26.6	—
4:1 mixture (C_{60} : C_{70})	73.4	—

Table 9.3 The quantity of C_{60} and C_{70} contributing to the solubility of the 4:1 mixture in *o*-DCB

Fullerenes	Quantity dissolved (g/L)	Molecular weight	Molarity (mmol/L)
C_{60}	46.4	720.66	64.4
C_{70}	27.0	840.77	32.1

Table 9.3 shows the quantity of C_{60} and C_{70} contributing to the solubility of the 4:1 mixture in *o*-DCB. Of the total quantity of 73.4 g/L (the solubility of the mixture), 46.4 g/L is contributed from C_{60} and the remaining 27.0 g/L is from C_{70} . By dividing each quantity by molecular weight (C_{60} : 720.66, C_{70} : 840.77), we obtained the molarity of 64.4 mmol/L for C_{60} and 32.1 mmol/L for C_{70} . That is, we have an extremely simple molarity ratio of 2 : 1 (C_{60} : C_{70}) in spite of the initial mole ratio of 4:1, which suggests that the fullerene mixture dissolves in *o*-DCB by forming units (or clusters) composed of two C_{60} molecules and one C_{70} molecule. Considering that the solubility of each fullerene is almost the same, it is quite surprising that the mixture dissolves without maintaining the initial mole ratio. The morphology of the units described above is not readily conceivable, and further study is needed to understand the dissolution mechanism of the fullerene mixture.

Nonetheless, from the above finding, the use of a 2:1 fullerene mixture for the preparation of $C_{60/70}@ZEP$ is recommended.

9.3.2 Resist Characteristics

We first investigated the characteristics of $C_{60}@PMMA$ [16, 17]. In what follows, the enhancement of etch resistance, sensitivity, and pattern quality are described.

The enhancement of etch resistance was evaluated by measuring etch rate of electron cyclotron resonance (ECR) dry etching under the Si etching condition (gas: Cl_2 , flow rate: 40 SCCM, pressure: 0.05 Pa, microwave power: 200 W). Figure 9.10 shows the normalized etch rate of $C_{60}@PMMA$ against C_{60} content. The relationship between the normalized etch rate and the enhancement of etch resistance or resistance enhancement (defined as a percentage of increase in resistance compared with pure resist) can be expressed as follows:

$$NER = 1 / (1 + \Delta RE / 100), \quad (9.1)$$

where NER is the normalized etch rate and ΔRE is the resistance enhancement (%). Rearranging (9.1), we obtain

$$\Delta RE = 100(1 / NER - 1). \quad (9.2)$$

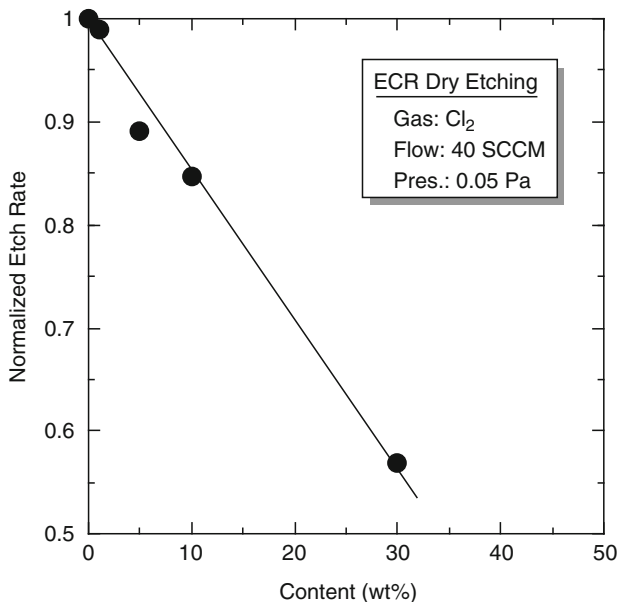


Fig. 9.10 Normalized etch rate of $C_{60}@PMMA$ against C_{60} content

From Fig. 9.10, it is clear that the rate decreases linearly with C_{60} content, and a resistance enhancement of about 10% is obtained at 5 wt% and about 80% at 30 wt%. This result proves that C_{60} is strongly etch resistant as expected.

Sensitivity was examined by obtaining sensitivity curves, which plot the normalized film thickness (NFT) against dose exposed on a large area (usually 50-100 μm). For a positive resist, sensitivity is defined as the dose at which NFT becomes zero on the sensitivity curve, or the dose required to clear the large area. As a general rule, when the dose required to clear the large area is small, sensitivity is said to be high. The resist solution was spin-coated on a Si substrate to a thickness of 50 nm and prebaked in an oven at 170°C for 30 min. Exposure was done with a 25-kV Gaussian electron-beam exposure system, JEOL-5FE, (JEOL stands for Japan Electron Optics Laboratory). The exposed sample was developed in a 1 : 5 mixture solution of 4-methyl-2-pentanone and 2-propanol and rinsed with 2-propanol. Figure 9.11 shows the sensitivity curves of pure PMMA (open circles) and 5 wt% C_{60} @PMMA (closed circles). Although 5 wt% C_{60} @PMMA showed a dissolution rate decrease due to the strong dissolution inhibiting effect of C_{60} , we could obtain the same sensitivity of $\sim 300 \mu\text{C}/\text{cm}^2$ by controlling development time: 2 min for pure PMMA and 5 min for 5 wt% C_{60} @PMMA.

Figures 9.12a, b show SEM (Scanning Electron Microscope) micrographs of 100- and 150-nm-pitch patterns of pure PMMA and 5 wt% C_{60} @PMMA. As clearly shown in the figure, the patterns of 5 wt% C_{60} @PMMA have a high contrast profile compared with those of pure PMMA. The strong dissolution inhibiting effect of C_{60} limits degradation in the underexposed and nonexposed areas during development, thereby enhancing pattern contrast.

After a preliminary study of C_{60} @PMMA, we investigated more practical systems of ZEP nanocomposites [16–18]. In what follows, enhancements of etch resistance (dry and wet) and thermal resistance, sensitivity, and pattern quality are described along with some examples of device fabrication.

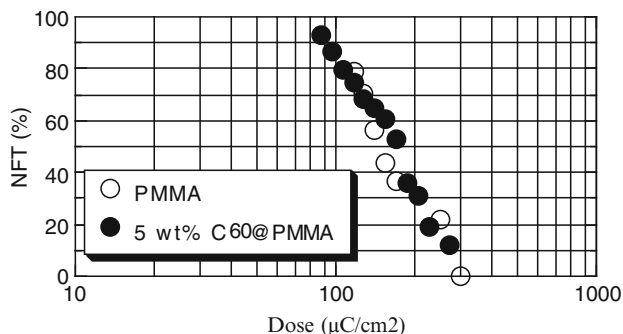


Fig. 9.11 Sensitivity curves of pure PMMA (open circles) and 5 wt% C_{60} @PMMA (closed circles). Film thickness is 50 nm. The samples were developed in a 1:5 mixture solution of 4-methyl-2-pentanone and 2-propanol and rinsed with 2-propanol. The development time: 2 min for pure PMMA and 5 min for 5 wt% C_{60} @PMMA. NFT stands for normalized film thickness

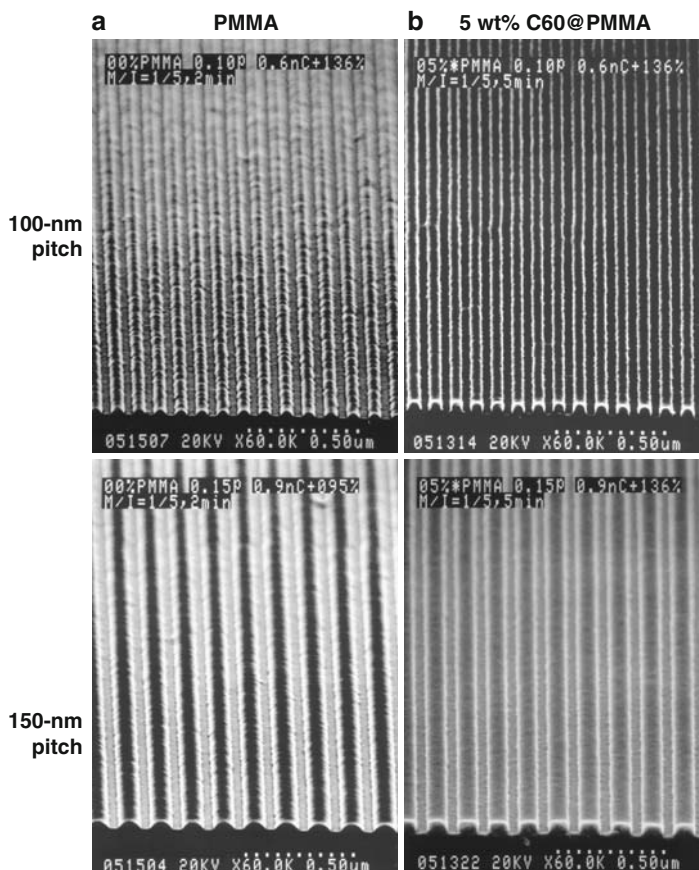


Fig. 9.12 Nanometer patterns of C_{60} @PMMA. Film thickness is 50 nm

The enhancement of etch resistance was evaluated by measuring etch rate of RIE under the SiO_2 etching condition (gas: C_2F_6 , flow rate: 40 SCCM, pressure: 2.0 Pa, rf power: 100 W). Figure 9.13 shows the dependence of normalized etch rate on fullerene content of C_{60} @ZEP, C_{70} @ZEP, and $C_{60/70}$ @ZEP. The etch rate decreases with fullerene content as it does for C_{60} @PMMA in Cl_2 ECR dry etching. A resistance enhancement of about 10% is obtained at 10 wt% and about 40% at 30 wt%. There is no noteworthy difference among the fullerene species, and this means that the enhancement effect of dry-etch resistance is independent of the fullerene species. In addition to the enhancement of dry-etch resistance, fullerene also enhances wet-etch resistance. This enhancement was evaluated by measuring the number of etched pits after dipping resist-coated samples in an etching solution. Pure ZEP and 5 wt% $C_{60/70}$ @ZEP were spin-coated on GaAs substrates to a thickness of 40 nm and baked in an oven at 165°C for 30 min. The samples were then dipped in a 20 : 1 wt% solution of citric acid/hydrogen peroxide, an etching solution widely used for the fabrication of GaAs devices [19], for 2 min and rinsed with water. After

Fig. 9.13 Normalized etch rates of C_{60} @ZEP, C_{70} @ZEP, and $C_{60/70}$ @ZEP as a function of fullerene content

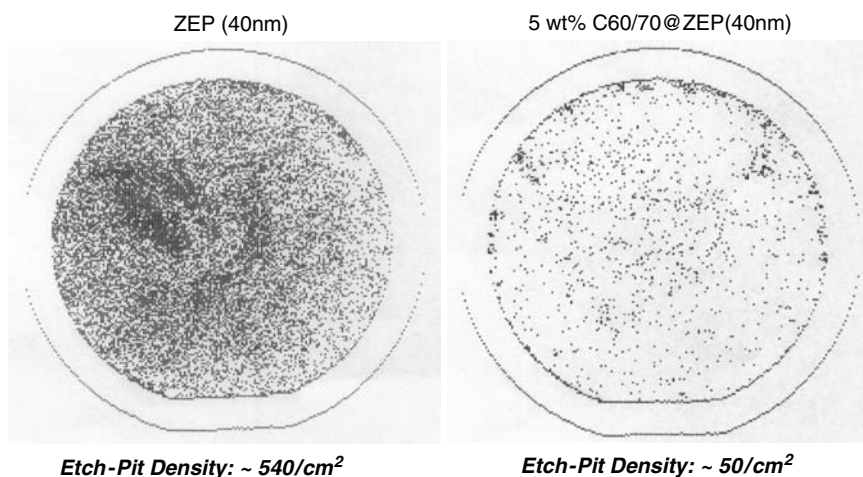
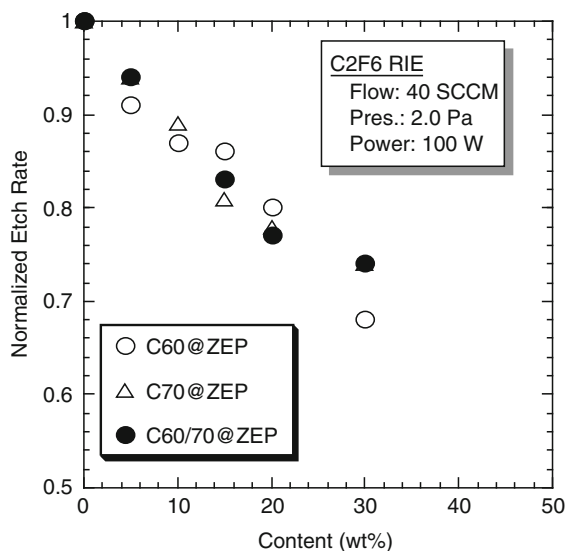


Fig. 9.14 An example of the enhancement of wet-etch resistance by fullerene. Pure ZEP and 5 wt% $C_{60/70}$ @ZEP samples spin-coated on GaAs substrates were dipped in a 20:1 solution of citric acid/hydrogen peroxide for 2 min and then, after rinsing and drying, scanned with a He-Ne laser surface scan tool to measure etch-pit density

rinsing, the resist film was removed with a resist remover (1-methyl-2-pyrrolidone) and dried with N_2 gas. Then, the samples were scanned with a He-Ne laser surface scan tool to measure etch-pit density.

Figure 9.14 shows laser-scanned outputs on the GaAs substrates. The etch-pit density of (a) pure ZEP is $\sim 540/cm^2$, while that of (b) 5 wt% $C_{60/70}$ @ZEP is $\sim 50/cm^2$. This significant difference is probably due to the strong chemical resistant

quality of the closely packed C_{60} and C_{70} molecules. And this result suggests that $C_{60/70}$ @ZEP has the potential for nanometer device fabrication in the area where a dry-etching technique cannot be employed because of the damage it causes.

An enhancement of thermal resistance was also observed in C_{60} @ZEP. Figure 9.15 shows an example of thermal resistance enhancement of C_{60} @ZEP. Although ZEP has a relatively high glass temperature of 145°C [11], it shows pattern swelling at around 120°C and completely flows at 150°C . On the other hand, 10 wt% C_{60} @ZEP shows no practically adverse swelling after heat treatment at 120°C and only slight deformation even at 150°C . This enhancement of thermal resistance facilitates metal deposition in a bilayer lift-off process, where the resist film is exposed to high temperatures during metal deposition.

Sensitivity was evaluated in the same way as C_{60} @PMMA. Resist solutions were spin-coated on an Si substrate to a thickness of 150 nm and prebaked in an oven at

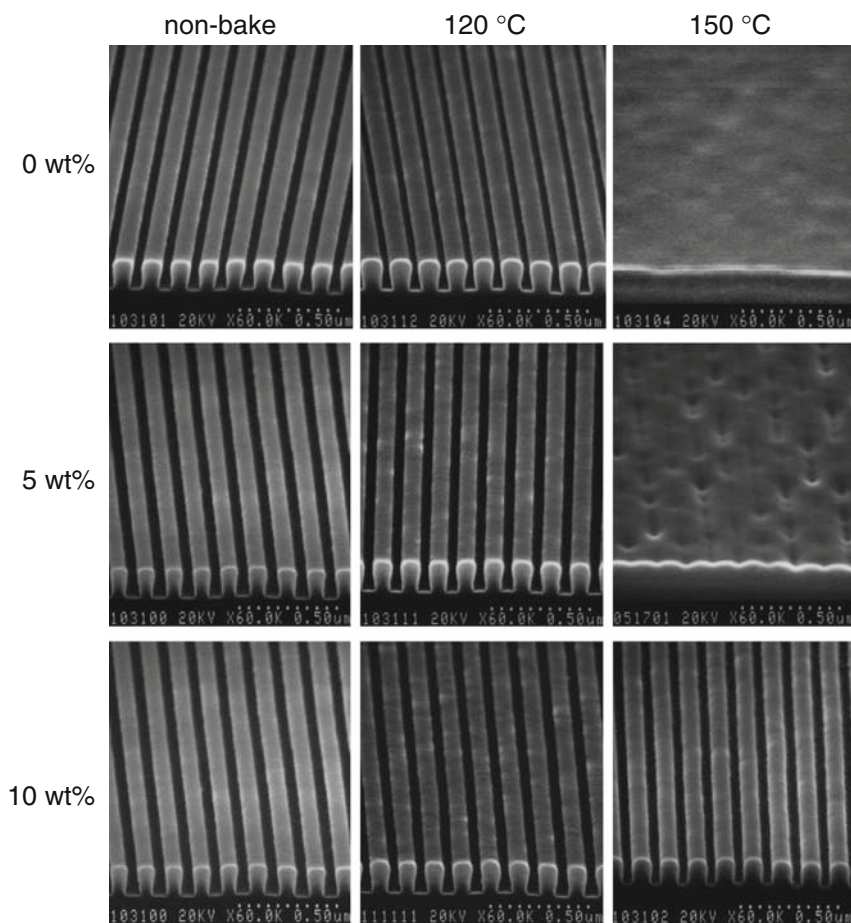


Fig. 9.15 An example of the enhancement of thermal resistance of C_{60} @ZEP. SEM micrographs show 150-nm pitch patterns of 0, 5, and 10 wt% after baking at 120 and 150°C

165°C for 30 min. Samples were exposed with the JBX-5FE and the exposed samples were developed in the ZEP520 developer ZED-N50 (pentyl acetate) for 30 s and rinsed in 2-propanol for 30 s.

Figure 9.16 shows sensitivity curves of $C_{60/70}$ @ZEP. Sensitivity decreases with increasing fullerene content: $\sim 50 \mu\text{C}/\text{cm}^2$ at 0 wt%, $\sim 70 \mu\text{C}/\text{cm}^2$ at 10 wt%, and $\gg 100 \mu\text{C}/\text{cm}^2$ at 30 wt%. This is due to the strong dissolution-inhibiting effect of fullerene. Fullerene C_{60} or C_{70} does not dissolve in the developer. The slope around 50% NFT of a sensitivity curve is called the γ -value. It is an indicator of resolution: The larger the γ -value of a resist is, the higher its resolution becomes. The γ -values of 0, 10, and 30 wt% $C_{60/70}$ @ZEP are 6.3, 6.1, and 4.8, respectively. It is expected that the resolution of 10 wt% is all but the same as that of 0 wt% and that the resolution of 30 wt% is even worse.

Like C_{60} @PMMA, C_{60} @ZEP also exhibits a contrast enhancement effect. Figure 9.17 shows an example of the contrast enhancement of patterns. The film thickness is 50 nm. The profile of ZEP patterns on the left is rounded at the top corners, while that of 5 wt% C_{60} @ZEP patterns on the right is not. As mentioned above, fullerene is insoluble in the developer and this limits the dissolution of 5 wt% C_{60} @ZEP at the upper corners of patterns, which are weakly exposed by the electron beam and removed in pure ZEP during development.

Figure 9.18 compares resolution among (a) pure ZEP, (b) C_{60} @ZEP, and (c) $C_{60/70}$ @ZEP. Resolution was evaluated by measuring 90-nm-pitch 250-nm-height line-and-space patterns. Pure ZEP patterns are not resolvable due to pattern

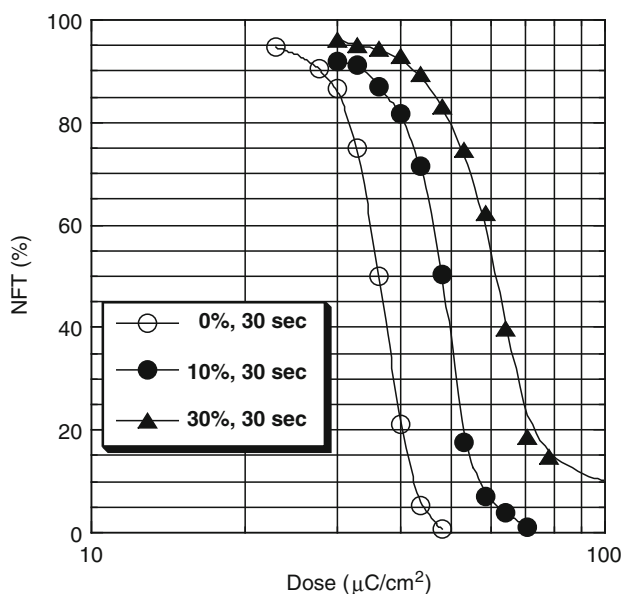


Fig. 9.16 Sensitivity curves of $C_{60/70}$ @ZEP. Film thickness is 150 nm. The samples were developed in ZED-N50 for 30 s

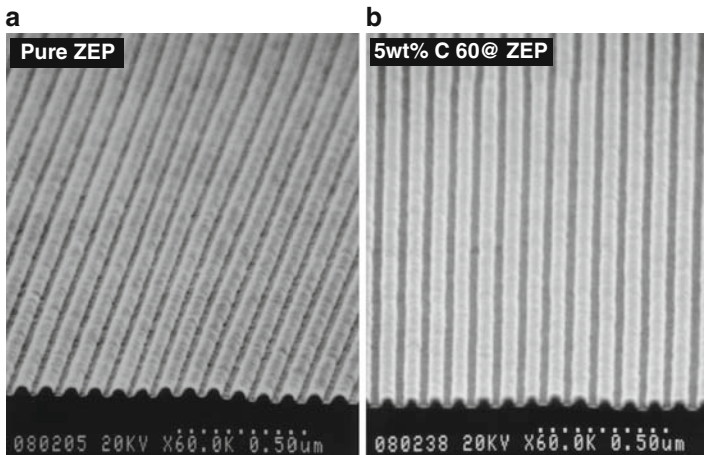


Fig. 9.17 An example of the contrast enhancement of C_{60} @ZEP. Pure ZEP patterns show rounding at upper corners, while 5 wt% C_{60} @ZEP patterns show steep profiles

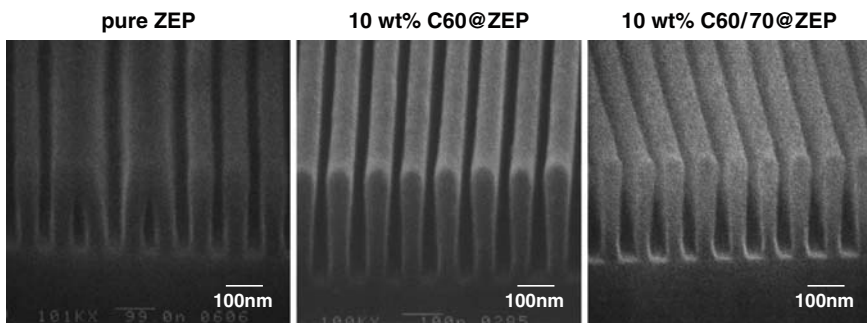


Fig. 9.18 Resolution comparison among (a) pure ZEP, (b) 10 wt% C_{60} @ZEP, and (c) 10 wt% $C_{60/70}$ @ZEP. Film thickness is 250 nm. Pitch is 90 nm. Patterns collapse in (a), while no pattern collapse is observed in (b) and (c)

collapse, while C_{60} @ZEP and $C_{60/70}$ @ZEP patterns are clearly resolved with no pattern collapse and exhibit an extremely high aspect ratio of more than 5. This proves that fullerene incorporation reinforces resist materials, or enhances their mechanical strength. Because there is no noticeable difference in the effects on resolution and on mechanical strength enhancement between C_{60} and C_{70} , $C_{60/70}$ @ZEP has a great advantage over C_{60} @ZEP for practical application.

In the following, some examples of device fabrication using $C_{60/70}$ @ZEP are described. Figure 9.19 shows an SEM micrograph of a 30-nm gate resist pattern of 10 wt% $C_{60/70}$ @ZEP for a high electron mobility transistor (HEMT). The pattern has a very sharp profile as expected from the contrast enhancement effect of fullerene.

Fig. 9.19 SEM micrograph of a 30-nm gate pattern delineated in a 200-nm thick film of 10 wt% C_{60/70}@ZEP

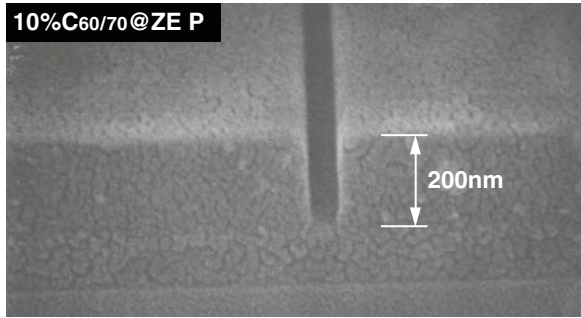
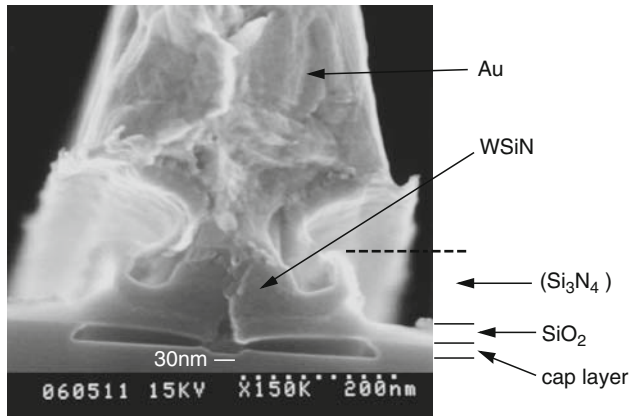


Fig. 9.20 Cross-sectional view of the 30-nm T-shaped gate of HEMT



The film thickness is 200 nm, which is not thick enough to etch the underlying substrate by RIE using pure ZEP.

Figure 9.20 is a SEM cross-sectional micrograph of the fabricated T-shaped gate. The bottom of the gate is 30-nm long as designed. The estimated cutoff frequency (f_T) is 350 GHz, which until recently was one of the highest values ever reported for any kind of transistor [20].

Figure 9.21 shows a cross-sectional view of 50-nm tantalum (Ta) absorber patterns of an X-ray mask. The Ta thickness is 400 nm and the aspect ratio is as high as 8. The mask was fabricated using 10 wt% C_{60/70}@ZEP. A layer of SiO₂ deposited over the Ta layer was first etched through the resist patterns by C₂F₆ RIE and then the Ta layer was etched through the SiO₂ mask by Cl₂ ECR. The mask composition and fabrication process are described in detail in [21]. This process can be applied to the fabrication of Fresnel zone plates for X-ray microscopy. Figure 9.22 shows an example of fabricated zone plates: (a) center area and (b) peripheral area. The diameter is 180 μm and the height is 180 nm. The width of the outermost ring is 35 nm.

Fig. 9.21 Fabricated Ta absorber of an X-ray mask with a feature size of 50 nm

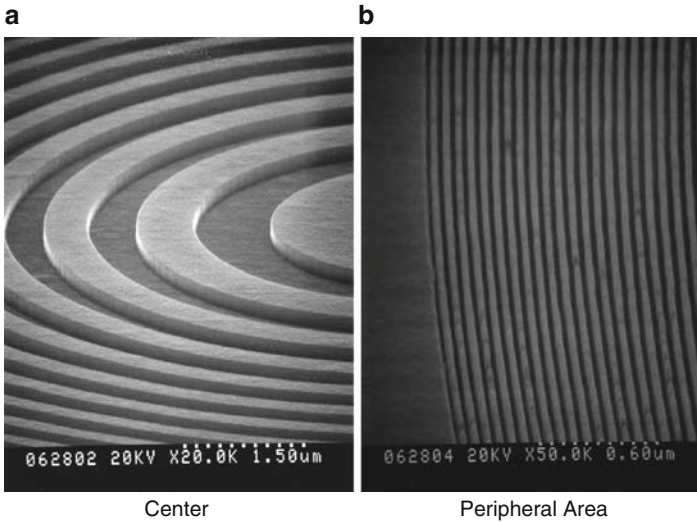
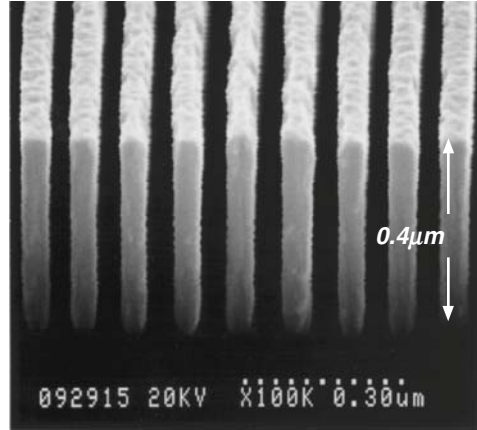


Fig. 9.22 An example of fabricated Fresnel zone plates: (a) center and (b) peripheral area. The diameter is 180 μm and the height is 180 nm. The width of the outermost ring is 35 nm. (Courtesy of NTT-AT Nanofabrication Co.)

Deep substrate etching using $C_{60/70}$ @ZEP has been demonstrated through the fabrication of distributed Bragg reflector (DBR) lasers and distributed feedback (DFB) lasers.

Figure 9.23 shows schematic drawings of (a) grooved-grating DBR and (b) DFB lasers. The grating etched in the upper-cladding AlGaAs layer acts as a mirror for laser oscillation. Because the grating is etched from the top surface into the upper-cladding layer after the epitaxial growth of the active layer, the DBR and DFB lasers can be fabricated without a high-temperature regrowth process, which

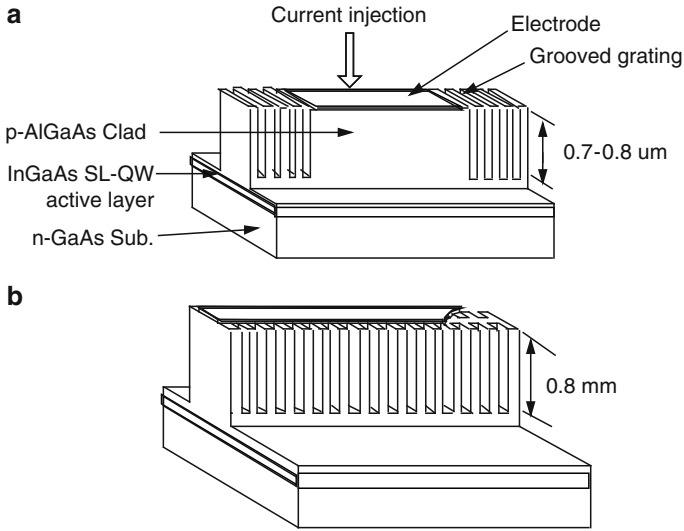
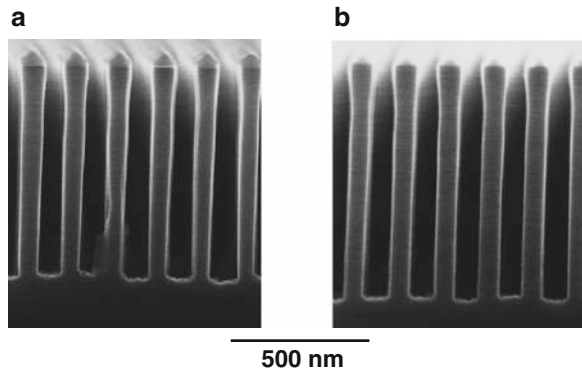


Fig. 9.23 A schematic drawing of grooved-grating: (a) DBR and (b) DFB lasers

Fig. 9.24 Cross-sectional SEM micrographs of deeply etched grooves for first-order diffracting grating: (a) DBR and (b) DFB lasers



simplifies the process and stabilizes the wavelength of the lasers. Cross-sectional SEM micrographs of extremely deep-groove-gratings etched into the AlGaAs layer are shown in Fig. 9.24: (a) 700 and (b) 800 nm. The period of each grating is 150 nm. The AlGaAs layer was etched through a 150-nm-thick SiO₂ mask. The SiO₂ mask was fabricated with a 150-nm-thick film of 10 wt% C_{60/70}@ZEP. We observed pattern collapse or pattern deformation in a pure ZEP film of 200 nm, which is a film thickness necessary for proper SiO₂ etching. The detailed process and lasing characteristics have been reported by Oku et al. [22].

9.3.3 Bilayer Resist System

One useful application of $C_{60/70}$ @ZEP to nanofabrication is to use it as a bilayer resist system for lift-off [23]. Arrays of dots with dimensions smaller than 50 nm are of great interest for the fabrication of quantum box arrays and nanoimprint molds. Nanometer dot patterns are generally produced by EBL, either by using a positive-type bilayer resist system of PMMA and the lift-off technique [12, 13], or by using a high-resolution negative-type resist, such as calixarene [24]. However, neither of them has sufficient sensitivity to write a large number of dot patterns. We have recently developed a new bilayer resist system composed of a $C_{60/70}$ @ZEP top layer and a pure ZEP bottom layer. The sensitivity of $C_{60/70}$ @ZEP can be easily changed by adjusting the fullerene content because of the dissolution inhibiting effect of fullerene. This unique characteristic enables us to make the sensitivity between the top and bottom layers different in the same manner as changing molecular weights in the PMMA bilayer system does. Because the sensitivity of ZEP is $\sim 50 \mu\text{C}/\text{cm}^2$, which is 5 or 6 times higher than that of PMMA and about 100 times higher than that of calixarene, the new bilayer system enables us to fabricate nanometer-scale dot arrays with a sensitivity that is practically viable. Additionally, because the sensitivity of the top layer can be easily optimized by changing

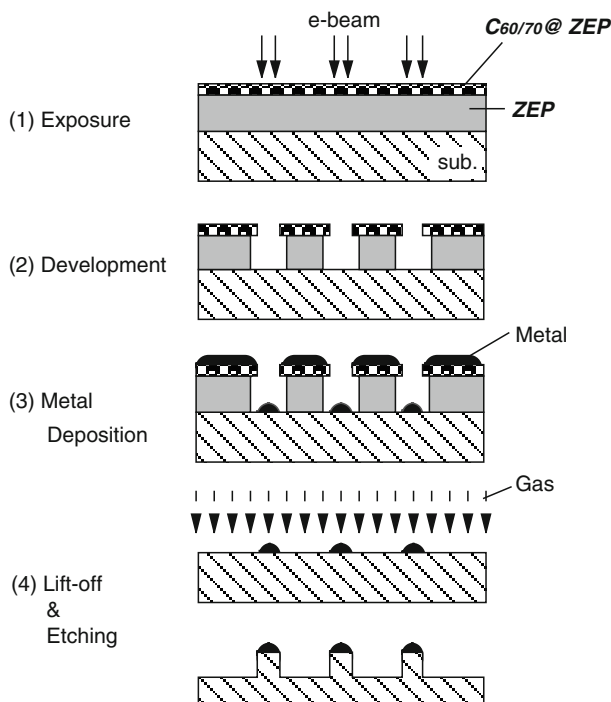


Fig. 9.25 Lift-off process of a bilayer resist system composed of a $C_{60/70}$ @ZEP top layer and a ZEP bottom layer. By changing the fullerene content, the sensitivity of the top layer is optimized to create an ideal overhang resist pattern for lift-off

the fullerene content, the new system also has an advantage over the PMMA bilayer system for sensitivity control to create ideal overhang patterns. In the PMMA system it is not always easy to prepare the best set of two polymers with different molecular weights.

Figure 9.25 shows a schematic drawing of the lift-off process of a bilayer resist system composed of a $C_{60/70}$ @ZEP520 top layer and a pure ZEP bottom layer. We prepared 10, 20, and 30 wt% $C_{60/70}$ @ZEP for the top layer. To minimize intermixing between the layers, we dissolved $C_{60/70}$ @ZEP in a 3:10 binary solvent of *o*-DCB and xylene because xylene is a good solvent for fullerenes but a poor solvent for ZEP. To clarify the difference in sensitivity between the single layer and bilayer systems, we made a bilayer system with a relatively thick film of 250 nm. Single layers of 0, 10, 20, and 30 wt% $C_{60/70}$ @ZEP with the equal thickness of 250 nm were prepared in the same manner as the top layer of the bilayer system.

ZEP was spin-coated on a Si substrate to a thickness of 200 nm and baked at 180°C for 30 min, and then $C_{60/70}$ @ZEP was spin-coated on the ZEP film to a thickness of 50 nm and baked at 165°C for 30 min (Fig. 9.25(1)). The film-coated substrate was exposed with the JBX-5FE, and the exposed substrate was developed in ZED-N50 for 1 min to form an overhang pattern (Fig. 9.25(2)). In lift-off experiments, we used a thinner film of 80 nm (30 nm for the top and 50 nm for the bottom) instead of the 250-nm film to improve the resolution. Titanium (Ti) was deposited on the patterned resist film to a thickness of 20 nm by electron-beam deposition (Fig. 9.25(3)). The Ti film on the resist film was lifted off with a resist remover (1-methyl-2-pyrrolidone) by ultrasonic agitation and then the Ti patterns were transferred to the substrate by dry etching (Fig. 9.25(4)).

We examined the sensitivity characteristics of the $C_{60/70}$ @ZEP single-layer and bilayer systems. The single-layer and bilayer systems of 10, 20, and 30 wt% are plotted in Fig. 9.26a-c, respectively, in comparison with the 0 wt% (pure ZEP) single-layer system. The sensitivity curves for all the bilayers change in the same manner as those for fullerene-incorporated single layers in the lower dose range, and deviate from the single layers and approach the curve for the pure ZEP single layer in the higher dose range. This is explained as follows: Each bilayer dissolves at the same rate as the corresponding fullerene-incorporated single layer until the interface of the top and bottom layers, because both the bilayer and the single layer contain the same amount of fullerene, and then starts to dissolve rapidly because of the absence of fullerene in the bottom layer. Because there is a large difference in sensitivity between the single layer and the bilayer in the 20 and 30 wt% systems compared with the 10 wt% system, it is expected that the 20 and 30 wt% bilayers can produce much more favorable overhang patterns for lift-off than the 10 wt% bilayer. In addition, the bilayer systems show a sensitivity of $\sim 60 \mu\text{C}/\text{cm}^2$, which is about 10% lower than that of pure ZEP but is still roughly 5 or 100 times higher than that of PMMA or calixarene. This verifies that nanometer dot patterns can be written in a much shorter time by using the $C_{60/70}$ @ZEP bilayer resist systems.

Figure 9.27 shows a cross-sectional view of 150-nm-pitch patterns formed in the 20 wt% bilayer. The patterns were exposed with a line dose of 0.4 nC/cm. The resist thickness is 50 nm for the top and 200 nm for the bottom layer, and the opening slit at the top surface is approximately 20 nm wide. Overhang patterns were successfully created as expected from the sensitivity curve measurement.

Figure 9.28 shows an array of about 35-nm-diameter and 75-nm-period Ti dots obtained after lift-off on a GaAs substrate. The dot patterns are formed with no

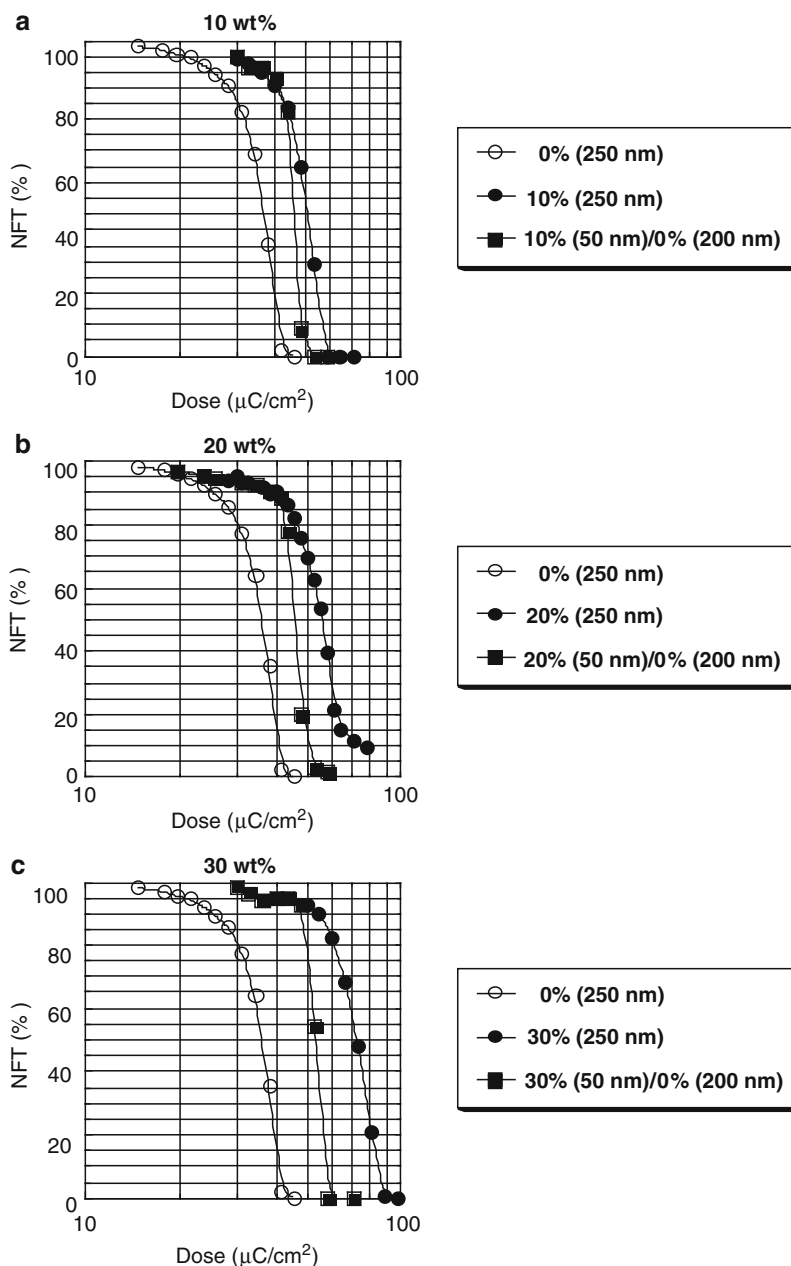


Fig. 9.26 Sensitivity curves of $\text{C}_{60/70}$ @ZEP bilayer resist systems in comparison with those of single layers. Fullerene content (the mixture of C_{60} and C_{70}) is as follows: (a) 10 wt%, (b) 20 wt%, and (c) 30 wt%, respectively. Film thickness is 250 nm in both the bilayer and the single-layer systems. All samples were developed in ZED-N50 for 1 min

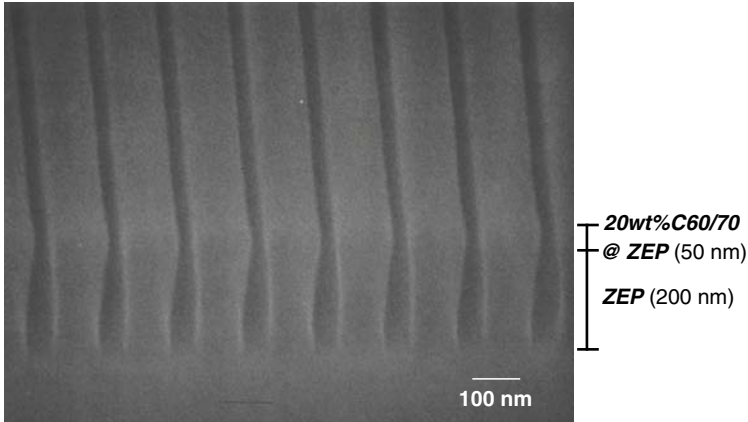
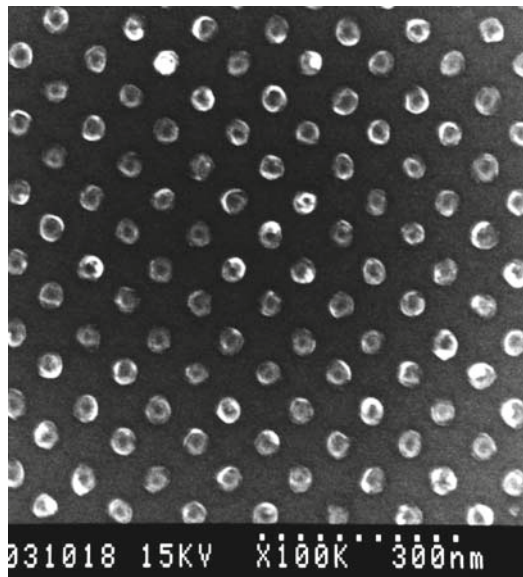


Fig. 9.27 Cross-sectional view of overhang patterns formed in the 20 wt% C_{60/70}@ZEP/ZEP bilayer resist system. Pitch is 150 nm and thickness is 250 nm (50 nm for the top and 200 nm for the bottom layer)

Fig. 9.28 An array of about 35-nm diameter and 75-nm period Ti dots obtained after lift-off on a GaAs substrate



detachment from the substrate and show good uniformity. During the Ti deposition by electron beam, no heat-induced deformation of resist patterns was observed owing to the enhanced thermal resistance of C_{60/70}@ZEP. This is also an advantage over the PMMA bilayer system.

We have successfully fabricated a quantum box array by using Ti dots formed by the bilayer lift-off as an etching mask. This fabrication is the first example of lithographically-initiated self-organization. The detailed fabrication process is described in [25]. Figure 9.29 shows an atomic force microscope (AFM) image of

Fig. 9.29 AFM image of an array of about 50-nm self-organized InGaAs/AlGaAs box-like structure

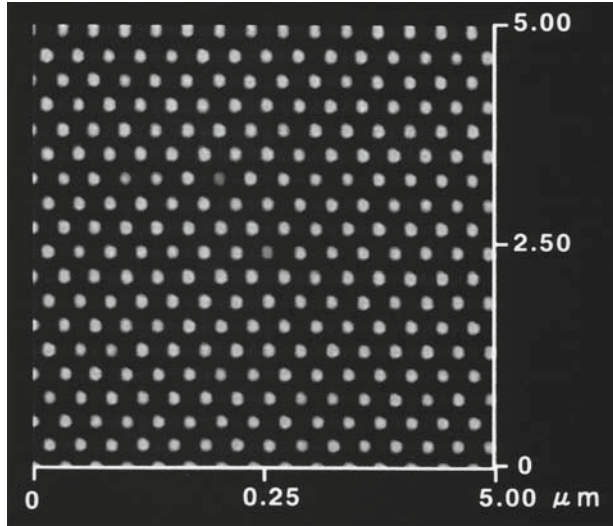
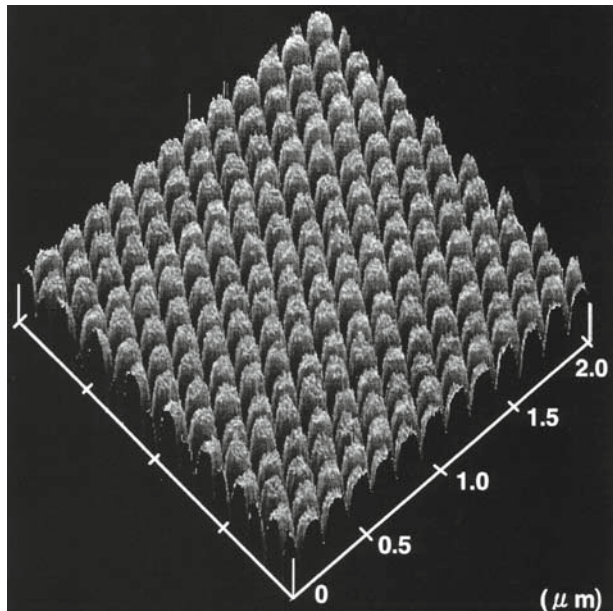


Fig. 9.30 AFM image of a SiC mold for nanoimprint. The pitch and height of the dots are 150 and 25 nm. The diameter at the top is about 95 nm. A nanometer hole array can be formed by simply pressing the mold onto a variety of substrates such as aluminum or polymer materials



an array of self-organized InGaAs/AlGaAs box-like structures. The diameter of the boxes is about 50 nm, and the 310-nm pitch of the initial Ti dots is reflected in the box-like structure array.

Another example of the bilayer lift-off application is a SiC mold for nanoimprint. Since SiC is a hard material with less likelihood of breakage or pattern distortion during pressing and inert to most chemicals used for cleaning, it is an ideal mold material for nanoimprinting. A mold with SiC dots was fabricated by C_2F_6 RIE using Ni dots as an etching mask. Figure 9.30 shows an AFM image of the fabricated mold. The diameter of the dots at the top is about 95 nm. The pitch and the height are 150 and 25 nm, respectively. These dot patterns can be inversely transferred to metals or polymer materials by simply pressing the mold onto the materials to produce a high-density nanometer hole array with high throughput [26].

9.4 C_{60} -Derivative Nanocomposite Resists

As described in the previous section, C_{60} has a strong dissolution inhibiting effect, which limits the amount of C_{60} incorporated into ZEP. One way to overcome this limit is to introduce a high-soluble functional group into a C_{60} molecule. We have synthesized several C_{60} derivatives and investigated the resist characteristics after preparing nanocomposite resists with ZEP.

In the following sections, the synthesis of C_{60} derivatives and the resist characteristics of C_{60} -derivative nanocomposite resists are described. The possibility of using a C_{60} derivative to make a chemical amplification nanocomposite resist is also examined.

9.4.1 Synthesis of C_{60} Derivatives

We synthesized eight C_{60} derivatives: (I) *N*-[4-{endo-methyl(trioxyethylene)oxycarbonyl}phenyl]azafullerene ($C_{60}NEO_3$), (II) *N*-[4-(1-naphthyl)iminocarbonyl]phenylazafullerene ($C_{60}NNp$), (III) *N*-[4-(4'-phenoxy)phenyliminocarbonyl]phenylazafullerene ($C_{60}N\phi O\phi$), (IV) *N*-[4-{endo-methyl(trioxyethylene)oxycarbonyl}phenyl]azafullerene (double adduct) [$C_{60}(NEO_3)_2$], (V) diphenylmethanofullerene ($C_{60}C\phi_2$), (VI) bis(*p*-methoxyphenyl)methanofullerene ($C_{60}CMO\phi_2$), (VII) diphenylmethanofullerene (double adduct) [$C_{60}(C\phi_2)_2$], (VIII) bis(*p*-methoxyphenyl)methanofullerene (double adduct) [$C_{60}(CMO\phi_2)_2$].

The molecular structure of derivatives is depicted in Fig. 9.31. The derivatives are grouped into two types: phenylazafullerene and methanofullerene, where the former includes derivatives (I), (II), (III), and (IV) and the latter derivatives (V), (VI), (VII), and (VIII). We selected these two types of derivatives because of the ease of their synthesis. The derivatives of the same type can be synthesized using basically the same process. Here, we describe the synthesis of (I) and (V) as examples of phenylazafullerene [27] and methanofullerene derivatives [28], [29]. Figures 9.32 and 9.33 outline the synthesis processes.

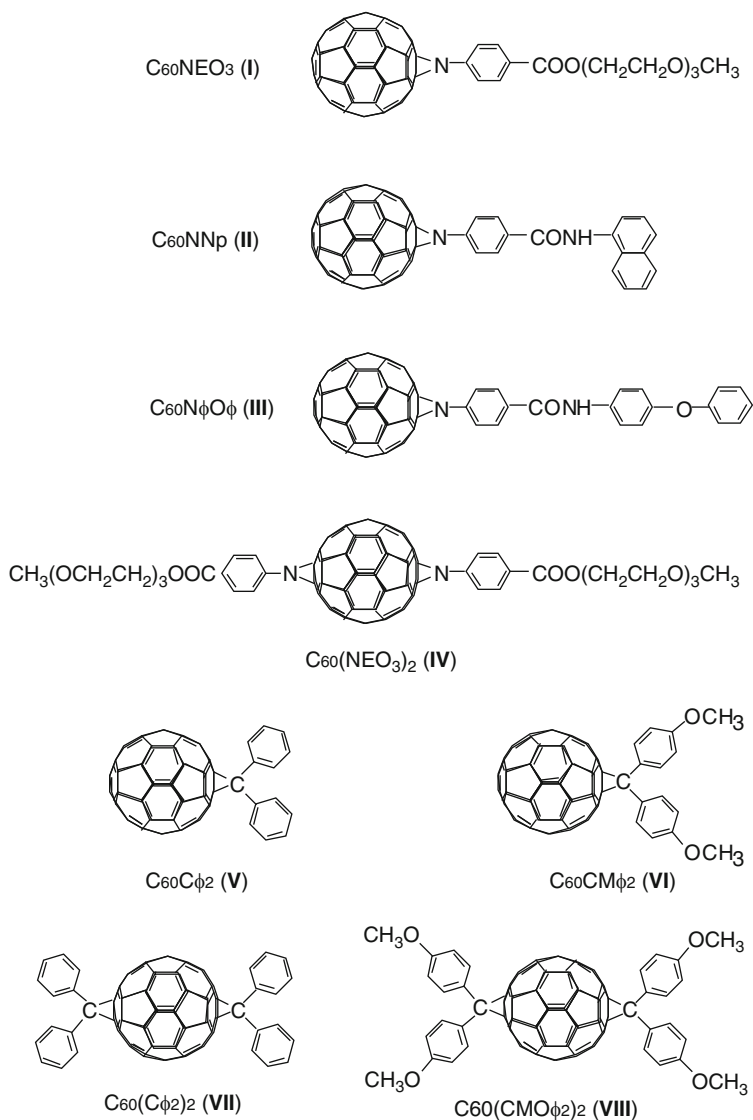
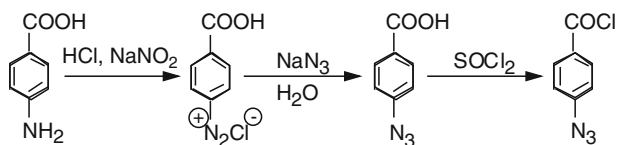


Fig. 9.31 C_{60} derivatives synthesized for nanocomposite resist formation

9.4.2 Phenylazafullerenes

(1) Synthesis of *p*-azidobenzoyl chloride

To a beaker with a stirring bar was added *p*-aminobenzoic acid (104.5 g, 0.762 mol) and concentrated hydrochloric acid (9.6 N, 400 mL), and the mixture was

(1) Synthesis of *p*-azidobenzoyl chloride

(2) Synthesis of 4-{endomethyl(trioxyethylene)oxycarbonyl}phenylazide

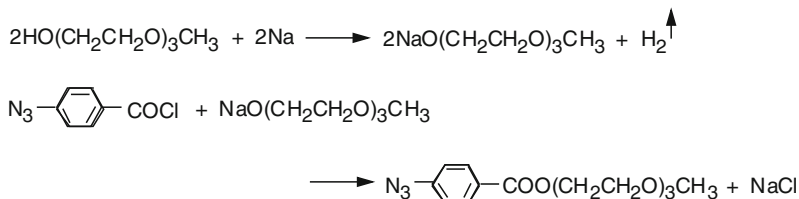
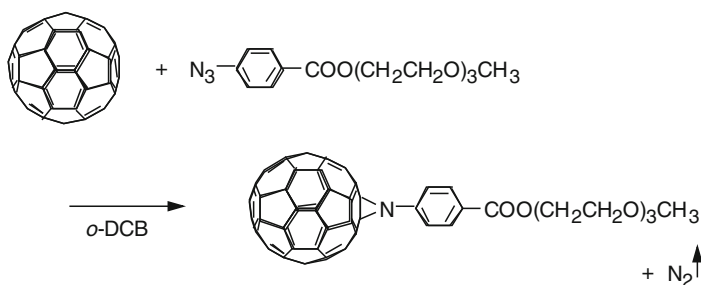
(3) Synthesis of C₆₀NEO₃

Fig. 9.32 Synthesis process of C₆₀ derivative (I): C₆₀NEO₃

stirred at room temperature. After the temperature had risen to 60°C, distilled water (2000 mL) was added to dissolve the mixture completely. Then, the beaker was moved to an ice bath for cooling, and an aqueous solution (600 mL) of sodium nitrite (46.60 g, 0.675 mol) was added to the mixture before the precipitation of a solid substance. Then, an aqueous solution (400 mL) of sodium azide (48.02 g, 0.696 mol) was slowly added to the mixture solution to form a yellowish-white foamy solid substance. The solid substance was collected by filtration and dried. The dried substance was dissolved in ethanol heated at 50°C and then the yellow part was removed by adsorption with activated carbon. Recrystallization by cooling the ethanol solution down to room temperature produced yellowish-white crystals of *p*-azidobenzoic acid (66.35 g, 53.39% yield). The product was confirmed by Fourier transform infrared (FT-IR) absorption spectroscopy.

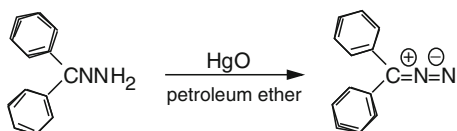
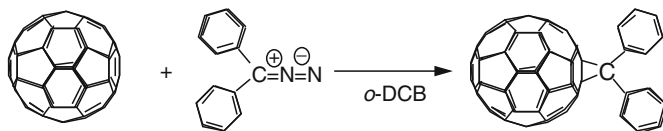
(1) Synthesis of diphenyldiazomethane(2) Synthesis of C₆₀Cφ₂

Fig. 9.33 Synthesis process of C₆₀ derivative (V): C₆₀Cφ₂

A four-necked round-bottom flask equipped with a stirrer, a nitrogen inlet, and a Dimroth condenser with a calcium chloride tube was heated and dried under nitrogen gas to completely remove water. The flask was charged with *p*-azidobenzoic acid (66.35 g, 0.407 mol) and then distilled thionyl chloride (350 mL). The mixture was heated to 80°C in an oil bath and was refluxed for 4 h. After refluxing, thionyl chloride was removed by reduced pressure and a quantity of an orangish-white solid of *p*-azidobenzoyl chloride was obtained. The product was confirmed by FT-IR, proton nuclear magnetic resonance (¹H-NMR) spectroscopy, and carbon nuclear magnetic resonance (¹³C-NMR) spectroscopy.

(2) Synthesis of 4-{endomethyl(trioxyethylene)oxycarbonyl}phenylazide

A four-necked round-bottom flask equipped with a stirrer, a nitrogen inlet, and a Dimroth condenser with a calcium chloride tube was heated and dried under nitrogen gas to completely remove water. The flask was charged with triethylene glycol monomethyl ether (45.25 g, 276 mmol) and metal sodium (0.642 g, 28.0 mmol). The mixture was heated to 65°C and was completely dissolved with the stirrer. After cooling the mixture to 0°C with ice, a tetrahydrofuran solution (100 mL) of *p*-azidobenzoyl chloride (5.04 g, 27.8 mmol) was slowly added to the mixture. The reaction was advanced at room temperature for 24 h. After the completion of the reaction, the by-product sodium chloride was filtered out and the solvent was removed by reduced pressure. The residual starting material was absorbed and removed with a large amount of water. Then the reaction product was dissolved in chloroform, rinsed with water, and subsequently dried. After removing the chloroform by reduced pressure, an orange-colored viscous liquid of 4-{endomethyl(trioxyethylene)oxycarbonyl}phenylazide was obtained (7.075 g, 82.4% yield).

(3) Synthesis of $C_{60}NEO_3$

A four-necked round-bottom flask equipped with a stirrer, a nitrogen inlet, and a Dimroth condenser with a calcium chloride tube was charged with *o*-DCB and C_{60} (2.00 g, 2.78 mmol). The mixture was slowly heated to 140°C to obtain a completely dissolved solution. Then, an *o*-DCB solution (30 mL) of 4-{endomethyl(trioxyethylene)oxycarbonyl}phenylazide (0.398 g, 2.78 mmol) was added to the mixture and the reaction was advanced for 13 h. After the reaction solution was concentrated by reduced pressure, the resulting solution was separated by styrene-gel column chromatography using *o*-DCB as an elution solvent. The second fraction was an *o*-DCB solution of $C_{60}NEO_3$. After removing the solvent, a black powder of $C_{60}NEO_3$ was obtained (650 mg).

The first fraction was an *o*-DCB solution of double adducts of NEO_3 , [$C_{60}(NEO_3)_2$], which contained some quantity of multiple adducts. Because it was difficult to control the relative position of the two NEO_3 's on the C_{60} molecule, the double adducts may also contain a variety of structural isomers. However, we assume that the isomers have little effect on the difference in dry-etch resistance because resistance enhancement is primarily provided by the C_{60} shell.

9.4.2.1 Methanofullerenes

(1) Synthesis of diphenyldiazomethane

A four-necked round-bottom flask equipped with a stirrer, a nitrogen inlet, and a Dimroth condenser with a calcium chloride tube was charged with benzophenone hydrazone (2.74 g, 13.9 mmol), dried petroleum ether (7.65 mL), and mercuric oxide (3.05 g, 13.9 mmol). The mixture was stirred at room temperature for 6 h. After filtering the reaction solution, the solvent was removed by reduced pressure. Then, the reaction product was dried in a vacuum at room temperature to obtain a reddish-purple solid of diphenyldiazomethane (2.31 g, 91.8% yield). The product was confirmed by FT-IR and 1H -NMR.

(2) Synthesis of $C_{60}C\phi_2$

A four-necked round-bottom flask equipped with a nitrogen inlet, a dropping funnel, and a Dimroth condenser with a calcium chloride tube was heated and dried under nitrogen gas to completely remove water. The flask was charged with fullerene (2.01 g, 2.91 mmol) and distilled *o*-DCB (50 mL). The mixture was stirred and an *o*-DCB solution (50 mL) of diphenyldiazomethane (2.10 g, 11.6 mmol) was slowly added through the funnel to the mixture. The reaction was advanced first at room temperature for 22 h and then at 50°C for 2 h. Then, the reaction solution was concentrated at 45°C by reduced pressure. Finally, the components of the reaction solution were separated by styrene-gel column chromatography using *o*-DCB as an elution solvent. The second fraction was an *o*-DCB solution of $C_{60}C\phi_2$. After removal of the solvent, a reddish-purple solid of $C_{60}C\phi_2$ was obtained. The product was confirmed by time-of-flight mass spectroscopy as well as by FT-IR and UV spectroscopy.

Table 9.4 Evaluation of C₆₀-derivative@ZEPs

Derivatives	Solubility (g/L)			Sensitivity (μC/cm ²)	Resolution	
	<i>o</i> -DCB	PGMEA	NER ^a		γ-values	50-nm L&S
(I) C ₆₀ NEO ₃	~100	0	1/0.9/0.85/0.88	50/52/55/87	6.3/9.2/8.1/7.9	Good
(II) C ₆₀ NNp	~50	0	1/0.93/0.84/0.92	50/43/59/63	6.3/14.3/6.3/5.4	Good
(III) C ₆₀ NφOφ	~50	0	1/0/92/0.84/-	50/62/62/-	6.3/22.9/9.4/-	Good
(IV) C ₆₀ (NEO ₃) ₂	>100	~50	1/0.96/0.9/0.89	170/170/190/215	5.7/5.7/5.1/4.9	Bridging
(V) C ₆₀ Cφ ₂	0	0	-	-	-	-
(VI) C ₆₀ CMOφ ₂	0	0	-	-	-	-
(VII) C ₆₀ (Cφ ₂) ₂	>100	0	1/0.98/0.91/0.84	170/200/280/300	5.7/6.3/8.1/5.7	Good
(VIII) C ₆₀ (Cφ ₂) ₂ C ₆₀ (CMOφ ₂) ₂	>100	>100	1/0.96/0.9/0.87	120/120/150/185	8.0/7.5/5.0/4.2	good

^aNER is normalized etch rate. A/B/C/D corresponds to the values at 0, 10, 30, and 50 wt%.

(I), (II), and (III) were exposed with a 50-kV EB machine and (IV), (VII), and (VIII) were done with a 100kV EB.

As in the case of the synthesis of C₆₀NEO₃, the first fraction was an *o*-DCB solution of double adducts, [C₆₀(Cφ₂)₂], which also contained some quantity of multiple adducts and a variety of structural isomers of the double adducts.

9.4.3 Resist Characteristics

We examined the solubility of C₆₀ derivatives and then investigated the resist characteristics after preparing nanocomposite resists with ZEP using the derivatives.

Table 9.4 summarizes the solubility data and the resist characteristics of the nanocomposite resists. The solubility of C₆₀ in *o*-DCB tends to increase by introducing functional groups. However, single adducts of metanofullerenes (C₆₀Cφ₂ and C₆₀CMOφ₂) are not soluble at all. Double adducts are, on the whole, more soluble than single ones. Two derivatives, C₆₀(NEO₃)₂ and C₆₀(CMOφ₂)₂, are soluble in a photoresist solvent, propylene glycol 1-monomethyl ether 2-acetate (PGMEA). Of these two, C₆₀(CMOφ₂)₂ is extremely soluble (>100 g/L) in PGMEA.

We prepared six C₆₀-derivative@ZEPs in the same manner as C₆₀@ZEP. They are denoted C₆₀NEO₃@ZEP, C₆₀NNp@ZEP, C₆₀NφOφ@ZEP, C₆₀(NEO₃)₂@ZEP, C₆₀(Cφ₂)₂@ZEP, and C₆₀(CMOφ₂)₂@ZEP for simplicity. The two single-adduct metanofullerene derivatives mentioned above could not be used for resist preparation because of their insolubility in *o*-DCB. Resist characterization was done in the same way as for C₆₀@ZEP or C_{60/70}@ZEP. The sensitivity and resolution of C₆₀NEO₃@ZEP, C₆₀NNp@ZEP, and C₆₀NφOφ@ZEP were evaluated with the JBX-5FE, while those of C₆₀(NEO₃)₂@ZEP, C₆₀(Cφ₂)₂@ZEP, and C₆₀(CMOφ₂)₂@ZEP were done with a 100-kV electron-beam machine (JBX-9300FS) [30]. Resolution was evaluated by measuring line-and-space patterns with 100-nm pitch and 150-nm height.

Figure 9.34 shows the normalized etch rate of the six C₆₀-derivative@ZEPs against fullerene-derivative content. On the whole, etch rates of all the C₆₀-derivative@ZEPs tend to decrease with content. However, the decrease is moderate, about

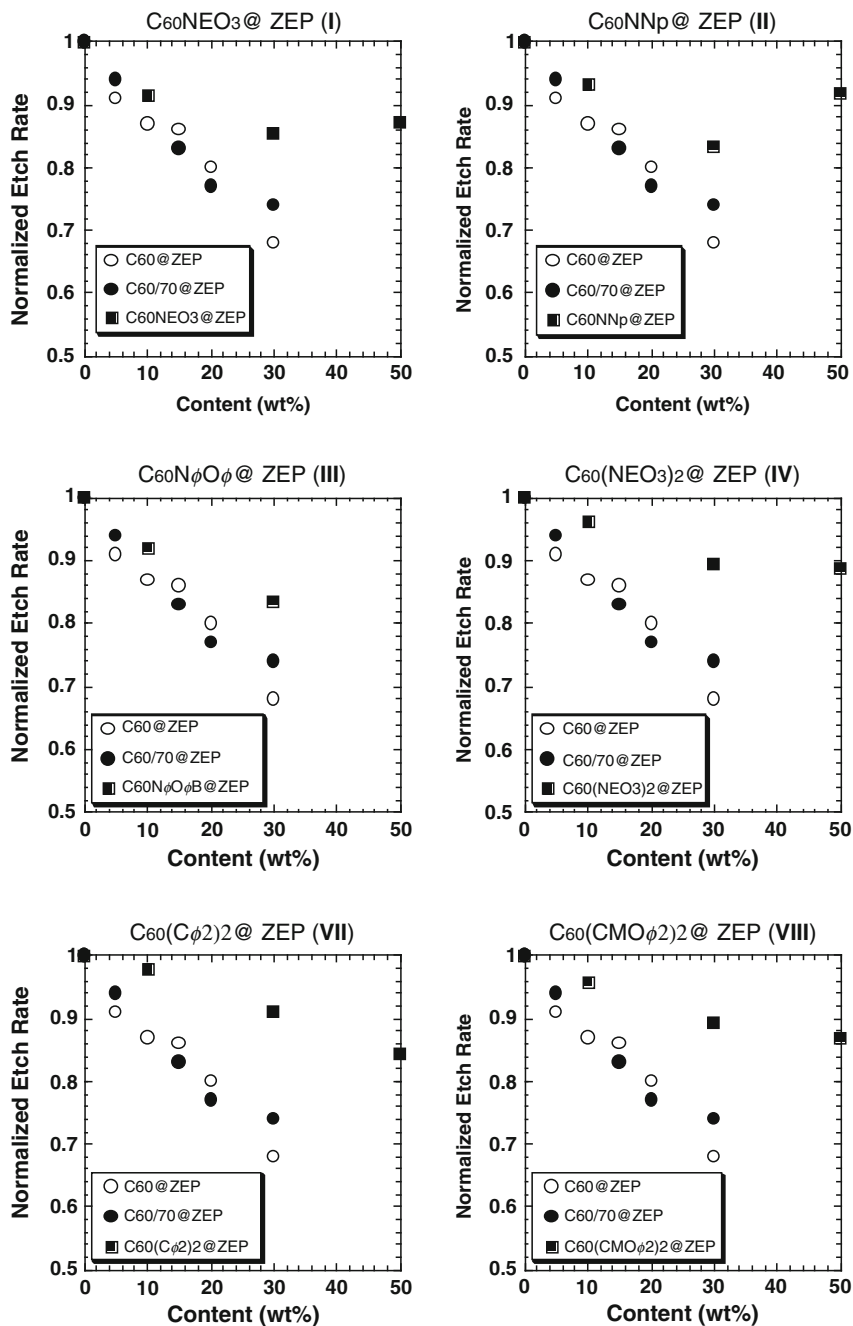


Fig. 9.34 Normalized etch rates of C₆₀-derivative@ZEPs against derivative content. The samples were etched by C₂F₆-RIE (flow: 40 SCCM, pressure: 2.0 Pa, rf power: 100 W)

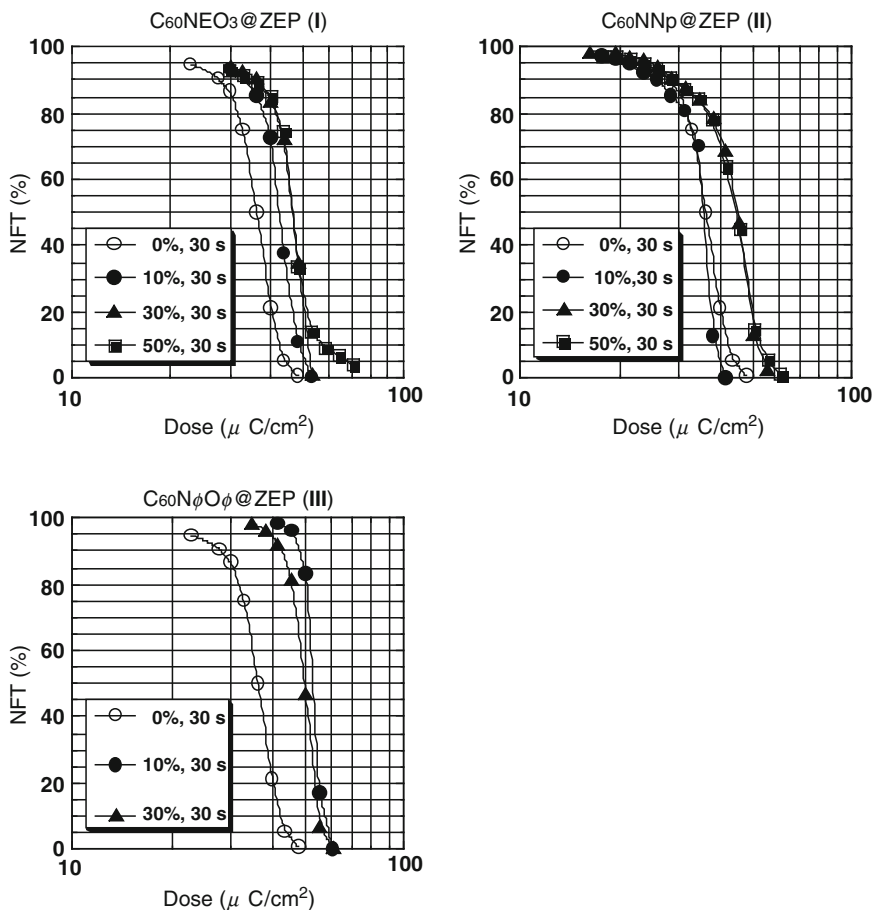


Fig. 9.35 Sensitivity curves of C₆₀-derivative@ZEPs: C₆₀NEO₃@ZEP (I), C₆₀NNp@ZEP (II), C₆₀φOφ@ZEP (III). Film thickness is 150 nm. The samples were exposed with a 25-kV exposure system and developed in ZED-N50 for 30 s

0.9–0.8, which corresponds to a resistance enhancement of about 10–25%, even at a higher content of 30–50 wt%, whereas the etch rate decreases to around 0.7 in C₆₀@ZEP or C_{60/70}@ZEP at 30 wt%. This means that dry-etch enhancement effect of the six derivatives is not so large compared with C₆₀ or C₇₀. Because the enhancement effect of fullerene nanocomposite resists primarily depends upon the number of C₆₀ and C₇₀ molecules incorporated, the effect should be lower for C₆₀ derivatives with bulky functional groups when they are incorporated in the matrix resist at the same weight percentage as C₆₀ or C₇₀. Thus, the C₆₀ derivatives should be as small as possible.

Figures 9.35 and 9.36 show the sensitivity curves of the six C₆₀-derivative@ZEPs. The sensitivity of C_{60/70}@ZEP decreases as the content increases as already

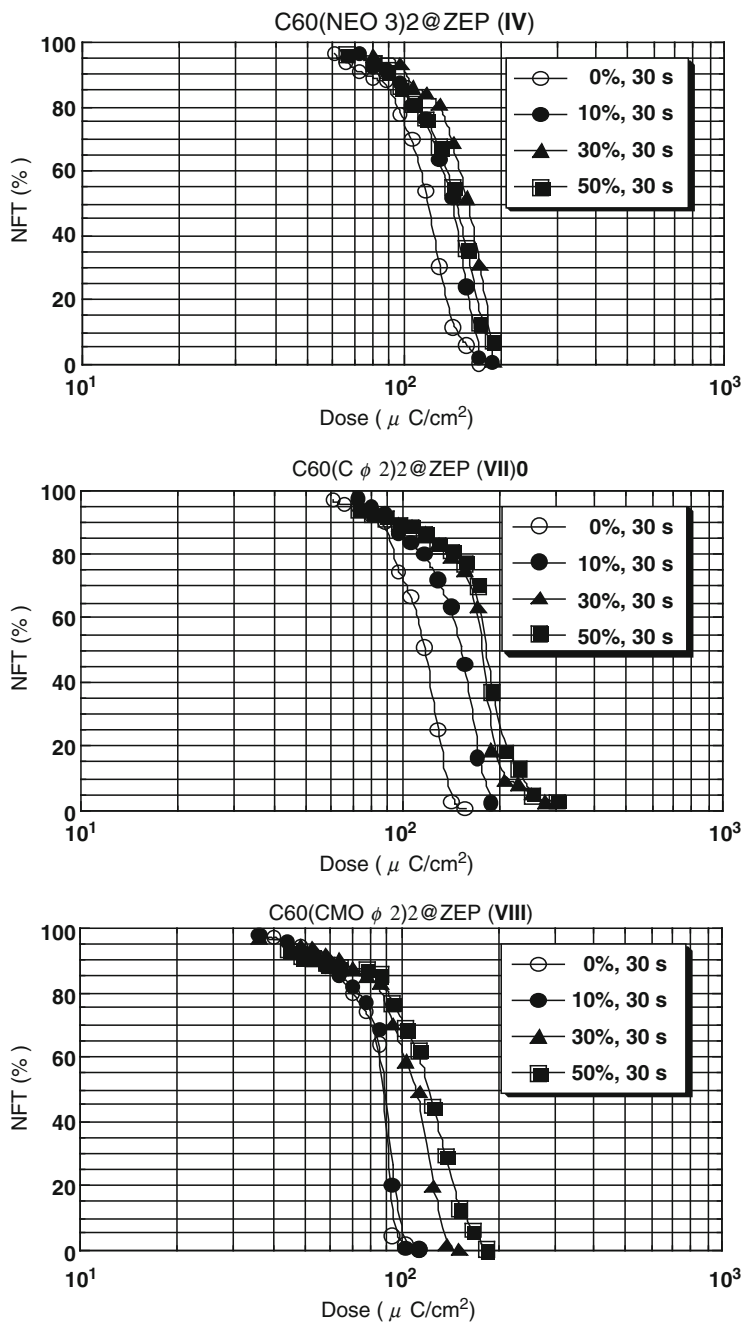


Fig. 9.36 Sensitivity curves of C_{60} -derivative@ZEPs: $C_{60}(\text{NEO}_{3/2})@ZEP$ (IV), $C_{60}(\text{C}\phi_2)_2@ZEP$ (VII), $C_{60}(\text{CMO}\phi_2)_2@ZEP$ (VIII). Film thickness is 150 nm. The samples were exposed with a 100-kV exposure system and developed in ZED-N50 for 30 s

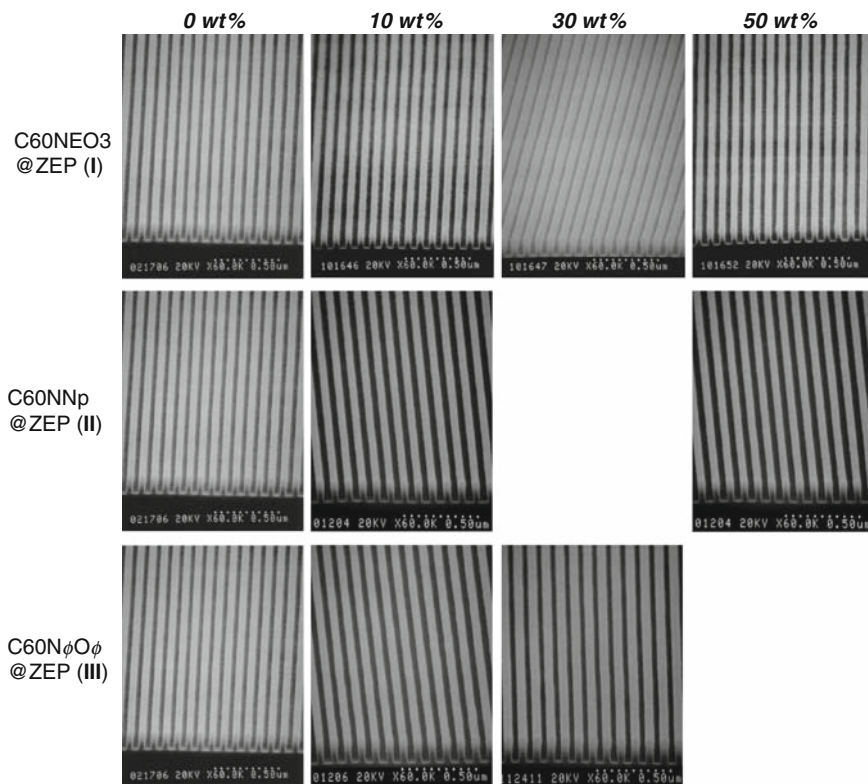


Fig. 9.37 100-nm pitch patterns of C_{60} -derivative@ZEPs: $C_{60}NEO_3$ @ZEP (I), $C_{60}NNp$ @ZEP (II), $C_{60}N\phi O\phi$ @ZEP (III). Film thickness is 150 nm. The samples were exposed with a 25-kV exposure system and developed in ZED-N50 for 30 s

shown in Fig. 9.16, but the sensitivity decrease is minimized in the C_{60} -derivative@ZEPs even at higher contents of 30 and 50 wt%. This is clearly because of the solubility enhancement provided by the C_{60} derivatives. The sensitivities evaluated with the 25-kV system are roughly 3–4 times higher than those evaluated with the 100-kV system. This is due to the general principle that sensitivity is approximately inversely proportional to acceleration voltage. It is noteworthy that 10 wt% $C_{60}N\phi O\phi$ @ZEP has an extremely high γ -value of 22.9, which is about three-and-a-half times higher than that of ZEP. This high γ -value is probably due to a large difference in the dissolution rate between the exposed and unexposed areas induced by $C_{60}N\phi O\phi$. The derivative has a moderate dissolution-inhibiting effect on the developer compared to C_{60} shown in the sensitivity curves, and a small amount of the derivative probably limits dissolution more effectively in the unexposed area than in the exposed area. Because the molecular weight of ZEP is unchanged in the unexposed area, the dissolution rate of ZEP can be further decreased in the unexposed area by incorporating a small amount of the derivative. On the other hand, in the

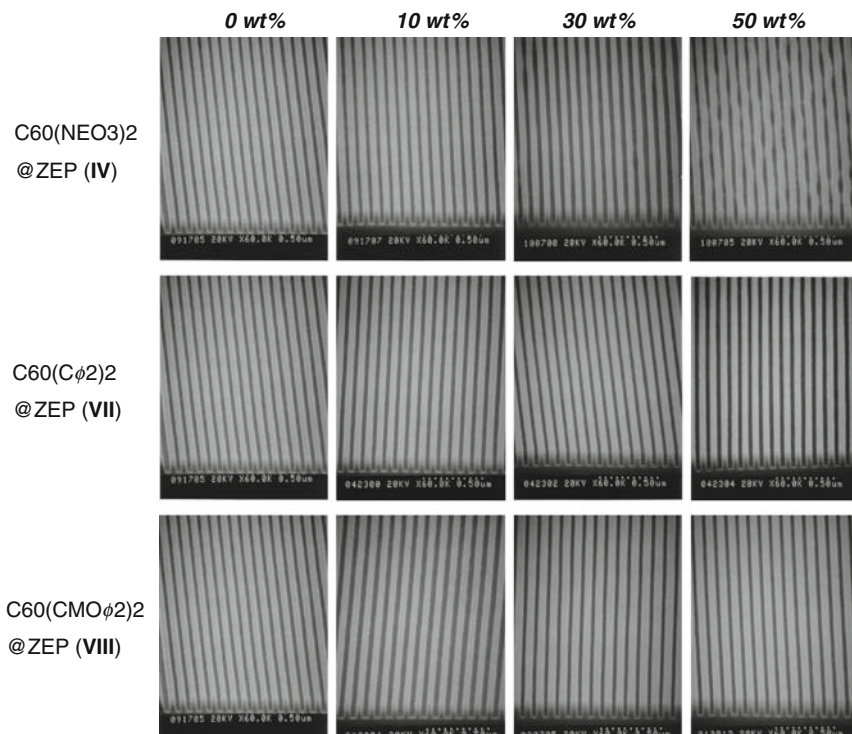


Fig. 9.38 100-nm pitch patterns of C_{60} -derivative@ZEPs: $C_{60}(\text{NEO}_3)_2$ @ZEP (IV), $C_{60}(\text{C}\phi_2)_2$ @ZEP (VII), $C_{60}(\text{CMO}\phi_2)_2$ @ZEP (III). Film thickness is 150 nm. The samples were exposed with a 100-kV exposure system and developed in ZED-N50 for 30 s

exposed area, where the molecular weights of ZEP are much smaller, the rate cannot be effectively decreased by the derivative as long as the incorporation content is low. In C_{60} -derivative molecular design, it is necessary to consider that the molecules are highly soluble in the resist solvent and also have a moderate dissolution-inhibiting effect on the resist developer.

Figures 9.37 and 9.38 show SEM micrographs of the 100-nm-pitch patterns of the six C_{60} -derivative@ZEPs. Micrographs for 30 wt% $C_{60}\text{-NNp@ZEP}$ and 50 wt% $C_{60}\text{-N}\phi\text{O}\phi\text{@ZEP}$ are missing because of inadequate sample preparation. All the resist samples except 50 wt% $C_{60}(\text{NEO}_3)_2$ @ZEP show high-quality patterns and are resolvable at least up to 50 nm. The bridging in the 50 wt% $C_{60}(\text{NEO}_3)_2$ @ZEP was caused by heating during SEM observation. It is assumed that the thermal enhancement effect of $C_{60}(\text{NEO}_3)_2$ is small because it has two rather flexible functional groups. The six C_{60} derivatives, on the whole, have the same effect on resolution as C_{60} or C_{70} . To verify the resolution enhancement by $C_{60}\text{-N}\phi\text{O}\phi$ expected from the extremely high γ -value, we need to evaluate resolution using patterns with dimensions smaller than 50 nm.

9.4.4 Chemical Amplification System

The chemical amplification resist drastically increases sensitivity by employing the mechanism in which acid generated upon exposure acts as a catalyst and initiates a chain reaction [31]. The first practically viable chemical amplification resist was developed by Ito and Willson et al. [32]. Since their pioneering work, chemical amplification resists have become the main focus of the research and development in the resist industry. Currently, high-sensitivity ArF chemical amplification resists are used for ULSI fabrication. Chemical amplification resists will be applied also to next-generation EUV lithography to meet the demand for high throughput [33]. A theoretical study has suggested that introducing aromatic groups into a polymer reduces absorption at 13-nm wavelength because of their small linear absorption coefficient [34]. This means that fullerene, which is aromatic, can be used as a resist material in EUV lithography.

We have examined a chemical amplification nanocomposite resist system that incorporates $C_{60}(C_{60}O\phi_2)_2$ into a chemical amplification positive-type electron-beam resist, CAP112PM (Tokyo Ohka Kogyo Co.). Because $C_{60}(C_{60}O\phi_2)_2$ is soluble in

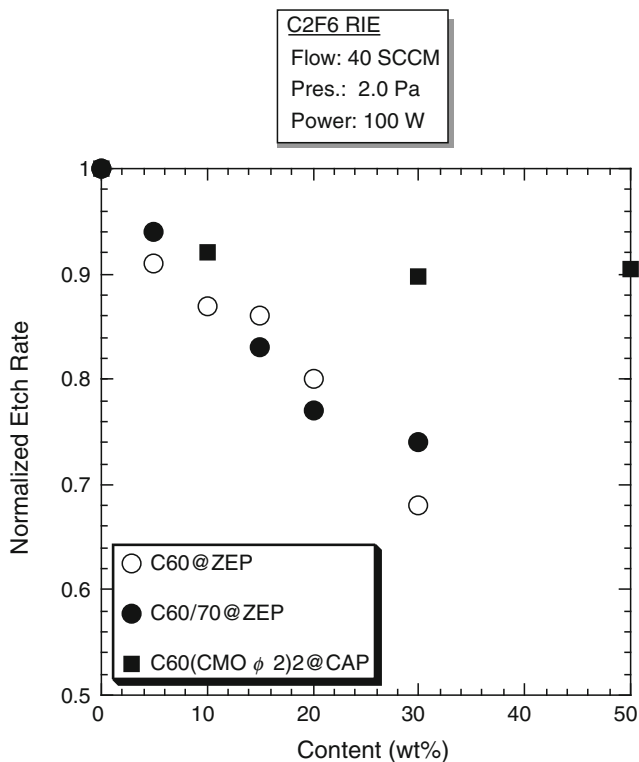


Fig. 9.39 Normalized etch rate of $C_{60}(C_{60}O\phi_2)_2$ @CAP

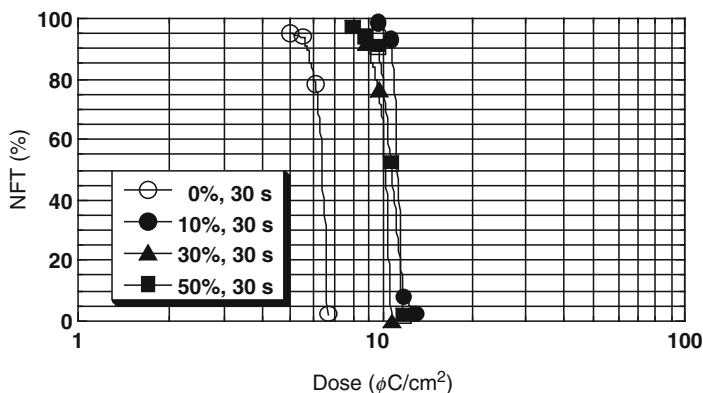


Fig. 9.40 Sensitivity curves of $C_{60}(C_{60}O\phi_2)_2@CAP$. Film thickness is 90 nm. The samples were exposed with a 100-kV exposure system and developed in TMAH for 30 s

PGMEA, the derivatives could be readily mixed with a PGMEA solution of CAP112PM (denoted $C_{60}(C_{60}O\phi_2)_2@CAP$). We prepared 0, 10, 30, and 50 wt% nanocomposite resist samples. Resist characteristics were examined in the same way as $C_{60}@ZEP$ or $C_{60/70}@ZEP$. The enhancement of the etch resistance was evaluated by measuring the etch rate of C_2F_6 RIE. Sensitivity was examined by plotting sensitivity curves. And resolution was measured by observing 100-nm-pitch 90-nm-height line-and-space patterns. Resist samples were prebaked on a hotplate at $90^\circ C$ for 90 s after spin-coating. The samples were exposed with the JBX-9300FS for sensitivity and resolution evaluation. The exposed samples were post-baked on the hotplate at $110^\circ C$ for 90 s and then developed in a 2.38% tetramethylammonium hydroxide (TMAH) aqueous solution for 30 s.

Figure 9.39 shows the normalized etch rate against $C_{60}(C_{60}O\phi_2)_2$ content. The etch rate tends to decrease like it does for $C_{60}(C_{60}O\phi_2)_2@ZEP$. Even at the highest content of 50 wt%, the normalized etch rate is around 0.9, that is, the resistance enhancement is about 10%. This moderate enhancement might be attributed to the bulkiness of the derivative as observed in C_{60} -derivative@ZEPs.

Figure 9.40 shows the sensitivity curves of $C_{60}(C_{60}O\phi_2)_2@CAP$. The film thickness is 90 nm. Sensitivity is $\sim 7 \mu C/cm^2$ for the pure CAP and $\sim 12 \mu C/cm^2$ for the $C_{60}(C_{60}O\phi_2)_2@CAP$ s. The sensitivity of the $C_{60}(C_{60}O\phi_2)_2@CAP$ s is roughly 20 times higher than that of C_{60} -derivative@ZEPs (at 100 kV). This demonstrates that the sensitivity of nanocomposite resists can be increased by using chemical amplification resists as the matrix resists.

Because the $C_{60}(C_{60}O\phi_2)_2@CAP$ s exhibits relatively high γ -values of 17.9, 16.3, 17.9, and 9.5 for 0, 10, 30, and 50 wt%, respectively, we expected that we could create high-contrast nanometer patterns. However, we could not create such patterns probably because of the effect of acid diffusion in CAP112PM.

Presently there are very few commercially available chemical amplification positive-type electron-beam resists for nanolithography other than CAP112PM. This limits our study of the chemical amplification nanocomposite resist system.

It is expected that high-performance chemical amplification electron-beam resists will be developed in a few more years and that this will accelerate the study of this new nanocomposite resist system. Because basic exposure mechanism is the same in both EBL and EUV lithography [35], [36] and fullerene is a potential material for EUV resists, we believe that the new system is a promising candidate for EUV resists as well as for electron-beam resists.

9.5 Conclusions

A new resist system that incorporates high-resistance and sub-nanometer-size fullerene molecules into a resist material has been examined for nanolithography. A system composed of fullerene (C_{60} and/or C_{70}) and a widely used positive-type electron-beam resist (ZEP520) exhibit about 10-40% enhancement of dry-etch resistance, which makes it possible to improve resolution by resist thinning. The enhanced thermal resistance of the system facilitates the fabrication of nanometer-size metal dot patterns by lift-off using the bilayer resist system. C_{60} -derivative nanocomposite systems (C_{60} -derivative@ZEPs) exhibit a moderate resistance enhancement (about 10-25%) and present nanometer patterns with a minimal decrease in sensitivity and without losing the potential resolution. Because of the similarity of the basic exposure mechanism and of the expected low absorption of fullerene to EUV, chemically amplified C_{60} -derivative nanocomposite systems are promising candidates for EUV resists as well as for electron-beam resists.

References

1. Reiser A (1989) Photoreactive Polymers. Wiley, New York
2. Willson CG, Dammel RA and Reiser A (1997) Photoresist Materials: A Historical Perspective. Proc. SPIE3049:28-41
3. ITRS (2005) <http://public.itrs.net/>
4. Kroto HW, Heath JR, O'Brien SC, Curl RF and Smalley RE (1985) C_{60} : Buckminsterfullerene. Nature **318**:162-163
5. Broers AN (1964) Micromachining by sputtering through a mask of contamination laid down by an electron beam. Proceedings of the First International Conference on Electron and Ion Beam Science and Technology, pp 191-204
6. Broers AN, Molzen WW, Cuomo JJ and Wittels ND (1976) Electron-beam fabrication of 80-Å metal structure. Appl. Phys. Lett. **29**(9):596-598
7. Gokan H, Esho S and Ohnishi Y (1983) Dry Etch Resistance of Organic Materials. J. Electrochem. Soc. **130**(1):143-146
8. Kakuchi M, Hikita M and Tamamura T (1986) Amorphous carbon films as resist masks with high reactive ion etching resistance for nanometer lithography. Appl. Phys. Lett. **48**(13):835-837
9. Tada T and Kanayama T (1996) Nanolithography using fullerene films as an electron beam resist. Jpn. J. Appl. Phys. **35**(1A):L63-L65
10. Thompson LF, Willson CG and Bowden MJ (1994) Introduction to Microlithography, 2nd ed. American Chemical Society, Washington, DC
11. Nakamura Y, Takechi S, Tsurunaga Y, Fujino K and Ban Y (1987) Resist characteristics of α -methylstyrene-methyl α -chloroacrylate copolymers. Polym. Preprints **36**(7):2078-2080

12. Chen W and Ahmed H (1993a) Fabrication of 5-7 nm wide etched lines in silicon using 100 keV electron-beam lithography and polymethylmethacrylate resist. *Appl. Phys. Lett.* **62**(13):1499–1501
13. Chen W and Ahmed H (1993b) Fabrication of high aspect ratio silicon pillars of < 10 nm diameter. *Appl. Phys. Lett.* **63**(8):1116–1118
14. Ruoff RS, Tse DS, Malhotra R and Lorents DC (1993) Solubility of C60 in a variety of solvents. *J. Phys. Chem.* **97**(13):3379–3383
15. Scrivens WA and Tour JM (1993) Potent solvents for C60 and their utility for the rapid acquisition of ¹³C NMR Data for fullerenes. *J. Chem. Soc. Chem. Commun.* **15**:1207–1209
16. Ishii T, Nozawa H and Tamamura T (1997a) A nano-composite resist system: A new approach to nanometer pattern fabrication. *Microelectron. Eng.* **35**:113–116
17. Ishii T, Nozawa H and Tamamura T (1997b) Nanocomposite resist system. *Appl. Phys. Lett.* **70**(9):1110–1112
18. Shibata T, Ishii T, Nozawa H and Tamamura T (1997) High-aspect-ratio nanometer-pattern fabrication using fullerene-incorporated nanocomposite resists for dry-etching application. *Jpn. J. Appl. Phys.* **36**(12B):7642–7645
19. DeSalvo GC, Tseng WF and Comas J (1992) Etch rates and selectivities of citric acid/hydrogen peroxide on GaAs, Al_{0.3}Ga_{0.7}As, In_{0.2}Ga_{0.8}As, In_{0.53}Ga_{0.47}As, In_{0.52}Al_{0.48}As, and InP. *J. Electrochem. Soc.* **139**(3):831–835
20. Suemitsu T, Ishii T, Yokoyama H, Enoki T, Ishii Y and Tamamura T (1999) 30-nm-gate InP-based lattice-matched high electron mobility transistors with 350 GHz cutoff frequency. *Jpn. J. Appl. Phys.* **38**(2B):L154–L156
21. Ozawa A, Ohoki S, Oda M and Yoshihara H (1994) Tantalum dry-etching characteristics for X-ray mask fabrication. *IEICE Trans. Electron.* **E77-C**(2):255–261
22. Oku S, Ishii T, Iga R and Hirono T (1999) Fabrication and performance of AlGaAs-GaAs distributed bragg reflector lasers and distributed feedback lasers utilizing first-order diffraction gratings formed by a periodic groove structure. *IEEE J. Sel. Top. Quant. Electron.* **5**(3):682–687
23. Ishii T, Tanaka H, Kuramochi E and Tamamura T (1998) Fabrication of nanometer-order dot patterns by lift-off using a fullerene-incorporated bilayer resist system. *Jpn. J. Appl. Phys.* **37**(12B):7202–7204
24. Fujita J, Ohnishi Y, Ochiai Y and Matsui S (1996) Ultrahigh resolution of calixarene negative resist in electron beam lithography. *Appl. Phys. Lett.* **68**(9):1297–1299
25. Kuramochi E, Temmyo J and Tamamura T (1997) Perfect spatial ordering of self-organized InGaAs/AlGaAs box-like structure array on GaAs (311)B substrate with silicon nitride dot array. *Appl. Phys. Lett.* **71**(12):1655–1657
26. Pang SW, Tamamura T and Nakao M (1998) Direct nano-printing on Al substrate using a SiC mold. *J. Vac. Sci. Technol.* **B16**(3):1145–1149
27. Murata Y (2001) Synthesis of fullerene derivatives and characterization of their composite resists. Master's thesis, Tokyo University of Agriculture and Technology, Tokyo
28. Kishimoto A (2002) Synthesis of fullerene derivatives and their application to nanocomposite resist system. Master's thesis, Tokyo University of Agriculture and Technology, Tokyo
29. Kohazame T (2004) Study of fullerene-derivative composite resists. Master's thesis, Tokyo University of Agriculture and Technology, Tokyo
30. Takemura H, Ohki H and Isobe M (2002) 100 kV high resolution e-beam lithography system, JBX-9300FS. *Proc. SPIE* **4754**:690–696
31. Smith GH and Bonham JA (1973) U.S. Patent 3,779,778
32. Ito H (1999) Chemically amplified resists: Past, present, and future. *Proc. SPIE* **3678**:2–12
33. Gonsalves KE, Thiyagarajan M, Choi JH, Zimmerman P, Cerrina F, Nealey P, Golovkina V, Wallace J, Batina N (2005) High performance resist for EUV lithography. *Microelectron. Eng.* **77**(1):27–35
34. Matsuzawa NN, Oizumi H, Mori S, Irie S, Shirayone S, Yano E, Okazaki S, Ishitani A and Dixon DA (1999) Theoretical calculation of photoabsorption of various polymers in an extreme ultraviolet region. *Jpn. J. Appl. Phys.* **38**(12B):7109–7113
35. Kozawa T and Tagawa S (2006) Acid generation efficiency in a model system of chemically amplified extreme ultraviolet resist. *J. Vac. Sci. Technol.* **B24**(6):L27–L30
36. Kinoshita H, Kurihara K, Ishii Y and Torii Y (1989) Soft X-ray reduction lithography using multilayer mirrors. *J. Vac. Sci. Technol.* **B7**(6):1648–1651

Chapter 10

Sol–Gel Hybrids for Electronic Applications: Hermetic Coatings for Microelectronics and Energy Storage

Andrei Jitianu and Lisa C. Klein

Abstract Hermetic seals are an essential part of microelectronics, namely, micro-electromechanical systems (MEMS) displays using organic-light emitting diodes (OLEDs) and electrochemical devices, such as microbatteries. Hermetic seals have to prevent humidity and other gases from reaching devices and degrading their performance. Typically, the barriers are applied once the devices have been assembled, and, consequently, the sealing material has to be hermetic at low processing temperatures. Hybrid organic–inorganic materials are capable of being applied in a sol–gel process at low temperature. A survey of sol–gel hybrid materials that are finding use in microelectronics is presented.

10.1 Introduction

New devices for the electronic and microelectronic industry present a challenge to materials chemistry research. Materials used for fabrication of microelectronics, microelectromechanical systems (MEMS), liquid crystal displays (LCDs), thin film transistors (TFTs), microbatteries, and especially for organic light emitting devices (OLEDs) have strict requirements, such as low cost, easy processibility, flexibility, transparency, chemical and physical inertness, and hermetic to water, oxygen and

L.C. Klein (✉)

Department of Materials Science and Engineering, Rutgers University,
607 Taylor Road, Piscataway, NJ 08854, USA
e-mail: licklein@rci.rutgers.edu

A. Jitianu

Department of Chemistry, Lehman College, City University of New York, 250 Bedford Park
Boulevard West, Bronx, NY 10468

other gases [1, 2]. Satisfying these requirements leads to better performance and longer lifetime. In particular, chemical and physical inertness means that there are no interactions between components during fabrication and assembly of the devices, and the components do not interact with the external environment.

Generally hermeticity describes the property of a package that contains the critical components of a device, which protects the components from the invasion of water and gases, and from external environmental contamination. The success of creating a hermetic barrier is a function of:

- Bulk permeability of the materials used for sealing
- Quality of Sealing [3]

Barrier materials are classified by their function as barriers against permeation of nitrogen or oxygen. Their efficacy is called oxygen (or nitrogen) transmission rate (OTR) $\text{cm}^3/\text{m}^2 \cdot \text{day}$, barriers against humidity for which the efficiency is measured by water vapor transmission rate (WVTR) $\text{g}/\text{m}^2 \cdot \text{day}$, and barriers which prevent permeation of both gases and humidity and their efficiency is measured by OTR and WVTR.

Chantham [4] showed that there are two mechanisms responsible for gas transport through materials under the influence of a pressure gradient applied across opposing faces of a thick barrier layer:

- Bulk diffusive flow via the solubility-diffusion mechanism (material property).
- Flow through defects in the materials (function of microstructure, meaning inhomogeneities, pinholes, microchannels or microcracks, and grain boundaries).

The mechanism of solubility-diffusion consists of several steps such as absorption of permeate onto barrier surface, solution of permeate into barrier material, diffusion of it through material and desorption onto the opposite surface. Consequently permeation is a function of permeate characteristics, such as size of molecules, molecular mass, chemical and physical interaction with barrier materials.

Besides hermeticity, what are the other desirable characteristics of a hermetic coating? Briefly, the coating must be a dielectric insulator. It should have a coefficient of thermal expansion that matches other components in the device. If the coating initially shows viscous flow, it should be rigid after curing. The coating should be shape conforming. In the long run, the coating must be abrasion resistant, hydrophobic, and oleophobic.

10.2 Humidity Barriers

One of the strictest requirements for new materials in the microelectronics industry is a hermetic barrier to humidity. Generally thin films have been investigated to achieve hermetic barriers. For example, a thin film hermetic barrier for OLED applications has to have a water vapor transmission rate (WVTR) not greater than $\sim 10^{-6} \text{g}/\text{m}^2 \cdot \text{day}$ at 25°C and 40% relative humidity [1, 5]. Figure 10.1 schematically shows the order of magnitude of protection required for various electronic devices and the actual protection given by various materials [1]. It is known that traditional polymeric materials are not efficient barriers to ensure the necessary hermeticity for an extended operating lifetime [2].

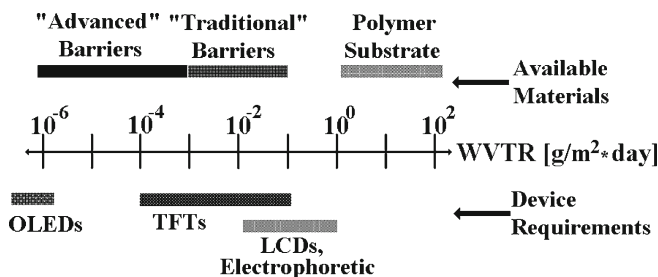


Fig. 10.1 Schematic scale of water vapor transmission rate (WVTR) requirements for common flexible electronic devices and the barrier performance provided by available materials (Reprinted with permission from Elsevier) [1]

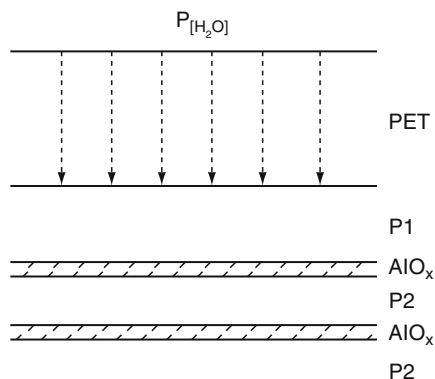
One approach to increase hermetic performance adopted by the food industry is to use metal- or metal oxide-coated plastic films. The barrier performance of these hybrid materials is limited by intrinsic defects [3, 5] and roughness [2]. In fact, it has been demonstrated that aluminum films reduce the permeability of atmospheric gases 1,000-fold when compared to the polymeric substrate. However, these metallized plastic materials do not have the desired hermeticity but have some undesirable electrical properties. DaSilva et al. [6] showed that SiO_2 and Si_xN_y transparent thin films deposited on polyester or polyethylene terephthalate by plasma-enhanced chemical vapor deposition (PECVD) provide an adequate hermetic barrier with insulator properties. The main problem for these materials is that they are brittle.

Another approach is to sputter alternating aluminum oxide and polyacrylate layers, using plasma-enhancement under vacuum [6, 7]. These hybrid transparent films obtained by plasma-enhanced chemical vapor deposition (PECVD) [5, 6] are extremely efficient as barriers even though they are very thin. It was shown [5, 8] that the inorganic layer has a critical coating thickness “ d ” where the oxygen transmission rate (OTR) and water vapor transmission rate (WVTR) decrease as much as 1,000-fold. This critical thickness “ d ” depends on the nature of the inorganic layer. For example, d is 15 nm for SiO_2 and ~ 8 nm for Si_xN_y coatings on polyester. Generally for these films the permeation is attributed to the microscopic defects that may have their origin in the dust particles present on the substrate surface, in geometric shadowing and stresses that appear during the film growth at sites of high surface roughness.

For hybrid double-layer coatings, Graff et al. [5] showed that an efficient hermetic barrier is achieved only if a near-defect-free inorganic layer in a low temperature process is obtained. They demonstrated by calculation that to achieve the required barrier performance for a single inorganic layer on a PET substrate the effective diffusivity of the oxide layer must be $<10^{-18}$ cm^2/s .

To address these issues, a multilayer barrier of polyacrylate–aluminum oxide pairs using the same PECVD technique was developed [2, 5] and is presented schematically in Fig. 10.2. The so-called dyads, polymer- AlO_x layers pairs, were repeated five times and a WVTR $\sim 8 \times 10^{-5}$ $\text{g/m}^2 \cdot \text{day}$ was achieved. Shaw et al. [9] introduced for the first time the dyads concept in 1994 when they reported a 0.1 $\text{cm}^3/\text{day}/\text{m}^2$ OTR using a hybrid barrier prepared by deposition of alternating

Fig. 10.2 Flexible polyethylene terephthalate (PET) substrate and multilayer thin-film barrier coating. *P1* and *P2* layers are vacuum-deposited acrylate polymers and the AlO_x layers are reactively sputtered aluminum oxide. (Reprinted by permission of AIP) [5]



thin film pairs of polyacrylate–aluminum metal on an oriented polypropylene substrate. For the multilayer hybrid barrier shown in Fig. 10.2, it was calculated that the defects in the AlO_x layers of the hermetic barrier stacks are so widely separated that the vapor diffusion vector is mostly parallel to the polymer P_1 layer, resulting in a very long effective diffusion pathway between AlO_x and PET layers.

The effective diffusion pathway “ l ” is schematically illustrated in Fig. 10.3 for a polymer with a physical thickness “ t ” and defect spacing “ s ”, when $t \ll s$. This effective diffusion pathway is ruled by the following equation:

$$l(P_1) = \left[t^2 + \left(\frac{s}{2} \right)^2 \right]^{\frac{1}{2}} \approx \frac{s}{2}. \quad (10.1)$$

An explanation for the efficiency of the multilayer structure could be the lag time effect. For a simple polymer layer PET- P_1 the lag time was demonstrated to be 1.72 h, while for four layers PET- P_1 - AlO_x - P_2 the lag time was 22.1 h. For a barrier with five dyads and with a defect spacing of 100 μm the lag time was calculated to be 1,752 h (~ 72 days); extrapolating to a defect spacing of 1 mm, the lag time is longer than 17,000 h (2 years).

10.3 Barriers for OLEDs

After Tang et al. [10] discovered green electroluminescence (EL) using OLEDs, there have been many attempts to obtain full color flat panel displays or flexible color displays [2] with longer lifetimes. OLEDs operate well in a controlled medium. Several authors [10–12] point out that OLEDs have a limited lifetime, indicated by decreasing EL efficiency, an increase in drive voltage, and the appearance of “dark spots” on the surface. It was shown that OLEDs prepared using $[\text{Al}(\text{q})_3]$ (where q is 8-hydroxyquinoline) lose 50% of EL intensity in 100 h of operation in dry Ar at an intensity of $I \sim 5 \text{ mA/cm}^2$. By using distyryl arylene derivatives for blue light OLEDs, a decrease of 90% from the initial EL intensity was observed, when

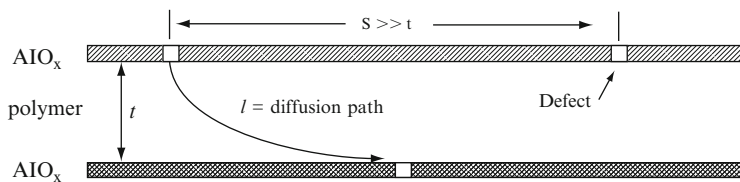


Fig. 10.3 Schematic illustration of the effective diffusional thickness “ l ” of the polymer layer (approximately half the AlO_x defect spacing). This results in a path length which is much longer than the polymer physical thickness (t). (Reprinted by permission of AIP) [5]

operated in dry N_2 at $I = 6 \text{ mA/cm}^2$. In comparison, OLEDs that operate in air lose 99% of EL initial intensity in 150 min.

Burrows et al. [2, 11–14] extensively studied OLEDs on glass or on silicon substrates for rigid flat displays [11, 14] or on a polymeric substrate for flexible OLEDs (F-OLED) [2, 12, 13]. They showed that to achieve an optimum operating lifetime for OLEDs a hermetic isolation of the OLEDs from atmospheric oxygen and moisture is necessary. Mainly, Ca and Mg used as cathodes oxidize in the presence of O_2 or H_2O and the organic semiconductor itself is damaged. Oxidation of 10% of the cathode resulted in the degradation of the EL properties of the devices. Losing even 5 \AA of metal at the metal-organic compound interface is very significant in the decay of the initial properties of the OLEDs. It was calculated that the maximum leakage tolerated for an OLED that contains an Mg cathode for 1-year lifetime is $1.5 \times 10^{-4} \text{ g/m}^2 \cdot \text{day}$.

To achieve better performance for their OLEDs, Burrows et al. [2, 12, 13, 15] engineered organic–inorganic multilayer flexible films, which are shown schematically in Fig. 10.4. For this hybrid material the permeation rate of water is $\sim 10^{-5} \text{ g/m}^2 \cdot \text{day}$. These organic–inorganic films were vacuum-deposited by roll-coating technology, commercially called BarixTM. They have a sandwich structure with multiple layers of aluminum oxide between polyacrylate layers, as is shown in Fig. 10.5. The vacuum roll-coating technology leads to encapsulation of the OLED active devices in a single step together with BarixTM preparation as is shown in Fig. 10.6. This approach produced very good results, in terms of lifetime stability of these devices.

As introduced above, defects such as pinholes, micropores, microchannels, and microcracks in the layers have an important role in the level of hermeticity. Recently, Groner et al. [16] and Carcia et al. [17] introduced atomic layer deposition (ALD) as a new method for hermetic barrier preparation. The ALD process is known for growing thin, conformal pinhole-free films with featureless microstructure and low stress. They showed [16, 17] that by using this ALD method, it is possible to obtain 25 nm layers of Al_2O_3 on polyethylene naphthalate and KaptonTM substrates with a WVTR $\sim 1.5 \times 10^{-3} \text{ g/m}^2 \cdot \text{day}$. Briefly, this new process consists of deposition of Al_2O_3 layer on a polymer substrate in a hot-wall ALD flow reactor at 120°C using sequential self-limiting exposures to trimethyl-aluminum and water with intermediate nitrogen gas purging steps. In this way defect-free films with ultra low permeability can be prepared.

Table 10.1 summarizes the main types of barriers presented in the literature, the method used for their fabrication and their efficiencies.

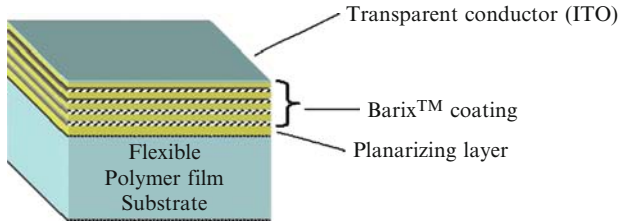


Fig. 10.4 Schematic cross-section of a Barix™ flexible engineered substrate (Reprinted with permission from Elsevier) [2]

Fig. 10.5 Scanning electron micrograph image of a barrier film cross section. (Reprinted by permission of AIP) [15]

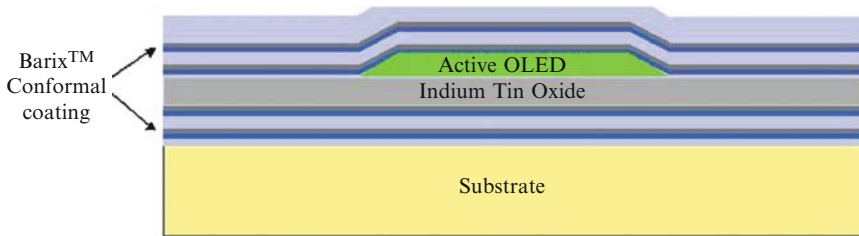
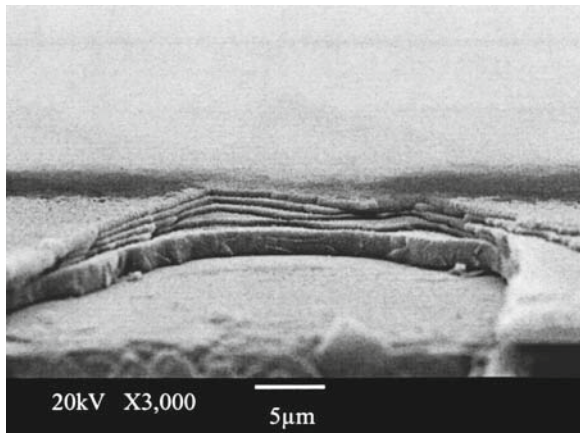


Fig. 10.6 Schematic cross-section of a Barix™ encapsulated OLED. (Reprinted by permission of SPIE) [12]

10.4 Performance Tests for Hermetic Barriers

In order to improve the properties of materials as hermetic barriers it is necessary to have reliable methods to determine and measure with accuracy the WVTR and OTR. These measurements are also important for the food packaging industry and

Table 10.1 Overview of barriers, thickness and their performances

Substrate	Coatings materials	Method of coating	Thickness (nm)	WVTR (g/m ² day)	OTR (cm ³ /m ² ·day)	References
PET	Six pairs polyacrylate-Al ₂ O ₃	Evaporation in a roll coating configuration	5 × 10 ³	<10 ⁻⁵	>5 × 10 ⁻³	[2, 5, 12, 24]
PET	SiO ₂	PECVD	8–200	–	1 × 10 ⁻¹	[6]
PET	SiN	PECVD	8–15	–	<5 × 10 ⁻³	[6]
Silicon wafers	Up to 500 pairs of polyacrylate-Al ₂ O ₃	Vacuum deposition and sputter with energetic plasma	500	>10 ⁻⁵	–	[7]
PET	Five pairs polyacrylate-Al ₂ O ₃	Flash evaporation in vacuum; UV curing	10–30	2 × 10 ⁻⁶	–	[15]
PEN	Al ₂ O ₃	ALD	25	<10 ⁻⁵	5 × 10 ⁻³	[16, 17]
Kapton™	Al ₂ O ₃	ALD	25	–	5 × 10 ⁻³	[16, 17]
Poly-carbonate	SiO ₂ + ITO Al ₂ O ₃ + ITO	PECVD	–	2–8 × 10 ⁻³	–	[18]

the pharmaceutical packaging industry, as well as high altitude science balloons. For the electronic devices such as OLEDs to be commercial, they need to have reliable performance and a lifetime that extends to 10,000 h of operation [18]. For this purpose, it was calculated that the new hybrid materials should have an OTR below 1 × 10⁻⁵ cm³/m²·day and WVTR approximately 1 × 10⁻⁶ g/m²·day at 39°C and 95% relative humidity (RH). In order to measure such small rates (WVTR and OTR) traditional, commercial equipment used for the food industry (available from MONCON [19, 20]) cannot be used. Commercial equipment is limited to 5 × 10⁻³ cm³/m²·day for O₂ and 5 × 10⁻³ g/m²·day. To extend the measurements, in order to be able to check the permeation rate of oxidizing species (O₂ and H₂O) through the hybrid barriers, new experiments have been proposed.

Permeation is defined as mass transfer of a substance (permeate) through a solid [21, 22]. Permeation rate is a function of diffusivity of permeates through solid and the solubility of the permeate in the solid. Nilsson and Forssell [23] used calcium as an indicator. Its physical, chemical, optical, and spectroscopic special properties, are due to its unoccupied d-band orbitals, that are just above the Fermi level. Based on this excellent review, Nisato et al. [24, 25] designed a calcium test to evaluate WVTR and OTR and high performance barriers such as Barix™. The cathodes for OLEDs consist of reactive metals that degrade very rapidly, making the calcium test a suitable one since calcium also has a high reactivity when in contact with water and oxygen. Mainly the reactions that take place are [26]:

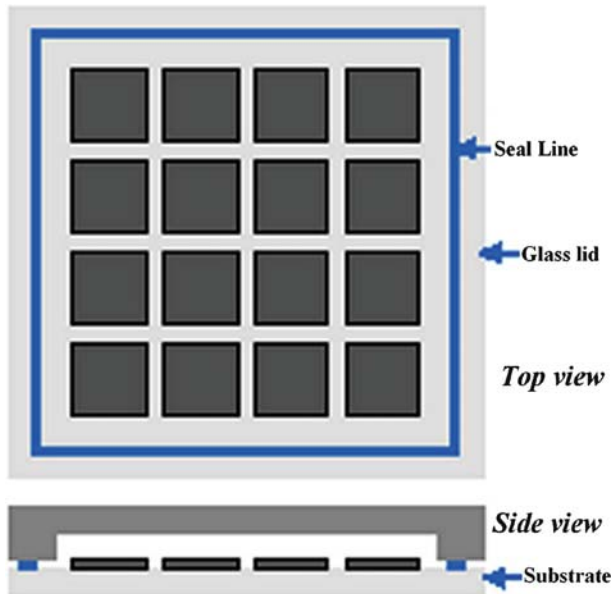


Fig. 10.7 Calcium test cell, a thin calcium film deposited on a substrate encapsulated with a glue line seal and glass lid. (Reprinted by courtesy of Koninklijke Philips N.V.) [24]



Water vapor and oxygen have distinct transmission rates due to the fact that these two permeates have different permeation mechanisms.

Nisato et al. [24, 25] designed a simple experiment. In a glove box, under controlled atmosphere, calcium layers were deposited on the plastic or hybrid substrate through a shadow mask. A glue line was drawn on glass lids and the calcium test cells were then assembled, as is shown in Fig. 10.7. The calcium layer has a highly reflecting metallic mirror. Once the calcium starts degrading due to permeation of water and oxygen, the layer becomes transparent due to the formation of the salt. Therefore, the effect of oxidation in decreasing the calcium layer was immediately noticeable.

Figure 10.8 shows the calcium test-cell permeation as a function of time. To evaluate the corrosion of calcium and the permeation of the studied hybrid layers, the test cells were placed in a dark box on top of a uniform light source together with a CCD camera to acquire images of the calcium layer at different time intervals. From these data, the average transmissions (grey value) of the calcium-covered areas were estimated. The gray values were then translated to the calcium thicknesses. Finally, they calculated the effective permeation from those data as a function of time.

To calculate the relative transmission T/T_0 for a calcium-pixel, the measured average black level I_{black} , average white level I_{white} and the gray-scale value I_{gray} (value 0.255) are used in the equation:

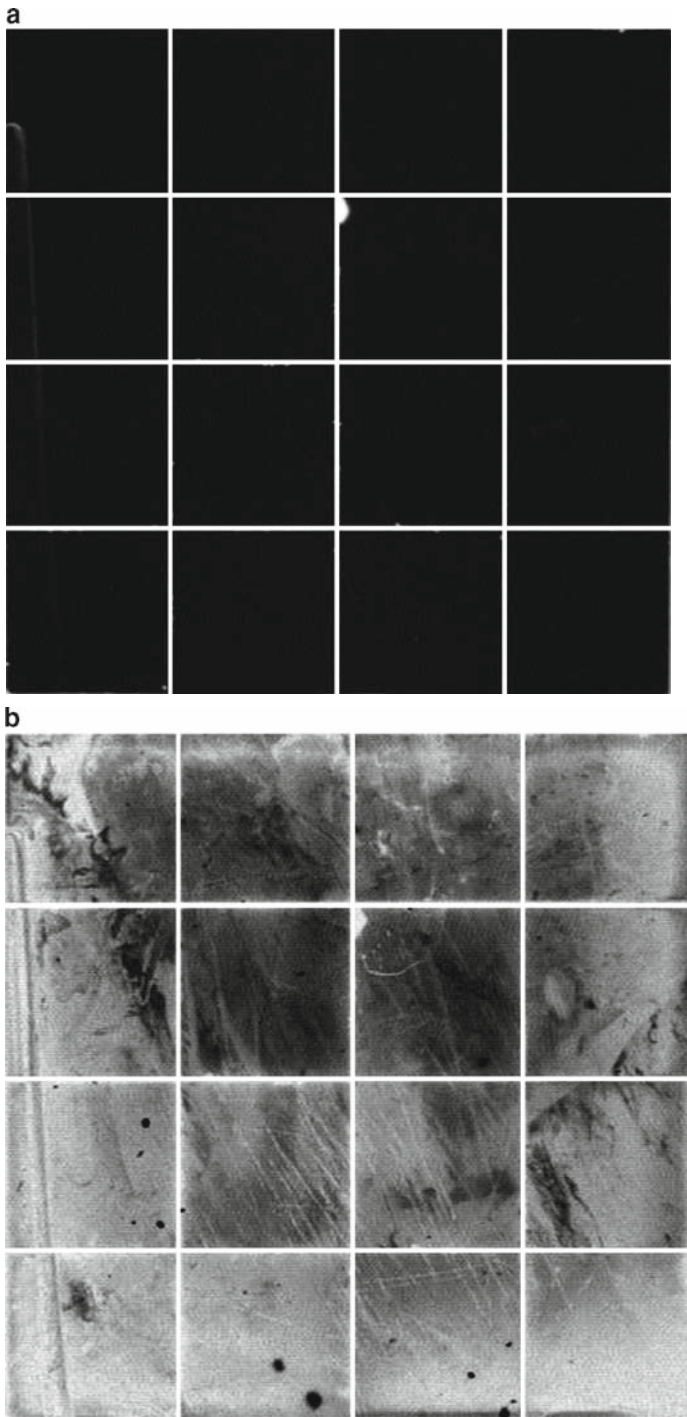


Fig. 10.8 The evolution of calcium test cells. The calcium square patterns are 5 mm wide. (Reprinted by courtesy of Koninklijke Philips N.V.) [24]

$$\frac{T}{T_o} = \frac{I_{\text{grey}} - I_{\text{black}}}{I_{\text{white}} - I_{\text{black}}}, \tag{10.2}$$

This equation was used to calculate the local calcium thickness d_{Ca} . The gray scale was calibrated as an effective calcium thickness. The results can be plotted as an amount of calcium not oxidized versus time or amount of water necessary to oxidize the calcium layer, this being the water absorbed by the cell. From the slope of the permeation curve the effective permeation constant of the cell was extracted. By using this method, they measured the WVTR at 50% RH for different materials at different temperatures as is listed in Table 10.2.

Carcia et al. [17] used the same Ca test for the hybrid layers obtained by ALD deposition of 25 nm layer of Al_2O_3 on polyethylene naphthalate (PEN). For a better accuracy of calculation, they controlled the Ca thickness using a quartz crystal microbalance. In this way, it was possible to obtain a semi-transparent calcium layer. Another improvement was to monitor the Ca decay by optical transmission measurements at 600 nm. The transmission increased with Ca consumption due to CaO or $\text{Ca}(\text{OH})_2$ formation. Figure 10.9 shows the optical change with time at different temperatures and at 85% RH. The WVTR at 38°C, and RH of 85% was $1.7 \times 10^{-5} \text{ g/m}^2 \cdot \text{day}$. This confirms that the Ca test method is very efficient in determining low permeation rates.

Paetzold et al. [26] monitored the calcium layer decay by measuring in situ the resistance of calcium. The cell used for these measurements is shown in Figure 10.10. This method determines the permeation rate with high accuracy,

Table 10.2 The WVTR calculated using the Ca test for different materials

Sample	Storage temperature (°C)	Effective WVTR (g/m ² day)	References
Glass	20	5×10^{-5}	[24]
Barix™	20	2×10^{-6}	[25]
	50	2×10^{-5}	[25]
	80	9×10^{-5}	[25]
Flexible glass 500	20	8×10^{-5}	[24]

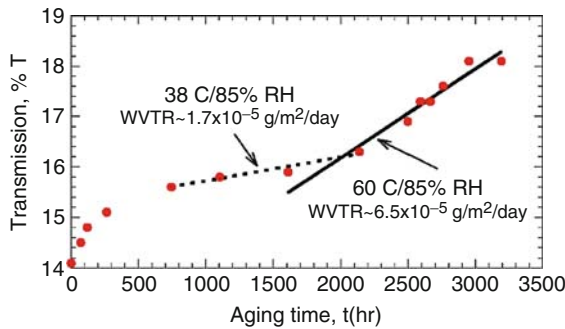


Fig. 10.9 Change in optical transmission with aging for a representative Ca thin-film square in a test cell where the lid was PEN, coated with 25 nm thick Al_2O_3 , grown by atomic layer deposition. Aging was at 38°C, 85% RH and 60°C 85% RH (Reprinted by permission of AIP) [17]

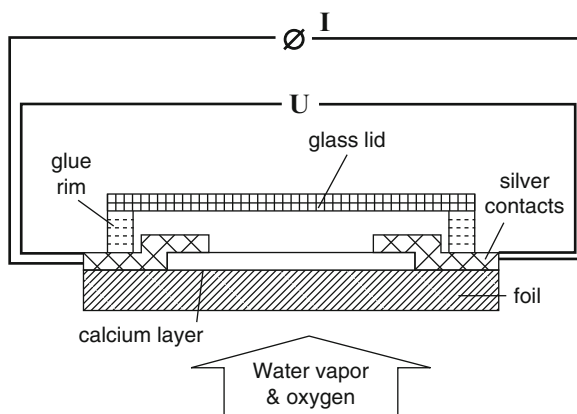


Fig. 10.10 Layout of the permeation sensor. The foil is covered with a calcium layer that is contacted by silver pads. The sensor is encapsulated with a glass lid. The oxidizing agents permeating through the foil oxidize the calcium. This is reflected by an increasing resistance that is monitored by a four-probe setup (Reprinted by permission of AIP) [26]

assuming that corrosion of the calcium layer from the substrate surface takes place uniformly. Here the resistance (R) is inversely proportional to the height (h) of remaining metallic calcium:

$$R = \frac{\rho l}{ah}, \quad (10.3)$$

where ρ is calcium resistivity, l is the length and a is the width of the Ca layer. The oxidized calcium species produced serve as insulators. The permeation rate P through the hybrid layer is proportional to the slope of the conductance curve $1/R$ vs. time:

$$p = -n \frac{M(\text{reagent})}{M(\text{Ca})} \delta \rho \frac{\ell}{b} \frac{d(1/R)}{dt}, \quad (10.4)$$

where n is the molar equivalent of degradation reaction (chemical reactions (a), (b) and (c)) and M the molecular masses of the reagent (water or oxygen) and δ is the density of calcium. Using this method, it was possible to measure very precisely the WVTR through barrier films of $\sim 1 \times 10^{-6} \text{ g/m}^2 \cdot \text{day}$.

Recently, Dunkel et al. [19] developed a very sensitive method to measure permeation using tritium-enriched water. The theoretical detection limit was calculated to be $2.4 \times 10^{-7} \text{ g/m}^2 \cdot \text{day}$. The apparatus developed can be used to measure the permeability of a polymer substrate with barrier coatings as well as perimeter sealing for OLED displays. The device shown in Fig. 10.11 consists of a gas supply system (in this case methane), a test chamber that contains a sample holder and the tracer material, an ionization chamber with a counter, and a recording device. The reservoir is initially loaded with 1 cm^3 of tritiated water (HTO) with a specific radioactivity of 1 Ci. Tritiated water is essentially a mixture of molecules of HTO and H_2O where every 1/1667th molecule is HTO.

All the measurements were performed at 38°C in RH ~ 100%. Equilibrium is reached very quickly for the sample analyzed. Methane was chosen as a diluting gas since it has a molecular mass similar to water, and it has a favorable ionization rate (half-life of tritium). The WVTR was calculated by converting the radioactivity counts per cubic meter of methane per 24 h per 1 m² of area. This method of detection has a lower theoretical limit of WVTR ~2.4 × 10⁻⁷ g/m² · day.

Groner [16] designed another experiment also using HTO to detect the permeation rate of the barrier obtained by ALD. The device used for these experiments is shown in Fig. 10.12. In this case, the atmosphere inside the barrier sample is saturated with HTO vapor. After some HTO permeates through the barrier, hygroscopic LiCl is used to absorb the HTO. The detection limit of WVTR using this method was calculated to be 1 × 10⁻⁶ g/m² · day.

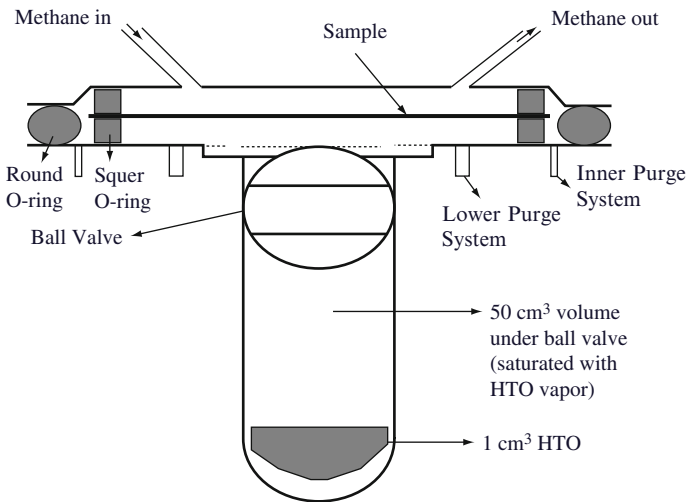


Fig. 10.11 Schematic of the radioactive tracer test. ©IEEE-2005; (Reprinted by permission of IEEE) [19]

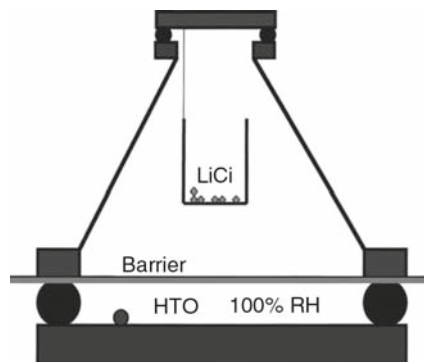


Fig. 10.12 Device used for HTO water test to measure the water vapor transmission rate (Reprinted by permission of AIP) [16]

Both methods that use HTO are able to detect very low levels, but the main problem is that they require special handling of radioactive materials. To address this issue, Vogt et al. [7] determined the permeation rate by measuring film swelling with X-ray and neutron reflectivity, as a function of exposure time to humidity and temperature. Instead of water they used deuterated water (D_2O). The detection limit of this method was calculated to be $>1 \times 10^{-6} \text{ g/m}^2 \cdot \text{day}$.

10.5 Formulating New Barrier Coatings

While PECVD and ALD methods lead to hermetic coatings, the equipment necessary for these processes is complicated and expensive. An alternate way to develop new protection materials is the sol–gel process, involving alkoxides and alkoxy silanes. Originally, the sol–gel process was used to prepare pure inorganic silica coatings to protect metals, alloys and stainless steel against oxidation and corrosion [27–31]. In addition to silica coatings, other ceramic coatings, such as ZrO_2 , Al_2O_3 , and SiO_2 – Al_2O_3 , were used to protect against gas and water corrosion [32]. Reed et al. [27, 28] obtained a multilayer coating on stainless steel, which was used for solar energy applications. Besides protecting against corrosion, these multilayer coatings were used for surface planarization.

Ideally, materials for electronic devices and for solar cells have flexibility, making rigidity the main problem of these inorganic coatings. The rigidity is tackled by using hybrid organic–inorganic coatings. Principally, hybrid materials offer lightweight, functional flexibility and ease of processing. In addition to organic light-emitting diodes, optically transparent ferromagnetic materials, environmentally stable, highly conductive macromolecules, piezo-sensitive multifunctional materials, are some of the materials needed to advance flexible display technologies, to allow portable video displays, and to take miniaturization to the next smaller level, all of which need flexible, hermetic, and, in many cases, transparent coatings.

10.6 The Sol–Gel Process for Organic–Inorganic Hybrids

In a sol–gel process carried out with a precursor containing identical alkoxy groups, for example, tetraethyl orthosilicate (TEOS) $Si(OC_2H_5)_4$, the hydrolysis and condensation polymerization reactions will generate an inorganic polymer with Si–O–Si links. In a sol–gel process with a precursor such as methyltrimethoxysilane (MTMS) $(CH_3)_3Si(OCH_3)_3$, there is a direct link between Si and C that does not undergo hydrolysis. Due to the combination of these precursors, the product of the sol–gel process is a hybrid.

Haas et al. [33, 34] showed that these kinds of precursors could be classified by their network-forming or network-modifying role. The precursors for hybrid materials were classified into four classes as follows:

- Type 1: Inorganic network formers, such as silicon alkoxides (tetramethoxysilane TMOS $\text{Si}(\text{OCH}_3)_4$, tetraethoxysilane TEOS $\text{Si}(\text{OC}_2\text{H}_5)_4$), aluminum (aluminium-tri sec butoxide $\text{Al}[\text{OC}(\text{CH}_3)_3]_3$), titanium alkoxides (titanium tri-isopropylate $\text{Ti}[\text{OCH}(\text{CH}_3)_2]_4$), etc.
- Type 2: Inorganic network formers that have organic non-reactive groups that are stable modifiers of the inorganic network, for example, methyltrimethoxysilane (MTMS).
- Type 3: Inorganic network formers with reactive organic modification for cross-linking/polymerization reactions; or monomers/polymers with silylated end groups for cross-linking/polycondensation via inorganic Si–O–Si bonds.
- Type 4: Organic monomers, which play the role of modifiers, which can react via chemical cross-linking/polymerization with modified alkoxide of Type 3.

A wide variety of silica-based type 2 precursors are commercially available due to the high stability of Si–C bond towards hydrolysis–polycondensation reactions [35, 36]. Figure 10.13 displays several organic modified precursors, Type 2 and 3. The Type 3 precursors have more than one reactive site capable of undergoing inorganic reactions (hydrolysis/polycondensation) and organic polymerization UV or thermally induced cross-linking (curing reactions).

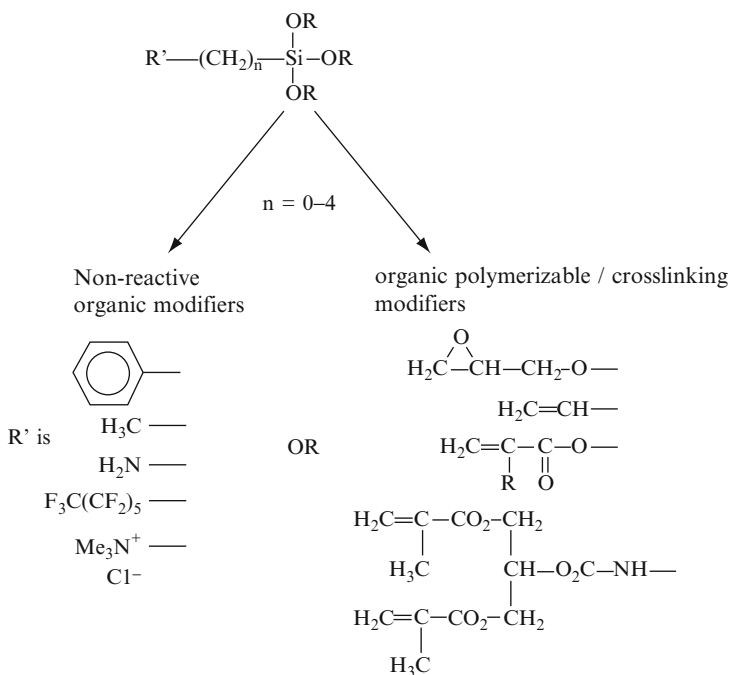
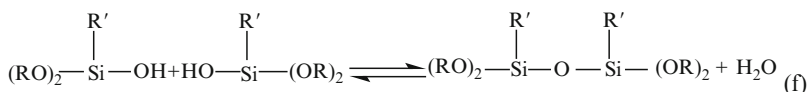
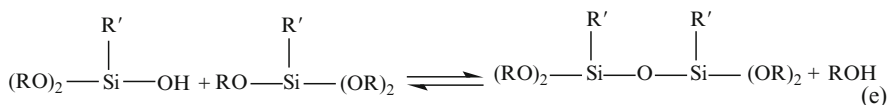
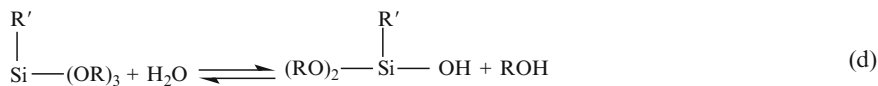


Fig. 10.13 Examples of organic modified silicon based alkoxide, type 2 and type 3 for synthesis of hybrid materials

The main reactions of hydrolysis–polycondensation that take place during the sol–gel processes with the organic modified alkoxides, Type 2 and Type 3 are the following:



where R is $-\text{O}-\text{C}_2\text{H}_5$ and R is $-\text{CH}_3$ in the case of methyltriethoxysilane.

The first reaction (d) is a hydrolysis reaction, while reactions (e) and (f) are condensation reactions. Many studies [35, 36] report that during the hydrolysis–polycondensation processes the silicon-carbon bonds are not involved. The silicon-carbon bonds were found to be unaffected by sol-gel processes in the final hybrid materials. The presence of the organic modifier groups R in the type 2 precursors decreases, generally, the cross-linking degree. The sol-gel processes are very complex, since these involve competitions between different reactions including reesterification, depolymerization, and transesterification [37].

The hybrid materials are often classified by the fact that there is a direct covalent bonding between the organic and inorganic parts. It is also possible to have hybrids without direct linking by covalent bonds, but where hydrogen bonding between organic and inorganic parts occurs, with anywhere from weak to relatively strong interactions. For these kinds of hybrid materials, the precursors of Type 1 and Type 4 are usually used.

Another way of classifying hybrids is either physical or chemical. In physical hybrids, the organic polymer and the inorganic polymer can form simultaneously or sequentially. An organic monomer may be the starting point for a thermal or UV-initiated polymerization. In the physical hybrids, the interaction between the organic polymer and the inorganic polymer is through hydrogen bonding. Categorizing physical hybrids is approximate at best, because of the processing factors that influence their structures, for example, phase separation, solubility as a function of molecular weight, and relative speeds of hydrolysis, polymerization, and gelling.

In chemical hybrids, the assumption is that the organic and inorganic components are covalently bonded. Many low temperature hybrids have been synthesized using the sol-gel process and methacrylate compounds [38, 39]. Other hybrids have been discussed in detail [40, 41].

Poly(methyl methacrylate) (PMMA)/ SiO_2 hybrids have been synthesized by a number of sol-gel processes. Typically, they have been prepared by mixing methyl methacrylate monomer (Type 4) with tetraethylorthosilicate (TEOS) (Type 1). Their polymerization is carried out simultaneously. Alternatively, TEOS has been polymerized first and then infiltrated with MMA monomer.

Recent work on PMMA/SiO₂ hybrids have reported on mechanical properties, and thermal stabilities. In such hybrids Van der Waals forces, hydrogen bonding or electrostatic attraction between organic and inorganic moieties are expected to influence the behavior.

In comparison to the sol–gel approach of using alkoxyisilyl-containing organic precursors or coupling agents, PMMA/SiO₂ hybrids that do not contain covalent bonding are simpler to prepare. Furthermore, it has also been shown that such an approach results in homogeneous hybrids with good mechanical and optical properties. For example, Landry found that homogenous, transparent PMMA/SiO₂ composites could be formed under acidic conditions, having improved mechanical properties and increased solvent resistance. Klein showed by infiltrating previously formed SiO₂ gels with MMA monomer, that the optical transparencies of PMMA/SiO₂ composites were similar to that of porous SiO₂ xerogels and the composites also had reasonable thermal shock resistance. With respect to optical properties, especially in the near infrared region (800 ~ 2,000 nm), most work on PMMA/SiO₂ is based on the hybrids, where covalent or ionic bonds between organic and inorganic moieties are the central concepts. One recent [42] process used vinyl triethoxysilane (VTEOS) to generate an oxide network with polymerizable vinyl groups. The advantage in this case of VTEOS over TEOS is the presence of an inorganic and organic network.

10.7 Organic/Inorganic Hybrid Flexible Films

The first attempt to use the hybrid films as a barrier was done in the middle 1990s by Amberg-Schwab et al. [46, 47] in order to obtain a barrier for oxygen, which can be used in the food industry to prevent the degradation of different flavors. Two different hybrid systems using 3-mercaptopropyl-trimethoxysilane and 1,1,1-tris-(hydroxymethyl)-propan-triacrilate – UV curable; and tetramethoxysilane, zirconium propoxide or aluminum-tri-sec-butoxide, and 3 amino-propyl-triethoxysilane – thermally curable were investigated. As supports for the above hybrid systems, they investigated biaxially oriented polypropylene (BOPP), polyethyleneterephthalate (PET) and regenerated cellulose were used. For the first system, UV-curable, deposited on BOPP, the efficiency of the barrier against penetration of the flavors was very high. Only two flavors (diphenyl oxide and cis-3-hexanol) out of seven investigated were detected through this barrier, and these only in traces. To reduce permeability of the water, oxygen and flavors, a vacuum deposition of SiO_x was employed between the polymer layer and thermally curable hybrid coating. By using this method, the OTR was lower than the detection method 0.05 cm³/g day used by the authors [46]. These PET-SiO_x-hybrid polymer-PET and BOPP-SiO_x-hybrid polymer structures (OTR <0.05 cm³/m²·day) present excellent adhesion and barrier properties even under high mechanical and thermal stress. These multilayer barriers can be used also as laminating agents as is shown in Fig. 10.14.

In another series of experiments in the thermal curable system beside tetramethoxysilane, zirconium propoxide or aluminum-tri-sec-butoxide, and 3 aminopropyl-triethoxysilane the 3-glycidoxypropyltrimethoxysilane (GLYMO) was introduced

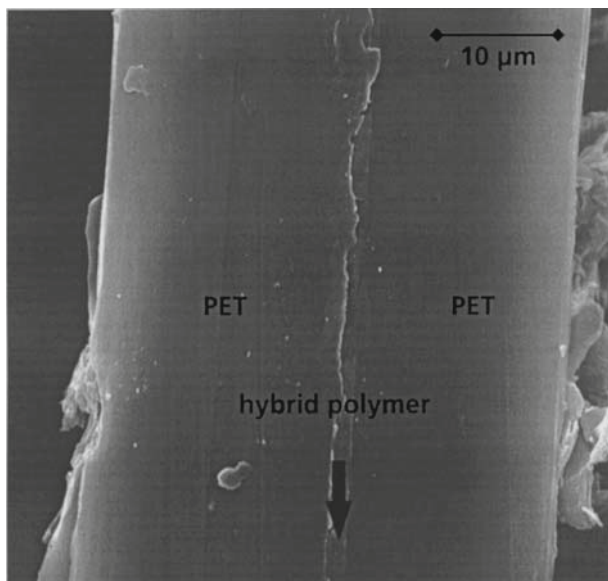
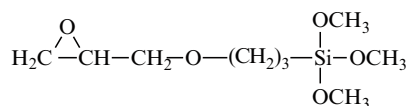


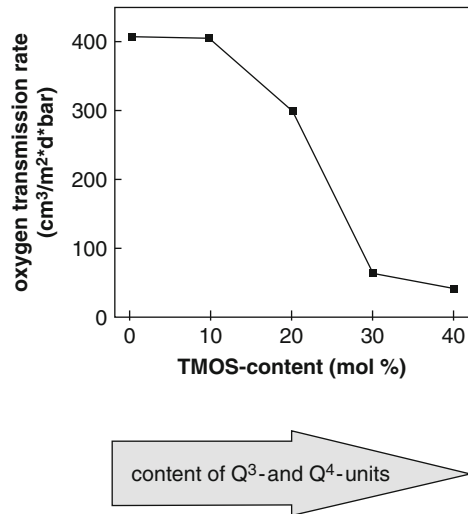
Fig. 10.14 SEM micrograph of the multilayer structure: PET-SiO_x-hybrid polymer-PET. (Reprinted by permission of Springer) [47]



[48, 49]. The epoxy groups from GLYMO have the role to form the organic network thermally cured (100°C/2 h) material. From chemical point of view, in order to be able to form the organic network the ring-opening reaction of GLYMO desired is with an epoxy from another oxirane. The result is formation of oligo- or poly-(ethyleneoxide) derivatives. It was demonstrated that the presence of aluminum-tri-sec-butoxide catalyzed the ring opening reactions of GLYMO [49]. Another important achievement for this system was that the control of polymerization-condensation of these molecular species was for the first time monitored by FT-Raman spectra, which is cheaper than NMR spectroscopy. The amount of inorganic component used, tetramethoxysilane (TMOS) varied from 0 to 40% (mol%) and it was shown that OTR decreased with increasing concentration of inorganic component deposited on polypropylene as illustrated in Fig. 10.15. This result was assigned to increase in the density of inorganic network, which hindered the penetration of the oxygen molecules through dense rigid hybrid network. For industrial applications, the thermal curing at 100°C for 2 h is not an economical approach, so this was replaced with an IR curing treatment for 3 min.

In contrast to the thermally cured barriers, there are some supports, e.g. polyolefins (polypropylene, PP) and plasticized PVC, which cannot be thermally cured [50]. For these types of supports the photochemical curable barrier was developed. Using this procedure anti-migration barriers of the plasticizer from PVC were developed.

Fig. 10.15 Dependence of the oxygen transmission rate on the TMOS-content of the barrier coating material (carrier foil polypropylene) (Reprinted by permission of Springer) [49]



For the hybrid coatings in the system methacryloxypropyl-trimethoxysilane and zirconiumpropoxide previously complexed with methacrylic acid, UV curable, it was shown that the efficiency of this improves the PP for oxygen barrier nine times, and improves the migration barrier of plasticizers from PVC with a factor of two. By introducing instead of zirconium-methacrylic complex an aluminium-sec-butoxide complexed with triethanolamine ($N(C_2H_4OH)_3$, TEA) the efficiency of OTR increases more than 14 times and the efficiency against plasticizer migration increases by a factor of 4. Another effect studied was the influence of increasing the concentration of aluminum complex in the last system. The efficiency of OTR remains constant being >14 times but the efficiency as a migration barrier is higher being nine times more efficient. The aluminum-TEA complex does not take part in the inorganic condensation process functioning as a network modifier, reducing the degree of inorganic cross-linking.

A revolutionary concept called “passive-active barrier” coatings prepared by sol-gel method was developed in the last years by major chemical companies as Chevron Chemical Company, Cryovac Incorporation, a subsidiary of Sealed Air Corporation and by Fraunhofer – Institut für Silicatiforschung [51]. Previously it was shown that the combinations between SiO_x , AlO_x inorganic layers and polymer layers give the WTR $< 10^{-3}$ g/m²·day or OTR $\ll 10^{-3}$ cm³/m²·day as it is illustrated in Fig. 10.16. By combination of these passive layers with active oxygen barrier layers, the efficiency of these barriers could increase dramatically.

Basically, the concept is an oxygen trap called “oxygen scavenger system” which is based on photo-initiation of a metal oxidation cyclo-olefin directly bonded to a silicate molecular chain. By this process, the formation of low molecular oxidation products, which decrease the quality of the package and integrity of the material, is prevented. However, more importantly the active layers consume the oxygen entrapped during the packaging process after UV activation. The inorganic network

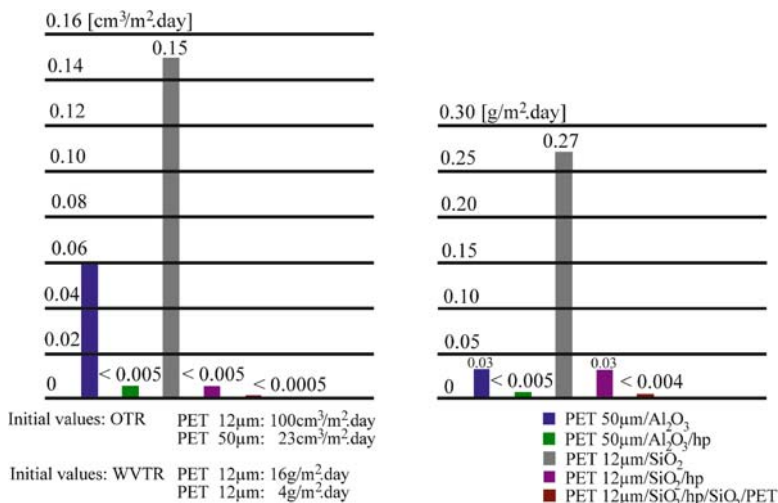
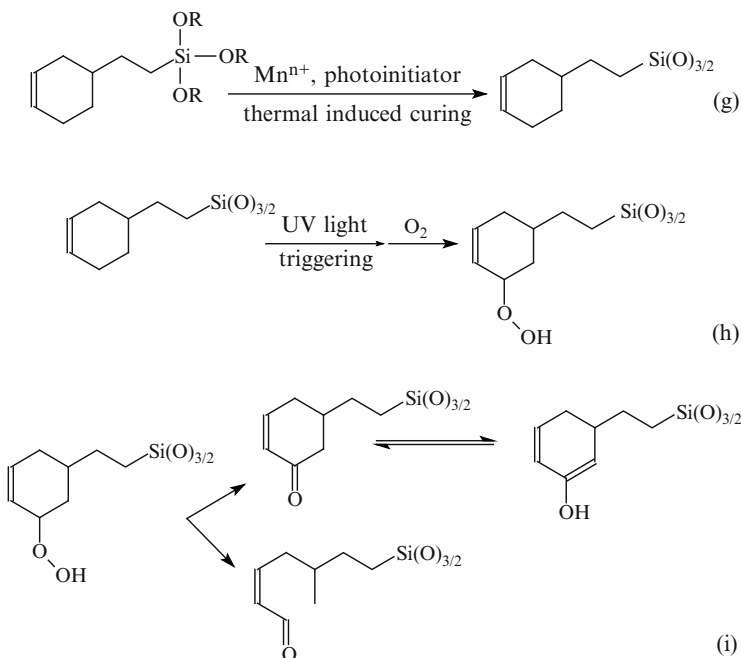


Fig. 10.16 Oxygen (OTRs, *left*) and water vapor (WVTRs, *right*) transmission rates of PET films with inorganic layers (PET-Al₂O₃ sputtered layer and PET – SiO_x PVD layer) and hybrid polymer based coatings (Reprinted by permission of Springer) [51]

is formed by hydrolysis-polycondensation and the sol formed can be easily applied to any substrate by classical coating techniques. The main reaction that takes place to form this scavenger films is:



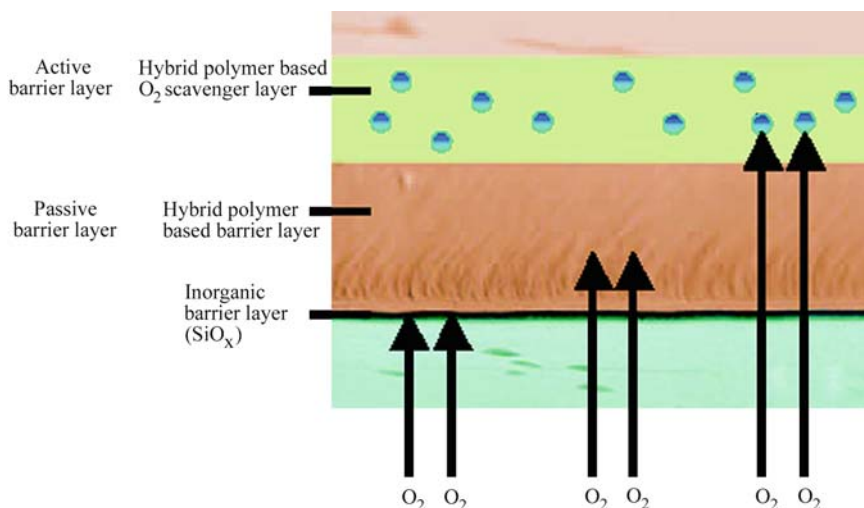


Fig. 10.17 Schematic way of combination of passive barrier layers with an active oxygen barrier layer (Reprinted by permission of Springer) [51]

These kinds of active layers can be deposited on any organic and inorganic layers. The schematic of how the active and passive layers can be combined is presented in Fig. 10.17. Amberg-Schwab et al. [51, 52] using the above described procedure developed flexible thin films for dye solar cells, which can be applied on non-planar surfaces as it is displayed in Fig. 10.18.

The main advantage of these coatings is that these solar cells could be in the future part of the construction components such as roofs or facades.

10.8 Permeable Layers

As mentioned before, permeation in a nonporous medium is controlled mainly by the diffusivity of the studied material and by the solubility of the permeant in the material. The organic polymers and especially silicones [43] are permeable to few gases. Moreover, the thin inorganic glasses have very low permeability. The hybrid organic–inorganic materials as a class of materials theoretically must be between the organic polymers and inorganic glasses, but synergetic effects are expected due to the high hydrophobicity and lack of porosity.

Conversely, hybrids could be used to generate highly permeable materials with selective permeation, when ion or proton conductive polymers are used [43]. While stable and reproducible conductivities have been demonstrated in thin films, the values of conductivity are still too low. Further advances in electrochromic devices are dependent on finding a solution to the electrolyte problem. Some recent studies on organically modified electrolytes are in the right direction [54, 55].



Fig. 10.18 Aspect of the hybrid coated solar cell modules with very high barrier properties (Reproduced by permission of Royal Society of Chemistry) [52]

Popall et al. [56] developed new organic–inorganic sulfonic-acid/sulfonamide functionalized protonic conductors for application as coatings, layers, or separators in film batteries as well as membranes in fuel cells under humid conditions. The main problem of these materials is the thermal stability which is up to 200°C and is limited by sulfonyl group. This is the main restriction to use these materials in the fuel cells that operate at higher temperatures.

10.9 Corrosion and Abrasion Resistant Coatings

Other interesting applications developed using the hybrid systems described above were to create antiadhesive and antistatic surfaces by controlling the hydrophobicity and oleophobicity of the surfaces. For this purpose fluoroalkyl modified silicon-based alkoxides were used [53]. Figure 10.19 displays an organic modified surface with oleophobic properties, while Fig. 10.20 shows the antistatic properties of the hybrid coatings. Izumi et al. [44, 45] studied the influence of firing conditions on adhesion of coatings prepared with methyltriethoxysilane (Type 2) for use as thick layer protection against corrosion of stainless steel.



Fig. 10.19 Anti-graffiti effect of an oleophobic organic–inorganic coating on glass towards acrylic spray paint. *Top*, uncoated glass surface; *bottom*, hybrid coated (Reprinted with permission from Elsevier) [53]

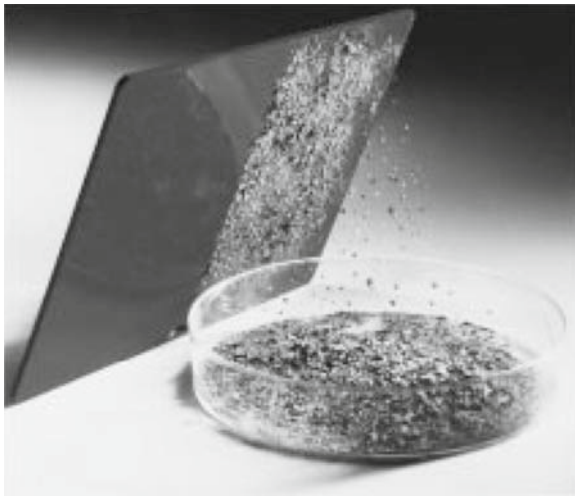


Fig. 10.20 Ash-test with an antistatic hybrid coating on a half side coated polycarbonate substrate (Reprinted with permission from Elsevier) [53]

While the primary focus is on hermeticity, it is also necessary to consider mechanical stability of coatings. Hybrid coatings have been developed to address abrasion resistance, particularly when it comes to coatings for optical fibers [57]. The requirements for this application are extremely demanding because these coatings must be applied to fibers during the fiber drawing operation, allowing the fiber to be spooled and cabled in high volume manufacturing operation.

The features of this coating system are that the coating (a) should be a one-component system, (b) have sufficient viscosity, and (c) show good wetting to the fiber substrate. Once the coating is applied to the fiber, the coating must UV cure quickly. Other properties of the coating are hardness to resist scratching, flexibility, toughness to resist

cracking, and optical transparency [58]. In addition, these coatings need to protect the fibers from fatigue, which is a time dependent process resulting from environmental exposure. Typically, UV-curable acrylates have been used [59]. A variety of acrylates have been modified with a sol–gel process that introduces chemical links between organic and inorganic components. Functional group substituted alkoxysiloxanes in the coatings promote adhesion to the fiber substrate [60].

10.10 Conclusions

In this chapter, we summarized the main methods of preparation of hybrid hermetic barriers, and the methods used for evaluation of their effectiveness. The main focus was on hybrid materials obtained by a sol–gel method, since this does not use expensive equipment, as is used in PECVD and ALD. Another advantage of the sol–gel method is the higher purity of the precursors and their ready availability.

The main advantages of using hybrid coatings are flexibility, low processing temperature and dual mechanism to assure hermeticity. The organic groups bonded directly to the silicon atoms both block the porosity of the film and increase hydrophobicity of the surface.

References

1. Lews J (2006) Material challenge for flexible organic devices. *Mater Today* 9: 38
2. Burrows PEGraff GLGross MEMartin PMSHi MKHall MMast EBonham CBennett WSullivan MB (2001) Ultra barrier flexible substrates for flat panel display. *Display* 22: 65.
3. Ely K (2000) Issues in hermetic sealing of medical products. *MDDIp*. 186.
4. Chatham H (1996) Oxygen diffusion barrier properties of transparent oxide coatings on polymeric substrates. *Surf Coat Tech* 78: 1.
5. Graff GLWilliford REBurrows PE (2004) Mechanisms of vapor permeation through multi-layer barrier films: lag time versus equilibrium permeation. *J Appl Phys* 96: 1840.
6. da Silva Sobrinho ASCzeremuskin GLatreche MWertheimer MR (2000) Defect-permeation correlation for ultrathin transparent barrier coatings on polymers. *J Vac Sci Technol A* 18: 149.
7. Vogt BDLee H-JPrabhu VMDeLongchamp DMLin EKWu W-I (2005) X-ray and neutron reflectivity measurements of moisture transport through model multilayered barrier films for flexible displays. *J Appl Phys* 97: 114509.
8. da Silva Sobrinho ASLatreche MCzeremuskin GKlemborg-Sapieha JEWertheimer MR (1998) Transparent barrier coatings on polyethylene terephthalate by single and dual-frequency plasma-enhanced chemical vapor deposition. *J Vac Sci Technol A* 16: 3190.
9. Shaw DGLanglois MG (1994) Use of vapor deposited acrylate coatings to improve the barrier properties of metallized film. 37th Annual Technical Conference Proceedings of Society of Vacuum CoatersQuimperFrancep. 240.
10. Tang CWvan Slyke SA (1997) Organic electroluminescent diodes. *Appl Phys Lett* 51: 913.
11. Burrows PEBulovic VForrest SRSapochak LSMcCarty DMThomson ME (1994) Reliability and degradation of organic light emitting devices. *Appl Phys Lett* 65: 2922.

12. Burrows PEGraff GLGross MEMartin PMHall MMast EBonham CBennett WMichalski LWeaver MBrown JFogarty DSapochak LS (2001) Gas permeation and lifetime test on polymer-based barrier coatings. *Proc SPIE* 4105: 75.
13. Gu GBurrows PEVenkatesh SFForrest SRThompson ME (1997) Vacuum-deposited nonpolymeric flexible organic light-emitting devices. *Opt Lett* 22: 172.
14. Baldo MA Lemansky SBurrows PETHompson MEForrest SR (1999) Very high-efficiency green organic light-emitting devices based on electrophosphorescence. *Appl Phys Lett* 75: 4.
15. Weaver MSMichalski LARajan KRothman MASilvernail JABrown JJBurrows PEGraff GLGross MEMartin PMHall MMast EBonham CBennett WZumhoff M (2002) Organic light-emitting devices with extended operating lifetimes on plastic substrates. *Appl Phys Lett* 81: 2929.
16. Groner MDGeorge SMMcLean SMCarcia PF (2006) Gas diffusion barriers on polymers using Al₂O₃ atomic layer deposition. *Appl Phys Lett* 88: 051907.
17. Carcia PFMcLean RSReilly MHGroner MDGeorge SM (2006) Ca test of Al₂O₃ gas diffusion barriers grown by atomic layer deposition on polymers. *Appl Phys Lett* 89: 031915
18. Kumar RSAuch MOu EEwald GJin CS (2002) Low moisture permeation measurement through polymer substrates for organic light emitting devices. *Thin Solid Films* 417: 120.
19. Dunkel RBujas RKlein AHornrdt V (2005) Method of measuring ultralow water vapor permeation for OLED displays. *Proc IEEE* 93: 1478.
20. www.mocon.com
21. Ranade AD'Souza NAWallace RMGnade BE (2005) High sensitivity gas permeability measurement system for thin plastic films. *Rev Sci Instrum* 76: 013902.
22. www.wikipedia.org
23. Nilsson POForsell G (1977) Optical properties of calcium. *Phys Rev B* 16: 3352.
24. Nisato GBouten PCPSlikkerveer PJBennett WDGraff GLRutherford NWiese L (2001) Evaluating high performance diffusion barriers: the calcium test. *Proceedings of the 21st Annual International Display Workshop/Asia Display*. 1435.
25. Nisato GKuilder MBouten PMoro LPhilips ORutherford N (2003) Thin film encapsulation for OLEDs: Evaluation of multi-layer barriers using a Ca test. *Proc Soc Info Display Symp Digest Tech Papers* 34: 550.
26. Paetzold RWinnacker AHenseler DCesari VHeuser K (2003) Permeation rate measurements by electrical analysis of calcium corrosion. *Rev Sci Instrum* 74: 5147.
27. Reed STAshley CS (1988) Sol-gel protective films for metal solar mirrors. *MRS Symp Proc* 121: 631.
28. Ashley CSReed STMahoney AR (1988) Planarization of metal substrates for solar mirrors. *MRS Symp Proc* 121: 635.
29. DeLima Neto PAtik MAVaca LAEgerter MA (1994) Sol-gel coatings for chemical protection of stainless steel. *J Sol gel Sci Technol* 2: 529.
30. Stoch AStoch JRakowska A (1994) An XPS and SEMS study of silica sol-gel/metal substrate interaction. *Surf Interf Anal* 22: 242.
31. DeLima Neto PAtik MAVaca LAEgerter MA (1994) Sol-gel ZrO₂ coatings for chemical protection of stainless steel. *J Sol gel Sci Technol* 1: 177.
32. Guglielmi M (1997) Sol-gel Coatings on metals. *J Sol gel Sci Tech* 8: 443.
33. Haas KH Wolter H (1999) Synthesis properties and applications of inorganic-organic copolymers (ORMOCER®s). *Curr Opin Solid State Mater Sci* 4: 571.
34. Haas KHRose K (2003) Hybrid inorganic/organic polymers with nanoscale building blocks: precursors processing properties and applications. *Rev Adv Mater Sci* 5: 47.
35. Sanchez CRibot F (1994) Chemical design of hybrid organic-inorganic materials synthesized via sol-gel. *New J Chem* 18: 1007
36. Jitianu ABritchi ADeleanu CBadescu VZaharescu M (2003) Comparative study of the sol-gel processes starting with different substituted Si-alkoxide. *J Non Cryst Solids* 319: 263.
37. Unger BJancke HHähner MStade H (1994) The early stages of the sol-gel processing of TEOS. *J Sol Gel Sci Tech* 2: 51.

38. Wojcik ABKlein LC (1995) Transparent inorganic/organic copolymers by the sol-gel process: copolymers of tetraethyl orthosilicate (TEOS)/vinyl triethoxysilane (VTES) and (meth)acrylate monomers. *J Sol Gel Sci Tech* 4: 57.
39. Wojcik ABKlein LC (1995) Transparent inorganic/organic copolymers by the sol-gel process: thermal behavior of copolymers of tetraethyl orthosilicate (TEOS)/vinyl triethoxysilane (VTES) and (meth)acrylate monomers. *J Sol Gel Sci Tech* 5: 77.
40. Wojcik ABKlein LC (1997) Organic/inorganic hybrids by the sol-gel process: classification of synthesis methods. *Appl Organomet Chem* 11: 129.
41. Avnir DKlein LCLevy DSchubert UWojcik AB (1998) Organo-silica Sol-Gel Materials. In Rappoport ZApeloig Y (eds) *The Chemistry of Organic silicon Compounds Vol. 2* Chapter 40. WileyLondonp. 2317.
42. Jackson AJitianu AKlein LC (2006) Development of a Hermetic Barrier Using Vinyl Triethoxysilane (VTEOS) and Sol-Gel Processing. *Materials Matters* 1: 11.
43. Haas KHAmberg-Schwab SBallweg T (2003) Synthesis and properties of hybrid inorganic-organic polymers based on organically modified Si-alkoxide and their use for permeation control. CIMTEC-2002-10th International Ceramics Congress and 3rd forum on New Materials; in Vincenzini P. (ed.) 10th International Ceramics Congress-Part BTechnap. 581.
44. Murakami MIZumi KDeguchi TMorita ATohge NMinami T (1989) Silica coating from triethoxymethylsilane on stainless steel sheets. *J Ceram Soc Jpn* 97: 91.
45. Izumi KTanaka HUCHida YTohge NMinami T. (1992) Influence of firing on adhesion of methyltrialkoxysilane-derived coatings on steel sheets. *J Non Crystalline Solids* 147,148: 483.
46. Amberg-Schwab SHoffmannMBaderH (1996) Barrierschichten für Verpackungsmaterialien: Barrierschichten aus anorganisch-organischen Hybridpolymeren. *Kunststoffe* 86: 660.
47. Amberg-Schwab SHoffmannMBader HGessler M (1998) Inorganic-organic polymers with barrier properties for water vaporoxygen and flavors. *J Sol Gel Sci Technol* 13: 141.
48. Hoffmann MAmberg-Schwab S (1998) Barrier properties of inorganic-organic polymers. *Mat Res Soc Symp Proc* 519: 309.
49. Amberg-Schwab SKatschorek HWeber UHoffmann MBurger A (2000) Barrier properties of inorganic-organic polymers: influence of starting compounds curing conditions and storage-scaling-up to industrial application. *J Sol gel Sci Tech* 19: 125.
50. Amberg-Schwab SKatschorek HWeber UBurger A (2003) Inorganic-organic polymers as migration barriers against liquid and volatile compounds. *J Sol gel Sci Tech* 26: 699.
51. Amberg-Schwab SWeber UBurger ANique SXalter R (2006) Development of passive and active barrier coatings on basis of inorganic-organic polymers. *Monatshefte für Chemie (Chemical Monthly)* 137: 657.
52. Sanchez CJulian BBelleville PPopall M (2005) Applications of hybrid organic-inorganic nanocomposites. *J Mat Chem* 15: 3559.
53. Haas KHAmberg-Schwab S Rose K (1999) Functionalized coating materials based on inorganic-organic polymers. *Thin solids films* 351: 198.
54. Dahmouche KATik MMello NCBonagamba TJPanepucci HAegerter MAJudeinstein P (1997) Investigation of new ion-conducting ormolytes: structure and properties. *J Sol Gel Sci Technol* 8: 711.
55. Judeinstein PTitman JStamm MSchmidt H (1994) Investigation of ion-conducting ormolytes: structure-property relationships. *Chem Mater* 6: 127.
56. Depre LIngram MPoinsignon C Poppal M (2000) Proton conducting sulfon/sulfonamide functionalized materials based on inorganic-organic matrices. *Electrochim Acta* 45: 1377
57. Wojcik ABKlein LCRondinella VVMatthewson MJFoy PR (1993) Organically modified silicate coatings for optical fibers. *SPIE* 2074: 135.
58. Rondinella VVMatthewson MJ (1993) Effect of loading mode and coating on dynamic fatigue of optical fiber in two-point bending. *J Am Ceram Soc* 76: 139.
59. Wei TSSkutnik BJ (1988) Effect of coating on fatigue behavior of optical fiber. *J Non Cryst Solids* 102: 100.
60. Nishiyama NHorie KAsakura T (1988) Adsorption behavior of a silane coupling agent onto a colloidal silica surface studies by ²⁹Si NMR spectroscopy. *J Colloid Interface Sci* 129: 113.

Chapter 11

Polymer–Iron Oxide Based Magnetic Nanocomposites

Mrinal Pal and Abhijit De

Abstract The thrust to develop magnetic particles, both fundamentally and technologically, arose out of the necessity for application of this in many spheres of the human race. Physical and chemical properties of lower dimension (nanoscale) particles are very much different from their bulk counterpart. Magnetic nanocomposites depicted quite a few unique properties like very low as well as very high coercivity, superparamagnetism, blocking temperature etc., which opened up new vistas in this area. It was quite evident that iron oxide, in different phases and alloys formed the basic macroscopic magnetic material. In the past few decades it was clear that besides developing magnetic particles as a pure material, there arose a tremendous compulsion to probe into diversions for an inter disciplinary area engulfing chemical and biological sciences for the benefit of mankind. One such effort resulted in determining the compatibility of nano-scale magnetic particles (metal oxides, particularly iron oxide) with polymeric materials to form organic/inorganic composites. Amongst the many questions, which generated with time, a few have been typically selected and addressed in this chapter. This chapter primarily concentrates on ways to prepare (both chemical and physical processes), understand structural aspects, magnetic behavior, electrical and optical properties of polymer–iron oxide based magnetic nanocomposites. Some interesting applications are discussed at the end of the chapter.

Abbreviations CCD: Charge coupled device; CM: Ceramic method; DTA: Differential thermal analysis; FTIR: Fourier transform infrared; GCR: Glass-ceramic route; HEBM: High-energy ball milling; IAA: Iron (III) tris (3-allylacetylacetonate); IO: Iron oxide; IS: Isomer shift; KG: Kilo gauss; MBE: Molecular beam epitaxy; MER: Magnetite epoxy resins; MF: Magnetic fluids; MS: Mössbauer spectroscopy; MW: Microwave; MZF: Manganese zinc ferrite; nm: Nanometer; NR: Natural rubber; NZF: Nickel zinc ferrite; PEG: Polyethylene glycol; PMAA: Poly-methacrylic acid; PVA: Polyvinyl acetate; PVB: Poly vinyl butyral; RFC: Rubber ferrite composite; SEM: Scanning electron micro-

M. Pal and A. De (✉)

Department of Physics, Presidency College, Kolkata 700 073, India
e-mail: abhijitde61@gmail.com

scopy; SGM: Sol-gel method; TEM: Transmission electron microscope; UV: Ultra-violet; VSM: Vibrating sample magnetometer; XPS: X-ray photoelectron spectroscopy; XRD: X-ray diffraction; μm : Micrometer; $\mu\text{-XRF}$: Micro-focus X-ray fluorescence; E_a : Anisotropy energy; E_z : Zeeman energy; H_c : Coercive force; H_{eff} : Hyperfine field; k : Boltzmann's constant; K : Anisotropy constant; M_s : Saturation magnetization of individual domain; M_{sa} : Saturation magnetization of the assembly or assembled particles; M_r : Remanence magnetization; T_B : Blocking temperature; T_c : Curie temperature; T_N : Néel temperature; V : Volume; Δ : Quadrupole splitting; β : Full width at half maximum (FWHM); λ : X-ray wavelength; τ : Relaxation time; μ : Magnetic moment.

11.1 Retrospect and Motivation

Why study magnetism and run after magnetic materials? If ever we were to ask such a question the answer is naturally – nature! Yes, there is no doubt that it was none other than nature that was primarily responsible to give us such a versatile topic and provide us with the material. We may recall our grandfather talking, where/when a man lazing with a stick was stunned to find the metal-end of the stick stuck to a *stone*. This was later termed *lodestone or magnetite*. Going a step ahead/further, fine particles of magnetite having single domain structure, existing inside living cells or organisms, are also known to depict *magnetotaxis (direction seeking)* effect governing their movement guided by earth's magnetic field. A strong technology driven motivation has been the guiding factor to exploit and enhance the properties in the area of high-density magnetic recording, ferrofluids, etc. Further tremendous impact on theoretical interests like, superparamagnetism, large coercivity, quantum tunneling of magnetization and giant magnetoresistance has been realized. Yet another additional aspect is miniaturization, which brings about convenience and economy. All throughout the development process of inorganic/organic magnetic materials the basic motivation was *sheer compulsion for applications critical to human race* which are technology related areas (communication, space science, etc.) and interdisciplinary avenues (drug delivery or target specific drugs for treatment for dreaded diseases like cancer). There are also some critical challenges to be met to encounter the ever-increasing problems threatening the human race.

11.2 Introduction to Magnetism

11.2.1 Brief Overview

The magnetic properties of solids generally originate from the motion or spin of electrons. Magnetic materials vary from one another depending on the differences

in the spin of electrons and their mutual interaction with the other quantum factors. The magnetic behavior of materials can be classified into the following five major groups:

1. Diamagnetism
2. Paramagnetism
3. Ferromagnetism
4. Ferrimagnetism
5. Antiferromagnetism

Materials in the first two groups are those that exhibit no collective magnetic interactions and are not magnetically ordered. Materials in the last three groups exhibit a long-range magnetic order below a certain critical temperature. Ferromagnetic and ferrimagnetic materials are usually what we consider as being magnetic (i.e., behaving like iron). The remaining three are so weakly magnetic that they are usually thought of as “nonmagnetic.”

1. Diamagnetism

Diamagnetism is a fundamental property of all matter, although it is usually very weak. This is due to the non-cooperative behavior of the orbiting electrons when exposed to an applied magnetic field. Diamagnetic substances are composed of atoms, which have no net magnetic moments (i.e., all the orbital shells are filled and there are no unpaired electrons). However, when exposed to a field, a negative magnetization is produced and thus susceptibility is negative.

2. Paramagnetism

In paramagnetic materials, some of the atoms or ions in the material have a net magnetic moment due to unpaired electrons in a partially filled orbital. One of the most important atoms with unpaired electrons is iron. However, the individual magnetic moments do not interact magnetically, and like diamagnetism, the magnetization is zero when the field is removed. In the presence of a field, a partial alignment of the atomic magnetic moments in the direction of the field results in a net positive magnetization and positive susceptibility.

3. Ferromagnetism

In ferromagnetic materials, the atomic moments exhibit very strong interactions. Electronic exchange forces results in a parallel or anti-parallel alignment of atomic moments which produce these interactions. Exchange forces are very large, equivalent to a field of the order 1,000 Tesla, or approximately a 100 million times the strength of the earth's magnetic field. The exchange force is a quantum mechanical phenomenon due to the relative orientation of the spins of two electrons. Ferromagnetic materials exhibit parallel alignment of moments resulting in large net magnetization even in the absence of a magnetic field. The elements Fe, Ni and Co and many of their alloys are typical ferromagnetic materials. Two distinct characteristics of ferromagnetic materials are their *spontaneous magnetization and the existence of magnetic ordering temperature*.

4. Ferrimagnetism

In ionic compounds, such as oxides, more complex forms of magnetic ordering can occur due to their crystal structure. One type of magnetic ordering is *ferrimagnetism*. In this case the magnetic structure is composed of two magnetic sub lattices (called A and B) separated by oxygen atom. The exchange interactions are mediated by oxygen anions. When this happens, the interactions are called *indirect or super-exchange interactions*. The strongest super-exchange interactions result in an anti-parallel alignment of spins between the A and B sub lattices. In ferrimagnets, the magnetic moments of the A and B sub lattices are not equal and result in a net magnetic moment. Ferrimagnetism is therefore similar to ferromagnetism. It exhibits all the hallmarks of ferromagnetic behavior of spontaneous magnetization, Curie temperature, hysteresis and remanence. However, ferro- and ferrimagnets have different magnetic ordering.

5. Antiferromagnetism

If the A and B sub lattice moments are exactly equal but opposite, the net moment is zero. This type of magnetic ordering is called *antiferromagnetism*. Antiferromagnetic materials also have zero remanence, no hysteresis, but a small positive susceptibility that varies in a peculiar way with temperature. The clue to antiferromagnetism is the behavior of susceptibility above a critical temperature, called the Néel temperature (T_N). Above T_N , the susceptibility obeys the Curie-Weiss law for paramagnets but with a negative intercept indicating negative exchange interactions (Fig. 11.1).

11.2.2 Ferrites

In ferromagnetic materials the electrons spin spontaneously and align in a net parallel direction, while in antiferromagnetic materials they are aligned anti-parallel leaving a small or negligible moment. In case of ferrimagnetic materials, cancellation of spin moment due to antiparallel alignment is partial, resulting in a high net moment. Ferrites were primarily known as *ceramic magnetic materials*.

Soft and hard ferrites are the two main synthetic ferrites. The soft ferrites have high permeability, low hysteresis and low eddy current losses. The magnetic properties of soft ferrites can be varied by:

1. Introducing structural defects (non-magnetic inclusions, voids, etc.) which may increase both the coercive force and the hysteresis by pinning the domain wall.
2. Growth of preferred crystal orientation in the direction of easy magnetization.

Soft ferrites usually have cubic structures of the inverse spinel type. These are the manganese – zinc ferrites, nickel ferrites and nickel – zinc ferrites. A different variety of magnetic material is achieved by varying the proportion of zinc to manganese or nickel or by inclusion of some other metal ion. Magnetite (Fe_3O_4),

Maghemite ($\gamma\text{-Fe}_2\text{O}_3$) are commonly known as ferrite materials. On the other hand, Hematite ($\alpha\text{-Fe}_2\text{O}_3$) shows interesting semiconducting properties.

11.2.3 Bulk vs. Fine Particles

The initial interest to work with fine particles and thin films of magnetic materials was kindled reading well-known texts [1, 2]. In contrast to macroscopic bulk features, fine particles of magnetic materials in pure form have shown some interesting features leading to fascinating technical applications. The spectrum of applications is tremendous which at one end we have high-efficiency motor, fridge magnet, and storage media devices and high frequency applications at the other. For such applications both very soft (FeCuNbSiB) and very hard (NdFeB) magnetic materials are essential for nanocomposites.

Superparamagnetism and exchange anisotropy are prime aspects where it is assumed that the particles are single-domain and uniaxial. Usually uniaxial refers to direction for easy axis of magnetization. Consider an assembly of uniaxial, single-domain particles. The anisotropy energy density E for such a system is:

$K \sin^2\theta$ (K is the anisotropy constant in erg/cm³, and θ is the angle between saturation magnetization M_s and easy axis). The energy barrier that must be overcome before a particle can reverse its magnetization is: $KV = \Delta E$ (ergs). The product of saturation magnetization of individual domain (M_s) and volume element of fine particle system (V) gives the magnetic moment of the system. When $K = 0$, each particle in a system has no anisotropy, and the moment/movement of each particle can have any direction as a result of the classical theory of paramagnetism. For such an assembly of magnetic particles (fine iron particles) in a non-magnetic matrix (solid mercury), the magnetization of such an assembly is:

$$M = n\mu L(a), \quad (11.1)$$

where $a = \mu H/kT$ and the saturation magnetization $M_{sa} = n\mu$, where n is the number of particles per unit volume of assembled particles and μ is the magnetic moment per particle. Initial (M_i) and remanence (M_r) magnetizations are related with relaxation time (τ) as

$$M_r = M_i \exp(-t / \tau). \quad (11.2)$$

The magnetization of fine-particle magnetic solids, M , is given by the Langevin equation,

$$M / M_{sa} = \coth(\mu H / kT - kT / \mu H), \quad (11.3)$$

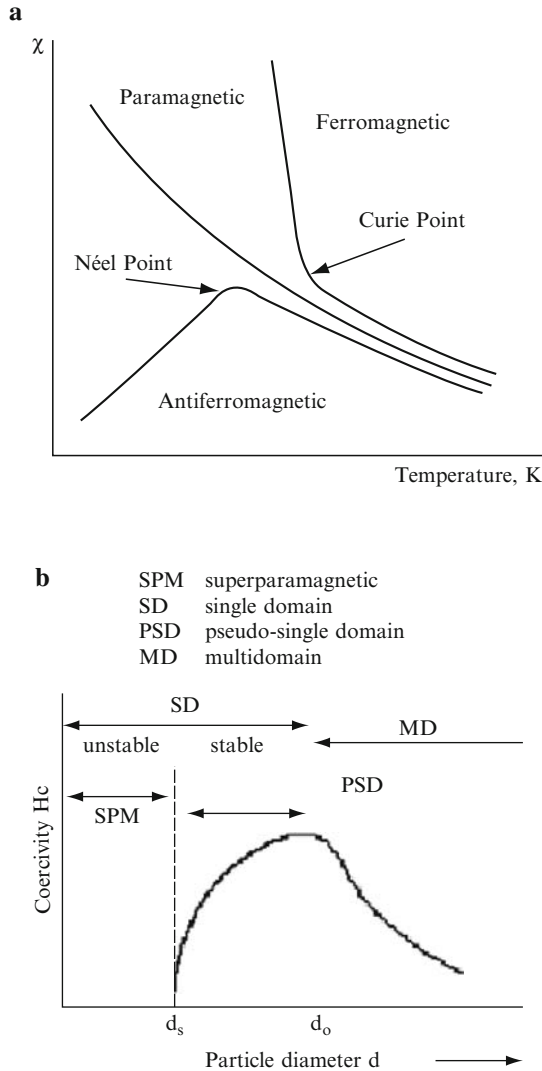


Fig. 11.1 (a) Variation of susceptibility of different magnetic materials with temperature. (b) Schematic diagram showing variation of coercivity (H_c) with particle diameter (d) for magnetic materials

where H is the field, T is the absolute temperature, $\mu (=M_s V)$ is the magnetic moment per particle, and k is the Boltzmann's constant [3].

Hysteresis appears and superparamagnetism disappears when particles of a certain size are cooled to a particular temperature, or when the particle size at constant temperature increases beyond a particular diameter D_p . This means that the determination of critical values of temperature or size is highly fundamental.

Initially spherical particles of iron of diameter about 50 Å dispersed in solid mercury at 200°K and 77°K depicted superparamagnetic nature. At 4.2°K the particles in the assembly do not have sufficient thermal energy for complete thermal equilibrium with the applied field during the time required for experimentation.

An assembly of fine particles of cobalt, say spherical particle Co of diameter 68 Å and τ of 0.1 s at room temperature, tries to reach thermal equilibrium (M_p) almost instantaneously and such particles attain superparamagnetic behavior.

Bean and Livingston [4] derived the following expression for the coercive force of a sub-domain particle:

$$H_c = 2KV[1 - 5(kT / KV)^{1/2}] / \mu, \quad (11.4)$$

where K is the magnetic anisotropy, V is the particle volume, μ is the magnetic moment, T is the absolute temperature, and k is the Boltzmann constant. With reference to this relation for H_c , at the onset of superparamagnetism and for temperatures below the blocking temperature T_B , the coercive force becomes zero. Thus

$$KV = 25kT_B. \quad (11.5)$$

For a plot of H_c vs. $T^{1/2}$, the intercept I at $T = 0$ is:

$$I = 2KV / \mu. \quad (11.6)$$

It has also been reported that for a size range distribution of superparamagnetic particles, a linear plot verified the validity of (11.4) and (11.5). For a plot of H_c and $T^{1/2}$ the distribution of data may show a linear relation for a finite value of I at $T = 0$, and $H_c = 0$ for $T = T_B$ (the blocking temperature). From (11.1), the slope S of the line becomes $[-10(kKV)^{1/2}] / \mu$ and gives:

$$\mu = 50kI / S^2. \quad (11.7)$$

Further, dividing the total magnetic moment in (11.7) by saturation magnetization of say, *magnetite*, the volume V per particle of magnetite may be estimated as:

$$V = 50kI / (M_s S^2). \quad (11.8)$$

If the particle is assumed spherical, an idea for a particle size can be estimated. The magnitude of coercive force increases rapidly with particle size.

So far, the description of fine particles of nano-scale dimension is primarily referred to as a solid state in powder form. The next question one encounters is what happens when such powdered substance is homogeneously dispersed in a medium which is non-magnetic? The non-magnetic medium may either be of a fixed matrix type (other non-magnetic metallic system or polymer medium viz. magnetic tape or disk) or of a free flowing type. This is commonly known as a *magnetic fluid*. A *magnetic fluid* is a colloidal dispersion of nano-sized magnetic particles in a

non-magnetic carrier. Non-magnetic materials could either be metallic for instance Hg systems [1] or any organic matrix compound. In a magnetic fluid, in contrast to bulk properties of magnetic materials in powder or solid state, the rotational freedom of the particles enables the magnetization process to be independent of particle anisotropy. So in ferrofluids the magnetization represents the degree of alignment of the magnetic moments of the particles. This is the Zeeman energy, $E_z = \mu H$, where μ is the magnetic moment of the particle and H the applied magnetic field. If a matrix is solidified in presence of an applied magnetic field, a *magnetically textured* sample is obtained which has particles of fixed orientation. In such a system, the Neel rotation of magnetic moments, away from the easy axis of the particle decides the *in-field magnetization process*. The applied magnetic field and the process temperature during sample preparation influence the statistical distribution of anisotropy axes. Basically, two types of *dispersed systems* have been of prime importance. Firstly, in a *mono-dispersed* system it was fundamental to estimate the difference between the normalized magnetization curves for *magnetically textured* samples and *ferrofluids*. Secondly, in a *poly-dispersed system* an increase in anisotropy energy ($E_a = KV$, where K is the effective anisotropy constant and $V =$ particle volume) is referred to *resistance to magnetization*. When $E_a \ll E_z$ the difference between magnetization of fluid and textured fluid is very small for a particular temperature.

The grain size, in the free state or in thin film or in any other configuration, is usually calculated using Scherrer's equation [5]

$$D = k\lambda / (\beta \cos\theta), \quad (11.9)$$

where D is the grain size, λ the X-ray wavelength, β (in radian) is the full width at half maximum (FWHM) of the peaks, θ the reflection angle and k is a constant of value ~ 1 .

11.2.4 Thin Films

The term thin film refers to “down-scale” of bulk material, which is reached when the thickness of the material is equal to less than 1 μm . This means the surface property of the material is dominant compared to its bulk counterpart. Such geometrical configuration of any material is unable to stand by itself and necessarily needs a substrate on which it is grown or deposited and is able to arrive at a lower strain energy to form stable films. In certain special cases “stand alone films” may be developed, but their uses have been rather limited. The substrate may be amorphous or crystalline in nature. The sticking probability of the deposited film material on the substrate material depends on the lattice matching between them. For low sticking probability, films tend to peel off the substrate surface.

Thin films are grown using either a physical or a chemical process. Contamination and undesired oxidation are serious problems during the growth of thin films, which can be overcome using ultra-high vacuum techniques. Usual physical processes to

grow thin films are sputtering, thermal evaporation, electron beam evaporation, molecular beam epitaxy (MBE), etc. MBE has the capability to grow films of thickness of a single atomic layer. Multilayer or sandwich structures are also possible to be grown in various configurations.

Under this section probably it may be more relevant to include the term film, which could engulf both thick and thin films. However, it will be discussed that inorganic oxides need an organic coating as holding or a support medium for very important applications.

As an ending note to this section, the magnetic materials are broadly classified as soft (easily magnetized) and hard (difficult to magnetize). “Soft” magnets (e.g., Ni/Fe alloy, Fe, etc.) have low magnetic coercive field (<10 Oe) and almost zero remanent magnetization. On the other hand, “hard” magnets (e.g., iron oxide doped with Co, CrO₂, Fe particles, barium ferrite, etc.) have high magnetic coercive field (>100 Oe) and significant remanent magnetization.

11.3 Preparation Methods

Some preparation methods for growing organic/inorganic magnetic nanocomposites are discussed below.

11.3.1 Chemical Methods

11.3.1.1 Co-precipitation Method

The process of co-precipitation deals with precipitation of multi-component or compound system in a matrix medium. Solid precipitates are formed and are filtered for a homogeneous matrix formation. A solution of inorganic or organic salt forms the co-precipitation agent. It is important that the essential compound be insoluble in the mother liquid. Mixing rate, pH, temperature, concentration, etc. are the main parameters, which need to be regulated carefully [6]. After proper drying and subsequent annealing, nanostructure materials are obtained in the system. Lot of care must be taken to maintain homogeneity of the nanostructure material in the matrix medium.

11.3.1.2 Sol-Gel Method (SGM)

The sol-gel chemistry is based on the hydrolysis and condensation of alkoxides, M(OR)_z, where M^{z+} is a metal, and “R” an alkyl group (R = Me, Et.). Alkoxides are not miscible with water so that a common solvent, usually the parent alcohol ROH, has to be used. The oxide network progressively grows from the solution, leading to the formation of oligomers, oxopolymers, colloids (sols or gels), and finally a solid phase [7].

Dispersions of colloids in liquids are basic to the formation of *sols*. *Gel* is short form of gelation implying growth and linking together of polymeric units to form a continuous network. It is interesting to note that at the very first stage of SGM an initial formation of amorphous network in the solution state precedes the process of crystallization. This is a distinct feature and in contrast to the crystallization process [8]. Mostly metal alkoxides, having a metal ion and alkyl group, are used as a starting compound. The process involves formation of an amorphous gel from solution through hydrolysis and poly-condensation reactions. Drying treatments in selected ambient are necessary as the obtained amorphous gel product contains sufficient amount of water and organic residues. Subsequent annealing of dehydrated gels is necessary to produce nanocrystalline materials. SGM favors low temperature processing. Large-scale application is rather discouraged as the parent metal alkoxides are highly expensive.

11.3.1.3 Solvent Evaporation Method

The process of solvent evaporation method is probably one of the simplest methods to select starting compounds, generate reaction pathways and treatment of end products. It has tremendous potential for large-scale production, variety of combination compatibility and applications. In fact, solvent evaporation method may be diverted towards spray drying, rapid evaporation, flame pyrolysis, and thermolysis to develop nanosized mixed-oxide powders from a polymer matrix based precursor solution [9–11]. In Sect. 5.1 a detailed description of this method has been discussed.

In the solvent evaporation method, the solvent can be retrieved in a closed system and can be made to use again, which is not the case under normal exhaust. Indeed, letting the solvent escape to the atmosphere is undesirable to both environment and economy.

11.3.1.4 Combustion Method

The two main aspects of the combustion method are externally induced and self-sustaining combustion synthesis. The self-sustaining combustion method is rapid and avoids formation of intermediate crystalline phases that require inter-diffusion for complete reaction.

11.3.2 Physical Methods

11.3.2.1 Conventional Ceramic Method

The ceramic method (CM) is one of the most primitive and well-proven methods to produce powder material. Primarily this process was used to develop ferrite materials even industrially. There are some typical steps followed for manufacture of polycrystalline ferrites in powder form [12]. CM begins with the usual weighing of

raw materials. Then it has to be either dry mixing i.e., pressing or wet mixing i.e., filtering and drying of compounds, to get the product materials. Then pre-sintering is done, then crushing follows. The next step is dry mixing or wet milling, filtering and dry powdering. Then the obtained material is mixed with a binder or lubricant. Granulation of the material is done for homogeneous product formation. This is followed by die pressing and finally sintering to get the net product.

One of the advanced versions of CM is the glass-ceramic route (GCR). Glass-ceramics basically refers to controlled crystallization of appropriate glasses. Precipitation of different types of nanocrystalline phases in selected parent glass systems is performed using two-stage heat treatment programs. Heat treatment at nucleation and crystallization temperature is highly critical during formation of glass materials. Differential thermal analysis (DTA) provides both, the crystalline temperature and the glass transition temperature from which the nucleation temperature is estimated. Pal et al. [13, 14] reported that nanoparticles of certain compounds remained well protected within the glass matrix.

11.3.2.2 Sputtering

For the process of sputtering, a target material which may be composed of a single element or compound form is selected as an electrode in a vacuum chamber. The requirement of high to ultra-high vacuum of the deposition chamber reduces the probability for contamination. Gas (argon or krypton or a reactive gas by combining with proportions of hydrogen or oxygen) plasma is generated thereby creating a mixture of ions of high energy, accelerated and bombarded onto the target. Atoms and clusters, both neutral and ionic, are ejected from the target, which are essential to the formation of films on selected substrates placed at required position inside the chamber. The sputtering parameters like, plasma environment, its pressure, sputtering power, duration for film growth, substrate temperature regulate ionic movement and control the type of film material. Stavroyiannis et al. [15] could estimate the ratio of atoms to clusters or ions to neutrals produced, depending on the mass and energy of the projectile ion and a variety of other experimental parameters. The process involving co-sputtering is more efficient for materials with low mutual solubility. In situ annealing of sputtered grown films has been known to control the material from being amorphous or crystalline. One of the major drawbacks for sputtering is formation of clusters in the film material. However, for large scale production or in-line process for film growth sputtering has proved to be of immense potential.

11.3.2.3 Molecular Beam Epitaxy (MBE)

MBE is one of the most advanced processes to grow highly precise controlled layered films. However, ultrahigh vacuum conditions and stringent technological setup are critical during film growth. This is a technique in which epitaxial layers are grown on temperature controlled substrates by impinging molecular or atomic beams evaporated from effusion sources under ultrahigh vacuum conditions. Inoue et al. [16]

reported that in contrast to conventional evaporation techniques the beam intensities of each source and the substrate temperature in MBE can be separately controlled to achieve epitaxial growth depending on the selection of substrate material.

11.3.2.4 Melt Spinning

Preparation of two-phase magnetic materials involving coupling of hard and soft magnetic materials have been possible employing the process of melt spinning. Alloy ingots are prepared selecting starting materials of about three to five elements. Combinations of such starting materials are usually heated by employing arc melting in some inert atmosphere. The alloy ingots are crushed into small pieces which are transferred to quartz crucibles with a nozzle diameter less than one millimeter. Melt spinning amorphous ribbon samples of various thicknesses are prepared using single roll melt spinning equipment with a copper roll in an inert atmosphere. Ping and Hono [17] reported amorphous samples which were sealed in an evacuated quartz tube and annealed for different time periods. The process of melts spinning offered minimum interface contamination and favored production of porosity free materials. Altering the annealing conditions controlled the grain sizes inside the samples. Melt spinning is a viable process for large-scale production of required material.

11.3.2.5 Mechanical Alloying

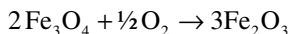
Mechanical alloying or mechanical milling or high-energy ball milling (HEBM) is usually employed to prepare nanocrystalline alloys. The starting powder material is introduced in a vial containing a number of milling balls and subjected to vigorous shaking. Such violent action brings about energy transfer to the powdered particles in the mills by virtue of shearing action or impact of the high velocity balls with the powder. This leads to the formation of nanostructured materials. The dimension and structure of nanoparticles in the powdered material depends on parameters like milling speed, type, size, size distribution of balls, ball to powder weight ratio, milling atmosphere, etc. [18]. The prime hindrance of HEBM is contamination from the ball material. HEBM is one of the present commercial technological processes for large-scale production of material.

11.4 Iron Oxide (IO)

11.4.1 Pure Phase

Iron ferrite is probably the oldest magnetic material known to mankind. Magnetite (Fe_3O_4), also known as *ferrous ferrite*, has a cubic structure. Their general form is $\text{MO} \cdot \text{Fe}_2\text{O}_3$, where M is a divalent metal ion like Mn, Fe, Ni, Co, Mg, etc.

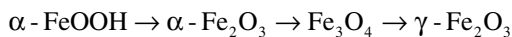
Maghemite ($\gamma\text{-Fe}_2\text{O}_3$) is ferrimagnetic in nature, has a cubic structure or spinel crystal structure, made by oxidizing magnetite:



Maghemite is unstable and transforms to hematite ($\alpha\text{-Fe}_2\text{O}_3$) on heating above 673 K in air. The magnetic ions (Fe^{3+}) in $\gamma\text{-Fe}_2\text{O}_3$ are identical in nature and ferrimagnetism is due to unequal distribution of such ions in the available sites. The tetragonal cell of $\gamma\text{-Fe}_2\text{O}_3$ is obtained as conversion from Fe_3O_4 . A unit cell of Fe_3O_4 contains eight molecules. Maghemite can be considered as a Fe (II)-deficient magnetite. The structure of $\gamma\text{-Fe}_2\text{O}_3$ has inverse spinel structure and is represented as $\text{Fe}^{3+}[\text{Fe}^{3+}_{40/3} \text{ }_{1/8}] \text{O}_{32}$, where represents the vacancy site present in the lattice. The Fe^{3+} ions outside the square bracket represent tetrahedral position and the Fe^{3+} ions inside the square bracket represent the octahedral position. The structure is based around a face centered cubic array of oxygen atoms with the cations filling either the tetrahedral or octahedral interstices within this array. There are 16 (out of 32) occupied octahedral sites and 8 (out of 64) occupied tetrahedral sites in the unit cell $\gamma\text{-Fe}_2\text{O}_3$. Thus a molecule of $\gamma\text{-Fe}_2\text{O}_3$ corresponding to a unit cell can be calculated to have a net moment of 2.5 μ_B .

The naturally occurring maghemite usually forms by weathering or low-temperature oxidation of spinels containing ferrous iron, commonly magnetic or titanium magnetite. They exist as widespread yellow pigment in sediments. Encyclopaedia Britannica says that maghemite exhibits strong magnetism and remanence. Its structure is isometric, of defective spinel form, and somewhat iron-deficient. It is metastable with respect to hematite and forms a continuous metastable solid with magnetite.

Usually $\gamma\text{-Fe}_2\text{O}_3$ is synthesized from α -goethite. The process of transformation of α -goethite to $\gamma\text{-Fe}_2\text{O}_3$ is represented as:



Compounds like lepidrocite [$\gamma\text{-FeO(OH)}$] when treated with pyridine and oxidized for long hours give complete conversion to $\gamma\text{-Fe}_2\text{O}_3$ having nanosized particle dimension (Venkataraman 2001). In some cases the conversion of Fe(OH)_2 to $\gamma\text{-Fe}_2\text{O}_3$ gets accelerated by heating and may take place through intermediates such as FeO(OH) and Fe_3O_4 [19].

Iron oxide particles are known to possess various shapes which depend on the routes for nucleation and growth from metal salt solutions. A few are tabulated in Table 11.1 [7].

Table 11.1 (Refer Sect. 2.1.1) Various shapes of IO

Particle type	Shape
Hematite Fe_2O_3	Ellipsoidal
	Spherical
	Cubic
	Spindle
	Disk
$\beta\text{-FeOOH}$	Rod
Fe_3O_4	Spherical

11.4.2 Composite

$\text{Ni}_{1-x}\text{Zn}_x\text{Fe}_2\text{O}_4$ (NZF) and $\text{Mn}_{1-x}\text{Zn}_x\text{Fe}_2\text{O}_4$ (MZF) are among zinc-based ferrite composites that have attracted attention [20–22]. Iron oxide was alloyed either with other *ferromagnetic/ferrimagnetic* or divalent elements. More details relevant to this compound will be discussed in the next section.

11.5 Metal Oxide Polymer Magnetic Nanocomposites

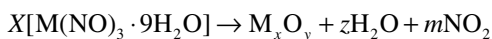
Metal salts (MX) when dissolved in an aqueous medium dissociate into ions in the solution. The negative charge of anions X^{z-} balances the positive charge of the atom M^{z+} [7]. When a *polymer structure provider* (polyvinyl alcohol – PVA, polyvinyl acetate, polyethylene glycol, etc.) is added to the metal compound, particularly nitrates, following the solution evaporation process, two phenomena are known to occur. Firstly, during addition of optimum amount of the polymer material to the mixed metal nitrate solution, the polar groups of the long chain polymer play a wrapping and covering role for the cations in the solution. A mutual contact between cations is restricted, which limits the growth of cations in size. Thus the metal ions remain uniformly distributed in the viscous liquid during evaporation. Secondly, complete evaporation of PVA gives out carbonaceous material, which provides heat through combustion for the formation of fine single-phase ferrite powders at a relatively low external temperature. Pramanik and Pathak [10] reported addition of urea to a mixture of metal compound, appropriate solvent, and *polymer structure provider*. It was observed that urea acted as a retardant which arrested the crystallization of the precursor powder during complete evaporation of the *polymer structure provider* added solution.

PVA is one of the most widely used polymers to support formation of metal oxide polymer nanocomposites. PVA of general structure $(-\text{C}_2\text{H}_4\text{O})_n$ has the following characteristics: crystal system – monoclinic, space group $\text{P2}_1/\text{m}-\text{C}_{2h}^2$, lattice constants – $a = 7.81 \text{ \AA}$, $b = 2.25 \text{ \AA}$, $c = 5.51 \text{ \AA}$ and $\beta = 91.7^\circ$, number of chains per unit cell – $N = 2$, molecular conformation – planar zigzag, and crystal density of 1.35 g/cc . PVA prepared from polyvinyl acetate has an *atactic structure* i.e., *at-PVA*. PVA prepared from *isotactic*-polyvinyl ethers by low temperature polymerization has *isotactic structure* i.e., *it-PVA*. Polarized infrared (IR) spectrum of *it-PVA* shows parallel dichroism bands at $3,340$ and $1,460 \text{ cm}^{-1}$, while for *at-PVA* it is observed at $1,141$ and 909 cm^{-1} [23].

11.5.1 Polymer Coated Magnetic Nanoparticles

To arrive at the formation of polymer coated magnetic nanoparticles, selection of parent compounds, and generation of precursor materials with follows up routes for final product formation are highly critical.

Recalling the Sect. 3.1.3 for *solvent evaporation method*, metal nitrates or equivalents may be selected as solute and hydrolyzed in aqueous medium to form a precursor solution. Let us concentrate on iron III nitrate ($\text{Fe}(\text{NO})_3 \cdot 9\text{H}_2\text{O}$) as a solute and 2methoxy-ethanol ($\text{CH}_3\text{-O-CH}_2\text{-CH}_2\text{-OH}$) as the solvent. Any potential reaction involving 2methoxy-ethanol (2ME) is not very likely, as the solution temperature was not raised above 443 K. It could be simple boiling and evaporation of the solvent rather than its decomposition. In general the reaction may be as:



This means a combination of iron III nitrate (I3N) with a solvent such as 2methoxy-ethanol and heating to dryness in air gives probable oxides of iron. The freshly prepared samples (Table 11.2) do not show any presence of oxy-hydrides but the tendency of their formation cannot be restricted if kept exposed to air. The process to grow iron oxide by the *solvent evaporation method* is briefly described below. Iron III nitrate is highly soluble in 2methoxy-ethanol giving a characteristic red color to the solution. The solutions were prepared as weight/volume (w/v) ratio; i.e., 1 mg iron III nitrate in 1 ml 2methoxy-ethanol giving 1:1 (w/v) solution (Table 11.2). They were transferred to crucibles containing 1 mg PVA in 10 ml-distilled water at room temperature. The crucibles were mounted on the hotplate, in the air, with constant stirring of the solution. The temperature of the hotplate was gradually raised in stages. At about 333 K bubbles appeared and at 353 K the solution began to boil. The temperature was kept constant to maintain the bubbling process till the solution became viscous. The heating process was continued to the final temperatures ranging from 393 K to 443 K for about 2 h till the viscous solution became a dry powdery mass. For rapid evaporation the solution temperature can be increased, but it was observed that increased vigorous bubbling led to the loss of the material. The end product was dry powdery mass, which easily crumpled to a homogeneous form. No heavy granules or coagulated particles were observed.

In the process of *solvent evaporation method* PVA having a molecular weight of about 125,000 to higher values were used [10, 11]. PVA [general structure $(-\text{C}_2\text{H}_4\text{O})_n$] having a degree of polymerization of 1,700 corresponding to a molecular weight $44 \times 1,700 = 74,800$ were tried for the same process [9].

Yogo et al. [24] could hydrolyse *Iron (III) tris (3-allylacetylacetonate)* [IAA] to form antiferrimagnetic $\alpha\text{-Fe}_2\text{O}_3$. This was possible, as Fe in IAA exists in trivalent

Table 11.2 (Refer Sect. 5.1): A set of powder samples grown by using the process of solvent evaporation method

Code	Preparation conditions	Product nature
Sample 1	1:5(w/v) I3N in 2ME, 443 K	Amorphous
Sample 2	1:1(w/v) I3N in 2ME, 443 K	Crystalline ($\gamma\text{-Fe}_2\text{O}_3$ & Fe_3O_4)
Sample 3	1:1(w/v) I3N in 2ME, 393 K	Crystalline ($\gamma\text{-Fe}_2\text{O}_3$)
Sample 4	1:1(w/v) I3N in 2ME, 443 K + 10%(w/v) sucrose solution	Crystalline ($\gamma\text{-Fe}_2\text{O}_3$, Fe_3O_4 & $\alpha\text{-Fe}_2\text{O}_3$)

form. Polymerization of IAA at 373 K for 42 h in ethanol resulted to IAA *oligomer*. An *oligomer* is a polymer having comparatively few monomer units in the molecule. IAA oligomer, which has good solubility in ethanol, hydrolyzes in hydrazine for conversion of Fe (III) to Fe (II). Ferrimagnetic iron oxide, having spinel oxide, resulted to IAA when the molar ratio was above 4 in the hydrolysis process.

In an interesting effort to develop iron oxide (IO) powders from organic based compounds, amorphous iron oxide was produced by the pyrolysis of iron pentacarbonyl [$\text{Fe}(\text{CO})_5$] in a modified domestic microwave (MW) oven in refluxing chlorobenzene as a solvent under air [25]. Initially a solution mixture of iron pentacarbonyl and chlorobenzene was irradiated and refluxed simultaneously for 20 min with 90% of the MW instruments power (90% meant that on/off irradiation cycles were in the ratio 9/1). The process of MW irradiation raised the temperature of the solution mixture. Cooling of the mixture was followed by centrifuge with chlorobenzene and pentane, and drying under vacuum (approximately 308 K and 15 mm Hg) for 24 h. When such iron oxide powders, amorphous Fe_2O_3 , were subjected to a heating process at 773 K under vacuum the final product was hematite.

Palchik et al. [25] employed differential scanning calorimetry (DSC) using nitrogen ambient and controlled heating rate (278 K/min) to detect the true amorphous nature of the as-prepared particles. Figure 11.2a of the DSC spectrum showed a sharp derivative line shape, starting with an exothermic peak at lower temperatures and converting to an endothermic transition at 523 K. This spectrum was explained on the basis that two broad peaks, was almost overlapping in shape and temperature with their peaks coinciding. The first band, the exothermic transition, gave a peak at lower temperatures. The second band, the endothermic peak shifted to higher temperatures by only a few degrees. The sum of these two peaks resulted in a sharp derivative spectrum. The exothermic peak was assigned to the disorder-order transition (crystallization) of the amorphous iron oxide. The crystallization of the amorphous iron oxide was reported at 541 K. The endothermic peak was attributed to desorption of the chlorobenzene solvent from the surface of the iron oxide. The thermo gravimetric

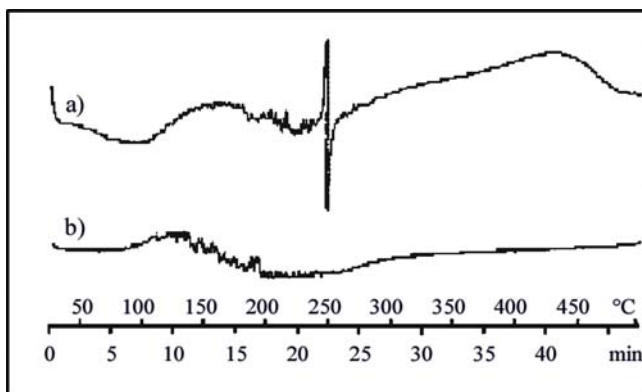


Fig. 11.2 DSC measurements: (a) as prepared Fe_2O_3 and (b) reheated sample[25]

analysis (TGA) spectrum supported the existence of the endothermic peak and attributed it to desorption of the material from the surface. On cooling the DSC-heated sample and reheating, a flat line was detected (Fig. 11.2b). The absence of any characteristic peak for reheating process indicated that the as-prepared sample was truly amorphous and not X-ray amorphous. The exothermic peak at 516 K was interpreted as the amorphous-crystalline transition.

11.5.1.1 Structural Aspects

The foremost work to develop any material pertains to its basic structure. No doubt, the most well proven X-ray diffraction (XRD) of the polymer based powdered ferrites (metal oxides) were performed to probe the phase (amorphous or crystalline or biphasic) existing in the material [9, 10, 25–29].

Initially, one may commence with a very simple route to form hybrid organic–inorganic magnetic nanocomposites. Considering the case for *solution evaporation method* it was observed that very less proportions of iron III nitrate in solution state (under heavy dilution) led to the formation of scanty precursors (Sample 1 in Table 11.2) [9]. This probably caused incomplete network structure in solid state and generated amorphous structured material. At a higher amount of solute in solution phase and maintaining a drying temperature of 393–453 K resulted in crystalline powdered materials. For 1:1 (weight/volume) iron III nitrate in 2ME and drying temperature of 393 K the powdered material (Sample 3) showed XRD peaks at $2\theta = 30^\circ, 35.2^\circ, 43.2^\circ, 54^\circ, \text{ and } 63.2^\circ$ corresponding to (220), (311), (400), (422) and (440) respectively. All such crystallographic planes confirm the presence of almost pure phase of $\gamma\text{-Fe}_2\text{O}_3$. At $2\theta = 54^\circ$ the situation is a bit tricky. This is because it refers to both (511) ($2\theta = 54.8^\circ$, [28]) and (422) ($2\theta = 53.8^\circ$) [10] corresponding to Fe_3O_4 and $\gamma\text{-Fe}_2\text{O}_3$; respectively. However, such a situation is not unlikely. Both $\gamma\text{-Fe}^{(III)}_2\text{O}_3$ and Fe_3O_4 ($\text{Fe}^{(III)}[\text{Fe}^{(II)}\text{Fe}^{(III)}]\text{O}_4$) belong to the spinel structure and have the lattice constants of 834 and 839 pm, respectively. Therefore, the exact phase is

Table 11.3 (Refer Sect. 5.1.1) – crystallographic planes and phases of IO from references – XRD analysis – [25–29]

Maghemite		Magnetite		Hematite	
$\gamma\text{-Fe}_2\text{O}_3$		Fe_3O_4		$\alpha\text{-Fe}_2\text{O}_3$	
2θ ($^\circ$)	(hkl)	2θ ($^\circ$)	(hkl)	2θ ($^\circ$)	(hkl)
30.4	(220)			24.4	(012)
35.6	(311)	35.2	(311)	33.2	(104)
37.3	(222)	38.2	(222)	36.0	(110)
43.4	(400)	44.5	(400)	38.9	(113)
53.8	(422)			48.6	(024)
57.4	(511)	54.8	(511)	54.3	(116)
63.0	(440)	64.8	(531)	57.7	(018)
		74.4	(533)	61.1	(214)

not determined by XRD (Table 11.3). Usually, fine particles reveal a smaller value of saturation magnetization compared with that of bulk. Under such circumstances existence of both phases may be declared. For a particular sample the *relative peak heights* (Table 11.4) were estimated from the peak intensities, which were normalized with respect to the dominant crystallographic plane. This has been done to understand crystallographic plane growth conditions. Sample 2 was prepared at a higher temperature of 443 K and was found to possess a mixed phase of both $\gamma\text{-Fe}_2\text{O}_3$ and Fe_3O_4 crystalline peaks (Table 11.2 and 11.4). A sample was tried (Sample 4) by including sucrose solution as suggested by Pramanik and Pathak [10]. It was observed that this sample (Sample 4) primarily had crystalline peaks corresponding to $\alpha\text{-Fe}_2\text{O}_3$ along with the dominant (311) peak of $\gamma\text{-Fe}_2\text{O}_3$. A comparison of peak positions with other references may not be always conclusive (Table 11.5). However, standard XRD peaks confirm the peak positions declared in the table for low molecular weight polymer based iron oxide. Figure 11.3 is supportive of the difference between Maghemite – C and Hematite XRD peak positions [27]. Samples prepared with the addition of sucrose to the parent solution during their growth provided higher energy routes for chemical reaction. As a result, Fe_3O_4 and $\gamma\text{-Fe}_2\text{O}_3$ got converted to $\alpha\text{-Fe}_2\text{O}_3$ at higher temperature. The main purpose to grow phases of pure iron oxide, by solvent evaporation, was to understand the conditions favoring formation of maghemite or hematite or magnetite

Some more processes are discussed to form a comparative study and develop a complete picture for structure formation in hybrid magnetic nanocomposites. Venkatraman et al. [29] showed conversion of $\alpha\text{-Fe}_2\text{O}_3$ to $\gamma\text{-Fe}_2\text{O}_3$ in presence of polyethylene glycol (PEG) in different weight ratios (Tables 11.6 and 11.7). For a comparison the *relative peak heights* were calculated from their data for sample giving pure $\gamma\text{-Fe}_2\text{O}_3$. The most dominant crystallographic peak was at (311). The normalized value of other peaks at (440), (220), (511), (400), (222) and (320) were 0.68, 0.27, 0.25, 0.21, 0.11 and 0.07; respectively (Fig. 11.4)

Jungk and Feldmann [27] used the polyol method to obtain iron oxide particles which were isolated by centrifugation. During the synthesis process, $\gamma\text{-Fe}_2\text{O}_3$ began to form at a temperature of 453 K indicating that the polyol medium was sufficient to produce the pure oxide instead of a hydroxide. A characteristic brownish red color confirmed $\gamma\text{-Fe}_2\text{O}_3$. However, at a higher temperature of 523 K the material transformed to $\alpha\text{-Fe}_2\text{O}_3$ giving a red colored powder (Fig. 11.3).

By now it is well known that processes involving higher heating profiles or stages favored a high degree of crystalline materials. In one of such cases, Pramanik and Pathak [10] reported XRD of NiFe_2O_4 , CoFe_2O_4 and ZnFe_2O_4 precursor powders, prepared in the presence of urea with varying calcinations, temperature and time. The virgin samples prepared at lower temperatures were amorphous. Heating samples at 723 K (for 2 h) led to the formation of crystalline peaks at (311) and (400). Continued heating at 723 K (for 24 h) caused a slight improvement to the peak formations. Further raising it to a higher temperature of 873 K (for 2 h) had a remarkable improvement of crystalline structure giving rise to peaks at (311), (220), (400), (422), (440) and (511). The growth of crystallinity in the precursor powders enhanced after thermal decomposition at 723 K and higher temperature

Table 11.4 (Refer Sect. 11.5.1.1) XRD analysis for low molecular weight polymer based IO [9]

Sample number 2				Sample number 3				Sample number 4			
2 θ ($^{\circ}$)	(hkl) plane	Phase	Relative Peak Height*	2 θ ($^{\circ}$)	(hkl) plane	Phase	Relative Peak Height*	2 θ ($^{\circ}$)	(hkl) plane	Phase	Relative Peak Height*
30	(220)	γ -Fe ₂ O ₃	0.3	30	(220)	γ -Fe ₂ O ₃	0.33	19.6	—	—	0.18
35.6	(311)	γ -Fe ₂ O ₃	1.0	35.2	(311)	γ -Fe ₂ O ₃	1.0	30	(220)	γ -Fe ₂ O ₃	0.26
44.8	(400)	Fe ₃ O ₄	0.35	43.2	(400)	γ -Fe ₂ O ₃	0.26	35.6	(311)	γ -Fe ₂ O ₃	1.0
54	(511) Or (422)	Fe ₃ O ₄ Or γ -Fe ₂ O ₃	0.24	54	(511) Or (422)	Fe ₃ O ₄ Or γ -Fe ₂ O ₃	0.21	48.8	(024)	α -Fe ₂ O ₃	0.26
62.8	(440)	γ -Fe ₂ O ₃	0.61	63.2	(440)	γ -Fe ₂ O ₃	0.3	54	(116)	α -Fe ₂ O ₃	0.12
64.8	(531)	Fe ₃ O ₄	0.24	—	—	—	—	57.2	(511)	γ -Fe ₂ O ₃	0.2
75.6	—	—	0.15	—	—	—	—	62.8	(531)	Fe ₃ O ₄	0.55
								64.8	(533)	Fe ₃ O ₄	0.19
								73.2	—	—	0.15

Table 11.5 (Refer sect. 5.1.1) – XRD data analysis (measured values of 2θ , B (FWHM) for polymer coated IO) (311) & (440) planes [9])

(311) – $\gamma\text{-Fe}_2\text{O}_3$			
Code	2θ ($^\circ$)	B ($^\circ$)	D (nm)
Sample 2	35.64	0.5443	34.06
Sample 3	35.63	0.609	30.45
Sample 4	35.59	0.6141	30.18
(440) – $\gamma\text{-Fe}_2\text{O}_3$			
Code	2θ ($^\circ$)	B ($^\circ$)	D (nm)
Sample 2	62.83	0.6434	32.14
Sample 3	62.95	0.7159	28.9

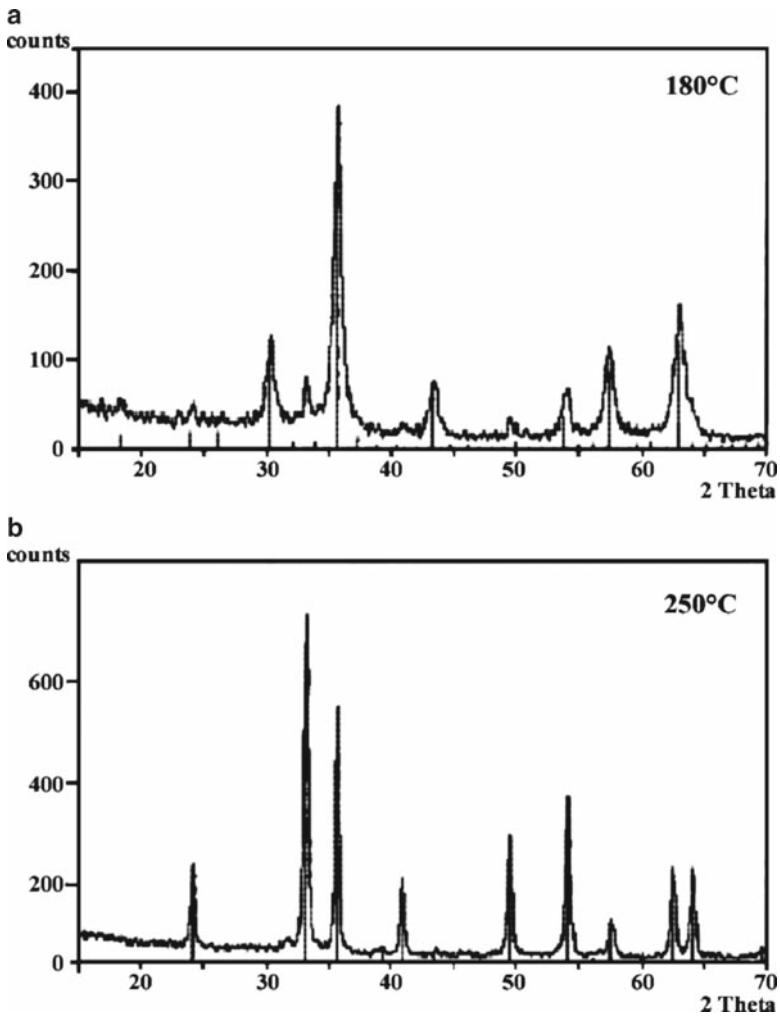


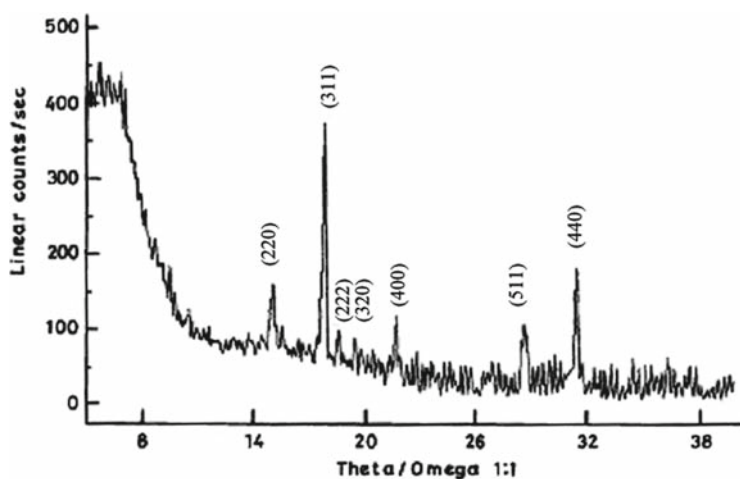
Fig. 11.3 (a) XRD of Fe_2O_3 particles after preparation, ICDD reference 39-1346, Maghemite-C, synthetic and (b) after heating to 523 K (ICDD reference 33-0664, Hematite, synthetic) [27]

Table 11.6 (Refer sect. 5.1.1) XRD data analysis of both α - Fe_2O_3 and γ - Fe_2O_3 for material based on phases of IO with polyethylene glycol (PEG) [29]

Weight ratio of α - Fe_2O_3 : PEG	Phases present (XRD data)	Crystallite size of α - and γ - Fe_2O_3 (\AA)
–	α -	22.76
1:2	α -/ γ -	22.76
1:3	α -/ γ -	22.76
1:4	α -/ γ -	22.76
1:5	γ -	22.76

Table 11.7 (Refer sect. 5.1.1) XRD data analysis of α - Fe_2O_3 films from Fe(III) 2-ethylhexanoate [41]

Preparation temperature on selected substrates	<104> crystal plane			<110> crystal plane		
	2θ ($^\circ$)	B ($^\circ$)	D (nm)	2θ ($^\circ$)	B ($^\circ$)	D (nm)
823 K on Quartz	33.09	0.419	21.9	35.57	0.361	25.7
923 K on Quartz	33.13	0.349	26.4	35.6	0.329	28.2
1,073 K on Quartz	33.24	0.334	27.5	35.73	0.319	29.1
1,073 K on Silicon substrate	33.04	0.242	38.0	35.51	0.232	39.9

**Fig. 11.4** XRD pattern of γ - Fe_2O_3 sample (Weight ratio of α - Fe_2O_3 ; Polyethylene glycol corresponded to 1:5) [29]

treatments. Increasing calcination temperature also increased the crystallite size in all the powder materials. At heat treatment temperatures of about 973 K, the powders prepared by PVA (molecular weight = 125,000) by the evaporation route, in the presence of urea, yielded finer crystallites (~17 nm) compared to the crystallites (~25 nm) of the powders prepared in absence of urea (Figs. 11.5 and 11.6).

The selection of polymer as a starting material to form organic–inorganic nanocomposite materials has been very critical. Why in many cases was PVA selected as the polymer provider? The reason was probably some interesting structural feature of PVA. From X-ray diffraction analysis, PVA prepared from polyvinyl acetate was found to be highly crystalline. It was suggested that the difference in size between acetate groups and hydrogen atoms is much too great to get accommodated and occupy equivalent positions in a crystal structure [30].

Let us begin addressing the foremost queries pertaining to bonding or bond structure formation in the hybrid organic–inorganic magnetic nanocomposites. The issues are:

- Identification, determination and conforming metal oxides,
- Original structure of polymeric compound which provides the organic base to the nanocomposite, and
- Retention of the molecular structure after organic–inorganic composite formation.

Pure FTIR spectrum of PVA is shown in Fig. 11.8a [9]. The molecular modes of vibration and existence are being given in Table 11.8. An initial comparison of PVA with those reported earlier FTIR absorption peaks at 3439.32 cm^{-1} and $1,455.35\text{ cm}^{-1}$ may be indicating type *it*-PVA [23]. However, confirmation for such a declaration demands a detailed analysis using FTIR with polarized radiation. FTIR spectroscopy of pyrrole shows peaks at 780 , $1,090$ and $3,400\text{ cm}^{-1}$ [28]. Moreover,

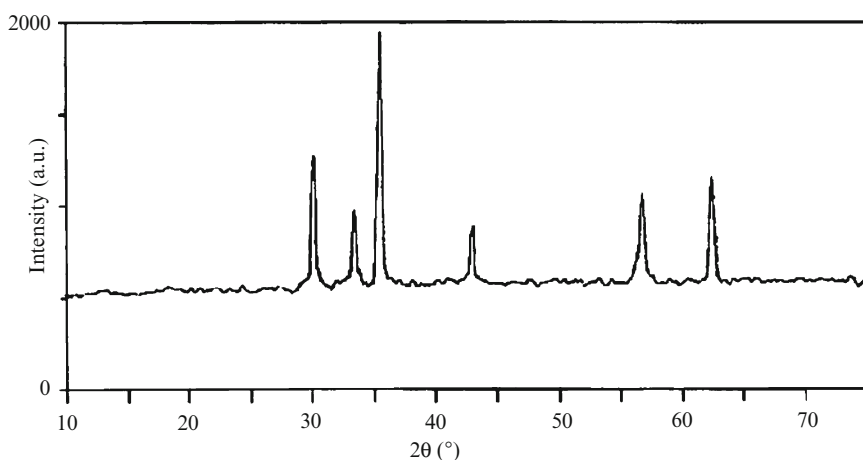


Fig. 11.5 XRD spectrum of Manganese zinc ferrite (MZF) ($\text{Mn}_{(1-x)}\text{Zn}_x\text{Fe}_2\text{O}_4$) where $x = 0.4$ [22]

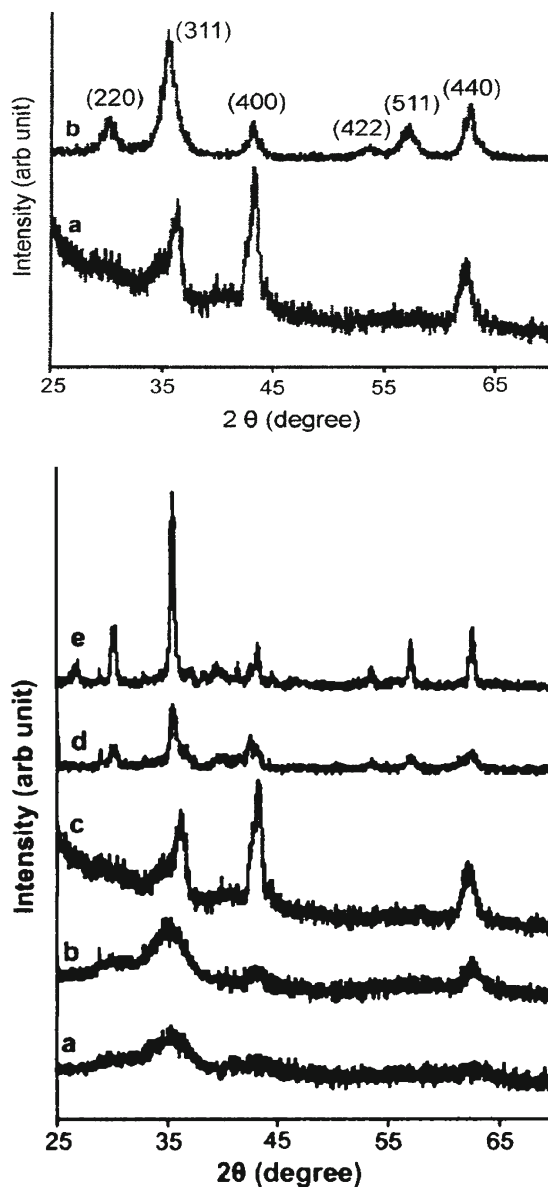


Fig. 11.6 (1) XRD spectra of 10 nm IO nanoparticles (a) without and (b) with oxidation by $(\text{CH}_3)_3\text{NO}$. (2) XRD spectra of (a) 3 nm, (b) 5 nm, (c) 10 nm, (d) 16 nm and (e) 25 nm IO particles without oxidation by $(\text{CH}_3)_3\text{NO}$ [9]

molecular bond structures of PVA were compared with polypyrrole (PPy) ($3,400\text{ cm}^{-1}$ ($-\text{NH}$ str), $3,100\text{ cm}^{-1}$ ($\text{C}-\text{H}$ str), $1,529\text{ cm}^{-1}$ ($\text{C}=\text{C}$ and $\text{C}-\text{C}$ str), $1,445\text{ cm}^{-1}$ ($\text{C}-\text{N}$ str), $1,295\text{ cm}^{-1}$ ($\text{C}-\text{H}$ and $\text{N}-\text{H}$ def), $1,242\text{ cm}^{-1}$ ($\text{C}-\text{N}$ str and $\text{C}-\text{H}$ def) and $1,050\text{ cm}^{-1}$ ($-\text{CH}$ def)) [31] (Fig. 11.7).

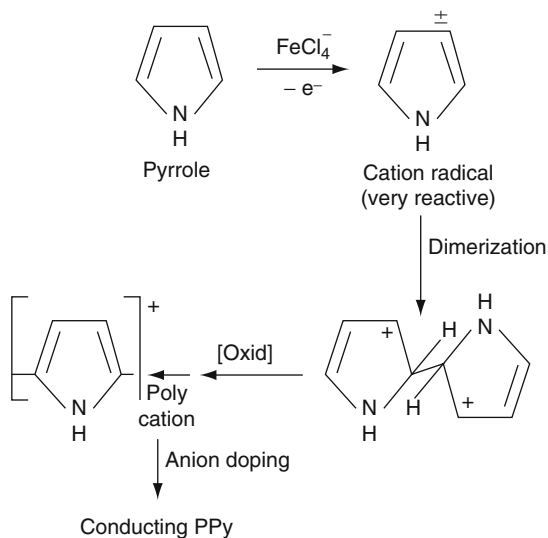


Fig. 11.7 Schematic showing results of the elemental analysis of polypyrrole grafted on fabric (after scraping from the surface) [31]

Table 11.8 (Refer sect. 5.1.1) – FTIR peak positions of PVA with reference to spectrum shown in Fig. 11.8a [9]

Mode	Wave number (cm^{-1})	PVA film [31]
–	4328.54	–
–	4022.92	–
O–H stretching vibration	3439.32	$3,330 \text{ cm}^{-1}$ (–OH str)
C–H stretching vibration	2920.66	$2,974 \text{ cm}^{-1}$ (–CH str)
–	2357.60	–
=CH–OH stretching vibration	1649.17	$1,652 \text{ cm}^{-1}$ (=CH–OH)
–CH δ ip	1455.35	$1,422 \text{ cm}^{-1}$ (–CH δ ip)
O–H bending vibration	1105.31	109 cm^{-1} (C–O str) 921 cm^{-1} (–CH op)

Concentrating on the molecular structure of organic–inorganic magnetic nanomaterials FTIR (Fourier Transform Infrared) spectroscopy proved to be a powerful tool [26, 31–34] was probably amongst the foremost who had reported in detail on infrared spectroscopy of ferrite materials (MFe_2O_4 , where M represented Co, Fe, Mg, Mn, Ni and Zn) in the range $280\text{--}2,500 \text{ cm}^{-1}$. Absorption bands arising from inter-atomic vibrations were measured and force constants calculated for the stretching of bonds between octahedral or tetrahedral metal ions and oxide ions. The values of force constants were found to agree with the elastic and thermodynamic properties of these compounds and were sensitive to distribution of metal ions between the

Table 11.9 (Refer sect. 5.1.1) – FTIR peak positions of PVA based IO grown using solution evaporation method [9]

Compound	Peaks at wave numbers (cm ⁻¹)
Sample 2	3424.2, 2339, 1618.6, 552.3, 445.7
Sample 3	3375.1, 2369.1, 1570.2, 1400, 557.9, 449.2
Sample 4	3403.1, 2362.4, 1560.5, 558.7

Table 11.10 (Refer Sect. 5.1.1) References for polymeric modes from FTIR

Mode	Wave number (cm ⁻¹)
OH Stretching vibration	3,600–3,100 – possibly from water of hydration
CH Stretching vibration	3,050–2,840 – includes PVA
CH–OH Stretching vibration	1,652 – For PVA
CH ₃ Bending vibration	1,360
OH Bending vibration	1,100–1,040
CO Stretching vibration	1,094 – For PVA

alternate sites. The measured values of integrated vibrational band intensities were found to be compatible with predominantly ionic bonding for these structures.

Waldron [34] suggested that *magnetite* shows strong absorption peaks between 600–500 cm⁻¹. More specifically, Hiremath and Venkatraman [33] declared pure γ -Fe₂O₃ (maghemite) had strong absorption peaks at around 3,450, 1,630, 546 and 458 cm⁻¹. However, pure α -Fe₂O₃ (hematite) had vibration absorption peaks at 3,419, 1,624, 1,400, 546 and 458 cm⁻¹. Both maghemite and hematite were prepared commencing with polyethylene glycol (PEG). This means that under such circumstances peaks at 546 and 458 cm⁻¹ were unable to distinguish between maghemite and hematite. However, such peak positions strongly suggested metal oxide stretching vibration. Similar, features were observed for iron oxide -PVA based samples (Table 11.9) [9]. In this table *sample 4* depicted only one peak at 558.7 cm⁻¹ compared to *sample 2 and 3*, which could mean that sucrose being “reaction energy provider” led to the formation of stronger metal-oxygen bond formation. The region 1,000–400 cm⁻¹ is important to search for metal-oxygen or other metal-oxyhydride bond formation. At this point, it will be wise to suggest searching for more evidence and a detailed study of such aspects before arriving at final conclusions.

Modes of vibration in FTIR spectroscopy in the 3,600–3,100 cm⁻¹ range (relating to antisymmetric and symmetric OH stretching) were assigned to water of hydration (Table 11.10). Hydrates were also ascribed to the 1,670–1,600 cm⁻¹ region. Similarly, broader bands associated with the lattice water molecule were in the 3,418 and 1,624 cm⁻¹ region. Carbonyl peaks are usually at 2,034 and 2,014 cm⁻¹ and oxyhydroxide [FeO (OH)] at 1,100 cm⁻¹.

With reference to data for sample 2, sample 3 and sample 4 the FTIR spectroscopy revealed absorption peaks in the 3,500 to 1,400 cm⁻¹ region. Absorption peaks

near 3,400–3,300 cm^{-1} were possibly due to water of hydration, while those about 1,650–1,550 cm^{-1} could be from =CH–OH and weaker modes of CH bonding contributed by PVA. So, it may be possible to say that some molecular contributions from PVA do exist, but the peak positions change from their parent configuration due to resultant effect in the nanocomposite.

Yu and Chow [35] reported on surface-functionalized magnetic nanoparticles by synthesis of poly-methacrylic acid (PMAA) coated maghemite nanoparticles in aqueous solution. Maghemite nanoparticles with an average diameter of about 6–10 nm were fabricated and were coated with PMAA by emulsion polymerization. From FTIR and thermal analysis chemical adsorption of methacrylic acid on the maghemite nanoparticle surface was confirmed and the existence of a symmetrical carboxylate bonding was suggested. It was further claimed that the free carboxyl group of PMAA provided the site for immobilization of foreign molecules.

An effort was made to understand some characteristic features of a memory device. For this purpose infrared spectroscopy (FTIR) of a piece of floppy disc (TDK) was done. The point of interest was to compare the vibration absorption spectrum of the organic–inorganic composite with that of the pure inorganic oxide magnetic material. This was the reason why the region from 1,000 to 400 cm^{-1} was scanned in particular. It can be observed that the polymer-based floppy disk has a very strong and characteristic absorption of infrared radiation. Such absorption behavior of molecules in the polymer of the floppy disk is predominant over absorption characteristics of the metal oxide. As a consequence, the infrared absorption modes of metal oxides are rather camouflaged. However, further work in this aspect may be interesting to the readers. A typical FTIR spectrum of a cut piece of floppy disc (TDK) has been shown (Figs 11.8b and 11.9).

In Sect. 5.1 preparation of amorphous iron oxide powders using microwave heating was described. Structural confirmation of amorphous and crystalline states of such iron oxide powders was done using X-ray photoelectron spectroscopy (XPS) and Mössbauer spectroscopy (MS). The MS spectra of amorphous and crystalline samples at 300 K are displayed in Fig 11.10 [25]. Figure 11.10a shows the MS spectrum for the amorphous sample. The central part of the spectrum exhibits only a broad doublet, which clearly indicates that no long-range magnetic ordering is present. The two quadrupole doublets with a relative ratio of ~2:1 were assigned to unequivalent Fe sites in the amorphous material. The hyperfine parameters of the major doublets were $IS = 0.38(1)$ and quadrupole splitting $\Delta = eqQ/2 = 0.56(1)$, and for the minor one $IS = 0.40(1)$ mm/s and $\Delta = 0.96(1)$ mm/s respectively, with a common line width of 0.30(1) mm/s. Such values are typical for Fe^{+3} in the high-spin state, and the doublets were attributed to Fe_2O_3 in the amorphous form. On the other hand, MS spectrum for the crystalline sample depicted clearly typical hyperfine magnetic splitting confirming long-range magnetic ordering at low temperatures. The interpretation of the spectrum resulted in a magnetic hyperfine field of $H_{\text{eff}} = 523(2)$ kOe, and $IS = 0.38(1)$ mm/s, with an effective quadrupole splitting of $\Delta_{\text{eff}} = 0.21(1)$ mm/s. The data was in good agreement with $\gamma\text{-Fe}_2\text{O}_3$: $H_{\text{eff}} = 520(1)$ kOe and $\Delta_{\text{eff}} = 0.22(1)$ mm/s.

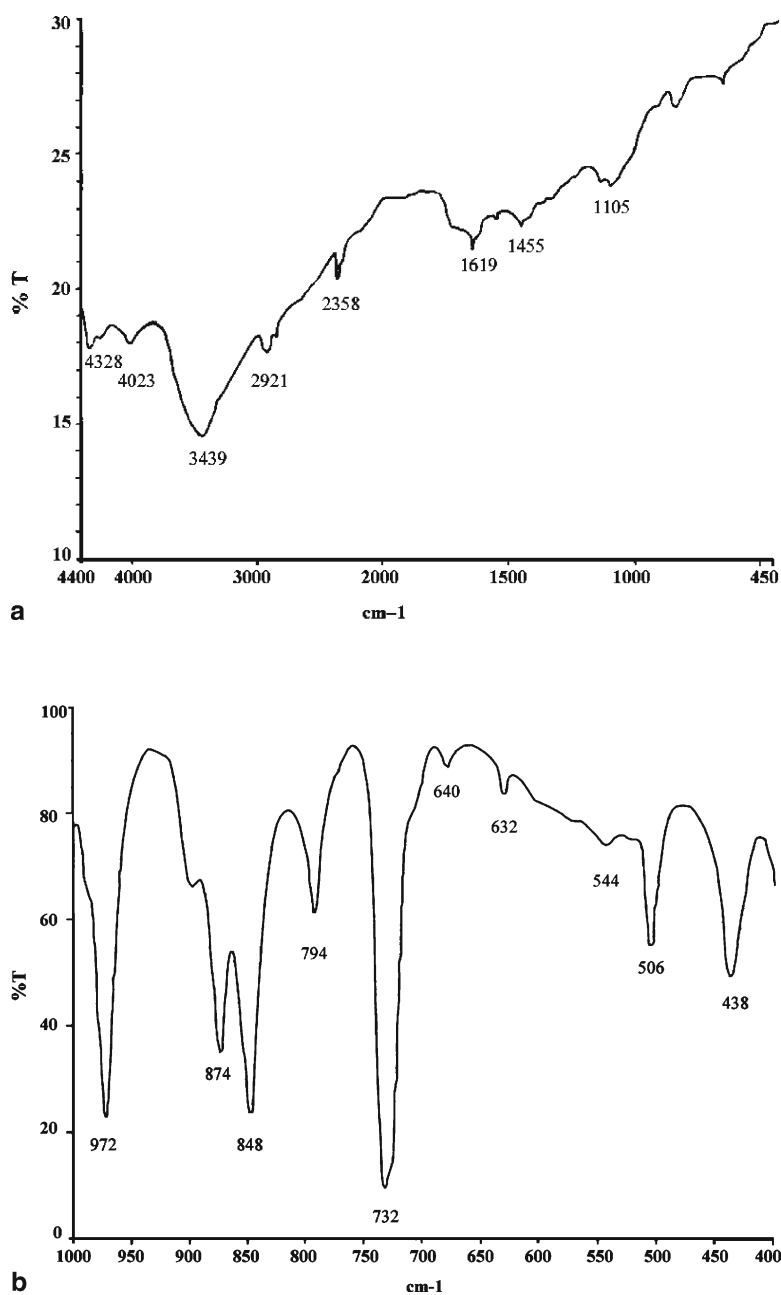


Fig. 11.8 (a) A typical FTIR spectrum of PVA [9]; (b) FTIR spectrum of plastic portion of floppy disc (TDK) usually used in computers in the range 1,000–400 cm^{-1}

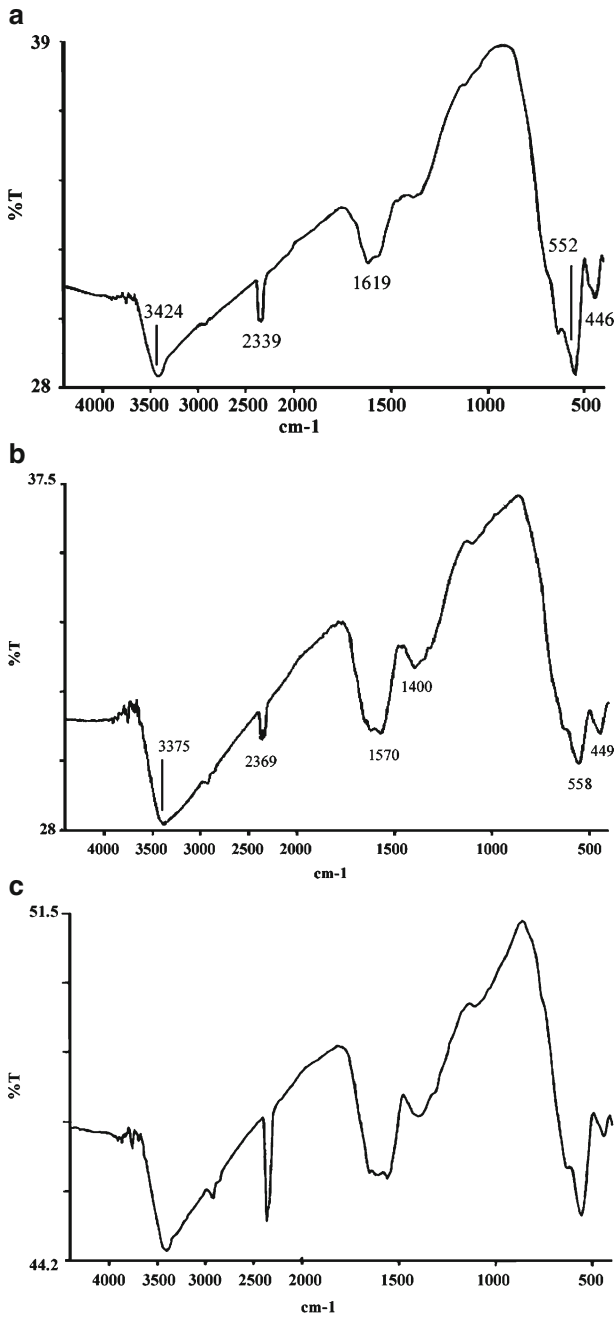


Fig. 11.9 FTIR spectra for Iron Oxide (a) Sample 2, (b) Sample 3, and (c) Sample 4 [9] as described in Table 11.2

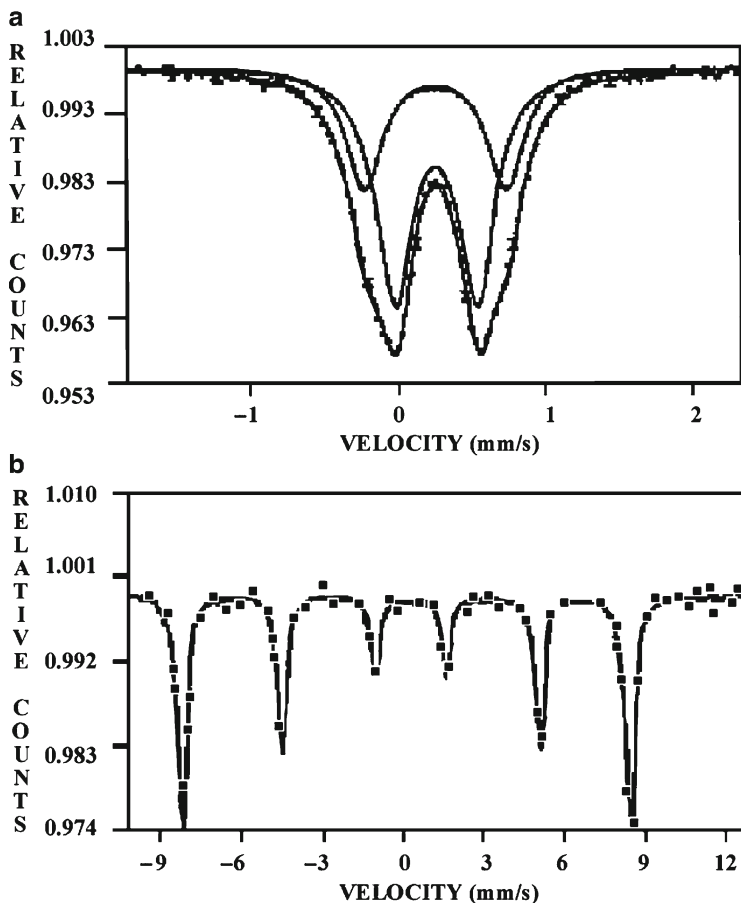


Fig. 11.10 Mössbauer spectra: (a) amorphous Fe_2O_3 and (b) heated to 773 K under vacuum amorphous Fe_2O_3 [25]

X-ray photoelectron spectroscopy (XPS) has proved to be one of the most powerful experimentations to obtain information about electronic structure of solids and their stoichiometry. Figure 11.11 represents XPS spectra, having resolution of 1 eV, of as-deposited iron oxide samples from organic base compounds [25]. XPS Fe2p core-level spectra confirmed that the short-range-ordering (SRO) as found in amorphous and crystalline compounds was almost identical. In Fig. 11.11a the O1s transitions represented triplet peaks, 530.5, 532.3 and 533.5 eV, for the as deposited amorphous iron oxide powders. The 530.5 eV peak was assigned to the surface O^{2-} ions of the iron oxide while the second and third peaks were ascribed to adsorbed oxygen species (532.3 and 533.5 eV), mostly water and carbonate. However, in the annealed sample which transformed to hematite, only one peak at 531 eV appeared. From XPS the oxygen to iron ratio was detected to be 3.1:2.

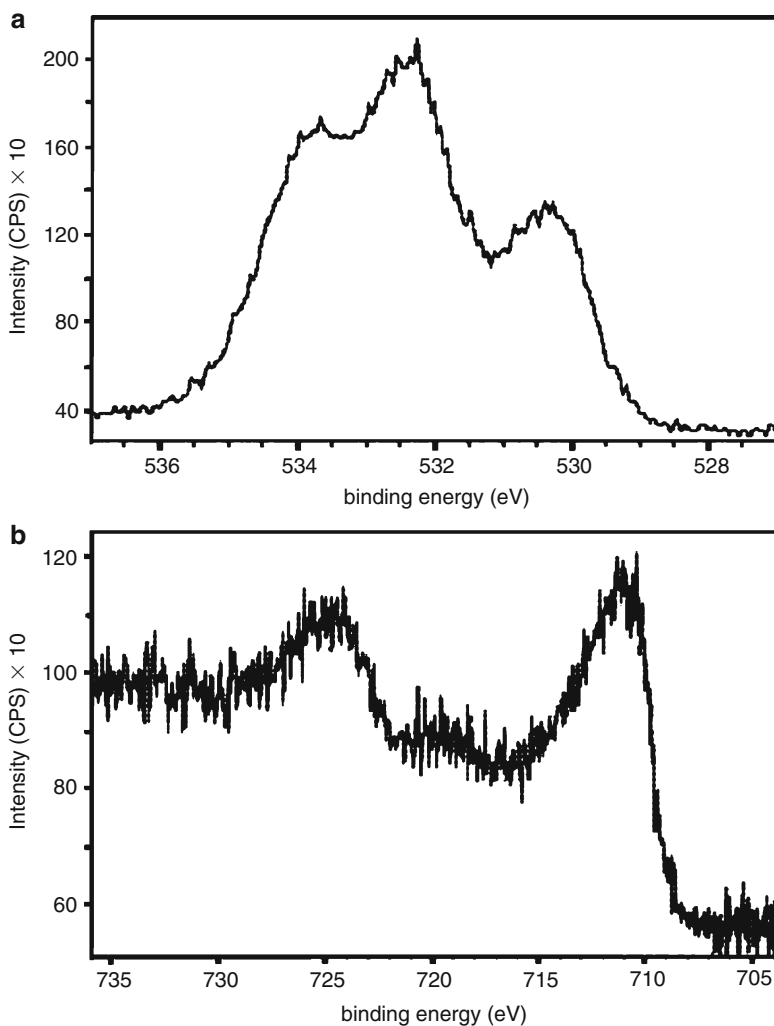


Fig. 11.11 X-ray photoelectron spectroscopy (XPS) spectra of the as-prepared product: (a) XPS spectra of the Fe2p core level and (b) spectra of the O1s transitions [25]

Figure 11.11b shows a doublet peak. The binding energy at 711 eV was assigned to the Fe2p_{3/2} transition and at 725 eV to the Fe2p_{1/2} transition.

11.5.1.2 Magnetic Behavior

In a very initial and simple step, demonstrated in an undergraduate laboratory, it was observed that placing a permanent magnet near to the crucible containing the powdered iron oxide attracted the total powdery mass. Further lowering of the magnet towards

the powdered iron oxide pulled the whole mass out of the crucible and nothing remained in the crucible. This indicated that despite using PVA as a non-magnetic substance in solution and heating process, no non-magnetic substance exists in the powdered material. However, it was expected that some residual non-magnetic substance remains in the crucible. This strongly suggests that either the polymeric substance decomposes/evaporates to the atmosphere or gets bonded to iron oxide in some form or the other.

Vibrating Sample Magnetometry (VSM) gives a description of the magnetic nature of the magnetic nanocomposite. Typical VSM results of magnetic nanocomposite materials are shown in many systems (Figs. 11.12, 11.16, 11.19, 11.20 and 11.23). In one of the cases it is interesting to observe the characteristic VSM of amorphous iron oxide prepared from organic compound (Fig. 11.12) [28]. The figure indicates a characteristic superparamagnetic behavior of iron oxide particles though saturation magnetization and hysteresis does not occur even at 15 Kgauss.

Yogo et al. [24] reported that in the case of hybrid IAA, oligomer methylhydrazine was a stronger reducing agent than hydrazine for the formation of spinel oxide. Selection of the reducing agent imposes a greater influence on the magnitude of saturation magnetization of iron oxide hybrid compared to variation in solution concentration. The molar ratio of iron, hydrazine derivative and water was maintained at 1:4:10 [24]. The hybrid formed at a higher solution concentration, the hydrolysis of Fe–O bonds and crystallization of magnetic particles precede more rapidly yielding magnetic particles with higher crystal regularity. A comparison of values for saturation magnetization is compiled in Table 11.11.

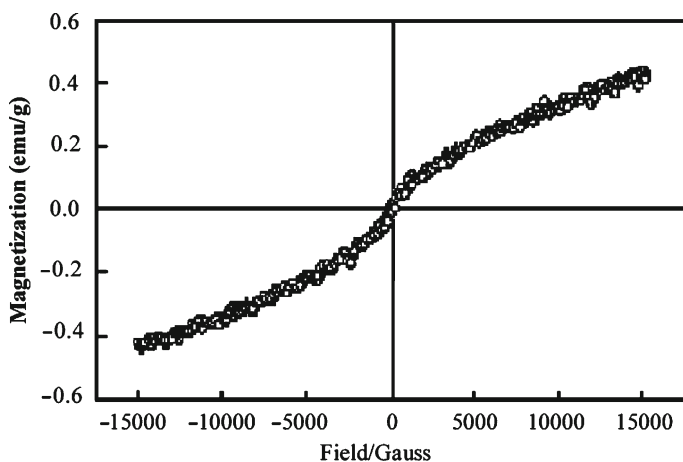


Fig. 11.12 Magnetic measurements of amorphous Fe₂O₃ (magnetization versus applied field) [25]

Table 11.11 (Refer sect. 5.1.2) Variable sample magnetometry (VSM) data for IO/polymer nanocomposite

IO/polymer nanocomposites	Temperature/ Magnetic Field	Saturation Magnetization	Susceptibility	Particle size	References
IO spinel (PVA based) polymer nanocomposite	300/8 K gauss	~25 emu/g		25–35 nm	[9]
γ -Fe ₂ O ₃ in Fe III ion-exchange resin	Room temperature/10 kG 293 K	Experimental value 15 emu/g calculated value 16.6 emu/g	d.c. magnetic (Faraday)	≤10 nm	Ziolo (1992)
γ -Fe ₂ O ₃ in Fe II ion-exchange resin	Room temperature/10 kG	46 emu/g		≤25 nm	Ziolo (1992)
Fe ₃ O ₄ (≤0.5%) in thick epoxy resin	Room temperature & Liquid N ₂ /~5kA. m ⁻¹	0.2Am ² kg ⁻¹		~10 nm	[38]
IO spinel/oligomer hybrid film	300 K/77 K	78 emu/g			[24]

11.5.1.3 Electrical Properties

We know that to understand basic electrical properties of *ferrite materials* (γ -Fe₂O₃, Fe₃O₄, and doped or alloyed with Ni, Cu, Mn, Co, Zn, etc.) the study of *dielectric properties or impedance or inductance spectroscopy* are essential. However, existence of the ferrite materials with organic substances forming composites will exhibit a totally different electrical property. On the other hand, α -Fe₂O₃ is nonmagnetic but shows semiconducting properties.

The nature of the matrix material, which is being discussed under the preview of this chapter, has a considerable influence. It is rather clear that electrically, either a *composite system is highly insulating or has some semiconducting behavior*. This means that the role of the organic matrix is highly critical. In any case, the organic substance must be non-magnetic or else it will camouflage the magnetic property of the basic ferrite material. If the organic compound is an insulator, the *magnetic nanocomposite* is highly insulating and only *ferrite material properties* are depicted. Another category of polymers exhibit conducting behavior and are commonly known as *conducting polymers*.

Conducting polymers are primarily responsible to bring about the feature of electrical conductivity in inorganic/organic hybrid nanocomposites. Conducting

polymers usually have electrical conductivity which can be tailored to desired values, and are organic electrochromic materials with chemically active surfaces. However, they are chemically sensitive and are mechanically unprocessable. Unique dimensional properties of nanomaterials offer more sites for surface reactivity and a high degree of porosity in sol form, improved mechanical properties, and disperses homogeneously in the matrix medium. Nanocomposites are a combination of conducting polymers and inorganic nanoparticles. These are highly useful and technologically important.

Polypyrrole, an example of *non-magnetic conducting polymer*, gives high degree nanocomposites. Iron oxide, as a magnetic nanomaterial, forms nanocomposites with polypyrrole by a process of simultaneous gelation of oxide. A variation of conductivity as a function of concentration of polypyrrole depicts an optimum maximum value rather than monotonic increase in conductivity. In a report it was observed that the electrical conductivity changed by almost 2 orders of magnitude, with a maximum value of 11.3 s cm^{-1} [28]. The electrical conduction phenomenon may be explained on basis of *percolation theory* [39]. Percolation theory predicts that for a certain optimum amount of concentration of the conducting polymer a full conducting path is formed for the flow of the current.

11.5.1.4 Optical Behaviour

Figure 11.13 shows diffuse reflection of $\gamma\text{-Fe}_2\text{O}_3$ and $\alpha\text{-Fe}_2\text{O}_3$, based on the polyol method, in the visible to near UV region. From 300 nm till about 550 nm both phases had no reflection. Above 550 nm till 800 nm a phase transformation from maghemite to hematite drastically increased the reflection. In accordance with the

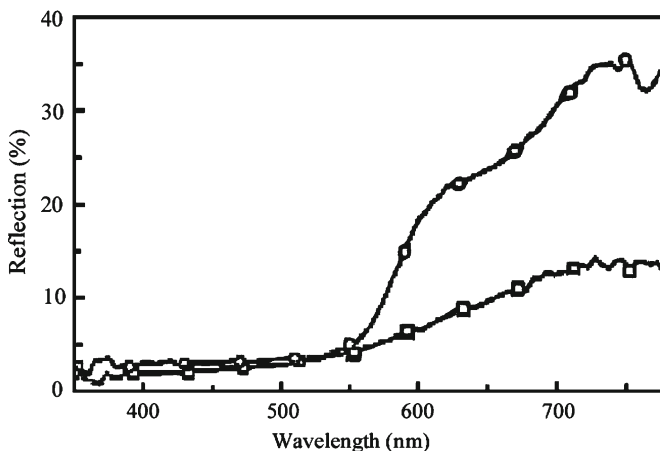


Fig. 11.13 Diffuse reflection of Fe_2O_3 particles after preparation (squares) and after heating to 523 K (circles) [27]

crystal structure, the color of the powder changed significantly from brownish red to characteristic red after heating to 523 K [27].

11.5.2 Embedded Magnetic Nanoparticles

11.5.2.1 Ion Exchange Resin

The polymer matrix may either be commercial based or in-lab synthesized ion-exchange resin. Ziolo et al. [36] selected a commercial ion-exchange resin, which was composed of sulphonated polystyrene cross linked with divinyl benzene to form a three-dimensional, porous polymer network. The dry resin exhibited the property of *cation exchange*. The cross linked resin was in the form of spherical beads of diameter 30–150 μm . The resin was exchanged with Fe (II) or Fe (III) from an aqueous solution of the respective chloride. The process of washing removed excess physisorbed Fe ions. From elemental analysis of the resins, Fe: S atom ratios of 1:2 or 1:3 confirmed complete ion exchange. Considering Fe (II) resin, exposure to a solution of NaOH caused a rapid change in color to green followed by a gradual change to deep red-black on exposure to air. Heating to 333 K followed by the drop wise addition of a dilute aqueous H_2O_2 solution accelerated the conversion to oxide formation. For Fe (III) resin, an aqueous suspension of the resin was heated and maintained at 333 K during drop wise addition of N_2H_4 with stirring. Aqueous NaOH was added in subsequent steps to make it highly alkaline (pH \sim 13–14). For both the resins the stirring was continued for many hours, then they were washed with water several times to bring them to neutral pH and finally dried. From elemental analysis of Fe (II) and Fe (III) resins, the Fe content was found to be 9.8 and 7.8%, respectively.

Structural Properties

Transmission electron microscope (TEM) analysis of Fe (II) in an ion-exchange resin (Fig. 11.14) [36] depicted a relatively uniform, high-density distribution of oxide in the polymer matrix (Fig. 11.15). The TEM micrograph showed the crystalline phase present in the material of either spherical or cubic shape, which were only due to iron oxide ($\gamma\text{-Fe}_2\text{O}_3$) particles. Higher iron oxide contents or loadings increased the particle size rather than their number. However, with multiple loadings of Fe initially the number (density) of particles increased in the polymer matrix rather than their size. By increasing the cyclic process many folds, the oxide particle size could be varied from about 5 to 25 nm.

Magnetic Properties

Using vibrating sample magnetometry (VSM), a Fe (II) ion-exchange resin composite having 15.28% Fe, meaning 21.8% by weight loading of $\gamma\text{-Fe}_2\text{O}_3$, was shown

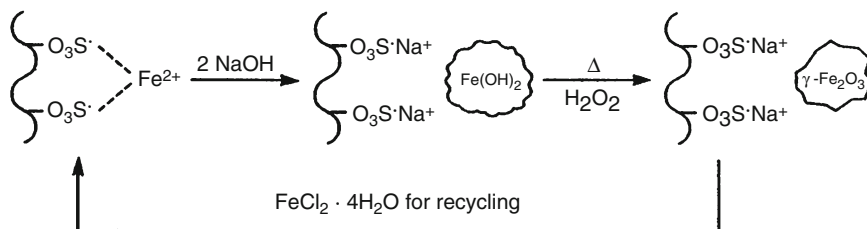


Fig. 11.14 Schematic of the $\gamma\text{-Fe}_2\text{O}_3$ precipitation process using Fe (II) in an ion-exchange resin [36]

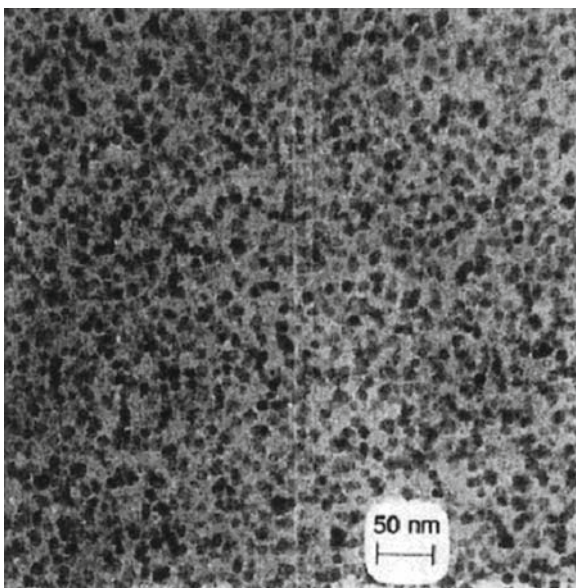


Fig. 11.15 Bright-field transmission electron micrograph of a microtomed section of composite containing 21.8% $\gamma\text{-Fe}_2\text{O}_3$ by weight in an 8% cross-linked polystyrene resin. The iron oxide particles range in size from 5 to 10 nm [36]

to possess a magnetic saturation moment of 15 emu/g (experimental value) at a magnetic field of 10 kG (Table 11.11) (Ziolo 1992). The superparamagnetic behavior of nanocomposites was also confirmed from measurements of dc magnetic susceptibility, determined by the Faraday method as a function of temperature and magnetic field. Field dependent magnetization at low temperatures (10 K), field cooled and zero field cooled, brought out the hysteresis in the iron oxide composites and confirmed that the particles were magnetically single-phased (Fig. 11.16). Coercivity of about 1 kOe indicated randomly oriented equiaxial particles with cubic magnetocrystalline anisotropy [40].

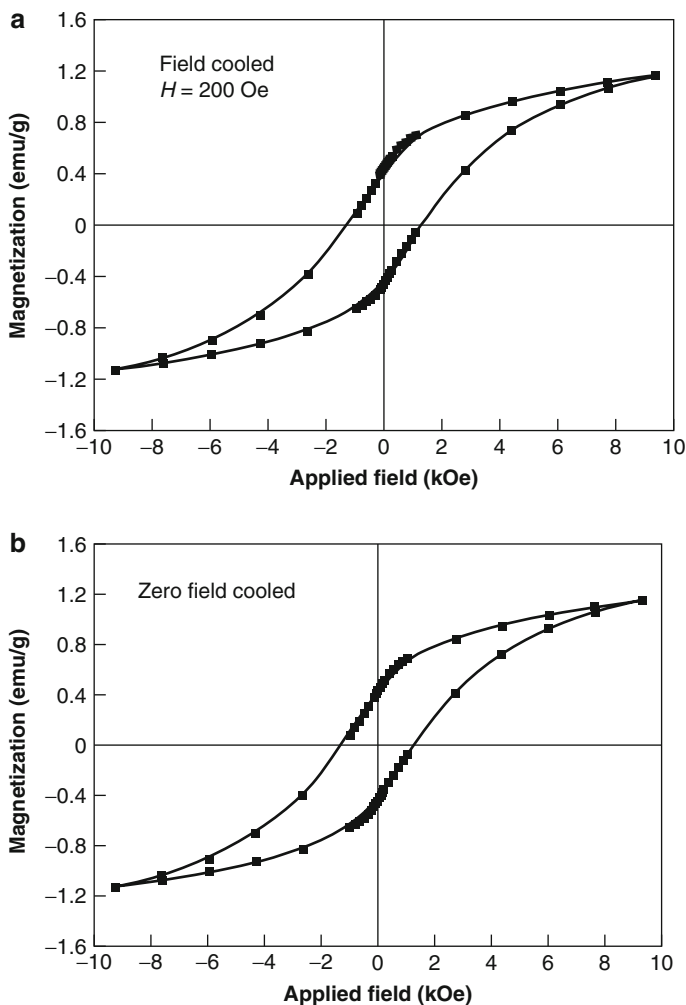


Fig. 11.16 (a) Field-cooled magnetization curve at 10 K and 200 Oe for a Fe (II) resin containing 8.5 nm γ - Fe_2O_3 at 2% by weight; (b) Zero-field-cooled curve at 10 K for the same sample [36]

Optical Nature

Optical absorption of the Fe (II) ion-exchange resin composite having the form of spherical beads of diameter about 45 μm was observed in the visible region (4,500–7,500 \AA) [36]. Using optical microprobe for the absorption measurements, the lens effects with field stops to limit the effective aperture near the optical axis under parallel illumination in the region 5–7 μm of the beads could be minimized, and the refractive index (calibrated depth-measurement scale) calculated (average refractive index = 1.6 ± 0.1 for the 21.8% by weight loaded beads) after correction for reflection loss.

Figure 11.17 compares the average absorption spectrum of the mesoscopic (nano-order) form of $\gamma\text{-Fe}_2\text{O}_3$, obtained from the optical density data of the composite, to that of the single-crystal form of $\gamma\text{-Fe}_2\text{O}_3$. The beads were considered as free-standing films of thickness equal to their diameter scaled by the volume loading fraction and assuming a uniform distribution of iron oxide throughout the bead. Ziolo (1992) gave evidence of two very important results (Fig. 11.17). Firstly, the mesoscopic form of $\gamma\text{-Fe}_2\text{O}_3$ was more transparent to visible light than the single-crystal form. The difference in absorption between the two forms ranged from nearly an order of magnitude in the “red” spectral region to a factor of 3 at 5,400 Å. The low value of absorption of mesoscopic $\gamma\text{-Fe}_2\text{O}_3$, $\alpha \leq 10^4 \text{ cm}^{-1}$, remained practically constant throughout the visible region. Secondly, in terms of wavelength difference between the main absorption edges in the mesoscopic and bulk spectra, the mesoscopic $\gamma\text{-Fe}_2\text{O}_3$ edge “red shifted” by 300–600 Å. It was a relatively large shift corresponding to 0.15–0.30 eV (~5–10% of the edge energy) and indicated a strong interaction, which affected the small-particle form of $\gamma\text{-Fe}_2\text{O}_3$. The low absorption of the mesoscopic $\gamma\text{-Fe}_2\text{O}_3$, compared to the single-crystal form, was characteristic of strongly reduced oscillator strength, which was attributed to high surface to volume ratio of the $\gamma\text{-Fe}_2\text{O}_3$ particles, cation impurities and vacancy distribution in the $\gamma\text{-Fe}_2\text{O}_3$, and chemical interaction with the matrix. Further, the reduction in oscillator strength arose due to confinement within dimensions of a few hundred angstroms inhibiting exchange coupling. The “step-like” behavior of the variation in absorption coefficient as a function of wavelength confirmed the signature of mesoscopic $\gamma\text{-Fe}_2\text{O}_3$.

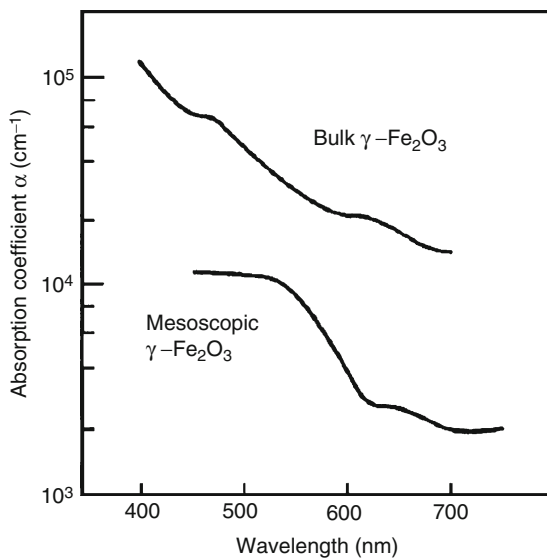


Fig. 11.17 Room temperature optical absorption spectra of mesoscopic and single-crystal $\gamma\text{-Fe}_2\text{O}_3$. Concerning mesoscopic $\gamma\text{-Fe}_2\text{O}_3$, refer to the sample in Fig. 11.15 [36]

11.5.2.2 Epoxy Resin

Thorpe et al. [38] worked with aqueous suspension of 10 nm magnetite particles (sizes about 1–2 μm across) in bis-phenol-based epoxy matrix, using sonication to attain uniform dispersion in the medium, and then hardening the resin by means of a polyamine-based hardener. It was observed using optical microscopy (126 \times) that for samples containing magnetite particles above 0.5% in the epoxy resin matrix, clumps of larger size introduced irregular spheroid shapes. The sizes were as large as several tens of microns across.

Structural Properties

Magnetite (approximately 5 wt%) phase was confirmed from XRD in magnetite epoxy resins (MER) [38]. Heating of such MER indicated absence of water in the material and an estimation of magnetostatic forces which confirmed spherical shapes of magnetites.

Optical microscopy of MER showed relatively large elongated clumps of magnetite particles in MER. Scanning electron microscopy (SEM) of MER revealed clumping formation of about 50 μm for samples containing 2% of magnetite, but nothing of that sort was observed at concentrations of 0.39% magnetite samples. Such a phenomenon was also confirmed from TEM results. It was concluded that in the case of the magnetite dispersion the magnetostatic forces produced the spherical agglomerates in the aqueous phase. After and during the hardening stage, the water was displaced by epoxy and the magnetite agglomerates maintained their spherical shape.

Micro-focus X-ray fluorescence ($\mu\text{-XRF}$) offers yet another way to detect magnetite agglomeration in MER or polymeric or glassy matrices, at much lower concentrations. The X-ray beam (white radiation) with a spot dimension of about 1–2 μm , a solid-state detector (to measure fluorescent radiation) and a background filtration are characteristic of $\mu\text{-XRF}$. A typical $\mu\text{-XRF}$ analysis of MER is represented in Fig. 11.18. Figure 11.18a indicates the difference in concentration, which is evident from the number of peaks in each sample. Figures 11.18b, c are subsequent scans (in a different position) for each sample on an expanded scale. Figure 11.18c is the best of the three spectra, as some of the background interference was filtered out. In Fig. 11.18c most of the peaks in the filtered spectrum fall into two categories, i.e., narrowest peaks with a base of about 7 μm , and the rest with considerable wider bases. The narrowest peaks probably correspond to single aggregates, whereas the wider peaks could be caused by a combination of aggregates at various depths. This was primarily due to the size of the beam and the dispersion of the X-rays in the sample. It was speculated that small angle X-ray detectors could examine aggregated or single particles of the order of 10 nm or better. With a high-intensity photon source, $\mu\text{-XRF}$ spectroscopy has shown its potential as a powerful tool for the characterization of solid nanodispersions at very low concentrations. On the other hand TEM could detect nanodispersions in thin samples (up to 200 nm) at concentrations of $>0.1\%$. At low concentrations TEM measurements

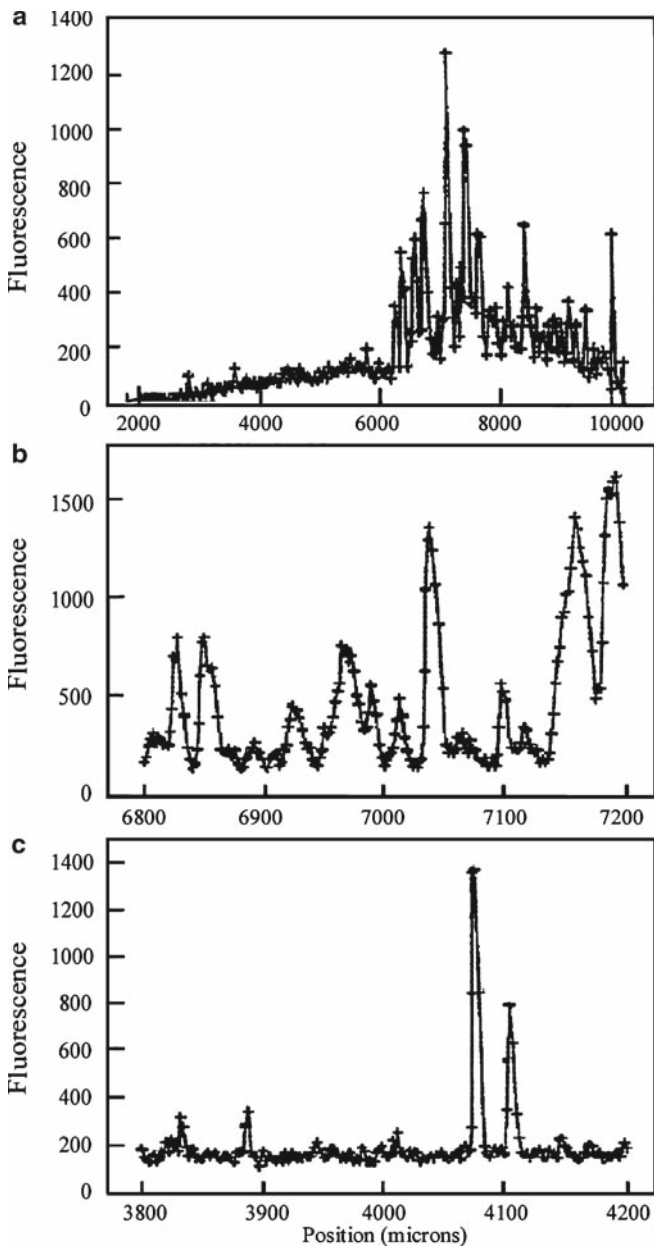


Fig. 11.18 (a) Fluorescence as a function of position for the 0.03% (*left* of 6,200 μm) and the 0.39% (*right* of 6,200 μm) magnetite (epoxy samples) using 200 scan points. (b) Expanded portion of the spectrum of the 0.39% magnetite/epoxy sample only. (c) Expanded portion of the spectrum of the 0.03% magnetite/epoxy sample with a discriminatory level set to filter out background noise [38]

were difficult because of the large inter-agglomerate distances. The synchro μ -XRF spectroscopy extended the range of sample size to several orders greater than the detection level of TEM. Moreover, it was also capable to detect small concentrations of particles in thick opaque samples. The absolute detection limit provided by synchro μ -XRF spectroscopy was very low ($\sim 10^{-16}$ g).

Magnetic Properties

It was interesting to learn that hysteresis curves for MER containing Fe_3O_4 concentrations greater than 1.5 wt% were irregular and not characteristic of bulk or mesoscopic (10 nm) magnetite. However, for MER containing about 0.39% magnetite in epoxy, typical hysteresis curves were obtained. It was suggested that at higher concentrations of magnetite, $\sim 3.4\%$ magnetite epoxy sample, clumping occurred resulting in irregular hysteresis curves. So, in a way low and high concentration of magnetite in MER referred to two-dimensional and three-dimensional agglomerates [38].

The coercive force ($40\text{--}60 \text{ Am}^{-1}$) of small non-interacting particles has been known to increase with particle size up to a certain optimum value ($\sim 5\text{--}20 \text{ nm}$). The saturation magnetization of the MER samples having low concentrations increased linearly with the concentration of magnetite in the epoxy. The individual particles were less than a single domain in size (superparamagnetic), and therefore it appeared that there was little interaction of particles below a concentration of $0.5\text{--}1 \text{ wt}\%$.

Optical Properties

The IAA oligomer hybrid films were cast on a fused silica substrate from an ethanol solution consisting of hybrid and 10 wt% poly (vinylbutyral) (PVB) [24]. The hybrid was prepared through hydrolysis of IAA oligomer with 4 equivalent of CH_3NHNH_2 and 1/6 equivalent of water at 50°C for 3 h, because the films were required to have not only magnetism but also transparency (Fig. 11.19). The hybrid films contained 10 wt% IO. The change of magnetization with applied field for the IAA oligomer hybrid film at 300 K has been shown (Fig. 11.20). The magnetic induction clearly indicates that the transparent film is magnetic, though the film has no coercive force.

A comparison of the optical transmittance and absorption coefficient as functions of wavelength and photon energy in the region $1,000\text{--}2,600 \text{ nm}$ for iron oxide spinel/oligomer hybrid film on a fused silica and absorption of PVB is highlighted in Fig. 11.21. It is observed that the absorption coefficient is small compared with that of bulk Fe_3O_4 . A single-crystal $\gamma\text{-Fe}_2\text{O}_3$ thin film having a thickness of about $0.3 \mu\text{m}$, epitaxially grown on an MgO substrate, showed a refractive index of about 3.0 corresponding to that of hematite (Ziolo 1992).

Xue et al. [41] prepared thin films of $\alpha\text{-Fe}_2\text{O}_3$ from Fe (III) 2-ethylhexanoate which is a metal organic compound, employing *spin-coating process* for film growth on silicon substrates. From FTIR of $\alpha\text{-Fe}_2\text{O}_3$ films, peaks at 1323.3 , 1423.5 , 1589.4 and 1716.7 cm^{-1} were attributed to C-H modes. The chain (ν (C-H)) in the

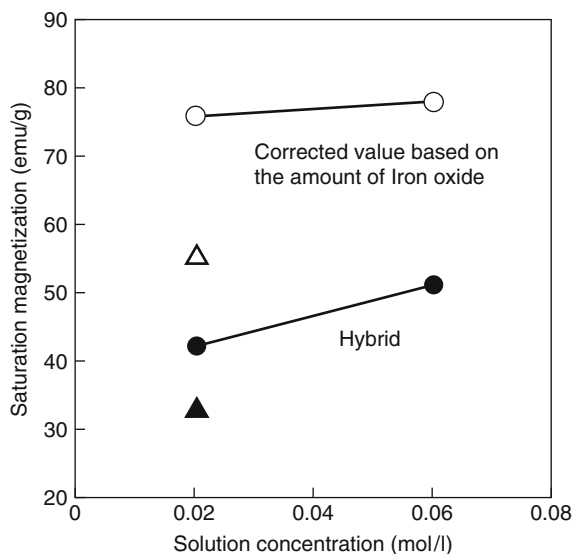


Fig. 11.19 Change of magnetization of hybrid (IAA oligomer) with solution concentration: (filled and open circles) methyl hydrazine; (filled and open triangles) hydrazine [24]

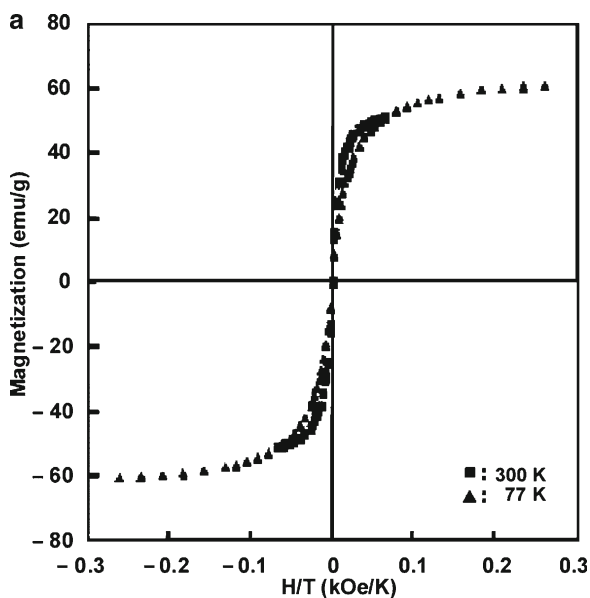


Fig. 11.20 (a) H/T superposition of two isothermal magnetization data at 77 and 300 K for hybrid synthesized from Iron allylacetylacetonate (IAA) oligomer synthesized at $\text{Fe}:\text{CH}_3\text{NHNH}_2:\text{H}_2\text{O} = 1:4:10$ ratio and at 353 K for 24 h; (b) Change of magnetization with applied field for a hybrid film (IO spinel/oligomer hybrid synthesized at $\text{Fe}:\text{CH}_3\text{NHNH}_2:\text{H}_2\text{O} = 1:4:1/6$ ratio and at 323 K for 3 h) on a silica glass [24]

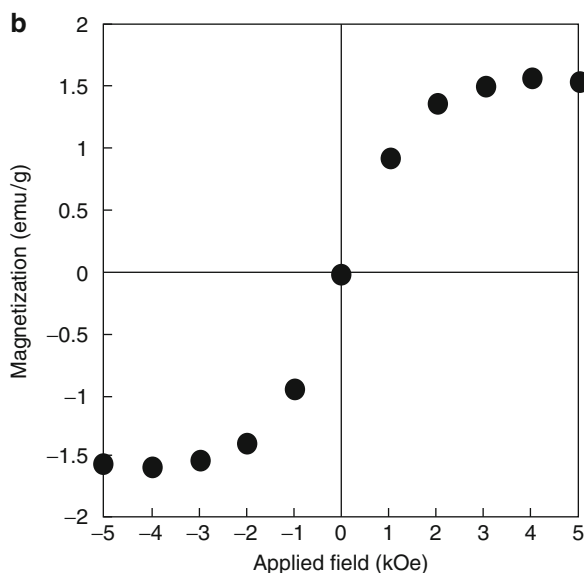


Fig.11.20 (continued)

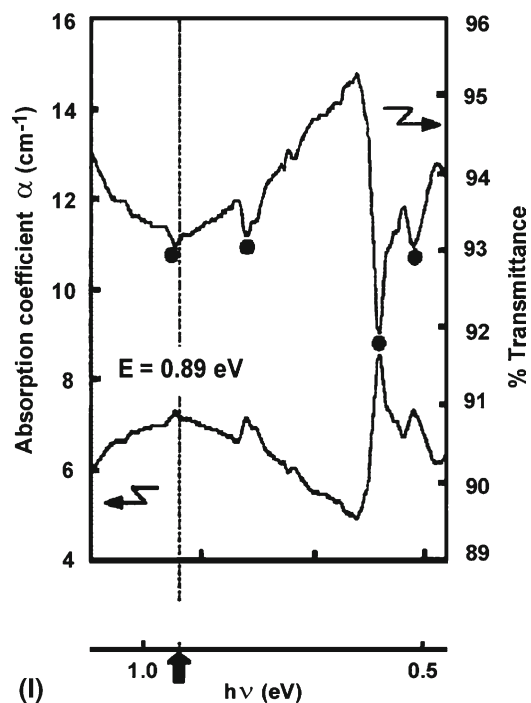


Fig. 11.21 (I) Optical transmittance and absorption coefficient as functions of wavelength and $h\nu$ for IO spinel/oligomer hybrid film on a fused silica substrate: (filled circle) absorption of poly (vinyl-butylal) PVB; (II) Optical transmittances as a function of wavelength for IO spinel/oligomer hybrid film and PVB film: (a) absorption edge of bulk γ - Fe_2O_3 , (b) absorption edge of bulk Fe_3O_4 , (a) magnetic hybrid film on a fused silica substrate, and (b) PVB film on a fused silica substrate [24]

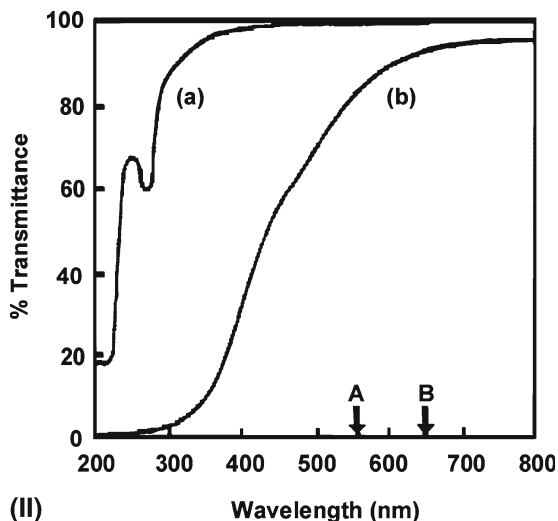


Fig. 11.21 (continued)

metal-organic molecule was identified at $2,961\text{ cm}^{-1}$. The amorphous $\alpha\text{-Fe}_2\text{O}_3$ films had a broad absorption band at 532 cm^{-1} , while crystalline $\alpha\text{-Fe}_2\text{O}_3$ films showed a $1,085\text{ cm}^{-1}$ band corresponding to FeO. The basic idea was to study the phase transition from amorphous to crystalline in the films, which occurred at an annealing temperature of about 733 K. The corresponding XRD data are being tabulated (Table 11.7).

11.5.2.3 Magnetic Fluids (MF)

Typically MF are realized as *ferrofluids*. It was a two-fold investigation. Firstly, magnetic particles of two ferrofluids differing in magneto-crystalline energy of the dispersed particles were considered. Secondly, textured fluids were introduced in paraffin wax under different texturing magnetic fields [42]. In one such type of a sample, *magnetite particles* showed anisotropy energy much greater than thermal energy at room temperature. In another type of a sample, *Mn-Zn ferrite particles* had thermal energy greater than the anisotropy energy. Chain formation in ferrofluid films was observed using CCD camera under different magnetic field [20] (Fig. 11.22).

11.5.2.4 Rubber Ferrite Composite (RFC)

Nickel zinc ferrites $\text{Ni}_{1-x}\text{Zn}_x\text{Fe}_2\text{O}_4$ (NZF) and $\text{Mn}_{1-x}\text{Zn}_x\text{Fe}_2\text{O}_4$ (MZF) [21, 22, 37] were prepared using the ceramic technique [12]. Natural rubber (NR) and butyl rubber (BR) were selected as the polymer matrix for mixing the magnetic filler

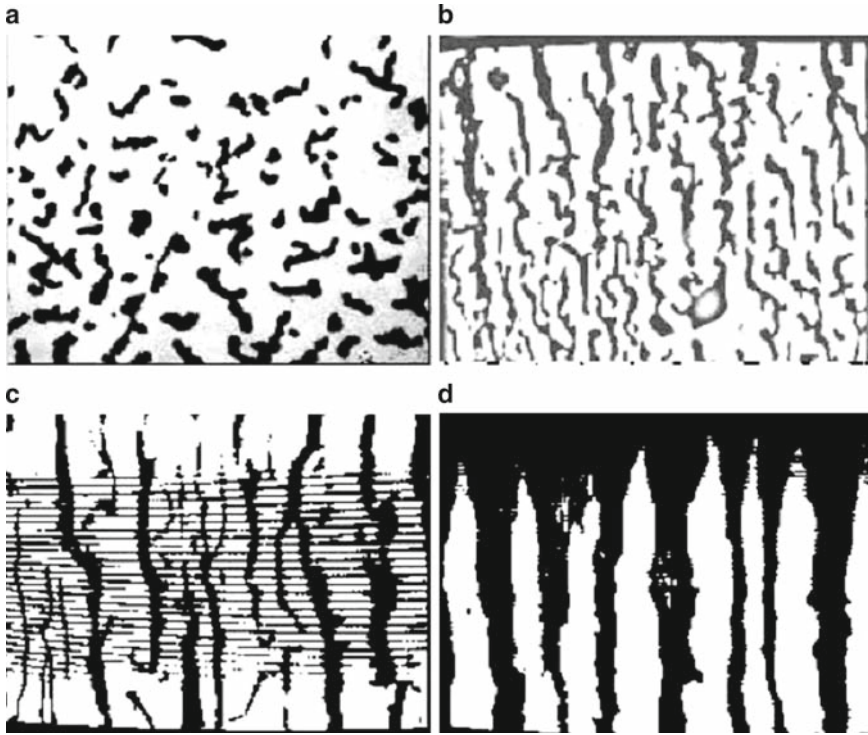


Fig. 11.22 Photographs showing the chain formation in ferrofluid films taken using a CCD camera for different magnetic field values (a): 1390 G, (b): 2210 G, (c): 2690 G, and (d): 3980 G [20]

(polycrystalline ferrite materials). Maintaining high degree tensile strength (serviceability of the elastomer) and modulus at different loadings of the magnetic filler was an objective during the synthesis.

Dielectric measurements conducted on MZF series with different compositions indicated a decrease in dielectric constant with the increase of frequency (100 kHz to 8 MHz). The temperature was also considered as a functional variation from 303 to 393 K. The increase of temperature shows an increase in dielectric constant in both ceramic MZF and RFC (Fig. 11.23).

11.6 Applications of Magnetic Nanocomposites

Application of nanostructure materials is vast and fascinating. The range of application includes cosmetic and sun block, nanofilters, coatings for cutting tools, tennis balls, materials for vehicles, catalysis, sensors, vitamins and additives in food and drug delivery etc. All such applications are for the benefit of mankind.

The basic iron oxide and its alloys were the initial soft ferrites which were applied to *high frequency applications – heavy duty and light duty multipliers* used in cores of transformers, generators and other communication equipments/microwave system components. Microwave applications have revolutionized both the domestic (cooking purpose) and the communication sector. Iron oxide and their alloys embedded in polymer materials are the basics to films or the matrix medium, which lead to development of magnetic memories (audio-video tapes, floppy discs, etc.). The thrust to develop natural and butyl rubber based ferrite composites (Rubber ferrite composites – RFC) was done in/with a view to arrive at flexible elastomer magnets [21, 22, 37]. RFCs have been proved as potential materials in microwave absorbers, designing of versatile magnets, noise filters, etc.

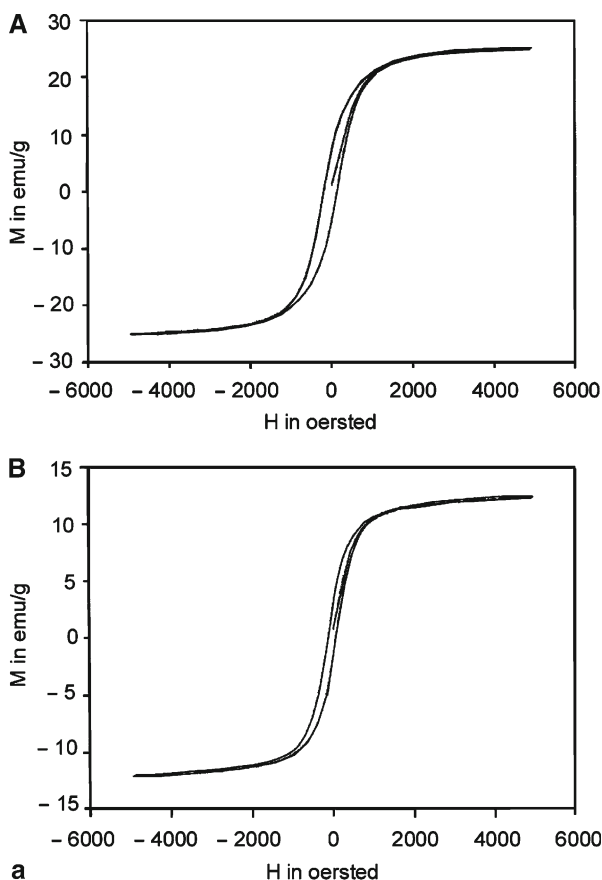


Fig. 11.23 (a) (A) Hysteresis loop of Mn_{1-x}Zn_xFe₂O₄ (MZF) (with reference to the sample in Fig. 11.5); (B) hysteresis loop of RFC (Rubber ferrite composites) having MZF (with reference to the sample in Fig. 11.5) [22]; (b) Representative hysteresis loop for A: Ceramic Ni_{1-x}Zn_xFe₂O₄ (NZF) and B: RFC (NZF in NR (Natural rubber)) [37])

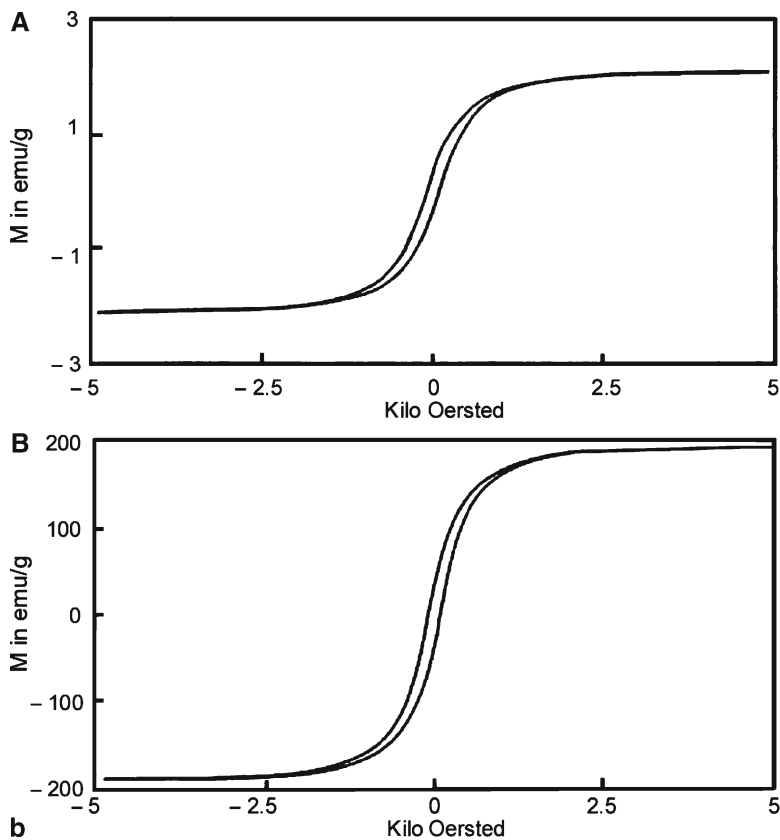


Fig. 11.23. (continued)

The application for polymer-iron oxide based magnetic nanocomposites is highly vital in thrust areas viz. environment, bioscience, conventional/alternative sources of energy and high technology sectors (space science, etc.).

Concentrating on environment pollution, pollutants in wastewater effluents from industrial or domestic sources contain plenty of organic chemicals, which must be removed or destroyed before recycling or discharging back to the environment. Ground and surface water may also contain such pollutants and needs proper treatment for sufficient purity for drinking purpose. Pollutant degradation by virtue of photo catalysis is a promising process for treating wastewater. Magnetic photo catalyst is a process, which allows easy recovery of photo catalyst from the treated water by magnetic force. Magnetic iron oxide core coated with titanium dioxide (TiO_2) forms the basis for magnetic photo catalyst.

Iron oxide mineral analogs for environmental research have found extensive application in environmental laboratory settings as substitutes for various subsurface soils. Behavior of these oxides is regulated by surface chemistry and morphology.

There are reports where iron oxide mineral analogs are characterized to represent natural iron oxide minerals in water distribution systems and in subsurface environments. Iron oxide mineral analogs were procured as crushed corrosion products from a water pipe and glass beads coated with iron oxide by a forced acid hydrolysis technique [43]. Corrosion products were found to be a mixture of five highly crystalline forms of iron oxide including goethite (α -FeOOH), ferrihydrite ($\text{Fe}_5\text{O}_7(\text{OH})_4\text{H}_2\text{O}$), iron hydroxide ($\text{Fe}(\text{OH})_3$), ferroxhyite (δ -FeOOH), and lepidocrocite (γ -FeOOH).

Though we have been mainly discussing on the soft magnetic materials, hard magnetic nanoparticles have shown immense potential for increasing magnetic storage devices.

Magnetic nanomaterials have also been used in filters to remove selected impurities from various types of fluids. The separation of organic contaminants such as polyaromatic hydrocarbons from water and the removal of sulfur compounds from hydrocarbon fuels are also being investigated with magnetic fluids.

The most promising aspect of pharmaceuticals and medicine as it relates to nanotechnology is currently *drug delivery*. In the area of biomedicine, nano-scale dimensional features are those for cell (10–100 μm), virus (20–450 nm), protein (5–50 nm). This is quite indicative that magnetic nanoparticles be associated with biomedicines. Magnetic nanoparticles can be coated with biological molecules to make them interactive with or bind to a biological entity, thereby providing a specific tag or address for controllable mechanism. The nanoparticles are magnetic, which means they obey Coulomb's law and can be manipulated by an external magnetic field gradient. This action at a distance, combined with the intrinsic penetrability of magnetic fields into human tissue, opens up many applications involving the transport and immobilization of magnetic nanoparticles, or of magnetically tagged biological entities. Thus a package can be delivered (say an anticancer drug) and targeted to the affected region of the body i.e., a tumor. There are reports on some special physical properties of magnetic nanoparticles for their potential application in biomedicine [44, 45].

In the area for cancer treatment, a relatively non-specific feature of chemotherapy is one of its major disadvantages. The therapeutic drugs are administered intravenously leading to general systematic distribution, resulting in deleterious side effects as the drug attacks normal, healthy cells in addition to the target tumor cells. However, if such treatments could be localized or brought exactly to the affected site, then the continued use of very potent and effective agents could be made possible. This was probably the main impetus to recognize the purpose to use magnetic carriers to target specific sites (generally cancerous tumors) within the body. In magnetically targeted therapy, a cytotoxic drug is attached to a biocompatible magnetic nanoparticle carrier [46]. The PMAA coated maghemite nanoparticles are recognized as potential magnetically targeted drug carriers by adsorbing an anticancer drug (carboplatin) by virtue of the ion-dipole interaction between CO_2^- of PMAA and carboplatin [35].

Towards mid-twentieth century, impetus for research in *space and astronomy* grew rapidly. There arose a necessity for controlling liquids in space (zero gravity

problems). This led to the development of *ferrofluids*, which are colloidal suspensions of magnetic nanoparticles (e.g., Fe_3O_4 of size about 10 nm) in a liquid. The response of ferrofluids to external magnetic fields offered smooth control of fluid movement required for mechanical or other physical action. Magnetic elements and their alloy oxides (Fe, Co, Zn, and Mn) were basic to ferrofluids. Mostly ferrofluids refer to magnetite (Fe_3O_4) nanoparticles in some liquid medium. It is essential that the nanoparticles remain separate from one another in the liquid medium forming a homogenous system. If there is any tendency for agglomeration of magnetic nanoparticles in the medium, it will cause anisotropic behavior of the ferrofluid, which in turn will spoil its purpose. Magnetic and van der Waals interactions must be overcome to prevent the particles from agglomeration into larger particles. Superparamagnetic property is highly dependent on particle size. Thermal motion of magnetic particles that are smaller than 10 nm in size is sufficient to prevent agglomeration due to magnetic interactions. Surfactants (oleic acid or tetramethylammonium hydroxide) are added to oil-based or aqueous-based ferrofluids to prevent the nanoparticles from approaching one another very closely. The surfactants are basically long-chain hydrocarbon with a polar head that attaches itself to the surface of the magnetite particle. The long chains comprising the tails, act as a repellent cushion and prevent the close approach of another particle. Spikes are observed when the ferrofluids are subjected to strong magnetic fields. Such spikes arise from a tendency of the particles to line up along the magnetic field lines to lower their energy. The presence of surface tension in fluids restricts the extent to which the particles can align themselves within the field. The main application areas of ferrofluids are:

1. Mechanical movements in regions not easily approachable viz. rotating shaft seals in X-ray generators and in vacuum chambers.
2. High speed computer disk drives.
3. Improving performance of loudspeakers (damping of unwanted resonance and dissipating heat in the coils).
4. Migratory sense of animals.
5. Biomedical applications (targeted medicines and magnetic resonance imaging MRI).

Magnetic materials (FeBO_3 and FeF_3) transparent in the visible region (absorption coefficient $\leq 40 \text{ cm}^{-1}$) at room temperature have caught up tremendous interest (Ziolo 1992) and [47]. This area included colored magnets, bead like magnets and low-density magnetic microphores.

11.7 Prospective Areas and Challenges

There are some excellent contributions in the area of organic–inorganic magnetic nanocomposites [2, 47–49], and Ziolo 1992.

Since early 1990s magnetic properties of molecular based materials caught the interest of physicists, chemists and mathematicians. A host of interdisciplinary areas opened up with bioscience providing the living conditions and man-made problems.

Structural based problems and their relation to different magnetic properties kindled the initial interest. To state a few are simple dinuclear or oligonuclear species, one-dimensional materials (Spin Hamiltonians). A few examples could be cited: molecular ferrimagnet (based on copper (II)-manganese (II) derivatives, organic building blocks (dithiocarbamate iron (III) complex), polycarbenes, Prussian blue compounds, etc.

Certain systems comprising of a finite number of interacting magnetic centers led to an interdisciplinary approach for zero-dimensional magnets, thanks to quantum effects in magnets. The main hurdles were to obtain assemblies of identical particles, which had to scale exponentially with the size of the particles. It was understood that magnetic interaction between the particles be minimized. To cite some examples viz. iron loaded ferritin, Mn_{12} (a cluster of twelve Mn ions) acetate, cluster of eight iron (III) ions, etc.

Yet another area of immense interest has been magnetic semiconductors and diluted magnetic semiconductors (ZnO: Co or Mn) [49–51].

We identify some challenges, which can be the goal setters for research in organic-inorganic magnetic nanocomposites:

- (a) Better synthesis method to ensure nanomaterials of desired size, distribution, shape, morphology and chemical composition resulting in the most required properties.
- (b) More sophisticated tools to characterize and study the nanomaterials.
- (c) Specific care to prevent coarsening of magnetic particles.
- (d) Clear understanding of the relationship between microstructure and related properties.
- (e) Especially, for magnetic nanocomposites one cannot go on reducing the size in the superparamagnetic region for higher storage capacity. This brings about instability in the system.

11.8 Concluding Remarks

In this chapter some aspects of iron oxide/organic magnetic nanocomposite materials have been addressed. The primary concern dealt with different ways to develop iron oxide and its alloys, which originated from organic based compounds. By pursuing so many different phases of iron oxide, amorphous and crystalline structures were studied. It is quite apparent that many more areas have not been included.

Molecular composition and bonding configurations existing in organic-inorganic nanocomposites were studied employing mainly infrared spectroscopy. It is this area which is still not yet fully understood.

It is very clear that there are host of routes to arrive at organic–inorganic magnetic nanocomposites. Till date plenty of research has been carried out. However, there are many questions still unanswered and not properly understood. The target and motivation to achieve such a goal, as briefly compiled in the application part, is also set. Everyday problems keep modifying our priority areas and it is not sure which pathway nanotechnology will follow but it can be concluded with certainty that world will be different from what we know now.

Acknowledgements I (AD) am highly grateful to the Department of Science and Technology (DST) – Funds for Improvement in Science and Technology (FIST) for providing essential support to build the basic infrastructure for research and development, and the graduate advance laboratory for academic development in our department. I am also thankful to the University Grants Commission (UGC) to provide me scope and funds by granting me a project UGC-MNR (2002–2004) in an area which was fairly new to me. I thank all my colleagues in our department and members of my family who provided me the impetus and encouragement to complete this chapter despite of many shortcomings. I am indebted to Dr M. Pal who on my request joined me as coauthor, in the final stage, to make this chapter a success. Finally, I must thank Prof. L. Merhari for giving me the opportunity to form such a chapter, providing me constant guidance and attending to any of my queries.

References

1. Cullity BD. (1972) Introduction to Magnetic Materials. Addison-Wesley, Reading, MA, pp383–441.
2. Blundell SJ. (2001) Magnetism in Condensed Matter. Oxford University Press, New York, pp180–182.
3. Morrish AH. (1965) The Physical Principles of Magnetism. Wiley, New York, p360.
4. Bean C and Livingston J. (1959) Suppl. *J. Appl. Phys.* 30, p1205.
5. Klug HP and Alexander LE. (1954) X-Ray Diffraction Procedures – For polycrystalline and Amorphous Materials. Wiley, New York, p687.
6. Pathak A and Pramanik P. (2001) Nanoparticles of Oxides Through Chemical Methods, *PINSA* 67 A(1), pp. 47–70.
7. Pierre AC. (1998) Introduction to Sol-Gel Processing. USA, Kluwer, p24–47; 110,161.
8. Roy R. (1987) Ceramics by the solution sol-gel route. *Science* 238, pp1664–1669.
9. De A. (2004) Low molecular weight polymer based nanostructured ferrite materials. In: Nano 2004 India: International Conference on Nano-Materials: Synthesis, Characterization and Application, Kolkata, India. Tata McGraw-Hill, New Delhi, India, 496–498.
10. Pramanik P and Pathak A. (1994) A new chemical route for the preparation of fine ferrite powders. *Bulletin of Materials Science* 17, pp967–975.
11. Pramanik P. (1999) A novel chemical route for the preparation of nanosized oxides, phosphates, vanadates, molybdates and tungstates. *Bulletin of Materials Science* 22, pp335–339.
12. Valenzuela R. (1994) Magnetic Ceramics. Cambridge University Press, Cambridge, New York.
13. Pal M, Brahma P, Chakravorty D, Bhattacharya D and Maiti HS. (1997) Preparation of nanocrystalline barium hexaferrite in a glass medium. *Nanostructured Materials* 8, pp731–738.
14. Pal M, Das D, Chintalapudi SN and Chakravorty D. (2000) Preparation of nanocomposites containing iron and nickel-zinc ferrite. *Journal of Materials Research* 15, pp683–688.

15. Stavroyiannis S, Panagiotopoulos I, Niarchous D. (1998) CoPt/Ag nanocomposites for high density recording media. *Applied Physics Letters A* 73, p3453
16. Inoue N, Kawamura Y and Morimoto K. (1997) Molecular beam epitaxy: Handbook of Nanophase Materials (ed.) A N Goldstein. Marcel Dekker, New York, pp83–140.
17. Ping DH and Hono K. (1998) Partitioning of Ga and Co atoms in a Fe₃B/Nd₂Fe₁₄B nanocomposite magnet. *Journal of Applied Physics* 83, p7769.
18. McCormick PG, Miao WF, Smith PAI, Ding J and Street R. (1998) Mechanically alloyed nanocomposite magnets. *Journal of Applied Physics* 83, p6256.
19. Craik DJ. (1975) *Magnetic Oxides* part 2. Wiley, New York, pp697–708.
20. Abraham VS, Swapna Nair S, Rajesh S, Sajeev US and Anantharaman MR. (2004) Magnetic field induced assembling of nanoparticles in ferrofluidic liquid thin film based on Ni_xFe_{1-x}Fe₂O₄. *Bulletin of Materials Science* 27, pp155–161.
21. Anantharaman MR, Sindhu S, Jagatheesan S, Malini KA and Kurian P. (1999) Dielectric properties of rubber ferrite composites containing mixed ferrites. *Journal of Physics D: Applied Physics* 32, pp1801–1810.
22. Mohammed EM, Malini KA, Kurian P and Anantharaman MR. (2002) Modification of dielectric and mechanical properties of rubber ferrite composites containing manganese zinc ferrite. *Materials Research Bulletin* 37, pp753–768
23. Tadakoro H. (1979) *Structure of Polymers*. Wiley-Interscience, San Francisco, pp213–214; 358; 381.
24. Yogo T, Nakamura T, Sakamoto W and Hirano S. (2000) Synthesis of transparent magnetic particle/organic hybrid films using iron-organics. *Journal of Material Research* 15(10), pp2114–2120.
25. Palchik O, Felner I, Kataby G and Gedanken A. (2000) Amorphous iron oxide prepared by microwave heating. *Journal of Materials Research* 15(10), pp2176–2181.
26. Chauhan P, Annapoorni S and Trikha SK. (1998) Preparation, characterization and optical properties of a-Fe₂O₃ films by sol-spinning process. *Bulletin of Material Science* 21, pp381–385.
27. Jungk H-O and Feldmann C. (2000) Nanoagglomerated, submicron a-Fe₂O₃ particles: Preparation and alication. *Journal of Material Research* 15, pp2244–2248.
28. Suri K, Annapoorni S and Tandon RP. (2001) Phase change induced by polypyrrole in iron-oxide polypyrrole nanocomposite. *Bulletin of Materials Science* 24, pp563–567.
29. Venkatraman A, Hiremath VA, Date SK and Kulkarni SD. (2001) A new combustion route to g-Fe₂O₃ synthesis. *Bulletin of Materials Science* 24, pp617–621.
30. Bunn CW. (1948) Crystal structure of polyvinyl alcohol. *Nature* 161, pp929–930.
31. Dhawan SK and Trivadi DC. (1993) Thin conducting polypyrrole film on insulating surface and its alications. *Bulletin of Material Science* 16, pp371–380.
32. Deb P, Biswas T, Sen D, Basumallick A and Mazumder S. (2002) Characteristics of Fe₂O₃ nanoparticles prepared by heat treatment of a non-aqueous powder precipitate. *Journal of Nanoparticle Research* 4, pp91–97.
33. Hiremath VA and Venkatraman A. (2003) Dielectric, electrical and infrared studies of g-Fe₂O₃ prepared by combustion method. *Bulletin of Material Science* 26, p391–396.
34. Waldron RD. (1955) Infrared spectra of ferrites. *Physical Review* 99, pp1727–1735.
35. Yu S and Chow GM. (2004) Carboxyl group (-CO₂H) functionalized ferromagnetic iron oxide nanoparticles for potential bio-applications. *Journal of Materials Chemistry* 14, pp2781
36. Ziolo RF, Giannelis EP, Weinstein BA, O'Horo MP, Ganguly BN, Mehrotra V, Russell MW, and Huffman DR. (1992) Matrix-mediated synthesis of nanocrystalline g-Fe₂O₃: A new optically transparent magnetic material. *Science* 257, pp219–223.
37. Anantharaman MR, Malini KA, Sindhu S, Mohammed EM, Date SK, Kulkarni SD, Joy PA and Kurian P. (2001) Tailoring magnetic and dielectric properties of rubber ferrite composites containing mixed ferrites. *Bulletin of Material Science* 24, pp623–631.
38. Thorpe AN, Senftle FE, Holt M, Grant J, Lowe W, Anderson H, Williams E, Monkres and Barkatt A. (2000) Magnetization, micro-X-ray fluorescence, and transmission electron micro-

- scopy studies of low concentrations of nanoscale Fe_3O_4 particles in epoxy resin. *Journal of Materials Research* 15, pp 2488–2493.
39. Stauffer D. (1985) *Introduction to Percolation Theory*. Taylor & Francis, London.
 40. Kneller E. (1969) *Magnetism and Metallurgy*, Vol. 1, chapter 1 (eds.) Berkowitz A.E. and Kneller E. Academic, New York.
 41. Xue S, Ousi-Benomar W and Lessard RA. (1994) $\alpha\text{-Fe}_2\text{O}_3$ thin films prepared by metalorganic deposition from Fe (III) 2-ethylhexanoate. *Thin Solid Films* 250, pp194–201.
 42. Gadhvi M, Upadhyay RV, Parekh K and Mehta RV. (2004) Magnetically textured ferrofluid in a non-magnetic matrix: magnetic properties. *Bulletin of Materials Science* 27, pp163–168.
 43. Borch T, Biederman JA, Mogk DW, Butterfield PW, Camper AK and Jordan RN. (2003) *Characterization of Two Iron Oxide Models for Environmental Research: Microscopic and Spectroscopic Studies – A Research Report*. Center for Biofilm Engineering, Montana State University, Bozeman, MT.
 44. Pankhurst QA, Connolly J, Jones SK and Dobson J. (2003) Applications of magnetic nanoparticles in biomedicine. *Journal of Physics D: Applied Physics* 36, ppR167–R181.
 45. Shinkai M. (2002) Functional magnetic particles for medical application. *Journal of Bioscience and Bioengineering* 94, pp606–613.
 46. Kačmár S, Koneracká M, Kopčanský P, Timko M, Sequiera A, De and Trevan M. (2001) Entrapment of anticancer drug 5 Fluorouracil in magnetoliposome vesicles. *Zborník konf. SSB*, 127.
 47. Ziolo RF. (1994) Magnets-value of the first step. *R&D Innovator* 3(11), p127.
 48. Kahn O. (1993) *Molecular Magnetism*. Wiley, Weinheim.
 49. Samarth N. (2006) Semiconductor physics: Magnetic manipulations. *Nature* 442, pp359–360.
 50. Rubi D, Calleja A, Arbiol J, Capdevila XG, Segarra M, Aragonès LI and Fontcuberta J. (2005) Structural and magnetic properties of ZnO: TM (TM: Co, Mn) nanopowders. *Journal of Magnetism and Magnetic Materials* 316(2), ppe211–e214.
 51. Pal M and Pal M. (2005) Nanocrystalline Mn-doped ZnO by chemical route. *Japanese Journal of Applied Physics* 44, pp 7901–7903.

Part III
Optical Applications

Chapter 12

Organic–Inorganic Hybrids for Light-Emitting Devices and Integrated Optics

L.D. Carlos, R.A. Sá Ferreira, and V. de Zea Bermudez

Abstract This work provides an overview of the latest advances in organic–inorganic hybrid materials with applications in light-emitting devices and integrated optics. The organization of the chapter intends to help the reader to gain a clear insight into the topic, from the description of the material’s synthesis to the photoluminescence results that emphasize the potential technological applications of these photonic materials for light-emitting purposes, integrated optics and non-linear optical effects.

In Sect. 12.2 conventional synthetic procedures that have been extensively used during the last decades to generate photoluminescent stable and efficient siloxane-based class I and class II disordered hybrids are described. The relevance of the sol–gel method in this context is highlighted. This section also covers recent and exciting progress in the emerging domain of hierarchically structured photonic hybrid materials prepared through the combination of sol–gel and self-assembly strategies. Reference is made to the assembly of nanobuilding blocks (NBBs) and to the few ordered materials that have been produced on the basis of the ordered hybrid approach.

In Sect. 12.3 several amorphous and highly-organized hybrid structures, lacking metal activator centres (Sect. 12.3.1) and incorporating optically-active centres (Sect. 12.3.2), are discussed. Emphasis is laid on their absorption and photoluminescent features and on the quantification of the colour emission and absolute external quantum yield. Due to their relevance to optical applications, particular attention is given to amine-functionalized cross-linked sol–gel derived hybrids in the non-doped and doped states which exhibit external photoluminescence quantum yields as high as 35 and 50%, respectively.

This review ends with Sect. 12.4 in which the requirements for developing integrated and non-linear optical devices based on hybrid materials are addressed.

L.D. Carlos(✉) and R.A. Sá Ferreira
Departamento de Física and CICECO, Universidade de Aveiro, 3810-193 Aveiro, Portugal
e-mail: lcarlos@ua.pt

V. de Zea Bermudez
Departamento de Química and CQ-VR, Universidade de Trás-os-Montes e Alto Douro 5001-081
Lila Deal, Portugal

12.1 Introduction

The drive to miniaturization, with corresponding demand for smaller machines and components using less resources and energy that occurred during the last two decades, have been rapidly pushing industry into the atomic and nanometer scale. Development of new synthesis strategies for advanced materials with enhanced properties and affording an effective control at the nanometer level is therefore required. Amongst the available synthetic methods employed for the development of nanosized systems, there are two main general approaches: “bottom-up” and “top-down”. The former applies to the creation of organic and inorganic structures, atom-by-atom or molecule-by-molecule. It implies the use of atoms or molecules as building blocks to design and assemble nanoarrangements of atoms in a functional form to give macroscopic systems.

The concept of “organic–inorganic hybrid” materials emerged very recently with the birth of “soft” inorganic chemistry processes, particularly the sol–gel process which is probably the supreme “soft” inorganic chemistry process allowing that tailored chemical design [1–9]. The unique low temperature processing characteristics of this process allow the chemical design of organic–inorganic hybrid materials through incorporation of low molecular weight organic molecules with appropriate functionalities into inorganic moieties, at temperatures at which the organic ones are not destroyed [1–4, 8–16].

The basic idea behind the development of hybrid materials is the combination of organic and inorganic components at the molecular scale to achieve a synergy of the most important properties of their constituents, such as high transparency (glass-like), low processing temperatures (polymer-like), and sufficient thermal stability (glass-like). These hybrid materials are easily accessible because of the unique availability of the respective precursors (usually, commercially available metal alkoxides, organoalkoxysilanes, as well as nanoparticles).

In the last few years it has become increasingly evident that complex inorganic materials can be synthesized across a range of length scales by constructional, morphological and hierarchical coding of precipitation reactions. This molecular tectonics concept has also been explored in the field of organic–inorganic hybrids for the development of organized sophisticated materials. Two main approaches have been employed to produce such systems: (1) classical self-assembly strategies involving the presence of organic templates that act as structure-directing agents [6, 7, 17–20]; (2) self-directed assembly strategies [21–28]. Self-organization of relatively simple precursor molecules has yielded complex hierarchical architectures with intricate structures, including several stages of organization.

Hybrids with tuneable attributes offering modulated properties have been designed during the last two decades, opening up exciting directions in materials science and related technologies with significant implications in the nanotechnological processing, which facilitate integration, miniaturization and multifunctionalization of devices. Promising applications are therefore expected in many fields, including optics, electronics, opto-electronics, ionics, mechanics, membranes, protective coatings, catalysis, sensors, biology, and others [1–3, 5–9, 12, 14–16, 29–37].

There is indeed a widespread agreement within the sol–gel scientific community that the inherent flexibility of the “soft” chemistry approach allows implementation of design strategies that are the basis of photonic hybrid materials [4, 11, 30–37]. In particular, siloxane-based hybrids present several advantages for designing materials for optical and photonic applications. Therefore, a significant number of innovative and advanced siloxane-based hybrids have been synthesized in the past few years with mechanical properties tuneable between those of glasses and polymers, and with improved optical properties as well. We can mention, for instance: – optical switching and data storage hybrid devices [33, 35, 38], – photoelectrochemical cells and coatings for solar energy conversion [33, 39, 40], – hybrid materials having excellent laser efficiencies and good photostability [41], fast photochromic responses [42], high and stable second-order non-linear optical responses [10, 43, 44] which can be used as original pH and fibre-optic sensors [45–48], – photopattern waveguiding structures for integrated optics [44, 49–52], and electroluminescent diodes [53, 54].

This survey attempts to cover the most recent advances in the field of photoluminescent stable and efficient siloxane-based hybrids prepared by means of conventional synthetic procedures (routes I and II in Sect. 12.2.1.1 and 12.2.1.2, respectively). Innovative photonic hybrid materials, whose structure and function are hierarchically organized, are also covered. Illustrative examples of these organized hybrid systems, prepared through the combination of sol–gel and self-assembly approaches (routes III and V in Sect. 12.2.2.1 and 12.2.2.3, respectively), are presented. The description of the major achievements obtained in the emerging area of organized hybrid materials with applications in optics is complemented with a reference to those optically active hybrid materials derived from the assembly of nanobuilding blocks (NBBs) (route IV in Sect. 12.2.2.2).

Examples of amorphous and highly-organized hybrid structures incorporating optically-active centres (organic dyes and lanthanide ions) are reviewed with emphasis on their absorption and photoluminescent features for light-emitting purposes and on the quantification of the colour emission and absolute external quantum yield.

Due to their relevance to optical applications, particular attention is given to amine-functionalized cross-linked sol–gel derived hybrids in the non-doped and doped states. Currently, several stable and efficient white-light photoluminescent amine-functionalized hybrids lacking metal activator ions are known [31, 55–62]. One such system – the aminepropyltriethoxysilane (APTES)-formic acid hybrid – exhibits the highest external photoluminescence (PL) quantum yield reported up to date (35%) [61]. The APTES-acetic acid phosphor analog displays two distinct emissions with quantum yields of 12 and 21% [55]. The values obtained for the non-doped di-urea and di-urethane cross-linked poly(oxyethylene) (POE)/siloxane hybrid frameworks (di-ureasils and di-urethanesils, respectively) are of the same order of magnitude (7–23%) [31, 58, 60, 63, 64]. As far as the doped amino-functionalized hybrid materials are concerned, emphasis is laid on those incorporating dye chromophores, such as the coumarin-153 (C-153)-doped di-ureasils which display laser action [65], and the rhodamine 6G-doped di-ureasils prepared

in the presence of zirconium(IV) *n*-propoxide (ZPO) modified with methacrylic acid (McOH), which show distributed feedback laser effect [66]. The emitted colour of di-ureasils and di-urethanesils incorporating lanthanide salts may be readily tuned across the Commission Internationale d'Éclairage (CIE) chromaticity diagram [31, 32, 67–73] and the Nd³⁺-doped di-urethanesils exhibit room temperature infrared emission [74]. Mention should also be made of the di-ureasil doped with the Eu(btfa)₃(4,4'-bpy)(EtOH) complex (where btfa and 4,4'-bpy stand for 4,4,4-trifluoro-1-phenyl-1,3-butanedione and 4,4'-bipyridine, respectively) displaying, to the best of our knowledge, the greatest emission quantum yield ever found in this sort of hybrid systems (50%) [75].

The review then proceeds with two sections describing the requirements to develop integrated and non-linear optic devices based on hybrid materials before conclusions are drawn. This allows the reader to gain an insight into the topic, from the description of the material's synthesis to the photoluminescent results that emphasize the potential technological applications of these photonic materials for light-emitting purposes, integrated optics, and non-linear effects.

12.2 Strategies for the Synthesis of Hybrids Incorporating Functional Groups

The structure, degree of order and main characteristics of nanohybrids [2] depend, not only on the chemical features of the organic and inorganic components, but also on the interaction that is established between them. As a consequence, the design of hybrid materials is primarily dictated by the nature, extent and accessibility of the inner interfaces [4, 6].

In the class of hybrid materials two distinct categories of materials – referred to as Class I and Class II hybrids – can be distinguished on the basis of the nature of the interactions occurring between the organic and inorganic components. Class I includes all hybrid systems in which both components interact in a weak manner (e.g., van der Waals contacts, π - π interactions and hydrogen bonding). Often, such systems form interpenetrated networks, as the first network is entrapped within the second network. In Class II we find all the hybrids in which at least a proportion of the organic and inorganic components are linked through strong chemical bonds (i.e., covalent, iono-covalent or acid-base bonds). However, tailoring of the hybrid networks is a function, not only of the type of interaction existing between the organic and inorganic species, but also of the chemical route employed to design the material. In the following, we will describe the approaches that have been explored in the last few years for the construction of non-organized and organized hybrid materials. Figure 12.1 summarizes general available synthetic routes for the design of hybrid materials, according to Sanchez et al. [6, 7, 35].

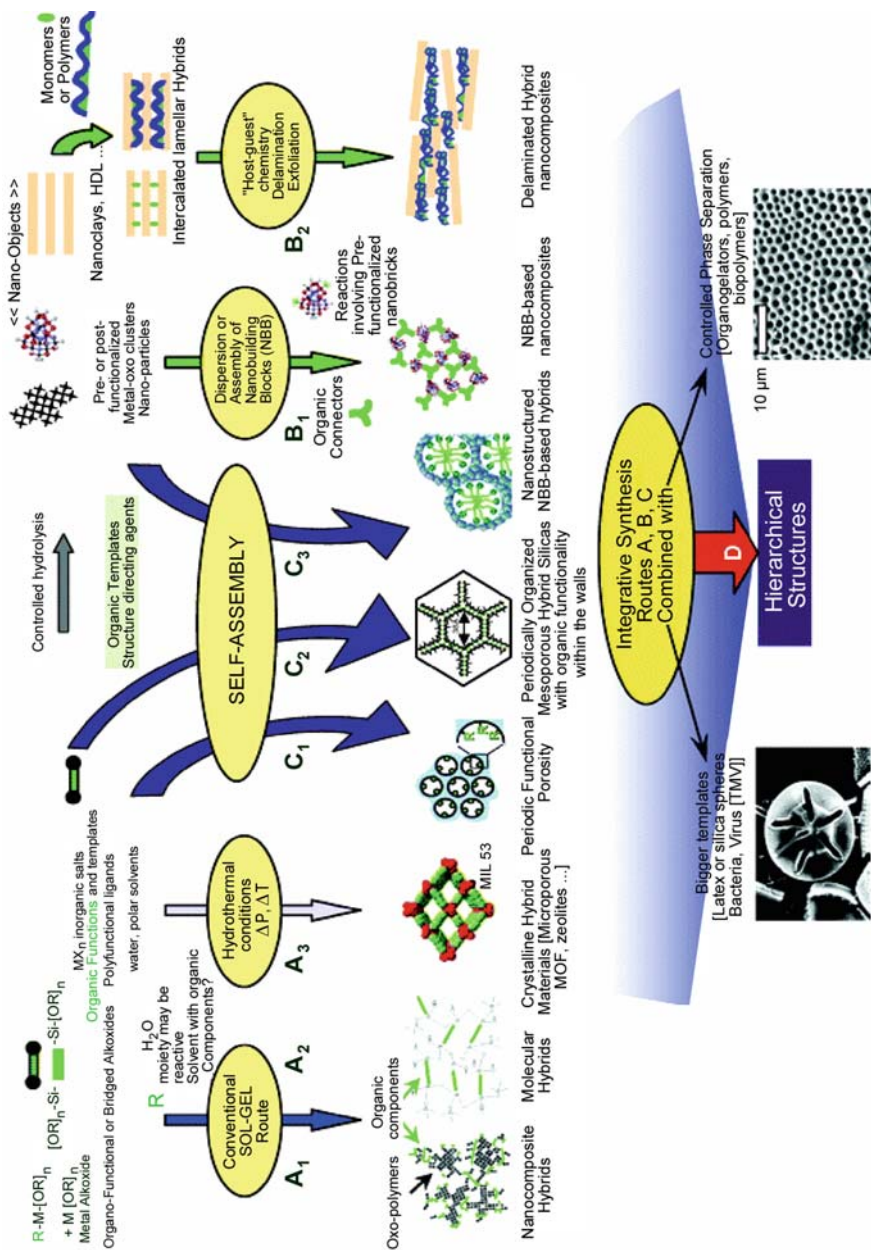


Fig. 12.1 Strategies for synthesis of hybrid materials. Reprinted from [33]

12.2.1 *Non-organized Hybrids*

12.2.1.1 **Route I: Synthesis of Class I Hybrids**

Preparation of siloxane-based Class I hybrid materials is quite simple. It involves embedding the organic components, such as dye molecules or macromonomers (e.g., polyethylene glycols) previously dissolved in the reaction solvent, within a solution of the growing siloxane network (typically from an alkoxy silane). Enhanced interfacial interactions through hydrogen bonding or π - π bonding usually promote intimate mixing and/or interpenetration between both components at the nanometer scale.

Synthesis of amorphous hybrid frameworks for optics has been essentially directed towards reduction or virtual suppression of groups responsible for quenching the luminescence (e.g., silanol (Si-OH) groups, residual solvent). The following five strategies have been proposed:

- Fine control of the sol-gel processing conditions. This may be achieved through optimization of water content, use of reactive hydrophobic precursors and thermal curing.
- Use of non-hydrolytic procedures, such as the modified sol-gel process usually designated as solvolysis or carboxylic acid method.
- Combination of the first strategy with the encapsulation of the emitting species through complexation or chelation. The complexes or chelates may be added directly to the matrix or formed in situ. In the latter case, appropriate ligands are grafted or anchored to the hybrid network itself prior to the addition of the lanthanide ions.
- Encapsulation of the lanthanide ions within nanoparticles. This route involves the combination of microemulsion techniques with the sol-gel process.
- Simultaneous introduction of inorganic and organic chromophores, i.e., lanthanide ions and organic dyes, into the hybrid structure.

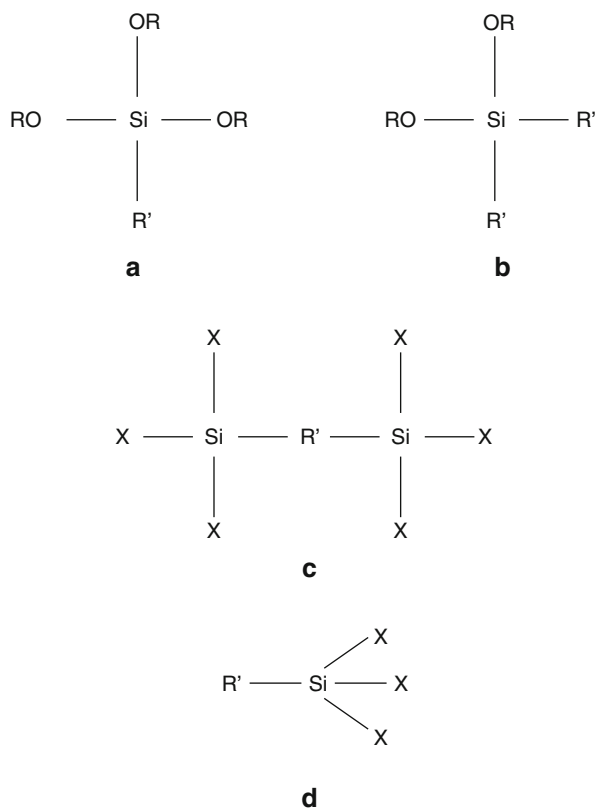
12.2.1.2 **Route II: Synthesis of Class II Hybrids**

Typically, preparation of siloxane-based Class II hybrids involves two steps. In the first stage, the organic and inorganic components are covalently grafted to form the sol-gel precursor hybrid molecule. In the second stage of the synthetic procedure, this organic-inorganic molecule undergoes hydrolysis and condensation reactions in the presence of water, leading to the growth of the oxopolymer framework. Therefore the strategy of construction of Class II hybrid compounds relies strongly on the relative chemical stability of the chemical bonds that associate the various components. The precursor molecules must incorporate at least two different functionalities: groups stable under the attack of water (Si-C bonds) and groups unstable with respect to hydrolysis (Si-O bonds).

1st Stage: Grafting Reaction

Two kinds of molecules have been used to produce siloxane-based Class II hybrids:

- Organosubstituted silicic acid esters (or organoalkoxysilanes) (Scheme 12.1a,b), where R is an alkyl group and R' is an organofunctional group that may play the role of network modifier or network former. If R' is a non-hydrolysable group (e.g., an alkyl group), it will have a network modifier effect. However, if R' is a group that may polymerize or copolymerize (e.g., methacryl or epoxy groups) or undergo hydrolysis and condensation reactions (e.g., trialkoxysilyl groups), it will act as a network former. In addition, R' can also be an organic dye molecule.
- Bridged silsesquioxane precursors (Scheme 12.1c), where X = Cl, Br, OR.



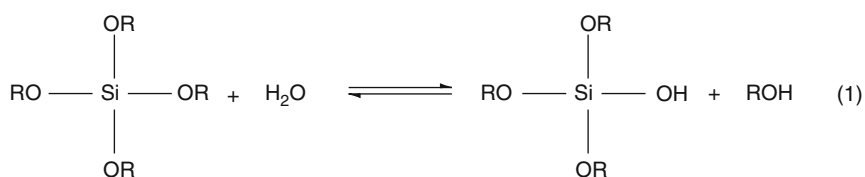
Scheme 12.1 Precursor molecules usually employed to produce siloxane-based Class II hybrids

2nd Stage: Sol–gel Reactions

Prior to presenting a brief overview of the sol–gel chemistry, it is worth emphasizing that although the hybrid concept is an old challenge that goes back to the industrial era, in recent years investigation on hybrid materials has exploded because of the recognition that the versatile sol–gel method is the most adequate route to produce these systems in a simple and inexpensive way.

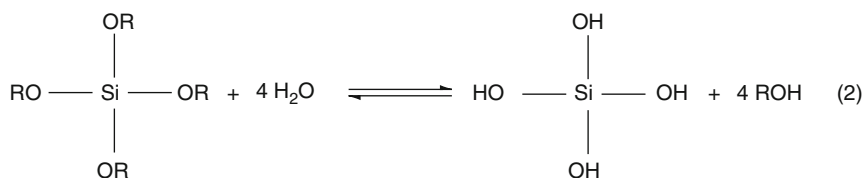
The sol–gel process is a chemical synthetic procedure that involves inorganic polymerization reactions, which lead to the formation of dispersed inorganic materials in solvents, through the growth of metal-oxopolymers [2].

a) Conventional sol–gel method



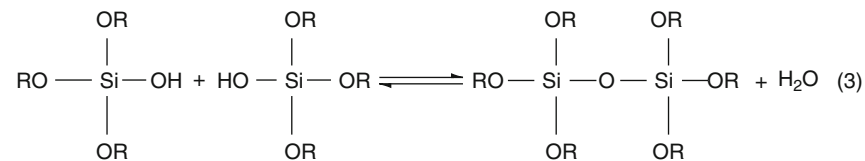
tetraalkoxysilane

hydroxyalkoxysilane

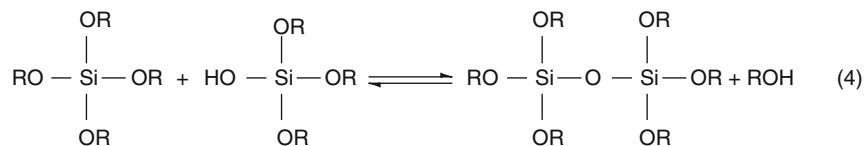


tetraalkoxysilane

tetrahydroxysilane



hydroxytrialkoxysilane hydroxytrialkoxysilane



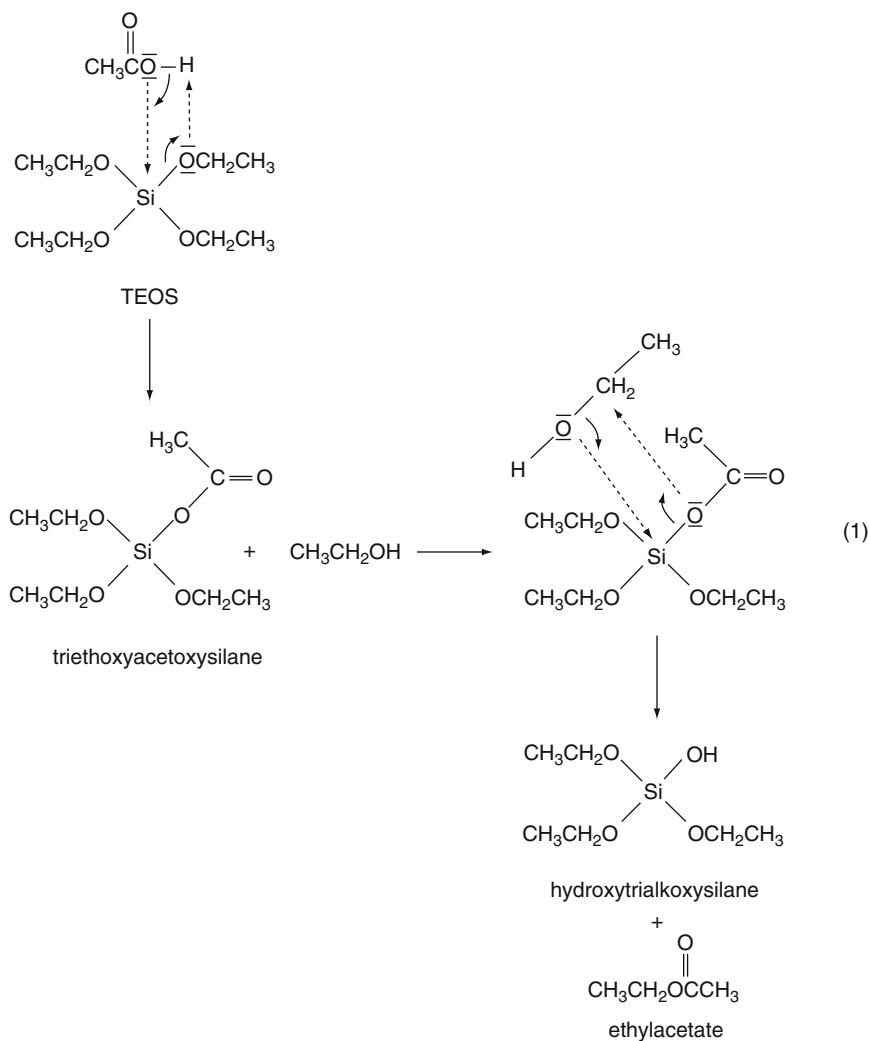
tetraalkoxysilane hydroxytrialkoxysilane

Scheme 12.3 Reactions of the conventional sol–gel process

This method involves hydrolysis and condensation reactions.

Hydrolysis Reaction

Because of their hydrolytic instability, metal alkoxides are the most extensively used precursors in this context. Under the attack of water, the alkoxy groups of such compounds are replaced by hydroxyl groups. In parallel, an alcohol molecule is



Scheme 12.4 Representative reactions of the modified sol-gel process (or solvolysis or carboxylic acid method)

formed. Depending on the amount of water and catalyst added, the hydrolysis may be partial (reaction 1 of Scheme 12.3) or complete (reaction 2 of Scheme 12.3).

Condensation Reactions

Through condensation, two partially hydrolyzed precursor molecules bind to each other and a small molecule is produced. When the molecule formed is water, the reaction is called aqueous condensation (reaction 3 of Scheme 12.3). If alcohol is the by-product, the reaction is known as alcoholic condensation (reaction 4 of Scheme 12.3).

Reactions (3) and (4) of Scheme 12.3 proceed to give rise to a giant silicon-containing molecule. When the molecule reaches macroscopic dimensions and extends throughout the solution, a gel results. The sol–gel transition takes place after the sol (i.e., colloidal suspension of solid particles in a liquid) is cast into a mould. After gelation, the sample is aged, a process that is accompanied by changes in its structure and properties. Aging may involve further condensation, dissolution and reprecipitation of monomers and oligomers, or phase transformations within the solid and liquid phases. Shrinkage of the gel network, originating from deformation of the network and transport of the liquid through the pores, occur when the gel is dried under normal conditions to evaporate the solvent. The volume of the dried gel – xerogel – is reduced by a factor of 5–10 with respect to that of the wet gel. Shrinkage will be lowest if the wet gel is dried under supercritical conditions in an autoclave. In the latter case, the product will be called aerogel. If the smallest dimension of the gel is greater than a few millimetres, the object is classified as a monolith. Alternatively, if gelation is produced by rapid evaporation of the solvent, films and fibres result. Most gels are amorphous, but many crystallize on heating. Upon sintering of the gel, a pore-free ceramic can be obtained.

A wide range of structures, microstructures, and compositions can be achieved through a careful control of the most critical process parameters, such as the H_2O/M ratio, the nature and concentration of the catalyst, and type of solvent.

b) Modified sol–gel method (or solvolysis or carboxylic acid method)

In 1986 Pope et al. [76] reported that the formation of hydroxyalcoxysilanes could take place in the absence of water, if the precursor molecule was reacted with a carboxylic acid. Scheme 12.4 illustrates the reaction mechanism proposed by these authors for the reaction of tetraethoxyortosilicate (TEOS) with acetic acid. Condensation reactions that take place after this non-hydrolytic stage proceed in a way similar to those occurring in the conventional sol–gel method.

12.2.2 *Organized or Texturized Hybrids*

As stated above, chemical routes I and II represent the main available pathways to produce non-organized hybrids. In fact, these materials not only exhibit infinity of

macrostructures, but they are generally polydisperse in size and locally heterogeneous in terms of chemical composition.

Chemical construction and patterning remain one of the greatest challenges in the science of organized matter chemistry [17]. Organization implies the controlled segregation at the nanoscopic level. The following routes prove that organization of a growing hybrid framework can be achieved using templates. Usually these species are organic molecules. In some cases, however, the growing supramolecular architecture or the precursor molecules may play the role of internal templates.

12.2.2.1 Route III: Template-directed Assembly

In this route, molecular or supramolecular templates are present as directing agents in the synthesis solution. These may take the form of discrete aggregates, such as micelles, or extended aggregates such as liquid crystalline mesophases. They can be self-assembled before or co-assembled during synthesis and in both cases act as organized substrates for inorganic deposition. The chemical, spatial and structural properties of the template should complement the reaction chemistry, bonding and packing consideration of the incipient inorganic phase. This requirement for interfacial matching is of paramount importance for the development of integrated hybrid systems capable of coordinated assembly.

a) Transcriptive synthesis – The formation of organized inorganic materials by direct templating using pre-formed self-assembled organic architectures can be described by the following sequence:

Self-assembly → transcription → replication.

Usually the organic template, which must be stable during the materials synthesis, is in place prior to formation of the inorganic phase. Incorporation of surface functional groups that direct interfacial events (e.g., nucleation from supersaturated solutions and adsorption of incipient or pre-formed nanoclusters from colloidal sols) produces inorganic replicas with high fidelity.

Templates with high specificity are chemically coded surfaces that are transcribed at the molecular level into inorganic nuclei with precise structural, orientational and positional properties. The repetition of these molecular processes leads to the inorganic replication of the organic architecture. Hybrids with micro-, meso-, and macroscale¹ patterns can thus be obtained. In general, in transcriptive mechanisms there is direct correspondence in size and shape between template and inorganic replica. For instance, supramolecular assemblies will be of limited use for chemical construction of micro- and macroscale structures.

¹According to the IUPAC, pores are classified on the basis of their diameter: micropores have diameters less than about 2 nm; mesopores have diameters between 2 and 50 nm; macropores have diameters greater than about 50 nm.

Recently it was demonstrated that porous pillared lamellar silicas could be prepared by confining hydrolysis and condensation of TEOS within the aqueous interlayer spaces of multilamellar vesicles preformed from the surfactant 1,12-diaminododecane [77]. The surfactant aggregates are sufficiently stable for the mineralized replicas to inherit the shape, size and ultrastructure of the preformed self-assembled vesicles: they are produced in the form of spherical micrometer-size particles of concentrically arranged laminated silica-surfactant nanostructures.

In the light of the same synthetic approach, an ordered liquid-crystalline hexagonal (HI) mesophase of the non-ionic surfactant octaethylene glycol monohexadecyl ether was used as an extended template for the formation of organized mesoporous silica [78]. Hydrolysis and condensation of tetramethylortosilicate (TMOS) was confined to the surface of the close packed rod-like micelles and as a consequence, a rigid monolith of the organized mesostructured material was produced by direct templating.

The transcriptive synthetic approach has also been explored in the field of biomineralization, highlighting the close relationship that exists between organized matter chemistry and biology. An organized bacterial superstructure (0.2 mm thick) consisting of coaligned 0.5 μm wide multicellular filaments of *Bacillus subtilis* (Note: this structure resembles the arrangement of surfactant cylinders in the HI liquid-crystalline phase, with the exception of an increase of length scale of 2 orders of magnitude) was used as macroscale organic template for the production of an ordered macroporous amorphous silica framework with uniform 0.5- μm -diameter channels oriented parallel to the fibre axis (Fig. 12.2) [79]. The 200 nm-wide interfilament spaces of the bacterial superstructural array represent a

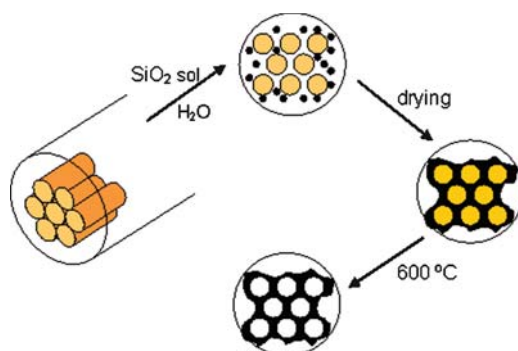


Fig. 12.2 Formation of an organized macroporous amorphous silica framework using a preorganized bacterial superstructural template. Infiltration and mineralization of the inter-filament spaces of the biological template (A), followed by drying, gives rise to a bioinorganic material (B). Removal of the organic material by controlled heating yields a macroporous replica (C). Adapted from [79]

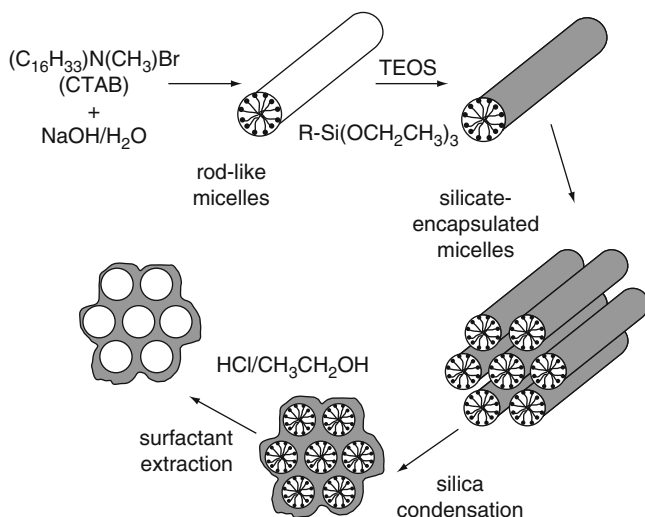


Fig. 12.3 Formation of an organized hybrid silica mesophase through synergetic synthesis (R = $-\text{C}_6\text{H}_5$, $-\text{C}_8\text{H}_{17}$ or $-\text{CH}_2\text{CHCH}_2-$). Adapted from [80]

continuum for patterned inorganic mineralization of preformed silica nanoparticles that play the role of construction units.

b) Synergetic synthesis – This strategy involves a mechanistic process in which cooperative interactions between different molecular components give rise to chemical construction of organized matter. Usually the interaction between inorganic precursors and amphiphilic organic molecules occurs in a three-step sequence:

Co-adaptation → co-assembly → replication

The synergetic synthetic approach has been explored for the development of organized covalently linked hybrid silica mesophases (Fig. 12.3) [80]. The co-condensation of siloxane (TEOS is the primary silica source) and organotrialkoxysilane precursors and their co-assembly with surfactant templates (micelles) provide a general route for the synthesis of organically functionalized, uniformly porous, ordered silica materials.

c) Integrative synthesis – This strategy is a combination of the previous two. It may be used to prepare materials with hierarchical structure and morphology in systems containing templates/directing agents having at least two different length scales.

Davis et al. [79] illustrated how supramolecular and supercellular templates can be combined for the fabrication of inorganic materials with structural hierarchy. In this study monolithic silica fibers with ordered porosity at both the meso- and micrometer scale were obtained. Preparation of the material involved coupling of the synergistic synthesis of silica-surfactant mesophases with higher order transcriptive patterning. Structural hierarchy was achieved by replacing the silica sol used in the synthesis of

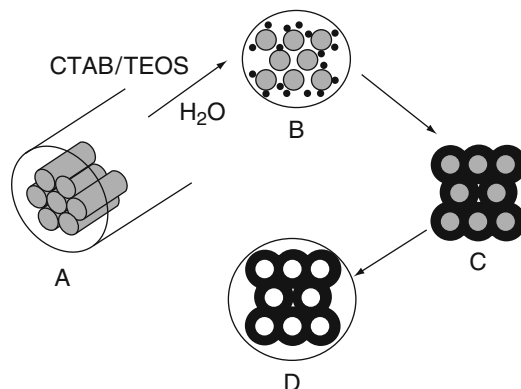


Fig. 12.4 Formation of a macroporous silica framework from a hierarchical silica-based structure using a preorganized bacterial superstructural template. Infiltration and mineralization (**B**) of the inter-filament spaces of the biological template (**A**), followed by drying, gives rise to a bioinorganic material (**C**). Removal of the organic material by controlled heating yields a macroporous replica (**D**). Adapted from [79]

the organized macroporous amorphous silica framework mentioned in subsection a) (see Fig. 12.2) by a synthesis mixture for the silica-surfactant mesophase MCM-41 (Fig. 12.4). The dried macroscopic bacterial product was infiltrated and mineralized within the interfilament spaces with the silica-surfactant mesophase. MCM-41 particles were found to be closely associated with the cell walls of the bacterial filaments. Controlled heating allowed removal of the organic material and production of a macroporous replica consisting of micrometer-size channels with walls of mesoporous silica. The organized composite was assembled by templating the mesophase on the surface of the bacterial filaments and not, as in the case of the pure silica material described above, from the consolidation of weakly associated nanoparticles within the interfilament spaces.

First reports on optical properties of hybrid photonic materials whose structure and function are organized hierarchically suggested that these solids are promising candidates for optical applications, such as lasers, light filters, sensors, solar cells, pigments, optical data storage, photocatalysis and frequency doubling devices [81].

Ordered periodic micro-, meso-, and macroporous materials allow the construction of composites incorporating many guest species, such as organic molecules, inorganic ions, semiconductor clusters and polymers. These guest/host materials combine the high stability of the inorganic host, new structure-forming mechanisms due to the confinement of guest species in well-defined pores, and a modular composition. Applications in switches, non-linear optics, and lasers might be envisaged.

²MCM-41 is a molecular sieve. Its structure is proposed to have a hexagonal stacking of uniform diameter porous tubes whose size may vary from about 15 to more than 100 Å.

Meng et al. [82] prepared a MCM-48 mesoporous material activated by the $\text{Eu}(\text{dbm})_3 \cdot 2\text{H}_2\text{O}$ complex (where dbm^- is dibenzoylmethanide) using a simple wet impregnation method. This method was also employed by Fu et al. to synthesize hybrid materials based on non-modified or APTES-modified MCM-41 doped with $\text{Eu}(\text{tta})_3 \cdot 2\text{H}_2\text{O}$ (where tta^- is thenoyltrifluoroacetate) [83]. Another example is the complexation of Eu^{3+} ions inside channels of highly ordered SBA-15 mesoporous silica containing phosphine oxide groups [84].

Covalent bonding of dye molecules to ordered or semi-ordered porous MCM-41 materials is of interest. The organic molecules can be dispersed and separated from each other, thus reducing intermolecular quenching of fluorescent features. Covalently linked chromophores might be used as sensors in separating processes to detect molecules located within the channel-like pores of thin membranes of MCM-41 materials. Moreover, as the optical characteristics of the chromophore are very sensitive to local environment, they could be used to probe the internal structure of mesostructured silicas.

Fowler et al. reported the direct synthesis of ordered mesoporous silica containing covalently linked fluorescent organic chromophore functionalities [85]. In principle it should be possible to incorporate a range of organic chromophores into surfactant-silica mesophases replicas without extensive modification of optical properties. An evaporation-induced self-assembly (EISA) procedure was used to process these mesostructured dye-functionalized silica systems as transparent films and monoliths [85]. Another interesting approach is the covalent bonding of a di-ureasil structure to the hexagonal array of one dimensional channels of MCM-41 [86]. The composites are photoluminescent displaying the intrinsic green emission of MCM-41 superposed on the blue and purplish-blue di-ureasil components [86].

Potential applications of hierarchically structured hybrid materials in ion transport devices have been recently proposed for the first time by Vallé et al. [20]. These authors demonstrated that the control of affinities between organic and inorganic components (hydrophilic/hydrophobic balance) in hybrid materials allows controlling the distribution of size scale, giving rise to tuneable functionalities and dimensional organization ranging from Å to cm. Transparent membranes hierarchically structured were obtained from *in-situ* synthesis of MCM-41 within a host polymer. The membranes have a well-defined mesostructured inorganic (hybrid) network homogeneously dispersed as submicrometre spheres in the dense transparent polymeric matrix (Fig. 12.5). To produce them, a new synthetic procedure was used, based on EISA [87] in a non-porogenic polymeric medium approach that relies on the addition of non-porogenic hydrophobic organic polymers to one-pot surfactant-templated synthesis of organosilicas to induce extra hierarchical levels. The liquid-like medium permits the materials to be processed as spin-coated thin films, membranes or solvent-cast monoliths. The *in-situ* grown-inorganic (hybrid) network is continuous and entrapped inside the polymer matrix, thus explaining the internal percolation of

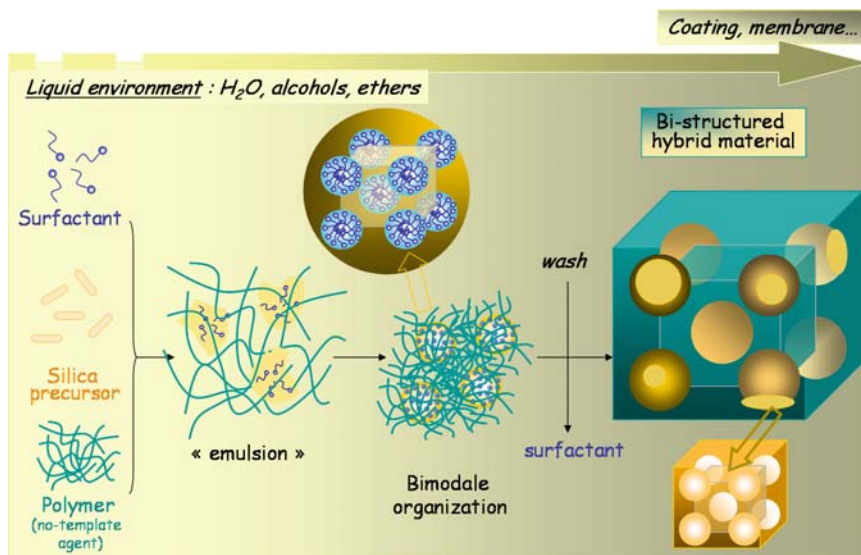


Fig. 12.5 General route of synthesis of ordered multimodal materials by using a template and polymeric environment. Reprinted from [20]

the former and the inner porosity and accessibility. Because of the resulting fast ion transport, ion-doped hierarchically-structured hybrid membranes offer high potentialities for ion transport devices. In addition to the improved mechanical properties, these membranes have high specific area and extraordinary water-uptake ability.

12.2.2.2 Route IV: Assembly of Well-defined Nanobuilding Blocks

Control of material structure can be achieved by the connection of preformed objects, such as clusters, nanoparticles or nanolayered compounds that keep their integrity in the final material. These NNBs are generally capped with polymerisable ligands or connected through organic spacers, such as telechelic molecules or polymers, or through functional dendrimers [6].

Multiscale ordering of functional colloidal particles is a powerful approach for the creation of macroscopic devices. Multiscale ordering can be performed through self-assembly. Building of such hybrid materials involves coupling of biomolecule-NBB, NBB-NBB, polymer-NBB and dendrimer-NBB systems.

Rhodes et al. described the preparation of a hierarchical zeolite material with ordered nano-, meso- and macroporosity using a novel combination of several strategies [88].

In a recent report on organic–inorganic hybrids prepared from ureapropyltriethoxysilane, methacryloxypropyltrimethoxysilane (MAPTMS) and McOH-modified ZPO precursors, used for the production of ultraviolet (UV) written low-losses planar waveguides [89], it was demonstrated that McOH acts as ZPO

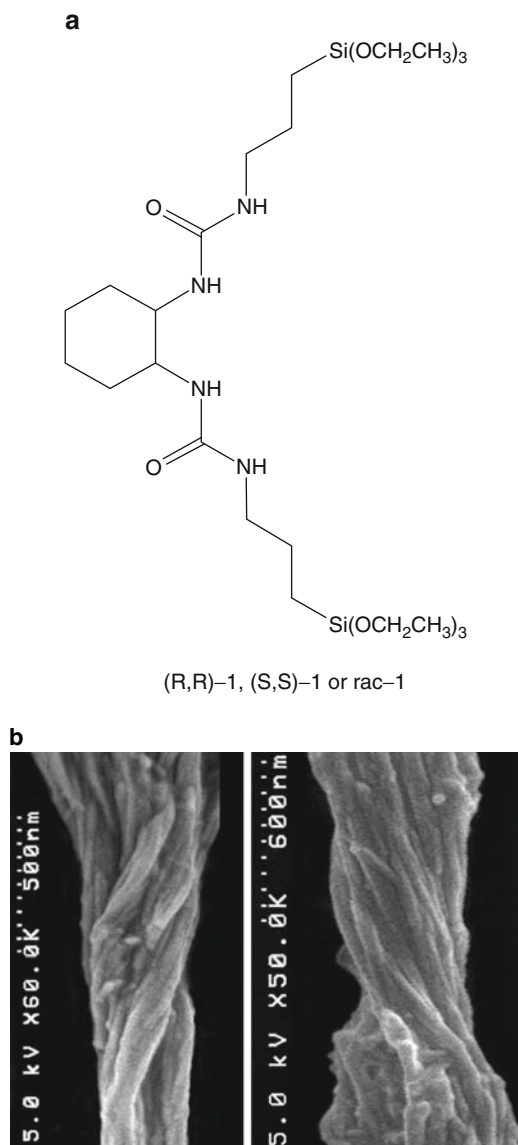


Fig. 12.6 (a) Chiral silylated diureidocyclohexyl derivative (R,R)-1, (S,S)-1, or rac-1; (b) right- or left-handed helical fibers formed from hydrolysis of the pure enantiomers (R,R)-1 or (S,S)-1; (c) ball-like structures and hollow tubular morphologies obtained, respectively, from the racemic mixture, rac-1HS, and from hydrolysis of enantiomerically pure compounds, (R,R)-1HS or (S,S)-1HS. Adapted from [18]

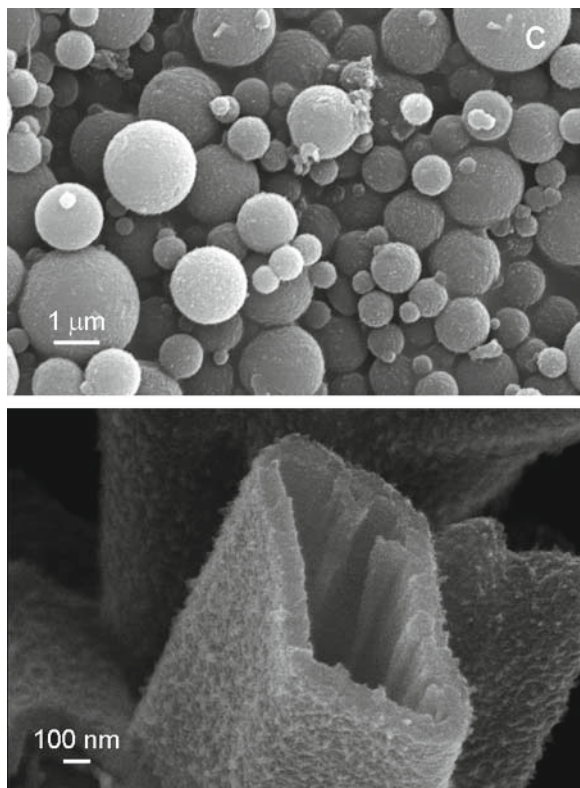


Fig. 12.6 (continued)

stabilizer, and allows UV patterning in the absence of photoinitiator. MeOH has also an impact on the local structure of the resulting hybrid, as it forms a complex with ZPO, that yields ordered nanoclusters dispersed within the hybrid host [90, 91]. These aggregates are similar to the NBBs described by Schubert et al. [92].

12.2.2.3 Route V: Self-directed Assembly

In silsesquioxane precursors $\text{RO}_3\text{-Si-R'-Si-O}_3\text{R}$ (Scheme 12.1c) and organosilanes R'-Si-X_3 (Scheme 12.1d, where $\text{X} = \text{OR}$ or Cl) self-assembly processes occur in the absence of an external template, yielding hierarchically structured ordered architectures with well defined morphologies at the macroscopic scale. Self-assembly of molecules relies on weak interactions (hydrogen bonds, hydrophobic interactions, π - π interactions) between R' groups, leading to supramolecular architectures that direct the organization of hybrid silicas under controlled hydrolysis.

Hybrids with helical morphology were created from a chiral silylated diureidocyclohexyl derivative (Fig. 12.6a) via self-directed assembly [19]. A left- or right-handed

helix was formed depending on the configuration of the organic substructure. The chirality transcription from the enantiopure precursors (Fig. 12.6a) depended on experimental conditions [18]: whereas in acidic aqueous medium right- or left-handed helical fibres formed (Fig. 12.6b) from the hydrolysis of the pure enantiomers (R,R)-1 or (S,S)-1, respectively, the hydrolysis of the racemic mixture of the precursors (rac-1) in the same medium led to a featureless granular solid. The hydrolysis of the same compounds under basic conditions yielded hollow tubular and spherical silicas (Fig. 12.6c). The tubular morphologies were obtained by means of hydrolysis of the enantiomerically pure compounds (R,R)-1 or (S,S)-1, whereas ball-like structures were obtained from the corresponding racemic mixture rac-1. The tubular shape is likely to result from the combination of two phenomena: self-association of the urea groups and self-templating of the organic crystalline precursor itself.

Self-directed assembly of lamellar-packed structures was investigated (Fig. 12.7 [24, 25] and Fig. 12.8 [23]). Long-range ordered lamellar di-urea cross-linked alkylene-bridged silsesquioxanes (Fig. 12.7a) with variable interlamellar distances were developed through a self-assembly process based on hydrogen bonding between urea groups and hydrophobic interactions between alkylene chains [18]. In these systems self-directed assembly is influenced by the synthetic procedure: while acid-catalyzed hydrolysis induced the formation of crystalline lamellar structures, F⁻-catalyzed hydrolysis yielded amorphous materials. Hybrids incorporating chains with less than 8 methylene groups were always amorphous. The materials consist of thin plates with a layered arrangement. Structural studies carried out on samples incorporating alkylene chains with variable length demonstrated that the interlamellar distances depend on the length of the organic spacer. In addition, as the number of methylene groups was increased, an increase of order resulted (Fig. 12.7b). Self-assembly was found to be influenced by the synthetic procedure chosen: acid-catalyzed hydrolysis in an excess of water induced the formation of

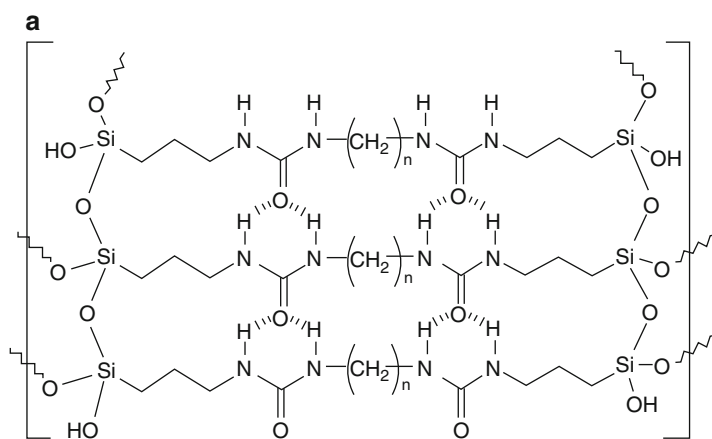


Fig. 12.7 Lamellar alkylene-bridged silsesquioxanes: (a) schematic formula; (b) TEM and SEM (c) images. Adapted from [24]

crystalline lamellar structures, whereas F⁻-catalyzed hydrolysis in ethanol, with a stoichiometric amount of water, yielded amorphous materials. If the number of methylene groups was lower/equal than/to 8, the hybrids were amorphous whatever the reaction conditions.

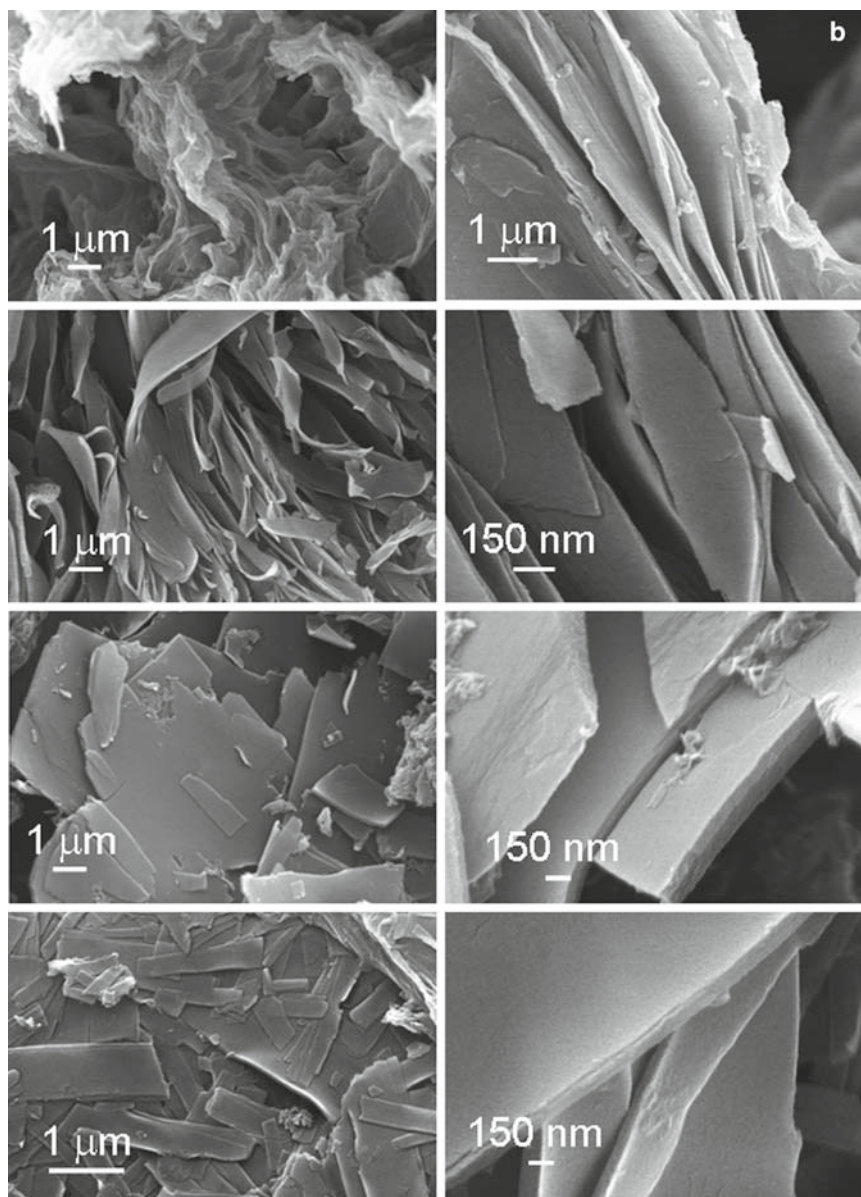


Fig. 12.7 (continued)

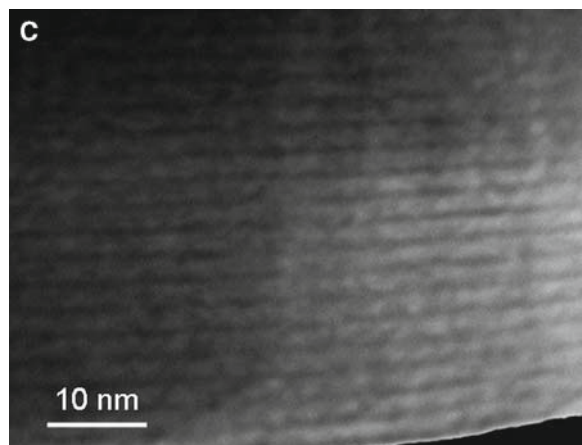


Fig. 12.7 (continued)

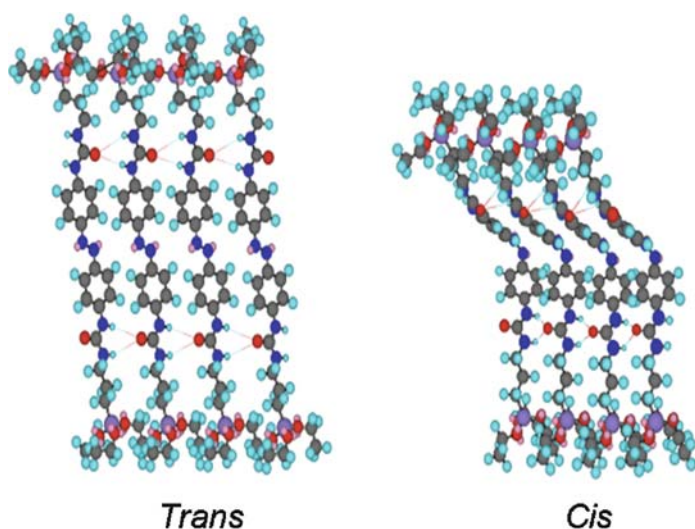


Fig. 12.8 Trans and cis forms of supramolecular structures of hybrid silicates formed by self-directed assembly from an azobenzene-bridged silsesquioxane. Reproduced from [23]

Hexagonal bidimensional structures (Fig. 12.9) [21] and ladder-type superstructures (Fig. 12.10) [28] were also produced by self-directed assembly.

Self-directed assembly of alkylenesilanes is less known. In this case, the design strategy relies on self-assembly of organophilic precursors that become amphiphilic as hydrolysis produces hydrophilic silanol groups. Alkylenesilanes adopt a bimolecular layered pattern of stacks of alkyne chains perpendicular to the layers. Examples of bilayered lamellar packing in alkylenesilanes are poly(octadecylsiloxane)s

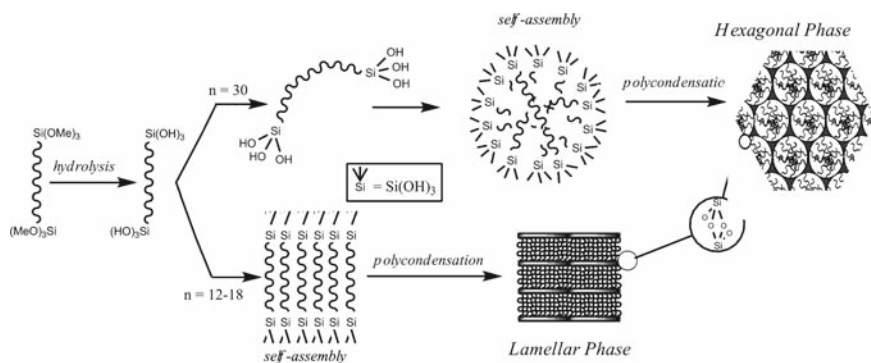


Fig. 12.9 Self-assembly of alkylene chains by hydrophobic interactions. Reproduced from [21]

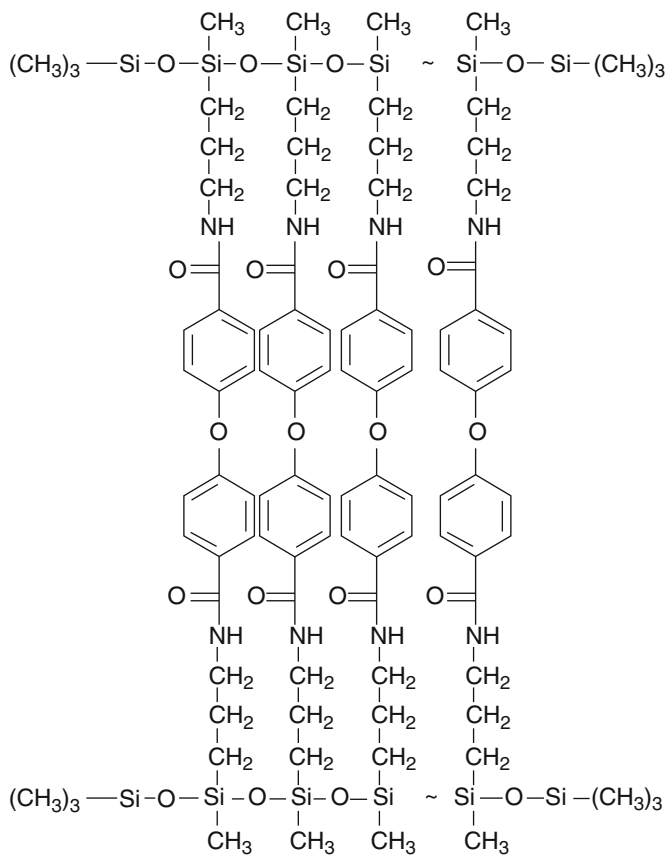


Fig. 12.10 Structure of aryl amide-bridged ladder-like polymethylsiloxane. Reproduced from [28]

[26] and hybrids synthesized from triethoxy [27]-based alkylsilanes. Hydrophobic interactions between the organic chains are the main force driving the formation of these van der Waals packing structures.

Recently we introduced a hierarchically-structured mono-amide cross-linked alkylene/siloxane hybrid where self-assembly is driven by a photoluminescent hierarchically-structured bilayer amide cross-linked alkylene/siloxane hybrid (named mono-amidosil), where self-assembly relies on: i) intermolecular hydrogen bonding between amide groups; ii) van der Waals interactions between all-*trans* alkylene chains assuming a partially interdigitated packing mode and an entropic term related to the phase separation between alkylene chains and siloxane nanodomains (Fig. 12.11) [22]. This material is the first example of a photoluminescent bilayered suprastructure displaying unique nanoscopic sensitivity. The two self-assembly forces are determinant for the emergence of a thermally-actuated optical memory effect induced by a reversible order-disorder phase transition of the alkylene chains. Recovery of emission energy is time-dependent.

12.3 Light-emitting Hybrids

12.3.1 Hybrids Lacking Metal Activator Centres

Representative photoluminescent organic–inorganic hybrids that lack metal activator centres are depicted in Fig. 12.12. Typically, they are almost transparent in most of the visible (VIS) spectral region. Their absorption edge occurs essentially from the UV to the blue spectral region as can be seen in Fig. 12.13a [55, 56, 61, 93]. The maximum of the excitation spectra (Fig. 12.13b) appears in a spectral region overlapping the absorption spectra, yet extending to longer wavelengths [31, 59, 61, 64, 93–95]. While the absorption spectrum reveals the spectral range over which the sample absorbs, independent of the occurrence (or not) of radiative transitions, the excitation spectrum corresponds to the specific region of the absorption spectrum which really contributes to the emission of light that can be observed.

When irradiated with UV light, the hybrids display a bright emission that appears white to the naked eyes, as shown in Fig. 12.13c. Such emission is characterized by a large broad band, typically Gaussian in shape, whose peak position depends on the hybrid type. For amine-based amorphous materials the hybrid emission is centred within the blue-green spectral region [22, 31, 55, 56, 58, 61, 64, 70, 93–96], whereas for bridged silsesquioxanes containing aromatic rings within their skeleton [25] the room temperature emission is deviated towards the blue [59]. Lowering the temperature down to 14 K induces minor changes in the photoluminescent features of the amine-based organic–inorganic hybrids with aliphatic organic counterparts, namely a deviation to the blue ($<1,000\text{ cm}^{-1}$) and an increase in the emission intensity (40–60%) [31, 94, 95]. However, some exceptions have been reported, in particular for those systems containing aromatic rings. Preliminary

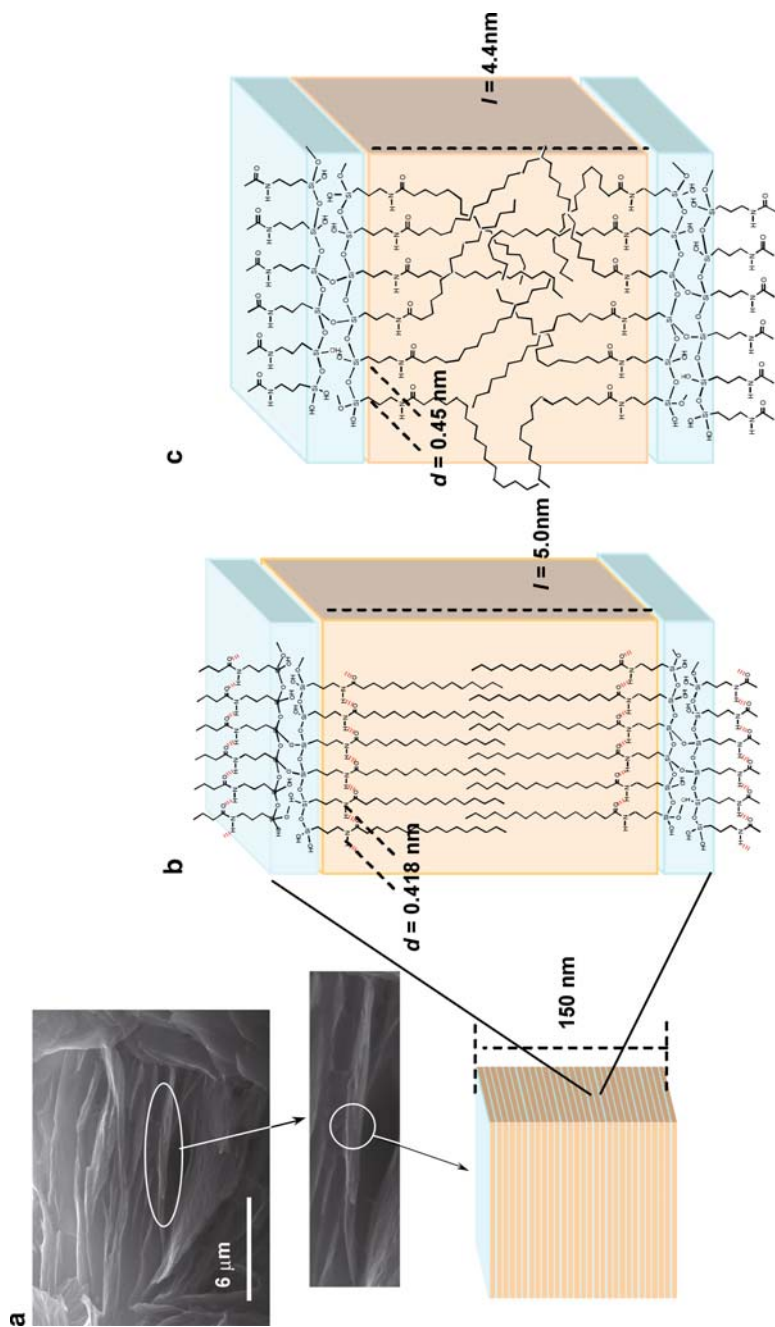


Fig. 12.11 SEM image and schematic representations of structure of mono-amidosil hybrid. (a) Lateral portion of a crystallite composed of a stack of bilayers. (b), (c) Bilayer at room temperature and at 120°C, respectively. Reprinted from [22]

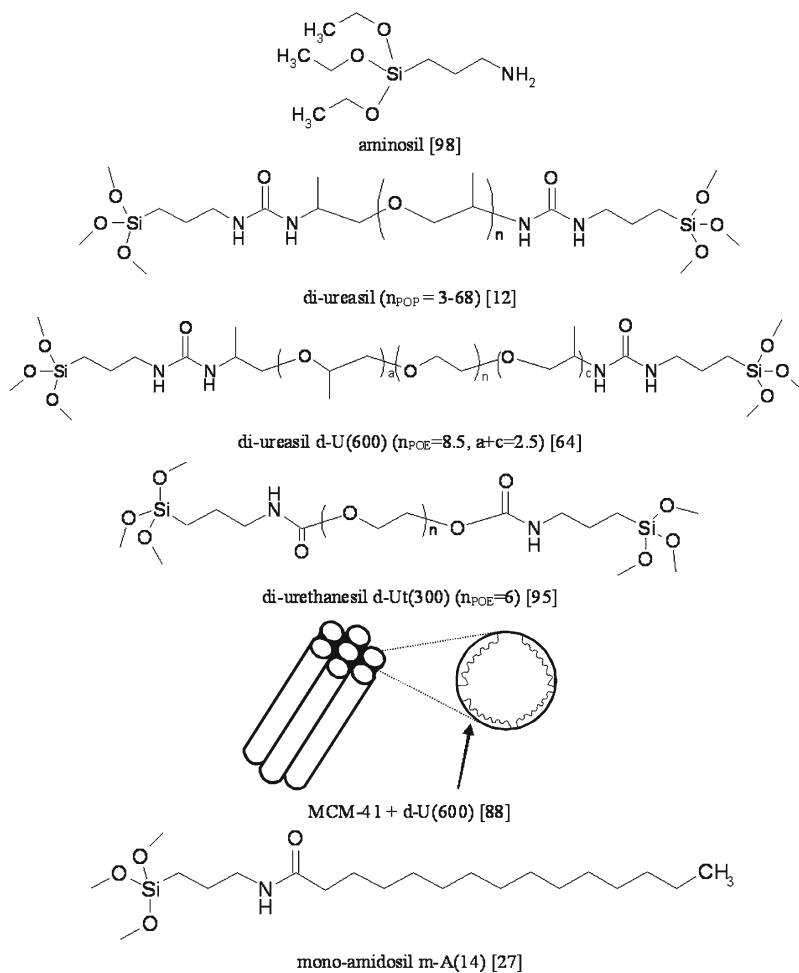


Fig. 12.12 Representative photoluminescent UV photostable organic-inorganic hybrids that lack metal activator centres

studies revealed that in the case of silsesquioxane hybrids tailored as amorphous materials, at 14 K, besides the presence of the room temperature component (Fig. 12.13), another band was observed at longer wavelengths (see Fig. 12.2 in [59]). Different behaviour of these components with respect to temperature variations was ascribed to distinct chemical origins; in particular the higher and lower energy emission bands were ascribed to the presence of the aromatic group and the urea group, respectively [59]. For amine-functionalized hybrids, in particular di-ureasils and di-urethanesils, a systematic study involving the photoluminescent features of hybrids, of non-hydrolyzed precursors and di-ureasils organic precursor (diamines)

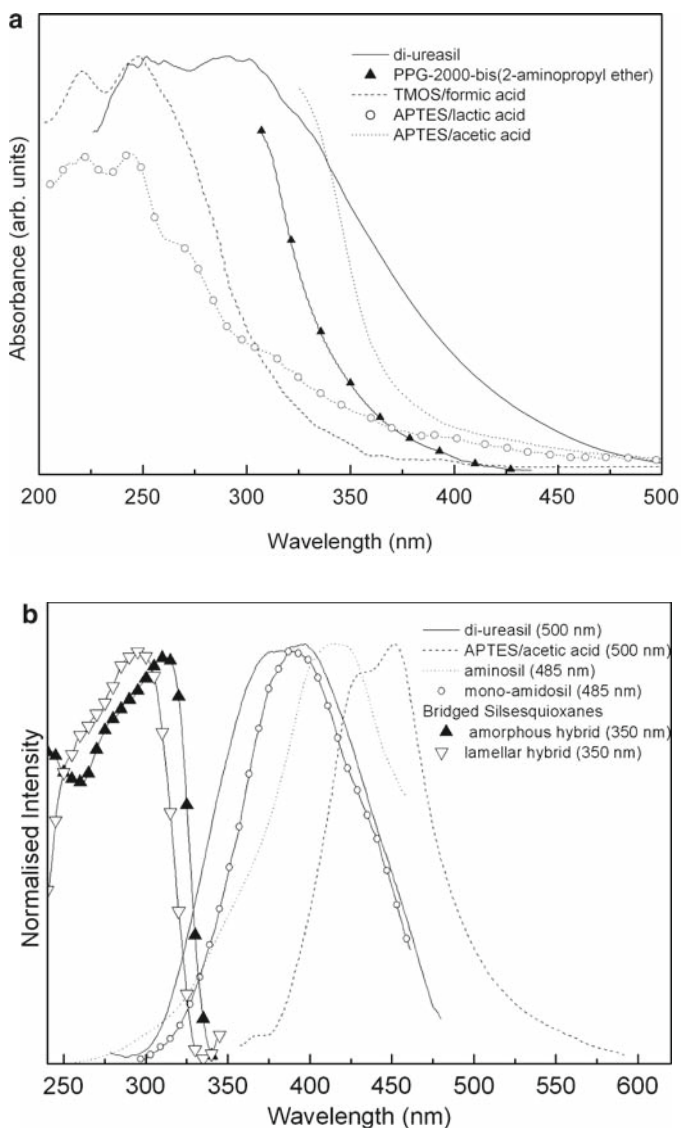


Fig. 12.13 (a) Absorption, (b) excitation, and (c) emission spectra of representative organic–inorganic hybrids. Di-ureasils [58], TMOS/formic acid and APTES/lactic acid [61]; PPG-2000-bis(2-aminopropyl ether) and APTES/acetic acid [93] Aminosil [60] Mono-amidosil [22]; Bridged Silsesquioxanes [59]

revealed that hybrids' emission results from the convolution of two distinct components, namely a higher energy one ascribed to the presence of siliceous nanodomains and a lower energy band associated with the NH/C=O groups [31, 58, 60, 94]. We will return below to the detailed chemical-physical nature of organic–inorganic hybrids intrinsic emission.

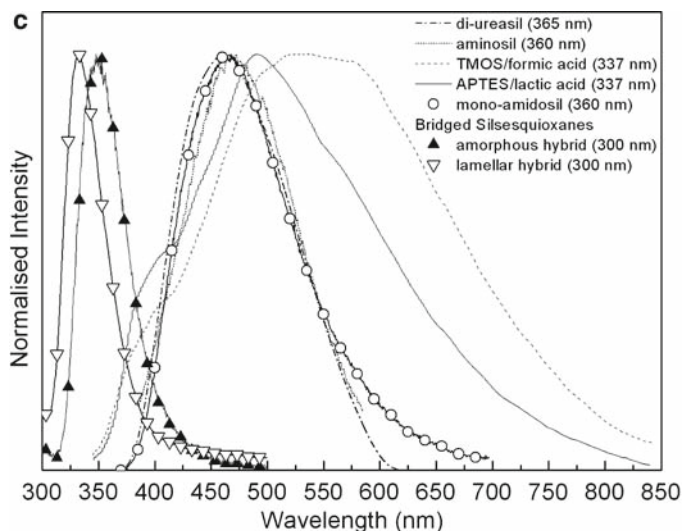


Fig. 12.13 (continued)

Another intrinsic photoluminescent property is related to the emission dependence on the excitation wavelength, in such a way that increasing the excitation wavelength results in an emission red-shift (deviation to lower energies), as illustrated in Fig. 12.14 for two representative amine-based hybrids [31, 55, 56, 58, 94, 97, 98]. The emission dependence on the excitation wavelength has not been completely understood, being often ascribed either to the different size of emitting monomers [55] or to defects occurring within siliceous domains that induce the presence of localized states [31, 97, 98]. The latter hypothesis was recently supported by the development of a model of thermal relaxation within localized states based on the extended multiple trapping framework [97, 98]. The model was simultaneously applied to classical and well known amorphous semiconductors, such as amorphous hydrogenated silicon, a-Si:H, and to the family of di-ureasil hybrids with different number of oxyethylene chains. From this model the energy gap of around 3.882 eV was estimated for di-ureasils and the density of localized states was characterized through the estimation of the β parameter (ranging between 4.36–12.08 eV⁻¹) that corresponds to the decay of the density of localized states within the gap. It should be noted that the estimated values are in good agreement with those achieved by other recombination models previously reported for classical semiconductors like a-Si:H [97]. This model was a first attempt to physically detail the emission wavelength dependence on the excitation wavelength, considering in an explicit way, the radiative and non-radiative transition mechanisms for carriers relaxing into localized states [97, 98].

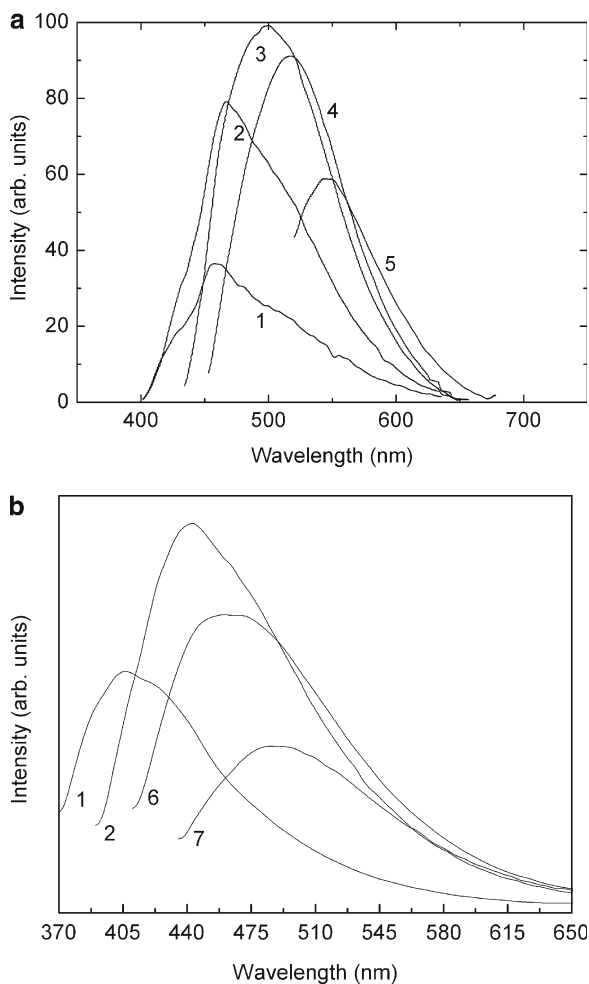


Fig. 12.14 Room-temperature emission spectra of (a) APTES-derived hybrid with acetic acid [55] and of (b) high molecular weight di-ureasil [d-U(2000)] under different excitation wavelengths, 1: 330–340 nm, 2: 375–380 nm, 3: 440 nm, 4: 470 nm, 5: 500 nm, 6: 395 nm and 7: 420 nm

12.3.1.1 Time-resolved Spectroscopy

The photoluminescent features of organic–inorganic hybrids that lack metal activator centres have also been studied by time-resolved spectroscopy, in particular time-resolved emission and by the acquisition of the emitting states decay curves, have enabled evaluation of the time-scale in which the processes behind the emission occur (dynamical evaluation). Moreover, time-resolved spectroscopy is a powerful technique allowing the unequivocal identification of different emission and excitation

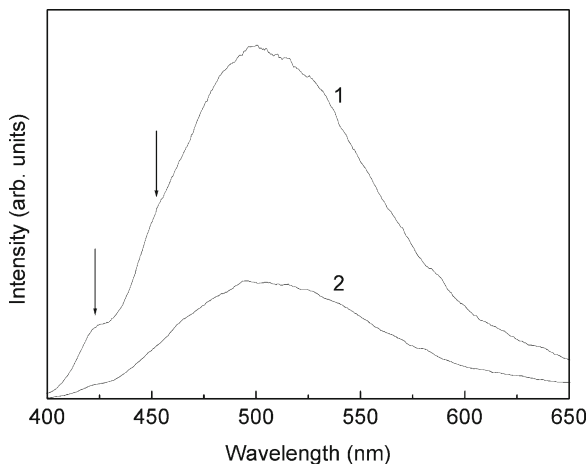


Fig. 12.15 Time-resolved emission spectra (14 K) of high molecular weight di-urethanesil [d-Ut(2000)] at an excitation wavelength of 360 nm for different starting delays, 1: 0.08 ms and 2: 5.00 ms. The spectra were acquired with an integration window of 20.00 ms

components with distinct time scales. Figure 12.15 illustrates that dynamical evolution showing an example of a time-resolved emission spectrum of an organic–inorganic hybrid belonging to the di-urethanesil class. The spectrum acquired at short delay time (0.08 ms) reveals the presence of a large broad band peaking at 500 nm, exhibiting two lower intensity peaks around 425 and 460 nm (marked with arrows in Fig. 12.15). When the starting delay is increased up to 5.00 ms, only the lower energetic peak can be discerned, thus indicating that the components at 425 and 460 nm may have the same nature, whereas the band peaking around 500 nm must have a different origin [31, 58, 60, 64, 70, 94–96].

To determine accurately the time scale behind each emission, a decay curve was monitored around the bands observed in the time-resolved spectrum for the di-ureasil hybrids [31, 58]. The shape of the decay curve depends on the starting delay, and on the monitoring wavelength. The decay curves monitored within 425 and 460 nm are approximately described by a single exponential function revealing a lifetime around 3.5 ms [31, 58], whereas the decay curves monitored within 500 nm are well reproduced by a single exponential function only for starting delays higher than 40.00 ms, yielding a lifetime value around 160 ms [31, 58]. The origin of the starting delay dependence of the decay curve has not yet been addressed in the literature.

The lifetime values were monitored as a function of the temperature, displaying different behaviours. The shorter lifetime followed a typical Arrhenius decrease for a temperature between 14 and 220 K. The longer lifetime remained approximately constant in the same temperature range [31, 58]. When increasing the temperature above 220 K, both lifetime values decreased substantially to about 10^{-8} s at room temperature [63, 99].

12.3.1.2 Emitting Centres and Recombination Mechanisms

The chemical-physical nature of the recombination centres behind the white light emission is a topic still under discussion in subject literature. Parallel efforts have been made to discuss either the chemical nature or the recombination mechanisms. This study involved the organic hybrid precursor used to prepare a di-ureasil hybrid (Jeffamine ED2001®) [31, 58, 60] and several types of amine-functionalized organic–inorganic hybrids, such as di-ureasils, di-urethanesils [31, 60] and di-amidosils [31, 95]. The discussion of the hybrid host emitting centres was extended to several types of amine-based hybrids, namely APTES-based hybrids containing carboxylic acids [61, 100] and TEOS-based hybrids containing acetylacetonate (acac^-) and ZPO [101].

The chemical origin of the emission features in the above-mentioned organic–inorganic hybrids was ascribed either to defects present in the as-prepared materials or to thermally activated ones. Evidences of the latter defects were reported for APTES-based hybrids. In particular, not only an increase in their luminescence intensity with the increase of the heat treatment temperature between 20 and 200°C was observed, but the luminescence intensity was also greater in the xerogels treated under vacuum than in hybrids treated in air [100]. These observations were interpreted as an indication that higher temperatures and vacuum conditions favour creation of oxygen-related defects [100]. Another defect type associated with thermal activated emitting centres, namely carbon impurities was proposed for sol–gel derived silica gels based on TEOS and TMOS incorporating a variety of carboxylic acids [61]. Under adequate heat treatments (at least above 520 K) a carbon impurity was created in the $-\text{O}-\text{Si}-\text{O}-$ network forming $-\text{O}-\text{C}-\text{O}-$ and/or $-\text{Si}-\text{C}-$ bonds [61].

The presence of oxygen-related defects was identified as the luminescent centres in organic–inorganic hybrids that are not subjected to any thermal treatment, such as TEOS-based hybrids incorporating acac and ZPO. Oxygen-related defects, namely $\cdot\text{O}-\text{O}-\text{Si}\equiv(\text{CO}_2)$, observed by electronic paramagnetic resonance (EPR) were also identified in di-ureasil hybrids [60, 101]. For the particular case of di-ureasils, the existence of oxygen-related defects was related to higher energy emission component.

Table 12.1 lists potential chemical defects thought to be at the origin of the respective emissions.

The identification of the recombination mechanisms was performed with the help of experimental data, namely the emission intensity dependence on the excitation power [31, 60, 95]. The emission intensity, I , depends on the excitation power, L , according to the power law $I \propto L^k$. When $1 < k < 2$ we are in the presence of exciton-like transitions; $k \leq 1$ is characteristic of free-to-bound and donor-acceptor ($D-A$) pairs [102, 103]. Deviations from this behaviour were observed either when variations of L extended over more than two orders of magnitude or when the selected excitation energy was resonant with the semiconductor band gap [102]. This is a procedure commonly used for classical semiconductors.

Table 12.1 Major optically-active defects observed in organic–inorganic hybrids and identified as the possible chemical origin of the photoluminescent features. The corresponding EPR signal is also indicated for two particular cases

Hybrid	Possible Defect
di-ureasil [40]	$\bullet\text{O}-\text{O}-\text{Si}\equiv(\text{CO}_2)$ EPR signal: $(g\parallel) = 2.035 \pm 0.007$; $(g\perp) = 2.018 \pm 0.007$ $\text{NH}_2^+/\text{NH}^-$
TEOS and methyltriethoxysilane with acac and ZPO [47]	$\equiv\text{Si}-\text{O}-\text{O}-\text{Si}\equiv$ or O_2^- EPR signal ($g=2.033$, under irradiation of 365nm)
APTES, TEOS and acetic acid (heat treatment 20–250 °C) [98]	$\text{NH}_3^+/\text{CH}_3\text{COO}^-$
TEOS and TMOS with carboxylic acids (heat treatment > 400 °C) [93]	thermal decomposition of the carboxylic acid, carbon impurity $\text{O}-\text{C}-\text{O}$ and/or $-\text{Si}-\text{C}-$

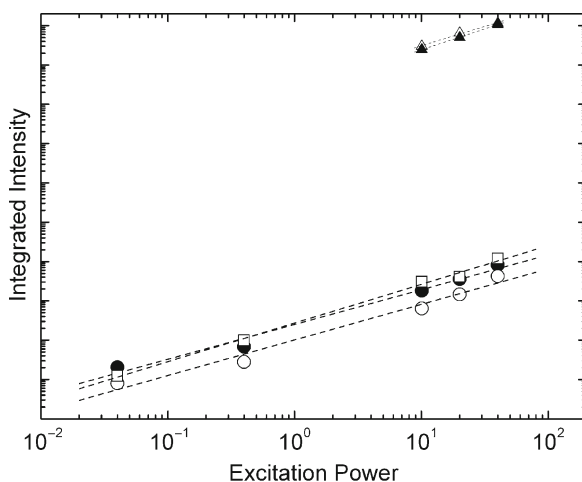


Fig. 12.16 Room temperature integrated intensity of d-U(2000) (*circles*) and d-A(8) di-amidosil (*triangles*) emission components, blue (*open symbols*) and purplish-blue (*solid symbols*) bands, and of the Jeffamine ED-2001® (*squares*) excited with an He-Cd laser (325 nm) at different power excitation. Dashed line corresponds to the data linear fit ($R > 0.99$)

Figure 12.16 represents the integrated intensity versus the incident power reported for the Jeffamine ED2001® and several organic–inorganic hybrids as well. For all the hybrids and the diamine, and for the two emission components, I depends sublinearly ($k \leq 1$) on L , pointing out that the recombinations mechanisms are mediated by $D-A$ pairs. Further arguments concerning the presence of $D-A$ pairs were found by combining steady-state and time-resolved emission - in particular

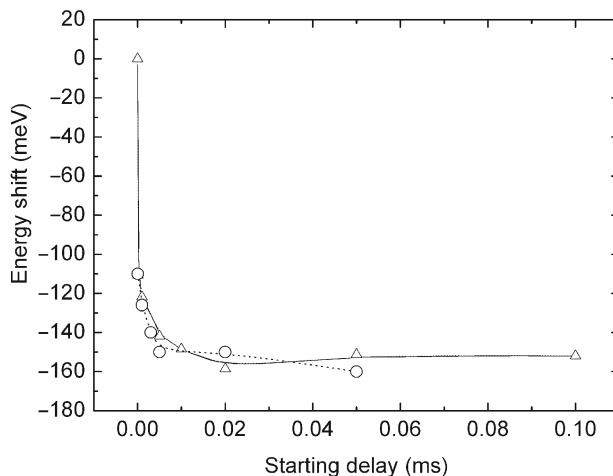


Fig. 12.17 Blue band peak position of the 14 K time-resolved spectra of d-U(2000) (*circles*) and d-A(8) (*triangles*), excited at 375 nm, measured for a fixed acquisition window of 10.00 ms and different starting delay times. Dashed lines are visual guides

the energy dependence on the starting delay. For longer delay times, a red shift in the spectrum is expected because distant pairs have smaller recombination probability. The respective energy levels therefore have larger lifetimes, a situation that is favoured with increasing delay time. As a consequence, recombination takes place at lower energies [104, 105].

Figure 12.17 depicts the energy shift (ΔE) between the energy at the maximum intensity of the time-resolved spectra, measured for starting delays between 5×10^{-5} and 0.1 s, and the corresponding value detected under continuous excitation for NH/C=O related emission. This emission shifts toward the red at smaller starting delays, being constant for starting delays around 10^{-2} s, whereas for the siliceous nanodomains the emission energy is independent of the starting delay [31, 60, 95]. The decrease of emission energy with increasing starting delay is consistent with *D-A* pair recombinations. With respect to the purplish-blue band, the results are restricted to a shorter time range because this emission occurs in a time scale, two orders of magnitude lower than the urea/urethane/amido-band recombination processes (not shown) [31, 60, 95]. Therefore, it was not possible to access corresponding phenomena observed for the other component. In fact, the emission energy does not vary within this starting delay interval, and thus may not controvert the *D-A* pair recombination mechanism [31, 60, 95, 103]. In fact, a similar behaviour was already reported for silicon nanocrystals, for which the room-temperature time-resolved spectra remained unchanged as the starting delay increased from 0 to 5×10^{-5} s, in spite of the fact that the emission intensity presented a sublinear excitation power dependence (indicating the presence of *D-A* pairs) [103].

12.3.1.3 Emission Colour Coordinates and Quantum Yield

The emission features of organic–inorganic hybrids were quantified through the estimation of their emission colours and quantum yields. Figure 12.18 depicts a CIE chromaticity diagram where emission colour of selected organic–inorganic hybrids is represented. The selected excitation wavelength corresponds to the one that maximizes emission intensity. Typically, emission colour coordinates range from the purplish/blue (bridged silsesquioxanes) to the green (APTES/acetic acid) spectral regions. Emission colour of the remaining hybrids lies in the blue region

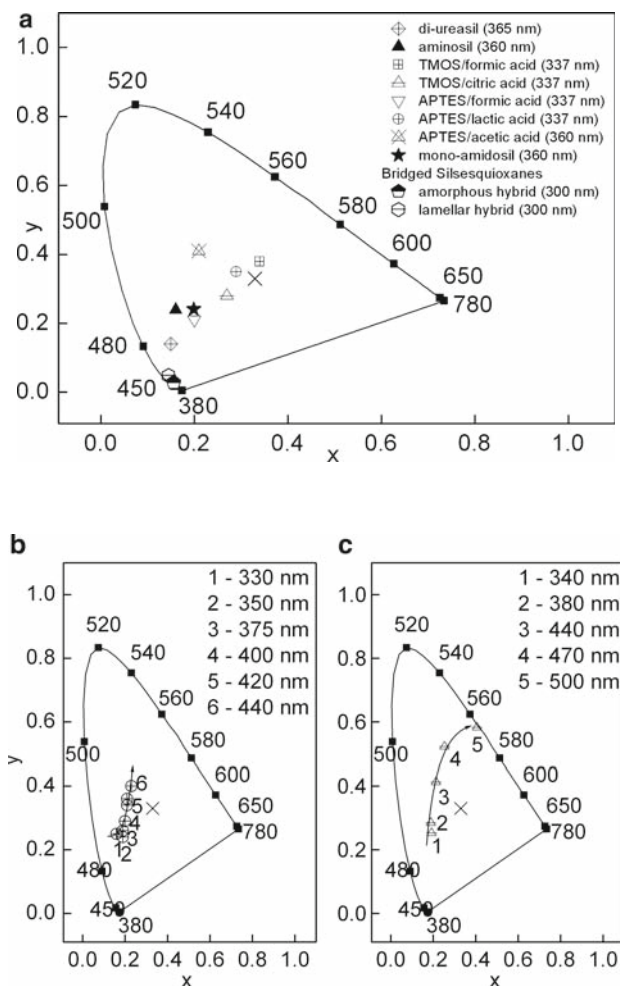


Fig. 12.18 CIE colour coordinates represented on the (x, y) diagram proposed in 1931 for (a) emission of representative organic–inorganic hybrids. Excitation wavelength is indicated in parenthesis; (b) d-U (2000) and (c) APTES-derived hybrid with acetic acid [55] under excitation wavelengths in the range 330–440 nm and 340–500 nm, respectively

Table 12.2 Colour coordinates (x , y), purity and quantum yields of emission of several representative organic–inorganic hybrids. The (x , y) coordinates were calculated according to CIE using a 2° standard observer

Hybrid	Excitation Wavelength (nm)	Colour coordinates		Purity (%)	Quantum Yield (%)	
		X	Y			
Di-ureasil [36,40,82]	365	0.15	0.14	78	6-20 ±2	
Aminosil [93]	360	0.16	0.24	65	*	
TMOS/formic acid [93]	337	0.34	0.38	20	*	
TMOS/citric acid [93]	337	0.27	0.27	25	*	
APTES/formic acid [93]	337	0.20	0.21	57	35 ±1	
APTES/lactic acid [93]	337	0.29	0.35	13	*	
APTES/acetic acid [12]	360	0.21	0.41	38	12-21 ±2	
Mono-amidosil [26]	360	0.20	0.24	50	3 ±1	
Bridged Silesquioxanes [38]	Lamellar	300	0.15	0.05	98	*
	Amorphous		0.16	0.03	98	*

*Not reported.

close to the white region (centre of the diagram marked with a cross symbol). CIE (x , y) coordinates are gathered in Table 12.2. Emission colour of the hybrids has low purity, except in the case of the bridged silesquioxanes whose (x , y) coordinates are closer to that of the well-known blue standard ZnS:Ag.

There are a few reports dealing with the determination of the absolute emission quantum yields in siloxane-based organic–inorganic hybrids. For powder samples the emission quantum yield, q_x , defined as the ratio between the number of emitted photons and the number of absorbed ones, is measured by the techniques described by Wrighton et al. [106] and by Brill et al. [107]. In this latter case, q_x is defined as:

$$q_x = \left(\frac{1 - r_{st}}{1 - r_x} \right) \left(\frac{\Delta\Phi_x}{\Delta\Phi_{st}} \right) q_{st}, \quad (12.1)$$

where r_{st} and r_x are proportions of exciting radiation reflected by the standard phosphor and by the sample, respectively, and q_{st} is the quantum yield of the standard phosphor. The terms $\Delta\Phi_{st}$ and $\Delta\Phi_x$ give the integrated photon flux (photons·s⁻¹) for the standard phosphor (sodium salicylate), and the sample, respectively. The values of r_{st} , r_x , $\Delta\Phi_{st}$ and $\Delta\Phi_x$ must be obtained for the same excitation wavelength, geometry and experimental conditions. In order to have absolute r values, barium sulfate (BaSO₄) is used as reflectance standard ($r = 0.91\%$) [108]. A detailed description of this method has been presented elsewhere [109, 110].

Wrighton et al. [106] define emission quantum yield as:

$$q_x = \frac{A}{R_s - R_H}, \quad (12.2)$$

where A is the area under the sample's emission spectrum and R_s and R_H are the diffuse reflectance of the reflecting standard (designated as white standard) and the

sample, respectively; a detailed description of this method has been presented elsewhere [106]. Experimental errors in the quantum yields values associated with this technique (within 20%) are larger than those obtained using the method of Brill et al. (~10%) [110].

The APTES-formic acid hybrid is one of the most efficient phosphors known amongst those not containing activator metal ions, with a quantum yield value of $35 \pm 1\%$ [61]. The APTES-acetic acid analogue exhibits two distinct emissions with quantum yields between 12 and 20% [55, 56] and similar values were reported for di-ureasils [31, 58, 60, 63, 94], di-urethanesils [31, 58, 60] and di-amidosils [95]. The lower value found for the mono-amidosil hybrid ($3 \pm 1\%$) was attributed to the presence of strong hydrogen-bonded amide-amide arrays that render difficult the photo-induced transfer between NH-based defects [22]. Table 12.2 lists the quantum yield values reported for several representative organic–inorganic hybrids lacking metal activator centres.

12.3.2 Hybrids Incorporating Optically Active Centres

12.3.2.1 Organic Dyes

Sol–gel derived dyes containing transparent matrices are an alternative to traditional liquid phase dye lasers since these gels are prepared under mild temperature conditions and they can be easily enriched with laser dyes without damaging them. Moreover, as the solubility of most dyes is limited in pure silica matrices, intensive efforts have been made in the last decade to synthesize dyes containing organic–inorganic hybrids [65, 66, 111–114]. Figure 12.19 depicts a few representative examples. Sensors, dye lasers, photochromic, non-linear optical and photovoltaic devices are among the possible applications for these materials [33–35].

Concerning laser emission, Avnir et al. [111] were the first to propose sol–gel derived glasses for the incorporation of laser dyes. After this first proposal, several other papers have appeared in literature showing laser action in dye containing organic–inorganic hybrids, such as rhodamine 6G doped-titania containing ormosils [112] and coumarin-153 (C-153) incorporated into transparent di-ureasils [65] (Fig. 12.19). The other two examples are samples obtained from a methyl-modified alkoxide incorporated rhodamine B and perylene red (laser emission using a stable planoconcave linear cavity) [114] and the distributed feedback laser effect observed in thin films of di-ureasil with MeOH modified ZPO containing rhodamine 6G [66]. Planar waveguides emitting in the infrared region up to 1.3 μm have been also reported through the successful doping of hybrid zirconia-based thin films with dye molecules (IR5 and IR1051) [113].

The development of dye containing organic–inorganic mesostructured hybrids has led to a number of advanced optical applications, such as optical switches and sensors and low-threshold waveguide microlasers [85, 115–117], with potential for fabrication of integrated optical circuits. For instance, waveguiding was enabled by

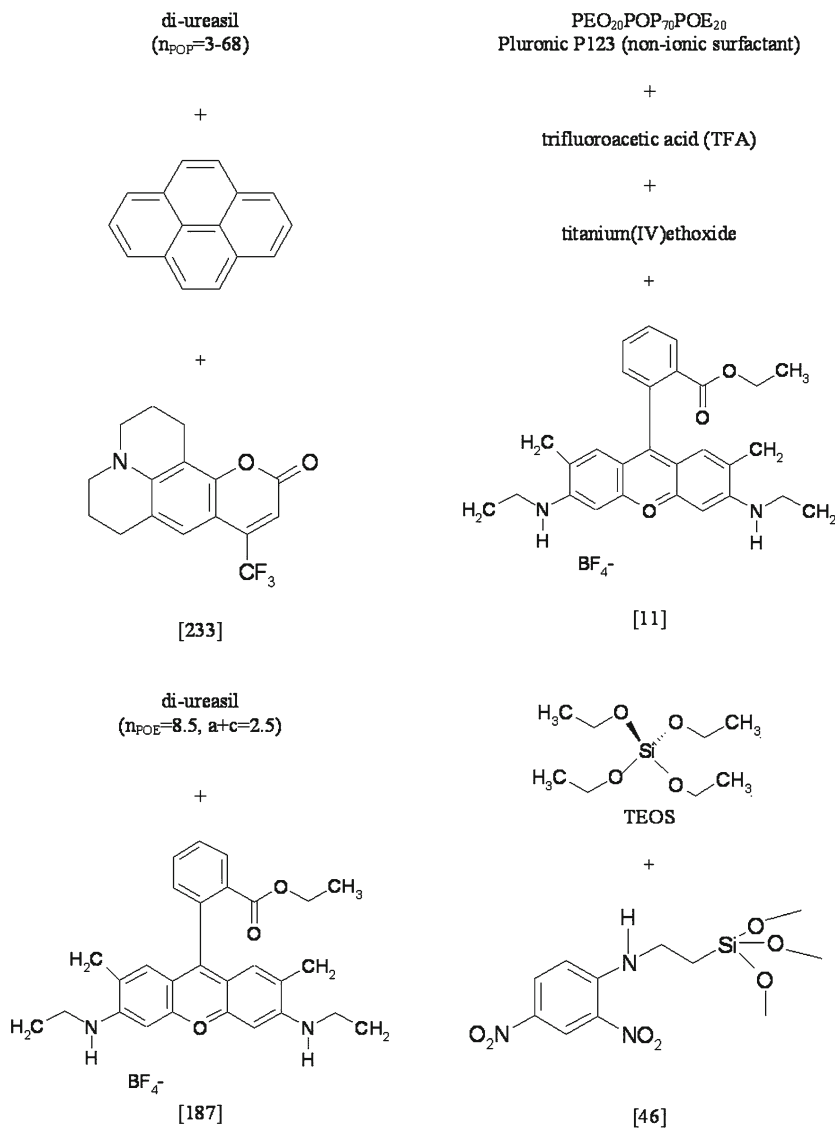


Fig. 12.19 Representative organized and non-organized organic–inorganic hybrids doped with dyes

the use of a low-refractive index (1.15) mesoporous silica thin film support incorporating rhodamine 6G. Amplified spontaneous emission with a low pumping threshold of 10 kW cm^2 was reported [115]. Additional examples of waveguides include optically transparent titania mesostructured organic–inorganic hybrids [84, 117] (Fig. 12.19). These materials have all the desired properties of their silica analogues, including nanoscopic domain separation and, with the important added

advantage of a higher refractive index (which makes possible planar waveguiding via one-step deposition onto simple glass substrates) [117].

12.3.2.2 Lanthanide Ions

The direct photoexcitation of lanthanide ions is not very efficient due to the ions' poor ability to absorb light, a consequence of the forbidden nature of the f-f transitions (Laporte's selection rule) [118, 119]. This can be overcome by using energy transfer from organic chromophores (for example) to lanthanide ions. Energy absorbed by such chromophores can be transferred to nearby lanthanide ions, which in turn undergo the corresponding radiative emitting process (the so-called sensitization of lanthanide luminescence or "antenna effect" [120, 121]). Lanthanide ions can form complexes with various organic molecules, such as β -diketones, aromatic carboxylic acids, and heterocyclic ligands, and these materials are of great interest for a wide range of photonic applications such as tuneable lasers, amplifiers for optical communications, components of the emitter layers in multilayer organic light emitting diodes (OLEDs) and efficient light conversion molecular devices (LCMDs) [108, 120–130]. In particular, these LCMDs have found a series of useful applications, such as luminescent labels in advanced time-resolved fluoroimmunoassays, light concentrators for photovoltaic devices and antennae in photosensitive bioinorganic compounds [108].

In spite of the fact that lanthanide complexes are characterized by highly efficient light emission under UV excitation (some of them even exhibit laser action in solution [131–133]), their low thermal and photochemical stability and poor mechanical properties are severe disadvantages that limit their technological applicability as tuneable solid-state lasers or phosphor devices. Moreover, most of those complexes are usually isolated as hydrates in which two or three water molecules are included in the first coordination sphere of the central ion, which quench emission due to activation of non-radiative decay paths [108, 128–130].

Among these generally undesirable properties, another serious drawback is the degradation of most of the lanthanide-based complexes under prolonged (in certain cases, only a few hours) UV irradiation (which decreases luminescence intensity). A typical example is the family of lanthanide β -diketonate chelates [75, 134–140]. While the origin of such degradation has not been yet completely understood, it is often attributed to photobleaching. The phenomenon of photobleaching (also commonly referred to as fading) occurs when the efficiency of the emission decreases due to photon-induced chemical damage and covalent modification of the complex. This mechanism can be used to assign the degree of photostability of the complex, and it has been used to develop lanthanide-thin-film based dosimeters with high sensitivity and selectivity to the three main UV regions related to skin damage effects: UV-A (365 nm), UV-B (315 nm), UV-C (290 nm) [135, 136].

One of the strategies adopted in the last few years to simultaneously improve thermal stability, mechanical features and light emission properties of lanthanide complexes is their encapsulation into sol-gel derived organic-inorganic hybrids

(particularly siloxane-based ones) through simple embedding of the complexes within the sol–gel matrix, or through the use of complexing ligands covalently grafted in-situ to the hybrid skeleton (see the examples given in Fig. 12.20). Generally, embedding of the salts and complexes gives rise to hybrid materials where one of the components is entrapped within a network of the other constituent (Class I hybrids). Despite the number of Class I organic–inorganic frameworks based on silica (SiO_2), alumina (Al_2O_3) or mixtures of SiO_2 and titania ($\text{SiO}_2/\text{TiO}_2$) or SiO_2 and zirconia ($\text{SiO}_2/\text{ZrO}_2$) [39, 139, 141–156] initially proposed, more recently research efforts have been concentrated essentially on Class II hybrid materials [57, 67–69, 72–75, 99, 157–171, 171–197].

The major interest of this approach is the possibility of preparing multifunctional nanoscale hybrid materials with tuneable design and suitable photonic features using the processing advantages of sol–gel matrices discussed in the introduction (e.g., flexible and versatile shaping and patterning, good mechanical integrity and excellent optical quality). Furthermore, this encapsulation into organic–inorganic hybrids may also contribute to decrease the rapid degradation of the complexes under UV exposure and promote efficient energy transfer between the hybrid host and the metal centre.

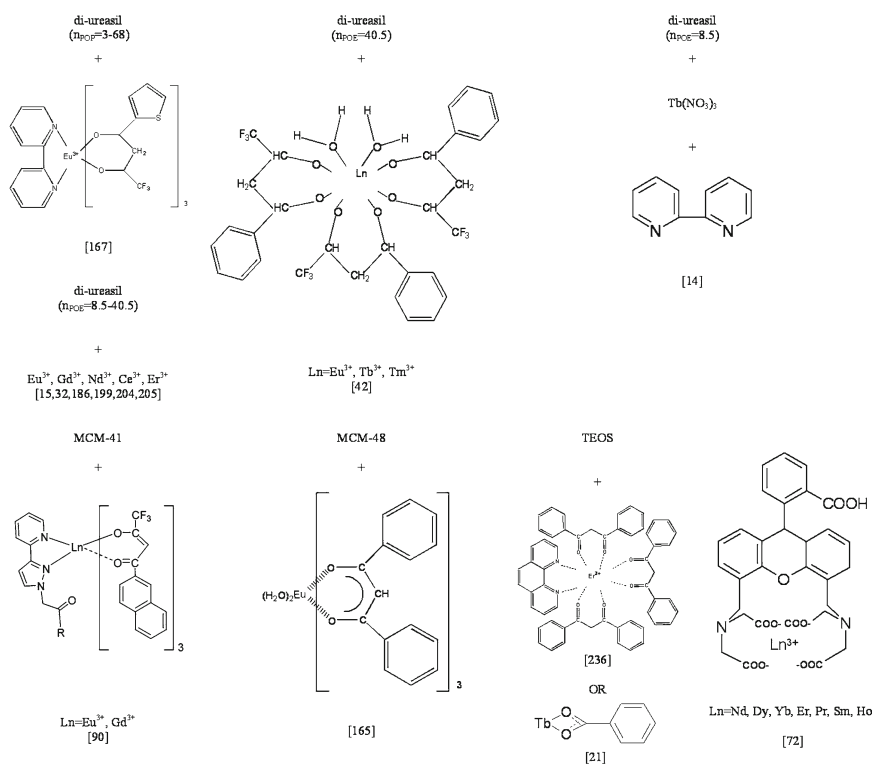


Fig. 12.20 Representative lanthanide-based organic–inorganic class I and class II hybrids

These organic–inorganic hybrids exhibit improved luminescent properties, with respect to the simple incorporation of lanthanide ions in silica-based matrices (see e.g., [164, 165]), essentially due to the following factors:

- Better dispersion of incorporated lanthanide ions within the matrix, avoiding clustering and allowing larger concentrations of emitting centres;
- Protection of the central lanthanide ions by the ligands, circumventing the quenching of the emission originating from residual water, Si-OH groups and dopant clustering [148, 198–201] and thus decreasing the non-radiative decay pathways;
- Encapsulation of metal ions by light-absorbing ligand-cage type structures which can give rise to efficient hybrid host-to-ligand-to metal and/or host-to-metal energy transfer.

Figure 12.20 depicts a few representative lanthanide-based organic–inorganic class I and class II hybrids.

Typically organic–inorganic hybrids are almost transparent in most of the visible spectral region. Maximum absorption occurs essentially from the UV to the blue spectral region. Due to the very low absorption cross-section of the Laporte forbidden f-f transitions, the absorption spectra of lanthanide-based hybrids are typically dominated by hybrid host and/or ligand absorption bands [165, 170, 172]. An illustrative example is seen in Fig. 12.21 which displays the absorption spectrum of the [Nd(calc45)]-doped silica-PEG hybrid (calc45 stands for 4',5'-bis-[N,N-bis(carboxymethyl)aminomethyl]fluorescein) [172] where the $\text{Nd}^{3+4}\text{G}_{5/2} \rightarrow {}^4\text{I}_{9/2}$ transition is indicated by the arrow.

For most hybrids the maximum of the excitation spectrum appears red-shifted relatively to that of the absorption spectrum (see e.g., [158, 165, 170]). This indicates that only the lower energy side of the absorption spectra is converted into efficient

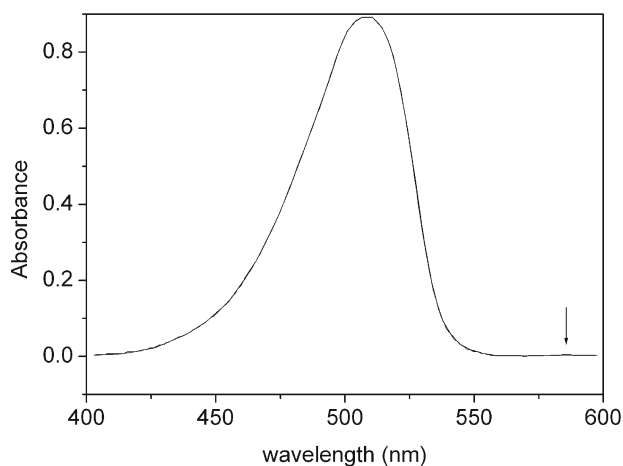


Fig. 12.21 Absorption spectrum of the [Nd(calc45)]-doped silica-PEG hybrid. Reprinted from [172]

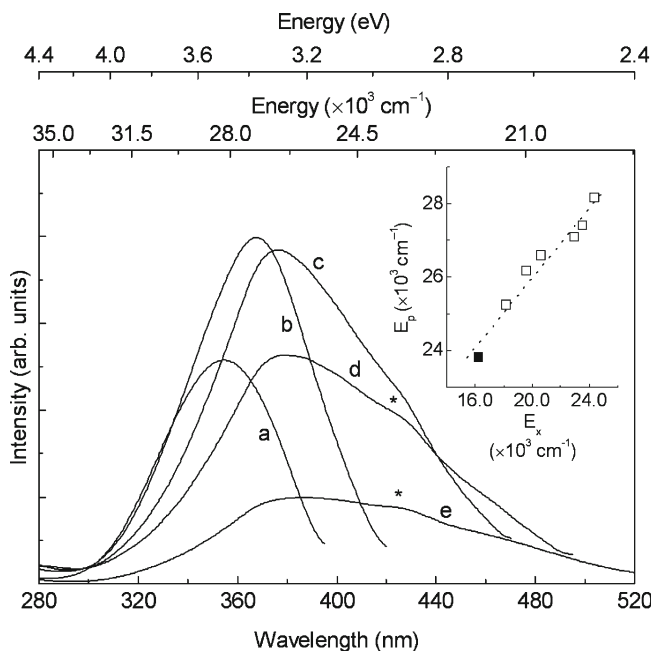


Fig. 12.22 Room temperature excitation spectra for d-U(2000) doped with $\text{Eu}(\text{CF}_3\text{SO}_3)_3$ monitored at different detection wavelengths: (a) 410 nm, (b) 435 nm, (c) 485 nm, (d) 510 nm, and (e) 550 nm. Inset shows the excitation maximum intensity position versus respective detection energy along the hybrid host emission band. *Solid square* represents excitation of the hybrids backbone detected around the strongest ${}^7\text{F}_2$ line, 616 nm. *Solid line* corresponds to data linear fit ($r > 0.99$). Reprinted from [73]

radiative emission. For lanthanide-based hybrids displaying emission arising from the hybrid host and/or ligand levels, the excitation spectra are strongly dependent on the detection wavelength. In these cases, a clear identification of the different components present in the spectra requires an independent discussion of the spectra monitored around the metal ion emission lines and along the hybrid host (or ligand levels) emission band [73, 99, 188]. Figure 12.22 presents an illustrative example of the excitation spectra for a Eu^{3+} -based di-ureasil monitored at detection wavelengths covering the hybrids' host emitting region (410–550 nm). With the increase of the detection wavelength the maximum intensity energy position shifts towards the red, and its full width at half maximum (FWHM) increases from 3,000 to 6,000 cm^{-1} [73]. When the detection wavelength is greater than 435 nm, a second band peaking around 420 nm is also discerned (marked with an asterisk in Fig. 12.22). As the detection wavelength increases, its relative intensity with respect to the spectrum maximum intensity increases and its peak position remains approximately independent of the monitoring wavelength, in contrast to what was observed for the maximum intensity energy position (E_p) that increases with the excitation energy (E_x) (inset of Fig. 12.22). These two components were already detected in the

excitation spectra of the non-doped di-ureasil host [31, 60, 94, 96], the less energetic band being assigned to the preferential excitation of the NH groups' D-A pairs and the more energetic one being attributed to the preferential excitation of the siliceous nanodomains [31, 60].

The excitation spectra for the Eu^{3+} -based di-ureasils monitored around the $^5\text{D}_0 \rightarrow ^7\text{F}_{2,4}$ transitions display two broad bands (centred at ~ 350 nm and 500 nm, the latter being most evident in the hybrids incorporating high molecular weight polymer chains) overlapped by a series of intra-4f⁶ lines [31, 73]). The high-energy band was assigned to ligand-to-metal charge transfer states, resulting from the interaction between the lanthanide ion and the first ligands [178], whereas the other band was ascribed to the excitation of the hybrid host emitting centres [73]. The relative intensity of the high-energy band strongly depends on the average polymer molecular weight of the polymer chains in accordance with the changes on the Eu^{3+} local coordination in the di-ureasils [67, 73, 178].

For organic–inorganic hybrids encapsulating rare-earth organic complexes such as β -diketonates, the excitation spectra monitored around the metal emission lines are composed of a large broad band in the UV/VIS region, ascribed to the superposition of ligand and hybrid host excitation, and some of the intra-4f transitions. The relative low intensity of the intra-4f transitions with respect to that band indicates an effective ligand-to-metal energy transfer mechanism. The complexes are encapsulated within the organic–inorganic matrix through either simple embedding [39, 139, 141–153], using ligands covalently grafted to the framework [99, 141, 157–174, 196, 202] or, in alternative, lanthanide ions anchoring to specific functional groups of the hybrid matrix [68, 75, 186, 187, 193]. As examples, we can refer to the excitation spectra of the Eu^{3+} -based hybrids prepared by Franville et al monitored around the cation most intense transition (Fig. 12.23) [159]. The spectra are mainly formed by a large broad band in the UV spectral region, 294–370 nm, resulting from $\text{S}_0 \rightarrow \text{S}_1$

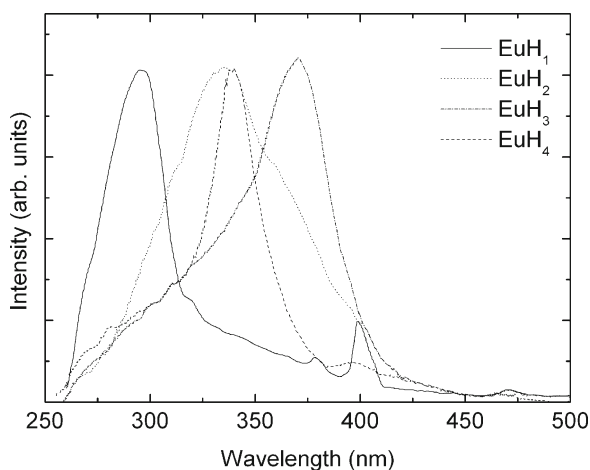


Fig. 12.23 Room temperature excitation spectra monitored around 616.0 nm for the EuH_i ($i = 1-4$) hybrid materials. Reprinted from [159]

absorption within the chromophore ligand, indicative of an efficient sensitizing of the luminescent centres by the organic ligands. Binnemans et al [171] and Sun et al [168, 169] reached essentially the same conclusion with respect to the excitation spectrum of Eu^{3+} - and $\text{Nd}^{3+}/\text{Yb}^{3+}/\text{Er}^{3+}$ - based hybrids, respectively.

Figure 12.24 displays the emission spectra of some organic–inorganic hybrids doped with Eu^{3+} -, Tb^{3+} -, Nd^{3+} - and Er^{3+} -based complexes that are representative of the structures depicted in Fig. 12.20. The spectra display a series of intra- $4f^N$ lines between energy levels schematically presented in Fig. 12.24. There is no emission either from the hybrid host or the ligand excited states, indicating efficient energy conversion from the hybrid emitting levels to the ligands and/or lanthanide ions.

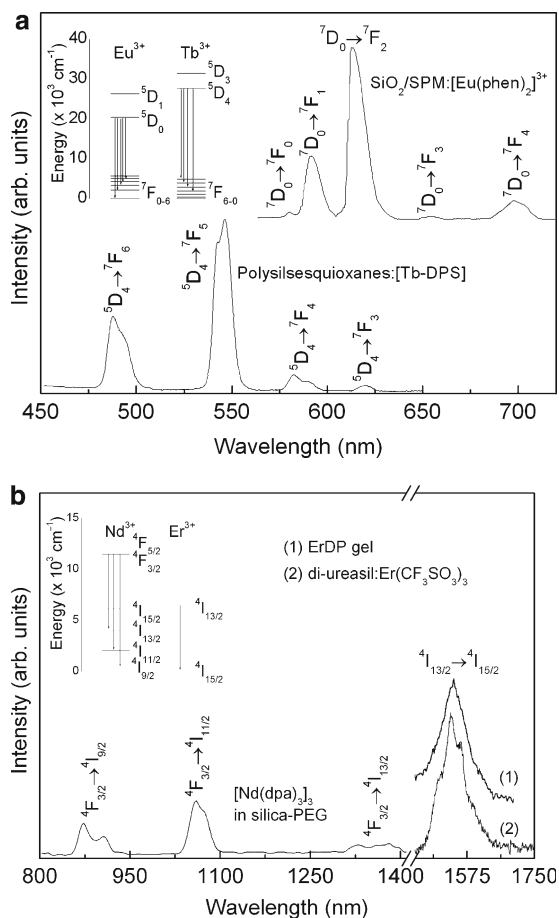


Fig. 12.24 Room-temperature emission spectra of (a) $\text{SiO}_2/\text{SPM}:[\text{Eu}(\text{phen})_2]^{3+}$ (SPM=tri(methoxysilyl)propyl-methacrylate and phen=1,10-phenanthroline), Polysilsesquioxane:[Tb-DPS](DPS=bis(propyltriethoxysilylureylene)pyridine) [146], (b) di-ureasil modified by $\text{Er}(\text{CF}_3\text{SO}_3)_3$ [185] ErDPD gel [169], and $[\text{Nd}(\text{dpa})_3]_3^-$ (dpa=pyridine-2,6-dicarboxylic acid) [172] in a silica-PEG excited under 300, 269, 488, 425 and 580 nm, respectively. Reprinted from [32]

The organic–inorganic hybrids incorporating lanthanide salts present usually an emission spectra characterized by a broad white-light emission associated to the hybrid host overlapped with the typical intra-4f transitions [67–69, 71–74, 178, 179, 183]. The relative intensity between these two emissions and therefore the emitted colour may be readily tuned across the CIE chromaticity diagram by changing chemical parameters – molecular weight of the organic precursors, type and amount of the lanthanide-based salt, synthetic conditions (H_2O/Si ratio, nature and concentration of the catalyst and type of solvent) – and physical parameters – excitation wavelength and temperature.

Figure 12.25 exhibits a CIE diagram with colour coordinates of the room temperature emission of a series of organic–inorganic hybrids for which energy transfer between the hybrid host emitting centres and the lanthanide ions is not really efficient. The colour coordinates of the hybrid materials encapsulating rare-earth organic complexes diverge from the centre of the diagram, representing in most of the cases pure colours, namely red (Eu^{3+}) and green (Tb^{3+}), as shown in the inset of Fig. 12.25. This evidence derives directly from the efficient intramolecular energy conversion from the ligands to the lanthanide ion that disables the emission arising from the hybrid host and/or the ligands. Consequently, the emission colour is dominated by the lanthanide photoluminescence, in contrast to the situation found in hybrids incorporating ionic salts (e.g., europium triflate, $Eu(CF_3SO_3)_3$, and europium perchlorate, $Eu(ClO_4)_3$), whose overall emission appears white to the naked eye, due to the contribution of the hybrid host emitting centres to the emission spectra.

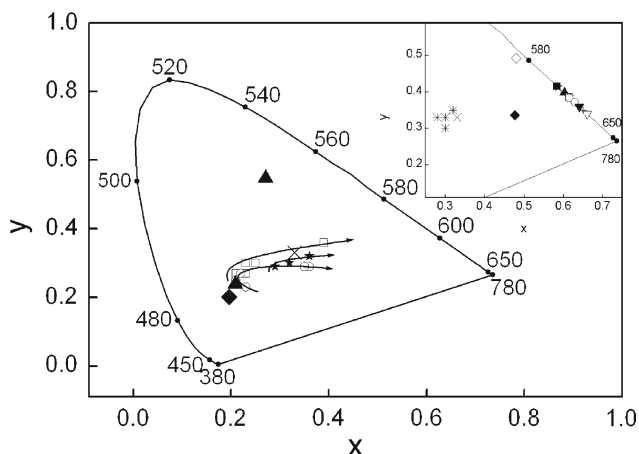


Fig. 12.25 CIE chromaticity diagram showing the (x, y) emission colour coordinates (calculated for the 2° standard observer) for (∇) U(2000)- $Eu(CF_3SO_3)_3$, ($-$) d-U(600)- $Eu(CF_3SO_3)_3$ (d-U(600) is a low molecular weight di-ureasil) (ξ) d-U(600)- $Eu(ClO_4)_3$, ethanolic solutions of the d-U(600) hybrid with (ζ) $Tb(NO_3)_3$ and with (η) a mixture of $Tb(NO_3)_3$ and 2,2-byp. Inset shows the CIE colour coordinates for the (ξ) $Eu(PA)_3$ complexes, (Δ) Hybrid I and (M) Hybrid II, Eu^{3+} -activated organic–inorganic hybrids materials with four different dicarboxylic acids ((ψ) EuH_1 , (∇) EuH_2 , ($-$) EuH_3 and (δ) EuH_4), phosphine oxides bonded to $Si(OR)_3$ groups treated with anhydrous europium salts ((B) $X_A 9a$ and (C) $X_A 9b$), (\square) SiO_2/SPM : terbium carbonyl complexes and ($+$) $SiO_2/SPM:Eu[(phen)_2]^{3+}$ and $SiO_2:Eu[(phen)_2]^{3+}$. Reprinted from [71]

Besides non-organized luminescent hybrids, light-emitting hierarchically structured hybrid materials are undoubtedly an interesting concept. Functionalization of ordered mesoporous silica by organic molecules and control of the optically active guest species location within the host architecture in order to achieve desired properties have recently received considerable attention and are also a great challenge. The periodic nanostructure of MCM-41 (and of other ordered mesoporous structures) makes it an ideal host for incorporation of optically active molecules. Examples have been given in Sect. 12.2.2.1. Mesoporous supports were used either in the purely siliceous or organically modified form and the photophysical properties of the encapsulated rare earth complexes depend greatly on the hydrogen-bonding interactions between host and guest.

Another interesting, yet largely unexplored, possibility concerns the complexation of lanthanides by ligands that are covalently anchored to the support. The potential advantage of this approach has recently been shown and is illustrated by three examples with lanthanide β -diketonate complexes. In the first case the complexes are grafted to sol–gel glasses and a Merrifield resin via covalently bound 1,10-phenanthroline [171, 173], whereas in the other two examples the β -diketonate complexes are covalently linked to the external surface of the MCM-41 channels functionalized by phenyltriethoxysilane (Ph-Si(OCH₂CH₃)₃) via a simple template-ion exchange method [203], or by a surface-bound pyrazolylpyridine ligand [204] (see Fig. 12.20).

Infrared luminescence has also been reported from Er³⁺, Nd³⁺ and Yb³⁺ β -diketonate complexes covalently bonded to MCM-41 and SBA-15 via functionalization of the external surface of their channels [205]. Upon excitation of the ligands absorption bands, these materials display the characteristic near infrared (NIR) luminescence of the corresponding lanthanide ions through intramolecular energy transfer from the ligands to the lanthanide ions. The excellent NIR-luminescent properties enable these mesoporous materials to have potential uses in optical amplifiers (operating at 1.3 or 1.5 μ m), laser systems, or medical diagnostics [205].

The formation of organic–inorganic ordered hybrid structures has been also achieved through non-aqueous sol–gel reaction between lanthanide alkoxides and benzyl alcohol. The synthesis leads to the formation of crystalline thin layers of lanthanide oxides equally spaced by an organic layer formed by benzoate molecules, and the periodic lamellar structure (thermally stable up to 400°C) is kept together by simple π - π interactions between the phenyl rings [206]. By doping the hybrids with Eu³⁺, Tb³⁺, Nd³⁺ or Er³⁺, it was possible to obtain phosphors showing a strong emission in the visible (quantum yield of $16 \pm 2\%$, for the Eu³⁺-based sample) [207] or in the infrared [208, 209]. Since the doped hybrids are excited in the organic sub-phase, where the excitation of the phenyl rings is effectively transferred to the emitting atoms, the energy needed for the excitation of the luminescent centres is substantially lower than that needed in their corresponding pure inorganic oxides.

There are very few reports analyzing the degree of photostability of organic–inorganic hybrids encapsulating lanthanide complexes under prolonged UV irradiation [75, 139]. One recent example involves incorporation of the [Eu(btfa)₃(4,4'-bpy)(EtOH)] complex into the di-ureasil host [75]. In contrast to the case of

the isolated complex, di-ureasils are nearly 100% photostable under UV-A excitation. On the other hand, photodegradation occurs in hybrids under UV-B and UV-C excitation (10–45% and 24–54%, respectively). In this case, Eu^{3+} luminescence quenching is irreversible, leading to a memory effect which nevertheless can be exploited. Indeed, through this effect, these hybrids are potential candidates for application in UV-B and UV-C dosimetry.

Emission Quantum Yield and Quantum Efficiency of an Atomic Level

Despite continuous world-wide interest in light emission features of lanthanide-doped organic–inorganic hybrids, only a handful of reports explicitly quantified improvement in the emission features of lanthanide complexes incorporated in hybrid materials. The absolute emission quantum yields [69, 73, 75, 186, 210] are measured by using techniques described by Wrighton et al., (12.1) [106], and Brill et al. (see (12.2)) [107]. For Ce^{3+} -based hybrids, Isakawi et al. [210] reported q values similar to those determined for di-ureasils or di-urethanesils incorporating $\text{Eu}(\text{CF}_3\text{SO}_3)_3$, namely 4.6–11.0% [69, 73], and di-ureasils incorporating $\text{Eu}(\text{nta})_3\cdot\text{bpy}$ (where nta and bpy stand for 1-(2-naphthyl)-4,4,4-trifluoro-1,3-butanedionate and 2,2'-bipyridine, respectively) [186]. A much higher quantum yield value $q\sim 50\%$ – indeed the largest one reported up to date for organic–inorganic hybrids incorporating lanthanide complexes – was recently reported for $[\text{Eu}(\text{btfa})_3(4,4'\text{-bpy})(\text{EtOH})]$ -containing di-ureasils [75].

Efficiency of the energy transfer between two species can be evaluated from different experimental data namely, the donor measured lifetime and absolute emission quantum yield, in the presence and absence of the acceptor, and by the emission of the acceptor ion excited at the donor absorption band, together with the emission excited via the acceptor [211]. For organic–inorganic hybrids encapsulating lanthanide complexes, the energy transfer efficiency between hybrid' emitting centres and lanthanide cations is controlled by the cation local coordination and has been estimated for a few examples through the measurements of the donor lifetime and absolute emission quantum yield in the presence and absence of the acceptor [71–73]. Decrease in the emission quantum yield (experimental lifetimes of the hybrid' emitting levels) observed for $\text{Eu}^{3+}(\text{Nd}^{3+})$ -based di-ureasils as the Eu^{3+} (Nd^{3+}) amount incorporated in the hybrid host increases, is a clear evidence of energy transfer between emitting centres of the matrix (donors) and metal ions (acceptors). Depending on the lanthanide content, energy transfer efficiency values range from 0.27 to 0.84 (Eu^{3+} -based di-ureasils) [73] and from 0.05 to 0.86 (Nd^{3+} -based analogues) [72].

The emission efficiency of Eu^{3+} -based materials could be estimated by calculating quantum efficiency of the ${}^5\text{D}_0$ level, η , instead of emission quantum yield. These two quantities should be similar when the ligand-to-metal energy transfer is very efficient and non-radiative deactivations of both ligand and ${}^5\text{D}_0$ levels are negligible. Furthermore since the calculation of η provides indication about the role of non-radiative deactivations in the Eu^{3+} emission it can be related to the ion local

coordination. Assuming that only non-radiative and radiative processes are essentially involved in the depopulation of the 5D_0 state, η can be defined as [67, 75, 134, 212, 213]:

$$\eta = \frac{k_r}{k_r + k_{nr}}, \quad (12.3)$$

where k_r and k_{nr} are the radiative and non-radiative transition probabilities, respectively ($k_{\text{exp}} = \tau_{\text{exp}}^{-1} = k_r + k_{nr}$). Emission intensity, I , taken as the integrated intensity S of the emission curves, for ${}^5D_0 \rightarrow {}^7F_{0-6}$ transitions, is expressed by:

$$I_{i \rightarrow j} = \hbar \omega_{i \rightarrow j} A_{i \rightarrow j} N_i \equiv S_{i \rightarrow j}, \quad (12.4)$$

where i and j represent the initial (5D_0) and final (${}^7F_{0-6}$) levels, respectively, $\hbar \omega_{i \rightarrow j}$ is the transition energy, $A_{i \rightarrow j}$ corresponds to Einstein's coefficient of spontaneous emission and N_i is the population of the 5D_0 emitting level [67, 75, 134, 212, 213]. Usually the branching ratio for the ${}^5D_0 \rightarrow {}^7F_{5,6}$ transitions can be neglected as they are not observed experimentally and we can ignore their influence on the depopulation of the 5D_0 excited state. Therefore the radiative contribution may be calculated from the relative intensities of the ${}^5D_0 \rightarrow {}^7F_{0-4}$ transitions and k_r can be calculated as:

$$k_r = \frac{A_{0-1} \hbar \omega_{0-1}}{S_{0-1}} \sum_{j=0}^4 \frac{S_{0-j}}{\hbar \omega_{0-j}}, \quad (12.5)$$

where A_{0-1} is the Einstein's coefficient of spontaneous emission between the 5D_0 and the 7F_1 Stark levels. The ${}^5D_0 \rightarrow {}^7F_1$ transition does not depend on the local ligand field seen by Eu^{3+} ions (purely magnetic dipolar) and, thus, may be used as a reference for the whole spectrum [214]:

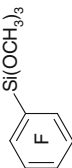
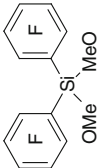
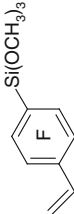
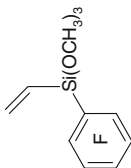
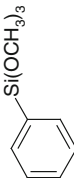
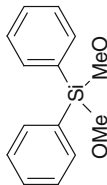
$$A_{0-1} = n^3 (A_{0-1})_{\text{vac}} \quad (12.6)$$

where *in vacuum* $(A_{0-1})_{\text{vac}} = 14.65 \text{ s}^{-1}$ [215]. Considering an average index of refraction n equal to 1.5 – typical of organic–inorganic hybrids [89, 216] – a value of $A_{0-1} \approx 50 \text{ s}^{-1}$ [188, 217] was obtained. Table 12.3 lists the parameters k_r , k_{nr} , η and q obtained for some representative examples of organic–inorganic hybrids encapsulating Eu^{3+} salts and complexes.

Local Coordination

The atomic-like 4f transitions are also often used to get further information about the local environment around the metal ions. This is particularly evident for Eu^{3+} which is a powerful local ion probe. Thus, changes in the number of Stark components of each intra-4f manifold, variations in relative intensity between them,

Table 12.3 Molecular structure, refractive index and attenuation coefficient of several organic–inorganic hybrids processed as waveguides.

Hybrid Type	Non-hydrolysed Precursors	Refractive Index	Attenuation Coefficient
ORMOCER® [117]		1.418	< 0.02 @ 1310 nm 0.18 @ 1550 nm
		1.450	< 0.02 @ 1310 nm 0.10 @ 1550 nm
		1.504	0.24 @ 1310 nm 0.32 @ 1550 nm
		1.436	0.18 @ 1310 nm 0.24 @ 1550 nm
		1.473	0.14 @ 1310 nm 0.36 @ 1550 nm
		1.545	0.18 @ 1310 nm 0.36 @ 1550 nm

0.22@1310 nm
0.46@1550 nm

1.505

0.44@1310 nm
0.44@1550 nm

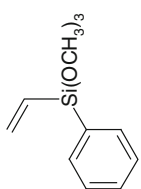
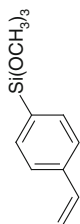
1.492

1.505

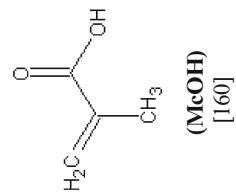
1.492

1.5212-1.5246
1.5050- 1.5090

0.4-0.6@632.8 nm
0.6-1.1@1550 nm



di-urea-propyltriethoxysilane (d-UPTES(600)) ($n_{POE} = 8.5$)



(continued)

Table 12.3 (continued)

Hybrid Type	Non-hydrolysed Precursors	Refractive Index	Attenuation Coefficient
	<p style="text-align: center;"> CH_3O CH_3O $\text{Si}(\text{CH}_2)_3\text{-C(=O)OCH}_3$ CH_3O MAPTMS + ZPO + McOH [167] </p>	1.42	0.13@1310 nm

differences observed in the energy of particular lines (induced by variations on the excitation wavelength and the temperature), and the analysis of the excited state decay curves, provide important information about the local coordination of the lanthanide ions such as:

- Existence of more than one local site
- Number of coordinated water molecules
- Local symmetry group
- Magnitude of the ligand field
- Importance of the covalency

Let us analyze all these aspects in more detail using illustrative examples of Eu^{3+} -based hybrids. The occurrence of changes in the energy, maximum splitting, FWHM and number of Stark components of the ${}^5\text{D}_0 \rightarrow {}^7\text{F}_{1-4}$ transitions as the excitation energy or the temperature varies, is a strong indication that more than one Eu^{3+} -local coordination site may exist. This can be further supported by the dependence of the non-degenerated ${}^5\text{D}_0 \rightarrow {}^7\text{F}_0$ energy with the excitation wavelength variation and by measuring the ${}^5\text{D}_0$ decay curve (monitored within different components of the ${}^5\text{D}_0 \rightarrow {}^7\text{F}_{0-4}$ transitions) under different excitation wavelengths. Moreover large values usually found for the FWHM of non-degenerated ${}^5\text{D}_0 \rightarrow {}^7\text{F}_0$ lines, ranging typically from ~ 20 to 30 cm^{-1} [178], point out that in organic–inorganic hybrids the Eu^{3+} ions are accommodated in a continuous distribution of closely similar local sites.

Generally, in Eu^{3+} -containing hybrids, the number of Stark components observed for the ${}^7\text{F}_{1-4}$ levels correspond to the $(2J+1)$ local-field maximum splitting (1, 3, 5, 7 and 9, respectively) indicating a low-symmetry Eu^{3+} local environment (belonging to the orthorhombic, triclinic or monoclinic crystallographic classes). The ligand field interaction is also of fundamental importance for the case of $4f-4f$ transition intensities. These transitions are in principle electric dipoles forbidden by Laporte's rule. However, provided that the site occupied by the rare earth ion does not present a centre of inversion, Laporte's rule is relaxed due to odd parity terms in the ligand field Hamiltonian [218]. Therefore, in organic–inorganic hybrids in which simultaneously emission spectrum is dominated by the ${}^5\text{D}_0 \rightarrow {}^7\text{F}_2$ transition, a $(2J+1)$ local-field maximum splitting for the ${}^5\text{D}_0 \rightarrow {}^7\text{F}_{1-4}$ lines is found, the ${}^5\text{D}_0 \rightarrow {}^7\text{F}_0$ transition is permitted, and the Eu^{3+} local point group is restricted to the $\text{C}_{1,2}$, C_s and C_{2v} ones [219].

In the so-called Horrocks method the number of water molecules, n_w , coordinated to Eu^{3+} ions may be obtained from decay time measurements performed in water and deuterated water (H_2O and D_2O , respectively) [220, 221] according to the empirical formula:

$$n_w = 1.05 \left[\frac{1}{\tau(\text{H}_2\text{O})} - \frac{1}{\tau(\text{D}_2\text{O})} \right], \quad (12.7)$$

where $\tau(\text{H}_2\text{O})$ is the decay time (ms) in H_2O and $\tau(\text{D}_2\text{O})$ is the decay time in D_2O . Recently a correction to the above formula was proposed by the same group [221] which is then written as:

$$n_w = 1.11 \left[\frac{1}{\tau(\text{H}_2\text{O})} - \frac{1}{\tau(\text{D}_2\text{O})} - 0.31 \right]. \quad (12.8)$$

However, working with Eu^{3+} as a structural probe has a drawback which lies in obtaining decay time values in D_2O . Indeed, D_2O is expensive and hygroscopic in the sense that fast D_2O - H_2O exchange occurs with atmospheric water. This problem can be overcome though, by assuming that the decay time observed in D_2O can be considered as a contribution of a purely radiative process. Therefore we will henceforth use k_r obtained from (12.5) instead of $\tau^{-1}(\text{D}_2\text{O})$ in (12.8), as proposed already in the literature [217].

The number of coordinated H_2O molecules has been estimated for several Eu^{3+} -containing organic-inorganic hybrids supporting, for instance, the discussion of the interaction between the Eu^{3+} ions and the hybrid framework [75, 203] and the possible replacement of Eu^{3+} first neighbours by H_2O (or vice-versa) [67, 178].

The maximum splitting of the ${}^5\text{D}_0 \rightarrow {}^7\text{F}_1$ transition opens the discussion of the ion's nearest ligands interaction potential between the Eu^{3+} ions and their nearest neighbours. Based on this maximum splitting, the $k=2$ contribution of the crystal-field strength (N_v) can be estimated using the methods developed by Auzel and Malta [222] and Malta et al. [223] as:

$$\Delta E_{\max} = \left[\frac{\frac{g_a}{g} \left\langle {}^7\text{F}_1 \left\| \sum_i C^2(i) \right\| {}^7\text{F}_1 \right\rangle^2}{\pi(2+a^2)} \right]^{\frac{1}{2}} N_v, \quad (12.9)$$

where $g=3$ is the degeneracy of the ${}^7\text{F}_1$ level ($g_a = g$ for J integer), $C^2(i)$ are the irreducible spherical tensor operators of rank 2, the index i runs over the 4f electrons, and a is a fraction which specifies the relative position of the intermediate ${}^7\text{F}_1$ Stark component, E_a , inside the interval ΔE , as

$$a = \frac{\Delta E / 2 - (E_a - E_{<})}{\Delta E / 2}, \quad \Delta E / 2 > (E_a - E_{<})$$

or

$$a = \frac{(E_a - E_{<}) - \Delta E / 2}{\Delta E / 2}, \quad \Delta E / 2 < (E_a - E_{<}), \quad (12.10)$$

where E_{ζ} is the energy of the lowest Stark component of the 7F_1 manifold [223]. This crystal-field strength parameter can also be estimated based on the interaction potential between the Eu^{3+} ions and their nearest neighbours, which relates the observed Stark energies to the ion-surrounding ligands local symmetry and is written as a phenomenological local-field interaction as

$$H_{\text{LF}} = \sum_i^6 \sum_{kq} B_q^k C_q^k(\theta_i, \phi_i) \quad (12.11)$$

with the spherical coordinates (r_i, θ_i, ϕ_i) fixing the location of the Eu^{3+} ion and the $4f$ electron and

$$C_q^k(\theta_i, \phi_i) = \left(\frac{4}{2k+1} \right)^{1/2} Y_q^k(\theta_i, \phi_i) \quad (12.12)$$

being spherical tensors written in terms of spherical harmonics Y^k , and B_q^k ($k=2,4,6$ and $-k \leq q \leq k$) being phenomenological parameters which encompass all the dynamics of the Eu^{3+} ions. These dynamical parameters express the spherical symmetry breaking of the free ion levels and determine their corresponding splitting to a maximum of $2J + 1$ Stark components, directly related to the point symmetry group of the ion-surrounding ligands. The eigenvalues of the matrix elements of the local-field perturbation are expressed in terms of the non-zero B_q^k 's associated with each point group and are determined by the best fitting between the observed Stark energies and the calculated eigenvalues. Based on these phenomenological B_q^k 's parameters N_v is estimated using methods developed by Auzel and Malta [222] and Leavitt [224] and its $k=2$ contribution is calculated separately as:

$$N_v = \left[\frac{4\pi}{5} \sum_q |B_q^2|^2 \right]^{1/2}. \quad (12.12)$$

These calculations have been performed for Eu^{3+} -containing hybrid materials linking high-energy ${}^5D_0 \rightarrow {}^7F_0$ line with high-field site (larger crystal-field strength) for which the Eu-ligands bonds are less covalent and the 5D_0 lifetime relatively shorter (and the Eu^{3+} ions are in a more flexible local structure). Moreover, low-energy ${}^5D_0 \rightarrow {}^7F_0$ lines were associated with low-field sites where the Eu-ligands bonds are more covalent, the 5D_0 lifetime relatively longer and the Eu^{3+} ions located in a more rigid structure [183].

The analysis of the ${}^5D_0 \rightarrow {}^7F_0$ energy allows drawing further conclusions regarding the Eu^{3+} local coordination site. The energy of this transition is related with the so-called *nephelauxetic* effect, in which the red shift observed for *d-d* and *f-f* energy differences, with respect to the free ion, is related to a decrease in the values of the Slater integrals F^k ($k = 2,4,6$) and spin-orbit coupling parameter ζ [225–228]. In fact, a phenomenological equation, expressing the *nephelauxetic* effect in terms of the red shift observed for the ${}^5D_0 \rightarrow {}^7F_0$ transition in a large series of Eu^{3+} compounds, has been proposed [229]. A purely phenomenological parameter δ , interpreted

as a covalency parameter, has been shown to correlate quite well with the observed red shifts and also with the *nephelauxetic* parameter h introduced by Jørgensen [225]. Therefore, changes occurring in the first-Eu³⁺ coordination shell (number, type of coordinated ligands and/or average radius) induce alterations in the energy of the ${}^5D_0 \rightarrow {}^7F_0$ transition in such a way that an increase of covalency reflects a shift towards lower energies [228, 230]. An ordinal scale of covalency for lanthanide compounds was recently formalized through a function of the overlap polarizability of a chemical bond (covalent fraction) [230]. This function depends on the average volume of the overlap region, of the order of 1.5% of the volume of the molecular-like pair lanthanide ion-ligating atom. A clear tendency of the *nephelauxetic* effect to increase with the covalent fraction was observed, in agreement with the idea that covalency, though small, is at the origin of the *nephelauxetic* effect in lanthanide compounds [230].

The red shift of the ${}^5D_0 \rightarrow {}^7F_0$, with respect to the value calculated for the free ion, was used to suggest a possible local charge distribution around the cations in Eu(CF₃SO₃)₃-doped high molecular weight di-ureasil hybrids [67, 178]. The Eu³⁺ first coordination shell was depicted as being formed by four carbonyl oxygens, five (or four) oxygen atoms from the SO₃ end groups of the triflate anions and two (or three) water molecules. The tendency of the first ligands to bond covalently to the metal cations discussed in terms of the ${}^5D_0 \rightarrow {}^7F_0$ red shift, pointed out a rather low covalency nature of the Eu³⁺ first coordination shell in those hybrids, when compared to that of analogous polymer electrolytes modified by europium bromide [178]. In the di-urethanesils the ${}^5D_0 \rightarrow {}^7F_0$ red shift was used (together with measurement of the 5D_0 lifetime and calculation of the crystal-field strength) to distinguish the degree of covalency of two distinct local Eu³⁺ environments [183].

Covalency and polarizability degree of the Eu³⁺ first coordination shell may also be inferred from the calculation of the Judd-Ofelt intensity parameters, Ω_λ ($\lambda = 2, 4, 6$) [67, 212, 213]. Usually, the Ω_λ intensity parameters are obtained from absorption data. However, for Eu³⁺-based compounds, the pure magnetic dipole character of the ${}^5D_0 \rightarrow {}^7F_1$ transition and the fact that the electric dipole ${}^5D_0 \rightarrow {}^7F_{2,4,6}$ transitions depend only on the U⁽²⁾, U⁽⁴⁾ and U⁽⁶⁾ reduced matrix elements, respectively, enables the determination of such parameters from the emission spectra [218]. It is important to keep in mind that theoretical calculations indicate the contribution of two different mechanisms to the values of the Ω_λ intensity parameters: forced electric dipole and dynamic coupling [212, 213, 218]. Jørgensen and Judd first reported the dynamic coupling mechanism in 1945 [231]. In a simple way, the dynamic coupling mechanism can be described assuming that the electric field of the incident radiation induces the formation of oscillating dipoles on the atoms in the neighbourhood of the Eu³⁺ cations, producing an additional oscillating electric field. An interesting aspect of these two mechanisms - forced electric dipole and dynamic coupling - is that they contribute with opposite signs to the value of the Ω_λ intensity parameters, so that when such parameters are phenomenologically evaluated,

it is not possible to individually identify each contribution [218]. Nevertheless, there are some empirical evidences that make relevant the phenomenological evaluation of the Ω_λ intensity parameters. The major contribution to the Ω_2 intensity parameter comes from the hypersensitivity electric dipole ${}^5D_0 \rightarrow {}^7F_2$ transition. It was empirically observed that in complexes where a higher degree of covalence in the Eu^{3+} first coordination shell should be expected, a higher value for the respective Ω_2 intensity parameter was simultaneously observed [211]. Another correlation was reported between $\Omega_{4,6}$ intensity parameters and local vibrational modes involving Eu^{3+} ions, suggesting that greater rigidity of the material is observed at higher values of such intensity parameters [211]. The Ω_6 intensity parameter is not usually calculated due to the low relative intensity of the ${}^3D_0 \rightarrow {}^7F_6$ transition, regarding the remaining intra- $4f^6$ transitions.

In summary, the expressions used in the calculation of the $\Omega_{2,4}$ intensity parameters are, respectively:

$$A_{0 \rightarrow 2} = \frac{4e^2}{3\hbar^4 c^3} (\hbar\omega_{0 \rightarrow 2})^3 \frac{n(n^2 + 2)}{9} \Omega_2 \left\langle {}^5D_0 \left\| U^{(2)} \right\| {}^7F_2 \right\rangle^2 \quad (12.13)$$

and

$$A_{0 \rightarrow 4} = \frac{4e^2}{3\hbar^4 c^3} (\hbar\omega_{0 \rightarrow 4})^3 \frac{n(n^2 + 2)}{9} \Omega_4 \left\langle {}^5D_0 \left\| U^{(4)} \right\| {}^7F_4 \right\rangle^2, \quad (12.14)$$

where e is the electron charge (in these equations an undimensional number equal to 1.16140×10^{-3}), \hbar the Planck constant (units $\text{cm}^{-1} \cdot \text{s}$), c the velocity of the light (in $\text{cm} \cdot \text{s}^{-1}$), $U^{(2)}$ and $U^{(4)}$ reduced matrix elements (values of 0.0032 and 0.0023, respectively [214]). Einstein's spontaneous emission coefficients $A_{0 \rightarrow 2}$ and $A_{0 \rightarrow 4}$ are calculated from (12.4) as:

$$\frac{\hbar\omega_{0 \rightarrow 2} A_{0 \rightarrow 2}}{\hbar\omega_{0 \rightarrow 1} A_{0 \rightarrow 1}} = \frac{S_{0 \rightarrow 2}}{S_{0 \rightarrow 1}} \quad (12.15)$$

and

$$\frac{\hbar\omega_{0 \rightarrow 4} A_{0 \rightarrow 2}}{\hbar\omega_{0 \rightarrow 1} A_{0 \rightarrow 1}} = \frac{S_{0 \rightarrow 4}}{S_{0 \rightarrow 1}}. \quad (12.16)$$

The $\Omega_{2,4}$ intensity parameters were calculated for a few examples of Eu^{3+} -containing hybrids, namely di-ureasils incorporating $\text{Eu}(\text{CF}_3\text{SO}_3)_3$ [67], $[\text{Eu}(\text{tta})_3(\text{H}_2\text{O})_2]$ [193], $[\text{Eu}(\text{btfa})_3(4,4'\text{-bpy})(\text{EtOH})]$ [75], and $\text{Eu}(\text{tpi})_3 \cdot 3\text{H}_2\text{O}$ and $\text{Eu}(\text{tpi})_3 \cdot 2\text{topo}$ (where tpi is 3-phenyl-4-(4-toluoyl)-5-isoxazolone and topo is tri-*n*-octylphosphine oxide) [187]. The relatively high values found for Ω_2 intensity parameters ($\sim 20 \times 10^{-20} \text{ cm}^2$) – typically larger than those of the precursors salts (or complexes) – indicate that

the local environment around Eu^{3+} ions is highly polarisable, unequivocally stating that the Eu^{3+} first coordination shell exhibits a more covalent character in the hybrid frameworks.

12.4 Integrated and Non-linear Optics

Each year, the telecommunication world experiences emergence of new services, new technologies and improvements to existing services; e.g., internet access induced a traffic explosion owing to applications like music and video sharing. To face this evolution and become more competitive, the market requires continuous improvement, and cost effective solutions, opening up a window of opportunity for low cost sol-gel derived components to be used in optical integrated circuits. Optical integrated circuits present several advantages when compared to the typical electronic integrated circuits - in particular larger bandwidth, low-loss coupling, smaller size, lower weight and power consumption, and immunity to electromagnetic interference. Sol-gel processing allows the combination in a single material of organic and inorganic counterparts, overcoming well known problems associated with each individual phase, namely low mechanical flexibility and high brittleness of inorganic glasses, their high-temperature processing requirements, which are not compatible with optoelectronic integration. On the other hand, polymers can exhibit relatively low heat and water resistance.

The first reports concerning the preparation of passive waveguides describe the combination of MAPTMS with an inorganic counterpart resulting from the mixture of ZPO stabilized in MeOH [232, 233]. MAPTMS contains a photopolymerisable organic group that enables easy patterning of such hybrids under UV light [see for e.g., [234]. The waveguides' optical properties depend on material intrinsic losses (e.g., vibrations of organic groups such as CH, NH, CO and OH oscillators of Si-OH moieties), on the processing mode and propagation wavelength. The best performance has been reported for waveguiding at 1,330 nm in a buried channel with propagation and coupling losses of 0.1 dBcm^{-1} and 0.5 dBcm^{-1} , respectively [50]. Recently, di-ureasils modified with a mixture of ZPO and MeOH have also been used as substrates for optical waveguides [89–91, 235]. Di-ureasils have been shown to simultaneously present acceptable transparency and mechanical flexibility leading to easier processing of thick films, enabling the production of self-patternable channels and monomode planar waveguides with low propagation losses ($<0.3 \text{ dB/cm}$), good thermal stability and large electro-optic coefficients at relevant wavelengths, especially 1,550 nm [89, 235]. Figures 12.26a, b show a photo of channel waveguides written in such hybrids and the output modal intensity distribution at 1,550 nm, respectively. Several organic-inorganic hybrids based on different organic precursors and commercially designated as ORMOCER® (trademark of the Fraunhofer-Gesellschaft zur Förderung der angewandten Forschung e.V. München) have also been used as substrates to UV written waveguides [236]. Table 12.4 lists several organic-inorganic hybrids and the corresponding non-hydrolyzed

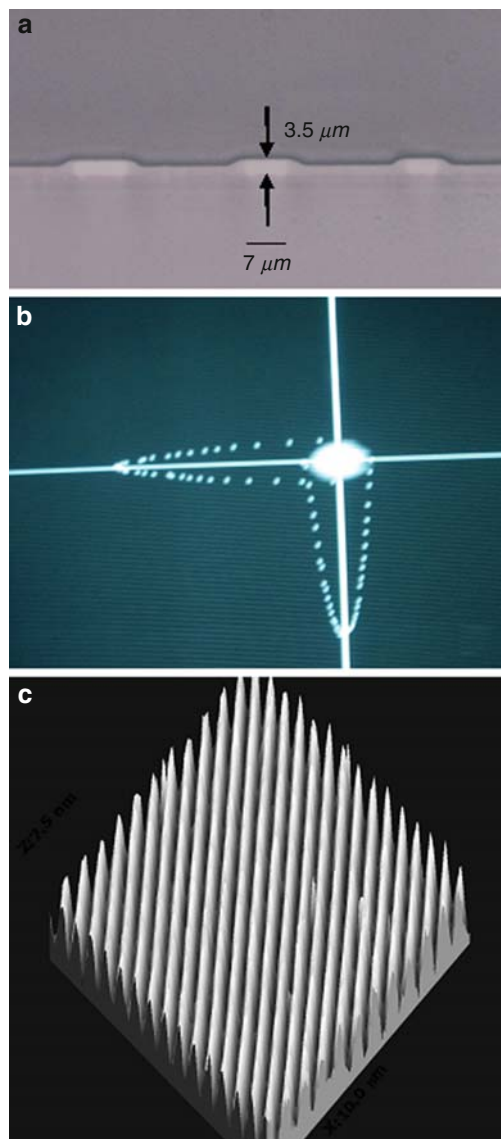
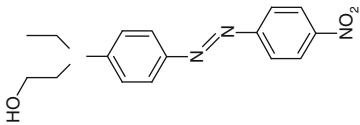
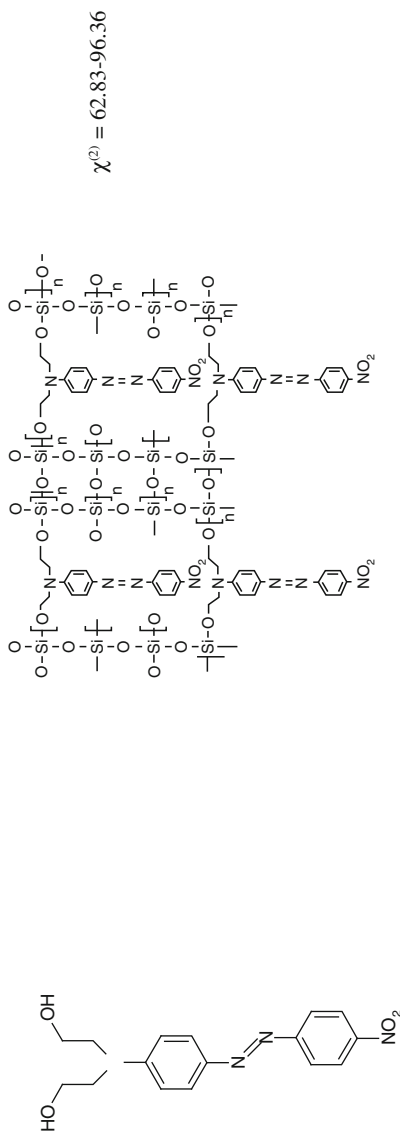


Fig. 12.26 (a) Optical microscope photograph of channel waveguides in d-U(600)-MAPTMS-ZPO hybrids by UV exposure through an amplitude mask. (b) Output modal intensity distribution at 1,550 nm for a 7- μm wide channel waveguide. Intensity profiles are superimposed, indicating modal dimensions of *Horizontal*: 2.6 μm , *Vertical*: 2.2 μm . Reprinted from. [89]; (c) 3D AFM representation of a grating with 500 nm pitch written on a di-ureasil modified by ZPO and McOH. Reprinted from [90]

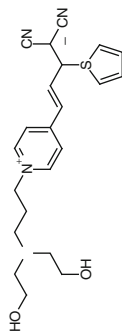
precursors that have demonstrated their capability of being processed as passive optical waveguides, together with their refractive index and attenuation coefficient at relevant wavelengths, namely 1,310 and 1,550 nm.

Table 12.4 Molecular structure of several organic–inorganic hybrids processed as waveguides and the respective refractive index and attenuation coefficient (dB cm⁻¹). Reprinted from [67]

Non-linear Chromophor	Matrix	Second-Order Non-linear features (pm/V)
N-(4-nitrophenyl)-(s)-prolinol [252]	CH ₃ SiO _{1.5} ZrO ₂	$d_{33} = 0.16$
4-(dimethylamino)-4'-nitrostilbene [173]	SiO ₂ -TiO ₂ TiO ₂	$\chi^{(2)} = 10.9$ $\chi^{(2)} = 11$ $d_{33} = 11$
	SiO ₂	$d_{33} = 55-75$
Dispersed Red1 (DR1) [109]	Red 17 functionalized with ICPTES	$d_{33} = 78-150$ $r_{33} = 20$
Dispersed Red 17 (DR17) [127]		



Dispersed Red 19 (DR19) [106]



[104]

AEAPTMS or
3-glycidoxypropyltri-methoxysilane-N-(3-
(trimethoxysilyl)propyl)-ethylenediamine
(GPTMS)

$d_{33} = 0.66$
 $d_{11} = 0.335$

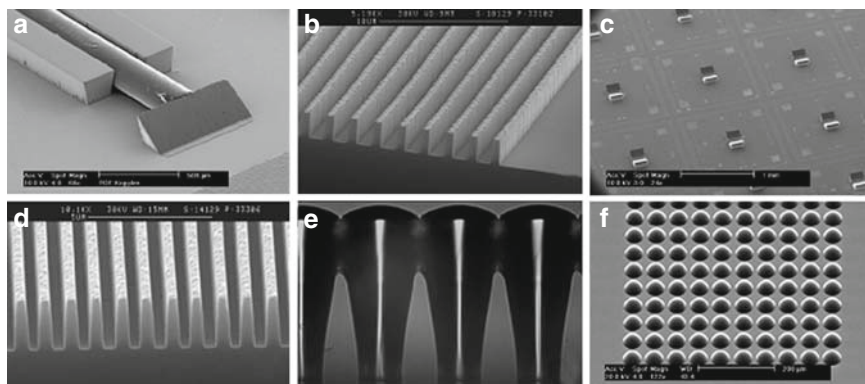


Fig. 12.27 Microoptical elements (lenses, lens arrays, gratings, prisms) fabricated by replication, lithography, or a combination of both. (a) Deflection prism (b) UV-moulded high aspect ratio grating in ORMOCER[®], (c) Replicated prisms on detector chip wafers, (d) UV-moulded grating, (e) Side view of 750- μm high ORMOCER[®] lenses on a GaAs wafer, (f) Replicated 10 \times 10 micro lens array. Taken from www.microresist.de

A diffraction grating with low rugosity (below 1 nm) and uniform modulation pattern was obtained through UV exposure of a di-ureasil hybrid [90, 91], opening up new perspectives for the development of new integrated optics devices. Figure 12.26c shows a diffraction grating written in di-ureasil hybrids. Figure 12.27 displays examples of various optical devices based on waveguides written on ORMOCER[®] organic–inorganic hybrids.

Organic–inorganic hybrids have been also considered potential candidates for the production of active optical waveguides due to their capability of acting as good host cages for the incorporation of large amounts of optically active ions from visible to infrared spectral regions of the electromagnetic spectrum [57, 71, 140, 154, 164, 165, 170, 172, 178]. Efforts have been made to use such devices in innovative light/laser sources working in visible and NIR regions. The great interest in infrared spectral region is due to the low-loss spectral windows of commercial silica-based transmission fibres that are located around 800, 1,310 and 1,550 nm (I, II and III telecommunication transmission windows, respectively). Therefore, optical features of organic–inorganic hybrids with technological potential for integrated optics must include low attenuation coefficients and optically active centres with efficient emission lines around such wavelengths. Although interesting results for light amplification have been reported, with large gain in the visible range, less promising results have been reported for infrared spectral region. The utilization of infrared-active elements is a complicated task as optical activity of the lanthanide ions like neodymium or erbium in the infrared is usually quenched at room temperature due to large number of hydroxyl and organic vibrational groups present in the organic–inorganic host. Owing to the need of high doping levels, other drawbacks concerning active waveguides doped with lanthanide ions may also occur, namely emission quenching due to concentration effects (energy transfer between close

ions followed by non-radiative deactivation in some recombination centres, lattice defects, for instance). Etienne et al. reported production of channels waveguides with low OH content using Er³⁺-doped dialkoxide hydrophobic silica precursor [237]. UV exposure results in a high guided mode confinement at 1,550 nm. For the first time, signal enhancement at 1,550 nm by pumping at 980 nm wavelength was observed in a hybrid material [237].

Organic chromophores (dyes) have also been used to fabricate channel waveguides. The covalent graft or embedding of molecules in hybrid hosts has the advantages of isolating active species from intermolecular interaction and intramolecular rearrangement [50], and contributing to thermal and mechanical stability of the chromophore. Casalboni et al. reported incorporation without degradation of the IR5 and IR1051 dyes in an ORMOCER[®] using 3-glycidylxypropyltrimethoxysilane (GLYMO) as the organic modifier, demonstrating the possibility of achieving emission in the 1,100–1,300 nm range. Laser action has been reported in titania–silica glass films doped with rhodamine 6G dye which exhibited a refractive index from 1.54 to 1.61 [238] and in rhodamine-activated hybrid organic–inorganic mesostructured titania which are also potential materials to be used as waveguides presenting high refractive indexes (1.8 ± 0.2).

Other applications in the field of photonics are based on non-linear processes. These non-linear optical processes may be divided into second-order effects, such as Pockels effect and second harmonic generation, and third-order non-linear effects like Kerr and Raman effects, four wave mixing, two-photon absorption and optical limiting power. High order susceptibilities are usually ignored.

The Pockels and Kerr effects are responsible for the refractive index changes (Δn) with the applied electrical field,

$$n(E) - n = -\frac{1}{2}r_{ij}n^3E + \frac{1}{2}s_{ij}n^3E^2,$$

where n is the refractive index for low intensity electric fields and r_{ij} and s_{ij} (tensors of rank 3) represent electro optical Kerr and Pockels coefficients, respectively. These tensors contain information about the direction of the polarization of the output wave with respect to polarization and propagation direction of the incident light. These non-linear effects are used to produce devices such as electro optical modulators. For crystals, r_{ij} and s_{ij} have typical values of $10^{-12} - 10^{-10}$ m/V and $10^{-18} - 10^{-14}$ m²/V², respectively. Non-linear refractive index due to Kerr effect is usually denoted as n_2 .

Second harmonic generation – the most probable non-linear effect during light absorption – may occur at high laser intensities, where the absorption of two photons produces only one hole-electron pair. Change in intensity of a beam as it propagates through a medium with linear and two-photon absorption, is given by $-(\alpha I + \beta I^2)$, where α and β are the linear and two-photon absorption coefficients, respectively. After two-photon absorption occurs, the medium may emit light with twice the frequency (half the wavelength) of the incident light. The so-called d_{lm} parameter (tensor of rank 3) contains information about the direction of polarization

of the output wave with respect to polarization and propagation direction of the incident light. Second-order non-linear effects cannot be observed in materials whose structure is characterized by an inversion centre (the second-order non-linear susceptibility is zero), as observed in most of the organic–inorganic hybrids which are tailored as amorphous materials. Two synthesis strategies have been adopted: i) the physical mixture of organic chromophores having non-linear properties into organic–inorganic host (Class I materials) [11, 239–245] and ii) the covalent graft between the organic chromophore and an inorganic skeleton (Class II materials) [10, 239, 245–247]. The latter method intends to increase thermal and chemical stability of the organic component and contribute to induce a permanent molecular alignment, contributing in turn to enhancement of the electro-optic coefficient. It has been demonstrated that the number of bonding sites and geometries affects the value of the electro-optic coefficient [10, 246]. The best results were obtained for two anchor sites in the vertical position with respect to the main chain. Data available in literature indicate that applying the poling technique is quite efficient for organic–inorganic hybrids, leading to electro-optic coefficients as high as 150 pm V^{-1} and temporal stability up to 10,000 h with azo dyes (e.g., DR1, DR17, DR19, DO) [10]. For comparison purposes we may recall that one of the most common materials for electro-optical devices with second-order non-linear optical properties is the inorganic crystal LiNbO_3 with an electro-optical coefficient ($r_{33} = 30.8 \text{ pm V}^{-1}$ and $d_{33} = 60 \text{ pm V}^{-1}$). Table 12.5 lists several organic chromophores and their respective non-linear properties.

Third-order non-linear effects have been observed in organic dyes containing conjugated π -electrons, due to their high polarizability [248–254]. Incorporation of the dyes into the hybrid host contributes both to increase their typical low chemical and thermal stability, prevents clustering and enhances the magnitude of third-order non-linear features. Table 12.5 lists several organic–inorganic hybrids with the respective third-order non-linear susceptibility value. Another important class of organic–inorganic hybrids with third order non-linear properties involves combination of nanosized organic and inorganic segments, taking advantage of the quantum confinement and dielectric confinement effects, and the possibility of incorporating high-doping levels of nanoparticles (Table 12.6) [255–261].

12.5 Conclusion and Perspectives

Organic–inorganic hybrids are a technologically key class of advanced multifunctional materials that fulfil the challenging strict requirements of the beginning of this century: higher levels of sophistication and miniaturization, recyclability, reliability, low energy consumption and environmental friendliness. The potential of these tailor-made materials with unparalleled performances, that are already entering niche markets, is basically due to the synergistic combination of organic, inorganic, and even biological components in a single system at the nanosize level.

Table 12.5 Examples of second-order non-linear hybrids. Reprinted from [67]

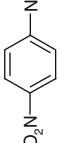
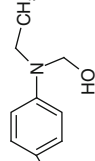
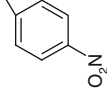
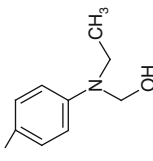
Third-Order Non-linear Chromophor	Matrix	Non-linear features
   	TEOS	$n_2 = -2.37 \times 10^{-5} \text{ cm}^2 \text{ W}^{-1}$
trans DRI [189] Rhodamine-6G [251]	SiO_2 - TiO_2	$\chi^{(3)} = 10^{-9}$ esu
4'-dimethylamino-N-methyl-4-stilbazolium iodide (DMSI) [169]	SiO_2	$\chi^{(3)} = 4.5 \times 10^{-14}$ esu
pseudisocyanine dyes [235] 1,1'-diethyl-2,2'-cyanine bromide [253]	SiO_2 SiO_2	$\chi^{(3)} = 10^{-7}$ esu $\chi^{(3)} = 5 \times 10^{-7}$ esu
metal dithiolenes and phthalocyanine dyes [87]	SiO_2 +polymethyl methacrylate (PMMA)	$\chi^{(3)} = 10^{-11}$ esu
0.8 (Poly(1,4-phenylene vinylene) + 0.2 (Poly(2,5-dimethoxy-1,4-phenylene vinylene)) [97]	SiO_2 (7)	$\chi^{(3)} = 7.9\text{--}59 \times 10^{-11}$ esu

Table 12.6 Examples of third-order non-linear hybrids. Reprinted from [67]

Third-Order Non-linear Nano-sized Hybrid	Non-linear features
nanocrystalline TiO ₂ +PMMA [248]	$\chi^{(3)} = 0.14-1.93 \times 10^{-9}$ esu $n_2 = 0.17-1.0 \times 10^{-11}$ cm ² .W ⁻¹ $\beta = 160-550 \times 10^{-9}$ cm W ⁻¹
TiO ₂ -PMMA [247]	$\chi^{(3)} = 1.05-5.27 \times 10^{-9}$ esu $n_2 = 1.3-6.2 \times 10^{-11}$ cm ² W ⁻¹ $\beta = 885-2260 \times 10^{-9}$ cm W ⁻¹
poly(styrene maleic anhydride)/TiO ₂ [236]	optical limiting lower continuous laser light Intensity (10 ⁷ W/m ²). $\beta = 200-960 \times 10^{-4}$ cm W ⁻¹ $\alpha = 0.45-1.2$ mm ⁻¹
nanometer-sized CdO CTAB [241]	$\chi^{(3)} = 1.67 \times 10^{-10}$ esu $n_2 = -155 \times 10^{-16}$ cm ² W ⁻¹ $\beta = 0.91 \times 10^{-9}$ cm W ⁻¹
	dodecylbenzene sulfonate $\chi^{(3)} = 1.22 \times 10^{-10}$ esu $n_2 = -697 \times 10^{-16}$ cm ² W ⁻¹ $\beta = 8.64 \times 10^{-9}$ cm W ⁻¹
CdS+PDMS-TEOS (PDMS= polydimethylsiloxane) or APTES [139]	$\chi^{(3)} = 10^{-6}$ esu
CdS+NaOAc+B(OC ₂ H ₅) ₃ +Si(OCH ₃) ₄ +Cd(OAc) ₂ ·2H ₂ O [229]	$\chi^{(3)} = 1.2-6.3 \times 10^{-7}$ esu
PbS+TMSPM+McOH+ZPO (TMSPM=3-(trimethoxysilyl) propyl methacrylate) [152]	$\chi^{(3)} = 1.8 \times 10^{-10} - 1.3 \times 10^{-7}$ esu $n_2 = -(3.1 \times 10^{-16}-6.7 \times 10^{-15})$ m ² W ⁻¹

The “soft” sol–gel process is of paramount importance for the creation of amorphous nanoscaled amorphous hybrid materials. More recently, association of this wet chemical method with a variety of self-assembly strategies has enabled the exploration of the concept of “synthesis with design and construction” of architecturally organized hybrid materials.

The photoluminescent features of the lanthanide-based disordered and ordered hybrid hosts reviewed here illustrate nicely the tremendous impact in photonics that results from the encapsulation of organic dyes and lanthanide complexes within siloxane-based matrices through simple embedding within the sol–gel derived matrix (Class I hybrid materials) or the use of coordinating ligands that are covalently grafted to the framework (Class II hybrid materials).

The expected advances in synthetic chemistry (involving even bio-inspired strategies) and the level of knowledge in nanoscience allow anticipation in the near future of an explosion in the number of emerging multiscale structured photonic organic–inorganic hybrids, hierarchically organized in terms of structure and optical functions, with unprecedented performance, exhibiting in particular a significant improvement in major properties: (1) mechanical integrity, transparency and optical loss of the host matrix; (2) emitting centre characteristics, such as chemical/thermal/photostability and optical efficiency; and (3) interaction between emitting centres and the host matrix due to a cage-type encapsulation with better chemical/thermal/photostability and with efficient host-to-emitting centre energy transfer processes.

Acknowledgments The support of the Network of Excellence FAME and of Fundação para a Ciência e Tecnologia, FCT (POCTI/P/CTM/46780/02; POCI/CTM/59075/04) is gratefully acknowledged. The authors thank the collaboration of L.S. Fu, N. J. O. Silva and S. S. Nobre (University of Aveiro) and S. C. Nunes (UTAD).

References

1. Avnir D (1995) Organic-chemistry within ceramic matrices – doped sol–gel materials. *Acc Chem Res* 28: 328–334
2. Brinker CJ, Scherer GW (1990) *Sol–gel Science, The Physics and Chemistry of Sol–Gel Processing*. Academic Press, San Diego.
3. Corriu RJP, Leclercq D (1996) Recent developments of molecular chemistry for sol–gel processes. *Angew Chem Int Ed Engl* 35: 1420–1436
4. Judeinstein P, Sanchez C (1996) Hybrid organic–inorganic materials: a land of multidisciplinary. *J Mater Chem* 6: 511–525
5. Sanchez C, Ribot F (1994) Design of hybrid organic–inorganic materials synthesized via sol–gel chemistry. *New J Chem* 18: 1007–1047
6. Sanchez C, Soler-Illia GJ de AA, Ribot F, Lalot T, Mayer CR, Cabuil V (2001) Designed hybrid organic–inorganic nanocomposites from functional nanobuilding blocks. *Chem Mater* 13:3061–3083
7. Sanchez C, Soler-Illia GJ de AA, Ribot F, Grosso D (2003) Design of functional nanostructured materials through the use of controlled hybrid organic–inorganic interfaces. *C. R. Chimie* 6: 1131–1151
8. Schmidt H, Jonschker G, Goedicke S, Mennig M (2000) The sol–gel process as a basic technology for nanoparticle-dispersed inorganic–organic composites. *J Sol–Gel Sci Technol* 19: 39–51.
9. Schubert U, Hüsing N, Lorenz A (1995) Hybrid inorganic–organic materials by sol–gel processing of organofunctional metal alkoxides. *Chem Mater* 7: 2010–2027
10. Lebeau B, Brasselet S, Zyss J, Sanchez C (1997) Design, characterization, and processing of hybrid organic–inorganic coatings with very high second-order optical nonlinearities. *Chem Mater* 9: 1012–1020
11. Lebeau B, Sanchez C (1999) Sol–gel derived hybrid inorganic–organic nanocomposites for optics. *Curr Opin Solid State Mater Sci* 4: 11–23
12. Livage J, Henry M, Sanchez C (1988) Sol–gel chemistry of transition metal oxides. *Prog Solid State Chem* 18: 259–341
13. Loy DA, Shea KJ (1995) Bridged polysilsesquioxanes – highly porous hybrid organic–inorganic materials. *Chem Rev* 95: 1431–1442
14. Novak BM (1993) Hybrid nanocomposite materials – between inorganic glasses and organic polymers. *Adv Mater* 5: 422–433
15. Schmidt H (1995) New type of non-crystalline solids between inorganic and organic materials. *J Non Cryst Solids* 73: 681–691
16. Schottner G (2001) Hybrid sol–gel-derived polymers: applications of multifunctional materials. *Chem Mater* 13: 3422–3435.
17. Mann S, Burkett SL, Davis SA, Fowler CE, Mendelson NH, Sims SD, Walsh D, Whilton NT (1997) Sol–gel synthesis of organized matter. *Chem Mater* 9: 2300–2310
18. Moreau JE, Vellutini L, Chi Man MW, Bied C (2003) Shape-controlled bridged silsesquioxanes: hollow tubes and spheres. *Chem Eur J* 9: 1594–1599
19. Moreau JE, Vellutini L, Chi Man MW, Bied C (2001) New hybrid organic–inorganic solids with helical morphology via H-bond mediated sol–gel hydrolysis of silyl derivatives of chiral (R,R)- or (S,S)-diureidocyclohexane. *J Amer Chem Soc* 123: 1509–1510

20. Vallé K, Belleville P, Pereira F, Sanchez C (2006) Hierarchically structured transparent hybrid membranes by *in situ* growth of mesostructured organosilica in host polymer. *Nat Mater* 5: 107–111
21. Alauzun J, Mehdi A, Reye C, Corriu RJP (2005) Hydrophilic conditions: a new way for self-assembly of hybrid silica containing long alkylene chains. *J Mater Chem* 15: 841–843
22. Carlos LD, de Zea Bermudez V, Nunes SC, Silva NJO, Sá Ferreira RA, Santilli CV, Ostrovskii D, Amaral VS, Rocha J (2006) Nanoscopic photoluminescence memory as a fingerprint of complexity in self-assembled alkylene/siloxane hybrids. *Adv Mater* 19: 341–348
23. Liu N, Yu K, Smarsly B, Dunphy DR, Jiang Y-B, Brinker CJ (2002) Catalyzed collapse and enhanced hydrogen storage of BN nanotubes. *J Am Chem Soc* 124: 14540–14555
24. Moreau JE, Vellutini L, Chi Man MW, Bied C, Dieudonné P, Bantignies J-L, Sauvajol J-L (2005) Lamellar bridged silsesquioxanes: self-assembly through a combination of hydrogen bonding and hydrophobic interactions. *Chem Eur J* 11: 1527–1537
25. Moreau JJE, Pichon BP, Chi Man MW, Bied C, Pritzkow H, Bantignies J-L, Dieudonné P, Sauvajol J-L (2004) A Better understanding of the self-structuration of bridged silsesquioxanes. *Angew Chem Int Ed* 43: 203–206
26. Parikh AN, Schivley MA, Koo E, Seshadri K, Aurentz D, Muelle r K, Allara DL (1997) n-Alkylsiloxanes: from single monolayers to layered crystals. The formation of crystalline polymers from the hydrolysis of n-Octadecyltrichlorosilane. *J Am Chem Soc* 119: 3135–3143
27. Shimojima A, Sugahara Y, Kuroda K (1997) Inorganic–organic layered materials derived via the hydrolysis and polycondensation of trialkoxy(alkyl)silanes. *Bull Chem Soc Jpn* 70: 2847–2853
28. Tang H, Sun J, Jiang J, Zhou X, Hu T, Xie P, Zhang R (2002) A novel aryl amide-bridged ladderlike polymethylsiloxane synthesized by an amido H-bonding self-assembled template. *J Am Chem Soc* 124: 10482–10488
29. Arkles B (2001) Commercial applications of sol–gel-derived hybrid materials. *Mater Res Soc Bull* 26: 402–408.
30. Avnir D, Braun S, Lev O, Levy D, Ottolenghi M (1994) Organically-doped sol–gel porous glasses: chemical sensors, enzymatic sensors, electro-optical materials, luminescent materials and photochromic materials. In: Klein L (ed) *Sol–Gel Optics, Processing and Applications*. Kluwer, Dordrecht, The Netherlands, ch 23, pp 539–582
31. Carlos LD, Sá Ferreira RA, de Zea Bermudez V (2003) Light emission from organic–inorganic hybrids materials and nanocomposites. In: Nalwa HS (ed) *Handbook of Organic–Inorganic Hybrid Materials and Nanocomposites*. American Scientific Publishers, Stevenson Ranch, CA, vol 1, pp 353–380
32. Carlos LD, Sá Ferreira RA, de Zea Bermudez V (2007) Hybrid materials for optical applications. In: KICKELBICK G (ed) *Hybrid Materials: Synthesis, Characterization, and Applications*. Wiley, Weinheim, pp 337–398
33. Sanchez C, Julian B, Belleville P, Popall M (2005) Applications of hybrid organic–inorganic nanocomposites. *J Mater Chem* 15: 3559–3592
34. Sanchez C, Lebeau B (2001) Hybrid organic–inorganic materials. In: Loy DA (eds) *Mater Res Soc Bull* 26: 377–387
35. Sanchez C, Lebeau B, Chaput F, Boilot J-P (2003) Optical properties of functional hybrid organic–inorganic nanocomposites. In: Romero PG, Sanchez C (eds) *Functional Hybrid Materials*. Wiley, Weinheim, pp. 122–168
36. Scott BJ, Wirnsberger G, Stucky GD (2001) Mesoporous and mesostructured materials for optical applications. *Chem Mater* 13: 3140–3150
37. Seddon AB (1997) Potential of organic–inorganic hybrid materials derived by sol–gel for photonic applications. In: Andrews MP, Najafi SI (eds) *Sol–gel and polymer photonic devices*. SPIE – The International Society of Optical Engineering – Series, Bellingham, WA, vol CR68, pp 143–171
38. Ptatschek V, Schreder B, Herz K, Hilbert U, Ossau W, Schottner G, Rahausser O, Bischof T, Lermann G, Materny A, Kiefer W, Bacher G, Forchel A, Su D, Giersig M, Muller G, Spanhel

- L (1997) Sol–gel synthesis and spectroscopic properties of thick nanocrystalline CdSe films. *J Phys Chem B* 101: 8898–8906
39. Jin T, Inoue S, Machida K, Adachi G (1997) Photovoltaic cell characteristics of hybrid silicon devices with lanthanide complex phosphor-coating film. *J Electrochem Soc* 144: 4054–4058
 40. Lancelle-Beltran E, Prené P, Boscher C, Belleville P, Buvat P, Sanchez C (2006) All-solid-state dye-sensitized nanoporous TiO₂ hybrid solar cells with high energy-conversion efficiency. *Adv Mater* 18: 2579–2582
 41. Faloss M, Canva M, Georges P, Brun A, Chaput F, Boilot JP (1997) Toward millions of laser pulses with pyrromethene- and perylene-doped xerogels. *Appl Opt* 36: 6760–6763
 42. Schaudel B, Guermeur C, Sanchez C, Nakatani K, Delaire JA (1997) Spirooxazine- and spiropyran-doped hybrid organic–inorganic matrices with very fast photochromic responses. *J Mater Chem* 7: 61–65
 43. Chamuel F, Jiang H, Kakkar A (2001) Sol–gel materials for second-order nonlinear optics. *Chem Mater* 13: 3389–3395
 44. Kim HK, Kang S-J, Choi S-K, Min Y-H, Yoon C-S (1999) Highly efficient organic–inorganic hybrid nonlinear optic materials via sol–gel process: synthesis, optical properties, and photobleaching for channel waveguides. *Chem Mater* 11: 779–788
 45. Aubonnet S, Barry HF, von Bultzingslowen C, Sabatie J-M, MacCraith BD (2003) Photopatternable optical chemical sensors based on hybrid sol–gel materials. *Electronics Lett* 39: 913–914
 46. Goncalves RR, Carturan G, Zampedri L, Ferrari M, Montagna M, Chiasera A, Righini GC, Pelli S, Ribeiro SJL, Messaddeq Y (2002) Low optical loss planar waveguides prepared in an organic–inorganic hybrid system. *App Phys Lett* 81: 28
 47. Levy D, Del Monte F, Otón JM, Fiksmán G, Matías I, Datta P, López-amo M (1997) Photochromic doped sol–gel materials for fiber-optic devices. *J Sol–Gel Sci Tech* 8: 931–935
 48. Rottman C, Grader G, De Hazan Y, Melchior S, Avnir D (1999) Surfactant-induced modification of dopants reactivity in sol–gel matrixes. *J Am Chem Soc* 121: 8533–8543
 49. Buestrich R, Kahlenberg F, Popall M, Dannberg P, Müller Fiedler R, Rösch O (2001) ORMOCER®s for optical interconnection technology. *J. Sol–Gel Sci Technol* 20: 181–186
 50. Casalboni M, Senesi R, Proposito P, De Matteis F, Pizzoferrato R (1997) Rigid-cage effects on the optical properties of the dye 3,3-diethyloxadicarbocyanine incorporated in silica-gel glasses. *Appl Phys Lett* 70: 2969–2971
 51. Najafi IS (1998) Sol–gel glass waveguide and grating on silicon. *J Lightwave Technol* 16: 1640–1642
 52. Yoon KB, Bae B-S, Popall M (2005) Fabrication of low-loss waveguides using organic–inorganic hybrid materials. *J Nonlinear Optic Phys Mater* 14: 399–407
 53. Dantas de Moraes T, Chaput F, Lahlil K, Boilot J-P (1999) Hybrid organic–inorganic light-emitting diodes. *Adv Mater* 11: 107–112
 54. Mitzi DB, Chondroudis K, Kagan CR (2001) Organic–inorganic electronics. *IBM J Res Dev* 45: 29–45
 55. Bekiari V, Lianos P (1998) Tunable Photoluminescence from a material made by the interaction between (3-Aminopropyl)triethoxysilane and organic acids. *Chem Mater* 10: 3777–3779
 56. Bekiari V, Lianos P (1998) Characterization of photoluminescence from a material made by interaction of (3-aminopropyl)triethoxysilane with acetic acid. *Langmuir* 14: 3459–3461
 57. Bekiari V, Stathatos E, Lianos P, Stangar UL, Orel B, Judeinstein P (2000) Optimization of the intensity of luminescence emission from silica/poly(ethylene oxide) and silica/poly(propylene oxide) nanocomposite gels. *Chem Mater* 12: 3095–3099
 58. Carlos LD, Sá Ferreira RA, de Zea Bermudez V, Ribeiro SJL (2001) Full-color phosphors from amine-functionalized crosslinked hybrids lacking metal activator ions. *Adv Func Mater* 11: 111–115
 59. Carlos LD, Sá Ferreira RA, Nobre SS, Man MWC, Moreau JJE, Bied C, Pichon B (2006) Photoluminescence changes induced by self-organisation in bridged silsesquioxanes. *Mater Sci Forum* 514–516: 118–122

60. Carlos LD, Sá Ferreira RA, Pereira RN, Assunção M, de Zea Bermudez V (2004) White-light emission of amine-functionalized organic–inorganic hybrids: emitting centers and recombination mechanisms. *J Phys Chem B* 108: 14924–14932
61. Green WH, Le KP, Grey J, Au TT, Sailor MJ (1997) White phosphors from a silicate-carboxylate sol–gel precursor that lack metal activator ions. *Science* 276: 1826–1828
62. Uchida Y, Nobu Y-I, Momiji I, Matsui K (2000) Luminescence of silica-pillared clays and gels derived from aminofunctional silanes. *J. Sol–Gel Sci Tech*, 19: 705–709
63. Fu LS, Sá Ferreira RA, Rocha J, de Zea Bermudez V, Hungerford G, Carlos LD (2008) Photoluminescence and quantum yields of organic–inorganic hybrids prepared through formic acid solvolysis. *Opt Mater* 30: 1058–1064
64. Fu LS, Sá Ferreira RA, Silva NJO, Carlos LD, de Zea Bermudez V, Rocha J (2004) Photoluminescence and quantum yields of urea and urethane cross-linked nanohybrids derived from carboxylic acid solvolysis. *Chem Mater* 16: 1507–1516
65. Stathatos E, Lianos P, Stangar UL, Orel B (2001) Study of laser action of Coumarine-153 incorporated in sol–gel made silica/poly(propylene oxide) nanocomposite gels. *Chem Phys Lett* 345: 381–385
66. Oliveira DC, Messaddeq Y, Dahmouche K, Ribeiro SJL, Gonçalves RR, Vesperini A, Gindre D, Nunzi J-M (2006) Distributed feedback multipeak laser emission in Rhodamine 6G doped organic–inorganic hybrids. *J Sol–Gel Sci Techn* 40:359–363
67. Carlos LD, Messaddeq Y, Brito HF, Sá Ferreira RA, de Zea Bermudez V, Ribeiro SJL (2000) Full-color phosphors from europium(III)-based organosilicates. *Adv Mater* 12: 594–598
68. Carlos LD, Sá Ferreira RA, Rainho JP, de Zea Bermudez V (2002) Fine-tuning of the chromaticity of the emission color of organic–inorganic hybrids co-doped with Eu^{III} , Tb^{III} , and Tm^{III} . *Adv Func Mat* 12: 819–823
69. Gonçalves MC, de Zea Bermudez V, Sá Ferreira RA, Ostrovskii D, Rocha J, Carlos LD (2004) Optically functional di-urethanesil nanohybrids containing Eu^{3+} ions. *Chem Mater* 16: 2530–2543
70. Sá Ferreira RA, Carlos LD, de Zea Bermudez V (1999) Excitation energy dependence of luminescent sol–gel organically modified silicates. *Thin Solid Films* 343: 476–480
71. Sá Ferreira RA, Carlos LD, de Zea Bermudez V (2004) Luminescent organic–inorganic nanohybrids. In: Nalwa HS (eds) *Encyclopedia of Nanoscience and Nanotechnology*. American Scientific Publishers, Stevenson Ranch, California, vol 4, pp 719–762
72. Sá Ferreira RA, Carlos LD, de Zea Bermudez V, Molina C, Dahmouche K, Messaddeq Y, Ribeiro SJL (2003) Room temperature visible/infrared emission and energy transfer in Nd^{3+} -based organic–inorganic hybrids. *J Sol–Gel Sci Technol* 26: 315–319
73. Sá Ferreira RA, Carlos LD, Gonçalves RR, Ribeiro SJL, de Zea Bermudez V (2001) Energy-transfer mechanisms and emission quantum yields in Eu^{3+} -based siloxane-poly(oxyethylene) nanohybrids. *Chem Mater* 13: 2991–2998
74. Gonçalves MC, Silva NJO, de Zea Bermudez V, Sá Ferreira RA, Carlos LD, Dahmouche K, Santilli CV, Ostrovskii D, Correia Vilela IC, Craievich AF (2005) Local structure and near-infrared emission features of neodymium-based amine functionalized organic–inorganic hybrids. *J Phys Chem B* 109: 20093–20104
75. Lima PP, Sá Ferreira RA, Freire RO, Almeida Paz FA, Fu L, Alves Jr S, Carlos LD, Malta OL (2006) Spectroscopic study of a UV-photostable organic–inorganic hybrids incorporating an Eu^{3+} β -diketonate complex. *Chem Phys Chem* 7: 735–746
76. Pope EJA, Mackenzie JD (1986) Sol–gel processing of silica: II. The role of the catalyst. *J Non-Cryst Solids* 87: 185–198
77. Tannev PT, Pinnavaia TJ (1996) Biomimetic templating of porous lamellar silicas by vesicular surfactant assemblies. *Science* 271: 1267–1269
78. Attard GS, Glyde JC, Göltner CG (1995) Liquid-crystalline phases as templates for the synthesis of mesoporous silica. *Nature* 378: 366–367
79. Davis SA, Burkett SL, Mendelson NH, Mann S (1997) Bacterial templating of ordered macrostructures in silica and silica-surfactant mesophases. *Nature* 385: 420–423

80. Burkett SL, Sims SD, Mann S (1996) Synthesis of hybrid inorganic–organic mesoporous silica by co-condensation of siloxane and organosiloxane precursors. *Chem Commun* 11: 1367–1368
81. Stein A, Melde BJ, Schroden RC (2000) Hybrid inorganic–organic mesoporous silicates – nanoscopic reactors coming of age. *Adv Mater* 12: 1403–1419
82. Meng QG, Boutinaud P, Franville A-C, Zhang HJ, Mahiou R (2003) Preparation and characterization of luminescent cubic MCM-48 impregnated with an Eu^{3+} β -diketonate complex. *Micropor Mesopor Mat* 65: 127–136
83. Fu LS, Zhang HJ, Boutinaud P (2001) Preparation, characterization and luminescent properties of MCM-41 type materials impregnated with rare earth complex. *J Mater Sci Technol* 17: 293–298
84. Corriu RJP, Embert F, Guari Y, Mehdi A, Reye C (2001) A simple route to organic–inorganic hybrid materials containing Eu^{3+} complexes. *Chem Commun* 1: 1116–1117
85. Fowler CE, Mann S, Lebeau B (1998) Covalent coupling of an organic chromophore into functionalized MCM-41 mesophases by template-directed co-condensation. *Chem Commun* 17: 1825–1826
86. Fu LS, Sá Ferreira RA, Valente A, Rocha J, Carlos LD (2006) Optically functional nanocomposites with poly(oxyethylene)-based di-ureasils and mesoporous MCM-41. *Micropor Mesopor Mater* 94: 185–192
87. Grosso D, Cagnol F, Soler-Illia GJAA, Crepaldi EL, Amenitsch H, Brunet-Bruneau A, Bourgeois A, Sanchez C (2004) Fundamentals of mesostructuring through evaporation-induced self-assembly. *Adv Funct Mater* 14: 309–322
88. Rhodes KH, Davis SA, Caruso F, Zhang B, Mann S (2000) Hierarchical assembly of zeolite nanoparticles into ordered macroporous monoliths using core-shell building blocks. *Chem Mater* 12: 2832–2834
89. Molina C, Moreira PJ, Gonçalves RR, Sá Ferreira RA, Messaddeq Y, Ribeiro SJL, Soppera O, Leite AP, Marques PVS, de Zea Bermudez V, Carlos LD (2005) Planar and UV written channel optical waveguides prepared with siloxane–poly(oxyethylene)–zirconia organic–inorganic hybrids. Structure and optical properties. *J Mater Chem* 15: 3937–3945
90. André PS, Nogueira R, Sá Ferreira RA, Gualdino A, Carlos LD, Silva NJO, Fu L, Teixeira ALJ, Pellegrini LP, Monteiro P (2006) Low cost UV patternable organic–inorganic sol–gel siloxanepoly(oxyethylene) materials for integrated optics. *Proceedings ICTON 223: WeC16–WeC17*
91. Sá Ferreira RA, Nogueira R, Gualdino A, Carlos LD, Silva NJO, Fu L, Teixeira ALJ, Pellegrino LP, Monteiro P, André PS (2006) Development of integrated photonic waveguides based on organic–inorganic hybrids. *Proceedings of the International Conference on Telecommunications ICT*
92. Schubert U, Völkel T, Moszner N (2001) Mechanical properties of an inorganic–organic hybrid polymer cross-linked by the cluster $\text{Zr}_4\text{O}_2(\text{methacrylate})_{12}$. *Chem Mater* 13: 3811–3812
93. Brankova T, Bekiari V, Lianos P (2003) Photoluminescence from sol–gel organic–inorganic hybrid gels obtained through carboxylic acid solvolysis. *Chem Mater* 15: 1855–1859
94. Carlos LD, de Zea Bermudez V, Sá Ferreira RA, Marques L, Assunção M (1999) Sol–gel derived urea cross-linked organically modified silicates. 2. Blue-light emission. *Chem Mater* 11: 58–588
95. Nunes SC, de Zea Bermudez V, Cybinska J, Sá Ferreira RA, Legendziewicz J, Carlos LD, Silva MM, Smith MJ, Ostrovskii D, Rocha J (2005) Structure and photoluminescent features of di-amide cross-linked alkylene–siloxane hybrids. *J Mat Chem* 15: 3876–3886
96. Carlos LD, Sá Ferreira RA, Orion I, de Zea Bermudez V, Rocha J (2000) Sol–gel derived nanocomposite hybrids for full colour displays. *J Lumin* 87–89: 702–705
97. Sá Ferreira RA, Ferreira AL, Carlos LD (2006) Modelling the emission red-shift in amorphous semiconductors and in organic–inorganic hybrids using extended multiple trapping. *Eur Phys J B* 50: 371–378
98. Sá Ferreira RA, Ferreira AL, Carlos LD (2006) Modelling of the emission red-shift in organic–inorganic di-ureasil hybrids. *J Non-Cryst Solids* 352: 1225–1229

99. Bekiari V, Lianos P, Judeinstein P (1999) Efficient luminescent materials made by incorporation of terbium(III) and 2,2-bipyridine in silica/poly(ethylene oxide) hybrid gels. *Chem Phys Lett* 307: 310–316
100. Han Y, Lin J, Zhang H (2002) Photoluminescence of organic–inorganic hybrid SiO₂ xerogels. *Mater Lett* 54: 389–396
101. Cordoncillo E, Guaita FJ, Escribano P, Philippe C, Viana B, Sanchez C (2001) Blue emitting hybrid organic–inorganic materials. *Opt Mater* 18: 309–320
102. Schmidt T, Lischka K, Zulehner W (1992) Excitation-power dependence of the near-band-edge photoluminescence of semiconductors. *Phys Rev B* 45: 8989–8994
103. Zhuravlev KS, Gilinsky AM, Kobitsky AY (1998) Mechanism of photoluminescence of Si nanocrystals fabricated in a SiO₂ matrix. *Appl Phys Lett* 73: 2962–2964
104. Street RA (1981) Luminescence and recombination in hydrogenated amorphous-silicon. *Adv Phys* 30: 593–676
105. Koyama H, Ozaki T, Koshida N (1995) Decay dynamics of the homogeneously broadened photoluminescence from porous silicon. *Phys Rev B* 52: 11561–11564
106. Wrighton MS, Ginley DS, Morse DL (1974) Technique for the determination of absolute emission quantum yields of powdered samples. *J Phys Chem* 78: 2229–2233
107. Brill A, De Jager-Veenis AW (1976) Quantum efficiency standard for ultraviolet and visible excitation. *J Electrochem Soc* 123: 396–398
108. de Sá GF, Malta OL, de Mello Donegá C, Simas AM, Longo RL, Santa-Cruz PA, Silva Jr EF (2000) Spectroscopic properties and design of highly luminescent lanthanide coordination complexes. *Coord Chem Rev* 196: 165–195
109. de Mello Donegá C, Alves Jr S, de Sá GF (1996) Europium(III) mixed complexes with β-diketones and o-phenanthroline-N-oxide as promising light-conversion molecular devices. *Chem Commun* 10:1199–1200
110. de Mello Donegá C, Ribeiro SJL, Gonçalves RR, Blasse G (1996) Luminescence and non-radiative processes in lanthanide squarate hydrates. *J Phys Chem Solids* 57: 1727–1734
111. Avnir D, Levy D, Reisfeld R (1984) The nature of the silica cage as reflected by spectral changes and enhanced photostability of trapped Rhodamine 6G. *J Phys Chem* 88: 5956–5959
112. Hu L, Jiang Z (1998) Laser action in rhodamine 6G doped titania containing ormosils. *Opt Commun* 148: 275–280
113. Casalboni M, De Matteis F, Proposito P, Pizzoferrato R (1999) Optical investigation of infrared dyes in hybrid thin films. *Appl Phys Lett* 75: 2172–2174
114. Nhung TH, Canva M, Chaput F, Goudket H, Roger G, Brun A, Manh DD, Hung ND, Boilot JP (2004) Dye energy transfer in xerogel matrices and application to solid-state dye lasers. *Opt Commun* 232: 343–351
115. Yang PD, Wirnsberger G, Huang HC, Cordero SR, McGehee MD, Scott B, Deng T, Whitesides GM, Chmelka BF, Buratto SK, Stucky GD (2000) Mirrorless lasing from mesostructured waveguides patterned by soft lithography. *Science* 287: 465–467
116. Hernandez R, Franville A-C, Minoofar P, Dunn B, Zink JI (2001) Controlled placement of luminescent molecules and polymers in mesostructured sol–gel thin films. *J Am Chem Soc* 123: 1248–1249
117. Bartl MH, Boettcher SW, Hu EL, Stucky GD (2004) Dye-activated hybrid organic–inorganic mesostructured titania waveguides. *J Am Chem Soc* 126: 10826–10827
118. Blasse G, Grabmaier BC (1994) *Luminescent Materials*. Springer, Berlin
119. Hüfner S (1978) *Optical Spectra of Transparent Rare Earth Compounds*. Academic Press, New York
120. Lehn J-M (1990) Perspectives in supramolecular chemistry – from molecular recognition towards molecular information processing and self-organization. *Angew Chem Int Ed Engl* 29:1304–1319
121. Sabbatini N, Guardigli M, Lehn J-M (1993) Luminescent lanthanide complexes as photochemical supramolecular devices. *Coord Chem Rev* 123: 201–228

122. McGehee MD, Bergstedt T, Zhang C, Saab AP, O'Regan MB, Bazan GC, Srdanov VI, Heeger AJ (1999) Narrow bandwidth luminescence from blends with energy transfer from semiconducting conjugated polymers to europium complexes. *Adv Mater* 11: 1349–1354
123. Adachi C, Baldo MA, Forrest SR (2000) Electroluminescence mechanisms in organic light emitting devices employing a europium chelate doped in a wide energy gap bipolar conducting host. *J Appl Phys* 87: 8049–8055
124. Werts MHV, Woudenberg RH, Emmerink PG, van Gassel R, Hofstraat JW, Verhoeven JW (2000) A near-infrared luminescent label based on YbIII ions and its application in a fluorooimmunoassay. *Angew Chem Int Ed* 39: 4542–4544
125. Kido J, Okamoto Y (2002) Organo lanthanide metal complexes for electroluminescent materials. *Chem Rev* 102: 2357–2368
126. Reyes R, Cremona M, Teotônio EES, Brito HF, Malta OL (2004) Voltage color tunable OLED with (Sm,Eu)- β -diketonate complex blend. *Chem Phys Lett* 396: 54–58
127. Reyes R, Cremona M, Teotônio EES, Brito HF, Malta OL (2004) Electrophosphorescence emission in organic light-emitting diodes based on (Sm + Eu) complexes. *Thin Solid Films* 469: 59–64
128. Bünzli J-CG, Piguet C (2005) Taking advantage of luminescent lanthanide ions. *Chem Soc Rev* 34: 1048–1077
129. Binnemans K (2005) Rare-earth beta-diketonates. In: Gschneidner Jr KA, Bünzli J-CG, Pecharsky VK (eds) *Handbook on the Physics and Chemistry of Rare Earths*. Elsevier, Amsterdam, vol 35, pp 107–272
130. Gawryszewska P, Sokolnicki J, Legendziewicz J (2005) Photophysics and structure of selected lanthanide compounds. *Coord Chem Rev* 249: 2489–2509
131. Samelson H, Lempicki A, Brecher C, Brophy VA (1964) Room temperature operation of europium chelate liquid laser. *Appl Phys Lett* 5: 173–174
132. Björklun S, Kellerman G, Hurt CR, Mcavoy N, Filipesc N (1967) Laser action from terbium trifluoroacetylacetonate in rho-dioxane and acetonitrile at room temperature. *Appl Phys Lett* 10: 160–162
133. Whittaker B (1970) Low threshold laser action of a rare earth chelate in liquid and solid host media. *Nature* 228: 157–158
134. Carlos LD, De Mello Donega C, Albuquerque RQ, Alves Jr S, Menezes JFS, Malta OL (2003) Highly luminescent Europium(III) complexes with naphthoiltrifluoroacetone and dimethyl sulfoxide. *Mol Phys* 101: 1037–1045
135. Gameiro CG, Achete CA, Simão RA, da Silva Jr EF, Santa-Cruz PA (2002) Molecular UV dosimeters of lanthanide complex thin films: AFM as a function of ultraviolet exposure. *J Alloys Comp* 344: 385–388
136. Gameiro CG, da Silva Jr EF, Alves Jr S, de Sá GF, Santa-Cruz PA (2001) Lanthanide complexes dispersed in enamel: a promising new material for photonic devices. *J Alloys Comp* 323–324: 820–823
137. Nockemann P, Beurer E, Driessen K, Van Deun R, Van Hecke K, Van Meervelt L, Binnemans K (2005) Photostability of a highly luminescent europium -diketonate complex in imidazolium ionic liquids. *Chem Commun* 34: 4354–4356
138. Pagnot T, Audebert P, Tribillon G (2000) Photostability study of europium dibenzolymethide embedded in polystyrene thin films with high concentration. *Chem Phys Lett* 322: 572–578
139. Qian G, Wang M (2000) Synthesis in situ, characterization, and photostability of europium β -diketonate chelates in organically modified silicates (ORMOSILs). *J Am Ceram Soc* 83: 703–708
140. Xu Q, Li L, Li B, Yu J, Xu R (2000) Encapsulation and luminescent property of tetrakis (1-(2-thenoyl)-3,3,3-trifluoroacetate) europium N-hexadecyl pyridinium in modified Si-MCM-41. *Micropor Mesopor Mat* 38: 351–358
141. Matthews LR, Knobbe ET (1993) Luminescence behavior of europium complexes in sol-gel derived host materials. *Chem Mater* 5: 1697–1700

142. Matthews LR, Wang X-J, Knobbe ET (1994) Concentration effects on the luminescence behavior of europium (III) chloride- and organoeuropium-doped silicate gels. *J Non-Cryst Solids* 178: 44–51
143. Serra OA, Nassa EJ, Zapparolli G, Rosa ILV (1994) Organic complexes of Eu^{3+} supported in functionalized silica gel: highly luminescent material. *J Alloys Compd* 207–208: 454–456
144. Serra OA, Nassa EJ, Rosa ILV (1997) Tb^{3+} molecular photonic devices supported on silica gel and functionalized silica gel. *J Lumin* 72–74: 263–265
145. Jin T, Inoue S, Tsutsumi S, Machida K, Adachi G (1998) Luminescence properties of lanthanide complexes incorporated into sol–gel derived inorganic–organic composite materials. *J Non-Cryst Solids* 223: 123–132
146. Li H, Inoue S, Machida K, Adachi G (1999) Preparation and luminescence properties of organically modified silicate composite phosphors doped with an europium(III) β -diketonate complex. *Chem Mater* 11: 3171–3176
147. Li H, Inoue S, Machida K, Adachi G (2000) Preparation and luminescence properties of inorganic–organic hybrid materials doped with lanthanide (III) complexes. *J Lumin* 87–89: 1069–1072
148. Kurokawa Y, Ishizaka T, Ikoma T, Tero-Kubota S (1998) Photo-properties of rare earth ion (Er^{3+} , Eu^{3+} and Sm^{3+})-doped alumina films prepared by the sol–gel method. *Chem Phys Lett* 287: 737–741
149. Zaiton MA, Kim T, Lin CT (1998) Observation of electron-hole carrier emission in the Eu^{3+} -doped silica xerogel. *J Phys Chem B* 102: 1122–1125
150. Zaiton MA, Goken DM, Bailey LS, Kim T, Lin CT (2000) Thermoanalysis and emission properties of $\text{Eu}^{3+}/\text{Eu}^{2+}$ in Eu^{3+} -doped xerogels. *J Phys Chem B* 104: 189–196
151. Tanner PA, Yan B, Zhang HJ (2000) Preparation and luminescence properties of sol–gel hybrid materials incorporated with europium complexes. *J Mater Sci* 35: 4325–4328
152. Ji X, Li B, Jiang S, Dong D, Zhang H, Jing XB, Jiang BZ (2000) Luminescent properties of organic–inorganic hybrid monoliths containing rare-earth complexes. *J Non-Cryst Solids* 275: 52–58
153. Li HR, Zhang HJ, Lin J, Wang SB, Yang KY (2000) Preparation and luminescence properties of ormosil material doped with $\text{Eu}(\text{TTA})_3\text{phen}$ complex. *J Non-Cryst Solids* 278: 218–222
154. Molina C, Dahmouche K, Santilli CV, Craievich AF, Ribeiro SJL (2001) Structure and luminescence of Eu^{3+} -doped class I siloxane-poly(ethylene glycol) hybrids. *Chem Mater* 13: 2818–2823
155. Ishizaka T, Nozaki R, Kurokawa Y (2002) Luminescence properties of Tb^{3+} and Eu^{3+} -doped alumina films prepared by sol–gel method under various conditions and sensitized luminescence. *J Phys Chem Solids* 63: 613–617
156. Cordoncillo E, Viana B, Escribano P, Sanchez C (1998) Room temperature synthesis of hybrid organic–inorganic nanocomposites containing Eu^{2+} . *J Mater Chem* 8: 507–509
157. Franville A-C, Zambon D, Mahiou R, Chou S, Troin Y, Cousseins JC (1998) Synthesis and optical features of an europium organic–inorganic silicate hybrid. *J Alloys Compd* 275–277: 831–834
158. Franville A-C, Zambon D, Mahiou R, Troin Y (2000) Luminescence behavior of sol–gel-derived hybrid materials resulting from covalent grafting of a chromophore unit to different organically modified alkoxysilanes. *Chem Mater* 12: 428–435
159. Franville A-C, Mahiou R, Zambon D, Cousseins J-C (2001) Molecular design of luminescent organic–inorganic hybrid materials activated by europium (III) ions. *Solid State Sci* 3: 211–222
160. Dong D, Jiang S, Men Y, Ji X, Jiang B (2000) Nanostructured hybrid organic–inorganic lanthanide complex films produced in situ via a sol–gel approach. *Adv Mater* 12: 646–649
161. Embert F, Mehdi A, Reyé C, Corriu RJP (2001) Synthesis and luminescence properties of monophasic organic–inorganic hybrid materials incorporating europium(III). *Chem Mater* 13: 4542–4549
162. Xu QH, Fu L, Li LS, Zhang HJ, Xu RR (2000) Preparation, characterization and photophysical properties of layered zirconium bis(monohydrogenphosphate) intercalated with rare earth complexes. *J Mater Chem* 10: 2532–2536

163. Fu LS, Meng QG, Zhang HJ, Wang SB, Yang KY, Ni JZ (2000) In situ synthesis of terbium-benzoic acid complex in sol–gel derived silica by a two-step sol–gel method. *J Phys Chem Solids* 61: 1877–1881
164. Liu F, Fu L, Wang J, Liu Z, Li H, Zhang H (2002) Luminescent hybrid films obtained by covalent grafting of terbium complex to silica network. *Thin Solid Films* 419: 178–182
165. Li HR, Lin J, Zhang HJ, Fu L, Meng QG, Wang (2002) Preparation and luminescence properties of hybrid materials containing Europium(III) complexes covalently bonded to a silica matrix. *Chem Mater* 14: 3651–3655
166. Guo JF, Fu L, Li HR, Zheng YX, Meng QG, Wang SB, Liu FY, Wang J, Zhang HJ (2003) Preparation and luminescence properties of ormosil hybrid materials doped with Tb(Tfacac)₃phen complex via a sol–gel process. *Mat Lett* 57: 3899–3903
167. Liu F, Fu L, Wang J, Meng Q, Li H, Guo J, Zhang H (2004) Preparation and luminescence properties of in situ formed lanthanide complexes covalently grafted to a silica network. *New J Chem* 28: 1137–1141
168. Sun LN, Zhang HJ, Meng QG, Liu FY, Fu L, Peng CY, Yu JB, Zheng GL, Wang SB (2005) Near-infrared luminescent hybrid materials doped with lanthanide (Ln) complexes (Ln = Nd, Yb) and their possible laser application. *J Phys Chem B* 109: 6174–6182
169. Sun LN, Zhang HJ, Fu L, Liu FY, Meng QG, Peng CY, Yu JB (2005) A new sol–gel material doped with an erbium complex and its potential optical-amplification application. *Adv Funct Mater* 15: 1041–1048
170. Bredol M, Jüstel T, Gutzow S (2001) Luminescence of sol–gel-derived silica doped with terbium-benzoate complex. *Opt Mater* 18: 337–341
171. Binnemans K, Lenaerts P, Driesen K, Görrler-Walrand C (2004) A luminescent tris(2-thenoyltrifluoroacetato)europium(III) complex covalently linked to a 1,10-phenanthroline-functionalised sol–gel glass. *J Mater Chem* 14: 191–195
172. Driesen K, Van Deun R, Görrler-Walrand C, Binnemans K (2004) Near-infrared luminescence of lanthanide calcein and lanthanide dipicolinate complexes doped into a silica-peg hybrid material. *Chem Mater* 16: 1531–1535
173. Lenaerts P, Storms A, Mullens J, D’Haen J, Görrler-Walrand C, Binnemans K, Driesen K (2005) Thin films of highly luminescent lanthanide complexes covalently linked to an organic–inorganic hybrid material via 2-substituted imidazo[4,5-f]-1,10-phenanthroline groups. *Chem Mater* 17: 5194–5201
174. Lenaerts P, Görrler-Walrand C, Binnemans K (2006) Luminescent europium(III) and terbium(III) nicotinate complexes covalently linked to a 1,10-phenanthroline functionalised sol–gel glass. *J Lumin* 117: 163–169
175. de Zea Bermudez V, Carlos LD, Duarte MC, Silva MM, Silva CJ, Smith MJ, Assunção M, Alcácer L (1998) Novel class of luminescent polymers obtained by the sol–gel approach. *J Alloys Compd* 275–277: 21–26
176. Carlos LD, de Zea Bermudez V, Sá Ferreira RA (1999) Multi-wavelength europium-based hybrid phosphors. *J Non-Cryst Solids* 247: 203–208
177. Silva MM, de Zea Bermudez V, Carlos LD, Passos de Almeida AP, Smith MJ (1999) Sol–gel processing and structural study of europium-doped hybrid materials. *J Mater Chem* 9: 1735–1740
178. Carlos LD, Sá Ferreira RA, de Zea Bermudez V, Molina C, Bueno LA, Ribeiro SJL (1999) White light emission of Eu³⁺-based hybrid xerogels. *Phys Rev B* 60: 10042–10053
179. Carlos L D, Sá Ferreira R A, de Zea Bermudez V (2000) An intra-Nd³⁺ visible to infrared conversion process in hybrid xerogels. *Electrochimica Acta* 45: 1555–1560
180. de Zea Bermudez V, Sá Ferreira RA, Carlos LD, Molina C, Ribeiro SJL (2001) Coordination of Eu³⁺ ions in siliceous nanohybrids containing short polyether chains and bridging urea cross-links. *J Phys Chem B* 105: 3378–3386
181. de Zea Bermudez V, Ostrovskii D, Gonçalves MC, Carlos L D, Sá Ferreira R A, Reis L, Jacobsson P (2004) Urethane cross-linked poly(oxyethylene)/siliceous nanohybrids doped with Eu³⁺ ions Part 1. Coordinating ability of the host matrix. *Phys Chem Chem Phys* 6: 638–648

182. de Zea Bermudez V, Ostrovskii D, Lavoryk S, Gonçalves MC, Carlos LD (2004) Urethane cross-linked poly(oxyethylene)/siliceous nanohybrids doped with Eu^{3+} ions Part 2. Ionic association. *Phys Chem Chem Phys* 6: 649–658
183. Carlos LD, Sá Ferreira RA, Gonçalves MC, de Zea Bermudez V (2004) Local coordination of $\text{Eu}(\text{III})$ in organic–inorganic amine functionalized hybrids. *J Alloys Compd* 374: 50–55
184. de Zea Bermudez V, Ostrovskii D, Gonçalves MC, Lavoryk S, Carlos LD, Sá Ferreira RA (2005) Eu^{3+} coordination in an organic–inorganic hybrid matrix with methyl end-capped short polyether chains. *J Phys Chem B* 109: 7110–7119
185. Nunes SC, de Zea Bermudez V, Sá Ferreira RA, Carlos LD, Morales E, Marques PVS, In: Organic–Inorganic Hybrid Materials-2004, Sanchez C, Schubert U, Laine RM, Chujo Y (eds) *Mater Res Soc Symp Proc*, Warrendale, PA, 2005, Vol 847, EE13311–6
186. Fu LS, Sá Ferreira RA, Silva NJO, Fernandes JA, Ribeiro-Claro P, Gonçalves IS, de Zea Bermudez V, Carlos LD (2005) Structure–photoluminescence relationship in $\text{Eu}(\text{III})$ β -diketonate-based organic–inorganic hybrids. Influence of the synthesis method: carboxylic acid solvolysis versus conventional hydrolysis. *J Mater Chem* 15: 3117–3125
187. Lima PP, Pavithran R, Sá Ferreira RA, Alves Jr S, Carlos LD, Malta OL, Reddy MLP (2006) Synthesis, characterization, and luminescence properties of Eu^{3+} 3-phenyl-4-(4-toluoyl)-5-isoxazonate based organic–inorganic hybrids. *Eur J Inorg Chem* 3923–3929
188. Ribeiro SJL, Dahmouche K, Ribeiro CA, Santilli CV, Pulcinelli SH (1998) Study of hybrid silica-polyethyleneglycol xerogels by Eu^{3+} luminescence spectroscopy. *J Sol–Gel Sci Technol* 13: 427–432
189. Dahmouche K, Santilli CV, Pulcinelli SH, Craievich AF (1999) Small-angle X-ray scattering study of sol–gel-derived siloxane-PEG and siloxane-PPG hybrid materials. *J Phys Chem B* 103: 4937–4942
190. Dahmouche K, Santilli CV, da Silva M, Ribeiro CA, Pulcinelli SH, Craievich AF (1999) Silica-PEG hybrid ormolytes: structure and properties. *J Non Cryst Solids* 247: 108–113
191. Molina C, Ribeiro SJL, Dahmouche K, Santilli CV, Craievich AF (2000) EXAFS, SAXS and Eu^{3+} luminescence spectroscopy of sol–gel derived siloxane-polyethyleneoxide hybrids. *J Sol–Gel Sci Tech* 19: 615–620
192. Dahmouche K, Carlos LD, de Zea Bermudez V, Sá Ferreira RA, Passos de Almeida AP, Santilli CV, Craievich AF (2001) Structural modelling of Eu^{3+} -based siloxane–poly(oxyethylene) nanohybrid. *J Mater Chem* 11: 3249–3257
193. Molina C, Dahmouche K, Messaddeq Y, Ribeiro SJL, Silva MAP, de Zea Bermudez V, Carlos LD (2003) Enhanced emission from $\text{Eu}(\text{III})$ β -diketonate complex combined with ether-type oxygen atoms of di-ureasil organic–inorganic hybrids. *J Lumin* 104: 93–101
194. Filho FAD, Ribeiro SJL, Gonçalves RR, Messaddeq Y, Carlos LD, de Zea Bermudez V, Rocha J (2004) Eu^{3+} doped polyphosphate–aminosilane organic–inorganic hybrids. *J Alloys Compd* 374: 74–78
195. Dahmouche K, Santilli CV, Pulcinelli SH, Sá Ferreira RA, Carlos LD, de Zea Bermudez V, Craievich AF (2006) Nanostructure and luminescent properties of sol–gel derived europium-doped amine functionalised hybrids. *J Sol–Gel Sci Tech* 37: 99–104
196. Moleski R, Stathatos E, Bekiari V, Lianos P (2002) Preparation of thin Ureasil films with strong photoluminescence based on incorporated europium–thenoyltrifluoroacetone–bipyridine complexes. *Thin Solid Films* 416: 279–283
197. Stathatos E, Lianos P, Lavrencic-Stangar U, Orel B (2002) A high-performance solid-state dye-sensitized photoelectrochemical cell employing a nanocomposite gel electrolyte made by the sol–gel route. *Adv Mater* 14: 354–357
198. Pope EJA, Mackenzie JD (1988) Nd-doped silica glass I: structural evolution in the sol–gel state. *J Non-Cryst Solids* 106: 236–241
199. Viana B, Koslova N, Ashehoug P, Sanchez C (1995) Optical properties of neodymium and dysprosium doped hybrid siloxane–oxide coatings. *J Mater Chem* 5: 719–724
200. Lochhead MJ, Bray KL (1995) Rare-Earth clustering and aluminum codoping in sol–gel silica: investigation using europium(III) fluorescence spectroscopy. *Chem Mater* 7: 572–577

201. Costa VC, Lochhead MJ, Bray KL (1996) Fluorescence line-narrowing study of Eu^{3+} -doped sol–gel silica: effect of modifying cations on the clustering of Eu^{3+} . *Chem Mater* 8: 783–790
202. Driesen K, Fourier S, Görrler-Walrand C, Binnemans K (2003) Judd–Ofelt analysis of lanthanide doped silica–PEG hybrid sol–gels. *Phys Chem Chem Phys* 5: 198–202
203. Guo XM, Fu L, Zhang HJ, Carlos LD, Peng CY, Guo JF, Yu JB, Deng RP, Sun LN (2005) Incorporation of luminescent lanthanide complex inside the channels of organically modified mesoporous silica via template-ion exchange method. *New J Chem* 29: 1351–1358
204. Gago S, Fernandes JA, Rainho JP, Sá Ferreira RA, Pillinger M, Valente AA, Santos TM, Carlos LD, Ribeiro-Claro PJA, Gonçalves IS (2005) Highly luminescent tris(β -diketonate) europium(III) complexes immobilized in a functionalized mesoporous silica. *Chem Mater* 17: 5077–5084
205. Sun LN, Zhang HJ, Peng CY, Yu JB, Meng QG, Fu L, Liu FY, Guo XM (2006) covalent linking of near-infrared luminescent ternary lanthanide (Er^{3+} , Nd^{3+} , Yb^{3+}) complexes on functionalized mesoporous MCM-41 and SBA-15. *J Phys Chem B* 110: 7249–7158
206. Pinna N, Garnweitner G, Beato P, Niederberger M, Antonietti M (2005) Synthesis of yttria-based crystalline and lamellar nanostructures and their formation mechanism. *Small* 1: 112–121
207. Karmaoui M, Sá Ferreira RA, Mane AT, Carlos LD, Pinna N (2006) Lanthanide-based lamellar nanohybrids: synthesis, structural characterization, and optical properties. *Chem Mater* 18: 4493–4499
208. Sá Ferreira RA, Karmaoui M, Nobre SS, Carlos LD, Pinna N (2006) Optical properties of lanthanide-doped lamellar nanohybrids. *ChemPhysChem* 7: 2215–2222
209. Karmaoui M, Sá Ferreira RA, Carlos LD, Pinna N (2007) Lanthanide-based lamellar nanohybrids: the case of erbium. *Mater Sci Eng: C* 27: 1368–1371
210. Isakawi M, Kuraki J, Ito S (1998) Preparation of Ce^{3+} -doped inorganic–organic hybrid materials using functionalized silanes. *J Sol–Gel Sci Technol* 13: 587–591
211. Reisfeld R, Jørgenson CK (1987) In: Gschneider KA Jr., Eyring L (eds) *Handbook on the Physics and Chemistry of Rare Earths*. Elsevier Science, Amsterdam, vol. 9, pp. 61
212. Malta OL, dos Santos MAC, Thompson LC, Ito NK (1996) Intensity parameters of 4f–4f transitions in the $\text{Eu}(\text{dipivaloylmethanate})(3) 1,10\text{-phenanthroline}$ complex. *J Lumin* 69: 77–84
213. Malta OL, Brito HF, Menezes JFS, Silva FRGE, Alves S, Farias FS, de Andrade AVM (1997) Spectroscopic properties of a new light-converting device $\text{Eu}(\text{thenoyltrifluoroacetate})(3) 2(\text{dibenzyl sulfoxide})$. A theoretical analysis based on structural data obtained from a sparkle model. *J Lumin* 75: 255–268
214. Carnall WT, Crosswhite H, Crosswhite HM (1977) Energy structure and transition probabilities of the trivalent lanthanides in LaF_3 . Argonne National Laboratory Report, unnumbered
215. Werts MHV, Jukes RTF, Verhoeven JW (2002) The emission spectrum and the radiative lifetime of Eu^{3+} in luminescent lanthanide complexes. *Phys Chem Chem Phys* 4: 1542–1548
216. Li H, Inoue S, Ueda D, Machida K, Adachi G (1999) Preparation of transparent inorganic–organic composite phosphors incorporated with europium (III) complexes. *Electrochem Solid State Lett* 2: 354–356
217. Hazenkamp MF, Blasse G (1999) Rare-earth ions adsorbed onto porous-glass – luminescence as a characterizing tool. *Chem Mater* 2: 105–110
218. Malta OL, Carlos LD (2003) Intensities of 4f–4f transitions in glass materials. *Quimica Nova* 26: 889–895
219. Carlos LD, Videira ALL (1994) Emission-spectra and local symmetry of the Eu^{3+} ion in polymer electrolytes. *Phys Rev B* 49: 11721–11728
220. Horrocks Jr WD, Sudnick DR (1979) Lanthanide ion probes of structure in biology – laser-induced luminescence decay constants provide a direct measure of the number of metal-coordinated water-molecules. *J Am Chem Soc* 101: 334–340

221. Supkowski RM, Horrocks Jr WD (2002) On the determination of the number of water molecules, q , coordinated to europium(III) ions in solution from luminescence decay lifetimes. *Inorganica Chimica Acta* 340: 44–48
222. Auzel F, Malta OL (1983) A scalar crystal-field strength parameter for rare-earth ions – meaning and usefulness. *J Physique* 44: 201–206
223. Malta OL, Antic-Fidancev E, Lemaitre-Blaise M, Milicic-Tang A, Taibi M (1995) The crystal-field strength parameter and the maximum splitting of the 7F_1 manifold of the Eu^{3+} ion in oxides. *J Alloys Compd* 228: 41–44
224. Leavitt RP (1982) On the role of certain rotational invariants in crystal-field theory. *J Chem Phys* 77: 1661–1663
225. Jørgensen CK (1962) *Progr Inorg Chem* 4:73
226. Newman DJ (1973) Slater parameter shifts in substituted lanthanide ions. *J Phys Chem Solids* 34: 541–545
227. Carlos LD, Videira ALL (1994) A mean radius for the first coordination shell in lanthanides. *J Chem Phys* 101: 8827–8830
228. Malta OL, Batista HJ, Carlos LD (2002) Overlap polarizability of a chemical bond: a scale of covalency and application to lanthanide compounds. *Chem Phys* 282: 21–30
229. Frey ST, De Horrocks Jr W (1995) On correlating the frequency of the ${}^7F_0 \rightarrow {}^5D_0$ transition in Eu^{3+} complexes with the sum of nephelauxetic parameters for all of the coordinating atoms. *Inorg Chim Acta* 229: 383–390
230. Carlos LD, Malta OL, Albuquerque RQ (2005) A covalent fraction model for lanthanide compounds. *Chem Phys Lett* 415: 238–242
231. Jørgensen CK, Judd BR (1964) Hypersensitive pseudoquadrupole transitions in lanthanides. *Mol Phys* 8: 281–290
232. Etienne P, Coudray P, Moreau Y, Porque J (1998) Photocurable sol–gel coatings: channel waveguides for use at 1.55 μm . *J Sol–Gel Sci Tech* 13: 523–527
233. Najafi SI, Li CY, Andrews M, Chiesham J, Lefebvre P, Mackenzie JD, Peyghambarian N (1995) Integrated optics devices by ultraviolet light imprinting in sol–gel silica glass. In: Armenise MN, Wong K.-K (eds) *Functional Photonics Integrated Circuits*. SPIE, Washington vol 2401, pp 110–115
234. Moreau Y, Arguel P, Coudray P, Etienne P, Porque J, Signoret P (1998) Direct printing of gratings on sol–gel layers. *Opt Eng* 37: 1130–1135
235. Sá Ferreira RA, Molina C, Dahmouche K, Ribeiro SJL, Gonçalves RR, de Zea Bermudez V, Carlos LD (2005) Photoluminescence-structure relationships in ormosils for integrated optical devices. *Mater Res Soc Symp Proc* 847: EE10.7.1–EE10.7.6
236. Kahlenberg F, Popall M (2006) ^{ORMOCER®} (organic–inorganic hybrid polymers) for telecom applications: structure/property correlations. *Mater Res Soc Symp Proc* 847: EE14.4.1
237. Etienne P, Coudray P, Porque J, Moreau Y (2000) Active erbium-doped organic–inorganic waveguide. *Opt Commun* 174: 413–418
238. Xiao-lei Z, Dennis L (2002) Sol–gel glass distributed feedback waveguide laser. *Appl Phys Lett* 80: 917–919
239. Zhang Y, Prasad PN, Burzynski R (1992) Second-order nonlinear optical properties of N-(4-nitrophenyl)-(s)-prolinol-doped sol–gel-processed materials. *Chem Mater* 4: 851–855
240. Nosaka Y, Tohriwa N, Kobayashi T, Fujii N (1993) Two-dimensionally poled sol–gel processing of titania film doped with organic compounds for nonlinear optical activity. *Chem Mater* 5: 930–932
241. Lebeau B, Sanchez C, Brasselet S, Zyss J, Froc G, Dumont M (1996) Large second-order nonlinearities in azo dyes grafted hybrid sol–gel coat. *New J Chem* 20: 13–18
242. Jiang H, Kakkar AK (1998) From simple acid-base hydrolytic chemistry to soluble high T_g inorganic–organic hybrid materials with large and stable second-order nonlinear optical susceptibilities. *Adv Mater* 10: 1093–1097
243. Innocenzi P, Miorin E, Brusatin G, Abbotto A, Beverina L, Pagani GA, Casalboni M, Sarcinelli F, Pizzoferrato R (2002) Incorporation of zwitterionic push-pull chromophores into hybrid organic–inorganic matrixes. *Chem Mater* 14: 3758–3766

244. Innocenzi P, Brusatin G, Abboto A, Beverina L, Pagani GA, Casalboni M, Sarcinelli F, Pizzoferrato R (2003) Entrapping of push-pull zwitterionic chromophores in hybrid matrices for photonic applications. *J Sol–Gel Sci Technol* 26: 967–970
245. Izawa K, Okamoto N, Sugihara O (1993) Stable and large second harmonic generation in sol–gel-processed poled silica waveguides doped with organic azo dye. *Jpn J Appl Phys* 32: 807–811
246. Innocenzia P, Lebeau B (2005) Organic–inorganic hybrid materials for non-linear optics. *J Mater Chem* 15: 3821–3831
247. Lee K-S, Kim T-D, Min YH, Yoon CS (2001) NLO activities of novel sol–gel processed systems with three different bonding directions. *Synth Met* 117: 311–313
248. Rosso V, Loicq J, Renotte Y, Lion Y (2004) Optical non-linearity in Disperse Red 1 dye-doped sol–gel. *J Non-Cryst Solids* 342: 140–145
249. Zhang X, Cao Z, Yang K, Long G (1998) Preparation and third-order non-linear optical property of rhodamine-6G-doped SiO_2 - TiO_2 sol–gel thin films. *Proc SPIE* 3175: 302–305
250. Gall GJ, King TA, Oliver SN, Capozzi CA, Seddon AB, Hill CAS, Underhill AE (1994) Third-order nonlinear optical properties of metal dithiolene- and phthalocyanine-doped sol–gel materials. *Proc SPIE* 2288: 372–381
251. Han W-T (1999) Synthesis and linear and non-linear optical properties of (0.8PPV + 0.2DMPPV)/silica glass composites by sol–gel process. *J Non-Cryst Solids* 259: 107–115
252. Watanabe T, Zhou HS, Honma I, Asai K, Ishigure K (2000) Synthesis and nonlinear optical susceptibility of cyanine dye J-aggregate doped silica film (I). *J Sol–Gel Sci Technol* 19: 257–261
253. Zhou HS, Watanabe T, Mito A, Asai K, Ishigure K, Honma I (2000) Synthesis and nonlinear optical susceptibility of cyanine dye J-aggregates doped silica film (II). *J Sol–Gel Sci Technol* 19: 803–806
254. Nakamura M, Nasu H, Kamiya K (1991) Preparation of organic dye-doped SiO_2 gels by the sol–gel process and evaluation of their optical non-linearity. *J Non-Cryst Solids* 135: 1–7
255. Yuwono AH, Xue J, Wang J, Elim HI, Ji W, Li Y, White TJ (2003) Transparent nanohybrids of nanocrystalline TiO_2 in PMMA with unique nonlinear optical behavior. *J Mater Chem* 13: 1475–1479
256. Yuwono AH, Liu B, Xue J, Wan J, Elim HI, Ji W, Li Y, White TJ (2004) Controlling the crystallinity and nonlinear optical properties of transparent TiO_2 –PMMA nanohybrids. *J Mater Chem* 14: 2978–2987
257. Wang SX, Zhang LD, Su H, Zhang ZP, Li GH, Meng GW, Zhang J, Wang YW, Fan JC, Gao T (2001) Two-photon absorption and optical limiting in poly(styrene maleic anhydride)/ TiO_2 nanocomposites. *Phys Lett A* 281: 59–63
258. Wu X, Wang R, Zou B, Wu P, Wang L, Xu J, Huang W (1997) The effects of different interfacial environments on the optical nonlinearity of nanometer-sized CdO organosol. *Appl Phys Lett* 71: 2097–2099
259. Li C-Y, Kao Y-H, Hayashi K, Takada T, Mackenzie JD, Kang KI, Lee S-G, Peyghambarian N, Yamane M, Zhang G-W, Najafi SI (1994) Improving CdS quantum-dot materials by the sol–gel method. *Proc SPIE* 2288: 151–162
260. Takada T, Yano T, Yasumori A, Yamane M, Mackenzie JD (1992) Preparation of quantum-size CdS-doped $\text{Na}_2\text{O} \cdot \text{B}_2\text{O}_3 \cdot \text{SiO}_2$ glasses with high non-linearity. *J Non-Cryst Solids* 147: 631–635
261. Martucci A, Innocenzi P, Fick J, Mackenzie JD (1999) Zirconia-ormosil films doped with PbS quantum dots. *J. Non-Cryst Solids* 244: 55–62
262. Corriu RJP, Mehdi A, Rey C, Thieuleux C, Frenkel A, Gibaud A (2004) Preparation of ordered SBA-15 mesoporous silica containing chelating groups. Study of the complexation of EuIII inside the pore channels of the materials. *New J Chem* 28: 156–160
263. de Zea Bermudez V, Carlos LD, Alcácer L (1999) Sol–gel derived urea cross-linked organically silicates. 1. Room temperature mid-infrared spectra. *Chem Mater* 11: 569–580

264. Dunn B, Zink JI (1991) Optical properties of sol–gel glasses doped with organic molecules. *J Mater Chem* 1: 903–914
265. Klein LL, Sanchez C (1995) Hybrid organic–inorganic materials. *J Sol–Gel Sci Tech* 5: 75–76
266. Vogel R, Meredith P, Kartini I, Harvey M, Riches JD, Bishop A, Heckenberg N, Trau M, Rubinsztein-Dunlop H (2003) Mesostructured dye-doped titanium dioxide for micro-optoelectronic applications. *ChemPhysChem* 4: 595–603
267. Xu J, Aubonnet S, Barry HF, MacCraith BD (2003) Preparation and characterization of erbium-doped ormosil planar waveguides. *Mater Lett* 57: 4276–4281

Chapter 13

Highly Photosensitive Sol–Gel Hybrid Nano Materials for Direct Photo-Fabrication of Micro-Optical Elements

Byeong-Soo Bae

Abstract In this review/chapter, the photosensitivity mechanisms in the sol–gel hybrid nanomaterials are covered with the aim of showing how large photoinduced changes in the refractive index and/or volume can be obtained. Applying the photo-fabrication technique to these highly photosensitive sol–gel hybrid nanomaterials, a series of micro-optical elements such as diffractive gratings, optical waveguides, and microlenses are described. The emphasis is laid on the advantages brought by such hybrid materials over many conventional photosensitive polymers or glasses, for practical application of the directly photo-fabricated micro-optical elements in optical communication, optical data storage, information displays, sensing, and imaging systems.

13.1 Introduction

Micro-optics is gaining increasing attention in recent years because of its potential applications in optical communication, optical data storage, information displays, sensing, and imaging systems [1–7]. Micro-optical elements, such as gratings, holograms, waveguides, microlenses, etc., of either refractive or diffractive types, can be realized/seen as continuous surface relief microstructures or as binary or multilevel relief. For the surface relief microstructures, several processing and manufacturing techniques as well as material categories have been introduced for micro-optics fabrication [1, 7, 8]. Conventional micro-optics fabrication uses a multi-step process, that includes patterning of a deposited photoresist film using mask lithography (UV or X-ray) or scanning lithography (laser or electron-beam scanning) followed by a development process. After patterning of the photoresist, reflow (or melting) process can be applied to further modify the shape of the

B.-S. Bae

Laboratory of Optical Materials and Coating (LOMC), Department of Materials Science and Engineering, Korea Advanced Institute of Science and Technology (KAIST), Daejeon, 305-701, Republic of Korea
e-mail: bsbae@kaist.ac.kr

photoresist. The resulting patterned resist surfaces can then be etched directly into the underlying material by using wet or dry etch transfer or used to produce tools suitable for replication. Conventional etch transfer processes are typically applied to materials that require high deposition temperatures, limiting the selection of the substrate materials. Conventional etch transfer techniques are well established methods but usually time consuming and expensive, especially when large etch depth is required. Thus, the etch transfer techniques are most suitable for fabrication of diffractive and refractive optical structures with small dimensions. Simpler photolithographic method to photo-pattern directly the micro-optical structures on a photoresist polymer without use of etch transfer process has been used. Replication of micro-optical structures can be also performed by embossing, casting, injection and compression moldings using polymers, glasses, or sol-gel materials [9–16]. The LIGA and diamond-turning techniques as well as laser micro-machining of optical structures into substrate materials have also been applied in the replication of tool fabrication [17–22]. More recently, non-lithographic techniques such as inkjet printing of optical structures using polymers and sol-gel materials have been investigated for micro-optics fabrication [23–26]. Plastic and glass molding techniques are also widely applied in micro-optics fabrication. By using molding techniques, large structure heights can be achieved. However, the mechanical machining and molding techniques are not always well suited for use with electronic components that are complex and relatively brittle. For glass and ceramic molding, high temperature is required during fabrication, which may eliminate various integration options. On the other hand, the plastic molding using polymers in micro-optics fabrication has a limitation due to their lack of thermal and chemical stability.

Compared to the conventional techniques described above, the direct photo-fabrication technique to imprint directly the micro-optical structures on the photosensitive materials without using a developing or an etching process can give simpler and contact-less fabrication of micro-structured surfaces. The photosensitive materials are defined as the materials that induce permanent changes in the refractive index and/or volume, upon light illumination. Thus, the photosensitive material is self-developed, in contrast to the photoresist material requiring developing process for fabrication of micro-structures. The photoinduced reactions like photo-polymerization, photolocking, and photoinduced migration in organics create volume expansion or compaction, or refractive index change that is large enough to fabricate micro-optical surface structures in the materials. These photosensitive polymers, called photopolymers, have been widely developed for many applications such as holograms or holographic optical elements and optical waveguides [27–38]. The photopolymers have been commercialized to be used in industries: the representative example is OmniDex and Polyguide from DuPont [29, 39]. Also, the azo-polymers to create orientational redistribution of the chromophores when illuminated with a polarized light have been used to fabricate periodic surface relief microstructures [40–45]. On the other hand, inorganic materials exhibit relatively small photosensitivity compared to polymers: photoinduced densification and condensation of silica network in silicate glasses [46, 47] and sol-gel glasses [48,

49], defect generation in germano-silicate glasses [50–54] and surface expansion of fluoride or chalcogenide glasses [55–57]. In particular, direct photo-fabrication of refractive index modulated diffraction gratings on the optical fibers using the photosensitivity in germano-silicate glass have been practically used in optical communication.

Sol–gel process offers a low-temperature chemical route for the synthesis of oxide-based materials [58, 59]. Based on the low temperature and the mild condition in the sol–gel process, the ability to trap organic functional molecules into inorganic glasses has been widely demonstrated. The sol–gel process also provides new materials, inorganic–organic hybrids, in which an inorganic network structure is organically modified at a molecular level [60–71]. These hybrids are extremely versatile in their composition, processing, and in optical and mechanical properties. In this chapter, sol–gel derived inorganic–organic hybrid material will be used as the terminology of *hybrimer* for the sake of convenience. The hybrimer means the hybrids of inorganic and organic components compared to the terminology of polymer. The introduction of organic groups into an inorganic network improves mechanical properties, leading to the easier processing of thick films. Recently, optically homogeneous and transparent inorganic–organic hybrids containing various inorganic and organic components have been synthesized. Also, the refractive index of the hybrimer is shown to be tailored in a wide range by the combination of inorganic and organic components. In addition, the modification of an inorganic network structure with organic groups gives large spaces for isomerization of organic photoactive molecules as compared to inorganic glasses or ceramics. This allows the hybrimers to incorporate easily the photoactive molecules to be used in efficient functional optical materials. Also, the organic modification in the inorganic network allows the formation of thick films for practical application, which is difficult in the sol–gel processed glasses or ceramics due to stress-induced cracking. Thus, the hybrimers are anticipated to be desirable materials for micro-optical applications.

Recently, it was found that the sol–gel derived inorganic-organic hybrid materials containing polymerizable organic groups can be negative-type photoresist materials to be photo-patterned by UV exposure followed by a simple development process [72–103]. This photo-patterning technology has been extensively studied to apply the hybrimers for simple fabrication of some micro-optical elements including optical waveguides. However, the developmental step still involved the use of organic solvents that may potentially decrease the surface quality of the optical elements. Moreover, it has been demonstrated that it is possible to fabricate directly the micro-optical structures in the hybrimers by using only a light exposure step [104]. This direct photo-imprinting enables the simple and cheap fabrication of micro-optical structures with improved surface qualities. Highly photosensitive hybrimers can undergo large changes both in the refractive index and topology, upon light exposure. The modulations of refractive index and volume in the photosensitive hybrimers are very dependent upon the photosensitive mechanisms which vary according to the composition and other parameters. Various photosensitive mechanisms in the hybrimers have been anticipated and proposed in many compositions to make micro-optical structures on the films. A better understanding of the

photosensitive mechanisms in the hybridizers can help design higher photosensitive hybridizers to be applied in simple fabrication of micro-optical elements

In this chapter, the photosensitivity mechanisms in the hybridizers which have been proposed in the literature will be summarized with a brief introduction of the hybridizers. Also, the micro-optical elements such as diffractive gratings, optical waveguides, and microlenses, etc. to be directly photo-fabricated on the hybridizer films using different photosensitive mechanisms creating different micro-optical modulations will be introduced. It should be reminded that the photo-fabrication of micro-optical components using a developing step to exploit the photoresist character of the hybridizers will be excluded in this chapter, even though extensive studies have been performed. The direct photo-fabrication technique of the hybridizers which can give better photosensitivity will provide many advantages for practical application of micro-optical elements over many conventional photosensitive polymers or glasses. This will enable the hybridizers to become potential materials for micro-optical applications in the future.

13.2 Sol–Gel Derived Hybrid Nano Materials (Hybridizer)

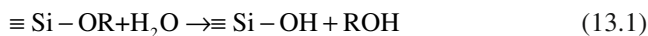
Sol–gel chemistry is based on the polycondensation of molecular precursors such as metal alkoxides to fabricate ceramics and glasses with improved or new properties [58, 59]. The mild reaction conditions (metallo-organic precursors, organic solvents, low reaction time, processing versatility of the colloidal state etc.) allow the mixing of inorganic and organic components at the nanometer scale. This led to a conceptually novel class of nanocomposites or nanohybrids composed of both inorganic and organic phases [60–71]. The concept was to combine properties of organic polymers (functionalization, ease of processing at low temperature, toughness) with properties of inorganic glasses or ceramics (hardness, chemical and thermal stability, transparency) in order to generate new/synergetic properties which are not accessible with classical composites. The nanocomposites and the nanohybrids are classified depending on the nature of the interface between inorganic and organic phases. The nanocomposites with weak bonding at the interfaces (Van der Waals, ionic or hydrogen bonds) can be organic molecules embedded in inorganic matrices, inorganic particles embedded in polymers, and interpenetrated network of organics and inorganics. Here, the inorganic particles and matrix networks can be formed by sol–gel reaction. On the other hand, the nanohybrids with strong covalent or ionic-covalent bonds at the interfaces can be synthesized in various ways. Among them, the sol–gel process using organo-alkoxysilanes can be used to fabricate typical siloxane based inorganic–organic nanohybrid materials. These nanocomposites or nanohybrids are extensively versatile in their composition, processing, and properties. The properties do not depend only on the organic and inorganic components but also on the interface between both phases, which can be used to tune many properties. Many reviews and literature on introduction, synthesis, properties

and applications of nanocomposites and nanohybrids have been published in the last decade [60–64, 66–71, 105–109].

13.2.1 Synthesis of Hybrimers

Siloxane-based hybrid materials (hybrimers) prepared by sol–gel process present many advantages for the design of materials [60–62, 66, 67, 71]. Firstly, many precursors are commercially available or can be modified or synthesized; secondly, the control of precursor reactivity can be achieved by controlling the catalysts; thirdly, transparent films or monoliths having good robustness can be easily processed; and finally, the resulting materials are not toxic. Figure 13.1 shows a schematic diagram of the synthesis of the hybrimers. Typical precursors of the hybrimers are organically modified silicone alkoxides (organo-alkoxysilanes) of general formula $R'_nSi(OR)_{4-n}$ where R' can be any organo-functional group and R is an alkyl group. The formation of siloxane $Si-O-Si$ network follows the classical sol–gel route which is as follows.

Hydrolysis:



Polycondensation:

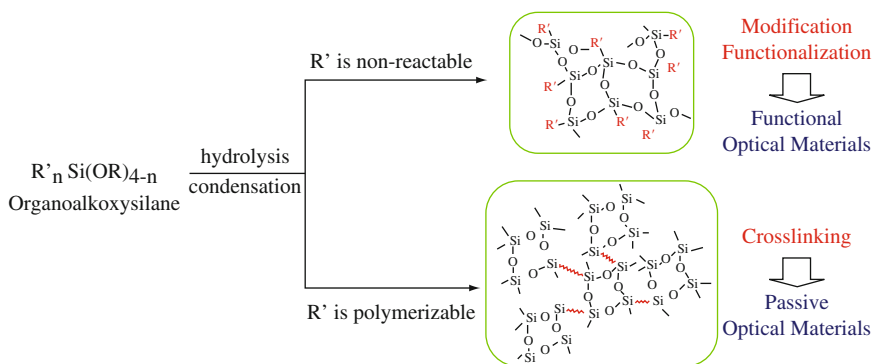
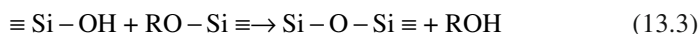
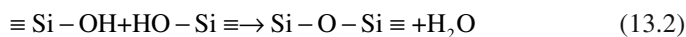


Fig. 13.1 Schematic diagram of synthesis of hybrimers. Different molecular structures in organoalkoxysilanes are formed depending on the chemical nature of organics in organoalkoxysilane

Depending on the chemical nature of organo-functional group R' in the organo-alkoxysilanes, different resulting molecular structures of the hybrimers are obtained as shown in Fig. 13.1. If R' is a simple non-hydrolysable group bonded to silicon through Si-C covalent bond (alkyl, phenyl, amino etc.), it will have a network modifying effect. In this case, the function of organics (hydrophobicity, hydrophilicity, photoactivity etc) in the stable siloxane network matrix is utilized to synthesize the active and functional optical materials. On the other hand, if R' is polymerizable by reaction with itself or additional components (methacrylate, epoxy etc), it will behave as another network former after polymerization of the organics. This cross-linked structure material can be used as a passive dielectric material in electrical and optical devices. In addition, organic monomers (acrylates, epoxides, diols) can also be used for reactions with organo-siloxane monomers or oligomers to increase the organic part of the hybrimer or enhance the polymerization of organic components. Also, unmodified alkoxysilanes (TEOS or TMOS), and other metal alkoxides like Al-, Zr-, Ti- alkoxides are used since they lead to high inorganic network density and increased stiffness. They can build up 3-dimensional inorganic networks. Aluminum, titanium, and zirconium compounds, beside their role as network formers, also act as efficient catalyst for siloxane condensation and epoxide polymerization. Thus, four different types of precursor owning a characteristic role are used to synthesize the hybrimers as represented in Fig. 13.2 [110]. The unmodified silicon alkoxides (type I) and the heterometal alkoxides (type II) form inorganic network by sol-gel reaction, while the reactive organically modified silicon alkoxides (type III) form organic network by polymerization, and the functional organically modified silicon alkoxides (type IV) modify the siloxane network. The modification of

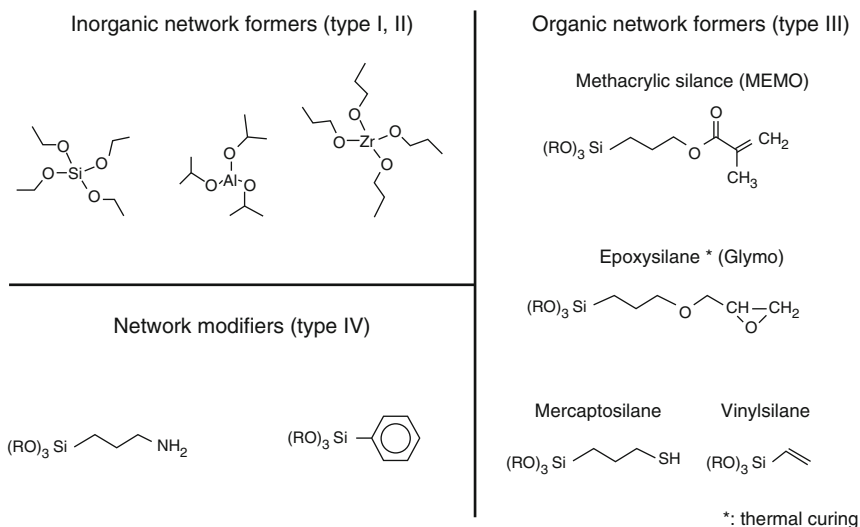


Fig. 13.2 Examples of precursors used in synthesis of hybrimers [110]

the hybrimer for specific application is mainly determined through the use of these four structural components and condition of forming inorganic and organic networks. In classical sol–gel processing of ceramics or glasses, a high temperature step is necessary to remove solvents and prepare the dense oxide network by sintering processes to produce drastic volume shrinkage. On the other hand, in the sol–gel processing of the hybrimers, no high temperature is necessary for the formation of a dense network and much less shrinkage occurs since the organic groups fill up the space in the oxide network. The organic structural groups, however, limit the maximum service temperatures compared with ceramics and glasses, although the thermal stability is better than that of the polymers.

The sol–gel process for synthesis of the hybrimers using organo-alkoxysilanes requires adding water for hydrolysis. This generates many limitations for practical applications. First of all, a thick film over 10 μm is very difficult to be formed, although organic modification gives sufficient elasticity to withstand shrinkage, due to the shrinkage induced by volatilization of solvents during heating. Second, due to the use of water, existence of silanol (SiOH) groups is inevitable. The silanol groups in the hybrimers would be vulnerable to chemical attack and near infrared absorption causing optical loss in the material. Also, the hybrimer solution in a solvent is not stable for long-term storage and cannot guarantee the reproducibility and reliability of the materials. Thus, the conventional hydrolytic sol–gel processed hybrimers have few chances to be applied practically in industries. Recently, as a result, new non-hydrolytic sol–gel process without the use of water for synthesis of the hybrimer has been widely investigated [111, 112]. The direct polycondensation between organo-silicon-halides or diols, and organo-silicon-alkoxides forms the siloxane network under non-aqueous conditions.



(X: OH, Cl etc.) organo-oligosiloxane alcohol, alkylhalide

The siloxane formation results in nano-sized organo-alkoxysilane oligomers with the byproduct of alcohol or alkylhalide. The formed organo-alkoxysilanes are cross-linked by the polymerization of organic chains resulting in 3D duroplastic materials. The hybrimers synthesized by condensation reaction of diphenylsilanediol (P2) with methacryloxypropyltrimethoxysilane (MPTS) or glycidylxypropyltrimethoxysilane (GPTS) have been investigated in many studies of electrical and optical applications [113–122]. The hybrimers contain a remarkably low content of silanol groups causing low optical loss and allowing it to form a thick film over 100 μm . Therefore, the hybrimers synthesized by non-hydrolytic sol–gel process are more desirable for use in micro-optics fabrication. Whether synthesized by hydrolytic or non-hydrolytic sol–gel process, the hybrimers form inorganic clusters with a size below 10 nm and siloxane ring structures rather than an inorganic network. This type of inorganic oxide compounds plays a very important role for the formation of inorganic structural units. Due to the

complexity of the reactions for forming the inorganic and subsequently the organic network, the understanding of the reaction steps in the fabrication of hybrimers is far from complete.

13.2.2 Characteristics and Applications of Hybrimers

Based on the above synthesis schemes, numerous hybrimers have been developed in recent years. This development yields many interesting new materials, with improved mechanical properties tunable between those of glasses and those of polymers, with improved optical properties (efficiency, stability, new functions, etc) and with improved catalytic or membrane based properties [60–62, 105–109, 119, 123, 124]. Due to the nano-scale structure and processing, the hybrimers are transparent amorphous materials with thermoset properties and show duroplastic behavior. Molding processes are possible only before or during the curing reactions, since after the complete formation of the inorganic and organic network structure the materials cannot be remolded without decomposition. Duroplastic behavior is generally connected with a high dimension and chemical stability of the materials. The inorganic structures of the hybrimers are responsible for their high stiffness and hardness compared with organic polymers. Due to the control of chemical structures, a wide span of mechanical properties can be tailored on a molecular scale for applications as coatings or bulk materials. Alternation of siloxane structure with other metal oxide structure (Ti–O–Ti, Al–O–Al or Zr–O–Zr) leads to higher stiffness and hardness of the hybrimers [110, 125]. On the other hand, thermal stability of the hybrimer is limited by the organic structures in their networks but usually better than organic polymers. If thermally very stable structures like phenyl or cyclophosphazane units are attached to the inorganic Si–O–Si network, thermal stability even above 400°C can be achieved [126]. High optical transparency with low birefringence of the hybrimers is mainly due to their amorphous nature and their lack of structures absorbing light in the visible region (e.g. conjugated electronic system, metallic structures or complexes). Therefore, the hybrimers can be used as low-loss matrices for optical applications [80, 90, 106, 114, 115, 118, 121, 124, 127]. Low-loss in the near infrared region can be achieved by partial fluorination. The hybrimers are highly electrically insulating materials comparable to inorganic glasses and non-polar organic polymers. However, the hybrimers can also be synthesized with polar or even ionic functions thereby reducing the surface resistivity for antistatic applications [110]. On the same principle, the oxygen permeability of the hybrimers can be very high for gas transport or separation process, or very low which makes them good candidates for barrier layer by adjustment of network density and matrix polarity [110]. Above all, the hybrimers present no transition temperature and no hysteresis during the heating cycle with a higher decomposition temperature than the polymers, to be used reliably [119].

One of the first and most important applications of the hybrimers was abrasion resistant coatings for a variety of substrates [110, 125, 128]. Due to their transparency and ease of processing, the hybrimers find widespread applications as coatings in transparent substrates which show high mechanical strength, hardness and abrasion resistance. The abrasion resistance also increases by using additional heterometal oxide based networks due to the enhanced condensation of inorganic network structure. In addition to the abrasion resistant coating, many coating applications have been explored in many types of substrates [110]. Anti-soiling, anti-fogging, and anti-static functions were provided to the coatings by granting organic functions in the network structure. Also, the barrier coatings and corrosion resistant coatings were developed.

The hybrimers have high electrical resistance, good barrier functions for water vapor and show also very good adhesion on substrates relevant in microelectronics. This makes them useful as passivation insulation layers in microelectronic and display devices. Due to their transparency, their isotropic nature, controllability of refractive index, and the patternability of the hybrimers, they are useful elements for optical applications [80, 90, 106, 114, 115, 118, 121, 124, 127]. Applications as planar optical waveguides afford low optical losses at wavelengths of optical signal processing at 1,300 and 1,550 nm. The hybrimers as solid polymer ionic conductors can be used in batteries, fuel cell, super capacitors, electrochromic devices [129–131]. The hybrimer electrolytes show good conductivities at room temperature in combination with increased dimensional stability compared to organic solid polymer electrolytes.

Compared to sol–gel processing of ceramics and glasses having a problem of shrinkage during drying, the hybrimers are easier to process in bulk form due to their organic modification which leads to better network relaxation properties. Thus, many bulk materials and composites based on the hybrimers have been developed in diverse industrial applications [110]. Also, the hybrimers can be processed as fiber and foils.

13.3 Photosensitivity Mechanisms in Hybrimers

The photosensitivity, defined as a permanent change in refractive index and/or volume upon light illumination, can be found both in inorganic and organic materials. Various permanent photoinduced phenomena have been explored in oxide glasses, fluoride glasses or chalcogenide glasses. Phenomena like photosensitivity can be quoted as photodarkening, photoexpansion etc. For the silicate glasses, the volume change can be negative or positive depending on the composition of glasses. The germanosilicate glasses exhibit densification accompanied with refractive index increase owing to Ge-related densification and oxygen deficient defects [46, 47, 51, 54, 132]. In contrast, the germanosilicate glass can also show decrease of density by dilation. The chalcogenide glasses and the fluorozirconate glasses create positive volume change when

exposed to sub-bandgap illumination [55–57]. It was also revealed that the photo-irradiation accelerates the hydrolysis and condensation in sol–gel processing of silica to increase the density and the hardness [48]. However, the photoinduced changes in refractive index and volume are relatively small to inscribe effectively the desired micro-optical structures on the surface. On the other hand, the organic component is more sensitive to light exposure to induce a large change in refractive index as well as volume. The available photoinduced phenomena to change refractive index and volume of the polymers are photo-polymerization, photoinduced decomposition, photolocking, and other photochemical reactions. Therefore, based on the concept of hybrimers, the high photosensitive hybrimers can be designed by combining different photosensitivity mechanisms of glasses and polymers, as represented in Fig. 13.3. A higher photosensitivity compared to glasses, and better stability and transparency compared to polymers can be achieved through better understanding of photosensitivity mechanisms in the hybrimers.

Polymerization of organic groups in the synthesis of the hybrimers is made by thermal or UV curing. Specially, photo-polymerization of methacrylate is the most common photoinduced reaction in the polymers resulting in changes in both refractive index and volume by cross-linking of methacrylates. Also, other photosensitivity mechanisms of the polymers are dominant in the methacrylate system. Thus, the methacrylate hybrimer system synthesized using methacryloxypropyltrimethoxysilane (MPTMS) has been usually considered for developing high photosensitive hybrimers. Also, since the UV curable methacrylate provides good optical transparency and easy processibility, the methacrylate hybrimers have been investigated to characterize their optical properties and apply for many optical applications. Thus, most photosensitive

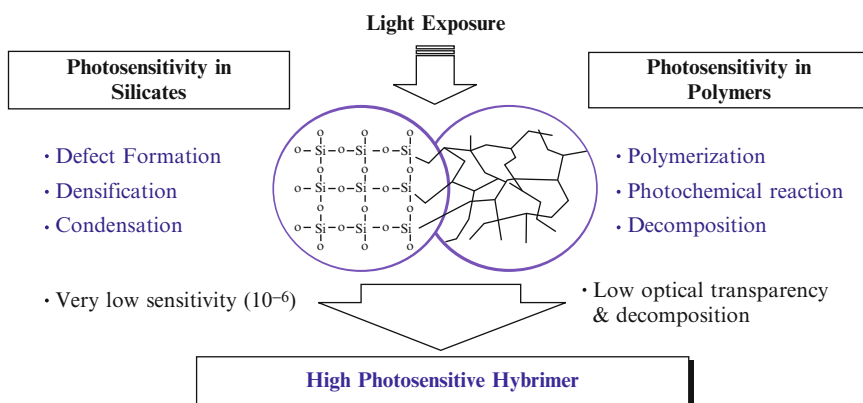


Fig. 13.3 Design of highly photosensitive hybrimers optimizing photosensitive mechanisms in silicates and polymers

hybrimers have been developed in the methacrylate hybrimer system using a precursor of MPTMS. Table 13.1 summarizes the hybrimer systems for different photosensitivity mechanisms, and the direct photo-fabrications of micro-optical elements.

Table 13.1 Summary of photosensitivity mechanisms for direct photo-fabrication of microoptical components

Mechanism	Materials (Precursors)	Photosensitivity (Vol/RI change)	Application (Fabrication)	Ref.
Densification	GI + DMDES GI + MPTMS		Grating (Photo) Microlens (Photo)	[133, 134]
Polymerization	MPTMS + TPO, MPTMS + TPO:MAA,ZPO:MAA	Compaction/+ Δn Grating (Photo, HI)	Grating (HI) [119, 136–139]	[135]
	d-U + ZPO, d-U+MPTMS+ZPO	Compaction/+ Δn	Waveguide (Photo)	[140]
Decomposition	MPTMS + PFAS	Compaction/– Δn	Grating (Photo, Phase)	[141–143]
	MPTMS + ZPO:MAA + BDK	Expansion/+ Δn	Waveguide (DLW, Photo)	[144–147]
Photolocking	MPTMS + PFAS + DPSD + BDK			
	MPTMS + PFAS+ZPO:MAA + AM	Expansion/+ Δn	Grating (HI) Fresnel lens (HI) Microlens (Photo)	[148, 149] [150] [151, 152]
	MPTMS + TPO:MAA	Expansion	Grating (HI)	[153]
	MPTMS + TPO	Expansion	Grating (DLW, Photo)	[154, 155]
Migration	PTMS + MPTMS + AM	Expansion	Microlens (Photo) Microlens (Photo)	[156] [157]
	GPTMS + SiCl ₄ + MPTMS	Expansion/– Δn	Microlens (Photo) Grating (Photo)	[158] [159]
	Silica sol + AM	+ Δn	Grating (HI)	[160]
Isomerization	Azo dye + TEOS	Expansion/+ Δn	Grating (HI)	[35, 161, 162]
Photochromism	D-TEOS + MTES	+ Δn	Waveguide (Photo)	[163, 164]
			Grating (Photo)	

GI: germanium isopropoxide, *DMDES*: dimethyldiethoxysilane, *MPTMS*: methacryloyloxypropyl trimethoxysilane, *TPO*: titanium propoxide, *MAA*: methacrylic acid, *ZPO*: zirconium propoxide, *AM*: acrylate monomer, *PFAS*: perfluoro-alkylsilane, *DPSD*: diphenylsilnaediol, *PTMS*: phenyltrimethoxysilane, *GPTMS*: glycidocypropyl trimethoxysilane, *TEOS*: tetraethoxysilane, *D-TEOS*: dithienylethene triethoxysilane, *MTES*: methyltriethoxysilane, *Photo*: photomask, *Phase*: phase-mask, *HI*: holographic interference, *DLW*: direct laser writing

13.3.1 Photoinduced Densification in Ge-Doped Hybrimer

Germanosilicate glass, which undergoes changes in refractive index under UV illumination, has been used for fabrication of grating devices with high reflectivity and broad bandwidth used in optical communication. In this case, photoinduced refractive index change through defect formation within the glass is small ($\sim 10^{-4}$) depending on the source and wavelength of light, and a surface relief pattern formation is rarely found. Thus, many researchers have focused on making the glass react more quickly to UV light and produce higher saturated refractive index changes. It was found that formation of more defects by heating in reduced atmosphere can enhance the photosensitivity in the glasses [50, 54]. The sol-gel derived germanosilicate and germanate thin films were fabricated for application of planar optical waveguides and their photosensitivity was investigated to write gratings on them [51–54, 132]. It was expected that the sol-gel derived films might offer higher photosensitivity due to their softness and porous structures undergoing densification under UV exposure. Furthermore, the Ge-doped hybrimer containing organics should enhance the photosensitivity with volume compaction since they contain organics resulting in softer and more porous structures. A Ge-doped hybrimer consisting of methyl-modified germanosilicate network structure exhibited considerable photosensitivity [134]. Large changes in its refractive index (6.5×10^{-3}) and volume were seen upon UV illumination. Figure 13.4a shows the changes in the refractive index and the density of Ge doped hybridizers as a function of UV fluence [134]. Refractive index increases linearly with the UV fluence up to $2,500 \text{ J/cm}^2$ and then saturates at 6.5×10^{-3} . Simultaneously, the density increases linearly up to 0.05 g/cm^3 with the UV fluence, as that seen for the refractive index change in Fig. 13.4a. The refractive index change Δn of a material is given by the differential form of the Lorentz-Lorentz equation:

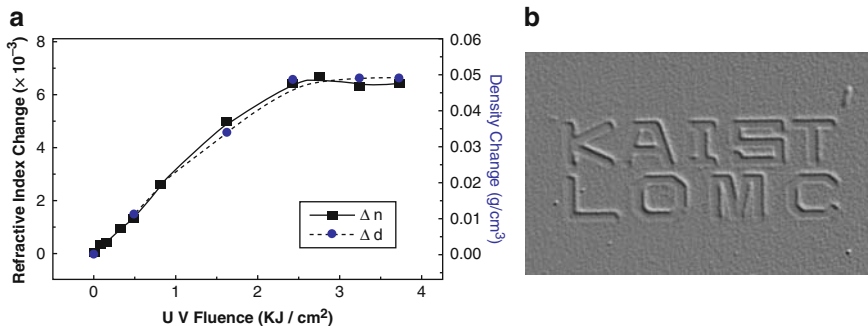


Fig. 13.4 (a) Change in refractive index and density of Ge-doped hybridizers with UV fluence of the 1,000 W Hg/Xe lamp (220–260 nm, 45 mJ/cm^2). (b) Optical micrograph of direct photo-imprinted letters on Ge-doped hybrimer [134]

$$\Delta n = \frac{(n^2 - 1)(n^2 + 2)}{6n^2} \left(\frac{\Delta\alpha}{\alpha} - \frac{\Delta V}{V} \right) \quad (13.5)$$

where $\Delta\alpha/\alpha$ and $\Delta V/V$ are the relative changes in polarizability and volume, respectively. Assuming a change in polarizability of the Ge-doped hybrimer upon UV irradiation, the refractive index change can be written as follows:

$$\Delta n = \frac{(n^2 - 1)(n^2 + 2)}{6n^2} \left(\frac{\Delta\rho}{\rho} \right) \quad (13.6)$$

where $\Delta\rho/\rho$ is the relative change in density. The calculated refractive index change based on measurement of density from the (13.6) is about 8×10^{-3} . This is in agreement with the experimental data indicating that the refractive index change is mainly induced by the densification. On the other hand, a methyl modified silicate hybrimer without germanium doping does not show any photoinduced changes either in refractive index or volume. It indicates that the densification is made by breakage of Ge-related bonds in the germanosilicate structures. As the Ge–O bonds are weaker than Si–O bonds they are more readily broken by low-energy radiation. Zachariassen’s random network theory provides the basic rules for the modeling of silica glass structures. The simple description of the silica glass structure is based on rings, which are closed circuits along nodal connection of tetrahedral network. In the tetrahedral network, the angle θ between two neighboring tetrahedra (Si–O–Si angle) is called bond angle. The densification of the silicate glass structure is mostly ascribed to the variation in angle θ . Usually, the frequency shifts in the Raman bands reveal structural changes in the glasses. Actually, the Raman spectra confirmed that the angle θ was reduced during photoinduced densification in Ge-doped hybrimer. Thus, it was assured that the change both in the refractive index and the volume was made only in Ge-doped hybrimers mainly by photoinduced densification. A surface relief pattern in the Ge-doped hybrimer was photo-fabricated by UV irradiation through a photomask. Figure 13.4b represents an optical micrograph of direct photo-inscribed letters on the Ge-doped hybrimer [134]. The volume compaction in the UV-illuminated region is the direct evidence for the photoinduced densification in the Ge-doped hybrimer. Moreover, in order to obtain higher photosensitivity producing more densification, Ge-doped polymerizable methacryl grafted hybrimer was prepared [133]. Larger and faster change both in refractive index and volume was observed due to simultaneous photo-polymerization of methacrylate and densification of siloxane in the hybrimer. Figure 13.5 shows images of AFM and optical microscopy of a concave type microlens array (MLA) that was directly photo-imprinted on the Ge-doped hybrimer using a binary photo-mask [133]. The shape of the microlens is sensitive to the UV exposure time and can be controlled easily as shown by the micro-structural evolution of the microlens directly photo-fabricated versus the UV fluence (Fig. 13.6). In addition, it was proved

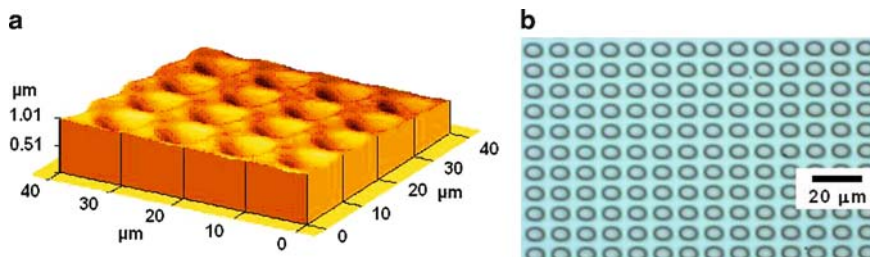


Fig. 13.5 (a) AFM image and (b) optical micrograph of directly photo-fabricated MLA on the Ge-doped methacrylate hybrimer [133]

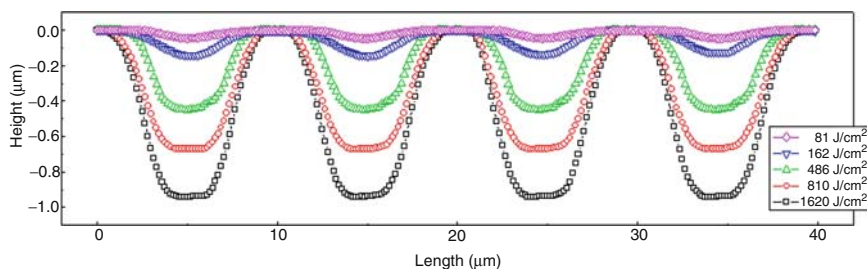


Fig. 13.6 Micro-structural evolution of microlenses directly photo-fabricated on the Ge-doped methacrylate hybrimer depending on the UV fluence

that the change in the refractive index and the volume in the Ge-doped hybridizers are permanent even at high temperature up to 200°C. The Ge-doped hybridizer has excellent optical qualities as well as good thermal and mechanical stability. It is therefore, suitable for the simple fabrication of effective microlenses and gratings.

13.3.2 Photo-polymerization of Methacrylate

The hybridizers synthesized from the polymerizable organic grafted organo-alkoxysilanes consist of a polymer network interpenetrated with the siloxane backbone. The inorganic part of the molecule is an alkoxy silane polymerized *via* hydrolysis and condensation reactions of the alkoxy groups at room temperature, thus leading to a glass-like material. The mild conditions under which the inorganic part of the material is prepared are compatible with the presence of an organic part. Simultaneously, polymerization of the organics in the organo-alkoxysilanes leads to a crosslinked polymer network in the

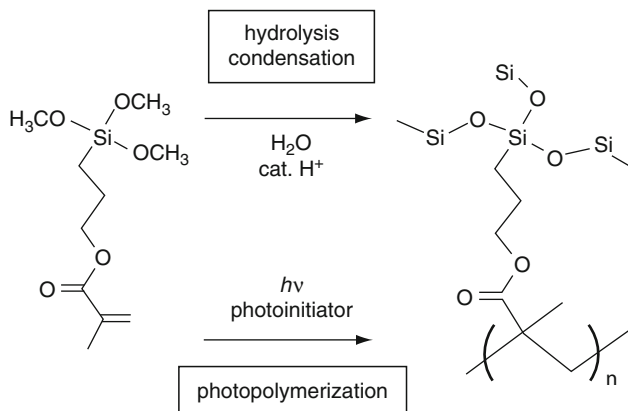


Fig. 13.7 Formation of inorganic network by condensation of siloxane and photo-polymerization of methacrylate in the methacrylate hybrimer [165]

hybrimer structure. In a methacryloxypropyltrimethoxysilane (MPTS), which is a precursor commonly used for the synthesis of the hybrimers for optical applications, methacryl groups can be photo-curable. Thus, the methacrylate hybrimer can be fabricated by photo-polymerization of methacrylate accompanied with hydrolysis and condensation reactions of alkoxy silane as illustrated in Fig. 13.7 [165].

This hybrimer combines qualities of photopolymers (suppleness, versatility) and the physical properties of glass (refractive index, heat and mechanical resistance), which can be adjusted by incorporating other metal alkoxides (Ti, Zr, Al, etc.). The photo-polymerization of methacrylate during processing produces a crosslinked polyacrylate network which is durable to wet etching. Thus, the selective photo-polymerization resulting in wet etching selectivity like a negative-tone photoresist allows the use of hybrimer films to fabricate micro-optical components by a developing process [72–103]. Also, the photo-polymerization induces changes in the refractive index and volume of the hybrimers, thus allowing direct photo-fabrication of micro-optical components without any etching step. In most cases, the volume shrinks and the refractive index increases due to the cross-linking during the polymerization. The volume compaction photoinduced by the photo-polymerization has been used in direct photo-fabrication of surface relief patterns [136, 137, 139, 140, 165, 166]. Figure 13.8 shows the volume shrinkage created only in the photo-illuminated area illustrating the photo-polymerization mechanism of the photosensitivity in the methacrylate hybrimer [137]. Photoinduced pressure gradients created from the internal strain caused by constrained photo-polymerization form the surface corrugation in the hybrimers. However, this competes with photoinduced migration or photolocking inducing volume expansion which is a reverse phenomenon. Thus, the volume shrinkage by photo-polymerization can be obtained when the photoinduced migration is inhibited by small additional monomers or thermal baking before

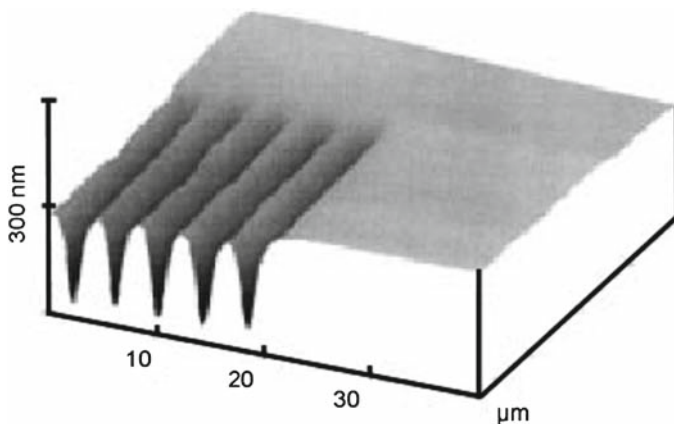


Fig. 13.8 AFM image of the micro-patterns directly photo-fabricated at the edge of the methacrylate hybrimer. The image shows volume compaction mainly due to photo-polymerization of methacrylate [137]

UV exposure. In addition to photosensitive or photo-patternable properties, the photo-polymerization makes a crosslinked structure with siloxane formation, thus leading to a mechanically and thermally stable material for practical application. Thus, understanding the photo-polymerization of the methacrylate is significant to achieve the objectives for the hybrimers. Few studies of photo-polymerization in the hybrimers have been conducted for scientific and technical interests [165, 167]. Differently from all-organic polymers, the presence of siloxane backbone in the hybrimers can be expected to affect the polymerization process of acrylate.

Radical polymerization of mono- and multifunctional acrylate and methacrylate monomers initiated by UV light has attracted much attention in applications such as coatings, printing inks, photoresists, photoadhesives, etc. The photochemical route for the polymerization of acrylate monomers has the advantages of fast curing, high final conversion and spatio temporal selectivity of the reaction [168]. Photo-polymerization can involve either a direct or a sensitized photoinduced process. The former is not in common use since direct formation of reactive species from the monomer is not efficient enough. Thus, the initiation step of the polymerization requires the presence of a photoinitiator that is a molecule capable of generating these reactive species (radicals or ions) under light excitation. The following conditions are essential to provide maximum efficiency of photo-polymerization: wide overlap between the emission spectrum of the light and the absorption spectrum of the photoinitiator, short life of excited states (single and triplet) of the photoinitiator to avoid quenching by molecular oxygen and high quantum yields for production of reactive radicals from excited states. Several types of radical-generating photoinitiators such as benzoyldimethylketal (BDK, $C_6H_5COC(OCH_3)_2C_6H_5$) and

1-hydroxycyclohexylphenylketone (HCPK, $\text{OHC}_6\text{H}_{11}\text{COC}_6\text{H}_5$) have been used in the methacrylate hybridizers. The photochemical step that leads to the primary monomer radical is followed by well-known mechanisms of propagation and termination. This scheme clearly shows that the overall efficiency of the reaction is strongly dependent on the photochemical process. Thus, understanding of the photochemical process is crucial to achieving total conversion of the acrylate bonds for the polymerization. A total conversion of the acrylate bonds is, however, hardly achievable due to the so-called occlusion process (i.e. loss of mobility of the growing reactive radicals resulting from gelification and vitrification of the mixture). These principles of the acrylate photo-polymerization also apply to the hybridizers. For the photochemical process, no influence of the siloxane formation is expected although the medium contains high polar water or alcohol. However, the siloxane matrices are known to exhibit high permeability to molecular oxygen. Therefore, oxygen diffusion through the hybridizer might conceivably become high enough to inhibit the photochemical process to some extent. Photoinitiator mobility should not be significantly affected by the presence of siloxane since its molecular size is small. However, mobility of the methacrylate attached to siloxanes is drastically reduced by the formation of the siloxane network. As a consequence, it is expected that the photo-polymerization of the hybridizers is slower than that of the polymers and high conversion degree is difficult to achieve.

Usually, the conversion degree of the acrylate for the polymerization can be examined using FTIR spectroscopy. Conversion degrees of the acrylate in some methacrylate hybridizers were characterized as a function of UV dose [115, 165]. One example of the FTIR spectra is shown in Fig. 13.9a. The decrease of the acrylate $\nu(\text{C}=\text{C})$ band at $1,638\text{ cm}^{-1}$ during the irradiation can be related to the consumption

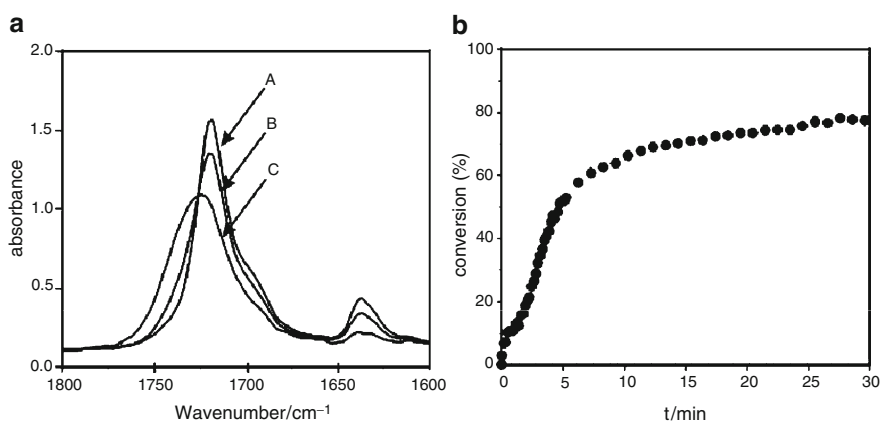


Fig. 13.9 (a) FTIR spectra of the methacrylate hybridizer and (b) calculated conversion degree of acrylate depending on UV exposure time A: 0 s, B: 10 s, C: 30 min. [165]

of the C=C double bonds by the photoinduced process [165]. The shift of the $\nu(\text{C}=\text{O})$ band at $1,718\text{ cm}^{-1}$ is a consequence of the loss of conjugation with the C=C double bond in the hybrimer. The area of the $\nu(\text{C}=\text{O})$ band, however, remains constant, which means that no evaporation of MPTS takes place. From the FTIR spectra, the conversion degree of the acrylates was calculated as the relative intensity of the acrylate $\nu(\text{C}=\text{O})$ band or more precisely using following equation.

$$\text{Conversion degree(\%)} = \left(1 - \frac{\left(\frac{A_{\text{C}=\text{C}}}{A_{\text{C}=\text{O}}} \right)_{\text{after UV}}}{\left(\frac{A_{\text{C}=\text{C}}}{A_{\text{C}=\text{O}}} \right)_{\text{before UV}}} \right) \times 100 \quad (13.7)$$

where $A_{\text{C}=\text{C}}$ and $A_{\text{C}=\text{O}}$ represent the integrated peak intensities of the C=C and C=O bands, respectively. Figure 13.9b represents the typical conversion degree of the acrylate as a function of UV irradiation time reaching finally 80% in the methacrylate hybrimer [165]. The conversion degree saturates to reach the plateau of the maximized value. Compared to thin films of conventional polymers, it takes a longer time to achieve the final conversion ratio. This result could be related to the poor mobility of acrylate moieties grafted onto the cross-linked siloxane backbone. However, it was found that the saturated conversion degrees of the methacrylate hybridizers are larger than 80% and enough to lead to efficient polymerization even in a viscous system. The conversion degree is very sensitive to composition, photoinitiator concentration, solvent, and processing parameter etc. Indeed, the conversion degree measured by FTIR spectra represents only a reduction of the C=C double bond, not the real polymerization degree. A closer examination of MAS ^{13}C NMR indicating the existence of a tetra-substituted C atom revealed that the methacrylate was crosslinked by efficient photo-polymerization. In the hybridizers, other metal oxides like zirconium oxide (ZrO_2) or titanium oxide (TiO_2) have been added to increase the refractive index of the hybridizers by forming the hetero Si–O–Ti bond, metal oxide nanocrystals, or metal-oxo-clusters. These metal alkoxides were usually used by complexing with bridging or chelating ligands such as β -diketones or carboxylic acid owing to their high reactivity. Methacrylic acid (MAA) has been widely used to be copolymerized with methacryl groups of MPTS as well as to be complexed with metal alkoxides. It was found that the addition of metal oxide catalyzes the condensation reaction of organo-alkoxysilanes and induces the polymerization of organic groups without adding a photoinitiator [125, 165]. In conclusion, the photo-polymerization in the methacrylate hybridizers, which is accompanied with condensation and densification of the inorganic backbone, makes volume shrinkage and refractive index increase by cross-linking of the network.

13.3.3 Photoinduced Decomposition of Methacrylate

Typically, organic polymers are susceptible to decomposition or degradation upon UV light. It is well known that poly(methylmethacrylate) (PMMA) is damaged and decomposed by long UV illumination [169, 170]. Ester groups in the PMMA chains absorb UV light in the 190–280 nm wavelength region. The extinction coefficient of ester groups at 216 nm is as high as $150 \text{ mol}^{-1} \text{ cm}^{-1}$. The resulting excitation leads to removal of ester groups from the main chains. The removed ester group remains as a radical subtracting H from main chains to form HCO_3CH_3 leading to the scission of the main polymeric chains. During this photolytic degradation reaction, the main chains are usually broken down and the polymeric fragments removed from the polymers are normally observed as gases such as CH_4 , CO_2 , CO etc. These small gas molecules diffuse out of the matrix, thus leading to a decrease of the density of PMMA as the exposure time to deep UV light increases. However, the breaking of the polymeric network induces cracks in the PMMA which deteriorates and cannot be optically used.

Similarly to PMMA, the methacryl radicals in the hybriders can be decomposed by long-time deep UV exposure. However, the hybriders are not deteriorated by the photoinduced decomposition of methacryl groups since the siloxane network can maintain the matrix network structure to be used in optics. It was found that both the refractive index and the film thickness of the methacrylate hybriders decreased with growing UV fluency [141–143]. Moreover, the changes in the refractive index and the thickness were enhanced with the addition of perfluoroalkyl groups as another organic modifier. Figure 13.10 shows the significant reduction of both the refractive index and film thickness in the fluorinated methacrylate hybriders synthesized from the precursors of MPTS and perfluoroalkyl

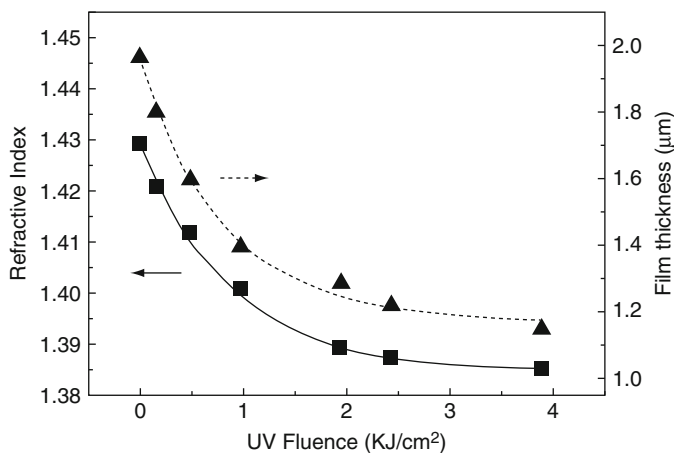


Fig. 13.10 Decrease in refractive index and thickness of the methacrylate hybrid film depending on UV fluence of 1 KW Hg/Xe lamp (200–260 nm, 45 mJ cm^{-2}) [142]

methoxysilane (PFAS) in a 3:1 ratio [142]. The refractive index decreases exponentially from 1.4298 down to 1.3853 with the UV cumulated fluence. Also, the film thickness decreases exponentially from 1.97 to 1.15 μm with increasing UV illumination time. Especially, the finally measured refractive index of 1.3853 is very low, and is comparable to the refractive indices of perfluorinated polymers such as Teflon[®]. This is not a usual observation because the volume compaction usually created by cross-linking the structure induces a refractive index increase. Thus, the reduction of the refractive index accompanied with volume compaction can be explained by the formation of micro-pores inside the material. As learned from the decomposition of the PMMA upon UV irradiation, UV excitation of the carbonyl group led to decomposition of the methacrylate chains in the hybrimer with formation of carbon and oxygen-containing volatile gaseous products. The decomposition of the methacryl chains under UV irradiation was evidenced by a decrease in peak intensity of the carbonyl $\nu(\text{C}=\text{O})$ stretching mode in the FTIR spectra versus UV fluence. It was also found that the decreases in the relative amounts of carbon and oxygen were related to the decomposition of methacryl groups. On the other hand, it was observed that the perfluoroalkyl groups do not decompose.

Based on the decomposition of methacryl groups in the hybridizers, the reduction of both refractive index and film thickness can be interpreted as follows. The organic methacryl groups fill the vacant spaces in the siloxane framework before UV exposure. Upon UV irradiation, the methacryl units decompose and are removed from the framework as gaseous products. Since bulky methacrylate chains which sterically hinder condensation reactions are removed upon UV irradiation, further condensation reaction of siloxane to extend the siloxane network is enhanced concurrently with the decomposition of methacryl groups. Thus, the film thickness decreases, as shown in Fig. 13.10, due to the shrinking of the inorganic network *via* photoinduced reactions. A refractive index change Δn of a material is given by the differential form of the Lorentz-Lorenz equation in (13.5) above. Two effects i.e. the polarizability change and the density change determine the refractive index change. Subsequent formation of micro-pores by decomposition of methacryl groups upon UV exposure can lower the density of the hybridizer. However, it was noticed that the contribution of a density change to a reduction of refractive index was not dominant in this hybridizer. Thus, the decrease in the refractive index upon UV irradiation is mainly due to the polarizability change. Generally, carbonyl groups are very polarized and hence induce high refractive indices in the materials. These carbonyl groups are removed upon UV illumination by the decomposition of methacrylate chains in the hybridizers. Thus, the polarizability reduction by removal of carbonyl groups contributes to the decrease in refractive index upon UV irradiation.

Using the photoinduced decomposition of methacrylate in the fluorinated methacryl hybridizer, surface relief patterns and gratings were directly imprinted on the hybridizers using a photomask lithography (12 μm period) and a phase-mask lithography (0.5 μm period) on the fluorinated methacryl hybridizer films

[141, 142]. These surface periodic patterns with extremely low refractive index in the light exposed region of the fluorinated methacrylate hybriimer imprinted via photoinduced decomposition mechanism can be applied to anti-refractive coatings and low dielectric materials in addition to micro-optical devices. However, since the photoinduced decomposition of methacrylate requires high and long-time exposure from only a deep UV source, it will be rarely used.

13.3.4 Photolocking of Photochemical Molecules

UV exposure usually (not always) increases the refractive index of the photo-polymerizable polymers and hybriimers. Generally, the refractive index increases abruptly with UV fluence at an early stage and then saturates after a certain UV dose. The increase in the refractive index from the unexposed state value to the saturated values represents the photosensitivity of the materials. This increment in the refractive index is mainly governed by photo-polymerization of the organic component and polycondensation of the inorganic component in the hybriimers. However, since the polycondensation of the inorganic groups is mainly made by thermal heating rather than by UV exposure, it can be neglected. Thus, the photoinduced refractive index increase of the hybriimers can be mainly ascribed to photo-polymerization. In this case, the refractive index increase by photo-polymerization should be identical regardless of concentration of doped photoinitiator because the photoinitiator has only a role of initiating the polymerization by photo-decomposed radicals. However, it was found that the refractive index was larger for higher photoinitiator concentration [144, 147]. It was also observed that the refractive index increase was slower than the polymerization kinetics although they should show the same slope if it is assumed that photo-polymerization is the main mechanism. This indicates that another factor raising the refractive index can be the incorporation of photoinitiators since the refractive index change is sensitive to the photoinitiator concentration. Therefore, the photoinitiator can also act as a refractive index modifier in the hybriimers. Actually, it was already found that the radicals produced by photo-decomposition of the photoinitiator were locked or fixed in methacrylate polymers to increase the refractive index while the undecomposed photoinitiators diffuse out during baking of the polymers [30, 31, 33, 34, 36, 38]. This photochemical reaction to increase the refractive index for fabrication of the optical waveguide circuits was named “photolocking”.

The photoinitiators such as benzoyldimethylketal (BDK, $C_6H_5COC(OCH_3)_2C_6H_5$) and 1-hydroxycyclohexylphenylketone (HCPK, $OHC_6H_{11}COC_6H_5$) are the photochemical molecules that are photo-decomposed into two radicals under UV illumination. These photo-decomposed radicals containing high refractive index phenyl groups can be locked or fixed into methacrylate matrix to increase the refractive index of the matrix during light exposure. Possible photochemical reactions for the photoinitiators to be fixed or locked in the methacrylate matrix

may be the attachment of the decomposed radicals to methacrylate groups or the coupling of the decomposed radicals. Schemes of the photochemical reactions of the BDK are shown in Fig. 13.11 [167]. When BDK is decomposed into radicals, the radicals may rapidly react with polymerizable methacryl groups and initiate the polymerization. The radicals can also undergo coupling of two benzoyl radicals to make a benzyl molecule. However, the coupling effect of the benzoyl radicals might be neglected in BDK-doped hybrimers as proved in a previous study [147]. The radicals produced by photo-decomposition of BDK have high electronic polarizability due to the phenyl groups in the radicals. Thus, the incorporation of the radicals in the hybrimers can increase the refractive index of the films. On the other hand, the unreacted photochemical molecules in the unexposed UV region are removed by vaporization during thermal baking. Usually, the photochemical molecules are susceptible to be volatile and mobile in the matrix. Thus, they thermally diffuse out through the surface and evaporate during thermal baking. Thus, the film thickness is smaller in the unexposed UV

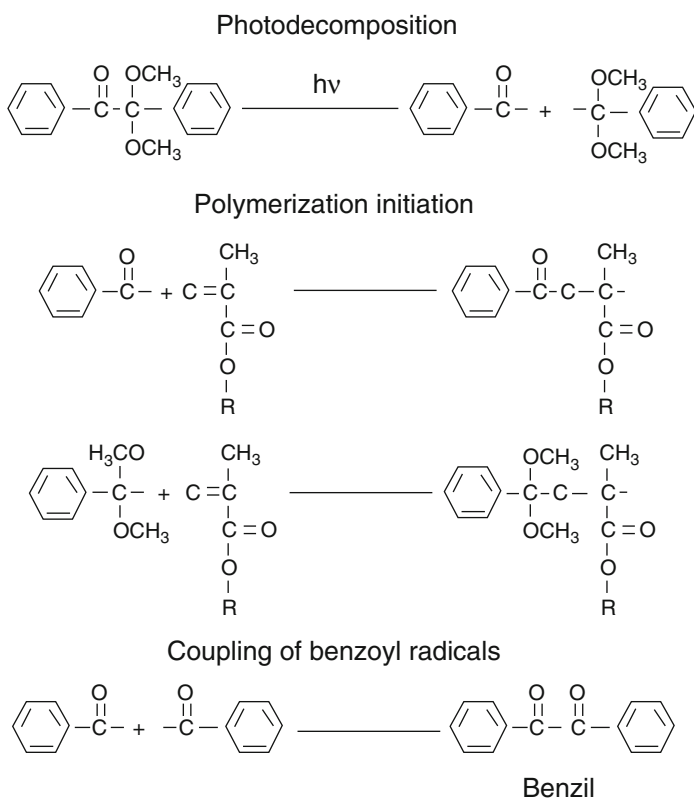


Fig. 13.11 Schematic diagram of possible photochemical reactions of BDK in the methacrylate hybrimer [167]

area whereas volume expansion occurs in the exposed area accompanied with refractive index increase. Apparently, it was observed that the refractive index and the film thickness increased with UV exposure and linearly rose with photoinitiator content as shown in Fig. 13.12 [135, 144]. As the UV exposure dose increases, both the refractive index and the film thickness first grow drastically and then similarly reach saturation. For the 30 mol% BDK doped hybrimer films, the refractive index change is 3.0×10^{-2} from 1.52 to 1.55 and the film thickness increases up to 1.5 times vs. UV dose increase. Thus, it is clear that the material is photosensitive as proved by the increase of the refractive index and the thickness of the films. Also, as the BDK content increases, the refractive index change increases almost linearly up to 43×10^{-3} and the film thickness grows up to more than 1.5 times of the film thickness. As more BDK are decomposed and locked into the hybrimer network, both the refractive index and the film thickness increase. At 50% of BDK content, the methacrylate hybrimers show an increase of 0.04 in the refractive index and 50% in the film thickness (can be dependent on the film thickness) under sufficient UV illumination. Also, a thickness step was observed at the boundary between the exposed and unexposed areas of the doped hybrimer film clearly indicating a photolocking mechanism [171]. Thus, selective UV exposure produces pattern expansions together with refractive index increase by photolocking of dopants in the exposed region. As in polymers, this selective pattern expansions together with refractive index increase have sufficient resolution to allow the fabrication of optical waveguides [135, 144, 146, 147]. Figure 13.13 illustrates the schematic diagram of the ridge optical waveguide fabrication using the photolocking of photoinitiator in the hybrimer films [144]. The UV exposure on the BDK-doped hybrimer films initiates the polymerization by the photo-decomposed BDK. The decomposed radicals are locked in the methacrylate matrix in the exposed area. On the other hand, the remaining BDK in the unexposed area which is mobile and volatile is removed

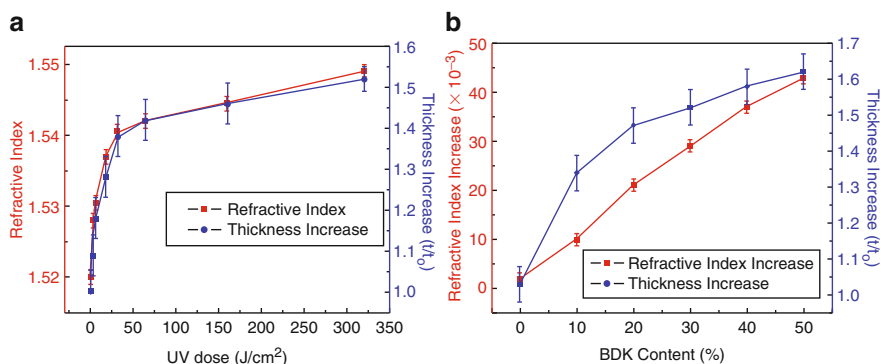


Fig. 13.12 Increase in refractive index and film thickness as a function of (a) UV fluence for 30 mol% BDK doped hybrimer film and (b) doped BDK concentration with 320 J/cm² UV fluence [135, 144]

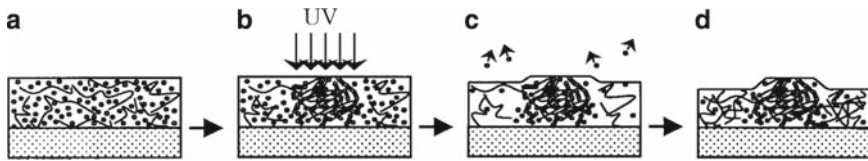


Fig. 13.13 Schematic illustration of photolocking of photoinitiator dopants in the hybrimer films: (a) film coating, (b) photo-polymerization and photolocking of photoinitiator dopants by UV exposure, (c) evaporation of photoinitiator dopants during baking process, (d) condensation and densification of the hybrimer films during baking process [144]

by evaporation during thermal baking process, lowering the refractive index and the film thickness. Finally, the condensation and densification of siloxanes are conducted to harden the film during baking process. This easy fabrication process of optical waveguides without using a developing process produced very smooth interfaces and low optical losses of ridge optical waveguides as shown in Fig. 13.14 [135]. This process has been called photochemical self-developing (PSD) process.

The photolocking mechanism to increase both the refractive index and the film thickness in the illuminated region is dependent on the kind of dopants and the matrix composition as well as the exposed UV wavelength. Thus, in order to achieve efficient photosensitivity for a specific application, the optimum hybrimer composition doped with a photolocking agent should be designed taking into account the UV wavelength. In addition to various photoinitiators, other photochemical or photoactive molecules such as acryl monomers, etc can be used as a photolocking agent. Even though many photosensitivity mechanisms can be applied to the hybrimers, it is obvious that the large refractive index increase under UV illumination is due to photolocking of dopants in the hybrimers.

13.3.5 Photoinduced Migration of Monomers or Oligomers

Volume deformation in the photosensitive materials can be either positive or negative, and depends on the material, system and composition. In the case of azo-polymers, liquid crystals and sol-gel materials, a negative volume change, compaction or shrinking in the exposed regions has been observed. The opposite deformation i.e. volume expansion has been found in some azo-polymers, fluoro-zirconate or chalcogenide glasses, and many photopolymers. Understanding of the mechanisms of deformation reactions is still evolving and some models have been proposed. For the azo-polymers, the *trans-cis* isomerization of azo chromophores upon photoexcitation is a major mechanism in the volume shrinkage deformation [41, 42, 44, 45]. Also, the liquid crystal can be shrunk through its reorientation [172], and sol-gel materials and general polymers can be densified by photoinduced condensation of silanol and polymerization of organics. On the other hand,

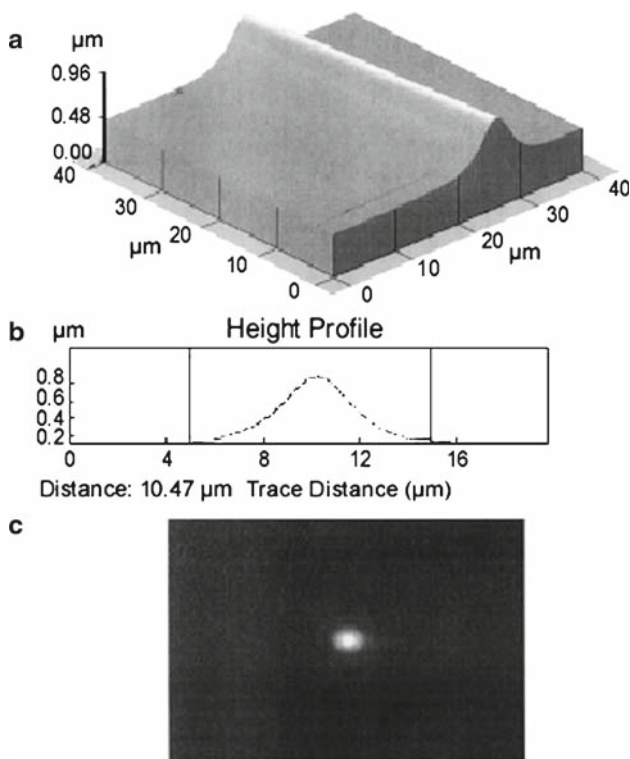


Fig. 13.14 (a) 3D AFM image, (b) 2D line profile AFM image and (c) near field mode profile of the directly photo-fabricated ridge optical waveguide in the BDK-doped hybrimer films using photolocking of BDK [135]

the azo chromophore migration from high to low light intensity regions can induce the volume expansion [40, 43]. For the glasses, the volume expansion was explained in terms of increase of structural randomness or structural reorganization by light illumination [55–57]. In the case of photopolymers, monomer diffusion from the non-illuminated to the illuminated regions has been used to explain the volume expansion [32, 37]. As in the case of the photosensitive materials described above, the volume deformation effect of the photosensitive hybrimers can be either negative (shrinkage) or positive (expansion) due to different photosensitive mechanisms depending on the hybrimer system and composition. It was known that the photopolymerization makes the volume shrink and refractive index increase. Thus, some hybrimers show volume shrinkage mainly governed by photo-polymerization as introduced in the previous section. However, most of the photo-polymerizable hybrimers doped with photoinitiator undergo volume expansion. This volume expansion is attributed to both the photolocking mechanism and the migration mechanism. The deposited film thickness increases under light exposure when the full area of the film is exposed, e.g., when no photomask is used during the exposure.

This confirms the photolocking mechanism taking place in the hybridizers. In addition, when selective illumination is performed on the coated films for fabrication of microstructures, e.g. when a photomask is used during the exposure, the surface relief height is greater than expected by photolocking mechanism. Thus, the monomer or oligomer diffusion process in the hybridizers can be assumed as demonstrated in photopolymers for fabrication of optical components.

The high surface relief deformation of the hybridizer films induced by the exposure step may be explained by diffusion reactions of the monomers and/or small molecular-weight oligomers in the films [148–150, 152–154, 156–160, 173]. When a coated hybridizer film is exposed, the photoinitiator in the film absorbs light, decomposes into free radicals initiating the polymerization. If a selective exposure is performed, e.g., with a patterned photomask, the photo-polymerization of the matrix and photolocking of the photo-decomposed radicals take place only in the illuminated area, leading to the formation of concentration and density gradients in the film. This selective exposure results in a diffusion of the constituents from the non-illuminated region to the illuminated region of the films, and a surface deformation is produced. The same diffusion behavior was found and explored in the photopolymers [32, 37]. The photopolymers containing a photo-polymerizable monomer, a photoinitiator, and a polymeric binder have been used to fabricate micro-optical elements such as microlenses, holograms, recording media etc. using surface relief formation by polymerization and monomer migration from “dark” areas to “bright” areas. Even though the migration mechanism was proposed in both the photopolymers and the photosensitive hybridizers, no experimental evidence has been given.

A recent study clearly demonstrated in situ photoinduced migration phenomena in high photosensitive hybridizers depending on UV exposure [151]. The high photosensitive hybridizer was designed and synthesized with an eye to inducing high levels of photoinduced migration of monomers and oligomers in subsequent processes. A large quantity of photo-chemical monomers (i.e. a photoinitiator or other photo-decomposable monomer) and a photo-active monomer (i.e. polymerizable acrylate monomer) were added to enhance photoinduced reactions. First of all, highly condensed fluorinated methacrylic zirconium oligosiloxane was synthesized by full condensation of 3-(methacryloxypropyl)-trimethoxysilane (MPTS) and heptadecafluorodecyl-trimethoxysilane (PFAS) with zirconium propoxide (ZPO) complexed with methacrylic acid (MAA). Here, PFAS was used to improve the optical transparency of the materials through fluorination of the methacryl-oligosiloxanes, and ZPO was used to catalyze the sol-gel reaction to form more condensed methacryl-oligosiloxanes. Also, by controlling the amount of PFAS and ZPO used in the reaction, it is possible to tune the refractive index of the hybridizers as required. After the condensation of the alkoxides, water and alcohol were evaporated to obtain a resin without any solvent. Then, benzylidimethylketal (BDK) (a photochemical monomer) dissolved in methylmethacrylic acid (MMA) (a photoactive monomer) were added into the synthesized highly condensed oligosiloxane resin as schematically presented in Fig. 13.15. The hybridizer resin composition containing many possibly diffusible monomers and oligomers can produce large photoinduced change in

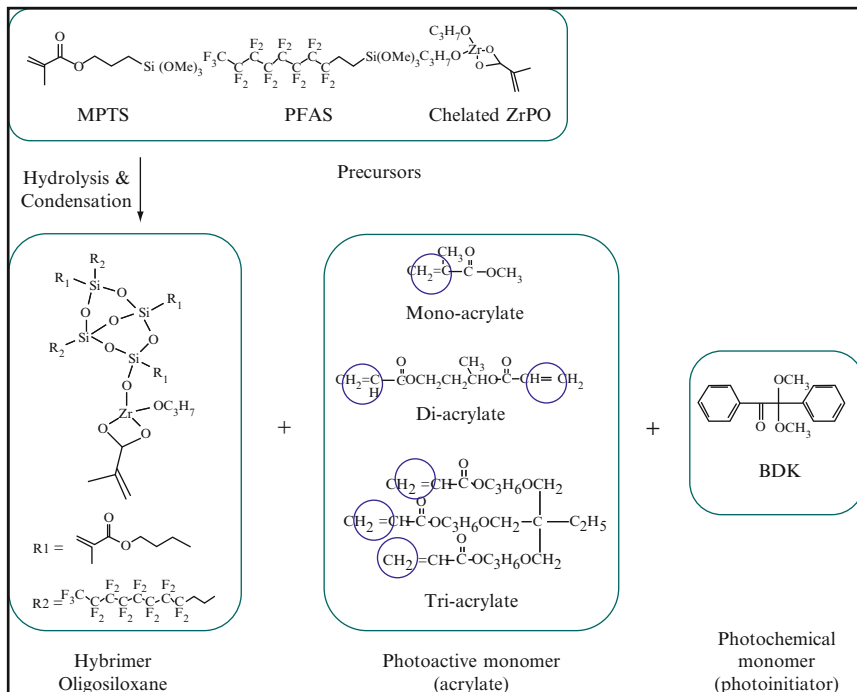


Fig. 13.15 Synthesis and design of highly photosensitive fluoro-methacrylic-zirconium hybrimer [171]

volume swelling and refractive index increase. When the deposited hybrimer film is exposed with a patterned photomask, the expanded patterns with a higher refractive index are generated through various complicated photosensitivity mechanisms. UV illumination induces the photo-polymerization of methacrylates in the oligosiloxanes and monomers including oligopolymerization, low-order polymerization, homopolymerization, and copolymerization initiated by photo-decomposed radicals from BDK. Also, the photo-decomposed radicals from BDK and methacryl radicals of the photoactive monomers are attached to the methacrylate of the oligosiloxanes. In addition, it may be expected to have polycondensation of oligosiloxanes by condensation of unreacted hydroxyls ($\text{SiOH} \rightarrow \text{SiO}$) to be densified under UV exposure. These photoinduced processes consume both monomers and oligomers to be polymerized in the exposed areas. Thus, substantial differences between the exposed and the unexposed areas are produced in the molecular structure including concentration of photoactive monomers or oligomers. The induced chemical gradient is subject to the diffusion of monomers or oligomers from the unexposed region to the exposed region, to be stabilized. This migration makes the exposed areas to swell making patterns with a higher refractive index compared to the unexposed area, which

shrinks due to removal of photochemical and photoactive monomers by the migration as well as by evaporation during heat treatment. The in situ migration behavior in the highly photosensitive hybrimers during UV exposure is represented in Fig. 13.16 [151]. Figure 13.16 shows a set of 3D scanning interferometer images of (a) line-shaped surface structures and (b) circle-shaped surface structures as a function

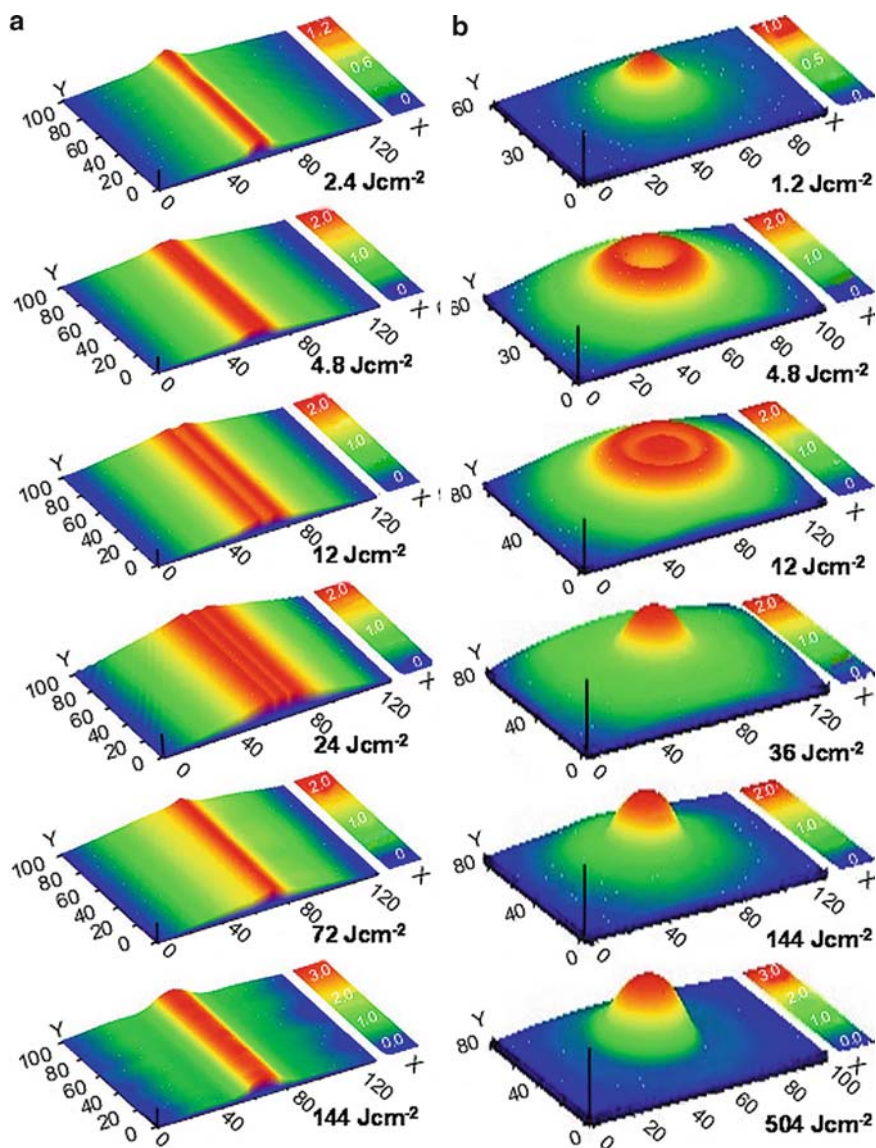


Fig. 13.16 Surface micro-structural evolution of micro-patterns depending on exposed UV dose by photoinduced migration of monomers or oligomers for (a) line-shaped and (b) circle-shaped surface structure [151]

of the UV dose. The line and circle width of a binary photo-mask for the line- and circle-shaped surface structuring were 10 μm and 30 μm , respectively. The photo-fabricated line- and circle-shaped surface structures exhibit various surface modulations as the UV dose increases. Initial UV dose creates a single peak in the exposed region mainly by the migration of monomers or oligomers from the unexposed region. The irradiated area becomes fixed and hardened due to the occurrence of intensive photoinduced reactions. Additional UV exposure makes the evolved pattern shapes to be more complex due to the relative subsidence of the central areas. This subsidence is the result of the hardening of the central region and the migration of oligosiloxanes and unreacted monomers from both the unexposed sides. This increases the height of the film around the exposed region. The migration continues, shifting the peaks towards the center and causing the uplift of the hardened central area along with the formation of another shoulder around the exposed area. This constant migration thus shapes the micro-patterns into three peaks. As the UV dose further increases, the peaks move toward the central peak due to more migration of monomers or oligomers, and finally combine into a single peak of line or circle on the micro-patterns. After this point, the width and the height of the photo-fabricated patterns are enhanced due to more migration, but the shape of the structure no longer changes. Finally, at saturation the peak height reaches a maximum whereas the peak width reaches a minimum, at the maximum UV dose to fabricate the desired line and circle shaped patterns. After building up the single peak, it becomes higher and narrower to form the desired surface structure by concentrating the diffusible monomers or oligomers. This in situ surface micro-structural evolution of the photo-fabricated micro-patterns, convincingly demonstrates the migration behavior of the constituents from the unexposed area to the exposed area in newly designed highly photosensitive hybriders. Furthermore, FTIR microscopy mapping was utilized to observe the chemical composition deviation around the exposed area showing the polymerization in the exposed region. Also, a refractive index profile similar to the topological profile was observed by a near field scanning optical microscopy (NSOM). Thus, it was shown that the expanded pattern in the exposed region has a higher refractive index than in the unexposed region. These micro-analyses confirm that all the photoinduced reactions of polymerization, migration and photolocking are present in the exposed area. In addition, a higher concentration of Ti in the exposed area than in the unexposed area was found in the titanium doped hybridizer showing the photoinduced migration of siloxane oligomers [153]

As mentioned above, the micro-patterned surface structure is dependent on the exposed area size (line width or circle diameter) as well as on the UV exposure. It is also expected that the migration is dependent on other composition and process parameters, which would result in variations in the micro-structural evolution of a given film as a function of the UV dose. By understanding this behavior, we can control the shape of the photo-fabricated micro-structures to produce a range of optical elements. Figure 13.17 illustrates the height and width changes of photo-fabricated micro-patterned surface structures as a function of various materials and process parameters [151]. First of all, as already described, the micro-patterned peak is divided into two or three peaks and then finally combines into a single peak with larger height and smaller width as UV exposure grows. As the exposed area

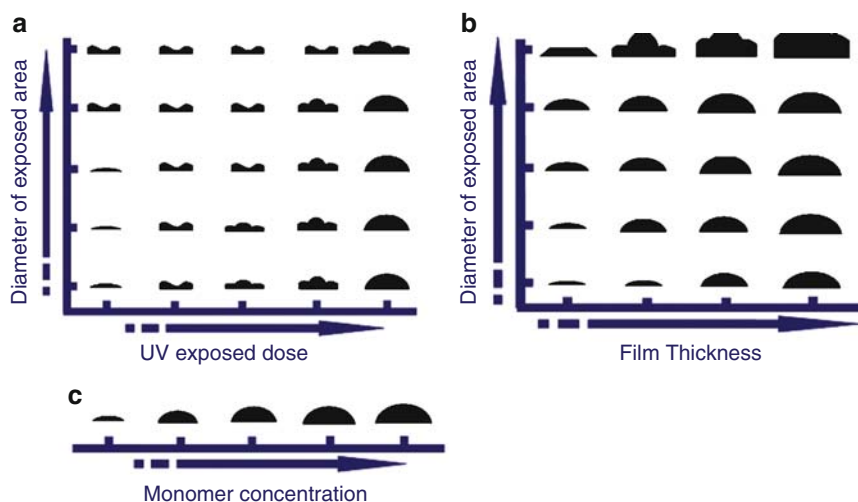


Fig. 13.17 Mapping of micro-pattern shapes directly photo-fabricated on hybrimer films depending on photo-migration parameters; (a) UV exposed dose, (b) concentration of photo active and photochemical monomers, and (c) film thickness [151]

size increases, the migration length becomes longer but not enough to reach the center of the exposed area. Thus, it needs higher UV dose to form the desired large sized shape of micro-patterns. Also, the micro-patterned surface structure is affected by the concentration of monomers. By increasing the number of diffusible monomers, the large size and height micro-patterns are inscribed. Finally, a thicker film leads to larger micro-patterned surface structures since it contains more diffusible moieties. However, in the case of excessively large pattern areas, the migration does not completely proceed to form the single desired shaped peak. Thus, the photoinduced migration is dependent on the diffusible monomer concentration and the migration length is determined by the exposed area. In order to form large sized patterns, it is required to increase the monomer concentration per unit area by growing the concentration or thickening the film or enhancing the light intensity to stimulate the migration. Overall, the photoinduced migration mechanism is a major factor to expand the volume in the photosensitive methacrylate hybrimers at the selected UV illumination. Thus, it allows the fabrication of the desired convex or concave microlenses, gratings, and optical waveguides of various sizes by controlling the material composition and process parameters.

In conclusion, various organic photosensitivity mechanisms in addition to simpler inorganic mechanisms are involved when the hybrimer film is selectively UV illuminated through a photomask or via direct laser writing. Figure 13.18 illustrates with a schematic diagram how to make the convex surface structure with increased refractive index in the UV illuminated region [151]. First of all, the photoinitiator is readily decomposed into two radicals that initiate the photo-polymerization

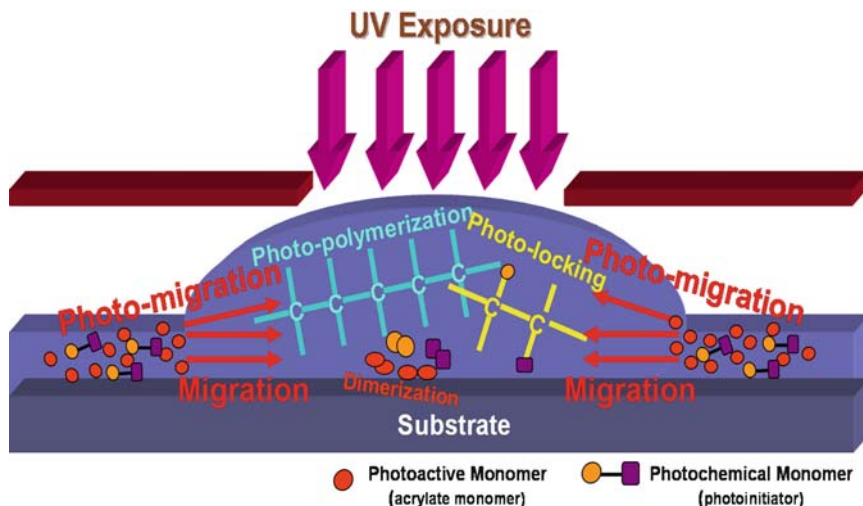


Fig. 13.18 Schematic diagram of photosensitivity mechanisms to form convex surface structure [151]

of the methacryl-oligosiloxanes and acrylate monomer. This photo-polymerization includes processes such as oligopolymerization, low-order polymerization, homopolymerization, and copolymerization. Also, the photo-decomposed radicals are fixed in the methacryl-oligosiloxane matrix or undergo a dimerization process in which two benzoyl radicals form benzyl molecules, as has been described above. The cross-linking and the attachment of doped molecules in the UV exposed area of the hybrimer film differentiate these areas from the mixed state of oligomers and monomers in the unexposed areas. This structural distinction causes substantial differences between the concentration of unreacted molecules in exposed and unexposed areas, as well as in the diffusivity, and the molecular size and weight of the constituents in these areas. The result is a chemical potential gradient between the exposed and unexposed areas, making it thermodynamically preferable for unreacted oligomers or monomers to migrate into the exposed area where they then react *via* photo-polymerization or photolocking. This migration will continue until all available sites for polymerization and photolocking in the exposed area are consumed, or until the diffusivity of the oligomers or monomers in the unexposed area drop below the level necessary to drive it. Thermal baking of the hybrimer film after UV exposure stabilizes it, allowing it to be patterned clearly. The heating may polymerize the methacryl-oligomers and the acrylate monomers in the film, and may also remove any photoinitiator which did not decompose during the UV exposure by evaporation. This latter process is likely to occur due to the photoinitiator's high diffusivity and volatility in the unexposed area. In any case, thermal baking hardens the surface of the exposed region, preventing further migration of either oligomers or monomers. In this way, stabilized surface structures with expanded volumes and higher refractive indices are formed in the exposed region.

13.3.6 *Wavelength Dependence of Photosensitivity Mechanisms*

As described above, the photosensitivity of the hybrimers is governed by many mechanisms and is complex, inducing different types of changes in the refractive index and in the volume. Among many photosensitivity mechanisms of organics in the polymerizable hybrimers, the most prominent mechanism is the polymerization that increases the refractive index and reduces the volume (which does not always occur and can be negligible in thin films). However, the main mechanism to increase the refractive index is the photolocking of the photo-decomposed monomers from the photoinitiator, whereas the mechanism to increase the volume predominantly is the photoinduced migration of monomers or oligomers from the unexposed area to the exposed area. On the other hand, the photosensitivity involving the inorganic phase in the hybrimers is due to the siloxane condensation and the Ge-related siloxane densification leading to drastic volume shrinkage and to refractive index increase. Thus, combining the photosensitivity mechanisms by optimizing the design of the composition, we can fabricate microstructures with the desired topological and optical profiles. Also, the photosensitivity of the hybrimer can be maximized in certain compositions by optimizing both the photosensitive mechanisms of the inorganic and organic components. Besides composition, other process conditions such as UV wavelength and atmosphere during UV illumination can affect the photosensitivity of the hybrimers. As a result, modulation of the fabricated microstructures profiles can be achieved by changing the UV wavelength and atmosphere during UV illumination. Thus, it was found that the photosensitivity of the Ge-doped methacrylate hybrimers was highly sensitive to the UV light used to produce results in fabricating different topographical microstructures [174]

First of all, since the photoinitiators are prone to be decomposed at the UV wavelength for effective polymerization initiation, the photolocking mechanism can be affected by the UV wavelength. It was found that the photolocking rarely occurred in some photoinitiator doped hybrimers over the whole wavelength spectrum [147]. It has been reported that the photo-polymerization of acrylates is dependent on the wavelength of the light employed [175]. Also, it is apparently known that the photoinduced densification of Ge-doped silica glass occurs only for light in the deep UV region of the spectrum [47, 51]. The Ge-doped methacrylate hybrimer consisting of methacrylate and Ge doped silica in the molecular structure showed high photosensitivity in the form of a refractive index increase accompanied with volume compaction [133]. It was found that the photosensitivity to which both the Ge-related densification in the silica network and the photo-polymerization of methacrylate contribution, is highly sensitive to the wavelength of the UV light used. Figure 13.19 shows the change in the refractive index and the film thickness as a function of UV light fluence of a Hg/Xe lamp (220–260 nm spectral range) and a Hg lamp (350–390 nm spectral range) which possess different UV spectral ranges [174]. The illumination of Hg/Xe lamp causes an initial drastic change in both the refractive index and the film thickness by photo-polymerization of the methacrylates and photoinduced-condensation of the siloxanes. Further refractive index increase

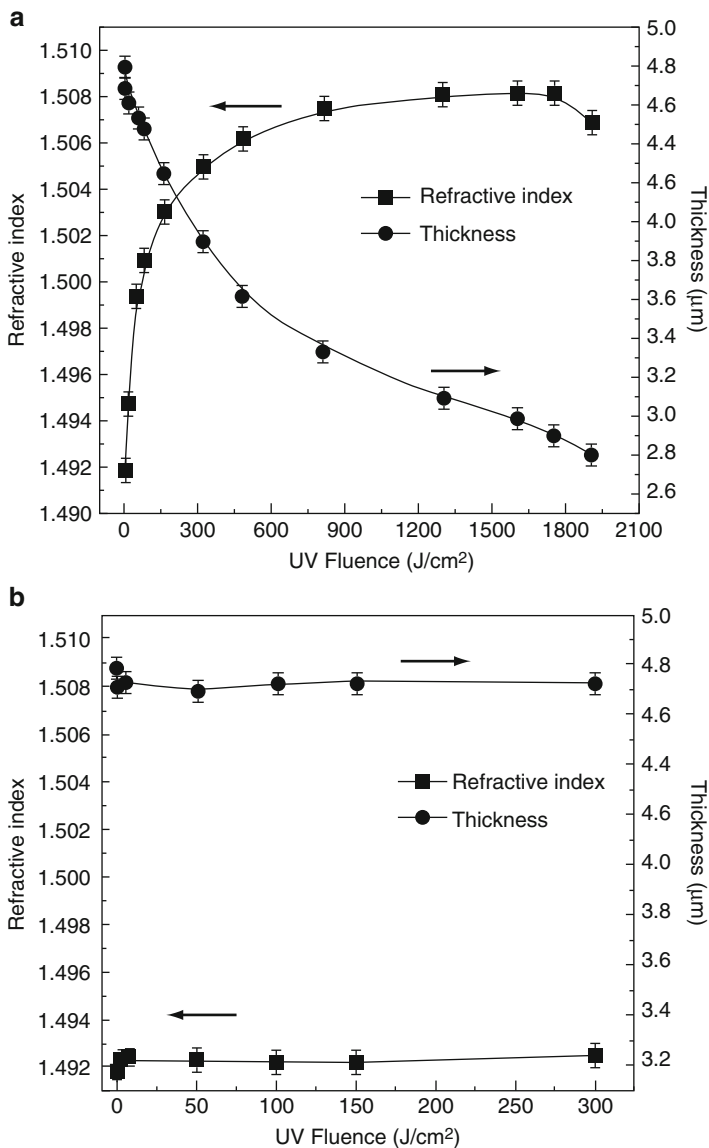


Fig. 13.19 Change in refractive index and film thickness of the Ge-doped methacrylate hybrimer as a function of UV fluence when illuminated by (a) a Hg/Xe lamp (220–260 nm) and (b) a Hg lamp (350–390 nm) [174]

and volume shrinkage are induced mainly by Ge-related densification. The changes saturate after exposure, for a long time and then finally start decreasing the refractive index due to the photoinduced decomposition of methacrylates initiated earlier. On the other hand, Hg lamp irradiation rarely changes both the

refractive index and the film's thickness, moreover the initial increase is small. Thus, short-wavelength UV lamps induce high photosensitivity whereas long-wavelength UV lamps trigger almost no photosensitivity. In other words, the photo-polymerization and the Ge-related densification with siloxane condensation are triggered only by the irradiation at shorter UV wavelength. It was also found that the photo-polymerization occurred at short-wavelength illumination without a photoinitiator being necessary and the photo-polymerization at long-wavelength exposure was enhanced by irradiation in an inert atmosphere. Large absorption and photon energy at short-wavelength UV allow the hybrimers as well as the polymers to be photo-polymerized without adding a photoinitiator. Inert atmosphere during UV exposure removes oxygen inhibition of free-radical photo-polymerization of acrylates. Therefore, the highest photosensitivity of the Ge-doped methacrylate hybrimers resulting in a maximum and simultaneous increase in the refractive index and volume compaction was obtained under short-wavelength illumination in an inert atmosphere. Direct photo-patterning of the Ge-doped methacrylate hybrimers was carried out using a UV fluence of $1,800 \text{ J/cm}^2$ through a quartz photomask consisting of a single $5 \mu\text{m}$ circle using both the Hg/Xe lamp and the Hg lamp. Figure 13.20 shows 3D AFM images of the single-circle patterns on the Ge-doped methacrylate hybrimer films with the different UV lamps [174]. Different lens-like shapes were patterned depending on which lamp was employed. The Hg/Xe lamp exposure makes concave lens-like shapes induced by volume compaction that is mainly the result of photo-polymerization and Ge-related densification (Fig. 13.20a), as expected. On the other hand, a convex lens-like shape is observed after direct photo-patterning using the Hg lamp (Fig. 13.20b), even though a little photoinduced reduction of the film's thickness was found in Fig. 13.19. This was made by the volume expansion in the exposed area due to the photoinduced migration of the monomers and/or small molecular oligomers, which is seldom sensitive to the UV wavelength, as explained previously. However, for the illumination with the Hg/Xe lamp the photoinduced migration was dominated by the other photosensitivity mechanisms mainly photo-polymerization of methacrylates and Ge-related densification. Thus, the bulges at the edge of the shape (see Fig. 13.20a) are the result of the occurrence of the photoinduced migration. These apparently opposite shapes of the direct photo-patterns assert the photosensitivity to be highly dependent on the UV lamp wavelength. Therefore, the appearance of the micro-optical structures can be controlled by changing the wavelength of the UV light employed and its fluence.

13.3.7 Photosensitivity Mechanisms in Functionalized Hybrimers

In the synthesis of hybrimers, the mild synthesis conditions offered by the sol-gel process allow for the incorporation of optically active organic molecules

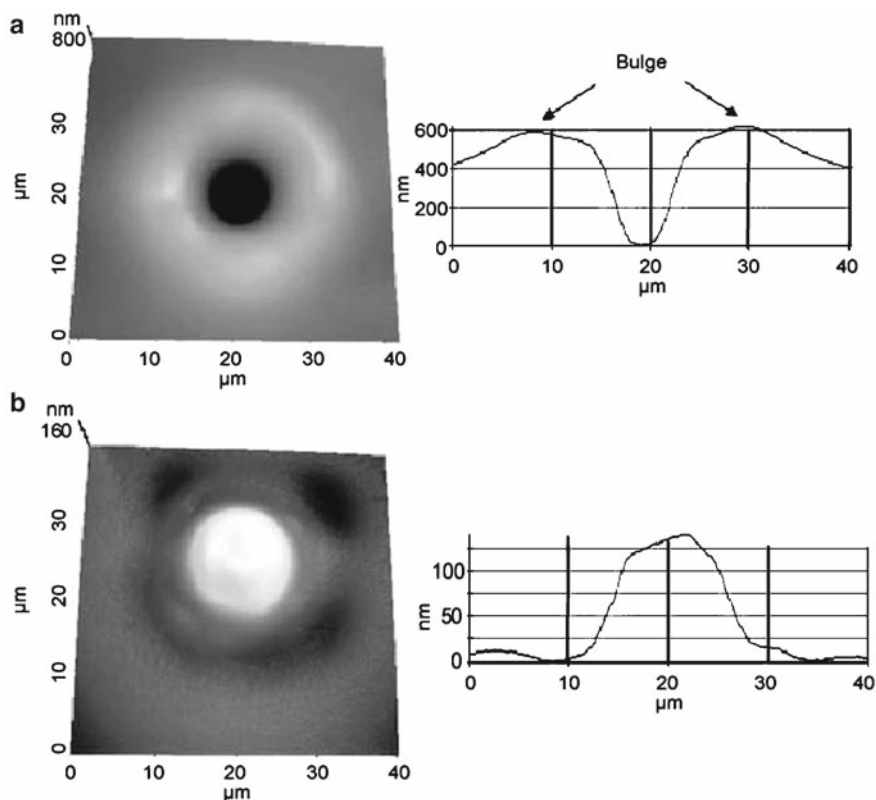


Fig. 13.20 AFM images of direct photo-patterned single circle on the Ge-doped methacrylate hybrimer film illuminated by (a) a Hg/Xe lamp (220–260 nm) and (b) a Hg lamp (350–390 nm) [174]

(laser dye, second-order nonlinear chromophores, reverse saturable absorbers, photochromic molecules, etc) into the siloxane matrix to form doped xerogels with specific optical properties. Thus, the optically functionalized hybrimers exposed to UV light are another type of photosensitive hybrimers for photo-fabrication of optical micro-structures. It is well known that a high birefringence (>0.01) can be created in materials containing azobenzene chromophores *via* the photo-excitation of azobenzene groups by polarized light. The mechanism involves successive *trans-cis* photo-isomerization and thermal *cis-trans* relaxation, whose process is illustrated in Fig. 13.21 [44, 45]. This leads to the alignment of azo groups in a direction perpendicular to the polarization of the incident light. The azobenzene incorporated into polymers, chemically bonded or not, often called azo-polymers, have been investigated for potential technological applications due to their interesting photosensitivity to induce anisotropy (birefringence and dichroism) as well as surface modulation [40–45]. The photoinduced

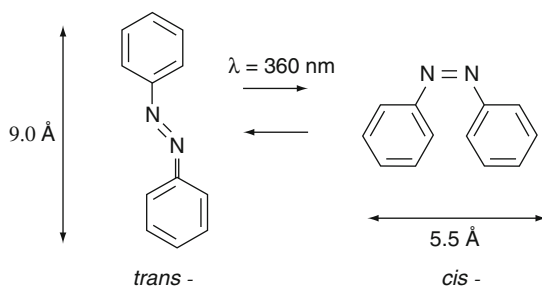


Fig. 13.21 Polarized light induced photo-isomerization of azobenzene group [44]

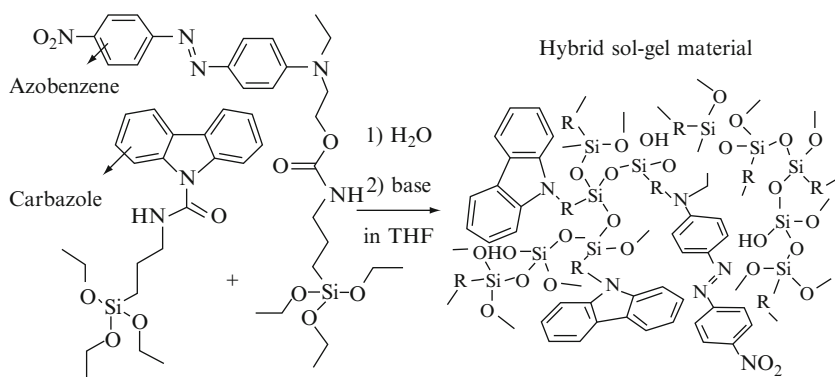


Fig. 13.22 Synthesis of azo-hybrid from azobenzene modified alkoxy-silanes [176]

birefringence and surface modulation in the azo-polymers are due to photoinduced alignment of the azobenzene chromophores and large-scale polymer chain migration, respectively. Thus, many studies have been performed on the formation of surface relief grating (SRG) on the azo-polymer films. Like azo-polymers, the azobenzene containing hybriders, azo-hybriders, were successfully synthesized using a sol-gel reaction of the azobenzene modified alkoxy-silanes, as represented in Fig. 13.22 [161, 162, 176]. Modified Disperse Red 1 (DR1) and carbazole grafted triethoxysilane monomers were mixed with tetraethoxysilane in acidic water with a mutual solvent (THF). After complete hydrolysis of the ethoxy groups, a small amount of base was added to the mixture in order to catalyze the condensation reactions. The presence of sterically hindered carbazole units prevents the azobenzene molecules from aggregating. It was found that its photosensitivity to change the birefringence and volume was comparable to that of the azo-polymers. Using the azo-hybrid, direct photo-fabrication of surface relief gratings (SRG) with high diffraction efficiencies was demonstrated [162, 176]. This photo-fabrication exploited the fact that only TM polarized (p-polarized)

light leads to high diffraction efficiency SRG, which is similar to the case of azo-polymers. Also, near-field optical patterning of the azo-hybrimer films with sub-wavelength resolution was made to provide potential applications to optical nanolithography and high density optical data storage. Figure 13.23 shows an example of near-field surface patterning of a 20 nm-thick film with a $\lambda/10$ resolution [177]. An array made of 9×9 nanodots of 55 nm-lateral size was inscribed in an area of $1 \times 1 \mu\text{m}^2$. In the profiles of two dot lines shown in Fig. 13.23, each nanodot is well separated from its closest neighbors. This near-field optical patterning enables to record binary data at a density as high as $80 \text{ bits } \mu\text{m}^{-2}$.

Dithienylethenes are photochromic molecules characterized by a large change in their UV-visible absorption spectrum, a thermal irreversibility for most of them, and high durability for recycle use [178–180]. The photoinduced electrocyclicization, responsible for the increase in the electronic delocalization of the molecules, generates an increase of the polarizability of the electronic cloud of the photochromes. They are then able to change the refractive index of the medium in which they are incorporated. Thus, the hybrimers doped with dithienylethene derivatives present a large photoinduced refractive index change ($\Delta n = 3 \times 10^{-3}$ at 785 nm) even with low doping concentration (0.7 wt%) [164]. However, the low solubility of the dithienylethene in the sol–gel medium prevents the refractive index change from increasing. To overcome this limit, the dithienylethene functionalized hybrimers in which the photochromic molecules are covalently attached to the siloxane network were synthesized by condensation of the newly synthesized triethoxysilylated dithienylethene with methyltriethoxysilane (MTES) precursors [163, 178]. These functionalized hybrimers showed a large refractive index change ($\Delta n \approx 4 \times 10^{-2}$ at 785 nm) which is at least an order

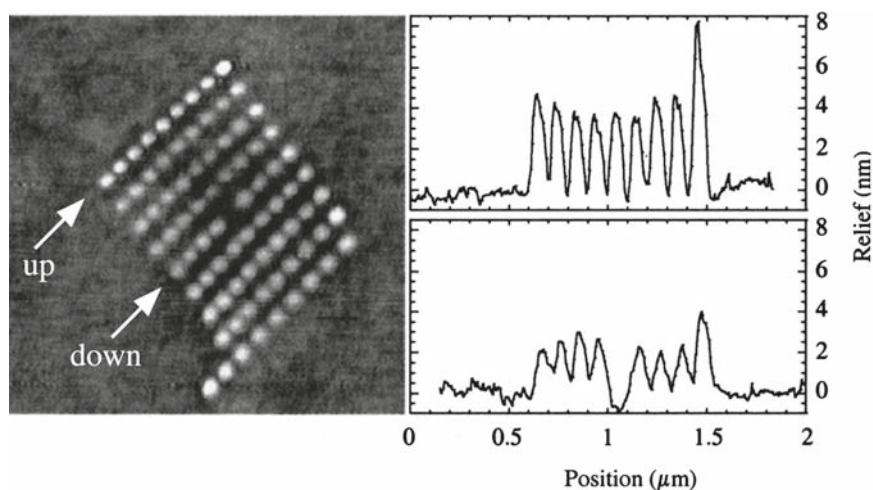


Fig. 13.23 Near-field optical patterning of an array of 9×9 bumps on a 20 nm-thick film. The lateral size of each bump is 55 nm, the mean height of the bumps is 5 nm [177]

of a magnitude higher than the values previously observed for other solids containing diarylethene units. Also, these had high photochromic reaction efficiency, thermal stability, and strong absorption in the colored state. This allows imprinting efficient ridge optical waveguides and gratings. Such a thermally irreversible photochromic material is a potential candidate for application in optically rewritable information storage media.

13.4 Direct Photo-Fabrication of Micro-Optical Elements

The emergence and rapid growth of the microelectronic technology combined with the optical technology need to couple and control light in and out of optical waveguides, together with concomitant drive for the miniaturization of components. A new area of optics termed “micro-optics” means optical elements of dimension of a millimeter or smaller [1, 7]. Mainly, this has implied lenses, or elements that act as lenses, as well as structures that redirect, polarize, and otherwise alter some state or direction of light. These would include elements like lenses, mirrors, gratings, and polarizers etc. made in micrometer scale. Also, optical waveguide structures can be considered in the broader classification under the name of “integrated optics” [3, 5]. These micro-optical elements are achieved by surface relief or refractive index modulation whose periods would be in the micrometer scale or of a submicron size comparable to the optical wavelength. The micro-optical structures are usually fabricated using multi-step processes including the photoresist and the etching processes based on the microelectronic fabrication technology. On the other hand, the direct photo-fabrication technology, in which the micro-optical structures are inscribed on the photosensitive materials just by selective light illumination, can remove the photoresist and the etching processes to simplify the fabrication of the micro-optical components. The elimination of the developmental step results in improved surface quality of the fabricated elements. Different selective light illumination technologies can be employed for the direct photo-fabrication. The simplest method is to use a photomask which gives the selective light-wave amplitude. However, with photomask illumination it is difficult to create submicron size patterns due to the limitation of the wavelength of light and resolution of the photosensitive materials. The phase-mask illumination producing light interference using a laser on the photosensitive materials can pattern submicron size relief or modulation. Also, the holographic interference using two or more laser beams, is the most useful method to pattern submicron size features in a large scale but is limited to imprint only periodic structures. Finally, the direct laser writing (DLW) has been applied for fabrication of various micrometer scale micro-optical structures. The DLW is a convenient method owing to its mask-free and non-contact features but is time consuming. For submicron size patterns, the electron beam writing can be used instead of using a laser. Direct photo-fabrication of micro-optical components such as gratings, optical waveguides, and microlenses on the photosensitive hybri-mers has been

reported using different fabrication technologies, as listed in Table 13.1. In this section, these will be introduced to prove the potential applicability of the photosensitive hybridizers.

13.4.1 Diffraction Gratings

A diffraction grating is a reflecting or transparent element, whose optical properties are periodically modulated [4]. Most commonly, the diffraction gratings appear as fine parallel and equally spaced grooves and refractive index differences on the material surface. When light impinges on a diffraction grating, diffractive and mutual interference effects occur, and light is reflected or transmitted in discrete directions, called diffraction orders. Because of their dispersive properties, the gratings are commonly used in monochromators and spectrometers.

There have been many reports on how to imprint the surface corrugation for the gratings on the hybridizer films using a line-patterned photomask to prove their photosensitivity [137–139, 154, 157–159]. Most of the surface relief gratings (SRG) have been printed mainly by the photoinduced migration mechanism to make volume expansion. It was also reported that the SRG was made by the photoinduced decomposition, photo-polymerization, and photoinduced densification to shrink the volume, and the refractive index modulated grating was inscribed by simple photo-polymerization. Generally, the imprinted feature size of the diffraction grating is dependent on the light exposure dose and the material composition.

The simplest method to fabricate a diffraction grating on the photosensitive hybridizers is to use a line-patterned (wider than 1 μm) photomask. Kärkkäinen et al. [157, 158] fabricated a diffraction grating which was printed by use of a photomask with a linewidth of 35 μm and a period of 70 μm . The UV exposure dose of 10.6 mJ/cm^2 resulted in a sinusoidal grating with a FWHM linewidth of 42.8 μm , a FWHM space width of 27.0 μm and a peak-to-valley height of 4.46 μm . The rms surface roughness was measured by AFM to be 4.4 nm. The linewidths of the printed gratings were larger than the linewidth of the openings on the photomask patterns due to the photoinduced migration. Also, a sinusoidal grating with a FWHM linewidth of 43.4 μm and a peak-to-valley height of 27.6 μm was fabricated using a binary photomask with a linewidth of 41 μm and a period of 82 μm . The rms surface roughness was measured by AFM to be 12.6 nm which is larger than the previous one. Rantala et al. [159] printed a diffraction grating with a period of 24 μm and a peak-to-valley depth of 0.685 μm using a UV dose of 2.78 J/cm^2 and measured the diffraction efficiencies, expecting an increase of the refractive index in the expanded volume region. In this study, the surface relief height was found to be proportional to the period of gratings in the photomask, due to more migration in the larger exposed area. The fabricated micro-structures had a smooth surface with rms surface roughness of around 2.2 nm with good chemical, mechanical and thermal stability. For example, the stability against organic solvents such as acetone

or alcohol was found to be excellent, which is not typically the case with conventional optical polymers. It was also found that a long accelerated aging test at 120°C had no effect on the optical properties of the materials. In addition to the use of binary photomasks, a gray-scale mask was used to fabricate saw-tooth gratings of different periods (6, 11, and 21 μm) which were formed by volume expansion [154]. The grating depth had a proportional relationship with the grating period, whereas the surface roughness had an inversely proportional relationship with the grating period. Contrary to the formation of SRG by volume expansion due to photoinduced migration, the SRG made by volume compaction due to photo-polymerization or photo-densification were also fabricated using a photomask. Blanc et al. [137] and Soppera et al. [139] recorded the diffraction gratings with a period as small as 1.4 μm using a UV dose of 0.9 J/cm². Figure 13.24 shows the patterned 4 μm period diffraction grating with amplitude of 785 nm and its diffraction pattern. The profile is sinusoidal, which offers the advantage of reducing the intensity diffracted into the higher orders. The diffraction efficiency of the grating was demonstrated by the high light intensity diffracted into the \pm first order. The diffraction efficiency was smaller for the gratings with narrower period and lower amplitude. Also, the measured diffraction efficiency was lower than the theoretically computed one due to the imperfect sinusoidal shape of the patterned surface. The patterned grating had a very smooth surface as low as 0.2 nm which is below the 1 nm limit for high-quality optical surfaces. In addition, the gratings are robust enough not to undergo changes of the diffraction efficiency after being dipped in a bath of isopropanol or water and being heated at high temperature. Pelissier et al. [138] recorded sinusoidal gratings with periods of 4 μm and 2 μm . This formation of surface corrugation was explained by the constrained densification induced by photo-polymerization in the exposed area. The diffraction efficiencies of the grating in the various orders were measured and compared with the theoretical value. Small discrepancies between the measured and the calculated diffraction efficiencies were explained by the imperfect shape of the corrugated surface. Also, the robustness of the gratings was proved by unchanged diffraction efficiencies after treatment in a solvent or water and baking at high temperature. Jang et al. [84, 85] demonstrated the fabrication of grating patterns on the bulk glass of the Ge-doped hybrimer with a linewidth of 6 μm using the photoinduced Ge-related densification to get volume compaction in the exposed region. It was observed that the volume compaction in the UV exposed area was associated with periodic pattern inscription, which was a direct evidence for photoinduced densification in the Ge-doped hybrimer.

Laser direct writing (LDW) has been used to pattern lines for the formation of diffraction gratings. However, LDW is not a common technology to fabricate diffraction gratings, since large laser beam size makes it hard to write submicron size line patterns. However, Kärkkäinen et al. [157, 158] presented the application of LDW with a bitmap exposure of 20 ns to print gratings whose lines and spaces were oriented along the fast scan direction with a period of 100 μm . The laser exposure of 10 mJ/cm² resulted in a grating with a FWHM linewidth of 61.7 μm , a space width of 42.2 μm and a peak-to-valley height of 1.93 μm with rms

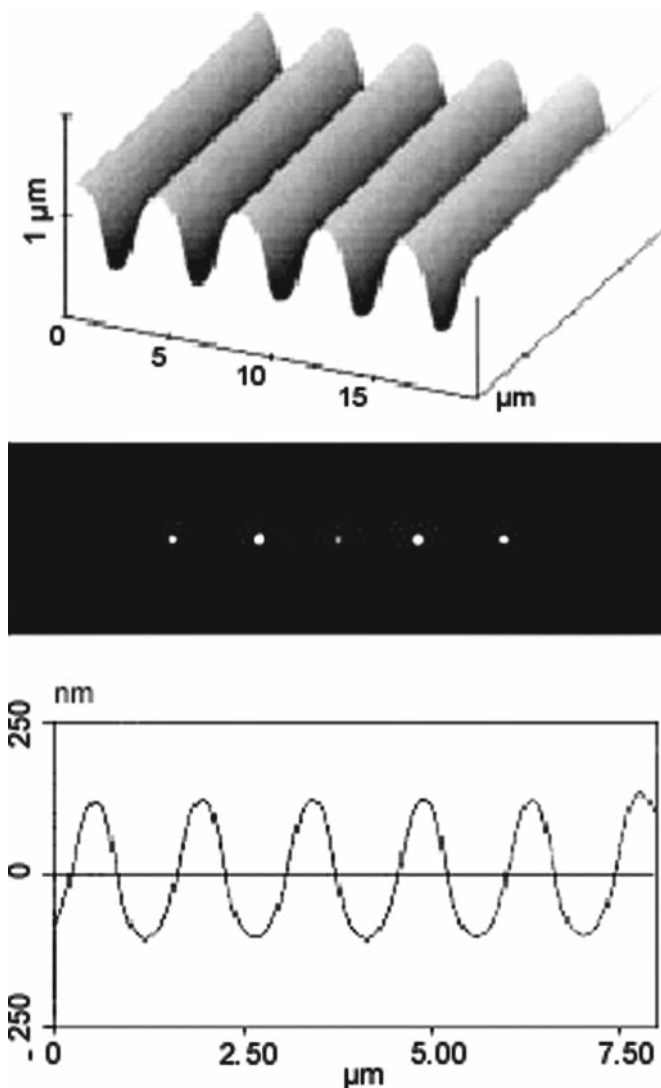


Fig. 13.24 AFM 3D image (*top*) and profile (*bottom*) of 4 μm period grating (*top*) and photograph of the Fraunhofer diffraction pattern (*center*) recorded on the hybrimer thin film [137]

surface roughness of 3.9 nm. When the laser exposure dose was raised from 6 mJ/cm^2 to 30 mJ/cm^2 , the peak-to-valley height increased from 1.2 μm to 6.8 μm . It was found that the gratings imprinted by UV exposure with a photomask and by the laser direct writing had different surface-topographies although they were exposed with the same UV dose. Also, Yu et al. [155] reported the LDW using a He-Cd laser for the fabrication of an array of lines with a period of 45 μm and a

maximum height of $1.17\ \mu\text{m}$. It was observed that the surface relief thickness increased with the laser beam intensity due to more monomer diffusion. Also, it was seen that the smoothest surface profile was produced with the smallest step size of the laser direct writing.

As described above, the photosensitive hyrimers are more suitable for fabrication of large period gratings and large dimensional optical elements with excellent surface smoothness. However, in the micro-optical systems, the diffraction gratings require submicron periods comparable to the optical wavelength for the application of wavelength dispersion, conversion, and modulation. However, with the photo-mask illumination and the LDW, it is difficult to imprint submicron patterns because of limits in the exposed light beam size and wavelength. Thus, the phase-mask illumination or the holographic interference enabling the patterning of submicron features should be rather used to fabricate diffraction gratings for practical applications. However, the monomer migration from the unexposed area to the exposed area still restricted the printing of submicron diffraction gratings in most photosensitive hyrimers. The phase-mask illumination using an excimer laser has been applied to fabricate sub-micron diffraction gratings on the hyrimer films. Figure 13.25 shows the schematic illustrations of the phase-mask illumination system using an excimer laser and the interference beam diffracted by a phase-mask to form periodically modulated beam intensity [141]. The light intensity profile with half the phase-mask pitch is made on the sample by interference of the diffracted beam from the phase-mask. Blanc et al. [136, 153] demonstrated imprinting of the diffraction gratings with periods of $1\ \mu\text{m}$ and $0.56\ \mu\text{m}$ using the phase-mask illumination. These were made by volume shrinkage due to the photo-polymerization or volume swelling due to the photoinduced migration. The $0.56\ \mu\text{m}$ period grating with a groove depth of $115\ \text{nm}$ was reported to have the first-order diffraction efficiency of $\sim 1.6\%$. The diffraction efficiency was stable up to a temperature of 220°C and remained unchanged when the samples were placed in alcohol or water for 30 min. Kang et al. [141] fabricated the SRG with a period of $528.36\ \text{nm}$ and a groove depth of $200\ \text{nm}$ by irradiation with the KrF excimer laser through a phase-mask with a $1050.50\ \text{nm}$ pitch. The gap between the thin film and the phase mask, as shown in Fig. 13.25, is

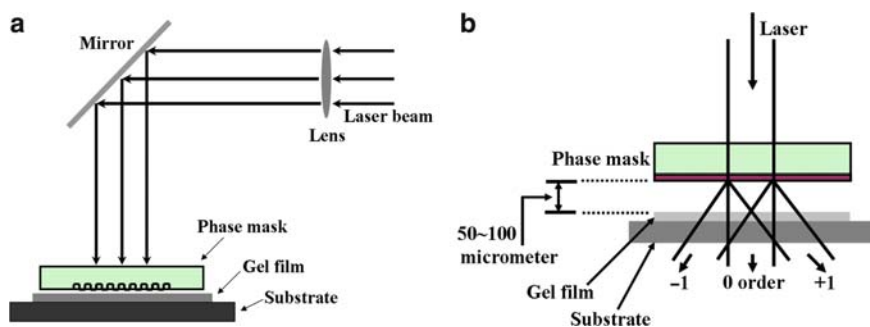


Fig. 13.25 Schematic illustrations of (a) phase-mask lithography using an excimer laser and (b) interference beam diffracted by a phase-mask [141]

an important parameter for making an excellent interference pattern on the thin film. During the formation of the diffraction grating, the power of the zero-order light has to be minimized, and the power of the first-order light has to be maximized. Thus, the optimum distance between the phase mask and the films was found to be about 50–100 μm . The measured first-order diffraction efficiency was dependent on the laser exposure time and optimized at $\sim 3.41\%$. Long laser exposure might cause the distortion of the grating shape or surface ablation by methacrylate decomposition. This could reduce the diffraction efficiency. In addition, Darracq et al. [162] photo-inscribed the SRG on the azo-hybrimer films using the holographic interference of the Ar^+ laser (514 nm) which is absorbed in the azo-hybrimer. It was found that high diffraction efficiency up to 40% was obtained and was dependent on the laser exposure energy. Also, Frey et al. [176] demonstrated the writing of the gratings on the azo-hybrimer films using the grating translation technique which is similar to holographic interferometer. For the azo-hybrimers whose photosensitivity depends on the polarization of light, the grating was fabricated only when TM polarized (p-polarized) light was used.

Even though the holographic interference is being widely used in photopolymers to produce the holograms since it is based on the non-contact mass production technology, few studies have reported on the photosensitive hybrimers. The holographic interference offers tunability over a wide range, good resolution, relatively simple apparatus and a large coverage of patterns. Imprinting of the diffraction gratings with a period larger than 1 μm by holographic interference was reported [181]. Also, the refractive index modulated grating with a period of 430 nm was printed and its diffraction was studied [166]. A different type of hybrimer, silica sol blended with diffusible high refractive index acrylate monomer, was used to fabricate a diffraction grating with near 100% grating efficiency for holographic storage [160]. Kang et al. [148] fabricated the diffraction gratings in a newly designed highly photosensitive hybrimer using the two-beam interference method. Figure 13.26 shows the schematic illustrations of the two-beam interference system and the interference beam obtained from the two-beam system [148]. The He-Cd laser is split into two-beams by a half mirror (HM) and then the respective beams are condensed onto the sample surface to form straight interference fringes after passing through a beam expander (L1), a 10 μm diameter pinhole (P) and a collimating lens (L2). When the system is used for the fabrication of diffraction gratings, the grating period is represented by the equation $\Lambda = \lambda/2 \sin \theta$, where λ is the wavelength of the He-Cd laser (325 nm), and θ is the incident beam angle on the hybrimer films. The spacing of the fringes was controlled by changing the incident angle of the two-beams ($\theta = \theta_1 = \theta_2$), which makes it possible to fabricate the diffraction gratings with various periods in the two-beam interference system. Thus, the diffraction gratings with a period from 5 μm down to 1 μm were fabricated on the photosensitive hybrimer films using the two-beam interference technique as shown in Fig. 13.27 [148]. The fabricated grating profiles were perfectly sinusoidal and the patterns were very homogeneous regardless of the grating pitch. In particular, in the case of the photomask patterning process, the fabrication of gratings with a submicrometer period was relatively difficult due to the diffraction limit between the sample and

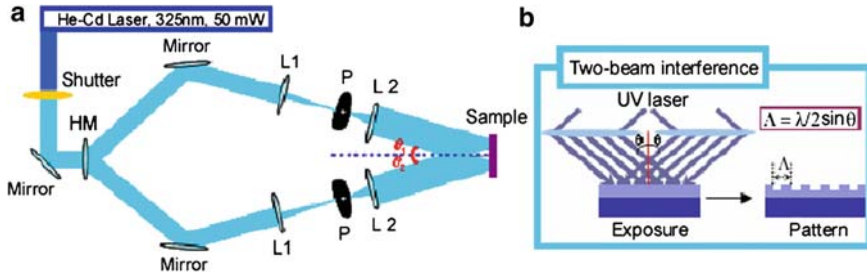


Fig. 13.26 Schematic illustration of (a) two-beam interference holography and (b) interference beam illuminated by the two-beam interference holography [148]

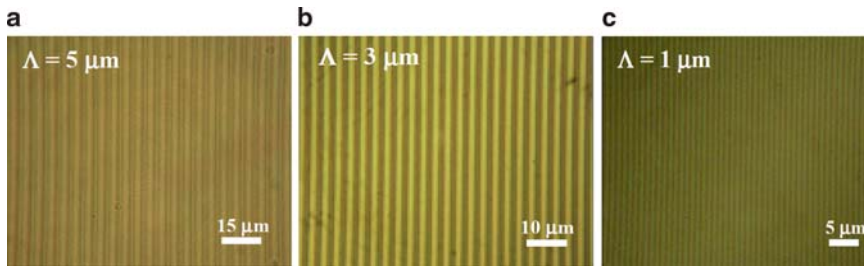


Fig. 13.27 Optical micrographs of diffraction gratings with periods of (a) $5 \mu\text{m}$, (b) $3 \mu\text{m}$, and (c) $1 \mu\text{m}$ fabricated by the two-beam interference holography (photo-fabrication: before baking, optical micrographs: after baking) [148]

the mask. Using the two-beam holographic interference method, the diffraction gratings with a submicrometer period were fabricated on the photosensitive hybriimer films. Figure 13.28 shows the AFM images of the diffraction gratings with periods of 600 nm and 500 nm [148]. Since the grating profile is related to the UV dose, the diffraction of gratings relies heavily on the laser beam intensity and the exposure time. The diffraction effects of the gratings were measured in situ and the calculated efficiency was plotted versus laser irradiated time, as shown in Fig. 13.29 [148]. As the exposure time increased, the diffraction effects were more pronounced and the gratings showed the strongest diffraction effects with the highest efficiency of 11.57% at an irradiation time of about 15 min . Furthermore laser illumination decreased the diffraction efficiency possibly because of the broadening of the gratings and the distortion of the grating shape. Thus, the diffraction effects and efficiencies of the gratings were heavily dependent on the UV exposure time and would be decreased by too high UV doses. The optimum UV dose to design the desired gratings is the most important factor to obtain the strongest diffraction effects of the gratings. Moreover, Kang et al. [149] fabricated 2D diffraction gratings by 3-beam or 4-beam interference made by using a triangular or rectangular

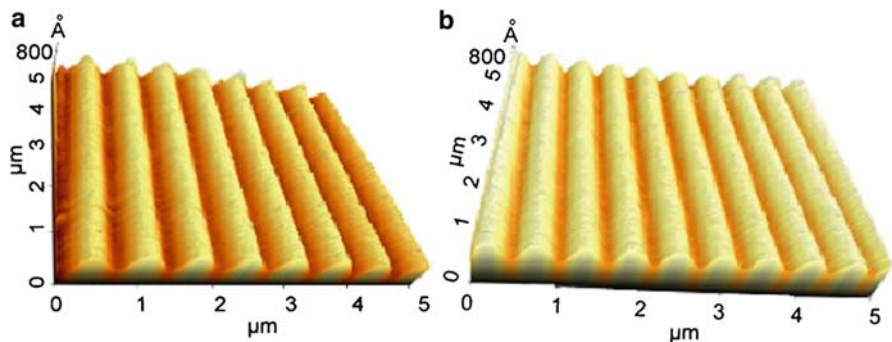


Fig. 13.28 AFM images of diffraction gratings with a period of (a) 600 nm and (b) 500 nm fabricated by the two-beam interference holography (photo-fabrication: before baking, AFM: after baking) [148]

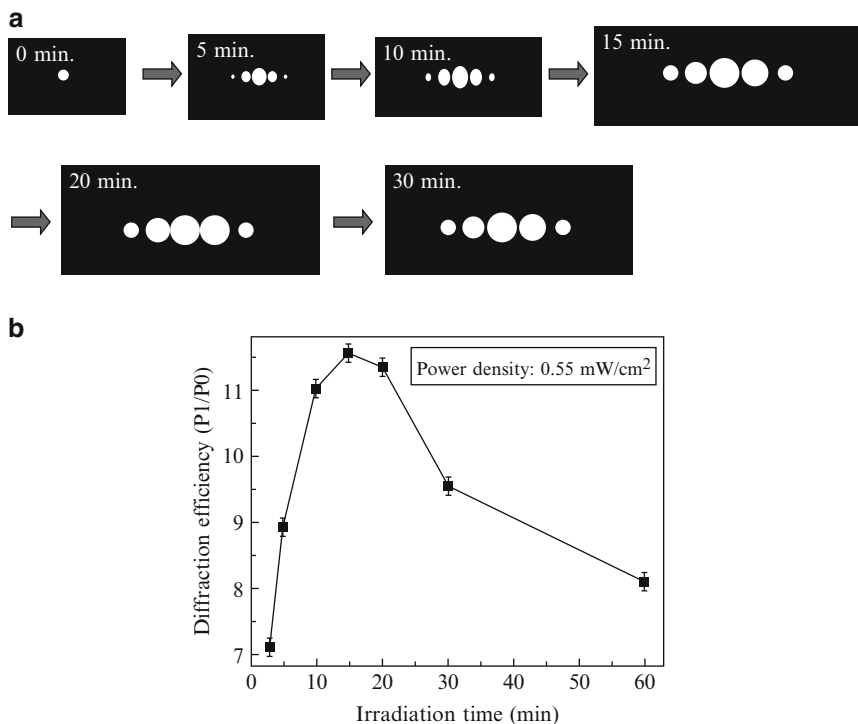


Fig. 13.29 (a) CCD images of diffraction effects of the gratings with a period of 5 μm depending on exposure time (diffraction effects in-situ measurement: before baking), and (b) diffraction efficiencies of gratings with a period of 0.7 μm depending on exposure time (diffraction efficiencies measurement: after baking) [148]

shaped diffraction optical element, respectively. The 3-beam interference and the 4-beam interference formed 2D hexagonal type and 2D rectangular type diffraction gratings with homogeneous surface structures, respectively, as shown in Fig. 13.30 [149]. For the formation of the 3-beam interference, a diffraction optical element with a triangular shaped line was used and the laser beam through this element was divided into three diffraction beams. These diffraction beams focused on one plane where the 3-beam interference was formed. In the case of 4-beam interference, the diffraction optical element with a rectangular shaped line made the laser beam divide into four beams. This allowed the formation of the 4-beam interference. Thus, these well shaped 2D diffraction gratings exhibited strong hexagonal or rectangular shaped diffraction patterns, as also demonstrated in Fig. 13.30. In addition, a well shaped Fresnel-type lens (FTL) with high efficiency and good focusing properties was inscribed on the photosensitive hybrimer using a very simple pin-hole diffraction (PHD, 1-beam interferometer) imaging [150]. Figure 13.31a illustrates the schematic configuration used to create PHD patterns. The PHD beam has circular diffraction patterns of different aperture sizes. The shape of the PHD fringes exhibits almost the same form as the FTL and these fringes could be applied to make a FTL on the photosensitive hybrimer films without a patterned mask. The FTL is made by the spatially controlled irradiation of the PHD beam with periodic changing of the irradiation intensity. In the PHD method, the setup parameters such as PH size and lens positions are easily changed to control the respective aperture sizes of PHD patterns. Thus, the focal length of the FTL is easily controllable through the PHD method. Figure 13.31b shows an optical micrograph of the FTL patterned by PHD on the photosensitive hybrimer films. The FTL exhibited the higher odd zones and lower even zones by the negative-type sensitivity depending on the spatially controlled exposure of PHD. In the patterned FTL, the first ring diameter was around 40 μm and a focal length measured experimentally was around 1 mm. Figure 13.31c, d show the focusing properties of the FTL from a CCD camera. In the absence of the FTL, the He-Ne laser beam shows no change of beam size (Fig. 13.31c), while the diffracted laser beams exhibit the focusing effect and are intensified (Fig. 13.31d). The diffraction efficiency of the FTL was highly dependent on the UV exposure dose and had the highest value at a dose of

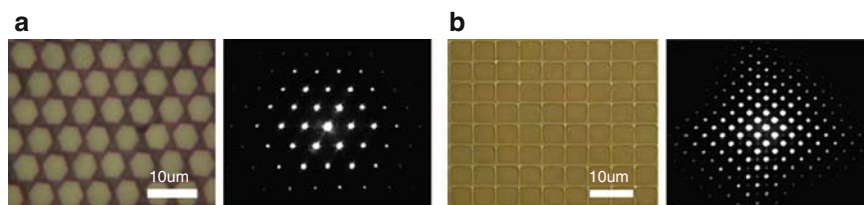


Fig. 13.30 Optical micrographs (*left*) of (a) 2D hexagonal type diffraction gratings fabricated by 3-beam interference and (b) 2D rectangular type diffraction gratings fabricated by 4-beam interference. CCD images (*right*) of diffraction effects of each grating [149]

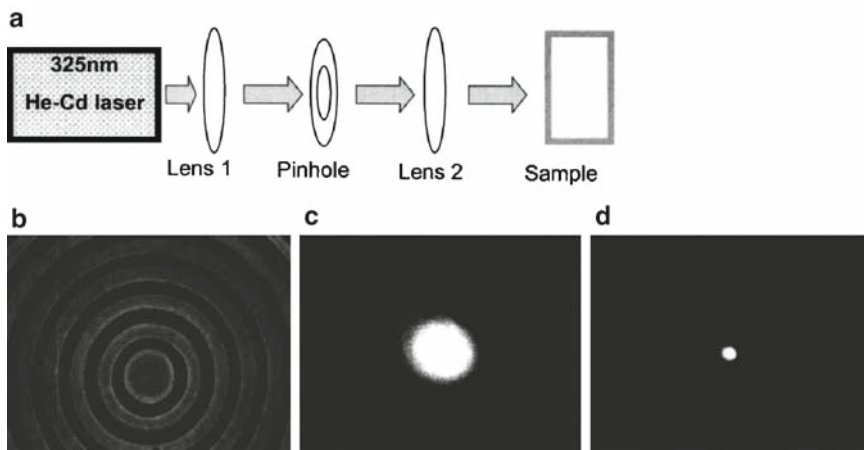


Fig. 13.31 (a) Schematic configuration for PHD patterning, (b) optical micrograph of a patterned FTL with a focal length of 1 mm, CCD images of collimated 632.8 nm light at focal plane (c) without patterned FTL, and (d) with patterned FTL [150]

330 mJ/cm². Also, it was found that the diffraction efficiency increased, approaching 85%, upon increasing the photoinitiator concentration up to 35 wt% in the hybrimer. Consequently, the patterning of FTL on the photosensitive hybrimer films resulted in a large change of the refractive index and volume between the odd and even zones on the FTL without damage to the film surface which has excellent uniformity. Moreover, the FTL did not exhibit a rectangular and a binary-type index and volume changes, but exhibited a gradient index and volume changes between odd and even zones. These lead to the highly efficient FTL suitable for various optical applications.

Overall, it has been found that the topological shape and the efficiency of the fabricated diffraction gratings are affected by the hybrimer composition, photoinitiator concentration, exposure dose, film thickness, exposure area, and prebaking and postbaking temperatures. All the created micro-structures of the gratings exhibit excellent chemical stability against organic solvents such as acetone or alcohols, which is not typically the case with conventional optical polymers. Also, they are thermally stable, allowing the diffraction to remain unchanged up to 220°C.

13.4.2 Optical Waveguides

Optical waveguides are micro-optical devices transmitting light by confining it within the high refractive index core surrounded by low refractive index cladding, through the phenomenon of total internal reflection [6]. Optical waveguides in

optically transparent dielectric materials such as silica and polymers have long been of interest for integrated optical circuit devices. Silica optical waveguides have the advantages of robustness, excellent optical characteristics, and compatibility with established silicon manufacturing protocols. The dominant techniques for fabricating silica waveguide integrated optical devices on silicon are flame hydrolysis (FHD) and chemical vapor deposition (CVD) which are high temperature processes since they require a step to consolidate the silica [182]. Low-temperature sol-gel processing has been also used to fabricate the silica waveguides [183–185]. The state-of-the art optical polymers have attracted attention for integrated optical waveguide devices because they offer rapid processibility, cost-effectiveness, high yield, high performance, such as lower optical loss and smaller birefringence compared to silica, power efficient thermal attenuation due to a larger thermo-optic coefficient than in silica, and compactness owing to a large refractive index contrast [186]. The techniques for fabricating polymer optical waveguides include casting polymer thick films and patterning channel optical waveguides. Common techniques for casting polymer films are spin coating, using doctor blade, extrusion, and lamination. The techniques that have been used for patterning channel optical waveguides in polymer films include photoresist-based patterning, direct photolithographic patterning, and micromolding patterning. Photoresist-based patterning is a standard semiconductor processing technology to pattern the channel optical waveguides using a selective reactive ion etching (RIE) after depositing a photoresist [145]. On the other hand, direct lithographic patterning consists in fabricating the channel optical waveguides by wet etching of the polymer films selectively exposed to light through a photo-mask or via direct laser writing [28, 29, 187, 188]. Recently, micromolding using a poly(dimethylsiloxane) (PDMS) mold/stamp was used to fabricate optical waveguides [189, 190].

Since the hybrimers exhibit excellent negative photoresist characteristics by photo-polymerization of organic groups, the optical waveguides can be fabricated using a direct photolithographic patterning. It is known that the unexposed area in the hybrimers is easily developed by common solvents to produce well defined patterns with a smooth wall surface. Many researches and developments of direct photolithographic patterning of the hybrimer waveguides and devices have been performed in the last decade [74–81, 89–91, 95–97, 103, 191, 192]. However, in order to compete with an already well-established polymer optical waveguide technology, it is required for the hybrimer optical waveguides to be fabricated more simply and with high robustness. Therefore, a self-developing process of the hybrimer optical waveguides using photosensitive hybrimers was firstly introduced in 2001 [144]. Single mode optical waveguides were fabricated by laser direct writing (LDW) on the hybrimer films doped with a large quantity of benzylidimethylketal (BDK). It was found that a slow laser writing speed induces a larger refractive index increase, thus producing more confined guided mode profiles. A photomask was also used in a direct photo-fabrication of ridge optical waveguides, as already shown in Fig. 13.14, to fabricate a 1×4 optical splitter [135]. The technique, called photochemical self-developing (PSD), forms directly the ridge optical waveguide on the hybrimer films without using a developing

process after light illumination. As illustrated in Fig. 13.13 with the fabrication of the ridge optical waveguide using the BDK-doped hybrimer, the refractive index increase and volume expansion are generated by a photolocking mechanism as well as by a photoinduced migration. As shown in Fig. 13.14a, b, the width of the fabricated waveguide is larger than the predefined photomask ($5\ \mu\text{m}$ opening) aperture due to the diffusiveness of the BDK. The photochemical self-developed waveguide shows a Gaussian shape, similar to that of the light beam. A symmetrical and intense single mode profile of the waveguide at $1,550\ \text{nm}$ can be seen in Fig. 13.14c. Using this process, a 1×4 optical splitter with a three-layer structure using the undoped hybrimer film as the cladding layers was successfully fabricated [135]. The same fabrication technique has been used for polymer optical waveguides [31, 36, 38]. In the case of polymer optical waveguides, photo-polymerization as well as photolocking were applied to induce the refractive index increase in the exposed region. Compared to the polymers, the hybrimers can undergo a larger refractive index increase due to their high photosensitivity triggered by complex mechanisms. The hybrimers containing a small quantity of photoinitiators can only undergo a refractive index increase with almost no volume expansion. Thus, the refractive index-modulated optical waveguide was imprinted using the LDW for fabrication of the 1×2 optical splitter, as presented in Fig. 13.32. The higher refractive index profile along the core region which was measured by near-field scanning optical microscopy (NSOM) was observed. Another direct photo-fabrication of the refractive index modulated optical waveguides has been reported for the photochromic molecule functionalized hybrimer films [163].

Recently, a multimode optical waveguide (MOW) with a large core structure has triggered interest for application in accessing network communication and optical interconnection since easy optical alignment is crucial for cheap production of integrated optical devices. The hybrimer was found convenient to produce thick films over $10\ \mu\text{m}$ through simple single spin coating. Then, the MOW with a

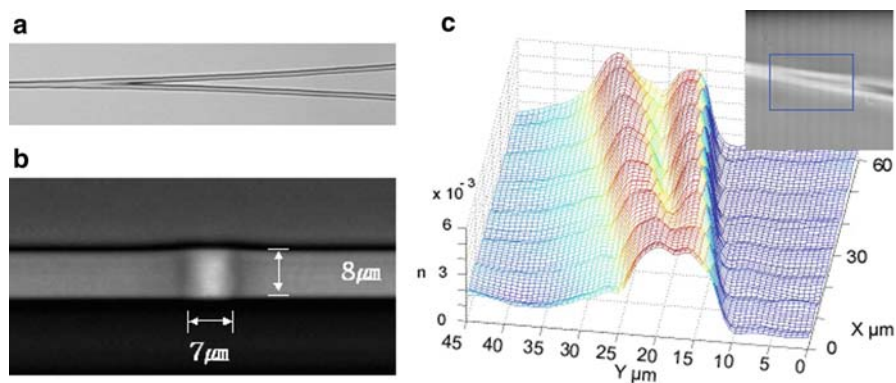


Fig. 13.32 Optical micrographs of (a) 1×2 optical splitter and (b) cross-section of refractive index modulated optical waveguide fabricated by LDW. (c) Refractive index profile of joint section of 1×2 optical splitter measured by using NSOM

well-shaped large core structure of 40 μm size was obtained by direct photo-fabrication using a photomask, as shown in Fig. 13.33 [146]. Figure 13.33a shows an optical micrograph of the MOW including its core structure and the underclad layer. A ca. 40 μm -thick film for the core layer with a large core structure could be formed evenly on the 15 μm -thick underclad layer. The series of photoinduced reactions in the photosensitive hybrimers cause a considerable refractive index increase as well as a volume expansion in the large core structure of the MOW. As shown in Fig. 13.33a, the contrast due to the refractive index difference between the UV exposed core structure and the unexposed area around the core structure and the underclad layer could be detected. The respective refractive indices of the clad layer and the core layer in the MOW were 1.486 and 1.501, respectively, at 1,550 nm. Figure 13.33b shows a 3D near-field scanning optical microscopy (NSOM) image of the reflection intensity that represents the large refractive index difference between the core and the area around the core in the MOW. Figure 13.33c exhibits the light propagation near-field image of the MOW showing strong light propagation performance. It was found that the fabricated MOW had an optical propagation loss as low as 0.13 dB cm at 850 nm due to the low optical absorption of the hybrimers in addition to a distinct refractive index difference between the core and the clad regions. Even though, the light has a limit of penetration in the matter, it was demonstrated that direct photo-patterning over a depth larger than 50 μm could be achieved. Recently, the direct photo-fabrication of MOW was made on hybrimer films deposited on PET film substrates to fabricate free-standing flexible film optical waveguides after removing the film substrate. Figure 13.34a shows the schematic procedure to fabricate the free standing flexible film MOW by direct photo-fabrication using a lamp or a laser. First, the surface of the PET substrate was modified with HMDS (1,1,1,3,3,3-hexamethyl-disilazane) before spin coating of the under-cladding hybrimer films without photoinitiator doping on a PET flexible film. This silylation step by HMDS decreases the adhesion between PET and hybrimer films for easy lift-off of the flexible waveguide from the PET film in the final step. Then the photosensitive hybrimer doped with photoinitiators is coated and UV lamp exposure through the photomask or LDW is performed to create the

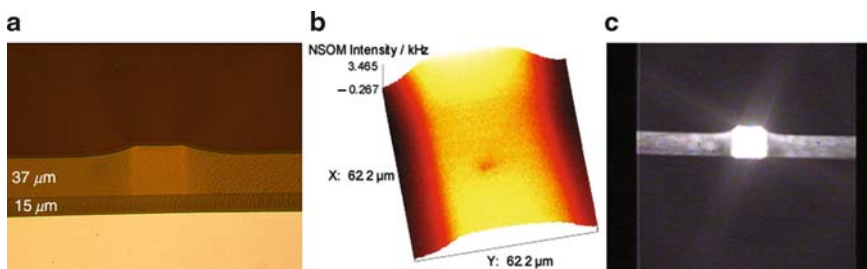


Fig. 13.33 (a) Optical micrograph of cross-section, (b) refractive index profile measured by NSOM, and (c) near-field image of optical propagation in the directly photo-fabricated multimode waveguide [146]

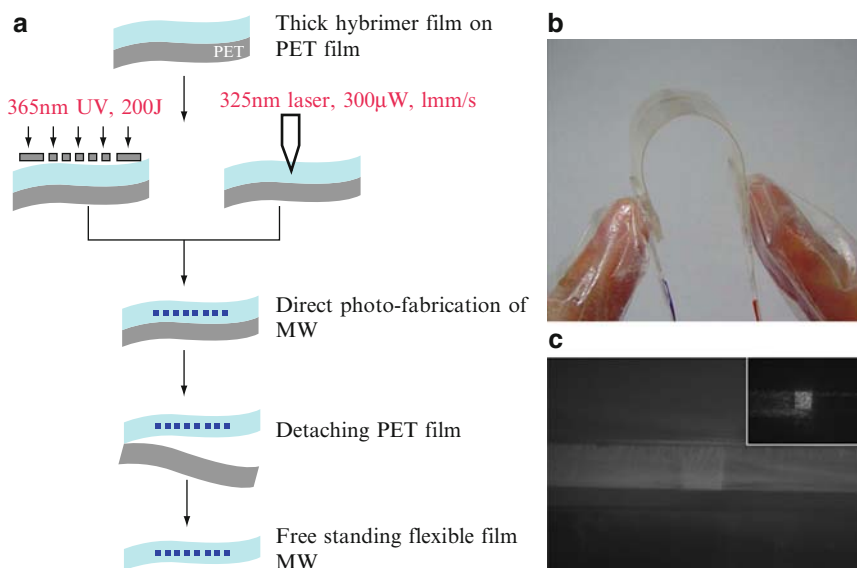


Fig. 13.34 (a) Schematic fabrication procedure, (b) photograph of free standing flexible film MW, (c) SEM micrograph of cross-section of the MW (inset: near-field image of optical propagation)

core structure. The over-cladding layer of the hybrimer without a photoinitiator doping is coated on the core layer. Finally, the fabricated flexible MOW is detached from the PET film. Figure 13.34b, c represents a picture of the fabricated free-standing flexible film MOW and its cross-section, respectively. Because of the easy and simple direct photo-fabrication and the robustness of the hybrimers, the hybrimer multimode optical waveguides will be potentially applicable in future optical areas such as accessing network communication, optical interconnection, optical PCB etc.

13.4.3 Microlens Arrays

Microlens arrays (MLA) in which the microlenses are arranged in 1D or 2D pattern in a plate are important micro-optical components for beam dispersion/expansion and conversion/collimation [2]. MLAs have been extensively used in many optical applications such as scanning system, large area display, beam homogenizer, optical coupling, and optical interconnection. Many researchers have been exploring various techniques to fabricate MLAs including the photoresist thermal reflow method, [8, 193] the ink-jet or droplet method, [24] the direct lithography method, [11, 194] molding or embossing, [13, 14] the LIGA process, [18], micro-machining, [195] and the self-assembly process [196] etc. Many methods, however, require

often complicated and multi-step processes before the required surface relief structures are revealed. Therefore, it is necessary to develop simpler cost-effective mass-fabrication methods of the desired MLAs with controllability of the focusing characteristics. Direct lithography of the MLA materials can be simpler for fabrication of MLAs because there is no need for photoresist and etching. Thus, photoresist polymers have been used as MLA materials but their limited chemical and thermal stability are a hindrance. Hybrimers treated as negative photoresists are more stable than the polymers, and can be better candidates for the fabrication of MLAs. He et al. [82–85] and Yuan et al. [197] fabricated several types of MLAs using a reflow technique of the hybrimers. After photolithography of the hybrimers using a photomask, the patterned hybrimers were reflowed by heating to achieve the desired spherical arrays.

Introduction of the photosensitive materials, which could be patterned by simple light exposure, offers the prospect of considerable improvement over conventional methods. As a result, typical photosensitive polymers such as photopolymers have been used to fabricate the MLAs by direct photo-patterning [37]. Direct light exposure of the photosensitive materials generated a spherical lens shape without any post treatment such as the reflow due to the Gaussian beam. In the recent years, some reports described MLAs obtained by direct photo-fabrication of the photosensitive hybrimers. Kärkkäinen et al. [157, 158, 173] reported the fabrication of the single microlenses as well as MLAs having a concave or convex shape on the hybrimer films by direct UV exposure. They used a gray-scale photomask as well as a binary photomask to achieve a better microlens shape. The gray-scale photomask was designed to have the lowest optical density in the center of a single-lens, and a gradual increase of that optical density toward the lens aperture edges. Consequently, the exposure dose through the gray-scale mask decreased gradually toward the edges of each single-lens pattern to generate a convex-microlens array. It was investigated whether the use of a gray-scale photomask could result in better controlled profiles than those fabricated with a binary photomask. The convex lens using a grayscale photomask with a UV exposure dose of 10.6 mJ/cm^2 had a peak-to-valley height of $1.57 \text{ }\mu\text{m}$ and an area size of $480 \times 480 \text{ }\mu\text{m}^2$. The surface profile of the lenslet was fitted with a model based on standard Zernike-polynomials. The measured rms surface roughness was 1.46 nm within a $50 \text{ }\mu\text{m}$ diameter circular region in the center of the lens. Using an optical design program and the Zernike-polynomial surface model, the effective focal length and maximum numerical aperture were estimated to be $55 \text{ }\mu\text{m}$ at 632.8 nm and 0.004 , respectively. A higher UV exposure dose of 21.2 mJ/cm^2 created a larger deformation height of $24 \text{ }\mu\text{m}$ with a larger rms surface roughness of 15 nm . The fabricated lens departed from rotational symmetry of the lenslet. The effective focal length and the corresponding maximum numerical aperture were estimated to be $5.7 \text{ }\mu\text{m}$ at 632.8 nm and 0.05 , respectively. In addition to the convex lens, a concave lens array structure was fabricated using a grayscale photomask. A UV exposure dose of 10.6 mJ/cm^2 resulted in a peak-to-valley depth of $1.56 \text{ }\mu\text{m}$ and an area size of $260 \text{ }\mu\text{m} \times 260 \text{ }\mu\text{m}$ with an rms surface roughness of 2.5 nm within a $50 \text{ }\mu\text{m}$ diameter circular region in the center of the lens. The surface profile of the lenslet was fitted with the Zernike-polynomial surface model and the

effective focal length was estimated to be $\sim 18\ \mu\text{m}$ at $632.8\ \text{nm}$. Yu et al. [156] also demonstrated the fabrication of a refractive microlens with a diameter of $140\ \mu\text{m}$ and a height of $2.13\ \mu\text{m}$ using a high-energy beam-sensitive (HEBS) gray-scale photo-mask. The microlens surface showed good optical smoothness with an rms surface roughness of $1.183\ \text{nm}$. Surface profiles of the fabricated microlenses were presented with Zernike-polynomial fit coefficients. Recently, Kang et al. [152] reported the first evaluation of the focal length of a directly photo-fabricated microlens on a hybrimer film depending on the hybrimer composition and the film thickness. It was discovered that the focal length was reduced as the photoactive monomer concentration and the film thickness increased owing to larger volume expansion with a higher refractive index increase by more monomer migration. Figure 13.35 shows the focusing profile of the directly photo-fabricated single microlens, including its 3D profile and its focal spot image [152]. Similarly, Fig. 13.36 shows the 3D profile image, the AFM rms surface roughness image, and the focal spot image of a directly photo-fabricated MLA exploiting the photoinduced migration mechanism in the photosensitive hybrimer [152]. The photolocking and the photoinduced migration mechanisms produce a considerable volume expansion as well as a refractive index increase in the exposed area. The fabricated convex-type MLA with a diameter of $30\ \mu\text{m}$ and a height of $1.25\ \mu\text{m}$ with uniform homogeneity functioned as microlenses as shown in Fig. 13.36c. All the fabricated MLAs without using any etching step presented excellent smoothness of the microlens surface with an rms surface roughness of $0.5\ \text{nm}$, as shown in Fig. 13.36b. The spot diameter value of $4.1\ \mu\text{m}$, based on the $1/e^2$ intensity of the peak, was found by fitting a Gaussian to the profile. As shown in Fig. 13.36c, the beams from the 2×2 array randomly measured on the

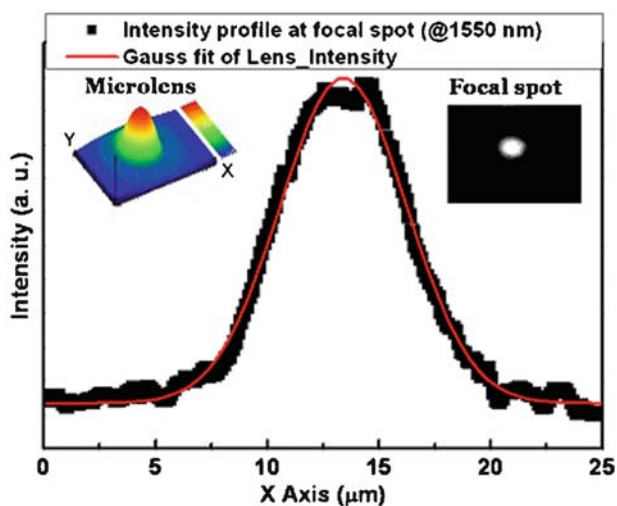


Fig. 13.35 Focusing profile at a focal spot of the directly photo-fabricated microlens. Microlens and focal spot images are shown in the inset [151]

directly photo-fabricated MLA exhibit a uniform profile. The high performance of the MLA resulted from the formation of the desired refractive index distribution and from surface relief modification via a controlled exploitation of the photoinduced migration mechanism. The curvature of the photo-fabricated MLA can be controlled by changing the UV dose, photoactive monomer concentration, and film thickness, as discussed in the section on photoinduced migration mechanisms. Thus, the focal length of the MLA was controlled to allow considerable freedom in the design and surface structuring during the fabrication of an efficient MLA. Figure 13.37 shows the change in the focal length of the directly photo-fabricated MLAs having 40 μm and 60 μm lens diameters, depending on the BDK/MMA concentration and on the film thickness [152]. The height and the refractive index distributions of the MLA increase as the BDK/MMA concentration and the film thickness increase due to a larger photoinduced migration and stronger photochemical reactions in the UV exposed area. The increase in the height and the refractive index changes of the

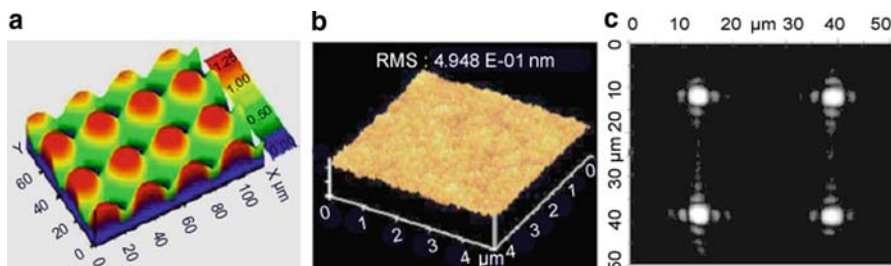


Fig. 13.36 (a) 3D profile image, (b) AFM surface roughness image, and (c) focal spot images on the focusing plane of the MLA directly photo-fabricated on the hybrimer films [152]

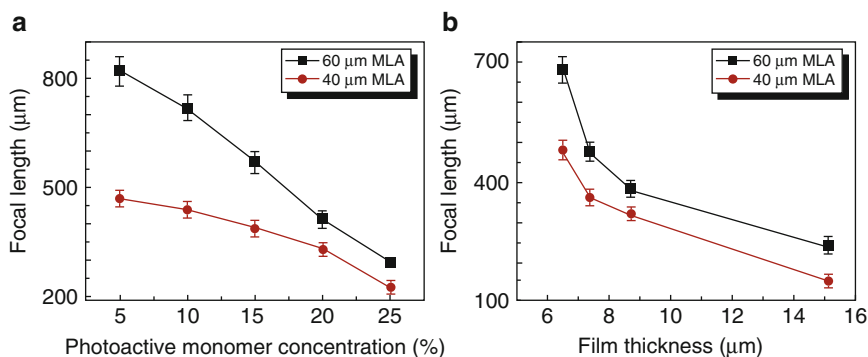


Fig. 13.37 Control of focal lengths of the MLAs directly photo-fabricated on the photosensitive hybrimer using the photoinduced migration mechanism. (a) Decrease of focal length with increasing BDK/MMA concentration. (b) Decrease of focal length with increasing film thickness [152]

MLAs play an important role in shortening the focal length and enhancing the focusing characteristics. Also, the MLAs fabricated on the photosensitive hybrimer films showed a high optical transmission of ~95% in the visible spectrum and in the near IR ranges, which can be useful for optical applications. Other studies on the photosensitive hybrid materials demonstrate the direct photo-fabrication of MLAs [147].

Contrary to the MLA fabrication via the photoinduced migration mechanism to create convex microlenses, concave microlenses are created in the Ge-doped hybrimer via photoinduced densification and polymerization resulting in volume compaction, as shown in Fig. 13.5 [133]. As seen in Fig. 13.6, the shape of the microlens can be easily controlled by changing the UV exposure dose.

13.5 Conclusion and Perspectives

The sol–gel derived hybrid materials (hybrimers) in which inorganic and organic components are mixed at the molecular scale can combine the specific characteristics of the inorganic and organic materials. Based on the concept of the hybrimer, the highly photosensitive hybrid materials, which undergo a permanent large change in volume and in refractive index, can be developed by combining the photosensitivity mechanisms of glasses and of polymers. Among the photosensitivity mechanisms occurring in the inorganic components, the photoinduced condensation and siloxane densification are expected to play a role but their effects are too small to be taken into account in the hybrid materials. On the other hand, Ge-related densification clearly induces both volume shrinkage and refractive index increase. Thus, the photosensitivity mechanism present in the inorganic component is found only in the Ge-doped hybrid material. All the photosensitivity mechanisms taking place in the polymers are also valid for the hybrid materials. Contrary to the photo-polymerization resulting in volume compaction and refractive index increase, the photolocking and the photoinduced migration expand the volume while simultaneously inducing a refractive index increase. Usually, when the hybrid materials containing a small quantity of extra monomers (photoinitiator or photoactive monomers) are exposed to light after thermal baking, the photo-polymerization becomes the dominant mechanism at the origin of the material shrinking since the migration and locking mechanisms are limited. The photolocking and the photoinduced migration occur easily in the methacrylate hybrid material system and generate positive change both in volume and refractive index. In addition, long exposure to deep UV decomposes the methacrylate in the hybrid material and reduces simultaneously the refractive index and the volume. Compared to the polymers which can be degraded under light illumination, the hybrid materials can present a higher photosensitivity without degradation due to the existence of the siloxane backbone. Therefore, the desired micro-optical structures can be designed in the hybrid materials through a control of the photosensitivity mechanisms, which is achieved by changing the composition and the process. Exploiting the photosensitivity mechanisms in the hybrid materials, micro-optical components such as

diffraction gratings, optical waveguides and microlens arrays have been directly photo-fabricated. Different fabrication techniques based on photomask, phase-mask, holographic interference and laser direct writing have been applied for direct photo-fabrication of the micro-optical components. The fabricated micro-optical components showed a smooth surface due to the elimination of the etching step. Also, it was found that the obtained micro-optical components were mechanically, chemically and thermally stable enough to be used practically. Through the demonstration of direct photo-fabrication, the applicability of the photosensitive hybrimers was confirmed. Thus, it is believed that the photosensitive hybrimers can replace the photopolymers that are already in the market.

Micro-optical technology has so far been used in high-performance applications rather than in mass-production due to its high cost. Recently, many industrial applications have demonstrated a need for micro-optical technologies at low cost for mass-production, e.g. to access network communication, optical PCB, microlens in digital camera, printer, scanner, projector etc. Thus, the development of low-cost materials and simple fabrication technologies for the production of micro-optical devices is required. The representative optical materials like glasses and polymers have their own limitations. It has been found that hybrimers possess many advantageous characteristics for optical applications compared to other materials. In addition to their superior optical characteristics, the hybrimers afford simple and direct photo-fabrication of micro-optical elements, which provides the potential for cost-effective technology readily applicable in mass-production industries. For the practical introduction of the photosensitive hybrimers, it is necessary to identify suitable industrial applications and to demonstrate the simpler fabrication of many micro-optical elements with good reliability and characteristics, acceptable to the current market.

References

1. Borrelli NF (2005) *Microoptics technology*. Marcel Dekker, New York
2. Daly D (2001) *Microlens arrays*. Taylor & Francis, New York
3. Hunsperger RG (2002) *Integrated optics*. 5th edition, Springer-Verlag, New York
4. Loewen EG (1997) *Diffraction gratings and applications*. Marcel Dekker, New York
5. Nishihara H, Haruna M, Sahara T (1989) *Optical integrated circuits*. McGraw Hill, New York
6. Okamoto K (2006) *Fundamentals of optical waveguides*. 2nd edition, Academic Press, Burlington
7. Sinzinger S, Jahns J (2003) *Microoptics*. 2nd edition, Wiley, Weinheim
8. Eisner M, Schwider J (1996) Transferring resist microlenses into silicon by reactive ion etching. *Opt Eng* 35:2979–2982
9. Dannberg P, Erdmann L, Bierbaum R, Krehl A, Bräuer A, Kley EB (1999) Micro-optical elements and their integration to glass and optoelectronic wafers. *Microsyst Technol* 6:41–47
10. Fu Y, Bryan NKA (2001) Novel one-step method of microlens mold array fabrication. *Opt Eng* 40:1433–1434

11. Gale MT, Rossi M, Pedersen J, Schutz H (1994) Fabrication of continuous-relief micro-optical elements by direct laser writing in photoresists. *Opt Eng* 33:3556–3566
12. Haruvy T, Gilath I, Maniewicz M, Eisenberg N (1997) Sol–gel replication of microoptical elements and arrays. *Chem Mater* 9:2604–2615
13. Kunnavaikkam MV, Houlihan FM, Schlax M, Liddle JA, Kolodner P, Nalamasu O, Rogers JA (2003) Low-cost, low-loss microlens arrays fabricated by soft lithography replication process. *Appl Phys Lett* 82:1152–1154
14. Ong NS, Koh YH, Fu YQ (2002) Microlens array produced using hot embossing process. *Microelectron Eng* 60:365–379
15. Seraji S, Wu Y, Jewell-Larson NE, Forbess MJ, Limmer SJ, Chou TP, Cao G (2000) Patterned microstructure of sol–gel derived complex oxides using soft lithography. *Adv Mater* 12:1421–1424
16. Shinmou K, Nakama K, Koyama T (2000) Fabrication of micro-optic elements by the sol–gel method. *J Sol Gel Sci Tech* 19:267–269
17. Gerlach A, Ziegler P, Mohr J (2001) Assembly of hybrid integrated micro-optical modules using passive alignment with LIGA mounting elements and adhesive bonding techniques. *Microsyst Technol* 7:27–31
18. Kupka RK, Bouamrane F, Cremers C, Megtert S (2000) Microfabrication: LIGA-X and applications. *Appl Surf Sci* 164:97–110
19. Mohr J (1998) LIGA – A technology for fabricating microstructures and microsystems. *Sens Mater* 10:363–373
20. Riedl MJ (2001) Stretching the optical envelope. *Photon Spectra* 35:130–132
21. Schaffer CB, Mazur E (2001) Micromachining and optical device fabrication using ultrashort pulses from a laser oscillator. *Opt Photon News* 12:20–23
22. Tsunetomo K, Koyama T (1997) Direct formation of a surface-relief grating on glass by ultraviolet visible laser irradiation. *Opt Lett* 22:411–413
23. Cox WR, Chen T, Hayes DJ (2001) Micro-optics fabrication by ink-jet printing. *Opt Photon News* 12:32–35
24. Danzebrink R, Aegerter MA (1999) Deposition of micropatterned coating using an ink-jet technique. *Thin Solid Films* 351:115–118
25. Keyworth BP, McMullin JN (1996) Method and apparatus for making optical components by direct dispensing of curable liquid. US Patent 5534101
26. Yoldas BE (1998) Design of sol–gel coating media for ink-jet printing. *J Sol Gel Sci Tech* 13:147–152
27. Booth BL (1975) Photopolymer material for holography. *Appl Opt* 14:593–601
28. Booth BL (1989) Low loss channel waveguides in polymers. *J Lightwave Technol* 7:1445–1453
29. Booth BL, Marchegiano JE, Chang CT, Furmanak RJ, Graham DM, Wagner RG (1997) Polyguide polymeric technology for optical interconnect circuits and components. *Proc SPIE* 3005:238–251
30. Bowden MJ, Chandross EA, Kaminow IP (1974) Mechanism of the photoinduced refractive index increase in polymethyl methacrylate. *Appl Opt* 13:112–117
31. Chandross EA, Pryde CA, Tomlinson WJ, Weber HP (1974) Photolocking—a new technique for fabricating optical waveguide circuits. *Appl Phys Lett* 24:72–74
32. Colburn WS, Haines KA (1971) Volume hologram formation in photopolymer materials. *Appl Opt* 10:1636–1641
33. Franke H (1984) Optical recording of refractive-index patterns in doped poly-(methyl methacrylate) films. *Appl Opt* 23:2729–2733
34. Franke H, Heuer W (1986) Photo-induced self-condensation, a technique for fabricating organic lightguide structures. *Proc SPIE* 651:120–125
35. Haugh EF (1972) Hologram recording in photo polymerizable layers. US Patent 3658526
36. Okamoto N, Tashiro S (1988) Optical waveguides of polymethyl methacrylate doped with benzophenone and coumarin. *Opt Commun* 66:93–96
37. Suzuki T, Todokoro Y, Komenou K (1989) Process for the production of optical elements. US Patent 4877717

38. Tomlinson WJ, Kaminow IP, Chandross EA, Fork RL, Silfvast WT (1970) Photoinduced refractive index increase in poly(methylmethacrylate) and its applications. *Appl Phys Lett* 16:486–489
39. Trout TJ, Schmiege JJ, Gambogi WJ, Weber AM (1998) Optical photopolymers: Design and applications. *Adv Mater* 10:1219–1224
40. Barrett CJ, Natansohn AL, Rochon PL (1996) Mechanism of optically inscribed high efficiency diffraction gratings in azo polymer films. *J Phys Chem* 100:8836–8842
41. Bian S, Li L, Kumar J, Kim DY, Williams J, Tripathy SK (1998) Single laser beam-induced surface deformation on azobenzene polymer films. *Appl Phys Lett* 73:1817–1819
42. Bian S, Williams JM, Kim DY, Li L, Balasubramanian S, Kumar J, Tripathy S (1999) Photoinduced surface deformation on azobenzene polymer films. *J Appl Phys* 86:4498–4508
43. Fiorini C, Prudhomme N, Veyrac DG, Maurin I, Raimond P, Nunzi JM (2000) Molecular migration mechanism for laser induced surface relief grating formation. *Synth Met* 115:121–125
44. Oliveira ON, dos Santos DS, Balogh DT, Zucolotto V, Mendoça CR (2005) Optical storage and surface-relief gratings in azobenzene-containing nanostructured films. *Adv Colloid Interface Sci* 116:179–192
45. Viswanathan NK, Kim DY, Bian S, Williams J, Liu W, Li L, Samuelson L, Kumar J, Tripathy SK (1999) Surface relief structures on azo polymer films. *J Mater Chem* 9:1941–1955
46. Bazylenko MV, Gross M, Moss D (1997) Mechanisms of photosensitivity in germanosilica films. *J Appl Phys* 81:7497–7505
47. Douay M, Xie WX, Taunay T, Bernage P, Niay P, Cordier P, Poumellec B, Dong L, Bayon JF, Pognant H, Delevaque E (1997) Densification involved in the UV-based photosensitivity of silica glasses and optical fibers. *J Lightwave Technol* 15:1329–1342
48. Maekawa S, Ohishi T (1994) Evaluation of SiO₂ thin films prepared by sol–gel method using photo-irradiation. *J Non-Cryst Solids* 169:207–209
49. Okusaki S, Ohishi T (2003) The effect of photo-irradiation in hydrolysis and condensation of silicon alkoxide. *J Non-Cryst Solids* 319:311–313
50. Hosono H, Kawazoe H, Muta K (1993) Preferred concentration enhancement of photobleachable defects responsible for 5 eV optical absorption band in SiO₂:GeO₂ glass preform by heating in a H₂ atmosphere. *Appl Phys Lett* 63:479–481
51. Jang JH, Koo J, Bae BS (1999) Photosensitivity of germanium oxide and germanosilicate glass sol–gel films. *J Non-Cryst Solids* 259:144–148
52. Jang JH, Koo J, Bae BS (2000) Fabrication and ultraviolet absorption of sol gel-derived germanium oxide glass thin films. *J Am Ceram Soc* 83:1356–1360
53. Jang JH, Koo J, Bae BS (2000) Photobleaching of sol–gel derived germanium oxide glass thin films. *J Mater Res* 15:282–284
54. Simmons KD, Potter BG, Stegeman GI (1994) Red photoluminescence and optical absorption in hydrogen treated GeO₂SiO₂ sol–gel derived planar waveguides. *Appl Phys Lett* 64:2537–2539
55. Hisakuni H, Tanaka K (1995) Optical microfabrication of chalcogenide glasses. *Science* 270:974–975
56. Hisakuni H, Tanaka K (1995) Optical fabrication of microlenses in chalcogenide glasses. *Opt Lett* 20:958–960
57. Sramek R, Smektala F, Xie WX, Douay M, Niay P (2000) Photoinduced surface expansion of fluorozirconate glasses. *J Non-Cryst Solids* 277:39–44
58. Brinker CJ, Scherrer GW (1990) Sol–gel science: the physics and chemistry of sol–gel processing. Academic Press, Boston
59. Schmidt H (1988) Chemistry of material preparation by the sol–gel process. *J Non-Cryst Solids* 100:51–64
60. Haas KH (2000) Hybrid inorganic-organic polymers based on organically modified Si-alkoxides. *Adv Eng Mater* 2:571–582

61. Haas KH (2003) Crosslinked heteropolysiloxanes as inorganic-organic polymers: precursors, synthesis, properties, and applications. In: Nalwa HS (ed) Handbook of organic-inorganic hybrid materials and nanocomposites: vol 1: hybrid materials. American Scientific Publishers, Stevenson Ranch, pp 207–239
62. Haas KH, Wolter H (1999) Synthesis, properties and applications of inorganic-organic copolymers (ORMOCER®s). *Curr Opin Solid State Mater Sci* 4:571–580
63. Lebeau B, Sanchez C (1999) Sol–gel derived hybrid inorganic-organic nanocomposites for optics. *Curr Opin Solid State Mat Sci* 4:11–23
64. Novak BM (1993) Hybrid nanocomposite materials-between inorganic glasses and organic polymers. *Adv Mater* 5:422–433
65. Sanchez C, Judeinstein P (1996) Hybrid organic-inorganic materials: A land of multidisciplinary. *J Mater Chem* 6:511–527
66. Sanchez C, Ribot F (1994) Design of hybrid organic-inorganic materials synthesized via sol–gel chemistry. *New J Chem* 18:1007–1047
67. Sanchez C, Ribot F, Rozes L, Alonso B (1999) Molecular design of hybrid organic-inorganic nanocomposites synthesized via sol–gel chemistry. *J Mater Chem* 9:35–44
68. Sanchez C, Soler-Illia GJAA, Ribot F, Grosso D (2003) Design of functional nano-structured materials through the use of controlled hybrid organic-inorganic interfaces. *CR Chimie* 6:1131–1151
69. Sanchez C, Soler-Illia GJAA, Ribot F, Lalot T, Mayer CR, Cabuil V (2001) Designed hybrid organic-inorganic nanocomposites from functional nanobuilding blocks. *Chem Mater* 13:3061–3083
70. Schmidt H (2000) Chemical routes to nanostructured materials. *Mater Sci Technol* 16:1356–1358
71. Schubert U, Hüsing N, Lorenz A (1995) Hybrid inorganic-organic materials by sol–gel processing of organofunctional metal alkoxides. *Chem Mater* 7:2010–2027
72. Äyräs P, Rantala JT, Honkanen S, Mendes SB, Peyghambarian N (1999) Diffraction gratings in sol–gel films by direct contact printing using a UV-mercury lamp. *Opt Commun* 162:215–218
73. Äyräs P, Rantala JT, Levy R, Descour MR, Honkanen S, Peyghambarian N (1999) Multilevel structures in sol–gel thin films with a single UV-exposure using a gray-scale mask. *Thin Solid Films* 352:9–12
74. Coudray P, Chisham J, Andrews MP, Najafi SI (1997) Ultraviolet light imprinted sol–gel silica glass low-loss waveguides for use at 1.55 μm . *Opt Eng* 36:1234–1240
75. Coudray P, Chisham J, Malek-Tabrizi A, Li CY, Andrews MP, Peyghambarian N, Najafi SI (1996) Ultraviolet light imprinted sol–gel silica glass waveguide devices on silicon. *Opt Commun* 128:19–22
76. Coudray P, Etienne P, Moreau Y, Porque J, Najafi SI (1997) Sol–gel channel waveguide on silicon: fast direct imprinting and low cost fabrication. *Opt Commun* 143:199–202
77. Du XM, Touam T, Degachi L, Guilbault JL, Andrews MP, Najafi SI (1998) Sol–gel waveguide fabrication parameters: an experimental investigation. *Opt Eng* 37:1101–1104
78. Etienne P, Coudray P, Moreau Y, Porque J (1998) Photocurable sol–gel coatings: channel waveguides for use at 1.55 μm . *J Sol Gel Sci Tech* 13:523–527
79. Fardad MA, Andrews MP, Milova G, Malek-Tabrizi A, Najafi SI (1998) Fabrication of ridge waveguides: a new solgel route. *Appl Opt* 37:2429–2434
80. Fardad MA, Mishechkin OV, Fallahi M (2001) Hybrid sol–gel materials for integration of optoelectronic components. *J Lightwave Technol* 19:84–91
81. Fardad MA, Touam T, Meshkinfam P, Sara R, Du XM, Andrews MP, Najafi SI (1997) UV-light imprinted Bragg grating in sol–gel ridge glass waveguide with almost 100% reflectivity. *Electron Lett* 33:1069–1070
82. He M, Yuan X, Bu J, Cheong WC (2004) Fabrication of concave refractive microlens arrays in solgel glass by a simple proximity-effect-assisted reflow technique. *Opt Lett* 29:1007–1009
83. He M, Yuan X, Ngo NQ, Cheong WC, Bu J (2003) Reflow technique for the fabrication of an elliptical microlens array in sol–gel material. *Appl Opt* 42:7174–7178

84. He M, Yuan XC, Ngo NQ, Bu J, Kudryashov V (2003) Simple reflow technique for fabrication of a microlens array in sol-gel glass. *Opt Lett* 28:731–733
85. He M, Yuan XC, Ngo NQ, Bu J, Tao SH (2004) Single-step fabrication of a microlens array in sol-gel material by direct laser writing and its application in optical coupling. *J Opt A: Pure Appl Opt* 6:94–97
86. Kärkkäinen AHO, Rantala JT, Descour MR (2002) Fabrication of micro-optical structures by applying negative tone hybrid glass materials and greyscale lithography. *IEEE Electron Lett* 38:23–24
87. Levy R, Descour MR (2000) Optical and opto-mechanical structures in hybrid sol-gel materials for use in micro-optics systems. *Proc SPIE* 3943:47–52
88. Levy R, Descour MR, Shul RJ, Willison CL, Warren ME, Kololuoma T, Rantala JT (1999) Concept for zero-alignment micro-optical systems. *Proc SPIE* 3897:167–173
89. Li CY, Chisham J, Andrews MP, Najafi SI, Mackenzie JD, Peyghambarian N (1995) Sol-gel integrated optical coupler by ultraviolet light imprinting. *Electron Lett* 31:271–272
90. Najafi SI, Touam T, Sara R, Andrews MP, Fardad MA (1998) Sol-gel glass waveguide and grating on silicon. *J Lightwave Technol* 16:1640–1646
91. Porque J, Coudray P, Moreau Y, Etienne P (1998) Propagation in sol-gel channel waveguides: numerical and experimental approaches. *Opt Eng* 37:1105–1110
92. Rantala JT, Äyräs P, Levy R, Honkanen S, Descour MR, Peyghambarian N (1998) Binary-phase zone-plate arrays based on hybrid sol-gel glass. *Opt Lett* 23:1939–1941
93. Rantala JT, Levy R, Kivimäki L, Descour MR (2000) Direct UV patterning of thick hybrid glass films for micro-opto-mechanical structures. *Electron Lett* 16:530–531
94. Rantala JT, Nordman N, Nordman O, Vähäkangas J, Honkanen S, Peyghambarian N (1998) Sol-gel hybrid glass diffractive elements by direct electron-beam exposure. *Electron Lett* 34:455–456
95. Saravanamuttu K, Du XM, Najafi SI, Andrews MP (1998) Photoinduced structural relaxation and densification in sol-gel-derived nanocomposite thin films: Implications for integrated optics device fabrication. *Can J Chem/Rev Can Chim* 76:1717–1729
96. Touam T, Du M, Fardad MA, Andrews MP, Najafi SI (1998) Sol-gel waveguides with Bragg grating. *Opt Eng* 37:1136–1142
97. Touam T, Milova G, Saddiki Z, Fardad MA, Andrews MP, Chrostowski J, Najafi SI (1997) Organoaluminumphosphate sol-gel silica glass thin films for integrated optics. *Thin Solid Films* 307:203–207
98. Wang YW, Yen CT, Chen WC (2005) Photosensitive polyimide/silica hybrid optical materials: Synthesis, properties, and patterning. *Polymer* 46:6959–6967
99. Yamada N, Yoshinaga I, Katayama S (1999) Processing and optical properties of patternable inorganic-organic hybrid films. *J Appl Phys* 85:2423–2427
100. Yu W, Yuan XC (2003) Variable surface profile gratings in sol-gel glass fabricated by holographic interference. *Opt Express* 11:1925–1930
101. Yu WX, Yuan XC, Ngo NQ, Que WX, Cheong WC, Koudriachov V (2002) Single-step fabrication of continuous surface relief micro-optical elements in hybrid sol-gel glass by laser direct writing. *Opt Express* 10:443–448
102. Yuan XC, Yu WX, Cheong WC, Ngo NQ (2002) Improved linear response to UV exposure and its interpretation of $\text{SiO}_2/\text{TiO}_2$ hybrid sol-gel glass. *J Phys D: Appl Phys* 34:L81–L84
103. Zhang X, Zhao Z, Qian M, Lee SY, Chin MK, Zeng X, Low DKY, Lu ACW, Plante P (2006) Planar waveguide devices based on sol-gel-derived photopatternable hybrid material. *J Cryst Growth* 288:176–179
104. Bae BS (2004) High photosensitive sol-gel hybrid materials for direct photo-imprinting of micro-optics. *J Sol Gel Sci Tech* 31:309–315
105. Beecroft LL, Ober CK (1997) Nanocomposite materials for optical applications. *Chem Mater* 9:1302–1317
106. Proposito P, Casalboni M (2003) Optical properties of functionalized sol-gel derived hybrid materials. In: Nalwa HS (ed) *Handbook of organic-inorganic hybrid materials and nanocomposites: vol 1 hybrid materials*. American Scientific Publishers, Stevenson Ranch, pp 83–123

107. Sanchez C, Julian B, Belleville P, Popall M (2005) Applications of hybrid organic-inorganic nanocomposites. *J Mater Chem* 15:3559–3592
108. Sanchez C, Lebeau B, Chaput F, Boilot JP (2003) Optical properties of functional hybrid organic-inorganic nanocomposites. *Adv Mater* 15:1969–1994
109. Schottner G (2001) Hybrid sol–gel derived polymers: Applications of multifunctional materials. *Chem Mater* 13:3422–3435
110. Haas KH, Amberg-Schwab S, Rose K, Schottner G (1999) Functionalized coatings based on inorganic-organic polymers (ORMOCER@s) and their combination with vapor deposited inorganic thin films. *Surf Coat Technol* 111:72–79
111. Hay JN, Raval HM (2001) Synthesis of organic-inorganic hybrids via the non-hydrolytic sol–gel process. *Chem Mater* 13:3396–3403
112. Vioux A (1997) Nonhydrolytic sol–gel routes to oxides. *Chem Mater* 11:2292–2299
113. Buestrich R, Kahlenberg F, Popall M, Dannberg P, Müller-Fiedler R, Rösch O (2001) ORMOCER@s for optical interconnection technology. *J Sol Gel Sci Tech* 20:181–186
114. Buestrich R, Kahlenberg F, Popall M, Martin A, Rösch O (2000) Low Si-OH ORMOCERs for dielectrical and optical interconnection technology. *MRS Symp Proc* 628:CC9.8.1–CC9.8.6
115. Eo YJ, Kim JH, Ko JH, Bae BS (2005) Optical characteristics of photo-curable methacryl-oligosiloxane nano hybrid thick films. *J Mater Res* 20:401–408
116. Eo YJ, Lee TH, Kim SY, Kang JK, Han YS, Bae BS (2005) Synthesis and molecular structure analysis of nano-sized methacryl-grafted polysiloxane resin for fabrication of nano hybrid materials. *J Polym Sci Part B: Polym Phys* 43:827–836
117. Houbertz R, Domann G, Cronauer C, Schmitt A, Martin H, Park JU, Frohlich L, Buestrich R, Popall M, Streppel U, Dannberg P, Wachter C, Brauer A (2003) Inorganic-organic hybrid materials for application in optical devices. *Thin Solid Films* 442:194–200
118. Houbertz R, Schulz J, Fröhlich L, Domann G, Popall M (2003) Inorganic-organic hybrid materials for polymer electronic applications. *MRS Symp Proc* 769:H7.4.1–H7.4.6
119. Moujoud A, Kim WS, Bae BS, Shin SY (2006) Thermally stable optical characteristics of sol–gel hybrid material films. *Appl Phys Lett* 88:101916
120. Nam KH, Lee TH, Bae BS, Popall M (2006) Condensation reaction of 3-(methacryloxypropyl)-trimethoxysilane and diisobutylsilanediol in non-hydrolytic sol–gel process. *J Sol Gel Sci Tech* 39:255–260
121. Popall M, Buestrich R, Kahlenberg F, Andersson A, Haglund J, Robertsson ME, Blau G, Gale M, Rösch O, Dabek A, Neumann-Rodekirch J, Cergel L, Lambert D (2000) Electrical and optical interconnection-technology based on ORMOCER-inorganic-organic hybrid materials. *MRS Symp Proc* 621:CC9.4.1–CC9.4.12
122. Schulz J, Frohlich L, Domann G, Popall M (2003) Inorganic-organic hybrid materials for polymer electronic applications. *MRS Symp Proc* 769:H7.4.1–H7.4.6
123. Boilot JP, Biteau J, Chaput F, Gacoin T, Brun A, Darracq B, Georges P, Lévy Y (1998) Organic-inorganic solids by sol–gel processing: optical applications. *Pure Appl Opt* 7:169–177
124. Seddon AB (1997) Potential of organic-inorganic hybrid materials, derived by sol–gel, for photonic applications. *Proc SPIE CR68:143–171*
125. Lee TH, Kang ES, Bae BS (2003) Catalytic effects of aluminum butoxyethoxide in sol–gel hybrid hard coatings. *J Sol Gel Sci Tech* 27:23–29
126. Schneider A, Kairies S, Rose K (1999) Synthesis of alkoxy-silyl substituted cyclophosphazenes and their properties in the sol–gel process. *Monatsh Chem* 130:89–98
127. Krug H, Schmidt H (1994) Organic-inorganic nanocomposites for micro optical applications. *New J Chem* 18:1125–1134
128. Sepeur S, Kunze N, Werner B, Schmidt H (1999) UV curable hard coatings on plastics. *Thin Solid Films* 351:216–219
129. Popall M, Du XM (1995) Inorganic-organic copolymers as solid state ionic conductors with grafted anions. *Electrochim Acta* 40:2305–2308

130. Popall M, Andrei M, Kappel J, Kron J, Olma K, Olsowski B (1998) ORMOCERs as inorganic-organic electrolytes for new solid state lithium batteries and supercapacitors. *Electrochim Acta* 43:1155–1161
131. Skaarup S, West K, Zachau-Christiansen B, Popall M, Kappel J, Kron J, Eichinger G, Semrau G (1998) Towards solid state lithium batteries based on ORMOCER electrolytes. *Electrochim Acta* 43:1589–1592
132. Simmons KD, Stegeman GI, Potter BG Jr., Simmons JH (1993) Photosensitivity of sol–gel derived germanosilicate planar waveguides. *Opt Lett* 18:25–27
133. Jang JH, Kang DJ, Bae BS (2003) Direct photo-imprinting in high photosensitive organically modified germanosilicate (ORMOGSIL) glasses. *MRS Symp Proc* 780:Y5.10.1–Y5.10.6
134. Jang JH, Kang DJ, Bae BS (2004) Large photoinduced densification in organically modified germanosilicate glasses. *J Am Ceram Soc* 87:155–158
135. Jung JI, Park OH, Bae BS (2003) Fabrication of channel waveguides by photochemical self-developing in doped sol–gel hybrid glass. *J Sol Gel Sci Tech* 26:897–901
136. Blanc D, Pélissier S (2001) Fabrication of sub-micron period diffraction gratings in self-processing sol–gel glasses. *Thin Solid Films* 384:251–253
137. Blanc D, Pelissier S, Saravanamuttu K, Najafi SI, Andrews MP (1999) Self-processing of surface relief gratings in photosensitive hybrid sol–gel glasses. *Adv Mater* 11:1508–1511
138. Pelissier S, Blanc D, Andrews MP, Najafi SI, Tishchenko AV, Parriaux O (1999) Single-step UV recording of sinusoidal surface gratings in hybrid solgel glasses. *Appl Opt* 38:6744–6748
139. Soppera O, Croutxe-Barghorn C, Carre C, Blanc D (2002) Design of photoinduced relief optical devices with hybrid sol–gel materials. *Appl Surf Sci* 186:91–94
140. Molina C, Moreira PJ, Gonçalves RR, Sá Ferreira RA, Messaddeq Y, Ribeiro SJL, Soppera O, Leite AP, Marques PVS, de Zea Bermudez V, Carlos LD (2005) Planar and UV written channel optical waveguides prepared with siloxane-poly(oxyethylene)-zirconia organic/inorganic hybrids. Structure and optical properties. *J Mater Chem* 15:3937–3945
141. Kang DJ, Park JU, Bae BS, Nishii J, Kintaka K (2003) Single-step photopatterning of diffraction gratings in highly photosensitive hybrid sol–gel films. *Opt Express* 11:1144–1148
142. Park JU, Kim WS, Bae BS (2003) Photoinduced low refractive index in a photosensitive organic-inorganic hybrid material. *J Mater Chem* 13:738–741
143. Park JU, Kang ES, Bae BS (2003) Photoinduced low refractive index patterning in a photosensitive hybrid material. *MRS Symp Proc* 780:Y3.7.1–Y3.7.6
144. Bae BS, Park OH, Charters R, Luther-Davies B, Atkins GR (2001) Direct laser writing of self-developed waveguides in benzyldimethylketal-doped sol–gel hybrid glass. *J Mater Res* 16:3184–3187
145. Kagami M, Ito H, Ichigawa T, Kato S, Matsuda M, Takahashi N (1995) Fabrication of large-core, high- Δ optical waveguides in polymers. *Appl Opt* 34:1042–1046
146. Kang DJ, Kim WS, Bae BS, Park HK, Jung BH (2005) Direct photofabrication of refractive-index-modulated multimode optical waveguide using photosensitive sol–gel hybrid materials. *Appl Phys Lett* 87:221106 1–3
147. Park OH, Kim SJ, Bae BS (2004) Photochemical reactions in fluorinated sol–gel hybrid materials doped with a photolocking agent for direct micropatterning. *J Mater Chem* 14:1749–1753
148. Kang DJ, Kim JK, Bae BS (2004) Simple fabrication of diffraction gratings by two-beam interference method in highly photosensitive hybrid sol–gel films. *Opt Express* 12:3947–3953
149. Kang DJ, Kim JK, Bae BS (2005) Fabrication of micro-optical devices by holographic interference of high photosensitive inorganic-organic hybrid materials (PhotoHYBRIMER). *MRS Symp Proc* 846:DD10.3.1–DD10.3.6
150. Kang DJ, Phong PV, Bae BS (2004) Fabrication of high-efficiency Fresnel-type lenses by pinhole diffraction imaging of sol–gel hybrid materials. *Appl Phys Lett* 85:4289–4291
151. Kang DJ, Bae BS (2007) Photo-imageable sol–gel hybrid materials for simple fabrication of micro-optical elements. *Acc Chem Res* 40: 903–912

152. Kang DJ, Jeong JP, Bae BS (2006) Direct photofabrication of focal-length-controlled microlens array using photoinduced migration mechanisms of photosensitive sol–gel hybrid materials. *Opt Express* 14:8347–8353
153. Blanc D, Pélissier S, Jurine PY, Soppera O, Croutxé-Barghorn C, Carré C (2003) Photo-induced swelling of hybrid sol–gel thin films: application to surface micro-patterning. *J Sol Gel Sci Tech* 27:215–220
154. Yu W, Yuan X (2004) Localized self-volume growth in hybrid sol–gel glass induced by ultraviolet radiation with a gray-scale mask. *Appl Opt* 43:575–578
155. Yu W, Yuan XC (2003) Volume growth initiated by point-to-point ultraviolet-laser direct writing in hybrid solgel glass for three-dimensional microfabrication. *Opt Lett* 28:1573–1575
156. Yu W, Yuan XC (2003) UV induced controllable volume growth in hybrid sol–gel glass for fabrication of a refractive microlens by use of a grayscale mask. *Opt Express* 11:2253–2258
157. Kärkkäinen AHO, Rantala JT, Tamkin JM, Descour MR (2003) Photolithographic processing of hybrid glasses for microoptics. *J Lightwave Technol* 21:614–623
158. Kärkkäinen AHO, Tamkin JM, Rogers JD, Neal DR, Hormi OE, Jabbour GE, Rantala JT, Descour MR (2002) Direct photolithographic deforming of organomodified siloxane films for micro-optics fabrication. *Appl Opt* 41:3988–3998
159. Rantala JT, Kärkkäinen AHO, Hiltunen JA, Keränen M, Kololuoma T, Descour MR (2001) UV light induced surface expansion phenomenon of hybrid glass thin films. *Opt Express* 8:682–687
160. Cheben P, Calvo ML (2001) A photopolymerizable glass with diffraction efficiency near 100% for holographic storage. *Appl Phys Lett* 78:1490–1492
161. Chaput F, Riehl D, Lévy Y, Boilot JP (1993) Azo oxide gels for optical storage. *Chem Mater* 5:589–591
162. Darracq B, Chaput F, Lahlil K, Lévy Y, Boilot JP (1998) Photoinscription of surface relief gratings on azo-hybrid gels. *Adv Mater* 10:1133–1136
163. Biteau J, Chaput F, Lahlil K, Boilot JP, Tsivgoulis GM, Lehn JM, Darracq B, Marois C, Levy Y (1998) Large and stable refractive index change in photochromic hybrid materials. *Chem Mater* 10:1945–1950
164. Biteau J, Tsivgoulis GM, Chaput F, Boilot JP, Gilat S, Kawai S, Lehn JM, Darracq B, Martin F, Levy Y (1997) Photochromism of dithienylethene derivatives trapped in sol–gel matrices. *Mol Cryst Liq Cryst* 297:65–72
165. Soppera O, Croutxé-Barghorn C, Lougnot DJ (2001) New insights into photoinduced processes in hybrid sol–gel glasses containing modified titanium alkoxides. *New J Chem* 25:1006–1014
166. Moreau Y, Arguel P, Coudray P, Etienne P, Porque J, Signoret P (1998) Direct printing of gratings on sol–gel layers. *Opt Eng* 37:1130–1135
167. Park OH, Jung JI, Bae BS (2001) Photoinduced condensation of sol–gel hybrid glass films doped with benzildimethylketal. *J Mater Res* 16:2143–2148
168. Decker C (1996) Photoinitiated crosslinking polymerisation. *Prog Polym Sci* 21:593–650
169. Dickens B, Martin JW, Waksman D (1984) Thermal and photolytic degradation of plates of poly(methyl methacrylate) containing monomer. *Polymer* 25:706–715
170. Gupta A, Liang R, Tsay FD, Moacanin J (1980) Characterization of a dissociative excited state in the solid state: photochemistry of poly(methyl methacrylate). *Photochemical processes in polymeric systems*. 5. *Macromolecules* 13:1696–1700
171. Kang DJ (2005) Synthesis and characterization of high photosensitive hybrid materials for direct photo-fabrication of micro and sub-micro structures. Ph.D dissertation, KAIST, Korea
172. Ramanujam PS, Holme NCR, Hvilsted S (1996) Atomic force and optical near-field microscopic investigations of polarization holographic gratings in a liquid crystalline azobenzene side-chain polyester. *Appl Phys Lett* 68:1329–1331

173. Kärkkäinen AHO, Rantala JT, Maaninen A, Jabbour GE, Descour MR (2002) Siloxane-based hybrid glass materials for binary and grayscale mask photoimaging. *Adv Mater* 14:535–540
174. Kim JK, Kang DJ, Bae BS (2005) Wavelength-dependent photosensitivity in a germanium-doped sol–gel hybrid material for direct photopatterning. *Adv Funct Mater* 15:1870–1876
175. Scherzer T, Decker U (1999) Kinetic investigations on UV-induced photopolymerization reactions by real-time FTIR-ATR spectroscopy: the efficiency of photoinitiators at 313 and 222 nm. *Nucl Instr and Meth Phys Res B* 151:306–312
176. Frey L, Darracq B, Chaput F, Lahlil K, Jonathan JM, Roosen G, Boilot JP, Levy Y (2000) Surface and volume gratings investigated by the moving grating technique in sol–gel materials. *Opt Commun* 173:11–16
177. Landraud N, Peretti J, Chaput F, Lampel G, Boilot JP, Lahlil K, Safarov VI (2001) Near-field optical patterning on azo-hybrid sol–gel films. *Appl Phys Lett* 79:4562–4564
178. Hoshino M, Ebisawa F, Yoshida T, Sukegawa K (1997) Refractive index change in photochromic diarylethene derivatives and its application to optical switching devices. *J Photochem Photobiol A: Chem* 105:75–81
179. Irie M, Mohri M (1988) Thermally irreversible photochromic systems. Reversible photocyclization of diarylethene derivatives. *J Org Chem* 53:803–808
180. Nakamura S, Irie M (1988) Thermally irreversible photochromic system. A theoretical study. *J Org Chem* 53:6136–6138
181. Jiang HJ, Yuan XC, Zhou Y, Chan YC, Lam YL (2000) Single-step fabrication of diffraction gratings on hybrid sol–gel glass using holographic interference lithography. *Opt Commun* 185:19–24
182. Poulsen MR, Borel PI, Fage-Pedersen J, Hübner J, Kristensen M, Povlsen JH, Rottwitt K, Svalgaard M, Svendsen W (2003) Advances in silica-based integrated optics. *Opt Eng* 42:2821–2834
183. Syms RRA, Schneider VM, Huang W, Ahmad MM (2004) High- Δn silica-on-silicon channel waveguides based on sol–gel germanophosphosilicate glass. *Electron Lett* 33:1216–1217
184. Ulrich R, Weber HP (1972) Solution-deposited thin films as passive and active light-guides. *Appl Opt* 11:428–434
185. Yeatman EM (1997) Sol–gel fabrication for optical communication components: prospects and progress. *Proc SPIE* CR68:119–142
186. Ma H, Jen AKY, Dalton LR (2002) Polymer-based optical waveguides: materials, processing, and devices. *Adv Mater* 14:1339–1365
187. Eldada L, Xu C, Stengel KMT, Shacklette LW, Yardley JT (1996) Laser-fabricated low-loss single-mode raised-rib waveguiding devices in polymers. *J Lightwave Technol* 14:1704–1713
188. Tomic D, Mickelson A (1999) Photobleaching for optical waveguide formation in a guest-host polyimide. *Appl Opt* 38:3893–3903
189. Lee BT, Kwon MS, Yoon JB, Shin SY (2000) Fabrication of polymeric large-core waveguides for optical interconnects using a rubber molding process. *IEEE Photon Technol Lett* 12:62–64
190. Rogner A, Pannhoff H (1994) Mass fabrication of passive polymer multimode and single-mode waveguide devices. *Conf Opt Fiber Comm, Technical Digest Series vol 4, Paper FB1* pp279–280
191. Moujoud A, Andrews MP, Najafi SI (2005) Fabrication of sol–gel optical waveguides by hot-dip coating process. *J Sol Gel Sci Tech* 35:123–126
192. Yoon KB, Bae BS, Popall M (2005) Fabrication of low-loss waveguides using organic-inorganic hybrid materials. *J Nonlinear Opt Phys Mater* 14:399–407
193. Syms RRA (2000) Refractive collimating microlens arrays by surface tension self-assembly. *IEEE Photon Technol Lett* 12:1507–1509
194. Yang R, Wang W (2004) Out-of-plane polymer refractive microlens fabricated based on direct lithography of SU-8. *Sensor Actuat A-Phys* 113:71–77

195. King CR, Lin LY, Wu MC (1996) Out-of-plane refractive microlens fabricated by surface micromachining. *IEEE Photonics Technol Lett* 8:1349–1351
196. Lu Y, Yin Y, Xia Y (2001) A self-assembly approach to the fabrication of patterned, two-dimensional arrays of microlenses of organic polymers. *Adv Mater* 13:34–37
197. Yuan XC, Yu WX, Ngo NQ, Cheong WC (2002) Cost-effective fabrication of microlenses on hybrid sol–gel glass with a high-energy beam-sensitive gray-scale mask. *Opt Express* 10:303–308

Chapter 14

Photonic Structures of Luminescent Semiconductor Nanocrystals and Spherical Microcavities

Yury P. Rakovich, John F. Donegan, and Andrey L. Rogach

Abstract This chapter introduces three-dimensional photonic structures of luminescent semiconductor nanocrystals and spherical microcavities made by a layer-by-layer assembly as a versatile bottom-up nanofabrication technique. Fabrication aspects are discussed here and fundamental optical properties are presented for these nanostructures where two main concepts of solid-state physics, the complete 3D electronic and photonic confinement are merged. Several applications of hybrid photonic structures as building blocks for coupled optical emitters and waveguides are demonstrated.

Abbreviations ABN: Anti-bonding; ASPL: Anti-Stokes photoluminescence; BN: Bonding; FSR: Free spectral region; GLMT: Generalized Lorentz-Mie theory; LbL: Layer-by-layer; LO: Longitudinal optical; MA: Mercaptoethylamine; MF: Melamine formaldehyde; MPD: 3-mercapto-1,2-propanediol; NCs: Nanocrystals; PDDA: Poly(diallyldimethylammonium chloride); PE: Polyelectrolyte; PL: Photoluminescence; PM: Photonic molecule; PS: Polystyrene; PSS: Poly(sodium 4-styrenesulfonate); QY: Quantum yield; SMTB: Single-mode tight-binding; TE: Transverse electric; TGA: Thioglycolic acid; TM: Transverse magnetic; TO: Transverse optical; WGM: Whispering gallery modes.

14.1 Introduction

In the last two decades semiconductor nanocrystals (NCs) have become the subject of vigorous investigation in one of the most rapidly growing branches at the interface between chemistry, physics and biology. They belong to a state of matter

Y.P. Rakovich(✉) and J.F. Donegan
School of Physics and Centre for Research on Adaptive Nanostructures and Nanodevices,
Trinity College Dublin, College Green, Dublin 2, Ireland
e-mail: Yury.Rakovich@tcd.ie

A.L. Rogach
Photonics & Optoelectronics Group, Physics Department & Center for Nanoscience (CeNS),
University of Munich, Amalienstrasse 54, 80799, Munich, Germany

lying in the transition regime between molecules and bulk materials. Due to the quantum confinement effect, NCs show unique physical and chemical properties, such as size-dependent bandgap, size dependent photoluminescence, and enhanced nonlinear optical properties [1–5]. Recently, novel hybrid materials based on NCs – polymer composites have become of enormous fundamental and technological interest [6–9].

The methods used for the assembly of ultrathin hybrid/NCs films are spin coating and solution casting, spraying, electrodeposition, polyion layer-by-layer (LbL) assembly, chemical self-assembly and Langmuir-Blodgett technique. Among others the LbL assembly has been demonstrated to be a very promising method in many applications due to its low cost and simplicity in ultrathin film preparation, its capacity to produce large area films, and its ability to achieve a good reproducibility of the film's quality and physical properties [10]. In addition, the LbL self-assembly method is unique for combining different types of materials such as polyelectrolytes (PE), anionic and cationic bipolar species, inorganic nanoparticles, dyes, proteins, DNA, and conducting polymers into one ultrathin film system [10]. Thus, it represents one of the key techniques in the so-called bottom-up strategy pursued in modern nanotechnology. Moreover, the LbL assembled films typically exhibit a much better quality than the thin films prepared by the Langmuir-Blodgett technique or spin coating and casting methods. All these advantages make the LbL assembled systems particularly promising in optoelectronic applications.

Originally this technique was used mostly for film preparation on macroscopically flat substrates. Recently, it was shown that the LbL method can also be extended to utilise other microtemplates, such as polymer or glass microspheres [11, 12] thereby permitting the construction of a new class of micrometer-size core-shell systems with controlled nanostructure and composition of the interfacial region. The nano-meter thick activation shell in these composites can be formed by assembling multilayers of charged polyelectrolytes and luminescent NCs via their consecutive electrostatic adsorption from the solution [13]. This technological achievement is of great importance for the development of novel micro-scale hybrid emitters and lasers. The spherical surface imposes boundary conditions on the propagation of NCs emission, which leads to the unique optical phenomenon – sharp resonances in the emission spectra called cavity modes or whispering gallery modes (WGM) [14–18]. As a result, the emission from the semiconductor NCs can be enhanced or inhibited when these nanoscale emitters are placed on the surface of a spherical microcavity.

This chapter provides an overview of the recent progress in fabrication and investigation of the optical properties of hybrid NCs/Microspheres composites produced by LbL assembly technique. The importance of the NC surface charge in the interaction with the PE multilayers is discussed as a critical step toward the fabrication of highly-emitting nano- and micro-scale devices. Optical properties of a novel NCs/microcavity system consisting of CdTe nanocrystals attached to melamine formaldehyde latex microspheres are further described. Recent advances in the use of these hybrid systems as building blocks for coupled-resonator optical emitters and waveguides are an important step in the development of complex photonic architectures with a strong coherent mode coupling.

14.2 Multilayers of Polyelectrolytes and Nanocrystals

Large surface-to-volume ratio is a key feature of semiconductor NCs in the quantum-confinement regime. The extent to which surface properties determine quantum efficiency and recombination dynamics of NCs is subject to a wide range of investigations [19–24]. During the chemical synthesis, the surface passivation and therefore surface charge can be modified by the addition or removal of organic ligands/inorganic materials without altering the intrinsic electronic properties of NCs [25–28]. The modified surface ensures solubility and stability. One can even alter the charge on the NCs surface by changing the short chain thiol stabilizers [27]. Efforts have been made to quantify the NCs surface charge [29]. The surface charge of NCs plays a key role in the controllable deposition of NCs on charged substrates using attractive electrostatic interaction. We will discuss below the importance of the surface charge in determining the optical emission properties of the NCs once they are incorporated into a PE multilayer structure on flat and spherical substrates using the LbL assembly technique.

14.2.1 *The Layer-by-Layer Deposition Technique*

The physical route described below makes use of the fact that well-defined multilayers can be formed by consecutive adsorption of oppositely charged polyelectrolytes. The process predominantly makes use of electrostatic interactions, however hydrophobic interactions and hydrogen bonding are also important factors to provide surface roughness of LbL films below 1 nm [30]. Prior to deposition of the PE multilayers, the quartz substrates should be thoroughly cleaned/ultrasonicated with NaOH and methanol. This renders the substrate hydrophilic in nature and facilitates the growth of the PE layers. The poly(diallyldimethylammonium chloride) (PDDA) solution is prepared by taking 150 μL (20 wt% in water) in 5 mL water. The poly(sodium 4-styrenesulfonate) (PSS) solution is prepared at a concentration of 0.412 mg mL^{-1} in water. Both can be obtained from Sigma-Aldrich. For each 5 mL of PDDA and PSS solutions, 1 mL of 3 M NaCl is added. A PE bilayer is self-assembled by sequentially dipping a quartz substrate into an aqueous solution of the positively charged PDDA for 20 min, followed by 20 min in the negatively charged PSS. After each dip the sample is rinsed with Millipore water to remove any loose molecules not ionically bonded to the surface. By repeating this dipping procedure, multilayer films are assembled to the required thickness. The thickness is approximately 1.4 nm for a single PDDA/PSS bilayer and 11.7 nm for a film composed of nine PDDA/PSS bilayers [31].

The proper choice of the NCs capping ligands is of great importance for their deposition on PE LbL film, as the strength of electrostatic attractive forces is determined by the NCs surface charge. Several successful syntheses of thiol-capped CdTe NCs were developed, demonstrating that the nature of the thiol influences the particle

growth, the PL quantum yield (QY) and the surface charge of as-synthesized CdTe NCs [27]. CdTe NCs stabilized by thioglycolic acid (TGA) or by mercaptoethylamine (MA) or by 3-mercapto-1,2-propanediol (MPD), show efficient luminescence as prepared and possess either negative, positive and neutral (slightly negative) surface charge, respectively. A monolayer of CdTe NCs can be deposited by dipping the PE multilayer in an aqueous NCs solution (concentration of 10^{-8} M) for 20 min. For the TGA (negative surface charge) and MPD (neutral/slightly negative charge) stabilized CdTe NCs, the final PE layer of the multilayer structure is bound to be a positively charged PDDA layer whereas for the MA stabilized (positive surface charge) NCs the final PE layer is required to be a negatively charged PSS layer.

14.2.2 Emission Properties of Colloidal Nanocrystals on Flat Polyelectrolyte Multilayers

The nature of surface ligands on NCs strongly affects the structure of NCs packing in the PE layers. In the strong electrostatic interaction regime (TGA or MA ligands) it can be expected that NCs adsorbed on a PE LbL film as a close-packed layer will remain mostly localized on or within the top PE layer [32, 33]. As a result the modification of the NCs optical emission could be caused by the interaction between the NCs and the top PE layer, and would be expected to be independent of the PE multilayer thickness. In contrast, a strong diffusion of MPD capped NCs through the PE multilayer structure can be expected taking into account the neutral nature of NCs surface states. However this idealized consideration does not take into account the morphology of the NCs film and the packing density of NCs – both of which can be affected by the interface roughness and the proximity of the quartz substrate.

The PL spectra, presented in Fig. 14.1a, are recorded from a monolayer of TGA-stabilized CdTe NCs adsorbed on a quartz substrate coated with PDDA, as well as on PE films of different thickness. The measured PL intensity remains constant as a function of the number of PE layers after initial increase in intensity (Figs. 14.1a, 14.3a). The lower PL intensity of CdTe NCs deposited on only one PDDA layer can be attributed to an enhanced non-uniformity of the PE layer deposited directly on the quartz substrate, which reduces the NCs packing density. As the subsequent PE layers are deposited the uniformity of the top PDDA layer is expected to improve, and therefore a greater number of NCs will be adsorbed onto the topmost PDDA layer. In contrast, as shown in Figs. 14.2a and 14.3c, for similar structures with a MPD-stabilized CdTe NCs strong enhancement of PL efficiency is observed with increased PE film thickness.

The CdTe NCs deposited on the 18-bilayer PE film show a ~25-fold increase in PL intensity compared to the emission from NCs deposited directly onto a PDDA coated quartz substrate (Fig. 14.3c). The PE film thickness dependence is an evidence of a strong diffusion of the MPD-stabilized NCs into the PE matrix, which plays a key role in the deposition kinetics of nominally neutral, but yet slightly

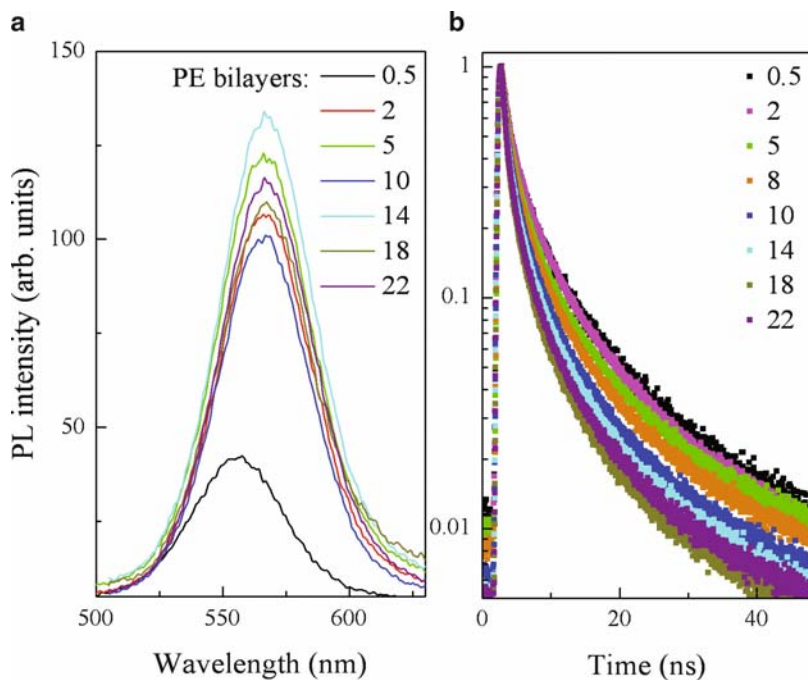


Fig. 14.1 PL spectra (a) and PL decay curves (b) of a monolayer of TGA stabilized CdTe NCs on PDDA coated quartz substrate (0.5 curve) and on a number of PE bilayers. The PL spectra were recorded using a Perkin-Elmer fluorescence spectrometer with 400 nm excitation wavelength. The PL decays were measured using a MicroTime200 system (PicoQuant) equipped with LDH-480 laser head. Reproduced with permission from The Institute of Physics

negative NCs. As a larger number of NCs is incorporated into the PE multilayer, there is an increased interaction between the NCs and the PE. This does not occur in the case of TGA- or MA-stabilized NCs. The difference is attributed to the larger surface charge of the TGA- or MA-stabilized NCs, which provides a sufficiently strong electrostatic interaction to ensure firstly a strong attraction to the topmost oppositely charged PE layer and secondly a strong electrostatic repulsion to the second PE layer in the multilayer film, which is of the same charge as the NCs. The combination of the two effects prevents diffusion of the more highly charged NCs through the PE matrix. It seems that the much weaker negative surface charge of the MPD-stabilized NCs is insufficient to form a localized monolayer. It is noteworthy that in the absence of absolute emission QY measurements, in order to ensure a qualitative comparison between the emission intensity of a different spectrum, the measurements should be done consecutively keeping fixed all the experimental conditions (optical set up, focal point and illuminated cross-section, sample holder, emission and excitation slits width).

Further insight into the mechanism of modification of NCs emission can be gained from time-resolved PL experiments. Figures 14.1b and 14.2b show that the decay dynamics of TGA- and MPD-stabilized NCs are strongly affected by the thickness

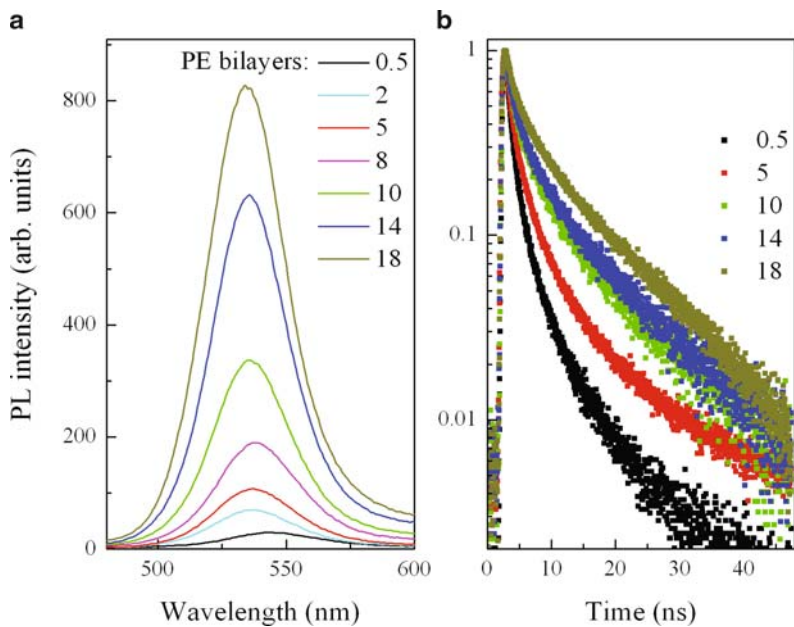


Fig. 14.2 PL spectra (a) and PL decay curves (b) of a monolayer of MPD-stabilized CdTe NCs on PDDA coated quartz substrate (0.5 curve) and on a number of PE bilayers. Reproduced with permission from Institute of Physics

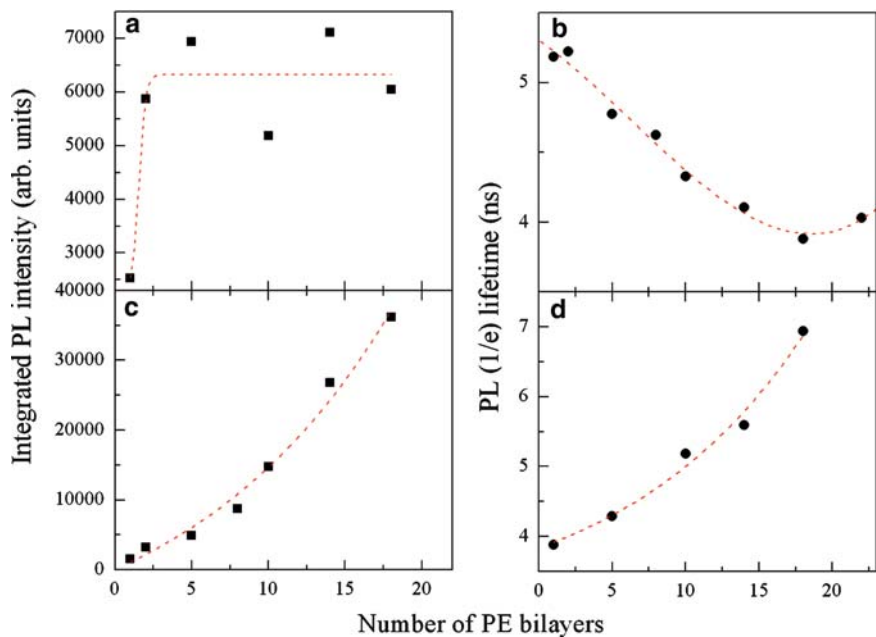


Fig. 14.3 Dependence of the integrated PL intensity of TGA (a) and MPD (c) stabilized CdTe NCs on a number of deposited PE bilayers. Panels (b) and (d) show the corresponding modification of the PL lifetime

of the PE layer, and that the recombination dynamics are different in two cases. For both TGA- and MPD-stabilized NCs, the PL decay curves can be successfully simulated using a two-exponential function [34, 35]. A detailed analysis reveals that the short lifetime component (~ 1 ns) is nearly the same in both cases, as would be expected for the intrinsic lifetime due to recombination of the excited NCs core population. However, there is a significant variation in the long timescale components ($4 \div 11$ ns), which are commonly accepted as being associated with surface states and are the most significant contributors to the QY of NCs [36]. An estimate of the average lifetime obtained from the time needed for the emission intensity to drop to $1/e$ of its initial value, shows the longer PL decay of MPD-stabilized CdTe NCs, observed for thicker PE layers (Figs. 14.2b, 14.3d). Since the observed experimental lifetime can be expressed as the sum of the radiative and non-radiative transition probabilities, this result clearly suggests that the increased interaction of the MPD-stabilized CdTe NCs with the PE chains suppresses the non-radiative recombination through reduction of the concentration of surface defects and/or less efficient carrier trapping at surface defects. Most likely, the dominant interaction is between the slightly negatively charged NCs and the positively charged PDDA PE. This can also result in a change in the polarity of the immediate NCs surroundings. As the PE multilayer thickness increases the contribution from the NCs within the multilayer becomes larger with respect to that coming from the NCs on the top surface of the PE layer.

In contrast, PL decay curves in TGA-capped CdTe NCs show a strong reduction in PL lifetime with an increasing thickness of the PE film (Figs. 14.1b, 14.3b) mostly due to the suppression of the long timescale components. In the absence of diffusion and with a constant PL intensity as a function of PE film thickness, it can be assumed that the number of TGA-stabilized NCs is approximately the same for each structure. Therefore, it must be concluded that the modification of the PL lifetimes is entirely due to the influence of the increasing PE film thickness. One option to be considered is a change in the electric field induced by NCs at the top surface of the PE multilayer. In response to a nanometer scale charged stimulus the PE film is prompt to adjust its chain distribution followed by modification of the surface electric field to the point of wrapping of individual NCs [37]. The result of this interaction can be two-fold. Firstly the electrostatic interaction between PE and wrapped NCs results in enhanced nonradiative transitions due to electrostatic interaction between oppositely charged species. Secondly the wrapping provides efficient separation of NCs from each other [37] thus eliminating resonance energy transfer between them. Both effects can cause the modification of PL lifetime seen in Fig. 14.3.

14.2.3 Spherical Microcavities with Semiconductor Nanocrystals

The formation of nanocomposite NCs/PE multilayer films on the surface of flat quartz substrates can be extended to other types of substrates like polymer or glass microspheres [12]. The preparation of semiconductor NCs multilayers on spherical

microcavities, is of immense interest given their tunable and desirable optical and electronic properties for various applications. In addition, such microspheres with shells containing NCs would exhibit a higher surface area than their counterparts fabricated on planar substrates. Among polymers, the high optical transparency, thermal and mechanical stability of melamine formaldehyde (MF) make it interesting as a potential candidate in optical microcavity applications. The refractive index of MF in the visible region ($n_r = 1.68$) is greater than that of polymethylmethacrylate ($n_r = 1.48$), silica ($n_r = 1.47$) or other glass materials ($n_r \sim 1.5$). Aqueous dispersions of MF microspheres of various sizes are available for example from Microparticles GmbH (Berlin). Monolayer NCs shells can be assembled on the surface of microspheres by depositing the negatively charged (TGA stabilized) CdTe NCs on the MF latex microspheres. The microspheres originally possessing a slightly positive surface charge can be modified with monolayers of negatively charged PSS and positively charged polyelectrolyte, poly(allylamine hydrochloride). This allows the three- or four-layer PE film pretreatment to increase the positive surface charge of the microsphere/PE system and provide high uniformity of the top PE layer. The build-up of the NCs monolayer is facilitated by the electrostatic interactions between the negatively charged $-\text{COOH}$ groups on the surface of CdTe NCs and the $-\text{NH}_3^+$ groups of PAH. High-resolution luminescence confocal microscopy imaging confirms the localization and the uniformity of NCs shell on the top of MF microsphere (Fig. 14.4).

Among others, optical quality of a microcavity is a key factor which determines various photonic applications of layered microspheres. In order to control this parameter the sectioning property of the confocal scanning microscopy can be utilized providing laser illumination below the bandgap of NCs [38]. In a confocal microscopy system (Fig. 14.5), the expanded collimated light is focused on the sample through an infinity corrected objective lens with a numerical aperture (NA) of 0.9 (Leitz, Germany). The backscattered light from the sample is collected by the objective lens, then focused onto a 30 mm diameter pinhole by a tube lens. The signal is detected by a photomultiplier tube (PMT) and analysed using an imaging software. The computer provides the control of a motorized stage moving in the x and y directions and a piezoelectric actuator driving the objective lens in the z direction.

The typical images of an isolated sphere of radius $R = 2.5 \mu\text{m}$ and a pair of touching spheres are shown in Fig. 14.6. The laser light was first focused on the surface of the substrate ($z = -R$) (near the back surface of the sphere) and only the shadow of the sphere can be seen in Fig. 14.6a. When the focal plane is moved towards the equatorial plane of the sphere ($z = 0$), bright rings appear in the periphery of the sphere (Fig. 14.6b, c). Since the distance from the plane $z = 0$ to the substrate is about 2.6 mm and the full width at half maximum (FWHM) of the system axial response of 0.8 mm is considerably less than this, light from the off-focused substrate will be blocked by the pinhole. In addition, other light scattering away from the focus will also be blocked by the pinhole. Hence bright rings can only be due to the light backscattered from the focused point of the sphere surface.

The bright center spot in Fig. 14.6c can be explained in terms of geometrical optics: when the light is focused on the centre of the sphere, rays propagate along

Fig. 14.4 Luminescence confocal image showing the 5.2 μm microspheres covered by a monolayer of 2.5 nm (green) and 4.4 nm (red) TGA stabilized CdTe NCs. The images were acquired by a fluorescence confocal microscopy workstation (Perkin-Elmer Life Sciences, Warrington, UK) (Nikon Eclipse TE 2000-U). Processing was performed using UltraView LCI

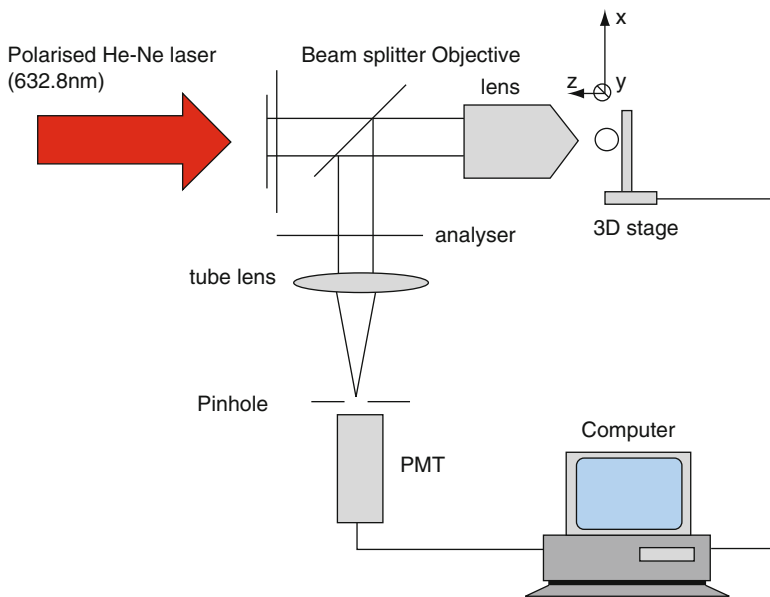
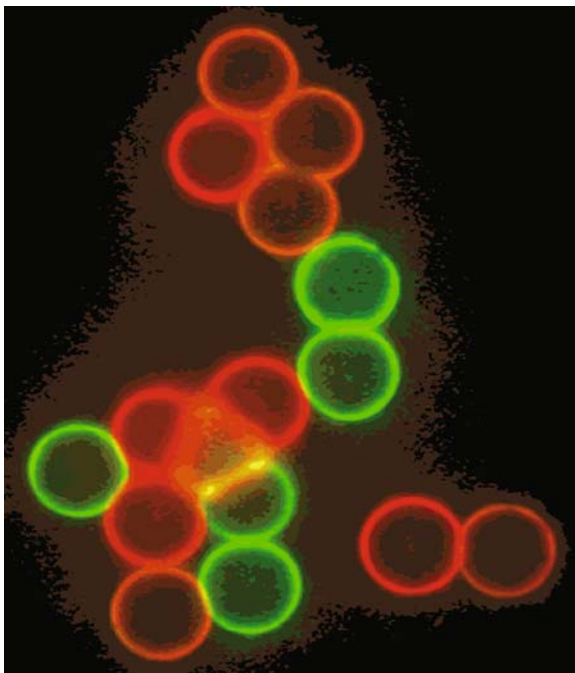


Fig. 14.5 Schematic of a confocal scanning polarization microscope. Reproduced with permission from Institute of Physics

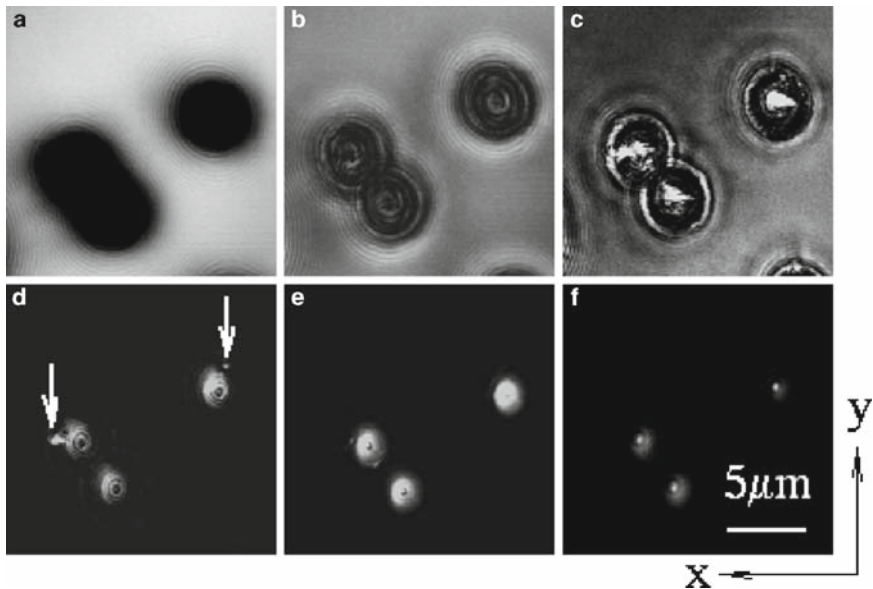


Fig. 14.6 Normalized confocal scanning images of microspheres covered by one monolayer shell of CdTe NCs, with different axial locations. From (a) to (f): $z = -R, -R/2, 0, R/2, R/2$ and R , respectively

radial directions and reflect back. The gain of the detector can be adjusted in order to see the rings around the sphere surface (Fig. 14.6b, d). However as this takes place, the centre of the sphere can be saturated. Figures 14.6d–f show the images near $z = R/2$ and R , respectively, with the same gain of the detector which is comparatively lower than that in Fig. 14.6c. Two point-like defects indicated by arrows in Fig. 14.6d, can be clearly seen inside the sphere near the region between $z = R/2$, which cannot be observed by conventional microscopy due to the poor sectioning property. Therefore the confocal imaging technique with laser illumination below the bandgap of NCs is an effective tool to control the quality of the spherical microcavity, locate any defects, and then select the spheres of highest quality.

14.3 Photons Confinement in Spherical Microcavities with Semiconductor Nanocrystals

Spherical microparticles show optical and spectroscopic properties distinct from those of a continuous medium, exhibiting a behaviour dependent not only on their composition, but also on their size. The unique spectroscopic properties of spherical particles arise from the confinement of photons. The circular optical modes in such microresonators, commonly observed as the ripple structure in elastic scattering efficiencies is now referred to by a number of names: cavity resonances,

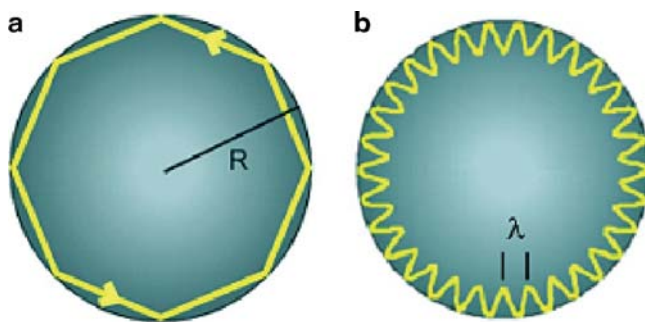


Fig. 14.7 Light confinement inside a microsphere in a geometric optics picture (a) and in a wave optics description (b)

Mie-resonances, morphology dependent resonances, or whispering gallery modes. In a geometric optics picture, WGM can be viewed as light rays that, once within the spherical particle, intersect repeatedly with the interface beyond the critical angle, undergoing total internal reflection (Fig. 14.7a). In a wave mechanics description, WGMs are internal standing waves, with an integer number of wavelengths circulating near the droplet interface (Fig. 14.7b).

The interest in the design and fabrication of optical structures for manipulation of light at the micrometer-length scale using semiconductor NCs or quantum dots, derives from both the fundamental study of the photon confinement with its quantum-electrodynamical consequences and from the potential applications. Various phenomena can be studied using NCs/microsphere hybride photonic structures, where both carriers and photons are confined within correspondingly nano- and micron length scales in three dimensions. These include cavity-quantum electrodynamics (QED) phenomena [39, 40], spontaneous emission control [15, 16, 41, 42], optical amplification and low-threshold lasing [43–47], ultra-fast carrier dynamic studies [48], enhanced Raman scattering [17, 49] and single-dot spectroscopy [50]. The basic effect of a microcavity on coupled NCs is enhancement or suppression of the radiative decay rate. As the spontaneous-emission rate is directly proportional to the fluorescence QY both can be modified when the emitting species is placed in a small-volume optical enclosure [51–53]. The above-discussed core-shell NCs/microsphere hybrid systems provide the exclusive coupling of quantum states of NCs with a microcavity mode which results in a strong exciton-radiation coupling.

14.3.1 Spherical Microcavities as Photonic Atoms

Extending the ideas of the linear combination of atomic orbitals method to the classical wave case, it was recently suggested that Mie resonances (WGM) of a single spherical microcavity play the same role as the atomic orbitals in the electronic case

and the spatial distributions of WGM can be described by analogy with the orbitals in a hydrogen atom [54]. In the absence of gain, the WGM resonances can be characterized by a mode number n (angular quantum number), a mode order l (radial quantum number), and an azimuthal mode number m (azimuthal quantum number). The value of n is proportional to the circumference divided by the wavelength of the light propagating within the microsphere, the mode order l indicates the number of maxima in the radial distribution of the internal electric field, and the azimuthal mode number m gives the orientation of the WGMs orbital plane. The modes offering the highest spatial photon confinement correspond to high values of angular momentum n , smaller values of l and to azimuthal numbers quantum numbers m close to n .

The electro-magnetic fields confined in a microsphere are given by [52]

$$\mathbf{E}_{\text{TE}} = j_n(nkr) \mathbf{X}_{nm}(\theta, \phi), \quad (14.1)$$

for modes having no radial components of the electric field (transverse electric or TE modes) and

$$\mathbf{E}_{\text{TE}} = \nabla \times j_n(nkr) \mathbf{X}_{nm}(\theta, \phi), \quad (14.2)$$

for the transverse magnetic (TM) modes (no radial component of the magnetic field).

Here $\mathbf{X}_{nm}(\theta, \phi)$ are the vector spherical harmonics given in spherical polar coordinates, $j_n(nkr)$ represents the spherical Bessel function, where $k = 2\pi/\lambda$ is the wavenumber, and λ is the free space wavelength.

On the other hand, the wave functions Ψ_{slm} for the electron confined in the hydrogen atom are given by [55]

$$\Psi_{slm} = R_{sl}(r) Y_{lm}(\theta, \phi), \quad (14.3)$$

where $R_{sl}(r)$ is known as the Laguerre polynomials. The eigenfunctions (1) and (3) are very similar and their spatial distributions are characterized by the three integer s , l and m (for hydrogen atom) and n , l and m (for microsphere), which correspond to the total angular, the radial and the azimuthal quantum numbers, respectively. Based on all above similarities, this approach has enabled small dielectric spheres to be considered as “photonic atoms” [54, 56, 57]. However, unlike energy states of an electron in the atom, photonic states in spherical microcavities are not localized due to finite storage time of photons in the resonant mode. This “photon lifetime” is controlled by the quality factor of WGM Q and therefore can be limited by diffractive losses, absorption, gain, shape deformation or refractive index inhomogeneity [52]. As a result, the resonant internal field of a spherical cavity is not completely confined to the interior of the microparticle. Decaying exponentially, the evanescent field extends a couple of micrometres into the surrounding and this very field distribution permits efficient coupling of NCs emission with WGM by placing the emitter (shell of NCs) just outside the high-refractive index microsphere. The theory suggests that by placing an excited emitter (like atom or molecule or NCs) near the surface of a spherical dielectric, the interaction of the emitter with its self-scattered field can produce enormous enhancements in its emission

rate at frequencies associated with WGM [58, 59]. This result can be clearly seen in Fig. 14.8.

In contrast to the broad, featureless PL band in the spectra of colloidal NCs, the emission spectra of a single MF/CdTe microsphere exhibit a very sharp periodic structure. The observed WGM peak structure is the result of coupling of electronic states in NCs and photon states of the microsphere. It is noteworthy that in many cases the WGM peaks in micro-PL spectra are superimposed on a background signal arising from part of the NC emission, which does not match any WGM of the microsphere [18, 60]. This background is missing from the micro-PL spectra presented in Fig. 14.8 indicating highly efficient coupling of NCs emission and photonic modes of the spherical microcavity. The placement and spacing between WGM peaks presented in Fig. 14.8 are determined by the size and refractive index of the microsphere while spectral intensity distribution depends on the parameters of NCs and can be easily modified by using NCs of different size.

To explore the optical processes in spherical microcavities, the Lorenz–Mie theory developed at the end of the nineteenth century is still widely used [61–63]. The theory gives a solution to the problem of scattering of plane electromagnetic waves of two polarizations on a sphere with an arbitrary complex refractive index n_r . The narrow optical resonances presented in Fig. 14.8 can be identified as optical

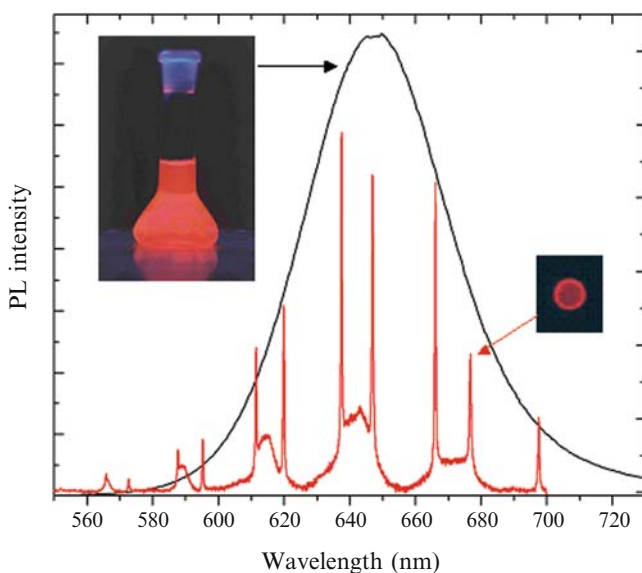


Fig. 14.8 PL spectra of CdTe NCs in water (*black*) and micro-PL spectra from a single MF microsphere of 3 μm in diameter covered by one monolayer shell of CdTe NCs (*red*). PL spectra of colloidal NCs were recorded using a Spex Fluorolog spectrometer. The micro-PL spectra from the single microsphere were recorded using a RENISHAW micro-Raman system. An Ar + laser (wavelength $\lambda = 514.5$ nm) was used in the micro-PL experiments

modes with TE and TM polarizations. For spherically symmetric microparticles the extinction cross-section is derived from the Lorenz-Mie theory [64]:

$$C_{ext} = \frac{2\pi}{k^2} \operatorname{Re} \sum_{n=1}^{\infty} (2n+1) (b_n(x, n_r) + a_n(x, n_r)), \tag{14.4}$$

where $x = 2\pi R/\lambda$ is the size parameter, R is the radius of the microsphere and the Mie scattering partial wave amplitudes $a_n(x, n_r)$ and $b_n(x, n_r)$ can be expressed in the following form [65]:

$$a_n(x, n_r) = \frac{A_n(x, n_r)}{A_n(x, n_r) + iC_n(x, n_r)} \quad \text{and} \quad b_n(x, n_r) = \frac{B_n(x, n_r)}{B_n(x, n_r) + iD_n(x, n_r)}. \tag{14.5}$$

The pairs of functions A_n, C_n and B_n, D_n are determined by the Mie scattering theory [66]. The resonance structure in the scattering spectra can be expected when the real part of a_n (or b_n) reaches a maximum value of 1 and the imaginary part is passing through 0 from the positive to the negative side. In other words the resonances in the Mie scattering characteristics occur when $C_n = 0$ or $D_n = 0$, which gives the following mathematical condition for a resonance [67]:

$$n_r \psi_n(x) \psi'_n(n_r x) - \psi_n(n_r x) \psi'_n(x) = 0 \tag{14.6}$$

or

$$n_r \psi_n(x) \psi'_n(n_r x) - \psi_n(n_r x) \psi'_n(x) = 0. \tag{14.7}$$

Note that, for given n and m , these equations have an infinite number of solutions at discrete values of x for TM and TE WGMs respectively. Also (14.6) and (14.7) are independent of the azimuthal mode number m because of the spherical symmetry implying that the m -modes are wavelength degenerated. The Riccati-Bessel functions of the first and second kind can be introduced as:

$$\psi_n(z) = z j_n(z) = \sqrt{\frac{\pi z}{2}} J_{n+\frac{1}{2}}(z) \quad \text{and} \quad \chi_n(z) = z y_n(z) = \sqrt{\frac{\pi z}{2}} Y_{n+\frac{1}{2}}(z) \tag{14.8}$$

where $J(z)$ and $Y(z)$ are the cylindrical Bessel functions of the first and second kind respectively. The use of Bessel functions for systems with cylindrical symmetry together with the recurrence relation $\Psi'_n(z) = -\frac{n}{z} \Psi_n(z) + \Psi_{n-1}(z)$ enables to reduce (14.6)–(14.7) to a form convenient for practical calculation of the position of WGMs. Thus for a real refractive index, the conditions for TM and TE resonances can be written in the following form:

$$\frac{1}{x} \left(\frac{n}{n_r} - n_r n \right) J_{n+1/2}(x) J_{n+1/2}(n_r x) + n_r J_{n+1/2}(n_r x) J_{n-1/2}(x) - J_{n+1/2}(x) J_{n-1/2}(n_r x) = 0, \tag{14.9}$$

$$n_r Y_{n+1/2}(x) J_{n-1/2}(n_r x) - J_{n+1/2}(n_r x) Y_{n-1/2}(x) = 0. \quad (14.10)$$

These conditions are transcendental equations, which can be solved for the size parameter x (position of a resonance) for given values of the refractive index m and for a given angular quantum number n . Thus comparing the calculated results with the spectral positions of the WGM in the experimental PL spectra, we can identify the indexes n and l for each mode and estimate the size of the sphere. The algorithm of the mode assignment can be as follows: (1) The resonant wavelengths corresponding to WGM resonances λ_i^{exp} ($i = 1, 2, \dots, N$) are determined from a PL spectrum of a single sphere; (2) We assume an approximate value for the microsphere radius based on technical specifications derived from the distribution of the sizes; (3) Theoretical resonance positions λ_i^{theor} are then calculated using (14.8) and (14.9); (4) Two lists of experimental and theoretical values are compared, and for each value of λ_i^{exp} , the closest value λ_i^{theor} is suggested while the difference between them Δ_i is calculated; (5) Taking into account the spectral resolution Δ , the

correlation $S = \frac{1}{N} \sum_1^N (1 + \Delta_i / \Delta)^{-1}$ is then maximized by adjusting only one fitting parameter, namely the size of the microsphere. Figure 14.9 shows the result of WGM identification in micro-PL spectra of NCs attached to two spheres of different sizes.

Among all the factors that cause a modification in the PL emission pattern due to spatial photon confinement in spherical microcavities, the polarization nature of the WGM plays an important role because of its potential use in all-optical switches

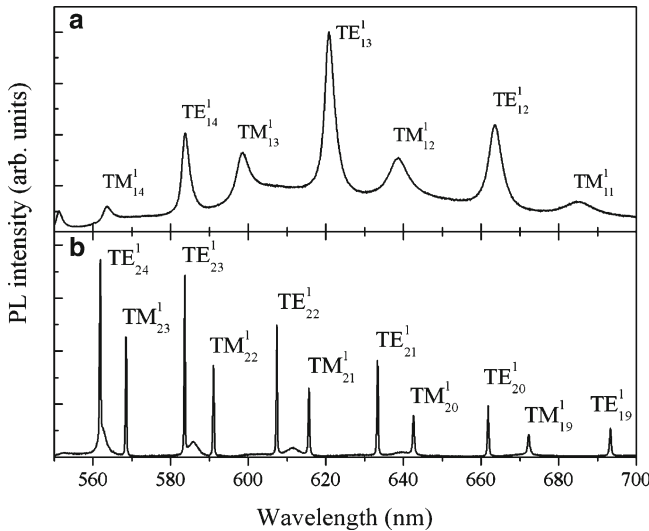


Fig. 14.9 Micro-PL spectra of two single microspheres with a monolayer of CdTe NCs, with diameters of 1.98 μm (a) and 3.06 μm (b). Reproduced with permission from American Institute of Physics

and logical devices [68]. Direct experimental identification of polarization states of WGMs can be performed by inserting a polarizer into the optical beam path in front of the detection system. In this case the polarizer selects only signals from NCs which emit components of the electromagnetic field parallel to the orientation of the polarizer axis.

For a focal spot on the top rim of a microsphere (Fig. 14.10, inset), the emission spectrum detected with a polarizer orientation parallel to the polarization plane of the laser is shown in Fig. 14.10a. Due to the higher excitation efficiency of transverse electric modes provided by this experimental scheme [69], the dominant spectral features in this case are WGMs of TE polarization. Rotating the polarizer by 90° leads to the similar WGM structure but with TM peaks dominating over the PL spectrum (Fig. 14.10b). This result confirms the polarization nature of WGM resonances; the two adjacent peaks representing TE and TM modes of a microcavity have orthogonal polarization states (Fig. 14.9). The experimental concept of polarization-sensitive mode analysis represents a convenient tool for determining the polarization properties, in particular for larger microspheres, without performing extensive numerical calculations.

Figure 14.9 also demonstrates two important aspects which can contribute to the understanding and interpretation of experimental results and to further applications. Firstly, the experimentally observable phenomenon is that the spectral spacing between two resonances of successive modes with the same order and polarization

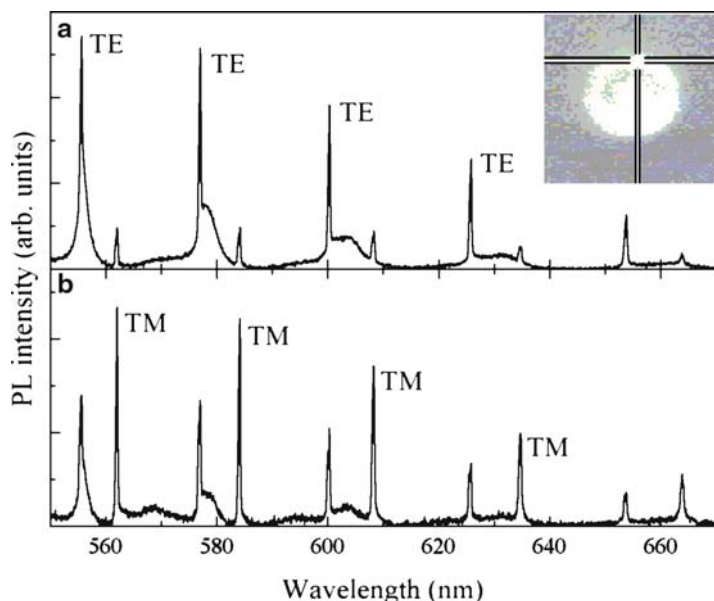


Fig. 14.10 Micro-PL spectra of a single microsphere with a monolayer of CdTe NCs with the polarizer orientation parallel to the polarization plane of the Ar⁺ laser (a), and with the polarizer rotated by 90° (b). The *inset* shows a microscope image of the microcavity with the crosshairs indicating the excitation-detection position

strongly depends on the size of the spherical microcavity. If the refractive index of the microsphere is constant and unchanged during the measurement this spectral spacing can be expressed in terms of size parameter as [70, 71]:

$$\Delta x = x_{n+1} - x_n \cong \frac{\tan^{-1}(n_r^2 - 1)^{1/2}}{n_r^2 - 1}, \quad (14.11)$$

for resonances with $x_{n,l} \gg 1$, $n \gg 1$, and $x_{n,l} \sim n$.

In the case of small spheres, when $|x-n| \gg 1/2$, the following relation applies [65]

$$\Delta x = x_{n+1} - x_n \cong \frac{x_n \tan^{-1}[(n_r x_n / n)^2 - 1]^{1/2}}{n[(n_r x_n / n)^2 - 1]^{1/2}}. \quad (14.12)$$

Since the experimental resonant spectrum can be precisely fitted using the Mie theory, it was shown that the difference between the mode spacing obtained by (14.11) or (14.12) and the experiment is $\sim 1\%$ [65]

For example, from the resonant spectrum in Fig. 14.9b, the mode spacing between resonances TE_{24}^1 and TE_{23}^1 measured in terms of wavelength is 21.8 nm, hence the experimental mode spacing can be fitted by the above asymptotic formulas with an accuracy within 1%, i.e. a deviation < 0.22 nm, when a suitable sphere size, refractive index and mode number are chosen. This simplified approach is largely exploited in current analysis of WGM structures, especially for large values of the size parameter which make the use of the whole machinery of Mie scattering theory algebraically or even computationally cumbersome.

The second phenomenon clearly seen in Fig. 14.9 is the significant broadening of WGM peaks in the spectrum corresponding to microspheres having a smaller size, compared to the spectrum corresponding to bigger microcavities, which reflects the lower quality factor Q of smaller microspheres. Due to the fact that WGMs are in fact leaky modes, the quality factor of a resonance is defined as [53, 72]:

$$Q = \frac{\text{Stored energy}}{\text{Energy lost per cycle}}. \quad (14.13)$$

Also, the Q -factor is the number of cycles required for the stored energy to decrease to $e^{-\pi}$ times of its original value. A high quality-factor is the basic reason for the interest in most of the suggested applications of microspheres.

Near a WGM, the electric field of a resonant mode inside the microcavity varies as:

$$E(t) = E_0 \exp \left[\left(i\omega_0 - \frac{\omega_0}{2Q} \right) t \right], \quad (14.14)$$

where ω_0 is the resonant frequency. The distribution of the energy of near-resonant modes in a microcavity $|E(t)|^2$ is therefore proportional to the Lorentzian

$$\frac{1}{(\omega - \omega_0)^2 + \left(\frac{\omega_0}{2Q} \right)^2}. \quad (14.15)$$

The spectral width between two points at which the energy is half of its maximum value is:

$$\Delta\omega = \frac{\omega_0}{Q}, \quad (14.16)$$

which also defines the average lifetime of the photon in a resonant mode as:

$$\tau = \frac{1}{\Delta\omega_0} = \frac{Q}{\omega_0}. \quad (14.17)$$

Aside from diffractive losses, the actual Q of a microcavity is determined by various factors like radiative losses, losses or gain attributable to absorption or emission by the material of the cavity, refractive index inhomogeneity or shape deformation. Also a strong decrease in the value of the Q-factor is expected when the curvature radius of microspheres is comparable to the resonant wavelength of WGM. This effect is accompanied by a broadening of the corresponding spectral peaks (Figs. 14.9a, b).

The typical value of the Q-factor for a composite MF/CdTe NCs microcavity of 3 μm size is $\sim 3,500$ which corresponds to an average photon storage time of ~ 1 ps. Decreasing the size of the microsphere down to 2 μm results in a Q value of ~ 800 and a corresponding modification of the photon lifetime.

14.3.2 Radiation-Pressure-Induced Modes Splitting in a Spherical Microcavity

The resonant photonic modes in spherical microcavities are highly sensitive to changes of the refractive index of the sphere itself [73] or to the environment in close vicinity to the sphere surface [74, 75]. In the latter case the sensitivity derives from the ability of the evanescent field of a WGM to explore the surrounding medium. Along with this property WGMs show remarkable sensitivity to deformation which allows for fine tuning of WGMs spectral position and Q-factor [76, 77].

As discussed earlier WGMs are wavelength degenerate with respect to the azimuthal m -modes because of the spherical symmetry of the microcavity, which means that orbits with various inclinations, described by various m -modes, have the same pathlengths and consequently the same resonance wavelengths. The total number of these m -modes, originating from a certain mode n , is governed by equations 1 and 2 and in the approach of the normal mode concept is equal to $2n + 1$.

One of the ways to reveal different m -modes is to deform the microsphere, for example by using a compression device [77]. Shape distortion breaks the azimuthal symmetry and results in lifting of the degeneracy. In a deformed sphere the photonic orbits with various inclinations have different pathlengths, therefore the spectral positions of the m -modes are no longer the same. In other words, a single WGM peak in the spectrum of a perfect sphere is now split into a series of azimuthal (m)

resonances. However, the m -modes with “+” and “-” signs designate clockwise and counter-clockwise rotations and therefore, still have the same resonance wavelength. As a result no degeneracy is removed between m and $-m$ modes in the deformed microsphere and the new degeneracy of WGMs is now $n + 1$ with m running from 0 to n . The perturbation theory provides an analytical expression for the frequency shifts and mode splitting of each of the WGMs for an oblate spheroid with a small amplitude of distortion $e = (r_p - r_e)/R \ll 1$, where the polar and equatorial radii are r_p and r_e , respectively [78]:

$$\lambda(m) = \lambda_{n,l} \left\{ 1 + \frac{e}{6} \left[1 - \frac{3m^2}{n(n+1)} \right] \right\}, \tag{14.18}$$

where $\lambda_{n,l}$ is the resonance wavelength for a perfect sphere.

The distortion amplitude e is defined to be positive for prolate spheroids and negative for oblate spheroids. For an oblate spheroid, the $m = \pm n$ equatorial mode has the lowest resonance frequency (i.e. the longest resonance wavelength) (Fig. 14.11). An m -mode with a given n value can be envisioned as filling n waveguides around the perimeter of the spheroid along the great circle of the m -mode. For an oblate spheroid, it then becomes physically intuitive to associate the smallest

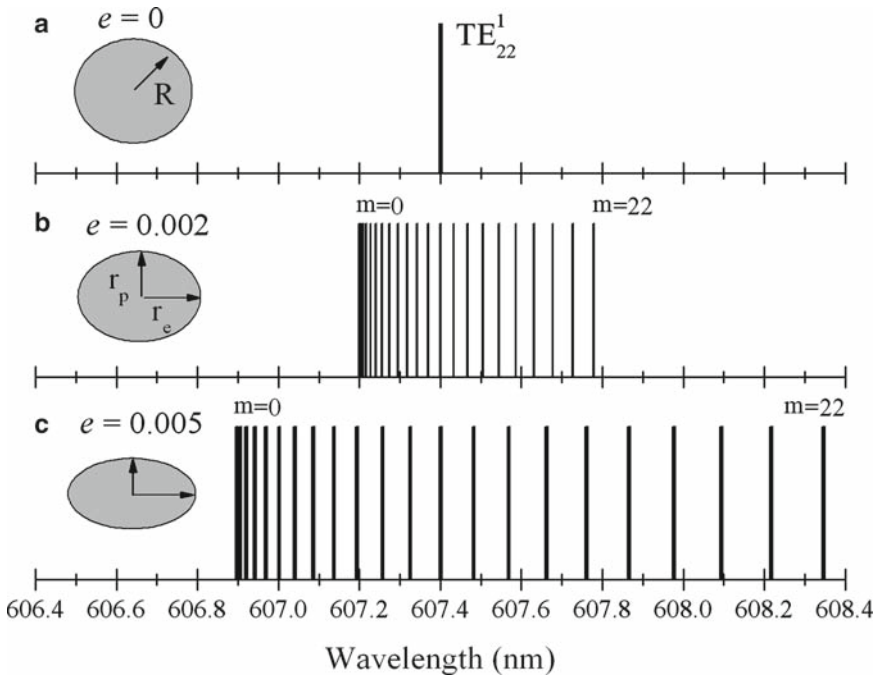


Fig. 14.11 The evolution of the WGM resonance from a perfect sphere (a) to a slightly distorted oblate spheroid (b) and to a severely distorted oblate spheroid (c). In (b) and (c), m -modes appear to be merged if spectrally unresolved, or are split if spectrally resolved

perimeter of the polar great circle $m = 0$ with a shorter wavelength and a higher frequency.

Apart from mechanical deformation of the microsphere, lifting of WGM degeneracy may be obtained by other means. The long evanescent tail of confined photonic states in a spherical microcavity implies high sensitivity of the WGM lineshape to the surface quality. In microspheres with a thin surface layer the evanescent tail of the field induces a dipole moment at the surface shell, causing a shift in the photon energy of the resonant state [79]. This is due to a change in the refractive index at the interface between the microsphere and the deposited layer.

The PE shell deposited on the surface of MF microspheres exhibits transient or permanent pores forming channels from the inside to the outside [30]. The value of the Young's modulus of PE LbL films (100–200 Mpa) falls in the range characteristic for highly cross-linked rubber and indicates that the LbL film is in fact a physically cross-linked network of PE molecules. Due to a large difference in the elastic properties of MF and PE multiplayer films [80], deformation of the PE shell may be the crucial factor controlling WGM structure in the micro-PL spectra of a microcavity. However, a controllable mechanical deformation of 3- μm microspheres combined with micro-PL spectroscopy is difficult to realize. The alternative is to use the radiation force acting on a microcavity near a substrate illuminated by a tightly focused laser beam. In this experimental scheme, instead of deforming the whole microsphere, only the soft PE layer is compressed under radiation pressure causing modification of WGM linewidth and structure.

It is well known that the radiation pressure created by the focused laser beam can be used to trap, levitate and manipulate micro- or nano-sized dielectric particles and biological cells [81, 82]. Although photons are massless particles, they can transfer their momentum to the matter. Let us suppose, that a spherical microcavity with PE/CdTe shell is positioned near a non-conductive homogeneous substrate. We assume the origin of the reference Cartesian coordinate system to be on the substrate surface, and z - and y -axes are normal and parallel to the substrate surface, respectively (Figs. 14.12 and 14.13). A laser beam of wavelength λ is tightly focused with an objective lens of high numerical aperture. The strong gradient of the electro-magnetic field intensity in the region of beam waist gives rise to the so-called gradient force (Fig. 14.13). Depending on the focus position, the gradient force can work against the gravitational forces, providing a means for the optical binding and the manipulation of ultra-fine particles and mesoscopic systems. Moreover, a beam of light can exert sufficient radiation pressure to move a microcavity along the direction of the beam propagation under the effect of a scattering force. The interplay between scattering and gradient forces provides a way of trapping the particle within the beam and thus its manipulation in the three dimensions. These two forces scale up linearly with light intensity and when the gradient force dominates the scattering force, a return force with a magnitude of piconewtons acts to confine the particle to the most intense region of the laser beam, thus creating a stable trap.

Apart from biological applications [82, 83], this radiation-pressure-induced optomechanical interaction shows great promises for a variety of applications in the field of optically actuated micro-optical-electromechanical systems (MEMS) [84, 85],

Fig. 14.12 Schematic of a spherical microcavity, showing the spatial orientation of three different m modes of the same n

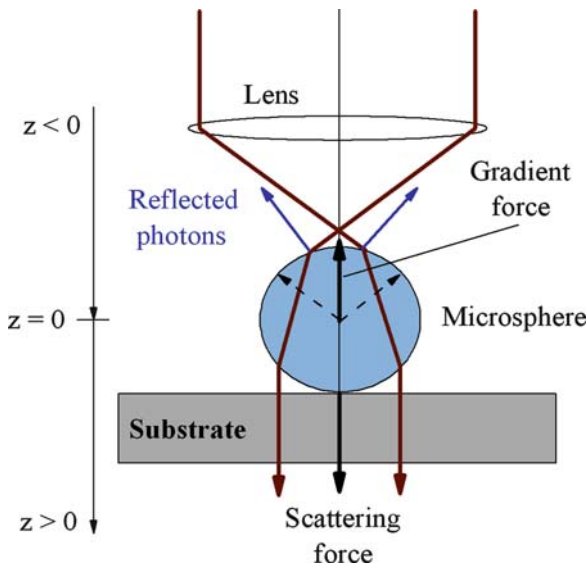
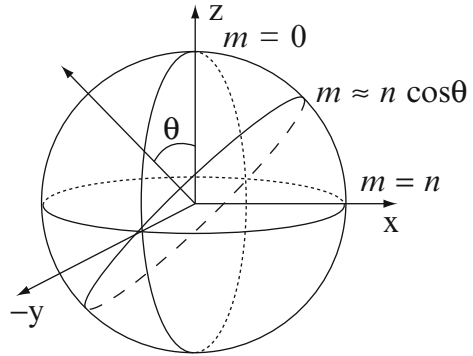


Fig. 14.13 Radiative forces on a spherical microcavity

laser cooling [86], spectrum analysis [87], optical information processing [85, 87], and quantum informatics [86].

For an object of radius R in air and a light beam with a wavelength λ and intensity I_0 , the force resulting from the light scattering is [82]:

$$F_{\text{scat}} = I_0 n_m \frac{\sigma \langle S \rangle}{c} \tag{14.19}$$

where n_m is the refractive index of the surrounding medium, $\langle S \rangle$ is the time-averaged Poynting vector, c is the speed of light, and σ is the particle's scattering cross-section, which in case of a spherical particle is given by:

$$\sigma = \frac{8}{3} \pi (kR)^4 R^2 \left(\frac{n_r^2 - 1}{n_r^2 + 2} \right)^2, \quad (14.20)$$

where n_r is the refractive index of the particle and $k = 2\pi/\lambda$ is the wave vector of the light.

The intensity gradient near the beam focus gives rise to a gradient force. This force is due to the Lorentz force acting on the dipole, induced by the electromagnetic field. In the field of the laser, the gradient force is given by [82]

$$F_{\text{grad}} = \frac{-n_m^3 R^3}{2} \left(\frac{n_r^2 - 1}{n_r^2 - 2} \right) \nabla (|E|^2) \quad (14.21)$$

where E is the electric field vector of the laser light. An essential feature predicted by this equation is that the gradient force is always directed towards the region of highest light intensity.

For a microcavity size larger than the wavelength of the laser radiation, the net force exerted on the microsphere by the focused Gaussian beam can be calculated via the generalized Lorentz-Mie theory (GLMT) [88]. The original Lorentz-Mie theory [89] is valid for the light scattering of a plane electromagnetic wave from the microparticle. The GLMT enables to calculate the spectrum of the scattered light for different positions of the particle in the beam and for different types of incoming waves. In this approach, the radiation pressure exerted by the laser beam propagating toward the positive z direction and impinging on a spherical microparticle located along the axis of the beam is expressed by:

$$F_{\text{rad}} = \frac{2P}{c\pi\omega_0^2} C_{\text{pr}}, \quad (14.22)$$

where P is the power of the laser beam, ω_0 the spot size of the focused beam and C_{pr} the radiation pressure cross-section which is given by [88]:

$$C_{\text{pr}} = \frac{\lambda^2}{2} \sum_{n=1}^{\infty} \left\{ \frac{2n+1}{n(n+1)} |g_n|^2 \operatorname{Re}(a_n + b_n - 2a_n b_n^*) \right. \\ \left. + \frac{n(n+2)}{n+1} \operatorname{Re}[g_n g_{n+1}^* (a_n + b_n + a_{n+1}^* + b_{n+1}^* - 2a_n a_{n+1}^* - 2b_n b_{n+1}^*)] \right\} \quad (14.23)$$

In this equation the beam shape coefficient g_n for an on-axis Gaussian beam is given by:

$$g_n = \left(1 + i2s \frac{z_0}{\omega_0} \right) \exp(ikz_0) \exp \left[\frac{-s^2 (n-1)(n+2)}{1 + i2(s z_0 / \omega_0)} \right], \quad (14.24)$$

where s is a parameter defined by $s = 1/k\omega_0$, and z_0 is the coordinate of the beam-waist center. The Mie-coefficients a_n and b_n are defined by (14.5).

Figure 14.14 shows the calculated radiation force F_{pr} for a variable focus position along the z -axis in the centre of the sphere having a diameter of 3 μm . A negative value of F_{pr} means a reversed radiation force exerted on the microsphere,

pulling the sphere in the opposite direction of the beam propagation. This happens when the resulting gradient force exceeds the scattering force. Positive F_{pr} pushes the sphere downwards on the solid substrate. The value $z = 0$ on the x -axis in Fig. 14.14 corresponds to the centre of the sphere (Fig. 14.13). Positive z values are focus positions below the centre towards the substrate and negative values of z correspond to a focus point above the sphere center (Fig. 14.13). A freely moving microsphere would be trapped at the point where the radiation force is zero. In these calculations, it is nearly $0.5 \mu\text{m}$ below the top of the sphere and $1 \mu\text{m}$ above the sphere centre respectively ($z = -1 \mu\text{m}$). If a laser beam is focused at that point, no radiation force is exerted on the sphere. If the focus is moved further up, the resulting radiation force is pulling the sphere upwards and if the focus is moved further down, the sphere is pushed on the substrate with a maximum radiation pressure at around $0.6 \mu\text{m}$ ($z = 0.9 \mu\text{m}$) above the substrate. These results clearly demonstrate the possibility to control the radiation pressure by tuning the focus position, implying a non-contact method for controllable tuning/modification of WGMs in a spherical microcavity having a compressible surface shell.

For exploring this possibility, the PL spectra of a single microsphere with 15-nm thick PE shell and a monolayer of CdTe NCs were taken at different focus positions and excitation power levels (see Fig. 14.15). In order to modify the stiffness of the PE shell, an additional chemical procedure was used. Before the spheres are coated with a NCs layer, the sample was kept for 3 days in a highly concentrated NaCl (3 Mol/L) solution. This treatment reduces the solidity of the PE layer resulting in a softer surface layer [90]. The soft layer is necessary to irreversibly deform the spherical shape of the PE shell by radiation pressure without requiring mechanical devices being in contact with the sphere.

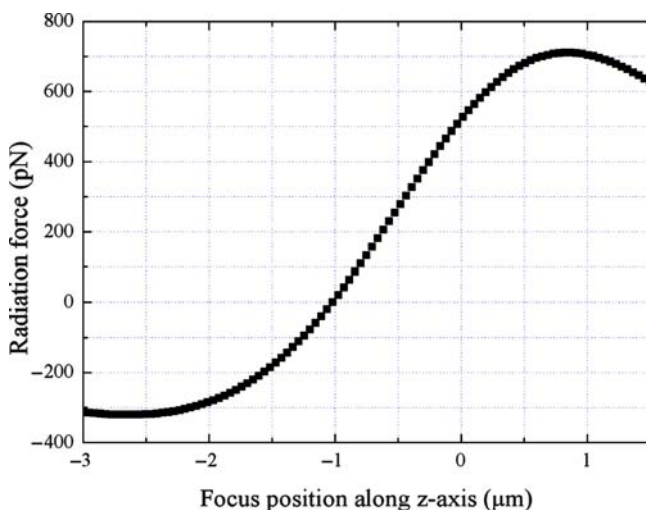


Fig. 14.14 Calculation of radiation pressure applied on a MF microsphere of $3 \mu\text{m}$ size along the z -axis. Excitation power $P = 20 \text{ mW}$

Figure 14.15 shows the results of two experiments. In these studies the Ar⁺-laser beam ($\lambda = 514.5$ nm) simultaneously serves the purpose of an optical tweezers setup, confining the sphere and applying a radiation pressure, and of an excitation source for the optically pumped semiconductor NCs. An *xyz*-table with a spatial resolution of 0.1 $\mu\text{m}/\text{step}$ allows an accurate focusing of the vertical laser beam through the high NA (0.9) microscope objective at 100 \times magnification. In the first case (Fig. 14.15a) the PL spectrum was recorded with a focus position of 1 μm above the microsphere. According to theoretical predictions (Fig. 14.14) an upward radiation pressure should be exerted on the sphere. The output power of the Ar⁺-ion laser is $P = 15$ mW. The spectrum shows the structure of the WGMs, which is typical for a sphere with a diameter of 3 μm . The more intense peaks in Fig. 14.15 were identified as TE modes, whereas the smaller peaks observed in micro-PL spectra are TM modes. All peaks broaden and show some indication of splitting due to the radiation pressure and the own weight of the sphere (1.6×10^{-12} N). When the focus position is inside the sphere near the substrate, a second peak is arising slightly red-shifted with respect to the original mode as shown in Fig. 14.15b. The broadening of the peak towards longer wavelength is in agreement with the theory, predicting that the deformation causes the lifting of the mode degeneracy and the shifting of the azimuthal modes to larger wavelengths (Fig. 14.11).

A simple model based on (14.18) can verify that the observed peak structure is caused by the lifted mode degeneracy. Within this model, individual WGMs can be approximated by the lorentzian-shaped azimuthal peaks. The superposition of these modes is plotted in Fig. 14.16 including the original peak of the undeformed sphere.

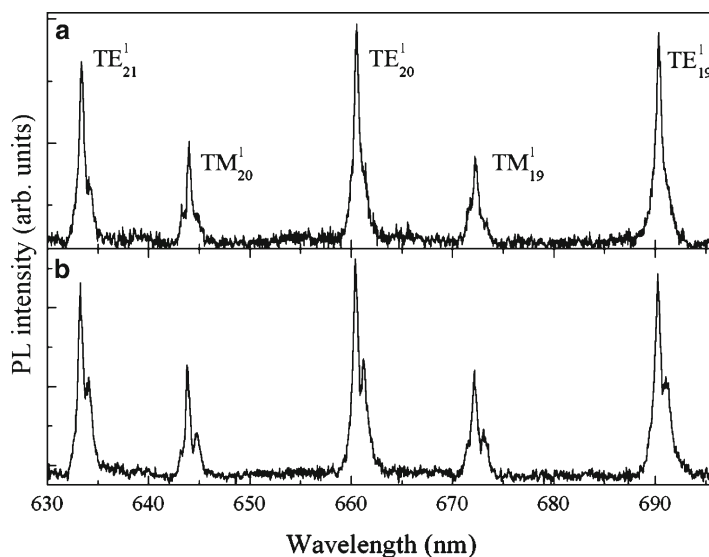


Fig. 14.15 PL spectra of microspheres with thin PE-shell and one monolayer of CdTe NCs recorded while trapped in a cw laser beam under radiation pressure. The focus position is 1 μm above the microsphere (a) and near the substrate (b)

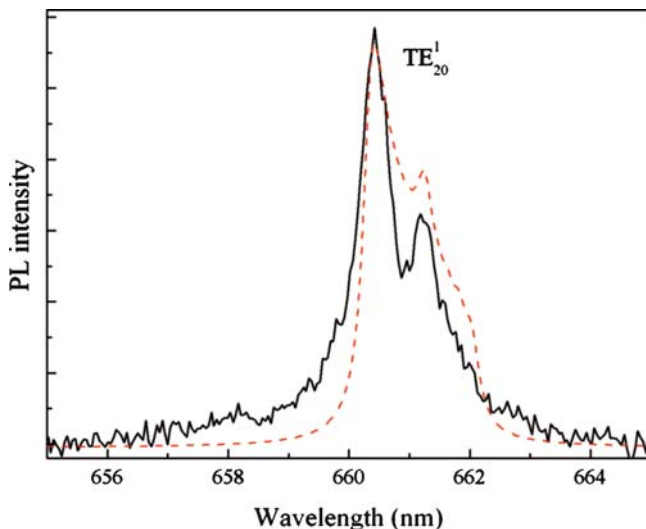


Fig. 14.16 Measured lineshape TE_{20}^1 mode (solid line) and simulated peak shape (dashed line)

The peak due to the perfectly shaped sphere is added to the model corresponding to an irregular deformation of the soft PE layer. As the solid sphere is not deformed but only the compressed PE layer is, we assume that there is still a strong resonance at the original resonance frequency of the WGM, assigned to the modes that travel around the sphere circumference in the region which is not affected by the distortion. Several parameters for the modelled peak such as the linewidth of the resonances (estimated to be $\Delta\lambda = 0.3$ nm) and the original resonance wavelength λ_0 are taken from the measured spectrum. The shape of the modelled peak is fitted to the measured peak by changing the ellipticity to the proper value. The result is shown in Fig. 14.16 demonstrating a good qualitative agreement between the calculated and measured line shapes of the peak. The estimated value of ellipticity $e = 8.5 \times 10^{-3}$ is equivalent to a decrease of the sphere radius by about 4 nm which is a reasonable value taken into account the thickness of PE shell.

14.3.3 Microcavity enhanced Raman Scattering and Anti-Stokes Emission

WGM microcavities (e.g.: microspheres, microcylinders, microrings and microtoroids) are ideally suited for observing nonlinear optical effects with extremely low threshold powers. High quality factors and large field densities associated with WGMs result in resonant enhancement of nonlinear interactions of various kinds [91–98]. These modes provide the opportunity to achieve a high nonlinear response

with weak electromagnetic fields, even if the cavity is fabricated from a material with low nonlinearity, as is usually the case for optically transparent materials. The quality factors of MF or polystyrene (PS) microspheres of $2 \div 70 \mu\text{m}$ in diameter with a thin shell of CdTe NCs were found to be high enough to provide the feedback required for nonlinear-optical processes such as enhanced Raman scattering [17, 49, 99]. It was also shown that Raman spectroscopy allows very efficient vibrational characterization of a monolayer of semiconductor NCs coating the microsphere [17]

The measured Raman spectrum of a single MF/PE/CdTe microsphere of $2.2 \mu\text{m}$ size with a shell thickness of only one monolayer reveals pronounced features as shown in Fig. 14.17. The use of the Si substrate provides the built-in standard of the Si TO mode at 520 cm^{-1} . The peak detected at 162.0 cm^{-1} originates from the longitudinal optical (LO) phonon mode of the CdTe NCs monolayer. The frequency of this peak is smaller than the corresponding bulk value of 168 cm^{-1} [100] by 6.0 cm^{-1} . This shift originates from two sources: a red shift due to the confinement of optical phonons [101, 102], and a blue shift caused by the lattice contraction [21, 103].

The 25.0 cm^{-1} width of the LO phonon line for CdTe NCs in our experiment reflects the somewhat broad size distribution of the quantum dots. It is noteworthy that no Raman signal was observed, under the same experimental conditions, from a monolayer of CdTe NCs directly deposited on top of the Si wafer. This is a compelling evidence that Raman signal from a monolayer of CdTe NCs was observed due to the strong coupling with the spherical microcavity.

As we discussed in Sect. 14.3.1, a strong increase in the value of the Q-factor is expected with increasing curvature radius of the microsphere. Increasing the size of the microsphere leads to a strong reduction of the mode volume and therefore to high

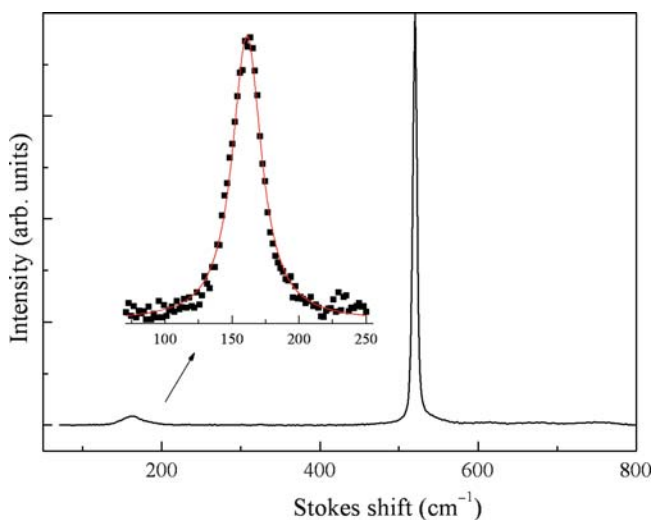


Fig. 14.17 Raman spectrum of a single MF/CdTe microsphere on a Si substrate. Excitation by an Ar⁺-laser ($\lambda = 488 \text{ nm}$). Reproduced with permission from the American Institute of Physics

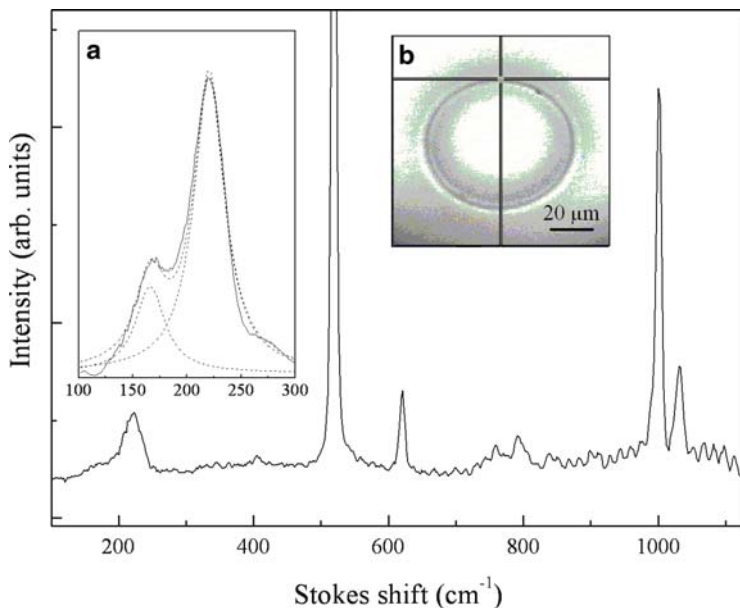


Fig. 14.18 Raman spectra of a single CdTe/PS microsphere on a Si substrate. Excitation by an Ar⁺-laser ($\lambda = 488$ nm). *Inset: (a)* The deconvolution of the lineshape of the Raman spectra in the region of CdTe LO phonon mode using Lorentzian functions. *(b)* microscope image of the CdTe/PS microsphere. The *dark cross* indicates the excitation position. Reproduced with permission from Elsevier

light circulating intensities, due to the cavity buildup factor. Fig. 14.18 shows the Raman spectrum of a microcavity-NCs system consisting of CdTe colloidal NCs coated onto a PS microsphere of $70 \mu\text{m}$ size. The recorded spectra at the resonance excitation by an Ar⁺-laser (488 nm) show a number of peaks which are characteristic of PS (220, 620, 759, 793, 1,001 and $1,031 \text{ cm}^{-1}$). In addition to these lines, the cavity-induced enhancement of the Raman scattering allows for the observation of the LO phonon mode from only a monolayer of CdTe NCs (166.0 cm^{-1}) (Insert, Fig. 14.18a), red-shifted due to the confinement of optical phonons [49]. However, the most remarkable experimental observation is the periodic (ripple) structure with very narrow regular peaks in the Raman spectra of the PS/NCs microsphere, which can be clearly seen in Fig. 14.18. This structure corresponds to the WGMs of the spherical microcavity and can be best detected by providing excitation at the rim of the microsphere (Insert, Fig. 14.18b). The resonant internal field of a spherical cavity corresponding to high-Q modes is mostly confined to the near-surface interior of the microsphere [104]. Therefore, a uniform intensity distribution within the rim of the microsphere in the volume determined by the WGM can be expected if the incident wave is resonant with a WGM. In such a situation, edge illumination with a focused beam excites the WGM of a microsphere more uniformly and more efficiently than an excitation focused at the microsphere center [49, 104].

Another feature, which can be clearly seen in Fig. 14.18, is that the intensity of WGM peaks decreases as they approach the excitation wavelength. The observed reduction of the peaks intensity in the Raman spectra of a CdTe/PS microsphere is due to the absorption by NCs that are coupled to the relevant WGM. It is well known that absorption, or gain, or refractive index variation alter the Q value of the spherical microcavity [18]. Because of the Stokes shift (30 nm) between the intrinsic PL peak and the absorption of CdTe NCs, the absorption coefficient is reduced in the long-wavelength part of the PL band [105], allowing a higher Q factor to be achieved in this spectral region.

Due to inhomogeneous broadening, the band edge emission was found to be strongly dependent on the excitation photon energy E_{ph} when E_{ph} is smaller than the fundamental absorption peak [106–108]. Resonant PL spectroscopy (size-selective excitation into the tail of the absorption onset) shows increasing fluorescence line narrowing with increasing excitation wavelength [108, 109]. When E_{ph} is close to the PL band maximum, efficient thermally-activated photon energy upconversion occurs leading to anti-Stokes photoluminescence (ASPL) [110–113], corresponding to the observation of an emission at energies higher than the excitation energy. The excitation of ASPL can be extremely efficient, and recent advances in a number of applications including laser technology [114], three-dimensional micro-fabrication and optical storage [115, 116], displays and optical limiting [114, 117], imaging techniques [118], and biological caging [119] have renewed interest in upconversion luminescence [120]. Upconversion of semiconductor NCs combined with photon confinement in three-dimensional microcavities has the greatest potential to be useful in micro-laser technology, optical data storage, lighting and bio-imaging applications.

Figure 14.19b shows the room-temperature spectrum of a single PS/CdTe microsphere on a Si substrate obtained using the low-intensity non-resonance excitation provided by a He-Ne laser. In that case, the strong coupling between the WGM of the spherical microcavity and the electronic states of the CdTe NCs results in an enhanced luminescence contribution to the Raman signal. This contribution appears simultaneously in both the Stokes and anti-Stokes spectral regions. The ASPL process is certainly highly efficient, with an intensity comparable to the Stokes PL as seen from Fig. 14.19b. We found that the integrated intensity of ASPL has an almost linear dependence on the excitation intensity under weak or moderate excitation ($< 200 \text{ W/cm}^2$). This dependence is very similar to the behaviour of ASPL in colloidal CdTe NCs where the progressive transition from Stokes PL to ASPL can be observed when changing the excitation wavelength to a wavelength below the band-gap region [111, 121–124]. A similar effect was recently reported in small (2 μm) microspheres with a thin shell of semiconductor NCs, and was explained by multiphonon-assisted excitation of an electron from the ground state to the excited state through the mediation of the shallow trap levels [17]. In the case of colloidal NCs such a low cross-section mechanism, like anti-Stokes excitation, can be only efficient in samples with high enough quantum yields [124, 125].

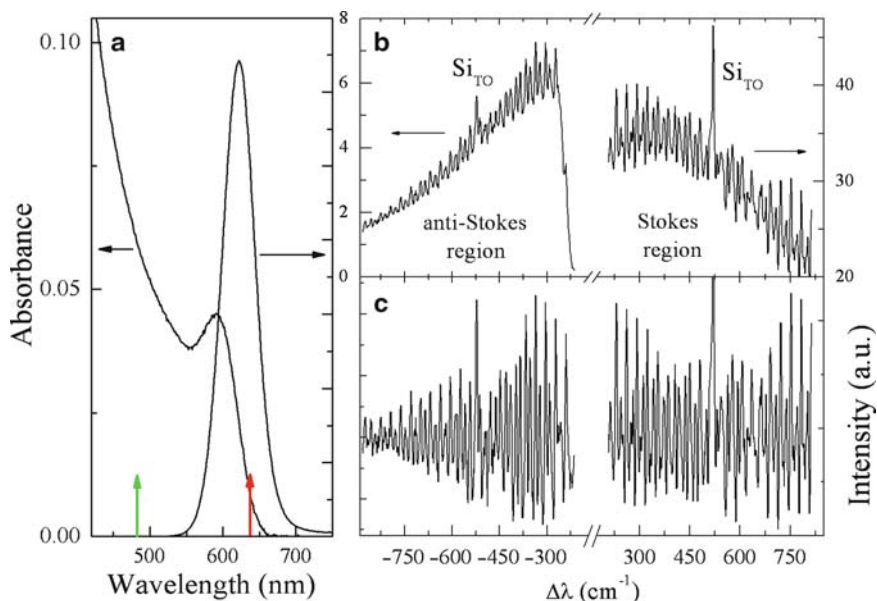


Fig. 14.19 Room temperature absorption and PL spectra of CdTe NCs in water (a). Arrows indicate the excitation wavelength used in micro-PL and Raman experiments. Raman spectrum of a single PS/CdTe microsphere on a Si substrate. Excitation by HeNe laser ($\lambda = 632.8$ nm) before (b) and after (c) PL background subtraction. Reproduced with permission from Elsevier

The observation of ASPL from a PS/CdTe microsphere can be attributed to the optical feedback via the microcavity with a WGM structure which leads to an increased probability of energy transfer to the emitting species.

Because of the very high PL quantum efficiency of NCs, the WGM peaks in the spectra presented in Fig. 14.19b are superimposed on a broad background PL signal. In order to show more clearly the WGM structure itself, this background may be subtracted using a multi-Gaussian function (Fig. 14.19c). This procedure made it possible to reveal one more feature which is typical for spherical microcavities, namely a slowly oscillating structure caused by interference between diffracted and transmitted light at the poles of the microsphere [126]. As can be seen in Fig. 14.19c, the WGM peaks are in fact grouped together and a periodic interference structure can be clearly seen both in Stokes and anti-Stokes spectral regions with a period of ~ 340 cm⁻¹ and ~ 230 cm⁻¹, respectively.

Similar to the PL spectra of a single microcavity, the Raman spectra (Figs. 14.18 and 14.19b, c) show a sequence of sharp peaks which only occur at discrete frequencies depending on the refractive index n_r and the radius R of the microsphere. The modes in the spectrum in Fig. 14.19b are arranged in pairs of pronounced peaks where the TE mode corresponds to the peak with higher intensity and the TM mode to the smaller peak, in agreement with polarization experiments. However in

contrast to the case of small ($<10\ \mu\text{m}$ size) microcavities, accurate identification of WGMs in $70\ \mu\text{m}$ -diameter microspheres is impossible due to the strong overlap of resonant peaks and a high Q-factor. Figure 14.20b shows an enlargement of the measured spectrum (Fig. 14.19b) where the periodic structure of WGM peaks can be seen in more detail, demonstrating that the modes in the PL spectrum are arranged in series of pairs of pronounced peaks, one peak of higher intensity than the second one. Moreover, a few extra tiny peaks can be distinguished in the spectral region between them. A Fourier analysis of the spectra allows to gain more insight into the WGM structure in the microcavity, making it possible to investigate the periodicity more thoroughly.

In the spectral frequency interval $0\text{--}3.5\ \text{nm}^{-1}$, we observed strong peaks corresponding to a periodicity of $1.31\ \text{nm}$, $0.65\ \text{nm}$, $0.44\ \text{nm}$ and $0.33\ \text{nm}$ (see bars in Fig. 14.20a, c). The highest periodicity value could be assigned to the free spectral range (FSR) between modes of the same polarization with radial order numbers $n = 1$. As TE modes have normally a higher quality factor than the TM modes, we can attribute the stronger peaks in Fig. 14.20b to the TE modes of the WGM. The good agreement between the measured FSR of $1.32\ \text{nm}$ between the TE modes supports this hypothesis. In turn, the periodicity of $0.65\ \text{nm}$ is attributed to the FSR between modes of different polarizations (i.e. between adjacent TE and TM modes) again in agreement with measured modes separation (Fig. 14.20b). Periodicities of

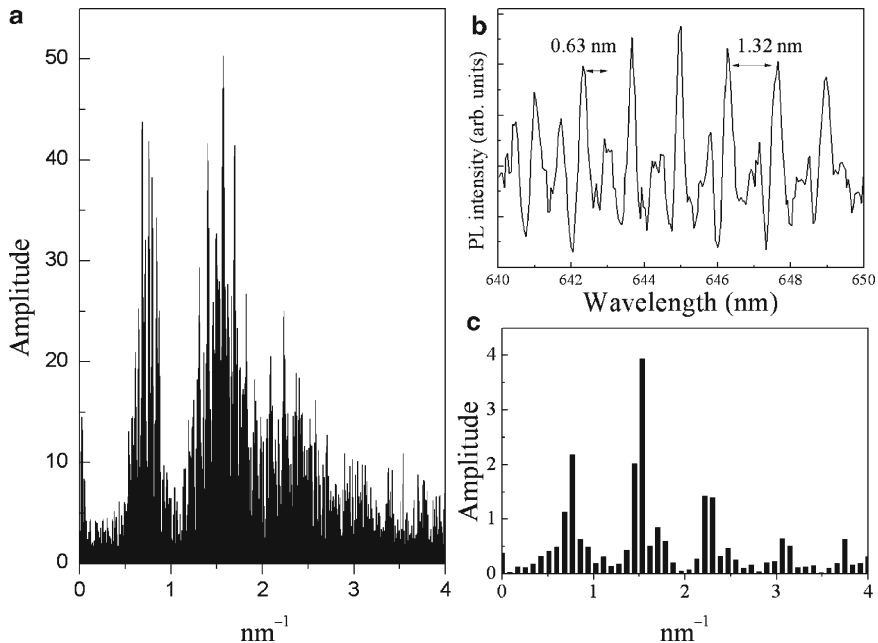


Fig. 14.20 Result of fast Fourier analysis over the whole spectral region (a). Expansion of the recorded spectrum (b) and corresponding result of fast Fourier analysis (c). *Arrows* indicate the free spectral range (FSR) and TE/TM mode splitting

0.44 and 0.33 nm, obtained from the Fourier analysis, are indicative of the TE and TM modes with radial order numbers which are greater than 1.

14.4 Coupled Spherical Microcavities with Semiconductor Nanocrystals

As discussed in Sect. 14.3.1, the resonant internal field of a spherical cavity is not completely confined to the interior of the microparticle. Depending on the size of the microsphere, the evanescent field can extend into the surroundings up to a couple of micrometers. It was recently recognized that the partial delocalization of Mie resonance states is of great importance because it suggests a possibility for coherent coupling between WGMs of two adjacent spherical particles with closely matched sizes. Such a system of coherently coupled photonic atoms may be called a “photonic molecule” (PM) [57, 127] and can be employed in order to manipulate photons on the micrometer length scale. By analogy with the formation of molecular electronic orbitals, the tight binding approximation provides two combinations for the electromagnetic field in a system of interacting microspheres: bonding and anti-bonding states (Fig. 14.21) [127–130].

Experimentally, the coupling of the photon modes of individual microspheres in the PM can cause a narrow resonance of a photonic atom to split into two modes of lower Q -factor [128]. This phenomenon has been demonstrated in a system of two square photonic dots coupled by a narrow channel [127], in a dye-stained bisphere system [129, 131, 132], in photonic dots doped by CdSe NCs [133], and in chains of polymer-blend microparticles [134]. However recent theoretical considerations [130] and experimental studies [42, 135] revealed a complex internal distribution

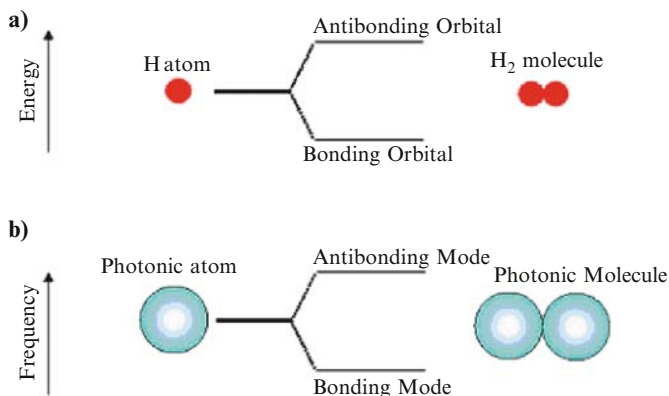


Fig. 14.21 Schematic of the splitting of the energy levels of hydrogen atoms (a). By analogy, the WGMs with the same resonant frequency split into two coupled modes

of density of photonic states of PM originating from lifting the degeneracy of PM modes with respect to the azimuthal index.

Recent proposals of coupled-resonator optical waveguides [136, 137], high-order optical filters [138], and optical-delay elements [139–141] stimulated further interest in systems of optically coupled microspheres such as linear chains [134, 142, 143], two-dimensional arrays or three-dimensional crystal structures [144]. In these systems a “photon hopping” transport between adjacent spheres should occur at the frequencies of the WGMs, providing the possibility of manipulating light paths as well as light dispersion at a microscopic scale.

14.4.1 *Modification of Confined Photon States in Weakly Coupled Spherical Microcavities with Semiconductor Nanocrystals*

The simplest experimental approach to investigate the propagation modes in interacting spherical microcavities can be the scanning of a sample along the longitudinal axis of the PM using the excitation/detection geometry as presented in Fig. 14.22 [42].

Figure 14.23 shows experimentally-obtained micro-PL spectra of coupled MF/CdTe microspheres and the result of the WGM identification by the algorithm described in Sect. 14.3.1. The shift in the position of the TE_{22}^1 , TE_{23}^1 , TM_{21}^1 , and TM_{22}^1 modes of the single microspheres, which can be clearly seen in Fig. 14.23, is the result of a size difference between the two microspheres of only 11 nm as calculated from the Mie theory. When the excitation is provided at the contact point between microspheres (Fig. 14.23b), the excited and emitted lights propagate efficiently along the longitudinal axis of the bisphere and the contribution of both microcavities can be clearly seen in the PL spectra at discrete WGM wavelengths. This contribution of PL signal from individual microcavities can be switched by changing the excitation position from the left to the right rim of the PM (Fig. 14.23a, c). In the above experiments, the excitation beam incidence was perpendicular to the longitudinal axis of the PM. For a given excitation and detection

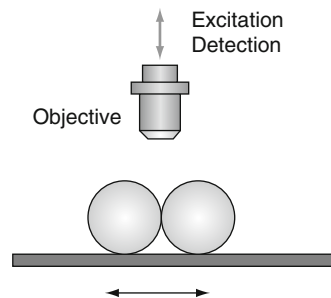


Fig. 14.22 Experimental geometry for scanning a PM along the longitudinal axis. Reproduced with permission from the International Society for Optical Engineering (SPIE)

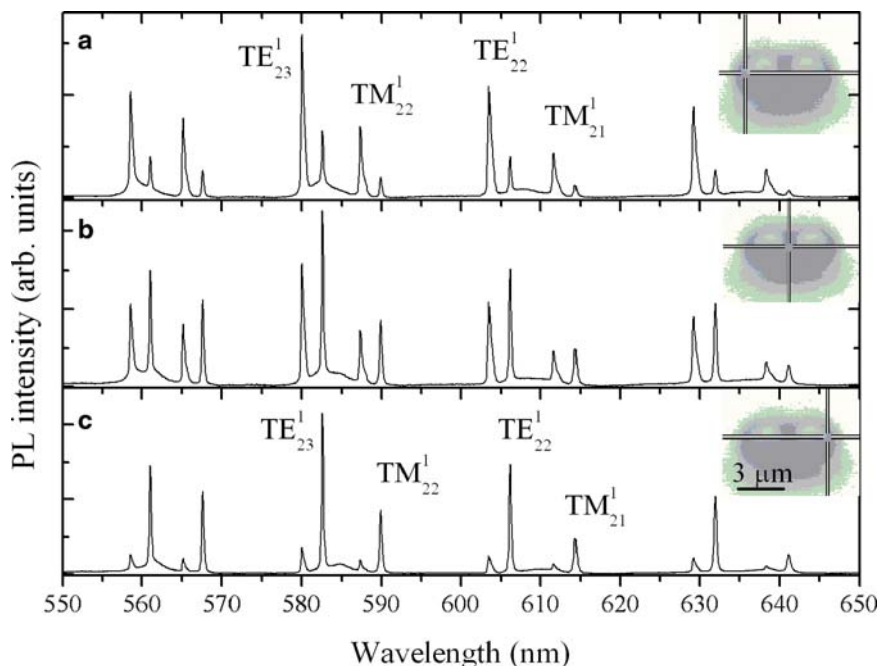


Fig. 14.23 PL spectra of a PM with excitation and detection at three different positions along its longitudinal axis. *Insets*: microscope images of the PM, with the cross-hairs indicating the excitation-detection position. Reproduced with permission from the International Society for Optical Engineering (SPIE)

configuration, no other new peak was observed in the PL spectra of the PM contrary to the case of single spheres, which is an indication of weak intermode coupling. The lack of intermode coupling in this configuration (Fig. 14.22) is not surprising because the coupling between the electro-magnetic fields of the spheres is expected to be minimum when the excitation and detection are set perpendicular to the axis of the PM [129]. However, the observed redistribution of intensity between the components of the WGM double structure clearly demonstrates waveguiding of the light along the PM and the possibility of wavelength switching in the PM depending on the excitation-detection geometry.

14.4.2 *Confined Optical Modes in Small Photonic Molecules with Semiconductor Nanocrystals in the Strong Coupling Regime*

Theoretical considerations [128–130] show that the inter-sphere coupling is expected to be maximum for the pair of modes whose orbitals include the contact point between the microspheres and lie in the same plane. Taking this into account,

the PL intensity of the coupled modes is anticipated to be maximum in the direction parallel to the PM axis, and the signal from the coupled inter-sphere modes should be more pronounced in the parallel configuration than in the perpendicular one.

Recently, a new approach to control the alignment of the spheres constituting the PM has been developed [42, 135] by utilizing a polystyrene substrate bearing a three-dimensionally ordered array of pores of $\sim 5 \mu\text{m}$ in size prepared through thermocapillary convection [145]. The ordered structures are formed by evaporating a solution of polystyrene in a volatile solvent, in the presence of moisture with forced airflow across the solution surface. A hexagonally-packed array of holes (microwells) of 3–5 μm depth then forms on the surface of the polymer (Fig. 14.24a). Only one pair of the 3 μm -size microspheres can be accommodated within each microwell, and the axis of the PM is close to the surface normal (Fig. 14.24b).

Figure 14.25b shows the PL spectrum of a PM accommodated in a microwell and the spectrum of the individual microspheres prior to being inserted into the microwell. A pronounced doublet structure in the spectrum presented in Fig. 14.25b, coinciding with the spectral positions of the WGM of the individual microspheres (Fig. 14.25a), is the result of the overlap of the uncoupled modes of the two spheres. The shift in the position of the WGM, which can be clearly seen in Figs. 14.25a, b is the result of a size difference between the two microspheres of only 25 nm. However, in contrast to the spectrum in Fig. 14.25a, this doublet is accompanied by two extra relatively broad peaks (indicated by arrows in Fig. 14.25b), which are indicative of strong mode coupling in the PM. The appearance of these two satellites can be interpreted as the result of the formation of BN and ABN orbitals in the PM [127] with the ABN peak observed at a lower wavelength than the BN peak. In terms of cooperative scattering theory [128], the observed satellites originate from the removal of the WGM degeneracy with respect to the m index. The shape of the satellite lines reflects the energy distribution among the coupled modes, because modes with different combinations of m can contribute to the PL

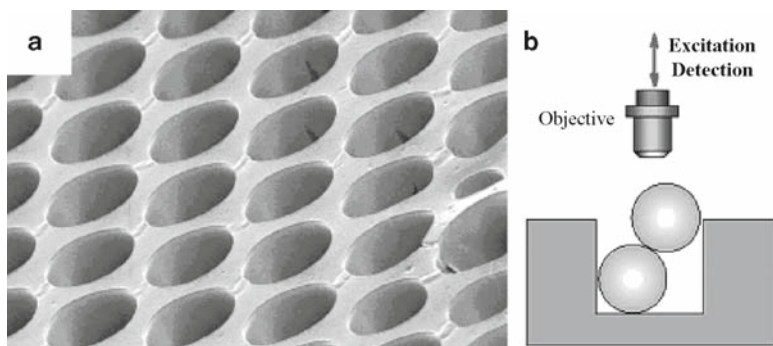


Fig. 14.24 Polystyrene film with an hexagonally ordered array of air-holes with diameters of about 5 μm (a), and experimental geometry for off-axis or parallel excitation and detection (b). Reproduced with permission from the International Society for Optical Engineering (SPIE)

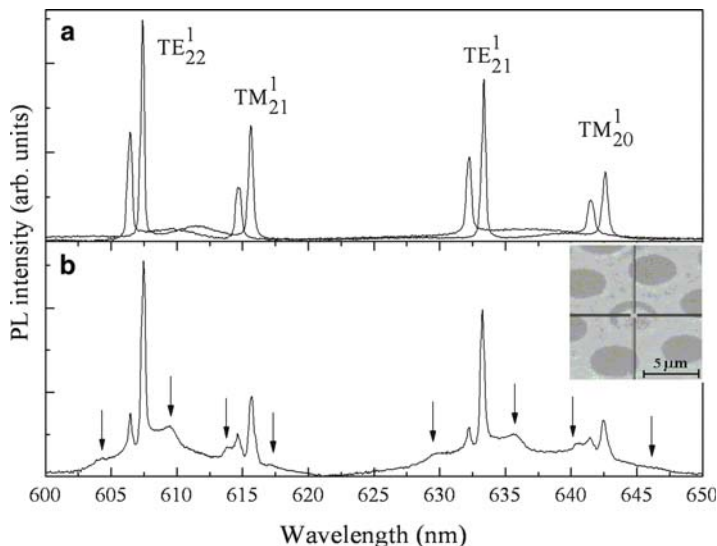


Fig. 14.25 PL spectrum of non-interacting microspheres (a) and PL spectrum of PM accommodated in a microwell (b). Arrows indicate the coupled modes. The dark cross indicates the excitation position. Reproduced with permission from the American Physical Society

spectra. The observation of an ABN peak broader than the BN peak reflects a decrease of the quality factor of the PM when compared with that of a single sphere, presumably due to the interaction with more dissipative modes of lower l [129]. The deconvolution of the line shape of resonances belonging to TE_{22}^1 WGM (Fig. 14.25a, b) using Lorentzian functions shows that the quality factors of PM peaks are ~ 8 times smaller than Q-factors of non-interacting microspheres.

14.4.3 Optical Modes in Photonic Molecules Formed from Spherical Microcavities

Photonic states in a PM can be described by a linear combination of the Mie resonance states of each microsphere [128] or by the more general phenomenological tight-binding model [130] which has been used recently to reproduce the band structure of two-dimensional photonic band-gap lattices composed of cylinders [54].

For a given WGM polarization, the value of the splitting between the BN and ABN modes of the PM can be obtained by using the maximum term approximation of the single-mode tight-binding (SMTB) method as [130]:

$$\Delta x_m = 2\Gamma_n \left| A_{n,m}(x_n) \right|, \quad (14.25)$$

where $x_n = 2\pi R/\lambda_n$ is the size parameter of a resonance with the mode number n , λ_n is the corresponding resonant wavelength, Γ_n is the width of the mode n in a single sphere, which can be calculated with the Mie-theory. For a given radius R of single spheres, the coefficient $A_{n,m}$ can be calculated as:

$$A_{n,m}(x_n) = -2n(-1)^{n+m} h_{2n}^{(1)}(k_0 Z) \times \sqrt{\frac{2n}{\pi(n+m)(n-m)}} \times \frac{n^{2n}}{(n+m)^{n+m}(n-m)^{n-m}}, \quad (14.26)$$

where $k_0 = x_n/R$ is the wavenumber, Z is the characteristic length [130] and the spherical Hankel function of the first kind can be estimated from:

$$h_{2n}^{(1)}(k_0 Z) \cong -i \frac{\exp[(2n+1/2)(\alpha - \tan h\alpha)]}{(n+1/2)\sqrt{\sec h\alpha \tan h\alpha}}. \quad (14.27)$$

Here, α is defined by $k_0 Z = (2n+1/2)/\cosh \alpha$. In the simplest approach, the positions of the m -resonances can be estimated as $x_m = x \pm \Delta x_m/2$.

Due to the high PL efficiency of CdTe NCs and the coupling of electronic transitions of NCs to the PM resonances, the BN and ABN branches were detected in a wide spectral region from 525 to 725 nm, corresponding to the full spectral range of the NC emission. This makes it possible to estimate the magnitude of the spectral spacing between the bonding and antibonding branches (Fig. 14.25) as a function of the angular mode number, for further comparison with theoretical calculations (Fig. 14.26).

Applying (14.24)–(14.26), we can see that the modelled data presented in Fig. 14.26 displays a behaviour which is in good agreement with experimental data. Continuous decrease of the splitting value between BN and ABN branches versus n can be seen in Fig. 14.26, where TE modes splitting is always larger than that of TM modes. Remarkably, the theory predicts the same behaviour. Although the maximum term approximation of the SMTB method overestimates the splitting value (Fig. 14.26), it is clear that this approach provides a good qualitative guide for the analysis of a variety of phenomena observed in PM.

It is worth noting that the observed disagreement between calculated and experimental values for the PM mode splitting (Fig. 14.26) may also have its origin in the fact that the magnitudes of splitting were estimated as spectral distances between maxima of ABN and BN peaks (indicated by arrows in Fig. 14.25b). However, a detailed study of the coherent mode coupling in PMs using the SMTB approach shows that the BN and ABN branches consist, in fact, of a number of very narrow peaks which are due to the presence of $m \neq \pm 1$ components [130]. The total number of these sharp peaks, originating from a certain mode n , is governed by the actual degeneracy of the Mie resonances which in the approach of the normal mode concept is $n+1$. Indeed, due to the dependence of the mode coupling on the orbital plane orientation, the interaction is limited to modes having the same m only, no degeneracy is removed between m and $-m$ and the new degeneracy of PM modes is now $n+1$ with $0 \leq m \leq n$. In the calculations within the SMTB model, the splitting was estimated as a spectral distance between outer peaks assigned to modes with $m = \pm 1$ which do not correspond to the maximum of the envelope of PM

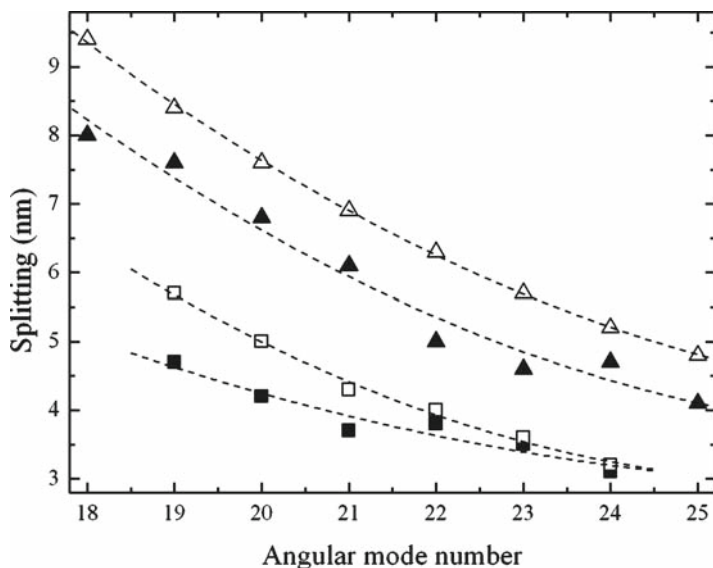


Fig. 14.26 Magnitude of spectral spacing between bonding and anti-bonding branches estimated from micro-PL spectra of a PM versus the angular mode number for TE (*solid up-triangles*) and TM (*solid squares*) modes. Open symbols show the result of theoretical calculations based on the maximum term approximation of the single-mode tight-binding method (14.24–14.26). The *dashed lines* are a guide to the eye. Reproduced with permission from the International Society for Optical Engineering (SPIE)

modes, therefore this may cause a discrepancy between estimated and observed values of the mode splitting. The fine structure of BN and ABN modes of the PM is of great interest to experimentalists because it suggests plenty of applications particularly in the field of information processing [135, 141]. However, in order to observe this phenomenon two conditions should be met. Firstly, the spacing between the m -resonances constituting the BN and ABN modes of the PM strongly depends on the angle of incidence of the electromagnetic wave θ [129, 130, 135]. For $\theta = 0^\circ$, i.e. when the incident light propagates parallel to the longitudinal axis of the PM, the incident wave can preferentially excite $m = \pm 1$ modes. The interaction with other dissipative modes of lower l causes the broadening of BN and ABN peaks and decreases the Q-factor compared to that of single spheres, as was observed in a number of papers [42, 128, 129, 135]. In the perpendicular configuration, when $\theta = 90^\circ$, the intermode coupling and spacing between m -resonances are expected to be minimal. In other words, in the case of perpendicular orientation of the PM with respect to excitation, all m -modes would merge into broad BN and ABN features and their fine structure would not be easily recognized. A compromise can be reached only for off-axis excitation with $0^\circ < \theta < 90^\circ$. Secondly, in order to reveal the $m \neq \pm 1$ components, the interacting cavities should not only have a similar size but also similar Q-factors. If the resonances of the two cavities are too

different in width, the coherent coupling is disturbed (at least to some extent) and as a consequence the fine structure of the PM modes cannot be detected.

One can see from the inset in Fig. 14.25b that excitation and detection in this case were located at the centre of the upper sphere forming the PM i.e. along the PM axis. In order to reveal the $m \neq \pm 1$ components in the PL spectra of the MF/CdTe PM, the WGM structure should be investigated at different excitation (and detection) positions across the upper sphere.

Figure 14.27a shows the micro-PL spectra of a PM formed by two almost identical microspheres with sizes of $3.0168 \mu\text{m}$ and $3.0189 \mu\text{m}$, recorded under an excitation (and signal collection) at the right edge of the upper microsphere (inset, Figure 14.27a). The presented PL spectra clearly reveal major features unique to a strong coherent coupling between the photonic states of the two microspheres forming the PM. One can clearly see a number of narrow peaks grouping on both sides arising from TE and TM resonances of the individual spheres and forming BN and ABN modes of the PM. The origin of this fine structure of BN and ABN modes lies in the lifting of the mode degeneracy in the PM [130, 135]. Therefore, this multi-peak structure would not radically be altered in scattering spectra or even in lasing, or stimulated Raman scattering in the same way that in a semiconductor laser the lasing does not alter the cavity resonances.

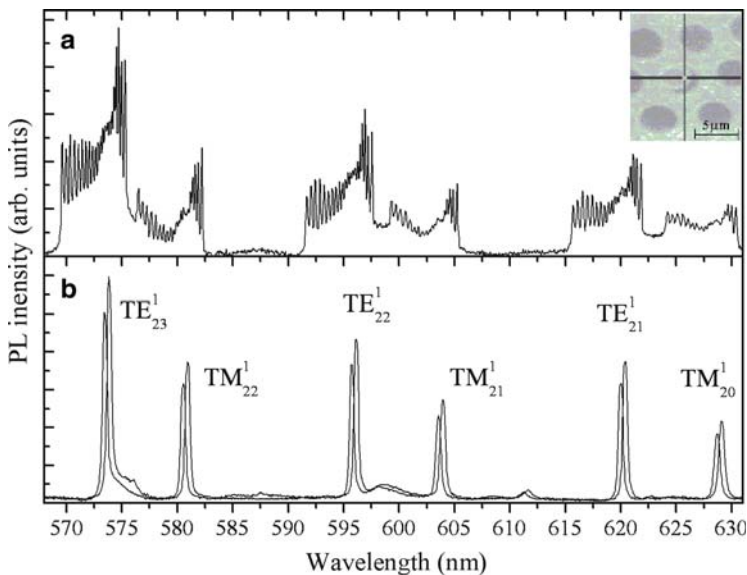


Fig. 14.27 PL spectra of the PM formed by two almost identical microspheres with off-axis excitation and detection (a), and PL spectra of non-interacting microspheres (b). *Inset*: microscope image of the PM in the microwell. The *dark cross* indicates the excitation position. Reproduced with permission from the American Physical Society

It is noteworthy that the number of experimentally resolved peaks increases with the angular mode number both for TE and TM modes, and is very close to the n value, although never in excess of n . Indeed we have observed 19 peaks in the spectral region of TE^1_{20} (19 peaks for TM^1_{20}), 21 peaks around the TM^1_{21} resonance (20 peaks for TM^1_{21}), 21 peaks in the region of the TM^1_{22} resonance (21 peaks for TM^1_{22}), 22 peaks for TM^1_{23} (22 peaks for TM^1_{23}) and 23 peaks around the TM^1_{24} resonance. Note that the spectral region occupied by a set of these narrow resonances is much wider than the linewidth of WGMs of non-interacting microspheres (Fig. 14.25).

The deconvolution of the lineshape of the m -resonances of the PM, using Lorentzian functions, shows that the m -resonances of the BN branch are always sharper than those of the ABN branch, providing a higher quality factor Q value for these modes and therefore a higher photon lifetime τ in the resonant modes. However, the most remarkable experimental fact is that the Q -factor of the m -resonances in the spectra of the PM exceeds the Q -value of single non-interacting microspheres, suggesting a corresponding modification of the photon lifetime in PM (τ_{PM}) with respect to photon storage time in single spherical microcavities before contact (τ_{SS}). These two facts along with the estimated value of BN/ABN splitting ($\sim 5\text{--}7$ nm) support the potential development of a new PM-based photonic device such as an optical delay line with controllable spectral and temporal tunability [141].

Figure 14.28b shows the spectral distribution of the ratios between photon lifetime of the m -modes of the PM and photon storage time in the WGMs of the single

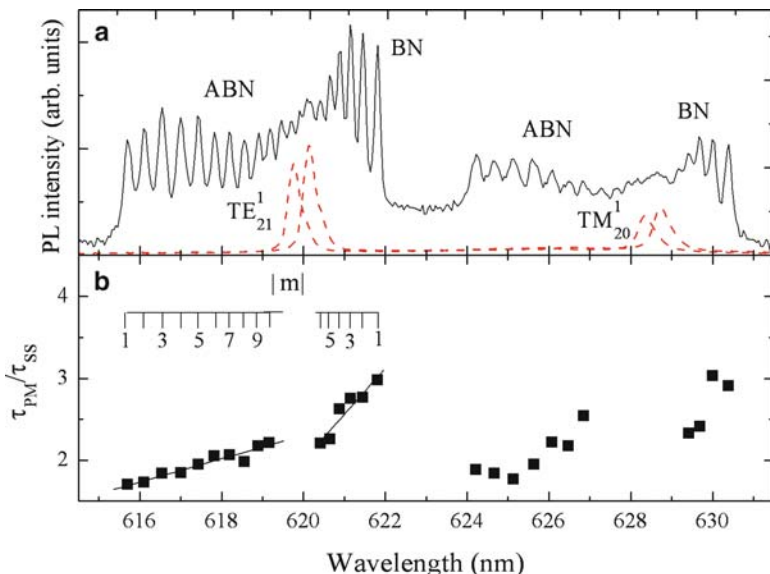


Fig. 14.28 (a) PL spectra of the PM (solid line) formed by two almost identical melamine-formaldehyde microspheres with off-axis excitation and detection. Dashed lines show the PL spectra of non-interacting microspheres. (b) Ratio between the photon lifetime of the m -modes of the photonic molecule and that of single spheres. The solid lines are the result of a linear fit

sphere. The ratios were calculated from the corresponding values of mode linewidth in the region of TM_{21}^1 and TM_{20}^1 resonances, demonstrating a threefold photon storage enhancement. It is evident from Fig. 14.28, that the interaction between spherical microcavities results in periodic-group delay spectra with peaks occurring at each of the m -resonant frequencies with larger delay times for higher m -values, which implies that the spectral components near these m -resonance spend more time traveling within the PM.

The relative increase in photon storage time $R = \tau_{PM}/\tau_{SS}$ shows an almost linear dependence on the azimuthal number m for a given mode number n (Fig. 14.29), however the slope of this dependence ($\Delta R/\Delta m$) in turn varies with n (Fig. 14.29, inset).

In all the experiments described here, the strong coupling phenomenon in the spectra of the PM was investigated in the visible and near-infrared spectral regions. However, recent achievements in the development of infra-red-emitting colloidal NCs can meet the first basic requirement for PM devices operating at such wavelengths, i.e. matching the basic communication spectral windows [146, 147]. Fig. 14.30a shows the values of spacing between adjacent m -resonances calculated in the spectral region of the C- and L- bands for PMs formed by two identical SiO_2 microspheres with sizes of 5 μm (a), 10 μm (b) and 16 μm (c). The standard for channel spacing $\sim 40\text{--}100$ GHz – in today’s optical communication systems [148] is taken

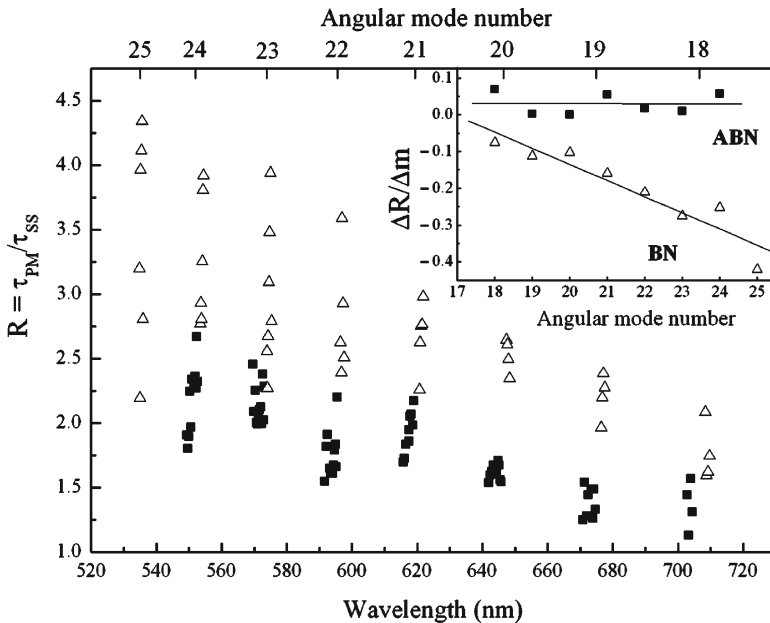


Fig. 14.29 Ratio between the photon lifetime of m -modes of the photonic molecule (τ_{PM}) and the photon storage time in the WGM of the single sphere (τ_{SS}). The *inset* shows the n -dependence of the $\Delta R/\Delta m$ slopes for BN and ABN modes. The *solid lines* are the result of a linear fit. Reproduced with permission from the International Society for Optical Engineering (SPIE)

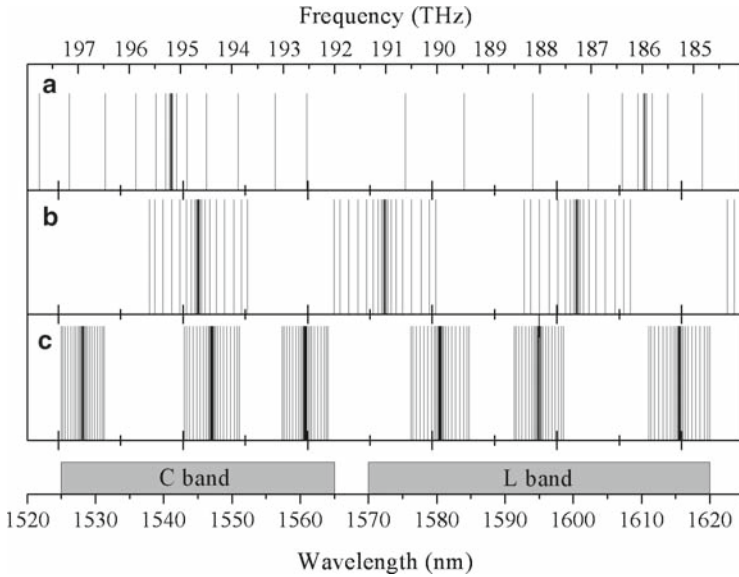


Fig. 14.30 Spectrum covering two major communication bands calculated for a PM formed by two identical SiO_2 microspheres with a refractive index $n_r = 1.4$ and sizes of $5 \mu\text{m}$ (a), $10 \mu\text{m}$ (b) and $16 \mu\text{m}$ (c)

into account for deciding on microsphere sizes. In this model, each m -resonance in the PM signal can be considered as a channel with the spacing between channels depending on the size of the microspheres and the azimuthal mode number.

For example for $10\text{-}\mu\text{m}$ individual microcavities, only one TE mode ($\lambda_{24} = 1,542.4 \text{ nm}$) is found in the C-band (Fig. 14.30b). A maximum splitting between BN and ABN modes (i.e. for $m = 1$) of 15.7 nm was estimated in this case. Calculating the positions of resonances for a single $16\text{-}\mu\text{m}$ microsphere, one can find 2 WGMs in the region of the C-band, namely TE_{40} ($\lambda = 1,544.6 \text{ nm}$) and TM_{39} ($\lambda = 1,559.6 \text{ nm}$). The maximum splitting in this case is much smaller, i.e. 8.8 nm for the TE_{40} WGM, but accommodates a larger number of m -resonances. These results clearly demonstrate that two coupled WGM spherical microcavities can generate a modal structure with a controllable number of peaks distributed over the major communication band. In contrast to the case of single spheres, the bandpass of the PM device can be as wide as the width of all communication bands and can be controlled by the size of the spherical microcavities forming the PM.

Figure 14.31b shows the estimated distribution of photon storage times between m -modes of the PM, assigning values of the photon storage time in single microspheres to $\tau_{\text{SS}} = 55 \text{ ps}$ for TM_{40}^1 , 3 ps for TM_{29}^1 and 0.9 ps for TM_{24}^1 as determined from calculations based on the Mie-theory. It can be anticipated that values of photon lifetime, τ_{PM} , calculated in such a way are underestimated because of the difference in Q-factor achievable for $3\text{-}\mu\text{m}$ spheres and $10\text{--}16 \mu\text{m}$ ones. Recent experimental studies clearly show a strong dependence of the Q-factors of

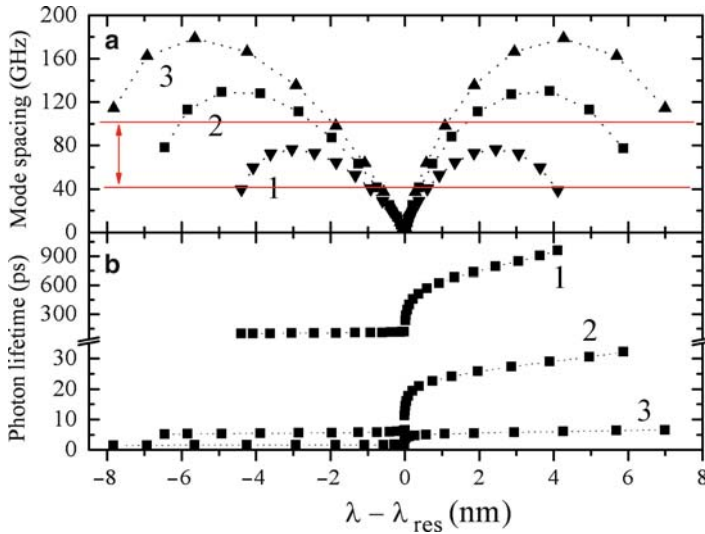


Fig. 14.31 (a) Spacing between adjacent m -modes calculated in the spectral region of the C-band for PMs formed by two identical SiO_2 microspheres with sizes of 10 μm (3), 12 μm (2) and 16 μm (1). (b) Calculated distribution of delay times between m -modes. The zero value on the wavelength axis corresponds to the position of TE_{24} , TE_{29} and TE_{40} WGM of the single spherical microcavity

m -resonances (and therefore photon storage times) on the quality factor of individual microspheres [42, 135].

The observed non-uniformity of spacing between m -resonances (Fig. 14.29, 14.30 and 14.31) provides a unique possibility to control the distribution of photon storage times in a particular spectral region (Fig. 14.31b). For all sizes of interacting microspheres, an initial increase of the spacing within the region of first three m -resonances was observed followed by a dip and then an increase in spacing again (Fig. 14.31a). This theoretical result is in good qualitative agreement with experimental data [135]. For the smallest PM size, 18 m -modes are available within a window of 12–200 GHz. The smaller Q-factor of WGMs in the individual spheres forming the PM results in a relatively moderate increase in photon lifetime – from 1.5 ps (obtained for ABN resonance with $m = 1$) up to 7 ps calculated for the corresponding m -resonance of BN mode of the PM. For microspheres of larger size, the number of available modes increases. Indeed, for 12- μm coupled spheres 20 m -resonances fit into the above-indicated spacing window, with the largest value of intermode spacing being ~ 130 GHz. Photon-storage times distributed between these m -modes increase from 5 ps up to 32 ps. The upper limit of intermode spacing drops even more for PMs formed from 16- μm microspheres. In that case, 22 m -resonances with spacing between 12 and 76 GHz can be seen in Fig. 14.31, providing discrete storage times found to be distributed between 94 ps and 960 ps. Remarkably, this maximum photon storage time provided by two interacting microspheres of 16- μm size corresponds to a ~ 15 cm length of silica-glass waveguide delay line.

Based on theoretical considerations of the internal field in the PM [130] and on a number of experimental works [129, 132, 135], it is anticipated that the size of the interacting microcavities is probably not the only parameter which allows to control the spacing between splitting modes and the distribution of photon storage times. Firstly, the efficiency of coupling between spherical microcavities forming the PM strongly depends on the spacing d between the microspheres. Indeed, the splitting of BN and ABN modes decreases exponentially with the increasing separation [130, 141]. For the present values of microsphere sizes, mode numbers and small d , the condition $2n + 1 > x_n (2 + d / a)$ is satisfied and the SMTB method yields an approximate equation for the coefficient $A_{n,m}(x_n, d)$:

$$A_{n,m}(x_n, d) = A_{n,m}(x_n) \times \exp \left[-x_n \frac{d}{a} \sqrt{\left(\frac{4n+1}{4x_n} \right)^2 - 1} \right]. \tag{14.28}$$

Replacing $A_{n,m}$ in Eqs. (14.24) by $A_{n,m}(x_n, d)$, we can estimate the mode spacing as a function of d .

Taking, for example, the PM formed by 10- μm microspheres (TE_{24} single-sphere resonance within C-band), the maximum splitting between BN and ABN modes shows a decrease by a factor of 1.3 as the spacing between spheres increases from 0 to 0.1 μm (Fig. 14.32). The corresponding modification of the $A_{n,m}(x_n, d)$ coefficient results in a significant decrease of the values of the channel spacing. While the delay time and the number of channels available between 12 and 200 GHz are unaffected, the upper limit of the channel spacing drops down to 139 GHz (22% decrease). For two 10- μm spheres separated by $d = 0.23 \mu\text{m}$, the spacings of all 18 channels are distributed between 12 and 100 GHz.

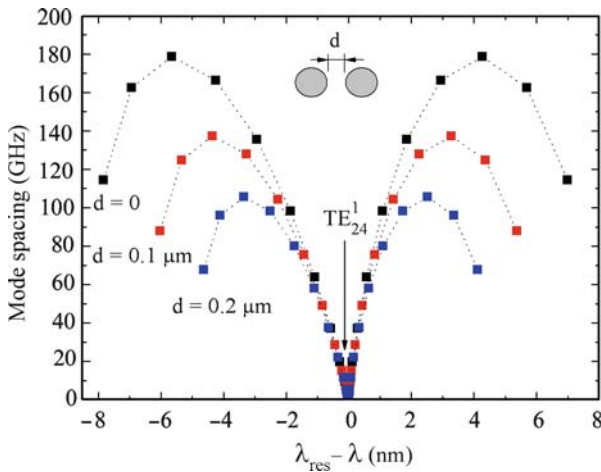


Fig. 14.32 Spacing between adjacent m -modes calculated for a PM formed by two identical SiO_2 microspheres with a size of 10 μm separated by a distance d

The next possibility to control the spacing between channels stems from the strong dependence of the splitting parameters of the PM modes on the angle θ of incidence of the electromagnetic wave. For $\theta = 0^\circ$, i.e. when the incident light propagates parallel to the longitudinal axis of the PM, the incident wave can only excite $m = \pm 1$ modes [129, 130, 135]. The interaction with other dissipative modes of lower n causes the broadening of the BN- and ABN-peaks and their Q -factor is lower than that of single spheres, as was observed in a number of studies [42, 128, 129, 135]. In the perpendicular configuration, i.e. when $\theta = 90^\circ$, the intermode coupling is expected to be minimal and the fine structure of the PM modes can hardly be resolved. In that case however, the Q -factor of the BN and ABN modes can be at least comparable to that of non-interacting microspheres, presumably due to the disappearance of one wing of these PM branches. The bandpass spectrum was demonstrated to be much more complicated for off-axis excitation, i.e. with $0^\circ < \theta < 90^\circ$, showing a number of tiny peaks between upper and lower peaks of $m = \pm 1$ [42, 129, 135]. Although further investigations need to be done on the angle-dependence of the fine structure of PM modes, recent investigations point clearly that the latter configuration is the basis for the development of PM-based optical delay devices with controllable spectral and temporal tunability.

Finally, it remains to be noted that the parameters of intercavity coupling in the PM can be governed also by the detuning of the microsphere sizes [129]. By forming PMs from pairs of microspheres of slightly different sizes, one can manipulate the spectral position of BN and ABN modes, thus controlling the symmetry of the splitting.

14.5 Conclusions

The universality and simplicity of the LbL technique enabled a comprehensive study of the interaction of semiconductor NCs with polyelectrolytes and an improved understanding of the photo-physics and nanoengineering of the assembled structures. This approach has the unique advantage of opening the way for the fabrication of composite photonic systems consisting of spherical microcavities and semiconductor nanocrystals. These systems are highly efficient for coupling out light from the NCs, enabling a new method for photonic mode coupling in photonic molecules. The study of microcavity/NCs structures, demonstrated here, reveals many fascinating questions and fundamental problems that appear when merging two main concepts of solid-state physics, namely the complete 3D electronic and photonic confinements in one structure. The dependence of WGM parameters on the characteristics of non-interacting microcavities suggests a myriad of photonic applications, in particular in the field of bio-sensing and quantum information processing.

Acknowledgements We thank Prof. J.J. Boland, Prof. A. Eychmuller, Dr. L. Bradley and Dr. N. Gaponik for helpful discussions and help with experimental arrangements. This work was supported by Science Foundation Ireland (SFI) under its CRANN CSET Project PR04 "Photonic Molecules." ALR acknowledges the Walton Award from the SFI.

References

1. Rogach AL (2008) *Semiconductor Nanocrystal Quantum Dots*. Springer, Wien
2. Weller H (1993) Colloidal semiconductor q-particles – chemistry in the transition region between solid-state and molecules. *Angew. Chem. Int. Ed.* 32: 41
3. Alivisatos AP (1996) Perspectives on the physical chemistry of semiconductor nanocrystals. *J. Phys. Chem.* 100: 13226–13239
4. Woggon U (1997) *Optical Properties of Semiconductor Quantum Dots*. Springer-Verlag, Berlin
5. Gaponenko SV (1998) *Optical Properties of Semiconductor Nanocrystals*. Cambridge University Press, Cambridge
6. Colvin V, Schlamp M, Alivisatos A (1994) Light-emitting diodes made with cadmium selenide nanocrystals. *Nature* 370: 6488–6491
7. Lee J, Sundar VC, Heine JR, Bawendi MG, Jensen KF (2000) Full colour emission from II-VI semiconductor quantum dot – polymer composites. *Adv. Mater.* 12: 1102–1105
8. Coe S, Woo WK, Bawendi M, and Bulovic V (2002) Electroluminescence from single monolayers of nanocrystals in molecular organic devices. *Nature* 420: 800–803
9. Achermann M, Petruska MA, Koleske DD, Crawford MH, Klimov VI (2006) Nanocrystal-based light-emitting diodes utilizing high-efficiency non-radiative energy transfer for color conversion. *Nano Lett.* 6: 1396–1400
10. Decher G, Schlenoff JB (2002) *Multilayer Thin Films: Sequential Assembly of Nanocomposite Materials*. Wiley, Weinheim
11. Sukhorukov GB, Donath E, Lichtenfeld H, Knippel E, Knippel M, Budde A, Möhwald H (1998) Layer-by-layer self assembly of polyelectrolytes on colloidal particles. *Coll. Surf. A* 137: 253–266
12. Susha AS, Caruso F, Rogach AL, Sukhorukov GB, Kornowski A, Möhwald H, Giersig M, Eychmüller A, Weller H (2000) Formation of luminescent spherical core-shell particles by the consecutive adsorption of polyelectrolyte and CdTe(S) nanocrystals on latex colloids. *Coll. Surf. A* 163: 39–44
13. Radtchenko IL, Sukhorukov GB, Gaponik N, Kornowski A, Rogach AL, Möhwald H (2001) Core-shell structures formed by the solvent-controlled precipitation of luminescent CdTe nanocrystals on latex spheres. *Adv. Mater.* 13:1684–1687
14. Fan X, Palinginis P, Lacey S, Wang H (2000) Coupling semiconductor nanocrystals to a fused-silica microsphere: a quantum-dot microcavity with extremely high Q factors. *Opt. Lett.* 25: 1600–1602
15. Artemyev MV, Woggon U, Wannemacher R, Jaschinski H, Langbein W (2001) Light trapped in a photonic dot: microspheres act as a cavity for quantum dot emission. *Nano Lett.* 1: 309–314.
16. Fan XD, Lonergan MC, Zhang YZ, Wang HL (2001) Enhanced spontaneous emission from semiconductor nanocrystals embedded in whispering gallery optical microcavities. *Phys. Rev. B* 64: 115310
17. Rakovich YP, Donegan JF, Gaponik N, Rogach AL (2003) Raman scattering and Anti-Stokes emission from a single spherical microcavity with a CdTe quantum dot monolayer. *Appl. Phys. Lett.* 83: 2539–2541
18. Rakovich YP, Yang L, McCabe EM, Donegan JF, Perova T, Moore A, Gaponik N, Rogach AL (2003) Whispering gallery mode emission from a composite system of CdTe nanocrystals and a spherical microcavity. *Sem. Sci. Techn.* 18: 914–918
19. Bawendi MG, Carroll PJ, Wilson W, Brus L (1992) Luminescence properties of CdSe quantum crystallites: resonance between interior and surface localized states. *J. Chem. Phys.* 96: 946–954.
20. Gao M, Kirstein S, Möhwald H, Rogach AL, Kornowski A, Eychmüller A, Weller H (1998) Strongly photoluminescent CdTe nanocrystals by proper surface modification. *J. Phys. Chem. B* 102: 8360–8363
21. Baranov AV, Rakovich YP, Donegan JF, Perova TS, Moore RA, Talapin DV, Rogach AL, Masumoto Y, Nabiev I (2003) Effect of ZnS shell thickness on the phonon spectra in CdSe quantum dots. *Phys. Rev. B* 68: 165306

22. Kimura J, Uematsu T, Maenosono S, Yamaguchi Y (2004) Photo-induced fluorescence enhancement in CdSe/ZnS quantum dot sub-monolayers sandwiched between insulating layers: influence of dot proximity. *J. Phys. Chem. B* 108: 13258–13264
23. Wuister SF, de Mello Donegá C, Meijerink A (2004) Influence of thiol capping on the exciton luminescence and decay kinetics of CdTe and CdSe quantum dots. *J. Phys. Chem. B* 108: 17393–17397
24. Poznyak SK, Osipovich NP, Shavel A, Talapin DV, Gao M, Eychmüller A, Gaponik N (2005) Size-dependent electrochemical behavior of thiol-capped CdTe nanocrystals in aqueous solution. *J. Phys. Chem. B* 109: 1094–1100
25. Murray CB, Norris DJ, Bawendi MG (1993) synthesis and characterization of nearly monodisperse CdE (E = S,Se,Te) semiconductor nanocrystallites. *J. Am. Chem. Soc.* 115: 8706–8715
26. Dabbousi BO, Rodriguez-Viejo J, Mikulec FV, Heine JR, Mattoussi H, Ober R, Jensen KF, Bawendi MG (1997) (CdSe)ZnS core-shell quantum dots: synthesis and characterization of a size series of highly luminescent nanocrystallites. *J. Phys. Chem. B* 101: 9463–9475
27. Gaponik N, Talapin DV, Rogach AL, Hoppe K, Shevchenko EV, Kornowski A, Eychmüller A, Weller H (2002) Thiol-capping of CdTe nanocrystals: an alternative to organometallic synthetic routes. *J. Phys. Chem. B* 106: 7177–7185
28. Gaponik N, Talapin DV, Rogach AL, Eychmüller A, Weller H (2002) Efficient phase transfer of luminescent thiol-capped nanocrystals: from water to non-polar organic solvents. *Nano Lett.* 2: 803–806
29. Yaroslavov AA, Sinani VA, Efimova AA, Yaroslavova EG, Rakhnyanskaya AA, Ermakov YA, Kotov NA (2005) What is the effective charge of TGA-stabilized CdTe nanocolloids? *J. Am. Chem. Soc.* 127: 7322–7323
30. Sukhorukov GB, Fery A, Brumen M, Möhwald H (2004) Physical chemistry of encapsulation and release. *Phys. Chem. Chem. Phys.* 6: 4078–4089
31. Caruso F (2001) Nanoengineering of particle surfaces. *Adv. Mat.* 13: 11–22
32. Mamedov AA, Belov A, Giersig M, Mamedova NN, Kotov NA (2001) Nanorainbows: graded semiconductor films from quantum dots. *J. Am. Chem. Soc.* 123: 7738–7739
33. Komarala VK, Rakovich YP, Bradley AL, Byrne SJ, Gun'ko YK (2006) Emission properties of colloidal quantum dots on polyelectrolyte multilayers. *Nanotechnology* 17: 4117–4122
34. Franzl T, Koktysh DS, Klar TA, Rogach AL, Feldmann J (2004) Fast energy transfer in layer-by-layer assembled CdTe nanocrystal bilayers. *Appl. Phys. Lett.* 84: 2904–2906
35. Franzl T, Shavel A, Rogach AL, Gaponik N, Klar TA, Eychmüller A, Feldmann J (2005) High-rate unidirectional energy transfer in directly assembled CdTe nanocrystal bilayers. *Small* 1: 392–395
36. Wang X, Qu L, Zhang J, Peng X, Xiao M (2003) Surface-related emission in highly luminescent CdSe quantum dots. *Nano Lett.* 3: 1103–1106
37. Tang Z, Wang Y, Kotov NA (2002) Semiconductor nanoparticles on solid substrates: film structure, intermolecular interactions, and polyelectrolyte effects. *Langmuir* 18: 7035–7040
38. Yang L, Taylor CM, Rakovich Y, McCabe EM (2003) The three-dimensional imaging of microspheres with confocal and conventional polarization microscopes. *Appl. Opt.* 42: 5693–5700
39. Kiraz A, Reese C, Gayral B, Zhang L, Schoenfeld WV, Gerardot BD, Petroff PM, Hu EL, Imamoglu A (2003) Cavity-quantum electrodynamics with quantum dots. *J. Opt. B* 5: 129–137
40. LeThomas N, Woggon U, Schöps O, Artemyev MV, Kazes M, Banin U (2006) Cavity QED with semiconductor nanocrystals. *Nano Lett.* 6: 557–561
41. Woggon U, Wannemacher R, Artemyev M, Möller B, LeThomas N, Anikeev V, Schöps O (2003) Dot-in-a-dot: electronic and photonic confinement in all three dimensions. *Appl. Phys. B* 77: 469–484
42. Rakovich YP, Gerlach M, Bradley AL, Donegan JF, Connolly TM, Boland JJ, Przyjalowski MA, Ryder A, Gaponik N, Rogach AL (2004) Confined optical modes in small photonic molecules with semiconductor nanocrystals. *J. Appl. Phys.* 96: 6761–6765
43. Lu S, Jiang D, Jia R, An L, Bian L, Liang X, Ma B, Sun B (2002) Lasing of CdSe_{1-x}S_x quantum dots in a glass spherical microcavity. *J. Phys.: Condens. Matter* 14: 6395–6401

44. Malko AV, Mikhailovsky AA, Petruska MA, Hollingsworth JA, Htoon H, Bawendi MG, Klimov VI (2002) From amplified spontaneous emission to microring lasing using nanocrystal quantum dot solids. *Appl. Phys. Lett.* 81: 1303–1305
45. Shopova SI, Farca G, Rosenberger AT, Wickramanayake WMS, Kotov NA (2004) Microsphere whispering-gallery-mode laser using HgTe quantum dots. *Appl. Phys. Lett.* 85: 6101–6103
46. Chan Y, Steckel JS, Snee PT, Caruge JM, Hodgkiss JM, Nocera DG, Bawendi MG (2005) Blue semiconductor nanocrystal laser. *Appl. Phys. Lett.* 86: 073102
47. Snee PT, Chan Y, Nocera DG, Bawendi MG (2005) Whispering-gallery-mode lasing from a semiconductor nanocrystal/microsphere resonator composite. *Adv. Mater.* 17: 1131–1136
48. Klimov VI, Bawendi MG (2001) Ultrafast carrier dynamics, optical amplification, and lasing in nanocrystals quantum dots. *MRS Bulletin* 26(12): 998–1004
49. Rakovich YP, Gerlach M, Donegan JF, Gaponik N, Rogach AL (2005) Three-dimensional photon confinement in a spherical microcavity with CdTe quantum dots: Raman spectroscopy. *Physica E* 26: 28–32
50. Zwiller V, Aichele T, Benson O (2004) Quantum optics with single quantum dot devices. *New J. Phys.* 6: 96
51. Hirschfeld T (1976) Quantum efficiency independence of the time integrated emission from a fluorescent molecule. *Appl. Opt.* 15: 3135–3139
52. Chang RK, Campillo AJ (1996) *Optical processes in microcavities*. World Scientific, Singapore
53. Jackson JD (1999) *Classical Electrodynamics*. Wiley, Hoboken
54. Lidorikis E, Sigalas MM, Economou EN, Soukoulis CM (1998) Tight-binding parametrization for photonic band gap materials. *Phys. Rev. Lett.*, 81: 1405–1408
55. Eisberg P, Resnick R. (1985) *Quantum Physics of Atoms, Molecules, Solids, Nuclei and Particles*. Wiley, New York
56. Arnold S, Comunale J, Whitten WB, Ramsey JM, Fuller KA (1992) Room-temperature microparticle-based persistent hole-burning spectroscopy. *J. Opt. Soc. Am. B* 9: 819–824
57. Arnold S (2001) Microspheres, photonic atoms and the physics of nothing. *Am. Sci.* 89: 414–421
58. Chew H (1987) Transition rates of atoms near spherical surfaces. *J. Chem. Phys.* 87: 1355–1360
59. Chew H (1988) Radiation and lifetimes of atoms inside dielectric particles. *Phys. Rev. A* 38: 3410–3416
60. Artemyev MV, Woggon U (2000) Quantum dots in photonic dots. *Appl. Phys. Lett.* 76: 1353–1355
61. Van de Hulst HC (1957) *Light Scattering by Small Particles*. Wiley, New York
62. Born M, Wolf E (1991) *Principles of Optics*. Pergamon Press, Oxford
63. Wang RT, van de Hulst HC (1991) Rainbows: Mie computations and the Airy approximation. *Appl. Opt.* 30: 106–117
64. Bohren CF, Huffman DR (1983) *Absorption and scattering of light by small particles*. Wiley, New York
65. Chylek P (1990) Resonance structure of Mie scattering: distance between resonances. *J. Opt. Soc. Am. A* 7: 1609–1613
66. Kerker M (1969) *The scattering of light and other electromagnetic radiation*. Academic Press, New York
67. Hunter BA, Box MA, Maier B (1988) Resonance structure in weakly absorbing spheres. *J. Opt. Soc. Am. A* 5: 1281–1286
68. Smirnov AY, Rashkeev SN, Zagoskin AM (2002) Polarization switching in optical microsphere resonator. *Appl. Phys. Lett.* 80: 3503–3505
69. Lock JA (1998) Excitation efficiency of a morphology-dependent resonance by a focused Gaussian beam. *J. Opt. Soc. Am. A* 15: 2986–2994
70. Chylek P (1976) Partial-wave resonances and the ripple structure in the Mie normalized extinction cross section. *J. Opt. Soc. Am.* 66: 285–287
71. Chylek P, Kiehl JT, Ko MKW (1978) Optical levitation and partial-wave resonances. *Phys. Rev. A* 18: 2229–2233

72. Barber PW, Chang RK (1998) *Optical Effects Associated with Small Particles*. World Scientific, Singapore
73. Teraoka I, Arnold S (2006) Theory of resonance shifts in TE and TM whispering gallery modes by non-radial perturbations for sensing applications. *J. Opt. Soc. Am. B* 23: 1381–1389
74. Arnold S, Khoshshima M, Teraoka I, Holler S, Vollmer F (2003) Shift of whispering-gallery modes in microspheres by protein adsorption. *Opt. Lett.* 28: 272–274
75. Teraoka I, Arnold S, Vollmer F (2003) Perturbation approach to resonance shifts of whispering-gallery modes in a dielectric microsphere as a probe of a surrounding medium. *J. Opt. Soc. Am. B* 20: 1937–1946
76. Tzeng HM, Long MB, Chang RK, Barber PW (1985) Laser-induced shape distortions of flowing droplets deduced from morphology-dependent resonances in fluorescence spectra. *Opt. Lett.* 10: 209–211
77. Ilchenko VS, Volikov PS, Velichansky VL, Treussart F, Lefevre-Seguin V, Raimond JM, Haroche S (1998) Strain-tunable high-Q optical microsphere resonator. *Opt. Commun.* 145: 86–90
78. Lai HM, Leung PT, Young K, Barber PW, Hill SC (1990) Time-independent perturbation for leaking electromagnetic modes in open systems with application to resonances in microdroplets. *Phys. Rev. A* 41: 5187–5198
79. Teraoka I, Arnold S (2006) Enhancing the sensitivity of a whispering-gallery mode microsphere sensor by a high-refractive-index surface layer. *J. Opt. Soc. Am. B* 23: 1434–1441
80. Lulevich VV, Andrienko D, Vinogradova OI (2004) Elasticity of polyelectrolyte multilayer microcapsules. *J. Chem. Phys.* 120: 3822–3826
81. Ashkin A (2000) History of optical trapping and manipulation of small-neutral particle, atoms, and molecules. *IEEE J. Quant. Electron.* 6:841–856
82. Molloy JE, Padgett MJ (2002) Lights, action: optical tweezers. *Contemp. Phys.* 43: 241–258
83. Kobayashi H, Ishimaru I, Hyodo R, Yasokawa T, Ishizaki K, Kuriyama S, Masaki T, Nakai S, Takegawa K, Tanaka N (2006) A precise method for rotating single cells. *Appl. Phys. Lett.* 88: 131103
84. Gauthier RC, Tait R, Mende H, Paulowicz C (2001) Optical selection, manipulation, trapping and activation of a microgear structure for applications in micro-optical-electromechanical systems. *Appl. Opt.* 40: 930–937
85. Sulfridge M (2002) Optical actuation of a bistable MEMS. *J. Microelectromech. Syst.* 11: 574–583
86. Metzger CH, Karrai K (2004) Cavity cooling of a microlever. *Nature* 432: 1002–1005
87. Dragoman D, Dragoman M (1999) Optical actuation of micromechanical tunneling structures with applications in spectrum analysis and optical computing. *Appl. Opt.* 38: 6773–6778
88. Ren KF, Grehan G, Gouesbet G (1996) Prediction of reverse radiation pressure by generalized Lorenz-Mie theory. *Appl. Opt.* 35: 2702–2710
89. Mie G (1908) Beitrage zur Optik trüber Medien, speziell kolloidaler Metallösungen. *Ann. Phys.* 25: 377–445
90. Lebedeva OV, Kim BS, Vasilev K, Vinogradova OI (2005) Salt softening of polyelectrolyte multilayer microcapsules. *J. Coll. Interf. Sci.* 284: 455–462
91. Hill SC, Benner RE (1986) Morphology-dependent resonances associated with stimulated processes in microspheres. *J. Opt. Soc. Am. B* 3: 1509–1514
92. Braginsky VB, Gorodetsky ML, Ilchenko VS (1998) Quality factor and non-linear properties of optical whispering-gallery modes. *Phys. Lett. A* 137: 393–397
93. Campillo AJ, Eversole JD, Lin HB (1991) Cavity quantum electrodynamic enhancement of stimulated emission in microdroplets. *Phys. Rev. Lett.* 67: 437–440
94. Gorodetsky ML, Ilchenko VS (1992) Thermal nonlinear effects in optical whispering-gallery microresonators. *Laser Phys.* 2: 1004–1009
95. Collot L, Lefevre-Seguin V, Brune M, Raimond JM, Haroche S (1993) Very high-Q whispering-gallery mode resonances observed on fused silica microspheres. *Europhys. Lett.* 23: 327–334
96. Hill SC, Leach DH, Chang RK (1993) Third-order sum-frequency generation in droplets: model with numerical results for third-harmonic generation. *J. Opt. Soc. Am. B* 10: 16–33

97. Hill SC, Boutou V, Yu J, Ramstein S, Wolf JP, Pan YL, Holler S, Chang RK (2000) Enhanced backward-directed multiphoton-excited fluorescence from dielectric microcavities. *Phys. Rev. Lett.* 85: p. 54–57
98. Spillane SM, Kippenberg TJ, Vahala KJ (2002) Ultralow-threshold Raman laser using a spherical dielectric microcavity. *Nature* 415: 621–623
99. Gaponik N, Rakovich YP, Gerlach M, Donegan JF, Savateeva D, Rogach AL (2006) Whispering gallery modes in photoluminescence and Raman spectra of a spherical microcavity with CdTe quantum dots: anti-Stokes emission and interference effects. *Nanoscale Res. Lett.*, 1: 68–73
100. Gorska M, Nazarewicz W (1974) Application of the random-element isodisplacement model to long-wavelength optical phonons in CdSe_xTe_{1-x} mixed crystals. *Phys. Stat. Sol. (b)* 65: 193–202
101. Trallero-Giner C, Debernardi A, Cardona M, Menéndez-Proupín E, Ekimov AI (1998) Optical vibrons in CdSe dots and dispersion relation of the bulk material. *Phys. Rev. B* 57: 4664–46
102. Byrne SJ, Corr SA, Rakovich TY, Gun'ko YK, Rakovich YP, Donegan JF, Mitchell S, Volkov Y (2006) Optimisation of the synthesis and modification of CdTe quantum dots for enhanced live cell imaging. *J. Mater. Chem.* 16: 2896–2902
103. Zhang JY, Wang XY, Xiao M, Qu L, Peng X (2002) Lattice contraction in free-standing CdSe nanocrystals. *Appl. Phys. Lett.* 81: 2076–2078
104. Serpengüzel A, Arnold S, Griffel G, Lock JA (1997) Enhanced coupling to microsphere resonances with optical fibers. *J. Opt. Soc. Am. B* 14: 790–795
105. Filonovich SA, Rakovich YP, Vasilevskiy MI, Artemyev MV, Talapin DV, Rogach AL, Rolo AG, Gomes MJM (2000) Probing the exciton density of states in semiconductor nanocrystals using integrated photoluminescence spectroscopy. *Chem. Monthly* 133: 909–918
106. Hoheisel W, Colvin VL, Johnson CS, Alivisatos AP (1994) Threshold for quasicontinuum absorption and reduced luminescence efficiency in CdSe nanocrystals. *J. Chem. Phys.* 101: 8455–8460
107. Rodrigues PAM, Tamulaitis G, Yu PY, Risbud SH (1995) Size selective photoluminescence excitation spectroscopy in CdSe nanocrystals. *Sol. Stat. Commun.* 94: 583–587
108. Rakovich Y, Walsh L, Bradley L, Donegan JF, Talapin D (2003) Size selective photoluminescence excitation spectroscopy in CdTe quantum dots. *Proc. SPIE* 4876: 432–437
109. Micic OI, Cheong HM, Fu H, Zunger A, Sprague JR, Mascarenhas A, Nozik A (1997) Size-Dependent spectroscopy of InP quantum dots. *J. Phys. Chem. B.* 101: 4904–4912
110. Talapin DV, Haubold S, Rogach AL, Kornowski A, Haase M, Weller H (2001) A novel organometallic synthesis of highly luminescent CdTe nanocrystals. *J. Phys. Chem. B* 105: 2260–2263
111. Rakovich YP, Filonovich SA, Gomes MJM, Donegan JF, Talapin DV, Rogach AL, Eychmüller A (2002) Anti-Stokes photoluminescence in II-VI colloidal nanocrystals. *Phys. Stat. Sol. (b)* 229: 449–452
112. Chen W (2005) Up-conversion luminescence from CdSe nanoparticles. *J. Chem. Phys.* 122: 224708
113. Joly AG, Chen W, McCready DE, Malm JO, Bovin JO (2005) Up-conversion luminescence of CdTe nanoparticles. *Phys. Rev. B* 71: 165304
114. Downing E, Hesselink L, Ralston J, MacFarlane R (1996) A three-color, solid-state, three-dimensional display. *Science* 273: 1185–1189
115. Parthenopoulos DA, Rentzepis PM (1989) Three-dimensional optical storage memory. *Science* 245: 843–845
116. Hehlen MP, Güdel HU, Shu Q, Rand SC (1996) Cooperative optical bistability in the dimer system Cs₃Y₂Br₇:10% Yb₃₊. *J. Chem. Phys.* 104: 1232–1244
117. Said AA, Wamsley C, Hagan DJ, Van Stryland EW, Reinhardt BA, Roderer P, Dillard AG (1994) Third- and fifth-order optical non-linearities in organic materials. *Chem. Phys. Lett.* 228: 646–650
118. Cahalan MD, Parker I, Wei SH, Miller MJ (2002) Two-photon tissue imaging: seeing the immune system in a fresh light. *Nat. Rev. Immunol.* 2: 872–880
119. Pettit DL, Wang SSH, Gee KR, Augustine GJ (1997) Chemical two-photon uncaging: a novel approach to mapping glutamate receptors. *Neuron* 19: 465–471

120. Auzel F (2004) Up-conversion and anti-stokes processes with f and d ions in solids. *Chem. Rev.* 104: 139–174
121. Rakovich YP, Gladyschuk AA, Rusakov KI, Filonovich SA, Gomes MJM, Talapin DV, Rogach AL, Eychmüller A (2002) Anti-stokes luminescence of cadmium telluride nanocrystals. *J. Appl. Spectr.* 69: 444–449
122. Filonovich SA, Gomes MJM, Rakovich YP, Donegan JF, Talapin DV, Gaponik NP, Rogach AL, Eychmüller A (2003) Up-conversion luminescence in colloidal CdTe nanocrystals. *MRS Proc.* 737: 157–162
123. Rakovich YP, Donegan JF, Filonovich SA, Gomes MJM, Talapin DV, Rogach AL, Eychmüller A (2003) Up-conversion luminescence via a below-gap state in CdSe/ZnS quantum dots. *Physica E* 17: 99–100
124. Rusakov KI, Gladyschuk AA, Rakovich YP, Donegan JF, Filonovich SA, Gomes MJM, Talapin DV, Rogach AL, Eychmüller A (2003) Control of efficiency of photon energy up-conversion in CdSe/ZnS quantum dots. *Opt. Spectr.* 94: 921–925
125. Wang X, Yu WW, Zhang J, Aldana J, Peng X, Xiao M (2003) Photoluminescence up-conversion in colloidal CdTe quantum dots. *Phys. Rev. B* 68: 125318
126. Chylek P, Zhan J (1989) Interference structure of the Mie extinction cross section. *J. Opt. Soc. Am. A* 6: 1846–1851
127. Bayer M, Gutbrod T, Reithmaier JP, Forchel A, Reinecke TL, Knipp PA, Dremin AA, Kulakovskii VD (1998) Optical modes in photonic molecules. *Phys. Rev. Lett.* 81: 2582–2585
128. Fuller KA (1991) Optical resonances and two-sphere systems. *Appl. Opt.* 30: 4716–4731
129. Mukaiyama T, Takeda K, Miyazaki H, Jimba Y, Kuwata-Gonokami M (1999) Tight-binding photonic molecule modes of resonant bispheres. *Phys. Rev. Lett.* 82: 4623–4626
130. Miyazaki H, Jimba Y (2000) Ab initio tight-binding description of morphology-dependent resonance in a bisphere. *Phys. Rev. B* 62: 7976–7997
131. Arnold S, Ghaemi A, Hendrie P, Fuller KA (1994) Morphological resonances detected from a cluster of two microspheres. *Opt. Lett.* 19: 156–158
132. Hara Y, Mukaiyama T, Takeda K, Kuwata-Gonokami M (2003) Photonic molecule lasing. *Opt. Lett.* 28: 2437–2439
133. Möller BM, Woggon U, Artemyev MV, Wannemacher R (2004) Photonic molecules doped with semiconductor nanocrystals. *Phys. Rev. B* 70: 115323
134. Barnes MD, Mahurin SM, Mehta A, Sumpster BG, Noid DW (2002) Three-dimensional photonic “molecules” from sequentially attached polymer-blend microparticles. *Phys. Rev. Lett.* 88: 015508
135. Rakovich YP, Donegan JF, Gerlach M, Bradley AL, Connolly TM, Boland JJ, Gaponik N, Rogach AL (2004) Fine structure of coupled optical modes in photonic molecules. *Phys. Rev. A* 70: 051801
136. Yariv A, Xu Y, Lee RK, Scherer A (1999) Coupled-resonator optical waveguide: a proposal and analysis. *Opt. Lett.* 24: 711–713
137. Mookherjee S, Yariv A (2002) Coupled resonator optical waveguides. *IEEE J. Sel. Top. Quant. Electron.* 8: 448–456
138. Little BE, Chu ST (2000) Toward very large-scale integrated photonics. *Opt. Photon. News* 11: 24–29
139. Maleki L, Matsko AB, Savchenkov AA, Ilchenko VS (2004) Tunable delay line with interacting whispering-gallery-mode resonators. *Opt. Lett.* 29: 626–628
140. Poon JKS, Scheuer J, Xu Y, Yariv A (2004) Designing coupled-resonator optical waveguide delay lines. *J. Opt. Soc. Am. B* 21: 1665–1673
141. Rakovich YP, Boland JJ, Donegan JF (2005) Tunable photon lifetime in photonic molecules: a concept for delaying an optical signal. *Opt. Lett.* 30: 2775–2777
142. Astratov VN, Franchak JP, Ashili SP (2004) Optical coupling and transport phenomena in chains of spherical dielectric microresonators with size disorder. *Appl. Phys. Lett.* 85: 5508–5510
143. Möller B, Woggon U, Artemyev MV (2006) Photons in coupled microsphere resonators. *J. Opt. A* 8: S113–S121

144. Furukawa H, Tenjimbayashi K (2002) Light propagation in periodic microcavities. *Appl. Phys. Lett.* 80: 192–194
145. Srinivasarao M, Collings D, Philips A, Patel S (2001) Three-dimensionally ordered array of air bubbles in a polymer film. *Science* 292: 79–83
146. Harrison MT, Kershaw SV, Burt MG, Rogach AL, Kornowski A, Eychmüller A, Weller H (2000) Colloidal nanocrystals for telecommunications. Complete coverage of the low-loss fiber windows by mercury telluride quantum dots. *Pure Appl. Chem.* 72: 295–307
147. Kershaw SV, Harrison M, Rogach AL, Kornowski A (2000) Development of IR-emitting colloidal II-VI quantum-dot materials. *IEEE J. Selec. Top. Quant. Electron.* 6: 534–543
148. Gumaste A, Antony T (2002) *DWDM Network Designs and Engineering Solutions*. Cisco Press. Indianapolis

Part IV
Biomedical Applications

Chapter 15

Biomedical Applications of Organic–Inorganic Hybrid Nanoparticles

María C. Gutierrez, María L. Ferrer, Pedro Tartaj, and Francisco del Monte

Abstract In this chapter, we discuss the application of various hybrid nanoparticles in different areas of biotechnology and biomedicine. The application of hybrid nanoparticles to these fields stems obviously from the intrinsic properties of nanoparticles (determined by high surface energy and large surface curvature) and also from the ability to design both the chemical nature of the nanoparticle surface (e.g., by attachment of organic moieties) and the nanoparticle structure (e.g., nanoparticle shape and surface structure). These features have allowed for the biocompatibility enhancement of the nanoparticles and hence, their routine use in contact with biological entities, from the most simple proteins and biomolecules to the most complex living organisms. The first part of this review focuses on biosensors, with optical, electrochemical and magnetic detection systems. Then, exploiting magnetic properties, an entire section is devoted to nuclear magnetic resonance imaging and hyperthermia. Finally, the use of different hybrid nanocapsules for drug delivery purposes is discussed.

15.1 Introduction

Nanotechnology is beginning to allow scientists, engineers, and physicians to work at the cellular and molecular levels to produce major benefits to the life sciences and health care [1]. Particularly the past couple of decades has witnessed an exponential growth of activities in the field of hybrid nanoparticles and nanocomposites worldwide, driven both by the excitement of understanding new science and by the potential hope for applications and economic impact [2]. This is not

M.C. Gutierrez (✉), M.L. Ferrer, P. Tartaj, and F. del Monte (✉)
Instituto de Ciencia de Materiales de Madrid,
CSIC, Campus Universitario de Cantoblanco,
Madrid 28049, Spain
e-mails: mcgutierrez@icmm.csic.es, delmonte@icmm.csic.es

surprising since the biological and physical sciences share a common interest in small structures [3].

The largest activity in the field of hybrid nanoparticles and nanocomposites at this time has been in the synthesis of new nanoparticles of different sizes and new shapes with applications in sensing, medical diagnosis, homogeneous catalysis, etc. The unraveling of the physics of these particles and the application of computation methods to understand their behavior are being investigated. Creating novel nanostructures requires new understanding of the properties of their surfaces. In most of their potential applications, the nature of the surface of nanoparticles will undoubtedly play the pivotal role in determining their functions. Being small could make the surface of a nanoparticle unstable due to the high surface energy and the large surface curvature. Thus the properties change as these particles are used. Not only could the surface structure and shape change, but the chemical nature of their surface could be altered too by the attachment of organic moieties. In addition, for device applications, these hybrid nanoparticles need to be connected to our macroscopic world. The perturbation at interconnects could have larger effects on the properties of nanoparticles than quantum confinement or other physical forces involved within the nanoparticle space. Thus it is clear that using these hybrid nanoparticles fully and effectively will depend on our understanding of their general properties and also of their surface properties and stability [4].

Besides hybrid nanoparticles, nanoporous hybrid materials have also called the attention of a number of research groups worldwide. The design, synthesis, and some optical properties of hybrid organic–inorganic nanocomposite materials are briefly presented. The properties that can be expected for such materials depend on the chemical nature of their components, but they also depend on the synergy of these components. Thus the interface in these nanocomposites is of paramount significance and one key point of their synthesis is the control of this interface. These nanocomposites are usually obtained by hydrolysis and condensation of hybrid metal alkoxydes (or simple metal alkoxydes whose hybrid character is introduced by post-functionalization), and by exfoliation of clay minerals and subsequent polymer intercalation.

In this chapter, we discuss the application of various hybrid nanocomposites in different areas of biotechnology and biomedicine. We first focus on biosensors, with optical, electrochemical and magnetic detection systems. Also based on magnetic properties, we devote an entire section to nuclear magnetic resonance imaging and hyperthermia. Later on, we discuss the use of different hybrid nanocapsules for drug delivery purposes, and finally we explore the use of hybrid nanoparticles and nanocomposites in biocatalytic processes. Due to the explosion of publications in this field, we do not claim that this review includes all the published work, but rather a presentation of some applications in biotechnology and biomedicine. We apologize to those authors whose excellent work has been unintentionally left out due to the large activity in this area.

15.2 Biosensors

Particularly with biomedicine there exists a need for enhanced speed, throughput and sensitivity, since many effects in biology are nonlinear, transient, complex, and very faint [5]. A gene may be expressed for a very short time, and in a specific location within a specific type of cell. Discerning this event within a large population of cells can be very difficult. Furthermore, many DNA analyses are limited by the scant amount of starting material, which in the case of forensics or epidemiology may be severely degraded. As an example, the concentration of a single gene (one DNA strand) within the volume of a typical mammalian cell is of the order of 10^{-12} M. If this one DNA strand is then diluted into a more conventional analysis volume of 10 μ L, the concentration drops to $<10^{-18}$ M. The most sensitive systems for nucleic acid analysis can detect concentrations in the femtomolar–picomolar range. Therefore reduction in assay volume is critical for the reliable detection of scarce biological analytes. As we describe it below, the use of hybrid nanoparticles and nanocomposites as analytical probes can lead to improved efficiency with respect to already established technologies.

15.2.1 Optical Biosensors

During the last three decades we have witnessed remarkable research and development activity aimed at the realization of optical sensors for the measurement of chemical and biological quantities. The first optical chemical sensors were based on the measurement of changes in the absorption spectrum and were developed for the measurement of CO_2 and O_2 concentrations [6]. Since then, a large variety of optical methods have been used in chemical sensors and biosensors including ellipsometry, spectroscopy (luminescence, phosphorescence, fluorescence, Raman), interferometry (white light interferometry, modal interferometry in optical waveguide structures), spectroscopy of guided modes in optical waveguide structures (grating coupler, resonant mirror), and surface plasmon resonance. In these sensors, a desired quantity is determined by measuring the refractive index, absorbance and fluorescence properties of analyte molecules or a chemo-optical transducing medium [7–10].

The most widely used and simple optical sensors making use of hybrid nanoparticles are based on the detection of analytes that either absorb or emit light and basically rely on the entrapment of biomolecules that contain chromophoric or fluorescent groups (i.e. flavoproteins, heme proteins, fluorescently-tagged proteins), or can be prepared by co-entrapping a biomolecule along with a chromophore or fluorophore that responds to the protein-mediated reaction (i.e. pH change, variation in O_2 levels). Alternatively, bioluminescence can also be used as a signal

to report on the presence of species that alter the function of luminescent proteins such as aequorin [11]. An interesting example mimicking cell function has been described for recognition of Listeriolysin O (LLO) [12]. LLO is a pore-forming hemolysin secreted by the foodborne pathogen *Listeria monocytogenes* and is required for bacterial virulence. Current detection methods for *L. monocytogenes* are time-consuming, labor-intensive, and expensive, which is impractical considering the limitations of food storage. To overcome these problems, Zhao et al. have developed a liposome-doped silica nanocomposite as a simple, inexpensive, and highly stable biosensor material that mimics existing whole-cell assays for LLO. Small unilamellar liposomes containing fluorescent dyes were immobilized within porous silica using alcohol-free sol-gel synthesis methods. The immobilized liposomes served as cellular surrogates for membrane insertion and pore formation by LLO. The integrity of liposomes in the solid-state sol-gel glass was investigated by fluorescence quenching and leaching assays. The materials were stable for at least 5 months in ambient conditions. Both free and immobilized liposomes responded to LLO at pH 6.0 with concentration-dependent kinetics. The pore formation of LLO in liposome-doped silica composites displayed similar kinetic curves as free liposomes but with slower rates. LLO insertion into the immobilized liposomes was pH dependent. No increase in membrane permeability was observed at pH 7.4 for the liposome-doped composites in the presence of LLO. Immobilized liposomes can detect LLO in ca 1.5 h using a steady state calibration and within 30 min using a kinetic calibration. These liposome silica composites potentially could be used for the detection of hemolysin-producing *L. monocytogenes* as well as many other bacteria that produce pore-forming toxins.

Attention has also been paid to the use of quantum dots for massively parallel and high-throughput analysis of a number of biological molecules. Han et al. reported the use of multicolor optical coding for biological assays by embedding different-sized quantum dots (zinc sulfide-capped cadmium selenide nanocrystals) into polymeric microbeads at precisely controlled ratios [13]. Their novel optical properties (e.g., size-tunable emission and simultaneous excitation) rendered these highly luminescent quantum dots ideal fluorophores for wavelength and intensity multiplexing. The use of ten intensity levels and six colors could theoretically code one million nucleic acid or protein sequences. Imaging and spectroscopic measurements indicated that the quantum dots-tagged beads are highly uniform and reproducible, yielding bead identification accuracies as high as 99.99% under favorable conditions. DNA hybridization studies demonstrated that the coding and target signals can be simultaneously read at the single-bead level. This spectral coding technology was expected to open new opportunities in gene expression studies, high-throughput screening, and medical diagnostics (Figs. 15.1 and 15.2)

The incorporation of fluorescence-quenching strategies into the sensing mechanism is of great interest because it allows extending the range of analytes to include nonabsorbing species that modulate decay properties of entrapped fluorescent species. Moreover, in the cases where fluorescent signaling is used, it allows enhancing the sensitivity limit up to single molecule detection limit. One recent new development taking advantage of such quenching strategies is a novel class of oligonucleotide

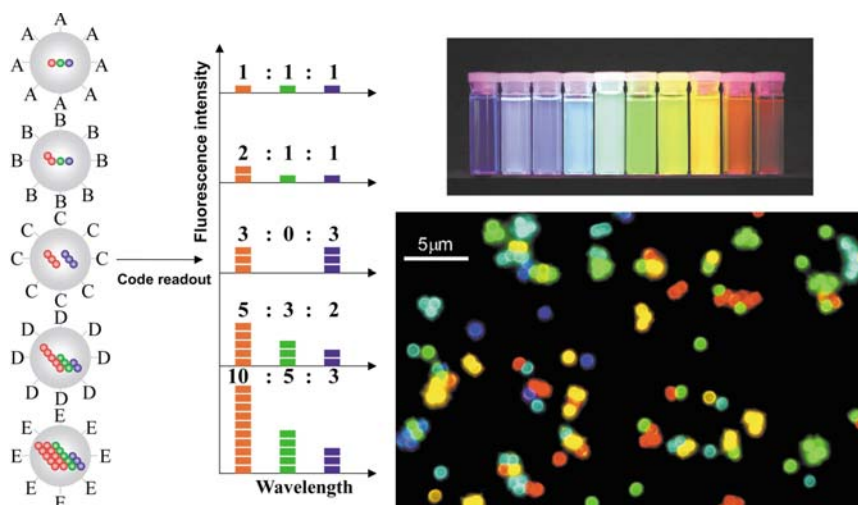


Fig. 15.1 (a) Schematic illustration of optical coding based on wavelength and intensity multiplexing. *Large spheres* represent polymer microbeads, in which small colored spheres (*multicolor quantum dots*) are embedded according to predetermined intensity ratios. Molecular probes (A–E) are attached to the bead surface for biological binding and recognition, such as DNA–DNA hybridization and antibody–antigen/ligand–receptor interactions. The number of colored spheres (*red, green, and blue*) does not represent individual quantum dots, but are used to illustrate the fluorescence intensity levels. Optical readout is accomplished by measuring the fluorescence spectra of single beads. Both absolute intensities and relative intensity ratios at different wavelengths are used for coding purposes; for example (1:1:1), (2:2:2), and (2:1:1) are distinguishable codes. (b) Ten distinguishable emission colors of ZnS-capped CdSe quantum dots excited with a near-UV lamp. From *left to right* (blue to red), the emission maxima are located at 443, 473, 481, 500, 518, 543, 565, 587, 610, and 655 nm. Fluorescence micrograph of a mixture of CdSe/ZnS quantum dots-tagged beads emitting single-color signals. The beads were spread and immobilized on a polylysine-coated glass slide, which caused a slight clustering effect. (Reprinted with permission from [13]; copyright Nature Publishing Group)

probes, called molecular beacons (MBs). MBs, first developed by Tyagi and Kramer, are single-stranded oligonucleotide probes that possess a stem-and-loop structure [14]. The loop portion of the molecule can report the presence of a specific complementary nucleic acid [14–19]. The five bases at the two ends of the MBs are complementary to each other, forming the stem. A fluorophore and a quencher are linked to the two ends of the stem as shown in Fig. 15.3. The stem keeps these two moieties in close proximity to each other, causing the fluorescence of the fluorophore to be quenched by energy transfer. When the probe encounters a target DNA molecule, it forms a hybrid that is longer and more stable than the stem, and its rigidity and length preclude the simultaneous existence of the stem hybrid. Thus the MB undergoes a spontaneous conformational reorganization that forces the stem apart and causes the fluorophore and the quencher to move away from each other, leading to the restoration of fluorescence. Therefore, at room temperature, the MBs emit an intense fluorescent signal only when hybridized to their

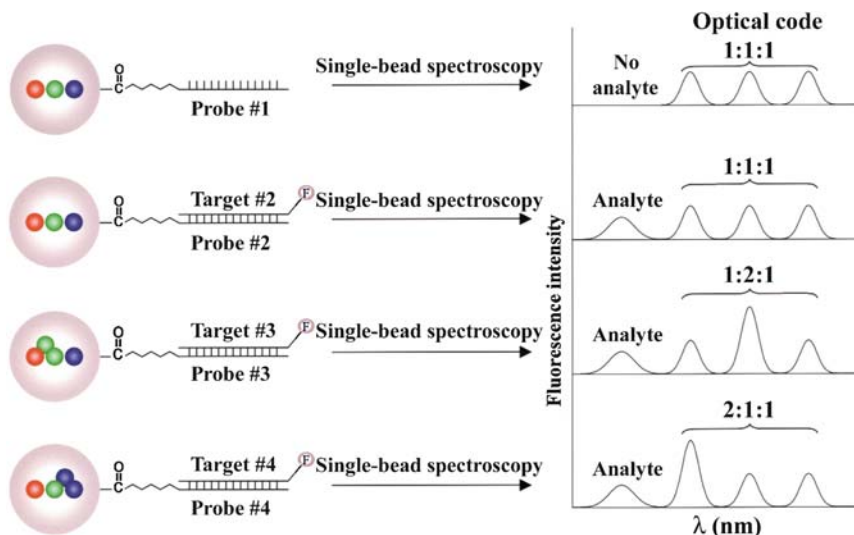


Fig. 15.2 Schematic illustration of DNA hybridization assays using quantum dots-tagged beads. Probe oligos (No. 1–4) were conjugated to the beads by crosslinking, and target oligos (No. 1–4) were detected with a blue fluorescent dye such as Cascade Blue. After hybridization, non-specific molecules and excess reagents were removed by washing. For multiplexed assays, the oligo lengths and sequences were optimized so that all probes had similar melting temperatures ($T_m = 66^\circ\text{--}99^\circ\text{C}$) and hybridization kinetics (30 min). (Reprinted with permission from [13]; copyright Nature Publishing Group)

target molecules [14–18, 21–23]. The size of the loop and its content can be varied by designing different MBs. Also, the quencher and the fluorophores can be changed according to the problem studied. There have been a variety of applications of MBs, [14–18, 21–23] including the real-time monitoring of polymerase chain reactions, [14] and even the investigation of HIV-1 disease progression [17, 18]. MBs have extremely high selectivity with single-base pair mismatch identification capability. They hold great promise for studies in genetics, disease mechanisms, and molecular interactions, for applications in disease diagnostics, and in new drug development.

MBs and colloidal gold nanoparticles have been combined to develop a new class of nanobiosensors that was able to recognize and detect specific DNA sequences and single-base mutations in a homogeneous format [20]. At the core of this biosensor was a 2.5-nm gold nanoparticle that functions as both a nanoscaffold and a nanoquencher (efficient energy acceptor). Attached to this core were oligonucleotide molecules labeled with a thiol group at one end and a fluorophore at the other. This hybrid bio/inorganic construct was found to spontaneously assemble into a constrained arch-like conformation on the particle surface. Binding of target molecules resulted in a conformational change, which restores the fluorescence of the quenched fluorophore. Unlike conventional MBs with a stem-and-loop structure, the nanoparticle probes did not require a stem, and their background fluorescence increased little with temperature. In comparison with the organic quencher

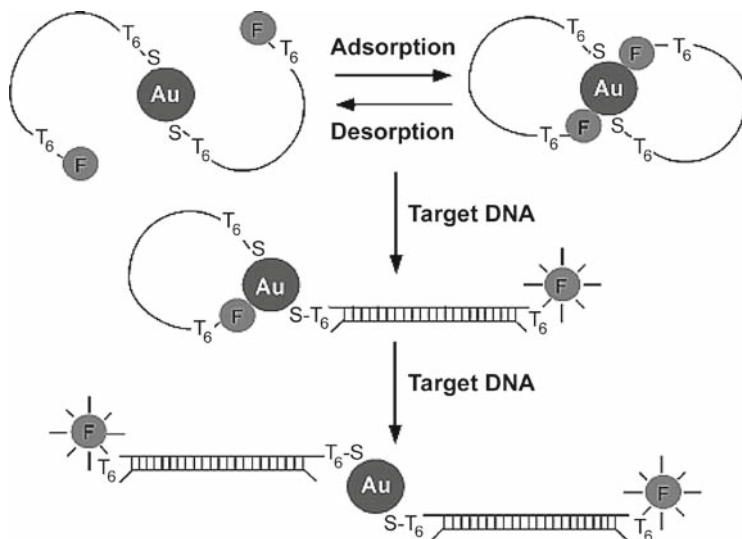


Fig. 15.3 Nanoparticle-based probes and their operating principles. Two oligonucleotide molecules (oligos) are shown to self-assemble into a constrained conformation on each gold particle (2.5 nm diameter). A T6 spacer (six thymines) is inserted at both the 3′- and 5′-ends to reduce steric hindrance. Single-stranded DNA is represented by a *single line* and doublestranded DNA by a *cross-linked double line*. In the assembled (closed) state, the fluorophore is quenched by the nanoparticle. Upon target binding, the constrained conformation opens, the fluorophore leaves the surface because of the structural rigidity of the hybridized DNA (double-stranded), and fluorescence is restored. In the open state, the fluorophore is separated from the particle surface by about 10 nm. See text for detailed explanation. *Au*, gold particle; *F*, fluorophore; *S*, sulfur atom. (Reprinted with permission from [20]; copyright ACS publications)

Dabcyl (4,4′-dimethylaminophenyl azo benzoic acid), metal nanoparticles have unique structural and optical properties for new applications in biosensing and molecular engineering.

However, the field where these sensors based on fluorescent emission of organic dyes and functionalized quantum dot nanoparticles are of great help is *in vivo* applications. A recent and interesting work in the field of *in vivo* imaging is the development and characterization of a highly-selective magnesium fluorescent optical nanosensor, made possible by PEBBLE (probe encapsulated by biologically localized embedding) technology [24]. A ratiometric sensor has been developed by co-immobilizing a dye that is both sensitive to and highly selective for magnesium. The sensors were prepared via a microemulsion polymerization process which entraps the sensing components inside a polymer matrix. The resultant spherical sensors were ca 40 nm in diameter. The Coumarin 343 (C343) dye, which by itself does not enter the cell, when immobilized in a PEBBLE was used as the magnesium-selective agent that provides the high and necessary selectivity over other intracellular ions, such as Ca^{2+} , Na^{+} , and K^{+} . The dynamic range of these sensors was 1–30 mM, with a linear range from 1 to 10 mM, with a response time of <4 s. In contrast to free dyes, these nano-optodes were not perturbed by proteins. They were

fully reversible and exhibit minimal leaching and photobleaching over extended periods of time. In vitro intracellular changes in Mg^{2+} concentration were monitored in C6 glioma cells, which remained viable after PEBBLE delivery via gene gun injection. The selectivity for Mg^{2+} along with the biocompatibility of the matrix provides a new and reliable tool for intracellular magnesium measurements.

An interesting alternative for in vivo imaging is the use of quantum dots. Fluorescent semiconductor nanocrystals (quantum dots) have the potential to revolutionize biological imaging, given their much higher fluorescent quantum yields and lower photobleaching than organic dyes. However, their use has been limited by difficulties in obtaining nanocrystals that are biocompatible. The encapsulation of individual nanocrystals in phospholipid block-copolymer micelles is of great help to address this problem, as recently demonstrated both in vitro and in vivo imaging [25] (Fig. 15.4). When conjugated to DNA, the nanocrystal-micelles acted as in vitro fluorescent probes to hybridize to specific complementary sequences. Moreover, when injected into *Xenopus* embryos, the nanocrystal-micelles were stable, nontoxic ($<5 \times 10^9$ nanocrystals per cell), cell autonomous, and slow to photobleach (Fig. 15.4). Nanocrystal fluorescence could be followed to the tadpole stage, allowing lineage-tracing experiments in embryogenesis.

A nice example for in vivo imaging has recently been reported. In particular, gold nanoparticle-oligonucleotide complexes were used as intracellular gene regulation agents for the control of protein expression in cells [26]. These oligonucleotide-modified nanoparticles had affinity constants for complementary nucleic acids that were higher than their unmodified oligonucleotide counterparts, were less susceptible to degradation by nuclease activity, exhibited greater than 99% cellular uptake, could introduce oligonucleotides at a higher effective concentration than conventional transfection agents, and were nontoxic to the cells under the conditions studied. By chemically tailoring the density of DNA bound to the surface of gold nanoparticles, the authors demonstrated a tunable gene knockdown. The authors conclude that despite these systems have not yet been optimized for maximum efficacy, the ability to systematically control the oligonucleotide loading on the nanoparticle surface makes it possible to identify several features that make them attractive candidates for antisense studies and therapies (Fig. 15.5). The ability to modify the gold nanoparticle surface allows one to realize unusual cooperative properties that led to enhanced target binding and allows the introduction of a variety of functional groups that have proven to be informative in terms of studying how the structure works within a cell. Moreover, this platform will allow to add functionality [27, 28] that could direct the oligonucleotide-modified nanoparticle agents to specific cell types and different components within the cell, thus opening the door for new possibilities in the study of gene function and nanotherapies.

For in vitro applications, the potential of sensors based on surface plasmon resonance (SPR) and evanescent-field waveguide optics (EF) for characterization of thin films [29] and monitoring processes at interfaces [30] has been widely recognized. EF and SPR sensors work similarly; both types of waves are guided, the waveguide modes by total internal reflection at the waveguiding film interface and the surface plasmon by the metal dielectric interface, and both sensors respond

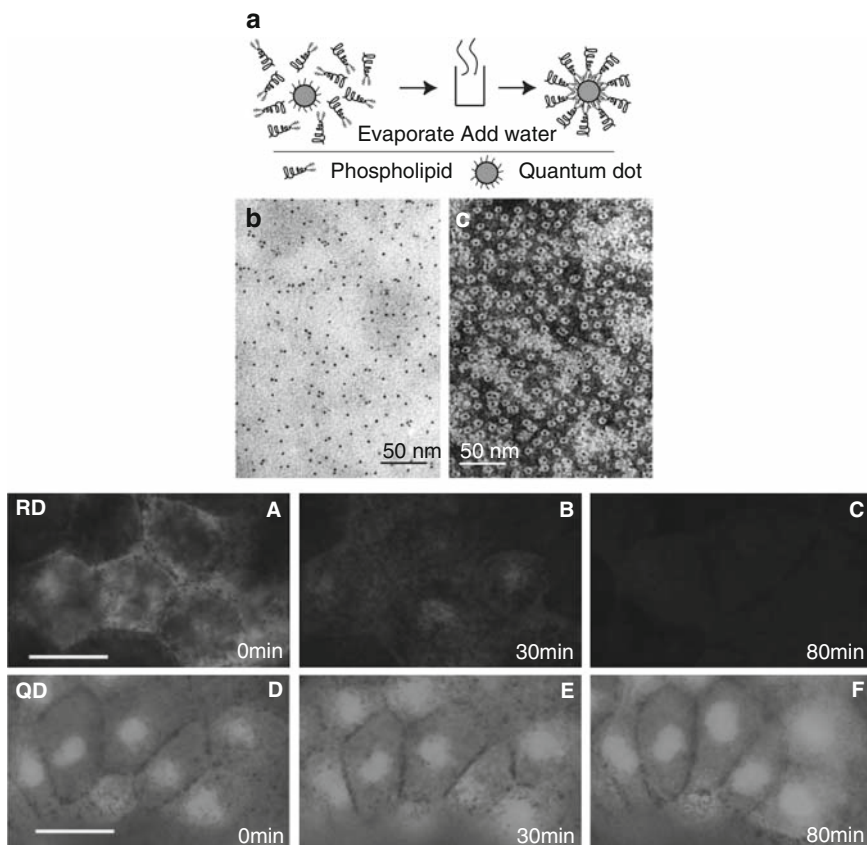


Fig. 15.4 *Top panel:* Quantum dot (QD)-micelle formation and characterization. (a) Schematic of single-QD encapsulation in a phospholipid block-copolymer micelle. (b) TEM image of QD-micelles dried on a carbon- Formvar-coated 200-mesh nickel grid. Only the QDs inside the micelle core are visible. The particles appear evenly spread on the surface. Although some clusters of two to four QDs are visible, most of the QDs are isolated, suggesting that a majority of micelles contain a single QD. (c) TEM image of the phospholipid layer obtained by negative staining with 1% PTA (phosphotungstic acid) at pH 7. With this technique, both the QD and the micelle can be visualized at the same time. The QD (*dark spot*) appears surrounded by a white disk of unstained phospholipids that stands out against the stained background. *Bottom panel:* Comparison of QD and RG-D (Rhodamine Green Dextran, Molecular Probes) for resistance to photobleaching. QDs and injection amounts are similar to those used in Fig. 15.3. For RG-D, 1 nL of a 25 mg/mL solution was injected. (a–c) Consecutive images of RG-D-injected *Xenopus* animal pole blastomeres. (d–f) Consecutive images of QD-injected *Xenopus* animal pole blastomeres. During each experiment, the injected embryos were excited continuously at 450 nm. (Reprinted with permission from [25]; copyright Science Magazine)

to a change in the refractive index induced by the adsorption or binding of molecules to the surface of the waveguiding (for EF) or metal film (for SPR). In the SPR technique, the adsorption or binding of a molecule on a metal surface is detected

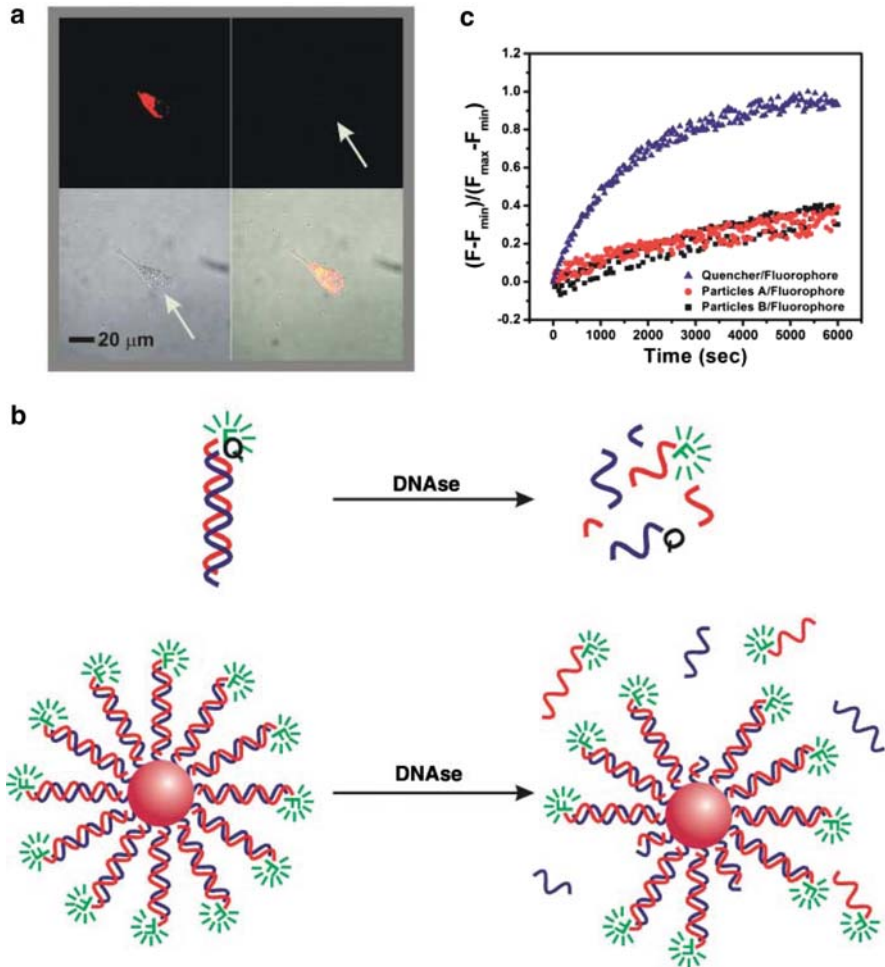


Fig. 15.5 Experiments aimed at understanding the intracellular stability of antisense nanoparticles. (a) Fluorescent microscopy images of C166-EGFP cells incubated 48 h with antisense particle B functionalized with dual-fluorophore labeled ASODNs (3' Cy3 and 5' Cy5.5'') only reveal fluorescence from Cy5.5 (706–717 nm, upper left). Negligible fluorescence is observed in the emission range of Cy3 (565–615 nm, upper right). Transmission and composite overlay images are shown in the lower left and lower right quadrants, respectively. The arrows indicate the location of the cell. Similar data collected from experiments using particle A are included elsewhere (23). (b) Duplexes composed of either quencher-modified SODN/fluorophore-modified complement or antisense particle/fluorophore modified complement were treated with DNase. (c) The ASODN duplex degraded much faster than the antisense particle duplex, as calculated using fluorescence spectroscopy, where F_{\min} is the fluorescence of the mixture at its initial, fully hybridized state and F_{\max} is the maximum fluorescence of the system at 80°C where all of the oligonucleotides are dehybridized. (Reprinted with permission from [26]; copyright Science Magazine)

by measuring the change in the surface plasmon wavevector, whereas in a waveguide EF sensor the presence of a molecule on the surface is detected by the induced change in the waveguide mode wavevector or effective index. EF waveguide

sensors can be more sensitive than SPR devices [31], while SPR sensors have had some success for label-free detection [32].

Worth-mentioning is a couple of examples where the remarkable detection limit of EF sensors is pointed out by Abel *et al.* in the design of a fiber-optic evanescent wave biosensor for the detection of oligonucleotides [33]. An automated optical biosensor system based on fluorescence excitation and detection in the EF of a quartz fiber was used to detect 16-mer oligonucleotides in DNA hybridization assays. A biotinylated capture probe was immobilized on the fiber surface via avidin or streptavidin. The hybridization with fluorescein-labeled complementary strands was monitored in real time by fluorescence detection. The double strands formed by hybridization could be dissociated by chemical or thermal regeneration, allowing one to perform hundreds of assay cycles with the same fiber. The signal loss during long-time measurements, *i.e.*, consecutive hybridization assays, can be described by a single-exponential function. Over more than 200 cycles, the net signal decreased by 50% with a signal variation of 2.4% after correction for this signal loss. By binding the capture probe with the 5'-end to the optical fiber surface, and by using a 50% (w/w) aqueous urea solution for chemical regeneration, the duration of an assay cycle could be reduced to 3 min. By applying longer assay cycles, the detection limit for the hybridization with a complementary fluorescein-labeled oligonucleotide was 2.0×10^{-13} M (24 fmol). To detect an unlabelled complementary 16-mer oligonucleotide, competitive hybridization assays were performed, resulting in a detection limit of 1.1×10^{-9} M (132 pmol). Poly-(acrylic acid) 5,100 sodium salt and tween 20 were used in the hybridization buffer to prevent nonspecific binding caused by ionic or hydrophobic interaction. The amount of nonspecific binding of noncomplementary oligonucleotides was in the range of 1–2%, compared with the specific binding in the different hybridization assays.

Liu *et al.* [34] also developed a fiber-optic EF DNA biosensor based on MBs such as those described above. The biotinylated MBs were designed and immobilized on an optical fiber core surface via biotin-avidin or biotin-streptavidin interactions. The DNA sensor based on this MB did not need labeled analyte or intercalation reagents. It can be used to directly detect, in real-time, target DNA/RNA molecules without using competitive assays. The sensor was fast, stable, highly selective, and reproducible. The concentration detection limit of the MB evanescent-wave biosensor was 1.1 nM. The authors applied the MB DNA biosensor to the analysis of specific γ -actin mRNA sequences amplified by polymerase chain reaction with satisfactory results.

Buckle *et al.* [35] described the application of a novel optical “evanescent wave sensor” (the Resonant Mirror, RM) to the direct study of biological recognition. In particular, measurement of antigen/antibody and enzyme/substrate/inhibitor interactions in real-time without labeling was detailed in their study. The RM, described in a preceding paper [36], detected changes in refractive index and/or thickness occurring within a few hundred nanometers of the sensor surface. Several methods for immobilization of biomolecules at the sensor surface have been investigated using antibodies and radioactively labeled antigens as model systems. One of the immobilization techniques involves deposition of carboxymethyl dextran on the sensor device and subsequent covalent attachment of biomolecules to the gel via their amino groups. With an anti-theophylline antibody, this method resulted in at least 212 femtomoles

of active antibody per mm^2 of the surface, a surface density equivalent to at least 9 monolayers of antibody. Immunoassays performed on the RM with immobilized antibodies resulted in sensitivities in the nM range for the complementary antigens. The specificity and sensitivity of the system was further improved by the use of sandwich or multi-site immunoassays and by the use of enhancer particles, such as colloidal gold particles. The broader applicability of the RM to studies on molecular interaction was demonstrated in an assay for the proteolytic enzyme trypsin and the specific inhibition of enzyme activity by al-antitrypsin.

Regarding SPR biosensors, there is a vast number of works published since 1983 [37]. Some representative examples are those published on the immobilization of proteins on a carboxymethyl-dextran-modified gold surface for biospecific interaction analysis [38]. Storhoff et al. describe a one-pot colorimetric differentiation of polynucleotides with single-base imperfections using gold nanoparticle probes [39]. Finally, the numerous works published by Van Duynes and coworkers are worth highlighting [40–46]. This group has demonstrated the ability of localized surface plasmon resonance (LSPR) nanosensors to work as sensitive platforms for the detection of streptavidin [46], anti-biotin [47], concanavalin [48], Alzheimer disease biomarkers [43], and many other biorecognition events [49].

Since many biomolecules contain visible chromophores, it is important to broaden the scope of LSPR sensing by exploring electronically resonant adsorbates in biosensing events. When resonant molecules are adsorbed on nanoparticles, the induced LSPR shift is found to be strongly dependent on the spectral overlap between the electronic resonance of the adsorbates and the plasmon resonance of the nanoparticles [50]. Specifically, a large red-shift occurs when the nanoparticles' LSPR is located at a slightly longer wavelength than the adsorbate's molecular resonance wavelength, that is, a factor of three greater than when the LSPR is distant from the molecular resonance. This resonant LSPR response opens up the possibility of detecting the binding of a low-molecular-weight analyte to a protein receptor adsorbed on a nanoparticle. Thus, one of the latest works published by Van Duynes and coworkers [40] has demonstrated that the binding of a small molecule (camphor) to a protein (CYP101(Fe^{3+})) can generate a LSPR spectral change. Amplified spectral response to substrate binding is achieved when the LSPR of the silver nanosensor was optimized to be close to the molecular resonance of the protein. The study revealed that strong coupling between the molecular resonance and the intrinsic LSPR of the nanoparticles results in an amplified LSPR shift that is modulated by substrate binding, providing further insight into possible uses of SPR spectroscopy. Application of this finding to the screening for inhibitors of human cytochrome P450s is under investigation.

15.2.2 Electrochemical Biosensors

Electrochemical biosensors, particularly enzyme electrodes, have enjoyed considerable popularity, culminating in commercial devices, ranging from self-testing meters for

blood glucose to high throughput analyzers for various metabolites [51–55]. All molecular-based biosensors rely on highly-specific recognition events to detect target analytes. The essential role of the sensor is to provide a suitable platform that facilitates formation of the probe-target complex in such a way that the binding event triggers a usable signal for electronic read-out. Because electrochemical reactions give an electronic signal directly, there is no need for expensive signal transduction equipment. A system displaying high sensitivity, good selectivity, and long-term stability would require the optimization of the proper immobilization of the biomolecule while ensuring no or little loss in its biological activity, sensitivity, and stability. However, the overall performance and the development of these biosensors will depend not only on the biocompatibility of the material and the immobilization method, but also on the physicochemical characteristics of the material, and on the existence of redox mediators and stabilizers.

Nanocomposites and nanoparticles are extremely suitable for designing new and improved electrochemical biosensing devices. To this end, a wide variety of compositions and configurations have been used for different electrochemical sensing systems such as enzyme biosensors, immunosensors and DNA sensors. The essential functions provided by these nanocomposites and nanoparticles include the immobilization of the biomolecules, the catalysis of electrochemical reactions, the enhancement of the electron transfer between the electrode surfaces and proteins, and the labeling of biomolecules for detecting biorecognition events [56]. Generally, metal nanoparticles and carbon nanotubes (CNT) have excellent conductivity and catalytic properties, which make them suitable for acting as “electronic wires” for enhanced protein-electrode electron transfer and as catalyst to increase electrochemical reactions. Oxide nanocomposites and CNT pastes are often used to immobilize biomolecules due to their biocompatibility, while semiconductor nanoparticles are mainly used as labels or tracers for electrochemical analysis. It is the aim of this section to summarize the recent advances in nanocomposite-based electrochemical biosensors and the role that the different materials play in the sensing systems

15.2.2.1 Metal and Semiconductor Nanoparticle-based Biosensors

The unique electronic and catalytic properties of metal and semiconductor nanoparticles render them ideal labels for biorecognition and biosensing processes. Thus, nanoparticles–biomolecule hybrids have been used to enhance electron transfer on biosensors, for biofuel-cell elements (i.e., a “wiring” of the enzyme redox centers to the macroscopic electrode) and for the detection of a biorecognition event on DNA and antibody–antigen analyses [54, 56–58].

Metal and Semiconductor Nanoparticle-enzyme Hybrids Systems

The electrical contacting of redox enzymes with electrodes is a key process in the design of enzyme electrodes for bioelectronic applications such as biosensors or

biofuel-cell elements. Although redox enzymes usually lack direct electrical communication with electrodes due to thick insulation protein shells surrounding the enzyme-active centers, electrical contacting of the proteins and electrodes have been reported by the application of diffusional electron mediators, the immobilization of the enzymes in redox-active polymers or the reconstitution of apo-enzymes on relay cofactor monolayers associated with electrodes [54, 59–62]. Biocatalytic electrodes for biosensor applications have been prepared by the co-deposition of redox proteins and metal nanoparticles on electrode supports. A well-known example in which the metal nanoparticles act as a nanoelectrode to electronically link the enzyme redox site to the macroscopic electrode is shown in Fig. 15.6 [63]. The gold nanoparticles (1.4 nm) were functionalized with *N*-(2-aminoethyl)-flavin adenine dinucleotide (FAD cofactor amine derivative 1), and then reconstituted with apo-glucose oxidase and assembled on a thiolate monolayer associated with the gold electrode. Alternatively, the functionalized gold nanoparticles could be first assembled onto the electrode through a thiolate monolayer and reconstituting apo-glucose oxidase subsequently. The resulting nanoparticle-enzyme electrode exhibited unprecedented efficient electrical communication with the electrode (electron

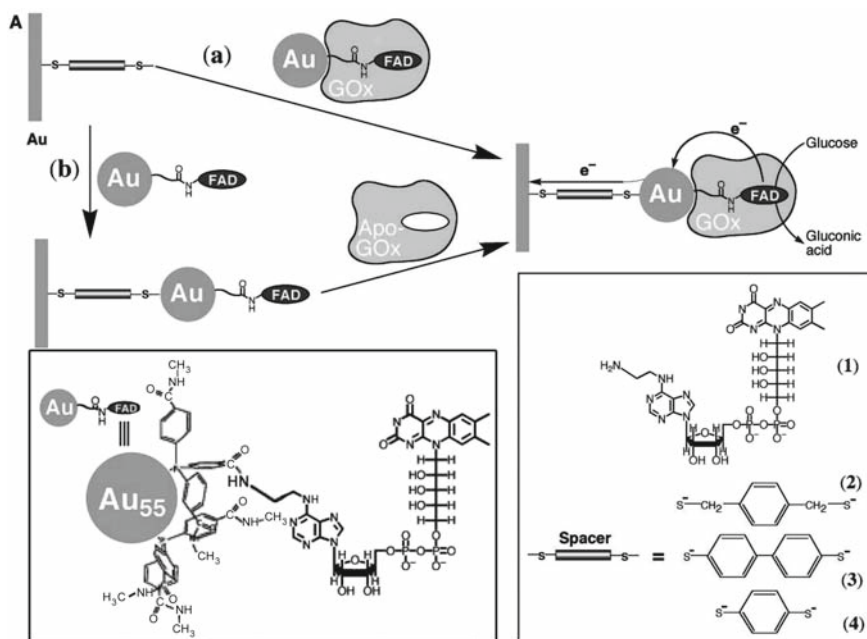


Fig. 15.6 Assembly of Au-NP–reconstituted GOx electrode by (a) the adsorption of Au-NP–reconstituted GOx to a dithiol monolayer associated with a Au electrode and (b) the adsorption of Au-NPs functionalised with FAD on the dithiol-modified Au electrode followed by the reconstitution of apo-GOx on the functional NPs. (Reprinted with permission from [63]; copyright Science Magazine)

transfer turnover rate $\sim 5000 \text{ s}^{-1}$); i.e., seven times faster than that between glucose oxidase and its natural substrate oxygen. Moreover, the enzyme electrode could be used for glucose detection without interference as the effective electrical contacting made it insensitive to oxygen or other common interferants, such as ascorbic acid.

Silver nanoparticles have also been employed to enhance the electron transfer between the electrode and different proteins such as, Cytochrome C, hemoglobin and myoglobin [64, 65]. Recently, the application of semiconductor nanoparticles for the enhancement of electron transfer between redox proteins and electrodes has been reported. Hemoglobin and CdS nanoparticles were mixed and immobilized onto pyrolytic graphite electrodes exhibiting direct electrochemistry [66]. Moreover, the use of enzyme nanoparticles hybrid systems in which the product generated by the catalytic process activates the photoelectrochemical functions of the nanoparticles has been demonstrated using acetylcholine esterase (AChE)-CdS nanoparticles hybrid monolayer on an Au electrode [67].

Metal and Semiconductor Hybrid Nanoparticles as Sensors of Biorecognition Events

Several electrochemical protocols currently offer great promise for ultrasensitive nanoparticle-based transduction of biological interactions (antigen–antibody and base-pairing of DNA). In such protocols the treated (dissolved) metal or semiconductor nanoparticles or polystyrene active beads can act as the reporter units of a recognition event. Stripping voltammetry (i.e., electroanalytical technique for trace metals measurements) has been particularly useful for detecting metal nanoparticles tags. Its remarkable sensitivity is attributed to the “built-in” preconcentration (electrodeposition) step during which the target metals are accumulated (plated) onto the working electrode lowering the detection limit by 3–4 orders of magnitude compared to pulse voltammetric techniques employed earlier to monitor DNA hybridisation [58]. The specific capturing of biomolecule-nanoparticles on the respective sensing interfaces allows the secondary dissolution of the captured nanoparticles and thus enables the amplified detection of the respective analyte by the release of many ions/molecules as a result of a single recognition event. Demonstrations of the use of gold nanoparticles tracers for the stripping-based electrochemical detection of antibody-antigen interactions and DNA hybridization were reported recently [68–70]. Such protocols relied on capturing the metal nanoparticles at the hybridized target or captured antibody followed by their dissolution and then stripping voltammetric measurements of the trace a metal (Fig. 15.7).

Since the sensitivity of the bioassay depends on the size of the metallic tag, a dramatic amplification of a single hybridization event using single reporter unit, such as metal or semiconductor nanoparticles, is expected with larger nanomaterial tracers. The catalytic enlargement of the gold tracer in connection to nanoparticle-promoted precipitation of gold or hydroquinone-induced silver, has promoted a second generation of amplified bioassays with subpicomolar detection limits [71, 72]. Solid-state measurements of the metal nanoparticles tag have also been

carried out through a magnetic collection of DNA–linked particle assembly onto an electrode transducer [73]. Such bioassays involved the hybridization of a target nucleotide to probe coated magnetic beads, followed by binding of the streptavidin-coated gold nanoparticles to the captured target, catalytic silver precipitation on the gold particle tags, magnetic collection of the DNA-linked particle assembly and constant current chronoamperometric detection (Fig. 15.8).

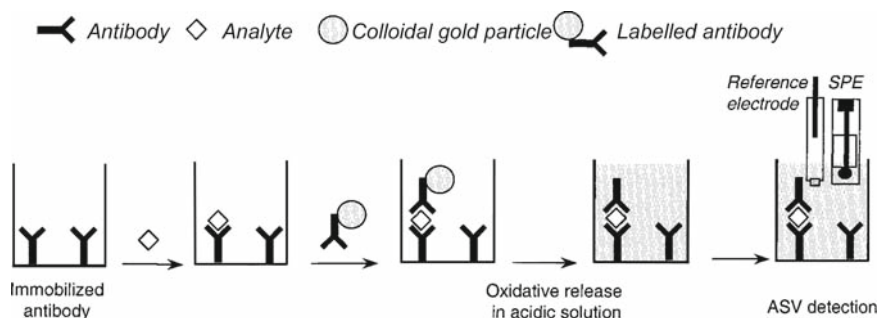


Fig. 15.7 Schematic of a noncompetitive heterogeneous electrochemical immunoassay based on a gold nanoparticle label. (Reprinted with permission from [68]; copyright ACS publications)

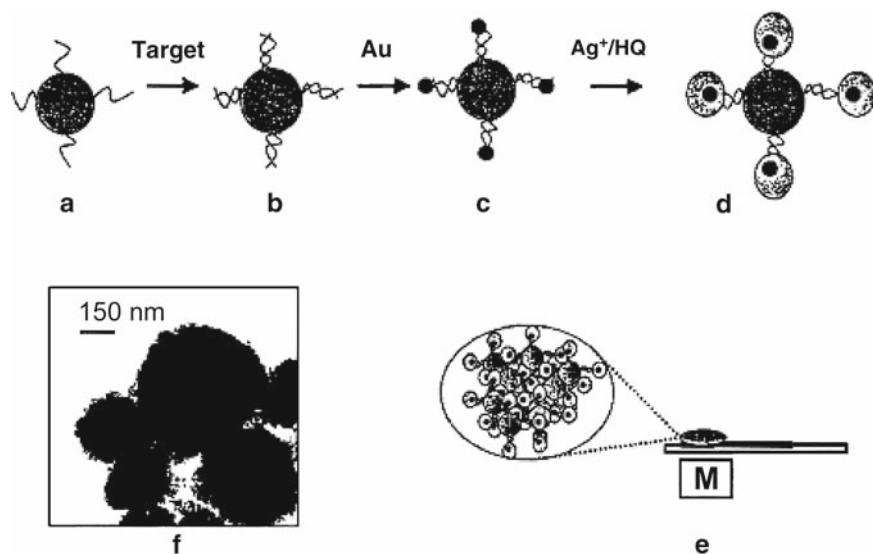


Fig. 15.8 Solid state magnetically induced electronic measurements of the metal nanoparticles tag. The catalytic growth of the gold tracer led to a second-generation bioassay. The external magnetic field is positioned under the electrode to attract the DNA-particle assembly to the surface and allows solid state detection. TEM micrograph of the DNA-particle assembly produced following a 20 min hybridization with the $50 \mu\text{g}/\text{mL}^{-1}$ target sample and 10 min silver precipitation. (Reprinted with permission from [73]; copyright ACS publications)

Another attractive route to enhance the sensitivity of DNA detection (by loading multiple tags per binding event) can be achieved by the internal encapsulation of the electroactive tag within carrier polymeric microbeads. Dramatic signal amplification was achieved by linking the biorecognition units to “electroactive beads” impregnated with the ferrocenecarboxaldehyde redox marker. Collection of the hybridized system and dissolution of the beads in an organic solvent released the immobilized redox label and allowed detection of the DNA target down to the 5×10^{-21} mol ($\sim 31,000$ molecules) level (Fig. 15.9b) [75].

Other approaches for amplified electrochemical sensing have been explored, giving promising results. For example, instead of using polymer carrier spheres it is also possible to encapsulate a huge amount of the signal-generating redox marker as a microcrystal in combination with a layer-by-layer technology [76]. It is also possible to increase the amount of metal marker and, therefore, the sensitivity of the detection by using micrometer-long metal nanowires. This protocol relies on the deposition of metal clusters along the DNA backbone rather than attaching them at the end of the probe and allows detection limits at the femto molar level [58, 77]. Semiconductor nanoparticles have also been extensively used as labels in electrochemical biosensors [78]. Thiolated oligonucleotides labeled with CdS semiconductor nanoparticles were employed as tags for the detection of DNA hybridization events [79]. Dissolution of the CdS nanoparticles and chronoamperometric stripping detection of dissolved Cd^{2+} ions provided the electric signal for the DNA analysis. Based on similar principles a multitarget simultaneous hybridization scheme was reported [80]. Nanoparticle-induced generation of conductivity paths across a microelectrode gap can also be exploited for highly sensitive detection of DNA hybridization [81].

15.2.2.2 Carbon Nanotube- based Electrochemical Biosensors

Carbon in many aspects is an ideal electrode substrate: it is versatile, it has access to a large positive potential range, it exhibits low residual currents and is suitable for chemical modifications. Among carbonaceous materials [82–84], CNTs are unique one-dimensional macromolecules whose outstanding properties have sparked abundant research since their discovery in 1991 [85]. Single-walled carbon nanotubes (SWCNT) are composed of a single sheet of graphite (diameter 0.4–2 nm), while multi-walled carbon nanotubes (MWCNT) consist of multiple concentric graphite cylinders of increasing diameter up to 100 nm [86]. Both SWCNT and MWCNT possess high tensile strengths, are ultra-light weight and have excellent thermal and chemical stability. They can also display metallic, semiconducting and superconducting electron transport making them extremely attractive for the task of electrochemical detection [87]. In addition to these properties, CNT-modified electrodes have been shown to accumulate important biomolecules such as nucleic acids and enzymes [88] making them extremely attractive for biosensing. To this end, biosensors ranging from amperometric enzyme electrodes to DNA hybridization biosensors have been developed [55, 57, 82, 89].

CNTs can enhance the electrochemical reactivity of important biomolecules and can promote the electron transfer reaction of proteins (including those where the redox centers are embedded deep inside the protein shell). To take advantage of the remarkable properties of these nanomaterials, the CNTs need to be properly functionalized and immobilized [86, 90]. The purification of CNTs with oxidizing acids creates surface acid sites (mainly carboxylic moieties), which provide sites for covalent linking to biorecognition elements or for their integration onto polymer structures. Several ways for confining both, modified and unmodified CNTs onto the electrode have been described and most of electrochemical biosensors reported to date have relied on two basic configurations including conducting bulk-modified composites and electrode coatings.

CNT-based Biocomposite Electrodes

CNT-based biocomposite electrodes rely on the use of CNT as the sole conductive component of the transducer rather than utilizing it as the modifier in connection to another electrode surface. Carbon nanotube paste enzyme electrodes were prepared by mixing CNT with mineral oil [91]. Such composites combine the advantages of paste electrode materials with the ability of CNT to promote electron transfer reactions. The incorporation of glucose oxidase and alcohol dehydrogenase/NAD⁺ within the three-dimensional CNT/Teflon matrix maintained a marked electrocatalytic activity toward hydrogen peroxide and NADH and permitted effective low-potential amperometric biosensing of glucose and ethanol, respectively [92]. CNT-based inks [55] are also highly suitable for the microfabrication of thick film electrochemical sensors (i.e., screen-printed strip electrodes).

CNT-coated Electrode Transducers

The purification of CNT provides sites for covalent linking to biorecognition elements or for their integration onto polymer structures. In early works CNT-modified electrodes relied on casting a CNT/sulphuric acid solution onto glassy carbon surface [93]. Modified single-wall and multi-wall CNTs were also solubilized in perfluorosulfonated polymer (Nafion) with dramatic enhanced redox activity of hydrogen peroxide at CNT/Nafion-coated electrodes for oxidase-based amperometric biosensors [94]. This electrode offered highly selective low potential (−0.05 V vs. Ag/AgCl) biosensing of glucose with effective discrimination against both neutral and anionic constituents. The deposition of platinum nanoparticles onto Nafion containing CNT glucose oxidase film led to higher sensitivity compared to devices based on CNT or Pt nanoparticles alone [95]. Non-hydrophilic CNT were also employed for the preparation of an amperometric biosensor based on the incorporation of SWCNT modified with enzyme into redox polymer hydrogel (Fig. 15.10) [96]. This approach resulted in 2- to 3-fold increase in the sensor current output while the amount of accessible redox centers increased up to tenfold.

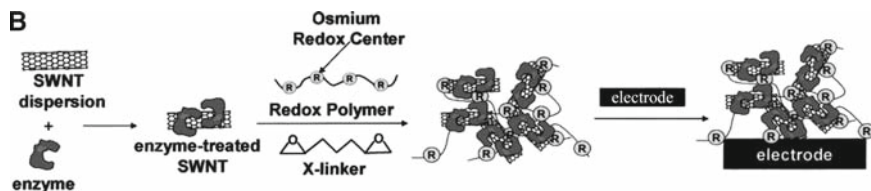


Fig. 15.10 Schematic of the construction of type-B sensors in which SWNTs were first incubated with an enzyme solution, before they were incorporated into the redox hydrogel. An aliquot of the redox hydrogel solution containing the enzyme-modified SWNTs was then cast on top of a bare glassy carbon electrode. (Reprinted with permission from [96]; copyright ACS publications)

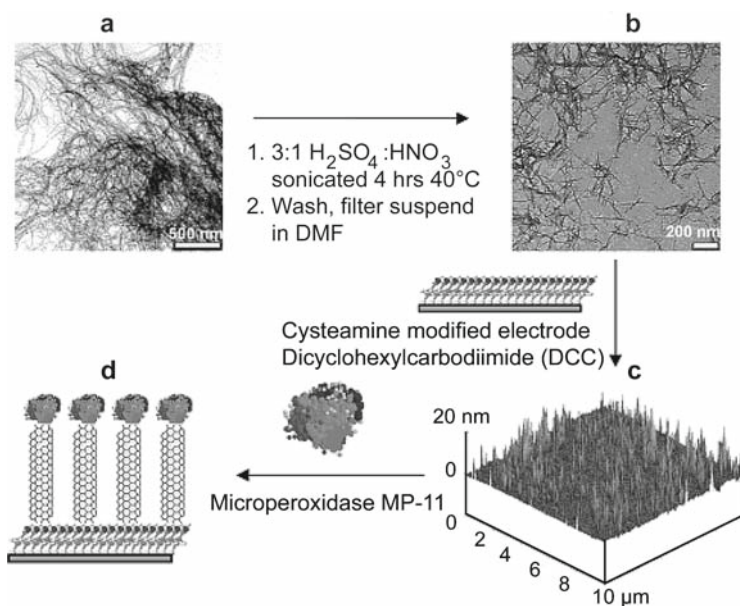


Fig. 15.11 Scheme showing the steps involved in the fabrication of aligned shortened SWNT arrays for direct electron transfer with enzymes such as microperoxidase (MP11). (Reprinted with permission from [97]; copyright ACS publications)

The electron transfer occurs when the tethered redox centers of the polymer collide with those of the CNT-immobilized enzyme.

A really effective CNT coating can be obtained by aligning short SWCNT normal to an electrode by self-assembling (Fig. 15.11). Such vertically aligned SWCNT act as molecular wires to allow electrical communication between the underlying electrode and the redox enzyme, i.e., the carboxylated open-end of nanotubes are used for enzyme immobilization and connection to electrode [97]. Their data indicates that “trees” of CNTs in the nanoforest behave electrically like a metal.

The direct electron transfer between the prosthetic group of the enzyme and electron surface of this configuration obviates the need for redox mediators, which is extremely attractive for developing reagent-less sensing devices. The reconstitution of glucose oxidase on a flavin-adenine-dinucleotide (FAD)-functionalized SWCNT associated with an Au electrode yields an electrically contacted biocatalyst [98]. The electrons were transported along distances higher than 150 nm, with the length of SWCNT controlling the rate of electron transport.

An attractive avenue for preparing amperometric biosensors was recently developed using CNT-nanoelectrode ensembles (NEEs) [89]. The low potential (-0.2 V vs. SCE) reductive detection of the hydrogen peroxide product led to highly selective amperometric monitoring of the glucose substrate along with linearity up to 30 mM glucose and a detection limit of 0.08 mM.

Enhanced electrochemical detection of biorecognition events, such as hybridization, has also been demonstrated using CNT. Highly-sensitive bioelectronic protocols for the detection of proteins and DNA were described recently based on the coupling of several CNT-derived amplification processes. In these procedures CNTs played a dual amplification role in both the recognition and transduction events, that is, as carriers for numerous enzyme tags and, for accumulating α -naphthol product of the enzyme reaction (Fig. 15.12). Coverage of around 9,600 enzyme molecules per CNT (i.e., binding event) was estimated. Such CNT-derived double step amplification procedure allows for the detection of DNA and proteins down to 1.3 and 160 zmoles respectively and indicates a great promise for PCR free DNA analysis [99].

15.2.2.3 Oxide Nanoparticles and Nanocomposites-based Electrochemical Biosensors

Oxide nanoparticles such as TiO_2 , ZrO_2 , Fe_3O_4 or MnO_2 have also been used to generate direct electron transfer between the protein and the electrode. For instance,

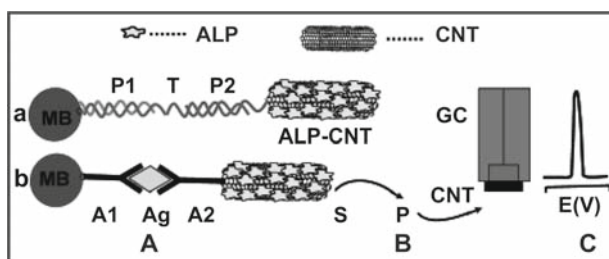


Fig. 15.12 Schematic representation of the analytical protocol: (A) Capture of the ALP-loaded CNT tags to the streptavidin-modified magnetic beads by a sandwich DNA hybridization (a) or A-Ag-A interaction (b). (B) Enzymatic reaction. (C) Electrochemical detection of the product of the enzymatic reaction at the CNT-modified glassy carbon electrode; *MB*, Magnetic beads; *P₁*, DNA probe 1; *T*, DNA target; *P₂*, DNA probe 2; *A₁*, first antibody; *Ag*, antigen; *A₂*, secondary antibody; *S* and *P*, substrate and product, respectively, of the enzymatic reaction; *GC*, glassy carbon electrode; *CNT*, carbon nanotube layer. (Reprinted with permission from [99]; copyright ACS publications)

horseradish peroxidase was mixed with TiO_2 nanoparticles and immobilized onto pyrolytic graphite electrode, which resulted in direct electron transfer [56]. Oxide nanoparticles can also be used as reporter units for biomolecules. Tris(2,2'-bipyridyl)cobalt (III) $[\text{Co}(\text{bpy})_3^{3+}]$ -doped SiO_2 nanoparticles labeled DNA probe was used to hybridize with target DNA immobilized on glassy carbon electrodes with a detection limit as low as 200 pM of the targeted nucleotide [100]. However, the use of SiO_2 for biosensing has been mainly realized in the form of nanoparticles networks (gels) that entrapped nanopores susceptible to be filled with active groups.

Sol-gel derived materials allow for a wide range of electrode compositions [51–53, 101–103]. Sol-gel-electrochemical biosensing materials, developed to date, have served primarily as microporous support matrices for the recognition element. The encapsulation of an enzyme within the oxide matrix is usually performed in the presence of conducting species including graphite, palladium, or colloidal gold [53, 104]. Ormosils (organically modified silica) and polymers are generally used to modulate enzyme activity. The organic mediator or metallic particle catalysts are easily dispersed into the resulting composites by adding them in the starting sol to facilitate communication between the enzyme and the conducting composite. Such processing technology has been used for the design of multilayer thin films in which the enzyme is sandwiched between the electrode surface and a silicate layer or between two silicate layers deposited as a three-layer architecture at the electrode/solution interface [101, 103, 105]. Sol-gel processing can be used for the preparation of electrochemical immunosensors [102]. The process has been coupled with the screen-printing technology to allow one-step mass production of low-cost antigen-containing strips. The encapsulated antigen is readily accessible to the enzyme (alkaline phosphatase)-labeled antibody, with dispersed graphite offering a facile amperometric detection of phenolic products. The sensor response can be tuned by tailoring the porosity of the ceramic-carbon matrix.

15.2.3 Magnetobiosensors

In recent years, there has been an increasing interest to use magnetic nanocomposites in biomedical applications. Magnetic nanoparticles are suitable for use in biosensor applications since their magnetic properties allow relatively easy (and remote) detection. Their large surface-to-volume ratio and mobility speed up the chemical reactions, e.g. in micro cavities where the mixing is otherwise slow. New methods have been presented in order to quantify the amount of biomolecules in a liquid using the magnetic properties of the nanocomposites [106, 107].

15.2.3.1 Magnetobiosensors Based on Magnetorelaxometry

Magnetorelaxometry was recently introduced as a method for the evaluation of immunoassays [108]. Magnetorelaxometry measures the magnetic viscosity, i.e.,

the relaxation of the net magnetic moment of a system of magnetic nanoparticles after removal of a magnetic field [109]. In a magnetic single domain (iron oxide ferrite nanoparticles normally used in these applications are single domain) there are two different relaxation mechanisms: Néel and Brownian mechanisms. When the internal magnetization vector of a nanoparticle relaxes in the direction of the easy axis inside the core, the so-called Néel relaxation is involved. The time constant of this process is:

$$\tau_{\text{Néel}} = \tau_0 \exp(KV_{\text{core}}/k_B T)$$

where τ_0 is usually approximated to 10^{-9} s. The Néel relaxation time depends exponentially on the energy barrier yielded by the product of core volume V_{core} and magnetic anisotropy constant K . In real systems of magnetic nanoparticles, the common distribution of the core volumes and anisotropy constants leads, via the Néel mechanism, to a modified logarithmic decrease in magnetization versus time [110]. Particles accomplish rotational diffusion in a carrier liquid, called Brownian relaxation, in which the corresponding relaxation time is often calculated according to [111]:

$$\tau_{\text{Brown}} = 4\pi r^3 \eta / k_B T$$

assuming non-interacting spherical particles with a hydrodynamic radius r , where η is the dynamic viscosity of the carrier liquid. For an ideal system of monodispersed particles, the time-dependence of the Brownian relaxation is a single exponential decay. For polydisperse nanoparticles with different particle sizes it can be described as a superposition of exponential decays. This relaxation signal still looks like an exponential decay. Therefore, Néel and Brownian relaxations can be distinguished by their different time dependence [112]. Furthermore, Brownian relaxation can take place only in liquids, whereas Néel relaxation does not depend on the state of the nanocomposites. The fact that magnetorelaxometry depends on the core size, the hydrodynamic size and the anisotropy allows this technique to distinguish between free and bound conjugates through their different magnetic behavior. Therefore this technique can be used as an analytical tool for the evaluation of immunoassays [109].

Measurement of the complex frequency-dependent magnetic susceptibility is a standard characterization method for magnetic liquids containing magnetic nanoparticles [113, 114]. Using this method [106] it is also possible to determine and quantify changes in relaxation mechanisms of magnetic nanoparticles after appropriate coating with biocompounds. The idea behind the method is to use magnetic nanocomposites that are thermally blocked in order to study the change in the Brownian relaxation time induced by changes of particle–fluid coupling, for example, when biomolecules are bound to the surface of the particles. When both the real χ' and imaginary χ'' components of the complex susceptibility $\chi = \chi' + \chi''$ are measured, a maximum in the imaginary component and a steep decrease in the real component at the frequency f_m are obtained:

$$f_m = 1/(2\pi\tau)$$

Determination of f_m and of the curves shapes of χ' and χ'' versus frequency enables one to study how the adsorption of biomolecules changes the Brownian relaxation time of the suspended particles. This change is mainly due to the varying hydrodynamic volume of the nanoparticles, since the change in the physical volume of the particle due to adsorption of biomolecules is negligible compared to the nanoparticle volume. The frequency shift will depend on the amount of biomolecules adsorbed by the nanoparticles.

15.2.3.2 Magnetobiosensors Based on Magnetoresistance

The idea of using a magnetic field sensor based on magnetoresistance technology in combination with magnetic nanoparticles working as magnetic labels for detecting molecular recognition events (antigen – antibody interaction, ligand –receptor binding) was first reported a few years ago [115]. Such a biosensor used magnetic nanoparticles encapsulated in polymer spheres for simultaneous characterization of many biomolecular interactions. An alternative geometry was proposed for a magnetoresistive prototype of biosensor to detect a single micron-sized magnetic sphere by a ring element based on anisotropic magnetoresistance [116].

In any case, it is clear that the next generation of magnetic biosensors must be based upon new physical properties that could allow high sensitivity, small size, low power consumption, stability of operation parameters, fast response, resistance to aggressive medium, and low price. To this end, a biosensor prototype based on giant magnetoimpedance has been recently developed [117]. These authors detect a change in giant magnetoimpedance when using superparamagnetic nanoparticles encapsulated in polymer microspheres that were coated with an antibody. Grancharov et al. have developed a novel method for detecting either protein binding or DNA hybridization at room temperature using 12-nm poly(ethylene glycol) phosphatidylethanolamine-manganese ferrite nanoparticles and a magnetic tunnel-junction-based biosensor situated in orthogonal magnetic fields [118].

15.3 Nuclear Magnetic Resonance Imaging (MRI)

The clinical introduction of MRI in the early 1980s revolutionized diagnostic imaging. The breathtaking progress in computer technology has made multidimensional imaging a reality, producing images within seconds without time-consuming data processing. These techniques allow physicians to accurately diagnose pathologies noninvasively [119]. Reflecting the fundamental importance and applicability of MRI in the medical field, Paul Lauterbur and Sir Peter Mansfield were awarded the 2003 Nobel Prize in Medicine for their discoveries concerning MRI.

The nucleus of an atom is built up of a number of protons and neutrons. Because the atomic particles are grouped in pairs that rotate in different directions, atoms with an even number of protons and neutrons display no external rotation. Nuclei in H^1 , F^{19} or P^{31} , display a weak external rotation or spin. Such nuclei also display a vibration effect or precession. Every object that can be made to vibrate will do so more strongly under the influence of a force applied at the same frequency as the natural resonant frequency of the object. A similar resonance effect occurs when atomic nuclei are subjected to electromagnetic waves at their own vibration frequency.

Among the substances in the human body that are important for MRI construction, namely H^1 , P^{31} , and Na^{23} , the first one (H^1) gives by far the strongest signal since it is present in almost all tissues and organs. When nuclei of elements with a weak external spin are placed in a strong homogenous magnetic field, they align themselves with the direction of the field. When a force is applied on the spinning atomic nuclei by a radio frequency at the so-called Larmor frequency, perpendicular to the direction of the magnetic field, the nuclei are tilted away from the aligned equilibrium direction and will perform a precession around the direction of the magnetic field. During this displacement from the equilibrium orientation the nuclei absorb energy. As soon as the radio frequency or excitation is removed, the nuclei will reorientate in the direction of the homogeneous field. The time constant describing the return movement of a group of nuclei to the field direction, or longitudinal direction, is known as the longitudinal or spin-lattice relaxation time T_1 . Since the local magnetic field strength is not homogeneous due to the presence of neighboring atoms, the nuclei precess at slightly different frequencies. As a result, the various nuclei fall out of phase with each other so that, although still rotating, they rapidly adopt different orientations in space. The resonance signal emitted from the nuclei interfere with each other, resulting in a rapid decay of the received signal. The time constant describing this process is known as the spin-spin relaxation time or transverse relaxation time T_2 . T_1 and T_2 are dependent on the temperature, magnetic field strength and on the chemical compound in which the atom is bound. In liquids, nuclei are relatively free so that T_2 is almost as long as T_1 . In solids, the interaction between nuclei is much greater so T_2 is much shorter than T_1 .

The development of the MRI as a clinical diagnostic modality has prompted the need for contrast agents. Characteristics of contrast agents and methods for their detection vary widely [120]. Historically, the most commonly used agents are small paramagnetic metal chelates, which act by shortening T_1 relaxation times [121]. MRI sensors have been constructed from these agents by coupling determinants of their T_1 relaxivity – solvent accessibility, rotational correlation time, or the spin and redox state of the metal to the presence of specific molecular targets. Sensors based on T_2 relaxation rate changes have also been produced, most recently by coupling the aggregation state of superparamagnetic iron oxide nanocomposites (SPIOs) to physiological signals of interest. Aggregation of SPIOs even in concentrations as low as 10 mg L^{-1} can change observed T_2 s quite dramatically. A third family of MRI sensors has been based on chemical exchange saturation transfer (CEST) effects [122]. Labile protons or water molecules bound to a CEST agent can be

selectively saturated and will exchange with bulk solvent protons to decrease the local MRI signal. In CEST-based sensors, the exchange rate or chemical shift of bound protons is modulated by interaction with the sensor's target.

15.3.1 Paramagnetic Contrast Agents

Bloch first described the use of a paramagnetic salt, ferric nitrate, to enhance the relaxation rates of water protons [123]. Later on, Lauterbur et al. were first to show the feasibility, exploiting paramagnetic agents for tissue discrimination on the basis of differential water proton relaxation times [124]. Since this pioneering work, many studies have been carried out on the use and development of paramagnetic contrast agents.

Focusing on hybrid nanocomposites, there is an active interest in the development of hybrid paramagnetic nanoparticles incorporating high payloads of paramagnetic substances with high molecular relaxivities to compensate for the inherent high threshold of detectability of MR contrast agents [125]. An approach that has recently been explored to enhance efficiency in MRI is based on the incorporation of paramagnetic substances in the protein nanocage of viruses [125, 126]. For example, the protein cage of Cowpea chlorotic mottle virus (CCMV), having 180 metal binding sites, is being explored to load Gd^{3+} contrast agents. In vivo CCMV binds Ca^{2+} at specific metal binding sites, however Gd^{3+} can also bind at these sites. The T_1 and T_2 relaxivities of solvent water protons in the presence of Gd^{3+} -bound CCMV is found to be unusually high as a result of the nanoparticle virus size and the large number of Gd^{3+} ions bound to the virus.

Dendrimers have emerged in biomedical research as versatile platforms for the preparation of nanomaterials with desired properties [127]. The term "dendrimer" is derived from the Greek "dendra" = tree and "meros" = part and describes graphically the structure of this new class of macromolecules which have highly branched, three-dimensional features that resemble the architecture of a tree [128]. A typical dendrimer consists of three main structural components: a multifunctional central core, branched units and surface groups. The branched units are organized in layers called "generations", and represent the repeating monomer unit of these macromolecules. The radial structure of the dendrimers was used for the first time in 1998 to prepare dendrimers-encapsulated metallic nanoparticles [129]. The high versatility of the dendrimers has been recently explored [130] for the preparation of paramagnetic contrast agents with dual functionality derived from the incorporation of fluorescence molecules in the Gd-dendrimer nanocomposites (Fig. 15.13).

Finally an area of recent interest in the use of hybrid nanocomposites as paramagnetic contrast agents for MRI is the development of nanoscale metal-organic frameworks. Particularly, Rieter et al. have recently prepared $Gd(BDC)_{1.5}(H_2O)_2$ nanorods (where BDC is 1,4-benzenedicarboxylate) that have been shown to exhibit large relaxivities and even luminescence when doped with Tb^{3+} dopants [131].

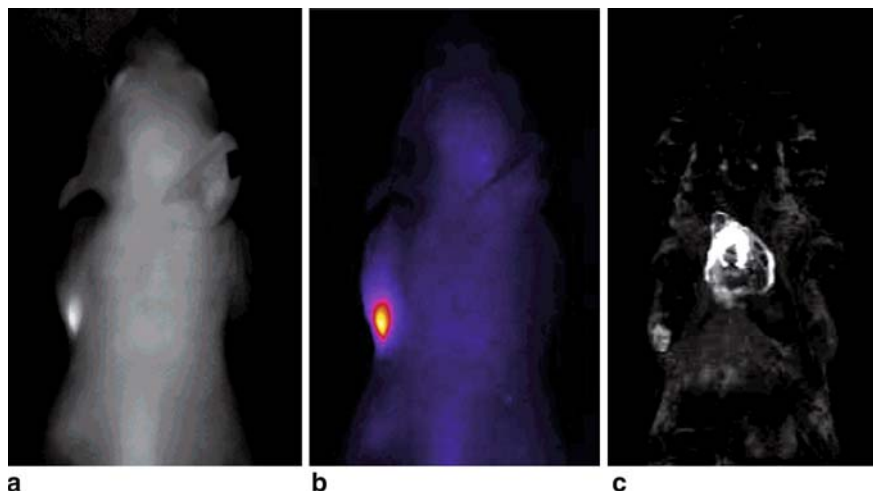


Fig. 15.13 Sentinel lymph node images of a normal mouse. **(a)** Optical image obtained under simultaneous white light and filtered (615–665 nm) excitation light detected with the emission filter set to 720 nm demonstrating fluorescence in the axillary lymph node of the mouse. The injection site cannot be seen because it is on the front of the mouse. **(b)** Image from **(a)** shown in false color. **(c)** Maximum intensity projection calculated from a 3D spoiled gradient echo MRI acquired using a GE Signa Excite 3T 30 min post-injection (TR, 9.5 ms; TE, 2.3 ms; FA, 30°), which illustrates the injection site in the mammary fat pad, the draining lymphatics, and axillary lymph node depicted in **(b)**. (Reprinted with permission from [130]; copyright ACS publications)

15.3.2 Superparamagnetic Contrast Agents

First introduced as contrast agents in the mid-1980s [132–134] hybrid superparamagnetic nanocomposites have been used in MRI for localization and diagnosis of brain and cardiac infarcts, liver lesions or tumors, where the nanoparticles tend to accumulate at higher levels due to the difference in tissue composition and/or endocytotic uptake processes ([135] and references therein). Especially promising results have been obtained in the improvement of sensitivity of detection and delineation of pathological structures, such as primary and metastatic brain tumors, inflammation and ischemia [136]. One of the potential applications of the magnetic nanoparticles is to enhance the sensitivity in order to image tissue microcirculation with the goal of direct quantitative measurement of blood flow and blood volume [137].

Superparamagnetic nanoparticles represent an alternative class of NMR contrast agents that are usually referred to as T_2 or T_2^* contrast agents, as opposed to T_1 agents such as paramagnetic chelates ([135] and references therein). The change in relaxation time produced by magnetic particles is a contribution of several complex mechanisms. The size and the composition of these particles represent the essential parameters. The particles possess very large magnetic moments in the presence of a static magnetic field, and dipolar interactions between the superparamagnetic

cores and surrounding solvent protons result in decreasing both longitudinal and transverse relaxation times.

For MRI, superparamagnetic contrast agents that consist of maghemite-magnetite core nanoparticles encapsulated in a polysaccharide of the dextran family are normally used ([135] and references therein). Usually, the way dextran is added to the magnetic nanoparticles is by coprecipitation from aqueous solutions containing the iron oxide precursors and the polysaccharides. Endorem[®] (magnetite nanoparticles coated with dextran) is the commercial name of superparamagnetic iron oxides (SPIOs) available on the market [138]. SPIO contrast agents are used for gastro-intestinal tract imaging and for liver and spleen diseases detection because of their relative large hydrodynamic size. In the case of Endorem[®], the massive uptake of nanoparticles by Kupffer cells allows to increase the contrast between the healthy and the diseased tissue, like tumors or metastases devoid of Kupffer cells [138].

In order to obtain aggregates with smaller hydrodynamic size and to increase the blood circulation time of the preparations, the addition of a higher proportion of dextran combined with ultrafiltration with Amicon YM300 membrane was carried out. Ultrafiltration assures the presence of smaller aggregates in the final dispersions while the addition of an extra amount of dextran assures invisibility against the plasma proteins, that is longer blood circulation times. The resulting colloidal composites are also known as Ultra small SuperParamagnetic Iron Oxides (USPIO) due to their extremely small hydrodynamic size (20–30 nm). Sinerem[®] (magnetite nanoparticles of 30 nm in diameter coated with dextran) is an example of an USPIO that could be commercialized [138]. Due to their long-circulating properties, USPIOs can be used for blood pool and tumor imaging (experimental imaging), based upon the detection and characterization of the lesions by their vascular appearance. Sinerem[®] has been used for lymphography of hyperplastic or metastatic (metastasis of a nickel-induced rhabdomyosarcoma) lymph nodes in rats, after intravenous administration. Another USPIO device consisting of monocrystalline iron oxide nanoparticles (MION-46, a nanoparticulate contrast agent designed specially for lymphography, coated by an extended dextran layer, exhibiting a hydrodynamic diameter of 20 nm) was also tested in rats and rabbits to detect lymph node metastases (metastasis of VX2 carcinoma) and tumor-associated lymph node hyperplasia, using different administration routes (subcutaneous, intravenous and intra-arterial) [139]. In both assays, hyperplastic lymph nodes showed NMR images consistent with an active uptake and a clustering inside the macrophages of lymphatic sinuses [139, 140].

One area of growing interest in the use of hybrid magnetic nanoparticles in medical imaging is specific cell tracking [141]. The ability to load enough nanosized particles in cell cultures using various methods, such as cell permeable peptides and transfection agents in combination with the magnetic nanoparticles, has provided a useful technique to label and track nonphagocytic cells *in vivo* using MRI [142]. This method has allowed researchers to study the distribution of stem cells [143].

Although commercial preparations are available on the market to be used as contrast agents, one area in which significant efforts are being carried out is the development of new synthetic routes able to produce preparations with improved properties. For example, biocompatible hybrid magnetic dispersions have been

prepared from hybrid Fe nanoparticles (12 nm) synthesized by continuous laser pyrolysis of $\text{Fe}(\text{CO})_5$ vapors [144]. The feasibility of these dispersions to be used as MRI contrast agents has been analyzed in terms of chemical structure, magnetic properties, ^1H NMR relaxation times and biokinetics. The results showed a contrast improvement of 60% in the liver with respect to commercial samples, which suggests that this product could be a suitable contrast agent for MRI imaging of liver and spleen.

Li et al. [145, 319] have recently reported a novel one-pot preparative approach based on the thermal decomposition of iron (III) precursors for the preparation of new USPIO contrast agents [145]. Using this method, the authors are able to synthesize magnetic nanoparticles (10 nm in size) covalently coated with mono-carboxyl-terminated poly(ethylene glycol) resulting in hydrodynamic sizes of about 20 nm. MRI experiments performed in living rats demonstrate that these particles have a very good biocompatibility and can be potentially used as contrast agents (Fig. 15.14). Particularly, the long-circulation time of these particles makes them useful for vascular compartment imaging. In fact, these authors mention that preliminary results have shown that small vessels in the cerebral tissue can be easily identified. Uniform hybrid magnetite nanoparticles synthesized by thermal decomposition of iron (III) acetylacetonate in a hot organic solvent and subsequently modified with 2,3-dimercaptosuccinic acid have also been tested for MRI [146]. It was observed that as the particle size increases from 4 to 12 nm, the T_2 -weighted MR signal intensity continuously decreases, which in turn leads to darker MR images, in accord with the increase in saturation magnetization. Furthermore, this material was tested for cancer diagnosis by conjugating the shell ligand with a cancer-targeting antibody, Herceptin, showing excellent selectivity.

Magnetoliposomes (magnetic nanoparticles encapsulated in liposomes) could also be used as MRI contrast agents ([147] and references therein). The advantage of using magnetic liposomes instead of USPIOs is that different biomedical functions can be implemented [148] through conjugation with biological ligands.

15.4 Drug Delivery

Engineering delivery systems of therapeutic agents has grown into an independent field, transcending the scope of traditional disciplines and capturing the interest of both academic and industrial research. At the same time, the acceleration in the discovery of new therapeutic moieties (chemical, biological, genetic, and radiological) has led to an increasing demand for delivery systems capable of protecting, transporting, and selectively depositing those therapeutic agents at desired sites [149, 150]. The use of an appropriate targeted drug delivery system can promote the efficiency of an active compound because the drug is only delivered to specific sites, thus avoiding the possible marked side-effects associated with abundant drug concentration in the case of nontargeted delivery.

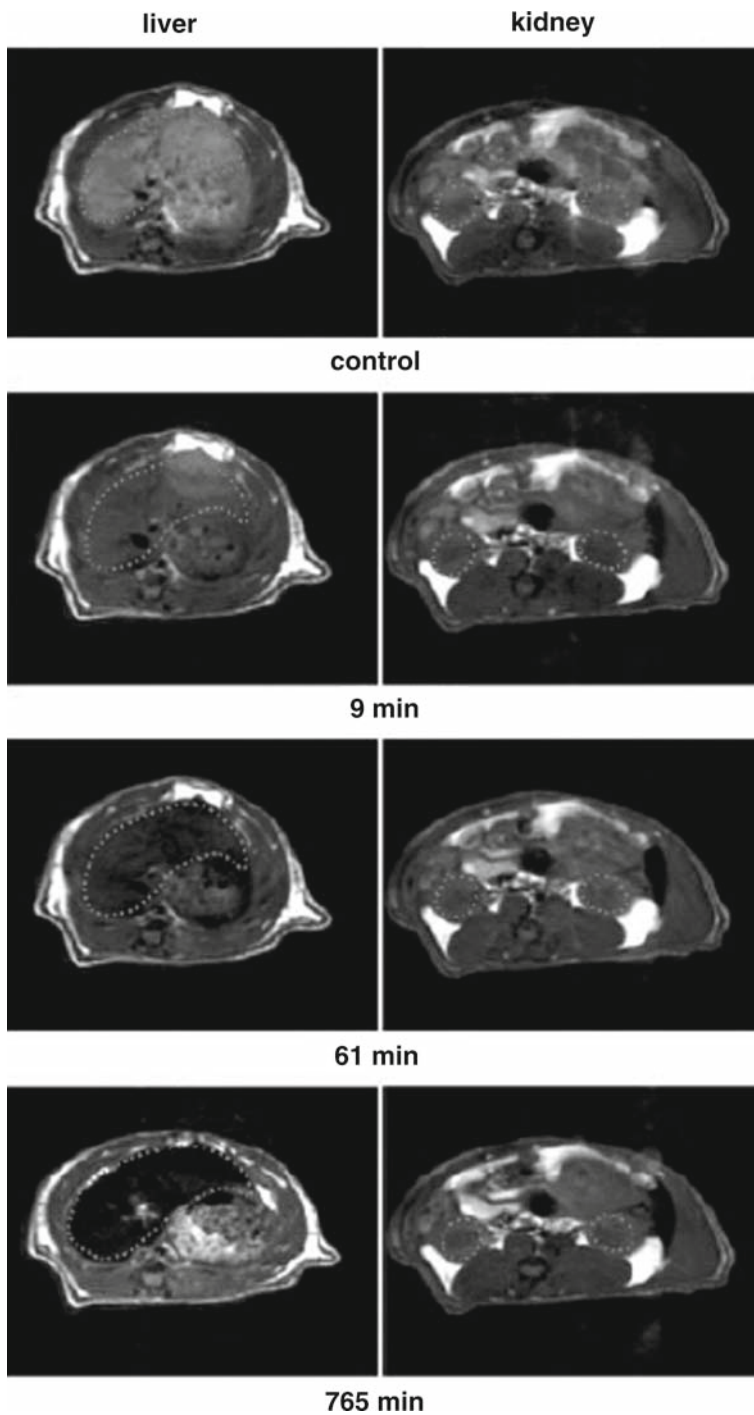


Fig. 15.14 Spin-echo abdomen magnetic resonance images of a living rat. Images in the first row were acquired before injection of the magnetic nanoparticles, and those from the second to the fourth row were captured at different times. (Reprinted with permission from [145]; copyright Wiley-VCH publications)

15.4.1 *Hybrid Nanocapsules as Vehicles for Drug Delivery*

Many natural and artificial objects are subjected to degradation by the surrounding environment. It is particularly important to protect compounds that can be damaged by irradiation, heating, oxidizing (reducing) agents, polymers, moisture, etc. at the molecular level during their storage and targeted delivery. Such substances are of practical importance in medicine (drugs), gene engineering (DNA, RNA), biotechnology (proteins, individual cells, enzymes), and in the food industry. The development of protective microenvironments combining the defense property with other properties, such as, for instance, the possibility of controlled release of the secured compound at the desired site in aggressive media, is of particular interest. Hybrid nanocapsules are probably the most suitable materials for this purpose. The use of hybrid nanocapsules is not casual because these latter aim to mimic the most sophisticated entities found in nature, working as carrier and vehicle to deliver and release substances or cells. Thus, liposomes, taken as models of biological membranes, are of fundamental importance because they serve as selective barriers for transport, as fluid matrixes for biosynthetic transformations, and as boundaries for the transfer of energy and information. Lipid bilayer vesicles are also well known nanomaterials, which have been extensively employed as supramolecular assemblies to construct molecular devices [151–159].

The performance of any of these biomimetic applications strongly depends on the membrane fluidity. For instance, the interest in using phospholipids vesicles as nanocapsules and vehicles to entrap, deliver and control-release functional substances (e.g. proteins, enzymes and drugs) resides in two main features [160]. Firstly, the bilayer can behave as a barrier and provide protection to the molecules encapsulated in the interior aqueous phase from the aggression of external denaturing agents. Secondly, entrapped molecules can be control-released in response to a variety of physical and chemical stimuli (including temperature, pressure, light, pH, and ions) that, as mentioned above, determine the bilayer fluidity and thus, its permeability [161]. In general, liposomes change their aggregate morphology by collapse and fusion when they interact with polyelectrolytes having the opposite charge. Obviously, a drastic increase in the morphological stability of liposomes seems to be quite desirable if one intends to apply these structures for practical purposes.

An example where the fragility of the liposome structure limits its applicability is that reported recently by Matsui et al. [162]. As the number of functions of nucleic acids continues to expand, there is a growing need for efficient delivery of functional nucleic acids. Since the discovery of lipofection [163], cationic lipids have been widely used as transfection agents in gene delivery [164]. They form liposomal bilayers in water. Polyanionic DNAs are readily bound to the resulting cationic liposomes to give complexes (lipoplexes) which are inserted in the cells via endocytosis to ultimately result in expression of the encoded gene. The bilayer-keeping forces are not very strong, and liposomes are not so rigid or robust. They are potentially fusible with cell membranes and hence toxic. They also easily undergo DNA-mediated/induced cross-linking/fusion to give larger particles (>> 100 nm) that have lower endocytosis susceptibility [164–167] and poorer vascular mobility. This problem has been challenged, occasionally, in the context of artificial

viruses, with different strategies of mostly multicomponent surface coverage such as stabilized plasmid–lipid particles [168], saccharide-manipulated particles [169], dimerizable cationic detergents [170, 171], liposome- μ -DNA systems [172, 173], glycoviruses [174], and PEG-stabilized plasmid nanoparticles [319].

The Nara group recently reported a ceramic-coated liposome and called it “cerasome” [175]. A cerasome is a novel bioinspired organic–inorganic hybrid composed of a liposomal membrane with a ceramic surface. The cerasomes were prepared from organoalkoxysilane proamphiphiles (**1** and **2** in Fig. 15.15) under sol–gel reaction conditions [162]. Formation of the bilayer vesicular structures of the cerasomes was confirmed by negative-staining transmission electron microscopy (TEM). The obtained diameter from TEM observation was 70–300 nm and 20–100 nm for the cerasomes prepared from **1** and **2** (Fig. 15.15), respectively. These cerasomes had characteristic properties as lipid bilayer vesicles, e.g. phase transition behavior from gel to liquid-crystalline state. The authors have focused on the consequence of surface rigidification of the cerasome as a gene carrier. They report that the cerasome retains its integrity in the complexation with plasmid DNA (pGL3) and the resulting DNA complex of infusible or monomeric cerasome in a viral size (~ 70 nm) exhibits a remarkable transfection performance (high activity, minimized toxicity and serum-compatibility). They experimentally examined the cerasome **1**-mediated transfection of HeLa (uterine) and HepG2 (hepatic) cells using a fixed amount (200 ng, 0.6 nM or 6.25 μ M P) of pGL3 and a variable amount

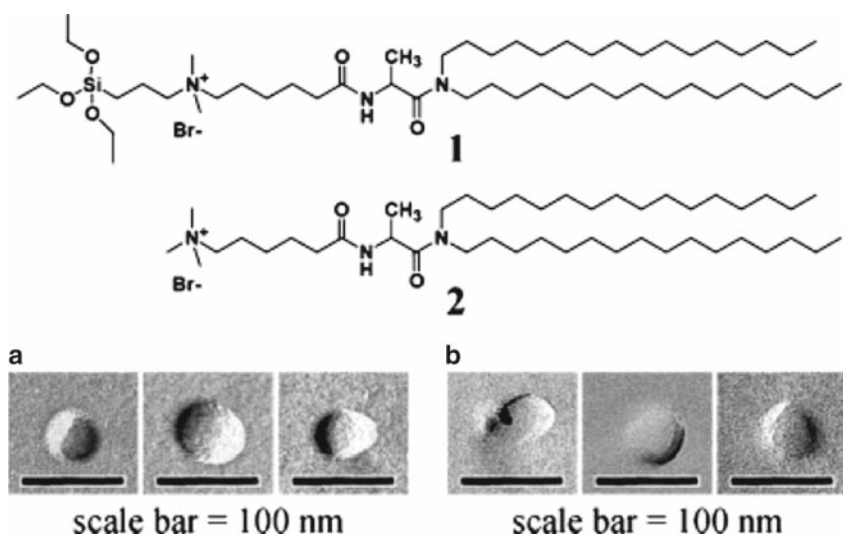


Fig. 15.15 Structures of lipids **1** and **2** and freeze-fracture TEM images of the liposomes formed with lipid **1** (a) or **2** (b) in water at 12.5 μ M. Approximately ten independent images were taken for each lipid; three of them, including the smallest one and the largest one, are shown. (Reprinted with permission from [162]; copyright ACS publications)

of lipid **1** [162]. The results indicate that neither the transfection-responsible cerasome-plasmid complex (~70 nm) nor the DNA-free cerasome (60–70 nm) is toxic under the present transfection conditions. Reference lipid **2**, on the other hand, turned out to be far less active and far more toxic. Interestingly, the big difference in activity of $1/2 = 10^{2-3}$ (serum-free) is in agreement with the size-activity correlation revealed for glycoviruses [174]. This large activity ratio can thus be explained primarily in terms of the difference between the sizes of *monomeric 1*-plasmid complex (~70 nm) and *fused 2*-plasmid complex (≥ 200 nm), although a possible difference in aggregation behavior should also be taken into account. The presented *monocomponent* silicon strategy provides a simple and widely applicable new tool to overcome these general problems inherent to the current technology of artificial gene delivery. Size control is particularly crucial for in vivo applications. Particles of viral size (mostly 30–100 nm) have not only good diffusion in vascular periphery, but also good permeation into malignant tissues by the so-called EPR effect [176].

The recently developed layer-by-layer (LbL) technology [177, 178] also offers the opportunity to fabricate multifunctional nanoengineered microcontainers. This technology is based on sequential deposition of oppositely charged polyelectrolytes on a surface of variable shape, which allows the formation of multilayer shells from a wide range of components with nanometer precision. Templating of LbL polyelectrolyte films on the surface of the micron- and submicron-sized isolated particles followed by their dissolution leads to the formation of hollow polyelectrolyte capsules [179–181]. The initial colloidal core determines the size of the capsules, which can be varied from 50 μm to 50 nm. The polyelectrolyte shell is permeable for small molecules and ions [182, 183], while large molecules and nanoparticles can be entrapped inside or banned from the capsule interior. Sustained release of the encapsulated furosemide, dextran and fluorescein molecules was demonstrated [184–186]. Different additional functionalities (magnetic, luminescent, sensing) can be imparted to the capsule shell by introducing nano- Fe_3O_4 , q-CdS, etc. as shell constituent [187, 188]. The protective character of polyelectrolyte microcapsules has been demonstrated in a recent work [189]. The protecting ability of the developed polyelectrolyte capsules was monitored by oxidation of encapsulated bovine serum albumin by H_2O_2 dissolved in aqueous solution. Two approaches for designing protective capsule microcontainers are demonstrated (Fig. 15.16): The “passive armor” approach is composed of a sacrificial reducing agent as a shell constituent, while the “active armor” approach includes the catalyst for H_2O_2 decomposition deposited onto the shell as the outer layer. In the latter case, the protective material is not consumed during the H_2O_2 treatment, thus prolonging the protection activity of the microcapsule. Advances in the field of capsules are in the direction of the combined use of LbL and organoalkoxysilane-type lipids (Si-lipid) with a polymerizable moiety in the headgroup, which yields robust lipid coatings on core-shell colloids [190]. The particle-supported Si-lipid membrane was found to be highly stable upon exposure to Triton X-100 and ethanol solutions, even at high concentrations. The enhanced stability of the Si-lipid film is attributed to the polymerized moiety in the headgroup of the synthetic lipids and H-bonding interactions between adjacent

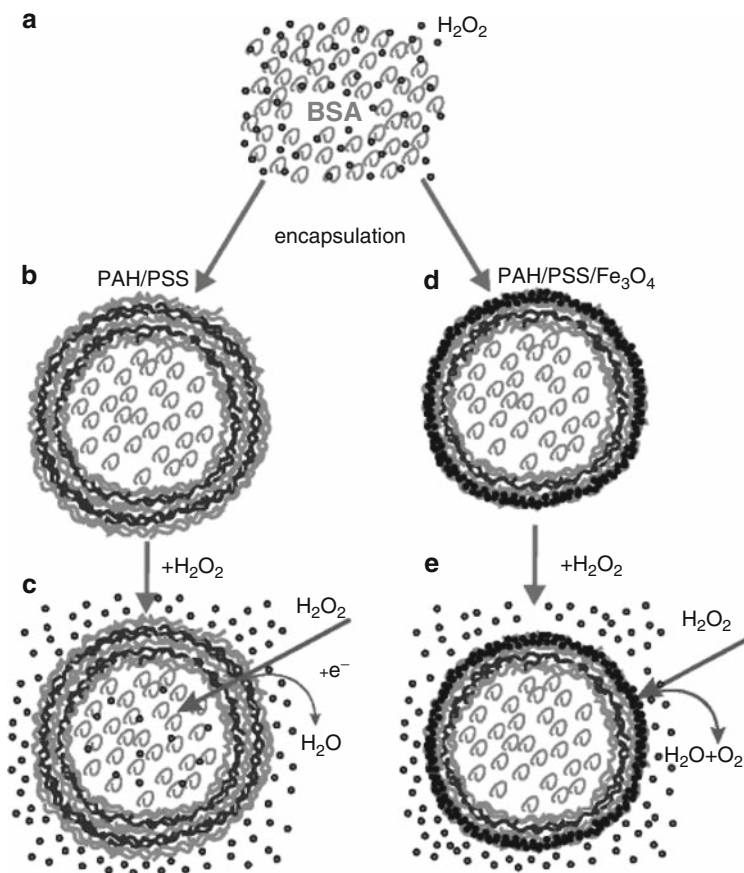


Fig. 15.16 Schematic overview of the “passive” and “active” protection approaches for nanoengineered polyelectrolyte capsules. (Reprinted with permission from [189]; copyright ACS publications)

Si-lipid molecules. The robustness of the inorganic lipid-based shell allows the removal of the core without significant delamination of the Si-lipid, providing a viable approach to the preparation of lipid-functionalized capsules.

There has also been increased interest in mesoporous silica materials for their use as carriers in controlled drug release. Amorphous mesoporous silica materials have been investigated as drug supports because of their nontoxic nature, adjustable pore diameter and very high specific surface area with abundant Si-OH bonds on the pore surface [191–200]. Several research groups have investigated the conventional mesoporous silica materials (such as MCM-41 and SBA-15) used as drug-delivery systems. These systems exhibit sustained-release properties, but their drug storage capacity is relatively low and, also, the irregular bulk morphology is not perfect for drug delivery. To overcome these disadvantages, one strategy is to

synthesize hollow mesoporous silica (HMS) spheres on the nanoscale with pore channels penetrating from the outside to the inner hollow core. Recently, Li et al. have successfully synthesized HMS spheres with a 3D pore-network shell [201, 202]. Later on, they proposed a strategy to combine the advantages of HMS spheres with a 3D pore network and polyelectrolyte multilayers with a stimuli-responsive property [203] (Fig. 15.17).

Nonetheless, inorganic hollow silica or polyorganosiloxane nanoparticles can also be prepared by direct template approaches. Schacht et al. have prepared the hollow silica spheres in oil/water emulsions, which resulted from an interfacial reaction [204]. Pinnavaia and coworkers introduced the silica into the interlayer regions of the multilamellar vesicles to form nearly spherical particles with stable lamellar mesostructures [205]. The ultrastable mesostructured silica vesicles were also reported by the same group using the neutral gemini surfactants as the

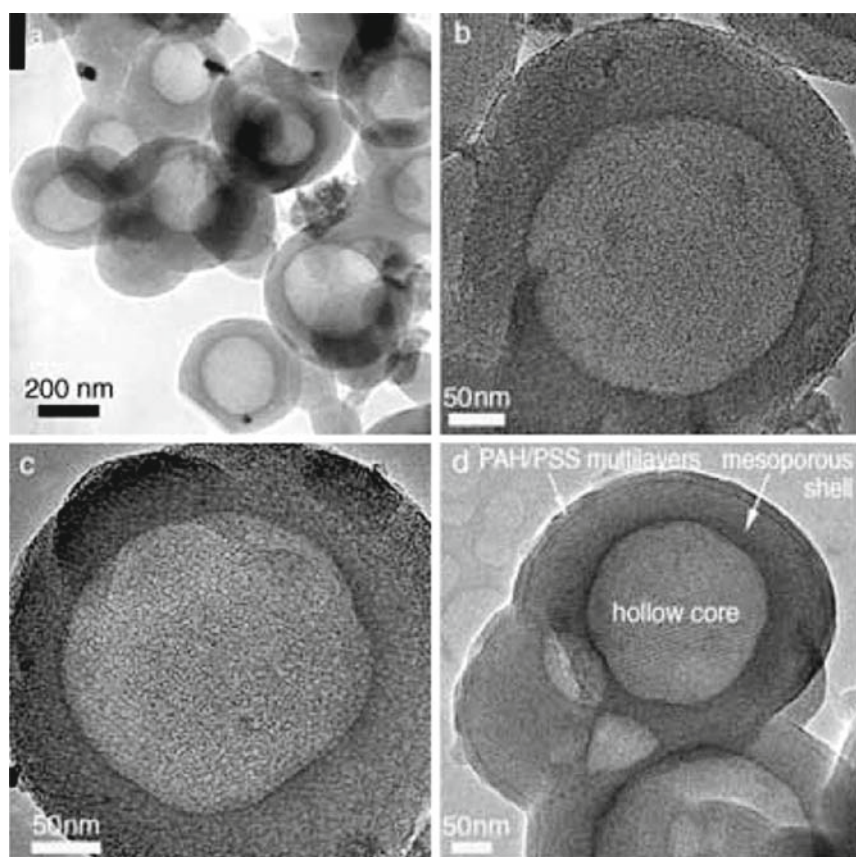


Fig. 15.17 TEM micrographs of HMS (a and b), the IBU-HMS system (c), and the IBU-HMS@PEM system (d). (Reprinted with permission from [203]; copyright Wiley-VCH publications)

structure-directing agents [206]. An organic/inorganic hybrid vesicle was prepared by gelation in the vesicles given by a lipid bearing an alkoxysilyl head, and a hierarchical vesicle assembly was made through an LbL approach [175, 207]. The colloids have been used as the templates for forming the inorganic shells. The linear polysiloxane colloids, as the templates formed *in situ* in an emulsion polymerization, were further coated with a cross-linked polysilsesquioxane shell by gelation of trimethoxymethylsilane, and the hollow particles were formed through extraction of the soluble core by a solvent [208, 209]. Functional molecules such as dyes were encapsulated in the siloxane network and in the cavity of the hollow particles [210].

In a very recent report, the hybrid core shell particles were prepared by coating the surfaces of monodisperse polystyrene beads with uniform silica shells [211]. Hollow silica spheres could be obtained by removing the polymer cores via calcination or by wet etching with toluene. The surfaces of block copolymer micelles have also been coated with a silica layer by reacting with an active silicate, making use of a few trimethoxysilane groups born on the corona-forming blocks of the micelles [212]. Recently, the same group has reported preliminary results on the preparation of such hollow nanoparticles using a novel reactive diblock copolymer, poly(ethyleneoxide)-*block*-poly[3-(trimethoxysilyl) propyl-methacrylate], which was synthesized by atom-transfer radical polymerization [213]. Pictures obtained by typical TEM and scanning electron microscopy -clearly showing the three-dimensional vesicular morphology- of the hybrid vesicles are presented in Fig. 15.18. The formation of these unique vesicles by this block copolymer was rather remarkable. In a recent work, the authors have studied how the preparation conditions and the copolymer compositions influenced the formation of these novel hybrid vesicles [214]. They conclude that the inorganic components impart stability.

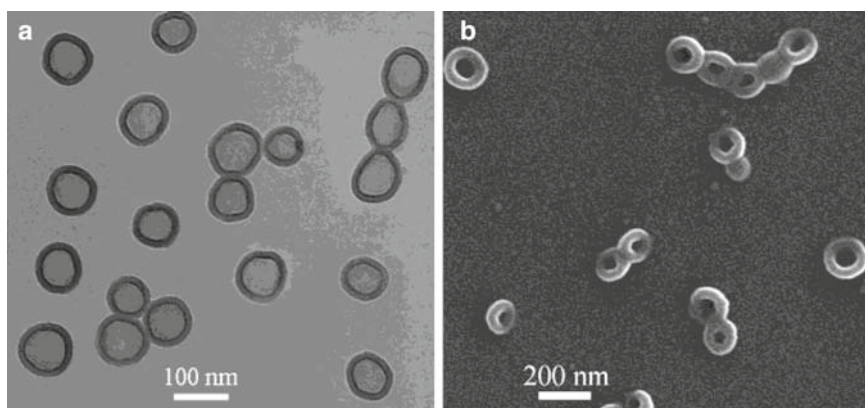


Fig. 15.18 (a) TEM images of the vesicles after addition of 1.3 wt% TEA in methanol/water 45:55 (w/w) at a polymer concentration of 0.45 g/L and (b) SEM image of the particles. (Reprinted with permission from [213]; copyright ACS publications)

15.4.2 Magnetic Drug Delivery

The use of magnetic targeted carriers containing hybrid nanomagnets for drug delivery aims to guide drugs to specific sites through the selective application of a magnetic field. Moreover, prolonged release of high, localized concentrations of drug is achieved by retention of the carriers in the region of interest [215]. The first clinical trial in humans, using magnetic-drug targeting therapy, was reported by Lübbe et al. [216]. These authors used magnetic nanoparticles to which the drug epirubicin was chemically bound.

The process of drug localization using magnetic delivery systems is based on the competition between forces exerted on the particles by blood compartment and magnetic forces generated from the applied magnet. When the magnetic forces exceed the linear blood flow rates in arteries (10 cm s^{-1}) or capillaries (0.05 cm s^{-1}), the magnetic particles are retained at the target site and maybe internalized by the endothelial cells of the target tissue [217]. Thus for drug delivery applications, an important parameter is the magnetophoretic mobility in a liquid (μ_m), which is the measure of the mobility of a magnetic carrier in a liquid medium under the influence of an applied inhomogeneous magnetic field. This parameter depends on the viscosity of the liquid medium, the carrier diameter and the effective susceptibility given by the difference in magnetic susceptibility between the carrier and the suspending medium. The susceptibility of the carrier depends on the size and the saturation magnetization of the magnetic carrier material. Thus, the highest magnetophoretic mobility should be achieved by using a carrier material with a large saturation magnetization.

A nice and illustrative example of the advantages and new trends in the use of hybrid magnetic carriers for the treatment of diseases was recently reported by Tanaka et al. [218]. These authors have tested magnetoliposomes containing the transforming growth factor (TGF)- β_1 for the treatment of articular cartilage defects in a rabbit model. TGF- β_1 is a cytokine that can increase bone formation and subsequent cartilage formation. However, cytokines show marked side effects when administered in abundant concentrations, therefore in this particular case, selective drug delivery is essential for the use of these compounds in the treatment of this disease.

Further research interest in the use of targeted hybrid magnetic nanoparticles is in the field of gene therapy [219]. Gene therapy represents an exciting development in medical treatment [220]. The theory is that by insertion of plasmid DNA into target cells, it may be possible to rectify genetic disorders, and to produce therapeutic agents in the form of peptides and proteins to stimulate the immune system. Magnetofection is a method in which magnetic nanoparticles associated with a DNA vector are transfected into cells by the influence of an external magnetic field [221].

15.5 Hyperthermia

Very simply stated, hyperthermia is the application of concentrated therapeutic heat to treat cancer. Due to its increasingly impressive research and clinical track records, it is considered as “main-stream” as surgery, chemotherapy, and radiation,

and is now recognized as the “fourth modality” in approved cancer treatment. However, due to its relatively recent acceptance in major medical circles, it is not well known – yet it is a treatment with genuine promises. A large body of medical evidence shows that when hyperthermia is used in combination with radiation therapy or chemotherapy, there is a dramatic improvement in response rates [222]. Since the heat generated is used to destroy the cancerous tissue, the primary question is which temperature range has to be chosen for the therapy [223]. According to the various mechanisms of cell damage, one has to differentiate between hyperthermia and thermoablation. Hyperthermia is known to use a moderate temperature elevation (treatments up to temperatures of 42°C for ~60 min) and it needs to be combined with other therapies (mostly irradiation or chemotherapy) to achieve a reliable destruction of tumor tissue. In contrast, thermoablation is conceived as a therapy modality that aims the thermal destruction of all tumor cells.

Hyperthermia can be produced by near-infrared laser irradiation of gold nanoparticles present in tumors and thus induce tumor cell killing via a bystander effect. To be clinically relevant, however, several problems still need to be resolved. In particular, selective delivery and physical targeting of gold nanoparticles to tumor cells are necessary to improve therapeutic selectivity. A very promising approach to improve the efficiency of gold nanoparticles in hyperthermia is to attach the gold nanoparticles to adenoviral vectors [224]. However, the form of hyperthermia to which more efforts are being devoted in the use of hybrid nanocomposites is magnetic hyperthermia

15.5.1 Magnetic Hyperthermia

Magnetic hyperthermia is a form of regional hyperthermia that aims to heat highly localized areas of the body. Fifty years ago, Gilchrist et al. reported on localized magnetic hyperthermia using fine magnetic particles [225]. Exposed to an alternating magnetic field these particles might act as localized heat sources at certain target regions inside the human body. The published results raised the hope to realize a powerful method for cancer treatment within a few years. During the following decades many investigations were carried out, and especially in vivo experiments with animals confirmed the general applicability to human patients.

The heating of magnetic oxide particles with low electrical conductivity in an external alternating magnetic field is mainly due to either loss processes during the reversal of coupled spins within the particles or due to frictional losses if the particles rotate in an environment of appropriate viscosity. Inductive heating of magnetic oxide particles (i.e., via eddy currents) is negligible due to the low electrical conductivity [223]. Hysteresis losses dominate when thermal energy is too low to facilitate reorientation. On the other hand, since the energy barriers decrease with a decreasing particle volume, thermal fluctuations facilitate the magnetisation reversal of small particles. Thus, relaxational losses dominate at the nanoparticle level when thermal energy can overcome the magnetic anisotropy barrier. Relaxational losses can be divided in Néel losses due to reorientation of the magnetic moment in a particle, and Brownian losses due to reorientation of the magnetic

particle itself in the fluid. In the first case the anisotropy barrier, and in the second case viscous friction determine the characteristic relaxation time. The characteristic relaxation times of the particle ensemble for Néel- or Brownian relaxation depend, in quite different manners, on the mean particle diameter. In principle, the heating power associated with hysteresis losses is higher than that based on the Brownian and Néel relaxation mechanisms, however, experimentally it is necessary to apply high magnetic field amplitudes which are at least larger than the effective anisotropy field. Unfortunately, these field amplitudes can rarely be used because of physiological and technological restrictions ([147] and references therein). The advantage of using superparamagnetic nanoparticles is that they absorb much more power at tolerable AC magnetic fields, compared to multidomain micron-sized particles subjected to the well-known hysteresis heating ([147] and references therein).

Recently, Wada et al. have proved the usefulness of magnetite nanoparticles coated with dextran for hyperthermia of oral cancer [226]. They found that the inhibition of the growth of tongue carcinoma in the four-time heating group was significantly greater than in the control group. Moreover, the survival rate was significantly higher in the heated groups than in the control group. Histological examination revealed accumulation of the magnetic nanoparticles at the stroma in the margin of the tumors. Many of the tumor cells disappeared at the site adjacent to this accumulation. New approaches to improve efficiency in hyperthermia treatment are based on the combination of this technique with some other tumor treatments. For example, Ito et al. have combined gene therapy with hyperthermia using magnetite cationic liposomes, i.e., liposomes filled with magnetic nanoparticles [227]. In nude mice, these magnetic liposomes induced cell death throughout much of the tumor area on heating under an alternating magnetic field.

It is worth mentioning a work by Gu et al. [228] who prepared hybrid nanocomposites based on iron oxide nanoparticles and porphyrin, with bimodal anticancer functionality. These nanocomposites can be used in the combinational treatment of malignancy by photodynamic therapy and hyperthermia therapy. Photodynamic therapy is an evolving modality for the treatment of superficial tumors [229]. The technique involves the systemic administration of a photosensitizer, which after a predefined time interval is followed by irradiation of the tumor site with nonthermal light. As a result, malignant cells become photochemically eradicated. Like any other anticancer treatment, photodynamic therapy aims at destroying tumor tissue without affecting healthy tissue. Due to the short half-life (0.6×10^{-6} s) and diffusion distance (0.1 μm) of singlet oxygen in aqueous media, photodynamic therapy can be considered as highly selective form of cancer treatment [230].

15.6 Biocatalysis

Catalysis plays a vital role in providing fuels, fine chemicals, pharmaceuticals, and means for strengthening environmental safeguards. More than 90% of chemical processes are based on catalysis. The enhancement in catalytic activity and selectivity and the reduction in cost of catalysts would benefit chemical industry enormously.

The large surface-to-volume ratios and special binding sites of fine particles in homogeneous and heterogeneous catalysis constitute part of the driving force in developing nanoparticle catalysts. An important aspect is that deliberate tailoring of the nanostructured catalysts could lead to new electronic and catalytic properties. Biocatalysis is even of greater interest, knowing the efficiency and specificity of enzymes. Unfortunately, their routine use in chemical transformations is severely limited by their high cost and poor stability. Immobilization of enzymes at solid surfaces can partly overcome these limitations [231, 232]. Immobilized enzymes can be recycled, thereby lowering their effective cost. The immobilized catalyst can be easily separated from the reaction mixture for easy workup, and reactions may be carried out in organic solvents. Immobilization can stabilize enzymes in specific cases, leading to improved activity and, in a few instances, the selectivity of the enzyme is altered in a desirable way [233]. Although the interaction between the protein and the support matrix is expected to play a major role in attenuating the immobilized enzyme properties, the effect of surfaces on the immobilized proteins is not well understood. Immobilization of proteins at well-defined surfaces and study of their properties are necessary for understanding immobilized protein behavior.

Developing a general methodology for the immobilization of proteins at well-defined hydrophilic solid surfaces and correlating their properties with the support surface characteristics are therefore of great interest. Such studies may be useful in identifying specific surfaces that improve the properties of the immobilized enzymes and in understanding the enzyme–matrix interactions. In addition to the above motivations, the importance of surface-bound proteins in biosensors, medical implants, enzyme reactors, and biomedical devices demands that a sufficient understanding of protein–surface interactions is developed. As a consequence, the support matrix surfaces can be designed on a rational basis to maximize protein function [233]. The support matrix, in general, should prevent enzyme aggregation, or spontaneous denaturation, and the matrix should not perturb the native properties of the immobilized protein to a significant extent or in an undesirable way. In addition, the support matrix should allow access to the immobilized enzymes by cofactors, substrates, or redox reagents [234]. In this context, enzymes have been immobilized using polymers, sol gels, surfactant films, and hydrogels [235–239]. The protective environment of these hosts can inhibit microbial degradation, hydrolysis and deamidation, and can extend the useful lifetime of these bound proteins while preserving their activity [240]. Binding of proteins at the surface of phospholipids [241, 242], Langmuir–Blodgett films and particles of different sizes and compositions has also been reported [243]. These various studies clearly established the advantages of enzyme immobilization, although the support surface characteristics are not well defined in many cases.

In the context of this section, emphasis will be only laid on studies about enzyme immobilization on the surface of discrete nanoparticles, nanotubes [244] and into the nanoporous structure of zeolites [245], including the galleries of alfa-zirconium phosphates [246], mesoporous MCM-41 [247] and mesoporous silica spheres [248]. As mentioned above, there are also quite interesting works about immobilization

on phospholipids bilayers and liposomes [249, 250], on self-assembled monolayers [251, 240], in Langmuir-Blodgett films [252, 253], within polymer matrixes [254, 255] and in thermally-evaporated lipid films [256, 257]. Each of the above support surfaces has its characteristic pros and cons versus inorganic counterparts, but here the aim is to focus on those materials of inorganic–organic hybrid nature.

The first relevant example is the use of nanoparticles as host for enzymes. A number of groups have studied the adsorption of proteins on inorganic colloidal nanoparticles of oxides and metals [258–262]. The effective enzyme loading on nanoparticles could reach up to 6.4 or 10 wt% due to a large surface area per unit mass of nanoparticles [262]. Further theoretical and experimental studies revealed that particle mobility, related to particle size and solution viscosity, could affect the intrinsic activity of the particle-attached enzymes [262].

In the area of metal nanoparticle-enzyme conjugate materials, Crumbliss, Stonehuerner and coworkers have studied both the formation and enzymatic activity of gold nanoparticles complexed with horseradish peroxidase, xanthine oxidase, glucose oxidase and carbonic anhydrase molecules [263–265]. A salient feature of their work is the demonstration that enzyme molecules are bound tightly to gold colloidal particles and retain significant biocatalytic activity in the conjugated form, whereas the enzyme molecules denature on adsorption to planar surfaces of gold.

More recently, there has been interest in bio-modified nanoparticles for constructing nanoparticle-based assemblies through specific biomolecular interactions [266–269]. Studies by Mirkin et al. and Alivisatos et al. showed that complementary DNA could be used to self-assemble DNA-modified gold nanoparticles into dimers and trimers or higher-order aggregates. Similarly, gold nanoparticles with chemisorbed antibodies [268] or a disulfide biotin-analogue [269] were cross-linked through the introduction of bivalent antigens and streptavidin, respectively, to form aggregated structures of the nanoparticles.

A recent example is the development, characterization, and activity studies of nanoassemblies of lignin peroxidase (LiP), and manganese peroxidase (MnP) from *Phanerochaete chrysosporium* on flat surfaces as well as on colloidal particles [270]. These assemblies of LiP and MnP were fabricated with polyelectrolytes – poly(ethylenimine) (PEI), poly(dimethyldiallylammonium chloride) (PDDA), and poly(allylamine) (PAH) – using LbL self-assembly. As above-mentioned the LbL approach has been shown to be a suitable means to assemble protein multilayer architectures on colloidal particles [271–276]. Multilayer films of bovine serum albumin [271], immunoglobulin G [271], β -glucosidase [272], glucose oxidase [273], and horseradish peroxidase have been assembled on polystyrene microspheres by the alternate deposition of the protein and oppositely charged polymer. The protein multilayer shell could be varied from several nanometers in thickness to hundreds of nanometers [271]. Biomacro-molecule multilayers are of interest in, for example, applications where the signal, as a result of biological interaction, needs to be amplified for the successful detection of various species, or where a higher efficiency of product from enzyme-substrate reactions is required [274–276].

Despite the promising features provided by nanoparticle-attached enzymes (i.e., nanoparticles provide the best results in terms of balancing the contradictory

issues including surface area, mass-transfer resistance, and effective enzyme loading), their dispersion in reaction solutions and their subsequent recovery for reuse are often a daunting task. Thus it appears that the use of nanofibers would overcome this problem while still keeping the advantageous features of nanometer-sized materials. Electrospinning has proven to be a simple and versatile method to prepare nanofibers from a variety of materials [277–286]. Electrospun nanofibers provide a large surface area for the attachment or entrapment of enzymes. In the case of porous nanofibers, they can reduce the diffusional path of the substrate from the reaction medium to the enzyme-active sites because of their small size, leading to better enzyme activity. Electrospinning can generate nonwoven mats or well-aligned arrays of nanofibers with controllable compositions and sizes in a matter of minutes [277–286]. Electrospun nanofiber mats are durable and easily separable and can also be processed in a highly porous form to relieve the mass-transfer limitation of the substrate through the mats. Because of these attractive features, electrospun nanofibers have generated much attention as supports for enzyme immobilization [83, 287–299]. As a first report, α -chymotrypsin was covalently attached to the polystyrene nanofibers of 120 nm diameter [287]. The observed enzyme loading reached up to 1.4% (wt/wt), corresponding to over 27.4% monolayer coverage of the external surface of nanofibers. The specific activity of the nanofibrous enzyme was over 65% of that of the native enzyme in aqueous solution, indicating a relatively low diffusional limitation. When the nanofibrous α -chymotrypsin was used in organic solvents, such as hexane and isooctane, it exhibited higher activity of over three orders of magnitude than that of its native counterpart. The half-life of the nanofibrous enzyme in anhydrous methanol was 18-fold higher than that of the native enzyme, suggesting that the covalent bonding improved the enzyme stability against structural denaturation. Recently Kim et al. successfully developed an active and stable enzyme system using electrospun nanofibers [300, 301]. They fabricated the enzyme aggregate coatings on the surface of electrospun polymer nanofibers. This approach employs the covalent attachment of seed enzyme molecules onto nanofibers, followed by the glutaraldehyde treatment cross-linking additional enzyme molecules or aggregates onto the covalently attached seed enzyme molecules. The apparent activity of α -chymotrypsin coatings based on per unit mass of fibers was nine times higher than that of covalently attached enzymes on nanofibers. The operational stability of enzyme coatings was greatly improved with no measurable loss of enzyme activity over a month of observation under vigorous shaking. This new approach of enzyme coatings on nanofibers, yielding high activity and stability, yields an economically viable enzyme system for using expensive enzymes with potential applications in various fields, such as biofuel cells, bioconversion, bioremediation, and biosensors.

Enzyme-polymer-(SWCNT) composites were prepared and examined for biocatalytic performance [302]. Improved enzyme activity was observed in comparison to similar enzyme-containing composites without using SWCNTs. It was discussed that the use of SWCNTs, which possess a high specific surface area, may effectively adsorb enzyme molecules and retain the enzyme within the

polymer matrix, whereas other forms of enzyme-composites may suffer from enzyme loss via leaching when they were placed in contact with aqueous solutions.

Hybrid nanotubes, composed of self-assembled lipids on ceramic or metal tubules, can also be promising in biomedical applications [244]. These authors have pioneered a technology, called template synthesis, for preparing monodisperse nanotubes of nearly any size and composed of nearly any material [303–305]. Several attributes make them potential candidates for biomedical applications. Firstly, nanotubes have inner voids that can be filled with species ranging in size from large proteins to small molecules. In addition, nanotubes have distinct inner and outer surfaces that can be differentially functionalized. The ability to control the dimensions allows tailoring tube size to fit the biomedical problem at hand. Finally, the ability to make these nanotubes out of nearly any material creates the possibility of making nanotubes with a desired property such as ruggedness or biodegradability [305]. Later on, these authors used template-synthesized silica nanotubes to demonstrate a number of these concepts. Silica nanotubes are ideal vehicles for such proof-of-concept experiments because they are easy to make, readily suspended in aqueous solution, and because silica surfaces can be derivatized with an enormous variety of chemical functional groups using simple silane chemistry with commercially available reagents. The silica nanotubes were synthesized within the nanopores of alumina template membranes using a sol–gel method [306]. Templates with pore diameters of either 60 or 200 nm were used for these studies [307].

While still embedded within the pores of the template membrane, the inner nanotube surfaces react following the first silane exposure. These silane molecules cannot attach to the outer nanotube surfaces because the outer surfaces are in contact with the template pore wall and thus masked. The template is then dissolved [304] to liberate the nanotubes, which unmask the outer nanotube surfaces. The nanotubes are then subjected to a second silane exposure to attach these silane molecules only to the outer nanotube surfaces. Thus, the authors developed a simple procedure for applying different functional groups to the inner versus outer surfaces of these nanotubes (e.g. hydrophilic chemistry on their outer surfaces and hydrophobic chemistry on their inner surfaces), which are ideal for extracting lipophilic molecules from an aqueous solution.

An additional interesting approach is the immobilization of enzymes in nanoporous structures. An elegant example mentioned above is provided by Mukhopadhyay et al., illustrating a combination between enzyme immobilization on metal nanoparticle and incorporation in a nanostructure matrix [245]. The authors demonstrate that gold nanoparticles bound at high surface coverage on 3-aminopropyltrimethoxysilane (APTS)-functionalized Na-Y zeolites are excellent candidates for the immobilization of pepsin. The assembly of gold nanoparticles on the zeolite surface occurs through the amine groups present in APTS. Pepsin was then bound to the Na-Y zeolite (core)-Au nano (shell) structures via interaction with the gold nanoparticles leading to a new class of biocatalysts. A highlight of the new biocatalyst wherein the enzyme is supported by a more massive biocompatible surface is the ease with which separation from the reaction medium may be achieved, i.e., by simple

sedimentation. The catalytic activity of pepsin in the bioconjugate was comparable to that of the free enzyme in solution. The pepsin-gold nano-zeolite bioconjugate material exhibited excellent activity over seven successive reuse cycles as well as enhanced pH and temperature stability.

Meanwhile, Bellezza et al. used zirconium phosphate $R-Zr(HPO_4)_2$ ($R-ZrP$) and zirconium phosphonates such as $R-Zr(C_6H_5-PO_3)_2$ ($R-ZrBP$) and $R-Zr(HOOCCH_2-CH_2PO_3)_2$ ($R-ZrCEP$) for the immobilization of myoglobin and lipase from *Candida rugosa* (CRL) [308, 309]. These layered inorganic solids have many positive features including an ordered structure, different surface areas, and well-defined hydrophilic/hydrophobic surface characteristics, which make them attractive candidates for the immobilization of bioactive materials. In the case of CRL, they obtained a selective immobilization of CRL isoenzymes that allowed the preparation of some biocomposites with different catalytic properties. Later on, the adsorption of myoglobin onto zirconium phosphonates allowed heterogeneous biocatalysts to be obtained, showing good catalytic efficiency, increased resistance toward inactivation by hydrogen peroxide, and that could be stored for months without a significant loss of catalytic activity [310]. Continuing their research on the immobilization of enzymes and proteins onto solid supports, they considered organic-inorganic hybrid nanocomposites based on zirconium oxide. These materials can be synthesized by grafting organic functions onto the surface of inorganic particles through strong chemical bonds. Due to the stable zirconium-phosphate bond, the zirconium oxide surface can be modified with different phosphates and phosphonates that provide the external surface of supports with specific functions that can interact with biomolecules [311–315].

Later on, they have investigated the adsorption and catalytic activity of myoglobin immobilized on colloidal particles of zirconia covalently grafted with phosphoric (ZrO_2-P) and benzenephosphonic acid (ZrO_2-BP) [316] (Fig. 15.19). The

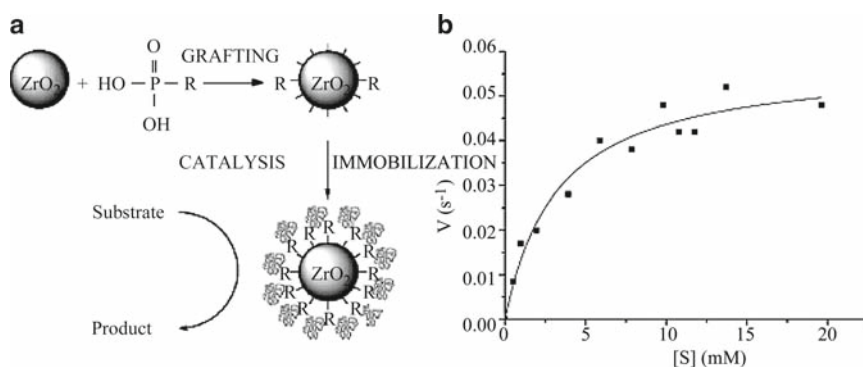


Fig. 15.19 (a) Schematic representation of processes involved in the nanobiocomposite assembly and its use in biocatalysis. (b) Initial rate of myoglobin (Mb)/ ZrO_2 -BP(1) catalyzed oxidation of 2-methoxyphenol as a function of substrate concentration. (Reprinted with permission from [316]; copyright ACS publications)

maximum adsorption was reached after 1 h of contact and was greater on the $\text{ZrO}_2\text{-P}$ hydrophilic support, compared to the $\text{ZrO}_2\text{-BP}$ hydrophobic support. The equilibrium isotherms fitted the Langmuir equation, suggesting the presence of a monolayer of protein molecules on the surface of the nanoparticles. The nanostructured biocomposites are active in the oxidation of 2-methoxyphenol (guaiacol) by hydrogen peroxide. The oxidation catalyzed by immobilized myoglobin followed a Michaelis-Menten kinetics, similar to that observed in the oxidation by free myoglobin (Mb) (Fig. 15.19). Furthermore, the catalytic efficiency is similar to that of free Mb and higher than that of “large-size” biocatalysts (with sizes larger than 1 μm). In the latter case, the kinetic parameters, k_{cat} and K_{M} , indicate that this efficiency is mostly due to an increased affinity of the nanobiocomposite for the substrate. The activity of the nanobiocomposites decreases slightly as the amount of adsorbed proteins increases. This is mainly due to the formation of a nonordered monolayer, which reduces the accessibility of the substrate to the active centers.

More recently, Caruso and coworkers [317] have reported on a facile process for encapsulating biomacromolecules within polyelectrolyte microcapsules using mesoporous silica spheres as sacrificial templates for both enzyme immobilization and polyelectrolyte multilayer capsule formation. The method yields microcapsules with a high enzyme loading, with retained enzyme activity and, notably for release purposes, with enzymes in a “free” (non-immobilized) state. The approach is also of significant value because it allows the encapsulation of a vast range of enzymes with sizes up to ca 40 nm in microcapsules comprised of a diverse range of polyelectrolytes. The encapsulation is not limited to enzymes that crystallize and the release can be easily tailored by altering the salt concentration or the solution pH.

Following this research line, the same group has immobilized various enzymes in mesoporous silica (MS) spheres followed by encapsulation via the layer-by-layer assembly of multilayered nanocomposite thin shells [248]. A range of enzymes with different molecular sizes and isoelectric points (pI) (e.g. catalase, peroxidase, cytochrome C, and lysozyme) has been examined in MS particles with a series of pore sizes. MS spheres with a bimodal mesoporous structure (BMS, 2–3 nm and 10–40 nm) show faster immobilization rates and significantly improved enzyme immobilization capacity than similar particles with only the smaller mesopores. High enzyme loadings (20–40 wt%) and rapid uptake (several minutes) were observed in BMS spheres for enzymes with a molecular size ≤ 3 nm and $\text{pI} \geq 10$. Finally, this group has prepared nanoporous biomacromolecule particles (and fibers) by immobilizing proteins in mesoporous materials, bridging the proteins by means of the infiltration of polyelectrolyte, followed by removal of MS template [318] (Fig. 15.20).

Nanoporous protein particles (NPPs) can be prepared with protein contents as high as 83 wt% and from a range of proteins and polyelectrolytes (PEs), including biocompatible bridging polymers such as polypeptides. The activity of NPP is largely retained after the processing steps used to generate the particles. Since MS has excellent adsorption ability for various proteins, this method is suitable for preparation of NPPs of controlled composition and functionality. The appreciable surface area and pore volume remaining after protein and PE infiltration in the MS templates

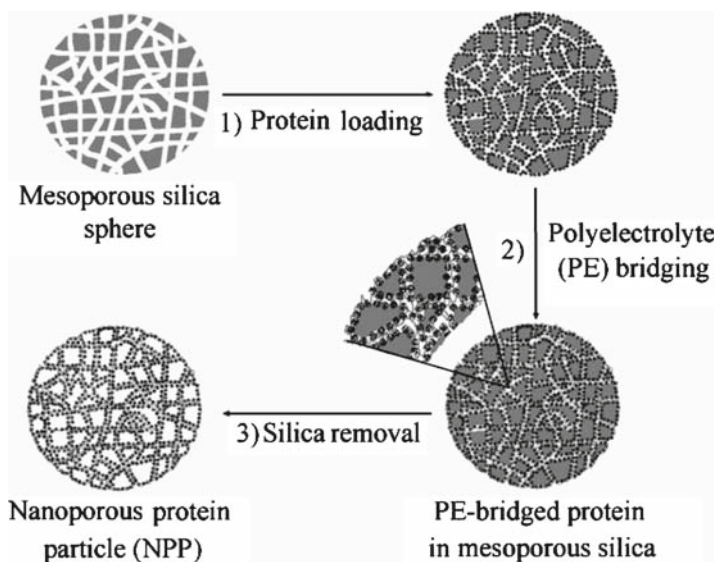


Fig. 15.20 Schematic illustration showing the preparation of nanoporous protein particles (NPPs). The protein is first loaded in the mesoporous silica spheres (step 1), after which the protein molecules are bridged by the infiltrated polyelectrolyte (step 2). When the bridging molecule is a weak polyelectrolyte (e.g., PAA, PGA), crosslinking of the protein and polyelectrolyte is accomplished using EDC. The mesoporous silica template is then dissolved by exposure to a $\text{HF-NH}_4\text{F}$ buffer solution (step 3), yielding intact NPPs. (Reprinted with permission from [318]; copyright Wiley-VCH publications)

indicate that it is possible to prepare NPPs with multiple proteins through sequential adsorptions with PEs. The attachment of targeting ligands to the NPPs through established coupling protocols would provide functional particles for protein-delivery applications. The authors focus their future work on the use of MS materials of different sizes, morphology and porosity, on the influence of the immobilization and infiltration conditions for various proteins and PEs, on the degree of crosslinking, and on the stability and activity of the nanoporous protein-based structures. Such materials are envisaged to find applications not only in biocatalysis, but also in biosensing, separations, and controlled drug delivery.

15.7 Outlook and Future Prospects

Looking to the 21st century, nanosciences will be one of the fields that will contribute to a high level of scientific and technological developments [3]. Nanostructured hybrid organic–(bio)–inorganic materials will play a major role in the development of advanced functional materials. Research in such materials is being mostly supported by the growing interest of chemists, physicists, biologists and materials

scientists to fully exploit this opportunity for creating smart materials benefiting from the best of the three realms: inorganic, organic and biological. Furthermore, while hybrid organic–inorganic nanostructured materials conquer more and more of the free spaces left between inorganic chemistry, polymer chemistry, organic chemistry, and biology, the progress in this field depends largely on the core competence of materials chemists to develop advanced materials with nano- and microstructures and with unprecedented performance. The challenge is not only to make any nanostructure of any shape and to know a great deal about its properties, but also to assemble them in any form, to control their structure at different space levels and to know about the properties of such assembled structures. Self-assembly of these nanoparticles by different techniques, either from the bottom-up techniques (assembling particles synthesized in solution) or from the top-down techniques (different lithographic methods), is being pursued. Although many future applications will make use of the properties of the individual nanoparticles (sensors, medical diagnostics, homogeneous catalysis, etc.), there are other important applications that would require self-assembled nanoparticles (nanoelectronics, optoelectronics, photonics, heterogeneous catalysis, etc). Even bio-inspired strategies are used to “mimic” the growth processes occurring in biomineralization and to design innovative multiscale structured hybrids (from nano- to millimetric scale), hierarchically organized in terms of structure and functions. The properties that can be obtained for such materials strongly depend on the synergy between the organic and inorganic nature of the components, but certainly rely on their nano/microstructure and degree of organization. Thus, the key point for the design of new hierarchically organized hybrid materials will not only be the tuning of the nature, but also the dimensions and accessibility of the inner interfaces.

Acknowledgements The financial support of MEC (MAT2006–02394), CM (S-0505/PPQ-0316), and CSIC-PIF (200660F0111) and MAT2008-03224/NAN are gratefully acknowledged.

References

1. Niemeyer CM (2001) Nanoparticles, proteins, and nucleic acids: Biotechnology Meets materials science. *Angewandte Chemie – International Edition* 40:128–158
2. Sanchez C, Gomez-Romero P (2004) *Functional Hybrid Materials*. Wiley, Weinheim
3. Whitesides GM (2003) The right size in nanobiotechnology. *Nature Biotechnology* 21:1161–1165
4. Whitesides GM, Alivisatos AP (2003) *Nanotechnology Research Directions*. IWGN Workshop, Report
5. Lagally ET, Mathies RA (2004) Integrated genetic analysis microsystems. *Journal Physics D-Applied Physics* 37:R245–R261
6. Lübbers DW, Opitz N (1975) The $p\text{CO}_2/p\text{O}_2$ -optrode: a new probe for measuring $p\text{CO}_2$ or $p\text{O}_2$ of gases and liquids (authors transl). Die $p\text{CO}_2/p\text{O}_2$ -Optrode: Eine neue $p\text{CO}_2$ - bzw. $p\text{O}_2$ -Messsonde zur Messung des $p\text{CO}_2$ oder $p\text{O}_2$ von Gasen und Flüssigkeiten. *Z. Naturforsch.* 30C:532–533
7. Wolfbeis OS (1991) *Fiber optic chemical sensors and biosensors*. CRC Press, Boca Raton

8. Brecht A, Gauglitz G (1995) Optical probes and transducers. *Biosensors and Bioelectronics* 10:923–936
9. Gauglitz G (1996) Opto-chemical and opto-immuno sensors, *Sensor Update* vol. 1, VCH Verlagsgesellschaft, Weinheim
10. Boisdé G, Harmer A (1996) Chemical and biochemical sensing with optical fibers and waveguides. Artech House, Boston
11. Blyth DJ, Poynter SJ, Russell DA (1996) Calcium biosensing with a sol–gel immobilized photoprotein. *Analyst* 121:1975–1978
12. Zhao J, Jedlicka SS, Lannu JD, Bhunia AK, Rickus JL (2006) Liposome-doped nanocomposites as artificial-cell-based biosensors: Detection of listeriolysin O. *Biotechnology Progress* 22:32–37
13. Han M, Gao X, Su JZ, Nie S (2001) Quantum-dot-tagged microbeads for multiplexed optical coding of biomolecules. *Nature Biotechnology* 19:631–635
14. Tyagi S, Kramer FR (1996) Molecular beacons: Probes that fluoresce upon hybridization. *Nature Biotechnology* 14:303–308
15. Tyagi S, Bratu DP, Kramer FR (1998) Multicolor molecular beacons for allele discrimination. *Nature Biotechnology* 16:49–53
16. Piatek AS, Tyagi S, Pol AC, Telenti A, Miller LP, Kramer FR, Alland D (1998) Molecular beacon sequence analysis for detecting drug resistance in *Mycobacterium tuberculosis*. *Nature Biotechnology* 16:359–363
17. Kostrikis LG, Huang Y, Moore JP, Wolinsky SM, Zhang L, Guo Y, Deutsch L, Phair J, Neumann AU, Ho DD (1998) A chemokine receptor CCR2 allele delays HIV-1 disease progression and is associated with a CCR5 promoter mutation. *Nature Medicine* 4:350–353
18. Kostrikis LG, Tyagi S, Mhlanga MM, Ho DD, Kramer FR (1998) Spectral genotyping of human alleles. *Science* 279:1228–1229
19. Fang X, Liu X, Schuster S, Tan W (1999) Designing a novel molecular beacon for surface-immobilized DNA hybridization studies. *Journal of the American Chemical Society* 121:2921–2922
20. Maxwell DJ, Taylor JR, Nie S (2002) Self-assembled nanoparticle probes for recognition and detection of biomolecules. *Journal of the American Chemical Society* 124:9606–9612
21. Giesendorf BAJ, Vet JAM, Tyagi S, Mensink EJMG, Trijbels FJM, Blom HJ (1998) Molecular beacons: A new approach for semi-automated mutation analysis. *Clinical Chemistry* 44:482–486
22. Ehrlich R, Kirner T, Ellinger T, Foerster P, McCaskill JS (1997) Monitoring the amplification of CATCH, a 3SR based cooperatively coupled isothermal amplification system, by fluorimetric methods. *Nucleic Acids Research*. 25:4697–4699
23. Gao W, Tyagi S, Kramer FR, Goldman E (1997) Messenger RNA release from ribosomes during 5'-translational blockage by consecutive low-usage arginine but not leucine codons in *Escherichia coli*. *Molecular Microbiology* 25:707–716
24. Park EJ, Brasuel M, Behrend C, Philbert MA, Kopelman R (2003) Ratiometric optical PEBBLE nanosensors for real-time magnesium ion concentrations inside viable cells. *Analytical Chemistry* 75:3784–3791
25. Dubertret B, Skourides P, Norris DJ, Noireaux V, Brivanlou AH, Libchaber A (2002) In vivo imaging of quantum dots encapsulated in phospholipid micelles. *Science* 298:1759–1762
26. Rosi NL, Giljohann DA, Thaxton CS, Lytton-Jean AKR, Han MS, Mirkin CA (2006) Oligonucleotide-modified gold nanoparticles for intracellular gene regulation. *Science* 312:1027–1030
27. Bergen JM, Pun SH (2005) Peptide-enhanced nucleic acid delivery. *MRS Bulletin* 30:663–667
28. Weissleder R, Kelly K, Sun EY, Shtatland T, Josephson L (2005) Cell-specific targeting of nanoparticles by multivalent attachment of small molecules. *Nature Biotechnology* 23:1418–1423

29. Pockrand I, Swalen JD, Gordon JG, Philpott MR (1978) Surface plasmon spectroscopy of organic monolayer assemblies. *Surface Science* 74:237–244
30. Gordon II JG, Ernst S (1980) Surface plasmons as a probe of the electrochemical interface. *Surface Science* 101:499–506
31. Lukosz W (1991) Principles and sensitivities of integrated optical and surface plasmon sensors for direct affinity sensing and immunosensing. *Biosensors and Bioelectronics* 6:215–225
32. Homola J (2003) Present and future of surface plasmon resonance biosensors. *Analytical and Bioanalytical Chemistry* 377:528–539
33. Abel AP, Weller MG, Duveneck GL, Ehrat M, Widmer HM (1996) Fiber-optic evanescent wave biosensor for the detection of oligonucleotides. *Analytical Chemistry* 68:2905–2912
34. Liu X, Tan W (1999) A fiber-optic evanescent wave DNA biosensor based on novel molecular beacons. *Analytical Chemistry* 71:5054–5059
35. Buckle PE, Davies RJ, Kinning T, Yeung D, Edwards PR, Pollard-Knight D (1993) The resonant mirror: A novel optical sensor for direct sensing of biomolecular interactions. Part II: Applications. *Biosensors and Bioelectronics* 8:355–363
36. Cush R, Cronin JM, Stewart WJ, Maule CH, Molloy J, Goddard NJ (1993) The resonant mirror: A novel optical biosensor for direct sensing of biomolecular interactions. Part I: Principle of operation and associated instrumentation. *Biosensors and Bioelectronics* 8:347–353
37. Liedberg B, Nylander C, Lundstrom I (1983) Surface plasmon resonance for gas detection and biosensing. *Sensors and Actuators* 4:299–304
38. Johnsson B, Lofas S, Lindquist G (1991) Immobilization of proteins to a carboxymethyl-dextran-modified gold surface for biospecific interaction analysis in surface plasmon resonance sensors. *Analytical Biochemistry* 198:268–277
39. Storhoff JJ, Elghanian R, Mucic RC, Mirkin CA, Letsinger RL (1998) One-pot colorimetric differentiation of polynucleotides with single base imperfections using gold nanoparticle probes. *Journal of the American Chemical Society* 120:1959–1964
40. Zhao J, Das A, Zhang X, Schatz GC, Sligar SG, VanDuyne RP (2006) Resonance surface plasmon spectroscopy: Low molecular weight substrate binding to cytochrome P450. *Journal of the American Chemical Society* 128:11004–11005
41. Lyandres O, Shah NC, Yonzon CR, Walsh JR, JT, Glucksberg MR, Van Duyne RP (2005) Real-time glucose sensing by surface-enhanced Raman spectroscopy in bovine plasma facilitated by a mixed decanethiol/mercaptohexanol partition layer. *Analytical Chemistry* 77:6134–6139
42. Zhang X, Young MA, Lyandres O, Van Duyne RP (2005) Rapid detection of an anthrax biomarker by surface-enhanced Raman spectroscopy. *Journal of the American Chemical Society* 127:4484–4489
43. Haes AJ, Chang L, Klein WL, Van Duyne RP (2005) Detection of a biomarker for Alzheimer's disease from synthetic and clinical samples using a nanoscale optical biosensor. *Journal of the American Chemical Society* 127:2264–2271
44. Haes AJ, Hall WP, Chang L, Klein WL, Van Duyne RP (2004) A localized surface plasmon resonance biosensor: First steps toward an assay for Alzheimer's disease. *Nano Letters* 4:1029–1034
45. Haes AJ, Zou S, Schatz GC, Van Duyne RP (2004) Nanoscale optical biosensor: Short range distance dependence of the localized surface plasmon resonance of noble metal nanoparticles. *Journal of Physical Chemistry B* 108:6961–6968
46. Haes AJ, Van Duyne RP (2002) A nanoscale optical biosensor: Sensitivity and selectivity of an approach based on the localized surface plasmon resonance spectroscopy of triangular silver nanoparticles. *Journal of the American Chemical Society* 124:10596–10604
47. Riboh JC, Haes AJ, McFarland AD, Yonzon CR, Van Duyne RP (2003) A Nanoscale optical biosensor: Real-time immunoassay in physiological buffer enabled by improved nanoparticle Adhesion. *Journal of Physical Chemistry B* 107:1772–1780
48. Yonzon CR, Jeoung E, Zou S, Schatz GC, Mrksich M, VanDuyne RP (2004) A comparative analysis of localized and propagating surface plasmon resonance sensors: The binding of

- concanavalin A to a monosaccharide functionalized self-assembled monolayer. *Journal of the American Chemical Society* 126:12669–12676
49. Dahlin A, Zach M, Rindzevicius T, Kall M, Sutherland DS, Hook F (2005) Localized surface plasmon resonance sensing of lipid-membrane-mediated biorecognition events. *Journal of the American Chemical Society* 127:5043–5048
 50. Haes AJ, Zou S, Zhao J, Schatz GC, VanDuyne RP (2006) Localized surface plasmon resonance spectroscopy near molecular resonances. *Journal of the American Chemical Society* 128:10905–10914
 51. Wang J (1995) Electroanalysis and biosensors. *Analytical Chemistry* 67:487R–492R
 52. Wang J (1999) Sol–gel materials for electrochemical biosensors. *Analytica Chimica Acta* 399:21–27
 53. Walcarius A (2001) Electrochemical applications of silica-based organic–inorganic hybrid materials. *Chemistry of Materials* 13:3351–3372
 54. Katz E, Willner I (2004) Integrated nanoparticle-biomolecule hybrid systems: Synthesis, properties, and applications. *Angewandte Chemie – International Edition* 43:6042–6108
 55. Wang J (2005) Carbon-nanotube based electrochemical biosensors: A review. *Electroanalysis* 17:7–14
 56. Luo XL, Morrin A, Killard AJ, Smyth MR (2006) Application of nanoparticles in electrochemical sensors and biosensors. *Electroanalysis* 18:319–326
 57. Drummond TG, Hill MG, Barton JK (2003) Electrochemical DNA sensors. *Nature Biotechnology* 21:1192–1199
 58. Wang J (2005) Nanomaterial-based amplified transduction of biomolecular interactions. *Small* 1:1036–1043
 59. Degani Y, Heller A (1988) Direct electrical communication between chemically modified enzymes and metal-electrodes. 2. Methods for bonding electron-transfer relays to glucose-oxidase and D-amino-acid oxidase. *Journal of the American Chemical Society* 110:2615–2620
 60. Willner I, Riklin A, Shoham B, Rivenzon D, Katz E (1993) Development of novel biosensor enzyme electrodes – Glucose-oxidase multilayer arrays immobilized onto self-assembled monolayers electrodes. *Advanced Materials* 5:912–915
 61. Emr SA, Yacynych AM (1995) Use of polymer-films in amperometric biosensors. *Electroanalysis* 7:913–923
 62. Raitman OA, Katz E, Buckmann AF, Willner I (2002) Integration of polyaniline/poly(acrylic acid) films and redox enzymes on electrode supports: An *in situ* electrochemical/surface plasmon resonance study of the bioelectrocatalyzed oxidation of glucose or lactate in the integrated bioelectrocatalytic systems. *Journal of the American Chemical Society* 124:6487–6496
 63. Xiao Y, Patolsky F, Katz E, Hainfeld JF, Willner I (2003) Plugging into enzymes: Nanowiring of redox enzymes by a gold nanoparticle. *Science* 299:1877–1881
 64. Liu T, Zhong J, Gan X, Fan C, Li G, Matsuda N (2003) Wiring electrons of cytochrome c with silver nanoparticles in layered films. *ChemPhysChem* 4:1364–1366
 65. Gan X, Liu T, Zhu X, Li G (2004) An electrochemical biosensor for nitric oxide based on silver nanoparticles and hemoglobin. *Analytical Sciences* 20:1271–1275
 66. Zhou H, Gan X, Liu T, Yang QL, Li GX (2005) Effect of nano cadmium sulfide on the electron transfer reactivity and peroxidase activity of hemoglobin. *Journal of Biochemical and Biophysical Methods* 64:38–45
 67. Pardo-Yissar V, Katz E, Wasserman J, Willner I (2003) Acetylcholine esterase-labeled CdS nanoparticles on electrodes: Photoelectrochemical sensing of the enzyme inhibitors. *Journal of the American Chemical Society* 125:622–623
 68. Dequaire M, Degrand C, Limoges B (2000) An electrochemical metalloimmunoassay based on a colloidal gold label. *Analytical Chemistry* 72:5521–5528
 69. Authier L, Grossiord C, Brossier P, Limoges B (2001) Gold nanoparticle-based quantitative electrochemical detection of amplified human cytomegalovirus DNA using disposable microband electrodes. *Analytical Chemistry* 73:4450–4456

70. Wang J, Xu DK, Kawde AN, Polsky R (2001) Metal nanoparticle-based electrochemical stripping potentiometric detection of DNA hybridization. *Analytical Chemistry* 73:5576–5581
71. Wang J, Polsky R, Xu DK (2001) Silver-enhanced colloidal gold electrochemical stripping detection of DNA hybridization. *Langmuir* 17:5739–5741
72. Cai H, Wang YQ, He PG, Fang YH (2002) Electrochemical detection of DNA hybridization based on silver-enhanced gold nanoparticle label. *Analytica Chimica Acta* 469:165–172
73. Wang J, Xu DK, Polsky R (2002) Magnetically-induced solid-state electrochemical detection of DNA hybridization. *Journal of the American Chemical Society* 124:4208–4209
74. Kawde AN, Wang J (2004) Amplified electrical transduction of DNA hybridization based on polymeric beads loaded with multiple gold nanoparticle tags. *Electroanalysis* 16:101–107
75. Wang J, Polsky R, Merkoci A, Turner KL (2003) “Electroactive beads” for ultrasensitive DNA detection. *Langmuir* 19:989–991
76. Mak WC, Cheung KY, Trau D, Warsinke A, Scheller F, Renneberg R (2005) Electrochemical bioassay utilizing encapsulated electrochemical active microcrystal biolabels. *Analytical Chemistry* 77:2835–2841
77. Braun E, Eichen Y, Sivan U, Ben-Yoseph G (1998) DNA-templated assembly and electrode attachment of a conducting silver wire. *Nature* 391:775–778
78. Merkoci A, Aldavert M, Marin S, Alegret S (2005) New materials for electrochemical sensing V: Nanoparticles for DNA labelling. *Trac-Trends in Analytical Chemistry* 24:341–349
79. Willner I, Patolsky F, Wasserman J (2001) Photoelectrochemistry with controlled DNA-cross-linked CdS nanoparticle arrays. *Angewandte Chemie – International Edition* 40:1861–1864
80. Wang J, Liu GD, Merkoci A (2003) Electrochemical coding technology for simultaneous detection of multiple DNA targets. *Journal of the American Chemical Society* 125:3214–3215
81. Park SJ, Taton TA, Mirkin CA (2002) Array-based electrical detection of DNA with nanoparticle probes. *Science* 295:1503–1506
82. Maalouf R, Soldatkin A, Vittori O, Sigaud M, Saikali Y, Chebib H, Loir AS, Garrelie F, Donnet C, Jaffrezic-Renault N (2006) Study of different carbon materials for amperometric enzyme biosensor development. *Materials Science and Engineering: C* 26:564–567
83. Wu J, Zou Y, Li X, Liu H, Shen G, Yu R (2005a) A biosensor monitoring DNA hybridization based on polyaniline intercalated graphite oxide nanocomposite. *Sensors and Actuators, B: Chemical* 104:43–49
84. Wu L, Yuan X, Sheng J (2005) Immobilization of cellulase in nanofibrous PVA membranes by electrospinning. *Journal of Membrane Science* 250:167–173
85. Iijima S (1991) Helical microtubules of graphitic carbon. *Nature* 354:56–58
86. Sun YP, Fu KF, Lin Y, Huang WJ (2002) Functionalized carbon nanotubes: Properties and applications. *Accounts of Chemical Research* 35:1096–1104
87. Baughman RH, Zakhidov AA, de Heer WA (2002) Carbon nanotubes - the route toward applications. *Science* 297:787–792
88. Shim M, Kam NWS, Chen RJ, Li Y, Dai H (2002) Functionalization of carbon nanotubes for biocompatibility and biomolecular recognition. *Nano Letters* 2:285–288
89. Lin Y, Lu F, Tu Y, Ren Z (2004) Glucose biosensors based on carbon nanotube nanoelectrode ensembles. *Nano Letters* 4:191–195
90. Hirsch A (2002) Functionalization of single-walled carbon nanotubes. *Angewandte Chemie – International Edition* 41:1853–1859
91. Rubianes MD, Rivas GA (2003) Carbon nanotubes paste electrode. *Electrochemistry Communications* 5:689–694
92. Wang J, Musameh M (2003) Carbon nanotube/Teflon composite electrochemical sensors and biosensors. *Analytical Chemistry* 75:2075–2079

93. Musameh M, Wang J, Merkoci A, Lin Y (2002) Low-potential stable NADH detection at carbon-nanotube-modified glassy carbon electrodes. *Electrochemistry Communications* 4:743–746
94. Wang J, Musameh M, Lin Y (2003) Solubilization of carbon nanotubes by Nafion toward the preparation of amperometric biosensors. *Journal of the American Chemical Society* 125:2408–2409
95. Hrapovic S, Liu Y, Male KB, Luong JHT (2004) Electrochemical biosensing platforms using platinum nanoparticles and carbon nanotubes. *Analytical Chemistry* 76:1083–1088
96. Joshi PP, Merchant SA, Wang Y, Schmidtke DW (2005) Amperometric biosensors based on redox polymer-carbon nanotube-enzyme composites. *Analytical Chemistry* 77:3183–3188
97. Gooding JJ, Wibowo R, Liu J, Yang W, Losic D, Orbons S, Mearns FJ, Shapter JG, Hibbert DB (2003) Protein electrochemistry using aligned carbon nanotube arrays. *Journal of the American Chemical Society* 125:9006–9007
98. Patolsky F, Weizmann Y, Willner I (2004) Long-range electrical contacting of redox enzymes by SWCNT connectors. *Angewandte Chemie – International Edition* 43:2113–2117
99. Wang J, Liu GD, Jan MR (2004) Ultrasensitive electrical biosensing of proteins and DNA: Carbon-nanotube derived amplification of the recognition and transduction events. *Journal of the American Chemical Society* 126:3010–3011
100. Zhu N, Cai H, He P, Fang Y (2003) Tris(2,2'-bipyridyl)cobalt(III)-doped silica nanoparticle DNA probe for the electrochemical detection of DNA hybridization. *Analytica Chimica Acta* 481:181–189
101. Avnir D, Braun S, Lev O, Ottolenghi M (1994) Enzymes and other proteins entrapped in sol-gel materials. *Chemistry of Materials* 6:1605–1614
102. Wang J, Pamidi PVA, Rogers KR (1998) Sol-Gel-Derived Thick-Film Amperometric Immunosensors. *Analytical Chemistry* 70:1171–1175
103. Jin W, Brennan JD (2002) Properties and applications of proteins encapsulated within sol-gel derived materials. *Analytica Chimica Acta* 461:1–36
104. Sampath S, Lev O (1996) Renewable, reagentless glucose sensor based on a redox modified enzyme and carbon-silica composite. *Electroanalysis* 8:1112–1116
105. Narang U, Prasad PN, Bright FV, Ramanathan K, Kumar ND, Malhotra BD, Kamalasanan MN, Chandra S (1994) Glucose biosensor based on a sol-gel-derived platform. *Analytical Chemistry* 66:3139–3144
106. Prieto AP, Ahrentorp F, Johansson C, Larsson K, Krozer A (2004) Biomolecular reactions studied using changes in Brownian rotation dynamics of magnetic particles. *Biosensors Bioelectronics* 19:945–951
107. Tartaj P (2006) Nanomagnets-From fundamental physics to biomedicine. *Current Nanoscience* 2:43–53
108. Weitschies W, Kötz R, Bunte T, Trahms L (1997) Determination of relaxing or remanent nanoparticle magnetization provides a novel binding-specific technique for the evaluation of immunoassays. *Pharmaceutical and Pharmacological Letters* 7:5–8
109. Rheinländer T, Kötz R, Weitschies W, Semmler W (2000) Magnetic fractionation of magnetic fluids. *Journal Magnetism Magnetic Materials* 219:219–228
110. Street R, Woolley JC (1949) A study of magnetic viscosity. *Proceedings Physical Society A* 62:562–572
111. Frenkel J (1955) *The Kinetic Theory of Liquids*. Dover, New York
112. Kötz R, Weitschies W, Trahms L, Brewer W, Semmler W (1999) Determination of the binding reaction between avidin and biotin by relaxation measurements of magnetic nanoparticles. *Journal Magnetism Magnetic Materials* 194:62–68
113. Fannin PC, Scaife BKP, Charles SW (1993) Relaxation and resonance in ferrofluids. *Journal Magnetism Magnetic Materials* 122:159–163
114. Hanson M, Johansson C (1991) Interaction effects in the dynamic response of magnetic liquids. *Journal Magnetism Magnetic Materials* 101:45–46

115. Baselt DR, Lee GU, Natesan M, Metzger SW, Sheehan PE, Colton R (1998) A biosensor based on magnetoresistance technology. *Biosensors Bioelectronics* 13:731–739
116. Miller MM, Prinz GA, Cheng SF, Bounnak S (2002) Detection of a micron-sized magnetic sphere using a ring-shaped anisotropic magnetoresistance-based sensor: a model for a magnetoresistance-based biosensor. *Applied Physics Letters* 81:2211–2213
117. Kurlyandskaya G, Levit V (2005) Magnetic dynabeads® detection by sensitive element based on giant magnetoimpedance. *Biosensors Bioelectronics* 20:1611–1616
118. Grancharov SG, Zeng H, Sun S, Wang SX, O'Brien S, Murray CB, Kirtley JR, Held GA (2005) Bio-functionalization of monodisperse magnetic nanoparticles and their use as bio-molecular labels in a magnetic tunnel junction based sensor. *Journal Physical Chemistry B* 109:13030–13035
119. Weinmann HJ, Ebert W, Misselwitz B, Schmitt-Willich H (2003) Tissue-specific MR contrast agents. *European Journal of Radiology* 46:33–44
120. Shapiro MG, Atanasijevic T, Faas H, Westmeyer GG, Jasanoff A (2006) Dynamic imaging with MRI contrast agents: quantitative considerations. *Magnetic Resonance Imaging* 24:449–462
121. Lauffer RB (1987) Paramagnetic metal complexes as water proton relaxation agents for NMR imaging: theory and design. *Chemical Review* 87:901–927
122. Ward KM, Aletras AH, Balaban RS (2000) A new class of contrast agents for MRI based on proton chemical exchange dependent saturation transfer (CEST). *Journal Magnetic Resonance* 143:79–87
123. Bloch F, Hanson WW and Packard M (1948), *Phys Rev* 70:474
124. Lauterbur PC, Mendoca-Dias MH, Rudin AM (1978) *Frontier of Biological Energetics*. Dutton PL, Leigh LS, Scarpa A, Eds. Academic, New York
125. Allen M, Bulte JWM, Liepold L, Basu G, Zywicke HA, Frank JA, Young M, Douglas T (2005) Paramagnetic viral nanoparticles as potential high-relaxivity magnetic resonance contrast agents. *Magnetic Resonance Medicine* 54:807–812
126. Anderson EA, Isaacman S, Peabody DS, Wang EY, Canary JW, Kirshenbaum K (2006) Viral nanoparticles donning a paramagnetic coat: Conjugation of MRI contrast agents to the MS2 capsid. *Nanoletters* 6:1160–1164
127. Svenson S, Tomalia DA (2005) Dendrimers in biomedical applications – reflections on the field. *Advanced Drug Delivery Reviews* 57:2106–2129
128. Aulenta F, Hayes W, Rannard S (2003) Dendrimers: a new class of nanoscopic containers and delivery devices. *European Polymer Journal* 39:1741–1771
129. Zhao M, Sun L, Crooks RM (1998) Preparation of Cu nanoclusters within dendrimer templates. *Journal American Chemical Society* 120:4877–4878
130. Talanov VS, Regino CAS, Kobayashi H, Bernardo M, Choyke PL, Brechbiel MW (2006) Dendrimer-based nanoprobe for dual modality magnetic resonance and fluorescence imaging. *Nanoletters* 6:1459–1463
131. Rieter WJ, Taylor KML, An H, Lin W, Lin WB (2006) Nanoscale metal-organic frameworks as potential multimodal contrast enhancing agents. *Journal American Chemical Society* 128:9024–9025
132. Mendonca MH, Lauterbur PC (1986) Ferromagnetic particles as contrast agents for magnetic resonance imaging of liver and spleen. *Magnetic Resonance Medicine* 3:328–330
133. Olsson MBE, Persson BRB, Salford LG, Schröder U (1986) Magnetic resonance imaging. Ferromagnetic particles as contrast agent in T2 NMR imaging. *Magnetic Resonance Imaging* 4:437–440
134. Renshaw PF, Owen CS, Maclaughlin AC, Frey TG, Leigh JS (1986) Ferromagnetic contrast agents: A new approach. *Magnetic Resonance Medicine* 3:217–225
135. Tartaj P, Morales MP, Gonzalez-Carreño T, Veintemillas-Verdaguer S, Serna CJ (2006) Synthesis, properties and biomedical applications of magnetic nanoparticles. *Handbook of Magnetic Materials*, Vol. 16, Ed. K.H.J. Buschow. Elsevier, Amsterdam, Chap. 5, pp. 403–482

136. Roberts PL, Chuang N, Roberts HC (2000) Neuroimaging: Do we really need new contrast agents for MRI. *European Journal Radiology* 34:166–178
137. Zavaljevski A, Holland SK, Dhawan AP (1999) Multilevel computed hemodynamic parameter maps from dynamic perfusion MRI. *IEEE Transactions on Instrumentation and Measurement* 48:711–720
138. Bonnemain B (1998) Superparamagnetic agents in magnetic resonance imaging: Physicochemical characteristics and clinical applications. A review. *Journal Drug Targeting* 6:167–174
139. Weissleder R, Heautot JF, Schaffer BK, Nossif N, Papisov A, Bogdanov A, Brady TJ (1994) MR lymphography: Study of a high-efficiency lymphotropic agent. *Radiology* 191:225–230
140. Clement O, Guimaraes R, de Kerviler E, Frija G (1994) Magnetic resonance lymphography: Enhancement patterns using superparamagnetic nanoparticles. *Investigative Radiology* 29:S226–S228
141. Laconte L, Mitin N, Bao G (2005) Magnetic nanoparticle probes. *Nanotoday* 1:32–38
142. Arbab AS, Yocum GT, Kalish H, Jordan EK, Anderson SA, Khakoo AY, Read EJ, Frank JA (2004) Efficient magnetic cell labelling with protamine sulfate complexed to ferumoxides for cellular MRI. *Blood* 104:1217–1223
143. Bulte JWM, Douglas T, Witwer B, Zhang SC, Strable E, Lewis BK, Zywicke H, Miller B, van Gelderen P, Moskowitz BM, Duncan ID, Frank JA (2001) Magnetodendrimers allow endosomal magnetic labelling and in vivo tracking of stem cells. *Nature Biotechnology* 19:1141–1147
144. Bomati-Miguel O, Morales MP, Tartaj P, Ruiz-Cabello J, Bonville P, Santos M, Zhao XQ, Veintemillas-Verdaguer S (2005) Fe-based nanoparticulate metallic alloys as contrast agents for magnetic resonance imaging. *Biomaterials* 26:5695–5703
145. Li Z, Wei L, Gao M, Lei H (2005) One-pot reaction to synthesize biocompatible magnetite nanoparticles. *Advanced Materials* 17:1001–1005
146. Jun Y, Hou Y, Choi JS, Lee JH, Song HT, Kim S, Yoon S, Kim KS, Shin JS, Su JS, Cheon J (2005) Nanoscale size effect of magnetic nanocrystals and their utilization for cancer diagnosis via magnetic resonance imaging. *Journal American Chemical Society* 127:5732–5733
147. Mornet S, Vasseur S, Grasset F, Duguet E (2004) Magnetic nanoparticle design for medical diagnosis and therapy. *Journal Materials Chemistry* 14:2161–2175
148. Mahato RI (2005) Water insoluble and soluble lipids for gene delivery. *Advanced Drug Delivery Reviews* 57: 699–712
149. Kostarelos K (2003) Rational design and engineering of delivery systems for therapeutics: biomedical exercises in colloid and surface science. *Advanced Colloid Interface Science* 106: 147–168
150. Lavan DA, McGuire T, Langer R (2003) Small-scale systems for in vivo drug delivery. *Nature Biotechnology* 21:1184–1191
151. Steinberg-Yfrach G, Liddell PA, Hung S-C, Moore AL, Gust D, Moore TA (1997) Conversion of light energy to proton potential in liposomes by artificial photosynthetic reaction centres. *Nature* 385:239–241
152. Steinberg-Yfrach G, Rigaud J-L, Durantini EN, Moore AL, Gust D, Moore TA (1998) Light-driven production of ATP catalysed by F0F1-ATP synthase in an artificial photosynthetic membrane. *Nature* 392:479–482
153. Gokel GW, De Wall SL (1999) Redox control of aggregation in synthetic vesicles. *Advances in Supramolecular Chemistry* 5:203–235
154. Westmark PR, Gardiner SJ, Smith BD (1996) Selective monosaccharide transport through lipid bilayers using boronic acid carriers. *Journal of the American Chemical Society* 118:11093–11100
155. Boon JM, Smith BD (1999) Facilitated phospholipid translocation across vesicle membranes using low-molecular-weight synthetic flippases. *Journal of the American Chemical Society* 121:11924–11925

156. Boon JM, Smith BD (2001) Facilitated phosphatidylcholine flip-flop across erythrocyte membranes using low molecular weight synthetic translocases. *Journal of the American Chemical Society* 123:6221–6226
157. Vandenburg YR, Zhang Z-Y, Fishkind DJ, Smith BD (2000) Enhanced cell binding using liposomes containing an artificial carbohydrate-binding receptor. *Chemical Communications*:149–150
158. Lasic DD (1993) *Liposomes: From Physics to Applications*. Elsevier, Amsterdam, The Netherlands
159. Gregoriadis G (Editor) (1993) *Liposome Technology*. CRC Press, Boca Raton, FL (USA)
160. Vamvakaki V, Fournier D, Chaniotakis NA (2005) Fluorescence detection of enzymatic activity within a liposome based nano-biosensor. *Biosensors and Bioelectronics* 21:384–388
161. Yatvin MB, Weinstein JN, Dennis WH, Blumenthal R (1978) Design of liposomes for enhanced local release of drugs by hyperthermia. *Science* 202:1290–1293
162. Matsui K, Sando S, Sera T, Aoyama Y, Sasaki Y, Komatsu T, Terashima T, Kikuchi J-I (2006) Cerasome as an infusible, cell-friendly, and serum-compatible transfection agent in a viral size. *Journal of the American Chemical Society* 128:3114–3115
163. Felgner PL, Gadek TR, Holm M, Roman R, Chan HW, Wenz M, Northrop JP, Ringold GM, Danielsen M (1987) Lipofection: a highly efficient, lipid-mediated DNA-transfection procedure. *Proceedings of the National Academy of Sciences of the United States of America* 84:7413–7417
164. Kabanov AV, Felgner PL, Seymour LW (Eds.) (1998) *Self-Assembling Complexes for Gene Delivery: From Laboratory to Clinical Trial*. Wiley, Chichester
165. Boussif O, Lezoualc'h F, Zanta MA, Mergny MD, Scherman D, Demeneix B, Behr J-P (1995) A versatile vector for gene and oligonucleotide transfer into cells in culture and in vivo: Polyethylenimine. *Proceedings of the National Academy of Sciences of the United States of America* 92:7297–7301
166. Rensen PCN, Sliedregt LAJM, Ferns M, Kieviet E, Van Rossenberg SMW, Van Leeuwen SH, Van Berkel TJC, Biessen EAL (2001) Determination of the upper size limit for uptake and processing of ligands by the asialoglycoprotein receptor on hepatocytes in vitro and in vivo. *Journal of Biological Chemistry* 276:37577–37584
167. Osaki F, Kanamori T, Sando S, Sera T, Aoyama Y (2004) A quantum dot conjugated sugar ball and its cellular uptake. On the size effects of endocytosis in the subviral region. *Journal of the American Chemical Society* 126:6520–6521
168. Zhang YP, Sekirov L, Saravolac EG, Wheeler JJ, Tardi P, Clow K, Leng E, Sun R, Cullis PR, Scherrer P (1999) Stabilized plasmid-lipid particles for regional gene therapy: Formulation and transfection properties. *Gene Therapy* 6:1438–1447
169. Bettinger T, Remy J-S, Erbacher P (1999) Size reduction of galactosylated PEI/DNA complexes improves lectin-mediated gene transfer into hepatocytes. *Bioconjugate Chemistry* 10:558–561
170. Dauty E, Remy J-S, Blessing T, Behr J-P (2001) Dimerizable cationic detergents with a low cmc condense plasmid DNA into nanometric particles and transfect cells in culture. *Journal of the American Chemical Society* 123:9227–9234
171. Zuber G, Zammuto-Italiano L, Dauty E, Behr J-P (2003) Targeted gene delivery to cancer cells: Directed assembly of nanometric DNA particles coated with folic acid. *Angewandte Chemie – International Edition* 42:2666–2669
172. Keller M, Harbottle RP, Perouzel E, Colin M, Shah I, Rahim A, Vaysse L, Bergau A, Moritz S, Brahimi-Horn C, Coutelle C, Miller AD (2003) Nuclear localisation sequence templated nonviral gene delivery vectors: Investigation of intracellular trafficking events of LMD and LD vector systems. *ChemBioChem* 4:286–298
173. Perouzel E, Jorgensen MR, Keller M, Miller AD (2003) Synthesis and formulation of neoglycolipids for the functionalization of liposomes and lipoplexes. *Bioconjugate Chemistry* 14:884–898
174. Nakai T, Kanamori T, Sando S, Aoyama Y (2003) Remarkably size-regulated cell invasion by artificial viruses. Saccharide-dependent self-aggregation of glycoviruses and its conse-

- quences in glycoviral gene delivery. *Journal of the American Chemical Society* 125:8465–8475
175. Katagiri K, Hamasaki R, Ariga K, Kikuchi J-I (2002) Layered paving of vesicular nanoparticles formed with cerasome as a bioinspired organic–inorganic hybrid. *Journal of the American Chemical Society* 124:7892–7893
 176. Maeda H, Wu J, Sawa T, Matsumura Y, Hori K (2000) Tumor vascular permeability and the EPR effect in macromolecular therapeutics: A review. *Journal of Controlled Release* 65:271–284
 177. Decher G, Hong JD, Schmitt J (1992) Buildup of ultrathin multilayer films by a self-assembly process: III. Consecutively alternating adsorption of anionic and cationic polyelectrolytes on charged surfaces. *Thin Solid Films* 210–211:831–835
 178. Decher G (1997) Fuzzy nanoassemblies: Toward layered polymeric multicomposites. *Science* 277:1232–1237
 179. Sukhorukov GB, Donath E, Davis S, Lichtenfeld H, Caruso F, Popov VI, Möhwald H (1998) Stepwise polyelectrolyte assembly on particle surfaces: A novel approach to colloid design. *Polymers for Advanced Technologies* 9:759–767
 180. Donath E, Sukhorukov GB, Caruso F, Davis SA, Möhwald H (1998) Novel hollow polymer shells by colloid-templated assembly of polyelectrolytes. *Angewandte Chemie – International Edition* 37:2202–2205
 181. Shchukin DG, Sukhorukov GB (2003) Selective YF₃ nanoparticle formation in polyelectrolyte capsules as microcontainers for yttrium recovery from aqueous solutions. *Langmuir* 19:4427–4431
 182. Farhat TR, Schlenoff JB (2003) Doping-controlled ion diffusion in polyelectrolyte multilayers: Mass transport in reluctant exchangers. *Journal of the American Chemical Society* 125:4627–4636
 183. Antipov AA, Sukhorukov GB, Möhwald H (2003) Influence of the ionic strength on the polyelectrolyte multilayers' permeability. *Langmuir* 19:2444–2448
 184. Sukhorukov GB, Brumen M, Donath E, Möhwald H (1999) Hollow polyelectrolyte shells: Exclusion of polymers and donnan equilibrium. *Journal of Physical Chemistry B* 103:6434–6440
 185. Ai H, Jones SA, De Villiers MM, Lvov YM (2003) Nano-encapsulation of furosemide microcrystals for controlled drug release. *Journal of Controlled Release* 86:59–68
 186. Antipov AA, Sukhorukov GB, Leporatti S, Radtchenko IL, Donath E, Möhwald H. (2002) Polyelectrolyte multilayer capsule permeability control. *Colloids and Surfaces A: Physicochemical and Engineering Aspects* 198–200:535–541
 187. Shchukin DG, Radtchenko IL, Sukhorukov GB (2003) Micron-scale hollow polyelectrolyte capsules with nanosized magnetic Fe₃O₄ inside. *Materials Letters* 57:1743–1747
 188. Gaponik N, Radtchenko IL, Sukhorukov GB, Weller H, Rogach AL (2002) Toward encoding combinatorial libraries: Charge-driven microencapsulation of semiconductor nanocrystals luminescing in the visible and near IR. *Advanced Materials* 14:879–882
 189. Shchukin DG, Shutava T, Shchukina E, Sukhorukov GB, Lvov YM (2004) Modified polyelectrolyte microcapsules as smart defense systems. *Chemistry of Materials* 16:3446–3451
 190. Katagiri K, Caruso F (2004) Functionalization of colloids with robust inorganic–based lipid coatings. *Macromolecules* 37:9947–9953
 191. Vallet-Regí M, Rámila A, Del Real RP, Pérez-Pariente J (2001) A new property of MCM-41: Drug delivery system. *Chemistry of Materials* 13:308–311
 192. Rámila A, Muñoz B, Pérez-Pariente J, Vallet-Regí M (2003) Mesoporous MCM-41 as drug host system. *Journal of Sol–Gel Science and Technology* 26:1199–1202
 193. Muñoz B, Rámila A, Pérez-Pariente J, Díaz I, Vallet-Regí M (2003) MCM-41 organic modification as drug delivery rate regulator. *Chemistry of Materials* 15:500–503
 194. Horcajada P, Rámila A, Pérez-Pariente J, Vallet-Regí M (2004) Influence of pore size of MCM-41 matrices on drug delivery rate. *Microporous and Mesoporous Materials* 68:105–109
 195. Doadrio AL, Sousa EMB, Doadrio JC, Pérez Pariente J, Izquierdo-Barba I, Vallet-Regí M (2004) Mesoporous SBA-15 HPLC evaluation for controlled gentamicin drug delivery. *Journal of Controlled Release* 97:125–132

196. Tourné-Péteilh C, Lerner DA, Charnay C, Nicole L, Bégu S, Devoisselle J-M (2003) The potential of ordered mesoporous silica for the storage of drugs: The example of a pentapeptide encapsulated in a MSU-Tween 80. *ChemPhysChem* 4:281–286
197. Fisher KA, Huddersman KD, Taylor MJ (2003) Comparison of micro- and mesoporous inorganic materials in the uptake and release of the drug model fluorescein and its analogues. *Chemistry – A European Journal* 9:5873–5878
198. Hata H, Saeki S, Kimura T, Sugahara Y, Kuroda K (1999) Adsorption of taxol into ordered mesoporous silicas with various pore diameters. *Chemistry of Materials* 11:1110–1119
199. Lai C-Y, Trewyn BG, Jeftinija DM, Jeftinija K, Xu S, Jeftinija S, Lin VS-Y (2003) A mesoporous silica nanosphere-based carrier system with chemically removable CdS nanoparticle caps for stimuli-responsive controlled release of neurotransmitters and drug molecules. *Journal of the American Chemical Society* 125:4451–4459
200. Mal NK, Fujiwara M, Tanaka Y (2003) Photocontrolled reversible release of guest molecules from coumarin-modified mesoporous silica. *Nature* 421:350–353
201. Li Y, Shi J, Chen H, Hua Z, Zhang L, Ruan M, Yan J, Yan D (2003) One-step synthesis of hydrothermally stable cubic mesoporous aluminosilicates with a novel particle structure. *Microporous and Mesoporous Materials* 60:51–56
202. Li Y, Shi J, Hua Z, Chen H, Ruan M, Yan D (2003) Hollow spheres of mesoporous aluminosilicate with a three-dimensional pore network and extraordinarily high hydrothermal stability. *Nano Letters* 3:609–612
203. Zhu Y, Shi J, Shen W, Dong X, Feng J, Ruan M, Li Y (2005) Stimuli-responsive controlled drug release from a hollow mesoporous silica sphere/polyelectrolyte multilayer core-shell structure. *Angewandte Chemie – International Edition* 44:5083–5087
204. Schacht S, Huo Q, Voigt-Martin IG, Stucky GD, Schuth F (1996) Oil-water interface templating of mesoporous macroscale structures. *Science* 273:768–771
205. Tanev PT, Pinnavaia TJ (1996) Biomimetic templating of porous lamellar silicas by vesicular surfactant assemblies. *Science* 271:1267–1269
206. Kim SS, Zhang W, Pinnavaia TJ (1998) Ultrastable mesostructured silica vesicles. *Science* 282:1302–1305
207. Katagiri K, Ariga K, Kikuchi J-I (1999) Preparation of organic–inorganic hybrid vesicle “Cerasome” derived from artificial lipid with alkoxysilyl head. *Chemistry Letters* 28:661–662
208. Emmerich O, Hugenberg N, Schmidt M, Sheiko SS, Baumann F, Deubzer B, Weis J, Ebenhoch J (1999) Molecular boxes based on hollow organosilicon micronetworks. *Advanced Materials* 11:1299–1303
209. Jungmann N, Schmidt M, Maskos M, Weis J, Ebenhoch J (2002) Synthesis of amphiphilic poly(organosiloxane) nanospheres with different core-shell architectures. *Macromolecules* 35:6851–6857
210. Jungmann N, Schmidt M, Ebenhoch J, Weis J, Maskos M (2003) Dye Loading of Amphiphilic Poly(organosiloxane) Nanoparticles. *Angewandte Chemie International Edition* 42:1713–1717
211. Lu Y, McLellan J, Xia Y (2004) Synthesis and crystallization of hybrid spherical colloids composed of polystyrene cores and silica shells. *Langmuir* 20:3464–3470
212. Koh K, Ohno K, Tsujii Y, Fukuda T (2003) Precision synthesis of organic/inorganic hybrid nanocapsules with a silanol-functionalized micelle template. *Angewandte Chemie – International Edition* 42:4194–4197
213. Du J, Chen Y, Zhang Y, Han CC, Fischer K, Schmidt M (2003) Organic/Inorganic hybrid vesicles based on a reactive block copolymer. *Journal of the American Chemical Society* 125:14710–14711
214. Du J, Chen Y (2004) Preparation of organic/inorganic hybrid hollow particles based on gelation of polymer vesicles. *Macromolecules* 37:5710–5716
215. Freeman MW, Arrot A, Watson HHL (1960) Magnetism in medicine. *Journal Applied Physics* 31: S404–S405

216. Lübke AS, Bergemann C, Riess H (1996) Clinical experiences with magnetic drag targeting: A phase I study with 4'-epidoxorubicin in 14 patients with advanced solid tumors. *Cancer Research* 56:4686–4693
217. Joubert JC (1997) Magnetic microcomposites as vectors for bioactive agents: The state of art. *Anales de Quimica* 93:S70–S76
218. Tanaka H, Sugita T, Yasunaga Y, Shimose S, Deie M, Kubo T, Murakami T, Ochi M (2005) Efficiency of magnetic liposomal transforming growth factor-beta 1 in the repair of articular cartilage defects in a rabbit model. *Journal Biomedical Materials Research A73*:255–263
219. Berry CC (2005) Possible exploitation of magnetic nanoparticle–cell interaction for biomedical applications. *Journal Materials Chemistry* 15:543–547
220. Ferrari S, Gedes DM, Alton EWF (2002) Barriers to and new approaches for gene therapy and gene delivery in cystic fibrosis. *Advanced Drug Delivery Reviews* 54:1373–1393
221. Gupta AK, Gupta M (2005) Synthesis and surface engineering of iron oxide nanoparticles for biomedical applications. *Biomaterials* 26:3995–4021
222. Van der Zee J (2002) Heating the patient: A promising approach. *Annals Oncology* 13: 1173–1184
223. Hilger I, Hergt R, Kaiser WA (2005) Use of magnetic nanoparticle heating in the treatment of breast cancer. *IEE Proceedings Nanobiotechnology* 152:33–39
224. Everts M, Saini V, Leddon JL, Kok RJ, Stoff-Khalili M, Preuss MA, Millican CL, Perkins G, Brown JM, Bagaria H, Nikles DE, Johnson DT, Zharov VP, Curiel DT (2006) Covalently linked Au nanoparticles to a viral vector: potential for combined photothermal and gene cancer therapy. *Nanoletters* 6: 587–591
225. Gilchrist RK, Medal R, Shorey WD, Hanselman RC, Parrott JC, Taylor CB (1957) Selective inductive heating of lymph nodes. *Annals Surgery* 146:596–606
226. Wada S, Tazawa K, Furuta I, Nagae H (2003) Antitumor effect of new local hyperthermia using dextran magnetite complex in hamster tongue carcinoma. *Oral Diseases* 9:218–223
227. Ito A, Shinkai M, Honda H, Kobayashi T (2001) Heat-inducible TNF-alpha gene therapy combined with hyperthermia using magnetic nanoparticles as a novel tumor-targeted therapy. *Cancer Gene Therapy* 8:649–654
228. Gu H, Xu K, Yang Z, Chang CK, Xu B (2005) Synthesis and cellular uptake of porphyrin decorated iron oxide nanoparticles – a potential candidate for bimodal anticancer therapy. *Chemical Communications*, 4270–4272
229. Derycke ASL, de Witte PAM (2004) Liposomes for photodynamic therapy. *Advanced Drug Delivery Reviews* 56:17–30
230. Gorman A, Killoran J, O'Shea C, Kenna T, Gallagher WM, O'Shea DF (2004) In vitro demonstration of the heavy-atom effect for photodynamic therapy. *Journal of the American Chemical Society* 126:10619–10631
231. Gübitz G, Künssberg E, Van Zoonen P, Jansen H, Gooijer C, Velthorst NH, Fei RW (1988) *Chemically Modified Surfaces in Science and Industry*. Vol. 2. Leyden DE, Collins WT, Eds. Gordon and Breach, London
232. Gorton L, Marko-Varga G, Domínguez E, Emneus J (1994) *Analytical Applications of Immobilized Enzyme Reactors*. Lam S, Malikin G, Eds. Blackie Academic & Professional, New York
233. Horbett TA, Brash JL (1995) *Proteins at interfaces II. Fundamentals and applications*, ACS symposium series 602, American Chemical Society, Washington, US
234. Rosevear A, Kennedy JF, Cabral JMS(Eds.) (1987) *Immobilized Enzymes and Cells*. Adam Higler, Bristol and Philadelphia
235. Yoshinaga K, Kito T, Yamaye M (1990) Effective immobilization of protein linked with polyethylene glycol on silica via hydrogels using silica sol. *Journal of Applied Polymer Science* 41:1443–1450
236. Tiberg F, Brink C, Hellsten M, Holmberg K (1992) Immobilization of protein to surface-grafted PEO/PPO block copolymers. *Colloid and Polymer Science* 270:1188–1193
237. Miksa B, Slomkowski S (1995) Polypyrrole core/polyacrolein shell latex for protein immobilization. *Colloid and Polymer Science* 273:47–52

238. Yoshinaga K, Kondo K, Kondo A (1995) Efficient immobilization of protein on monodispersed colloidal silica particles modified by copolymers of maleic-anhydride and styrene or methyl-methacrylate. *Polymer Journal* 27:98–100
239. Shabat D, Grynszpan F, Saphier S, Turniansky A, Avnir D, Keinan E (1997) An efficient Sol Gel reactor for antibody-catalyzed transformations. *Chemistry of Materials* 9:2258–2260
240. Fang J, Knobler CM (1996) Phase-separated two-component self-assembled organosilane monolayers and their use in selective adsorption of a protein. *Langmuir* 12:1368–1374
241. Hamachi I, Fujita A, Kunitake T (1994) Enhanced N-demethylase activity of cytochrome c bound to a phosphate-bearing synthetic bilayer membrane. *Journal of the American Chemical Society* 116:8811–8812
242. Fujita A, Senzu H, Kunitake T, Hamachi I (1994) Enhanced peroxidase activity of cytochrome c by phosphate bilayer membrane. *Chemical Letters*:1219–1222
243. Koilpillai L, Gadre RA, Bhatnagar S, Rajan CR, Ponrathnam S, Kumar KK, Ambekar GR, Shewale JG (1990) Immobilization of penicillin G acylase on methacrylate polymers. *Journal of Chemical Technology and Biotechnology* 49:173–182
244. Mitchell DT, Lee SB, Trofin L, Li N, Nevanen TK, Söderlund H, Martin CR (2002) Smart nanotubes for bioseparations and biocatalysis. *Journal of the American Chemical Society* 124:11864–11865
245. Mukhopadhyay K, Phadtare S, Vinod VP, Kumar A, Rao M, Chaudhari RV, Sastry M (2003) Gold nanoparticles assembled on amine-functionalized Na - Y zeolite: A biocompatible surface for enzyme immobilization. *Langmuir* 19:3858–3863
246. Kumar CV, McLendon GL (1997) Nanoencapsulation of Cytochrome c and horseradish peroxidase at the galleries of α -zirconium phosphate. *Chemistry of Materials* 9: 863–870
247. He J, Li X, Evans DG, Duan X, Li C (2000) A new support for the immobilization of penicillin acylase. *Journal of Molecular Catalysis – B Enzymatic* 11:45–53
248. Wang Y, Caruso F (2005) Mesoporous silica spheres as supports for enzyme immobilization and encapsulation. *Chemistry of Materials* 17:953–961
249. Hamachi I, Fujita A, Kunitake T (1994) Enhanced N-demethylase activity of cytochrome c bound to a phosphate-bearing synthetic bilayer membrane. *Journal of the American Chemical Society* 116:8811–8812
250. Chen X, Hu N, Zeng Y, Rusling JF, Yang J (1999) Ordered electrochemically active films of hemoglobin, didodecyldimethylammonium ions, and clay. *Langmuir* 15:7022–7030
251. Mrksich M, Sigal GB, Whitesides GM (1995) Surface plasmon resonance permits *in situ* measurement of protein adsorption on self-assembled monolayers of alkanethiolates on gold. *Langmuir* 11:4383–4385
252. Nicolini C, Erokhin V, Antolini F, Catasti P, Facci P (1993) Thermal stability of protein secondary structure in Langmuir-Blodgett films. *Biochimica et Biophysica Acta – General Subjects* 1158:273–278
253. Boussaad S, Dziri L, Arechabaleta R, Tao NJ, Leblanc RM (1998) Electron-transfer properties of cytochrome c Langmuir-Blodgett films and interactions of cytochrome c with lipids. *Langmuir* 14:6215–6219
254. Yang Z, Mesiano AJ, Venkatasubramanian S, Gross SH, Harris JM, Russell AJ (1995) Activity and stability of enzymes incorporated into acrylic polymers. *Journal of the American Chemical Society* 117:4843–4850
255. Franchina JG, Lackowski WM, Dermody DL, Crooks RM, Bergbreiter DE, Sirkar K, Russell RJ, Pishko MV (1999) Electrostatic immobilization of glucose oxidase in a weak acid, polyelectrolyte hyperbranched ultrathin film on gold: Fabrication, characterization, and enzymatic activity. *Analytical Chemistry* 71:3133–3139
256. Sastry M (2002) Entrapment of proteins and DNA in thermally evaporated lipid films. *Trends in Biotechnology* 20:185–188
257. Sastry M, Rao M, Ganesh KN (2002) Electrostatic assembly of nanoparticles and biomacromolecules. *Accounts of Chemical Research* 35:847–855

258. Daubresse C, Grandfils C, Jérôme R, Teyssié P (1996) Enzyme immobilization in reactive nanoparticles produced by inverse microemulsion polymerization. *Colloid and Polymer Science* 274:482–489
259. Martins MBF, Simões SID, Cruz MEM, Gaspar R (1996) Development of enzyme-loaded nanoparticles: Effect of pH. *Journal of Materials Science: Materials in Medicine* 7:413–414
260. Caruso F, Schüller C (2000) Enzyme multilayers on colloid particles: Assembly, stability, and enzymatic activity. *Langmuir* 16:9595–9603
261. Liao M-H, Chen D-H (2001) Immobilization of yeast alcohol dehydrogenase on magnetic nanoparticles for improving its stability. *Biotechnology Letters* 23:1723–1727
262. Jia H, Zhu G, Wang P (2003) Catalytic behaviors of enzymes attached to nanoparticles: The effect of particle mobility. *Biotechnology and Bioengineering* 84:406–414
263. Crumbliss AL, Perine SC, Stonehuerner J, Tubergen KR, Zhao J, Henkens RW (1992) Colloidal gold as a biocompatible immobilization matrix suitable for the fabrication of enzyme electrodes by electrodeposition. *Biotechnology and Bioengineering* 40:483–490
264. Stonehuerner J, Zhao J, O'Daly JP, Crumbliss AL, Henkens RW (1992) Comparison of colloidal gold electrode fabrication methods: The preparation of a horseradish peroxidase enzyme electrode. *Biosensors and Bioelectronics* 7:421–428
265. Zhao J, O'Daly JP, Henkens RW, Stonehuerner J, Crumbliss AL (1996) A xanthine oxidase/colloidal gold enzyme electrode for amperometric biosensor applications. *Biosensors and Bioelectronics* 11:493–502
266. Mirkin CA, Letsinger RL, Mucic RC, Storhoff JJ (1996) A DNA-based method for rationally assembling nanoparticles into macroscopic materials. *Nature* 382:607–609
267. Alivisatos AP, Johnsson KP, Peng X, Wilson TE, Loweth CJ, Bruchez Jr MP, Schultz PG (1996) Organization of 'nanocrystal molecules' using DNA. *Nature* 382: 609–611
268. Shenton W, Davis SA, Mann S (1999) Directed self-assembly of nanoparticles into macroscopic materials using antibody-antigen recognition. *Advanced Materials* 11:449–452
269. Connolly S, Fitzmaurice D (1999) Programmed assembly of gold nanocrystals in aqueous solution. *Advanced Materials* 11:1202–1205
270. Patel DS, Aithal RK, Krishna G, Lvov YM, Tien M, Kuila D (2005) Nano-assembly of manganese peroxidase and lignin peroxidase from *P. chrysosporium* for biocatalysis in aqueous and non-aqueous media. *Colloids and Surfaces B: Biointerfaces* 43:13–19
271. Caruso F, Möhwald H (1999) Protein multilayer formation on colloids through a stepwise self-assembly technique. *Journal of the American Chemical Society* 121:6039–6046
272. Caruso F, Fiedler H, Haage K (2000) Assembly of β -glucosidase multilayers on spherical colloidal particles and their use as active catalysts. *Colloids and Surfaces A: Physicochemical and Engineering Aspects* 169:287–293
273. Schüller C, Caruso F (2000) Preparation of enzyme multilayers on colloids for biocatalysis. *Macromolecular Rapid Communications* 21:750–753
274. Caruso F, Niikura K, Furlong DN, Okahata Y (1997) Part 2. Assembly of alternating polyelectrolyte and protein multilayer films for immunosensing. *Langmuir* 13:3427–3433
275. Jordan CE, Frutos AG, Thiel AJ, Corn RM (1997) Surface plasmon resonance imaging measurements of DNA hybridization adsorption and streptavidin/DNA multilayer formation at chemically-modified gold surfaces. *Analytical Chemistry* 69:4939–4947
276. Decher G, Lehr B, Lowack K, Lvov Y, Schmitt J (1994) New nanocomposite films for biosensors: Layer-by-layer adsorbed films of polyelectrolytes, proteins or DNA. *Biosensors and Bioelectronics* 9:677–684
277. Reneker DH, Chun I (1996) Nanometre diameter fibres of polymer, produced by electrospinning. *Nanotechnology* 7:216–223
278. Fang X, Reneker DH (1997) DNA fibers by electrospinning. *Journal of Macromolecular Science – Physics* 36:169–173
279. Norris ID, Shaker MM, Ko FK, MacDiarmid AG (2000) Electrostatic fabrication of ultrafine conducting fibers: Polyaniline/polyethylene oxide blends. *Synthetic Metals* 114:109–114
280. MacDiarmid AG, Jones Jr WE, Norris ID, Gao J, Johnson AT Jr, Pinto NJ, Hone J, Han B, Ko FK, Okuzaki H, Llaguno M (2001) Electrostatically-generated nanofibers of electronic polymers. *Synthetic Metals* 119: 27–30

281. Megelski S, Stephens JS, Chase DB, Rabolt JF (2002) Micro- and nanostructured surface morphology on electrospun polymer fibers. *Macromolecules* 35:8456–8466
282. Frenot A, Chronakis IS (2003) Polymer nanofibers assembled by electrospinning. *Current Opinion in Colloid and Interface Science* 8:64–75
283. Li D, Wang Y, Xia Y (2003) Electrospinning of polymeric and ceramic nanofibers as uniaxially aligned arrays. *Nano Letters* 3:1167–1171
284. Wnek GE, Carr ME, Simpson DG, Bowlin GL (2003) Electrospinning of nanofiber fibrinogen structures. *Nano Letters* 3:213–216
285. Li D, Wang Y, Xia Y (2004) Electrospinning nanofibers as uniaxially aligned arrays and layer-by-layer stacked films. *Advanced Materials* 16:361–366
286. Li D, Xia Y (2004) Direct fabrication of composite and ceramic hollow nanofibers by electrospinning. *Nano Letters* 4:933–938
287. Jia H, Zhu G, Vugrinovich B, Kataphinan W, Reneker DH, Wang P (2002) Enzyme-carrying polymeric nanofibers prepared via electrospinning for use as unique biocatalysts. *Biotechnology Progress* 18:1027–1032
288. Smith D, Kataphinan W, Reneker D, Dabney S (2002) Preservation of biological materials using fiber-forming techniques. WO 2002100628
289. Al-Sheheri HA. The use of electrospinning technology in enzymes preservation and chemical warfare protective clothing applications. The University of Akron, Dissertation, 2003
290. Wang Y, Hsieh Y-L (2003) Polymer Preparation. (American Chemical Society, Division of Polymer Chemistry) 44: 1212–1213
291. Xie J, Hsieh Y-L (2003) Ultra-high surface fibrous membranes from electrospinning of natural proteins: Casein and lipase enzyme. *Journal of Materials Science* 38: 2125–2133
292. Zeng ZSJ, Hou H, Kissel T, Wendorff JH, Greiner A (2003) Functional polymer nanofibers and nanotubes via electrospinning: chemical modifications for selected applications. *Polym Prep (American Chemical Society, Division of Polymer Chemistry)* 44:76–77
293. Bruno FF, Drew C, Nagarajan R, Wang X, Kumar J, Samuelson LA (2004) Conductive polymer complexes from macromolecule inspired biocatalysis. *Polymeric Materials: Science and Engineering* 90:234–235
294. Gouma P, Simon S, Jha PK, Sawicka K (2004) Bio-composite oxides for resistive detection of pathogens. *Chemical Senses* 20:72–73
295. Hsieh Y-L, Xie JB, Wang YH, Chen H, Li L, Zhang LF (2004) Generation of polymer-based nano-porous fibers and protein or enzyme membrane compositions. PCT International Application WO 2004044281
296. Wang Y, Hsieh Y-L (2004) Enzyme immobilization to ultra-fine cellulose fibers via amphiphilic polyethylene glycol spacers. *Journal of Polymer Science, Part A: Polymer Chemistry* 42:4289–4299
297. Zeng J, Chen X, Liang Q, Xu X, Jing X (2004) Enzymatic degradation of poly(L-lactide) and poly(β -caprolactone) electrospun fibers. *Macromolecular Bioscience* 4:1118–1125
298. Chua K-N, Lim W-S, Zhang P, Lu H, Wen J, Ramakrishna S, Leong KW, Mao H-Q (2005) Stable immobilization of rat hepatocyte spheroids on galactosylated nanofiber scaffold. *Biomaterials* 26:2537–2547
299. Kim J (2005) Enzyme-polymer composites with high biocatalytic activity and stability. *Polymer Material: Science Engineering* 92:552–553
300. Kim BC, Nair S, Kim J, Kwak JH, Grate JW, Kim SH, Gu MB (2005) Preparation of biocatalytic nanofibres with high activity and stability via enzyme aggregate coating on polymer nanofibres. *Nanotechnology* 16:S382–S388
301. Kim J, Jia H, Wang P (2006) Challenges in biocatalysis for enzyme-based biofuel cells. *Biotechnology Advances* 24:296–308
302. Rege K, Raravikar NR, Kim D-Y, Schadler LS, Ajayan PM, Dordick JS (2003) Enzyme-polymer-single walled carbon nanotube composites as biocatalytic films. *Nano Letters* 3:829–832
303. Martin CR (1994) Nanomaterials: A membrane-based synthetic approach. *Science* 266:1961–1966

304. Miller SA, Young VY, Martin CR (2001) Electro-osmotic flow in template-prepared carbon nanotube membranes. *Journal of the American Chemical Society* 123:12335–12342
305. Cepak VM, Martin CR (1999) Preparation of polymeric micro- and nanostructures using a template-based deposition method. *Chemistry of Materials* 11:1363–1367
306. Steinle ED, Mitchell DT, Wirtz M, Lee SB, Young VY, Martin CR (2002) Ion channel mimetic micropore and nanotube membrane sensors. *Analytical Chemistry* 74:2416–2422
307. Hornyak GL, Patrissi CJ, Martin CR (1997) Fabrication, characterization, and optical properties of gold nanoparticle/porous alumina composites: The non-scattering Maxwell-Garnett limit. *Journal of Physical Chemistry B* 101:1548–1555
308. Bellezza F, Cipiciani A, Costantino U, Elena Negozio M (2002) Zirconium phosphate and modified zirconium phosphates as supports of lipase. Preparation of the composites and activity of the supported enzyme. *Langmuir* 18:8737–8742
309. Bellezza F, Cipiciani A, Costantino U (2003) Esterase activity of biocomposites constituted by lipases adsorbed on layered zirconium phosphate and phosphonates: Selective adsorption of different enzyme isoforms. *Journal of Molecular Catalysis B: Enzymatic* 26:47–56
310. Bellezza F, Cipiciani A, Costantino U, Nicolis S (2004) Catalytic activity of myoglobin immobilized on zirconium phosphonates. *Langmuir* 20:5019–5025
311. Schafer WA, Carr PW, Funkenbusch EF, Parson KA (1991) Physical and chemical characterization of a porous phosphate-modified zirconia substrate. *Journal of Chromatography* 587:137–147
312. Randon J, Blanc P, Paterson R (1995) Modification of ceramic membrane surfaces using phosphoric acid and alkyl phosphonic acids and its effects on ultrafiltration of BSA protein. *Journal of Membrane Science* 98:119–129
313. Gao W, Dickinson L, Grozinger C, Morin FG, Reven L (1996) Self-assembled monolayers of alkylphosphonic acids on metal oxides. *Langmuir* 12:6429–6435
314. Clausen AM, Carr PW (1998) Chromatographic Characterization of Phosphonate Analog EDTA-Modified Zirconia Support for Biochromatographic Applications. *Analytical Chemistry* 70:378–385
315. Carrière D, Moreau M, Barboux P, Boilot J-P, Spalla O (2004) Modification of the surface properties of porous nanometric zirconia particles by covalent grafting. *Langmuir* 20:3449–3455
316. Bellezza F, Cipiciani A, Quotadamo MA (2005) Immobilization of myoglobin on phosphate and phosphonate grafted-zirconia nanoparticles. *Langmuir* 21:11099–11104
317. Yu A, Wang Y, Barlow E, Caruso F (2005) Mesoporous silica particles as templates for preparing enzyme-loaded biocompatible microcapsules. *Advanced Materials* 17:1737–1741
318. Wang Y, Caruso F (2006) Nanoporous protein particles through templating mesoporous silica spheres. *Advanced Materials* 18:795–800
319. Li W, Huang Z, MacKay JA, Grube S, Szoka Jr. FC (2005) Low-pH-sensitive poly(ethylene glycol) (PEG)-stabilized plasmid nanolipoparticles: Effects of PEG chain length, lipid composition and assembly conditions on gene delivery. *Journal of Gene Medicine* 7:67–79

Chapter 16

Development of Bioactive Organic–Inorganic Hybrids Through Sol–Gel Processing

Toshiki Miyazaki, Masanobu Kamitakahara, and Chikara Ohtsuki

Abstract Bioactive ceramics have attractive features for bone repair because they spontaneously bond to a living bone when implanted in bony defects. However their clinical application is limited to repairs requiring only low loads of material due to their insufficient mechanical performance such as higher brittleness and lower flexibility than those of natural bones. It has been reported that the essential condition for artificial materials to show bioactivity is the formation of bone-like apatite on their surfaces through chemical reactions with body fluids. Fundamental studies concerning apatite formation on bioactive glasses and glass-ceramics have reported that the formation of surface apatite is triggered by both the release of calcium ions and by Si–OH groups formed on the surface of materials. These findings led the authors of the present chapter to the idea that new bioactive materials with mechanical properties similar to those of natural bones can be designed by organic modification of calcium silicate. After a brief critical review of the state-of-the-art on artificial bones, the authors report on their work, emphasizing how bioactive organic–inorganic hybrids have been designed and developed from various organic polymers by addition of Si–OH groups and calcium ions. Similar chemical modification is also effective for providing conventional polymethylmethacrylate (PMMA)-based bone cement with bioactivity. The added-value of bioactive organic–inorganic hybrids is experimentally demonstrated while future prospects show the promises of such new bionanocomposites.

T. Miyazaki (✉)

Graduate School of Life Science and Systems Engineering, Kyushu Institute of Technology,
2-4 Hibikino, Wakamatsu-ku, Kitakyushu, 808-0196, Japan
e-mail: tmiya@life.kyutech.ac.jp

M. Kamitakahara

Graduate School of Materials Science, Nara Institute of Science and Technology,
8916-5 Takayama-cho, Ikoma-shi, Nara 630-0192, Japan

C. Ohtsuki

Department of Crystalline Materials Science, Graduate School of Engineering,
Nagoya University, Furo-cho, Chikusa-ku, Nagoya 464-8603, Japan

16.1 Introduction

Our body tissues and organs lose their functions due to diseases, accidents and aging. When the level of damage is not too severe, the tissues and functions can be spontaneously repaired by the self-reconstructing ability of the body through normal nutritious supply and recuperation. Reconstruction can be assisted by artificial means such as medicine, radial rays, and thermal treatment. However, when the damage to tissue is too large to benefit from full self-reconstruction, the lost tissue and function may induce further problems to peripheral tissues. In such a case, the damaged tissues are reconstructed with alternative materials. The most popular technique is called “autograft” and consists of transferring healthy tissue from another part of the body of the same patient. Autografting has the intrinsic problem of inducing damages to healthy tissues of the patient, because the bone graft is extracted from the patient himself. Another candidate technique is called “allograft” and consists of transferring tissues from other persons. The allograft faces problems of infection due to certain disease-causing substances when it is implanted into the patient. In addition, lack of donors is also a significant problem.

We therefore expect that artificial materials could be used to substitute or to support function of organs. Materials designed for such purposes are called biomaterials. Biomaterials are defined as materials intended to interface with biological systems in order to evaluate, treat, augment or replace any tissue, organ or function of the body. Several artificial materials including ceramics and metals have been used for repairing bony defects. However the problem is that materials implanted in bony defects get encapsulated by fibrous tissues to be isolated from the surrounding bone [1]. This is a normal reaction for protecting our living body from foreign substances. This type of biological response is called bioinertness.

16.2 Bioactive Ceramics

In the early 1970s, Hench et al. developed a novel glass, so-called Bioglass[®], in the $\text{Na}_2\text{O}-\text{CaO}-\text{SiO}_2-\text{P}_2\text{O}_5$ system [2–4]. It has quite attractive characteristics for making direct bone-bonding in the body. This type of bone-bonding ability is called bioactivity. The typical composition (wt%) of this glass is Na_2O (24.5%), CaO (24.5%), SiO_2 (45%), P_2O_5 (6%). With such a composition, the glass displays the highest rate of bone-bonding among $\text{Na}_2\text{O}-\text{CaO}-\text{SiO}_2-\text{P}_2\text{O}_5$ systems. Bioglass[®] has such high biological affinity that it bonds not only to hard tissues but also to soft tissues. The high biological affinity of Bioglass[®] expands its clinical application to artificial middle ear, and fillers for alveolar ridge reconstruction. However, the mechanical strength of Bioglass[®] is as low as that of conventional glasses; therefore its clinical application is restricted to reconstructions where a large material loading is not required. Development of bioactive glass-ceramics has been undertaken in order to improve the mechanical properties of bioactive glasses. Kokubo et al. synthesized a bioactive glass-ceramic A-W, that has oxyfluorapatite ($\text{Ca}_{10}(\text{PO}_4)_6(\text{O},\text{F}_2)$) and β -wollastonite crystals in the $\text{MgO}-\text{CaO}-\text{SiO}_2$ glassy matrix. This synthesis was based on heat-

treatment of a glass having the following composition in weight%: MgO (4.6%), CaO (44.7%), SiO₂ (34.0%), P₂O₅ (16.2%), CaF₂ (0.5%) [5, 6]. This glass-ceramic contains β-wollastonite (CaO·SiO₂) which consists of silicate chains of SiO₄ in the tetrahedral structure, to increase its mechanical strength, as well as oxyfluorapatite. In other words, glass-ceramic A-W is a kind of ceramic–ceramic hybrid that contains 38 wt. % of oxyfluorapatite and 34 wt. % of β-wollastonite grains having a size of approximately 50–100 nm. Glass-ceramic A-W shows a bending strength of approximately 200 MPa in air, which is larger than that of the human cortical bone.

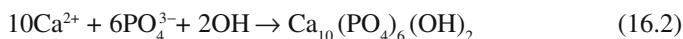
When a rectangular specimen of glass-ceramic A-W is implanted in a rabbit tibia, it bonds to the living bone within 4 weeks. It bonds so tightly that, after applying a load perpendicular to the interface a fracture occurred not within the glass-ceramics but within the bony tissues. Thanks to its excellent bioactivity and mechanical properties, the glass-ceramic A-W was clinically used as artificial iliac crest, vertebrae, and bone fillers from 1991 to 2000. Clinical applications involved this material in more than 45,000 cases until 2000.

Hydroxyapatite (Ca₁₀(PO₄)₆(OH)₂) is known as the main inorganic component of natural bones which comprise 70 wt % of bone matrix. Synthetic hydroxyapatite prepared by the sintering process also exhibits bioactivity [7]. It was commercialized in the late 1980s as bone substitute in the form of dense body, porous body and granules.

The sol–gel process is also suitable for synthesis of hydroxyapatite ceramics [8, 9]. Calcium alkoxide such as Ca(OC₂H₅)₂ and phosphorus alkoxide such as P(OC₂H₅)₃ and PO(OC₂H₅)₃ are often used as precursors. In this technique, the hydroxyapatite thin-films can be easily coated on various ceramics and metals [10].

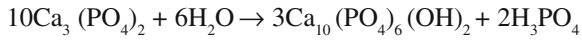
Apatite cements are also developed to be applied as injectable bone substitutes. In these cements, a calcium phosphate paste is prepared by mixing powder of calcium phosphates in an aqueous liquid. The paste can be formed into desirable shapes for several minutes. It precipitates low-crystalline hydroxyapatite after setting and fills bone defects.

Brown and Chow developed apatite cement from tetracalcium phosphate (TTCP, Ca₄(PO₄)₂O) and anhydrous calcium hydrogen phosphate (DCPA, CaHPO₄) [11]. The setting reaction of the cement is as follows:



Calcium and phosphate ions are released from TTCP and DCPD (dicalcium phosphate dihydrate) into the surrounding liquid after mixing the powder with the liquid. Solubility of TTCP and DCPA in water is higher than that of hydroxyapatite [1]. Therefore the surrounding liquid becomes supersaturated with respect to the apatite after dissolving of TTCP and DCPA. As a result, the cement sets through precipitation of the apatite, locking together the formed apatite crystals. The solubility of TTCP in water is higher than that of DCPA. In order to match the dissolution rates of TTCP and DCPD, the particle size of TTCP is adjusted to be ten times that of DCPA.

Monma et al. found that α-tricalcium phosphate (α-TCP) precipitates hydroxyapatite by hydrolysis as follows [12]:



Apatite cement based on α -TCP has been also developed. However, the rate of hydrolysis of α -TCP is lower in comparison with the apatite precipitation of the cement based on TTCP and DCPD. In order to improve reactivity with the liquid, TTCP or an organic acid such as malic acid and succinic acid is added to the cement.

16.3 Bone-Bonding Mechanism of Bioactive Ceramics

According to earlier reports on the observation of the interface between the bioactive ceramics and the bone in vivo, these ceramics bond to the living bone through an apatite layer formed at the interface via a chemical reaction with the body fluid, as shown in Fig. 16.1 [13, 14]. Exceptionally, TCP ceramics exhibit bioactivity without formation of such an apatite layer [15]. This apatite layer is composed of carbonate hydroxyapatite with both a structure and a composition similar to those of natural bone. Therefore, it is expected that fibroblastic cells do not proliferate on the apatite layer, which results in a direct contact of the bone with the surface of the materials, without the fibrous tissue interfering. In the above case, a tight chemical bond may be formed between the surface apatite and the bone apatite in order to decrease

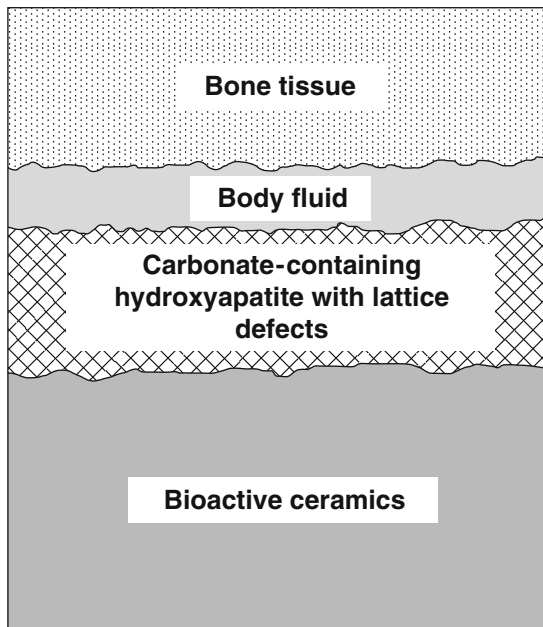


Fig. 16.1 Bone-bonding mechanism of bioactive ceramics

interface energy between them. The bone-bonding ability therefore depends on the rate of apatite formation when the materials are exposed to body fluids.

The apatite formation on bioactive ceramics and glass-ceramics can be well reproduced even in a simulated body fluid (SBF) that has concentrations of inorganic ions almost similar to those of the human blood plasma, as shown in Fig. 16.2 [16–19]. The apatite formation is caused by chemical reaction between the material surface and the surrounding fluid, because SBF does not contain any cell or protein. Materials which grow the apatite layer on their surface in SBF have the potential to bond to living bones. This SBF can be used for the evaluation of bioactivity of not only artificial materials *in vitro*, but also apatite coating on various materials under biomimetic conditions.

Ion concentrations of SBF are shown in Fig. 16.2. The pH of SBF is adjusted to pH 7.25 at 36.5°C. When the apatite-forming ability of the specimen is not very high, the pH of SBF is sometimes adjusted to 7.40. This fluid is a metastable solution containing calcium and phosphate ions and is already supersaturated with respect to the apatite. Therefore SBF is prepared as follows, using bottles and wares washed with HCl solution, neutral detergent, and ultrapure water. Firstly, 700 cm³ of ion-exchanged distilled water is poured into a 1,000 cm³ polyethylene bottle, and is stirred with a magnetic stirrer, and the reagent-grade chemicals are added into the water, one by one in the given order, after each reagent is completely dissolved. Temperature of the solution in the bottle is adjusted to 36.5°C with a water bath, and the pH of the solution to 7.25 by titrating 1 kmol/m³ HCl solution. Once the pH is adjusted, the solution is transferred from the polyethylene bottle to a volumetric glass flask. Ultrapure water is added to adjust the total volume of the solution to one liter, and the flask is shaken. The solution is transferred from the flask to a polyethylene or polystyrene bottle, and stored in a refrigerator at 5–10°C. The fluid can be preserved for more than one month in a refrigerator. A solution with ion concentrations

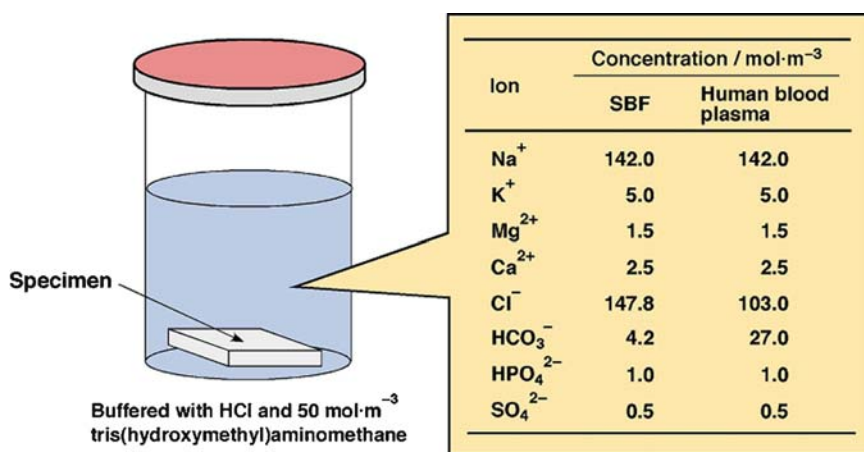


Fig. 16.2 Ion concentrations of SBF in comparison with those of human blood plasma

1.5 times of SBF (1.5SBF) can be also prepared by following a modified protocol to accelerate the apatite formation in biomimetic apatite coating.

Although chemical reactions between materials and the body fluid *in vitro* are well reproduced in SBF, there is still a gap in the composition between SBF and the human extracellular fluid *i.e.* SBF contains larger amount of Cl^- ions and smaller amount of HCO_3^- ions. Therefore the apatite which was formed in SBF also contains a larger amount of Cl^- ions and a smaller amount of HCO_3^- than the natural bone. A novel simulated body fluid with inorganic ion concentrations exactly equal to those of the human extracellular fluid has been proposed by revising the protocol of preparation including the type and amount of chemical reagents [19, 20].

16.4 Basic Composition for Exhibiting Bioactivity

It was shown that bioactive materials can be designed by selecting a material with apatite-forming ability. The ability of apatite formation is dependent on the composition and structure of materials. For instance, the rate of apatite formation increases in the following order: sintered hydroxyapatite < glass-ceramic A-W < Bioglass® [21–23]. Sintered hydroxyapatite also forms a bone-like apatite phase when it is exposed to body fluids, through an ion-exchange reaction with those surrounding fluids [24, 25]. However the reaction rate is small. In contrast, the reaction rate is higher for glass-ceramic A-W which contains CaO, SiO_2 -based glassy phase, as well as crystalline oxyfluorapatite and β -wollastonite. This glassy phase will contribute to rapid apatite deposition.

Which components constitute the basic composition of bioactive ceramics? Ohtsuki et al. fundamentally investigated the compositional dependence of apatite formation on the surface of glasses in the $\text{CaO-SiO}_2\text{-P}_2\text{O}_5$ system after soaking in SBF [26]. It was noted that surface apatite formation is restricted to areas composed of the $(\text{CaO}, \text{SiO}_2)$ system, but not the $(\text{CaO}, \text{P}_2\text{O}_5)$ system. Both the calcium ions released from $(\text{CaO}, \text{SiO}_2)$ -based glasses and the phosphate ions released from $(\text{CaO}, \text{P}_2\text{O}_5)$ -based glasses increased almost equally the degree of supersaturation of the surrounding fluid with respect to the apatite. In spite of that, the former glasses grow the surface apatite layer, but not the latter. This indicates that the surface of $(\text{CaO}, \text{SiO}_2)$ -based glasses exclusively provides favorable sites for apatite nucleation.

The glasses form a silica hydrogel layer prior to forming the apatite layer and dissolve an appreciable amount of silicate ions. This means that highly hydrated silica, thus involving silanol (Si-OH) groups, is abundant on the surface of the glasses. It is speculated that the silanol groups effectively induce heterogeneous nucleation of the apatite. This is confirmed by the observation that a pure silica gel, prepared by a sol-gel method, forms bone-like apatite on its surface in a SBF at pH 7.40 [18, 27]. This suggests that a certain type of silanol groups is responsible for the apatite deposition on bioactive materials. The released Ca^{2+} ions will increase the degree of supersaturation of the surrounding fluid with respect to the apatite,

which is already supersaturated even before its exposure to the glass-ceramics. Once apatite nuclei are formed on the surface of the materials, they can grow spontaneously by consuming calcium and phosphate ions of the surrounding body fluid. Addition of a small amount of Al_2O_3 and TiO_2 significantly reduces the apatite formation in SBF [28, 29]. This is because the release of Ca^{2+} from the glasses into the surrounding fluid is suppressed, and the apatite-forming ability of hydrated silica containing Al_2O_3 and TiO_2 is thought to be lower than that of pure hydrated silica formed on CaO-SiO_2 glasses.

Li et al. prepared $\text{CaO-SiO}_2\text{-P}_2\text{O}_5$ glass powders by sol–gel process [30]. They showed that the apatite-forming ability of sol-gel-derived glasses was higher than that of melt-derived ones of the same composition. This is attributed to large pore volume and surface area of the sol-gel-derived glasses. They also showed that the sol–gel process can expand the SiO_2 -content range across which the apatite formation in SBF can be observed, namely from 60 mol% in the melt-derived glasses to as large as 85 mol%.

The initial stage of the apatite formation on $(\text{CaO}, \text{SiO}_2)$ -based bioactive glasses and on sintered hydroxyapatite has been precisely investigated by using techniques such as transmission electron microscopy (TEM), energy-dispersive X-ray (EDX) spectroscopy, and zeta potential measurements [24, 25, 31]. The results of the above research have revealed that the apatite formation progresses through the following mechanisms. Firstly, Ca^{2+} ions in SBF are selectively adsorbed onto negatively charged surfaces. Then phosphate ions are adsorbed on the Ca-rich surfaces to form a kind of amorphous calcium phosphate. Finally, the formed amorphous calcium phosphate is converted into low-crystalline apatite, since hydroxyapatite is a thermodynamically stable phase among calcium phosphates in neutral conditions. As a summary, selective adsorption of Ca^{2+} in SBF onto negatively charged surfaces of materials is a key issue for inducing apatite formation.

16.5 Design of Bioactive Organic–Inorganic Hybrids by the Sol–Gel Process

Based on the mechanism of apatite formation on bioactive glasses and glass-ceramics, hybrid materials with bone-bonding ability can be developed *via* organic modification of Si-OH and Ca^{2+} at the nanometer level. Molecular design of bioactive organic–inorganic hybrids is schematically illustrated in Fig. 16.3.

In order to develop such organic–inorganic hybrids, only limited heat treatment at lower temperature is allowed during synthesis, since organic polymers are prone to thermal decomposition. The sol–gel processing enables synthesis of various ceramics and oxide gels at lower temperature, and therefore is one of the attractive methods to prepare organic–inorganic hybrids.

Mackenzie et al. have already reported that organically-modified silicates can be synthesized from tetraethoxysilane (TEOS) with incorporation of poly(dimethylsiloxane) (PDMS). The synthesized organic–inorganic hybrid, called

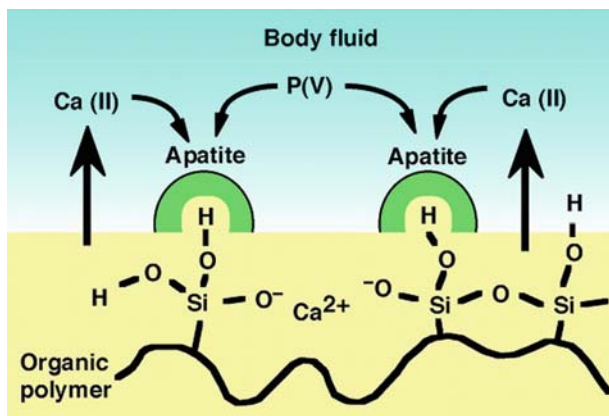


Fig. 16.3 Design of bioactive organic-inorganic composites

ORMOSIL, may combine the thermal stability of the silica block with the flexibility of the polymer chain [32].

Osaka et al. exploited the fact that ORMOSILS contain a lot of Si-OH groups and reported that incorporation of calcium nitrate in ORMOSILS during the sol-gel processing gave the hybrids the apatite-forming ability in SBF [33]. Si-OH groups and Ca²⁺ ions on ORMOSILS trigger nucleation of the apatite in SBF. This means that calcium salt-incorporated ORMOSILS show the bone-bonding property when implanted in the body. Chen et al. modified the protocol of synthesis and obtained TEOS-PDMS-Ca(NO₃)₂ hybrids with higher mechanical strength [34].

Synthesis of bioactive organic-inorganic hybrids has been also reported using vinyltrimethoxysilane (VS; H₂C=CHSi(OCH₃)₃) and methacryloxypropyl trimethoxysilane (MPS; H₂C=C(CH₃)COO(CH₂)₃Si(OCH₃)₃) as starting materials [35, 36]. Vinyl and methacryloyl groups in the starting organic substances were first radically polymerized to form organic polymers. The polymers were then incorporated with Ca²⁺ ions by mixing with calcium salts and subjected to hydrolysis with water to form Si-OH groups. The synthesized organic-inorganic hybrids formed an apatite layer on their surfaces in SBF.

16.6 Bioactive Organic-Inorganic Hybrids Synthesized from MPS and HEMA

We attempted the synthesis of bioactive organic-inorganic hybrids by incorporation of MPS (CH₂=C(CH₃)COO(CH₂)₃Si(OCH₃)₃) and calcium chloride into 2-hydroxyethylmethacrylate (HEMA, CH₂=C(CH₃)COO(CH₂)₂OH) [37]. HEMA has high hydrophilicity and biological affinity, and is used for medical applications such as contact lenses and coating agent on artificial blood vessels [38].

MPS and HEMA were dissolved in ethanol with a molar ratio of MPS:HEMA = 1:9, at a total concentration of 1 mol/dm³. The solution of 100 cm³ was heated at 75°C for 3 h with 0.001 mol benzoylperoxide (BPO) as initiator of the polymerization of HEMA and MPS. The obtained polymer solution was then mixed with 20 cm³ of ethanol containing 0.01 mol calcium chloride (CaCl₂). In some of the solutions, addition of 1 cm³ of either 1 mol/dm³ HCl or 1 mol/dm³ NH₃ aqueous solution catalyzed the hydrolysis. The resultant solutions were cast in polypropylene containers and dried at room temperature. After gelation, the gels were allowed to further dry under ambient condition at room temperature until weight loss of the sample became less than 2% in 24 h. Hybrids without and with addition of HCl and NH₃ were denoted as “NO”, “HC” and “NH”, respectively. Tensile mechanical properties of the hybrids were evaluated using a universal testing machine under ambient conditions according to Japanese Industrial Standard (JIS) K7113. Nine specimens were subjected to tensile test for NO, and seven specimens for HC and NH. Bioactivity of the obtained hybrids was evaluated by examining the apatite formation on their surfaces in SBF.

Figure 16.4 shows representative stress-strain curves for the MPS–HEMA hybrids. Their tensile strength increased in the following order: HC (0.15 ± 0.02 MPa) < NO (0.68 ± 0.04 MPa) < NH (2.10 ± 0.18 MPa). Their Young’s modulus also increased in the same order: HC (0.24 ± 0.02 MPa) < NO (2.65 ± 0.19 MPa) < NH (41.1 ± 1.8 MPa). The Young’s modulus of the hybrids is quite similar to those of the human cancellous bone (50–500 MPa) and articular cartilage (1–10 MPa). Such hybrids are expected to bring a novel material for reconstruction of cancellous bones and articular cartilages.

SEM photographs of hybrids before and after soaking in SBF for 7 days are shown in Fig. 16.5. After soaking, spherical particles were formed on the surfaces of hybrids NO and NH, but not on the hybrid HC. TF–XRD patterns in Fig. 16.6

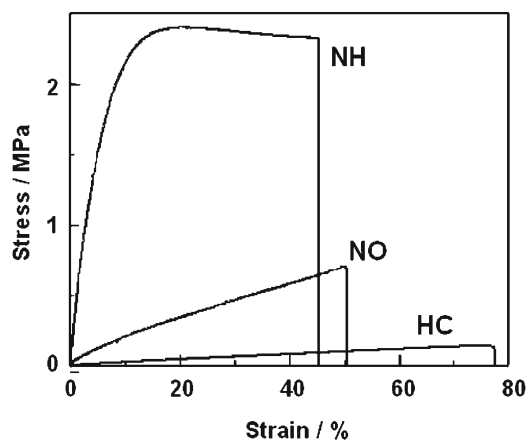


Fig. 16.4 Representative stress-strain curves of the MPS–HEMA hybrids prepared with different catalysts



Fig. 16.5 SEM pictures of the MPS-HEMA hybrids prepared with different catalysts before and after soaking in SBF for 7 days

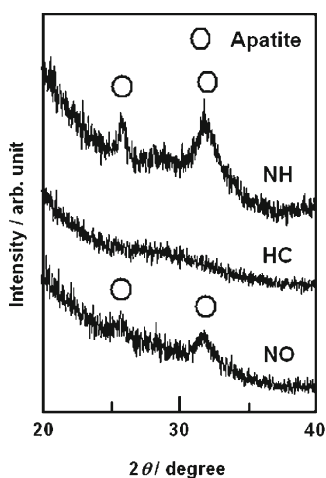


Fig. 16.6 TF-XRD patterns of surfaces of MPS-HEMA hybrids prepared with different catalysts before and after soaking in SBF for 7 days

show peaks assigned to poorly crystalline apatite at about 26° and 32° for hybrids NO and NH after the soaking, but not for the hybrid HC.

Our results indicate that hybrids NO and NH are expected to form apatite in the body and bond to living bones. In contrast, hybrid HC does not show bioactivity, in spite of the existence of silanol groups and release of calcium ions. Release of HCl in hybrid HC decreases the degree of supersaturation of the surrounding fluid with respect to the apatite, and consequently suppresses apatite formation. There also remains the possibility that silanol groups did not have the appropriate structure after addition of HCl, because the structural effect of silica gel on the ability of apatite formation is also affected by the fabrication process of the silica gel [39, 40].

After polymerization of the MPS and HEMA solution, a copolymer consisting of MPS and HEMA is produced. The alkoxy silane groups in the copolymer are hydrolyzed by atmospheric water or catalysts to form silanol groups during aging and drying processes [41, 42]. The silanol groups then condense to form siloxane bonds ($\equiv\text{Si}-\text{O}-\text{Si}\equiv$), which allows cross-linking in the MPS-HEMA copolymer.

When HCl is added to the copolymer solution, linear siloxane chains are mainly formed by polycondensation of silanol groups [42]. In contrast, when NH_3 is added to the copolymer solution, 3-dimensional siloxane networks are predominantly formed. Therefore, hybrid NH has a harder structure caused by the high concentration of siloxane network, in comparison with hybrids NO and HC. The lower Young's modulus of hybrid HC may be attributed to a lower concentration of siloxane network in the hybrids structure.

Various natural and synthetic polymers are available for synthesis of hybrids. Recent research works have reported preparation of bioactive organic–inorganic hybrids from materials like chitosan and polycaprolactone *via* their modification with Si–OH and Ca^{2+} [43, 44].

16.7 Bioactive Starch-Based Hybrids

Starch is a natural organic polymer that is known as a constituent of various kinds of crop. Starch-based materials are getting a lot of attention as novel bone substitutes [45]. Miyazaki et al. attempted the preparation of bioactive organic–inorganic hybrids from starch by addition of glycidoxypolytrimethoxysilane (GPS, $\text{CH}_2(\text{O})\text{CHCH}_2\text{O}(\text{CH}_2)_3\text{Si}(\text{OCH}_3)_3$) and CaCl_2 [46].

In this procedure potato starch was dissolved in dimethylsulfoxide. CaCl_2 , GPS, ultrapure water and divinylsulfone (DS) as cross-linking agent were then added to the solution. The prepared sol was subsequently poured into a Teflon dish and kept *in vacuuum* at room temperature for 3 days to remove bubbles in the solution. It was then dried at 60°C for 21 days for further progress of the sol–gel reaction. Mass ratio of starch to the total of GPS and starch was fixed at 0.50, while the molar ratio of CaCl_2 to GPS was fixed at 0.05. Molar ratio of H_2O to GPS was fixed at 2.0. Mass ratio of divinylsulfone to starch was varied from 0 to 0.05. The specimen with $(\text{DS})/(\text{DS} + \text{starch}) = \chi$ weight% was denoted as “DS x”. The obtained gels were then soaked in SBF at pH 7.40 at 36.5°C for 7 days. Surface structural changes on the hybrids after soaking in SBF were examined by SEM and TF–XRD. Dumbbell-shaped specimens with the following dimensions were prepared: 115 mm in length, 25 ± 1 mm in width at the center and 6 ± 0.4 mm in width at the edges. Five specimens were subjected to tensile tests by using the Instron-type material testing machine, following the JIS 7127.

Figure 16.7 shows SEM pictures of the surfaces of the specimens after soaking in SBF for 7 days. Fine particles were observed on all the surfaces of the hybrids. The particles were identified as poorly crystalline apatite by TF–XRD. Figure 16.8 shows stress–strain curves of the representative specimens with various contents of divinylsulfone. Their tensile strength increased in the following order: DS0 (3.73 ± 0.66 MPa) < DS3 (9.68 ± 2.30 MPa) < DS5 (18.52 ± 1.27 MPa). Their Young's modulus also increased in the same order: DS0 (190 ± 20 MPa) < DS3 (292 ± 32 MPa) < DS5 (910 ± 36 MPa). The specimen with divinylsulfone 3 wt% to GPS showed mechanical properties analogous to those of human cancellous bones.

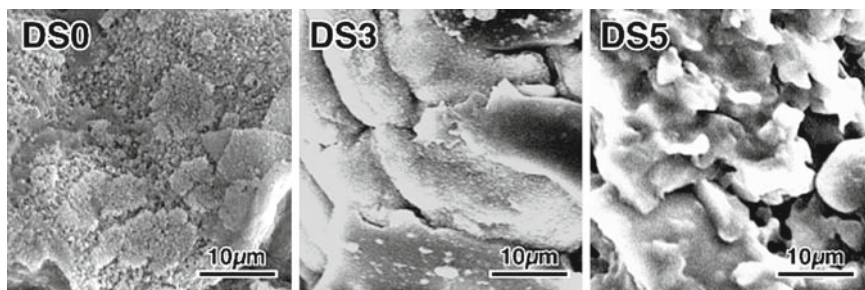
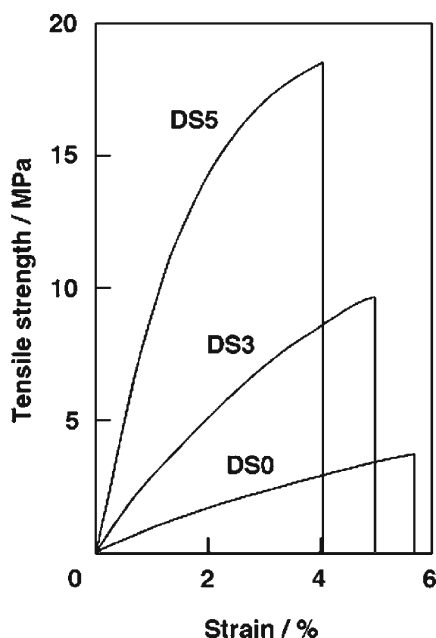


Fig. 16.7 SEM pictures of surfaces of GPS–starch hybrids with different divinylsulfone contents, after soaking in SBF for 7 days

Fig. 16.8 Representative stress–strain curves of GPS–starch hybrids with different divinylsulfone contents, before soaking in SBF



Organic–inorganic hybrids prepared from starch by addition of alkoxy silane and calcium salts were found to form apatite on their surfaces in SBF, irrespective of the divinylsulfone content. This means that addition of divinylsulfone as cross-linking agent does not generate an adverse effect on their bioactivity. Results of tensile tests show that the mechanical properties of the hybrids can be easily controlled by the content of cross-linking agent. The added divinylsulfone will bond to hydroxyl groups in starch to induce cross-linking, leading to improvement of the mechanical strength of the hybrid [47].

16.8 Bioactive Chitin-Based Hybrids

Chitin is a natural organic polymer, known as a constituent of club shell. Its chemical structure is shown in Fig. 16.9. Chitin has attractive features for implant materials, such as high hydrophilicity and low toxicity [48]. Miyazaki et al. attempted the preparation of bioactive organic–inorganic hybrids from chitin through modification with glycidoxypropyltrimethoxysilane (GPS, $\text{CH}_2(\text{O})\text{CHCH}_2\text{O}(\text{CH}_2)_3\text{Si}(\text{OCH}_3)_3$) and calcium chloride (CaCl_2) [49].

Compositions of the prepared specimens are shown in Table 16.1. A powder of chitin was dissolved in *N,N*-dimethylacetamide (DMAc) solution containing lithium chloride (LiCl) at 6.6 weight%. Then GPS, divinylsulfone and CaCl_2 were added to the solution. The prepared sol solution was subsequently poured into a glass dish and dried in an air oven at 100°C for 24 h. The mass ratio of chitin to the total of GPS and chitin was fixed at 0.25, while the molar ratio of CaCl_2 to GPS ranged from 0 to 0.50. Ca-free gels were added with divinylsulfone to advance cross-linking. The bulk gels obtained were cut into rectangular specimens of $10 \times 10 \times 1 \text{ mm}^3$ section, and then soaked in 30 mL of SBF.

Homogeneous organic–inorganic hybrids can be successfully synthesized from chitin by modification with GPS and CaCl_2 . Chitin is known to have high chemical durability due to tight intra- and intermolecular hydrogen bonds between the $\text{C}=\text{O}$ groups and the $\text{N}-\text{H}$ groups, and between the $\text{C}=\text{O}$ groups and the OH groups [50]. Therefore chitin is quite difficult to dissolve in conventional aqueous and organic solvents. However, the LiCl/DMAc mixed solvent can easily dissolve chitin because Li^+ ions break the hydrogen bonds [51]. Bulk gels of organic–inorganic

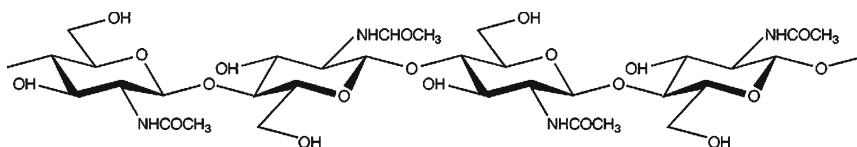


Fig. 16.9 Chemical structure of Chitin

Table 16.1 Compositions of GPS–Chitin hybrids

Sample	Mass ratio		Molar ratio
	Chitin/(Chitin+GPS)	DS/Chitin	CaCl_2/GPS
Ca0	0.25	0.05	0
Ca025	0.25	0	0.25
Ca05	0.25	0	0.50

GPS: Glycidoxypropyltrimethoxysilane

DS: Divinylsulfone

hybrid based on chitin can be synthesized using such a mixed solvent. Figure 16.10 shows SEM pictures of the surfaces of the specimens after soaking in SBF for 7 days. Deposition of fine particles was observed on the surfaces of all specimens after soaking. Figure 16.11 shows TF-XRD patterns of the surfaces of specimens

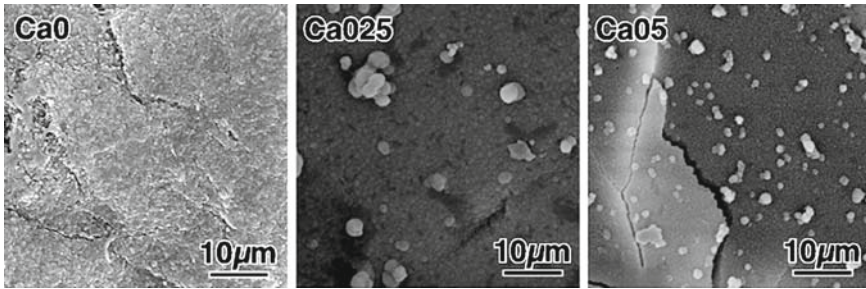


Fig. 16.10 SEM pictures of surfaces of GPS-Chitin hybrids with different calcium contents, after soaking in SBF for 7 days

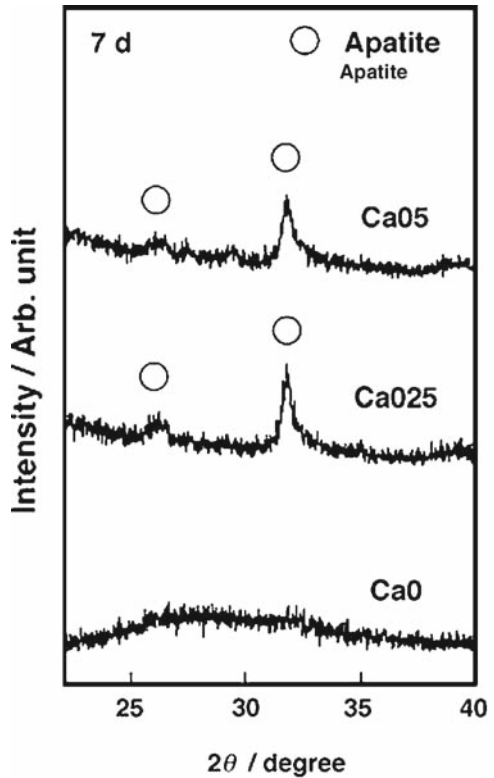


Fig. 16.11 TF-XRD patterns of surfaces of GPS-Chitin hybrids with different calcium contents, after soaking in SBF for 7 days

after soaking in SBF for 7 days. Broad peaks assigned to poorly crystalline apatite were observed at $2\theta = 26^\circ$ and 32° in the XRD patterns of the specimens except for specimen Ca0 after soaking. Figure 16.12 shows EDX spectra of the surface of specimen Ca0 after soaking in SBF for 7 days. Peaks assigned to Ca and P were observed.

Even Ca-free hybrids grow a kind of calcium phosphate on their surface in SBF, although it is not identified as apatite. The apatite formation can be significantly enhanced by adding CaCl_2 . This means that high bioactivity will be achieved on the chitin-based hybrids by addition of only a small amount of Ca^{2+} . It is reported that release of a large amount of Ca^{2+} in bioactive hybrids decreases the mechanical strength in body environment [52]. This type of chitin-based hybrid is attractive for flexible bone substitutes resistant to degradation in the body.

16.9 Bioactive Bone Cements Prepared by Organic Modification of Calcium Silicate

We applied organic modification of Si–OH and Ca^{2+} for the development of bioactive materials that can be injected into bony defects. Generally, bone cement consisting of poly(methyl methacrylate) (PMMA) powder and methyl methacrylate (MMA) liquid, in which they are mixed and polymerized, is clinically used for fixation of implants such as artificial hip joints [53]. Significant problems of the PMMA bone cement include loosening at the interface between the bone and the cement because

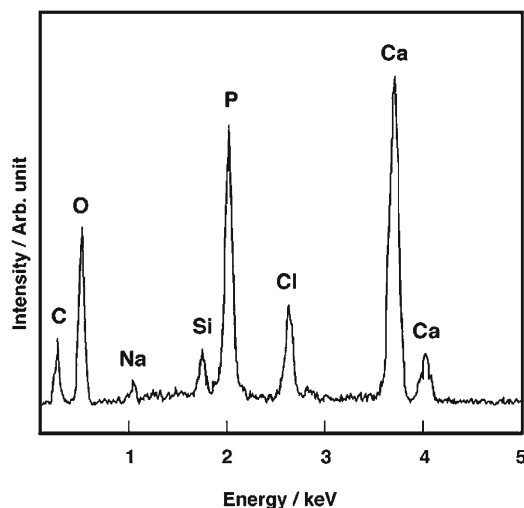


Fig. 16.12 EDX spectra of surface of sample Ca0 after soaking in SBF for 7 days

of a lack of bioactivity. Several studies have been conducted to develop bioactive cements through a method based on mixing powders of bioactive ceramics with the PMMA cement [54, 55]. In such a method, large amounts of ceramic powder should be incorporated into the cement to induce bioactivity, since the bioactive ceramic powder is almost covered with the PMMA matrix and thus hardly exposed to body fluids. Novel strategies for obtaining bioactive PMMA bone cements need to be therefore developed on the basis of a fundamental study on bonding mechanisms of artificial materials to living bones. We therefore attempted the preparation of bioactive PMMA bone cements by incorporating calcium silicate gels resulting from MPS and various calcium salts [56–58].

We used a PMMA powder having a molecular weight of about 100,000 and an average particle size about 14 μm . The PMMA powder was mixed with a calcium salt selected from CaCl_2 , calcium acetate ($\text{Ca}(\text{CH}_3\text{COO})_2$), calcium hydroxide ($\text{Ca}(\text{OH})_2$), calcium lactate ($\text{Ca}(\text{CH}_3\text{CHOHCOO})_2$) and calcium benzoate ($\text{Ca}(\text{C}_6\text{H}_5\text{COO})_2$) at 20 wt% of the powder. BPO was then added to the powder as a polymerization initiator. MMA liquid was mixed with MPS at 20 wt% of the liquid. *N,N*-dimethyl-*p*-toluidine (NDT) was then added to the liquid as a polymerization accelerator. The composition of the cements is shown in Table 16.2. The cement denoted as “Reference” has a composition similar to that of the commercially available bone cement CMW[®]-1 (CMW Depuy), containing neither MPS nor calcium salt. The powder was mixed with the liquid at a powder to liquid ratio of 1:0.5 at $23 \pm 2^\circ\text{C}$. The paste was shaped into a rectangular specimen with a size of $10 \times 15 \times 1 \text{ mm}^3$. At half the setting time of the specimens, they were soaked in 35 cm^{-3} of SBF at pH 7.25 for 7 days to examine their apatite-forming ability. Compressive strengths of the cements with and without exposure to SBF were measured with a universal material testing machine.

Figure 16.13 shows SEM pictures of surfaces of cements modified with MPS and various kinds of calcium salts after soaking in SBF for 7 days. Assemblies of fine particles were observed on cements modified with CaCl_2 , $\text{Ca}(\text{CH}_3\text{COO})_2$ and $\text{Ca}(\text{OH})_2$ after soaking. The formed particles were identified as poorly crystalline apatite by TF-XRD as shown in Fig. 16.14. Figure 16.15 reveals the compressive strengths of cements modified with MPS and various calcium salts before and after soaking in SBF for 7 days. The compressive strengths of modified cements decreased after exposure to SBF, except for cement modified with $\text{Ca}(\text{OH})_2$. Of the cements examined in this study, those modified with $\text{Ca}(\text{CH}_3\text{COO})_2$, $\text{Ca}(\text{OH})_2$ or $\text{Ca}(\text{CH}_3\text{CHOHCOO})_2$ showed a compressive strength close to the lower limit required by ISO5833.

Table 16.2 Compositions of cements

Sample	Powder (Mass ratio)			Liquid (mass ratio)		
	PMMA	Calcium Salt	BPO	MMA	MPS	NDT
Reference	0.971	0.000	0.029	0.992	0.000	0.008
Modified cement	0.776	0.194	0.029	0.794	0.198	0.008

MPS: Methacryloxypropyltrimethoxysilane

BPO: Benzoyl peroxide

NDT: *N,N*-dimethyl-*p*-toluidine

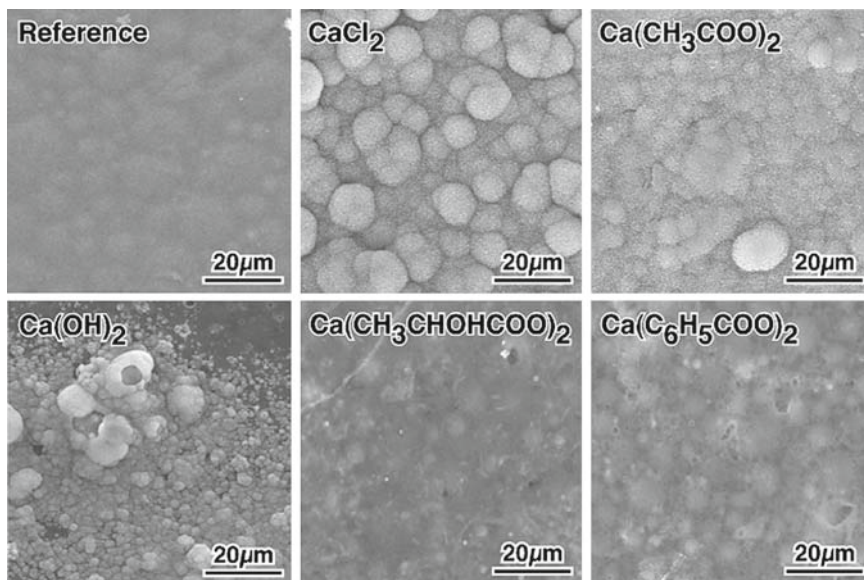


Fig. 16.13 SEM pictures of surfaces of cements modified with MPS and various kinds of calcium salts after soaking in SBF for 7 days

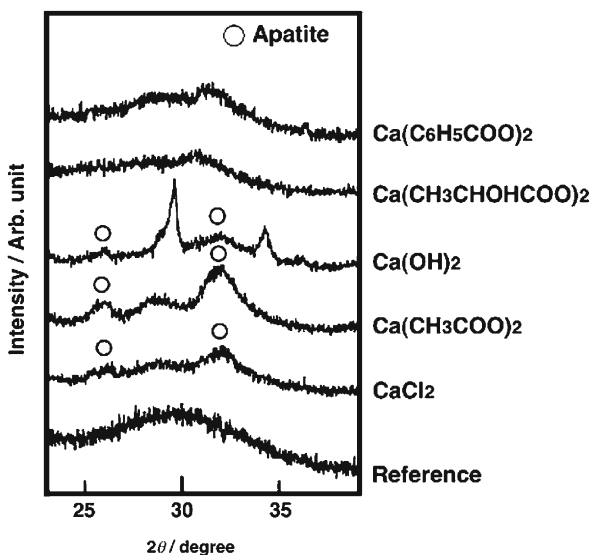


Fig. 16.14 TF-XRD patterns of surfaces of cements modified with MPS and various kinds of calcium salts after soaking in SBF for 7 days

Modification of PMMA cements by incorporation of MPS and appropriate types of calcium salts allows these cements to grow apatite when implanted in a patient body. Incorporated alkoxy silane and calcium salts form calcium silicate gels during setting and/or after exposure to SBF through sol–gel reaction. The formed calcium

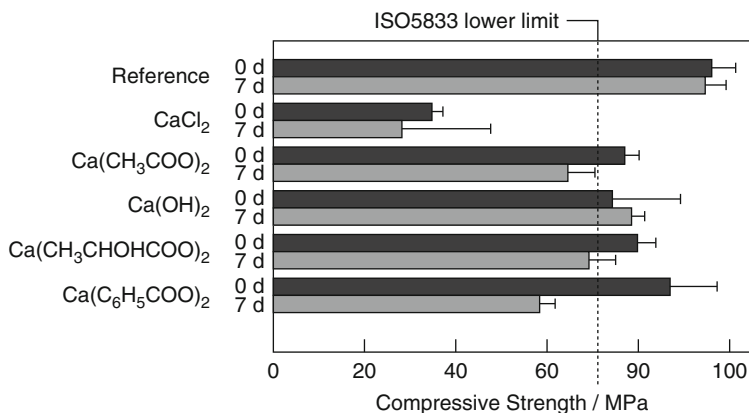


Fig. 16.15 Compressive strength of cements modified with MPS and various calcium salts before and after soaking in SBF for 7 days

silicate gels induce apatite nucleation in SBF. The solubility of the calcium salt in water decreases in the following order: $\text{CaCl}_2 > \text{Ca}(\text{CH}_3\text{COO})_2 > \text{Ca}(\text{CH}_3\text{CHOHCOO})_2 > \text{Ca}(\text{C}_6\text{H}_5\text{COO})_2 > \text{Ca}(\text{OH})_2$. Cements modified with highly water-soluble calcium salts have tendency to grow apatite in SBF. It is worth noting that cement modified with $\text{Ca}(\text{OH})_2$ still formed apatite in SBF, despite the fact that the solubility of $\text{Ca}(\text{OH})_2$ is the lowest compared to the calcium salts used in this study. The pH of the surrounding solution remarkably increased after soaking of cement modified with $\text{Ca}(\text{OH})_2$ in SBF. The increase in pH accelerates the apatite nucleation, since OH^- is a component of the apatite. These observations indicate that increase in pH as well as release of Ca^{2+} govern the apatite formation on modified cements. All cements but that modified with $\text{Ca}(\text{OH})_2$ showed a decrease in their compressive strength after soaking in SBF. This is attributed to release of Ca^{2+} ions from the cement into the solution. When Ca^{2+} ions are rapidly released, pores are formed inside the cement, leading to a decrease in compressive strength. An appropriate rate of release of Ca^{2+} is desirable to keep a high mechanical strength of the cement.

16.10 Bioactive Organic–Inorganic Hybrids Based on Various Metal Hydroxides

What kind of surface structure is effective for inducing bioactivity? In order to clarify this point, apatite deposition on various materials such as oxide gels prepared by sol–gel process, self-assembled monolayers (SAMs), and chemically-treated metal substrates was investigated in SBF. As a result, it appeared that not only Si–OH groups but also various functional groups such as Ti–OH [27, 59, 60], Zr–OH [61, 62], Ta–OH [63, 64], Nb–OH [65], Mo–OH [66], COOH [67–69],

PO_4H_2 [67] and SO_3H [70–72] are effective at triggering heterogeneous nucleation of the apatite. These findings led us to the idea that various bioactive organic–inorganic hybrids can be designed by organic modification of inorganic substances that provide the functional groups described above.

Uchida et al. reported that titania (TiO_2) having the anatase structure exhibits a higher ability for apatite formation in SBF than titania having either a rutile or an amorphous structure [60]. On the basis of these findings, Kamitakahara et al. synthesized bioactive anatase-poly(tetramethylene oxide) (PTMO) hybrids [73]. Anatase crystals with a size of about 10 nm precipitate after hot-water treatment of the organic–inorganic hybrids obtained from PTMO and titanium tetraisopropoxide ($\text{Ti}(\text{OCH}(\text{CH}_3)_2)_4$). The synthesized hybrids form the apatite in SBF within 3 days. It is worth noting that this type of hybrids grows the apatite, even if it does not contain Ca^{2+} . This means that Ca-free bioactive organic–inorganic hybrids can be designed by appropriately controlling the chemical state of the metal hydroxides. According to a similar molecular design, bioactive tantalum oxide (Ta_2O_5)–PTMO hybrids can be obtained [74]. Such Ca-free bioactive hybrids are expected to maintain their strength even in the patient body, in contrast to Ca-containing hybrids where release of Ca^{2+} is reported to decrease their strength in body fluids [52].

Miyazaki et al. prepared organic–inorganic hybrids based on poly(vinyl alcohol) (PVA) by modification with molybdenum hydroxide as well as hydrated silica, and compared their apatite-forming ability [75]. PVA is an organic polymer that has been studied extensively because of its high hydrophilicity, film-forming ability and processability [76, 77]. Further, in the medical field PVA is attractive for making artificial cartilages [78–80]. PVA with a molecular weight of 86,000 was dissolved in a mixed solvent of ultra-pure water and ethanol to form a 5 wt% solution at 80°C. Then followed the addition of tetraethoxysilane (TEOS, $\text{Si}(\text{OC}_2\text{H}_5)_4$) or bis(acetylacetonato) dioxomolybdenum(VI) (BADM, $\text{MoO}_2(\text{CH}_3\text{COCHCOCH}_3)_2$) under vigorous stirring, before $\text{Ca}(\text{NO}_3)_2$ was finally added to the solution. Compositions of the prepared hybrids are shown in Table 16.3.

Table 16.3 Compositions of PVA-based hybrids

Sample	Alkoxide	Mass ratio		Molar ratio	
		Alkoxide/(PVA+Alkoxide)		$\text{CaCl}_2/\text{Alkoxide}$	
Si60Ca007	TEOS	0.6		0.07	
Si60Ca010	TEOS	0.6		0.10	
Si60Ca015	TEOS	0.6		0.15	
Mo40Ca10	BADM	0.4		1.0	
Mo40Ca15	BADM	0.4		1.5	
Mo40Ca20	BADM	0.4		2.0	

TEOS: Tetraethoxysilane ($\text{Si}(\text{OC}_2\text{H}_5)_4$)

BADM: Bis(acetylacetonato) dioxomolybdenum (VI)
($\text{MoO}_2(\text{CH}_3\text{COCHCOCH}_3)_2$)

For all compositions, crack-free, homogeneous and transparent monolithic films were obtained. Figure 16.16 shows SEM pictures of the surfaces of PVA/silica and PVA/molybdenum oxide hybrids soaked in SBF. Numerous particles were observed on surfaces of all PVA/silica hybrids after soaking. In the case of PVA/molybdenum oxide hybrids, particles were observed on the surface of hybrids after the soaking when Ca/Mo molar ratio was 1.5 or more. Figure 16.17 shows TF-XRD patterns of surfaces of PVA/silica and PVA/molybdenum oxide hybrids soaked in SBF. Broad peaks assigned to low crystalline apatite were detected for all the examined PVA/silica hybrids. On the other hand, peaks assigned to the apatite were observed for PVA/molybdenum oxide hybrids with Ca/Mo molar ratio of 1.5 or more. In addition, peaks ascribed to calcium molybdate were detected for samples described above after the soaking.

The results show that bioactive organic-inorganic hybrids can be obtained through the sol-gel process from PVA by addition of silicon or molybdenum alkoxide, as well as calcium salt. Compared to PVA/Silica hybrids, addition of larger amount of calcium salt is necessary to induce the apatite formation on PVA/molybdenum oxide hybrids. Results of TF-XRD indicate that a kind of calcium molybdate as well as apatite is formed on the former after soaking in SBF. It is assumed that Ca^{2+} ions incorporated into the PVA/molybdenum oxide hybrids bind to not only phosphate ions but also molybdenum hydroxide to form water-insoluble calcium molybdate. These phenomena consequently suppress the release of Ca^{2+} , leading to lower ability of the apatite formation. It is also assumed that Mo-OH groups on surfaces of hybrids have lower apatite-forming ability than Si-OH counterparts.

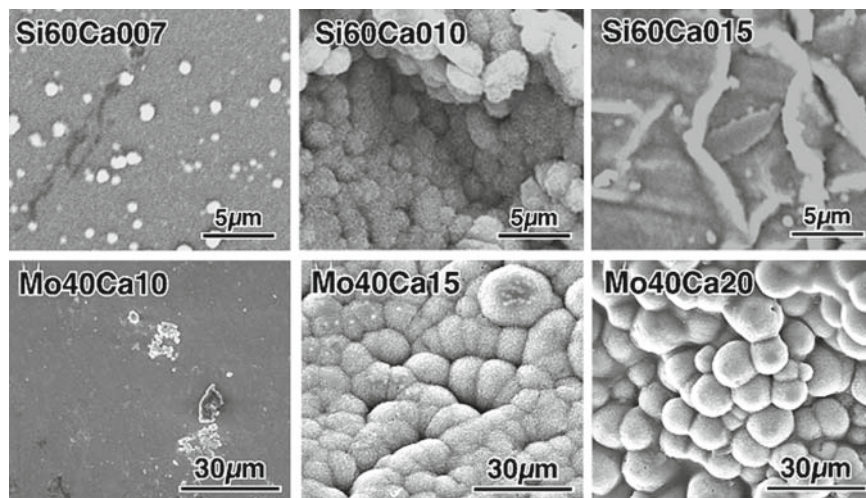


Fig. 16.16 SEM pictures of surfaces of PVA-based hybrids modified with silicon or molybdenum alkoxide, after soaking in SBF. Soaking period was 2 days and 3 days for PVA/silica and PVA/molybdenum oxide hybrids, respectively

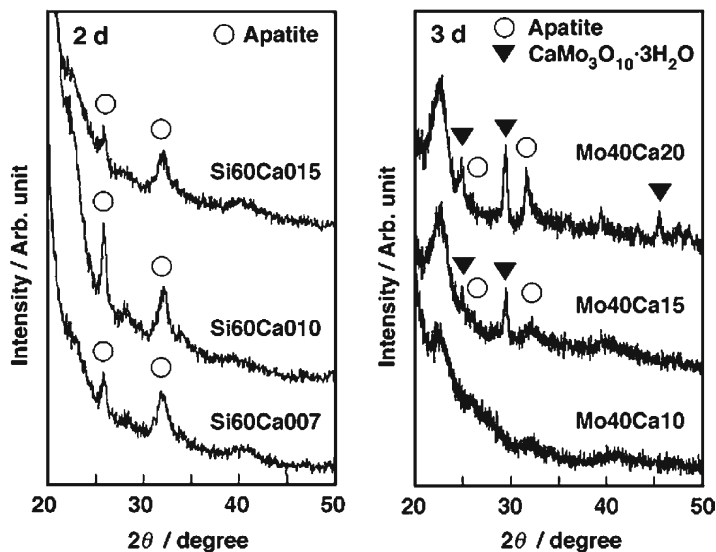


Fig. 16.17 TF-XRD patterns of surfaces of PVA-based hybrids modified with silicon or molybdenum alkoxide, after soaking in SBF. Soaking period was 2 days and 3 days for PVA/silica and PVA/molybdenum oxide hybrids, respectively

16.11 Conclusion

After carefully selecting various kinds of oxide gels that induce apatite deposition when in body fluids, bone-bonding bioactive nanohybrids can be designed by chemical modification of these gels with flexible organic polymers. Sol–gel process is a promising technique for obtaining such nanohybrids, and the described strategy of material design is expected to produce novel high-added-value biomaterials.

Acknowledgments This study was supported by a Grant-in-Aid for Encouragement of Young Scientists ((B)16700365) of the Japanese Society for the Promotion of Science.

References

1. Hench LL, Wilson J (1993) *An Introduction to Bioceramics*. World Scientific, Singapore
2. Hench LL, Splinger RJ, Allen WC, Greenlee TK (1972) Bonding mechanisms at the interface of ceramic prosthetic materials. *J Biomed Mater Res Symp* 2:117–141
3. Hench LL (1991) Bioceramics: from concept to clinic. *J Am Ceram Soc* 74:1487–1510
4. Hench LL (1998) Bioceramics. *J Am Ceram Soc* 81:1705–1728
5. Kokubo T, Shigematsu M, Nagashima Y, Tashiro M, Nakamura T, Yamamuro T, Higashi S (1982) Apatite- and Wollastonite-containing glass-ceramics for prosthetic application. *Bull Inst Chem Res Kyoto Univ* 60:260–268

6. Kokubo T, Kim HM, Kawashita M (2003) Novel bioactive materials with different mechanical properties. *Biomaterials* 24:2161–2175
7. Jarcho M (1976) Hydroxyapatite synthesis and characterization in dense polycrystalline forms. *J Mater Sci* 11:2027–2035
8. Deptula A, Lada W, Olczak T, Borello A, Alvani C, Dibartolomeo A (1992) Preparation of spherical powders of hydroxyapatite by sol-gel process. *J Non-Cryst Solids* 147:537–541
9. Jillavenkatesa A, Condrate RASr (1998) Sol-gel processing of hydroxyapatite. *J Mater Sci* 33:4111–4119
10. Chai CS, Ben-Nissan B (1999) Bioactive nanocrystalline sol-gel hydroxyapatite coatings. *J Mater Sci Mater Med* 10:465–469
11. Chow LC (1991) Development of self-setting calcium phosphate cements. *J Ceram Soc Jpn* 99:954–964
12. Monma H (1987) Tricalcium Phosphate Ceramics Complexed with Hydroxyapatite. *Yogyo-Kyokai-Shi* 95:814–818
13. Ohtsuki C, Kushitani H, Kokubo T, Kotani S, Yamamuro T (1991) Apatite formation on the surface of ceravital-type glass-ceramic in the body. *J Biomed Mater Res* 25:1363–1370
14. Neo M, Kotani S, Nakamura T, Yamamuro T, Ohtsuki C, Kokubo T, Bando Y (1992) A comparative study of ultrastructures of the interfaces between four kinds of surface-active ceramic and bone. *J Biomed Mater Res* 26:1419–1432
15. Ohtsuki C, Kokubo T, Neo M, Kotani S, Yamamuro T, Nakamura T, Bando Y (1991) Bone-bonding mechanism of sintered β -3CaO·P₂O₅. *Phosphorus Res Bull* 1:191–196
16. Kokubo T, Kushitani H, Sakka S, Kitsugi T, Yamamuro T (1990) Solutions able to reproduce in vivo surface-structure changes in bioactive glass-ceramic A-W. *J Biomed Mater Res* 24:721–734
17. Ohtsuki C, Aoki Y, Kokubo T, Bando Y, Neo M, Nakamura T (1995) Transmission electron microscopic observation of glass-ceramic A-W and apatite layer formed on its surface in a simulated body fluid. *J Ceram Soc Jpn* 103:449–454
18. Cho SB, Nakanishi K, Kokubo T, Soga N, Ohtsuki C, Nakamura T, Kitsugi T, Yamamuro T (1995) Dependence of apatite formation on silica gel on its structure: effect of heat treatment. *J Am Ceram Soc* 78:1769–1774
19. Kokubo T, Takadama H (2006) How useful is SBF in predicting in vivo bone bioactivity? *Biomaterials* 27:2907–2915
20. Oyane A, Kim HM, Furuya T, Kokubo T, Miyazaki T, Nakamura T (2003) Preparation and assessment of revised simulated body fluid. *J Biomed Mater Res* 65A:188–195.
21. Oonishi H, Kushitani S, Yasukawa E, Iwaki H, Hench LL, Wilson J, Tsuji E, Sugihara T (1997) Particulate bioglass compared with hydroxyapatite as a bone graft substitute. *Clin Ortho Rel Res* 334:316–325
22. Oonishi H, Murata N, Saito M, Wakitani S, Imoto K, Kim N, Matsuura M (1998) Comparison of bone growth behavior into spaces of hydroxyapatite and AW glass ceramic particles. In: LeGeros RZ, LeGeros JP (eds) *Bioceramics Vol. 11*. World Scientific, Singapore, pp. 411–414
23. Oonishi H, Hench LL, Wilson J, Tsuji E, Kin S, Yamamoto T, Mizokawa S (2000) Quantitative comparison of bone growth behavior in granules of Bioglass®, A-W glass-ceramic, and hydroxyapatite. *J Biomed Mater Res* 51:37–46
24. Kim HM, Himeno T, Kokubo T, Nakamura T (2005) Process and kinetics of bonelike apatite formation on sintered hydroxyapatite in a simulated body fluid. *Biomaterials* 26:4366–4373
25. Kim HM, Himeno T, Kawashita M, Kokubo T, Nakamura T (2004) The mechanism of biomineralization of bone-like apatite on synthetic hydroxyapatite: an in vitro assessment. *J R Soc Interface* 1:17–22.
26. Ohtsuki C, Kokubo T, Yamamuro T (1992) Mechanism of apatite formation on CaO-SiO₂-P₂O₅ glasses in a simulated body fluid. *J Non-Cryst Solids* 143:84–92
27. Li P, Ohtsuki C, Kokubo T, Nakanishi K, Soga N, de Groot K (1994) The role of hydrated silica, titania, and alumina in inducing apatite on implants. *J Biomed Mater Res* 28:7–15
28. Ohtsuki C, Kokubo T, Yamamuro T (1992) Compositional dependence of bioactivity of glasses in the system CaO-SiO₂-Al₂O₃; its in vitro evaluation. *J Mater Sci Mater Med* 3:119–125

29. Ohtsuki C, Osaka A, Kokubo T (1994) Effects of Al_2O_3 and TiO_2 on bioactivity of CaO-SiO_2 glasses. In Andersson OH, Yli-Urpo A (eds) *Bioceramics Vol. 7*. Butterworth-Heinemann, Oxford, pp. 73–78
30. Li R, Clark AE, Hench LL (1991) An investigation of bioactive glass powders by sol–gel processing. *J Appl Biomater* 2:231–239
31. Takadama H, Kim HM, Kokubo T, Nakamura T (2000) Mechanism of apatite formation induced by silanol groups-TEM observation. *J Ceram Soc Jpn* 108:118–121
32. Hu Y, Mackenzie JD (1992) Rubber-like elasticity of organically modified silicates. *J Mater Sci* 27:4415–4420
33. Tsuru K, Ohtsuki C, Osaka A, Iwamoto T, Mackenzie JD (1997) Bioactivity of sol–gel derived organically modified silicates, Part I: in vitro examination. *J Mater Sci Mater Med* 8:157–161
34. Chen Q, Miyaji F, Kokubo T, Nakamura T (1999) Apatite formation on PDMS-modified $\text{CaO-SiO}_2\text{-TiO}_2$ hybrids prepared by sol–gel process. *Biomaterials* 20:1127–1132
35. Osaka A, Ohtsuki C, Tsuru K (1995) Preparation of bioactive polymers modified with silanol groups. In: Wilson J, Hench LL, Greenspan D (eds), *Bioceramics Vol. 8*. Elsevier Science, Oxford, pp. 441–445
36. Yabuta T, Tsuru K, Hayakawa S, Ohtsuki C, Osaka A (2000) Synthesis of bioactive organic–inorganic hybrid with γ -methacryloxypropyl trimethoxysilane. *J Sol-Gel Sci Tech* 19:745–748
37. Miyazaki T, Ohtsuki C, Tanihara M (2003) Synthesis of bioactive organic–inorganic nanohybrid for bone repair through Sol–gel processing. *J Nanosci Nanotech* 3:511–515
38. Ratner BD, Hoffman AS, Schoen FJ, Lemons JE (2004) *Biomaterials science* 2nd edition, Elsevier Academic Press, Amsterdam
39. Cho SB, Nakanishi K, Kokubo T, Soga N, Ohtsuki C, Nakamura T (1996) Apatite formation on silica gel in simulated body fluid: its dependence on structures of silica gels prepared in different media. *J Biomed Mater Res (Appl. Biomater.)* 33:145–151
40. Cho SB, Miyaji F, Kokubo T, Nakanishi K, Soga N, Nakamura T (1998) Apatite formation on silica gel in simulated body fluid: effects of structural modification with solvent-exchange. *J Mater Sci Mater Med* 9:279–284
41. Plueddemann EP (1991) *Silane Coupling Agents* 2nd edition, Plenum, New York
42. Brinker CJ, Scherer GW (1990) *Sol–Gel Science*, Academic Press, San Diego
43. Yamada A, Tsuru K, Hayakawa S, Osaka A (2002) Chitosan-organosiloxane hybrids for biomedical applications. In: Abstract of the 3rd Asian international Symposium on Biomaterials and Drug Delivery Systems
44. Rhee SH (2004) Bone-like apatite-forming ability and mechanical properties of poly(ϵ -caprolactone)/silica hybrid as a function of poly(ϵ -caprolactone) content. *Biomaterials* 25:1167–1175
45. Mendes SC, Reis RL, Bovell YP, Cunha AM, van Blitterswijk CA, de Bruijn JD (2001) Biocompatibility testing of novel starch-based materials with potential application in orthopaedic surgery: a preliminary study. *Biomaterials* 22:2057–2064
46. Miyazaki T, Yasunaga S, Ishida E, Ashizuka M, Ohtsuki C (2005) Development of bioactive organic–inorganic hybrid based on starch. *J Jpn Soc Powder and Powder Metall* 52:360–363 (in Japanese)
47. Kabra BG, Gehrke SH, Spontak RJ (1998) Microporous, responsive hydroxypropyl cellulose gels. 1. Synthesis and microstructure. *Macromolecules* 31:2166–2173
48. Khor E. (2001) *Chitin: Fulfilling a Biomaterials Promise*, Elsevier, Amsterdam
49. Miyazaki T, Ohtsuki C, Tanihara M, Ashizuka M (2004) Apatite deposition on organic–inorganic hybrids prepared from chitin by modification with alkoxysilane and calcium salt. In: Barbosa MA, Monteiro FJ, Correia R, Leon B(eds), *Bioceramics Vol. 16*. Trans Tech Publications, Switzerland, pp. 545–548.
50. Khor E, Lim LY (2003) Implantable applications of chitin and chitosan. *Biomaterials* 24:2339–2349
51. Chen BQ, Sun K, Zhang KB (2004) Rheological properties of chitin/lithium chloride, N,N-dimethyl acetamide solutions. *Carbohydr Polym* 58:65–69

52. Kamitakahara M, Kawashita M, Miyata N, Kokubo T, Nakamura T (2004) Degradation of bioactive polydimethylsiloxane-CaO-SiO₂-TiO₂ and poly(tetramethylene oxide)-CaO-TiO₂ hybrids in a simulated body fluid. *J Am Ceram Soc* 87:235–239
53. Kühn KD (2000) *Bone Cement*. Springer, Berlin
54. Harper EJ (1998) Bioactive bone cements. *Proc Inst Mech Eng H* 212:113–120
55. Shinzato S, Kobayashi M, Mousa WF, Kamimura M, Neo M, Kitamura Y, Kokubo T, Nakamura T (2000) Bioactive polymethyl methacrylate-based bone cement: comparison of glass beads, apatite- and wollastonite-containing glass-ceramic, and hydroxyapatite fillers on mechanical and biological properties. *J Biomed Mater Res* 51:258–272
56. Ohtsuki C, Miyazaki T, Kyomoto M, Tanihara M, Osaka A (2001) Development of bioactive PMMA-based cement by modification with alkoxysilane and calcium salt. *J Mater Sci Mater Med* 12:895–899
57. Miyazaki T, Ohtsuki C, Kyomoto M, Tanihara M, Mori A, Kuramoto K (2003) Bioactive PMMA bone cement prepared by modification with methacryloxypropyltrimethoxysilane and calcium chloride. *J Biomed Mater Res* 67A:1417–1423
58. Mori A, Ohtsuki C, Sugino A, Kuramoto K, Miyazaki T, Tanihara M, Osaka A (2003) Bioactive PMMA-based bone cement modified with methacryloxypropyltrimethoxysilane and calcium salts - effects of calcium salts on apatite-forming ability. *J Ceram Soc Jpn* 111:738–742
59. Kim HM, Miyaji F, Kokubo T, Nakamura T (1996) Preparation of bioactive Ti and its alloys via simple chemical surface treatment. *J Biomed Mater Res* 32:409–417
60. Uchida M, Kim HM, Kokubo T, Fujibayashi S, Nakamura T (2003) Structural dependence of apatite formation on titania gels in a simulated body fluid. *J Biomed Mater Res A* 64:164–170
61. Uchida M, Kim HM, Kokubo T, Miyaji F, Nakamura T (2001) Bonelike apatite formation induced on zirconia gel in a simulated body fluid and its modified solutions. *J Am Ceram Soc* 84:2041–2044
62. Uchida M, Kim HM, Miyaji F, Kokubo T, Nakamura T (2002) Apatite formation on zirconium metal treated with aqueous NaOH. *Biomaterials* 23:313–317
63. Miyazaki T, Kim HM, Miyaji F, Kokubo T, Kato H, Nakamura T (2000) Bioactive tantalum metal prepared by NaOH treatment. *J Biomed Mater Res*. 50:35–42
64. Miyazaki T, Kim HM, Kokubo T, Kato H, Nakamura T (2001) Induction and acceleration of bonelike apatite formation on tantalum oxide gel in simulated body fluid. *J Sol-gel Sci Tech* 21:83–88
65. Miyazaki T, Kim HM, Kokubo T, Ohtsuki C, Nakamura T (2001) Bonelike apatite formation induced on niobium oxide gels in simulated body fluid. *J Ceram Soc Jpn* 109:934–938
66. Wakabayashi G, Miyazaki T, Ishida E, Ashizuka M, Kokubo T, Ohtsuki C (2003) Development of bioactive molybdenum metal by alkali treatment. In Okazaki M, Ishikawa K, Yamashita K, Doi Y, Ban S (eds), *Archives of BioCeramics Research Vol. 3*. Saga Printings, pp. 288–292
67. Tanahashi M, Matsuda T (1997) Surface functional group dependence on apatite formation on self-assembled monolayers in a simulated body fluid. *J Biomed Mater Res* 34:305–315
68. Kawashita M, Nakao M, Minoda M, Kim HM, Beppu T, Miyamoto T, Kokubo T, Nakamura T (2003) Apatite-forming ability of carboxyl group-containing polymer gels in a simulated body fluid. *Biomaterials* 24:2477–2484
69. Miyazaki T, Ohtsuki C, Akioka Y, Tanihara M, Nakao J, Sakaguchi Y, Konagaya S (2003) Apatite deposition on polyamide films containing carboxyl group in a biomimetic solution. *J Mater Sci Mater Med* 14:569–574
70. Kawai T, Ohtsuki C, Kamitakahara M, Miyazaki T, Tanihara M, Sakaguchi Y, Konagaya S (2004) Coating of apatite layer on polyamide films containing sulfonic groups by biomimetic process. *Biomaterials* 25:4529–4534
71. Miyazaki T, Imamura M, Ishida E, Ashizuka M, Ohtsuki C, Tanihara M (2005) Apatite formation on organic-inorganic hybrid containing sulfonic group. In Li P, Zhang K, Colwell CW Jr (eds), *Bioceramics Vol. 17*. Trans Tech Publications, Switzerland, pp. 725–728

72. Leonor IB, Kim HM, Balas F, Kawashita M, Reis RL, Kokubo T, Nakamura T (2005) Surface charge of bioactive polyethylene modified with -SO₃H groups and its apatite inducing capability in simulated body fluid. In Li P, Zhang K, Colwell CWJr (eds) *Bioceramics Vol. 17*. Trans Tech Publications, Switzerland, pp. 453–456
73. Kamitakahara M, Kawashita M, Miyata N, Kokubo T, Nakamura T (2003) Apatite-forming ability and mechanical properties of CaO-free poly(tetramethylene oxide) (PTMO)-TiO₂ hybrids treated with hot water. *Biomaterials* 24:1357–1363
74. Kamitakahara M, Kawashita M, Miyata N, Kim HM, Kokubo T, Ohtsuki C, Nakamura T (2004) Apatite-forming ability and mechanical properties of poly(tetramethylene oxide) (PTMO)-Ta₂O₅ hybrids. In Barbosa MA, Monteiro FJ, Correia R, Leon B (eds), *Bioceramics Vol. 16*. Trans Tech Publications, Switzerland, pp. 521–524.
75. You C, Miyazaki T, Ishida E, Ashizuka M, Ohtsuki C, Tanihara M (2005) Apatite deposition on organic–inorganic hybrids synthesized from poly(vinyl alcohol) and various metal oxides. In Li P, Zhang K, Colwell CWJr (eds), *Bioceramics Vol. 17*. Trans Tech Publications, Switzerland, pp. 469–472
76. Huang RYM, Rhim JW (1993) Modification of poly(vinyl alcohol) using maleic-acid and its application to the separation of acetic-acid water mixtures by the pervaporation technique. *Polym Int* 30:129–135
77. Gimenez V, Mantecon A, Cadiz V (1996) Modification of poly(vinyl alcohol) with acid chlorides and crosslinking with difunctional hardeners. *J Polym Sci A Polym Chem* 34:925–934
78. Oka M, Ushio K, Kumar P, Ikeuchi K, Hyon SH, Nakamura T, Fujita H (2000) Development of artificial articular cartilage. *Proc Inst Mech Eng H J Eng Med* 214:59–68
79. Kobayashi M, Oka M (2004) Characterization of a polyvinyl alcohol-hydrogel artificial articular cartilage prepared by injection molding. *J Biomater Sci Polym Ed* 15:741–751
80. Nakashima K, Sawae Y, Murakami T (2005) Study on wear reduction mechanisms of artificial cartilage by synergistic protein boundary film formation. *JSME Int J Ser C* 48:555–561

Chapter 17

Silica Sol–Gel Biocomposite Materials for Sensor Development

Wai Tak Yip, Yongyao Zhou, Tami A. Martyn, and James W. Gilliland

Abstract The performance of a silica sol–gel biosensor is intimately related to the characteristics of an encapsulated guest molecule. The effect of charge, size, and polarity on the behavior of the encapsulate was investigated using both ensemble measurements and single-molecule spectroscopy. Simply by monitoring the mobility of individual encapsulates, the heterogeneous microscopic environment within a silica sol–gel was directly revealed. Regardless of molecular charges, all small molecules are sufficiently immobilized in alcogels. On the other hand, a floppy, non-polar molecule can display surprisingly high rotational mobility inside an alcogel. Such behavior is attributed to the disruption of molecular templating by active conformation fluctuations during the gelation process. In a more porous hydrogel, however, Coulombic interactions dictate molecular mobility. For biosensor development, molecular templating continues to be a major concern in the synthesis of active silica biocomposite materials, where large enzyme molecules are routinely encapsulated. To circumvent this problem, liposomes are used to template the formation of large silica pores to maintain unimpaired conformational flexibility necessary for the normal functioning of an enzyme. The use of liposome also keeps an enzyme from hazardous chemical environments while a hydrogel is forming, making it less likely to become inactive. This strategy appears applicable to the encapsulation of both robust and fragile enzymes and produces active silica biocomposites for biosensor development. In a separate front, silica alcogel is embedded inside a polyelectrolyte multilayer scaffold to produce a hybrid film. The hybrid architecture allows one to vary the response time of a sensing device through the precision control of film thickness. This approach can be further exploited to strengthen a hydrogel thin film structure, which may eventually replace the slow monolithic hydrogel sensor by a faster and sturdier hybrid thin film sensor. This chapter illustrates the above concepts and techniques while providing the reader with a promising strategy for pH-sensor development.

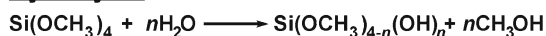
W.T. Yip (✉), Y. Zhou, T.A. Martyn, and J.W. Gilliland
Department of Chemistry and Biochemistry, University of Oklahoma, Norman,
OK 73071, USA
e-mail: ivan-yip@ou.edu

17.1 Introduction

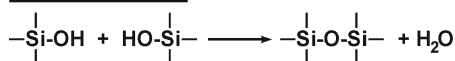
The sol–gel process is a low temperature synthetic route to the preparation of inorganic oxides. Scheme 1 illustrates the two reactions that best summarize the sol–gel process. The synthesis employs a metal alkoxide (e.g. $\text{Si}(\text{OCH}_3)_4$, TMOS, $\text{Si}(\text{OCH}_2\text{CH}_3)_4$, TEOS) as a starting material [1]. In Scheme 1, TMOS is first hydrolyzed into silanol, which then undergoes condensation to produce a highly porous and disorganized three-dimensional network of silicon oxide. The stochastic nature of solution chemistry leaves many unreacted alkoxy and hydroxyl terminal groups randomly distributed throughout the silica framework and produces an amorphous material that is both structurally and chemically heterogeneous. Unreacted alkoxy and hydroxyl groups also leave behind silica pores of dimension ranging from a few nanometers to hundreds of nanometers. The porous nature of silica sol–gel not only provides a viable platform to immobilize active biomolecules, but it also permits small molecules to diffuse inside and interact with the encapsulated biomolecules. The room-temperature sol–gel silica formation process is also suitable for the encapsulation of biomolecules that are prone to denaturation at high temperatures. The nanoscopic confinement inside a silica sol–gel also offers extra protection to entrapped proteins against proteolysis and thermal denaturation, making it ideal for the design and fabrication of biosensors for medical applications.

The first attempt to encapsulate proteins in silica hydrogels by Dickey in 1955 produced weakly active biocomposite materials [2]. His observations went unnoticed, and no further investigation on the wider application of silica hydrogel for active bio-encapsulation was reported for another 16 years. The true potential of silica hydrogel biocomposite was subsequently revealed by Johnson in 1971 when he reported that 34% trypsin activity could be retained upon hydrogel encapsulation [3]. Despite this exciting finding, Johnson's work again failed to ignite further interest in silica biocomposite materials. The somewhat unfortunate outcome of the groundbreaking work demonstrated by Dickey and Johnson was perhaps partly due to the process by which silica hydrogels were directly obtained *i.e.* from the acidification of a sodium silicate precursor. Since this approach does not offer enough flexibility to optimize the activity of an entrapped enzyme, it was probably not perceived as an effective way to deliver a wide variety of active biocomposite materials. As silane chemistry continued to mature in the 80s, the room-temperature sol–gel process began to show promise as a more flexible alternative to the encapsulation and manipulation of organic, inorganic, and biomolecules in silica. The interest in

Hydrolysis



Condensation



Scheme 1

silica sol–gel biocomposite materials eventually took off when Avnir and coworkers reported in 1990 that as much as 30% bioactivity could be retained when alkaline phosphatase was encapsulated inside silica hydrogels [4]. Thereafter, the seminal work by Zink, Brennan, Bright, and Gill continued to broaden the scope and strategy for silica sol–gel bio-encapsulation [5–16]. The last decade has witnessed a rapid increase in the number of biomolecules successfully encapsulated inside silica hydrogels. With seemingly an endless number of biomolecules on the horizon, the possibility of silica sol–gel biocomposite materials appears to be unlimited. Indeed, the successful entrapments of nucleic acids, antibodies, enzymes, membrane proteins, whole cells, and even live microbes have already stimulated widespread interest in the biosensor and biocatalysis research communities [17–26].

One serious limitation of silica sol–gel bio-encapsulation is that there appears to have no unifying strategy that is applicable to the encapsulation of all enzymes. This has been one of the major issues that severely limits the progress of silica sol–gel biocomposite materials for sensor development. Presumably, nucleation of silica sol surrounding a molecule during gel formation is strongly influenced by the surface charge and topography of the molecule itself, dictating the physical characteristics of the pore where the molecule will eventually reside. Since the nanoscopic confinement imposed by a silica pore dramatically enhances protein–silica interactions and alters protein behavior in a significant way, it is not surprising to see that the physical properties as well as the bioactivity of an encapsulated protein are rarely predictable. As a result, every protein comes with a unique encapsulation protocol that maximizes the activity of the resultant silica sol–gel biocomposite material. For example, organically modified silicates (ORMOSIL) have been used to tailor the hydrophobicity of silica pores for the active encapsulation of lipophilic proteins like human serum albumin (HSA) and lipase [6, 27]. Lipase also displayed a higher activity when poly(ethylene glycol) (PEG) was added to reduce the polarity of silica pores and enhance protein dynamics [12, 28]. It has also been demonstrated that the activity of lactate and glycolate oxidases could be rescued upon forming a complex with poly(ethyleneimine) prior to silica sol–gel encapsulation [29]. Sorbitol has been shown to increase chymotrypsin and ribonuclease T1 activity by altering their hydration inside silica pores [30]. In addition to the engineering of the microenvironment surrounding an encapsulated protein, new precursors for the making of sol–gel silica with higher biocompatibility have been constantly developing. Thus Gill and Ballesteros produced highly active silica biocomposite with high encapsulation efficiency from polyol esters of silicates and siloxane precursors [20]. Brennan et al. used sugar-modified silane precursors to enhance biocompatibility and reduce shrinking in silica biocomposites [31–33]. More recently, silaffin polypeptides and silicatein biomimetics were employed to eliminate hazardous chemical environments by catalyzing silica sol–gel formation at neutral pH [34, 35]. Last but not least, the gelation of silica sol in the presence of organic polymers or biopolymers has been shown to produce hybrid materials that exhibit higher long-term structural stability with remarkable biocompatibility [20, 36–39].

Regardless of how a silica biocomposite is made, the highly cross-linked sol–gel framework presents a serious mass transport problem for both substrates and products

of an encapsulated enzyme, rendering most biocatalysis in silica hydrogel diffusion-controlled. This problem is particularly serious for cationic species in neutral and higher pH environments where a silica hydrogel usually acquires negatively charged surfaces, leading to Coulombic attractions that dramatically impair cation diffusion. As a result of slow diffusion, biological activities are usually confined to near the surface of a thick silica hydrogel monolith. Since no substrate can reach far below the monolith surface within a short period of time, enzymes deep inside the monolith become practically useless in applications that require fast response. This problem is partly alleviated by opening up both the encapsulation volume and the interconnecting channels in a hydrogel using organic additives to disrupt protein–silica interactions and accelerate mass transport, producing more active biocomposite materials with faster response time [30, 40]. Alternatively, silica sol–gel biosensors have been built into thin film configurations on flat, irregular, as well as fiber surfaces in order to shorten the response time. The latest development in the applications of silica sol–gel biocomposite materials as biosensors and bioreactors has been reviewed recently [41].

To further improve the efficacy of bio-encapsulation and to transform silica sol–gel biocomposite into a more competitive sensor technology, it is imperative to understand how the behavior of encapsulated protein and substrate guests can be influenced by a silica host. Using mobility to probe the extent of guest–host interactions, our work focuses on examining intermolecular interactions that are likely to affect the behavior of guest molecules confined within microscopic silica pores. We employed both conventional and single-molecule spectroscopy to unravel genuine molecular events that would otherwise be reduced into mere statistical averages in ensemble measurements because of the heterogeneous microenvironments found inside sol–gel silica. The latest advances in solid-state technology have allowed the optical detection of single molecules at room temperature [42]. Since then, new single-molecule spectroscopic techniques have been constantly developed to meet new challenges. Newly developed techniques such as total internal reflection microscopy [43, 44], three-dimensional orientation measurements [45–47], photon bunching and anti-bunching [48, 49], dual-color excitation [50, 51], fluorescence correlation spectroscopy [52, 53], polarization modulation [54, 55], fluorescence lifetime [42, 56], fluorescence anisotropy [57–63], and surface-enhanced Raman spectroscopy [64] have rapidly transformed single-molecule spectroscopy into a powerful tool particularly suitable for the study of heterogeneous molecular dynamics relevant to both physical and biological sciences [65].

17.2 Guest–Host Interactions inside Sol–Gel Silica

17.2.1 *Hydrophobic Repulsion*

Sol–gel silica is a hydrophilic host and is incompatible with the encapsulation of hydrophobic dyes like Nile Red. Attempts to trap Nile Red in sol–gel silica have shown to result in poor encapsulation efficiency [66]. The mismatch in polarity forces Nile Red away from a silica surface, leading to poor encapsulation efficiency.

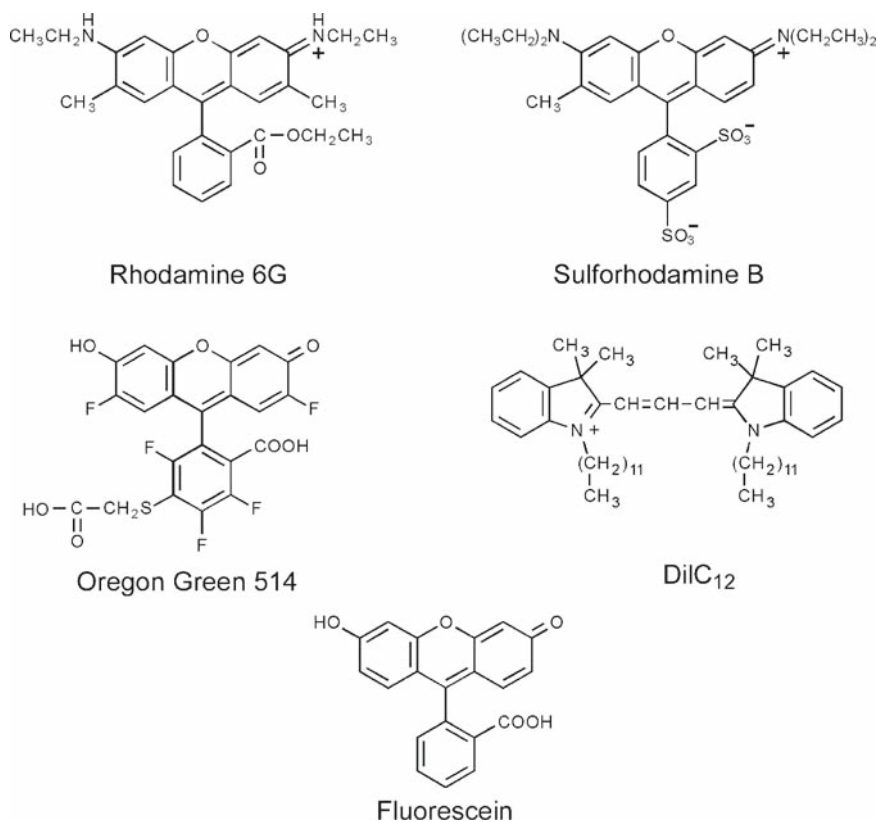


Fig. 17.1 Molecular structures of all fluorophores examined in this chapter

This bias against hydrophobic molecules suggests that Nile Red would not be a suitable candidate for monitoring the effect of hydrophobic repulsion in a sol–gel silica since successful encapsulation of Nile Red is not facilitated by hydrophobic repulsion but the lack thereof or the complete domination by other interactions that favor encapsulation. Instead, the effect of hydrophobic repulsion was subtly revealed through the study of silica sol–gel encapsulated 1,1'-didodecyl-3,3,3',3'-tetramethylindocarbocyanine (DiIC₁₂), an indocarbocyanine that carries two long hydrophobic methylene chains (Fig. 17.1).

In this study, the polarization of emission from a single DiIC₁₂ molecule was used to determine the mobility of the molecule [67]. As illustrated in Fig. 17.2, single-molecule emission is resolved into parallel $I_{\parallel}(t)$ and perpendicular $I_{\perp}(t)$ polarization components, where $I_{\parallel}(t)$ and $I_{\perp}(t)$ are simultaneously monitored by two detectors upon continuous laser excitation. From the measured $I_{\parallel}(t)$ and $I_{\perp}(t)$, emission polarization $P(t)$ at all time can be calculated according to the following equation.

$$P(t) = \frac{I_{\parallel}(t) - I_{\perp}(t)}{I_{\parallel}(t) + I_{\perp}(t)}$$

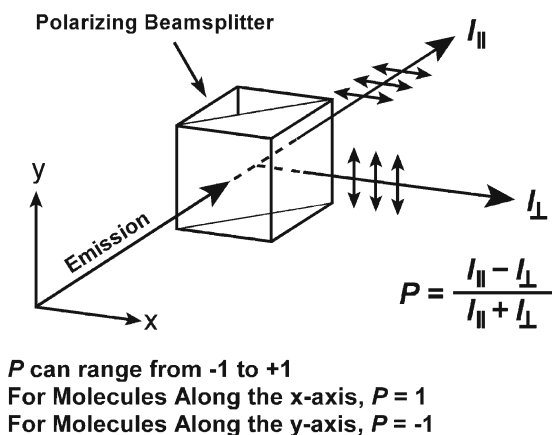


Fig. 17.2 Schematic for single-molecule polarization (P) measurements

A freely “tumbling” DiIC₁₂ molecule should emit equally along the parallel and perpendicular polarization axes, leading to zero $P(t)$. On the other hand, a DiIC₁₂ molecule is classified as “fixed” if it maintains a constant non-zero $P(t)$. If a DiIC₁₂ molecule changes its orientation during the course of a measurement and thus changes $P(t)$, it is classified as “intermediate” to designate that it is neither a freely tumbling nor a permanently immobilized molecule.

Figure 17.3 depicts how the three different types of behavior manifested themselves in the emission intensity time traces together with the associated $P(t)$ and the corresponding average mobility over time \bar{P} . Excluding the intermediate molecules where \bar{P} does not carry any physical meaning, Fig. 17.4 presents the distributions of \bar{P} for all tumbling and fixed DiIC₁₂ molecules. The intense spike around zero polarization suggests that silica sol–gel encapsulated DiIC₁₂ exhibits remarkable mobility. A total of 101 DiIC₁₂ molecules studied were found to be tumbling, which account for 48% of the 212 molecules we investigated. Apparently, the positive charge on the indocarbocyanine moiety in DiIC₁₂ induces immobilization through hydrophilic attractions toward the silica surface, leading to the encapsulation of fixed molecules. On the other hand, the fact that DiIC₁₂ is a non-polar molecule that is almost insoluble in water suggests that the hydrophilic interaction between DiIC₁₂ and silica is unlikely to be strong. This weak hydrophilic interaction between DiIC₁₂ and silica is vulnerable to any disruption caused by the long hydrophobic chains of DiIC₁₂ because of the mismatch in polarity, leading to the encapsulation of tumbling molecules.

The distinct mobility between tumbling and fixed DiIC₁₂ is a strong indication that the two groups of molecules are residing in different local environments. This provides a unique opportunity to examine how the confinement of DiIC₁₂ in different microenvironments may affect its behavior. Indeed, when the survival lifetime of tumbling and fixed DiIC₁₂ molecules are compared in Fig. 17.5, it becomes clear that

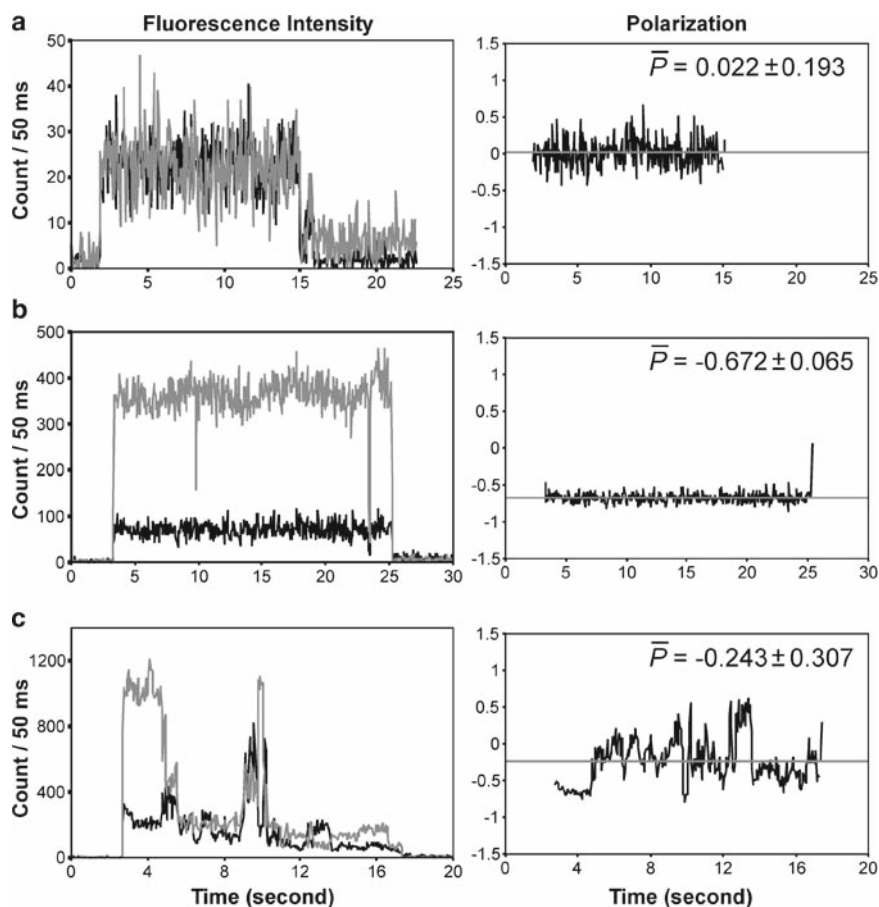


Fig. 17.3 The fluorescence intensity and polarization of three single DiIC₁₂ molecules that display three different behaviors. (a) A molecule that tumbles freely with an average polarization close to zero. (b) A molecule that is completely immobilized with an average polarization equal to -0.672 . (c) A molecule that switches between tumbling and immobilized or between different orientations. *Black* and *gray* lines in the fluorescence traces represent $I_{\parallel}(t)$ and $I_{\perp}(t)$ respectively. The *gray* line in the polarization plot indicates the average polarization (\bar{P}) of the molecule. Reproduced with permission from [68]. Copyright 2003 American Chemical Society

fixed DiIC₁₂ displays a higher photostability than tumbling DiIC₁₂ upon continuous laser excitation. This observation is consistent with the notion that immobilization helps eliminate dynamic interactions that are responsible for photo-degradation and thereby enhancing photostability [69]. In the case of DiIC₁₂, our single-molecule study indicated that this effect amounts to a threefold increase in the photostability of fixed over tumbling molecules. This translates to a practical approach to extend the operational lifespan of silica sol–gel based optical sensor devices simply by choosing molecules that favor immobilization in view of their higher resultant photostability.

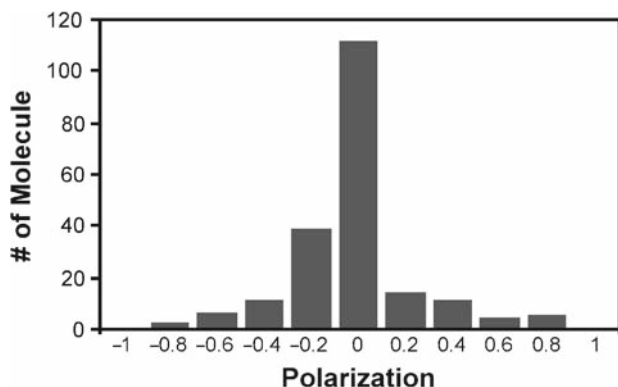


Fig. 17.4 Polarization distributions of tumbling and fixed DiIC₁₂ molecules. The sharp increase in the number of molecules at zero polarization indicates the presence of a substantial fraction of tumbling DiIC₁₂ molecules. Reproduced with permission from [68]. Copyright 2003 American Chemical Society

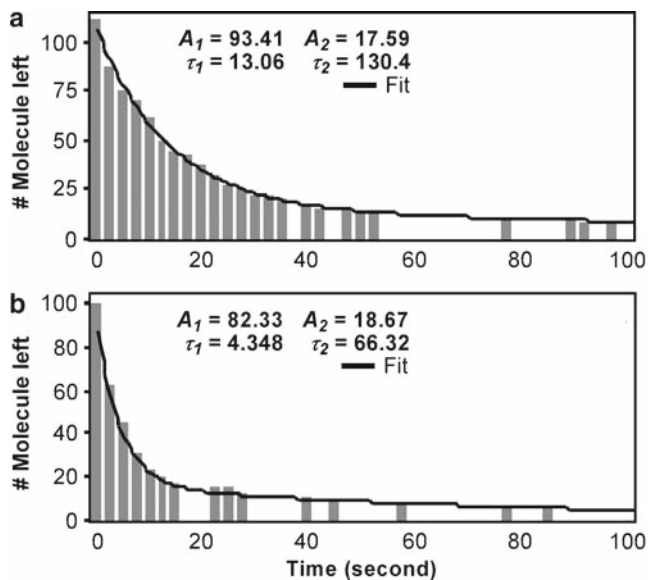


Fig. 17.5 The survival histograms of single DiIC₁₂ molecules upon continuous excitation at 543.5 nm. (a) Fixed and (b) tumbling molecules. Both histograms are fitted with a bi-exponential decay function with the number of molecules left = $A_1 \exp(-t/\tau_1) + A_2 \exp(-t/\tau_2)$. Reproduced with permission from [68]. Copyright 2003 American Chemical Society

17.2.2 Coulombic Interactions

In general, one of the most dominant forms of protein-silica interactions is believed to be Coulombic attraction. The isoelectric point of silica is 2.0 ± 0.2 [70]. At physiological pH, most unreacted silanol in a silica hydrogel will ionize to produce negatively charged pore surfaces. Under microscopic confinement where intermolecular separations are short, these surface charges are expected to strongly influence the adsorption of encapsulated organic dyes, DNA, RNA, and protein molecules. By determining the mobility of single fluorophores that carry different charges, we were able to reveal the influence of Coulombic interactions on the mobility of a silica sol–gel encapsulate [71]. Fig. 17.6 illustrates the mobility distributions of rhodamine 6G (R6G) and Oregon Green 514 (ORG) encapsulated in sol–gel thin films, representing positively charged (+1) and negatively charged (–3) fluorophores, respectively. Since the positive charge in R6G delocalizes throughout the entire xanthene moiety, the iminium proton normally does not participate in acid–base equilibria. R6G fluorescence is therefore insensitive to pH except at pH higher than 11 where its ester group will begin to hydrolyze [72]. As for ORG, its fluorescence is strongly pH dependent. Depending on its surrounding pH, ORG can be either a neutral (weakly fluorescent) or an anionic (strongly fluorescent) molecule. Since the carboxylic acid groups in ORG have low pK_a values, their fluorescence gradually becomes pH insensitive beyond pH 6.0. Due to the significant contrast in fluorescence intensity, it is worth pointing out that our single-molecule fluorescence studies were skewed toward the detection of the highly fluorescent anionic ORG by default.

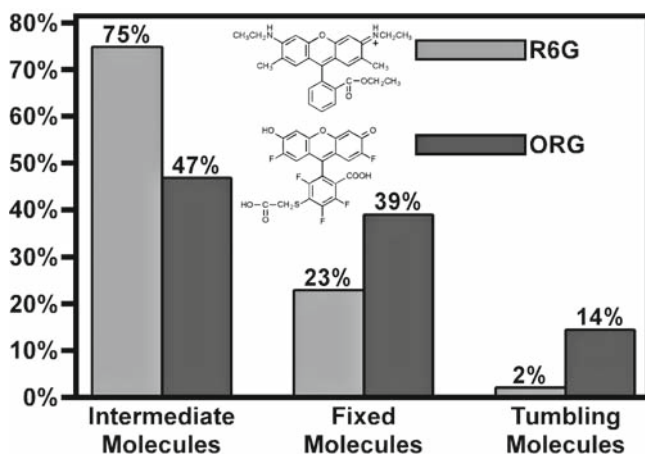


Fig. 17.6 Single-molecule mobility distributions of R6G and ORG encapsulated in silica sol–gel thin films

Given a similar molecular skeleton between R6G and ORG, the sevenfold higher percentage tumbling molecules found in ORG ($14 \pm 2\%$) relative to R6G ($2 \pm 1\%$) shown in Fig. 17.6 is a strong indication that a more disruptive interaction existed between ORG and a silica surface. This disruptive interaction is attributed to the long-range electrostatic repulsion experienced by an encapsulated ORG molecule. Charge–charge repulsion between ORG and a pore surface promotes ORG mobility by preventing it from adhering strongly to the pore surface. The effect of Coulombic repulsion on ORG was further confirmed by examining its mobility inside a wet silica film that was in contact with a pH 7.0 phosphate buffer. The percentage of tumbling ORG was found to increase from $14 \pm 2\%$ to $23 \pm 4\%$ upon wetting. Presumably, at pH much higher than the isoelectric point of silica, most surface Si–OH groups should have been deprotonated. As a result of the additional negative charges that were left on a pore surface, encapsulated ORG molecules appeared to experience stronger Coulombic repulsion and became more mobile.

The most intriguing feature in Fig. 17.6 is that despite strong Coulombic repulsion, the majority of silica sol–gel encapsulated ORG were found to be either completely immobilized or only capable of changing orientation occasionally. Wetting the film with a pH 7.0 buffer only enhanced mobility marginally with more than 75% of ORG remaining either as fixed or intermediate. This implies that Coulombic interactions only have a moderate effect on the mobility of molecules confined within silica pores. In addition to Coulombic interaction, the confinement imposed by a microscopic pore may also favor shorter range interactions such as van der Waals interactions and H-bonding. There is also a good possibility that most immobilized ORG are being confined on a purely physical basis, a phenomenon commonly described as molecular templating or imprinting [73, 74]. With regard to R6G, Coulombic attraction between R6G and a silica pore surface would only favor surface adsorption, dramatically reducing mobility as well as the percentage of tumbling molecules.

In a silica biocomposite, it is plausible to argue that a similar type of long-range Coulombic interactions can be prevalent between a protein and a silica surface. Since the morphology of different silica pores in an amorphous gel is unlikely to be identical, Coulombic interactions are expected to influence the conformation of different proteins differently and lead to unpredictable biocomposite activity. One approach to suppress Coulombic attraction, and thereby minimizing protein–silica interactions, is to modify the hydration shell of an enzyme using polymeric additives such as glycerol [75], polyvinyl alcohol, poly(ethylene glycol) [12], poly(vinylimidazole) (PVI), or poly(ethyleneimine) (PEI) [29]. These additives are said to electrostatically complex with an encapsulated enzyme, thereby neutralizing Coulombic attraction and restoring enzymatic activity. A major obstacle in generalizing this approach is that the effect of an additive is strongly protein specific, which usually leads to unpredictable outcomes. For example, silica sol–gel encapsulated glucose oxidase, lactate oxidase, and glycolate oxidase respond to polycationic PVI and PEI differently [29]. Subsequent structural analysis suggested that the differences originated from the FAD binding pocket in glucose oxidase *versus*

the FMN binding pocket in lactate oxidase and glycolate oxidase [76]. Another more popular approach to manipulate protein–silica interaction is to alter the surface characteristics of a silica pore by mixing organically modified silica precursors with TMOS during the sol–gel synthesis process. The silica pore inside the resultant ORMOSIL can be tailored to exhibit a hydrophobic, hydrophilic, cationic, or anionic surface, depending on the non-hydrolyzable substituent on the organically modified precursors [19, 77, 78]. This design flexibility in ORMOSIL is instrumental to the successful encapsulation of enzymes that are otherwise less active, or even inactive, in purely TMOS-derived silica hydrogels [79–82]. Despite the apparent advantage of ORMOSIL, the presence of non-hydrolyzable substituent will inevitably decrease the extent of cross-linking. This will lead to an extremely porous framework and weaken the overall structural integrity of the resultant ORMOSIL [66]. Accordingly, an ORMOSIL will crumble into pieces before a high degree of surface modification can be achieved. Even if the mechanical structure of an ORMOSIL could remain intact, the level of surface modification would never reach 100% [19].

17.2.3 Hydrogen Bonding

In an attempt to further manipulate mobility with Coulombic interaction, we examined the mobility of silica sol–gel encapsulated sulforhodamine B (SRB). SRB is a positively charged fluorophore that contains two highly acidic sulfonic groups ($pK_a < 1.5$) [83]. Ionization of both sulfonic groups at moderate to high pH generates two additional negative charges and turns SRB into a zwitterion that carries one net negative charge. The zwitterionic nature of SRB has been demonstrated to interact with both cationic and anionic aquifer materials such as sandstone and limestone, respectively [83, 84]. As a result, even with a net negative charge, SRB was found to exhibit a mobility distribution that more resembles that of R6G than ORG [85]. This suggests that a single negative charge is insufficient to counter all other interactions that favor immobilization. In addition to molecular templating, the positive charge on SRB may help anchor the molecule onto a pore surface through Coulombic interactions and further limit its mobility. By comparing the photostability of silica sol–gel encapsulated R6G and SRB in water and ethanol, we also identified evidence of H-bonding in SRB from the increase in photostability upon solvation. This is in stark contrast to the behavior of R6G, which showed a lower photostability in both water and ethanol compared to that of a dry sample. Since R6G and SRB share an almost identical xanthene skeleton, any structurally related interaction through the xanthene moiety can be safely ruled out as the source of additional photostability in SRB. This leaves the benzyl ring as the most probable place through which SRB acquires additional photostability. A sulfonic group is known to form a special type of H-bonding network with surfactants like bis(2-ethylhexyl) sulfosuccinate (AOT) through bridging water molecules [86]. We attributed that the sulfonic groups in SRB are also capable of forming such a H-bonding network inside a silica pore,

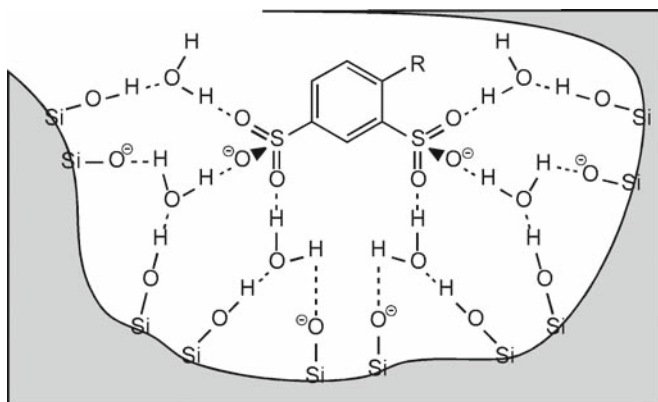


Fig. 17.7 Special hydrogen bonding network that might hold SRB in place and help reduce molecular motions surrounding a silica sol-gel encapsulated SRB. *R* represents the xanthene ring in SRB. Reproduced with permission from [87]. Copyright 2005 American Chemical Society

indirectly anchoring SRB onto a pore surface. As shown in Fig. 17.7, the microscopic pore dimension would serve to provide additional stability to the H-bonding network and further reduce molecular motions within the entire silica pore. With most molecular motions slowed by the H-bonding network, dynamic interactions that lead to the photo-degradation of SRB would likely be suppressed. On the other hand, R6G is incapable of H-bonding. Upon solvation, R6G would only be subjected to more active solvent dynamics with no other interactions to counteract the effect. Since more active dynamic motions inevitably create interactions that cause additional photo-degradation, this explains why silica sol-gel encapsulated R6G becomes less photostable upon wetting.

17.2.4 Molecular Templating

The significant amount of fixed ORG in Fig. 17.6 also suggests that even three negative charges are incapable of breaking ORG completely free from a silica surface, implying that Coulombic interaction is not the major factor that governs mobility. The presence of these immobilized ORG was attributed to a molecular templating effect that is ubiquitous in silica sol-gel composite [73, 74]. Here, a dopant guest molecule can serve as a template for silica pore formation when a liquid sol gradually gels into a solid composite, trapping the guest molecule inside a pore of similar shape and dimension. Apparently, this purely physical entrapment is sufficient to overcome strong repulsive interaction between ORG and silica, leading to a substantial popula-

tion of permanently immobilized ORG in the silica composite. Recently, the molecular templating effect has been employed to create silica molds of a wide variety of molecules. Bearing similar size and shape of the real molecules, these silica molds have been demonstrated to selectively recognize the real molecules that fit the molds [68, 88–90]. This completely reagentless approach is expected to impact the design and fabrication of sensors used in hostile environments where organic molecules and biomolecules are unlikely to survive, conditions that may be frequently encountered in deep-sea and space explorations.

If molecular templating can exert a moderate effect on the mobility of a small molecule like ORG, its influence on much larger protein molecules would be even more considerable. An intuitive strategy to combat molecular templating is to open up pore dimension by diluting the liquid sol with a suitable solvent before gelation sets in. This approach has been the common thread in numerous protocols developed for the fabrications of active silica sol–gel biocomposite materials since the 1990s. Typically, a target biomolecule dissolved in a stabilizing aqueous buffer is employed to dilute the liquid sol, which upon solidification forms a hydrogel. With a less constricted environment, many biomolecules can function normally to produce very active silica biocomposite materials for biosensor and bioreactor applications [41]. This prompts us to examine how molecular templating in hydrogels differs between the encapsulation of big and small molecules. In our work, the extent of molecular templating was inferred from the mobility of fluorescein (FL) and R6G, representing small molecules that are negatively and positively charged, respectively. In previous sections where fluorophores were encapsulated in silica alcogel samples, molecular templating was found to dominate Coulombic interactions. The study of FL and R6G mobility in hydrogels should reveal if Coulombic interactions would ever become significant in determining mobility, and possibly provide an easily controllable way to manipulate molecular properties inside silica hydrogels. Green fluorescent protein (GFP) was also used to assess the effect of size on molecular templating. Folded into a β -barrel that measures 3 nm in diameter and 4 nm long, GFP represents a big molecule constituted of 238 amino acid residues that has an isoelectric point around pH 6.0. GFP becomes negatively charged at pH 7.0 or above, which should disfavor the adsorption onto a silica pore surface. If molecular templating in hydrogel would become less significant in large molecules, the mobility of GFP would be enhanced.

When FL, R6G, and GFP were trapped inside silica hydrogels at neutral pH, their differences in mobility were clearly discernible in their respective fluorescence images shown in Fig. 17.8. The hydrogel samples studied were made from 1 part of HCl acidified TMOS liquid sol mixed with 10 parts of 10 mM phosphate buffer pH 7.0 doped with FL, R6G, or GFP. In addition to ensuring biocompatibility, the significant amount of aqueous buffer used makes the hydrogel extremely porous to help suppress molecular templating. This is in contrast to dye-doped alcogel samples discussed in previous sections where the silica network is densely packed and thus only very small amount of water remains in the resultant silica

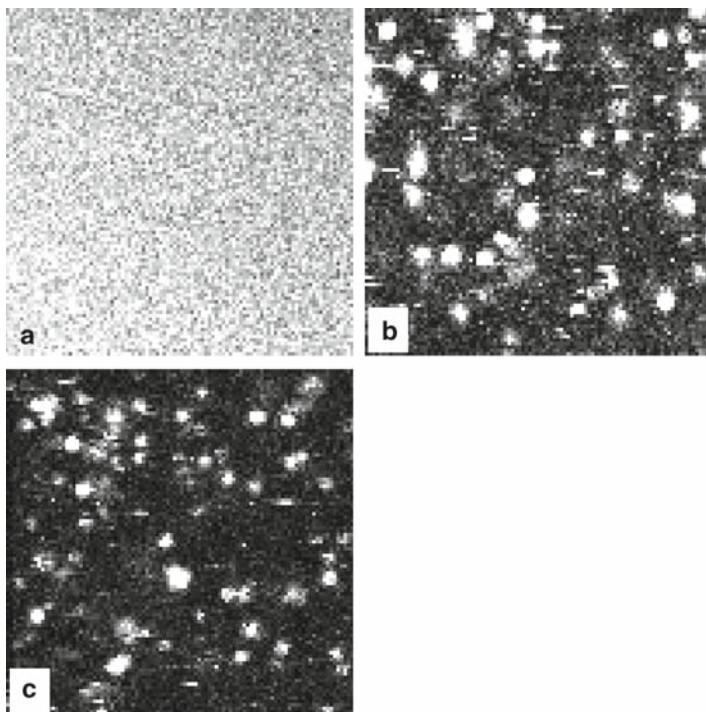


Fig. 17.8 Scanning confocal images of (a) fluorescein, (b) rhodamine 6G, and (c) green fluorescent protein encapsulated in silica hydrogels. All image sizes are $10\ \mu\text{m} \times 10\ \mu\text{m}$. Approximately 12 min were required to raster scan the $100\ \mu\text{m}^2$ area. In the images, each stationary fluorescence spot represents a molecule that remains immobilized during the 12 min scan time

films. The effect of the enhanced porosity in hydrogels is very well reflected by the fluorescence image of negatively charged FL in Fig. 17.8a, in which no discernable fluorescent spot from immobilized FL can be identified. The entire image is characterized by a moderate fluorescence background, which implies that FL molecules diffused freely while the image was recorded, and that molecular templating was completely eliminated in the porous hydrogel network. The same FL molecule would have been immobilized in a denser alcogel network. On the contrary, Coulombic attraction slowed R6G diffusion to a halt inside the same hydrogel network and produced distinct fluorescence spots from immobilized single R6G molecules in Fig. 17.8 b [91]. The completely opposite behavior displayed by FL and R6G clearly demonstrate the full range of Coulombic interactions while molecular templating is absent. Despite a similar molecular structure in FL and R6G, our observations suggest that Coulombic interaction alone can render a molecule diffusing freely like FL or completely immobilized like R6G.

While FL diffusion is slightly hindered in a highly porous silica hydrogel, the same may not translate well to the diffusion of bigger molecules like proteins. At neutral pH, GFP is not expected to be strongly attracted to a silica surface. Nevertheless, the distinctive fluorescence spots shown in Fig. 17.8 c clearly indicate

that the mobility of the hydrogel encapsulated GFP must be severely retarded. This may be purely due to the bigger size of GFP relative to FL such that despite being similarly prepared, the hydrogel does not have sufficient channels that are wide enough to support unhindered diffusion of big molecules. Thus, while the pores and channels in the hydrogel are wide enough for FL diffusion, they are still too small relative to GFP to support its translational diffusion [92, 93]. Attempts to loosen up the silica network further by adding more than 10 parts phosphate buffer to the TMOS sol did not translate to higher GFP mobility. The aqueous sol mixture eventually failed to gel when more than 20 parts of phosphate buffer was used. Another explanation to the apparent immobility of GFP found in hydrogels is that the positively charged domains on a GFP surface can still be attracted toward a silica surface in spite of an overall negative charge. This attraction is expected to impair GFP diffusion, as in the case of R6G shown in Fig. 17.8 b. Finally, there is also a remote possibility that the hydroxyl group of serine, threonine, and tyrosine in GFP might react with silanol during the polymerization reaction while liquid sol was solidifying, thereby forming a covalent linkage to the silica surface and rendering the GFP immobilized.

17.3 Enzyme-Doped Liposomes for Silica Sol–Gel Bio-Encapsulation

All protein-silica interactions considered above can be detrimental to the normal functioning of an encapsulated enzyme. An enzyme that experiences restricted flexibility under microscopic confinement may not be as effective a catalyst as if it were free in an aqueous buffer. Since different enzymes experience protein–silica interactions to different extents, a protocol that is developed for the encapsulation of one enzyme may not work well for others; hence the unpredictable biological activities of silica sol–gel biocomposite materials. If that is the case, then a truly generic approach to active silica sol–gel biocomposite material can be developed only if all protein–silica interactions can be eliminated during the biocomposite formation process. In light of this, we recently devised a new silica biocomposite protocol in which protein–silica interactions are completely ruled out using enzyme-doped liposomes [87]. As illustrated in Fig. 17.9, an enzyme is first trapped inside a liposome, which also serves as a protective coating to prevent the enzyme from being directly in contact with any silane reagent during the sol–gel formation process. This shall prevent the hydroxyl groups in serine, threonine, and tyrosine from reacting with silanol and becoming covalently attached to the silica network. After the aqueous TMOS sol mixture solidifies, the resultant hydrogel is shocked by electrical pulses that are strong enough to shatter the liposome and release the entrapped enzyme. Instead of residing in a silica pore that is comparable to its own molecular dimension, the newly released enzyme will be encased in a cavity that was once occupied by the liposome before it broke. In this case, the liposome replaces the enzyme as a template for pore formation. Thus simply by enclosing an enzyme in large liposomes, any effect of molecular templating on the enzyme is practically eliminated. The much larger silica pore created relative to the size of an

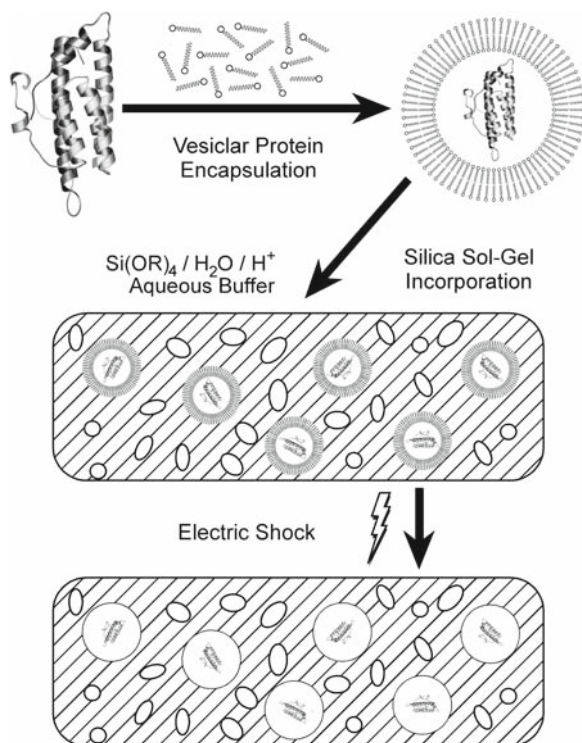


Fig. 17.9 The newly designed silica sol-gel bio-encapsulation protocol, through which molecular templating effect can be eliminated and an encapsulated enzyme can be stored inside silica pores of known dimension

enzyme also ensures that, though trapped, the enzyme has enough room to maneuver without compromising its flexibility, and therefore catalytic activity. An additional benefit of this strategy is that simply by varying the size of the liposome prepared, the resultant silica pore size can be adjusted accordingly. This capability provides an easy yet independent control for optimizing the activity of silica biocomposite materials while allowing one to prepare hydrogels of different porosities that will strike the balance between maximizing substrate diffusion and minimizing enzyme leakage.

The ability of this protocol to yield active silica biocomposite was examined using horseradish peroxidase (HRP) as the encapsulated enzyme. In the presence of luminol and H_2O_2 , HRP will produce a blue chemiluminescence at ~ 430 nm. It has been reported on numerous occasions that HRP can withstand the harsh conditions encountered in a silica sol-gel formation process and that it is capable of retaining a fair amount of activity upon direct encapsulation [94–96]. In this experiment, liposome-protected HRP was encapsulated in a silica hydrogel in the presence of luminol and H_2O_2 to ensure that both substrates were homogeneously distributed throughout the entire hydrogel. Each sample was prepared by adding 1 part acidified TMOS sol to 10 parts phosphate buffer containing a designated mixture of free

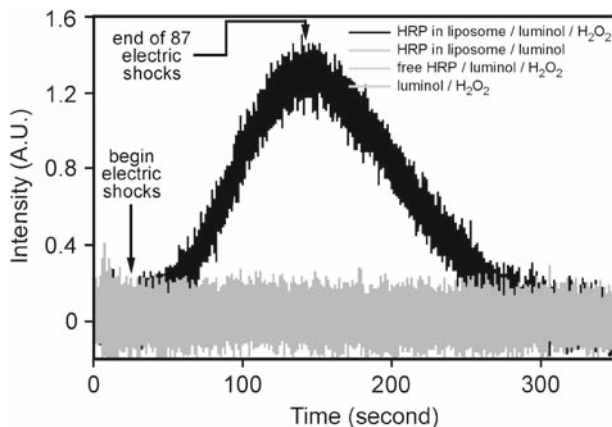


Fig. 17.10 Electric-shock-induced chemiluminescence time traces from different silica hydrogel biocomposites. Since all control samples produce no detectable chemiluminescence, their intensity time traces are all represented by the same gray color. Reproduced with permission from [98]. Copyright 2005 American Chemical Society

HRP, liposome-protected HRP, luminol, and H_2O_2 . To protect HRP, 200 nm liposomes were routinely prepared in accordance with the protocol reported in the literature [97]. Fig. 17.10 compares the time traces of chemiluminescence intensity from different biocomposite hydrogels as electric shocks were being applied. The figure clearly indicates that only the hydrogel that contained liposome-protected HRP, luminol, and H_2O_2 could produce chemiluminescence upon the application of electric shocks.

No chemiluminescence was observed from all control samples where either HRP or one of the substrates was missing. As for free HRP that was not protected by the liposome, it became inactive immediately after the addition of the 1 part liquid TMOS sol to a chemiluminescing mixture containing free HRP, luminol, and H_2O_2 . As a vivid reminder of the hostile environment encountered by proteins during the silica hydrogel fabrication process, Fig. 17.11 illustrates the rapid quenching of HRP chemiluminescence upon adding the liquid TMOS sol.

The chemiluminescence traces in Fig. 17.10 are a clear indication that shocking the hydrogel helps bring the protected HRP and its substrates together, which were initially separated by the liposomes. Electric shocks are known to cause dielectric breakdown and induce temporary nano-pore formation on the surface of a liposome. This would allow luminol and H_2O_2 to reach the protected HRP and produce chemiluminescence. Normally, reversible sealing of the liposomes would have stopped substrate infusion and terminated chemiluminescence [99, 100]. Instead, high voltage and long electric pulses were deliberately used to inflict permanent damage to the liposomes. As a result, the HRP biocomposite was able to maintain chemiluminescence long after the firing of the last electric pulse. Chemiluminescence began to subside when all substrates near the newly released HRP had been consumed and the reaction gradually switched back to diffusion control.

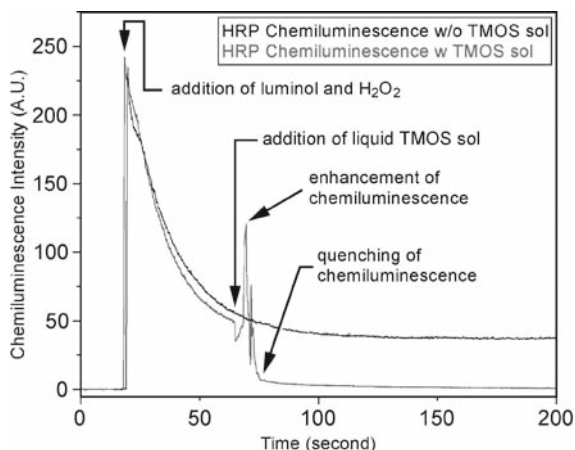


Fig. 17.11 Chemiluminescence from unprotected HRP in a luminol/ H_2O_2 solution with and without the addition of liquid TMOS sol. There is a sudden increase in chemiluminescence intensity upon the addition of the TMOS sol, which is then immediately followed by a rapid quenching to nearly zero chemiluminescence, suggesting that HRP has been inactivated

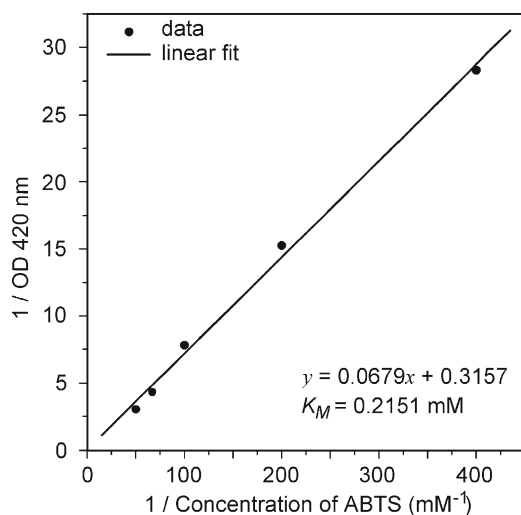


Fig. 17.12 Lineweaver-Burk plot of silica hydrogel encapsulated HRP prepared by the new bio-encapsulation protocol. Activity of HRP was assayed after 87 1.5 kV/20 ms electric shocks were applied to the biocomposite. Since HRP is a two-substrate enzyme, the K_M was measured against 1 mM of H_2O_2

Figure 17.12 illustrates a Lineweaver-Burk plot obtained from an HRP biocomposite prepared according to the new protocol. In this sample, liposome-protected HRP was encapsulated in a hydrogel in the absence of luminol and H_2O_2 . As a result, liquid TMOS sol would no longer be able to inactivate free HRP, which had to be

removed prior to the addition of the liquid sol. Briefly, the buffer that contained both free HRP and liposome-protected HRP was first precipitated with anti-peroxidase, which was then eluted through a protein A column to capture all free HRP. Addition of a TMOS sol to the eluate that mostly contained liposome-protected HRP completed the hydrogel synthesis. After the HRP biocomposite solidified, liposome-protected HRP was freed by high voltage electric shocks and its activity was assayed against the oxidation of azino-bis(3-ethylbenzothiazoline-6-sulfonate) (ABTS) in the presence of H_2O_2 . The oxidized form of ABTS absorbs strongly at 420 nm, which was used to monitor the rate of biocatalysis. The linear fit shown in Fig. 17.12 suggests that similar to others, our HRP biocomposite also conforms to Michaelis-Menten kinetics. The new encapsulation protocol therefore does not affect the catalytic mechanism of HRP in any significant way. However, the slower diffusion permissible in a silica hydrogel is reflected by a larger K_M value.

To determine whether the same protocol is also applicable to the encapsulation of more fragile enzymes, we replaced HRP with firefly luciferase (LUC). Unlike HRP, LUC is an extremely fragile enzyme that is known to denature easily when trapped directly inside a silica hydrogel. As a result, several alternative approaches have been developed to immobilize LUC in silica hydrogel while maintaining its bioactivity. This includes the use of sodium silicate as the silica precursor to eliminate the liberation of alcohol during hydrogel formation [20]. Successful encapsulation of LUC using sugar-modified silica precursor have also been reported [101]. Most recently, biomimetic catalysts have shown some moderate progress in encapsulating active LUC in hydrogels as well [35].

Due to the fragile nature of LUC, we made no attempt to separate free LUC from liposome-protected LUC when preparing LUC silica biocomposite hydrogel. All free LUC would be denatured by the hydrogel-formation process. Hydrogels were made from 1 part TMOS sol and 10 parts phosphate buffer that contained either liposome-protected or free LUC. After gelation, all samples were subjected to multiple electric shocks to release any liposome-protected LUC before assaying their bioluminescence activity. In the presence of oxygen, D-luciferin, and adenosine triphosphate (ATP), LUC oxidizes D-luciferin through an ATP driven process and produces bioluminescence. It is apparent in Fig. 17.13 that we were able to produce an active biocomposite when we employed our new protocol to encapsulate LUC in a TMOS-derived silica hydrogel.

Bioluminescence is clearly discernable in Fig. 17.13 when D-luciferin and adenosine triphosphate (ATP) was added to an active LUC biocomposite where the liposomes had been shattered by the repeated application of electric shocks. Although the retention of bioactivity was not quantified, the burst of bioluminescence is an unmistakable signature of LUC bioactivity, which is well-documented in earlier investigations [102, 103]. As a control experiment where LUC was directly trapped inside a similarly prepared silica hydrogel without the protection by any liposome, however, no bioluminescence was produced upon the addition of D-luciferin and ATP. The fact that both active HRP (robust) and LUC (fragile) enzymes can be encapsulated in silica hydrogels in a similar fashion without the need to develop any elaborated enzyme specific optimization procedure suggests

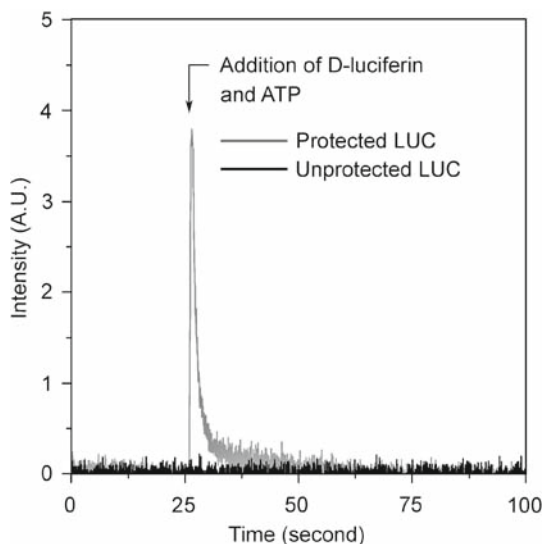


Fig. 17.13 Comparison of firefly luciferase activity in TMOS-derived hydrogels prepared using liposome-protected and unprotected firefly luciferase. Activity of firefly luciferase was assayed after 87 1.5 kV/20 ms electric shocks were applied to both biocomposites

that our protocol may be equally applicable to a wide variety of enzymes. This protocol may provide a powerful platform to transform silica biocomposite into a more competitive technology for biosensor and bioreactor developments.

17.4 Polyelectrolyte Multilayer Silica Sol–Gel Composite Thin Films Sensors

Due to their flexibility in processing, porous silica composite materials have been demonstrated to support a wide range of sensor formats such as monolith, thin film, and fiber coating of very diverse shapes and dimensions. While a dense silica network contributes to high structural stability, it inevitably slows molecular diffusion. The higher the density of a silica network, the more sturdy the biocomposite structure, but the slower the molecular diffusion. Slow diffusion is an undesirable feature in sensor applications since it leads to slow sensor response. As such, silica thin film rather than monolith is the most widely adopted configuration for sensors that aim at delivering fast responses. In a recent attempt of using ORG to construct thin film pH sensors, we identified a response hysteresis caused by impaired diffusion even in ~200 nm thin silica films. ORG in bulk solution responds to pH variation with changes in both intensity and emission spectrum. While the fluorescence intensity of ORG increases with pH, the emission spectrum simultaneously shows a red shift in λ_{max} . Silica thin film pH sensors based on the pH response of ORG

were constructed from an 8.8 wt% SiO_2 TEOS sol solution that contained 1 : 8 : 7 molar ratio of TEOS : ethanol : water and 34 nM ORG. Freshly prepared liquid sol was allowed to age for 16–20 h before it was spun-cast onto a microscope coverglass to make a thin pH sensing film. To investigate the influence of pH on the sensor response, the film-coated coverglass was used to seal one end of a polystyrene tube to make a small sample cuvette that can hold more than 1,000 μL of buffer. In a typical experiment, 1,000 μL of buffer at different pHs was first transferred into the cuvette and the sensing film was allowed to equilibrate with the buffer for a designated period prior to recording an ORG emission spectrum, from which the film's pH response would be evaluated. To examine the time it takes for a sensing film to equilibrate with an external buffer, ORG emission spectra were collected at different equilibration times after the addition of a buffer. To repeat the measurement at a different pH, the old buffer in the cuvette was vacated and a new buffer was added.

We found that the dry to wet transition occurred rapidly and a reasonably steady ORG spectrum was usually obtained within five to ten minutes after buffer addition. Subsequent measurements made over the next two hours revealed little change in ORG emission, indicating that equilibration with the solvent was complete within the first 10 min. As illustrated in the inset in Fig. 17.14, significant response hysteresis was observed when the sensing film was not given enough time to equilibrate with a pH buffer. Similar response hysteresis in rapidly cycled silica sol–gel films has been reported, with the effect diminishing upon repeated use [104]. This hysteresis was attributed to the fraction of dyes that were contained within isolated, slowly equilibrating pores [104, 105]. The delayed response to pH from isolated pores broadens

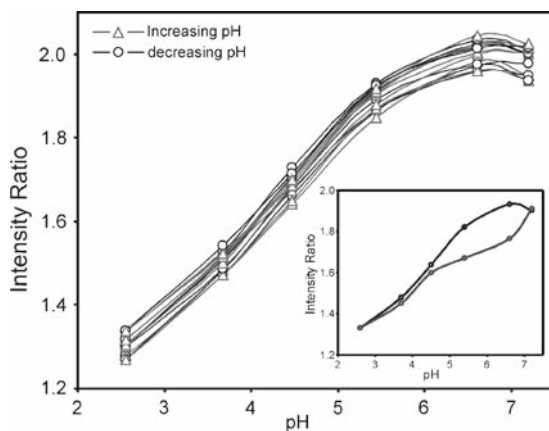


Fig. 17.14 The pH response of a 200-nm thick silica film doped with ORG as the sensor was subjected seven times to pH variation cycles between pH 7.2 and pH 2.6. A 20-min equilibration was allowed every time the sensor was dipped into a new pH buffer. The y-axis reports the shoulder to peak fluorescence intensity ratio of ORG at 524 nm and 554 nm, respectively. Hysteresis is obvious in the inset when there was insufficient time (only 5 min) for the thin film sensor to equilibrate with the external pH buffers

the distribution of local environments in a wet film, altering the emission intensity and changing the spectral shape. It has been shown that the response hysteresis can be largely suppressed by cycling a sensing film repeatedly through a series of buffers. This will gradually shift the pH inside all isolated pores to a steady value and thus reduce the hysteresis to a mere constant pH-insensitive response that contributes to part of the total signal [104]. Alternatively, hysteresis can also be eliminated at the expense of response time if extended equilibration is allowed.

One way to shorten the equilibration time and therefore accelerate sensor response is to use a thinner silica film to construct the sensor. This can be accomplished by adjusting the aging time of a liquid sol before it is drawn or spun into a thin film either by dip-coating or spin-coating, respectively. Since the viscosity of a liquid sol increases with time as the condensation of silanol continues, shortening the aging time should result in a thinner silica film. In practice, however, aging time is never an ideal parameter for controlling film thickness as it is easily affected by the choice of silane precursor, pH of the liquid sol, conditions used for hydrolysis, and the temperature and relative humidity during the long aging hours. In order to afford precision thickness control, preferably down to the nanometer length scale, we recently integrated the polyelectrolyte multilayer technology into the fabrication of thin silica films for sensor development.

First demonstrated by Decher and coworkers in the early 1990s, the layer-by-layer self-assembly deposition soon became a powerful technique to prepare thin polymer films of desirable thickness [106, 107]. On the basis of electrostatic attraction and entropic driving forces, thin layers of oppositely charged polyelectrolytes can be assembled onto a glass surface in a layer-by-layer fashion simply by dipping the glass alternately in the positive and negative polyelectrolyte solutions. In polyelectrolyte multilayers, the film thickness can be precisely controlled by the number of polyelectrolyte layers assembled, which in turn equals the total number of dips used for the multilayer film preparation. As a result of its simplicity, the layer-by-layer approach to thin film fabrication has been rapidly generalized into the deposition of other charged species including organic and inorganic molecules [108–112], biomolecules [113, 114], as well as metallic and inorganic nanoparticles [115–124] to produce new sensors and photonic materials.

In our latest work, we employed polyelectrolyte multilayers as a mechanically stable scaffold to hold together an otherwise fragile silica sol–gel thin film. The strategy to fabricate polyelectrolyte multilayer silica sol–gel composite thin films is summarized in Fig. 17.15. A polyelectrolyte multilayer film is first synthesized according to standard protocols [125, 126]. Then one edge of the porous multilayer film is dipped into a liquid sol to draw the sol into the multilayer scaffold through capillary actions. The mesoscopic porosity inside a multilayer structure ensures that there are plenty of capillary actions, which should allow the liquid sol to travel a long distance up the polyelectrolyte film. After removing it from the liquid sol, the wet film is then left to dry into a multilayer silica composite thin film. In this approach, the film thickness is almost exclusively defined by the thickness of the multilayers, which depends on the number of polyelectrolyte layers deposited. The aging time of the liquid sol becomes irrelevant as viscosity affects capillary actions but not the film thickness. Liquid sol of high viscosity is undesirable here as it impairs capillary actions and limits the traveling distance of the liquid sol up the

multilayers, possibly leading to thicker, and uneven composite films. As a result, freshly prepared liquid sol is recommended in preparing multilayer silica composite thin films.

In our experiment, poly(allylamine hydrochloride) (PAH) and poly(acrylic acid) (PAA) were used respectively as the positive and negative polyelectrolytes to assemble multilayer thin films. Both PAH and PAA are weak polyelectrolytes. Aqueous solutions of PAH and PAA at 0.02 M monomer concentration were adjusted to pH 7.5 and 3.5, respectively, prior to multilayer assembling. Synthesis of multilayer films with different number of bilayers was accomplished by dipping a microscope slide alternately into the PAH and PAA solutions each for 15 minutes, with the slide thoroughly rinsed with 18 M Ω Millipore water and dried with N₂ between consecutive dips. Figure 17.16 illustrates how the thickness of a PAH–PAA multilayer film builds up linearly with the number of bilayers assembled.

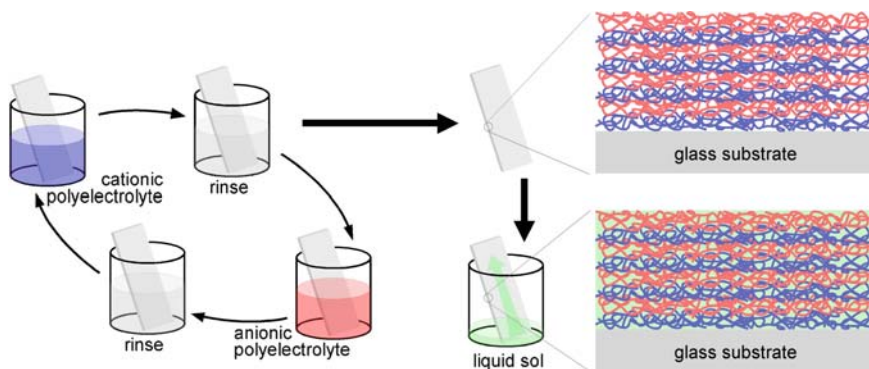


Fig. 17.15 The schematic for polyelectrolyte multilayers silica composite thin film preparation

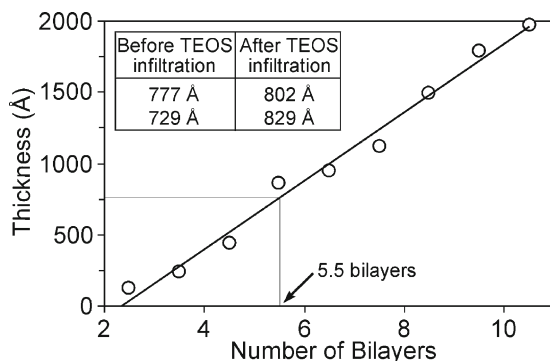


Fig. 17.16 The thickness dependence of a polyelectrolyte multilayer on the number of poly(allylamine hydrochloride) – poly(acrylic acid) (PAH–PAA) bilayers. The table enclosed indicates the change in thickness of a 5.5 bilayer film before and after the infiltration by a liquid TEOS sol

To construct a multilayer silica composite thin film, an acidified TEOS sol was employed to infiltrate the mesoporous structure of a 5.5 bilayer film. The table in Fig. 17.16 indicates that in two separate attempts, there is a moderate increase in the thickness of the composite films relative to the original 5.5 bilayer polyelectrolyte films. Swelling of polyelectrolyte multilayer upon contact with a liquid medium has been reported in numerous occasions [37, 125, 127]. In this case, the absorption of liquid sol probably caused the multilayer film to swell, producing a thicker scaffold for the liquid sol to impregnate. Despite swelling, the thickness of the composite film is still fairly restrained by the original multilayer framework, implying that polyelectrolyte multilayers can be a practical approach to the synthesis of composite thin film sensors with desirable thickness. It is also worth mentioning that, excluding areas near the TEOS dip line, multiple thickness measurements on a composite film parallel to the direction along which the TEOS sol was drawn up yielded a steady value, indicating that the thickness of the composite film was very well maintained by the underlying polyelectrolyte multilayers framework. However, due to an excess of TEOS sol accumulated through direct contact, the film became heavily wedged near the TEOS dip line.

To prepare a multilayer silica composite pH sensor, ORG-doped TEOS sol was used to infiltrate a 5.5 bilayer PAH-PAA film. After drying, the composite sensor was subjected to a series of buffers to evaluate its pH response. The normalized emission spectra of the composite film-encapsulated ORG at different pHs are summarized in Fig. 17.17.

The most striking feature in the figure is the change in spectral shape with external pH displayed by the ORG-based composite sensor. Although not clear in the normalized spectra, the fluorescence intensity of the composite sensor also varied

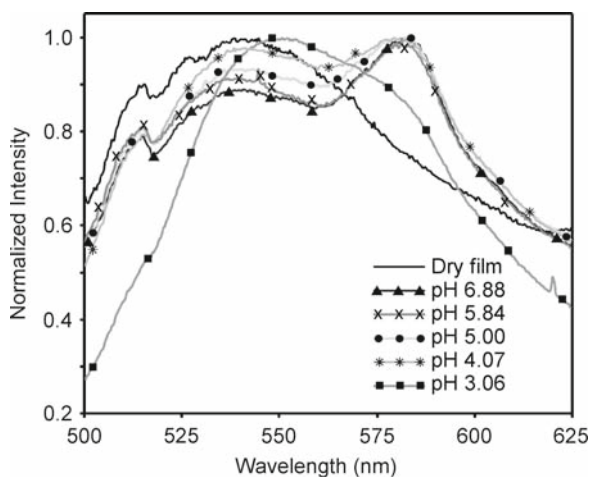


Fig. 17.17 Normalized emission spectra of ORG encapsulated inside a composite film of silica and 5.5 bilayers PAH-PAA polyelectrolyte multilayers at different pHs

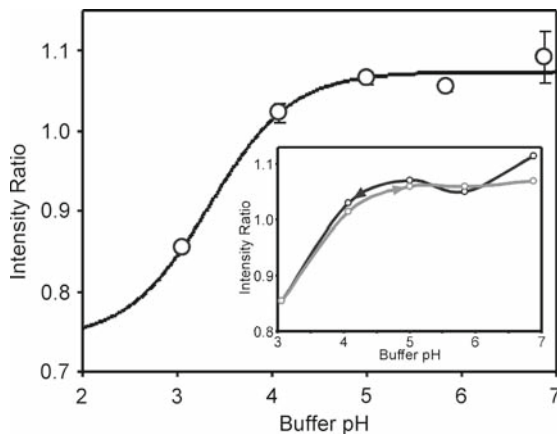


Fig. 17.18 pH response of the polyelectrolyte multilayers silica sol–gel composite thin film that was doped with ORG. Intensity ratios at 584.5 to 543.5 nm are calculated from the spectra in Fig. 17.12. The *solid line* represents a Henderson-Hasselbalch fit to the intensity ratio. The inset indicates a small hysteresis despite a short equilibration time of 2 min was used

steadily with external pH. From the normalized spectra, the fluorescence intensity ratio at 584.5 ± 2.5 nm to 543.5 ± 2.5 nm was employed to monitor the sensor's pH response. It is noteworthy to emphasize that all spectra were measured within the first 5 min after the addition of each pH buffer, with a majority of spectra recorded after less than 2 min of equilibration time. Figure 17.18 illustrates the sensor response to pH cycled from pH 6.88 to 3.06 and back to pH 6.88. Despite a shorter equilibration time, the 5.5 bilayers, 80 nm thick composite sensor displays a response hysteresis that is substantially less than that of the 200 nm thick silica sensor shown in Fig. 17.14. These results are consistent with the assumptions that thinner films respond faster than thicker films and that a polyelectrolyte multilayer silica composite is capable of delivering thin film sensors where the film thickness can be accurately controlled.

17.5 Future Outlook

Relative to organic and inorganic molecules, the trapping of enzymes into a silica sol–gel biocomposite thin film sensor presents additional challenges. First, as of the most popular ways to cast thin films, spin coating is incompatible with the preparation of active silica sol–gel biocomposite films. Most enzymes do not survive the sheer force they encounter during the spin coating process and become denatured, producing biocomposite thin films with little or no biological activity [128]. Second, active silica sol–gel biocomposites are usually prepared in the presence of an aqueous buffer to stabilize an encapsulated enzyme. This generally leads to the formation of hydrogel monoliths that contain a large proportion of aqueous content.

A hydrogel that contains too much water lacks the critical silica mass to build a sturdy framework. Water then becomes essential to maintain the overall hydrogel structure. As a result, the silica hydrogel cracks into pieces and collapses if left to dry by evaporation. Cracking is expected to become a more serious problem in thin film configurations specifically designed to deliver quick sensor responses. A hydrogel thin film by itself is therefore inherently unstable. Evaporation is accelerated by the large surface area available from a thin film, leading the film to shrink, crack, and collapse rapidly. By extending the current study to embedding a fragile silica hydrogel inside a sturdy multilayer framework, we anticipate that our new approach to sensor fabrication will be particularly attractive to the development of thin film hydrogel-based biosensors.

References

1. Brinker CJ and Scherer G. (1989) *Sol-Gel Science, The Physics and Chemistry of Sol-Gel Processing*. San Diego, Academic Press.
2. Dickey FH. (1955) Specific adsorption. *J. Phys. Chem.* 59: 695–707.
3. Johnson P and Whateley TL. (1971) Use of polymerizing silica gel systems for immobilization of trypsin. *J. Coll. Inter. Sci.* 37: 557–563.
4. Braun S, Rappoport S, Zusman R, Avnir D and Ottolenghi M. (1990). Biochemically active sol-gel glasses: the trapping of enzymes. *Mater. Lett.* 10: 1–5.
5. Brennan JD. (1999). Using intrinsic fluorescence to investigate proteins entrapped in sol-gel derived materials. *Appl. Spectrosc.* 53: 106A–121A.
6. Brennan JD, Hartman JS, Ilnicki EI and Rakic M. (1999). Fluorescence and NMR characterization and biomolecule entrapment studies of sol-gel-derived organic-inorganic composite materials formed by sonication of precursors. *Chem. Mater.* 11: 1853–1864.
7. Doody MA, Baker GA, Pandey S and Bright FV. (2000) Affinity and mobility of polyclonal anti-dansyl antibodies sequestered within sol-gel-derived biogels. *Chem. Mater.* 12: 1142–1147.
8. Dunn B, Miller JM, Dave BC, Valentine JS and Zink JJ. (1998). Strategies for encapsulating biomolecules in sol-gel matrices. *Acta Mater.* 46: 737–741.
9. Ellerby LM, Nishida CR, Nishida F, Yamanaka SA, Dunn B, Valentine JS and Zink JJ. (1992). Encapsulation of proteins in transparent porous silicate glasses prepared by the sol-gel method. *Science* 255: 1113–1115.
10. Flora KK and Brennan JD. (2001) Effect of matrix aging on the behavior of human serum albumin entrapped in a tetraethyl orthosilicate-derived glass. *Chem. Mater.* 13: 4170–4179.
11. Gill I, Pastor E and Ballesteros A. (1999) Lipase-silicone biocomposites: Efficient and versatile immobilized biocatalysts. *J. Am. Chem. Soc.* 121: 9487–9496.
12. Keeling-Tucker T, Rakic M, Spong C and Brennan JD. (2000) Controlling the material properties and biological activity of lipase within sol-gel derived bioglasses via organosilane and polymer doping. *Chem. Mater.* 12: 3695–3704.
13. Narang U, Prasad PN, Bright FV, Kumar A, Kumar ND, Malhotra BD, Kamalasanan MN and Chandra S. (1994) A novel protocol to entrap active urease in a tetraethoxysilane-derived sol-gel thin-film architecture. *Chem. Mater.* 6: 1596–1598.
14. Wang R, Narang U, Prasad J and Bright FV. (1993) Affinity of antiluorescein antibodies encapsulated within a transparent sol-gel glass. *Anal. Chem.* 65: 2671–2675.
15. Zheng L, Flora K and Brennan JD. (1998). Improving the performance of a sol-gel-entrapped metal-binding protein by maximizing protein thermal stability before entrapment. *Chem. Mater.* 10: 3974–3983.

16. Zink JI, Valentine JS and Dunn B. (1994). Biomolecular materials based on sol–gel encapsulated proteins. *New J. Chem.* 18: 1109–1115.
17. Avnir D, Braun S, Lev O and Ottolenghi M. (1994) Enzymes and other proteins entrapped in sol–gel materials. *Chem. Mater.* 6: 1605–1614.
18. Ferrer ML, Del Monte F, Levy D. (2002) A novel and simple alcohol-free sol–gel route for encapsulation of labile proteins. *Chem. Mater.* 14: 3619–3621.
19. Gill I. (2001) Bio-doped nanocomposite polymers: Sol–gel bioencapsulates. *Chem. Mater.* 13: 3404–3421.
20. Gill I and Ballesteros A. (1998) Encapsulation of biologicals within silicate, siloxane, and hybrid sol–gel polymers – an efficient and generic approach. *J. Am. Chem. Soc.* 120: 8587–8598.
21. Gill I and Ballesteros A. (2000) Bioencapsulation within synthetic polymers.(Part 1): sol–gel encapsulated biologicals. *Trends Biotechnol* 18: 282–296.
22. Jin W and Brennan JD. (2002) Properties and applications of proteins encapsulated within sol–gel derived materials. *Anal. Chim. Acta* 461: 1–36.
23. Liu DM, Chen IW. (1999) Encapsulation of protein molecules in transparent porous silica matrices via an aqueous colloidal sol–gel process. *Acta Materialia* 47: 4535–4544.
24. Livage J, Coradin T and Roux C. (2001) Encapsulation of biomolecules in silica gels. *J. Phys.: Condens. Matter* 13: R673–R691.
25. Luo TJM, Soong R, Lan E, Dunn B, Montemagno C. (2005) Photo-induced proton gradients and ATP biosynthesis produced by vesicles encapsulated in a silica matrix. *Nat. Mater.* 4: 220–224.
26. Pierre AC. (2004) The sol–gel encapsulation of enzymes. *Biocatal. Biotransform.* 22: 145–170.
27. Reetz MT, Tielmann P, Wiesenhofer W, Konen W and Zonta A. (2003) Second generation sol–gel encapsulated lipases: Robust heterogeneous biocatalysts. *Adv. Synth. Catal.* 345: 717–728.
28. Baker GA, Jordan JD and Bright FV. (1998) Effects of poly(ethylene glycol) doping on the behavior of pyrene, rhodamine 6G, and acrylodan-labelled bovine serum albumin sequestered within tetramethylorthosilane-derived sol–gel-processed composites. *J. Sol Gel Sci. Technol.* 11: 43–54.
29. Chen Q, Kenausis GL and Heller A. (1998) Stability of oxidases immobilized in silica gels. *J. Am. Chem. Soc.* 120: 4582–4585.
30. Brennan JD, Benjamin D, DiBattista E and Gulcev MD. (2003). Using sugar and amino acid additives to stabilize enzymes within sol–gel derived silica. *Chem. Mater.* 15: 737–745.
31. Brook MA, Chen Y, Guo K, Zhang Z and Brennan JD. (2004) Sugar-modified silanes: precursors for silica monoliths. *J. Mater. Chem.* 14: 1469–1479.
32. Chen Y, Zhang Z, Sui XH, Brennan JD and Brook MA. (2005) Reduced shrinkage of sol–gel derived silicas using sugar-based silsesquioxane precursors. *J. Mater. Chem.* 15: 3132–3141.
33. Cruz-Aguado JA, Chen Y, Zhang Z, Brook MA and Brennan JD. (2004) Entrapment of Src protein tyrosine kinase in sugar-modified silica. *Anal. Chem.* 76: 4182–4188.
34. Luckarift HR, Spain JC, Naik RR and Stone MO. (2004) Enzyme immobilization in a biomimetic silica support. *Nat. Biotech.* 22: 211–213.
35. Roth KM, Zhou Y, Yang WJ and Morse DE. (2005) Bifunctional small molecules are biomimetic catalysts for silica synthesis at neutral pH. *J. Am. Chem. Soc.* 127: 325–330.
36. Coradin T, Allouche J, Boissiere M and Livage J. (2006) Sol–gel biopolymer/silica nanocomposites in biotechnology. *Curr. Nanosci.* 2: 219–230.
37. Dubas ST and Schlenoff JB. (2001) Swelling and smoothing of polyelectrolyte multilayers by salt. *Langmuir* 17: 7725–7727.
38. Miao Y and Tan SN. (2001) Amperometric hydrogen peroxide biosensor with silica sol–gel/chitosan film as immobilization matrix. *Anal. Chim. Acta* 437: 87–93.
39. Sanchez C and Lebeau B. (2001) Design and properties of hybrid organic-inorganic nanocomposites for photonics. *MRS Bull.* 26: 377–387.
40. Wei Y, Xu JG, Feng QW, Lin MD, Dong H, Zhang WJ and Wang C. (2001) A novel method for enzyme immobilization: Direct encapsulation of acid phosphatase in nanoporous silica host materials. *J. Nanosci. Nanotechnol.* 1: 83–93.

41. Avnir D, Coradin T, Lev O and Livage J. (2006) Recent bio-applications of sol–gel materials. *J. Mater. Chem.* 16: 1013–1030.
42. Xie XS and Dunn RC. (1994) Probing single molecule dynamics. *Science* 265: 361–364.
43. Funatsu T, Harada Y, Tokunaga M, Saito K and Yanagida T. (1995) Imaging of single fluorescent molecules and individual ATP turnovers by single myosin molecules in aqueous solution. *Nature* 374: 555–559.
44. Tokunaga M, Kitamura K, Saito K, Iwane AH and Yanagida T. (1997) Single molecule imaging of fluorophores and enzymatic reactions achieved by objective-type total internal reflection fluorescence microscopy. *Biochem. Biophys. Res. Commun.* 235: 47–53.
45. Bartko AP and Dickson RM. (1999) Imaging three-dimensional single molecule orientations. *J. Phys. Chem. B* 103: 11237–11241.
46. Bartko AP, Xu KW and Dickson RM. (2002) Three-dimensional single molecule rotational diffusion in glassy state polymer films. *Phys. Rev. Lett.* 89: art. no.–026101.
47. Sick B, Hecht B and Novotny L. (2000) Orientational imaging of single molecules by annular illumination. *Phys. Rev. Lett.* 85: 4482–4485.
48. Bernard J, Fleury L, Talon H and Orrit M. (1993) Photon bunching in the fluorescence from single molecules: a probe for intersystem crossing. *J. Chem. Phys.* 98: 850–859.
49. Moerner WE, Dickson RM and Norris DJ. (1997) Single-molecule nanophotonics in solids. *Mater. Sci. Eng. B* 48: 169–174.
50. Blab GA, Cognet L, Harms GS, Lommerse PHM and Schmidt T. (2001) Simultaneous “dual-color and dual-polarization imaging” as a tool for colocalization and fluorescence resonant energy transfer studies of single molecules. *Biophys. J.* 80. (Annual Meeting Abstracts): 150b.
51. Cognet L, Harms GS, Blab GA, Lommerse PHM and Schmidt T. (2000) Simultaneous dual-color and dual-polarization imaging of single molecules. *Appl. Phys. Lett.* 77: 4052–4054.
52. Maiti S, Haupts U and Webb WW. (1997) Fluorescence correlation spectroscopy – Diagnostics for sparse molecules. *Proc. Natl. Acad. Sci. U.S.A.* 94: 11753–11757.
53. Moore KJ, Turconi S, Ashman S, Ruediger M, Haupts U, Emerick V and Pope AJ. (1999) Single molecule detection technologies in miniaturized high throughput screening: Fluorescence correlation spectroscopy. *J. Biomol. Screen.* 4: 335–353.
54. Forkey JN, Quinlan ME and Goldman YE. (2000) Protein structural dynamics by single-molecule fluorescence polarization. *Prog. Biophys. Mol. Biol.* 74: 1–35.
55. Ha T, Laurence TA, Chemla DS and Weiss S. (1999) Polarization spectroscopy of single fluorescent molecules. *J. Phys. Chem. B* 103: 6839–6850.
56. Dunn RC, Holtom GR, Mets L and Xie XS. (1994) Near-field fluorescence imaging and fluorescence lifetime measurement of light harvesting complexes in intact photosynthetic membranes. *J. Phys. Chem.* 98: 3094–3098.
57. Del Monte F, Ferrer ML, Levy D. (2001) Probing the chemical environment at the porous cage of ormosils through the fluorescence of oxazine 1. *J. Mater. Chem.* 11: 1745–1751.
58. Ferrer ML, Del Monte F. (2003) Study of the adsorption process of sulforhodamine B on the internal surface of porous sol–gel silica glasses through fluorescence means. *Langmuir* 19: 650–653.
59. Ferrer ML, Del Monte F, Levy D. (2001) Microviscosities at the porous cage of silica gel-glasses and ormosils through fluorescence anisotropy. *J. Phys. Chem. B* 105: 11076–11080.
60. Ha T, Glass J, Enderle T, Chemla DS and Weiss S. (1998) Hindered rotational diffusion and rotational jumps of single molecules. *Phys. Rev. Lett.* 80: 2093–2096.
61. Schaffer J, Volkmer A, Eggeling C, Subramaniam V, Striker G and Seidel CAM. (1999) Identification of single molecules in aqueous solution by time-resolved fluorescence anisotropy. *J. Phys. Chem. A* 103: 331–336.
62. Sharma J, Tleugabulova D, Czardybon W, Brennan JD. (2006) Two-site ionic labelling with pyranine: Implications for structural dynamics studies of polymers and polypeptides by time-resolved fluorescence anisotropy. *J. Am. Chem. Soc.* 128: 5496–5505.
63. Tleugabulova D, Zhang Z, Chen Y, Brook MA, Brennan JD. (2004) Fluorescence anisotropy in studies of solute interactions with covalently modified colloidal silica nanoparticles. *Langmuir* 20: 848–854.

64. Nie SM and Emery SR. (1997) Probing single molecules and single nanoparticles by surface-enhanced Raman scattering. *Science* 275: 1102–1106.
65. Tamarat P, Maali A, Lounis B and Orrit M. (2000) Ten years of single-molecule spectroscopy. *J. Phys. Chem.* 104: 1–16.
66. Bardo AM, Collinson MM and Higgins DA. (2001) Nanoscale properties and matrix-dopant interactions in dye-doped organically modified silicate thin films. *Chem. Mater.* 13: 2713–2721.
67. Viteri CR, Gilliland JW and Yip WT. (2003) Probing the dynamic guest-host interactions in sol–gel films using single molecule spectroscopy. *J. Am. Chem. Soc.* 125: 1980–1987.
68. Graham AL, Carlson CA and Edmiston PL. (2002) Development and characterization of molecularly imprinted sol–gel materials for the selective detection of DDT. *Anal. Chem.* 74: 458–467.
69. Avnir D, Levy D and Reisfeld R. (1984) The nature of the silica cage as reflected by spectral changes and enhanced photostability of trapped rhodamine 6G. *J. Phys. Chem.* 88: 5956–5959.
70. Park GA. (1965) The isoelectric points of solid oxides, solid hydroxides, and aqueous hydroxo complex systems. *Chem. Rev.* 65: 177–198.
71. Gilliland JW, Yokoyama K and Yip WT. (2004) Effect of coulombic interactions on rotational mobility of guests in sol–gel silicate thin films. *Chem. Mater.* 16: 3949–3954.
72. El Baraka M, Deumie M, Viallet P and Lampidis TJ. (1991) Fluorescence properties and partitioning behavior of esterified and unesterified rhodamines. *J. Photochem. Photobiol. A-Chem.* 62: 195–216.
73. Fireman-Shoresh S, Avnir D and Marx S. (2003) General method for chiral imprinting of sol–gel thin films exhibiting enantioselectivity. *Chem. Mater.* 15: 3607–3613.
74. Katz A and Davis ME. (2000) Molecular imprinting of bulk, microporous silica. *Nature* 403: 286–289.
75. Nassif N, Roux C, Coradin T, Rager MN, Bouvet OMM and Livage J. (2003) A sol–gel matrix to preserve the viability of encapsulated bacteria. *J. Mater. Chem.* 13: 203–208.
76. Heller J and Heller A. (1998) Loss of activity or gain in stability of oxidases upon their immobilization in hydrated silica: Significance of the electrostatic interactions of surface arginine residues at the entrances of the reaction channels. *J. Am. Chem. Soc.* 120: 4586–4590.
77. Rottman C, Grader G and Avnir D. (2001) Polarities of sol–gel-derived ormosils and of their interfaces with solvents. *Chem. Mater.* 13: 3631–3634.
78. Seddon AB and Ou DL. (1998) CdSe quantum dot doped amine-functionalized Ormosils. *J. Sol–Gel Sci. Technol.* 13: 623–628.
79. Kadnikova EN and Kostic NM. (2002) Oxidation of ABTS by hydrogen peroxide catalyzed by horseradish peroxidase encapsulated into sol–gel glass. Effects of glass matrix on reactivity. *J. Mol. Catal. B-Enzym.* 18: 39–48.
80. Kauffmann C and Mandelbaum RT. (1998) Entrapment of atrazine chlorohydrolase in sol–gel glass matrix. *J. Biotech.* 62: 169–176.
81. Reetz MT. (1997) Entrapment of biocatalysts in hydrophobic sol–gel materials for use in organic chemistry. *Adv. Mater.* 9: 943–954.
82. Reetz MT, Zonta A and Simpelkamp J. (1995) Efficient heterogeneous biocatalysts by entrapment of lipases in hydrophobic sol–gel materials. *Angew. Chem.-Int. Edit. Engl.* 34: 301–303.
83. Kasnavia T, Vu D and Sabatini DA. (1999) Fluorescent dye and media properties affecting sorption and tracer selection. *Ground Water* 37: 376–381.
84. Sabatini DA. (2000) Sorption and intraparticle diffusion of fluorescent dyes with consolidated aquifer media. *Ground Water* 38: 651–656.
85. Gilliland JW, Yokoyama K and Yip WT. (2005) Solvent effect on mobility and photostability of organic dyes embedded inside silica sol–gel thin films. *Chem. Mater.* 17: 6702–6712.
86. Li Q, Weng SF, Wu JG and Zhou NF. (1998) Comparative study on structure of solubilized water in reversed micelles. I. FT-IR spectroscopic evidence of water/AOT/n-heptane and water/NaDEHP/n-heptane systems. *J. Phys. Chem. B* 102: 3168–3174.
87. Li Y and Yip WT. (2005) Liposomes as protective capsules for active silica sol–gel biocomposite synthesis. *J. Am. Chem. Soc.* 127: 12756–12757.

88. Carlson CA, Lloyd JA, Dean SL, Walker NR and Edmiston PL. (2006) Sensor for fluorene based on the incorporation of an environmentally sensitive fluorophore proximal to a molecularly imprinted binding site. *Anal. Chem.* 78: 3537–3542.
89. Marx S, Zaltsman A, Turyan I and Mandler D. (2004) Parathion sensor based on molecularly imprinted sol–gel films. *Anal. Chem.* 76: 120–126.
90. Tao ZY, Tehan EC, Bukowski RM, Tang Y, Shughart EL, Holthoff WG, Cartwright AN, Titus AH and Bright FV. (2006) Templated xerogels as platforms for biomolecule-less biomolecule sensors. *Anal. Chim. Acta* 564: 59–65.
91. Narang U, Wang R, Prasad PN and Bright FV. (1994) Effects of aging on the dynamics of rhodamine-6 g in tetramethyl orthosilicate-derived sol–gels. *J. Phys. Chem.* 98: 17–22.
92. Chirico G, Cannone F, Beretta S, Diaspro A, Campanini B, Bettati S, Ruotolo R and Mozzarelli A. (2002) Dynamics of green fluorescent protein mutant2 in solution, on spin-coated glasses, and encapsulated in wet silica gels. *Protein Sci.* 11: 1152–1161.
93. Gottfried DS, Kagan A, Hoffman BM and Friedman JM. (1999) Impeded rotation of a protein in a sol–gel matrix. *J. Phys. Chem. B* 103: 2803–2807.
94. Bhatia RB, Brinker CJ, Gupta AK and Singh AK. (2000) Aqueous sol–gel process for protein encapsulation. *Chem. Mater.* 12: 2434–2441.
95. Lloyd CR and Eyring EM. (2000) Protecting heme enzyme peroxidase activity from H₂O₂ inactivation by sol–gel encapsulation. *Langmuir* 16: 9092–9094.
96. Smith K, Silvernail NJ, Rodgers KR, Elgren TE, Castro M and Parker RM. (2002) Sol–gel encapsulated horseradish peroxidase: A catalytic material for peroxidation. *J. Am. Chem. Soc.* 124: 4247–4252.
97. Nguyen T, McNamara KP and Rosenzweig Z. (1999) Optochemical sensing by immobilizing fluorophore-encapsulating liposomes in sol–gel thin films. *Anal. Chim. Acta* 400: 45–54.
98. Martinez Y, Retuert J, Yazdani-Pedram M and Colfen H. (2004) Hybrid ternary organic-inorganic films based on interpolymer complexes and silica. *Polymer* 45: 3257–3265.
99. Kinoshita K, Hibino M, Itoh H, Shigemori M, Hirano K, Kirino Y and Hayakawa T. (1992) Events of Membrane Electroporation Visualized on a Time Scale from Microsecond to Seconds. *Guide to Electroporation and Electrofusion*. Eds: Chang DC, Chassy BM, Saunders JA and Sowers EE. San Diego, Academic Press: 29–46.
100. Tsong TY. (1991) Electroporation of cell-membranes. *Biophys. J.* 60: 297–306.
101. Cruz-Aguado JA, Chen Y, Zhang Z, Elowe NH, Brook MA and Brennan JD. (2004) Ultrasensitive ATP detection using firefly luciferase entrapped in sugar-modified sol–gel-derived silica. *J. Am. Chem. Soc.* 126: 6878–6879.
102. DeLuca M and McElroy WD. (1974) Kinetics of the firefly luciferase catalyzed reactions. *Biochemistry* 13: 921–925.
103. McElroy WD, Seliger HH and White EH. (1969) Mechanism of bioluminescence, chemiluminescence and enzyme function in the oxidation of firefly luciferin. *Photochem. Photobiol.* 10: 153–170.
104. Yang L and Saavedra SS. (1995) Chemical sensing using sol–gel derived planar wave-guides and indicator phases. *Anal. Chem.* 67: 1307–1314.
105. Fu Y, Collinson MM and Higgins DA. (2004) Single-molecule spectroscopy studies of microenvironmental acidity in silicate thin films. *J. Am. Chem. Soc.* 126: 13838–13844.
106. Decher G, Hong JD and Schmitt J. (1992) Buildup of ultrathin multilayer films by a self-assembly process: III. Consecutively alternating adsorption of anionic and cationic polyelectrolytes on charged surfaces. *Thin Solid Films* 210–211: 831–835.
107. Decher G and Schmitt J. (1992) Fine-tuning of the film thickness of ultrathin multilayer films composed of consecutively alternating layers of anionic and cationic polyelectrolytes. *Prog. Colloid Polym. Sci.* 89: 160–164.
108. Ariga K, Lvov Y and Kunitake T. (1997). Assembling alternate dye-polyion molecular films by electrostatic layer-by-layer adsorption. *J. Am. Chem. Soc.* 119: 2224–2231.
109. Cooper TM, Campbell AL and Crane RL. (1995) Formation of polypeptide-dye multilayers by an electrostatic self-assembly technique. *Langmuir* 11: 2713–2718.

110. He JA, Mosurkal R, Samuelson LA, Li L and Kumar J. (2003) Dye-sensitized solar cell fabricated by electrostatic layer-by-layer assembly of amphoteric TiO_2 nanoparticles. *Langmuir* 19: 2169–2174.
111. Jaiswal A, Collins J, Agricole B, Delhaes P and Ravaine S. (2003) Layer-by-layer self-assembly of Prussian blue colloids. *J. Colloid Interface Sci.* 261: 330–335.
112. Place I, Penner TL, McBranch DW and Whitten DG. (2003) Layered nanocomposites of aggregated dyes and inorganic scaffolding. *J. Phys. Chem. A* 107: 3169–3177.
113. Szyk L, Schaaf P, Gergely C, Voegel JC and Tinland B. (2001) Lateral mobility of proteins adsorbed on or embedded in polyelectrolyte multilayers. *Langmuir* 17: 6248–6253.
114. Szyk L, Schwinte P, Voegel JC, Schaaf P and Tinland B. (2002) Dynamical behavior of human serum albumin adsorbed on or embedded in polyelectrolyte multilayers. *J. Phys. Chem. B* 106: 6049–6055.
115. Ariga K, Lvov Y, Ichinose I and Kunitake T. (1999) Ultrathin films of inorganic materials. (SiO_2 nanoparticle, montmorillonite microplate, and molybdenum oxide) prepared by alternate layer-by-layer assembly with organic polyions. *Appl. Clay Sci.* 15: 137–152.
116. Ariga K, Lvov Y, Onda M, Ichinose I and Kunitake T. (1997) Alternately assembled ultrathin film of silica nanoparticles and linear polycations. *Chem. Lett.* 125–126.
117. Boal AK, Galow TH, Ilhan F and Rotello VM. (2001). Binary and ternary polymer-mediated “bricks and mortar” self- assembly of gold and silica nanoparticles. *Adv. Funct. Mater.* 11: 461–465.
118. Bogdanovic G, Sennerfors T, Zhmud B and Tiberg F. (2002). Formation and structure of polyelectrolyte and nanoparticle multilayers: Effect of particle characteristics. *J. Colloid Interface Sci.* 255: 44–51.
119. Evans CR, Spurlin TA and Frey BL. (2002). In situ FT-IR measurements of competitive vapor adsorption into porous thin films containing silica nanoparticles. *Anal. Chem.* 74: 1157–1164.
120. Goldenberg LM, Jung BD, Wagner J, Stumpe J, Paulke BR and Gornitz E. (2003) Preparation of ordered arrays of layer-by-layer modified latex particles. *Langmuir* 19: 205–207.
121. Lvov Y, Ariga K, Onda M, Ichinose I and Kunitake T. (1997). Alternate assembly of ordered multilayers of SiO_2 and other nanoparticles and polyions. *Langmuir.* 13: 6195–6203.
122. Lvov YM, Rusling JF, Thomsen DL, Papadimitrakopoulos F, Kawakami T and Kunitake T. (1998) High-speed multilayer film assembly by alternate adsorption of silica nanoparticles and linear polycation. *Chem. Comm.* 1229–1230.
123. Sennerfors T, Bogdanovic G and Tiberg F. (2002). Formation, chemical composition, and structure of polyelectrolyte-nanoparticle multilayer films. *Langmuir* 18: 6410–6415.
124. Zhang JH, Bai LT, Zhang K, Cui ZC, Zhang G and Yang B. (2003). A novel method for the layer-by-layer assembly of metal nanoparticles transported by polymer microspheres. *J. Mater. Chem.* 13: 514–517.
125. Hiller J and Rubner MF. (2003). Reversible molecular memory and pH-switchable swelling transitions in polyelectrolyte multilayers. *Macromolecules* 36: 4078–4083.
126. Shiratori SS and Rubner MF. (2000). pH-dependent thickness behavior of sequentially adsorbed layers of weak polyelectrolytes. *Macromolecules* 33: 4213–4219.
127. Kügler R, Schmitt J and Knoll W. (2002). The swelling behavior of polyelectrolyte multilayers in air of different relative humidity and in water. *Macromol. Chem. Phys.* 203: 413–419.
128. Narang U, Prasad PN, Bright FV, Ramanathan K, Kumar ND, Malhotra BD, Kamalasanan MN, and Chandra S. (1994) Glucose biosensor based on a sol–gel-derived platform. *Anal. Chem.* 66: 3139–3144.

Index

A

- AAO. *See* Anodic alumina template; Anodic aluminum oxide
- Abel, A. P., 713
- Abraham, A., 213
- Abrasion resistant coatings and corrosion, 444–446, 591
- Acetylcholine esterase (AChE), 717
- ACPA. *See* 4,4'-Azobis(4-cyanopentanoic acid)
- ACPC. *See* 4,4'-Azobis(4-cyanopentanoic chloride)
- Adenosine triphosphate (ATP), 809
- Adjacent *m*-modes, 691
- Aerogels, 135–136. *See also* Silica-based porous materials
- AFM. *See* Atomic force microscopy
- AFM image
 BDK-doped hybriimer films photolocking of, 607
- AFM surface roughness image, 636
- Agostiano, A., 340
- Ahn, J. H., 247
- AIBN. *See* 2,2'-Azobisisobutyronitrile
- Air Mass 1.5 Global, 328
- ALD. *See* Atomic layer deposition
- Alivisatos, A. P., 329, 340, 743
- AlkoxySilane endcapped oligomer, 8, 41
- Amato, G., 264
- Amberg-Schwab, S., 440, 443
- Aminepropyltriethoxysilane, 507
- Amino groups grafting onto silica nanoparticles, 94–95. *See also* Polymers grafting onto nanoparticle surfaces, in solvent-free dry-system
- 3-Aminopropyltrimethoxysilane (APTS), 745
- Amorphous hybrid synthesis, strategies for, 510
- Anodic alumina template, 359
- Anodic aluminum oxide, 361
- Anomalous SAXS, 199
- Antiferromagnetism, definition of, 454.
 See also Magnetism
- Anti-Stokes photoluminescence, 676
- Apatite cements tetracalcium phosphate (TTCP), 767
- Apatite-forming ability bioactive materials, 770
- APFO-3. *See* Poly(2,7-(9,9-dioctyl-fluorene)-alt-5,5-(4',7'-di-2-thienyl-2,'1',3'-benzothiadiazole))
- APTES. *See* Aminepropyltriethoxysilane
- APTES-formic acid hybrid, 540
- Argon fluoride (ArF), 385
- Aryl amide-bridged ladder-like polymethylsiloxane, structure of, 527
- ASAXS. *See* Anomalous SAXS
- ASO. *See* AlkoxySilane endcapped Oligomer
- ASPL. *See* Anti-Stokes photoluminescence
- Assemble monolayer protected gold nanoclusters, 255
- Assink, R. A., 11
- ATES. *See* (3-Aminopropyl)triethoxysilane
- Atomic force microscopy, 10, 347, 407
- Atomic layer deposition, 429
- Atomic nuclei, 727
- Atomic orbitals method, linear combination of, 659
- Atom-transfer radical polymerization, 89, 256
- ATRP. *See* Atom-transfer radical polymerization
- AuMPCs. *See* Assemble monolayer protected gold nanoclusters
- Au-NP-reconstituted GOx electrode, assembly of, 716
- Autograft, 766
- Auzel, F., 556, 557

- Avnir, D., 540
 Azimuthal quantum numbers, 660
 Azobenzene group
 azo-hybrimer
 synthesis of, 618
 photo-isomerization of
 polarized light, 618
 4,4'-Azobis(4-cyanopentanoic acid), 119
 4,4'-Azobis(4-cyanopentanoic chloride), 100
 2,2'-Azobisisobutyronitrile, 113, 114
 Azochromophores
 trans-cis isomerization of, 606
 Azo-hybrimer films
 sub-wavelength resolution, 619
 Azo-polymers, 584, 617
- B**
- Bai, Y., 238
 Barix™ technology, 429
 Basic benzyl dimethyl amine, 12
 BaTiO₃/polyvinylidene fluoride, 242
 Battery, ionic diffusion processes in, 290
 Bauer, C., 341
 BDK. *See* Benzyl dimethyl ketal
 BDK-doped hybrimer films, UV exposure, 605
 BDMA. *See* Basic benzyl dimethyl amine
 Bean, C., 457
 Beck Tan, N. C., 70
 Becquerel, E., 321
 Beek, W. J. E., 340, 345, 368
 Bein, T., 148
 Bellezza, F., 746
 Benzoyl peroxide, 113, 114
 Benzyl dimethyl ketal, 608, 630
 Biaxially oriented polypropylene, 440
 Bicontinuous phase morphology
 model, 29–31
 Bilayer resist system, in fullerene
 nanocomposite resists, 404–409
 Bimodal anticancer functionality, 741
 Bimodal mesoporous structure (BMS), 747
 Binary photo-mask, 610
 Binnemans, K., 547
 Bioactive bone cements
 calcium silicate
 cements, compositions of, 780
 methyl methacrylate (MMA) liquid, 779
 PMMA powder, 780
 poly(methyl methacrylate) (PMMA)
 powder, 779
 Si–OH and Ca²⁺ organic modification
 of, 779
- Bioactive ceramics
 apatite cements, 767
 apatite formation
 simulated body fluid (SBF), 769
 bone-bonding mechanism, 766
 ceramics bond, 768
 TCP ceramics exhibit bioactivity, 768
 glass-ceramic A-W, 767
 hydroxyapatite, 767
 Bioactive chitin-based hybrids
 chemical structure, 777
 GPS, compositions, 777
 GPS, SEM pictures of surfaces, 778
 GPS, TF–XRD patterns of
 surfaces, 778
 sample CaO, EDX spectra, 779
 Bioactive organic–inorganic composites,
 design, 772
 Bioactive organic–inorganic hybrids
 metal hydroxides
 poly(vinyl alcohol) (PVA), 783
 PVA-based hybrids, compositions, 783
 self-assembled monolayers, 782
 sol–gel process, design of
 apatite formation, mechanism, 771
 synthesis of, 772
 Bioactive organic–inorganic hybrids synthesis
 from MPS and HEMA
 in ethanol, 773
 hydrophilicity and biological affinity, 772
 NO, tensile test for, 773
 polymerization, 774
 SEM pictures, 774
 silanol groups, 774
 stress-strain curves for, 773
 TF–XRD patterns, 774
 Bioactive starch-based hybrids
 GPS–starch hybrids, SEM pictures, 776
 GPS–starch hybrids, stress-strain curves, 776
 SBF, SEM pictures, 775
 starch-based materials, 775
 Biocatalysis
 chemical processes, 741
 chemical transformations, 742
 enzymes, 742
 Bioglass, 766
 Bioluminescence, 705
 Biomimetic applications, membrane fluidity,
 733
 Bipolar junction transistors, 232
 BJTs. *See* Bipolar junction transistors
 Blanc, D., 622, 624
 Block copolymer micelles, 738

- BOPP. *See* Biaxially oriented polypropylene
- BPO. *See* Benzoyl peroxide
- Brennan, J. D., 155, 792, 793
- Brick, C. M., 266
- Bridged polysilsesquioxanes materials.
See also Hybrid porous materials
with hierarchical porosity, 164–165
porous silsesquioxanes by sol-gel
processing, 158–160
templated bridged silsesquioxanes,
160–164
- Brill, A., 539, 540, 550
- Broers, A. N., 387
- Brownian losses, 740
- BSA. *See* 4,4′-[1,3 phenylenebis
(1-methylidene)] bis(aniline)
- BT/PVDF. *See* BaTiO₃/polyvinylidene
fluoride
- Buckle, P. E., 713
- Bulk-heterojunction
concept, 299
photovoltaic devices, 324
solar cell, 300, 302–303
- Burrows, P. E., 429
- C**
- Cadmium selenide (CdSe), 329
- Cadmium telluride, 302, 332
- Calcium test method
evolution, 433
importance, 434–435
permeation, 432
- Carmichael A.J., 113
- Capacitors
applications, 234
importance, 292
- Carbon nanotubes (CNT), 254, 297, 715
and conducting polymer, nanocomposites,
297–298
- Carbon nuclear magnetic resonance, 412
- Carbon resist, definition, 387
- Carcia, P. F., 429, 434
- Carter, S. A., 349, 356
- Casalboni, M., 565
- Cavity-quantum electrodynamics (QED), 659
- C₆₀-derivative nanocomposite resists
chemical amplification system, 420–422
phenylazafullerenes, 410–414
resist characteristics, 414–419
synthesis of, 409–410
- CdSe and CdTe nanoparticles, 329–333. *See also* Nanoparticle-polymer hybrid
solar cells
- CdS nanoparticles, preparation, 200–206.
See also Hybrid organic-inorganic
nanocomposites
- CdTe. *See* Cadmium telluride
- CdTe nanocrystals, 650
- CdTe NCs monolayer
longitudinal optical (LO) phonon mode,
674
Raman signal, 674
- CdTe NCs, water
room temperature absorption and PL
spectra, 677
- Cements, surfaces of
SEM pictures of, 781
TF-XRD patterns of, 781
- Ceramer, synthesis, 174–175
- Ceramic magnetic materials. *See* Ferrites
- Ceramic method (CM), for magnetic
nanocomposites preparation,
460–461. *See also* Organic/
inorganic magnetic nanocompos-
ites, preparation methods for
- Chantham, H., 426
- Chapin, D. M., 321
- Chashechnikova, I., 274
- Chemical amplification system, in C₆₀-
derivative nanocomposite resists,
420–422
- Chemical mechanical polishing, 252
- Chemical shift anisotropy, 214
- Chemical vapor deposition, 249, 630
- Chen, Q., 772
- Chen, W. X., 245
- Che, S., 154
- Chiteme, C., 241
- Chow, G. M., 476
- Class I hybrids, synthesis, 510. *See also*
Hybrids incorporating functional
groups, synthesis of
- Class II hybrids, synthesis, 510–515. *See also*
Hybrids incorporating functional
groups, synthesis of
- CMP. *See* Chemical mechanical polishing
- C₆₀-NEO₃, synthesis, 412–413
- ¹³C-NMR. *See* Carbon nuclear magnetic
resonance
- CNs. *See* Carbon nanotubes
- CNT-based biocomposite electrodes, 721
- CNT-coated electrode transducers,
721–723
- CNT-derived amplification processes
analytical protocol, schematic
representation of, 723
- CNTs. *See* Carbon nanotubes

- Colloidal semiconductor nanocrystals, optical property, 333
- Commission Internationale d'Éclairage (CIE), 508
- Composite sensor, ORG, emission spectra, 814
- Conducting organic polymers, 254, 290, 296, 298
 application of, 306
 hybrid nanocomposite materials and, 293–294
 in ss-DSSC, 306
- Conducting polymers, 323–324
 and CNs, nanocomposites, 297–298
 definition, 482–483
 electrical conductivity and, 482–483
 and POMs, nanocomposites, 295–297
- Confocal imaging technique, 658
- Confocal scanning polarization microscope, schematic, 657
- Conjugated polymers
 blending nanoparticles and, 326
 metal oxide networks and
 in situ blends on TiO₂, 365–367
 in situ blends on ZnO, 367–371
 nanoporous semiconductors and, 355–358
 and nanostructured inorganic electrodes filling in, 326–327
- COPs. *See* Conducting organic polymers
- Corrosion and abrasion resistant coatings, 444–446
- Coumarin 343 (C343), 709
- Coupled spherical microcavities
 with semiconductor nanocrystals
 confined photon states, modification, 680–681
 photonic molecule, 679
 photonic molecules, confined optical modes in, 681–683
 spectral spacing, magnitude, 685
 spherical microcavities, optical modes in, 683
- Cowpea chlorotic mottle virus (CCMV), 728
- Crivello, J. V., 60
- CRL isoenzymes, immobilization, 746
- CSA. *See* Chemical shift anisotropy
- CuInS₂ and CuInSe₂ nanoparticles, 338
- CVD. *See* Chemical vapor deposition
- Cylindrical Bessel functions, 662
- D**
- Dang, Z. M., 240
- Darracq, B., 625
- Das, D., 240
- da Silva Sobrinho, A. S., 427
- Davies, W. E. A., 30
- Davis, S. A., 518
- DBR. *See* Distributed Bragg reflector
- DBTDL. *See* Dibutyltin dilaurate
- DD. *See* Dipolar decoupling
- DDM. *See* Diaminodiphenylmethane
- DDS. *See* Diaminodiphenyl sulfone
- Decher, G., 812
- Deoxyribonucleic acid (DNA), 743
- DES. *See* Dielectric spectroscopy
- DGEBA. *See* Diglycidyl ether of Bisphenol A
- Diamagnetism, definition, 453.
See also Magnetism
- Diaminodiphenylmethane, 6
- Diaminodiphenyl sulfone, 6
- Dibutyltin dilaurate, 12
- Dielectric spectroscopy, 9
- Differential scanning calorimetry, 8, 466
- Differential thermal analysis, 461
- Diffraction gratings
 AFM/CCD images, 627–628
 AFM 3D image, 623
 diffraction efficiency, 622
 Fraunhofer diffraction pattern, 623
 holographic interference, 624
 homogeneous surface structures, 628
 hybrimer films, 624
 imprinting of, 625
 laser direct writing, 622
 light impinges, 621
 micro-optical systems, 624
 optical micrographs of, 626, 628
 photomask, 622
 photosensitive hybrimer, 625
 photosensitivity mechanisms, 638
 postbaking temperatures, 629
- Digital signal processors, 232
- Diglycidyl ether of Bisphenol A, 6
- DiIC₁₂ molecules, 798
- DiI molecules, 797
- Dimethyldiethoxysilane, 184
- Dimethyl sulfoxide, 119
- Diphenyldiazomethane, synthesis, 413
- Dipolar decoupling, 220
- Direct laser writing, 620
- Directly photo-fabricated single microlens, 635
- Direct photo-fabrication
 of micro-optical elements
 diffraction gratings (*see* Diffraction gratings)
 microelectronic technology, 620
 microlens arrays, 633–637

- optical waveguides, 629–633
 - phase-mask illumination, 620
 - refractive index modulation, 620
 - Disperse Red 1, 618
 - Distorted-wave Born approximation, 212
 - Distributed Bragg reflector, 402
 - Distributed feedback (DFB) lasers, 402
 - Dithienylethenes, photochromic molecules, 619
 - Djurišić, A.B., 359
 - DLS. *See* Dynamic light scattering
 - DLW. *See* Direct laser writing
 - DMA. *See* Dynamic mechanical analysis
 - DMDES. *See* Dimethyldiethoxysilane
 - DMSO. *See* Dimethyl sulfoxide
 - DNA hybridization assays, schematic illustration, 708
 - do Nascimento, G. M., 222
 - DR1. *See* Disperse Red 1
 - DRAMs. *See* Dynamic random access memories
 - Drug delivery system, 731
 - hybrid nanocapsules as vehicles for cerasome, 734
 - gene engineering, 733
 - hollow mesoporous silica (HMS) spheres, 737
 - lipid bilayer vesicles, 733
 - liposomes, TEM images, 734
 - mesoporous silica materials, 736
 - transmission electron microscopy (TEM), 734
 - magnetic drug delivery
 - hybrid nanomagnets, 739
 - DSC. *See* Differential scanning calorimetry
 - DSPs. *See* Digital signal processors
 - DSSC. *See* Dye sensitized solar cells
 - DTA. *See* Differential thermal analysis
 - Dunkel, R., 435
 - Duroplastic behavior, 590
 - DWBA. *See* Distorted-wave Born approximation
 - Dyakonov, V., 330, 338
 - Dye sensitized solar cells, 325
 - Dynamic light scattering, 9
 - Dynamic mechanical analysis, 9
 - Dynamic random access memories, 385
- E**
- EAcAc. *See* Ethyl acetoacetate
 - EBL. *See* Electron beam lithography
 - EBM. *See* Equivalent box model
 - EC. *See* Epoxy-functional clusters
 - ECR. *See* Electron cyclotron resonance
 - EDA. *See* Ethylenediamine
 - EISA. *See* Evaporation-induced self-assembly
 - Eisenberg, P., 37–38
 - Electrical conductivity and conducting polymers, 482–483
 - Electrochemical biosensors
 - carbon nanotube-based electrochemical biosensors, 720–723
 - enzyme electrodes, 714
 - metal and semiconductor nanoparticle-based biosensors, 715–720
 - oxide nanocomposites-based electrochemical biosensors, 723–724
 - Electrochemical detection, biorecognition events, 723
 - Electrochemical supercapacitor
 - hybrid organic-inorganic materials in, 294–295
 - CNs and conducting polymer, nanocomposites, 297–298
 - POMs and conducting polymers, nanocomposites, 295–297
 - role of, 292–293
 - types of, 295
 - Electroluminescence (EL), 428
 - Electromagnetic wave, 692
 - Electron beam lithography, 387
 - Electron cyclotron resonance, 394
 - Electronic paramagnetic resonance, 535
 - Electron spin resonance, 330
 - Electrospinning, 744
 - Electrospun nanofiber mats, 744
 - Embedded capacitors, hybrid nanocomposites in, 235–242. *See also* Hybrid organic-inorganic nanocomposites
 - Emission quantum yield, definition, 539–540
 - Energy conversion devices vs. energy storage, 291–293
 - Energy-dispersive X-ray (EDX), 771
 - Epoxy-functional clusters, 44
 - Epoxy resin, in metal oxide polymer magnetic nanocomposites, 488–493
 - Epoxy-silica hybrid network, phases, 29
 - Epoxy-silica/silsesquioxane networks, in nanocomposites synthesis, 6–10
 - Epoxy-silica/SSQO nanocomposites, mechanical properties, 80–82
 - EPR. *See* Electronic paramagnetic resonance
 - EQE. *See* External quantum efficiency
 - Equivalent box model, 29
 - Ernst, R. R., 213
 - ESR. *See* Electron spin resonance
 - ETA. *See* Extremely thin absorber
 - Ethyl acetoacetate, 175

- Ethylenediamine, 94
 Etienne, P., 565
 Evaporation-induced self-assembly, 520
 External quantum efficiency, 328
 Extremely thin absorber, 300
 Extreme ultraviolet (EUV) lithography, 387
 Ezhilvalavan, S., 273
- F**
- Fabricated grating profiles, 625
 Fan, Q., 350
 Fasce, D. P., 35
 Feher, F. J., 35, 59
 Feldmann, C., 468
 Ferrimagnetism, definition, 454. *See also*
 Magnetism
 Ferrites, 455. *See also* Magnetism
 Ferrofluids, application area, 498
 Ferromagnetism, definition, 453.
See also Magnetism
 FETs. *See* Field-effect transistors
 FHD. *See* Flame hydrolysis
 Fiber-optic EF DNA biosensor, 713
 Field-effect transistors, 232, 233, 253, 254
 Fill factor (FF), 327–328
 Film thickness, UV exposure, 605
 Flame hydrolysis, 630
 Flat bilayer, architectures, 326
 Flat bilayers cells
 bilayers with TiO₂, 349–354
 junctions of doped polymers, 354–355
 Flat panel displays, 274–276. *See also* Hybrid
 organic-inorganic nanocomposites
 Flexible OLEDs, 429
 Flory-Erman (F-E) rubber elasticity theory, 55
 Fluorescein, scanning confocal images, 804
 Fluorescence-quenching strategies, 706
 Fluorescent microscopy images, 712
 Fluorescent semiconductor nanocrystals, 710
 Fluorescent signal, 707
 Fluorophores, molecular structures, 795
 Folded sheet materials, 137
 F-OLEDs. *See* Flexible OLEDs
 Forssell, G., 431
 Fourier analysis, spectral region, 678
 Fourier Transform Infrared (FTIR) spectroscopy, 8, 474
 Fowler, C. E., 520
 FPD. *See* Flat panel displays
 Franville, A.-C., 546
 Fréchet, J. M. J., 331, 351
 Fresnel-type lens, 628–629
 Frey, L., 625
 Friend, R. H., 299
 FSM. *See* Folded sheet materials
 FTIR. *See* Fourier transform infrared
 FTIR microscopy mapping, 611
 FTIR spectroscopy, methacrylate hybrimer, 599
 FTL. *See* Fresnel-type lens
 Fu, B. X., 60
 Fu, L. J., 246
 Fuller, C. S., 321
 Fullerene nanocomposite resists
 bilayer resist system, 404–409
 concept of, 388–390
 preparation of, 390–394
 resist characteristics, 394–403
 types of, 387, 388
 Full width at half maximum, 197, 458,
 545, 656
 Fu, L. S., 520
 Functionalized quantum dot nanoparticles, 709
 Functional nucleic acids, 733
 FWHM. *See* Full width at half maximum
- G**
- γ -Aminopropyltriethoxysilane, 93
 γ -APS. *See* γ -Aminopropyltriethoxysilane
 Gaussian beam, 670
 GCR. *See* Glass-ceramic route
 Geckeler, 255
 Ge-doped hybrimers
 optical micrograph of, 594
 photoinduced densification in, 595
 refractive index and density of, 594
 UV irradiation, 595
 Ge-doped methacrylate hybrimers
 AFM images of, 616
 direct photo-patterned single circle
 AFM images of, 617
 methacrylate and Ge doped silica, 614
 refractive index and film thickness, change
 in, 615
 UV light, 614
 Gelloz, B., 264
 Generalized Lorentz-Mie theory, 670
 Germanosilicate glasses
 densification, 591
 refractive index
 UV illumination, 594
 GID. *See* Grazing-incidence diffraction
 Gilchrist, R. K., 740
 Gilot, J., 375
 GISAXS. *See* Grazing incidence small angle
 scattering
 Glass-ceramic route, 461

- GLMT. *See* Generalized Lorentz-Mie theory
3-Glycidoxypropyltrimethoxysilane, 440, 565
Glycidyloxypropyltrimethoxysilane, 589
GLYMO. *See*
 3-Glycidoxypropyltrimethoxysilane
Gokan, H., 387
Gold-tagged beads, 719
Goossens, A., 350, 351
GPTS. *See*
 Glycidyloxypropyltrimethoxysilane
Graetzel, M., 306
Graff, G. L., 427
Grancharov, S. G., 726
Gratings, diffraction effects, 627
Grätzel, M., 325
Gray-scale photomask, 634
 binary photomask, 634
 high-energy beam-sensitive (HEBS), 635
Grazing incidence diffraction, 199
Grazing incidence small angle scattering, 194
Green fluorescent protein (GFP), 803, 804
Greenham, N. C., 329, 330, 332, 340
Groner, M. D., 429, 436
GTMS. *See* (3-Glycidyloxypropyl)
 trimethoxysilane
Gu, H., 741
Günes, S., 338
- H**
Haas, K.-H., 437
Han, M., 706
Hashimoto, K., 364
HCP. *See* Hexagonally close-packed array
HEBM. *See* High-energy ball milling
Heeger, A. J., 323, 358, 371
Hegeer, A. J., 299
HEMT. *See* High electron mobility transistor
Hench, L. L., 766
Heptadecafluorodecyl-trimethoxysilane
 (PFAS), 608
Hermetic barrier
 function of, 426
 in microelectronics industry, 426–428
 tests for, 430–437
Hexagonally close-packed array, 260
Hg lamp irradiation, 615
HgTe nanoparticles, 338
High electron mobility transistor, 400
High-energy ball milling, 462
Highly photosensitive hybridmers, design, 592
High performance liquid chromatography, 166
High photosensitive sol–gel hybrid
 nanomaterials, 583
Himmel, B., 18
Hiremath, V. A., 474
HNSC. *See* Hybrid nanocrystal-polymer
 solar cell
Hole-transport material, 300–301
Hollow mesoporous silica (HMS), TEM
 micrographs, 737
Holographic interference, 625
Hono, K., 462
Horseradish peroxidase (HRP), 806
 luminol/H₂O₂ solution,
 chemiluminescence, 808
 silica hydrogel encapsulated
 lineweaver-Burk plot of, 808
 silica hydrogel, immobilize LUC, 809
 TMOS sol, 809
HPLC. *See* High performance liquid
 chromatography
HSC. *See* Hybrid organic–inorganic solar
 cells; Hybrid solar cells
HTM. *See* Hole-transport material
HTO water test, device for, 436
Huang, H. H., 31
Huisman, C. L., 340
Human serum albumin (HSA), 793
Hüsing, N., 141, 164
Hybrid coatings, features, 445–446
Hybrid magnetic nanoparticles, gene
 therapy, 739
Hybrid materials
 classes of, 508
 precursors for, 437–438
 synthesis of, 509
Hybrid nanocomposite materials
 application, biosensors
 DNA analyses, 705
 electrochemical biosensors,
 714–724
 magnetic nanoparticles, 724
 magnetobiosensors, 724–726
 optical biosensors, 705–714
 and COPs, 293–294
 in electrochemical supercapacitors, 295
 future prospects of, 310
 in hybrid solar cells, 298–301
 HSC and ss-DSSC, 305–308
 with inorganic semiconductors,
 301–305
 processability and large-scale
 fabrication, 308–309
 role of, 294
Hybrid nanocrystal-polymer solar
 cell, 301
Hybrid nanoparticles, synthesis, 704

- Hybrid nanotubes
 - self-assembled lipids, 745
 - silica nanotubes, 745
- Hybrid organic-inorganic materials, in
 - electrochemical supercapacitors, 294–295
 - CNs and conducting polymer, nanocomposites, 297–298
 - POMs and conducting polymers, nanocomposites, 295–297
- Hybrid organic-inorganic nanocomposites, 174
 - application of mechanically flexible surface and bioactive properties of, 187–188
 - thermally conductive property of, 188
 - tribological property, 185–187
 - electronic applications of
 - embedded capacitors, 235–242
 - historical background of, 232–235
 - integrated circuits, 251–253
 - LEDs, 263–273
 - liquid crystal displays and flat panel displays, 274–276
 - Lithium ion batteries, 243–251
 - telecommunication networks, 258–262
 - transistors, 253–258
 - ULSI devices, 273–274
 - mechanical flexibility of organosiloxane-based, 175–177
- M(OR)_n-PDMS-derived
 - chemical modification of metal alkoxides, 178–181
 - Dimethyldiethoxysilane usage, 184–185
 - formation behavior and structure, 181–183
 - mechanical properties of, 183–184
- properties of, 231–232
- SSNMR in structural characterization of, 213–215
 - PLS nanocomposites, 222–223
 - semiconductor nanoparticles, 215–222
- TEOS-PDMS derived, 177–178
- X-ray scattering techniques in structural characterization of, 194–195
 - nanoparticles nanocomposites, 199–206
 - polymer-layered silicate nanocomposites, 206–213
- Hybrid organic-inorganic solar cells, 290
- Hybrid paramagnetic nanoparticles, 728
- Hybrid polymer-inorganic photovoltaic cells, performance, 372–374
- Hybrid-polymer solar cells, 324–327
- Hybrid porous materials
 - bridged polysilsesquioxanes, 156–158
 - with hierarchical porosity, 164–165
 - porous silsesquioxanes by sol-gel processing, 158–160
 - templated bridged silsesquioxanes, 160–164
 - chemical and covalent modification of, 143–144
 - classes and synthesis of, 142–143
 - in situ synthesis, 150–156
 - post-synthesis treatment, 145–150
- Hybrid silicates, supramolecular structures, 526
- Hybrids incorporating functional groups, synthesis, 508–509
 - non-organized hybrids
 - route A, 510
 - route B, 510–515
 - organized or texturized hybrids, 515–516
 - route C, 516–521
 - route D, 521–523
 - route E, 523–528
- Hybrid solar cells, 299, 305–308
 - hybrid nanocomposite materials in, 298–301
 - HSC and ss-DSSC, 305–308
 - with inorganic semiconductors, 301–305
 - processability and large-scale fabrication, 308–309
 - photovoltaic properties of, 300
- Hybrimers
 - acrylate photo-polymerization
 - principles of, 599
 - BDK-doped, 604
 - BDK, photochemical reactions of
 - schematic diagram of, 604
 - films, photoinitiator dopants, photolocking of, 606
 - high electrical resistance, 591
 - highly electrically insulating materials, 590
 - methacryl groups
 - decomposition of, 602
 - oxygen permeability of, 590
 - photolithography of, 634
 - photolocking mechanism, 608
 - photosensitivity of, 614
 - silanol groups, 589
 - synthesis of
 - micro-optics fabrication, 589
 - polymerization of, 592

- precursor used in, 588
 - schematic diagram of, 587
 - sol-gel processing of, 589
 - thermal stability of, 590
 - Hybrimers, photosensitivity mechanisms
 - Ge-doped hybrimer
 - photoinduced densification in, 594–596
 - methacrylate
 - photoinduced decomposition of, 601–603
 - photo-polymerization of, 596–600
 - photoinduced migration, monomers/oligomers
 - azo chromophores, *trans-cis* isomerization of, 606
 - 3D AFM image, 607
 - diffusion process, 608
 - exposed/unexposed areas, 609
 - high photosensitive hybrimer, 608
 - light intensity regions, 607
 - thermal baking of, 613
 - UV exposed dose, 610–612
 - UV illumination, 612
 - photolocking
 - of photochemical molecules, 603–606
 - refractive index and film thickness, 605
 - UV wavelength, 606
 - photosensitivity mechanisms
 - in functionalized hybrimers, 616–620
 - wavelength dependence of, 614–616
 - Hydrogen atoms, energy levels splitting
 - schematic of, 679
 - Hydrolysis–polycondensation, reactions, 438
 - Hyperbranched poly(amidoamine) grafting
 - onto silica nanoparticle surface, 92–93, 95–98. *See also* Polymers grafting onto nanoparticle surfaces, in solvent-free dry-system
 - amino groups grafting onto silica nanoparticles, 94–95
 - experimental methods of, 93–94
 - polar solvents effects on, 98
 - reaction conditions and amino group content effects on, 99–100
 - Hyperthermia
 - magnetic hyperthermia, 740
 - magnetic oxide particles
 - heating of, 740
 - near-infrared laser irradiation
 - of gold nanoparticles, 740
 - therapeutic heat, application of, 739
 - Hysteresis losses, 740
- I**
- IAA. *See* Iron (III) tris (3-allylacetylacetonate)
 - ICPTES. *See*
 - 3-Isocyanatepropyltriethoxysilane
 - ICs. *See* Integrated circuits
 - Immobilized catalyst, 742
 - Indium tin oxide, 269, 329
 - Infra-red-emitting colloidal nanocrystals, 688
 - Inhomogeneous magnetic field, 739
 - Inorganic materials, definition, 173–174
 - Inorganic nanoparticles, role, 88
 - Inorganic semiconductors
 - and hybrid nanocomposite materials, 301–305 (*see also* Hybrid solar cells)
 - and hybrid solar cells, 301–305 (*see also* Hybrid nanocomposite materials)
 - Inoue, N., 461–462
 - InP nanoparticles, 338–339
 - Integrated and non-linear optics, 560–566
 - Integrated circuits. *See also* Hybrid organic-inorganic nanocomposites
 - applications of, 233–234
 - hybrid nanocomposites in, 243–251
 - Interpenetrating network, 13
 - Inverse opal structures, 138–139.
 - See also* Silica-based porous materials
 - Ion exchange resin, in metal oxide polymer magnetic nanocomposites, 484–487
 - IPN. *See* Interpenetrating network
 - Iron oxide (IO)
 - composite, 464
 - nanoparticles, 741
 - pure phase of, 462–463
 - Iron (III) tris (3-allylacetylacetonate), 465
 - Isakawi, M., 550
 - 3-isocyanatepropyltriethoxysilane, 512
 - ITES. *See* (3-isocyanatopropyl)triethoxysilane
 - ITO. *See* Indium tin oxide
 - Ito, A., 741
 - Ito, H., 420
 - Izumi, K., 445
- J**
- Jang J. H., 622
 - Jordens, K., 48
 - Jørgensen, C. K., 558
 - Joshi, M., 60
 - Judd, B. R., 558
 - Jungk, H.-O., 468

K

Kakuchi, M., 387
 Kamitakahara, M., 783
 Kang, D. J., 624, 635
 Kang, Y., 361
 Kärkkäinen, A. H. O., 621, 622, 634
 Kay, B. D. J., 11
 Keefer, K. D., 15
 Kerner-Nielsen model, 28
 Kim, J. K., 357
 Kim, S. S., 744
 Kinoshita, H., 422
 Klimov, V. I., 336, 337
 Kokubo, T., 766
 Koshida, N., 264
 Krausch, K. R., 371, 375
 Krebs, F., 350
 Kresge, C. T., 137
 Kumar, S., 257
 Kwong, C. Y., 340

L

Laguerre polynomials, 660
 Lamellar alkylene-bridged silsesquioxanes, formula, 524
 Langmuir-Blodgett films, 742
 Langmuir equation, 747
 Larmor frequency, 727
 Laser direct writing, 630
 diffraction gratings, formation of, 622
 photomask illumination, 624
 refractive index-modulated optical waveguide, 631
 Lauterbur, P. C., 728
 Lavrentyev, V. I., 59
 LbL method, 650
 LbL polyelectrolyte films, 735
 LCDs. *See* Liquid crystal displays
 LCDMs. *See* Light conversion molecular devices
 LDW. *See* Laser direct writing
 Lead salts, multiple exciton generation in, 335–337
 Lead selenide (PbSe), 333
 Lead sulfide (PbS), 333
 Leavitt, R. P., 557
 LEDs. *See* Light-emitting diodes
 Lee, A., 60–61
 Lee, B., 210, 212
 Lee, J., 266
 Lee, T. W., 269
 Lee, Y. J., 253
 LESR. *See* Light-induced ESR

Lichtenhan, J. D., 59, 60
 Li, G., 148, 309
 Light conversion molecular devices, 542
 Light-emitting diodes. *See also* Hybrid organic-inorganic nanocomposites
 applications of, 235
 hybrid nanocomposites in
 polymer-based materials in, 265–273
 Si-based nanocomposite materials in, 263–265
 Light-emitting hybrids
 hybrids incorporating optically active centres
 emission quantum yield and quantum efficiency, 550–551
 lanthanide ions, 542–550
 local coordination, 551–560
 organic dyes, 540–542
 hybrids lacking metal activator centres, 528–533
 emission color coordinates and quantum yield, 538–540
 emitting centres and mechanisms, 535–537
 time-resolved spectroscopy, 533–534
 Light-induced ESR, 330
 Lignin peroxidase (LiP), nanoassemblies, 743
 Li, G. Y., 60
 Li, H., 249
 Li, L., 239
 Lindén, M., 140
 Liquid crystal displays, 425. *See also* Hybrid organic-inorganic nanocomposites
 applications of, 235
 hybrid nanocomposites in, 274
Listeria monocytogenes, 706
 Lithium (Li) ion batteries. *See also* Hybrid organic-inorganic nanocomposites
 applications of, 234–235
 hybrid nanocomposites in, 243–251
 Lithographic process, for device fabrication, 384
 Liu, W., 209
 Liu, X., 713, 771
 Livingston, J., 457
 Li, W., 731, 737
 Li, Y., 332
 Localized surface plasmon resonance (LSPR), 714
 Lopez, H. A., 265
 Lorentzian functions, 687
 Lorentzian-shaped azimuthal peaks, 672
 Lorentz-Lorenz equation, 594
 Lorenz-Mie theory, 662

- Lübbbers, D. W., 739
Luminescence confocal image, 657
- M**
- MAA. *See* Methacrylic acid
MacDiarmid, A. G., 323
Mackenzie, J. D., 175, 177, 771
MacKenzie, K. J. D., 213
Macquarrie, D. J., 154
Macromolecular scale structure detection, scattering methods in, 9–10
Magic angle spinning, 217
Magnetic fluid (MF), 457–458, 493
Magnetic nanocomposites
 applications of, 494–498
 preparation, co-precipitation method in, 459 (*see also* Organic/inorganic magnetic nanocomposites, preparation methods for)
Magnetism, 452–455
 bulk *vs.* fine particles, 456–458
 ferrites, 455
 thin films, 458–459
Magnetite epoxy resins, 488
Magnetobiosensors
 magnetoimpedance, 726
 magnetorelaxometry, 724
 magnetoresistance technology
 magnetic nanoparticles, 726
 magnetoresistive prototype, 726
 relaxation mechanisms
 Brownian relaxation, 725
 Néel mechanism, 725
Magnetofection, 739
Magnetoliposomes, MRI contrast agents, 731
Magnetophoretic mobility, 739
Mahima, S., 255
Malta, O. L., 556, 557
Manganese peroxidase (MnP), 743
Mann, S., 154
MAPTMS. *See*
 Methacryloxypropyltrimethoxysilane
Mark, J. E., 23, 177
Martos, M., 246
MAS. *See* Magic angle spinning
Mathias, L. J., 223
Matsui, K., 733
Maximum power point, 345
MB DNA biosensor, 713
MBE. *See* Molecular beam epitaxy
McGehee, M. D., 358, 359
McLachlan, D. S., 241
MCM. *See* Mobil Composition of Matter MCM-41 particles, importance, 519, 520
MDMO-PPV. *See* Poly [2-methoxy-5-(3'-7'-dimethyloctyloxy)-1,4-phenylene vinylene]
Measured line shapes, of peak, 673
MEC. *See* *t*-butylperoxy-2-methacryloyloxyethylcarbonate
MEH-PPV. *See* Poly [2-methoxy-5-(2'-ethylhexyloxy)-1,4-phenylene vinylene]
M3EH-PPV. *See* Poly [2,5-dimethoxy-1,4-phenylene-1,2-ethenylene-2-methoxy-5-(2-ethylhexyloxy) (1,4-phenylene-1,2-ethenylene)]
Meissner, D., 338
Melamine formaldehyde, 656
Memory, J. D., 213
MEMS. *See* Microelectromechanical systems; Micro-optical-electromechanical systems
Meng, Q. G., 520
MeOZO. *See* 2-Methyl-2-oxazoline
MER. *See* Magnetite epoxy resins
Meredith, P., 334, 335
Mesoporous silica spheres
 multilayered nanocomposite thin shells, 747
Metal/insulator/metal, 239
Metal nanoparticle-enzyme conjugate materials, 743
Metal nanoparticles
 enzyme immobilization on, 745
 solid state magnetically induced, 718
Metal organic chemical vapor deposition, 236
Metal-organic frameworks, 135, 166
Metal oxidation and corrosion, sol-gel process for, 437
Metal oxide networks and conjugated polymers
 in situ blends on TiO₂, 365–367
 in situ blends on ZnO, 367–371
Metal oxide polymer magnetic nanocomposites
 embedded magnetic nanoparticles
 epoxy resin, 488–493
 ion exchange resin, 484–487
 MF, 493
 RFC, 493–494
 polymer coated magnetic nanoparticles, 464–467
 electrical properties of, 482–483
 magnetic behavior of, 480–482
 optical behavior of, 483–484
 structural aspects of, 467–480

- Methacrylate hybrimer
 AFM image of, 598
 film UV, refractive index and thickness, 601
 FTIR spectroscopy, 599
- Methacrylic acid, methacryl groups
 copolymerized with, 600
- Methacryloxypropyltrimethoxysilane, 522, 589, 592
- 3-(Methacryloxypropyl)-trimethoxysilane (MPTS), 608
- Methylmethacrylic acid (MMA), 608
- 2-Methyl-2-oxazoline, 108
- Methyltriethoxysilane (MTES), 619
- Methyltrimethoxysilane, 437
- MF. *See* Melamine formaldehyde
- MF/CdTe microcavity, Q-factor, 666
- MF/CdTe microsphere, emission spectra, 661
- MF microsphere, radiation pressure calculation, 671
- MF/PE/CdTe microsphere, Raman spectrum, 674
- Microcavity enhanced Raman scattering and anti-stokes emission, 673
- Microelectromechanical systems, 425
- Micro-focus X-ray fluorescence, 488
- Micro lens arrays, 633
 AFM and optical microscopy, 595, 596
 photoresist thermal reflow method, 633
- Micro-optical-electromechanical systems, 668
- Micro-optical modulations, 586
- Micro-optical structures, photosensitive materials, 584
- Micro-optics
 diamond-turning techniques, 584
 elements of, 583
 fabrication, sol-gel materials, 584
 photo-fabrication of, 586
 photolithographic method to photo-pattern, 584
 potential applications in, 583
- Micro-PL spectra
 CdTe NCs, water, 661
 of single microspheres
 monolayer of CdTe NCs, 663, 664
 WGM peaks, 665
- Micro-PL spectroscopy, 668
- Microprocessor units (MPUs), 385
- Mie scattering theory, 662
- MIM. *See* Metal/insulator/metal
- Mirkin, C. A., 743
- Miyazaki, T., 775, 777, 783
- MLA. *See* Microlens arrays
- MLA directly photo-fabricated focusing plane of, 636
- MMT. *See* Montmorillonite
- Mobil Composition of Matter, 137
- MOCVD. *See* Metal organic chemical vapor deposition
- MOF. *See* Metal-organic frameworks
- Molecular beacons (MBs), 706
- Molecular beam epitaxy, 459, 461–462
- Monma, H., 767
- Mono-amidosil hybrid, structure of, 529
- Monocomponent silicon strategy, 735
- Monolayer protected nanoclusters, 255
- Montmorillonite, 274
- Mössbauer spectroscopy (MS), 476
- MOW. *See* Multimode optical waveguide
- MPCs. *See* Monolayer protected nanoclusters
- MPP. *See* Maximum power point
- MPTMS. *See* Methacryloxypropyltrimethoxysilane
- MPTS. *See* Methacryloxypropyltrimethoxysilane
- MQ-MAS. *See* Multiple-quantum magic-angle spinning
- MRI. *See* Nuclear magnetic resonance imaging
- MRI sensors, chemical exchange saturation transfer (CEST) effects, 727
- M41S-materials, 137–138. *See also* Silica-based porous materials
- MTMS. *See* Methyltrimethoxysilane
- Mukhopadhyay, K., 745
- Multimodal materials, synthesis of ordered, 521
- Multimode optical waveguide, 631
- Multiple-quantum magic-angle spinning, 214
- Multi-walled carbon nanotubes (MWCNT), 245, 720
- Murray, C. B., 200, 202
- MWNTs. *See* Multi-walled carbon nanotubes
- μ -XRF. *See* Micro-focus X-ray fluorescence
- N**
- Nair, S., 210
- Nakanishi, K., 140, 141, 155, 164
- Nanobiocomposite assembly, schematic representation, 746
- Nanobuilding blocks, 6, 505, 507
 assembly of, 521–523
- Nanocrystals, multilayers
 capping ligands, 651
 coupled spherical microcavities, 679
 microsphere hybrid systems, 659
 optical emission properties of, 651

- PL decay curves, 655
 - semiconductor, preparation of, 655
 - spherical microcavities
 - photons confinement, 658
 - with semiconductor nanocrystals, 655–658
 - Nanoengineered polyelectrolyte capsules
 - schematic overview of, 736
 - Nanofibrous α -chymotrypsin, 744
 - Nanoparticle-attached enzymes, 743
 - Nanoparticle-based probes, 709
 - Nanoparticle-polymer hybrid solar cells
 - CdSe and CdTe nanoparticles, 329–333
 - light absorbing nanoparticles, 338–339
 - PbS, PbSe, and PbTe nanoparticles, 333–337
 - TiO₂ nanoparticles, 339–340
 - ZnO nanoparticles, 340–341
 - morphology of nc-ZnO, 347–348
 - photophysics of, 341–343
 - photovoltaic properties of nc-ZnO, 343–347
 - Nanoparticles nanocomposites, structural characterization, 199–206
 - Nanoporous hybrid materials, 704
 - Nanoporous inorganic semiconductors, infiltrating polymers into, 326
 - Nanoporous protein particles (NPPs), 747
 - schematic illustration of, 748
 - Nanoporous semiconductors and conjugated polymers, 355–358
 - Nanostructured inorganic electrodes and conjugated polymers, 326–327
 - NBBs. *See* Nanobuilding blocks
 - nc-ZnO-polymer blends
 - morphology of, 347–348
 - photovoltaic properties of, 343–347
 - Near field scanning optical microscopy, 611
 - reflection intensity, image of, 632
 - Near-field surface patterning
 - refractive index profile measured, 632
 - thick film, 619
 - Nelson, J., 357, 363
 - Nephelauxetic effect, 557, 558
 - NFT. *See* Normalized film thickness
 - Ng, L. V., 18
 - Nguyen, T.-Q., 269
 - Nielsen, L. E., 27
 - Nilsson, P. O., 431
 - Nisato, G., 431, 432
 - NMR. *See* Nuclear magnetic resonance
 - Noncompetitive heterogeneous electrochemical immunoassay
 - schematic of, 718
 - Non-faradaic electrical energy storage, 292
 - Non-interacting microspheres, PL spectra, 686, 687
 - Normalized film thickness, 395
 - Nozik, A. J., 336, 337
 - NSOM. *See* Near field scanning optical microscopy
 - n-type semiconductor, in situ synthesis, 327
 - Nuclear magnetic resonance, 8
 - Nuclear magnetic resonance imaging
 - applicability of, 726
 - development of, 727
 - paramagnetic contrast agents, 728–729
 - superparamagnetic contrast agents, 729–731
 - Nucleic acid-Au nanoparticles-functionalized beads
 - DNA, amplified detection of, 719
 - N-vinyl-2-pyrrolidone, 110
 - NVPD. *See* N-vinyl-2-pyrrolidone
- O**
- o*-DCB. *See* *ortho*-dichlorobenzene
 - Ohnishi parameter, definition, 387
 - Ohtsuki, C., 770
 - Okamoto, M., 207
 - Oku, S., 403
 - OLEDs. *See* Organic light-emitting diodes
 - Olson, D. C., 363
 - Optical biosensors, 705
 - Optical coding wavelength, schematic diagram, 707
 - Optical integrated circuits, advantages, 560
 - Optical microcavity applications, 656
 - Optical micrograph, of cross-section, 632
 - Optical nanolithography, 619
 - Optical waveguides
 - fabrication process of, 606
 - fabrication technique, 631
 - micro-optical devices, 629
 - micro-optics, 620
 - photo-polymerization of, 630
 - photosensitivity mechanisms, 638
 - polymer films, 630
 - reactive ion etching, 630
 - Organically modified silicates (ORMOSIL), 793
 - Organic dyes, in light-emitting hybrids, 540–542. *See also* Light-emitting hybrids
 - Organic-inorganic hybrids
 - emission features of, 538–540

- Organic-inorganic hybrids (*cont.*)
flexible films, 440–443
lanthanide-based, 543
luminescent properties, factors for, 544
molecular structure of, 562–563
optically-active defects in, 536
role in active optical waveguides
production, 564
sol-gel process for, 437–440
- Organic/inorganic magnetic nanocomposites
preparation methods for
chemical, 459–460
physical, 460–462
prospects and challenges in, 498–499
- Organic-inorganic (O-I) nanocomposite
polymers, methods of synthesis, 5
epoxy-silica/silsesquioxane networks, 6–10
formation, structure and morphology of,
77–79
interphase interaction and structure
ordering, 79–80
nanobuilding blocks in
epoxy-POSS networks, 60–76
polyhedral oligomeric silsesquioxanes,
58–60
- Organic-inorganic networks and in situ
generated silica/SSQO nanodomains. *See also* Organic-inorganic (O-I) nanocomposite polymers, methods of synthesis
with defined interphase covalent bonding
epoxy networks with SSQO grafted
along chain, 56
O-I copolymer networks with SSQO
domains, 41–56
trialkoxysilanes polymerization, 32–41
interpenetrating epoxy-silica networks
formation of, 14–21
morphology and structure of, 21–24
network DGEBA-D2000-TEOS, 13–14
thermomechanical properties and
interphase interaction, 24–31
network DGEBA-D2000-ATES nanocomposite, 56–58
sol-gel process, 10–13
- Organic light-emitting diodes, 235, 425, 542
barriers for, 428–430
- Organic materials, definition, 173–174
Ormosils, enzyme activity, 724
ortho-dichlorobenzene, 391
solubility of fullerenes in, 393
Osaka, A., 772
OTR. *See* Oxygen transmission rate
Oxygen scavenger system, definition, 442
- Oxygen transmission rate, 426
Ozin, G. A., 148
- P**
- PAA. *See* Porous anodic alumina
Paetzold, R., 434
Palchik, O., 466
Pal, M., 461
PA-PPV. *See* Phenylamino-*p*-phenylene
vinylene
Paramagnetism, definition, 453. *See also*
Magnetism
Passive-active barrier coating, preparation, 442
Pathak, A., 464, 468
Payne effect, 10
PbS, PbSe, and PbTe nanoparticles, 333–337.
See also Nanoparticle-polymer
hybrid solar cells
lead salts, multiple exciton generation in,
335–337
photovoltaic devices, 333–335
PCBs. *See* Printed circuit boards
PCL4. *See* Poly(ϵ -caprolactone)
PCNEPV. *See* Poly[oxa-1,4-phenylene-1,2-(1-
cyano)ethenylene-2,5-dioctyloxy-
1,4-phenylene-1,2-(2-cyano)
ethenylene-1,4-phenylene]
 π -conjugated polymers, properties, 323
PDMDPS. *See* Polydimethyldiphenylsiloxane
PDMS. *See* Polydimethylsiloxane
PE. *See* Polyelectrolytes
Pearson, G. L., 321
PECVD. *See* Plasma-enhanced chemical vapor
deposition
PEDOT. *See* Poly(3,4-ethylenedioxy
thiophene)
PEDOT:PSS. *See* Poly(3,4-ethylenedioxythiophene):poly(styrenesulfonate)
PE LbL film, deposition on, 651
Pelissier, S., 622
PEMA. *See* Polyethylene grafted with maleic
anhydride
PEN. *See* Polyethylene naphthalate
PEO. *See* Poly(ethylene oxide)
PEO-POSS. *See* Poly(ethylene oxide)-
polyhedral oligosilsesquioxane
PEP. *See* Photoelectrochemical polymerization
Percolation theory, concept, 483
Perfluoroalkyl methoxysilane, 602
Periodic mesoporous organosilicas, 162
Perkin-Elmer fluorescence spectrometer, 653
Perturbation theory, frequency shifts, 667
PE-shell, microspheres, 672

- PET. *See* Polyethyleneterephthalate
- PGE. *See* Phenyl glycidyl ether
- PGMEA. *See* Propylene glycol 1-monomethyl ether 2-acetate
- Phase-mask illumination
- light interference
 - laser, photosensitive materials, 620
 - using excimer laser, 624
- Phase-mask lithography
- schematic diagram, 624
 - using excimer laser, 624
- PHD. *See* Pinhole diffraction
- Phenylamino-*p*-phenylene vinylene, 349
- 4-Phenylazide, synthesis, 412
- 4,4'-[1,3 phenylenebis(1-methylidene)] bis(aniline), 6
- Phenyl glycidyl ether, 66
- Phenyltriethoxysilane, 187
- Phospholipids bilayers, 743
- Photochemical self-developing, 630
- Photo-decomposed radicals, 603
- Photoelectrochemical polymerization, 307
- Photofabricated micro-patterned surface structures
- mapping of, 611, 612
- Photoinduced absorption spectroscopy, 330
- Photoinduced decomposition, of
- methacrylate, 602
- Photoinduced electrocyclization, 619
- Photoinduced migration mechanism
- convex microlenses, 637
 - surface micro-structural evolution, 610
- Photoinduced reactions, 584
- Photolocking, 613
- refractive index and film thickness, 606
 - UV wavelength, 614
- Photoluminescence (PL), 330
- Photoluminescent UV photostable
- organic-inorganic hybrids, 530
- Photomultiplier tube, 656
- Photonic molecule (PM), 679
- Photon lifetime
- photon storage time, ratio between, 688
- Photon storage times
- PM, *m*-modes, 689, 690
- Photo-polymerization, 607
- efficiency of, 598
 - of methacrylate, 592
- Photopolymers, 584
- Photosensitive fluoro-methacrylic-zirconium hybri-mer
- synthesis and design of, 609
- Photosensitive hybri-mer films, 628
- Photosensitive hybri-mers, 585, 628
- doped with photoinitiators, 632
 - MLAs directly photo-fabricated
 - focal lengths of, 636
 - UV exposure, 610
- Photosensitive methacrylate hybri-mers
- UV illumination, 612
- Photosensitive polymers. *See also* Photopolymers
- holograms, 584
- Photosensitivity mechanisms
- direct photo-fabrications of micro-optical elements, 593
 - schematic diagram of, 613
 - UV lamp wavelength, 616
- Photo-storage times distribution, 690
- Photovoltaic device, principle, 322
- PhSi(OEt)₃. *See* Phenyltriethoxysilane
- P3HT. *See* Poly(3-hexylthiophene)
- PIA. *See* Photoinduced absorption spectroscopy
- Ping, D. H., 462
- Pinhole diffraction, 628
- schematic configuration for, 629
- Pinnavaia, T. J., 737
- Planar optical waveguides, 591
- Plasma-enhanced chemical vapor deposition, 427
- PLS. *See* Polymer-layered silicate
- PL spectra, 652
- PMAA. *See* Poly-methacrylic acid
- PM-based photonic device, 687
- PMMA. *See* Poly(methyl methacrylate); Poly(methyl methacrylate); Poly(methylmethacrylate); Polymethylmethacrylate
- PMMA cements, modification, 781
- PMOs. *See* Periodic mesoporous organosilicas
- PmPV. *See* Poly(m-phenylene vinylene-co-2,5-dioctoxy-*p*-phenylene)
- PMSSQ. *See* Poly(methylsilesquioxane)
- PMT. *See* Photomultiplier tube
- p*-*n* junction type silicon solar cell, 322
- POE. *See* Poly(oxyethylene)
- Point of zero charge, 133
- Poly(*p*-phenylene vinylene), 254, 266
- Poly(2,7-(9,9-dioctyl-fluorene)-alt-5,5-(4',7'-di-2-thienyl-2,'1',3'-benzothiadiazole)), 332
- Poly(3,4-ethylenedioxy thiophene), 254, 306
- Poly(3-hexylthiophene), 325
- Poly(3-nonylthiophene) (P3NT), 367
- Poly(3-octylthiophene) (P3OT), 340
- Poly(chloro-*p*-xylylene), 273

- Poly(diallyldimethylammonium chloride) (PDDA), 651, 743
- Poly(dimethylsiloxane) (PDMS), 359, 630, 771
- Poly(ϵ -caprolactone), 210
- Poly(ethylene oxide), 140
- Poly(ethylenimine) (PEI), 743
- Poly(m-phenylene vinylene-co-2,5-dioctoxy-*p*-phenylene), 254
- Poly(methyl methacrylate), 390
- Poly(methylmethacrylate), 439
- UV illumination, 556
- UV irradiation, 602
- Poly(methylsilsesquioxane), 210
- Poly(*N*-vinyl carbazole), 297
- Poly(oxyethylene), 507
- Poly(oxypropylene), 43
- Poly(*p*-phenylene vinylene), 324
- Poly(sodium 4-styrenesulfonate) (PSS), 651
- Polyaniline (PANI), 296
- Polyanionic DNAs, 733
- Poly [2,5-dimethoxy-1,4-phenylene-1,2-ethenylene-2-methoxy-5-(2-ethylhexyloxy) (1,4-phenylene-1,2-ethenylene)], 349–350
- Polydimethyldiphenylsiloxane, 186–187
- Polydimethylsiloxane, 175
- Polyelectrolyte microcapsules, 747
- Polyelectrolyte multilayers silica
- sol-gel composite thin films sensors
 - molecular diffusion, 810
 - ORG spectrum, 811
 - pH response of, 811
 - pH sensors, 810
 - polyelectrolyte multilayers film, 812
 - schematic for, 813
 - thickness dependence of, 813
 - using ORG, 810
- Polyelectrolyte multilayers silica sol-gel composite thin film
- pH response of, 815
- Polyelectrolytes, 650
- Polyelectrolyte shell, 735
- Polyelectrolytes, multilayers of
- colloidal quantum dots
 - emission properties of, 652–655
 - film thickness, 652
 - layer-by-layer deposition technique, 651–652
 - PL decay curves, 653, 654
 - spherical microcavities
 - with semiconductor nanocrystals, 655–658
 - TGA, integrated PL intensity of, 654
- Polyethylene glycol (PEG), 468, 474
- Polyethylene grafted with maleic anhydride, 210
- Polyethylene naphthalate, 434
- Polyethyleneterephthalate, 440
- Polyhedral oligomeric silsesquioxanes, 6, 58–60, 266. *See also* Organic-inorganic (O-I) nanocomposite polymers, methods of synthesis of
- Polyion layer-by-layer (LbL) assembly, 650
- Polymer coated magnetic nanoparticles, formation, 464–467. *See also* Metal oxide polymer magnetic nanocomposites
- electrical properties of, 482–483
 - magnetic behavior of, 480–482
 - optical behavior of, 483–484
 - structural aspects of, 467–480
- Polymer-layered silicate, 222
- nanocomposites, structural characterization, 206–213
- Polymer nanocomposites
- bottom-up technique in preparation, 5
 - properties of, 5–6
- Polymer optical waveguides, 631
- fabrication technique, 631
- Polymer photovoltaic devices, steps in, 324
- Polymer poly(triphenylamine acrylate), 333
- Polymers and structured inorganic semiconductors
- oriented nanorods, 360–364
 - structured porous TiO₂, 358–360
- Polymers grafting onto nanoparticle surfaces, in solvent-free dry-system
- advantages of, 91–92
 - cationic grafting of polymers onto carbon black surface, 110–113
 - cationic grafting of polymers onto silica nanoparticles, 107–110
 - grafting of hyperbranched poly(amidoamine), 92–100
 - vinyl monomers, radical polymerizations of, 100–107
 - in ionic liquid, 113–126
- Poly-methacrylic acid, 476
- Poly [2-methoxy-5-(3' 7'-dimethyloctyloxy)-1,4-phenylene vinylene], 330
- Poly [2-methoxy-5-(2'-ethylhexyloxy)-1,4-phenylene vinylene], 329
- Polymethylmetacrylate, 359
- Polyorganosiloxane nanoparticles, 737
- Poly[oxa-1,4-phenylene-1,2-(1-cyano)ethenylene-2,5-dioctyloxy-1,4-phenylene-1,2-(2-cyano)ethenylene-1,4-phenylene)], 350
- Polyoxometalates, 295–297

- Poly(3,4-ethylenedioxythiophene):poly(styrene sulfonate), 343
- Poly(ethylene oxide)-polyhedral oligosilsesquioxane, 253
- Polystyrene (PS) microspheres, 674
- POMs. *See* Polyoxometalates
- POP. *See* Poly(oxypropylene)
- Popall, M., 444
- Pope, E. J. A., 515
- Porous anodic alumina, 258
- Porous silicon oxide, 264
- Porphyrin, 741
- POSS. *See* Polyhedral oligomeric silsesquioxanes
- Pothukuchi, S., 240
- PPV. *See* Poly(*p*-phenylene vinylene)
- PPXC. *See* Poly(chloro-*p*-xylylene)
- Pramanik, P., 464, 468
- Prasad, P. N., 335
- Printed circuit boards, 236
- Printed wiring board, 236
- Probe encapsulated by biologically localized embedding (PEBBLE), 709
- Propylene glycol 1-monomethyl ether 2-acetate, 414
- Proteins immobilization, 742
- PSD. *See* Photochemical self-developing
- PS/NCs microsphere, Raman spectra, 675
- PSO. *See* Porous silicon oxide
- p*-toluenesulfonic acid, 12
- PTPAA. *See* Polymer poly(triphenylamine acrylate)
- PVA-based hybrids, surfaces
- SEM pictures, 784
 - TF-XRD patterns of, 785
- PVA/molybdenum oxide hybrids, 784
- PVA/silica hybrids, 784
- PVK. *See* Poly(*N*-vinyl carbazole)
- PWB. *See* Printed wiring board
- PZC. *See* Point of zero charge
- Q**
- Qian, L., 269
- Quantum dots (QD), 710
- micelle formation and characterization, 711
- R**
- Radical polymerization
- UV light, multifunctional acrylate, 598
- RAM. *See* Random access memory
- Ramamurthy, P. C., 256
- Raman scattering, 686
- Raman spectra, 595
- Ramesh, C., 210
- Random access memory, 232
- Rankin, S. E., 46, 360
- Rantala, J. T., 621
- Ravirajan, P., 304, 357
- Reactive ion etching, 387, 630
- Reed, S. T., 437
- Refractive index, UV exposure, 605
- Relaxational losses, 740
- Rentzepis, P. M., 259
- RFC. *See* Rubber ferrite composite
- R6G fluorescence
- single-molecule mobility distributions, 799
- Rhodamine 6G (R6G)
- mobility distributions of, 799
 - scanning confocal images of, 804
- Rhodes, K. H., 521
- RIE. *See* Reactive ion etching
- Rieter, W. J., 728
- Room-temperature sol-gel silica formation process, 792
- Rubber ferrite composite, 493–494
- S**
- Sanchez, C., 6, 262, 308, 508
- Sargent, E. H., 334
- Sariciftci, N. S., 299, 338, 350, 357
- Savenije, T. J., 349, 351, 353, 369
- SAXS. *See* Small-angle X-ray scattering
- Scanning electron microscopy, 10, 395, 488
- Schacht, S., 737
- Schaefer, D. W., 15
- Schmidt-Rohr, K., 213
- Schubert, U., 523
- Serosati, B., 243
- SEC. *See* Size exclusion chromatography
- Self-assembled monolayers (SAMs), 782
- Selmarten, D., 339
- Šelmic, S., 337
- Selvan, R. K., 247
- SEM. *See* Scanning electron microscopy
- Semiconductor hybrid nanoparticles
- biorecognition events, sensors of, 717–720
- Semiconductor nanocrystals (NCs), 649
- Semiconductor nanoparticle-enzyme hybrids systems, 715–717
- Semiconductor nanoparticles, electron transfer, 717
- Senkevich, J. J., 273
- Shaw, D. G., 427
- Shindo, T., 187
- Ship-in-the-bottle synthesis, of hybrid porous materials, 146
- Shirakawa, H., 293, 323

- Short-range-ordering, 479
- Silica and silsesquioxane, 7
- Silica-based porous materials, 135–141
- Silica biocomposite
- Coulombic interactions, 800
- Silica hydrogel biocomposites
- electric-shock-induced chemiluminescence time traces, 807
- Silica hydrogel layer, 770
- Silica sol–gel bio-encapsulation
- enzyme-doped liposomes for horseradish peroxidase (HRP), 806
 - liposome, 805
 - protein-silica interactions, 805
 - silica pores, 806
- limitation of, 793
- Silica sol–gel biosensor
- guest–host interactions
 - Coulombic interactions, 799–801
 - fluorophores, molecular structures of, 795
 - hydrogen bonding, 801–802
 - hydrophobic repulsion, 794
 - molecular templating, 802–805
- Silica sol–gel encapsulated SRB
- hydrogen bonding, 802
- Silicate glass structure
- densification of, 595
- Silica thin film pH sensors, 810
- Silicon solar cells, 322
- Siloxane-based class I hybrid materials,
- preparation, 510
- Siloxane-based class II hybrid materials,
- preparation, 510
 - condensation reactions, 515
 - grafting reaction, 511–512
 - hydrolysis reaction, 514–515
 - sol-gel reactions, 513–514
- Siloxane-based hybrids, advantages, 507
- Silver nanoparticles, electron transfer, 717
- Simulated body fluid (SBF)
- apatite nucleation in, 782
 - divinylsulfone, 776
 - ion concentrations of
 - human blood plasma, 769
- pH of, 769
- Single CdTe/PS microsphere, Raman spectra, 675
- Single-molecule polarization (*P*)
- measurements
 - schematic for, 796
- Single PS/CdTe microsphere, on Si substrate, 676
- Single-Pulse excitation, 219
- Single-walled carbon nanotubes (SWCNT), 245, 254, 720
- CNT-nanoelectrode ensembles (NEEs), 723
 - flavin-adenine-dinucleotide (FAD), 723
 - redox polymer hydrogel
 - schematic of, 722
- Sinha Ray S., 207
- SIP. *See* System-in-a-package
- Siwick, B. J., 260
- Size exclusion chromatography, 8
- Slooff, L. H., 350, 367
- Small-angle X-ray scattering, 9, 194
- Smith, D. M., 149
- Smith, M. E., 213
- Solar cells, 321–323
- characterization of, 327–329
- Sol–gel-electrochemical biosensing materials, 724
- Sol–gel materials
- micro-optics fabrication, 584
- Sol-gel method (SGM), in magnetic nanocomposites preparation, 459–460. *See also* Organic/inorganic magnetic nanocomposites, preparation methods for
- Sol-gel process
- hybrid nano materials
 - hybrimers, characteristics and applications, 590–591
 - hybrimers, photosensitivity mechanisms (see Hybrimers, photosensitivity mechanisms)
 - hybrimers, synthesis of, 587–590
 - iono-covalent bonds, 586
- hybrimers, synthesis of, 589
- inorganic–organic hybrid material
- hybrimer, 585
- on low temperature, 585
- materials design, advantages for, 587
- for metal oxidation and corrosion, 437
- for organic-inorganic hybrids, 437–440
- polycondensation of, 587
- molecular precursors, 586
- principles of, 132–135
- siloxane-based hybrid materials, 587
- Sol–gel thin films
- Oregon Green 514 (ORG) encapsulated, 799
- Solid-state dye-sensitized solar cell, 291, 305–308
- Solid-state nuclear magnetic resonance, 213
- Solid-state sol–gel glass
- liposomes, integrity of, 706

- Solvent evaporation method
for iron oxide formation, 465
in magnetic nanocomposites preparation,
460 (*see also* Organic/inorganic
magnetic nanocomposites,
preparation methods for)
- Soppera, O., 622
- SPE. *See* Single-Pulse excitation
- Spectral coding technology
DNA hybridization, 706
- Spectrum covering
SiO₂ microspheres, 689
- Spherical Bessel function, 660
- Spherical microcavities
photons confinement, semiconductor
nanocrystals
anti-stokes emission, 673
microsphere, light confinement, 659
photonic atoms, 659
quantum dots, 659
radiation-pressure-induced modes, 666
Raman spectrum of, 675
spherical microparticles, 658
- Spherical microcavity
Lorenz–Mie theory, 661
with PE/CdTe shell, 668
photonic atoms, 659
radiative forces on, 669
schematic of, 669
transverse magnetic (TM) modes, 660
WGM, polarization nature of, 663, 664
WGMs of, 675
WGMs orbital plane, 660
WGMs, tuning/modification of, 671
- Spherical microparticle, 670
- Spiess, H. W., 213
- Spin-echo abdomen magnetic resonance
images
of living rat, 732
- SPIO contrast agents, 730
- SPIOs. *See* Superparamagnetic iron oxide
nanocomposites
- SPR biosensors, 714
- SRG. *See* Surface relief gratings
- SRO. *See* Short-range-ordering
- ss-DSSC. *See* Solid-state dye-sensitized solar
cell
- SSNMR. *See* Solid-state nuclear magnetic
resonance
- SSQO. *See* Silica and silsesquioxane
- Stavroyiannis, S., 461
- Stein, A., 154
- Stejskal E. O., 213
- Storhoff, J. J., 714
- Sun, L. N., 547
- Supercapacitors, double-layer, 291, 293
- Superparamagnetic iron oxide
nanocomposites, 727
- Superparamagnetic nanoparticles
NMR contrast agents, 729
- Surface grafting of polymers onto nanoparticles,
methodologies, 89–91
- Surface plasmon resonance (SPR), 710
- Surface relief gratings, 618
azo-hybrimer films, 625
direct photo-fabrication of, 618
- Suzuki, N., 262
- SWNTs. *See* Single-walled carbon nanotubes
- System-in-a-package, 236
- T**
- Tada, T., 387
- Tanaka, H., 739
- Tang, C. W., 428
- t*-butylperoxy-2-methacryloyloxyethylcar-
bonate, 106
- TDI. *See* Toluene-2,4-diisocyanate
- Telecommunication networks, hybrid
nanocomposites in, 258–262. *See also* Hybrid organic-inorganic
nanocomposites
- TEM. *See* Transmission electron microscopy
- TEOS. *See* Tetraethoxysilane; Tetraethyl
orthosilicate
- TEOS-PDMS-derived organic–inorganic
hybrid nanocomposites, 177–178
- TE polarization, WGMs, 664
- Tetraethoxyortosilicate, 515
- Tetraethoxysilane, 11, 174
- Tetraethyl orthosilicate, 437, 439
- Tetraglycidyl diaminodiphenylmethane, 6
- Tetrahydrofuran (THF), 365
- Tetramethoxyortosilicate, 517
- Tetramethoxysilane, 11, 440
- Tetramethylammonium hydroxide, 421
- TFT. *See* Thin film transistor
- TGA. *See* Thermal gravimetry analysis
- TGDDM. *See* Tetraglycidyl
diaminodiphenylmethane
- Thermal gravimetry analysis, 10
- Thermally stimulated depolarization currents, 10
- Thick hybrimer film, on PET film, 633
- Thin film transistor, 257, 271, 425
- Thiolated oligonucleotides, 720
- Thorpe, A. N., 488

- Time resolved microwave conductivity, 343
 Time-resolved spectroscopy, in light-emitting hybrids, 533–534. *See also* Light-emitting hybrids
- TiO₂
 flat bilayers cells and, 349–354
 nanoparticles, 339–340
 structured porous, 358–360
- Titanium doped hybrimer, 611
- TLCT. *See* True liquid crystal templating
- TMAH. *See* Tetramethylammonium hydroxide
- TMOS. *See* Tetramethoxyortosilicate; Tetramethoxysilane
- TMOS-derived hydrogels
 firefly luciferase activity, comparison, 810
- Toluene-2,4-diisocyanate, 119
- TOPO. *See* Trioctylphosphineoxide
- Transforming growth factor (TGF), 739
- Transient absorption spectroscopy technique, 304
- Transistors. *See also* Hybrid organic-inorganic nanocomposites
 applications of, 232–233
 hybrid nanocomposites in, 253–258
- Transmission electron microscopy (TEM), 10, 484, 771
- α -Tricalcium phosphate (α -TCP), 767
 (3-aminopropyl)triethoxysilane, 56
 (3-isocyanatopropyl)triethoxysilane, 43
 (3-glycidylloxypropyl)trimethoxysilane, 33
- Trioctylphosphineoxide, 329–330
- TRMC. *See* Time resolved microwave conductivity
- True liquid crystal templating, 138
- TSA. *See* *p*-toluenesulfonic acid
- Tsang, W. M., 275
- TSDC. *See* Thermally stimulated depolarization currents
- Tseng, T. Y., 273
- Two-beam interference holography, 626
- Two-step acid-base polymerization, of TEOS, 17–20
- U**
- Uchida, M., 783
- ULSI. *See* Ultra large scale integrated devices; Ultra-large-scale integrated circuits
- Ultra-large-scale integrated circuits, 384
- Ultra large scale integrated devices, 232. *See also* Hybrid organic-inorganic nanocomposites
 hybrid nanocomposites in, 273–274
- Ultra-small angle scattering regime, 195
- Ultra small SuperParamagnetic Iron Oxides, 730
- USAXS. *See* Ultra-small angle scattering regime
- USPIO. *See* Ultra small SuperParamagnetic Iron Oxides
- UV illumination
 methacrylates, photo-polymerization of, 609
- UV-visible absorption spectrum, 619
- V**
- Vaia, R. A., 209
- Vallé, K., 520
- VanderHart, D. L., 222
- van der Waals interactions
 and H-bonding, 800
- Van Hal, P. A., 365
- Varlot, K., 207
- Venkatraman, A., 468, 474
- Vesicles, TEM images, 738
- Vibrating sample magnetometry, 481, 484
- Vinyl monomers, radical polymerizations of.
See also Polymers grafting onto nanoparticle surfaces, in solvent-free dry-system
 copolymer with pendant peroxycarbonate groups, grafting of, 105–106
 experimental methods of, 100–101
 grafting of copolymer onto silica nanoparticle surface, 101–102
 in ionic liquid
 advantage of, 113–114
 grafting of vinyl polymers onto carbon black, 114–118
 grafting of vinyl polymers onto silica nanoparticles, 118–125
 recycle of, 125–126
 peroxycarbonate groups grafting onto the silica nanoparticle, 106–107
 peroxycarbonate groups initiation of, 107
 postpolymerization of, 106
 silica-azo initiation of, 102–105
- Vinyl triethoxysilane, 440
- Vogt, B. D., 437
- Voronkov, M. G., 59
- VSM. *See* Vibrating sample magnetometry
- VTEOS. *See* Vinyl triethoxysilane
- W**
- Wada, S., 741
- Waldron, R. D., 474
- Wang, G. X., 249
- Wang, K. H., 210
- Wang, L., 367
- Wang, Y.-P., 89

- Water vapor transmission rate, 426
 measurement of, 436
WAXS. *See* Wide-angle X-ray scattering
Wen, J. Y., 23
WGM. *See* Whispering gallery modes
WGM microcavities, 673
WGM resonance, evolution of, 667
WGM resonances, 660
WGM spherical microcavities, 689
WGM structure
 Fourier analysis of spectra, 678
Whispering gallery modes, 650
White, M. S., 375
Wide-angle X-ray scattering, 10, 194
Wilkes, G. L., 48, 175, 177
Wilkes' morphological model, 32
Willson, C. G., 420
Wong, C. P., 239
Wong, E. W., 238
Wrighton, M. S., 539, 550
WVTR. *See* Water vapor transmission rate
- X**
Xenopus embryos, 710
XPS. *See* X-ray photoelectron spectroscopy
X-ray diffraction, 194, 195, 467
X-ray photoelectron spectroscopy, 365, 476, 479
X-ray reflectivity, 195
X-ray scattering techniques, in hybrid composites study, 194–199. *See also* Hybrid organic-inorganic nanocomposites
XRD. *See* X-ray diffraction
XRR. *See* X-ray reflectivity
Xue, S., 490
Xu, H. Y., 60
Xu, J., 335
- Y**
Yanagida, S., 306, 307
Yanagisawa, T., 137
Yang, D. K., 223
Yang, J., 245
Yang, S. H., 269
Yang, X., 238
Yao, Z. L., 255–256
Yogo, T., 465, 481
Yoshinaga, K., 89
Yu, S., 476
Yu, W., 623, 635
- Z**
Zachariassen's random network theory, 595
Zakhidov, A. A., 335
Zax, D. B., 223
Zeolites, 136–137. *See also* Silica-based porous materials
Zeolite surface
 gold nanoparticles, assembly of, 745
Zernike-polynomial surface model, 634
Zhao, J., 706
Ziolo, R. F., 484, 485, 487, 490, 498
Zirconium n-butoxide, 187
Zirconium(IV) n-propoxide, 508
Zirconium propoxide (ZPO), 608
ZnO nanoparticles, 340–341.
 See also Nanoparticle-polymer hybrid solar cells
 morphology of nc-ZnO, 347–348
 photophysics of, 341–343
 photovoltaic properties of nc-ZnO, 343–347
ZOL materials, 163–164. *See also* Bridged polysilsesquioxanes materials
ZPO. *See* Zirconium(IV) n-propoxide
 $\text{Zr}(\text{O}_n \text{C}_4 \text{H}_9)_4$. *See* Zirconium n-butoxide